

Print ISSN : 2395-1990

Online ISSN : 2394-4099

www.ijsrset.com



**International Conference on
Recent Trends In Mechanical
Engineering
(ICRTIME-2022)**

Organized By

Department of Mechanical Engineering,
Government Engineering College, K R Pet – 571426,
Mandya District, Karnataka, India

VOLUME 9, ISSUE 9, JANUARY-FEBRUARY-2022

**INTERNATIONAL JOURNAL OF SCIENTIFIC
RESEARCH IN SCIENCE,
ENGINEERING AND TECHNOLOGY**

Email : editor@ijsrset.com Website : <http://ijsrset.com>

International Conference on Recent Trends In Mechanical Engineering ICRTIME-2022

14th and 15th March, 2022

Organised by



Department of Mechanical Engineering, Government Engineering
College, K R Pet – 571426, Mandya District, Karnataka, India

In Association with



International Journal of Scientific Research in Science, Engineering and
Technology

Online ISSN : 2394-4099 | Print ISSN : 2395-1990

Volume 9, Issue 9, January-February-2022

Published By



website : www.technoscienceacademy.com

About the College

Our Institution Government Engineering College, K R Pet is started during the year 2007 by Karnataka state Government under the Department of Higher Education (Technical). The Institution is recognized and approved by All India Council for Technical Education, New Delhi and affiliated to Visvesvaraya Technological University, Belagavi, Karnataka. The following four under graduate programmes are available in the institution, namely, Civil, Mechanical, Electronics and Communication and Computer science and Engineering. In connection with research activities, institution is having Research and Development centers in all the departments with modern research facilities. Many research scholars are pursuing their Ph.D. and M.Sc. (Engg.) by research under the ambience of renowned state technological university, VTU, Belagavi

About the Department

Department of Mechanical Engineering was established in the year 2007 with an intake of 60. The department has highly qualified and experienced faculty specialized in the areas of Design, Thermal, Manufacturing and other areas of Mechanical Engineering. Department is well equipped with CAED, CIM, CAD/CAM, CAMA, Design, Heat and Mass transfer and Fluid Machines laboratories. Mechanical Engineering department is a recognized research centre of Visvesvaraya Technological University, Belagavi. It has achieved academic excellence by securing 7th University Rank during the university examination of 2017. Department has industry – interaction cell through which MOU has been initiated. The premier institute, GTTC is our institution –industry partner extending technological services to the Department.

About the conference

First International Conference on Recent Trends in Mechanical Engineering (ICRTIME 2022) is organized by the Department of Mechanical Engineering, Government Engineering College K R Pet. The aim of this conference is to create a platform to meet all the creative minds of under graduates, Post Graduates and Research scholars, experts, industrialists and other eminent personalities who may guide the budding researchers in the areas of Mechanical Engineering. Mainly the conference focuses on the following trends in Mechanical Engineering: i) Shape Memory Polymers , ii) Processing, characterization and testing of Engineering Materials , iii) Robotics and automation, iv) Computational fluid dynamics , v) Design in Mechanical Engineering , vi) Fluid

mechanics vii) Heat transfer and its applications, viii) Dimensional analysis, ix) Vibrations in Mechanical structures, x) ANN, DOE, CCD Techniques applied to Mechanical Engineering, xi) CAD/CAM/CIM/CNC/DNC and Machining of metals, welding technologies, 3D printing and xii) Production technologies and others related to Mechanical Engineering field.

Chief Patrons:

Shri. Kumar Naik, I.A.S

Additional Chief Secretary to Government, Higher Education Department

Shri. Pradeep P, I.A.S

Commissioner, Department of Collegiate and Technical Education, Government of Karnataka

Shri R Manjunath,

Director, Department of Technical Education, Government of Karnataka

Organizing chair:

Dr. K R Dinesh, Principal, GEC K R Pet

Conveners:

Dr. Lokesh T,

Head of the Department,
Mechanical Engineering, GEC K R Pet
Mobile No.: 9448620533

Dr. Praveen Kumar B S,

Mechanical Engineering, GEC, K R Pet
Mobile No.: 9611290235

Organizing secretary:

Dr. Rudresh B M

Mechanical Engineering, GEC, K R Pet

Co-ordinators:

Dr. Sathisha N S, HOD, Civil Engineering

Mr. Raveendra K, HOD, E and C Engineering

Dr. Hareesh K, HOD, CS and Engineering

Dr. Nagabhushan H M, Training and Placement Officer, GEC K R Pet

Mrs. Pushpavathi S M

Mechanical Engineering, GEC K R Pet

Mrs. Sowjanya N S

Mechanical Engineering, GEC K R Pet

Mr. Suhail Ahmed

Mechanical Engineering, GEC K R Pet

Technical Advisory Committee:

1. **Dr. Carl Santulli,** Universita Degli studi di Camerino school of Science and Technology, Camerino, Italy
2. **Dr. Chakravarthy P,** Department of Aerospace Engineering, IISST, Trivandrum,
3. **J.Paulo Davim,** Professor, University of Aveiro, Portugal
4. **Dr. Venkateshvarulu,** Principal Scientist, NAL, Bangalore
5. **Dr. G Pundarika,** Principal, GEC, Ramanagara
6. **Dr. K G Chandrashekar,** Principal, GSKSJTI, Bengaluru
7. **Dr. Sadashive Gowda,** Principal, VVCE, Mysuru
8. **Dr. Suresha Bheemappa,** Professor, NIE, Mysuru
9. **Dr. U S Mallikarjun,** Professor, MED, SIT, Tumkur
10. **Dr. Raghunandan K,** MIT, Manipal
11. **Dr. M S Govindgowda,** Director, ATME, Mysuru
12. **Dr. Madhu D,** Professor, MED, GEC, Ramanagar
13. **Dr. Rangswamy T,** Principal, GEC Mosalehosally
14. **Dr. D P Girish,** Professor, MED, GEC Mosalehosally
15. **Dr. K I Parashivamurthy,** Professor, MED, GEC, Chamarajnagar
16. **Dr. M M Benal,** Principal, GEC, Challakere
17. **Dr. Virupaxi Bagodi,** Principal, GEC, Talakal
18. **Dr. Seenappa,** Principal, GEC, Khushal Nagar
19. **Dr. Ganaraj,** Professor, PESCE, Mandya
20. **Dr. Y Vijay Kumar,** Principal, GMIT, Davanagere
21. **Dr. Narendra Babu B R,** Professor, VVIT, Mysuru
22. **Dr. Sreerama Reddy T V,** Professor, MED, BIT, Bangalore
23. **Dr. Ravi Kumar B N,** Professor, MED, BIT, Bangalore
24. **Dr. Suresh M R,** Professor, MSRUAS, Bangalore
25. **Dr. Lingesh B V,** MED, BIT, Bangalore

CONTENTS

Sr. No	Article/Paper	Page No
1	Effect of Nanoparticles and Jathropa Biofuel Diesel Fuel Blends on Common Rail Direct Injection (CRDI) Diesel Engine Chandan A M, Chethan S, Indresh C L	01-08
2	Optimization of Process Parameters of Hydrodynamic Journal Bearing: MOGA Approach Ravindra K G, Rudresh B M, Prasanna Kumar M K, Praveen Kumar M R	09-18
3	Optimization of Disc Brake Using Dual Calipers Shawn Hrithik, Sudeep Y A, Madhu H C, H S Shivashankar	19-26
4	Estimation and Comparison of Welding Performances in P-GMAW for SS 316 Material Using MRA and ANN Rudreshi Addamani, Gurupavan H R, Dr. Gayathri Devi S K, Mallikarjun Bhovi, Prathik Jain S	27-34
5	Literature Review of Load Balancing Approaches in Data Center Networks Nagaraju T A, Dr. Panduranga Rao M V, Dr. Revanna C R	35-41
6	Locomotive Aid for Paralysed People Leelavathi V V	42-71
7	Change Detection for Critical Infrastructure Protection System Rudrappa K M	72-79
8	Change Detection for Critical Infrastructure Protection System Rudrappa K M	80-87
9	Automation of Hydroponics Greenhouse Farming Using Arduino and IOT Veena Yadav S, Deepa V P	88-99
10	Design and Implementation of Heart Attack Detection and Medication Using Ad a fruit Flora Module Deepak H A, Tayab Mustaq Ahmed, Deepak R, Sharath S	100-110
11	Wireless Multifunctional Robot for Military Applications Nagabhushana H M, Rudrappa K M	111-120
12	Preparation and Mechanical Properties Evaluation of Aluminium-Alumina Metal Matrix Composite Mallikarjuna G B, E Basavaraj	121-127
13	Optimization of MRR for CNC Turning of Steel Surendra Kumar Saini	128-133
14	Synthesizing of Polymer Derived Ceramic Foams and Its Applications -	134-143

	A Review Sree Krishna M, Kiran B Gowda, H C Madhu	
15	Effect of NanoTiO₂ Particles on Microstructural and Wear Behaviour of AA8011 Metal Matrix Composites S. Viswanath, G. Bhanodaya Reddy	144-152
16	Aluminium Hybrid Metal Matrix Composites - A Review C R Vishwanath, M S Raviraj	153-159
17	Performance Evaluation of Thermo-Acoustic Refrigerator (TAR) with Different Stack Materials Sadanda Megeri, Irappa Hunagund, Pundarika G, Madhu D	160-174
18	Experimental Studies on Oscillating Heat Pipe using conventional and Nano Fluids Parashuram A K, K. Rama Narasimha, K. Gopalakrishna	175-184
19	Effect of Cooling Rate on Mechanical Properties of ASTM Grade Steel Devaraj M R, Mohan kumara K C, Niranjan Kumar V S, Joel Hemanth	185-194
20	Stiffness Variation Study of Fingers in Finger Seal Rajesh P, J Sharana Basavaraja, V Arun Kumar	195-202
21	Plain Points Picking (PPP) Algorithm - A New Method of Slicing In 3D Printing Ashwin N, Anoop N, Dr. Raviraj M S, Dr. Muniraju M	203-208
22	Microstructure and Mechanical Behaviour of Chromium Oxide reinforced LM26Based Metal Matrix Composites T V Nagaraja, Dr. Ravindra Sagar	209-219
23	Effect of Injecting Bio-Diesel from the Used Cooking Oil and Graphene Nano Platelets on Performance, Combustion and Emission Characteristics of Diesel Engine Nagaprasad K S, Rajesh Kumar Kodi, Prakash Raju S, Madhu. D	220-229
24	Variation of Tensile, Hardness, Impact and Natural Frequency in Jute/E-Glass Epoxy Composite For Varying Fiber Loading and Addition of Shear Thickening Fluid Dr. Abhishek M R, Dr. Suresh P M, Dr. Mruthunjaya M, Dr. Balaji B	230-241
25	Finite Element Analysis of Hybrid Biodegradable Composite Praveenkumara B M, Vignesh Kumar R	242-250
26	Influence of Nano graphite based Vegetable oils as Cutting Fluids for Mild Steel Drilling Viraja Deshpande, P. N. Jyothi	251-264
27	Design of Reconfigurable Manufacturing Systems : A Review N Swamy, Dr. U. M. Daivagna, Dr. A Thimmana Gouda, Dr. Veerabhadrappe Algur	265-272
28	Performance of Different Refrigerants in a Four-Wheeler Automobile	273-286

	AC Condenser H. M. Gurudatt, G. S. V. L. Narasimham, B. Sadashive Gowda	
29	Influence of Cerium Oxide on Wear Characteristics of GFRP Composites Vithal Rao Chavan, Dr. K. R. Dinesh, Dr. Veerabhadrappe Algur, Dr. K. Veeresh	287-293
30	Investigations on Effect of Fill Ratio and Heat Input on Thermal Performance in Oscillating Heat Pipe using Acetone Working Fluid M. Prashanth, Santhosh Gotaganaki	294-300
31	Intelligent Autonomous Braking System for Accident Prevention Prashanth K P, Amruth K U, Chandru M K, Sanman S, Yashaswini T C	301-309
32	Influence of Deccan Hemp Biodiesel over the Performance and Emissions of a CI Engine N. Srujana, G. Bhanodaya Reddy, J Subramanyam	310-317
33	Nursery Monitoring System using IoT Sanjay H S, Hemanth U, Vaidesh B, Harisha V R, Lakshmi D L, Goutham V	318-322
34	A Review on Microstrip Patch Antennas Imran Khan, Vaishnavi H T, Kiran K B, Yuktha M, Kavya M R	323-335
35	Minimizing of Latency in Cognitive Radio Based IoT Systems for SDR Applications Prathibha. S	336-349
36	Touch less Touch Screen Using Gesture Processing Komala K V, Deepa V P	350-359
37	Face Recognition Based Attendance Marking System Prathibha S	360-375
38	Study on Paper Making Process Using Agricultural Waste as Raw Material Vinay J S, Vinay K R, Ekanthappa, H S Shivashankar	376-384
39	Smart Multipurpose Surveillance Robot Deepak H A, Deepak R, Sharath S, Sowmyashree	385-392
40	The Effect of Heat Treatment Process on the Microstructure and Micro Hardness of AlSi10Mg Alloy Samples Fabricated by Additive Manufacturing Manjunath Prasad R, U N Kempaiah, Santhosh N	393-400
41	IOT Based Industrial Pollution Monitoring and Controlling System Rajani, Lakshmi D L, Hamsashree M K, Shama Firdose U	401-407
42	Effect of Graphene Loading on The Thermal Behaviour of Glass Epoxy Nano Composites M. S. Aswathnarayan, Munirju. M, Reddappa H N, B M. Rudresh	408-415

43	Effect of Sliding Pressure on Wear Behaviour of Polypropylene Natural Composites Mahesha A, Rudresh B M, Reddappa H N, Madhu D	416-427
44	3D Design Model of Miniature Sugarcane Harvesting Machine Irappa Hunagund, Sadananda Megeri, Deepak S Gasthi, Kiran R P, Bharath B M	428-445
45	Study, Optimization of Cutting Parameters of Non-Ferrous Metal by Turning Operation in Lathe Machine Nagesha N, B S Praveen Kumar	446-455
46	Effect of Nano and Hybrid Micro fillers on Two Body abrasive wear Behaviour of Polyamide 66 and Polyamide 6 (PA66/PA6) Blend Based Composites Umesh G L, Rudresh B M, Krishna Prasad N J, Madhu D	456-467
47	Determination of Optimum Pressure Loss Coefficient and Flow Distribution at Unsymmetrical Pipe Trifurcation Using Experimental and Numerical Technique Basappa Meti, Nagaraj Sitaram	468-476
48	Investigation of Various Mg Alloy and Nano Composite for Enhancing Mechanical Properties, Corrosion Protection for Light Weight Component for The Application of Automobile Industry Amit Tiwari, Dr. Neeraj Kumar	477-497
49	An Experimental Study on Mechanical Characterization of Fiber Based Hybrid Polymer Composites Pradeepkumar G R, Paraveej Shirahatti, H K Shivanand, Sadashiva M	498-507
50	Tribological Studies of Structural Steels - A comprehensive Study Hemaraju, Santosh Kumar TC, Sharath N, Sudesha Shetty M	508-515
51	Energy Efficient Automated Hydraulic Power Unit Nikhil Kumar K, Paraveej Shirahatti, S. Shiva Prakash, Gujjala Anil Babu, H. K. Shivanand	516-532
52	Effect of Heat Flux on Free Convection Heat Transfer in Porous Trapezoidal Enclosures Vijaya Kumara V M, Aswatha, Hemanth Kumar C B	533-541
53	A Review on Mechanical and Tribological Properties of Natural Fiber Reinforced Polymer Composites Prashanth N, Dr. Ranganatha Swamy L, Dr. Hemaraju	542-556
54	Mechanical Characterization of Coconut Spathe and Bast Papaya Fiber Reinforced Epoxy Polymer Composite Pradeepkumar G R, Shiva Prakash S, Paraveej Shirahatti, Gujjala Anil Babu, Sampathkumar R	557-574
55	The Effect of Heat Treatment Process on the Microstructure and Micro	575-583

	Hardness of AlSi10Mg Alloy Samples Fabricated by Additive Manufacturing Manjunath Prasad R, U N Kempaiah, Santhosh N	
56	Effect of Heat Treatment on Dry Sliding Wear Behaviour of AA6061-Gr Metal Matrix Composites by Taguchi Techniques Lokesh T, Rudresh B M	584-593
57	Study of Corrosion of Aluminium 6061 Based Metal Matrix Composite Sunitha V, Girisha H N, Madhu D	594-600
58	Study of Mechanical Properties of Aluminium 7075 Alloy Reinforced with Cenosphere and E-Glass Fibres Sunitha. V, Girisha H N, Dr. Girish D P, Suhael Ahmed S	601-611
59	Numerical Study of Heat Flux Variation Around A Re-Entry Module at High Altitude K. S. Santhosh, Siddharth G	612-623
60	Effect of Crosshead Speed on Mechanical Behavior of Bagasse Reinforced Polymer Composites Sandesh S Nayak, Muniraju M, Rudresh B M	624-630
61	Green Synthesis of Silver Nanoparticles Using Leaf Extract of Hyptis Capitata and Evaluation of their Catalytic Efficiency Revathy R, Jebin Joseph, Sajini T, Cyril Augustine, Beena Mathew	631-636
62	Propulsion Option for Deep Space Travel Lakshmi Prasad L, Amrutha. G, Bharath B H, Divya H S, Kousik S	637-651
63	Detection of Cyber Threats Using Machine Learning Naveen T. H, Sudhakar K. N	652-656
64	Review of Cloud Computing Security on Amazon Web Service Monika B A, Jeethendra S R, Prof. Annaiah H	657-663
65	Review on RDPC : Secure Cloud Storage with Duplication Technique Ashwathnarayan, Rachitha M, Prof. Annaiah H	664-665
66	A Smart Stick : Senior Citizen's Friend Dr. Shivashankara S	666-678
67	Electrical Conductivity (dS/m) Study for Agricultural Benefits after Optimization of Bio-Methanated High TDS Spent wash from Distilleries Lalitha D, Sathish Ns, Ramesh N, Manju B	679-681
68	Mechanical Characterization of Aluminium Based Hybrid Composites Reinforced with Boron Carbide and Alumina Paraveej Shirahatti, H. K Shivanand, Ranjth R Hombal, Ajeet Shivaji Mankani, Sadashiva M	682-698
69	A Study on Parametric Optimization of Co2 Welding Process by Taguchi Method on Structural Steel Plates Praveen Math, Dr. B S Praveen Kumar	699-708

70	Design and Development of Regeneration of Electricity Ranjith R Hombal, Pavan Kumar D, Paraveej Shirahatti, Kiran G K, H. K. Shivanand	709-709
71	Influence of Server Density in Racks on Data Centre Thermal Management : A Numerical Study Chethana G D, Dr. Sadashive Gowda B	710-718
72	NVH Analysis of Acoustic Materials by Using Aluminium, Steel and Carbon Fiber Vijaykumar, Dr. Vinay V. Kuppast	719-727
73	Enhancing Surface Layer Properties of Al6061-B4C Composite by Controlled Shot Peening Dr. Suresh Kumar. S, Rathan Kumar K	728-736
74	Friction Reduction Using Electrical Water Pump in I C Gasoline Engine Danesh Warad, A P Singh	737-745
75	Anti-Friction Coatings for I C Engine Piston Danesh Warad, A P Singh	746-755
76	Lowering Friction Torque Using AFC on Engine Bearings Danesh Warad, A P Singh	756-765
77	Profile Generation of a Subsonic Aircraft Wing with NACA 64-215 at the Root and NACA 64-210 at the Tip Nataraj Kuntoji, Vinay V Kuppast	766-779
78	Mechanical Characterization of Micro B4C Particles Reinforced Al6061 Alloy Metal Composites Murali Mohan R, Madeva Nagaral	780-789
79	Study on Effect of Process Parameters on Kerf Width using Wire Electrical Discharge Machining of Cu-Al-Mn Shape Memory Alloys N Praveen, U S Mallik, A. G. Shivasiddaramaiah	790-797
80	Dielectric Properties of Lanthanum Doped Nano Copper Ferrite Chikkappa Udagani	798-806
81	Spatial Variation and Fluoride Contamination of Drinking Water using GIS in the Bagepallitaluk of Chikkaballapura District, Karnataka, India Sridhara M K, Sadashivaiah C, Kiran D A	807-813
82	WSN Framework for Rose Greenhouse Monitoring Devika	814-822
83	A survey on Performance Analysis and Comparison among Different Task Scheduling Algorithms in Cloud Computing Sakshi T, Rachana S B, Prof. Annaiah H	823-828
84	Locomotive Aid for Paralysed People Leelavathi V V	829-853
85	Development of a 2D-DWT based Image Compression and	854-862

	Decompression Algorithm Nandeesh R, Shanmugam M	
86	Statistical Assessment of Water Quality Parameters for Bellandur Lake Water, Bangalore Urban Area Ramesh. N	863-869
87	P3O4 Contents Present in The Soil, After Spraying the Distillery Spent Wash Obtained from Optimized Bio Methanation Process Lalitha D, Ramesh N, Sathish Ns, Manju B	870-873
88	K2O Contents Present in The Soil, After Spraying the Distillery Spent Wash Obtained from Optimized Biomethanation Process Lalitha D, Manju B, Ramesh N, Sathish Ns	874-877
89	Fabrication and Characterization of Hybrid Fibers Thermoplastic Blend Composites Lingesh B V, B M Rudresh	878-887
90	Effect of Aerobic Exercises on Selected Motor Fitness Variables Among School Level Soccer Players Dr. Kanthraj S	888-892
91	Effect of Muscle Relaxation Training on Competitive Anxiety of School Level Boys Foot Ball Players Srinivasa Murthy	893-897



Effect of Nanoparticles and Jathropa Biofuel Diesel Fuel Blends on Common Rail Direct Injection (CRDI) Diesel Engine

Chandan A M¹, Chethan S¹, Indresh C L¹

Richa Sharma, Prof. Pooja Thakre

Department of Mechanical Engineering, Malnad Collage of Engineering, Hassan -573202, Karnataka, India

ABSTRACT

In this study, the components of Ricinus communis plant such as leaves and seeds are effectively utilized as a green source for the synthesis of copper oxide nanoparticles (CuO) and production of biodiesel, respectively. The Copper oxide nanoparticles were successfully utilized for the biodiesel synthesis using Ricinus communis oil as feedstock by varying the reaction parameters.

Biofuels are receiving tremendous attention worldwide as renewable and alternative source of energy production. Biofuels can be produced with the help of various materials through different extraction methods and conversion processes. The combustion of bio fuel takes place completely in engine and increase in power with increase in load.

Keywords: Ricinus communis, synthesis, biodiesel, tremendous.

I. INTRODUCTION

Biofuels are a class of renewable energy derived from living materials. The most common biofuels are corn ethanol, biodiesel, and biogas from organic by-products. Energy from renewable resources puts less strain on the limited supply of fossil fuels, which are considered non-renewable resources. The use of biofuel in Common Rail Direct Injection (CRDI), it can direct injection of the fuel into the cylinders of a diesel engine via a single, common line, called the common rail which is connected to all the fuel injectors.

II. METHODOLOGY

The basic methods used for the successful operation of the above concept is initially nanoparticles (mg) are obtained by synthesizing novel nanoparticles like green synthesis from leaves and flowers, organic synthesis. And then trans esterification flash, fire and pour point is known. Further biofuel – fuel blends are prepared process is done by adding these nanoparticles to bio fuel (ml). By this many basic fuel properties like viscosity, density, flash, fire and pour point is known. And now performance study of CRDI engine is done and the final method is emission analysis of the engine.

III. MATERIAL SELECTION

The material used are Ricinus communis leaves, chemical such as Cupric nitrate $\text{Cu}(\text{NO}_3)_2$

Preparation of Ricinus communis leaves extract:

Ricinus communis leaves were washed with water and allowed to shade dry. And they were crushed to make coarse/fine powder. The resultant 50 gram of powder and 1:4 proportion of water was placed in 500 ml flask. The mixture was heated about 3 hours at 700 c. The resultant extract was filtered and the filtrate was again heated at 800 c for 3 hours. Finally the water extract of Ricinus communis leaves was obtained.

Preparation of COPPER OXIDE (CuO) Nanoparticles:

COPPER OXIDE (CuO) Nanoparticle catalyst was prepared by solution combustion synthesis. Initially 5 ml, 10 ml and 15 ml of plant extract and 1gram of cupric nitrate was added to each extract and homogenized for 10 minute to make uniform solution with the help of stirrer. The resulting solutions was kept in a muffle furnace at 5000 c for 15 minute. then the obtained Copper oxide Nanoparticles were kept in airtight vials for further characterizations and applications. Ricinus communis leaves + Cupric nitrate $\text{Cu}(\text{NO}_3)_2 \rightarrow$ Copper oxide (CuO) + $\text{N}_2\uparrow$ + $\text{O}_2\uparrow$



Fig1. Shadow Dry crushing



Fig 2. 1st stage

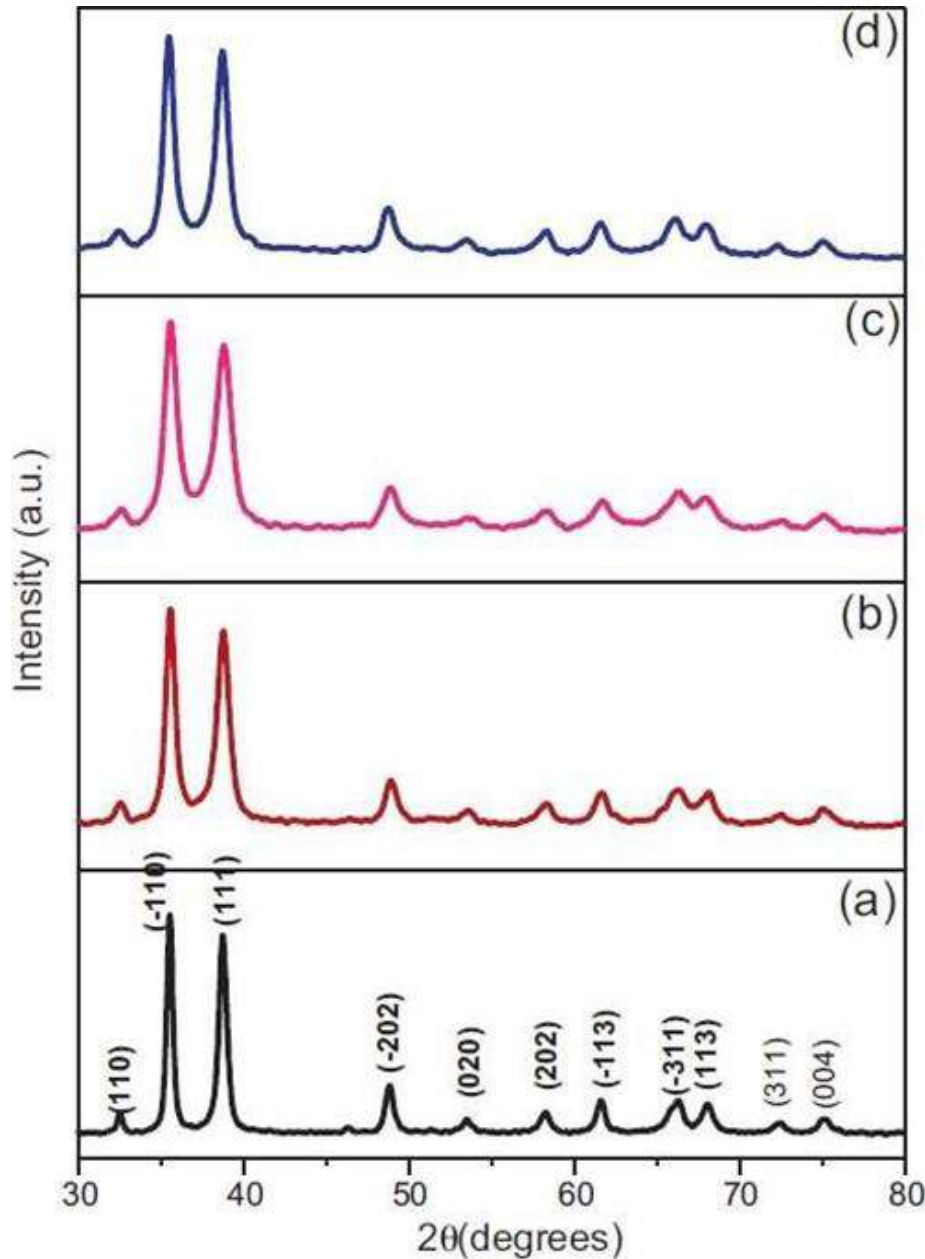


Fig 3. Fine powdered of Ricinus leaves



Fig 4. Water extract Communis

IV. RESULTS OF COPPER OXIDE NANOPARTICLES

X-RAY DIFFRACTION(XRD) Patterns of Copper oxide Nanoparticles:

XRD patterns of copper oxide nanoparticles prepared at different concentrations of plant extract 5ml, (b) 10ml, (c) 15ml and (d) 20 ml

Summary:

When the intensity of the nanoparticle increases with the increase in moment of the nanoparticle in degrees for various plant extract as shown in the above figure. The intensity of the nanoparticle is maximum when the moment of the nanoparticle moment is between 35 to 40 degrees.

4.1 TRANSESTERIFICATION USING SODIUM HYDROXIDE (NAOH) NANOPARTICLE:

Transesterification is done by heating 1 liter of Raw jathropa fuel at 60 degree Celsius using Magnetic stirrer as shown in figure (a), After heating the raw fuel to 60 degree Celsius, Titration should be done using 10.1 gram of heated Raw fuel, added 2 drop of indicator (Phenolphthalein) and 0.4 gram of sodium hydroxide (NAOH) solution dissolved in 50 ml of water and to get the brick color shown in figure.

The formula used in titration and to find the 1st index and the amount of nanoparticles to be used is given by,
 FFA: $28.2 \times 0.1 \times \text{Burette reading} / \text{weight of sample taken in gram}$

Where,

FFA: Free Fatty Acid 28.2: FFA Molar mass 0.1: FFA Constant

Calculation:

$$\text{FFA}: 28.1 \times 0.1 \times 29 / 10.1$$

$$\text{FFA} = 8.2 \text{ grams.}$$

After titration, found that it is a 2 index process.

In the 1 index, added 8.2 grams of H₂SO₄ (the amount of H₂SO₄ is obtained by titration) and 150 ml of methanol and heated for 2 hours at 60 degree Celsius, after heating poured the fuel into separation funnel and kept 8 hours for settling of glycerin and catalyst.

After 8 hours, separated the settled glycerin and catalyst then went for 2 index, again heated the bio fuel to 60 degree Celsius and took a sample of 10.1 gram of heated bio fuel, added 2 drop of indicator and 0.4 gram of NAOH solution dissolved in 50 ml of water and to get the brick color.

The formula used in titration and to find the 2nd index and the amount of nanoparticles to be used is given by,
 FFA: $28.2 \times 0.1 \times \text{Burette reading} / \text{weight of sample taken in gram} + 3.5$

Where,

FFA: Free Fatty Acid. 28.2: FFA Molar mass. 0.1: FFA Constant.

Calculation:

$$\text{FFA} = 28.2 \times 0.1 \times 5.3 / 10.1 + 3.5$$

$$\text{FFA} = 5 \text{ grams.}$$

After titration added 5 grams of sodium hydroxide (NAOH) (the amount of NAOH is obtained by titration) and 150 ml of methanol and heated for 2 hours and poured into separation funnel and kept 8 hours for settling of glycerin and catalyst as shown in figure (c). Can see the glycerin and catalyst settled in the bottom of the funnel shown in figure (d). After separating glycerin and catalyst got the Bio fuel.

The next process was washing and drying. Washed the bio fuel using hot water at 60 degree or above, for 10 times, at last stage got pure bio fuel, which is settled in top of the funnel as shown in figure.

After washing, the drying process is done to remove the glycerin and water content in the fuel, where the bio fuel is heated for 135 to 140 degree Celsius and kept for cooling.

After cooling, Measured the pure bio fuel using measuring funnel and got 800 ml of pure bio fuel using 1000 ml of raw fuel shown in figure.

After that blended the bio fuel into the diesel in the ratio of,

- B10 → 900ml of diesel and 100ml of bio fuel.
- B20 → 800ml of diesel and 200ml of bio fuel.
- B100 → Pure bio fuel.

We converted bio fuel into Bio diesel.



V. RESULT AND DISCUSSION

The experimental results obtained from the tests carried out on engine performance and combustion characteristics are presented in this graph. The results which obtained are significantly comparable to pure diesel.

(a) BRAKE THERMAL EFFICIENCY

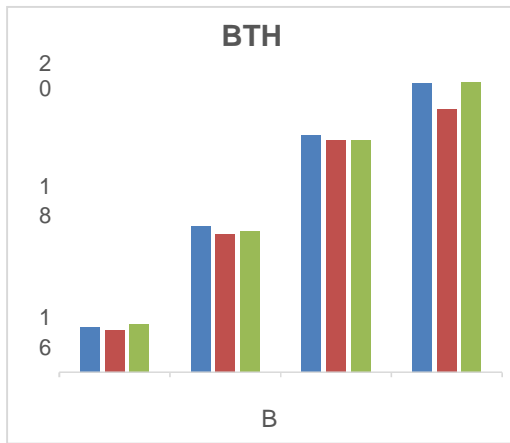


Figure: Variation of brake thermal efficiency with respect to brake power.

Where,

Blue = Diesel Red = B10

Green= B20

The above figure shows the Brake thermal efficiency is increasing with increasing brake power for all blends of biodiesel and diesel.

The combustion of bio fuel takes place completely in engine and increase in power with increase in load. It may be because of the presence of oxygen in biodiesel which enhance the combustion as compared to diesel and biodiesel is more lubricant than diesel that provides additional lubrication.

(b) SPECIFIC FUEL CONSUMPTION

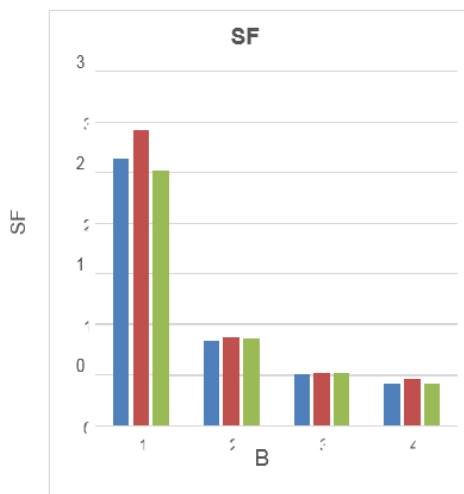


Figure: Variation of specific fuel consumption with respect to brake power.

The above figure shows the specific fuel consumption with respect brake power. When using blends, biodiesel fuel is expected to decrease as compared to the consumption of diesel fuel. Specific fuel consumption (SFC) decreased sharply with increase in brake power for all fuel sample.

(c) MECHANICAL EFFICIENCY:

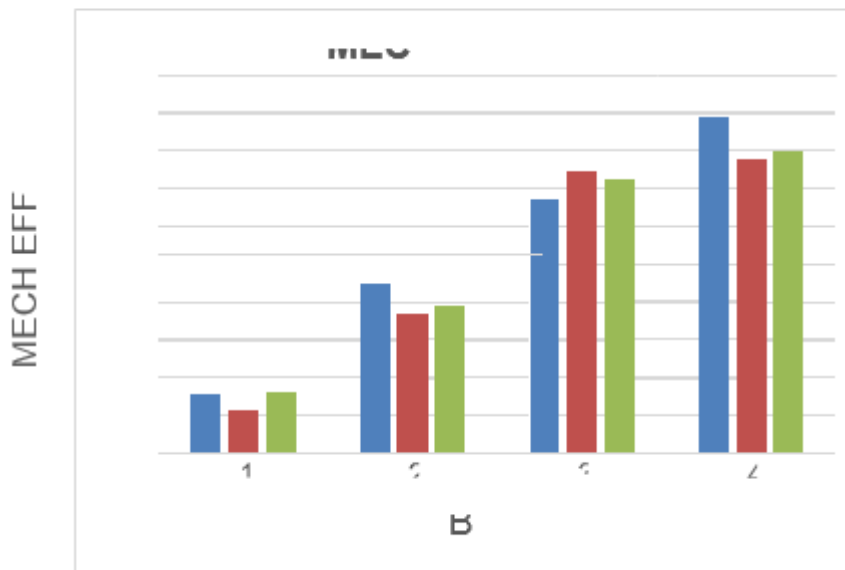


Figure: Variation of Mechanical efficiency with respect to brake power.

The variation of mechanical efficiency with brake power for pure diesel and blends are shown in figure. The mechanical efficiency of pure diesel is slightly higher than the blend fuel. In this case the diesel and are almost nearer to B10 and B20 each other in BP. From the graph it is evident that as the percentage of biodiesel increases in diesel the mechanical efficiency goes on decreasing. This happens due to lower calorific value of biodiesel compared to diesel.

VI. CONCLUSION

Experiments were conducted with different blends of mixed biodiesel in CI engine for various brake power and the results as follows:

- Break thermal efficiency is same for blends and pure diesel
- Fuel consumption reduces with increase in brake power for biofuel than pure diesel.
- Mechanical efficiency decreases with increasing the brake power specially in full load condition.
- Unburnt Hydrocarbon (HU) % reduces B10 and B20 comparatively Diesel.

VII. REFERENCES

- [1]. Production of Biodiesel (B100) from JATROPHA Oil Using Sodium Hydroxide as Catalyst– Joshua Folaranmi.
- [2]. A Systematic evaluation of the Mechanical Extraction of JATROPHA CURCAS L. oil for biofuels production– Andrea V. Yate _ et.al.

- [3]. Effect of Sr@ZnO nanoparticles and RICINUS COMMUNIS biofuel-diesel fuel blends on modified CRDI diesel engine characteristics— Manzoore Elahi M.Soudagar _ et.al.
- [4]. Green synthesis of colloidal silver nanoparticles by sonochemical method—M Darroudi, A.Zak, M. R. Muhamad, N. M.Huang, and M. Hakimi, Mater Lette 66 (2012).
- [5]. Larvicidal activity, phytochemical composition, and antioxidant properties of different parts of five populations of Ricinus communis from L.Ghnimi Wafa, Industrial Crops and Products 56 (2014).



Optimization of Process Parameters of Hydrodynamic Journal Bearing: MOGA Approach

Ravindra K G^{1*}, Rudresh B M², Prasanna Kumar M K¹, Praveen Kumar M R¹

¹Department of Mechanical Engineering, Bangalore Institute of Technology, Bangalore-560004, Karnataka, India

²Department of Mechanical Engineering, Government Engineering College, K R Pet-571426, Karnataka, India

ABSTRACT

Optimization of hydrodynamic journal bearing is most required because of their usage supports machineries which rotate at high speeds such as compressors and turbines. It is difficult to optimize the bearing parameters using conventional algorithms as they require non-linear optimization with constraints. Genetic Algorithms (GAs) are the class of algorithms and it is a general purpose algorithm that could achieve the process parameters with all the available constraints. In this work, the geometric parameters and their range such as variance ratio (0 - 1), journal radius (25 - 65), radial clearance (30 - 60), dynamic viscosity (0.026 - 0.046), surface pattern parameters (1/6) and surface roughness parameter (15 - 30) were used as an input for training the ANN model and to evaluate the performance that would result in optimal value of minimum fluid film thickness, frictional torque and critical journal mass of journal bearing. It has been carried out for the bearings having longitudinal type of roughness patterns using the Multi Objective Genetic algorithm (MOGA) approach. Using Pareto optimal concept, the optimization of design parameters has been evaluated. The designed model using MOGA Approach shows a satisfying response compared to experimented data for the roughness pattern.

Keywords: MOGA, Hydrodynamic bearing, ANN, Genetic Algorithm, Film thickness

I. INTRODUCTION

Hydrodynamic journal bearing shows a satisfactory performance for functioning of pumps, compressors etc. It operates continuously at high speed and heavy loads [1]. They have good load-carrying capacity, excellent stability, durability and low coefficient of friction. Journal bearings are of many designs for compensating varying load requirements such as speeds, cost with many dynamic properties. The journal bearings are more critical to any rotary operation from the point of view of durability and performance. Hence, the techniques for the development of engine bearing analysis have been received attention over the years. The design of such bearings rely upon thin-film hydrodynamic lubrication theory, which shown a separation of two surfaces in relative motion. In many of the real applications, the journal bearing designers face more problem for the

simultaneous optimization of several objectives together. Those of the objectives are often incomparable and conflicting. Bearing parameters optimization is of non-linear optimization along with constraints [2], By conventional optimization algorithms it is difficult to solve this problem because of problems of convergence speed or accuracy. In increasing demand of initial and running costs for the bearings, to withstand the competition, so prompted engineers to apply optimization methods in the design of bearings. Hashimoto.et.al [3] studied the journal bearings optimization models with hydrodynamic case and their applications to elliptical bearing design for machineries which rotating at very high speeds. The prime objective is to finding out the values of the variables that lead to an optimal value of the function, satisfying all the constraints.

The problem in a multi-objective optimization can be mathematically represented as shown in Equation 1.

$$\text{optimize } f(r) = \begin{bmatrix} f_1(r) \\ f_2(r) \\ \cdot \\ \cdot \\ f_n(r) \end{bmatrix} \text{ subjected to } c(r) \geq 0; n \geq 2 \quad \text{----- (1)}$$

Here, r is the parameter vector, $f(r)$ is the objective vector and $c(r)$ is the constraint vector.

The concept of genetic algorithms is new in the field of bearing analysis design, and a limited work has been carried out in rotor-bearing system using genetic algorithms. Artificial Neural Network (ANN) model have been developed which predicts the value of various stability characteristics in journal bearing design, based on geometric and operating conditions. A genetic algorithm was then applied to the trained ANN model to determine the geometric parameters that results in a nearest value.

II. METHODOLOGY

The following methodology has been adopted for the development of the concepts of ANN and MOGA Approach.

2.1 Optimization of Journal Bearing

By using the concepts of Artificial Neural Networks (ANNs) and Genetic Algorithms (GAs), The following steps must be carefully designed in evaluating the performance of the designed parameters. They may be: 1. Selection of design variables 2. Hydrodynamic Simulation 3. Use of Artificial Neural networks and 4. Optimization of the process.

2.1.1 Design of ANN for Journal Bearing Optimization

The typical model of an artificial neuron along with a multi layered neural network is shown in Figure.1. The signal flow in the direction of inputs $x_1, x_2, x_3, \dots, x_n$ were considered as a single directional shown by arrows as a signal output (O). The output O is shown as per Equation 2.

$$O = f(\text{net}) = f\left(\sum_{j=1}^n w_j x_j\right) \text{----- (2)}$$

Where w_j is weighted vector and the function $f(\text{net})$ could refer as a transfer function or activation function. The term 'net' is defined as the product of scalar of vectors of the weights and inputs (Equation 3).

$$\text{net} = w^T x = w_1 x_1 + \dots + w_n x_n \text{----- (3)}$$

Where T is transpose of a matrix, output O in simple form is stated as (Equation 4),

$$O = f(\text{net}) = \begin{cases} 1 & \text{if } w^T x \geq \theta \\ 0 & \text{otherwise} \end{cases} \text{----- (4)}$$

Where θ is the level of thresholds.

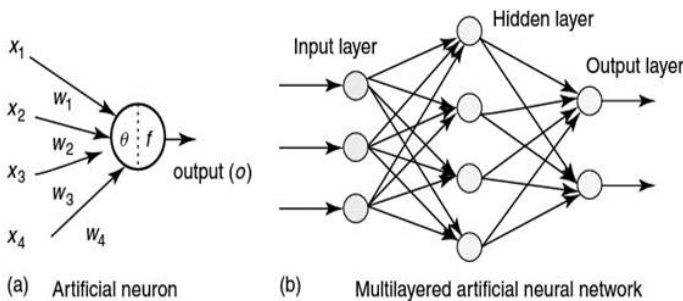


Figure. 1. Schematic of an artificial neuron and a multi layered artificial neural network

2.1.2 Genetic Algorithm

Genetic algorithms in brief are used as a class of algorithms in search spaces that could be of discontinuous and nonlinear. As compared to other optimization techniques, they do not rely on local derivatives for guiding the search process.

2.1.3 Objective functions

These are the functions which could significantly specify the quantities to be maximized or minimized under the prescribed level of constraints. In the design of hydrodynamic journal bearing, three important objective functions used are mainly minimum oil film thickness (h_{min}), critical journal mass (\overline{M}_{CJ}) and frictional torque on journal surface (\overline{T}_{FJ}). The objective functions for Multi Objective Genetic Algorithm (MOGA) connected to testing model of ANN are

$f(1) = \text{simulation}(\text{net1}, r)$

$f(2) = -\text{simulation}(\text{net2}, r)$

$f(3) = -\text{simulation}(\text{net3}, r)$

Where 'r' is the design variable vector and net1, net2 and net3 are the networks for the target vectors of h_{min} , \overline{M}_{CJ} and \overline{T}_{FJ} respectively.

III. RESULTS AND DISCUSSION

The MOFT (h_{min}), frictional torque on journal surface (\overline{T}_{FJ}) and critical journal mass (\overline{M}_{CJ}) for a journal bearing is computed in the hydrodynamic model for the following fixed geometric parameters of the bearing:

Speed of the bearing = 3000 rpm

Maximum load on bearing = 15000 N

Aspect ratio, $\lambda = L/D = 1.0$

Power law index, $n = 1.0$

Supply pressure, $P_s = 0.5 \text{ N/mm}^2$

3.1 Pareto Optimal Concept

In the multi objective optimization, a vector $x=[x_1,x_2,\dots,x_k]$ are considered as a more optimal than a vector $y=[y_1,y_2,\dots,y_k]$ if x dominated y. The set of Pareto optimal called as a non-dominated solutions forms a Pareto surface P (Figure 2) maximization of required objective function can be obtained by assigning negative value so that the minimization of negative objective function is same as its maximization [2, 5]. Hence, maximization of objective function can be obtained from these entire Pareto front plots by neglecting its negative values.

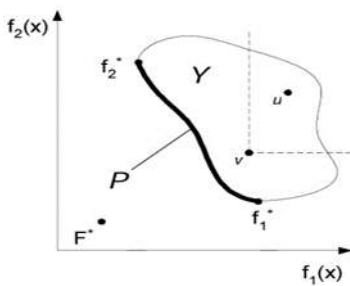


Figure 2: Pareto optimal front

3.2 Genetic Algorithm Implementation

Table 1: The options set up for the MOGA approach [6, 7]

Sl. No.	Options	Specification
1	Population type	Double vector
2	Population size	15*number of variables
3	Selection function	Tournament
4	Tournament size	2
5	Crossover fraction	0.8
6	Mutation function	Constraint dependent
7	Crossover function	Heuristic
8	Crossover ratio	1.0

9	Migration direction	Forward
10	Migration fraction	0.2
11	Migration Interval	20
12	Distance measure function	@distance crowding
13	Pareto front population fraction	0.35
14	Maximum generation	200*number of variables
15	Time limit	Infinity
16	Fitness limit	-Infinity
17	Stall generations	100
18	Function tolerance	1e-4
19	Plot function	Pareto front
20	Evaluate fitness function	In serial

3.3 Optimization Results

The optimization results of variance ratio (V_{rj}), journal radius (R_j), radial clearance (c) and dynamic viscosity (μ) for the maximization of MOFT (h_{min}) and critical journal mass (\bar{M}_{CJ}) and minimization of friction torque (\bar{T}_{FJ}) are presented in the form of Pareto front in Figures 3 and 4. These results are also tabulated in Table 2 and Table 3

3.1.1 Optimization results for longitudinal roughness patterns

Table 2: Pareto optimal designs for maximization of \bar{h}_{min} and \bar{M}_{CJ} for bearing with longitudinal roughness pattern ($\gamma=6$)

Design options	\bar{h}_{min}	\bar{M}_{CJ}	V_{rj}	R_j (mm)	c (μm)	μ (Pas)	Λ
1	0.99925	75.488	0.85431	50.995	33.469	0.042122	16.7345
2	0.99193	84.948	0.99763	48.553	31.162	0.042143	15.581
3	0.9829	94.819	0.99264	46.276	31.668	0.042664	15.834
4	0.98158	98.117	0.99523	45.587	31.782	0.042341	15.891
5	0.97778	100.9	0.98494	45.017	31.651	0.042643	15.8255
6	0.9731	106.79	0.99322	43.871	31.961	0.042373	15.9805
7	0.96558	111.69	0.99716	42.967	31.018	0.043014	15.509
8	0.96131	116.83	0.8512	42.006	30.644	0.042799	15.322
9	0.94905	127.54	0.97901	40.191	30.35	0.04267	15.175
10	0.94283	131.39	0.9975	39.55	30.393	0.042791	15.1965
11	0.93367	134.19	0.98777	39.081	31.544	0.043103	15.772

12	0.93217	138.69	0.71774	38.269	30.34	0.042416	15.17
13	0.92928	140.14	0.99069	38.091	30.444	0.042538	15.222
14	0.92244	144.73	0.99697	37.327	30.077	0.042345	15.0385
15	0.9127	148.32	0.85864	36.695	30.567	0.042353	15.2835
16	0.8982	148.42	0.99835	36.731	30.942	0.044687	15.471
17	0.89629	153.3	0.99936	35.903	30.229	0.043768	15.1145
18	0.88562	155.43	0.99633	35.547	30.233	0.044621	15.1165
19*	0.86934	158.68	1	35	30	0.046	15

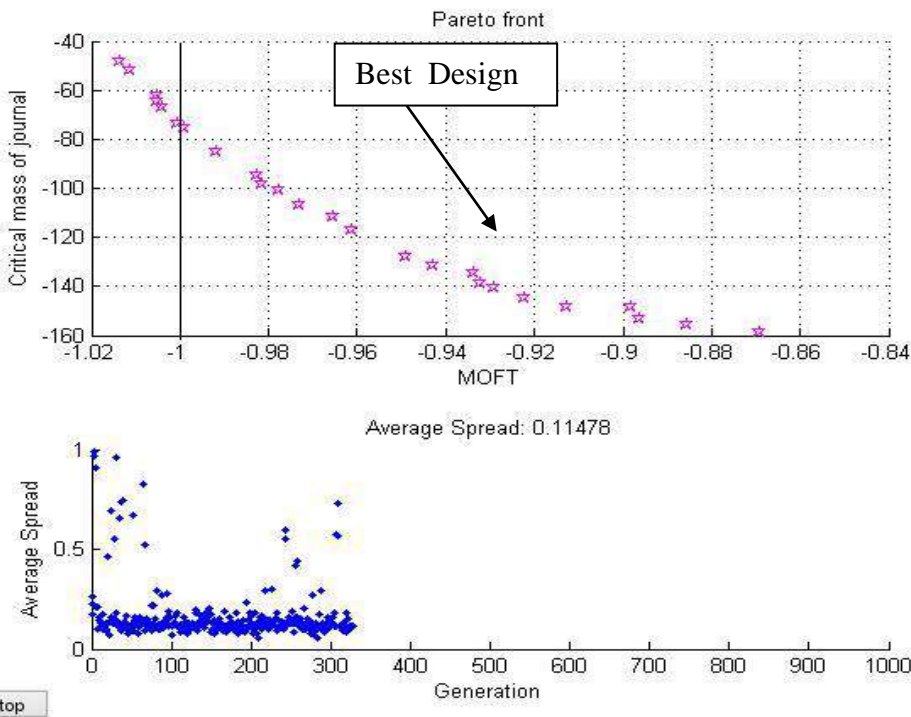


Figure 3: MOGA results for maximization of \bar{h}_{\min} and \bar{M}_{CJ} for bearing with longitudinal roughness pattern ($\gamma = 6$) (a) Pareto front and (b) Average spread of individual.

For longitudinal type roughness ($\gamma = 6$), Figure 3 show the Pareto front for the combination of objective function \bar{h}_{\min} and \bar{M}_{CJ} . Pareto optimality has provided totally 19 design options for longitudinal roughness pattern case.

The design parameters for the above selected options for the cases of longitudinal roughness pattern; $V_{rj} = 1$, $R_j = 35$ mm, $c = 30$ μ m, $\mu = 0.046$ Pas.

From figure 3(b) the average spread is terminated at 334 generations and found to be 0.11478.

Table 3: Pareto optimal designs for maximization of \bar{M}_{CJ} and minimization of \bar{T}_{FI} for bearing with longitudinal roughness pattern ($\gamma = 6$)

Design options	\bar{M}_{CJ}	\bar{T}_{FJ}	V_{rj}	R_j (mm)	c (μm)	μ (Pas)	Λ
1	158.31	437.8	0.75992	35	32.496	0.045999	16.248
2	158.25	426.31	0.76899	35	32.545	0.044754	16.2725
3	158.13	409.91	0.77299	35.004	32.509	0.042635	16.2545
4	158.07	398.03	0.80092	35.001	32.556	0.041355	16.278
5	157.95	383.63	0.79661	35.002	32.556	0.039785	16.278
6	157.84	374.87	0.78749	35.006	32.505	0.038813	16.2525
7	157.79	366.28	0.78347	35.005	32.665	0.038294	16.3325
8	157.58	358.83	0.95041	35.003	35.642	0.044579	17.821
9	157.57	352.37	0.95938	35.003	36	0.044605	18
10	157.49	334.16	0.9675	35.007	37.026	0.044552	18.513
11	157.49	331.76	0.96491	35.005	37.064	0.044256	18.532
12	157.39	310.41	0.95812	35.003	38.56	0.044649	19.28
13	157.19	287.39	0.95246	35.005	39.169	0.041872	19.5845
14	157.13	273.44	0.94103	35.004	40.667	0.042867	20.3335
15	157.09	267.08	0.96774	35.005	40.709	0.04162	20.3545
16	156.98	251.33	0.96504	35.004	42.09	0.041481	21.045
17*	156.7	228.5	0.96148	35.007	43.299	0.039142	21.6495
18	156.61	218.71	0.9656	35.007	45.247	0.040471	22.6235
19	156.45	205.18	0.95991	35.007	46.256	0.039047	23.128
20	156.28	200.52	0.92587	35.005	47.065	0.039195	23.5325
21*	156.16	189.8	0.91639	35.006	46.212	0.036227	23.106
22	155.51	164.79	0.9633	35.007	45.894	0.029133	22.947
23	155.2	154.75	0.74855	35.007	50.426	0.032691	25.213
24	154.92	134.63	0.95943	35.007	52.879	0.028442	26.4395
25	154.62	127.9	0.90342	35.008	56.07	0.028871	28.035
26	154.29	122.69	0.8577	35.01	56.969	0.027414	28.4845
27	153.68	117.08	0.64722	35.004	57.966	0.026007	28.983

Figure 4: MOGA results for maximization of \bar{M}_{CJ} and minimization of \bar{T}_{FJ} for bearing with longitudinal roughness pattern ($\gamma = 6$) (a) Pareto front and (b) Average spread of individual.

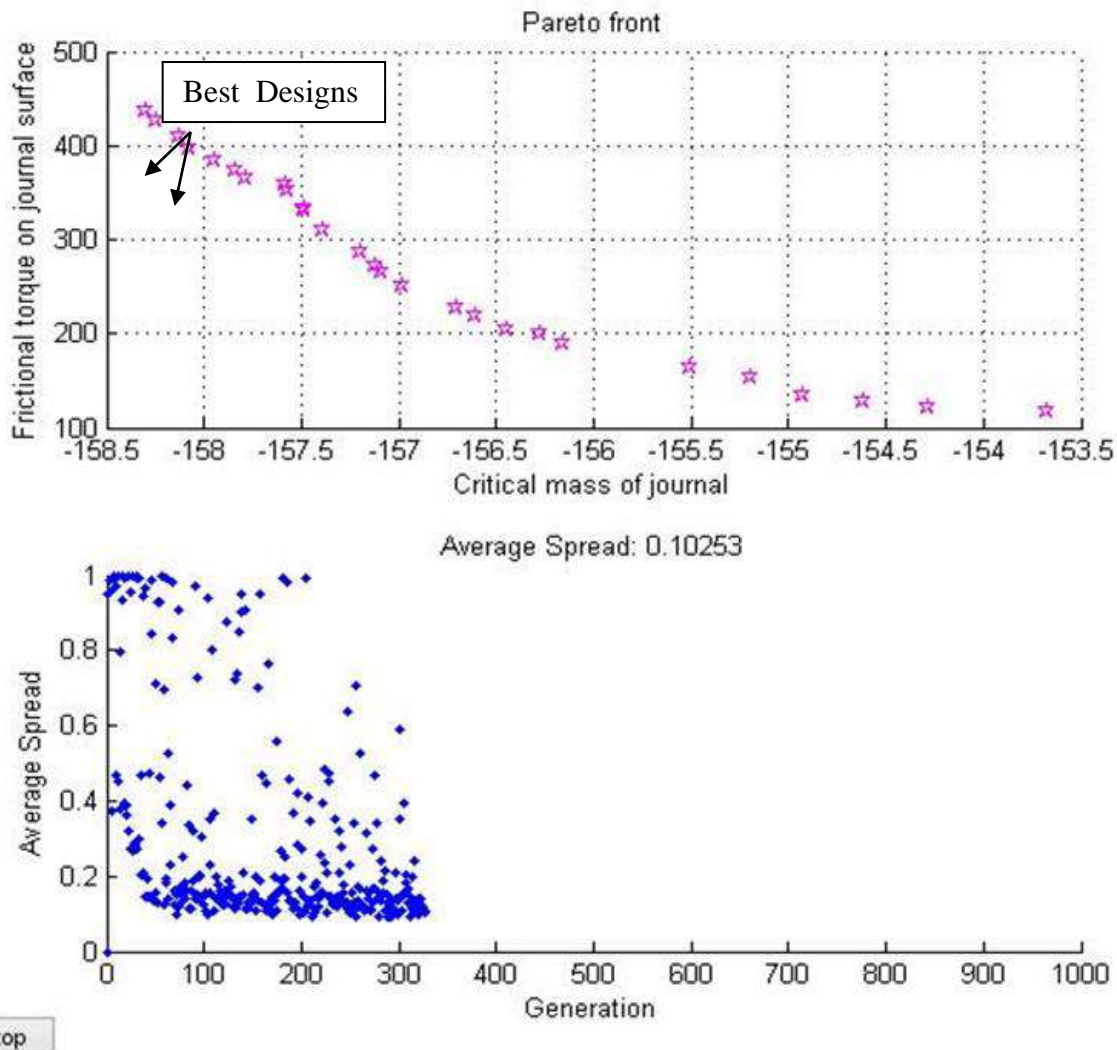


Figure 4: MOGA results for maximization of \bar{M}_{CJ} and minimization of \bar{T}_{FJ} for bearing with longitudinal roughness pattern ($\gamma = 6$) (a) Pareto front and (b) Average spread of individual.

Pareto optimal concept has provided total of 27 design options and are tabulated in Table 3 for longitudinal roughness respectively. It is observed that the design option starts from point A and upto point B, drastic decreases in \bar{T}_{FJ} with marginal reduction in \bar{M}_{CJ} . So point B and its corresponding design option is selected as best design. Then from point B to C, \bar{M}_{CJ} starts decreasing with simultaneous reduction in \bar{T}_{FJ} . The selected design options and their corresponding design parameters as per the first (point B) and second choice (point C) of the designer are, $V_{rj} = 0.96148$, $R_j = 35.007$ mm, $c = 43.299 \mu\text{m}$, $\mu = 0.039142 \text{Pas}$ and the other selected design option are $V_{rj} = 0.91639$, $R_j = 35.006$ mm, $c = 46.212 \mu\text{m}$, $\mu = 0.036227$ Pas respectively.

IV. CONCLUSION

1. Genetic algorithm has been developed and customized to use the Artificial Neural Network simulation results of objective functions for the optimization process.
2. The suitability of combining both Artificial Neural Network (ANN) and Multi-objective Genetic Algorithm (MOGA) techniques of MATLAB in the difficult and important task has been achieved.
3. Achievement of regression value above 99% and close agreement between expected and predicted value of all the three output functions shows the suitability of ANN in Multi-objective Genetic Algorithm optimization problem.
4. The optimization process was carried out for the optimization of design variables: variance ratio, journal radius, radial clearance and dynamic viscosity. Further Pareto optimal concept was utilized to predict the best design options for the maximization and/or minimization of two selected objective functions together.
5. For the maximization of minimum oil film thickness and minimization of frictional torque of bearing having longitudinal roughness, the optimum values was found to be 0.99388.

V. REFERENCES

- [1]. Hashimoto.H., (1997), "Optimum design of high speed short journal bearings by Mathematical programming," *STLE Tribology Transactions* 40.2.pp.283-293.
- [2]. Wang.N., Li Ho.C., and Cha.K.C., (2000), "Engineering Optimum Design of Fluid-Film Lubricated Bearings," *Tribology Transactions*, 43:3.pp.377-386.
- [3]. Hashimoto.H., and Matsumoto.K., (2000), "Improvement of Operating Characteristics of High-Speed Hydrodynamic Journal Bearings by Optimum Design: Part I – Formulation of Methodology and Its Application to Elliptical Bearing Design," *ASME*.
- [4]. Ghorbanian.J., Ahmadi.M., and Soltani.R., (2011), "Design predictive tool and optimization of journal bearing using neural network model and multi-objective genetic algorithm," *Scientia Iranica*, 18(5).pp.1095-1105.
- [5]. Cook.D.F., Ragsdale.C.T., and Major.R.L., (2000), "Combining a neural network with a genetic algorithm for process parameter optimization," *Engg. Application of Artificial Intelligence*, 13.pp.391-396.
- [6]. Gupta.S., Tiwari.R., and Naira.S.B., (2007), "Multi-objective design optimization of rolling bearings using genetic algorithms," *Journal of Mechanism and Machine theory*, 42.pp.1418-1433.
- [7]. Roy.L., and Kakoty.S.K., (2013), "Optimum Groove Location of Hydrodynamic Journal Bearing Using Genetic Algorithm," *Advances in Tribology*. Article ID 580367.
- [8]. Zuperl.U., and Cus.F., (2000), "Optimization of Cutting Conditions During Machining by Using Neural Networks," *Production Engineering Institute, Faculty of Mechanical Engineering, Maribor, Slovenia*.
- [9]. Hirani.H., and Suh.N.P., (2005), "Journal bearing design using multi-objective genetic algorithm and axiomatic design approaches," *Tribol. Int.*38.pp.481-491.
- [10]. Saruhan.H., Rouch.K.E., and Raso.C.A., (2004), " Design optimization of tilting-pad journal bearing using genetic algorithm," *Int. Jr. of rotating machinery*.10(4).pp.301-307.

- [11]. Samanta.B., Al-Balushi.K.R., and Al-Araimi.S.A., (2005), "Artificial neural networks and genetic algorithm for bearing fault detection," Springer. 10.pp.264-271.
- [12]. Taha.Z., and Widiyati.K., (2009), "Artificial neural network for bearing defect detection based on acoustic emission," Springer. 50. pp.289-296.
- [13]. Dongare.A.D., and Kachare.A.D., (2012), "Predictive Tool: An Artificial Neural Network," IJEIT. Volume 2.
- [14]. Vijay.H., and Chaturvedi.D.K., (2010), "Parameters Estimation of an Electric Fan Using ANN," Journal of Intelligent Learning Systems and Applications, 2.pp.33-38.
- [15]. Nagaraju.T., Sharma.S.C., and Jain.S.C., (2006), "Study of orifice compensated hole-entry hybrid journal bearing considering surface roughness and flexibility effects," Tribology International. 39. pp.715-725.
- [16]. Patir N. and Cheng H. S., "An Average Flow Model for Determining Effect of Three-Dimensional Roughness on Partial Hydrodynamic Lubrication", Trans. ASME Jr. of Lub. Tech., vol. 100, pp. 12-17, 1978.
- [17]. Patir N. and Cheng H. S., "Application of Average Flow Model to Lubrication between Rough Sliding Surfaces", Trans. ASME Jr. of Lub. Tech., vol. 101, pp. 220-230, 1979. Kirankumar.B.P. and Prajapati.J.M., (2012), "A brief review on Optimum Design of A Journal Bearings for I.C. Engine," IJERT, Volume 1.
- [18]. Svozil.D., KvasniEka.V., and Pospichal.J.E., (1997), "Introduction to multi-layer feed-forward neural networks," Chemometrics and Intelligent Laboratory Systems, 39.pp.43-62.
- [19]. Hykin.S., "Neural Networks – A comprehensive foundation," McMaster University, Hamilton, Cannada.
- [20]. Pratap.R., "Getting Started with MATLAB," Department of Mechanical Engineering Indian Institute of Science, Bangalore.
- [21]. Hamburg.A.P., (2005), "Genetic algorithms for optimization," TU-Sofia.



Optimization of Disc Brake Using Dual Calipers

Shawn Hrithik¹, Sudeep Y A¹, Madhu H C², H S Shivashankar³

¹UG Student, Department of Mechanical Engineering, Siddaganga Institute of Technology, Tumakuru-573103, Karnataka, India

²Assistant professor, Department of Mechanical Engineering, Siddaganga Institute of Technology, Tumakuru-573103, Karnataka, India

³Associate professor, Department of Mechanical Engineering, Siddaganga Institute of Technology, Tumakuru-573103, Karnataka, India

ABSTRACT

Brakes are the mechanical device which are used to control/stop the movement of a machine or automobile. The disc is sandwiched between two pads activated by cylinders backed in a caliper mounted on the stud shaft. When the brake lever is pressed using pressurized hydraulic, pressurized fluid is constrained into the chambers pushing the contradicting cylinders and brake pads into frictional contact with the disc. In general practice/literature review we found only single caliper are analyzed. In this work an attempt is made to analyze and optimize the performance of disc brake having dual coupled calipers using finite element method (FEM) analysis under severe braking conditions i.e., panic braking (26.48m/s² deceleration). FEM analysis was carried out using Ansys 2021 Software version to determine the distribution of temperature, stresses and deformation across the disc brake under various braking conditions.

Keywords: Disc brake, caliper.

I. INTRODUCTION

A Disc brake is a type of brake that uses the calipers to squeeze pairs of pads against a disc or a rotor to create friction. When a brake pedal is pressed, the push rod which is connected to lever or pedal and master cylinder piston pushes the cylinder piston. This movement allows the master cylinder piston to slide and push the return spring inside the bore of master cylinder, which generates pressure in reservoir tank. At this moment a primary seal allows the brake fluid of reservoir tank to flow over it into the brake hosepipes. A secondary seal ensures that the brake fluid does not go other side. Then the fluid enters in to cylinder bore of caliper assembly via brake hosepipes and pushes the caliper piston or pistons. At this time the piston ring moves in rolling shape with piston. Then the caliper piston pushes brake pad. This movement causes brake pads to stick with brake disc which creates friction and stops the brake disc/rotor to rotate. This way disk brake system stops or slows down the vehicle. When the brake lever or pedal is released the piston ring pushes the calliper piston back to

cylinder bore of calliper till both, calliper piston and piston ring come into their original shape. Currently retraction spring pushes the brake pads to their original position. The return spring in master cylinder assembly pushes the master cylinder piston back into its original position and allows the fluid to flow back to reservoir via hosepipe and master cylinder bore.



Disc Brake coupled with dual calipers[13]

II. LITERATURE REVIEW

Mahmood Hasan Dakhil et.al [1] have reported a research paper on the design and structural analysis of disc brakes in automobiles which discussed optimized design of disc brake using finite element analysis. This was done to evaluate the performance of the brake under severe braking conditions. The cast iron and stainless steel were used as disc brake materials. They have taken a actual condition and calculated the required forces and estimated the braking distance for the discbrakes of cast iron and stainless-steel material, both were found to be under the allowable limits.

Mit Patel et.al [2] reported on design of the disc brake's rotor. In this paper design of the disc brake's rotor was carried out. The aim of their study was to analyse the thermo-mechanical behaviour of the brake disc during the braking phase. The coupled thermal-structural analysis was used to determine the deformation and the Von Mises stress. Hence, to estimate enhanced performance of the rotor disc. A comparison between analytical and results obtained from FEM analysis was done and all the values obtained from the analysis were less than their allowable values. They have designed a disc rotor based on the calculation of braking force.

Subhasis Sarkar et.al [3] conducted research on modelling and simulation of disc brake to analyze temperature distribution using FEM. The objective of their study was to investigate and analyze the temperature distribution of rotor disc and to identify critical temperature during operation using FEA analysis. Static thermal analysis had been carried out on the disc rotor to evaluate and compare their performance and the temperature distribution was analyzed considering cooling parameters (convection and radiation). Comparative study was carried out between different materials i.e., Aluminium metal matrix composite (AMMC), Asbestos, and Grey Cast Iron (GCI) etc. They had concluded that disc brake design plays an important role in heat transfer as other

variables such as plate and vane thickness, material and flow pattern. They concluded on the basis of their results that with increase in the vehicle speed the temperature increases for both the material but the rate of heat generation was less for AMMC as compared to GCI with speed

Kumaragurubaran SB et.al [4] reported on design and analysis of disc brake rotor. Their work deals with the thermal analysis of disc brake of a vehicle. Heat generation and dissipation of disc brake were analyzed. The objective of their work was to investigate and analyze the temperature distribution of rotor disc during operation using Ansys. In their research work design of a disc brake is proposed with copper liner on its brake disc, the heat transfer of existing and hybrid disc was calculated for finding the effectiveness of heat transfer.

Bhuvneshwar Pancholi et.al [5] published a paper on the refinement and optimization of disc brake. They focused on the shortcomings of the existing stainless-steel brakes using Ansys, a 3D CAD model was imported into Ansys so that they could monitor and analyse the shortcomings. They calculated the braking distance of the vehicle (Bajaj 220f) and performed Structural and thermal analysis on it after applying boundary conditions. They also made comparisons between Silicon-carbide brakes and Stainless-Steel brakes using Ansys and also compared the Braking distances.

K.N.V. Sreedevi et.al [6] published a paper on the modelling and analysis of a disc brake. The aim of the paper was to model a disc brake used in Honda Civic. structural and Thermal analysis was done on the disc brake with three different materials. The materials used are Stainless Steel, Cast Iron and Aluminium Alloy.

The motive of our research is to design and analyse a disc brake with dual calipers simulating under a real-world conditions and comparing it with the conventional single caliper disc.

III. CALCULATIONS

Considering a real-world problem, the following assumptions were made and these values are considered for analysis work

1. Overall Weight of the car (m): 1250 kg[1]
2. Centre of Gravity height (h) = 8.2 inches = 0.208m.
3. Deceleration(d) = 26.48m/s²
4. Wheel Base (Wb) = 2.35m or 2350mm
5. Wt. Distribution: Front – 40% = 0.4×1250 = 500 kg

Rear – 60% = 0.6×1250 = 750 kg

Static Wt. distribution factor = 1250×0.66 = 833.33kg Dynamic Wt. = $(h \times m \times d) \div (Wb \times gravity) = 298.644$ kg

Braking Force Front = Static wt. on axle + Dynamic Wt.

= 1131.97kg = 11.10 kN

Braking Force Rear = Static Wt. on axle – Dynamic Wt.

= 534.68 kg = 5.24 kN.

Torque required = BF (Front) × Coefficient of friction b/w tyre and road × rolling radius of tyre

= 11.10×103×0.02×95% of radius of tyre

= 11.10×103×0.02×0.95×0.19 = 40.071 N-m

Area of rubbing force acting on disc A = 2×3.14×0.0847135

Kinetic energy $= (1/2) \times m \times v^2 = (1/2) \times 1250 \times 27.762^2 = 479.55 \text{ kJ}$ Heat per wheel for a disc (car 4 wheels) $= 479.55/4 = 119.88 \text{ kJ}$ Surface area of disc $= 0.084 \text{ m}^2$

Heat flux = Heat generated / Time / Twice the projected area $= 119.88 / 6.87 / 2 \times 0.084 = 103.86 \text{ kW / m}^2$

Heat flux at front = 40% of heat flux $= 0.4 \times 103.86$

$= 41.544 \text{ kW / m}^2$

IV. MODELLING AND ANALYSIS

The design of the disc was done on SolidWorks 2021 version.

Procedure:

The disc brake was designed using dimensions assumed nearby the standard value. The disc diameter is about 288mm.

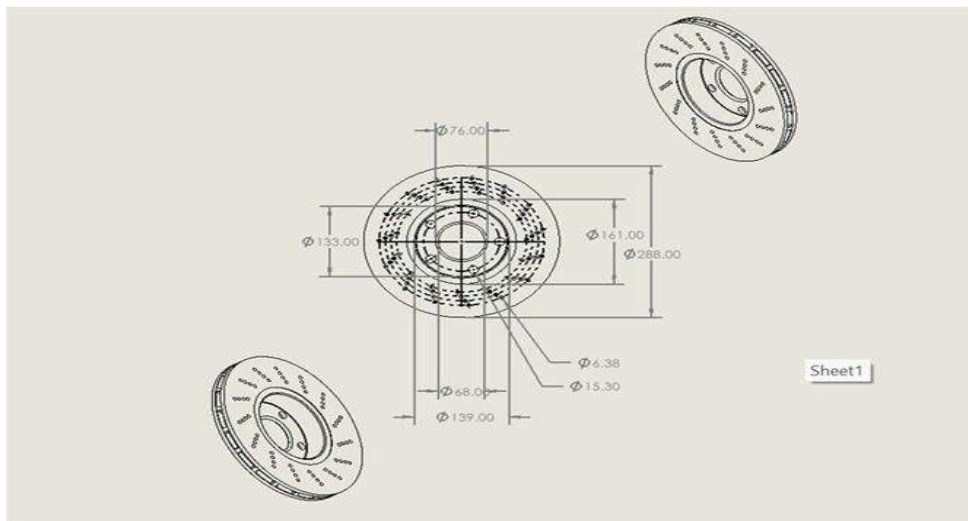


Figure 1: Dimension of Disc Brake Designed

This final model which is shown in the figure was imported to the Ansys 2021 software for the analysis.

We did this considering two materials

1. Stainless steel 316 (SS-31)
2. Grey Cast Iron

The properties of the materials are shown in the table [12]:

Material	Stainless Steel 316 grade	Grey Cast Iron
Yield Strength	230 MPa	200 MPa
Tensile Strength	520 MPa	450 MPa
Modulus of Elasticity (E)	$193 \times 10^3 \text{ MPa}$	$180 \times 10^3 \text{ MPa}$
Poisson's ratio	0.28	0.29
Melting point	1380 deg Celsius	1180 deg Celsius

In the software the material should be selected. The mesh size was adjusted to 5mm, mesh used is triangular mesh. Area where natural convection takes place is to be considered and then heat flux is calculated. From this,

an iteration is run and max temperature value is estimated. After this, max temperature value is to be imported to find the von-mises stress. The disc is fixed at the centre and pressure is applied on two sides of the disc at different radius. The von-Mises stress is obtained.

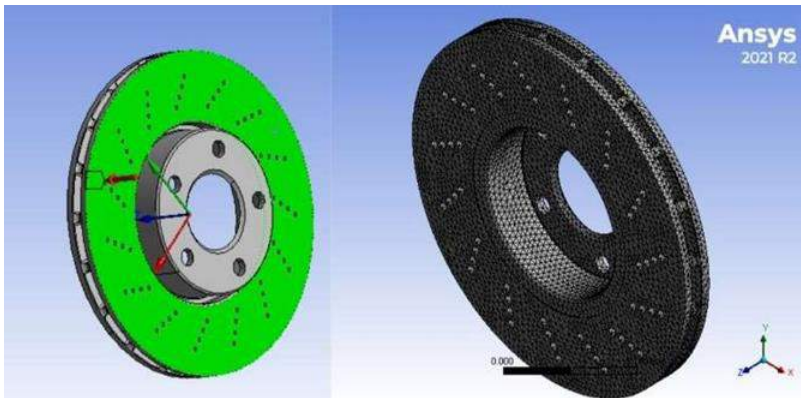


Figure 2: Pressure applied on the disc and meshed view of the brake disc
The pressure applied on the disc brake which is assumed to be the clamping force of the caliper on two sides of the disc brake at different radius is shown in figure 2.

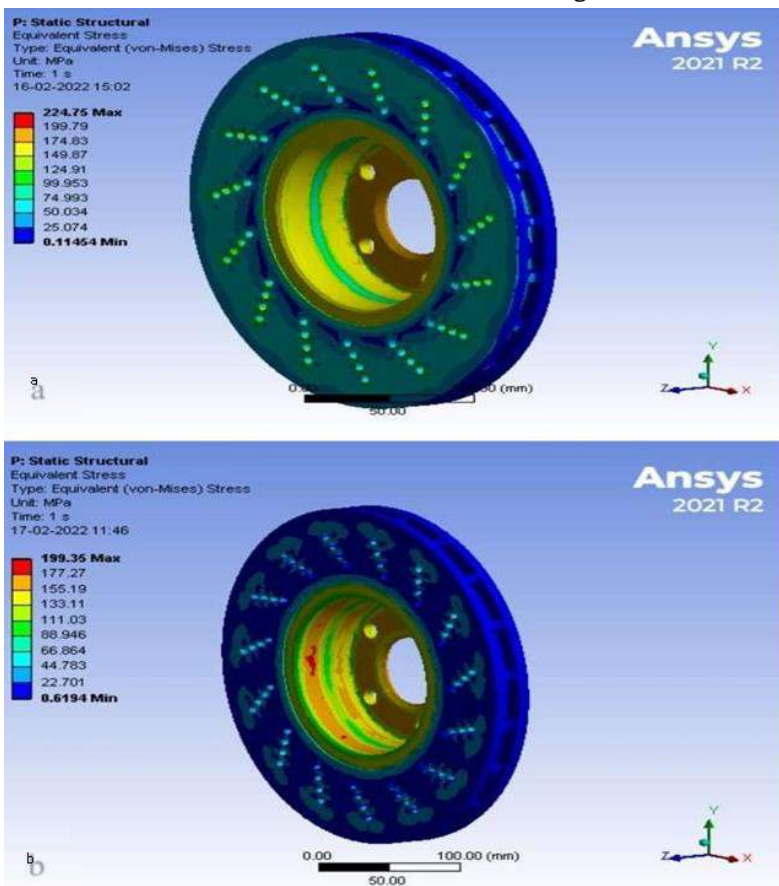


Figure 3: von-Mises Stress of a) SS-316 and b) GCI

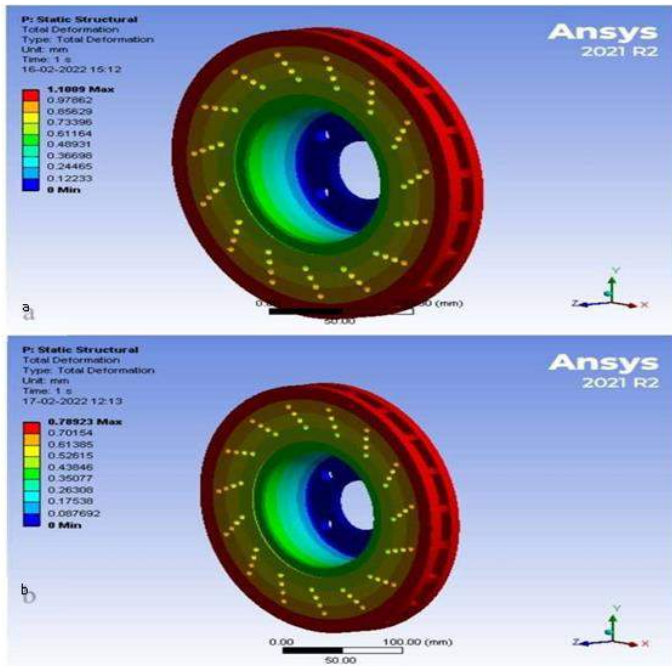


Figure 4: Total deformation of a) SS-316 and b) GCI

In the Figure 3 and 4, the result of von-Mises stress and total deformation is shown of two different materials i.e., SS-316 and GCI. The properties of SS-316 and GCI are compared and it is observed that GCI material had better characteristics compared to that of SS-316 material and hence, GCI material is considered for the analysis.

V. RESULTS AND DISCUSSION

The analysis result conducted based on the assumed calculations are shown in the figures below

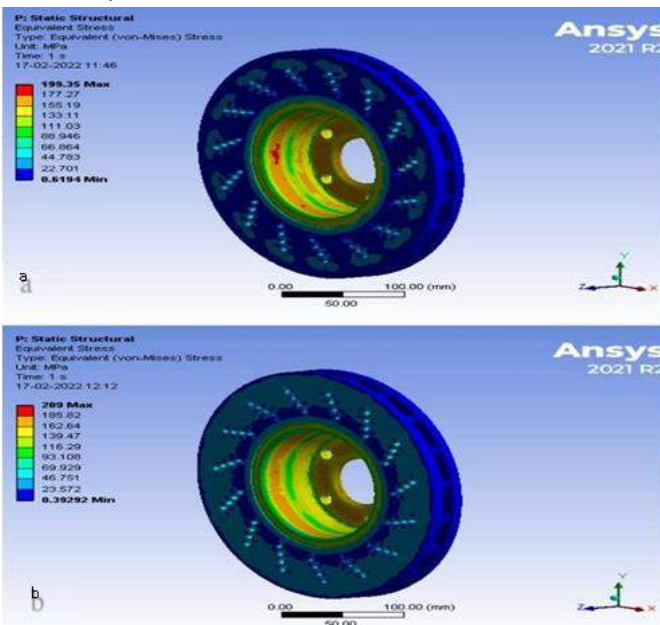


Figure 5: von-Mises stress of GCI having a) Dual caliper and b) Single caliper

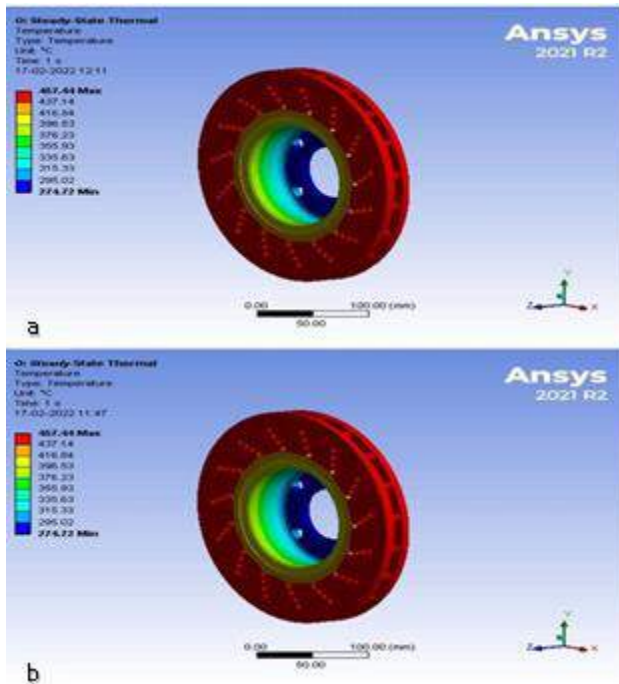


Figure 6: Temperature distribution of GCI having a) Dual caliper and b) Single caliper

As per the analysis, the following result is obtained and been tabulated:

Characteristics	Single caliper	Dual caliper
von-Mises stress	209 MPa	199.36 MPa
Temperature Distribution	457.44 deg Celsius	457.44 deg Celsius

From the above tabulated result obtained from FEM analysis, it is observed that maximum von-Mises stress in single caliper is 209 MPa, while the maximum von-Mises stress in dual caliper is 199.36 MPa, as shown in Figure 5.

The temperature distribution in single and dual caliper is found to be same i.e., 457.44 deg Celsius. Figure 6 represents the temperature distribution of GCI having single and dual caliper.

VI. CONCLUSIONS

Based on the analysis done on the Ansys software, it is found that grey cast iron is better in its characteristics and also using double caliper is comparatively better than using a single caliper as it showed lesser von-Mises stress at maximum temperature as compared to the single caliper.

VII. REFERENCES

[1]. Mahmood Hasan dakhil, A. K. Rai, P. Ravinder reddy & ahmed abdulhussein jabbar(2014), design and structural analysis of disc brake in automobiles IJMPERD |IISN(e): 2249-8001Vol. 4, issue 1, 95-112.

- [2]. Prof. Mit Patel, Mansi Raval, Jenish Patel (2016), Design of Disc Brake's Rotor IJEDR | Volume 4, Issue 4 | ISSN: 2321-9939.
- [3]. Subhasis Sarkar (Dr.) Pravin P Rathod, A. J. Modi (2014) IJSRD | Vol 02 Issue 03 ISSN (online): 2321-0613
[4]Venkatramanan R, Kumaragurubaran SB, Vishnu Kumar C, Sivakumar S , Saravanan B (2015) IJAER| Vol.10 Number 19.
- [4]. Bhuvneshwar Pancholi, Mahendra Dutta, Poojan Bharatia, Basit Lone, Sarfaraz Shaikh (2020) Refinement & Optimzation of Disc Brake, IRJMETS | Volume: 2/Issue: 12.
- [5]. K. N. V. Sreedevi, P. Radha Krisha Prasad, M. V. S. Murali Krishna, Gangireddy(2018), Modeling analysis of a Disc Brake, IJSR Volume 8 Issue 2.
- [6]. R.S. Kurmi and J.K. Gupta, (2008). Machine Design, Division of S. Chand and Company Ltd, Ram Nagar, New Delhi.
- [7]. Joe Y.G. Cha, Analysis of disc brake instability due to friction induced vibration, International of automotive technology, vol 9, No 2, PP 169-171.
- [8]. Utz von Wagner, (2011) Influence of dynamic brake pad properties on automotive disc brakeSqueal, PAMM,vol 11, Issue 1, Paper 345-346.
- [9]. Haripal Singh and Harsh Deep Shergill, (2012) Thermal Analysis of Disc Brake Using Comsol International Journal on Emerging Technologies.
- [10]. Daniel Das. A, Christo Reegan Raj. V, Preethy. S and Ramya Bharani G. (2013). Structural and Thermal Analysis of disc braking in Automobiles. "International Journal of Latest Trends in Engineering and Technology". [12]<https://www.makeitfrom.com/materialproperties/Grey-Cast-Iron>
- [11]. <http://www.safebraking.com/name-the-car/>



Estimation and Comparison of Welding Performances in P-GMAW for SS 316 Material Using MRA and ANN

Rudreshi Addamani*¹, Gurupavan H R¹, Dr. Gayathri Devi S K², Mallikarjun Bhovi³, Prathik Jain S⁴

¹Department of Mechanical Engineering, P.E.S. College of Engineering, Mandya, Karnataka, India

²Department of Mechanical Engineering, B.M.S. College of Engineering, Bengaluru, Karnataka, India, CFDS, RUAS, Bangalore, Karnataka, India

³Department of Mechanical Engineering, P.D A. College of Engineering, Kalaburgi, Karnataka, India

⁴Department of Aeronautical Engineering, DSCE, Bengaluru- 78, Karnatka, India

ABSTRACT

Pulsed Gas Metal Arc Welding (P-GMAW) is considered as one of the most important arc welding processes in fabrication, which is used in high-technology industrial applications. In order to control and recognize the P-GMAW process parameters, it is necessary to determine the input and output relationship of the welding processes. P-GMAW offers an enhancement in quality and productivity over regular Gas Metal Arc Welding (GMAW). The process enables low mean current and low net heat input with stable spray transfer. This paper describes the estimation and comparison of welding process parameters viz., current, Gas Flow Rate (GFR) and Wire Feed Rate (WFR) on Ultimate Tensile Strength (UTS), Yield Strength (YS) and Percentage of Elongation. Experiments have been performed by taking SS 316 material based on Taguchi's L27 standard orthogonal array. Estimation of welding performances have been carried out using sophisticated mathematical models viz., Multiple Regression Analyses (MRA) and Artificial Neural Network (ANN) and compared. The output developed by ANN model is used to compare with the output obtained through MRA. Estimation and comparison of welding performances were carried out using MRA and ANN techniques.

I. INTRODUCTION

High quality and productivity of welding in fabrication process is generally achieved by using Pulsed Gas Metal Arc Welding (P-GMAW) in high technology industries. To improve wetting, suitable selection of pulse parameters is required, but the penetration remains finger type penetration. The weld beads are either deep and narrow in the penetration or convex are seen in generally through experiments. A variety of parameters which influence the P-GMAW process which are viz., wire size and wire feed rate for penetration and arc stability, shielding gas for weld bead shape, arc stability, metal transfer mode and molten droplet detachment, welding speed for penetration and metal transfer. Mean current, base current peak current, peak time and pulse duration are the other parameters which influences the P-GMAW process in terms of metal transfer mode,

tapering of electrode, penetration, molten metal droplet detachment, number of droplets detached per pulse, temperature of transferred metal, width of weld pool, wetting in weld bead and drop size. At a given wire feed rate, P-GMAW exhibits greater arc characteristics, less fume generation, lower heat input and reduced spatter significantly than spray transfer in steady current GMAW.

The main characteristic of P-GMAW under steady current conditions is a spray type metal transfer at low average currents, which would produce globular metal transfer. It introduces additional parameters such as pulse duration (T_p), pulse frequency (f), peak current (I_p), background current (I_b) and background time (T_b) shown in Fig. 1. The appropriate selection of pulse parameters provides required droplet velocity and control over weld pool to achieve desired geometrical characteristics of weld joint. The different nature of metal transfer and thermal behaviour of the deposited droplet at various pulse parameters give rise to different geometrical, metallurgical and mechanical characteristics in the weld joint [1].

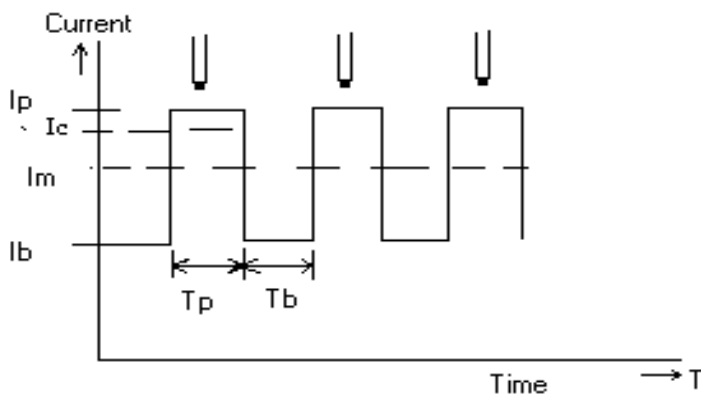


Fig. 1. Pulsed current waveform

Several researchers focus on friction welding process parameter optimization with a hybrid technique of ANN and different optimization algorithms. ANN based approaches could model this welding process of INCOLOY 800H in both forward and reverse directions efficiently, which are essential for the automation. Five different training algorithms were used to train ANN for both forward and reverse mapping and ANN tuned force approach was used for optimization. The results showed that GANN with 4-9-3 for forward and 4-7-3 for reverse mapping arrangement could outperform the other four approaches in most of the cases but not in all. Experiments on tensile strength (TS), microhardness (H) and burn off length (BOL) of the joints were performed with optimised parameter. It is concluded that this ANN model with genetic algorithm may provide good ability to predict the friction welding process parameters to weld Incoloy 800H [2]. Weld joint strength monitoring in Pulsed Metal Inert Gas Welding (PMIGW) process was performed. Response surface methodology is applied to perform welding experiments. A multilayer neural network model has been developed to predict the UTS of welded plates. Six process parameters, namely pulse voltage, back-ground voltage, pulse duration, pulse frequency, wire feed rate and the welding speed, and the two measurements, namely root mean square (RMS) values of welding current and voltage, are used as input variables of the model and the UTS of the welded plate is considered as the output variable. Furthermore, output obtained through multiple regression analysis is used to compare with the developed ANN model output. It was found that the welding strength predicted by the developed ANN model is better than that based on multiple regression analysis [3]. Efforts have been made towards the monitoring of friction stir welding (FSW) process using real-

time torque signals in their research work. Signals were analyzed using discrete wavelet transform and statistical features namely dispersion, asymmetry and excess are computed. The computed features are further processed to develop effective methodology for internal defect identification in FSW process. The prediction accuracy of the model with computed signal features are found to be more than the model developed with process parameters. The comparison of the developed support vector regression (SVR) model with ANN model and general regression model yields that prediction performance of SVR is superior to ANN and general regression model [4]. Ultrasonic welding was carried out on aluminum-steel dissimilar alloys to investigate the influences of welding parameters on joint strength. Designed and conducted a 3-factor, 3-level comprehensive test. Vibration time significantly impact the tensile strength although its significance level is close to the threshold. The interaction between welding parameters all can significantly impact the tensile strength. The artificial neural network optimized by Genetic Algorithm was used to establish an analytical model. The supplemental experiment and residual analysis were conducted to verify the accuracy of the analytical model. The analytical model show that with the increase of clamping force, the changes of optimal and minimum strength are limited, but the range of welding parameters to obtain a higher strength change significantly; the optimal welding parameters from lower vibration amplitude and higher vibration time shifts towards to higher vibration amplitude and shorter vibration time gradually; for 0.3 Mpa clamping force, the influences of vibration amplitude and vibration time on tensile strength are not significant [5].

II. EXPERIMENTAL WORK

DC electrode positive power supply Lorch welding machine was used to conduct trials. Experimental trial pipe specimens are 300 mm in overall length (each specimen is cut in to 150 mm length) with wall thickness of 3 mm, outer diameters of 25 mm and inner diameter of 22 mm. Edge preparation is done with an angle of 60° and tack welded. Copper coated mild steel electrode of 1.2 mm diameter was used to carry out welding. Argon (85%) and CO₂ (15%) gas mixture was used for shielding. The experimental setup consists of a rotating disk which rotates with a constant speed of 5 rpm in to which work sample was mounted. The working ranges for the process parameters were selected from the American Welding Society (AWS) hand book, literature review and experts advise as shown in Table 1. Single pass welding was performed on SS 316 pipes by varying the process parameters. Fig 2 & 3 shows the welding and tensile experimental set up respectively. Ultimate Tensile Strength (UTS), Yield Strength (YS) and percentage of elongation are considered as output variables. The Experiments were conducted according to L₂₇ orthogonal array.

Input parameters	Levels		
	I	II	III
Current (Amp)	60	65	70
GFR (LPM)	15	16	17
WFR (mm/min)	120	125	130

Table1. Welding settings used in experiments

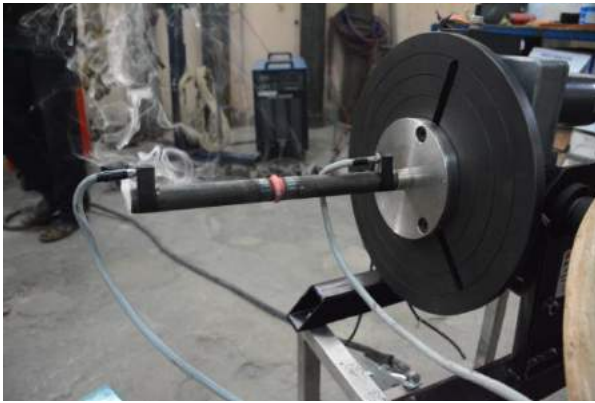


Fig. 2. Welding Experimental Setup



Fig. 3. Tensile Experimental Setup

III. RESULT AND DISCUSSIONS

1.1 Multiple Regression Analysis (MRA)

The objective of multiple regression analysis is to construct a model that explains as much as possible, the variability in a dependent variable, using several independent variables. The model fit is usually a linear model, though some times non linear models such as log-linear models are also constructed. When the model constructed is a linear model, the population regression equation is

$$Y_i = \alpha + \beta_1 X_{1i} + \dots + \beta_m X_{mi} + e_i \tag{1}$$

Where Y_i is the dependent variable and $X_{1i} \dots X_{mi}$ are the independent variables for i^{th} data point and e_i is the error term. Error term is assumed to have zero mean. This error term is the combined effect of variables that are not considered explicitly in the equation, but have an effect on the dependent variable. The coefficients $\alpha, \beta_1, \dots, \beta_m$ are not known and estimates of these values, designated as a, b_1, \dots, b_m have to be determined from the sampled data. For this least squares estimation is used, which consists of minimizing.

$$SS = \sum_{i=1}^n e_i^2 = \sum_{i=1}^n (Y_i - a - b_1 X_{1i} - \dots - b_m X_{mi})^2 \tag{2}$$

With respect to each of the co-efficient a, b_1, \dots, b_m . This will give $k+1$ equations from which a, b_1, \dots, b_m . can be obtained. These least squared estimates are the best linear unbiased estimates and hence give the best linear unbiased estimate of the dependent variable.

$$Y = a + b_1 X_1 + b_2 X_2 + \dots + b_m X_m \tag{3}$$

The obtained regression model for estimating UTS for SS 316 material is,

$$UTS = 5.74 \times A - 24.74 \times B - 4.37 \times C + 720.69 \tag{4}$$

The obtained regression model for estimating YS for SS 316 material is,

$$\text{Yield Stress} = 2.34 \times A - 8.11 \times B - 9.4 \times 10^{-1} \times C + 221.87 \tag{5}$$

The obtained regression model for estimating % of Elongation for SS 316 material is,

$$\% \text{ of Elongation} = 2.2 \times 10^{-1} \times A - 4.5 \times 10^{-1} \times B - 1.38 \times 10^{-1} \times C + 12.12 \tag{6}$$

1.2 Artificial Neural Network (ANN)

A neural network is an artificial representation of human brain that tries to simulate its learning process. ANN is an interconnected group of artificial neurons that uses a mathematical model or computational models for information processing based on a connectionist approach to computation. The ANN are made of interconnecting neurons which may share some properties of biological neurons. ANN is an information processing paradigm that is inspired by procedure in the biological nervous system. Neural networks are non linear mapping systems that consist of simple processors which are called neurons, linked by weighed connections. Each neuron has inputs and generates an output that can be seen as the reflection of local information that is stored in connections. The output signal of a neuron is fed to other neurons as input signals via interconnections Fig. 4 shows the network architecture of ANN.

The neuron has a bias b , which is summed with the weighted inputs to form the net input n .

$$n = w_{1,1}p_1 + w_{1,2}p_2 + \dots + w_{1,R}p_R + b \tag{7}$$

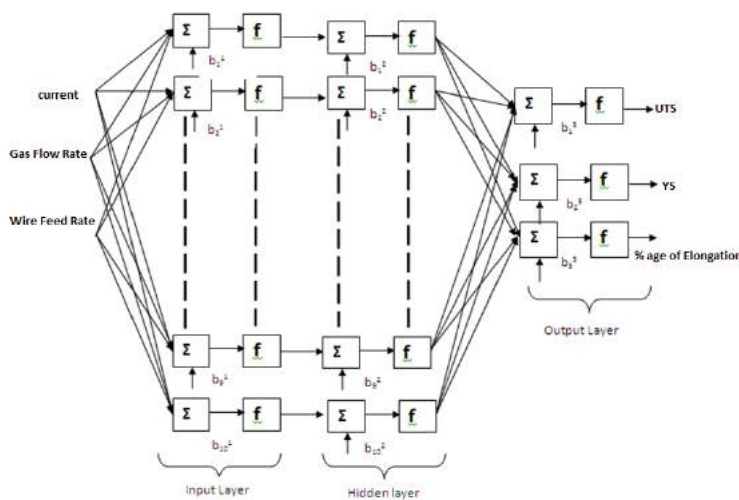


Fig. 4. Network architecture

Various input to the neurons are represented by ' X_n '. Each of these inputs is multiplied by a connection weighed, represented by ' W_n ' and added to the bias ' φ ' to compute activation ' a_n ' which is converted into the output ' O_n ' via transfer function. Various input to the neurons are represented by ' X_n '. Each of these inputs is multiplied by a connection weighed, represented by ' W_n ' and added to the bias ' φ ' to compute activation ' a_n ' which is converted into the output ' O_n ' via transfer function.

$$a_n = W_n X_n^T + \varphi \tag{8}$$

$$O_n = f(a_n) \tag{9}$$

After conducting the experiment, response values are noted down and analysis has been done. The experiment was conducted in the same environmental condition for all the runs so that environmental noise factors can be minimized.

1.3 Prediction of response variables of SS 316 material

The prediction of responses was carried out using MRA and ANN. When the training is completed, it is necessary to check the network performance and determine if any changes need to be made to the training process, network architecture or the data sets.

Fig. 5, Fig. 6 and Fig. 7 gives the measured and estimated responses with the number of runs using MRA for UTS, YS and % of elongation. Referring to the below figure, it was observed that most of these estimates are correlating well with the measured responses at lower and higher welding conditions than at intermediate welding conditions. From the Fig. 5 and Fig. 6 it is observed that the UTS and YS increases with higher current and gas flow rate. With reference to graphs, it is noticed that predicted results are in good agreement with the measured responses at higher welding conditions than at lower and intermediate welding conditions.

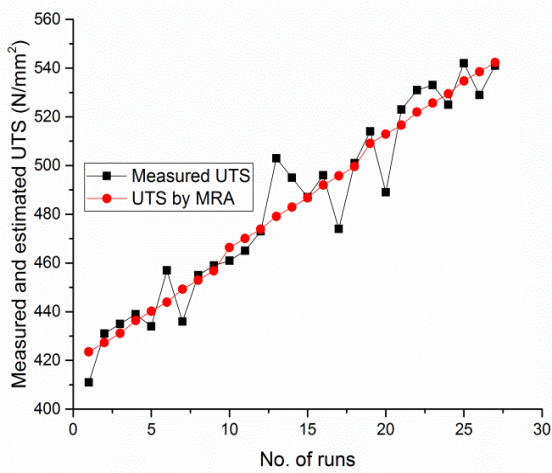


Fig. 5. Measured and estimated UTS by MRA

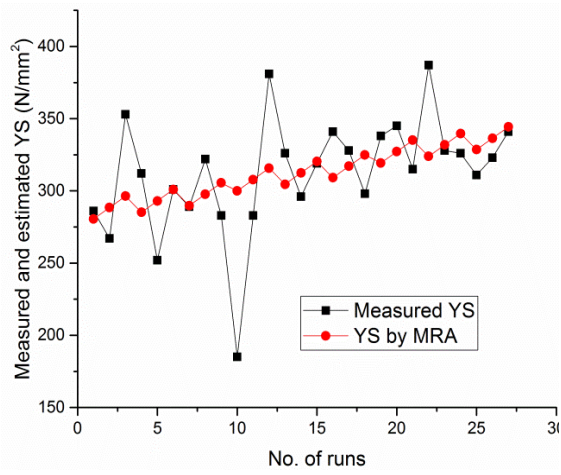


Fig. 6. Measured and estimated YS by MRA

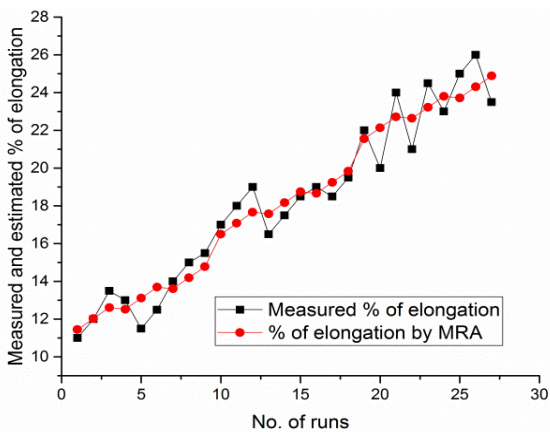


Fig. 7. Measured and estimated % of elongation by MRA

Comparison of responses using MRA and ANN were carried out. It is observed from the Fig. 8, Fig. 9, Fig. 7 and Fig. 10, predicted UTS, YS and % elongation of 70% of the data set by ANN exhibits better correlation with the measured UTS, YS and % elongation when compared to the MRA.

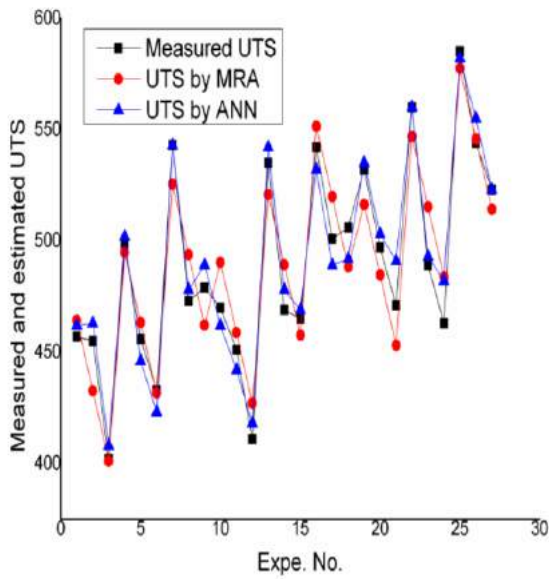


Fig. 8. Comparison of UTS by MRA & ANN

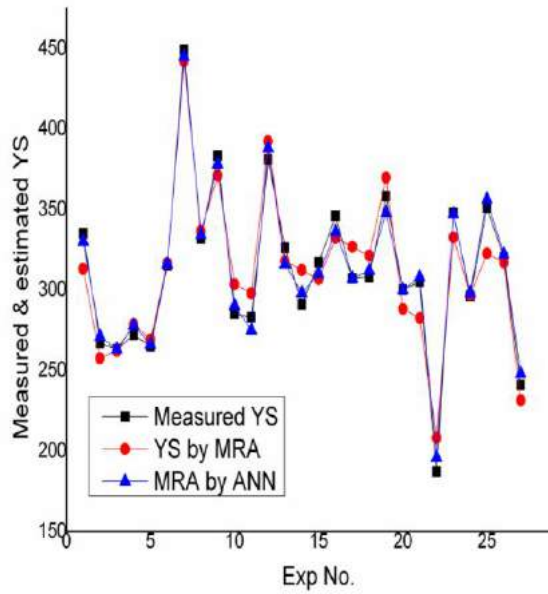


Fig. 9. Comparison of YS by MRA & ANN

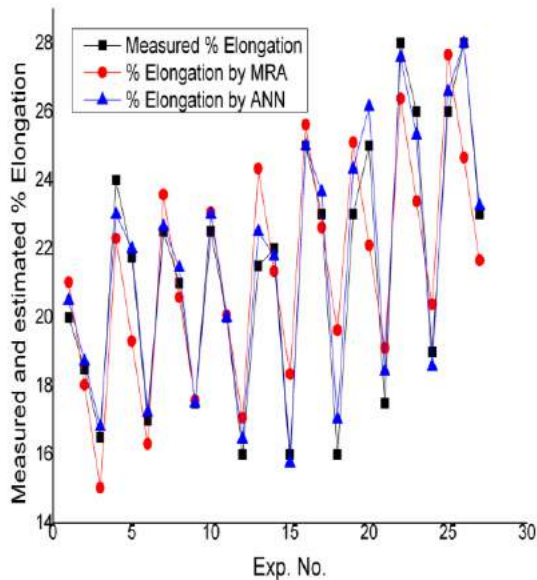


Fig. 10. Comparison of % elongation by MRA & ANN

IV. CONCLUSION

This paper has presented an investigation on the estimation and prediction of welding parameter on ultimate tensile strength, yield strength, percentage of elongation and hardness. It was found that, each control factors are affecting the response variables to different extent. We have also seen that MRA and ANN is a preferred tool for estimating the welding performances for SS 316 material.

Comparison of the two theoretical methods for estimation of welding performances, it was found that, ANN fitting function has an edge over MRA method. Thus, predicted response variables of 70% training set correlates well with the measured response variables. ANN function gave better prediction than MRA.

V. REFERENCES

- [1]. P.Srinivasa Rao, O.P.Gupta, S.S.N.Murty, "A study on the weld bead characteristics in pulsed gas metal arc welding with rotating arc " Proceedings of OMAE04 23rd International Conference on Offshore Mechanics and Arctic Engineering June 20-25, 2004, Vancouver, British Columbia, Canada, OM AE2004-51580.
- [2]. K. Anand, Birendra Kumar Barik, K. Tamilmannan, P. Sathiya, "Artificial neural network modeling studies to predict the friction welding process parameters of Incoloy 800H joints ", Engineering Science and Technology, an International Journal, Vol. 18, 2015, pp- 394 -407.
- [3]. Sukhomay Pal, Surjya K. Pal, Arun K. Samantaray, "Artificial neural network modeling of weld joint strength prediction of a pulsed metal inert gas welding process using arc signals ", journal of materials processing technology, Vol. 202, 2008, pp - 464-474.
- [4]. Bipul Das, Sukhomay Pal, Swarup Bag, "Torque based defect detection and weld quality modeling in friction stir welding process ", Journal of Manufacturing Processes, Vol. 27, 2017, pp. 8-17.
- [5]. Dewang Zhao, Daxin Ren, Kunmin Zhao, Sun Pane, Xinglin Guo, "Effect of welding parameters on tensile strength of ultrasonic spot welded joints of aluminum to steel – By experimentation and artificial neural network", Journal of Manufacturing Processes, vol. 30, 2017, vol. 63-74.



Literature Review of Load Balancing Approaches in Data Center Networks

Nagaraju T A¹, Dr. Panduranga Rao M V², Dr. Revanna C R³

¹Assistant professor, Department of Electronics and Communication, Government Engineering College,
Ramanagara, Karnataka, India

²Professor Department of ISE, Jain University, Bengaluru, Karnataka, India

³Assistant professor, Department of Electronics and Communication, Government Engineering College,
Ramanagara, Karnataka, India

ABSTRACT

Data center networks typically uses an output model to provide bandwidth for the top two categories of applications. A large amount of data is required for frequent transfers between servers on multiple paths. However, standard load balancing algorithms such as the Equal-Cost Multi-Path route are not suitable for instantaneous traffic on data center networks. Based on the topology of a specialized data center and traffic characteristics, researchers have recently come up with new ways to plan traffic to measure traffic. This paper provides a comprehensive survey of contemporary elucidations for load balancing in data center networks.

Keywords: Data Center Networks, load balancing

I. INTRODUCTION

In recent years, businesses and companies are slowly falling apart to change their services such as web search and online gaming in cloudy places. Supporting these ever-growing one's cloud services, a large number of data centers have been suspended. Today's data centers typically use a scale model, such as FatTree [1], VL2 [2], DCell [3], connecting a large number of asset servers and thus supports size to count. In these data center buildings, it is usually the case with many alternatives between the pairs of final hosts. Therefore, it is important to evenly measure the volume of traffic across many ways. However, traffic patterns in such data center networks is very different from the traditional Internet [4]. First, big data computer systems like MapReduce and Dyrad remove the partition / combination pattern, when the server is in the middle assign tasks to distributed servers for processing and integration results from them. This is a multi-to-one connection pattern may cause output collapse. Second, flow processes for other applications follow OPEN patterns, which increase explosion and insecurity traffic matrix. Third, most of the flow in data centers is short size, like 10 KB. But there is a small amount of large flow they impact on many bytes of traffic and may even lead to more traffic jams.

Due to special topology and traffic characteristics, traditional uploading algorithms are not well suited for data the middle environment. On the other hand, load balancing schemes traditional networks designed with a large system times and fail to properly measure data traffic institutions. On the other hand, standard measurement of static load Algorithms cannot be combined with congestion information, which is possible leads to congestion in some cases. For example, in general The ECMP uses a fixed acceleration method according to a few fields in the pack headers, as a source IP and local IP, then map the hash value of cost-effective methods to the next hop. ECMP is simple will be distributed to existing networks. However, it is easy causes congestion due to the large flow of flow in the data center networks. Apart from topology and traffic, load balancing formation operating system faces a few new challenges in the data center networks. The first challenge is how to do it on time and accurately find congestion and measure bottle bandwidth way. As the data center traffic explodes too RTT (Round-Trip-Time) network is in microseconds Standard, load rating should respond to congestion in RTT times Second, load balancing should be being strong against reorganization. Packets from the same flow can be balances in different network modes, which may result TCP resets. Reset it not only affects the output of TCP, but also sets it up important overheads of calculation for hosts. Third, the burden scaling uses randomly algorithms of the same set short and long flow. However, the short flow is much delayed sensitivity rather than long flow, so these two types of flow require should be treated in a very different way. Fourth, link failure has been shown to be frequent and disruptive to data centers, thus load balancing should effectively manage the asymmetry created by link failure. In the end, the load balances are facing many small supply challenges in data centers. such as, the implementation of new load balancing algorithms changes and feel all the way to the final hosts, to control the flow path of the final hosts.

II. BACKGROUND

In recent years, data center communication has attracted a lot of attention from both academics and industry. There are available survey documents on data center networks, such as traffic control, bandwidth allocation, data center recognition. Since the design of data center measurement methods requires primarily consideration of data center topology and traffic features, this section provides basic information about data center network structures and data center traffic network applications. In addition, some data center load balancing methods consider power consumption as an important metric. There are different applications running in data center networks ranging from latency-sensitive services like web search, to throughput-sensitive tasks like database update, with the growing applicability of data centers in a wide variety of scenarios, there have been several systematic measurement studies of data center usage to guide practical issues in data center operations

The three key issues for data center network design are

Data Center Traffic Analysis

The traffic originated from a rack in a data center is ON/OFF in nature, where the ON/OFF durations both fit heavy-tailed distributions. But the total traffic matrix is random in nature and lacks predictability.

Data Center Congestion Analysis

It is intuitive to think that loss rates are positively associated with link utilization, but recent studies show that they are irrelative and some special traffic pattern with cause severe packets loss. Besides, link utilization grows

rapidly in higher layers. For example, links in core layers are often observed to achieve as high as 70% link utilization. However, core links surprisingly exhibit the smallest loss rates despite their high link utilizations

Failures in Data Centers

Data centers usually provide high reliability by setting backup equipment's and redundant paths. But link failures and device failures still happen at times in data centers . The reliability and survivability of data center networks are related to network topologies.

III. LOAD BALANCING

As today's data centers provide high path diversities between hosts and exhibit special traffic characteristics, a proper load balancing mechanism is required to improve application performance and network utilization. The main target of load balancing algorithms in data centers is to evenly assign flows among different paths to improve network utilization.

The four primary objectives of the load balancing algorithm:

- High performance
- Scalability
- Robustness
- Energy-efficiency

High performance: There are a variety of different applications in today's data centers, resulting in specific requirements for their flows. Therefore, load balancing mechanisms in data centers should also assign flows based on their requirements. Two main requirements that need to be considered are throughput and latency.

Scalability: The enterprises and organizations are continuously moving their services into data centers, the scale of data center grows sharply in recent years. Most of load balancing mechanisms require to collect or store link utilization information. Some schemes perform optimally in small-scale scenarios, but when the topology scales up, they may become prohibitively expensive to be deployed in practical data center networks.

Robustness: It is stated that link failures and switch crashes happen at times even though the commodity devices in data centers are highly reliable. These failures, if not be quickly processed, will greatly degrade the performance of applications since flow length in data centers are mostly small in size. Besides, topology changes are common in data centers due to software or hardware updates, which will incur paths change between hosts. Therefore, how load balancing algorithms react to failures and topology changes in data centers is a critical issue.

Energy Efficiency: With the growing concern of energy consumption for the Information and Communication Technologies (ICT) industry, much work has been done in the area of energy-efficient framework for data center services such as big data systems and content delivery networks Today's data centers adopt a variety of topologies to provide large bisection bandwidth and multiple backup paths for applications. However, these redundancies in data centers also cause huge energy consumption even when the load is much less stressed.

A typical centralized architecture is shown in Fig. 1. Centralized mechanisms usually employ a global controller. The control plane (determining how to forward traffic) is separated from the data plane (forwarding flows based on the policy of control plane). A controller can collect global information and deal with link failures automatically, and provide a promising manner for centralized real-time traffic scheduling.

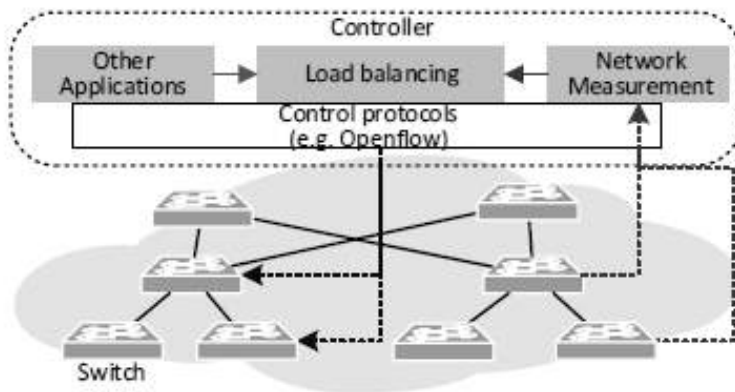


Fig. 1: A typical centralized architecture. The effect of fiber loading on the tensile behaviour of

IV. LITRATURE SURVEY

The Existing data center load balancing mechanisms could be broadly classified into Centralized Mechanisms and Distributed Mechanisms according to their methods of scheduling flows.

Energy-agnostic Centralized Mechanisms. The main purpose of the traffic planning system lies in balancing the load and thus improving overall capacity and reducing flow time. Therefore, a series of traffic planning processes are designed for data centers without regard to power consumption.

M. Al-Fares et.al. [5] Hedera, a central and idle algorithm that aims to measure maximum flow in data centers. It argues that ECMP is unable to properly regulate large flow and may also cause flow collisions. Therefore, Hedera proposes a way to measure the maximum flow and allocate it in the middle to maximize network usage with a smaller schedule. Specifically, for the first time, it gets a large flow in the switch cables. Second, assign methods for this large flow according to the set algorithms. Finally, the controller installs routes to related switches.

FDALB [6] Separates the flow into short distances and long flows and organizes them in different ways. Compared to the Mahout, the limit for short-distance and long-distance separation is read by finalists and can be familiar with different traffic patterns. Long flows are marked with markers for end hosts. Short flows are transmitted alternately using static schemes such as ECMP, while long flows are regulated by a central controller according to global congestion information.

Energy-aware Centralized Mechanisms. Energy efficiency becomes an important factor in data center communication processes. Some of the latest uploading algorithms proposed for data networks also consider power consumption. It is ideal for centralized schemes to collect server information and links. The key points are to make the right trade-off between power efficiency, performance, and durability. Recent power algorithms are very focused on energy efficiency, and simply schedule a load to avoid exceeding link bandwidth or server power.

A highly efficient server-first action plan (MESF) [7] is proposed by cloud-based data centers to reduce server power consumption and meet operational deadline limits. In MESF, the central editor is used to process arrival tasks based on real-time server scores. Server score is determined by the server computing capacity and the type of data center. In order to ensure the completion time of tasks, the server capacity to maintain the type of tasks is set equal to the deadline for these types of tasks. There are two different ones

Data Center Energy-efficient Network-aware Scheduling (DENS) [8] is designed for a data center to reduce energy consumption and improve network performance. When processing tasks, DENS selects appropriate computer resources based on load and communication capacity of servers. Communication power represents the amount of bandwidth from end to end of each server or group of servers. DENS assesses the capacity of each server when new work arrives and uses metric M to represent its score.

Congestion-aware Distributed Mechanisms. In asymmetric topologies, balancing load only according to egress port status may have worse performance when the link congestion occurs in downstream switches. Thus, collecting congestion information and leveraging this information to balance load becomes the motivation of congestion-aware schemes.

Instead of using a single TCP connection, Multipath TCP (MPTCP) [9] leverages the multi-paths between end-hosts and setups multiple sub-connections to make full use of the bandwidth and improve throughput. MPTCP uses the initial SYN to negotiate the use of MPTCP. After the successive establishment of a TCP connection, the client learns from SYN packet that there are additional IP addresses or TCP ports the server may have. Then additional connections can be established using different IP addresses or ports. During the transmission, each MPTCP subflow has its own sequence number and maintains its own congestion window. To make multiple subflows work together.

CONGA [10] is a distributed load balancing system designed for efficiency in 2-tier Leaf-Spine topology. It recognizes that intermediate systems are too slow to respond to congestion and pure local systems are difficult to gather information on global congestion. CONGA is developing a distributed algorithm to detect global congestion between leaf switches. VxLAN technology [11] used for overlay networks is used to manage method information.

Expeditus [12], for Clos-based topology, such as the fat-tree and VL2 to store information on congestion in leaf transformation requires significant memory costs. Therefore, it is almost impossible to gather information on global density in real time. To address this issue, Expeditus suggests two top tree topology designs, a collection of information on one hops and a two-stage selection.

Congestion-agnostic Distributed Mechanisms. Selecting flow paths taking into account congestion information can benefit almost complete performance. However, collecting too much information on congestion requires large hardware or protocol modification, which prevents the use of large amounts.

RepFlow [12] is a simple program that aims to reduce short-term finishing time without adjustment of switches or kernel hosts. RepFlow investigates that short flows in data centers may be affected by long distances while other methods may be used. Therefore, it simply duplicates each short flow and transmits new flow in other ways by creating another TCP connection to the receiver. The flow to RepFlow is transmitted using ECMP and the hash value of the repeated flow is different from the original.

TRILL [14]. It is short for transparent interconnection of lots of links. It is proposed to solve the problems caused by traditional Ethernet networks, such as the convergence problem of STP when there are frequent topology changes, and the bandwidth waste problem because of the single flow tree. Different load balancing algorithms can be implemented based on TRILL. The load balancing algorithm based on TRILL that distributes messages with different MAC addresses in a VLAN evenly between multiple R Bridges. As a result, an R Bridge is only responsible for forwarding messages with allocated MAC addresses.

V. CONCLUSION

Load balancing becomes an important research area that facilitates the completion of flow time, increasing bandwidth usage, and saving energy on data center networks. First, we introduced the data center network topology, traffic features, and key structures and objectives of upload evaluation processes. Then, the difference between load balancing in data centers and traffic engineering over WAN is introduced. This article attempts to briefly evaluate current load balancing technologies.

VI. REFERENCES

- [1]. M. Al-Fares, A. Loukissas, and A. Vahdat, "A Scalable, Commodity Data Center Network Architecture," in Proc. ACM SIGCOMM, 2008, pp. 63–74.
- [2]. A. Greenberg, J. R. Hamilton, N. Jain, S. Kandula, C. Kim, P. Lahiri, D. A. Maltz, P. Patel, and S. Sengupta, "VL2: A Scalable and Flexible Data Center Network," in Proc. ACM SIGCOMM, 2009, pp. 51–62.
- [3]. C. Guo, H. Wu, K. Tan, L. Shi, Y. Zhang, and S. Lu, "Dcell: A Scalable and Fault-tolerant Network Structure for Data Centers," in Proc. ACM SIGCOMM, 2008, pp. 75–86.
- [4]. T. Benson, A. Anand, A. Akella, and M. Zhang, "Understanding Data Center Traffic Characteristics," in Proc. ACM SIGCOMM, 2010, pp. 92–99.
- [5]. M. Al-Fares, S. Radhakrishnan, B. Raghavan, N. Huang, and A. Vahdat, "Hedera: Dynamic Flow Scheduling for Data Center Networks," in Proc. USENIX NSDI, 2010, pp. 19–19.
- [6]. S. Wang, J. Zhang, T. Huang, T. Pan, J. Liu, and Y. Liu, "FDALB: Flow Distribution Aware Load Balancing for Datacenter Networks," in Proc. IEEE/ACM IWQoS, 2016, pp. 1–2.
- [7]. N. Liu, Z. Dong, and R. Rojas-Cessa, "Task Scheduling and Server Provisioning for Energy-efficient Cloud-computing Data Centers," in Proc. IEEE ICDCS, 2013, pp. 226–231.
- [8]. D. Kliazovich, P. Bouvry, and S. U. Khan, "DENS: Data Center Energy-efficient Network-aware Scheduling," Springer Cluster Computing, vol. 16, no. 1, pp. 65–75, 2013.
- [9]. C. Raiciu, S. Barre, C. Pluntke, A. Greenhalgh, D. Wischik, and M. Handley, "Improving Datacenter Performance and Robustness with Multipath TCP," in Proc. ACM SIGCOMM, 2011, pp. 266–277.
- [10]. M. Alizadeh, T. Edsall, S. Dharmapurikar, R. Vaidyanathan, K. Chu, A. Fingerhut, F. Matus, R. Pan, N. Yadav, G. Varghese et al., "CONGA: Distributed Congestion-aware Load Balancing for Datacenters," in Proc. ACM SIGCOMM, 2014, pp. 503–514.

- [11]. M. Mahalingam, D. Dutt, K. Duda, P. Agarwal, L. Kreeger, T. Sridhar, M. Bursell, and C. Wright, "Virtual Extensible Local Area Network (VXLAN): A Framework for Overlaying Virtualized Layer 2 Networks over Layer 3 Networks," RFC 7348, 2014.
- [12]. W. Wang, Y. Sun, K. Zheng, M. A. Kaafar, D. Li, and Z. Li, "Freeway: Adaptively Isolating the Elephant and Mice Flows on Different Transmission Paths," in Proc. IEEE ICNP, 2014, pp. 362–367.
- [13]. H. Xu and B. Li, "Reflow: Minimizing Flow Completion Times with Replicated Flows in Data Centers," in Proc. IEEE INFOCOM, 2014, pp. 1581–1589.
- [14]. "Load Balancing Based on TRILL," <https://patents.google.com/patent/WO2012171462A1/en>



Locomotive Aid for Paralysed People

Leelavathi V V

¹Department of Electronics and Communication Engineering, Government Engineering College,
Chamarajanagar-571313, Karnataka, India

ABSTRACT

This project discusses about a brain-controlled wheel chair based on Brain-computer interfaces (BCI). BCI's are systems that can bypass conventional channels of communication (i.e., muscles and thoughts) to provide direct communication and control between the human brain and physical devices by translating different patterns of brain activity into commands in real time. The intention of the project work is to develop a robot that can assist the disabled people in their daily life to do some work independent of others. Here, we analyse the brain wave signals. Human brain consists of millions of interconnected neurons, the pattern of interaction between these neurons are represented as thoughts and emotional states. According to the human thoughts, this pattern will be changing which in turn produce different electrical waves. A muscle contraction will also be generating a unique electrical signal. All these electrical waves will be sensed by the brain wave sensor and the different pattern is used for controlling a wheel chair.

Keywords: brain-computer interface, wheel-chair, eeg sensor

I. INTRODUCTION

Paralysis is the inability whether temporary or permanent to move a part of the body. In almost all cases, paralysis is due to nerve damage, and it is not because of injury to the affected region. For instance, an injury in the middle or lower regions of the spinal cord is likely to disrupt function below the injury, including the ability to move the feet or feel sensations, even though the actual structures are as healthy as ever. Because of this in patients at least one of the following symptoms results. The brain is unable to relay a signal to an area of the body due to injuries to the brain. Brain-Computer Interface (BCI) also known as "direct neural interface" can provide a direct communication and interaction channel between the user's brain and the computer. BCI helped to direct in assisting, augmenting, or repairing human cognitive or even sensory-motor functions. BCI provides a new direction to construct an interactive system which can translate human Channel based on brain waves and muscles to allow users to communicate without movement with the external world. A BCI system is just to translate EEG signals from a reflection of brain activity into user action through system's hardware and software. [1].

II. OVERVIEW

2.1 Problem Statement Disabled person has trouble moving from one place to other without the help of others. The present system doesn't provide much help since they are manually operated wheel chair. Hence there is need for autonomous system which aid disabled person to move on their own.

2.2 Existing System Existing system consist of manually operated wheel chair which consists of wheel pully which should be rotated by hand to move the wheel chair .The other version consists of motorized wheel chair which is also operated by a remote on the wheel chair. These systems are inefficient when the person using it is physically challenged or disabled due to old age / paralysis.

2.2 Proposed System Our proposed idea consists of a motorized wheel chair, which is controlled using brain signals. This system doesn't depend on operating switches manually or rotating a pully. Since the control mechanism works by intercepting brain signal, it overcomes the main limitation of existing system. Thus, allowing physically challenged and disabled person to use without effort.

2.3 Motivation behind proposed work The motivation of the EEG-controlled wheelchairs is to facilitate assistance in mobility in order to accomplish complex navigational tasks in realistic environments for the paralyzed patients. It includes the development of automatic navigation strategies and personalized interactive assistance to enable the patients to move effectively and easily. One attempt attracting considerable attention in those fields involves the utilization of bio-signals such as an electroencephalogram (EEG) or electromyogram (EMG); obtainable from the human body as a means for interaction with the surrounding world. In the field of brain-computer interface (BCI), meaningful information derived directly from a user's brain activity has been used to manipulate systems. However, despite the definite advantage unique to EEG signals that allows a system to be controlled only by one's thoughts, the poor signal-to-noise ratios in the spontaneous EEG signals and the lack of consistency in the signal ` patterns still make their application impractical.

2.4 Scope of the proposed project

- Advancements in robotics, sensor technology and artificial intelligence promises enormous scope for developing an advanced wheelchair.
- The proposed work deals with engineering an interface between the human brain and an electric wheelchair using a portable EEG brainwave headset and firmware signal processing and filtering.
- The project eliminates the drawbacks of conventional EEG by using a dry sensor technology to pick up EEG signals instead of using a conductive gel and reducing the time it takes to setup.
- This project aims at creating a cost-efficient solution, later intended to be distributed as an add-on conversion unit for a normal wheelchair. Doing so would be of noble and of importance to "brain-active-body-paralyzed patients providing them the independence of mobility.
- The main purpose of this project is to design a wheelchair for severely disabled person move them voluntarily. Their movement of wheelchair can be controlled with their own mind waves.

2.5 Objectives

Independent mobility is a necessity to live everyday life for human beings. A person with physical challenges has restricted mobility. For these people, Brain Computer Interface (BCI) provides a promising solution. The major design objectives of this project are given below.

- To reduce user effort in controlling the wheelchair.
- To ensure the safety during movement.
- A smart wheelchair using inexpensive hardware and open-source software.
- To monitor the activity of the person in real time using sensors
- The designed system should be portable for the user.

III. LITERATURE SURVEY

1. Cecilia L. Maeder; Claudia Sannelli; Stefan Haufe; Benjamin Blankertz: PreStimulus “**Sensorimotor Rhythms Influence Brain-Computer Interface Classification Performance**”: The influence of pre-stimulus ongoing brain activity on post-stimulus task performance has recently been analysed in several studies. While pre-stimulus activity in the parieto-occipital area has been exhaustively investigated with congruent results, less is known about the sensorimotor areas, for which studies reported inconsistent findings. In this work, the topic is addressed in a brain-computer interface (BCI) setting based on modulations of sensorimotor rhythms (SMR). The goal is to assess whether and how peristimulus SMR activity influences the successive task execution quality and consequently the classification performance. Grand average data of 23 participants performing right and Lefthand motor imagery were analysed. Trials were separated into two groups depending on the SMR amplitude in the 1000ms interval preceding the cue, and classification by common spatial patterns (CSPs) pre-processing and linear discriminant analysis (LDA) was carried out in the post-stimulus time interval, i.e., during the task execution. The correlation between trial group and classification performance was assessed by an analysis of variance. As a result of this analysis, trials with higher SMR amplitude in the 1000 ms interval preceding the cue yielded significantly better classification performance than trials with lower amplitude. A further investigation of brain activity patterns revealed that this increase in accuracy is mainly due to the persistence of a higher SMR amplitude over the ipsilateral hemisphere. Our findings support the idea that exploiting information about the ongoing SMR might be the key to boosting performance in future SMR-BCI experiments and motor related tasks in general.

2. Murat Akcakaya; Betts Peters; Mohammad Moghadamfalahi; Aimee R Mooney; Umut Orhan; Barry Oken; Deniz Erdogmus: “**Noninvasive Brain-Computer interfaces for Augmentative and Alternative Communication**”: Brain-computer interfaces (BCIs) promise to provide a novel access channel for assistive technologies, including augmentative and alternative communication (AAC) systems, to people with severe speech and physical impairments (SSPI). Research on the subject has been accelerating significantly in the last decade and the research community took great strides toward making BCI-AAC a practical reality to individuals with SSPI. Nevertheless, the end goal has still not been reached and there is much work to be done to produce real-world worthy systems that can be comfortably, conveniently, and reliably used by individuals with SSPI with help from their families and care givers who will need to maintain, setup, and debug the systems at home. This paper reviews reports in the BCI field that aim at AAC as the application domain with a consideration on both technical and clinical aspects.

3. C Guger, H Ramoser, G Pfurtscheller: “**Real time EEG analysis with subjectspecific spatial patterns for a brain-computer interface (BCI)**”: Electroencephalogram (EEG) recordings during right and left motor imagery

allow one to establish a new communication channel for e.g., patients with amyotrophic lateral sclerosis. Such an EEG-based brain-computer interface (BCI) can be used to develop a simple binary response for the control of a device. Three subjects participated in a series of on-line sessions to test if it is possible to use common spatial patterns to analyse EEG in real time in order to give feedback to the subjects. Furthermore, the classification accuracy that can be achieved after only three days of training was investigated. The patterns are estimated from a set of multichannel EEG data by the method of common spatial patterns and reflect the specific activation of cortical areas. By construction, common spatial patterns weight each electrode according to its importance to the discrimination task and suppress noise in individual channels by using correlations between neighbouring electrodes. Experiments with three subjects resulted in an error rate of 2,6 and 14 days of training and make common spatial patterns a promising method for an EEG-based brain-computer interface.

4. Md. Arif Abdulla Samy; Md. Mirazur Rahman; Tafsir Ahmed Khan: "Extracting and discriminating selective brain signals in non-invasive manner and using them for controlling a device": A cost-efficient approach to brain computer interface (BCI): Publisher: IEEE: The interface through which a human brain establishes links with external devices is generally called Brain Computer Interface. Although there are some significant amounts of ongoing researches on how an overall efficient BCI can be developed are going on, making a cost-efficient approach while dealing with limitless brain patterns is found to be more challenging. In this work, feasibility of a cheaper but appropriate way of extracting and discriminating of several non-invasive EEG signals and using those for controlling devices such as a wheel chair has been proved. To assist the argument of this project, numerous experimental data has been processed to produce several signals, such as, right turn, moving forward, stop etc. for the wheel chair. In the experiment the above mentioned three signals were well distinguished from each other. A microcontroller has been used for processing the signals collected from the brain and hence sending to the wheel chair controlling motors. Despite the challenges of dealing with very low but noise sensitive brain signals, their limitless patterns, and limited scope of necessary circuitries, this work has opened up the scope of feasibility of BCI technology in practical life with a simpler and easier approach.

5. R. S. Naveen; Anitha Julian: "Brain computing interface for wheel chair control: Publisher: IEEE:" Brain-computer interfaces (BCIs) or mind machine interface (MMI) is the direct communication path between brain and external devices. Currently it is difficult for the persons suffering from strokes, amyotrophic lateral sclerosis (ALS) can lead to complete paralysis. Therefore, the BCI system may be used to improve the quality of life of such patients. In this paper we overcome this challenge by introducing a BCI system which helps the patient to navigate the wheelchair from one place to another based-on motor imagery model to control a brain actuated wheelchair. This allows the user to control the direction for four movements left turn, right turn, forward and backward movement, of the simulation or real wheelchair. Experimental trials are to be conducted to assess the BCI control; both a simulated wheelchair in a virtual environment and a real wheelchair were tested. The system will be realized as a standalone hardware unit and will be tested in the field.

6. Nafiul Hasan; Md. Mahmudul Hasan; Md. Akramul Alim: "Design of EEG Based Wheel Chair by Using Color Stimuli and Rhythm Analysis Publisher": IEEE: A novel methodology of brain controlled intelligent wheelchair by using color stimuli is proposed here. A general methodology is applied to find out most effective rhythm for color classification. Primary colors RGB and secondary color yellow were chosen for left, right, forward and stop command. Alpha, Beta, Theta, Delta rhythms were analysed for three different subjects. Using dissimilar

features of time and frequency domain twelve artificial neural network were built to decide the best rhythm. Principal component analysis was made for each EEG signal to remove the background effect of color stimuli. Comparing the findings, it is visualized that beta rhythm is the most efficient rhythm with minimum mean square error of 4.845×10^{-9} among all designed ANN for color classification.

7. Danny Wee-Kiat Ng; Ying-Wei Soh; Sing-Yau Goh: "Development of an Autonomous BCI Wheelchair Publisher: IEEE:" In the society, most of the disabled people especially completely movement impaired ones live like burdens and suffer from severe depression as they have to depend on others for day-to-day activities and cannot contribute to the community. These people may not be able to move their arms or legs but they can certainly think. If their ability to think and make decisions can be utilized in decision making situations and also if they can further be included in industrial automation structure, they will no longer be burden rather they will become man-power to the society. One of the major challenges of involving these people in such processes is making a low-cost device that is affordable by the mass, made with locally available components and also interprets the person's choice accurately. As these people are physically disable, comprehending their electroencephalogram (EEG) signal for blink detection can be an effective solution for translating their choices. EEG-based controlling devices are mobile and can serve as powerful aids for severely disabled people in their daily life. In this work, a low-cost EEG sensor is made with readily available components and a framework is developed to detect voluntary eye blinks. A graphical user interface (GUI) is also developed which is suitable for the impaired person. The eye blinks of the person act as bridge between a set of choices pointed in the GUI and his/her selection interest and thus help the person control home appliances, wheel chair and even computer without depending on others.

8. Soumya Sen Gupta; Sumit Soman; P. Govind Raj; Rishi Prakash: "Detecting eye movements in EEG for controlling devices. Publisher: IEEE:" Eye blinks and lateral eye movements are prominent in EEG signals which are obtained by placing electrodes in the frontal region of the brain. This paper presents a machine learning approach to detect eye movements and blinks from EEG data and map them as intents to control external devices like a computer desktop or a wheel chair.

9. C. S. Ashwin; K. R. Rangarajan; S. Ramachandran: "Disance (enhance the disabled) brain mapped mobility for physically challenged. Publisher: IEEE:" This paper proposes an intelligent robotic wheelchair with user-friendly human computer interface (HCI) based on EEG signal, face directional gesture, and voice. Electroencephalography (EEG) is the recording of electrical activity along the scalp produced by the firing of neurons within the brain. The user has to just think the direction in which the wheel chair has to move. Additionally, at unavoidable circumstances he can use voice or other gestures to signal the movement. The user's intention is transferred to the wheelchair via the HCI, and then the wheelchair is controlled to the intended direction. Additionally, the wheelchair can detect and avoid obstacles autonomously using sonar sensors. By combining HCI into the autonomous functions, it performs safe and reliable motions while considering the user's intention. The proposed robotic Wheelchair is feasible for the disabled and the elderly with severe motor disabilities. This concept gives the user the flexibility to use the device in unknown and evolving scenarios.

10. Lamiya Rahman; Jannatul Adan; Quazi Mutasim Billah; Md Kamrul Islam; A.H.M Mostafa Kamal; Sazzad Hossain: "A low-cost Human Computer Interface for Disabled People based on Eye Blink detection using Brain

Signal :Publisher: IEEE.” In the society, most of the disabled people especially completely movement impaired ones live like burdens and suffer from severe depression as they have to depend on others for day-to-day activities and cannot contribute to the community.

These people may not be able to move their arms or legs but they can certainly think. If their ability to think and make decisions can be utilized in decision making situations and also if they can further be included in industrial automation structure, they will no longer be burden rather they will — 25 become man-power to the society. One of the major challenges of involving these people in such processes is making a low-cost device that is affordable by the mass, made with locally available components and also interprets the person's choice accurately. As these people are physically disable, comprehending their electroencephalogram (EEG) signal for blink detection can be an effective solution for translating their choices. EEG-based controlling devices are mobile and can serve as powerful aids for severely disabled people in their daily life. In this work, a low-cost EEG sensor is made with readily available components and a framework is developed to detect voluntary eye blinks. A graphical user interface (GUI) is also developed which is suitable for the impaired person. The eye blinks of the person act as bridge between a set of choices pointed in the GUI and his/her selection interest and thus help the person control home appliances, wheel chair and even computer without depending on others.

IV. COMPONENTS USED IN THE SYSTEM

4.1 Software Requirement:

1. Arduino IDE

4.2 Hardware Requirement:

1. Arduino Uno
2. Heart beat sensor
3. Blood oxygen sensor (spO2)(MAX30100)
4. Temperature sensor(LM35)
5. Motor Driver(LM239D)
6. DC motor
7. Battery(12V)
8. EEG sensor
9. LCD Display

4.3 Hardware Description

1. ARDUINO UNO The Arduino Uno is an open-source microcontroller board based on the Microchip ATmega328P microcontroller and developed by Arduino.cc. The board is equipped with sets of digital and analog input/output (I/O) pins that may be interfaced to various expansion boards (shields) and other circuits. The board has 14 digital I/O pins (six capable of PWM output), 6 analog I/O pins, and is programmable with the Arduino IDE (Integrated Development Environment), via a type B USB cable. It can be powered by the USB cable or by an external 9-volt battery, though it accepts voltages between 7 and 20 volts. It is similar to the

Arduino Nano and Leonardo. While the Uno communicates using the original STK500 protocol, it differs from all preceding boards in that it does not use the FTDI USB-to-serial driver chip. Instead, it uses the Atmega16U2 (Atmega8U2 up to version R2) programmed as a USB-to-serial converter.

Features of Arduino

The key features of Arduino have been discussed below as follows:

- Arduino boards are able to read analog or digital input signals from different sensors and turn it into an output such as activating a motor, turning LED on/off, connect to the cloud and many other actions.



Figure 4-1 ARDUINO UNO

- You can control your board functions by sending a set of instructions to the microcontroller on the board via Arduino IDE (referred to as uploading software).
- Unlike most previous programmable circuit boards, Arduino does not need an extra piece of hardware (called a programmer) in order to load a new code onto the board. You can simply use a USB cable.
- Additionally, the Arduino IDE uses a simplified version of C++, making it easier to learn to program. Finally, Arduino provides a standard form factor that breaks the functions of the microcontroller into a more accessible package. Arduino UNO board description We chose the Arduino UNO board because it is the most popular board in the Arduino board family. In addition, it is the best board to get started with electronics and coding. Some boards look a bit different from the one given below, but most Arduino have majority of these

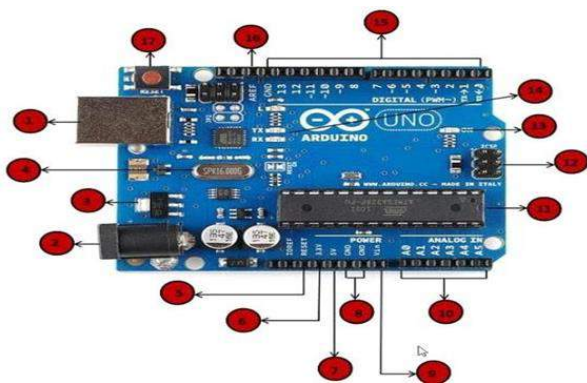


Figure 4 - 2 Arduino UNO Board

components in common. The pin configuration of the Arduino UNO Board is discussed in the below Table 4-1:

Pin No.	Description
1	Power USB: Arduino board can be powered by using the USB cable from your computer. All you need to do is connect the USB cable to the USB connection (1).
2	Power (Barrel Jack): Arduino boards can be powered directly from the AC mains power supply by connecting it to the Barrel Jack (2).
3	Voltage Regulator: The function of the voltage regulator is to control the voltage given to the Arduino board and stabilize the DC voltages used by the processor and other elements.
4	Crystal Oscillator: The crystal oscillator helps Arduino in dealing with time issues. How does Arduino calculate time? The answer is, by using the crystal oscillator. The number printed on top of the Arduino crystal is 16.000H9H. It tells us that the frequency is 16,000,000 Hertz or 16 MHz
5,17	Arduino Reset: You can reset your Arduino board, i.e., start your program from the beginning. You can reset the UNO board in two ways. First, by using the reset button (17) on the board. Second, you can connect an external reset button to the Arduino pin labelled RESET (5).
	Pins (3.3, 5, GND, Vin) 3.3V (6) : Supply 3.3 output volt

2. DC MOTOR

- A DC motor converts DC electrical energy into mechanical energy.
- Basic principle: When a current-carrying conductor is placed in a magnetic field, it experiences a torque and has a tendency to move.
- DC Motor – 100RPM – 12Volts geared motors are generally a simple DC motor with a gearbox attached to it.
- These motors have a 3 mm threaded drill hole in the middle of the shaft thus making it simple to connect it to the wheels or any other mechanical assembly.
- They are very easy to use and available in standard.

5V (7) : Supply 5 output volt

6,7
8,9

(Most of the components used with Arduino board works fine with 3.3 volt and 5 volts.)

GND (8- Ground): There are several GND pins on the Arduino, any of which can be used to ground your circuit.

Vin (9) : Even this pin can be used to power the Arduino UNO board from an external power source, like AC mains power supply.

Analog pins: This board has six analog input pins A0 to A5. These pins can read

10

the signal from an analog sensor like the humidity sensor or temperature sensor and convert it into a digital value that can be read by the microprocessor.

Main microcontroller: Each Arduino board has its own microcontroller (11). You can assume it as the brain of your board. The main IC (integrated circuit) on the Arduino is slightly different from board to board. The microcontrollers are usually of the ATME L Company. You must know what IC your board has before loading up a new program from the Arduino IDE. This information is available on the top of the IC. For more details about the IC construction and functions,

11

you can refer to the data sheet.

ICSP pin: Mostly, ICSP (12) is an AVR, a tiny programming header for the Arduino

12

consisting of MOSI, MISO, SCK, RE SE T, VCC, and GND. It is often referred to as an SPI (Serial Peripheral Interface), which could be considered as an "expansion" of the output. Actually, you are slaving the output device to the master of the SPI bus.

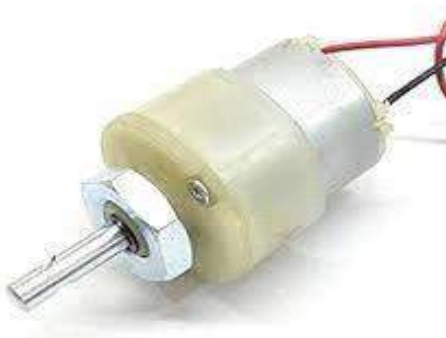


Figure 4 - 3 DC motor

13

Power LED indicator: This LED should light up when you plug your Arduino into a power source to indicate that your board is powered up correctly. If this light does not turn on, then there is something wrong with the connection.

14

TX and RX LEDs: On your board, you will find two labels: TX (transmit) and RX (receive). They appear in two places on the Arduino UNO board. First, at the digital pins 0 and 1, to indicate the pins responsible for serial communication. Second, the TX and RX led (13). The TX led flashes with different speed while sending the serial data. The speed of flashing depends on the baud rate used by the board. RX flashes during the receiving process.

15

Digital I/O: The Arduino UNO board has 14 digital I/O pins (15) (of which 6 provide PWM (Pulse Width Modulation) output. These pins can be configured to work as input digital pins to read logic values (0 or 1) or as digital output pins to drive different modules like LEDs, relays, etc. The pins labelled “~” can be used to generate PWM.

16

ARE F: AREF stands for Analog Reference. It is sometimes, used to set an external reference voltage (between 0 and 5 Volts) as the upper limit for the Analog input pins.

3. MOTOR DRIVER (L298N) Motor driver is a small Current Amplifier whose function is to take a low-current control signal and then turn it into a higher-current signal that can drive a motor. The most popular L298N H-bridge module with onboard voltage regulator motor driver can be used with this motor that has a

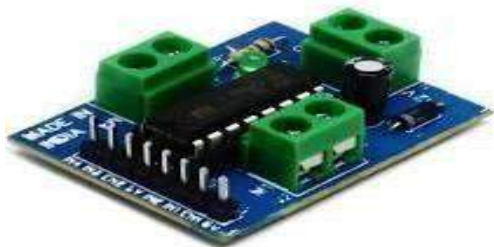


Figure 4 - 4 Motor driver

voltage of between 5 and 35V DC. Nuts and threads on the shaft to easily connect and internally threaded shaft for easily connecting it to the wheel.

4. EEG SENSOR

- The Electroencephalography (EEG) sensor is a non-invasive sensor.
- It has a bipolar configuration with two measurement electrodes which detects the electrical potentials in the specific scalp region and is used in combination with a reference electrode, placed at a region of low muscular activity. The resulting signal is the amplified difference between these two signals and the result of the brain's electrical activity in the monitored scalp region.
- EEG Muscle Sensor Module V3.0 with Cable and electrodes will measure the filtered and rectified electrical activity of a muscle and gives the output 0-Vs Volts depending on the amount of activity in the selected muscle, where Vs signifies the voltage of the power source.
- This Muscle Sensor V3 measures, filters, rectifies and amplifies the electrical activity of a muscle and produces an analog output signal that can easily be read by Arduino microcontroller. Important Features:
- Improved adjustable gain (more rugged).
- Onboard port for new cables .
- Connects to the board straight out of the box.
- Power Supply: Normally $\pm 9V$ dual power supply, minimum voltage is $\pm 3.5V$.
- The body temperature of the patient is measured using this sensor.
- Any abnormality in body temperature will be alerted.
- LM35 is a precision Integrated circuit Temperature sensor, whose output voltage varies based on the temperature around it.
- It is a small and cheap IC which can be used to measure temperature anywhere between $-55^{\circ}C$ to $150^{\circ}C$.
- It can easily be interfaced with Arduino.
- The body temperature of the patient is measured using this sensor.



Figure 4 - 5 Electroencephalography (EEG) sensor

- Power the IC by applying a regulated voltage like +5V (VS) to the input pin and connected the ground pin to the ground of the circuit. Now, you can measure the temperature in form of voltage as shown below:

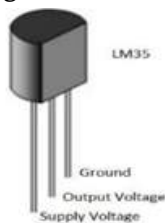


Figure 4 - 6 Temperature sensor: (LM35)



Figure 4-8 A to Mini-B Cable

Step 2 - Download Arduino IDE Software:

One can get different versions of Arduino IDE from the Download Page on the Arduino Official website. We must select our software, which is compatible with our operating system (Windows, IOS, or Linux). Unzip the file, after downloading it completely.

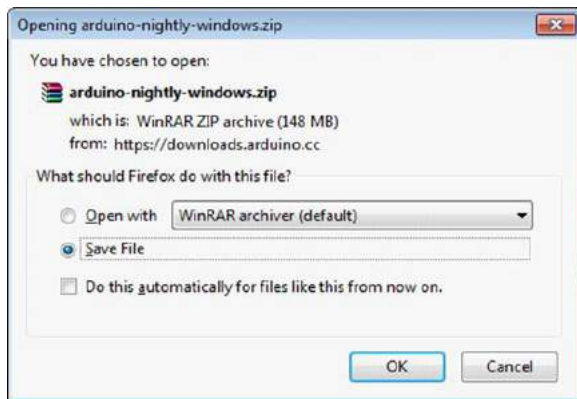


Figure 4 -9 Downloading Arduino IDE

Step 3 - Power up your board:

The Arduino Uno, Mega, Duemilanove and Arduino Nano automatically draw power from either, the USB connection to the computer or an external power supply. If you are using an Arduino Diecimila, you have to make sure that the board is configured to draw power from the USB connection. The power source is selected with a jumper, a small piece of plastic that fits onto two of the three pins between the USB and power jacks. Check that it is on the two pins closest to the USB port. Connect the Arduino board to computer using the USB cable. The green power LED (labelled PWR) should glow.

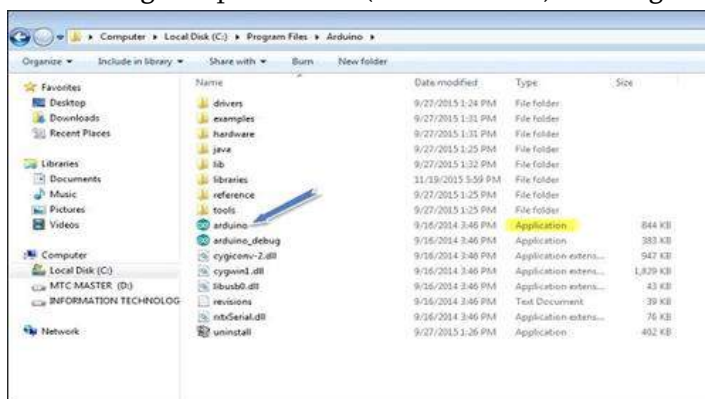


Figure 4 - 10 Launch Arduino IDE

Step 4 -Launch Arduino IDE :

After your Arduino IDE software is downloaded, you need to unzip the folder. Inside the folder, you can find the application icon with an infinity label (application.exe). DoubleClick the icon to start the IDE.

Step 5 - Open your first project:

Once the software starts, we have two options:

- Create a new project. To create a new project, select File →New, as shown in Fig 4-11.

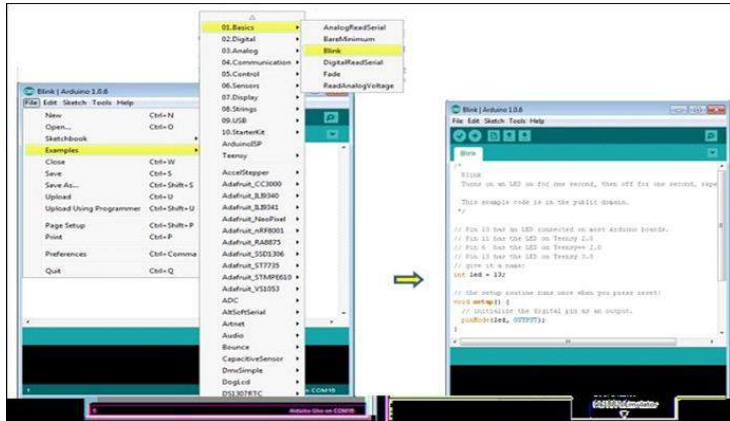


Figure 4 - 11 Creating a New Project

- Open an existing project example. To open an existing project example, select File → Example → Basics → Blink, as shown in Fig. 4.-12. Here, we are selecting just one of the examples with the name Blink. It turns the LED on and off with some time delay. We can select any example from the list.

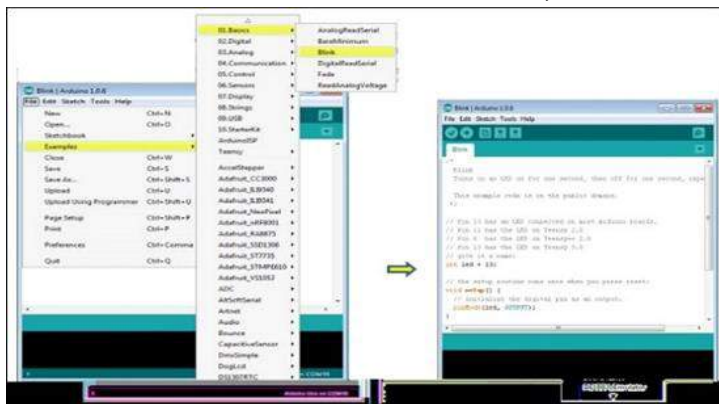


Figure 4 - 12 Opening an Existing Project

Step 6 -Select the respective Arduino board:

To avoid any error while uploading our program to the board, we must select the correct Arduino board name, which matches with the board connected to our computer. Go to Tools → Board and select the board.

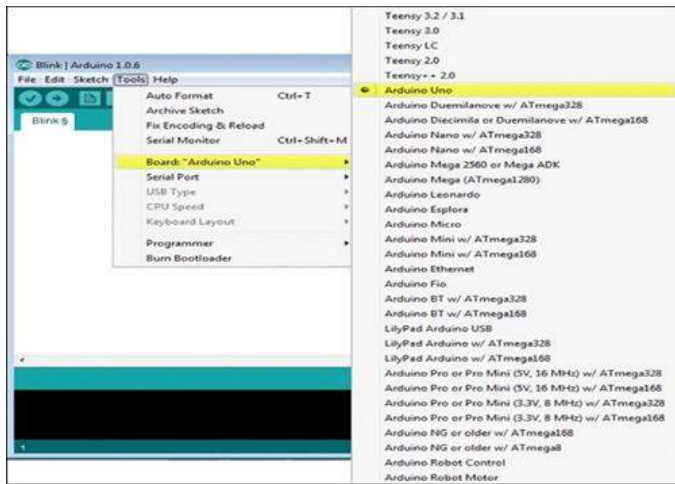


Figure 4 - 13 Selecting the Arduino Board

Step 7 - Select the serial port:

Select the serial device of the Arduino board.

Go to Tools → Serial Port menu.

This is likely to be COM3 or higher (COM1 and COM2 are usually reserved for hardware serial ports).

To find out, you can disconnect your Arduino board and re-open the menu, the entry that disappears should be of

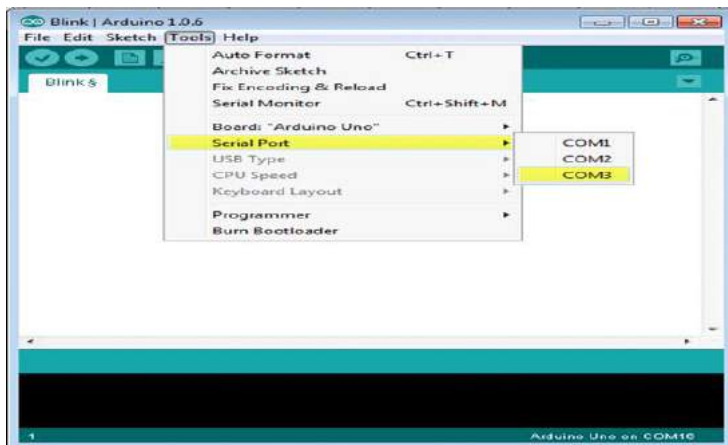


Figure 4 - 14 Selecting the Serial Port

the Arduino board. Reconnect the board and select that serial port.

Step 8 -Upload the program to the board:



Figure 4 - 15 Arduino IDE Toolbar

Before explaining how to upload our program to the board, we should know the function of each symbol appearing in the Arduino IDE toolbar.

- A. Used to check if there is any compilation error.
- B. Used to upload a program to the Arduino board.
- C. Shortcut used to create a new sketch.
- D. Used to directly open one of the example sketches.
- E. Used to save your sketch.
- F. Serial monitor used to send and receive the serial data from the board.

Now, simply click the "Upload" button in the environment. Wait few seconds; we will see the RX and TX LEDs on the board, flashing. If the upload is successful, the message " Done uploading" will appear in the status bar.

• Program Structure

In this section, we will study in depth, the Arduino program structure and we will learn more new terminologies used in the Arduino world. The Arduino software is open-source. The source code for the Java environment is released under the GPL and the C/C++ microcontroller libraries are under the LGPL. Arduino programs are called "sketch".

Arduino programs can be divided in three main parts: **Structure**, **Values** (variables and constants), and **Functions**. Let us learn about the Arduino software program, step by step, and how to write the program without any syntax or compilation error. Let us start with the Structure. Software structure consist of two main functions:

- Setup() function
- Loop() function

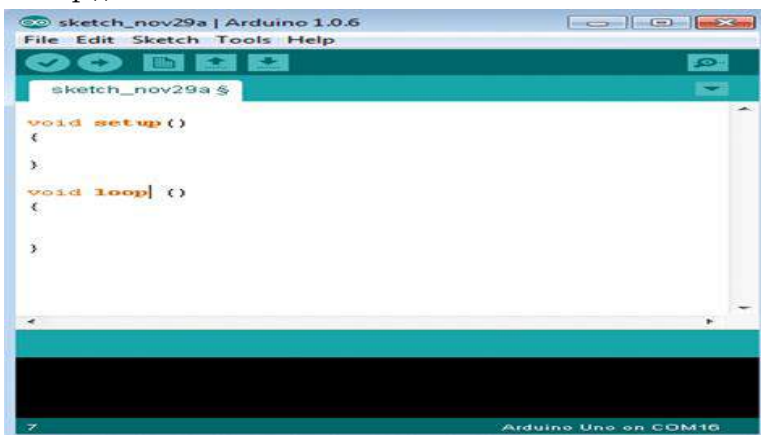


Figure 4 - 16 Structure of a Sketch

The setup () function is called when a sketch starts. It is used to initialize the variables, pinmodes, start using libraries, etc. The setup function will only run once, after each power up or reset of the Arduino board.

After creating a setup () function, which initializes and sets the initial values, the loop() function does precisely what its name suggests, and loops consecutively, allowing our program to change and respond. It actively controls the Arduino board.

• Programming using Embedded C

C is a high-level programming language intended for system programming. Embedded C is an extension that provides support for developing efficient programs for embedded devices. Yet, it is not a part of the C language.

In our internship program, we employed Embedded C programs to write sketches to be dumped on Arduino Uno.

Introduction to Embedded C

Embedded C programming language is an extension to the traditional C programming language that is used in embedded systems.

The only extension in the Embedded C language from normal C Programming Language is the I/O Hardware Addressing, fixed-point arithmetic operations, accessing address spaces, etc.

- Basic Structure of Embedded C Program: The embedded C program has a structure similar to C programming. The five layers of Embedded C programming structure are:
 - Comments
 - Pre-processor directives
 - Global declaration
 - Local declaration
 - Main function ()

The whole code follows the below outline. This is the basic structure of the embedded c program. Each code has a similar outline. Now let us learn about each of this layer in detail.

Outline of an Embedded C code is as shown below:

1. Multiline CommentsDenoted using `/*.....*/`
2. Single Line Comments..... Denoted using `//`
3. Pre-processor Directives.....`#include` or `#define`
4. Global VariablesAccessible anywhere in the program
5. Function Declarations.....Declaring Function
6. Main Function..... Main Function, execution begins here
7. {
8. Local Variables.....Variables confined to main function.
9. Function Calls.....Calling Other Functions
10. Infinite LoopLike while (1) or for (;)
11. Statements
12.
13.
14. }
15. Function DefinitionsDefining the Functions
16. {
17. Local Variables.....Local Variables confined to this Function
18. Statements
19.
20.
21. }

- **Comment Section:** Comments are simple readable text, written in code to make it more understandable to the reader. Usually comments are written in // or /* */. Example: //Test program
- **Global Declaration Section:** The global variables and the user-defined functions are declared in this part of the code. They can be accessed from anywhere.

```
void delay (int);
```

- **Local Declaration Section:** These variables are declared in the respective functions and cannot be used outside the main function.
- **Main Function Section:** All C programs need to have the main function. So does an embedded C program. Each main function contains 2 parts. A declaration part and an Execution part. The declaration part is the part where all the variables are declared. The execution part begins with the curly brackets and ends with the curly close bracket. Both the declaration and execution part are inside the curly braces.

Example:

```
1. void main(void) // Main Function
2. {
3. P1 = 0x00;
4. while(1)
5. {
6. P1 = 0xFF;
7. delay(1000);
8. P1 = 0x00;
9. delay(1000);
10. }
11. }
```

Function Definition Section: The function is defined in this section.

- Arduino Code libraries – Library Structure
- A library is a folder comprised with C++ (.cpp) code files and C++ (.h) header files.
- The .h file describes the structure of the library and declares all its variables and functions.
- The .cpp file holds the function implementation. – **Importing Libraries**

The first thing to do is to find the library we want to use out of the many libraries available online. After downloading it to our computer, we just need to open Arduino IDE and click on Sketch Include Library Manage Libraries. We can then select the library we want to import. Once the process is complete the library will be available in the sketch menu.

- **Arduino Code Explanation** Arduino code is written in C++ with an addition of special methods and functions. C++ is a human-readable programming language. When we create a 'sketch' (the name given to Arduino code files), it is processed and compiled to machine language.

• **Code Structure**

The basic concepts which one should know to write a program on Arduino IDE are discussed below:

– **Libraries**

In Arduino, much like other leading programming platforms, there are built-in libraries that provide basic functionality. In addition, it's possible to import other libraries and expand the Arduino board capabilities and features. These libraries are roughly divided into libraries that interact with a specific component or those that implement new functions. To import a new library, we need to go to Sketch > Import Library.

In addition, at the top of our file, we have to use 'include' to include external libraries. We can also create custom libraries to use in isolated sketches.

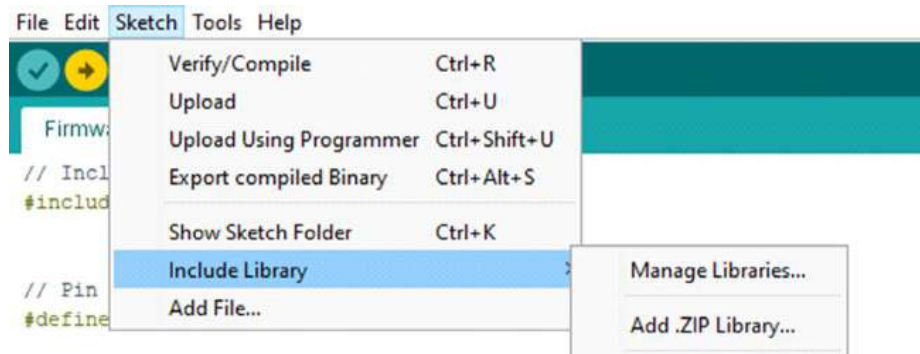


Figure 4 - 17 Include library

– Pin Definitions

To use the Arduino pins, we need to define which pin is being used and its functionality. A convenient way to define the used pins is by using: 'define pinName pinNumber'. The functionality is either input or output and is defined using the pinMode () method in the setup section.

– Declarations

– **Variables** Whenever we're using Arduino, we need to declare global variables and instances to be used later on. In a nutshell, a variable allows us to name and store a value to be used in the future. For example, we would store data acquired from a sensor in order to use it later. To declare a variable, we simply define its type, name and initial value. It's worth mentioning that declaring global variables isn't an absolute necessity. However, it's advisable to declare variables to make it easy to utilize our values further down the line.

– Instances

In software programming, a class is a collection of functions and variables that are kept together in one place. Each class has a special function known as a constructor, which is used to create an instance of the class. In order to use the functions of the class, we need to declare an instance for it.

– Setup()

Every Arduino sketch must have a setup function. This function defines the initial state of the Arduino upon boot and runs only once. Here we'll define the following: * Pin functionality using the pinMode function

- * Initial state of pins
- * Initialize classes
- * Initialize variables
- * Code logic

– Loop()

The loop function is also a must for every Arduino sketch and executes once

setup () is complete. It is the main function and as its name hints, it runs in a loop over and over again. The loop describes the main logic of our circuit.

– Code Logic

The basic Arduino code logic is an “if-then” structure and can be divided into 4 blocks:

– Setup

It will usually be written in the setup section of the Arduino code, and performs things that need to be done only once, such as sensor calibration.

– Input

At the beginning of the loop, read the inputs. These values will be used as conditions (“if”) such as the ambient light reading from an LDR using analogRead ().

– Manipulate Data

This section is used to transform the data into a more convenient form or perform calculations. For instance, the AnalogRead () gives a reading of 0-1023 which can be mapped to a range of 0- 255 to be used for PWM. (See analogWrite ()).

– Output

This section defines the final outcome of the logic (“then”) according to the data calculated in the previous step. Looking at an example of the LDR and PWM, turns on an LED only when the ambient light level goes below a certain threshold.

• From Software to Hardware

There is a lot to be said of Arduino’s software capabilities, but it’s important to remember that the platform is comprised of both software and hardware. The two works in tandem to run a complex operating system. Code → Compile → Upload → Run At the core of Arduino, is the ability to compile and run the code. After writing the code in the IDE we need to upload it to the Arduino. Clicking the Upload button (the rightfacing arrow icon), will compile the code and upload it if it passed compilation. Once the upload is complete, the program will start running automatically.

V. PROPOSED SYSTEM DESIGN (HARDWARE)

5.1 Detailed block diagram

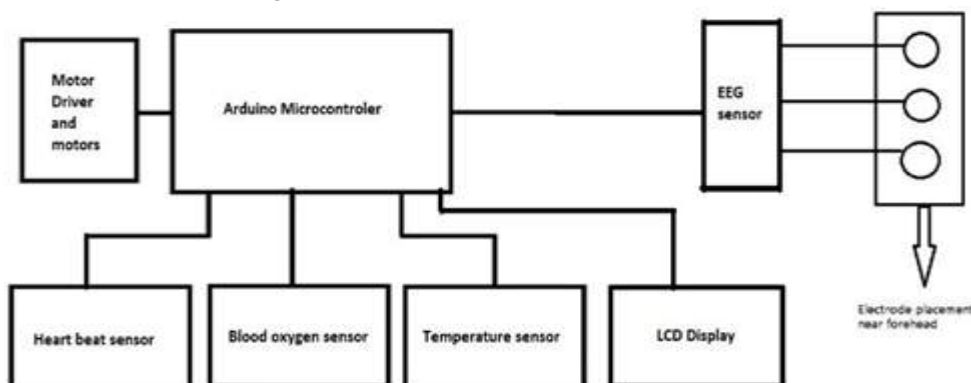


Figure 5 - 1 Block Diagram

5.2 Detailed design

The brain of the system is Arduino microcontroller. The system is designed to control the movement of wheel chair using EEG sensor. EEG sensor intercepts and measures the electrical signal sent by brain to control muscle movement. The electrodes from EEG sensors are attached near forehead when person tries to move eyes, The signal is intercepted. The system is de-signed to recognize different pattern of eye movement, like blinking, blinking fast, hard blink and these patterns are used to control the direction of wheel chair.

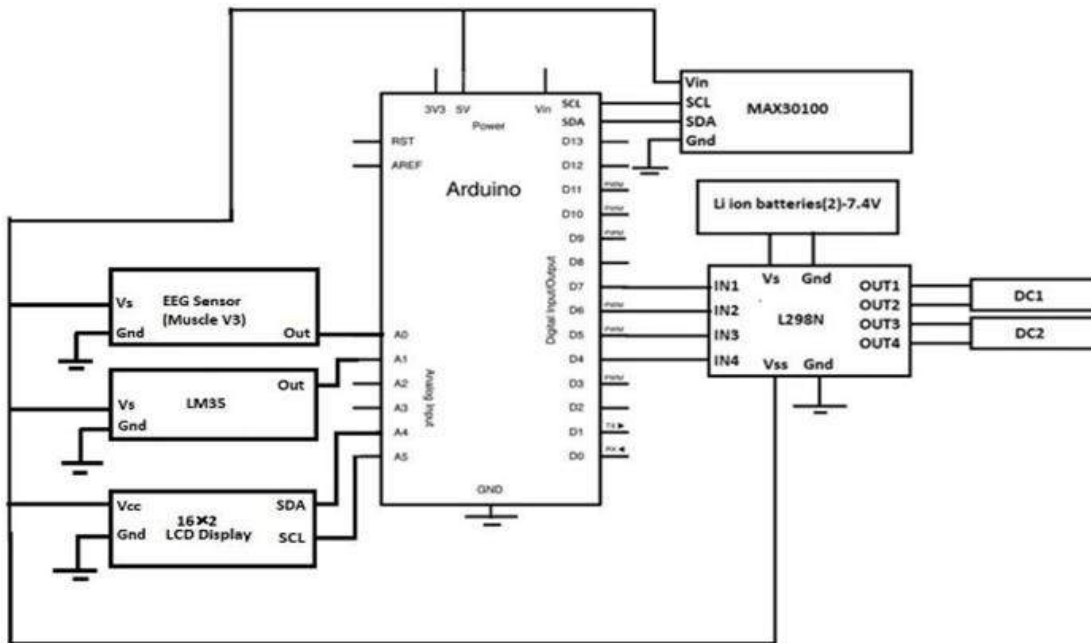
Various other sensors are used to monitor the health of the patient.

1. Heart beat sensor: The heart beat sensor is attached to micro con- troller, it measures the heart rate of patient, and if the heart rate is too low or high than the threshold value, micro controller gives alert sound.

2. Blood Oxygen Sensor: This sensor measures the oxygen concentration level in blood of patient. This is very important parameter to be checked because paralyzed patients don't have control on their lungs and other diseases like asthma may worsen the effect. If the measured value is less than threshold value an alert will be given by the system.

3. Temperature sensor: The body temperature of the patient is measured using this sensor, any abnormality in body temperature will be alerted.

5.3 Designed circuit



VI. PROPOSED SYSTEM DESIGN (SOFTWARE)

6.1 Program

```
int brainSignalThreshold =250 ; // variable used to store threshold value of brain
////////////////////////////////////// #include<wire.h>
#include "MAX30100_PulseOximeter.h" // MAX30100 library
#define REPORTING_PERIOD_MS 1000 // setting the time gap (ms) at which new measurement
```

```

PulseOximeter pox; // creating object 'pox' for class PulseOximeter
uint32_t    tsLastReport    =    0;    //    creating    variable    to    store    time
//////////////////////////////////////////////////// //lcd declaration
#include<LiquidCrystal_I2C.h> // library to interface lcd LiquidCrystal_I2C lcd(0x27,16,2); // initializing lcd
with    address    0x27    ,and    its    variables    used    in    temperature    sensor
////////////////////////////////////////////////////
int ThermistorPin = A2; // thermistor connected to pin A2
int Vo;
float R1 = 1000; // resistor connected to thermistor and its value in ohm
float logR2, R2, T;
float c1 = 1.009249522e-03, c2 = 2.378405444e-04, c3 = 2.019202697e-07;
//////////////////////////////////////////////////// //motor pin assign
int left_motor_1 = 4; // left motor first pin to pin 4
int left_motor_2 = 5; // left motor second pin to pin 5
int right_motor_1 =7;// right motor first pin to pin 7
int right_motor_2 =8;// right motor second pin to pin 8
////////////////////////////////////////////////////

//variable used in functioning of wheel chair movement
long currentTime ,pastTime=0; // variable to store time
int mode=0; // this variable decides mode of vehicle i.e 0= forward ,1= backward

////////////////////////////////////////////////////
void setup()
{ // put your setup code here, to run once:
Serial.begin(9600); // declare all motor pin as output pinMode(left_motor_1,OUTPUT);
pinMode(left_motor_2,OUTPUT); pinMode(right_motor_1,OUTPUT);
pinMode(right_motor_2,OUTPUT); //Set State of Pins all to LOW (0) digitalWrite(left_motor_1,0);
digitalWrite(left_motor_2,0);
digitalWrite(right_motor_1,0);
digitalWrite(right_motor_2,0);

////////////////////////////////////////////////////
lcd.init(); // INITIALIZE THE LCD
lcd.backlight(); // IT WILL TURN ON BACK LIGHT
lcd.clear();
lcd.setCursor(0,1);
lcd.print(" FORWARD");
delay(500);

```



```

if(mode==1){
  mode=2;
  lcd.setCursor(0,1);
  lcd.print(" BACKWARD");
  break;
}
}
break;// break out of action } } // while loop end
}
else {
stopcar();
}
////////////////////////////////////
}
void moveChair()
{
if (mode ==0){
  forward();
}
if(mode == 1){
backward();
}
if(mode == 2){
right();
}
if(mode == 3){
left();
}
} //////////////////////////////////////////////////
void check_health(){
  pox.update();
if (millis() - tsLastReport > REPORTING_PERIOD_MS) {
  lcd.setCursor(0,0);
  lcd.print(" ");
  Vo = analogRead(ThermistorPin);
  R2 = R1 * (1023.0 / (float)Vo - 1.0);
  logR2 = log(R2);
  T = (1.0 / (c1 + c2*logR2 + c3*logR2*logR2*logR2));
  T = T - 273.15;
}

```



```
T = (T * 9.0) / 5.0 + 32.0;
lcd.setCursor(0,0); // TO SET WRITING POSITION ON LCD ( COL,ROW)
lcd.print(int(pox.getHeartRate()));
lcd.print(" B/S:");
lcd.print(int(pox.getSpO2())); // (" ")
lcd.print(" T:");
lcd.print(int(T));
tsLastReport = millis();
}
}
void forward(){
digitalWrite(left_motor_1,1); //Turn digital out left_motor_1 to High
digitalWrite(left_motor_2,0); //Turn digital out left_motor_2 to Low
digitalWrite(right_motor_1,1); //Turn digital out right_motor_1 to High
digitalWrite(right_motor_2,0); // turn digital out right_motor_2 to low
}
void backward(){
digitalWrite(left_motor_1,0);
digitalWrite(left_motor_2,1);
digitalWrite(right_motor_1,0);
digitalWrite(right_motor_2,1);
}

void left(){
digitalWrite(left_motor_1,0);
digitalWrite(left_motor_2,1);
digitalWrite(right_motor_1,1);
digitalWrite(right_motor_2,0);
}
void right(){
digitalWrite(left_motor_1,1);
digitalWrite(left_motor_2,0);
digitalWrite(right_motor_1,0);
digitalWrite(right_motor_2,1);
}

void stopcar(){
digitalWrite(left_motor_1,0);
```

```
digitalWrite(left_motor_2,0);
digitalWrite(right_motor_1,0);
digitalWrite(right_motor_2,0);
}
void onBeatDetected()
{
Serial.println("Beat!");
}
```

6.2 Flowchart

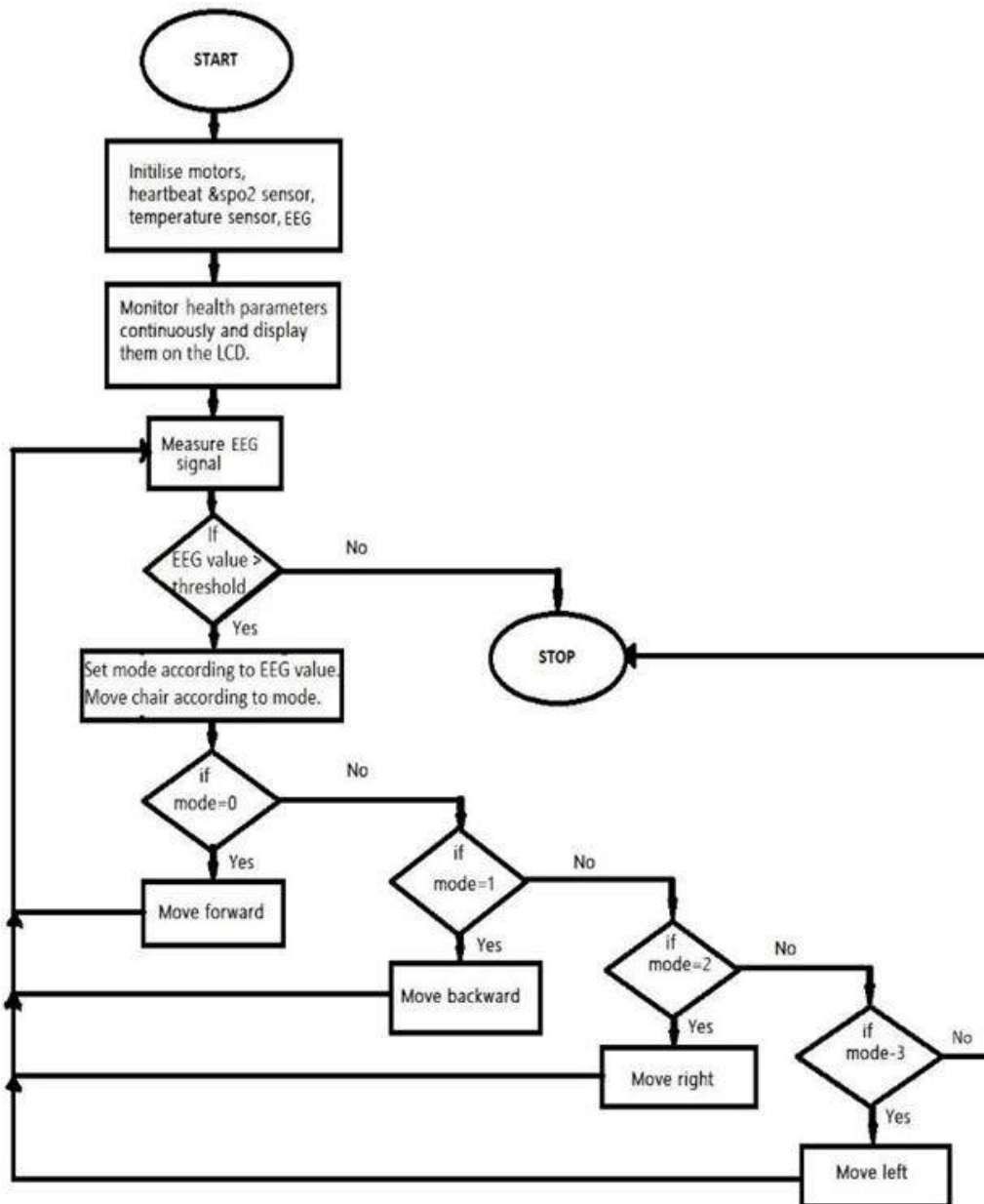


Figure 6-1 Flow chart

VII. RESULTS AND DISCUSSION

7.1 Project model result. CASE 1: Temperature and Heartbeat is measured continuously and displayed on LCD screen.

- In this case, Temperature sensor reading showing 85 degrees Celsius.



Figure 7 - 1 Temperature sensor reading

- In this case, MAX30100 sensor readings showing pulse rate as 102 bpm and oxygen concentration as 95%.



Figure 7 - 2 MAX30100 sensor readings

CASE 2: Direct modes can be changed by concentrating greater than 1 second and less than 2 seconds. The modes are FORWARD, BACKWARD, RIGHT and LEFT. • In this case, Display showing wheelchair moving in FORWARD direction



Figure 7 - 3 Display showing FORWARD movement

- In this case, Display showing wheelchair moving in BACKWARD direction.



Figure 7-4 Display showing BACKWARD movement

- In this case, Display showing wheelchair moving in LEFT direction.



Figure 7-5 Display showing LEFT direction

- In this case, Display showing wheelchair moving in RIGHT direction.



- Figure 7-6 Display showing RIGHT direction

CASE 3: The wheelchair can be moved in set direction mode by concentrating for more than 2 seconds.

7.2 Final Result Image

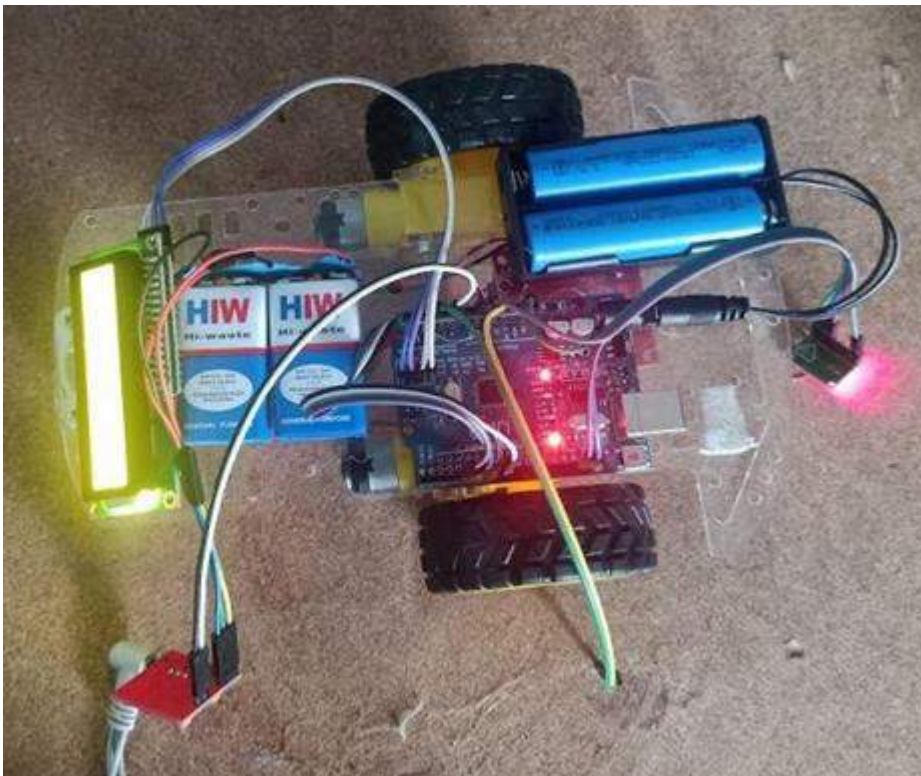


Figure 7-7 Working model of wheelchair controlled using brain as bio-sensor

7.3 Advantages

- The wheel chair without the tiresome turning of the wheels is a simple step ahead of the electrical wheelchairs.
- It may prove beneficial for every individual for locomotion purposes without the need of manual labour.
- The simultaneous EEG acquisition may detect any substantial improvement in the condition of the body.

7.4 Disadvantages

- The fixing of the electrodes must be done before any further course.
- The mental state must be stable at all times.
- Some training is must before it is fully efficient and used for practical purposes.

7.5 Applications

- The developments in the field of brain computer interface are a juvenile step towards the improvement of the wheel chair.
- The wheel chair controls only two wheels whereas the same condition may be used to drive a car with four wheels.
- The functionality of the brain can be used to trounce many other manual works at industries as well as household levels.
- The day today gadgets may be evolved to work using mind waves.

VIII. CONCLUSION

Appropriate assistive technology often helps people with disabilities compensate, at least in part, for a limitation. This specialized technology promotes independence and decreases the need for other support.

IX. REFERENCES

- [1]. Cecilia L. Maeder; Claudia Sannelli; Stefan Haufe; Benjamin Blankertz: PreStimulus Sensorimotor Rhythms Influence Brain-Computer Interface Classification Performance.
- [2]. Murat Akcakaya; Betts Peters; Mohammad Moghadamfalahi; Aimee R Mooney; Umut Orhan; Barry Oken; Deniz Erdogmus: Noninvasive Brain-Computer interfaces for Augmentative and Alternative Communication.
- [3]. C Guger, H Ramoser, G Pfurtscheller: Real time EEG analysis with subject-specific spatial patterns for a brain-computer interface (BCI).
- [4]. Md. Arif Abdulla Samy; Md. Mirazur Rahman; Tafsir Ahmed Khan: Extracting and discriminating selective brain signals in non-invasive manner and using them for controlling a device: A cost-efficient approach to brain computer interface (BCI): Publisher: IEEE.
- [5]. R. S. Naveen; Anitha Julian: Brain computing interface for wheel chair control: Publisher: IEEE.

- [6]. Nafiul Hasan; Md. Mahmudul Hasan; Md. Akramul Alim:Design of EEG Based Wheel Chair by Using Color Stimuli and Rhythm Analysis Publisher: IEEE.
- [7]. Danny Wee-Kiat Ng; Ying-Wei Soh; Sing-Yau Goh:Development of an Autonomous BCI Wheelchair Publisher: IEEE.
- [8]. C. S. Ashwin; K. R. Rangarajan; S. Ramachandran:Disance (enhance the disabled) brain mapped mobility for physically challenged Publisher: IEEE.
- [9]. Lamiya Rahman; Jannatul Adan; Quazi Mutasim Billah; Md Kamrul Islam; A.H.M Mostafa Kamal; Sazzad Hossain:A low-cost Human Computer Interface for Disabled People based on Eye Blink detection using Brain Signal :Publisher: IEEE.
- [10]. Soumya Sen Gupta; Sumit Soman; P. Govind Raj; Rishi Prakash: Detecting eye movements in EEG for controlling devices Publisher: IEEE.



Change Detection for Critical Infrastructure Protection System

Rudrappa K M

Associate Professor & HOD, Department of EEE, GEC, Mosalehosahalli, Hassan, Karnataka, India

ABSTRACT

In real world applications, tracking target in low resolution video is a challenging task because there is loss of discriminative detail in the visual appearance of moving object. The existing methods are mostly based on the enhancement of LR (low resolution) video by super resolution techniques. But these methods require high computational cost. This cost further increases if we are dealing with events detection. This paper presents an algorithm which is able to detect unusual events without such type of conversion and well suited for enhancement of security of ATMs where conventional low resolution cameras are generally used due to their low cost.

Proposed algorithm only uses close morphological operation with disk like structuring element in the pre-processing steps to cope up with low resolution video. It further uses rolling average background subtraction technique to detect foreground object from dynamic background in a scene. The proposed algorithm is able to recognize the occurrence of uncommon events such as overcrowding or fight in the low resolution video simply by using statistical property, standard deviation of moving objects. It is fast enough because it process low resolution frames and could be helpful in surveillance system for enhancing the security of ATMs where conventional camera of low resolution are still used. It does not use any classifier and avoids the requirement of training the system initially.

Keywords: ATM, MATLAB, Face detection, resolution

I. INTRODUCTION

An Automated Teller Machine (ATM) [1-2] allows customers to perform banking transactions [3] any and at any time without the need of human teller. By using a debit or ATM card at an ATM, individuals can withdraw cash from current or savings accounts, make a deposit or transfer where money from one account to another or perform other functions.

As is often the case with inventions, many inventors contribute to the history of an invention. In the case of the ATM, Don Wetzel invented the first successful and modern ATM in the USA, however he was not first inventor to create an ATM. In 1939, Luther George Simian started patenting an earlier and not-so-successful version of an ATM. An automatic teller machine or ATM allows a bank customer to conduct their banking transactions from almost every other ATM machine in the world. Don Wetzel was the conceptualist and chief

conceptualist of the automated teller machine, an idea he said he thought of while waiting in line at a Dallas bank.

At the time (1968) Wetzel was the Vice President of Product Planning at Ductal, the company that developed automated baggage-handling equipment. The other two inventors listed on the patent were Tom Barnes, the chief mechanical engineer and George Chastain, the electrical engineer. It took five million dollars to develop the ATM. The concept of the modern ATM first began in 1968, a working prototype came about in 1969 and Ductal was issued a patent in 1973. The first ATMs were off-line machines, meaning money was not automatically withdrawn from an account. The bank accounts were not (at that time) connected by a computer network to the ATM. Therefore, banks were at first very exclusive about who they gave ATM privileges to.

II. TYPES OF ATM ATTACK ON ATM

There are a variety of ATM attacks because it is such an attractive target. There are three basic types of ATM attacks:

Physical attack:

Brute force attack to ATM machines with the intention of gaining access to cash within the safe.

ATM Fraud:

The gang will remove the device with the cash glued on it using their special prying tool.

Software and network attack:

Theft of sensitive information or controlling ATM spew out bills automatically

Money lost by ATM attacks:

In the past few decades, significant efforts in the field of moving object detection and tracking have been done to make following applications reliable, robust and efficient: video surveillance, robotics, authentication system, media production, biological research etc. But there are many challenges which produce hurdles in the improvement of these applications. These challenges may include illumination change, dynamic background, camouflage, occlusion, shadow etc. These obstacles become more cumbersome when we perform object tracking in low resolution video. In low resolution video it is very difficult to accurately find out the object of interest because most of the discriminative details such as visual features and primitives have been lost. It results in inaccurate object tracking which further lead to inefficient event detection. But there are certain benefits of using low resolution video such as it requires low storage, transmission.

III. EXISTING METHODS

In the literature of abnormal event detection, most of the methods as in uses classifiers to recognize the events and does not use video input. These classifiers require learning time and careful attention on training dataset. Some approaches require manual setup initially in the automated event detection system and have high computational cost. From the literature we come to the fact that we need an algorithm which deals with uncommon even detection in video to assist a fully automated surveillance [4] system.

METHODOLOGY: The methodology consists of two sections such as Transmitter and receiver sections. The block diagrams of transmitter and receiver sections are as shown in the figure 1 and figure 2 respectively.

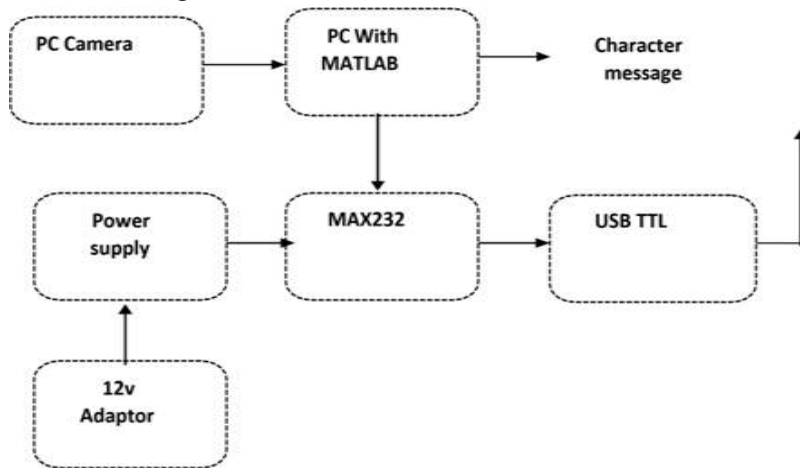


Figure 1: Transmitter Section

The characters from the MATLAB coding is Transmitted to the Hardware in order to get the exact Event that had occurred inside the ATM. The simulation part consists where the code helps us to identify the exact picturization of events. The MAX232 is a integrated circuit which is designed bu Maxim integrated Products that converts signals from a RS-232 serial port to signals suitable for use in TTL-compactable digital logic circuits.

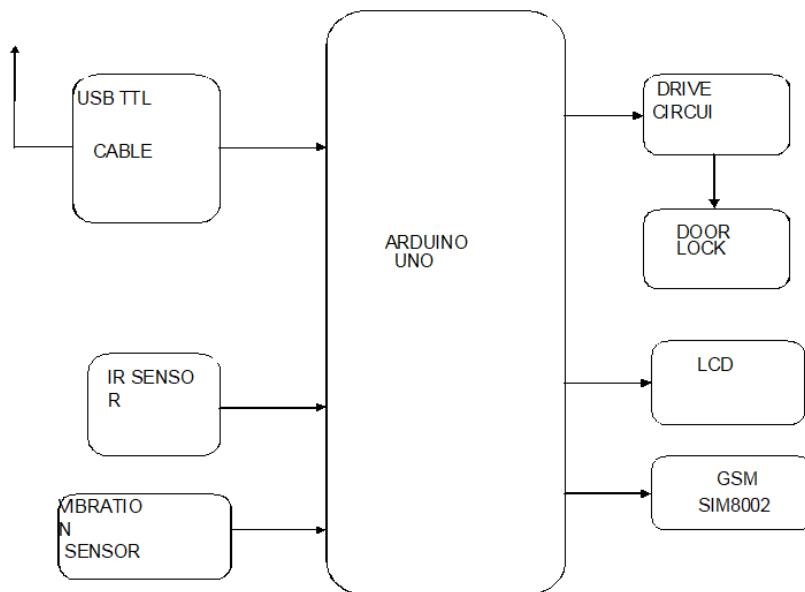


Figure 2: Receiver section

The receiver part of Block Diagram is as shown in the figure 2. The detailed description of each and every block is explained in Hardware requirements Section. The Character from the transmitter end is received by USB TTL Cable and hence transfer it into controlled called Arduino UNO, where the controller identifies the event that ad happened inside the ATM with the help of MATLAB code. Thus the respective results will be displayed with the help of LCD, Automatic message to owner and in charged person will be sent through GSM and hence automatically door will be locked up in order to caught the victims

Software Implementation

MATLAB

I have chosen MAT Lab to use as the programming language. It is a high-level language that specializes in data analysis and computing mathematical problems. Mat lab's official website can be found at www.mathworks.com.

The program environment has an interactive command window that allows users to test and experiment with the code line by line. Users can also save their codes into an M-file and run the program. The Mat lab Help Navigator is also very useful. It properly categorizes and provides detailed explanations and sample usages of all functions. Just like C++ and Java, the language syntax provides loops and condition statements for programming purposes.

The language was chosen over C++ and Java because there are a lot of built-in functions that are specific for image processing. As well, the compiler can compute large mathematical equations faster than other languages. These advantages suit the project perfectly due to the large matrix computations required during the extraction process.

EMBEDDED C PROGRAMMING:

The soul of the processor functioning inside each and every embedded system we come across in our daily life, such as mobile phone, washing machine, and digital camera. Each processor is associated with an embedded software. The first and foremost thing is the embedded software that decides functioning of the embedded system. Embedded C language is most frequently used to program the microcontroller.

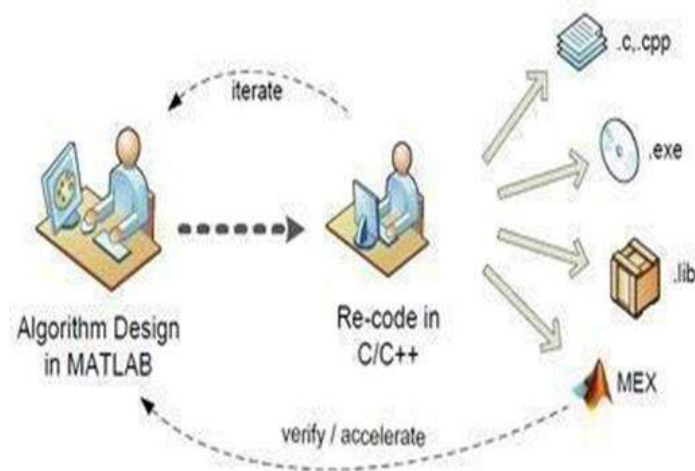


Figure 3: Embedded C Programming

FLOW CHART FOR WORKING:

The flow chart for working of change detection for critical infrastructure protection is as shown in the figure 4.

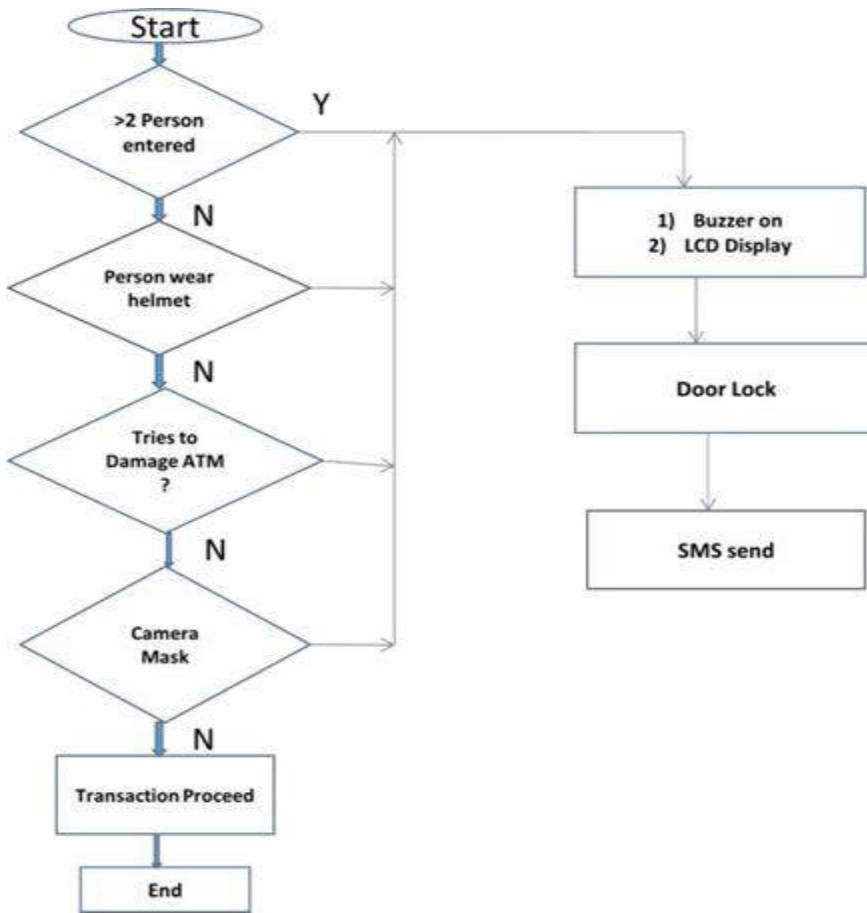


Figure 4: Working flow chart

FLOW CHART FOR CODING:

Similarly, the flow chart for programming is as shown in the figure 5.

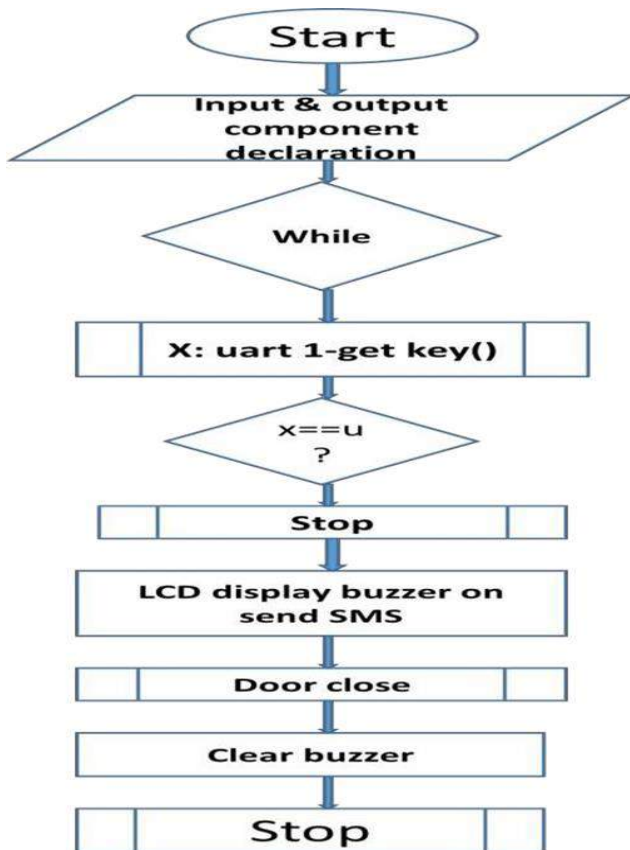


Figure 5: Coding flow chart

IV. RESULTS

The results were considered for various possibilities.

When Person is detected:

Initially the motion is detected in the ATM. If there is any motion it will start the process of person detection and after person detection output is shown in the terminal and the user is allowed to access the ATM. The process wise results are shown in following figures 6(a) to 6(d).



Figure 6 (a): First Validation Message



Figure 6(b): Motion Detected in ATM

When ATM damaged:

Initially the vibration is detected in the ATM. If there is any vibration is detected it will start the process after output is shown in the terminal.

When multiple persons entered

Initially counts the number of persons entered in the ATM. If there is more than 2 persons entered it will start the process after output is shown in the terminal.

When person wearing a helmet:

Initially recognizes the person wearing helmet inside the ATM. If there is any person wearing the helmet it will start the process after output is shown in the terminal.



Figure 6(c): Unusual Event Detection

When person wearing a mask:

Initially recognizes the person wearing mask inside the ATM. If there is any person wearing the mask it will start the process after output is shown in the terminal.

When person receives SMS through GSM:

Figure 6(d): SMS through GSM

V. CONCLUSION

ATM model developed is more reliable in providing security. The implementation of ATM surveillance by using smart sensors and GSM modem took advantages of the stability and reliability of sensor characteristics. The security features were enhanced largely for protection of ATM's when compared to previous systems. The security features were enhanced largely for protection of ATM's when compared to previous systems. The system will be built on the technology of embedded system which makes the system more safe, reliable and easy to use. Once the Unusual Event is detected for longer duration of time through the GSM (Global system for mobile communication) the message signal is immediately sent to the higher authority person. Similarly, when crowd is detected, through the GSM the message signal is immediately sent to the higher authority person. This method is secure and efficient in terms of computational complexity and threshold values. Thus this system will be able to what physical attacks on the ATM and alerts necessary people to take action at any time and save people from lot of hardships involved in the ATM attacks

VI. REFERENCES

- [1]. Sudhir Goswami, Jyoti Goswami, Nagresh Kumar, "Unusual Event Detection in Low Resolution Video for enhancing ATM security", 2nd International Conference on Signal Processing and Integrated Networks (SPIN), 2015.
- [2]. Saleem Ulla Shariff ; MaheboobHussain ; Mohammed Farhaan Shariff, "Smart unusual event detection using low resolution camera for enhanced security", 2017 International Conference on Innovations in Information, Embedded and Communication Systems (ICIIECS), 17-18 March 2017
- [3]. Jignesh J. Patoliya; Miral M. Desai, "Face detection based ATM security system using embedded Linux platform", 2017 2nd International Conference for Convergence in Technology (I2CT), 7-9 April 2017.
- [4]. Sharayu Sadashiv Phule; Sharad D. Sawant, "Abnormal activities detection for security purpose unattended bag and crowding detection by using image processing", 2017 International Conference on Intelligent Computing and Control Systems (ICICCS), 15-16 June 2017.
- [5]. G. Renee Jebaline, S. Gomathi, "A Novel Method to Enhance the Security of ATM using Biometrics," 2015 International Conference on Circuit, Power and Computing Technologies [ICCPCT] 978-1-4799- 7075-9 ©2015 IEEE.
- [6]. Vikas Tripathi, Durgaprasad Gangodkar, Vivek Latta, and Ankush Mittal, "Robust Abnormal Event Recognition via Motion and Shape Analysis at ATM Installations", Journal of Electrical and Computer Engineering, Volume 2015.
- [7]. S.Shriram, Swastik B.Shetty, Vishnuprasad P. Hegde , KCR Nisha, Dharmambal V , "Smart ATM Surveillance System", 2016 International Conference on Circuit, Power and Computing Technologies [ICCPCT].



Change Detection for Critical Infrastructure Protection System

Rudrappa K M

Associate Professor & HOD, Department of EEE, GEC, Mosalehosahalli, Hassan, Karnataka, India

ABSTRACT

In real world applications, tracking target in low resolution video is a challenging task because there is loss of discriminative detail in the visual appearance of moving object. The existing methods are mostly based on the enhancement of LR (low resolution) video by super resolution techniques. But these methods require high computational cost. This cost further increases if we are dealing with events detection. This paper presents an algorithm which is able to detect unusual events without such type of conversion and well suited for enhancement of security of ATMs where conventional low resolution cameras are generally used due to their low cost.

Proposed algorithm only uses close morphological operation with disk like structuring element in the pre-processing steps to cope up with low resolution video. It further uses rolling average background subtraction technique to detect foreground object from dynamic background in a scene. The proposed algorithm is able to recognize the occurrence of uncommon events such as overcrowding or fight in the low resolution video simply by using statistical property, standard deviation of moving objects. It is fast enough because it process low resolution frames and could be helpful in surveillance system for enhancing the security of ATMs where conventional camera of low resolution are still used. It does not use any classifier and avoids the requirement of training the system initially.

Keywords: ATM, MATLAB, Face detection, resolution

I. INTRODUCTION

An Automated Teller Machine (ATM) [1-2] allows customers to perform banking transactions [3] any and at any time without the need of human teller. By using a debit or ATM card at an ATM, individuals can withdraw cash from current or savings accounts, make a deposit or transfer where money from one account to another or perform other functions.

As is often the case with inventions, many inventors contribute to the history of an invention. In the case of the ATM, Don Wetzel invented the first successful and modern ATM in the USA, however he was not first inventor to create an ATM. In 1939, Luther George Simian started patenting an earlier and not-so-successful version of an ATM. An automatic teller machine or ATM allows a bank customer to conduct their banking transactions from almost every other ATM machine in the world. Don Wetzel was the conceptualist and chief

conceptualist of the automated teller machine, an idea he said he thought of while waiting in line at a Dallas bank.

At the time (1968) Wetzel was the Vice President of Product Planning at Ductal, the company that developed automated baggage-handling equipment. The other two inventors listed on the patent were Tom Barnes, the chief mechanical engineer and George Chastain, the electrical engineer. It took five million dollars to develop the ATM. The concept of the modern ATM first began in 1968, a working prototype came about in 1969 and Ductal was issued a patent in 1973. The first ATMs were off-line machines, meaning money was not automatically withdrawn from an account. The bank accounts were not (at that time) connected by a computer network to the ATM. Therefore, banks were at first very exclusive about who they gave ATM privileges to.

II. TYPES OF ATM ATTACK ON ATM

There are a variety of ATM attacks because it is such an attractive target. There are three basic types of ATM attacks:

Physical attack:

Brute force attack to ATM machines with the intention of gaining access to cash within the safe.

ATM Fraud:

The gang will remove the device with the cash glued on it using their special prying tool.

Software and network attack:

Theft of sensitive information or controlling ATM spew out bills automatically

Money lost by ATM attacks:

In the past few decades, significant efforts in the field of moving object detection and tracking have been done to make following applications reliable, robust and efficient: video surveillance, robotics, authentication system, media production, biological research etc. But there are many challenges which produce hurdles in the improvement of these applications. These challenges may include illumination change, dynamic background, camouflage, occlusion, shadow etc. These obstacles become more cumbersome when we perform object tracking in low resolution video. In low resolution video it is very difficult to accurately find out the object of interest because most of the discriminative details such as visual features and primitives have been lost. It results in inaccurate object tracking which further lead to inefficient event detection. But there are certain benefits of using low resolution video such as it requires low storage, transmission.

III. EXISTING METHODS

In the literature of abnormal event detection, most of the methods as in uses classifiers to recognize the events and does not use video input. These classifiers require learning time and careful attention on training dataset. Some approaches require manual setup initially in the automated event detection system and have high computational cost. From the literature we come to the fact that we need an algorithm which deals with uncommon even detection in video to assist a fully automated surveillance [4] system.

METHODOLOGY: The methodology consists of two sections such as Transmitter and receiver sections. The block diagrams of transmitter and receiver sections are as shown in the figure 1 and figure 2 respectively.

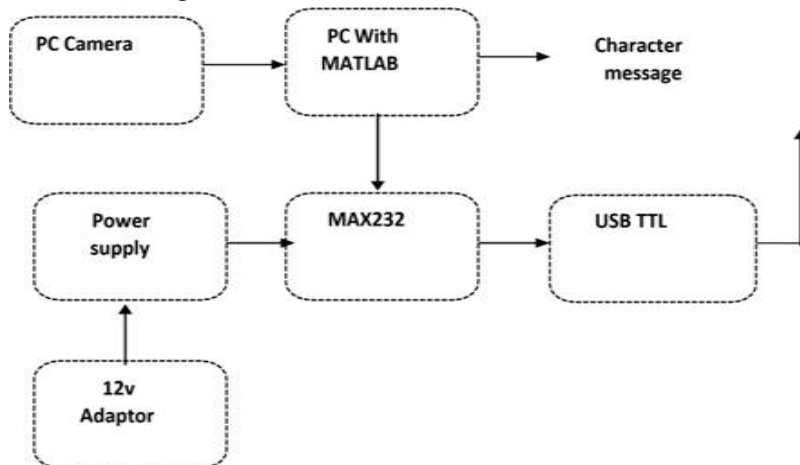


Figure 1: Transmitter Section

The characters from the MATLAB coding is Transmitted to the Hardware in order to get the exact Event that had occurred inside the ATM. The simulation part consists where the code helps us to identify the exact picturization of events. The MAX232 is a integrated circuit which is designed bu Maxim integrated Products that converts signals from a RS-232 serial port to signals suitable for use in TTL-compactable digital logic circuits.

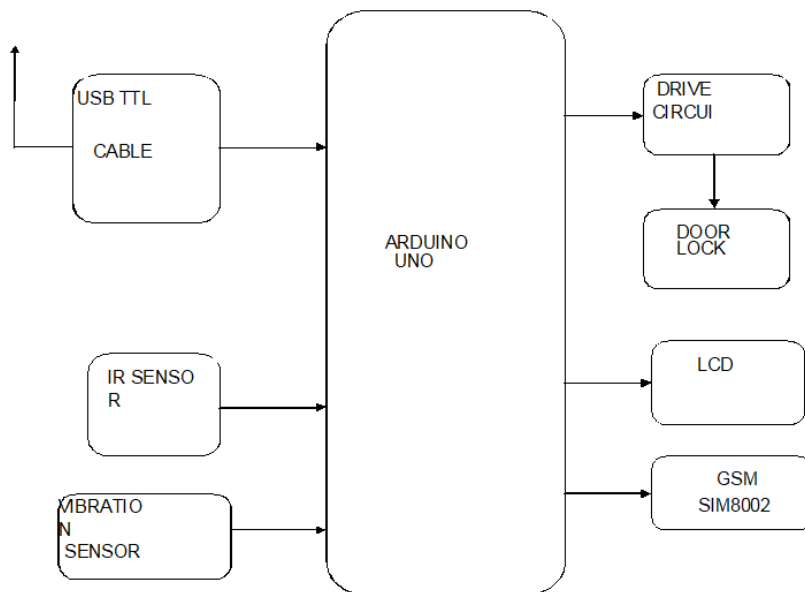


Figure 2: Receiver section

The receiver part of Block Diagram is as shown in the figure 2. The detailed description of each and every block is explained in Hardware requirements Section. The Character from the transmitter end is received by USB TTL Cable and hence transfer it into controlled called Arduino UNO, where the controller identifies the event that ad happened inside the ATM with the help of MATLAB code. Thus the respective results will be displayed with the help of LCD, Automatic message to owner and in charged person will be sent through GSM and hence automatically door will be locked up in order to caught the victims

Software Implementation

MATLAB

I have chosen MAT Lab to use as the programming language. It is a high-level language that specializes in data analysis and computing mathematical problems. Mat lab's official website can be found at www.mathworks.com.

The program environment has an interactive command window that allows users to test and experiment with the code line by line. Users can also save their codes into an M-file and run the program. The Mat lab Help Navigator is also very useful. It properly categorizes and provides detailed explanations and sample usages of all functions. Just like C++ and Java, the language syntax provides loops and condition statements for programming purposes.

The language was chosen over C++ and Java because there are a lot of built-in functions that are specific for image processing. As well, the compiler can compute large mathematical equations faster than other languages. These advantages suit the project perfectly due to the large matrix computations required during the extraction process.

EMBEDDED C PROGRAMMING:

The soul of the processor functioning inside each and every embedded system we come across in our daily life, such as mobile phone, washing machine, and digital camera. Each processor is associated with an embedded software. The first and foremost thing is the embedded software that decides functioning of the embedded system. Embedded C language is most frequently used to program the microcontroller.

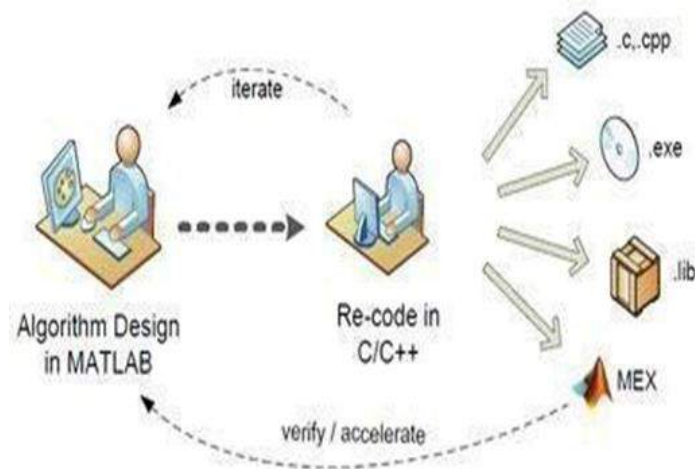


Figure 3: Embedded C Programming

FLOW CHART FOR WORKING:

The flow chart for working of change detection for critical infrastructure protection is as shown in the figure 4.

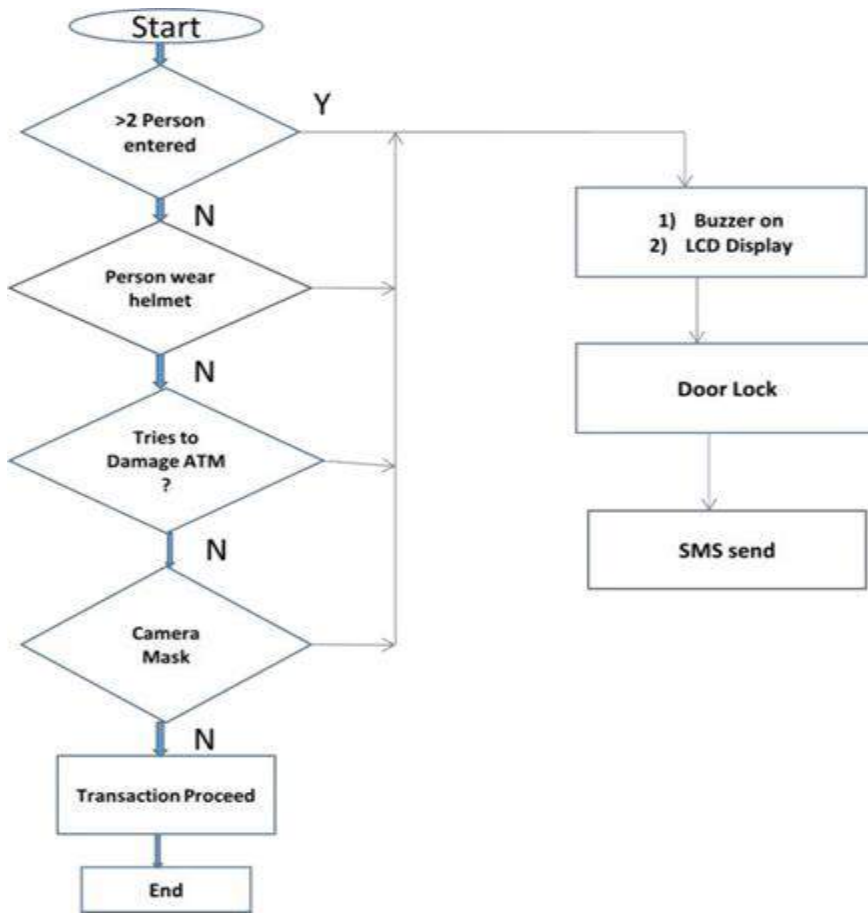


Figure 4: Working flow chart

FLOW CHART FOR CODING:

Similarly, the flow chart for programming is as shown in the figure 5.

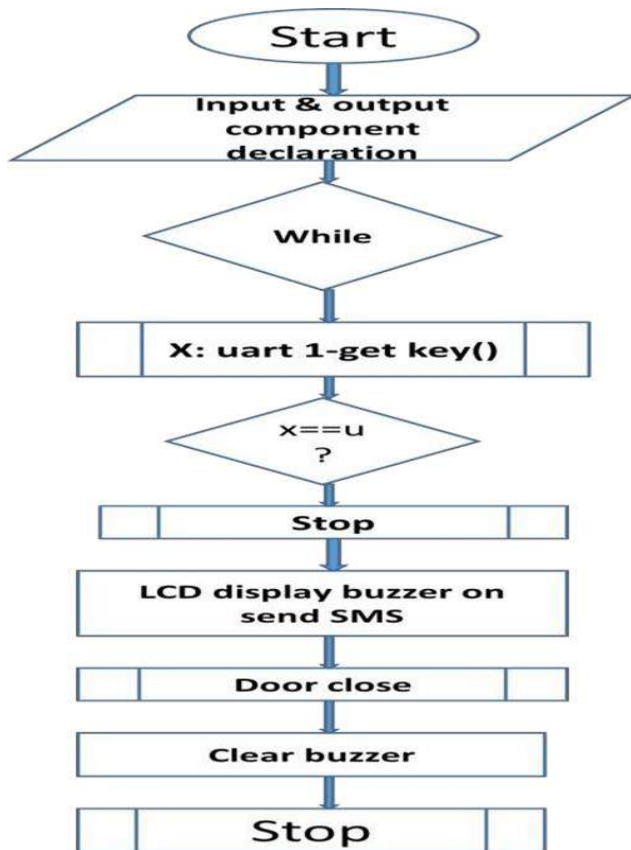


Figure 5: Coding flow chart

IV. RESULTS

The results were considered for various possibilities.

When Person is detected:

Initially the motion is detected in the ATM. If there is any motion it will start the process of person detection and after person detection output is shown in the terminal and the user is allowed to access the ATM. The process wise results are shown in following figures 6(a) to 6(d).



Figure 6 (a): First Validation Message



Figure 6(b): Motion Detected in ATM

When ATM damaged:

Initially the vibration is detected in the ATM. If there is any vibration is detected it will start the process after output is shown in the terminal.

When multiple persons entered

Initially counts the number of persons entered in the ATM. If there is more than 2 persons entered it will start the process after output is shown in the terminal.

When person wearing a helmet:

Initially recognizes the person wearing helmet inside the ATM. If there is any person wearing the helmet it will start the process after output is shown in the terminal.



Figure 6(c): Unusual Event Detection

When person wearing a mask:

Initially recognizes the person wearing mask inside the ATM. If there is any person wearing the mask it will start the process after output is shown in the terminal.

When person receives SMS through GSM:

Figure 6(d): SMS through GSM

V. CONCLUSION

ATM model developed is more reliable in providing security. The implementation of ATM surveillance by using smart sensors and GSM modem took advantages of the stability and reliability of sensor characteristics. The security features were enhanced largely for protection of ATM's when compared to previous systems. The security features were enhanced largely for protection of ATM's when compared to previous systems. The system will be built on the technology of embedded system which makes the system more safe, reliable and easy to use. Once the Unusual Event is detected for longer duration of time through the GSM (Global system for mobile communication) the message signal is immediately sent to the higher authority person. Similarly, when crowd is detected, through the GSM the message signal is immediately sent to the higher authority person. This method is secure and efficient in terms of computational complexity and threshold values. Thus this system will be able to what physical attacks on the ATM and alerts necessary people to take action at any time and save people from lot of hardships involved in the ATM attacks

VI. REFERENCES

- [1]. Sudhir Goswami, Jyoti Goswami, Nagresh Kumar, "Unusual Event Detection in Low Resolution Video for enhancing ATM security", 2nd International Conference on Signal Processing and Integrated Networks (SPIN), 2015.
- [2]. Saleem Ulla Shariff ; MaheboobHussain ; Mohammed Farhaan Shariff, "Smart unusual event detection using low resolution camera for enhanced security", 2017 International Conference on Innovations in Information, Embedded and Communication Systems (ICIIECS), 17-18 March 2017
- [3]. Jignesh J. Patoliya; Miral M. Desai, "Face detection based ATM security system using embedded Linux platform", 2017 2nd International Conference for Convergence in Technology (I2CT), 7-9 April 2017.
- [4]. Sharayu Sadashiv Phule; Sharad D. Sawant, "Abnormal activities detection for security purpose unattended bag and crowding detection by using image processing", 2017 International Conference on Intelligent Computing and Control Systems (ICICCS), 15-16 June 2017.
- [5]. G. Renee Jebaline, S. Gomathi, "A Novel Method to Enhance the Security of ATM using Biometrics," 2015 International Conference on Circuit, Power and Computing Technologies [ICCPCT] 978-1-4799- 7075-9 ©2015 IEEE.
- [6]. Vikas Tripathi, Durgaprasad Gangodkar, Vivek Latta, and Ankush Mittal, "Robust Abnormal Event Recognition via Motion and Shape Analysis at ATM Installations", Journal of Electrical and Computer Engineering, Volume 2015.
- [7]. S.Shriram, Swastik B.Shetty, Vishnuprasad P. Hegde , KCR Nisha, Dharmambal V , "Smart ATM Surveillance System", 2016 International Conference on Circuit, Power and Computing Technologies [ICCPCT].



Automation of Hydroponics Greenhouse Farming Using Arduino and IOT

Veena Yadav S¹, Deepa V P²

¹Department of Electronics and Communication, Government Engineering College, K.R. Pet-571426, Karnataka, India

²Department of Electronics and Communication, Government Engineering College, Ramanagara-562159, Karnataka, India

ABSTRACT

Over the years, traditional farming for harvesting with the use of soil takes longer time to decompose making it prone to diseases and expensive. Hydroponics system means growing plants without soil with better results, especially in areas with space and environment unsuitable. This system has no adverse effect on environment or quality on crops. Here the proposed system presents intelligent Plant Care Hydroponic that exercises environment driven control methods through an Internet- of -Things (IOT). IOT provides a scalable and configurable software for users to easily and quickly add/remove/exchange the sensors and actuators and program their interactions.

Keywords: Hydroponics, Greenhouse Farming, Arduino, IOT

I. INTRODUCTION

Human require air, food, water and living space in order to survive. These things are not endless in nature and thus humans are dependent upon the optimization of land areas and the preservation of biodiversity. The human population is increasing and predicted to expand from 7.0 billion to 9.5 billion people within the next 40 years. An ever increasing demand for food species is implied and it is estimated that food production will have to be doubled in order to compensate and provide availability to all.

The word "Hydroponic" define as any means to grow plants via a medium that does not include the use of soil but involves inorganic nutrients or nutrient solution. One of the basic principles for vegetable production, both in soil and in hydroponic systems is to provide all the nutrients the plant needs. The implantation of IOT in hydroponics would help the farmers to automate the whole farming process thereby ensuring better yield and the quality of the produce. The main aim of this paper is to make a compact system to automate nutrient dose, PH, water supply and temperature of a greenhouse hydroponic farm.

II. LITERATURE SURVEY

In literary survey, we analyze critically and concisely earlier research and literature related to a particular research problem, and utilize them for their own research purposes. It helps in understanding the significance of new research and its connections to earlier work. The survey may display an insufficiency in the literature, which a new research can correct. In such case, the survey focuses on what is known about the topic and what is not known.

According to Rahul nalwade and Tushar Mote [1] India is at number 4 among the leading food producing countries. This field to start up with the initial setting up of a hydroponic plant. In order to make the process much easier, the concept of IOT is used to control and monitor multiple parameters by using an android application, and also alert the users whenever the farm is in abnormal condition.

According to Saket Adhau, Rishikesh Surwase and K H Kowdiki, with the recent advancements in technology and improvements in hydroponics method of growing there is a rapid demand for automated system. Although there are some automated systems available, but they haven't made much of an effective breakthrough. This paper is intended to efficiently make use of the sensor data in real-time. They specify the work that aims to build a self- controlled fully automated hydroponic system which is intelligent enough to provide proper amount of required nutrients by using the present day technology. The real-time data collected from multiple sensors are imported into an AVR microcontroller board and the process of automating and monitoring these real time data is carried out. They have provided a cost efficient method of implementing a good automated hydroponic control system. The system is subjected to be rigorous tests for correctness and validation. Once it meets all the required criteria, the system is then provided to the consumers in and across India.

According to the study of P Sihombing, N A Karina, J T Tarigan and M I Syarif the developments in technology along with the combination of science has been resulted in some of the brilliant ideas that could improve the way the agricultural practices have been carried out. In this paper they have developed a control tool that could automatically control the flow of nutrients to the hydroponics plants by using a smartphone. Arduino Uno microcontroller is used as the base of hardware part and Arduino programming is used in programming. Simple if statements are used to control the flow of nutrients. Various parameters like Fluid level, temperature and humidity are continuously monitored using the smartphone. The height of the nutrients in the reservoir is determined by using an ultrasonic sensor, which is used to fill the water or nutrients solution to a specified level after which the flow of water is automatically stopped. The temperature is measured by using an LM35 temperature sensor. The reading from these sensors are directly displayed on the LCD display. This helps the farmers to control different parameters of their farm from remote areas. The only limitation in country like India is internet connection. If the sufficient amount of internet speed is available, the controlling happens without any lags.

III. METHODOLOGY

The implementation of hydroponic farming is the fastest growing sector of agriculture and it could very well dominate the food production in the future. Hydroponic farms require 90-95% less water than the conventional farms and the farm can be placed anywhere as no soil is required. The main aim of our project is to make a compact system to automate nutrient dose, PH, water supply and temperature of a greenhouse hydroponic farm. In this technique, we ensure that plant gets all nutrients from the water solution.

Hydroponic system can accomplish this by allowing crop production in urban environments not available for conventional farming. In our project, the parameters are controlled automatically. Also, the cultivators can know the conditions of the plant growth and control the parameters remotely by using IOT technology. Here we have considered the Arduino micro controller with three types of sensors such as temperature sensor, PH sensor and LDR for both plant 1 and plant2. ESP8266 is a Wi- Fi module to communicate by using internet of things with the server. The GSM module is to communicate and relay is used to automatically turn on/off the water supply from the pumping motor.

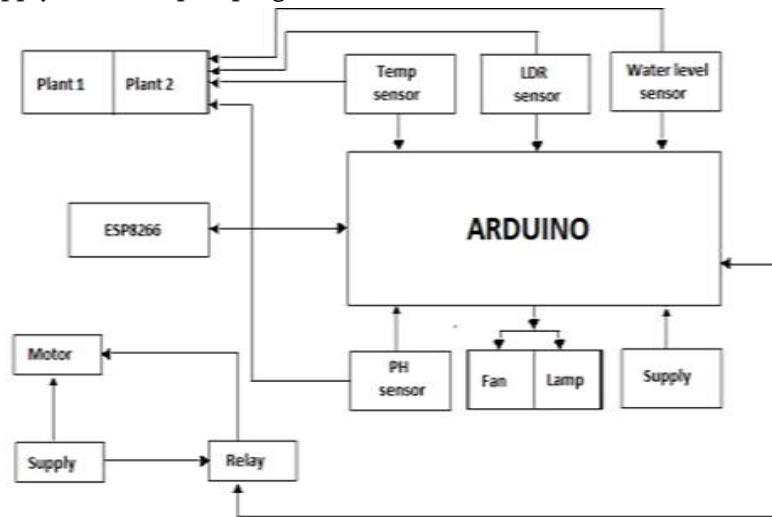


Fig. Block diagram of automated hydroponic farm

Nutrients/Chemicals required for plant growth To survive and grow, plants need:

- Oxygen
 - Carbon Dioxide
 - Lights
 - Water
 - Nutrients.
- Any good Hydroponic nutrient should contain all of these elements; Nitrogen (N), Potassium (K), Phosphorous (P), Calcium (Ca), Magnesium (Mg), Sulphur (S), Iron (Fe), Manganese (Mn), Copper (Cu), Zinc (Zn), Molybdenum (Mo), Boron (B), Chlorine (Cl)

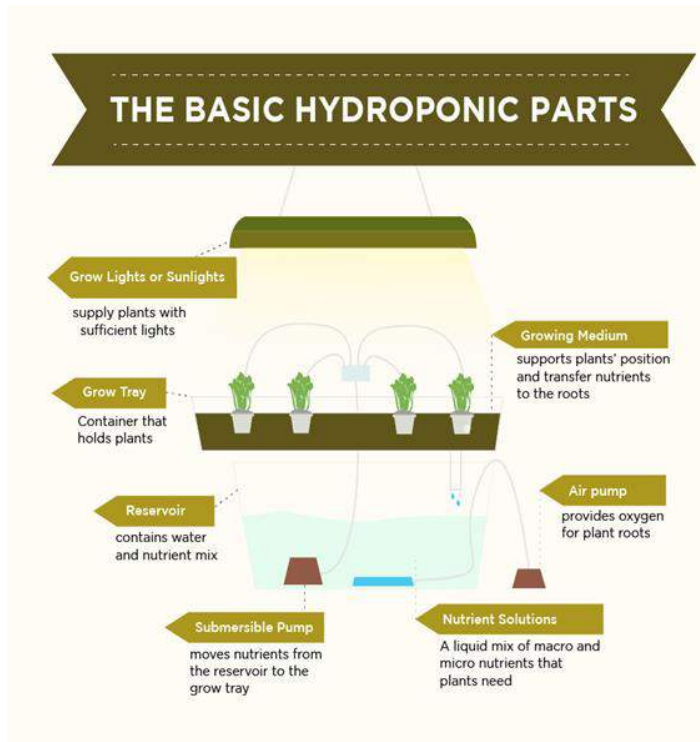
Hardware required

- Arduino Microcontroller
- Temperature sensor:- LM35

- PH sensor :- glass electrode
- LDR
- Ultrasonic sensor
- ESP8266
- Relay
- Dc motor

Software

- Arduino IDE
- ThingSpeak(IoT)



A) The Basic Hydroponic Parts Why Hydroponics?

Hydroponics come up with several obvious benefits that the soils cannot compare to. Let's see.

Better growth rate

It's not uncommon to see that Hydroponically grown plants than enjoying a 20-30% better rate than those in the soil, grown in the similar conditions. This is because plant roots directly contact with the nutrients rather than searching for food in the soils. All of these energies will be instead consumed in its growth, and in producing fruits and flowers. Growers are also in charge of the whole growing system

- nutrients, temperature, lights, and so on. By this, you can provide with the ideal conditions that plants require.

Hydroponics saves water

It is estimated that agriculture consumes 80% of fresh water. Meanwhile, the FAO predicted that the food production would increase by 70% when the population hugely expands. That would be a huge issue to deal with for future farming. It's when Hydroponics is adopted as a viable solution. This soilless growing method

uses only 10% water in comparison to soil agriculture. It is able to do that because of its efficient recirculated system. Hydroponic plants get the sufficient water while the run-off ones are captured and get back to the system.

No soils needed

This comes with two great benefits:

1. You can grow crops anywhere whether in arable or heavily contaminated places. It saves the lands by growing plants in convenient locations like large-scale indoor greenhouses, or even in your apartment.
2. All of the weeds and soil-related pests and disease are eliminated in a Hydroponic system.

Effective use of nutrients

All nutrients are added to the solution, and you are 100% controlling giving the specific amounts of foods (nutrients) that plants need. Unlike the soil, nutrients are not lost because they are held in the reservoir.

B) Hydroponic Nutrient Guide

What plants require are still the same in any environment - organic compost (C, O, N, H), macro and micronutrients. However, plants grown hydroponically don't have the similar ways to get the necessary nutrients they need.

What Plants Need

To survive and grow, plants need:

- Oxygen
- Carbon Dioxide
- Lights
- Water
- Nutrients

Plants get oxygen and carbon dioxide from the environment for respiration.

Lights supply plants with energy, which is used in the photosynthesis process to make foods. They get lights from the natural lights of the sun or artificial lights from grow bulbs.

Water gives plants moisture. Nutrients in the water are what the soilless growers are in total control to let plants reach their full potential growth.

C) Which Plants Are Best Grown In Hydroponics

We can grow anything in Hydroponics provided that you create a proper set-up and supply plants with sufficient nutrient balance. But we should not take that mind- set and grow anything we want.

This is because some plants will grow absolutely well in Hydroponics while others do not bring expected yields. At the same time, some plants need us for their special care and installation to survive. To give some recommendations for beginners, it's better that we begin with something easy and thrives in Hydroponics first.

Let's go to the list

- Vegetables: Lettuce, Spinach, tomatoes, kale
- Herbs: Basil, chive, oregano, mint
- Fruits: Strawberries, hot peppers

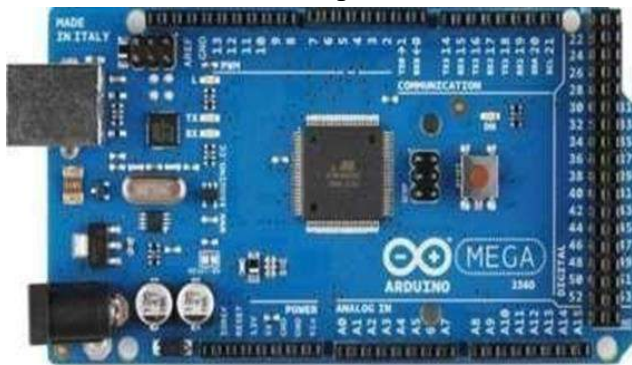
D) Motivation

Farmers will be able to produce crops faster hydroponically, which will allow them to plant more during the season. They will spend less time in weeding and doing other work because there is no soil to fuss with.

E) Objectives

- Automation in hydroponics agriculture
- Increases the health of plants
- Increase in the production
- Increase the quality of crop
- Controlled nutrients for plants automatically using IoT
- Efficient way of agriculture

F) Hardware Arduino Mega



The Arduino Mega is a microcontroller board based on the ATmega1280 (datasheet). It has 54 digital input/output pins (of which 14 can be used as PWM outputs), 16 analog inputs, 4 UARTs (hardware serialports), a 16 MHz crystal oscillator, a USB connection, a power jack, an ICSP header, and a reset button. It contains everything needed to support the microcontroller; simply connect it to a computer with a USB cable or power it with a AC-to- DC adapter or battery to get started.

LM35



LM35 is an integrated analog temperature sensor whose electrical output is proportional to the Degree Centigrade. They are used in your daily household devices from Microwave, fridges, AC to all fields of engineering.

PH sensor



The most common PH sensor is the glass electrode. It's used in many industry applications and in a wide variety of fields. The glass electrode method has high reproducibility, and it can measure PH of various solutions. A PH electrode is a potentiometric or electrochemical sensor that has a voltage output.

LDR



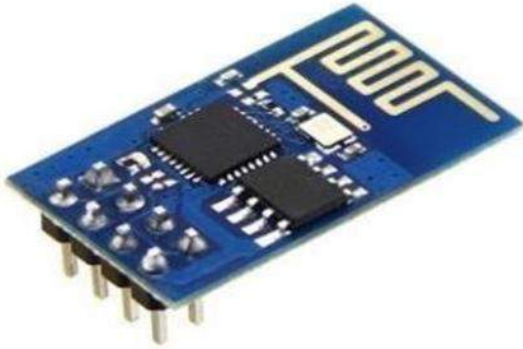
A light-dependent resistor alternatively called an LDR, photo resistor, photoconductor, or photocell, is a variable resistor whose value decreases with increasing incident light intensity. An LDR is made of a high-resistance semiconductor. The resulting free electron conducts electricity, thereby lowering resistance.

ULTRASONIC SENSOR



An ultrasonic sensor is an electronic device that measures the distance of a target object by emitting ultrasonic sound waves, and converts the reflected sound into an electrical signal. Ultrasonic waves travel faster than the speed of audible sound (i.e. the sound that humans can hear). Ultrasonic sensors have two main components: the transmitter (which emits the sound using piezoelectric crystals) and the receiver (which encounters the sound after it has travelled to and from the target).

WIFI MODULE (ESP 8266)



ESP8266 is a 3V WiFi module very popular for its Internet of Things applications. ESP 8266 maximum working Voltage is 3.6V and its very important to note. You must know how to power it, how to serial-connect it with ARDUINO safely, how to ping and many other things. You should use software like Circuito.io, Tinkercad, Fritzing to simulate and work with the board safely. You should also use Logic Level Controller to use with ESP8266 module.

SOFTWARE

ABOUT THINGSPEAK

Getting Started

- Sign Up for New User Account – <https://www.thingspeak.com/account/new>
- Create a New Channel by selecting Channels and then Create New Channel
- Follow a tutorial for common devices and applications

Channels

Channels are where your application stores and retrieves any type of data. Each channel has a Private View and a Public View. The Private View is only accessible by signing into your ThingSpeak.com user account. The Public View is what other viewers will see when they visit your ThingSpeak Channel. You can have different info on each view, customize the view with Plugins, and even disable the Public View.

Channels API

To read and write to a ThingSpeak Channel, your application must make requests to the ThingSpeak API using HTTP requests. Each ThingSpeak Channel allows for 8 fields of data (both numeric and alphanumeric formats), location information, and a status update. Each entry is stored with a date and time stamp and is assigned a unique Entry ID (entry_id). After the data is stored, you can retrieve the data by time selection or by Entry ID. In addition to storing and retrieving numeric and alphanumeric data, the ThingSpeak API allows for numeric data processing such as timescaling, averaging, median, summing, and rounding. The channel feeds supports JSON, XML, and CSV formats for integration into applications

Charts API

Use the Charts API to present numerical data stored in ThingSpeak Channels on charts. Supported chart types are line, bar, column, and step. Options include size, color, and labels.

Open Source API

The ThingSpeak API is available on GitHub and includes the complete ThingSpeak API for processing HTTP requests, storing numeric and alphanumeric data, numeric data processing, location tracking, and status updates. The open source version follows the same documentation as the ThingSpeak hosted service.

Apps

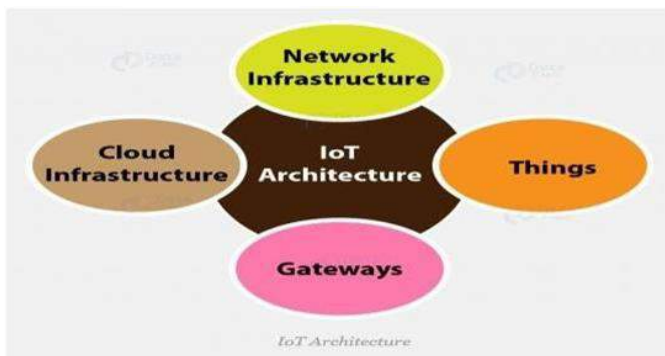
ThingSpeak Apps are apps that make it easier for devices to access resources on the web such as social networks, web services, and APIs.

Thing HTTP

ThingHTTP is for connecting things to web services via HTTP requests. ThingHTTP supports GET, POST, PUT, and DELETE methods, HTTP/1.0, HTTP/1.1, SSL, custom HTTP headers, and Basic Authentication.

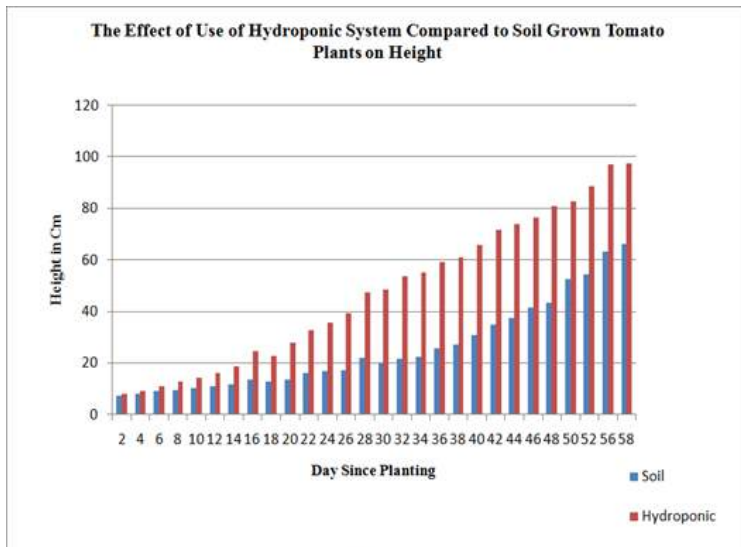
G) INTERNET OF THINGS (IOT)

Kevin Ashton, in a presentation to Proctor & Gamble in 1999, coined the term “Internet of Things”. Almost all, every area, every device, every sensor, every software are connected to each other. The ability to access these devices through a smart phone or through a computer is called IoT. These devices are accessed remotely. IoT is basically a platform where we connect everyday things embedded with electronics, software, and sensors to the internet enabling them to collect and exchange data. In this way, each of your devices will learning from the experiences of other devices, just as humans do. With IoT, the interdependence in the human will expand- i.e to interact, collaborate and contribute to things. The „Thing“ in IoT can refer to any device that might comprise any kind of built- in- sensors with the ability to collect and transfer data over a network or internet without manual intervention.



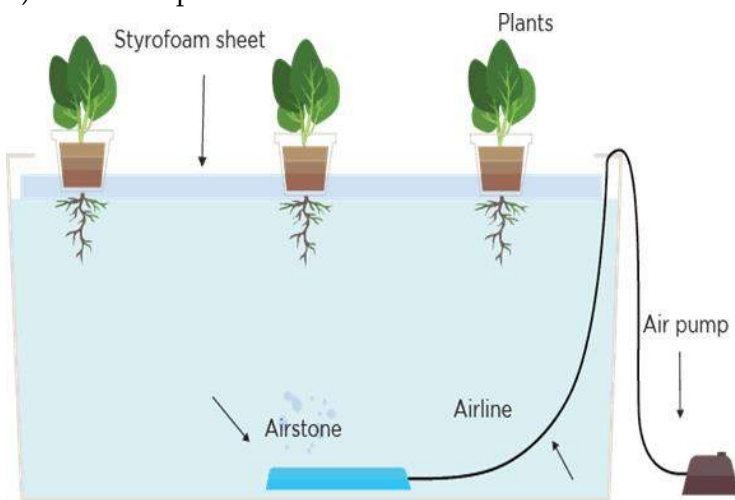
IV. RESULTS AND DISCUSSION

- a) Below graph shows the difference between conventional method and hydroponics method with example of tomato plant.

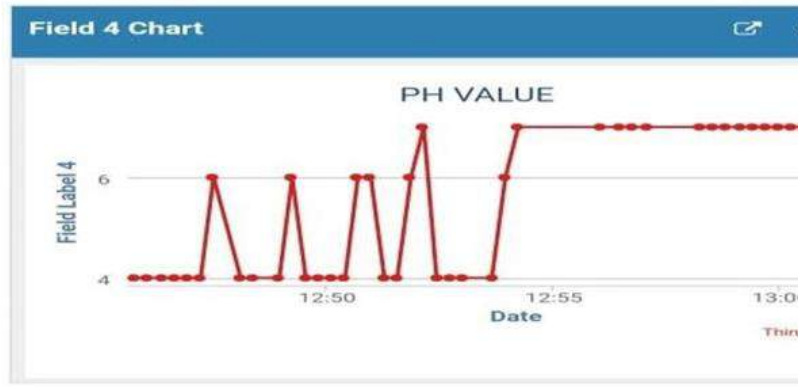
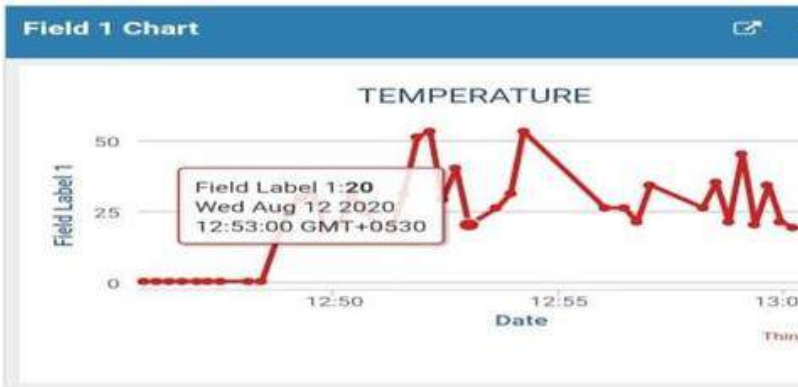


Graph 1

b) Plant setup



c) Data uploaded to ThingSpeak



V. CONCLUSION

Hydroponically grown plants do not come in contact with soil borne pests and diseases thus saves costs of soil preparation, insecticides and fungicides.

Since the amount of nutrients is fed directly to the plants, there is no wastage of water due to run off or evaporation.

Progress has been on large scale and results obtained in various countries in the world have proved that this technology is thoroughly practical and has very definite advantages over conventional methods of crop production.

VI. REFERENCES

- [1]. Dr.Hector Munoz. (2010). Home Based Vegetable Production System.Date of retrieval 28.01.201
- [2]. Zhai Yanni, Chen Xuedong. Design of smart home remote monitoring system based on embedded system.
- [3]. IEEE International Conference on Computing, Control and Industrial Engineering (CCIE), 2011, 41 -44.
- [4]. M. Azaza , C.Tanougast , E.Fabrizio , A.Mami, "Smart greenhouse fuzzy logic based control system enhanced with wireless data monitoring", vol. 61,pp.297-307, March 2016.
- [5]. I. Mohanraj, Field, "Monitoring and Automation Using IoT in Agriculture Domain", Procedia Computer Science, vol. 93, pp.931-939,2016.
- [6]. R Nalwade, T Mote - Hydroponics farming, Trends in Electronics and Informatics (ICEI 2017)
- [7]. Somchoke Ruengittinun, Sitthidech Phongsamsuan – Applied internet of thing for smart hydroponic farming ecosystem (HFE) (Ubi..2017)



Design and Implementation of Heart Attack Detection and Medication Using Ad a fruit Flora Module

Deepak H A¹, Tayab Mustaq Ahmed², Deepak R¹, Sharath S³

¹Assistant professor, Department of Electronics and communication, NAVKIS College of Engineering, Hassan, Karnataka, India

²Department of Research and Development, Malnad Techno head Business Solutions Private Limited, Shivamogga, Karnataka, India

³Assistant Professor, Department of Electronics and Communication, GEC KR Pet, Mandya, Karnataka, India

ABSTRACT

In this project we are trying to decrease the rate of death due to the lack of timely medication during a situation of a heart attack. As we all know the risk of having a heart attack is more now a day's due to mental stress in daily life. But at the time of a heart attack, if the patient gets the prescribed medicine in time, then the death of the patient can be avoided. So, we have designed a watch which will regularly monitor the heart rate of the person wearing it and then according to the rate of heart beat it will calculate whether the heartbeat of the patient is normal or not. Because in both the case of low heart beat and high heart rate can cause a heart failure. A bradycardia is a condition in which the heart rate is too low, and a tachycardia is a condition in which the heart rate is too high. Thesetwo situations may potentially result in a heart attack or heart failure. The model we created will monitor the heart rate on a regular basis, and if the person's heart rate becomes too high, it will have the prescribed prescription stored in two compartments of the smartwatch. This may aid in the early treatment of the patient and maybe save many lives.

Keywords—Heart Beat, Hemoglobin, MAXREFDES117, MAXREFDES117, Pulse, Photo Sensor, Thumb, LED, Monitor, Medication, Photo detector

I. INTRODUCTION

In addition to the timing function, a smart watch is a "universal networked computer with multiple sensors" that can be worn on the wrist [5]. Smart watches can change health care by supporting / assessing health in daily life because: (1) most people are familiar with them; (2) they are becoming more and more available as consumer devices ; (3) in a near real-time manner Provide continuous monitoring of physical activity and physiological indicators; (4) Support personalized messages and reminders; (5) Realize communication between patients, family members and health care providers; (6) Including on-site behaviour review, small surveys and Sensory measurement.[5].

The normal heart rate of an average person is around 72 beats per minute. Coronary artery pressure increases steadily during exercise and gradually returns to the cost of relaxation after exercise. Exercise with a normal heart rate is a sign of human health. A lower-than-normal heart rate usually indicates a condition called bradycardia, while a heart rate higher than normal is called tachycardia. Hardware or software implemented to eliminate overload harmonics and symbol noise, and then use a set of zero-crossing rules to determine the number of hits in a given time interval (e.g., zero and zero). This is a powerful method that can automatically filter out any time noise within the character. Coronary artery heart load display is a gated monitoring tool through which anyone can assess heart load in real time or record it for further examination. In the case that a heart attack can be detected early, the patient's heart rate is monitored by a pulse sensor and a temperature sensor, and then it is connected to the microcontroller. The sensor is installed in a portable device. [9]. Early fashion included a tracking container with a set of electrode cables connected to the chest. The ischemic load of a healthy, relaxed human heart is about 72 beats per minute (heartbeats per minute), compared to about 120 for a young child. Beat every minute, while the heart rate of older children is about 90 beats per minute. Charging when the heart rate is normal is a sign of human health. This is called tachycardia. Heart rate is genuinely measured by placing the thumb on the patient's arterial pulse and measuring, measuring and counting the pulse, usually within a 30-second period. Although this method is not always correct, and can cause errors when overloaded. Most modern strategies for assessing coronary artery load used digital methods. Myocardial infarction (MI), commonly called a heart attack, is a serious medical emergency in which the blood supply to the heart is suddenly blocked, usually due to a blood clot in the coronary arteries [6,8]. Insufficient blood supply to the heart can severely damage the heart muscle and endanger life. Heart attacks can be divided into three types: ST-segment elevation myocardial infarction (STEMI), non-ST-segment elevation myocardial infarction (NSTEMI) and coronary artery spasm [11]. An electrocardiogram (ECG) is one of the most common strategies for measuring coronary heart pressure, but it is also an expensive instrument. Watches with other internal shapes can also be used to measure the instantaneous electrical charge of the heart. The instrument can provide correct measurement results, but its cost usually exceeds thousands of rupees, so it is not economical. Therefore, the proposed use of a heart rate sensor to determine coronary artery pressure is undoubtedly a useful tool for determining the position and temperature of the patient's heart rate. In medicine, "pulse" is defined as the rhythmic expansion and contraction of the arteries that describe each heart beat [13]. Therefore, the pulse is the same as the beating of the human heart. The pulse rate per minute can be measured on the neck and wrist. The most important points for measuring heart rate are the fingers, wrist (radial artery), neck (carotid artery), inner elbow (brachial artery), behind the knee (popliteal artery), and ankle (posterior artery). Shin). Higher or lower indicates an abnormality in the body [6]. Some devices can correctly analyze the coronary artery load, use optical age, use ordinary infrared light-emitting diodes (LED) and photoelectric sensor to calibrate the coronary artery load of the heart with the index finger.

The microcontroller is programmed to collect signals of use from its built-in analog-to-virtual converter ADC, and use the reading to calculate the coronary artery pressure on the heart; finally, the analysis results are displayed digitally on the LCD screen.

TABLE 1: COMPARISON OF ERROR RATES OF VARIOUS HEART BEAT RATE MONITORING SYSTEMS [3]

Device	Error % at 80 90 BPM	Error rate at 160 170 BPM
Garmin vivofit	10.7	0.0
Withings pulse 02	5.3	57.5
Basis carbon steel	10.2	57.1
Samsung gear fit	4.2	unable to read
Samsung galaxy S5	3.1	0.2

II. EXISTING METHODS

1) OPTICAL METHOD

An Android-based heart rate monitor that uses a camera and flash to determine the user's heart rate (in beats per minute). Use data smoothing on an integer matrix to calculate the total value of the red pixels in the photo. Average, determine the heart beat, and the total value of the red pixels in the heart condition photo is greater than the smoothed average value. Portable devices with optical heart rate video displays have small LEDs on the side. Beneath it illuminates the pores and the green light on the baby's skin. The light waves from these light emitters are related to the blood flowing through the wrist. When this light is refracted (or reflected) by the flowing blood, another sensor inside the wearable device records the information. This data, along with the exercise records captured by the device's accelerometer, can then be processed using algorithms that provide clear heart rate readings. Pressing firmly on the top of the index finger on the camera may shut off blood flow. Lead to inaccurate readings. Devices with optical sensors that read data from the wrist (rather than fingertip) have the greatest difficulty in monitoring heart rate. This method requires light to penetrate multiple layers, and the darker the person, the more light that needs to be restored. This technology compensates for skin tone problems. [3].

2) ELECTRICAL METHODS

Electrical method Heart rate monitors use electrodes to monitor the voltage generated by the heartbeat [3]. The receiver recognizes these electrode records based on the radio signals from the chest strap. These records are used to determine your heart rate. Some video display devices also contain a "scrambling signal," which uses a unique code in the radio signal to

prevent the receiver from receiving radio transmissions from nearby locations. channel. This is usually not a big problem, but it can be a problem. The disadvantage of digitization is that your data may be harmed or damaged. There are dangers in this method, such as false results, deterioration of pressure compounds in the body [3].

III. LITERATURE REVIEW

1. In the paper namely "IoT on Heart Attack Detection and Heart Rate Monitoring" authors Mamidi Manisha, Katakam Neeraja, Vemuri Sindhura, Paruchuri Ramaya have explained about Life is valuable. Many people die of heart attacks, and because the seizures are discovered too late, we cannot save lives. Usually, heart attack detection is done traditionally using specialized hardware devices. With the help of increased technology, we should be able to capture and monitor the changes in our body. In this paper we propose a system which will detect heart attack with help of different scenarios i.e., monitoring heart attack but also other heart diseases. To get rid of these heart attacks or to reduce this heart disease we are developing this system to reduce the death rate.
2. In the paper "HEART RATE MONITORING AND HEART ATTACK DETECTION USING WEARABLE DEVICE" authors Yashasvi Yadav, Manasa S Gowda have explained about A portable device used to monitor heart rate and detect heart attacks. Life is precious. Many of us died of heart attacks. This is due to our diet, age, less physical activity and many other factors. The main cause of death worldwide is heart attack. A heart attack is not easy to detect, and the symptoms of a heart attack vary from person to person. To overcome heart disease and heart attack and help our society, we are developing a system that will help reduce mortality and detect heart attack early.
3. In the paper "Real Time Heart Attack and Heart Rate Monitoring Android Application" authors Kainat Zeba, Lakshmi S Patil, Sanjana R Gowda, Varsha R, Mrs. Shobha Chandra K have explained about Technological innovations in disease prevention and patient health have promoted the development of surveillance systems and other fields. This concept is related to heart attack detection and heart rate monitoring. This is an Android application that can continuously monitor the patient's heart. Speed and send appropriate notification to registered users. This will help doctors monitor the health of remote patients and create smart health systems. This project can help save the lives of patients at the last minute.

IV. PROPOSED SYSTEM

As we all know the risk of having a heart attack is more nowadays. But at the time of a heart attack, if the patient gets the prescribed medicine in time, then the death of the patient can be avoided. So, we have designed a watch which will monitor the heart rate of the person wearing it and then according to the rate of heart beat it will calculate whether the heart beat of the patient is normal or not. If the heart rate of the person is low or high it will give the prescribed medicine for both the cases which will be stored

in one compartment of the smart watch. In this project we are trying to lessen the rate of death due to the lack of timely medication during a heart attack. As we all know the risk of having a heart attack is more nowadays. But at the time of a heart attack, if the patient gets the prescribed medicine in time, then the death of the patient can be avoided. So, we have designed a watch which will monitor the heart rate of the person wearing it and then according to the rate of heart beat it will calculate whether the heart beat of the patient is normal or not.

If the heart rate of the person is low or high it will give the prescribed medicine for both the cases which will be stored in one compartment of the smart watch.

V. CIRCUIT DIAGRAM

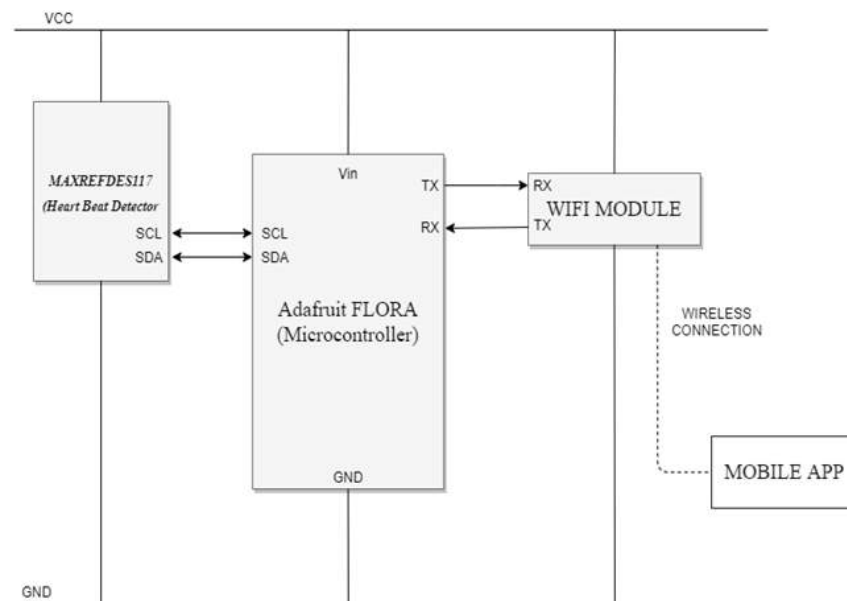


Fig1: Block Diagram of heart attack detecting and medication System

VI. HARDWARE AND SOFTWARE REQUIREMENTS

A. HARDWARE REQUIREMENTS

- Adafruit FLORA
- MAXREFDES117 (HEART-RATE AND PULSE-OXIMETRY MONITOR)
- SmartPhone
- Bluetooth Module

B. SOFTWARE REQUIREMENTS

- Arduino IDE
- MIT App Inventor

VII. WORKING PRINCIPLE OF HEART BEAT SENSOR

The working principle of using a heart rate sensor to detect a heart attack is photoplethysmography (PPG) technology. It uses an infrared light source to illuminate the finger on one side, while the other side of the finger uses a photodetector. Placed, it can measure a small variation within the transmitted light intensity. Heart rate measurement uses substances that gently absorb hemoglobin. The light from the infrared light source under the monitor illuminates the blood vessels under the skin. The light detector detects soft light that is not absorbed but reflected back. The variations within the photodetector mark are related to changes in the distribution of blood in the tissue. When visible light is irradiated on the photodetector again, the photodetector will send out an electrical signal. The signal we get from the sensor is an analog signal, which becomes the signal on the right. In addition, the signal can be filtered and then amplified to obtain an ideal PPG (PhotoPlethysmoGraph) waveform synchronized with the heartbeat [3]. The heart rate detection is based on the calculation of the Fourier transform of the heart rate signal under the assumption of excessive overshoot. The heart rate is 120 beats per minute.

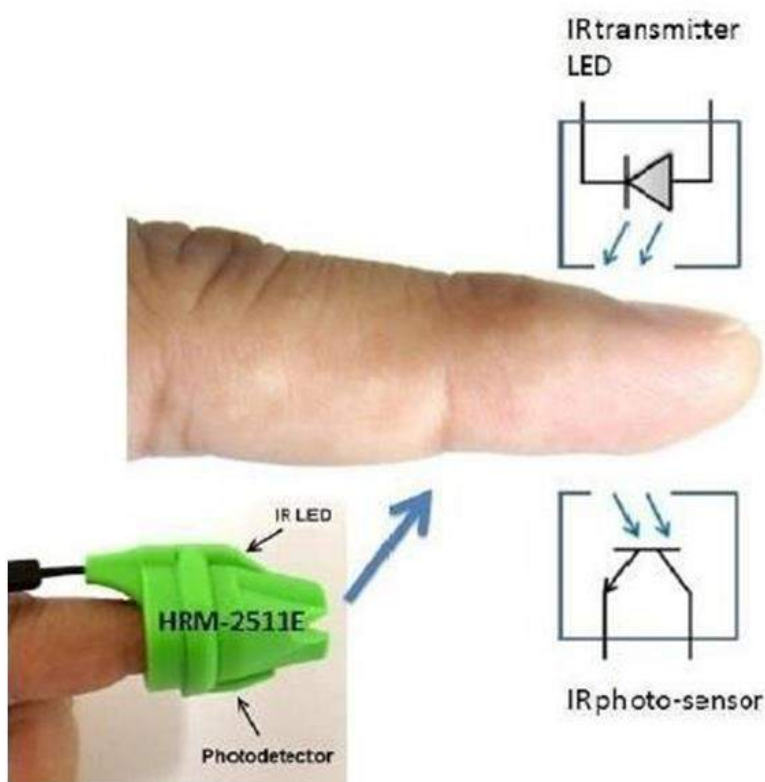


Fig2: Heart Beats sensor working principle

The heart beat/second = $120/60 = 2$ bps

The PPG sensor used can correctly analyze the coronary heart rate. The coronary heart rate can be calculated by understanding the terms in the PPG curve. Two heart rates are calculated based on three consecutive PPG peaks and their combined values. The value is displayed as the instant heart rate. Our tool calculates beats per second and estimates the size, not the safest limit for the problem at hand. The safest heart rate can be calculated based on the gender and type of

the problem. Various methods are used in the clinical profession to calculate the safest bpm, for example: B. Martha, Londeree Moeschberger, Miller and others.

- The pulse sensor is a sensor used to detect irregular heart rhythms. The sensor is sent to the Adafruit FLORA microcontroller.
- The Adafruit FLORA microcontroller acts as the controller processor and can use the heart rate sensor for heart rate measurement.
- The circuit module ESP8266 is a media interface for real-time data transmission module from microcontroller to smartphone [4].

TABLE 2: AGE-WISE THRESHOLD VALUES FOR ADAPTIVE ALARMING MECHANISM [3]

Percentage/Age	18-35	36-64	Above 64
Normal heart rate	72-75 (BPM)	76-79 bpm	70-73 bpm
Bradycardia	HR \leq 55	HR \leq 60	HR \leq 65
Tachycardia	HR \geq 110	HR \geq 120	HR \geq 100
Hypertension	BP \geq 150/100	Bp \geq 145/95	Bp \geq 140/90
Hypotension	Systolic BP < 85 mmHg	Systolic BP < 96 mmHg	Systolic BP < 117 mmHg

VIII. METHODOLOGY

In this project the main microcontroller we are using is Adafruit FLORA because, FLORA is an Adafruit's fully-featured wearable electronics platform. Due to its round and small size we are choosing this device. For the checking of the heart rate the sensor we are using is the MAXREFDES117 which is a heart rate and pulse-oximetry monitor. This sensor is used because of its accuracy. The algorithm used for heart-rate monitoring is a beat-finding algorithm. The beat-finding algorithm is a peak detection-based algorithm and the algorithm is based on a "PULSE SENSOR RAMPED" website [7].

The MAXREFDES117 will collect the pulse and send it to the microcontroller then the value of the heart rate of the person is calculated by the microcontroller. By referring this value of the heart rate, the microcontroller will check where there is a hike or sudden decrease in the heart rate and display the heart rate on the mobile app which will be connected through Bluetooth or WIFI module. In accordance with the problem, it will provide the tablets which are stored in one of the compartments present in the smartwatch. The compartment contains two tablets which is prescribed by the doctor for

both conditions like hike or decrease in the heartbeat. By using this technique, the rate of death due to heart attack can be decreased.

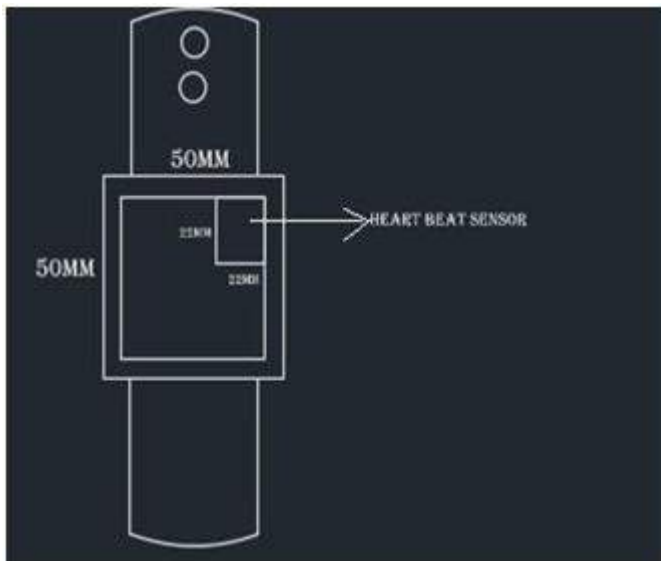


Fig3: Front view of the smart watch

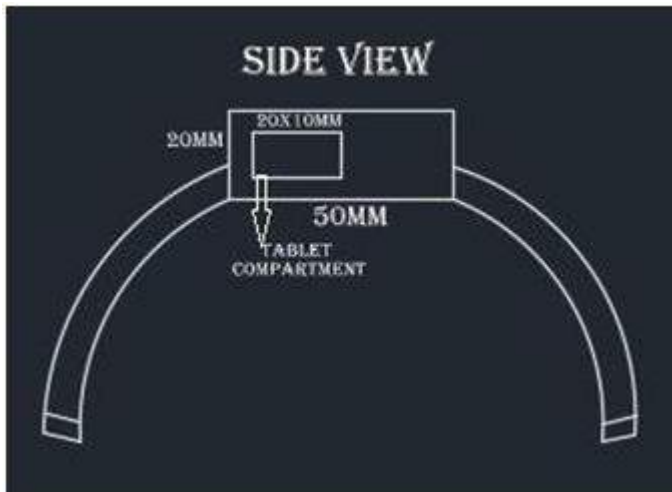


Fig4: Side view of the smart watch

As we can see in the above figure 3 it shows the design view of the one side of the smart watch in which we can observe that there is a compartment present. This compartment is provided to store the tablet. These tablets are helpful in a serious condition of low heart rate and also the hyper heart rate.

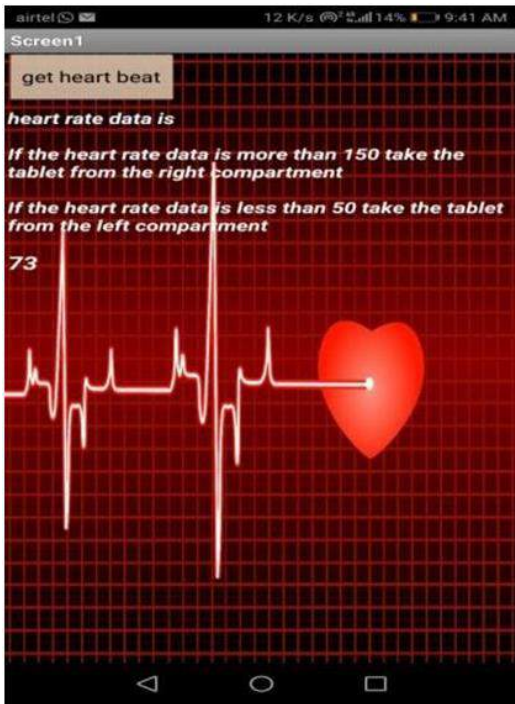


Fig5:SnapShotsofMobileapplication

above Fig 5 Shows the mobile app which is built using MIT App Inventor Platform. The APP contains a button named “get heart beat”. Whenever the user presses the button, the data from the microcontroller will be received by the mobile app and then after a time interval of 6 seconds the data of the rate of heart beat will be displayed on the app [2] and then the data will be passed to the registered number through the SMS.

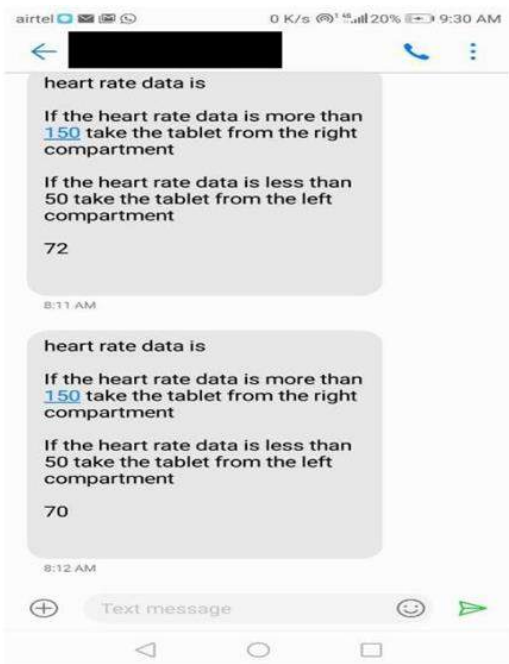


Fig6:Snap ShotsofMessagereceivedbythefamilymember

The above fig 6 shows the message received by the user where he can get the heart rate data on their mobile phones.

IX. FUTURE IMPLEMENTATION

- Further we can also add the feature showing time and body temperature on the smartwatch.
- We can also link the data of the heart rate to the cloud and store that for the further process or for the doctor's report

X. LIMITATION

- This device cannot be used while jogging or exercise time.
- The patient needs the doctor's consultation to keep the right tablets in the watch compartment.

XI. CONCLUSION

The proposed is aimed towards checking the heart rate of the person and then detect the risk of heart attack and if there is any chance of getting the heart attack the module will contain 2 chambers which will be containing the tablets for the two cases of the heart attack one is whenever the heart rate is too low and another is for when the heart rate is very high and there is an app provided to check the heart rate and then then it will intimate the user to take the tablet from the required compartment. And simultaneously the data will be passed to the registered user so that the family members of the patient shall get an intimating message to get the heart beat data of the patient.

This project will be useful for the early detection of the heart attack to control the rate of death by providing medication at the right time so that the life of the patients shall be saved.

XII. REFERENCES

- [1]. Padmavathi Kora, A Rajani, M C Chinnaiah, K Swaraja, K Meenakshi, "IoT Based Wearable Monitoring structure for detecting Abnormal Heart" 2021 International Conference on Sustainable Energy and Future Electric Transportation (SEFET), 10.1109/SeFet48154.2021.9375787.
- [2]. Dev V. Savla, Soham Parekh, Ankit R. Gupta, Devansh Agarwal, Narendra M. Shekokar, "ResQ-Smart Safety Band Automated heart rate and fall monitoring system" 2020 Fourth International Conference on I-SMAC (IoT in Social, Mobile, Analytics and Cloud) (I-SMAC), 10.1109/ISM4C49090.2020.9243548
- [3]. G. Arunkumar; N.G. Hrisheekesh; Nehanaj Gadwal; J. Prajwal; Praveen Kumar, "2020 IEEE International Conference on Electronics, Computing and Communication Technologies (CONECCT)", 10.1109/CONECCT50063.2020.9198570
- [4]. Mamidi Manisha, Katakam Neeraja, Vemuri Sindhura, Paruchuri Ramaya "IoT on Heart Attack Detection and Heart Rate Monitoring", International Journal of Innovations in Engineering and Technology.

- [5]. YashasviYadav,ManasaSGowda,“HEARTRATEMONITORING AND HEART ATTACK DETECTION USINGWEARABLEDEVICE”,InternationalJournalofTechnicalResearch and Applications e-ISSN: 2320-8163, Volume 4, Issue3 (May-June,2016).
- [6]. Kainat Zeba, Lakshmi S Patil, Sanjana R Gowda1, Varsha R,Mrs.ShobhaChandraK,“RealTimeHeartAttackandHeartRateMonitoringAndroidApplication”,IJCSMC,Vol.7,Issue.4, April2018,pg.115–124
- [7]. Poltak Sihombing, Mangasa Manullang, Dahlan Sitompul,Imelda Sri Dumayanti “Communication at a Real Time to AvoidSudden Death” The 3rd International Conference on ComputingandAppliedInformatics2018,doi:10.1088/1742-6596/1235/1/012044
- [8]. BlaineReeder,AlexandriaDavid,“Healthathand:Asystematicreviewofsmartwatchusesforhealthandwellness” JournalofBiomedicalInformatics
- [9]. Gibson, A.L.; Wagner, D.; Heyward, V. Advanced FitnessAssessmentandExercisePrescription,8E;HumanKinetics:Champaign, IL,USA,2018.
- [10]. “PulseSensorAmped,”2015.[Online].Available:http://pulsesensor.com/pages/pulse-sensor-amped-arduino-v1dot1.
- [11]. Bhopal,R.S.EpidemicofCardiovascularDiseaseandDiabetes:Explainingthe Phenomenonin South Asians Worldwide;OxfordUniversityPress:Oxford,UK,2019.
- [12].C. Santhanakrishnan, N. Gayathri Poojitha, Jahnavi Reddy L“ASurveyonTracingHeartAttacksbyPulseMonitoringinIoT”International Conference on Physics and Photonics Processes inNanoSciences,doi:10.1088/1742-6596/1362/1/012093
- [13]. <https://store.arduino.cc/usa/arduino-uno-rev3>
- [14].Mechanic, O.J.; Shamai, A.G. Acute Myocardial Infarction;StatPearls[Internet];StatPearlsPublishing:Tampa/St.Petersburg,FL,USA,2019.
- [15]. Yadav, Yashasvi, and Manasa Gowda. "HeartRateMonitoringandHeartAttackDetectionusingWearableDevice."InternationalJournalfortechnicalresearchandApplication(2016).
- [16]. Komkrit, C. & Pongpat, M. 2016. Wireless Heart RateMonitoring System Using MQTT. Procedia Computer Science86(2016):160-163.



Wireless Multifunctional Robot for Military Applications

Nagabhushana H M^{*1}, Rudrappa K M²

^{*1}Department of Electronics and Communication Engineering, Government Engineering College,
Krishnarajapete, Karnataka, India

²Department of Electronics and Communication Engineering, Government Engineering College,
Mosalehosahalli, Karnataka, India

ABSTRACT

Robot is an electro-mechanical machine or device which is controlled either by set of computer programs or by electronic circuit to perform various of tasks. With the development in robotic technology technocrats proposed new ideas and inventions of robots. In the modern life style robots are becoming indispensable part of human life. The robotic technology also provides automation in factories, hospitals, offices and even in some hotels. Besides automation this technology also used in defence forces, Entertainment, Space exploration, Security systems and many dangerous mission executions. As the terror is always remains India's first enemy so, the robots are going to use for saving human life. Countries like India are still facing and confronting with regular threats from terrors. Both Kashmir and Mumbai terror attacks have consummated that as far as possible the future of warfare will be handle by robot and unmanned machines to protect human life. Currently, the Indian Army has Daksh Military robot to combat in battle field. As the technology proliferate rapidly in automation field by incorporating Military Robots as soldiers in war field to reduce grievance and demise in war fields. In defence areas, Robot are usually miniature in size so they are enough capable to enter in tunnels, mines and small holes in building and also have capability to survive in harsh and difficult climatic conditions for life long without causing any harm.

Keywords: Wireless, Robot, NRF, Missile System, GSM Module, Gunn System

I. INTRODUCTION

The developments in India's immediate neighborhoods over the past decade have led India an essential need to develop and upgrade its military. There is a widely sensed need for the rapid modernization of the Indian armed forces, which is being reflected in some of the key initiatives that have been taken up by the Indian government so far (such as Make in India). However, the pace of modernization of the Indian armed forces over the years has been rather slow, and technologically, they are not where they should have been. Indigenous development of modern defense hardware continues to remain a concern.

By keeping in mind, the value of each and every soldier, we can't risk their life by letting them to do surveillance tasks, risky jobs like bomb diffusing. All these works can be performed by using remotely operated robots to encounter terrorists and also to launch a rocket remotely without the presence of the soldiers in dangerous missions. Indian military is lagging behind in technology for these problems compared to other nations.

As the terror is always remains India's first enemy so, the robots are going to use for saving humans life. Countries like India are still facing and confronting with regular threats from terrors. Both Kashmir and Mumbai terror attacks have consummated that as far as possible the future of warfare will be handle by robot and unmanned machines to protect human life.

To ensure that the soldiers are on frontline is empowered with modern technologies and not to risk our soldiers' lives. The proposed work in this paper acts as a substitute for a soldier in battle ground and in any critical missions. In our Indian army there is no modern combat robot technology.

The present robots in Indian army are only capable of doing surveillance during day and night and are not capable of doing combat operations. The proposed work is capable of providing surveillance and is also capable of performing combat operations by its Gun and missile systems that can be operated remotely. Currently existing robots have limited range of coverage as they are based on Zigbee and Wi-Fi. These robots sense only one or two physical quantities. They are not capable of doing combat operations. Their cost of production is also more.

TABLE I COMPARISION WITH EXISTING ROBOTS

Features	Robots			
	DHRONA	DAKSH	DAKSH SPOTTER	DAKSH WARRIOR
Surveillance	PIR and GAS	PIR	-	PIR
Sensors	Need not be in line of sight	In line of sight	In line of sight	Need not be in line of sight
Operation	1100 meters (can be extended using next version of NRF module)	400-500 meters	600 meters	700 meters
Gun System	Yes	No	No	Yes
Missile System	Yes	No	No	No
Robotic arm	Yes	No	Yes	No

The above stated problems can be overcome by implementing the proposed work which uses NRF24L01 RF module with Arduino for the long-range operation of the robot. The robot will have night vision and day vision camera for surveillance that can be transmit data for long range.

The Robot will have GAS sensor to detect harmful gases like carbon dioxide, carbon monoxide, sulphur dioxide. The Robot also has oxygen sensor to measure the amount of oxygen in the air. The detected gases are sent to the operator using the GSM module. The Robot also has passive infrared sensor to detect humans, animals and send the detected information to the operator through the GSM module. For the bomb diffusing task, the robot has a robotic arm [1] which is mounted on the robot controlled remotely by means of gesture control. The gesture control is the easy means for controlling the robotic arm.

The present missile system is not operated remotely, means that the missile has to be launched by the presence of operator near the missile system. That is not possible near the border and enemy areas. This can be overcome by mounting the missile system on the robot, driving the robot near the border areas and firing the missile. The impact and advantages of military robot use are often lifesaving. These robots are easily replaceable at a cost, unlike human life. Robots can also endure damage caused by bombs or other types of weaponry that would otherwise destroy living beings. These robots are used to terminate any life-threatening operations. They are also equipped with gun and missile like features that make these robots as the substitute in combat zones thus saving human lives.

The Robot is user friendly and can perform multiple tasks like detecting harmful gases which is deadly for the human beings, PIR sensor for detecting living things.

Shreedhar A Joshi et al. [2] presented a wireless controlled military combat robot system. In this system the robot is controlled by a RF (Radio Frequency) transmitter and receiver module. The transmitted signal is encoded using (HT12E), which converts the parallel data into serial data and transmits through RF transmitting antenna with oscillating frequency of 434MHz. The RF receiver receives the serial data from RF transmitter by receiving antenna with frequency of 434MHz. The decoder (HT12D) converts the serial data into parallel data and fed to the driver unit. This robot can be used to detect toxic gases and can used as fire fighter with help of sensors.

E Amareswar et al. [3] proposed a multipurpose military service robot interfaced to the Bluetooth module though UART protocol. Mobile robotics with suitable sensors and cameras can perform different missions like reconnaissance patrol and relay back video images to an operator. With the development of modern technology and Android smartphone, Bluetooth technology aims to exchange data wirelessly at a short distance using radio wave transmission comprising features to create ease, perception and controllability. In this work designed a robot that can be controlled using an application running on an android controller. The phone. It sends control command via Bluetooth which is interfaced to the controller.

Tarunpreet kaur et al. [4] developed a wireless multifunctional robot for military applications. This paper presents a modern approach for surveillance at remote and border areas using multifunctional robot based on 3G technology used in defense and military applications. This robotic vehicle has an ability to substitute the soldier at border areas to provide surveillance. This multisensory robot used to detect human, bombs, harmful gases and fire at remote and war field areas. Conventionally, wireless security robot obsoletes due to limited frequency range and limited manual control. These limitations are surmounted by using 3G technology which has limitless range. This robotic vehicle is designed for reconnaissance as well as surveillance under certain circumstances.

The proposed multifunctional robot system uses NRF24L01 RF module with Arduino for the long-range operation of the Robot. The robot will have night vision and day vision camera for surveillance that can be transmit data for long range. The Robot will have GAS sensor [5, 6] to detect harmful gases like carbon dioxide, carbon monoxide, Sulphur dioxide. The Robot also has oxygen sensor to measure the amount of oxygen in the air. The detected gases are sent to the operator using the GSM module. The Robot also has Passive infrared sensor to detect humans, animals and send the detected information to the operator through the GSM module. For the bomb diffusing task, the robot has a robotic arm which is mounted on the robot. The robotic arm can be controlled remotely by means of gesture control [7]. The gesture control is the easy means for controlling the robotic arm. In addition to these, the robot is equipped with the GUN and Missile system that can be operated remotely. The gun is capable of taking down targets and is also capable of destroying the bombs.

II. PROPOSED WIRELESS MULTIFUNCTIONAL ROBOT FOR MILITARY APPLICATIONS

The block diagram of the robotic vehicle is shown in the figure 1. The Arduino controller [9] used in this work is a heart of the entire system. All the sensor modules, motor driver modules, Gun system, Communication module are interfaced with the Arduino Controller.

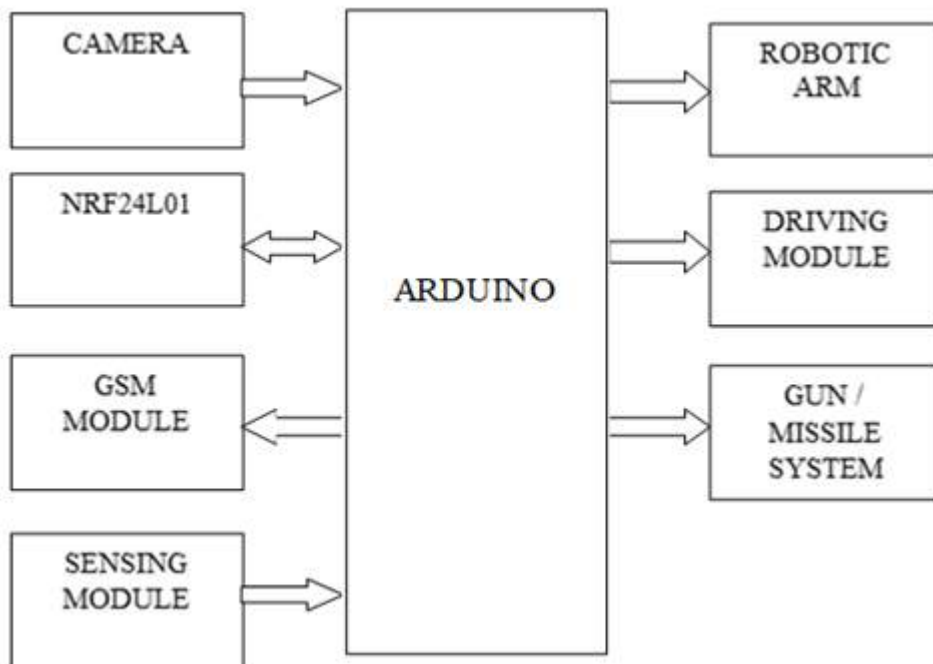


Figure 1: Block diagram of robotic vehicle

Arduino is an open source computer hardware and software that designs and manufactures microcontrollers kits for building digital devices and interactive objects that can sense and control objects in the physical and digital world. A pre-assembled Arduino board includes a microcontroller, which is programmed using Arduino programming language and the Arduino development environment. In essence, this platform provides a way to build and program electronic components.

The system also consists of GSM module [8] which is used to send information regarding the motion detected by the PIR sensor and any presence of harmful Gases. The GSM module sends the information to the control

centre. The SIM800A is a complete Dual-band GSM/GPRS solution in a SMT module which can be embedded in the customer applications. The communion Module also consists of RF Wi-Fi transmitter and receiver modules for the control of the robot from the command centre. It is a single-chip radio transceiver for the worldwide 2.4-2.5 GHz ISM band. The radio transmitters and receivers include frequency generator, enhanced shock burst mode controller, power amplifier, crystal oscillator modulator and demodulator.

The Robotic Arm in this work is used to diffuse explosives, carry medical aids, and perform dangerous jobs which are considered as life threatening for humans. The main feature of the robotic arm in this work is that the arm is gesture controlled by the movement of the human hand. The arm can move 360 degrees with 6 degree of freedom and has a payload capacity of 2 to 3 kgs. There are three types of operational envelope in the six degrees of freedom. These types are Direct, Semi-direct (conditional) and Non-direct. The designed robotic arm is shown in the figure 2.



Figure 2: Robotic arm

The speed of robotic vehicle depends upon the Size and RPM (Rotation per Minute) of DC motor. In order to drive the motors a driving module L293D is used to provide supply to motors. A single L293D contains two H bridge to rotate the motor in both clockwise and anticlockwise direction. A remote missile/gun system also known as a remote weapon system, (RWS) is a remotely operated weaponized system often equipped with fire-control system for light and medium calibre weapons which can be installed on ground combat vehicle or sea and air-based combat platforms. Such equipment is used on modern military vehicles, as it allows a gunner to remain in the relative protection of the vehicle. The gun can be rotated 180-degree clock wise and anti-clock wise direction. The gun can fire up to a maximum range of 100 meters. The fin system is mounted on a geared motor of 30 RPM for aiming the gun towards the target. The remote gun system is shown in the figure 3. The FPV camera is a micro-size and ultra-lightweight all-in-one device, integrating a 5.8G 25mW image transmission module of 48 frequency points and a 600-TVline (TVL) camera with a dipole whip antenna (SF-C01) or a 4-Leaf-Clover antenna.

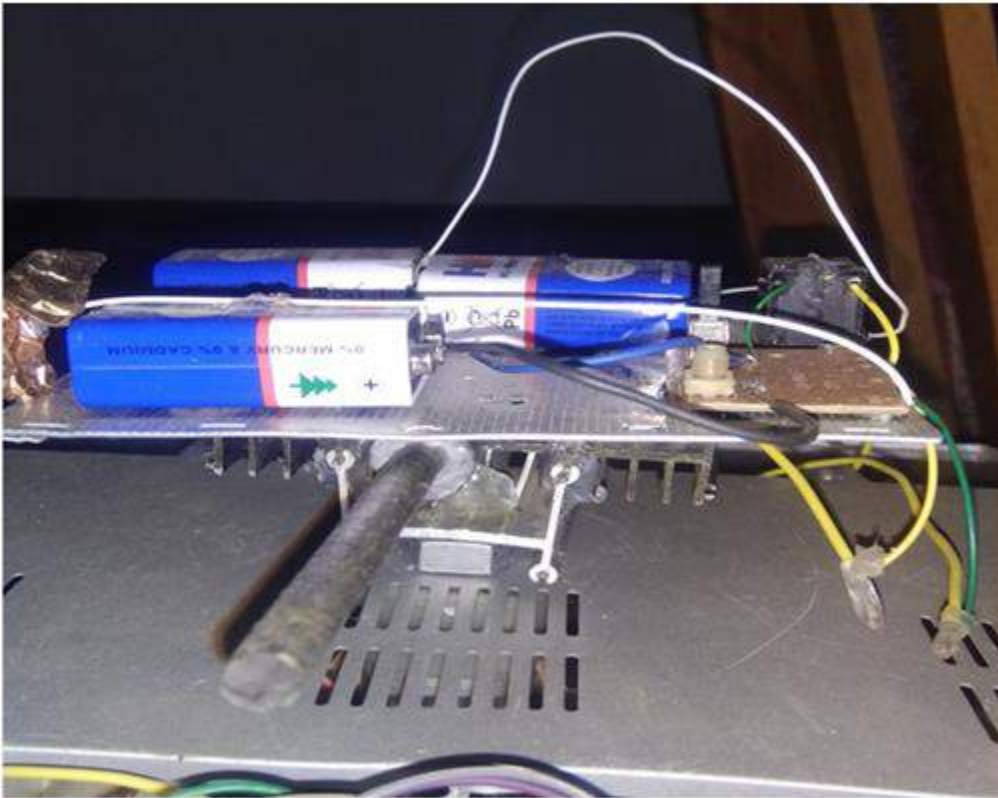


Figure 3: Remote gun system

A gas detector is a device that detects the presence of gases in an area, often as part of a safety system. This type of equipment is used to detect a gas leak or other emissions. A gas detector can sound an alarm to operators in the area where the leak is occurring, giving them the opportunity for rescue. PIR sensors are commonly used in security alarms and automatic lighting applications. PIR sensors detect general movement, but do not give information on who or what moved, so an active IR sensor is required.

III. RFABRICATION OF THE PROPOSED ROBOTIC VEHICLE AND WORKING

The robotic body can be fabricated using three quarter inch PVC tubes as they are light weight and can be cut easily into desired shapes and lengths. The initial fabricated robotic body of the system is shown in the figure 4. The transmitter circuit consists of arduino uno as the controller, NRF24L01 RF module as the antenna and the joystick which is used to control the robotic vehicle. The receiver circuit consists of another arduino, connected to another NRF24L01 module and to the motor driver module. The robot wheel DC motors are connected to the L293D motor driver module. The robotic Arm in our project has to be controlled wirelessly. For this we make use of arduino mega and DC motors and a 5 DOF robotic arm and motor driver IC for controlling the movement of the robotic arm.

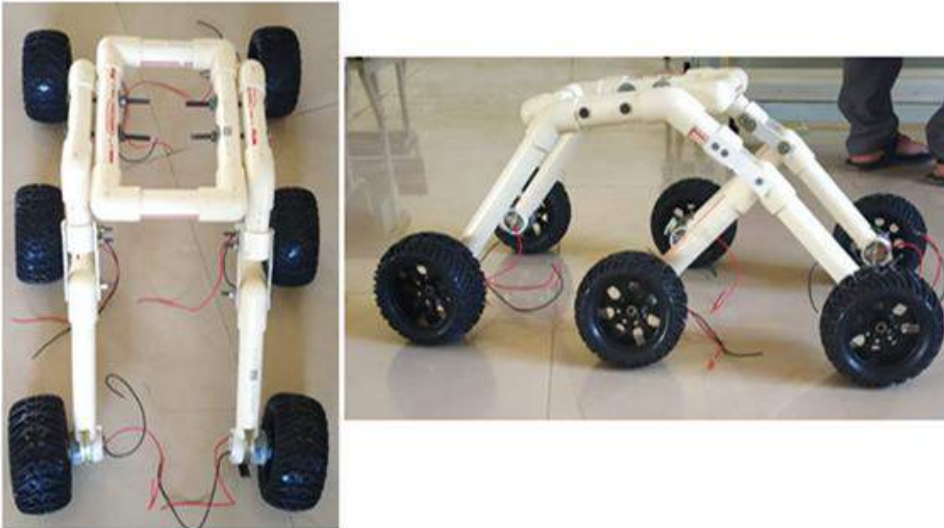


Figure 4: Fabricated robotic body

The PIR sensor and Gas sensor are used in the system. A PIR sensor can detect changes in the amount of infrared radiation impinging upon it, which varies depending on the temperature and surface characteristics of the objects in front of the sensor. A gas sensor is a device that detects the presence of gases in an area, often as a part of safety system. This type of equipment is used to detect a gas leak or other emissions and can interface with a control system so that the process can be automatically shut down. A gas detector can sound an alarm to operators in the area where the leak is occurring, giving them the opportunity to leave. The final assembled robotic vehicle is shown in the figure 5 and 6.



Figure 4: The final assembled robot



Figure 6: Wireless multifunctional robot module

The pictograph of the gun firing demonstration is shown in the figure 7 and 8.



Figure 7: Gun firing demonstration



Figure 8: Gun firing demonstration

IV. CONCLUSION

The model of wireless multifunction robot is described to build using night vision wireless camera run by Arduino controller. Controlling of robot can be performed through wireless communication using Wi-Fi and NRF24L01. The function of robot can be enhanced by adding features like gas sensors, PIR sensor and bomb defuse kit together with gun and missile launching system. The gun can be fired remotely by means of remote control using NRF24L01 radio Wi-Fi module. As the terror is always remains India's first enemy so, the robots are going to use for saving human life. Countries like India are still facing and confronting with regular threats from terrors. Both Kashmir and Mumbai terror attacks have consummated that as far as possible such circumstances will be handle by robot and unmanned machines to protect human life. To ensure that a soldier on the frontline is empowered with nice technologies and not to risk our soldier's lives. The presented work acts as a substitute for a soldier in battle ground and in any critical missions.

I. REFERENCES

- [1]. McMorran, Darren Chung, Dwayne Chung Kim Li, and Jonathan Muradoglu, "Adapting a Low-Cost Selective Compliant Articulated Robotic Arm for Spillage Avoidance," *Journal of Laboratory Automation*, vol 21, No 6, 2016.
- [2]. Shreedhar A Joshi, Girishkumar A, A K Vidyashree and Sampada Ranade, "Wireless Controlled Military Combat Robot System," *International Conference on Communication and Electronics System*, 2017.
- [3]. E Amareswar, G Shiva Sai Kumar Goud, S Aashraya and T Naveen, "Multi-Purpose Military Service Robot," *International Conference of Electronics, Communication and Aerospace Technology*, Vol 2, 2017.

- [4]. Tarunpreet Kaur and Dilip Kumar, "Wireless Multi-Functional Robot for Military Applications," International Conference on Recent Advances in Engineering and Computational Sciences, 2017.
- [5]. C. F. Tsai and M. S. Young, "Pyroelectric Infrared Sensor-based Thermometer for Monitoring Indoor Objects", Review of Scientific Instruments, vol 74, No 12, pp 5267–5273, 2003.
- [6]. D. Hallee, "Passive Infrared Sensors: A Brief Overview". In Home Safety Guide..org, 2016.
- [7]. Lang M A, "Divers Alert Network," DAN Nitrox Workshop Proceedings. Durham, pp. 197, 2009.
- [8]. "GSM Global system for Mobile Communications," 4G Americas, 2014.
- [9]. "Microcontroller Maniacs Rejoice: Arduino Finally Releases the 32-Bit Due". Retrieved 20 Feb 2018.
- [10]. Schmidt, M. "Arduino: A Quick Start Guide," Pragmatic Bookshelf, pp 201, 2011.
- [11]. Smith, "Differences Between the Arduino Uno Revision 2 and Revision 3". startingelectronics.org. 2018.
- [12]. Wali and Russeen, "An electronic nose to differentiate aromatic flowers using a real-time information-rich piezoelectric resonance measurement," Procedia Chemistry, pp 194–202, 2012.
- [13]. Billing, Rius, Fleischner and Richard. "Mars Science Laboratory Robotic Arm," 15th European Space Mechanisms and Tribology Symposium, 2011.



Preparation and Mechanical Properties Evaluation of Aluminium-Alumina Metal Matrix Composite

Mallikarjuna G B¹, E Basavaraj²

¹Department of Mechanical Engineering, Kalpataru Institute of Technology, Tiptur, Tumkur-572201, Karnataka, India

²Department of Mechanical Engineering, Jawaharlal Nehru National College of Engineering, Shivamogga-577204, Karnataka, India

ABSTRACT

Aluminium based MMC's find wide applications in aerospace, automobiles and marine sectors. Metal matrix composites (MMCs) possess significantly improved properties compared to unreinforced alloys. The mechanical properties of aluminium alloy matrix composites are strongly dependent on microstructure parameters like shape, size, volume fraction and distribution of reinforcement particles. Therefore, judicious selection of the variables is important to optimize the properties of the composites. Among various particulates used, alumina is one of the most inexpensive and low density reinforcement available in large quantity in nature. In this study, aluminium alloy LM13 and 3%, 6%, 9% and 12% (by weight) alumina of composites were prepared by stir casting liquid metallurgical method. For characterization optical microscope is used to identify the structure of the prepared composites. It is observed that the uniform distribution of silica particles in the matrix and also exists in a good bonding between matrix and reinforcement. The hardness of the composites was increased with increasing the amount of alumina in aluminium. An experimental result shows that there are enhanced mechanical properties, when alumina weighing 9% was added to the base aluminium LM13 alloy.

Keywords: Al alloy LM13, Alumina, Mechanical properties, Stir casting

I. INTRODUCTION

Technology related to industry is growing at a very rapid rate now days and consequently there is demand for modern materials. Particulate reinforced composites constitute a large portion of these modern advanced materials [1]. Metal matrix composite (MMC's) is a combination of the metal as matrix material and hard particle/ceramic as reinforcement to get good properties. MMC's are used for the space shuttle, commercial airliners, electronic substrates, bicycles, automobiles, golf clubs, and a variety of other applications [2-3]. A good combination of high strength and ductility of the Aluminum based metal matrix composites (MMC's) have introduced the new material to a wide area of possible advanced applications. In general stir casting

technology was used to preparation of MMC's in the processing time it melt of the selected matrix material, followed by reinforcement material is introducing into the melt, obtaining a suitable dispersion through stirring process. Its advantages are simplicity, flexibility and applicability to large quantity production. It is also attractive because, in principle this method suitable for engineering application in terms of production capacity and cost efficiency [4]. In metal matrix composites Aluminium is the most popular matrix material. Due to its lower density aluminium is quite attractive, their strengthened capability to be by precipitation, good resistance to corrosion, high thermal and high electrical conductivity and damping capacity. The demand for structural materials are to be cost effective and also to provide high performance has resulted in continuous attempts to composites develop as serious competitors to the traditional engineering alloys[5]. In the recent years, usage of particle ceramic as a reinforcement in metal matrix composites (MMC's) is steadily enhancing because of their advantages like good isotropic properties and the secondary processing possibility [6]. Composites based Al alloy have replace the other costlier material in many engineering applications significantly. The requirements concerning safety factor and reliability are always improving and therefore the properties like mechanical are more important [7].

II. METHODS AND MATERIALS OF COMPOSITES

In this work aluminium LM13 alloy used as a matrix material and 355 μ m size of alumina as a particulate reinforcement with different weight percentages (in wt.% 3, 6, 9 and 12) are used. The composites were prepared by using stir casting method. Permanent mould made from cast iron is used for preparing composite castings. ASTM standards are followed to prepare testing specimens of the prepared composites. The toughness and formability of 12% silicon aluminum alloy can be combined with the reinforcement particles. The matrix material LM13 aluminum alloy chemical compositions are shown in Table 1. Alumina provides excellent hardness properties on incorporation into the soft alloy, thereby using it better where hardness is desirable applications. Figure 1 shows the setup of stir casting method.

Table.1: Chemical Composition of Al alloy LM13 by Wt. %.

Elements	Zn	Mg	Si	Ni	Fe	Mn	Al
Wt. %	0.5	1.4	12	1.5	1.0	0.5	Balance



Figure.1: Stir casting method setup.

III. PROCEDURE FOR PREPARED COMPOSITES TESTING

The cast composites were machined and the specimens for the measurement of tensile strength and impact behavior were prepared as per the ASTM standards. The tensile strength (E8M) properties and Impact test (E23) properties were evaluated in laboratory as per the standards. The specimens prepared for hardness, tensile test and impact test as shown in figure 2.



Figure 2: Hardness, Tensile test specimen and Impact test specimen

IV. RESULTS AND DISCUSSIONS

Microstructure Examination:

Microstructure is visualized with the help of optical microscope. The microstructural images of the different specimens containing 3% to 12% weight of alumina for the microns size of 355 μ m as shown in below figure 3. These are typical micrographs of the MMC's showing that the alumina particles are uniformly dispersed in the matrix aluminium alloy. The micrograph shows the increased reinforcement contents in the prepared composites.

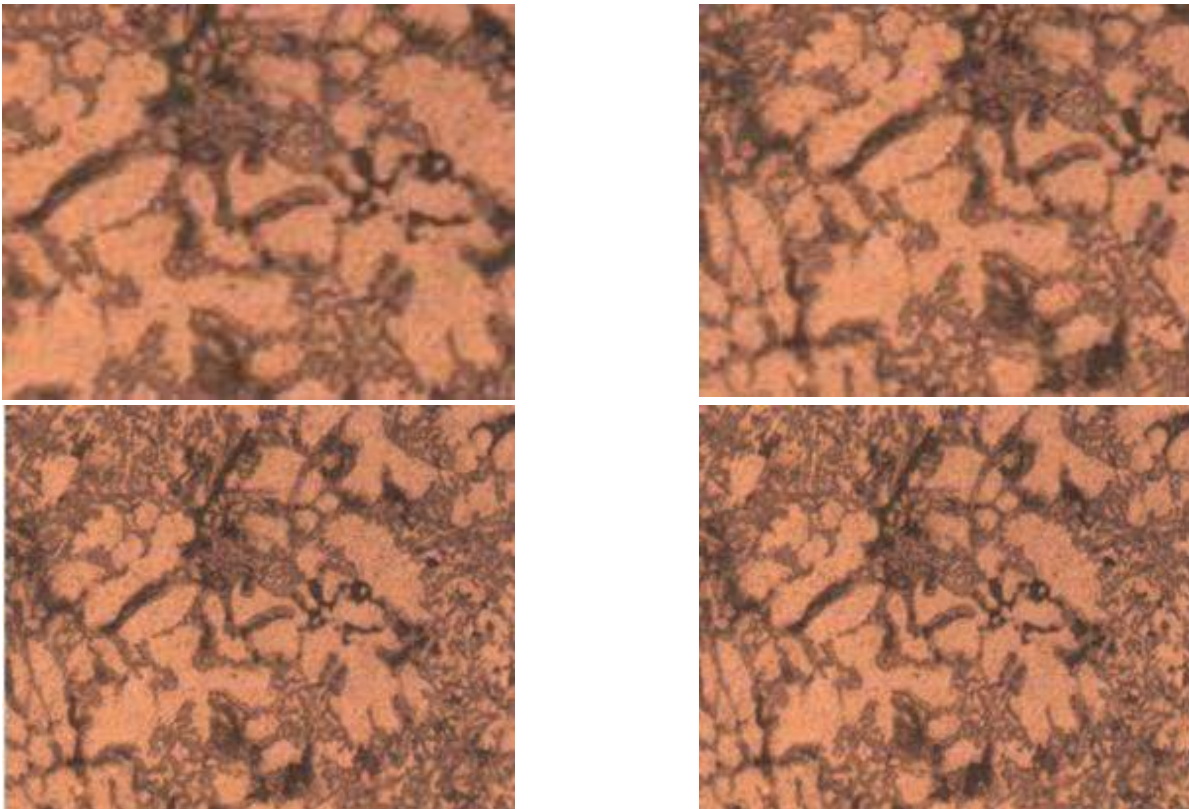


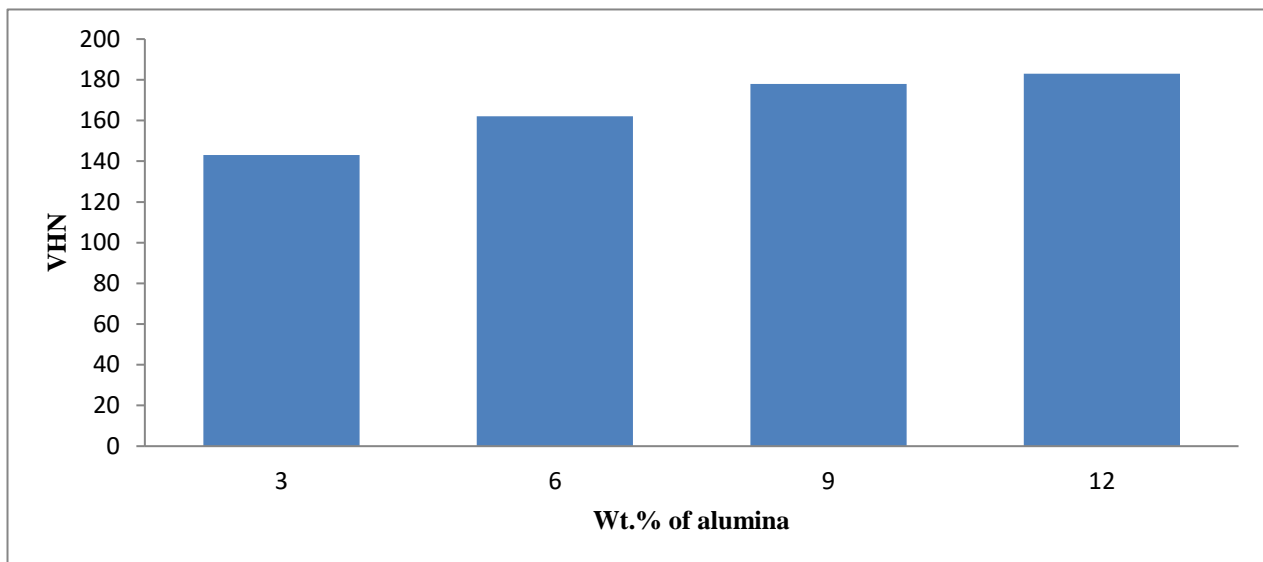
Figure 3: Microstructure of Al LM13 alloy with wt. % of alumina for 355 micron size.

Hardness:

The prepared composites vicker hardness test results are tabulated in Table 2. To know the reinforcement effect in the matrix material, the hardness tests were conducted on Al alloy LM13- Al_2O_3 of various micron size composites. The specimens prepared were tested using Zwick Vickers microhardness testing machine. The hardness was determined by recording the indentation produced on specimen. Figure 4 shows the microhardness test results of the prepared composites. The composite containing 355micron size and wt.% of alumina reinforcement. From the Figure 4 clearly reveals the hardness number of the prepared composite material is much higher than that of its base metal hardness number. It is also shown that the prepared composite materials hardness number was increases with increased weight percentage of reinforcement content.

Table.2: VHN for 355 micron size of reinforcement alumina with weight percentage.

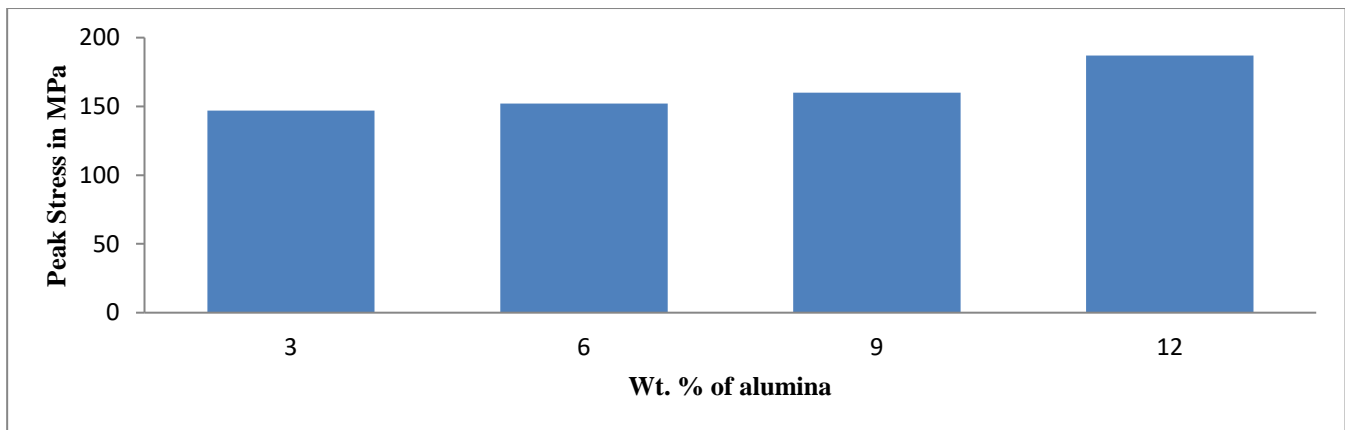
Weight Percentage	VHN
3%	143
6%	162
9%	178
12%	183

**Figure.4: VHN v/s Wt. % of alumina reinforcement.****Tensile Test:**

The tensile test results of the prepared composite are tabulated in Table 3. The values of tensile strength for 355 micron size weight percentage of Al_2O_3 are shown in Figure 5. Addition of reinforcement Al_2O_3 in base metal increases the tensile strength. Tensile strength increases because the bonding strength between reinforcement and matrix material increases. The figure 5 shows tensile strength increases with the addition of reinforcement particle. The addition of reinforcement makes the base alloy more ductile.

Table.3: Tabulation of results is as follows showing tensile properties for the prepared composites in Mpa.

Weight percentage	Tensile Strength (MPa)
3%	147
6%	152
9%	160
12%	187

**Figure.5: Peak stress v/s Wt. % of alumina reinforcement.****Impact Test:**

The strength, ductility and toughness of material are modified when impact loads are used instead of static loads. Toughness is a measure of the energy that the material absorbs during plastic deformation before its failure under impact loading. The impact tests were done on the samples using Charpy test as ASTM E23 standards. The values for the impact tests have been given in Table 4 and it's been clear that the sample with varying weight percentage of alumina absorbs more energy than base alloy. Figure 6 shows the variation of impact energy with weight percentage of reinforcement.

Table 4: Tabulated Impact Energy value of the prepared composite

Weight percentage	Impact Energy (N-m or Joules)
3	3
6	3
9	6
12	7

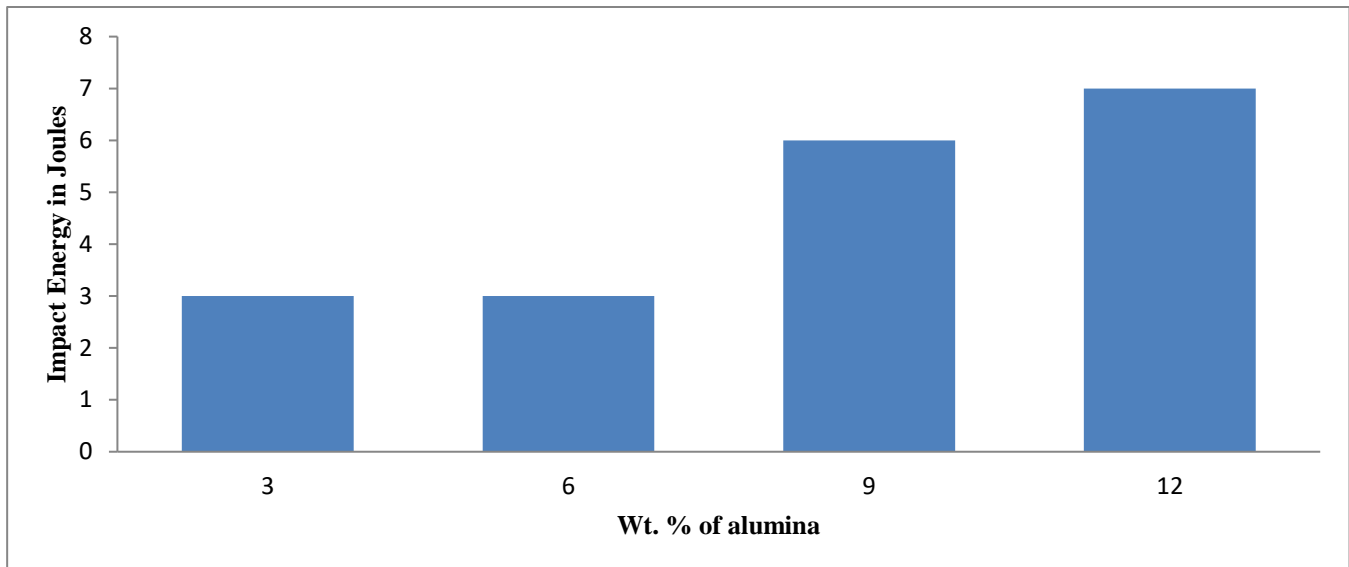


Figure.6: Impact energy v/s Wt. % of alumina reinforcement

V. CONCLUSION

- Al alloy LM13-Alumina composites are prepared successfully by using stir casting method.
- The microstructures observation shows the distribution of the alumina particles (reinforcement) in the aluminium base alloy (matrix material) is uniform.
- Hardness and tensile strength were increased with addition of reinforcement alumina reinforcement.
- Impact energy was increased with the addition of reinforcement material.
- In overall, in this study the Al LM13 alloy - Alumina composites obtained excellent mechanical properties compare to base alloy metal.

VI. REFERENCES

- [1]. A.M.S. Hamouda , S. Sulaiman , T.R Vijayaram , M. Sayuti , M.H.M. Ahmad, "Processing and characterisation of particulate reinforced aluminium silicon matrix composite", Journal of Achievements in Materials and Manufacturing Engineering, volume 25 Issue 2 December 2007.
- [2]. Manoj Singla, D.Deepak Dwivedi et al, "Development of Aluminium Based Silicon Carbide Particulate Metal Matrix Composite", Journal of Minerals & Materials Characterization & Engineering, Vol. 8, No.6, pp 455-467, 2009.
- [3]. Mallikarjuna G B, K V Srinivas, "Preparation and property evaluation of Aluminium-Silica composite by casting route", ISSN 2278 – 0149, Vol. 1, No. 3, October 2012, IJMERR.
- [4]. M. N. Wahab, A. R. Daud and M. J. Ghazali, "Preparation And Characterization of Stir Cast- Aluminum Nitride Reinforced Aluminum Metal Matrix Composites", International Journal of Mechanical and Materials Engineering (IJMME), Vol. 4 (2009), No. 2, 115-117.

- [5]. H. Zuhailawati*, P. Samayamutthirian and C.H. Mohd Haizu, "Fabrication of Low Cost Of Aluminium Matrix Composite Reinforced With Silica Sand", *Journal of Physical Science*, Vol. 18(1), 47–55, 2007.
- [6]. J. Babu Rao*, D. Venkata Rao and N.R.M.R. Bhargava, "Development of light weight ALFA composites", *International Journal of Engineering, Science and Technology* Vol. 2, No. 11, 2010, pp. 50-59.
- [7]. Joel Hemanth, "Quartz (SiO₂p) reinforced chilled metal matrix composite (CMMC) for automotive applications" *Materials and Design* 30 (2009) 323–329 @ Elsevier Ltd.
- [8]. Sudarshan and M.K. Surappa, "Dry sliding wear of fly ash particle reinforced A356 Al composites", *Wear* 265 (2008) 349–360 at www.sciencedirect.com.



Optimization of MRR for CNC Turning of Steel

Surendra Kumar Saini

Department of Mechanical Engineering, Poornima College of Engineering, Jaipur -302022, Rajasthan, India

ABSTRACT

Stainless steel is mainly used for manufacturing of different parts like bio-implants, milk and food containers drink cans, surgical tools and structural components. It possesses excellent chemical and mechanical properties. Turning of this steel with digital control lathe enhance the material removal rate as well other desired quality characteristics than conventional lathe. Therefore in the present study digitally control lathe that is computer numerical control (CNC) lathe used to machine stainless steel. Turning on work material conducted using orthogonal array twenty seven by varying control factors speed, feed and depth of cut. Significant factor is evaluated using analysis of variance method. Depth of cut is found as significant control factor followed by feed and speed.

Keywords: steel, CNC turning, orthogonal array, coated carbide tool, Taguchi method

I. INTRODUCTION

Computer numerical control (CNC) lathe digitally control the distinct control parameters that affects the quality characteristics. However these parameters can be control manually in conventional lathe. Evaluation of optimum turning parameters for different materials may have a reference values for emerging industries. Therefore researchers have reported their work based on turning of different hard materials. Later suggested optimum values of process parameters obtained from different statistical methods [1-6]. Akhtar et al. conduct turning on aluminium alloy using orthogonal array and revealed optimum values of parameters [7]. Rizvi and Ali analysed the surface and material characteristics of CNC turned steel using hybrid approach [8]. Qinge et al. [9] had done turning to optimize turning parameters. They used hybrid method i.e. fuzzy logic and data mining for optimization of power consumption during turning. Their experimental and simulation finding were superimposed. Riadh et al. [10] studied parametric effects on surface roughness and material removal rate for turning of cobalt alloy. Tamizharasan et al. [11] used Taguchi methodology for investigation of chip thickness ratio during CNC turning of metal matrix composite. They reported that cutting speed has more effect on chip thickness ratio. Palanisamy et al. [12] used orthogonal array during turning of nickel based super alloy. Surface roughness, micro-hardness and material characteristics of work material have investigated. Ngoc et al. [13] used Taguchi-adaptive neuro-fuzzy inference system-teaching learning based model to find the optimum values of process parameters for carbon steel turning. Surface finish of analysed by varying control factors feed, speed

and depth of cut for turning of steel [14-15]. Accuracy of developed techniques found robust. From the short literature review, author unable to find CNC turning of hard steel (AISI 304) using CNC Turn 250 (Model Manufacturer: EMCO Concept) with coated carbide cutting tool made of ceratizit. Orthogonal arrays (L27) are used for conduct the experiment. The main aim of present study is to obtain the optimum value of CNC lathe control factors (i.e. spindle speed, feed and depth of cut) for material removal rate. Values of optimum control factors have been obtained using Taguchi and analysis of variance methods. In this analysis it is found that the depth of cut is most significant.

II. MATERIALS AND METHODS

The Stainless steel (AISI304) is elected because it has wide applications like bio-implants, milk and food containers drink cans, surgical tools and structural components, textile equipments, cryogenic vessels and coal hopper etc. Chemical composition of work material is shown in Table I. The work piece tensile strength (MPa) = 124, experimentally calculated density (Kg/m³) = 7964, thermal conductivity (W/m-k) = 116 and melting temperature (°C) = 885. Coated carbide cutting tool made of ceratizit used for cutting (turning) and CNC Turn 250 made of EMCO Concept lathe (Figure 1) used for turning. Control factors spindle speed (rpm), feed (mm/rev) and depth of cut (mm) and their associated levels are selected based on preliminary literature review and catalogue provided by cutting tool manufacturer for machining of AISI 304 stainless steel. The levels of turning process parameters are shown in Table II. Material removal rate is calculated by the weight difference of the work piece before and after machining using weighing machine then divide by the machining time multiply with the density of the selected material. Material removal rate is measured in term of (mm³/min). To determine the MRR in term of signal to noise ratio (SNR) equation (1) is used.

TABLE I CHEMICAL COMPOSITION OF WORK PIECE (IN PERCENTAGE)

Fe	Si	Mn	P	S	Cr	Ni	N	C
66-74	1.0	2.0	0.045	0.03	18-20	8-11	0.10	0.08



Figure 1: Photograph of EMCO Concept Turn 250 machine tool used for turning.

Table II Levels of control factors

Factors	Units	Levels		
		i	ii	iii
Spindle Speed (SS)	RPM	1400	1600	1800
Feed	mm/rev	0.08	0.14	0.2
Depth of Cut (DOC)	mm	0.4	0.8	1.2

Signal-to-Noise Ratio for MRR:

$$\left[\frac{s}{N} = -10 \log \left(\frac{\left(\sum \frac{1}{Y_i^2} \right)}{n} \right) \right] \quad (1)$$

Larger – The – Better

III. RESULTS AND DISCUSSION

Turning operation performed on work material using CNC lathe with coated carbide cutting tools. Material removal rate is calculated by the weight difference of the work piece before and after turning using weighing machine then divide by the machining time multiply with the density of the selected material. The experimental values of MRR are present in Table III.

TABLE III ORTHOGONAL ARRAY LAYOUT (L_{27}) AND CORRESPONDING VALUE OF MRR

Exp. No.	Input parameters			MRR	
	SS	Feed	DOC	Experimental values (mm ³ /min)	Signal to noise ratio (dB)
1	1400	0.08	0.4	1711.991	64.6700
2	1400	0.08	0.8	3358.02	70.5217
3	1400	0.08	1.2	5087.312	74.1298
4	1400	0.14	0.4	2674.663	68.5454
5	1400	0.14	0.8	6588.058	76.3751
6	1400	0.14	1.2	9660.706	79.7002
7	1400	0.20	0.4	4158.724	72.3792
8	1400	0.20	0.8	8566.931	78.6565
9	1400	0.20	1.2	13432.547	82.5632
10	1600	0.08	0.4	2154.555	66.6672
11	1600	0.08	0.8	5004.753	73.9877
12	1600	0.08	1.2	54175.257	94.6760
13	1600	0.14	0.4	5129.8157	74.2020

14	1600	0.14	0.8	10146.888	80.1267
15	1600	0.14	1.2	11329.797	81.0844
16	1600	0.20	0.4	6134.568	75.7557
17	1600	0.20	0.8	12022.136	81.5996
18	1600	0.20	1.2	18293.522	85.2459
19	1800	0.08	0.4	2719.479	68.6897
20	1800	0.08	0.8	5569.003	74.9155
21	1800	0.08	1.2	7774.587	77.8135
22	1800	0.14	0.4	4988.176	73.9588
23	1800	0.14	0.8	8768.331	78.8583
24	1800	0.14	1.2	12614.619	82.0175
25	1800	0.20	0.4	6717.615	76.5443
26	1800	0.20	0.8	12144.053	81.6873
27	1800	0.20	1.2	12905.436	82.2155

Analysis of Variance (ANOVA) method was introduced by Sir Ronald Fisher to evaluate different statistical components like sums of squares, degrees of freedom, error variance and F-values. Maximum material removal rate is always desired on CNC turned work part. Therefore higher is better type quality characteristic used to evaluate the signal to noise (S/N) ratio as shown in Table III. Rank of control factors evaluated by Taguchi method that is shown in Table IV. The ANOVA test performed at the significance level of 5% and confidence level of 95% [16]. From Table V, depth of cut found high than other control factors. It means depth of cut is more responsible for high material removal rate. This validates the results obtained using Taguchi method based optimization. The Figure 2 depicts the effect of control factors.

TABLE IV EVALUATION OF SIGNIFICANT CONTROL FACTORS

Levels	SS	Feed	DOC
i	74.17	74.01	71.27
ii	79.26	77.21	77.41
iii	77.41	79.63	82.16
Difference of maximum and minimum	5.09	5.62	10.89
Rank	3	2	1

Table V ANOVA TEST RESULT

Factors	DOF			
		SS	MS	F-value
SS	2	283727854	141863927	1.75
Feed	2	29506189	14753095	3.18

DOC	2	684455765	342227882	4.22
SS*Feed	4	269312890	67328223	0.83
Feed*DOC	4	242266043	60566511	0.75
SS*DOC	4	368326042	92081510	1.13
Error	8	649193073	81149134	
Total	26	252678785		
S = 9008.28 R-Sq = 74.31% R-Sq (adj) = 16.50%				



Figure 4: Main effect of SNR versus control factors

IV. CONCLUSION

Turning on stainless steel (grade AISI304) conducted using computer numerical control turn machine. Material removal rate of work material has analyzed using Taguchi and analysis of variance methods. Following observations are found from present study.

- Orthogonal array design used for turning on work material.
- Analysis of variance test done on 95% of confidence level.
- Depth of cut is found significant parameter.

V. REFERENCES

- [1]. Saini S. K., Pradhan S. K., Soft Computing Techniques for the Optimization of Machining Parameter in CNC Turning Operation, International Journal of Emerging Technology and Advanced Engineering, 4 (2014) 117-124.
- [2]. Joshi V, Kumar H. Optimization of CNC Lathe Turning: A Review of Technique, Parameter and Outcome. Advances in Manufacturing and Industrial Engineering 73 (2021) 963.

- [3]. Natarajan C., Muthu S., Karuppuswamy P., Prediction and analysis of surface roughness characteristics of a non-ferrous material using ANN in CNC turning, *International Journal of Advance Manufacturing Technology* 57 (2011) 1043-1051.
- [4]. Saini S. K. and Pradhan S. K., Optimization of multi-objective response during CNC turning using taguchi-fuzzy application. *Procedia Engineering* 97 (2014) 141-149.
- [5]. Saini S. K. and Pradhan S. K., Optimization of machining parameters for CNC turning of different materials. *Journal of Applied Mechanics and Materials* 592-594 (2014) 605-609.
- [6]. Pradhan S. K. and Saini S. K., Multi-objective optimization of CNC turning machining parameters. *Journal of Advanced Materials Research* 1016 (2014) 172-176.
- [7]. Akhtar MN, Sathish T, Mohanavel V, Afzal A, Arul K, Ravichandran M, Rahim IA, Alhady SS, Bakar EA, Saleh B. Optimization of Process Parameters in CNC Turning of Aluminum 7075 Alloy Using L27 Array-Based Taguchi Method. *Materials* 14 (2021) 4470.
- [8]. Rizvi SA, Ali W. Analysis of surface roughness and material removal rate in machining of AISI 1040 steel using CNC turning process. *International Journal of Innovation in Engineering* 3 (2021) 8-19.
- [9]. Qinge X., Congbo Li, Ying T., Lingling Li, Li Li, A knowledge-driven method of adaptively optimizing process parameters for energy efficient turning, *Energy* 166 (2019) 142-156.
- [10]. Riadh S., Brahim B. F., Tarek M., Salim B., Mohamed A. Y., Modeling and optimization of the turning parameters of cobalt alloy (Stellite 6) based on RSM and desirability function. *The International Journal of Advanced Manufacturing Technology* 100 (2019) 2945-2968.
- [11]. Tamizharasan T., Senthilkumar N., Selvakumar V., Dinesh S. Taguchi's methodology of optimizing turning parameters over chip thickness ratio in machining P/M AMMC, *SN Applied Physics* 1-160 (2019).
- [12]. Palanisamy A., Selvaraj T., Sivasankaran S., Optimization of turning parameters of machining incoloy 800h superalloy using cryogenically treated multilayer cvd-coated tool. *Arabian Journal for Science and Engineering* 43 (2018) 4977-4990.
- [13]. Ngoc L. C., Minh-Quan N., Thanh-Phong D., Shyh-Chour H., Te-Ching H., Du D., Van A. D., An effective approach of adaptive neuro-fuzzy inference system-integrated teaching learning-based optimization for use in machining optimization of S45C CNC turning. *Optimization and Engineering* 20 (2019) 811-832.
- [14]. Saini S. K. and Kumar P., CNC turning process parameters optimization for stainless steel. *Applications of Advanced Computing in Systems* pp 59-64. https://doi.org/10.1007/978-981-33-4862-2_6.
- [15]. Pradhan S K, Saini S. K., Multi-Objective Optimization of CNC Turning Machining Parameters. *AMR* 2014;1016:172-6. <https://doi.org/10.4028/www.scientific.net/amr.1016.172>.
- [16]. Saini S. K. and Dubey A. K., Study of material characteristics in laser trepan drilling of ZTA. *Journal of Manufacturing Processes* 44 (2019) 349-358.



Synthesizing of Polymer Derived Ceramic Foams and Its Applications – A Review

Sree Krishna M¹, Kiran B Gowda², H C Madhu³

¹Department of Mechanical Engineering, Siddaganga institute of technology, Tumkur, Karnataka, India

ABSTRACT

Ceramics foams have immensely influenced development of humanity. Their role in automobile industries to heat-shields in space applications are noteworthy mentions. Due to their low density, chemical stability and temperature resistance, novel applications for them are developed every day. This is especially true for porous ceramics. However, ceramics are brittle, due to lack mechanisms such as dislocation or twins. This results in low toughness and resistance to thermal shock. These true ceramics can be synthesised by self-propagating reaction, sol-gel precipitation methods or polymer pyrolysis methods. The main aim of this review is to provide better understanding of polymer derived ceramics synthesizing strategy.

Silicon based ceramics which are derived from preceramic polymer are generally called as polymer derived ceramics. Transformation process from polymer to ceramic foam contains different stages namely shaping, cross-linking, pyrolysis and crystallization. Silicon based polymer derived ceramics can be easily synthesized by preceramic organosilicon polymer. Also, this process has control over porosity, intermediate processing temperature (600°C – 1000°C), less processing cost, simple methodology. The obtained ceramic will possess low density, high thermal resistance, chemical stability and also control over permeability. In addition to this some polymeric properties such as ductility, solubility in organic compounds. For example, polysiloxane polymers have high ceramic yield because of high cross-linking tendency.

Keywords: Polymer derived ceramics (PDC), Cross-linking, Pyrolysis, Ceramic Foams.

I. INTRODUCTION

Polymer derived ceramic foams are foams obtained by pyrolyzing the polymeric precursor. It is also called as cellular ceramics because of high number of pores. Ceramic foams' basic structural unit consists of solid struts and pores surrounded by them. It is possible to produce such advanced ceramic foams by liquid polymer precursors, so that it will be easier in shaping process when compared to conventional powder sintering process.

Ceramic foams have unique properties such as low thermal conductivity, low density, high thermal shock resistance, high permeability, high specific strength and chemical stability. These properties of cellular ceramic

materials are influenced by their morphology, size and distribution of pores. These properties can be varied depending on the type of synthesizing techniques which includes sol-gel precipitation method, self-propagating reaction method and polymer derived ceramic method i.e., replica technique, sacrificial technique, direct foaming and reaction technique). Reported data shows that the SiOC derived from replica technique is the most studied ceramic because of low cost and availability of the precursors, which are easy to handle. Ceramics and its composites have immense applications in the area such as thermal protection systems, automobile bike brake disc, heat exchangers, light weight structures, filtering molten metals or hot gases and other space applications.

II. MATERIALS AND SYNTHESIZING TECHNIQUES

The microstructure, phase distribution and morphology of the ceramic foams will be influenced by the molecular structure and type of preceramic precursor. The physical properties of ceramics can be varied by the selection of proper molecular precursor structure.

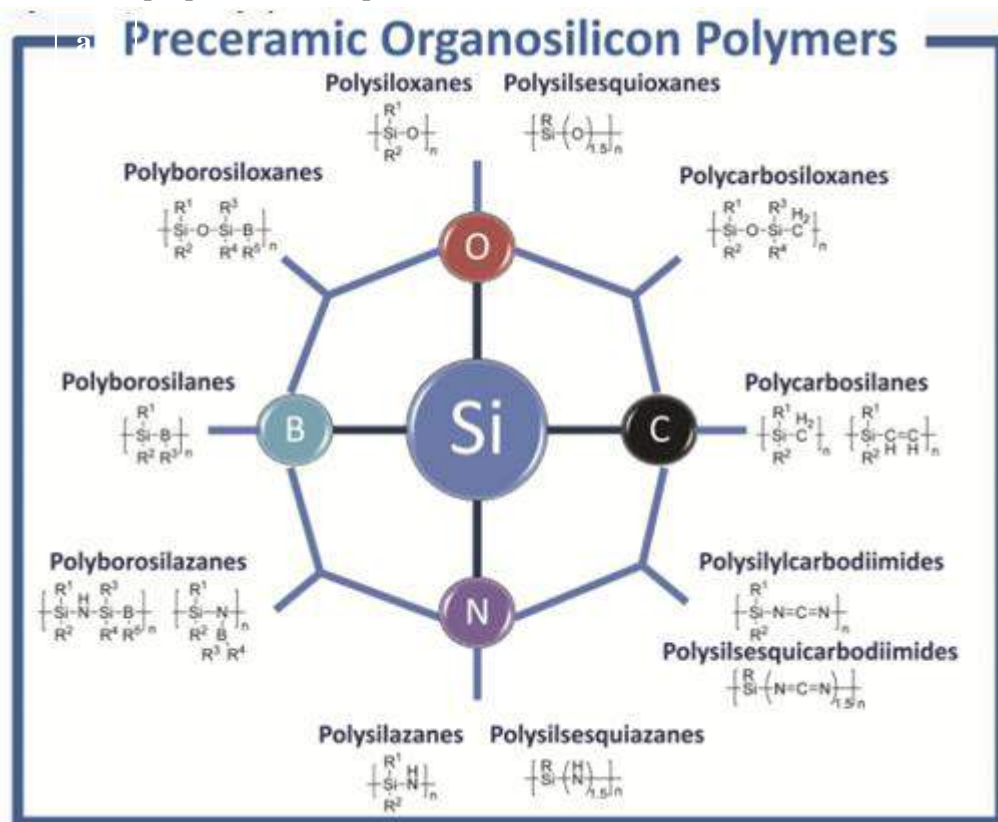


Figure1:Materials [4]

Polyorganosiloxanes are the most widely used precursors. Polymer which contains Si-O-Si linkage with organic compounds attached to the silicon are called as polyorganosiloxanes. The method of preparing polysiloxanes contains the reaction of chlorogano silanes with water. For example, PHMS (polyhydromethylsiloxne) and PDMS (polydimethylsiloxane).

Polyorganosilanes are synthesized by wurtz-type reductive dehalogenation reaction. There is another alternate method to produce polyorganosilanes is catalytically dehydrogenative oligomerization of hydrosilanes with transition metals.

Polyorganocarbosilanes are derived from polyorganosilane using the reaction called thermal reorganization of polymethylsilane. It is known as kumada rearrangement. The method used for synthesizing polyorganosilazanes is ammonolysis of organosilicon chlorides. Due to its high molecular weight, its yield will be generally high. [1,4]

Polymer derived ceramics

Ceramics which are obtained by pyrolyzing the organosilicon polymers. There are several methods with which we can achieve PDC are replica technique, sacrificial technique, direct foaming and reaction technique.

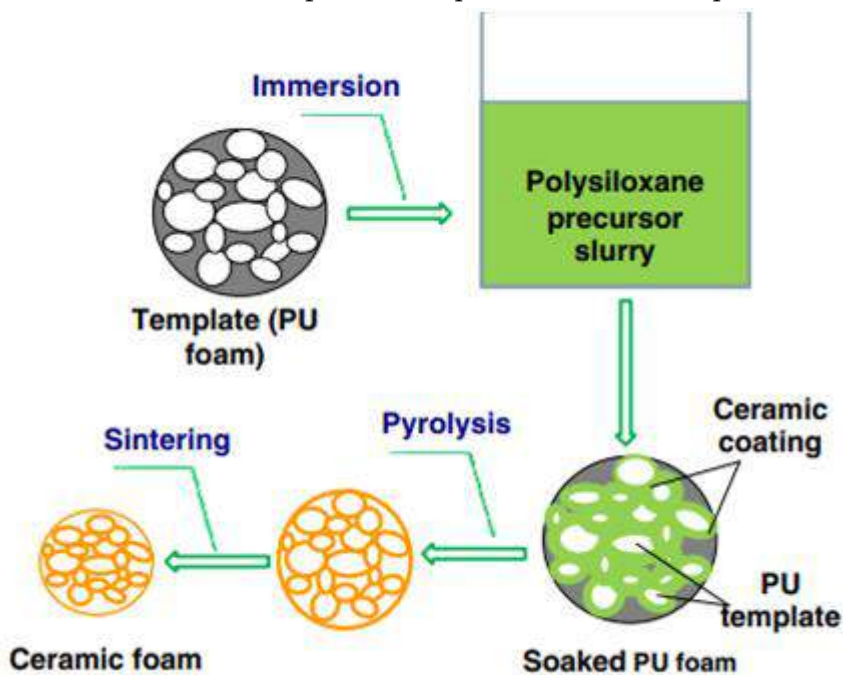


Figure2:Replica technique[6]

The **Replica technique** is the most widely used in synthesizing the cellular ceramic foams. In replica method, the porous structured polyurethane foam is immersed in polymer precursor, then allow it to cross-link for few hours. The process of formation of covalent bonds between the polymer chains is called cross-linking. Then the templates and precursor become more rigid. Then it is subjected to pyrolysis at high temperature (600°C to 1000°C). After pyrolysis, ceramic foams with cell size greater than $150\ \mu\text{m}$ would be formed.

Some researchers found another way of producing ceramic foams using wood template followed by cross-linking and pyrolysis. This technique has added additional yield that prevent cracking before and after pyrolysis. [6,7]

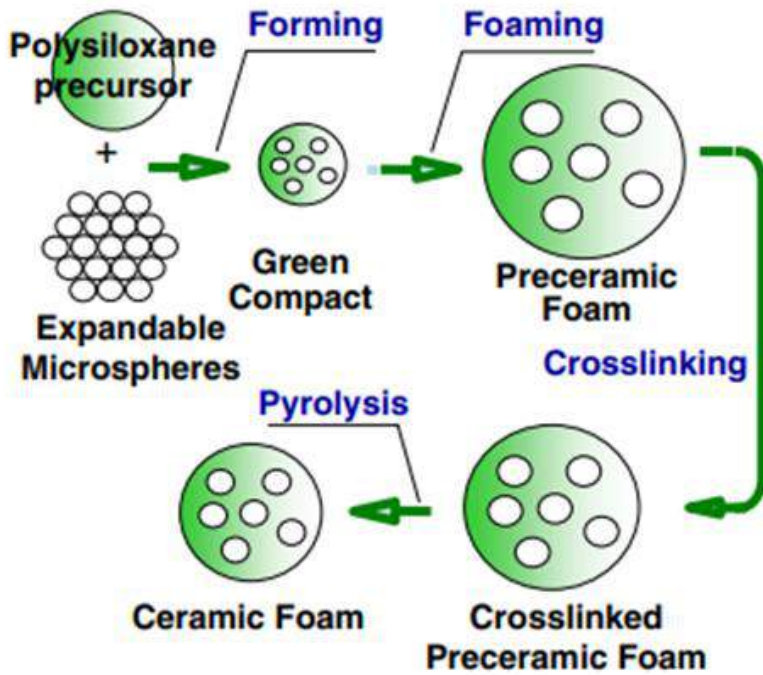


Figure3:Sacrificial technique [6]

In **Sacrificial Technique**, a composite containing expandable sacrificial template with preceramic polymer is to be prepared, followed by foaming, cross-linking and pyrolysis to get the porous PDC. The sacrificial template materials are usually extracted by chemical means such as salts. After pyrolysis, the cell size of ceramic foams ranges from 10-100 μm . [6,7]

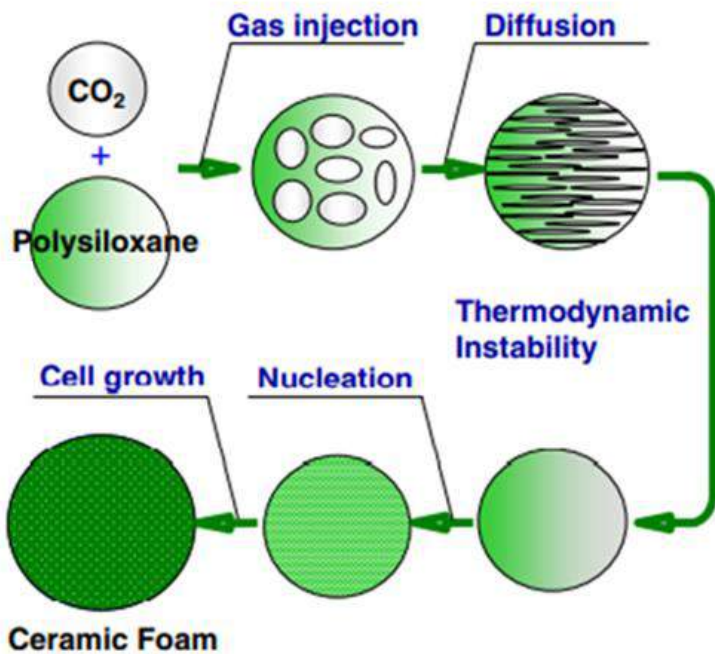


Figure4:Direct Foaming [6]

The direct foaming is the fastest way to device ceramics. We can obtain the foam structure by blowing CO₂ gas into the polysiloxane precursor. Then the bubbles are generated in the precursor, upon heating the porous ceramic yields. Apart from CO₂, blowing agents can be volatile liquids such as freon& pentane and solid agent like calcium carbonate. To control the stability of the ceramic foams' thin layers may rupture when the cellular ceramics becomes thin due to drainage of precursor and shrinkage of bubbles. Here porosity and pore size are depends on the amount of blowing agent and polymer precursor.the cell size of ceramic foams ranges from 2-50 μm.[6,7]

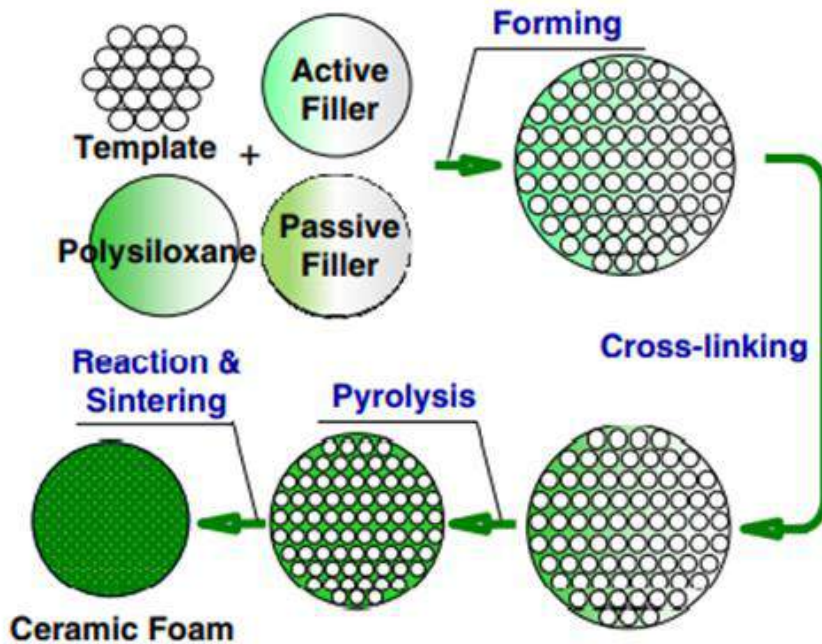


Figure5:Reaction technique [6]

Reaction technique is the oldest technique to synthesize the structural ceramic foams. Sacrificial template is being used along with the mixture of polymer precursor and active & passive fillers such as aluminium oxide, kaolin and silicon carbide.i.e., 80% polysiloxane, 3% kaolin, 2% aluminium oxide and 15% template by weight. After pyrolysis, the cell size of ceramic foams ranges from 10-45 μm.[6,7]

Sol-gel precipitation and self-propagating reaction

The processing of sol-gel is a liquid to solid transformation. Sol-gel precipitation is a wet chemical technique used for the fabrication of both glassy and ceramic materials. The sol SiO₂ is mixed with H₂/Ar by situ gas evolution method. Then the foamed sol will be converted into gel. In this process, it needs metal salts as starting compounds and H₂/Ar in reduction step. Since there is no contamination in this process, it is suitable for synthesizing high purity ceramic foams. The cell size usually ranges from 10-600 μm. Self-propagating reaction method is used for producing both organic and inorganic compounds. This process contains exothermic combustion reactions in solids of different nature. [1]

III. MICROSTRUCTURES

1. SEM and Tomography:

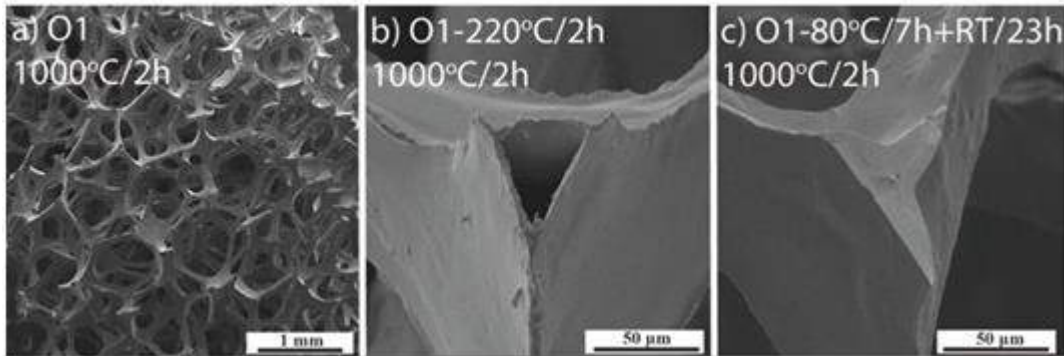


Figure6: SEM micrographs of O1, O2 and C1 samples with 100% PHMS at 1000 ° C. [3]

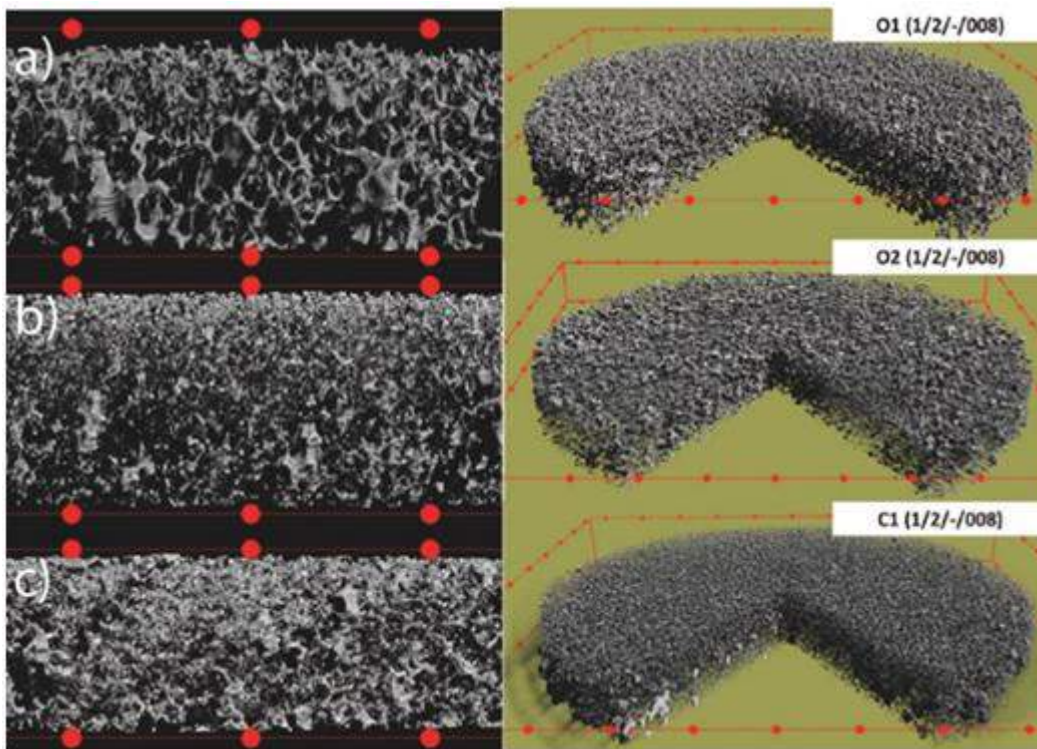


Figure7:3DTomography images of O1, O2 and C1 sample surfaces [3]

Figure 6 shows the SEM micrographs obtained from the surfaces of SiOC ceramic foams with 100% PHMS polymer. Here O1 and O2 indicates that PU foams have open cell structures and C1 has closed cell structure.

Figure 7 shows the 3D images obtained by microtomography of O1, O2 and C1 samples. The yielded O1 and O2 ceramic foam have thinner struts with interconnected and non-aligned cells, where as C1 yielded foam had solid dense matrix with lower porosity. [3]

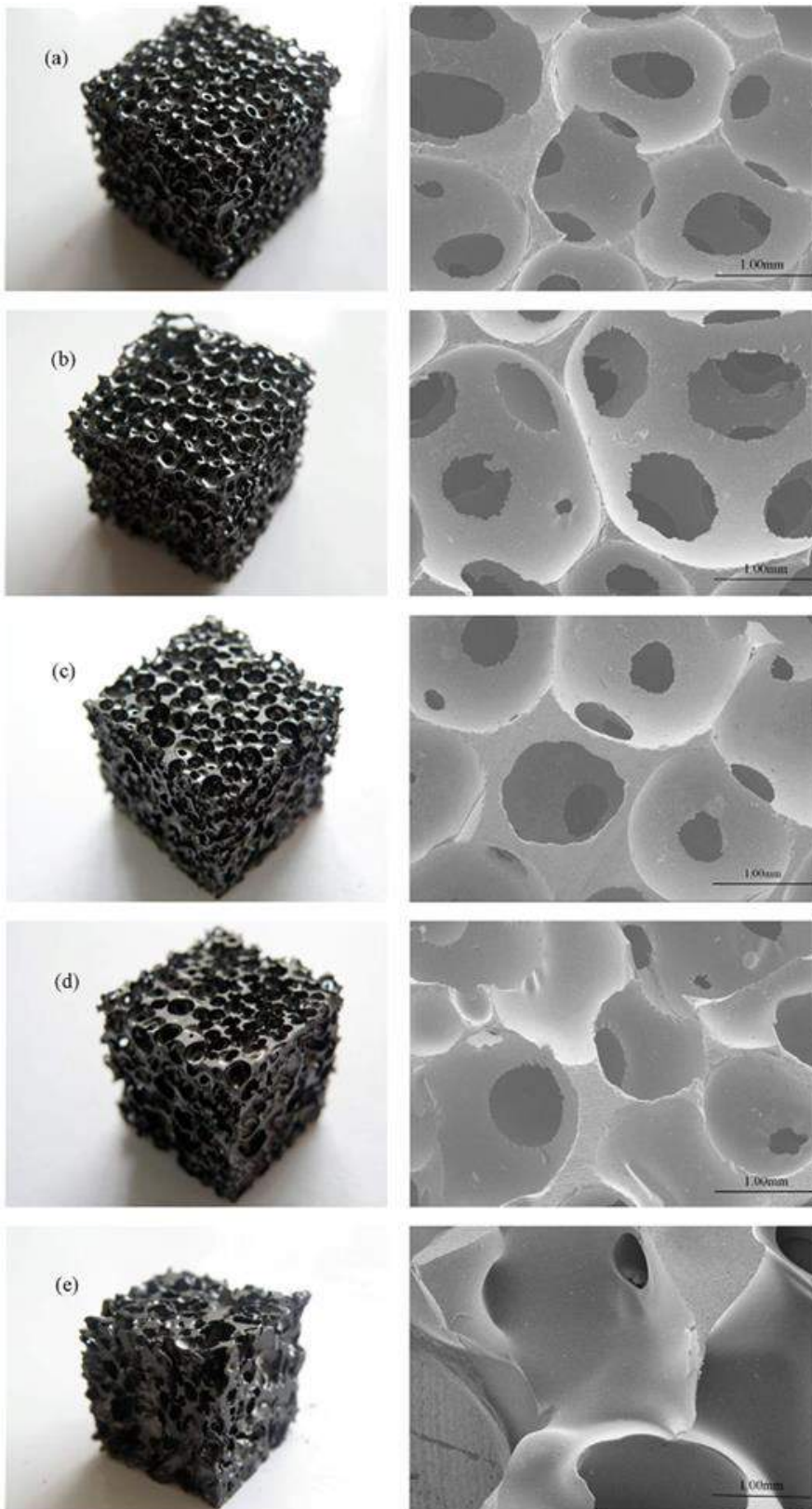


Figure8:SEM images at various rate of change in temperature during pyrolysis. a) 0.25 ° C/min, b) 0.5 ° C/min, c) 1 ° C/min,d) 2 ° C/min,e) 3 ° C/min. [8]

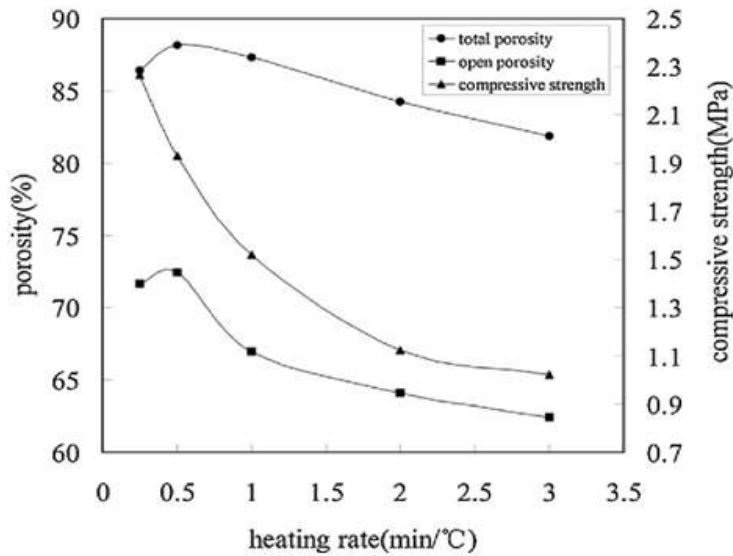


Figure9:Porosity and compressive strength [8]

Figure 8 shows the effect of heating rates on the surfaces of SiOC and also on SEM micrographs. Surface porosity will be higher at lower heating rates when compared to higher heating rates (0.25 ° C/min to 3 ° C/min). Figure 9 shows the graph of porosity & compressive strength versus the rate of heating. The Total porosity obtained is 88% and open porosity of 73%. Also, compressive strength decreases with increase in rate of heating.[8]

IV. APPLICATIONS



Figure10:Porsche ceramic disc brakes (PCDB) [11]

Porsche has developed a new high performance disc brakes with involute cooling ducts for an efficient cooling. Actually, in the early days, the disc brakes were made from conventional brittle materials. Hence Porsche made carbon fibre reinforce brake disc to overcome the brittle property. PCCB is made of short carbon fibres, carbon powder and precursor mixture at 1000° C.

Grey cast iron disc weighs heavier which reduces the acceleration & deacceleration and increases the usage of fuel. Ceramic disc brakes weigh less but gives similar track properties, these were used in F1 racing cars, bikes etc.

Apart from fuel, it also reduces unsprung masses of car, this results in improved performance of shock absorbers and thus, transmissibility will be less. Porsche has achieved 100 to 0 KMPH in just 3 sec. other cars which uses CDB are F1, 911GT2 and Mercedes Benz vision GST.[11]

Other applications:

- Filtering molten metals or hot gases.
- Thermal protection system.
- Heat exchangers.
- Light weight structures with appropriate strength.
- Space applications.

V. CONCLUSION

From the above review it can be stated that, replica process is the optimum technique to synthesize the polymer derived ceramics. Further, pyrolysis done at a heating rate of 0.25 – 0.50°C/min, yields optimal porosity and compressive strength in ceramic foams. Depending on the application open or closed structure can be chosen. Open structure yields thin struts while closed structure yields solid dense matrix. Furthermore, the shrinkage can be controlled by varying the concentration of polysiloxane in precursor solution. Since the above-mentioned polymers are in liquid state, it will be suitable for adding composites such as carbon fibers, aluminum & carbon powder to improve its mechanical properties such as toughness, hardness and strength.

VI. REFERENCES

- [1]. Mao, Xiaojian. "Processing of ceramic foams." *Recent Advances in Porous Ceramics* 31 (2018).
- [2]. Greenough, M., Zhao, Z., Jacobsohn, L. G., Tong, J., & Bordia, R. K. (2021). Low/intermediate temperature pyrolyzed polysiloxane derived ceramics with increased carbon for electrical applications. *Journal of the European Ceramic Society*, 41(12), 5882-5889.
- [3]. Semerci, T., de Mello Innocentini, M. D., Marsola, G. A., Lasso, P. R. O., Soraru, G. D., & Vakifahmetoglu, C. (2020). Hot air permeable preceramic polymer derived reticulated ceramic foams. *ACS Applied Polymer Materials*, 2(9), 4118-4126.
- [4]. Colombo, Paolo, and Michele Modesti.(1999) "Silicon oxycarbide ceramic foams from a preceramic polymer." *Journal of the American Ceramic Society* 82.3: 573-578.

- [5]. Biasetto, L., Pena-Alonso, R., Soraru, G. D., & Colombo, P. (2008). Etching of SiOC ceramic foams. *Advances in applied ceramics*, 107(2), 106-110.
- [6]. Kumar, B. M., & Kim, Y. W. (2010). Processing of polysiloxane-derived porous ceramics: Science and Technology of Advanced Materials, 11(4), 044303.
- [7]. Colombo, Paolo, Gabriela Mera, Ralf Riedel, and Gian Domenico Soraru,(2010) "Polymer-derived ceramics: 40 years of research and innovation in advanced ceramics." *Journal of the American Ceramic Society* 93, no. 7: 1805-1837.
- [8]. Tian, H. and Ma, Q.S., (2012) Effects of heating rate on the structure and properties of SiOC ceramic foams derived from silicone resin. *Ceramics International*, 38(3), pp.2101-2104.
- [9]. Riedel, Ralf, Gabriela Mera, Ralf Hauser, and Alexander Klönczyski.(2006) "Silicon-based polymer-derived ceramics: synthesis properties and applications, *Journal of the Ceramic Society of Japan* 114, no. 1330: 425-444.
- [10]. Fu, S., Zhu, M., & Zhu, Y. (2019). Organosilicon polymer- derived ceramics: An overview. *Journal of advanced ceramics*, 8(4), 457-478.
- [11]. Crouse, W. H., & Crouse, W. H. *Automotive mechanics*. Tata McGraw-Hill Education.



Effect of NanoTiO₂ Particles on Microstructural and Wear Behaviour of AA8011 Metal Matrix Composites

S. Viswanath¹, G. Bhanodaya Reddy¹

¹Department of Mechanical Engineering, Sri Venkateswara University, Tirupati 517502, Andhra Pradesh, India

ABSTRACT

Aluminium based MMCs are widely used in several industries because of their improved properties over other traditional materials in the scopes of automotive, marine and aerospace applications. Wear behaviour, as a chief inferiority for AA8011, was tried to be enhanced by incorporating Titanium Dioxide (TiO₂) Nano particles creating a wear resistant composite that fulfils with tribological uses such as brake components. Composites reinforced with different percentages of Nano TiO₂ (0, 3, 6, 9, and 12 wt.%) using stir casting technique. The primary phase structure and micro-hardness were assessed by XRD and Vickers hardness tester respectively. The addition of the TiO₂ deeply affected the hardness and wear performance of AA8011 alloy. It was found to be a maximum of 51±0.93 HV by adding 12% Nano TiO₂ particles. Abrasive and adhesives were the dominant wear mechanisms present in the composites, as it was observed by worn surface morphology through SEM after the wear test. MMC with 12 wt.% of TiO₂ had showed lowest wear and more friction coefficient was elevated in the composite with 3wt.% TiO₂ than the composite with 12 wt.% of TiO₂ during friction process.

Keywords: Metal Matrix Composites; AA8011; Titanium dioxide (TiO₂); Microhardness, Friction coefficient; Wear.

I. INTRODUCTION

The utilization of aluminium based metal matrix composites (AMMCs) is rising daily in the overall manufacturing sectors due to their superior properties such as better durability, good mechanical strength and high specific strength [1]. AMMCs reinforced with ceramic particles possessing enhanced the wear resistance, hardness and strength than the pure aluminium and hence they are prescribed in automobile, aviation and civil applications particularly for sliding components [2]. Sliding components specifically in case of braking system like braking pads which are mounted in brake rotor discs of each wheel [3]. The brake pad materials should satisfy the requirements such as stable coefficient of friction and low wear rate at different operating conditions. These requirements can be fulfilled when the brake pads are manufactured by MMCs because of their high strength to weight ratio, lighter weight and economically cheap [2]. AMMCs are recommended for such areas

due to their superior strength with moderate toughness by its ductile matrix and good bonding between matrix and reinforcement particles.

Among the various ceramic particles such as TiO_2 , SiC, B_4C , Al_2O_3 , TiC etc., the Titanium dioxide (TiO_2) possessing properties like excellent optical transparency, nontoxicity, high refractive index, chemically inert and it is economically cheap [4]. Moreover, TiO_2 has high hardness with good modulus [5], and sustainable to wear resistance, exhibiting better mechanical properties. Kumar and Raja durai [2] have studied the hardness and wear behaviour of AMMCs fabricated by powder metallurgy process, results observed that the TiO_2 shows clear effect on wear behaviour, the weight loss of specimen has been decreased with increasing TiO_2 percentage and increased the friction coefficient. In another examination [4], where the TiO_2 as reinforcement to Al7068 matrix composite has been prevented material loss from the specimen during wear test and imparted extreme hardness in the surface of the composite.

The use of AA8011 as matrix material for fabrication of AMMCs is very scanty till today and AA8011 matrix with iron and silicon as major alloying elements having excellent formability, superior strength characteristics and corrosion resistance and hence they have been used for cosmetic bottles and in air conditioning [6]. The wear behaviour of AMMCs with combination of AA8011 matrix and TiO_2 nanoparticles reinforcement is not found in the literature. Many processing routes have been applied to produce particulate MMCs but stir casting is the most advantageous because of its simplicity paving to effective casting for mass production and cost effectiveness [7-9].

Aim of this attempt is to study the effect of different fractions of TiO_2 such as 3, 6, 9 and 12 wt.% on microstructure, micro hardness and wear properties of AA8011/ TiO_2 nano composite fabricated by using stir casting and results are compared with as-received AA8011 alloy.

II. EXPERIMENTAL WORK

2.1 Materials

Aluminium alloy AA8011 was stir casted with incorporation of TiO_2 as reinforcement to produce AA8011/ TiO_2 MMCs. The chemical composition of AA8011 alloy is shown in Table 1. That was imported from JINDAL Aluminum Ltd. Bangalore India.

Table 1. Composition of AA8011 (wt%)

Si	Fe	Cu	Mn	Mg	Cr	Zn	Ti	Al
0.62	0.82	0.02	0.05	0.06	0.02	0.05	0.03	Bal.

Few specifications of TiO_2 are presented in Table 2 and Fig.1 shows Scanning Electron Microscope (SEM) image of TiO_2 in as-received condition with particles size distribution graph.

Table 2. Properties of TiO_2 nanoparticles

Purity (%)	>99.9
Avg. Particle size range (nm)	20-50
Density (g/cm^3)	4.3
Morphology	Near Spherical

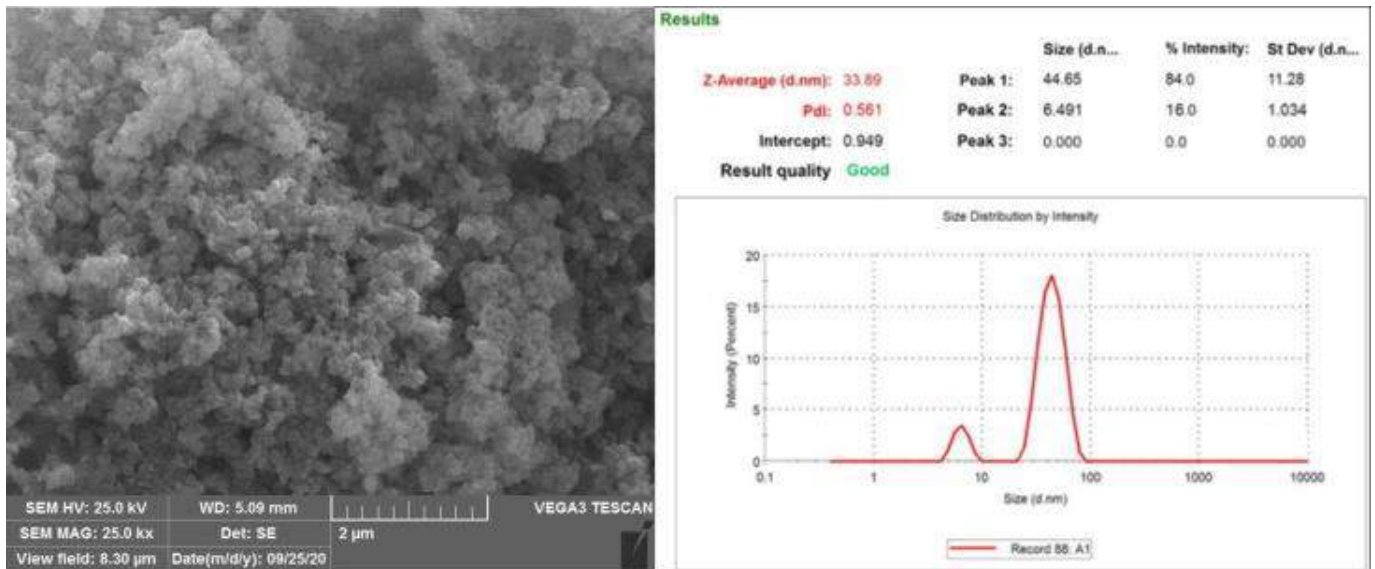


Fig. 1. TiO₂ SEM image with size distribution graph

2.2 Composite preparation

Fig. 2 shows the stir casting set-up, it was used to prepare AA8011 composites reinforced with TiO₂ by different percentages such as 0, 3, 6, 9, and 12 wt.%. By using digital electronic weighing machine, the pre-determined fraction of TiO₂ nano particles weighed firstly, then the measured quantity of TiO₂ submitted to preheating furnace and heated up to 200 °C. The temperature for melting AA8011 alloy accelerated up to 850 °C, then the alloy turned into molten completely. The measured quantity of TiO₂ in preheated condition was added slowly to the vortex of AA8011 alloy and also Degas tablet to prevent oxidation of AA8011 was supplied. The mixture was being stirred for 25 min at a speed of 450 rpm using graphite mixer, the mixture was poured into cast-iron mould (which was pre-heated to 250 °C).

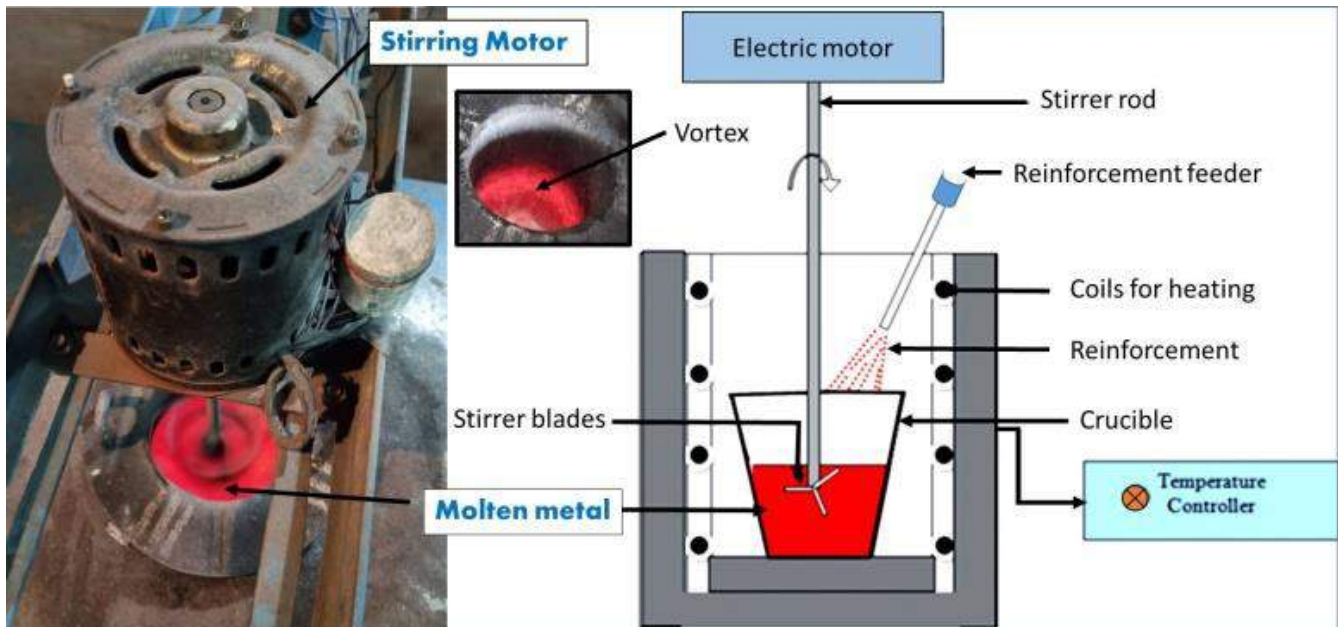


Fig. 2. Stir casting setup

2.3 Microhardness and Wear test

Phase and structure of composite samples determined by using X-ray Diffractometer (Bruker, Model: D-8 Advance) with Cu-K α radiation ($\lambda=1.54\text{\AA}$). The microhardness of the composite samples was characterized by using Digital micro hardness tester (Wilson Wolpert 401-MVD) as per the ASTM E 92 standards. A load of 500g applied for a dwelling time of 20 s by diamond pyramid of $136^{\circ}\pm 5$ angle between opposite faces of working edge with square base.

Dry sliding wear tests were conducted as per ASTM G 99, in an ambient temperature using pin-on-disc apparatus using Ducom (TR20) as shown in Fig. 3. The wear samples with length of 30 mm and diameter of 10 mm were subjected to sliding under a load of 50 N against the rotating stainless steel (EN32) disc which had a hardness of 50HRC. The disc was rotating with a linear velocity of 1.65 m/s up to a sliding distance of 890 m.

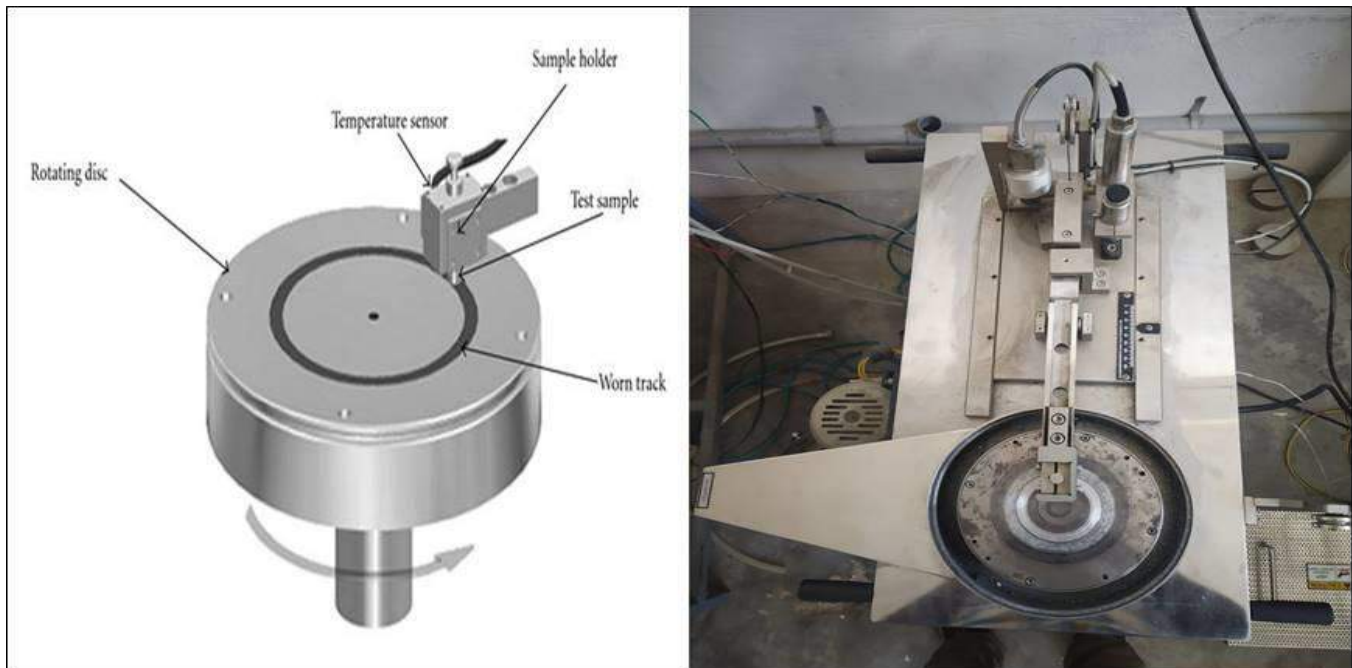


Fig. 3. Pin-On-Disc setup

III. RESULTS AND DISCUSSION

3.1 Structure analysis by XRD and Grain size determination

The XRD results of fabricated composite samples are shown as patterns in **Fig. 4 (a)**, which are identified and scanned by varying diffraction angle (2θ) from 30° to 90° . The intensified peaks of Al are presented in the form of phase i.e., (111), (200), (220), (311), and (222) and are clearly visible at positions of 38.34° , 44.59° , 64.98° , 78.12° , and 82.32° respectively. Increase in peak integral width of XRD, which is also referred as Full width at half maximum (FWHM) broadening is occurred and it is increased as increasing the percentage of the TiO_2 particles. Indeed, the larger grains can reduce the FWHM values and smaller grains can increase the FWHM values. Therefore, it confirms that the grain size is decreases as increasing the FWHM values, it is attributed to the increasing the percentage of TiO_2 in the composite samples.

The average grain size of samples in this work are determined using Scherrer and Wilson equation [10] and these values are plotted as shown in Fig. 4 (b).

$$D = \frac{0.94\lambda}{\beta \cdot \cos \theta_{\beta}} \quad (1)$$

Where D is the average grain size, λ is the X-ray wavelength (1.54\AA), θ is the Bragg angle and β is the peak broadening($^{\circ}$).

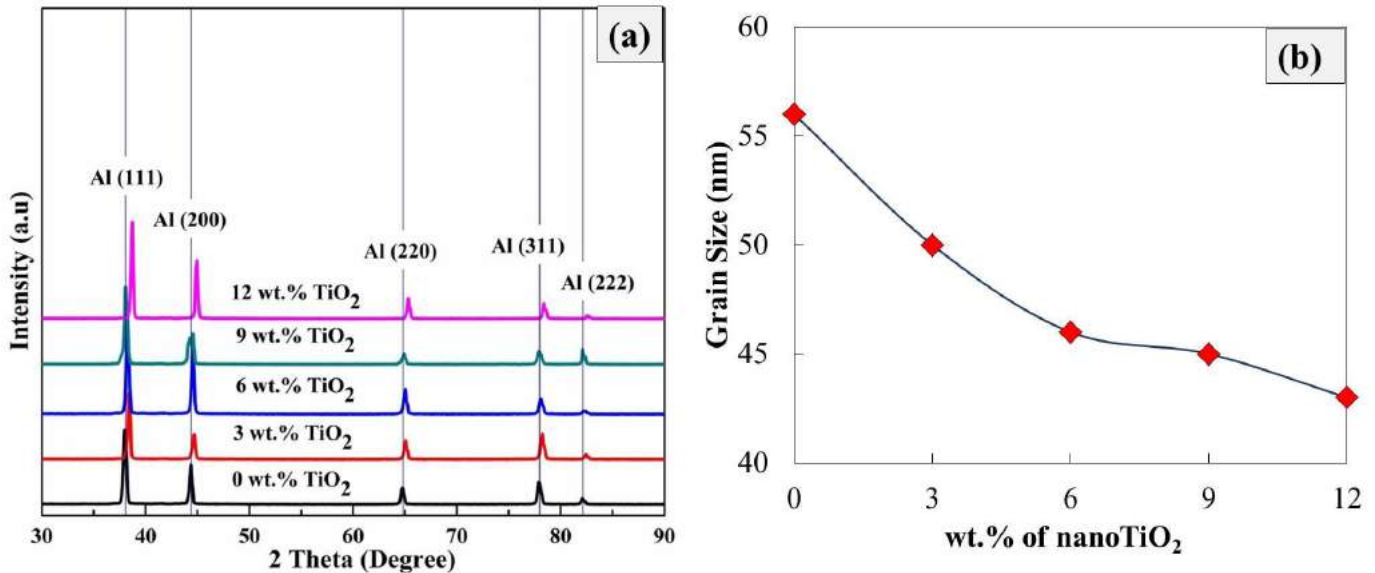


Fig. 4 AA8011 composites (a) XRD patterns (b) Grain size.

The retardation of dislocations from continuously moving slip plane is due to the presence of nano particles and TiO₂ particles which plays a primary role in controlling the grain size. As shown in Fig. 4 (b) it is very clear that the grain size of the composite have been decreased as increasing the reinforcement percentage, and hence the increase in weight fraction of TiO₂ and corresponding decrease in grain size could led to generate fine and dense structure in the composite. Moreover, the reduction of grain size of the composite causing for the strengthening of composite, according to Hall-Petch theory.

3.2 Microhardness

Fig. 5 illustrates the micro hardness variation by the effect of TiO₂ nano particles in the AA8011 composite samples. The graph shows that the micro hardness values increases as increasing the TiO₂ amount and the value of hardness increased from 37 ± 0.28 HV (as-received AA8011) to 40 ± 0.37 HV (TiO₂ with 3 wt.%) and maximum of this value raised to 51 ± 0.93 HV by the addition of 12 wt.% of TiO₂. The incorporation of ceramic particles which are basically very hard caused in enhancing the hardness of aluminium matrix. Apart from this, the composite hardness depends on several factors such as reinforcement particles in nano-size, retardation of dislocation movements by increasing their density, grain refinement, heat input and finally by fabrication process [11]. The grain size of the composite has been decreased as increasing the TiO₂ content (Fig. 4 (b)), and also causing restriction of plastic deformation and increases the dislocation density by the broadening of FWHM values analysed from the XRD patterns (Fig. 4 (a)). The hardness values are having an inverse relation with grain size, increasing the hardness values by decreasing of grain size of the samples observed in the present work.

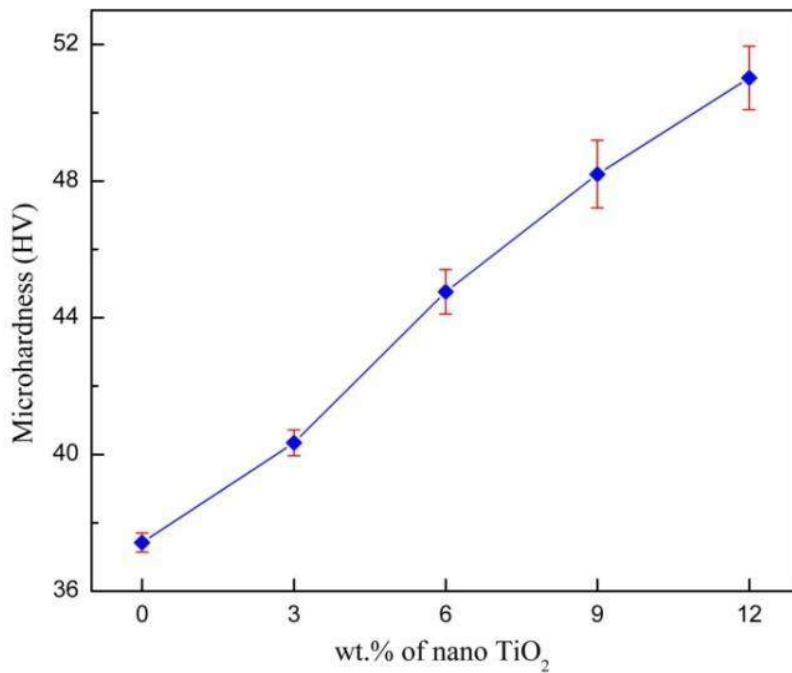


Fig. 5 Microhardness of AA8011 with varying TiO₂ percentage.

3.3 Wear behaviour

The dry sliding wear was observed by measuring weight loss. The wear rate of the samples used in this work was determined with weight loss/ sliding distance ($\mu\text{g}/\text{m}$) relationship. For AA8011, the wear rate is $7.2\mu\text{g}/\text{m}$, and friction coefficient is 0.486. For composite of 3 wt.% TiO₂, the wear rate is $4.3\mu\text{g}/\text{m}$, and friction coefficient is 0.496. For composite of 6 wt.% TiO₂, wear rate is $2.8\mu\text{g}/\text{m}$ and friction coefficient is 0.374. For composite of 9 wt.% TiO₂, wear rate is $1.3\mu\text{g}/\text{m}$ and friction coefficient is 0.351. Finally for composite of 12 wt.% TiO₂, wear rate is $0.8\mu\text{g}/\text{m}$ and friction coefficient is 0.349. It is clear that wear rate and friction coefficient is less for composite of 12 wt. % TiO₂. Fig. 6 shows wear rate and friction coefficient with respect to wt.% TiO₂. From the Fig. 6(a) it is observed that the trend of wear rate is decreased as increasing the wt.% TiO₂ to AA8011 matrix, which is due to the presence of hard ceramic particles of nano size, increasing hardness as imparted from smaller grains and increase of dislocation density as seen in the above discussion. And the less wear rate is obtained in this work from the composite contained with 12 wt.% TiO₂ among all the wear samples.

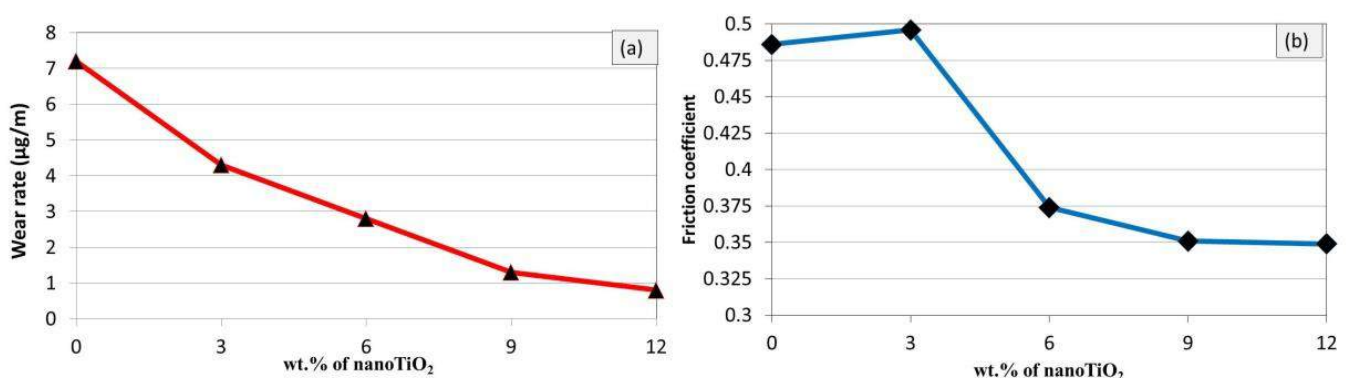


Fig. 6 Wear test results (a) Wear rate (b) Friction coefficient.

Fig. 6(b) shows that the friction coefficient is slightly increased after incorporation of TiO₂ (3 wt.%) to composite as compared with as-received AA8011 matrix. After the addition of reinforcement with 6, 9, and 12 wt.% of TiO₂, the friction coefficient values are gradually decreased. Since, the micro structural changes occurred in the composite by the presence of hard ceramic particles with their increasing percentage and enhancement in micro hardness shown favour to yield less friction coefficient during wear test.

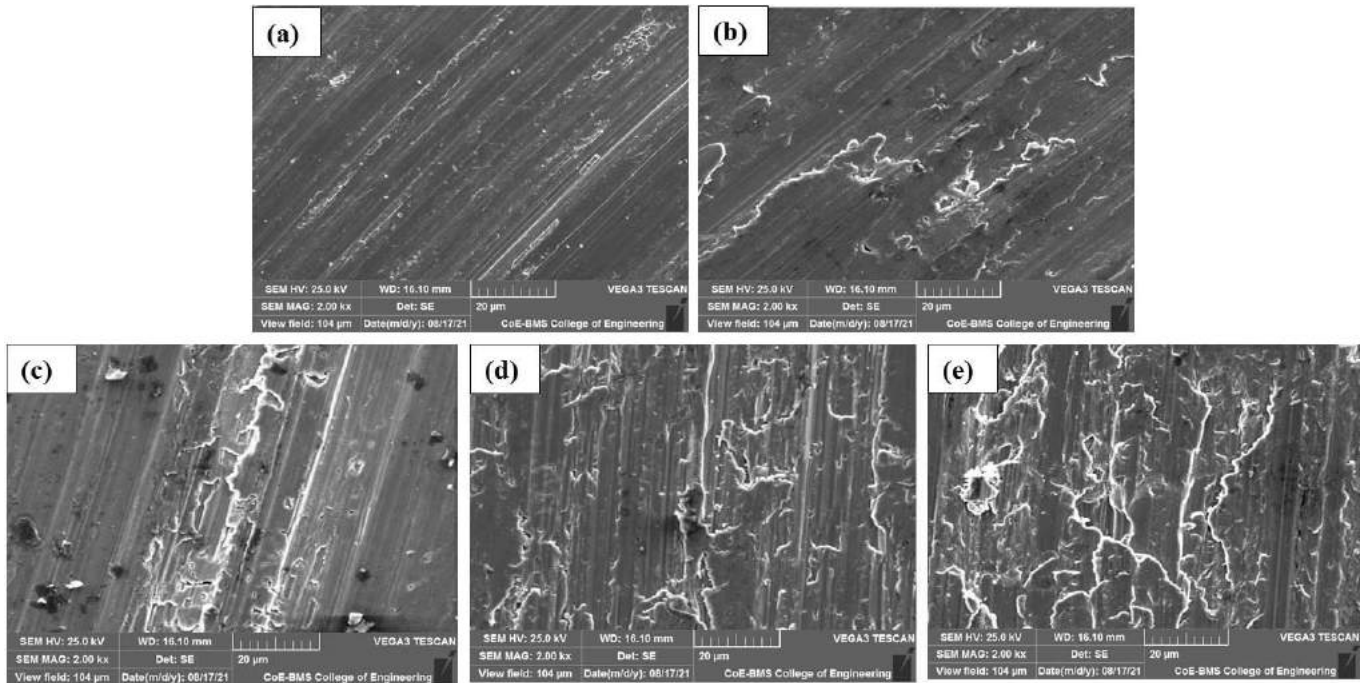


Fig. 7 SEM images of worn surface (a) As-received AA8011 (b) AA8011/3 % TiO₂ (c) AA8011/6 % TiO₂ (d) AA8011/9 % TiO₂ (e) AA8011/12 % TiO₂

After wear test on Pin-On-Disc apparatus at conditions load 50N, sliding speed 1.65 m/s and sliding distance 890 m, microstructure of the worn surfaces of AA8011 with 0, 3, 6, 9, and 12 wt.% TiO₂ compositions is analysed by using SEM. The images scanned by SEM shows the surfaces in the form of scratches and grooves as seen in the **Fig. 7(a-e)**. The **Fig. 7a** is evident for AA8011 matrix ductility, due to this property the material separated during wear test in the form of micro ploughing caused by action of counterpart hard disc. The Abrasive and adhesives were the dominant wear mechanisms in the AA8011 with presence of TiO₂ hard nano particles and they have hindered the material removal from the sample surfaces. **Fig 7 (b-e)** illustrates the SEM images of AA8011 with 3%, 6%, 9%, and 12% of TiO₂ particles, which are more evident for formation of oxide layer which is also referred as passive layer or protective layer could prevent the wear loss. This protective layer appears in white colour from the SEM images and its formation increased as increasing the TiO₂ content to AA8011 matrix. This layer becomes denser as increasing TiO₂ content. Indeed, this passive layer formation occurs in the materials possessing smaller grains, such material structure is known as Nano-crystalline structure produced due to increase in dislocation density [10]. In this work, this mechanism employed with decreased grain size, FWHM broadening enhanced hardness from the addition and increasing of TiO₂ to AA8011 matrix and these changes obviously shown favour to lower the wear loss of the composite samples.

IV. CONCLUSIONS

The dry sliding wear behaviour of AA8011/TiO₂ nano composites produced by stir casting route has been studied with effect of TiO₂ percentage and the results of this work leads to the following conclusions.

- (i) AA8011/TiO₂MMCs were successfully casted by incorporation of nano TiO₂ as 3, 6, 9, and 12 wt.% to AA8011 matrix.
- (ii) Grain size of the samples was determined from XRD analysis and grain size of the composite samples was decreased as increasing TiO₂ content.
- (iii) The micro hardness of the composite samples increased with increase in nano TiO₂ particulate percentage and was found to be having a maximum of 51±0.93 HV for an addition of 12 wt.% TiO₂ nano particles.
- (iv) Abrasive and adhesive wears were found to be the dominant mechanisms and the wear rate of the composites decreased as increasing micro hardness and smaller grains obtained by the increasing of TiO₂ wt.% to AA8011 matrix.
- (v) The friction coefficient was reduced by incorporation of ceramic particles, which acts as lubricant during sliding and observed the formation of passive layer on the worn surface morphology from SEM images which mitigates the wear loss in the composite samples.

V. REFERENCES

- [1]. Thirumoorthy A, Arjunan TV, Kumar KS. Latest research development in aluminum matrix with particulate reinforcement composites—a review. *Materials Today: Proceedings*. 2018 Jan 1;5(1):1657-65.
- [2]. Kumar CA, Rajadurai JS. Influence of rutile (TiO₂) content on wear and microhardness characteristics of aluminium-based hybrid composites synthesized by powder metallurgy. *Transactions of Nonferrous Metals Society of China*. 2016 Jan 1;26(1):63-73.
- [3]. Abhik R, Umasankar V, Xavior MA. Evaluation of properties for Al-SiC reinforced metal matrix composite for brake pads. *Procedia Engineering*. 2014 Jan 1;97:941-50.
- [4]. Joshua KJ, Vijay SJ, Selvaraj DP. Effect of nano TiO₂ particles on microhardness and microstructural behavior of AA7068 metal matrix composites. *Ceramics International*. 2018 Dec 1;44(17):20774-81.
- [5]. Ramesh CS, Khan AA, Ravikumar N, Savanprabhu P. Prediction of wear coefficient of Al6061-TiO₂ composites. *Wear*. 2005 Jul 1;259(1-6):602-8.
- [6]. Shi C, Shen K. Twin-roll casting 8011 aluminium alloy strips under ultrasonic energy field. *International Journal of Lightweight Materials and Manufacture*. 2018 Jun 1;1(2):108-14.
- [7]. Jawalkar CS, Verma AS, Suri NM. Fabrication of aluminium metal matrix composites with particulate reinforcement: a review. *Materials Today: Proceedings*. 2017 Jan 1;4(2):2927-36.
- [8]. Sijo MT, Jayadevan KR. Analysis of stir cast aluminium silicon carbide metal matrix composite: A comprehensive review. *Procedia technology*. 2016 Jan 1;24:379-85.
- [9]. Selvam JD, Smart DR, Dinaharan I. Synthesis and characterization of Al6061-Fly Ashp-SiCp composites by stir casting and compocasting methods. *Energy procedia*. 2013 Jan 1;34:637-46.

- [10]. Pandey V, Singh JK, Chattopadhyay K, Srinivas NS, Singh V. Influence of ultrasonic shot peening on corrosion behavior of 7075 aluminum alloy. *Journal of Alloys and Compounds*. 2017 Nov 5;723:826-40.
- [11]. Mirjavadi SS, Alipour M, Emamian S, Kord S, Hamouda AM, Koppad PG, Keshavamurthy R. Influence of TiO₂ nanoparticles incorporation to friction stir welded 5083 aluminum alloy on the microstructure, mechanical properties and wear resistance. *Journal of Alloys and Compounds*. 2017 Jul 25;712:795-803.



Aluminium Hybrid Metal Matrix Composites –A Review

C R Vishwanath¹, M S Raviraj¹

¹Department of Mechanical Engineering, Government Engineering College, Chamara Nagar, Karnataka-571313, India

ABSTRACT

MMCs typically consist of a low-density matrix metal such as aluminium, titanium or magnesium, reinforced with particulate or fibre reinforcement. Light weight MMC's be able to prepared by dispersing the particles or fibres of one or more(hybrid) reinforcement materials in the metal matrix phase to achieve desirable properties. This paper presents a review of the effect of the addition of different particulate reinforcement materials in Al metal matrix phase. Most of the light weight composites are reinforced with ceramic material such as silicon carbide (SiC), boron carbide (B₄C), Aluminium oxide (Al₂O₃), TiC and/or graphite. For producing light weight and high strength MMCs, several methods and techniques such as powder metallurgy, melt stirring, squeeze casting, stir casting, spark plasma sintering methods etc. may be employed to fabricate these composites. The properties of MMCs are based on the parameters such as, volume fraction of matrix and reinforcements and also on the size, shape and proportion of the reinforcement particles. Mechanical and thermal behaviour of these composites is extensively studied and documented. Because of the significant improvement in the properties of these composites and potential in their applications to the engineering society, future research perspectives in these composites is promising and challenging.

Keywords: Silicon carbide, Graphite, melt stirring, squeeze casting, stir casting, Hybrid composites

I. INTRODUCTION

Metal Matrix Composites (MMCs) are one of the most widely used materials in modern days because of their adaptability to different situations and the excellent mechanical and thermal properties compared to conventional or traditional materials in the areas such as, automobiles, aerospace and other industrial applications. Compared with unreinforced metals, MMCs offer higher specific strength and stiffness, higher operating temperature, and greater wear resistance, as well as the opportunity to tailor these properties for a particular application. MMCs permit to overcome the technical barriers and limitations of using conventional materials to serve specific purposes and exhibit desirable properties.

Hybrid metal matrix composites are made by dispersing two or more reinforcement materials in metal matrix. Hybrid metal matrix composites are advanced materials used for light weight, high strength, high wear resistance, and good dimensional stability which suit the applications in aerospace and automobile sector.

TABLE I PROPERTIES OF SOME ENGINEERING MATERIALS

Material	Density (ρ)gm/cc	Tensile modulus (E)(GPa)	Tensile Strength (σ)(GPa)	Specific modulus (E/ ρ)	Specific strength (σ/ρ)
Cast iron	7	100	0.14	14.3	0.02
Steel, AISI1045	7.8	205	0.57	26.3	0.073
A12024-T4	2.7	73	0.45	27	0.17
A16061-T6	2.7	69	0.27	25.5	0.1

II. ALUMINIUM / SILICON CARBIDE / GRAPHITE HYBRID MMCS

S A Mohan Krishna .et al. [2] have investigated the thermal properties of aluminium-silicon carbide-graphite hybrid metal matrix composites. Their investigation proposes, aluminium matrix composites reinforced with the particles of silicon carbide possess high yield strength, low coefficient of thermal expansion or thermal expansively, high modulus of elasticity and excellent wear resistance by maintaining volume proportion up to 20% and it is necessary to evaluate different percentage combinations of reinforcements with matrix Aluminium to check for thermal stability and to measure thermal conductivity and coefficient of thermal expansion.

S. CemOkumus .et al. [3] have prepared aluminium-silicon based hybrid composites reinforced with silicon carbide and graphite particles were prepared by liquid phase particle mixing (melt stirring) and squeeze casting. The thermal expansion and thermal conductivity behaviours of hybrid composites with various graphite contents (5.0; 7.5; 10 wt.%) and different silicon carbide particle sizes (45 μm and 53 μm) were investigated. Results indicated that increasing the graphite content improved the dimensional stability, and there was no obvious variation between the thermal expansion behaviors of the 45 μm and the 53 μm silicon carbide reinforced composites. The thermal conductivity of hybrid composites was reduced due to the enrichment of the graphite component.

S A Mohan Krishna .et al. [4] made Micro structural characterization & investigation of thermal conductivity behaviour of Al 6061-SiC-Gr-hybrid MMC with varying percentage(2.5%,5%,7.5% & 10%) reinforcements were carried out using optical microscope ,scanning electron microscope, energy dispersive spectroscopy thermal characterization analysis were made. It has been observed that dispersion concentration of the reinforcement has been homogeneous & negligible porosity has been noticed.

Basavarajappa. et al [11] reported application of Taguchi techniques to study dry sliding wear behaviour of metal matrix composites. Aluminium alloy 2219 was used as the matrix. Two composites were fabricated by liquid metallurgy (stir casting), one with 15 wt% of SiC reinforcement particles of size 25 μm and other with 15% SiC reinforcement particles, 3 wt% of graphite is added with a particle size of 45 μm . The wear of the composite materials were studied as a meaning of the sliding distance, applied load and the sliding speed. In the present investigation, an L27 orthogonal array was chosen, which has 27 rows and 13 columns. The wear parameters chosen for the experiment was (i) sliding speed of 1.53 m/s, 3.06 and 4.59 m/s (ii) load of 9.81 N, 19.6 N and

39.2 N (iii) sliding distance of 500 m, 1000 m & 1500 m. And the results showed percentage contribution of all factors for SiCp reinforced composite were sliding distance ($p = 57.57\%$), load ($p = 24.34\%$) and sliding speed ($p = 6.8\%$). Though, the relations between sliding speed and load is ($p = 2.15\%$) and other factors were least. In case of Graphitic hybrid composite, the percentage contribution (p) of factors were sliding speed ($p = 57.24\%$) load ($p = 22.58\%$) and sliding speed ($p = 9.66\%$). However, the interactions between the factors were minimum. Sliding distance was the most predominant wear factor that had the maximum physical as well as statistical influence on the wear of both composites.

III. Aluminium-Magnesium/Silicon Carbide (SiC)/Aluminium oxide (Al₂O₃) hybrid MMCs

Md. AI Mehedi et. al [14] reported Tribological characteristics of aluminium matrix hybrid composites reinforced with SiC and Al₂O₃. Pure aluminium ingot (> 99.5% Al) and magnesium ribbons were used to make the matrix alloy. SiC and Al₂O₃ of particle size 106 μm were used as particulates. Pin on disc machine was used to analysis the wear. The results showed that weight loss had increased as the sliding speed increased for all samples. When reinforced with reinforcements weight loss gradually decreased for speed 1.89 m/s and 2.10 m/s. When the percentage of SiC was increased i.e. doubled the weight loss decreased considerably. SiC particles were found to be superior wear resistant. The increase of load decreased the wear and increase of sliding velocity increased the wear rate. The increase in load moves the wear mechanism from abrasion to delamination wear mechanism.

Kenneth Kanayo Alaneme et. al. [10] reported Corrosion and wear behaviour of Al–Mg–Si alloy matrix hybrid composites reinforced with rice husk ash and silicon carbide. Al–Mg–Si alloy was chosen as aluminium matrix for the research. Silicon carbide (SiC) of particle size 28 μm and rice husk ash (RHA) of particle size under 50 μm were chosen as reinforcement materials for the fabrication of the hybrid composites. The Al–Mg–Si alloy matrix hybrid composites reinforced with RHA and SiC were manufactured by double stir casting technique. The quantitative amounts of rice husk ash (RHA) and SiC required to produce 5, 7.5, and 10 wt% reinforcement consisting of RHA and SiC in weight ratios 0:1, 1:3, 1:1, 3:1, and 1:0 respectively. The results showed similar wear surface topographies characterized typically by abrasive wear which occasional worn debris welded to the surface of the samples. The samples C5 and A0 were the little exceptions that showed extra main adhesive wear mechanism due to the great accumulation of debris noticeable on the surfaces.

TABLE II ILLUSTRATION OF DIFFERENT MATRIX/REINFORCEMENT MATERIALS IN MMC'S AND ITS BEHAVIOURS

Type of Matrix	Type of Reinforcement	Fabrication Method	Outcome	Reference
Aluminium	SiC (45 μm & 50 μm)/ Gr (5, 7.5 & 10wt%)	Melt Stirring and Squeeze Casting	Improved dimensional stability and reduced thermal conductivity with enrichment of graphite	[3]
Al2219 Alloy	SiC(15wt% at 25 μm)/Gr	Liquid Stir casting	Established relations between sliding distance, applied load and sliding speed	[11]

	(3wt% at 45 μm)	Technique	which concluded that the sliding distance is the predominant factor which influence the wear	
Al/Mg alloy	SiC(28 μm)/RHA	Double Stir Casting Technique	Improved corrosion resistance and OCP	[10]
Al/Mg alloy	Graphite Flakes (50vol.%)	Spark Plasma Sintering Method	Thermal expansion coefficient values reduced to zero or negative values and the thermal conductivity increased by four times compared to copper	[1]
Al2219	SiC (50nm and 150nm)(0.5, 1, 1.5, and 2 wt%)	High intensity ultrasonic cavitation process	Increased ultimate tensile strength and hardness. Achieved uniform dispersion of nano particles of SiC with low porosity	[6]
Al6061	SiC/Gr (2.5, 5, 7.5 and 10 vol%)	Stir Casting	Dispersion concentration of the reinforcement is homogeneous & negligible porosity has been noticed.	[4]

IV. ALUMINIUM-MAGNESIUM ALLOY/GRAPHITE METAL MATRIX COMPOSITES

Valerio Oddone. et al. [1] prepared the composites of aluminium alloy and magnesium alloy by spark plasma sintering method to produce light metal-graphite composites with an excellent combination of the properties such as high thermal conductivity, low thermal expansion and low density. By adding up to 50 vol.% of macroscopic graphite flakes, the thermal expansion coefficient of magnesium and aluminium alloys was tuned down to zero or negative values, while the specific thermal conductivity was over four times higher than in copper.

Omriani E .et al. [5] their paper summarizes various tribological aspects of self-lubricating aluminium composites of graphite reinforcement & the influence of various factors such as (a) material factors, graphite size and volume fraction, and (b) mechanical factors, applied load and sliding speed on the tribological properties of self-lubricating aluminium composites. Bringing self-lubricating composites into different operating systems is a solution to reduce the use of external toxic petroleum-based lubricants in sliding contacts in a way to help the environment and reduce energy dissipation in industrial components for strategies toward sustainability and energy efficiency.

V. ALUMINIUM/SILICON CARBIDE METAL MATRIX NANO COMPOSITES

N V Murthy .et al. [6] have prepared the SiC based Aluminium metal matrix nano composites by high intensity ultrasonic cavitation process and evaluated the mechanical and tribological properties. The ultrasonic assisted stir casting helped agitation was successfully used to fabricate Al 2219 metal matrix of alloy reinforced with (0.5,

1, 1.5 and 2) Wt. % of nano silicon carbide (SiC) particles of different sizes 50nm and 150nm. The micrographs of scanning electron microscopy of nano composite were investigated it reveals that the uniform dispersion of nano particles silicon carbide in aluminium alloy 2219 matrix and with the low porosity. And the mechanical properties showed that the ultimate tensile strength and hardness of metal matrix nano composite Al2219 / nano SiC of 50nm and 150nm lean to augment with increase weight percentage of silicon carbide content in the matrix alloy.

TABLE III COMPARATIVE EVALUATION OF THE DIFFERENT MANUFACTURING TECHNIQUES

Method	Range of Shapes and Size	Range of Volume fraction	of Damage reinforcement	of Cost
Stir Casting	Wide range of shapes	Up to 0.3	No Damage	Less expensive
Squeeze Casting	Limited range of shapes (Up to 2cm ht.)	Up to 0.45	Severe Damage	Moderately expensive
Powder Metallurgy	Wide range; restricted size	0.3 - 0.5	Reinforcement Fracture	Expensive
Spray Casting	Limited shape; Large size	0.3 - 0.7	Reinforcement Fracture	Expensive

VI. Stir casting procedure for Al6061/SiC MMCs

Gowri Shankar M.C .et al. reported that, during processing of SiC particle-reinforced aluminum matrix composites, the particles are preheated at 600–800° C for 2 h in order to remove the volatile substances and to maintain the particle temperature closer to melt temperature of 750° C. Also, in SiC particles preheating leads to the artificial oxidation of the particle surface forming SiO₂ layer. This SiO₂ layer helps in improving the wettability of the particle. The Al6061 billets were charged into the furnace and melting was allowed to progress until a uniform temperature of 750° C (which is above the liquidus temperature) was attained, subsequently degassed by passing hexachloroethane (C₂Cl₆) solid degasser. The melt was then allowed to cool to 600° C (slightly below the liquidus temperature) to a semi-solid state. At this stage, the silicon carbide mixture was added to the melt and manual stirring of the slurry was performed for 20 minutes. An external temperature probe was utilized in all cases to monitor the temperature readings of the furnace. After the manual stirring, the composite slurry was reheated and maintained at a temperature of 750° C 10° C (above the liquidus temperature) and then mechanical stirring was performed. The stirring operation was performed for 10 minutes at an average stirring rate of 400rpm. Casting was then performed on prepared sand moulds at a pouring temperature of 720°C.

VII. SUMMARY

The aluminium based hybrid composites reinforced with silicon carbide and graphite particles exhibits higher thermal conductivity with negligible or zero coefficient of thermal expansion as compared to conventional metals. Some researchers have also found that MMCs with silicon carbide and graphite reinforcement having particle size 50 μ m to 20 μ m shows improved dimensional stability, machinability and higher wear resistant characteristics. Thus, it is evident that as the size of the reinforcement reduces, the surface area of the reinforcement particle increases and there will be a drastic improvement in thermal conductivity at low thermal coefficient of expansion. Hence there is a huge scope for the researchers to investigate the thermal behaviours and wear characteristics of the aluminium based hybrid nano composites

VIII. REFERENCES

- [1]. Valerio Oddone, BenjiBoerner and Stephanie Reich "Composites of aluminium alloy and magnesium alloy with graphite showing low thermal expansion and high specific thermal conductivity", Science and Technology of Advanced Materials, 2017,pp 180-186
- [2]. S A Mohan Krishna, T N Shridhar, and L Krishnamurthy "Utility of Aluminium-Silicon Carbide-Graphite Hybrid Metal Matrix Composites to Investigate Thermal Properties for Engineering Applications" IJREST, Volume-3, Issue-7, Jul-2016.
- [3]. S. CemOkumus, SerdarAslan, RamazanKarslioglu, DenizGultekin, HatemAkbulut "Thermal Expansion and Thermal Conductivity Behaviors of Al-Si/SiC/graphite Hybrid Metal Matrix Composites (MMCs)" MatSc/article/view/3093(2012)
- [4]. S A Mohan Krishna, T N Shridhar& L Krishnamurthy "Micro structural charectrization & ivestigation of thermal conductivity behaviour of Al 6061-Sic-Gr-hybrid MMC" Indian journal Engineering & Material Scinces Vol.23, Aug 2016, pp 207-222.
- [5]. Omrani E, Moghadam, A.D, Menezes, P.L. et al. Int J Adv Manuf Technol "Influences of graphite reinforcement on the tribological properties of self-lubricating aluminium matrix composites for green tribology, sustainability, and energy efficiency" 2016 pp 83: 325.
- [6]. N V Murthy, A Prasad Reddy, N Selvaraj, C S P Rao "Preparation of SiC based Aluminium metal matrix nano composites by high intensity ultrasonic cavitation process and evaluation of mechanical and tribological properties" Materials Science and Engineering 149 2016 012106
- [7]. T. Wejrzanowski, M. Grybczuk, M. Chmielewski, K. Pietrzak, K.J. Kurzydowski, A. Strojny "Thermal conductivity of metal-graphene composites" <http://doi.org/10.1016/j.matdes.2016.03.06922>.
- [8]. Y. Sahin, "Optimization of testing parameters on the wear behaviour of metal matrix composites based on the Taguchi method", Materials Science and Engineering A 408 (2005) 1-8.
- [9]. Sudarshan , M.K. Surappa, "Dry sliding wear of fly ash particle reinforced A356 Al composites", Wear 265 (2008) 349-360

- [10]. Kenneth KanayoAlaneme, TolulopeMoyosoreAdewale, Peter ApatOlubambi, "Corrosion and wear behaviour of Al-Mg-Si alloy matrix hybrid composites reinforced with rice husk ash and silicon carbide", *Journal of Materials Research*, 2014;3 (1):9-16.
- [11]. S. Basavarajappa a*, G. Chandramohan a, J. Paulo Davim, "Application of Taguchi techniques to study dry sliding wear behaviour of metalmatrix composites", *Materials and Design* 28 (2007) 1393-1398.
- [12]. Mohsen Hossein-Zadeh, OmidMirzaee, PeymanSaidi, "Structural and mechanical characterization of Al-based composite reinforced with heat treated Al₂O₃ particles", *Materials and Design* 54 (2014) 245-250.
- [13]. N. Natarajan a, S. Vijayarangan b, I. Rajendran, "Wear behaviour of A356/25SiCp aluminium matrix composites sliding against automobile friction material", *Wear* 261 (2006) 812-822.
- [14]. Md AI Mehedi, K. M. H. Bhadhon and Prof. Dr. M.N. Haque, "Tribological characteristics of aluminium matrix hybrid composites reinforced with SiC and Al₂O₃", *Aluminium* · XX/2011.
- [15]. J P Patak, J K Singh, S Mohan, "Synthesis and characterization of aluminium - silicon- silicon carbide composites", *Indian journal of Engineering and material science*, vol. 13; june 2006; pp 238-246.
- [16]. B. N. PramilaBai, "Dry sliding wear of A356-Al-SiC, composites", *Wear*, 157 (1992) 295-304.



Performance Evaluation of Thermo-Acoustic Refrigerator (TAR) with Different Stack Materials

Sadanda Megeri^{1*}, Irappa Hunagund¹, Pundarika G², Madhu D³

^{1*}Assistant Professor, Department of Mechanical Engineering, Government Engineering College Ramanagar- 562159, Karnataka, India

²Principal, Department of Mechanical Engineering, Government Engineering College, Ramanagar- 562159, Karnataka, India

³Professor and Head, Department of Mechanical Engineering, Government Engineering College, Ramanagar- 562159, Karnataka, India

ABSTRACT

Thermo acoustic refrigeration is an innovative alternative for cooling that is both clean and inexpensive. The objective of this article is to investigate effect of stack material on performance of thermo acoustic refrigerator. Through the construction of a functional model in fluidyne software, this work demonstrate the effectiveness of thermo acoustics for modern cooling. Hence, simulation of thermo acoustic refrigerator is performed using fluidyn software. Performance evaluation is carried out using different stack materials and different working fluids. Simulation of thermo acoustic refrigerator was done successfully by using fluidyne software. The various stack materials used in simulation software are aluminium, copper, foam, lexan, and paper. Hot heat exchanger temperature is 300k and cold heat exchanger temperature is 297k, so the temperature difference is less and hence refrigeration effect is very small in thermo acoustic refrigerator.

Keywords: Thermo-acoustic, refrigerator, temperature, gradient, frequency

I. INTRODUCTION

Thermo acoustic Refrigeration System mainly consist of a loudspeaker attached to an acoustic resonator filled with a gas. In the resonator, a stack consisting of a number of parallel plates and two heat exchangers are installed. The loudspeaker, which acts as the driver, sustains acoustic standing waves in the gas at the fundamental resonance frequency of the resonator. The acoustic standing wave displaces the gas in the channels of the stack while compressing and expanding respectively leading to heating and cooling of the gas. The gas, which is cooled due to expansion absorbs heat from the cold side of the stack and as it subsequently heats up due to compression while moving to the hot side, rejects the heat to the stack. Thus the thermal interaction between the oscillating gas and the surface of the stack generates an acoustic heat pumping. The

heat exchangers are used so that heat interaction with the surrounding takes place. Heat is pumped from the cold end heat exchanger to the hot end heat exchanger. The pressure variation and displacement of sound waves in thermo acoustic-refrigerator system

A stack material should be selected first so that its properties can be taken into account while choosing other parameters. The material chosen should have a low thermal conductance. As a TAR's main purpose is to move heat from one end of the stack to the other, heat conduction in the opposite direction (from the hot end to the cold end) results in a reduction of efficiency.

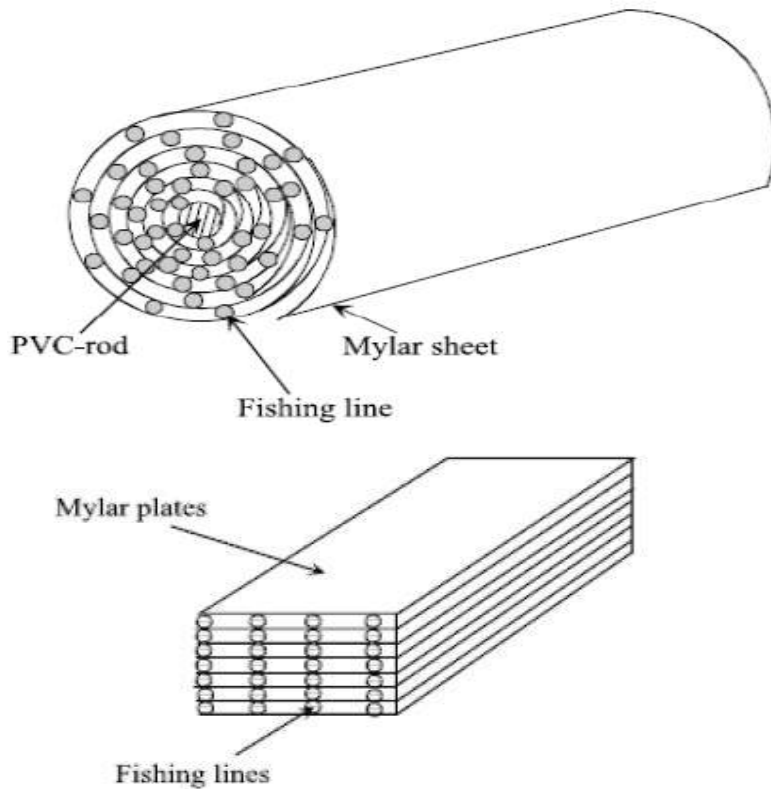


Figure 1. Cylindrical and flat stack arrays

The thermal conductivity is too high, the situation is analogous to carrying water uphill with a leaky bucket. The material should also have a larger specific heat capacity than the gas. A stack with a larger heat capacity is less affected by the temperature oscillations of the nearby gas, which is desirable because it allows the temperature gradient along the stack walls to remain steady, increasing the effectiveness of the gas in transporting thermal energy from the cold end to the hot end of the stack. Due to the necessary thermal properties, ceramic and plastic materials are often chosen as stack materials.

In the present work the concept of Computational Fluid Dynamics (CFD) is used to simulate the TAR. CFD is the simulation of fluids engineering systems using modeling (mathematical physical problem formulation) and numerical methods (discretization methods, solvers, numerical parameters, grid generations, etc.). To solve this problem, physical properties of stack materials are set in the software. Then we used Navier-Stokes Equation and it is the governing equation of CFD. As the Navier-Stokes Equation is analytical, human can understand it and solve them on a piece of paper.

In CFD software, we can compare and analyze the simulation results with experiments and the real problem. If the results are not sufficient to solve the problem, we have to repeat the process until find satisfied solution. This is the process of CFD. Figure 2 shows process of CFD.

The objectives of present work are: 1) Simulation of the thermo-acoustic refrigerator, 2) To investigate the effect of stack material on performance thermo-acoustic refrigerator,

The experiment suggests that thermo-acoustic refrigerators could one day be viable replacements for conventional refrigerators.

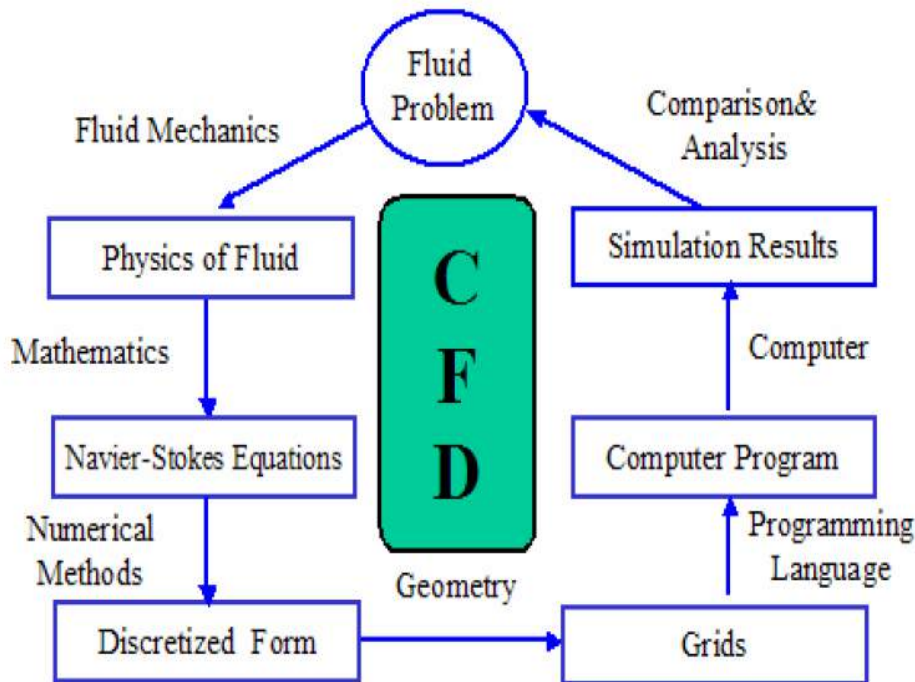


Figure 2. Process of Computational Fluid Dynamics

II. LITERATURE REVIEW

Rijke [1], in 1859, discovered that placing a heated wire mesh in the bottom half of an open tube produced sound waves. The highest intensity was obtained when the mesh was placed at one-fourth the length of the tube as measured from the bottom. Rijke [1] also observed that convective transport of air through the tube was necessary to produce the thermo-acoustic effect. The stack forms the heart of the refrigerator where the heat-pumping process takes place, and it is thus an important element that determines the performance of the refrigerator. The heat conductivity through the stack material and gas in the stack region has a negative effect on the performance of the thermo-acoustic refrigerators. The stack material must have low thermal conductivity and a heat capacity much larger than the heat capacity of the working gas in order that the temperature of the stack plates remains steady Swift [2]. In a typical thermo-acoustic device a stack usually occupies less than 10% of the overall device volume Swift [2]. Stacks are finely subdivided into many parallel channels or pores in order to maintain moderate (standing-wave) or good (traveling-wave) thermal contact

between the working gas and the stack across large cross-sectional areas. Stacks are available in different sizes and shapes; honeycombs, spiral rolls, parallel plates, circular pores, and pin arrays are examples of stacks commonly used in thermoacoustic engines and refrigerators. Figures 3 show examples of stack arrangement used in thermo-acoustic devices Swift [2]. Due to the necessary thermal properties, ceramic and plastic materials are often chosen as stack materials. Swift and Keolian [3] have proposed a new geometry, the pin array stack, and derived expressions for velocity and temperature in the pin array. They have shown that devices with this stack geometry can have significantly higher efficiency relative to the previous parallel-plate stack design. Construction of such stacks will be challenging since the crucial characteristic of the pin stack is the convexity of the gas-solid interface, on a length scale comparable to the penetration depths.

A thermo-acoustic theory for a bulk porous medium has developed by Roh et al. [4] from that for a single pore, parallel, capillary-tube-based theories. The authors have introduced the tortuosity, the viscous dynamic shape factor, and the thermal dynamic shape factor to extend the thermo-acoustic theory to a bulk porous medium. Comparisons of thermo-acoustic properties of RVC and aluminum foam developed by Tasnim [5] shown good agreement with the experiment. This prediction has shown that random porous media stacks should perform as well as parallel pore stacks in high-frequency prime movers. A more complete analysis is necessary for small refrigerators since enhanced viscosity may affect the performance.

The thermo-acoustic properties of fibrous porous materials are studied by Jensen and Rasper [6] using a computational fluid simulation. Tasnim [7] analyzes random porous thermoacoustic stack systems analytically, experimentally, and numerically with a primary objective to develop a comprehensive analytical porous media modeling for random porous (such as Reticulated Vitreous Carbon (RVC) foams) environment.

Lotton et al. [8] have presented analytical modelling for predicting the transient temperature profile in thermo-acoustic refrigerators. In their modelling, the authors have included the transverse heat conduction in the stack, heat leakages through the duct walls, heat generated by viscous losses in the stack, heat generated by vorticity at the ends of the stack, and heat transfer through both ends of the stack. The theoretical transient response of temperature of a thermo-acoustic refrigerator is compared with experimental measurements. A good qualitative agreement is obtained between analytical and experimental results after fitting empirical coefficients. Also, there exist different explanations about temperature distribution along with the stack in different works of literature.

Reid and Swift [9] have shown both experimentally and theoretically that temperature oscillations within a stack are linear for low-temperature differences between the two ends of the stack. Their theoretical prediction is based on inviscid boundary-layer, short-stack approximations, and neglecting the ordinary conduction of heat down the temperature gradient, as it is small compared to the hydrodynamic one. The experimental measurement provided by the authors is only for a single stack location within a standing wave thermo-acoustic refrigerator.

Worlikar and Knio [10] have developed a low Mach-number compressible flow model to simulate acoustically driven flows around a thermo-acoustic stack (finite thickness) for a wide range of drive-ratios. Worlikar and Knio have found that a periodic vortex dominates the flow near the edges of the stacks. Worlikar et al. [11] have extended the idea of Worlikar and Knio [10] by using a numerical solver for the energy equations of the

fluid and the stack plates, and by using a fast solver for the velocity potential. The modified model can handle unsteady thermally stratified flows in two-dimensional (2-D) thermo acoustic stacks.

Worlikar and Knio [12] have further extended their model by adding heat exchangers to the thermoacoustic stack assuming that the heat exchangers (one hot and one cold) are isothermal and in perfect thermal contact with stack plates. Their results reveal optimum stack performance is achieved when the length of the heat exchanger is nearly equal to peak-to-peak fluid particle displacement.

N.M. Hariharan et al [13] have built an experimental setup based on the linear thermo acoustic model and some simple design parameters. The engines produce acoustic energy at the temperature difference of 325–450 K imposed along with the stack of the system. This work illustrates the influence of stack parameters such as plate thickness (PT) and plate spacing (PS) with resonator length on the performance of thermoacoustic engines, which are measured in terms of onset temperature difference, resonance frequency, and pressure amplitude using air as a working fluid. The results obtained from the experiments are in good agreement with the theoretical results from DeltaEc.

Ahmed et al. [14] gave software analysis of a simple Thermo-acoustic Refrigerator (TAR). Two software were used for simulating the TAR; ANSYS Fluent and DeltaEC. ANSYS Fluent was used to predict the turbulent and oscillatory nature of the thermo-acoustic effect with the simulation. DeltaEC was used to calculate the final achievable temperature gradient of the TAR. Haggag et al. [15] designed the TAR system and manufactured using a PVC material. The effect of the stack center position and frequency on the system coefficient of performance (COP) is experimentally and theoretically investigated. The working medium used is Helium-Air mixture. Kajurek et al [16] demonstrated the design procedure of a small thermo-acoustic refrigerator with nominal cooling power of 10 W. Authors explain the design choices with the reasons for using specific parameters. The simulation results show that the cooling power of the refrigerator increases with the increase in the drive ratio and with the increase in the temperature of the cold heat exchanger. Tartibu [17] summarizes recent development with regards to the designing and the performance of highly efficient traveling-wave thermo-acoustic refrigerators. Desai et al. [18] performed experimental investigations on a half-wavelength standing wave type thermoacoustically driven thermoacoustic refrigerator also known as TADTAR. Authors shown that longer resonator and He-Ar mixture as working gas among the choices is better for a TADTAR system for achieving better performance.

Shivakumar and Bheemasha [19] investigated the effect of the spacing of a parallel plate stack on the performance of the thermo-acoustic refrigerator (TAR). Three parallel plate stacks have been used to study the performance of TAR considering different porosity ratios by varying the gap between the parallel plates.

Ali Namedar [20] used OpenFOAM package to simulate the thermo-acoustic refrigerator. For simulating oscillating inlet pressure, authors implemented cosine boundary condition into the Open-FOAM. The governing equations are the unsteady compressible Navier–Stokes equations and the equation of state. The computational domain consists of one plate of the stack, heat exchangers, and resonator. The main result of this paper includes the analysis of the position of the cold heat exchanger versus the displacement of the pressure node at large amplitude for successful operation of the refrigerator. In addition, the effect of the input power on the successful operation of the apparatus has been investigated. It is observed that for higher temperature difference between heat exchangers, the time of steady state solution is longer.

From the literature review, no work is observed on use of different stack materials to simulate TAR systems using software. Hence in the present work it is proposed to use aluminium, copper, foam, lexan, and paper as stack materials to investigate the performance of the TAR system.

III. RESEARCH METHODOLOGY

The present work involves only theoretical investigation of effect of operating variables on the performance of thermo-acoustic refrigerator using Fluidyn software. The model developed in Fluidyn software is focused on the different stack materials to evaluate the performance of TAR. The working fluids chosen for the analysis is helium with different stack material. The temperature gradient will develop across the length of the stack. The various geometric values, mean parameters, stack material properties and working fluid properties for simulation are given in Table 1 to Table 7.

Geometric Value and Mean Parameters

Table 1: Parameters for simulation

$C_p \text{ fluid} = 1007 \text{ J/ kg/ K}$	$K_w = 2p/k = 3.619/ \text{ m}$
$K_{\text{fluid}} = 0.0263 \text{ W/m /K}$	$f = 200 \text{ Hz}$
$L_{\text{fluid}} = 0.1846 _ 10_4 \text{ N sm_2}$	$DR = pA/p_m = 0.01$
$s = 1/f = 0.005 \text{ s}$	$T_m = 300 \text{ K}$
$Dt = 10_5 \text{ s}$	$R = 287 \text{ J kg_1 K_1}$
$K = a/f = 1.736 \text{ m}$	$p_m = 100 \text{ kPa}$
$K_{\text{solid}} = 1.05 \text{ Wm_1 K_1}$	$q_m = 1.1614 \text{ kg m_3}$
$C_{p\text{solid}} = 840 \text{ J kg_1 K_1}$	$pr = 0.707$
$q_{\text{solid}} = 2600 \text{ kg m_3}$	$c = 1.4$
$a = 347.2 \text{ m s_1}$	$L = 0.07 \text{ m}$
$L_1 = 0.01 \text{ m}$	$L_2 = 0.005 \text{ m}$
$L_3 = 0.7108 \text{ m}$	$L_4 = 0.0002 \text{ m}$
$L_5 = 0.0004 \text{ m}$	$L_6 = 0.0002 \text{ m}$
$L_7 = 0.0002 \text{ m}$	$L_8 = k/2 = 0.868 \text{ m}$

Material properties:

Gas properties:

Table 2: Helium properties

Name to the gas	Helium
Material Type	Gas
Dynamic Viscosity	$1.97e-005 \text{ m}^2/\text{sec}$
Thermal Conductivity	0.155
Gamma	1.4
Molecular Weight	4

Solid properties:

MATERIALS	THERMAL CONDUCTIVITY W/m-k	DENSITY Kg/m3	SPECIFIC HEAT J/Kg-K
LEXAN	0.18	1119	1300
FOAM	0.033	1040	1300
PAPER	0.18	930	1340
ALUMINIUM	180	2790	902
COPPER	401	8940	385

Table 3: Stack properties

After choosing the various parameters for simulation software, the pre-processing settings and data are set to the simulation model. In Pre-Processing part various settings and creations like loading fluid mesh file, Group creation, creating fluid boundary faces for cold and hot zones, material assignment, defining zone interaction, entering boundary and initial conditions are made. After the pre-processing the Output controls are defined and solution control parameters settings are made in the solver. At the end of simulation Post – Processing is set in the software to Create Contour plots, Create Trace plots and to Create Profile line plots.

IV. RESULTS AND DISCUSSION

The results obtained from the fluidyne software simulation are plotted on the graph. The plotted graphs are accurate for the given results. The simulation is carried out with copper, foam, lexan, and paper as stack materials. The effect of these stack materials on various working conditions like fluid pressure, velocity and temperature are show in the below graphs at different at stack length.

4.1 Aluminium stack effect on thermo acoustic refrigerator performance

The effect of aluminium stack plate in between cold heat exchanger and hot heat exchanger in thermo acoustic refrigerator. The simulation conducted results and the graph plotted as below

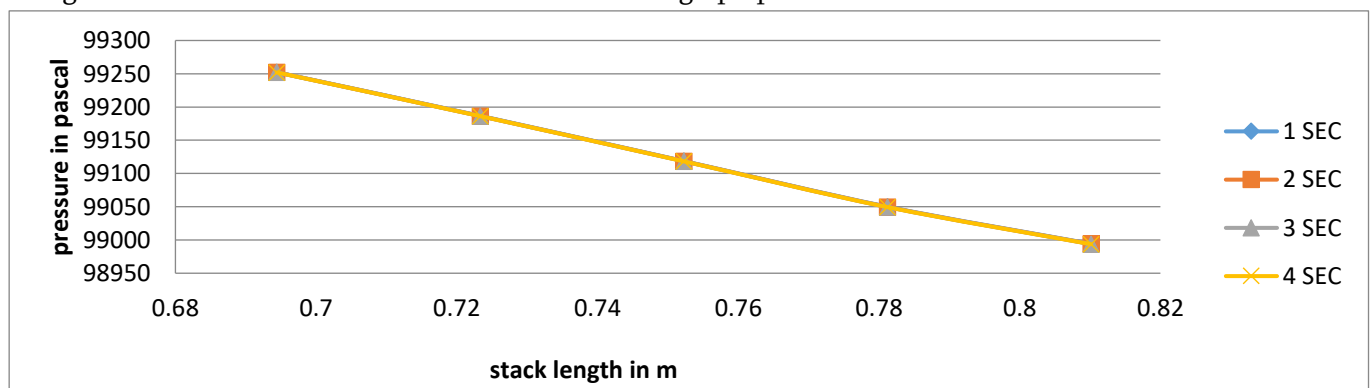


Figure 3. Aluminium stack length v/s pressure

Figure 3 shows the pressure variation at different stack length. As the stack length increases pressure decreases along the stack length.

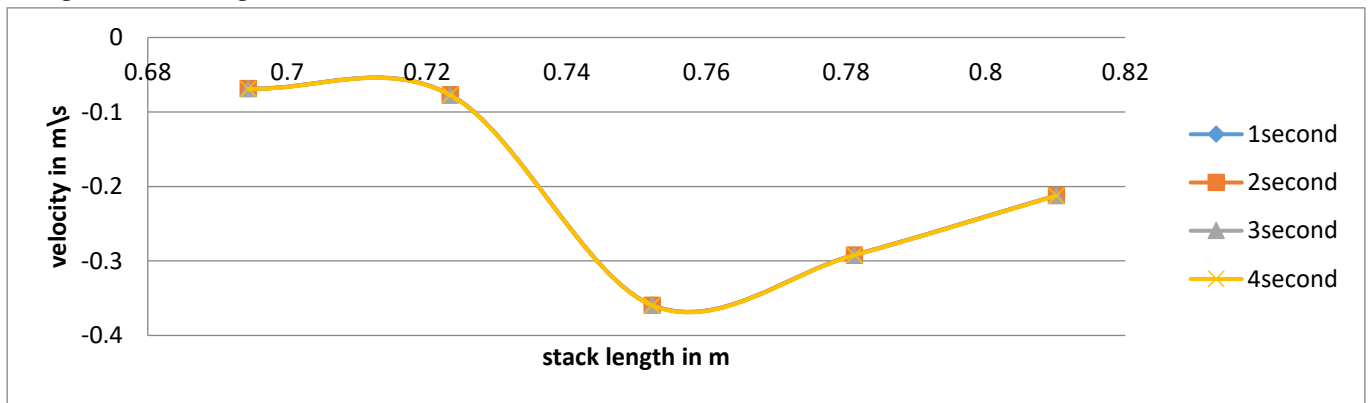


Figure 4. Stack length v/s velocity

In Figure 4, velocity varies at different stack length. Initially as the stack length increases the velocity is decreasing, after some stack length the velocity start raising up.

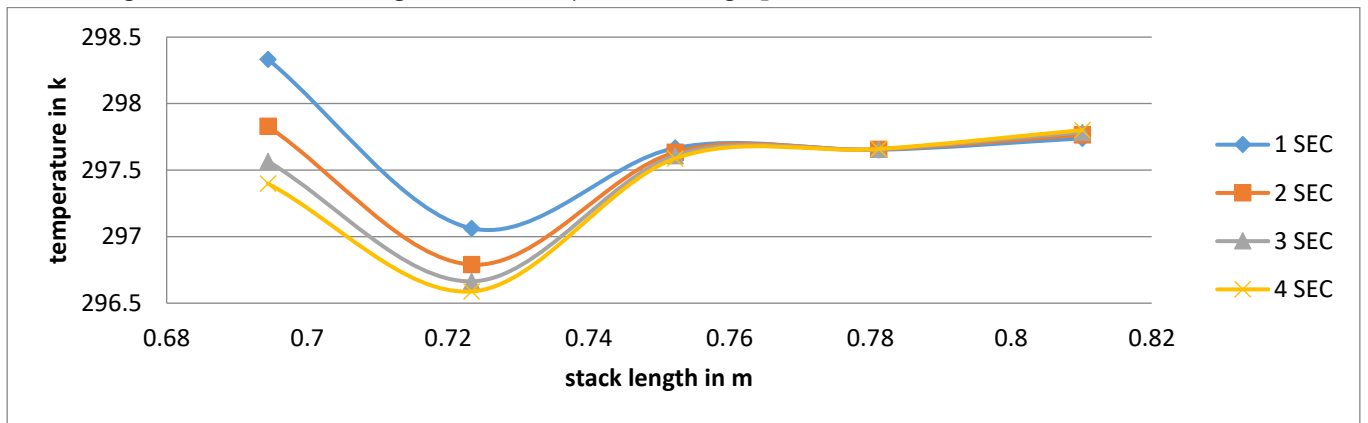


Figure 5. Stack length v/s temperature

Figure 5 shows that temperature reduction at cold side of the stack and increase in temperature on hot side of stack. This results shows that as the operating pressure is increases, the temperature gradient also increases but too much operating pressure may be causes the damage of resonator tube.

4.2 Copper stack effect on thermo acoustic refrigerator performance

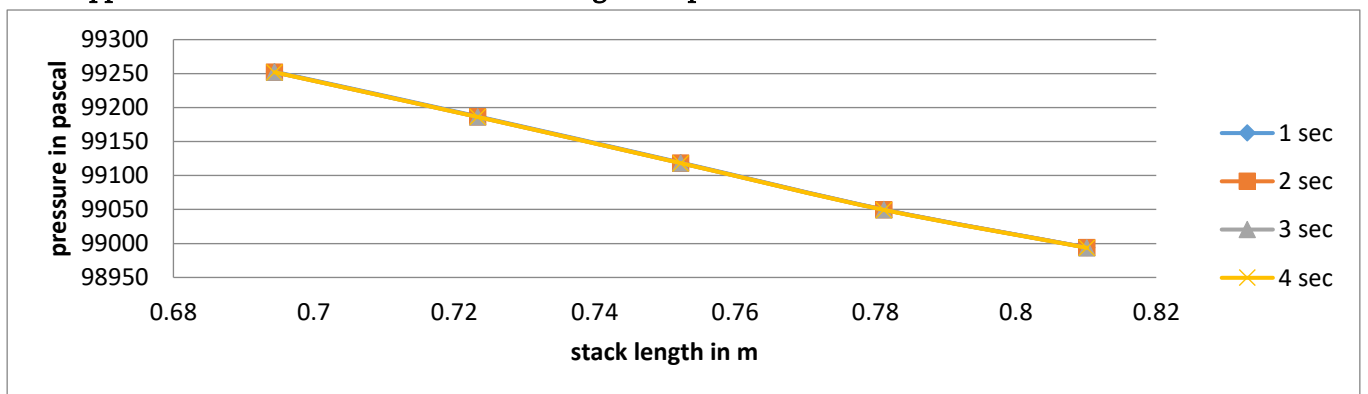


Figure 6. Stack length v/s pressure

Figure 6 shows the results of using copper stack material instead of aluminium. Because copper containing heat dissipates more than aluminium and low thermal conductivity here graphs illustrates pressure will flow cold heat exchanger to hot heat exchanger decelerates along stack length.

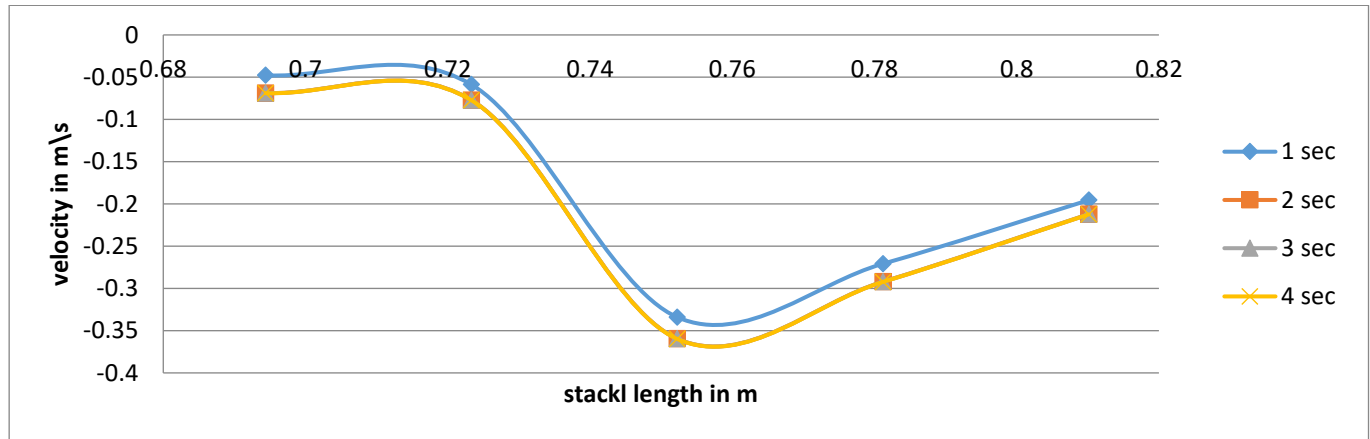


Figure 7. Stack length v/s velocity

The velocity and pressure are inversely proportional to each other so when velocity increase along the stack length the pressure will be decrease but sometimes velocity is decreases along the length of stack with time in its temperature. Similarly, it rejects heat to the gas molecules nearby during expansion, thus maintaining stable temperature. It is obvious that large amplitudes of pressure lead to an increase in heat transfer since it generates larger temperature difference between the fluids and the solid.

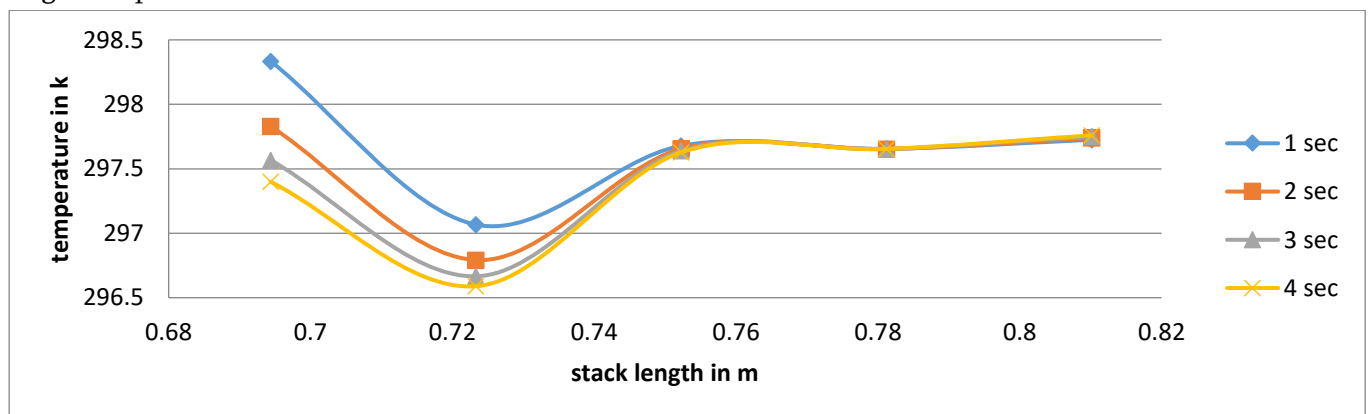


Figure 8. Stack length v/s temperature

Figure 8 shows temperature effect along length of stack heat capacity of solid generally quite greater than that of fluids the solid absorbs heat without much change in its temperature. Similarly, it rejects heat to the gas molecules nearby during expansion, thus maintaining stable temperature. It is obvious that large amplitudes of pressure lead to an increase in heat transfer since it generates larger temperature difference between the fluids and the solid.

4.3 Foam stack effect on thermo acoustic refrigerator performance

Foam stack is one of the stack material used in thermo acoustic refrigerator it is more less thermal conductivity compare to other stack materials and heat capacity also more.

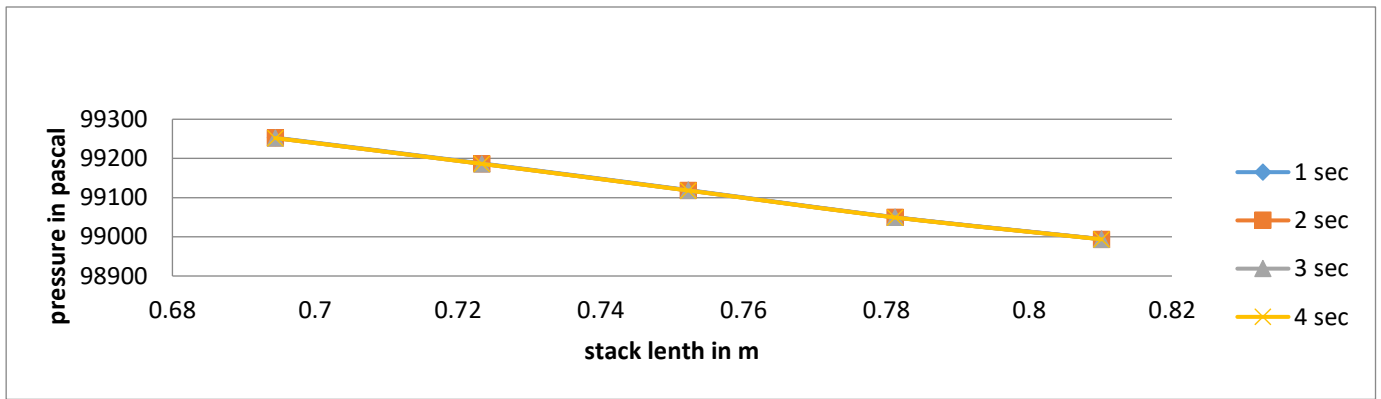


Figure 9. Pressure various along stack length

Figure 9 represents in foam stack the pressure will be maximum at hot heat exchanger because temperature is high at hot heat exchanger and pressure will minimum at cold side heat exchanger in thermo acoustic refrigerator the both temperature at cold and hot are iso-thermal so that pressure will moves along hot to cold it is decreases along the stack length.

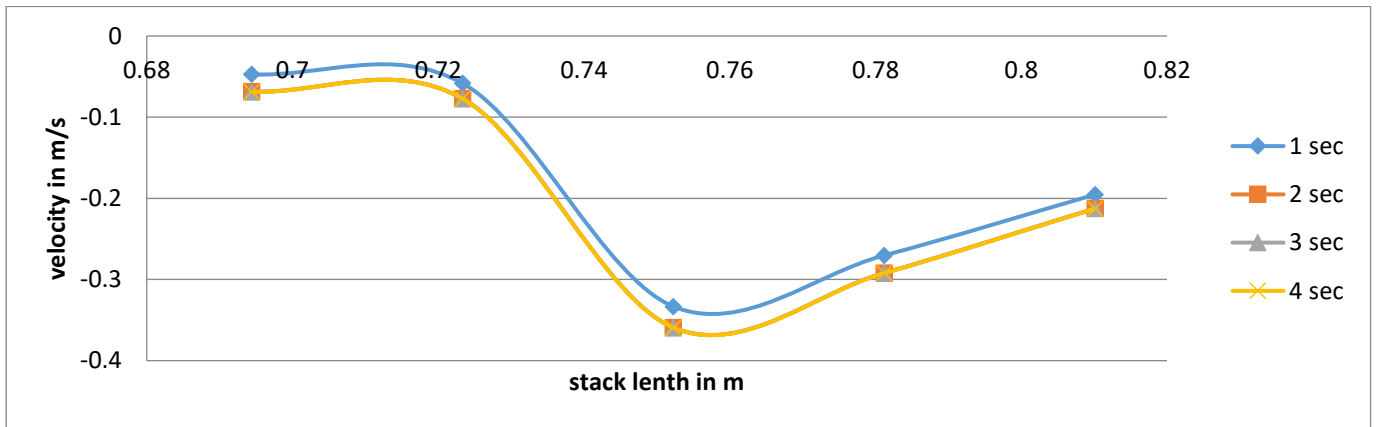


Figure 9. Velocity variation along stack length

Figure 9 represents the velocity variation along foam stack length. The velocity is high at cold heat exchanger but low at hot heat exchanger because of velocity and pressure are the inversely proportional to each other.

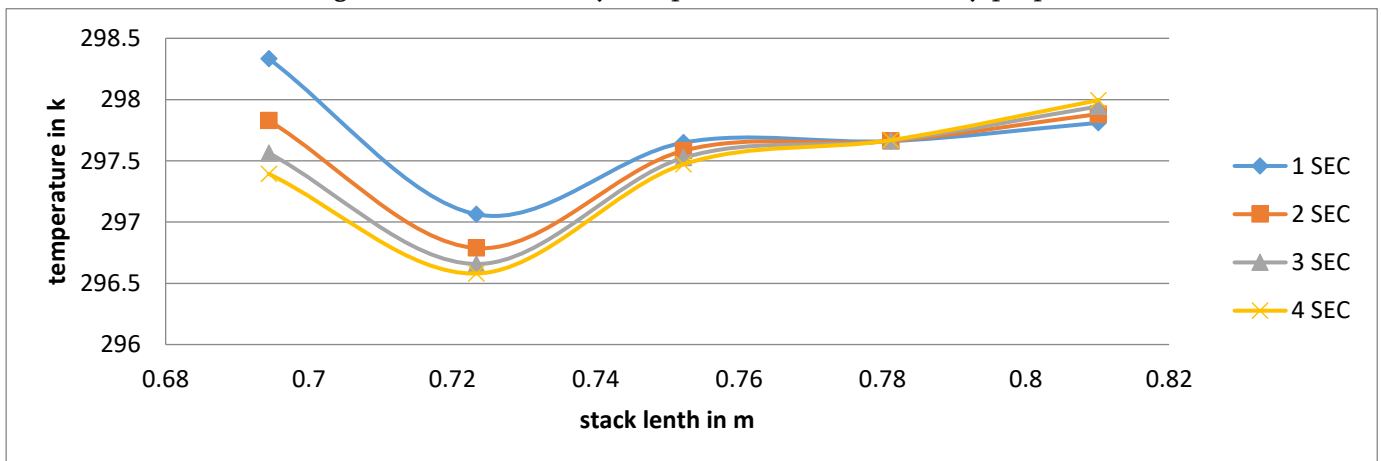


Figure 10. Stack length v/s temperature

A foam stack with a larger heat capacity is less affected by the temperature oscillations of the nearby gas, which is desirable because it allows the temperature gradient along the stack walls to remain steady, increasing the effectiveness of the gas in transporting thermal energy from the cold end to the hot end of the stack. Due to the necessary thermal properties.

4.4 Lexan stack effect on thermo acoustic refrigerator performance

Lexan is also one of the stack material used in thermo acoustic refrigerator it has low thermal conductivity compare to aluminium and copper stack materials.

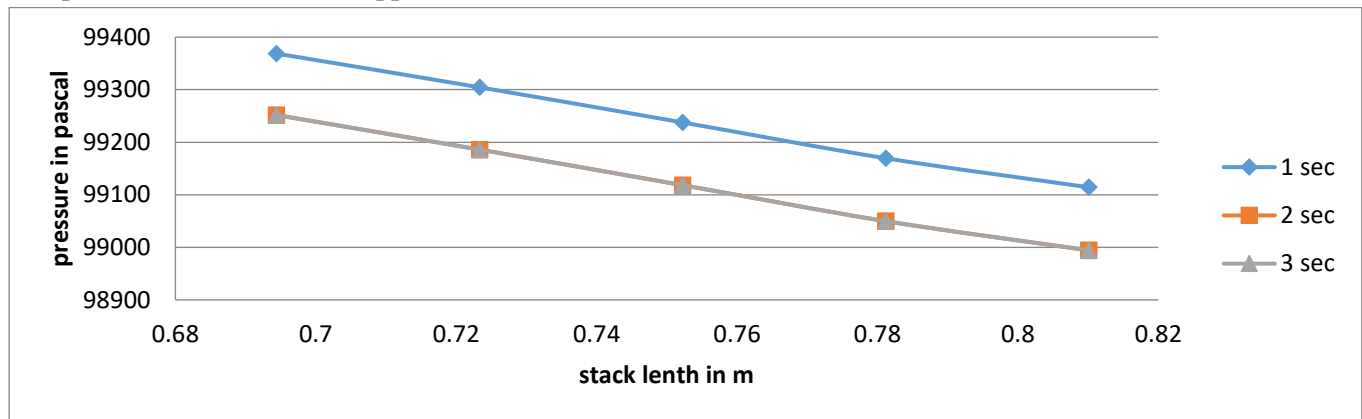


Figure 11. Pressure variation along stack length

Figure 11 shows pressure variations along lexan material stack length. Pressure variation is different with different timings. The varying pressure is high at time equal to 1sec, that is at hot heat exchanger but at timings 2&3 sec it is slightly varies and pressure decreases along stack length.

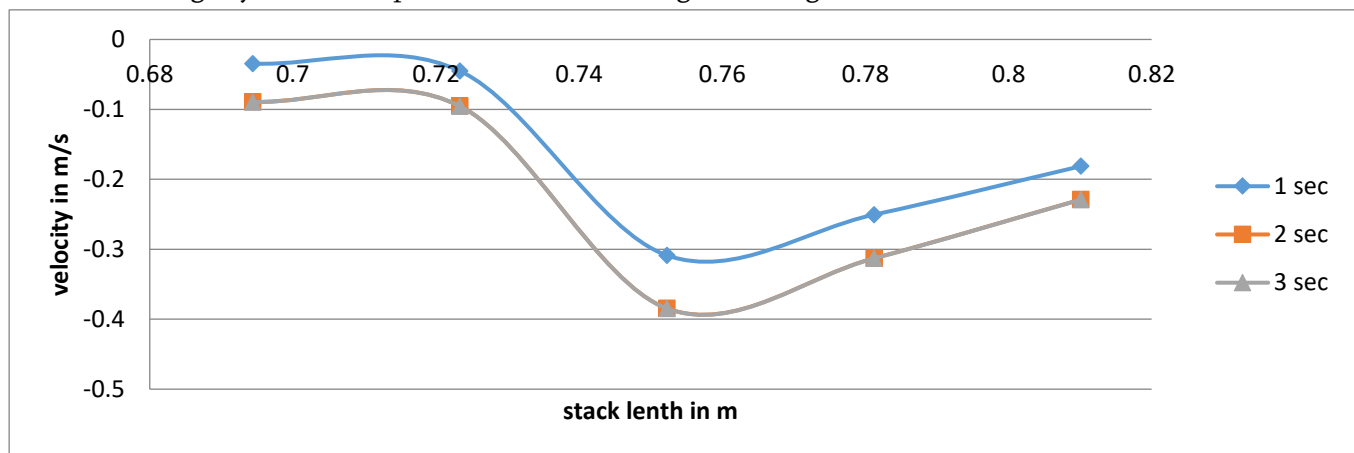


Figure 12 Velocity variation along stack length

Figure 12 shows the variation of velocity along Lexan stack length. The velocity is increases at cold heat exchanger decreases at hot heat exchanger with stack length.

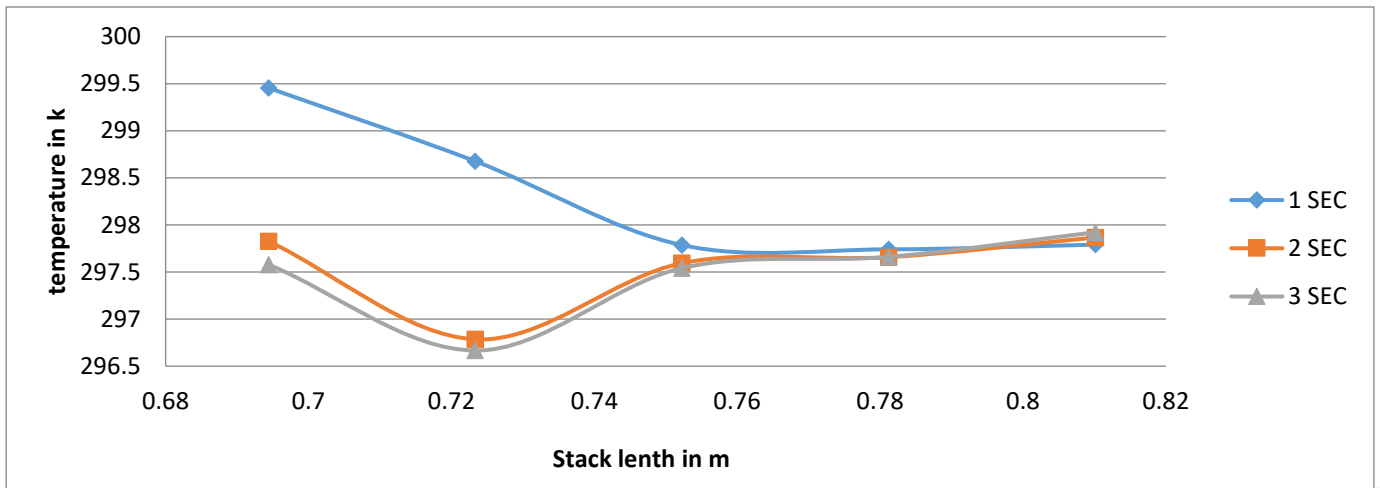


Figure 13 stack length v/s temperature

Figure 13 shows the temperature is high at hot end and low at cold end heat exchanger

4.5 paper stack effect on thermo acoustic refrigerator performance

Paper stack also good heat dissipates properties

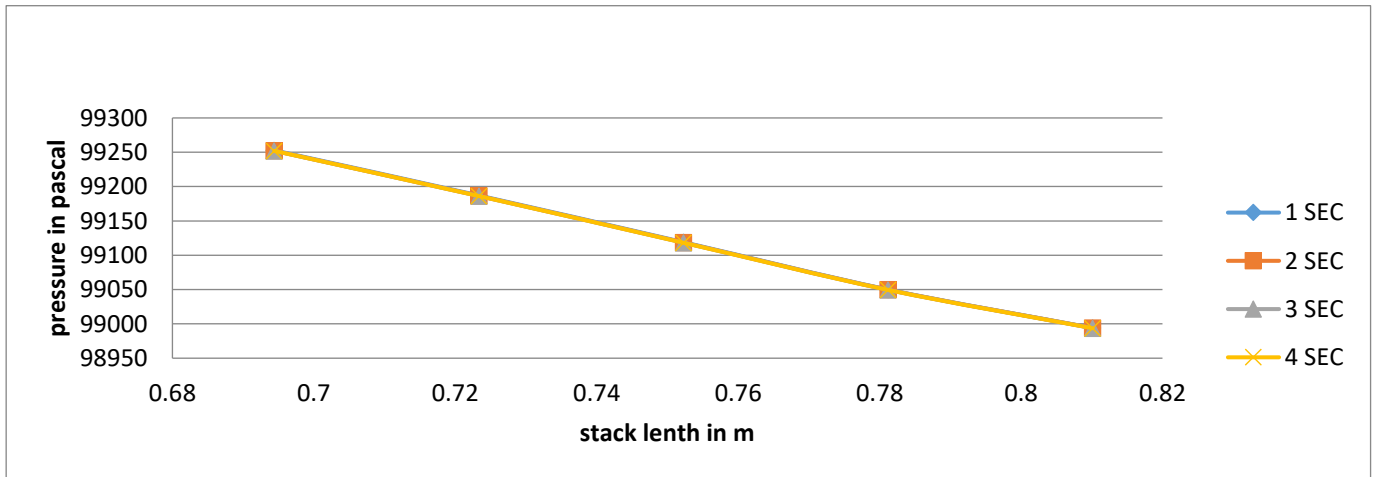


Figure 14. Stack length v/s pressure

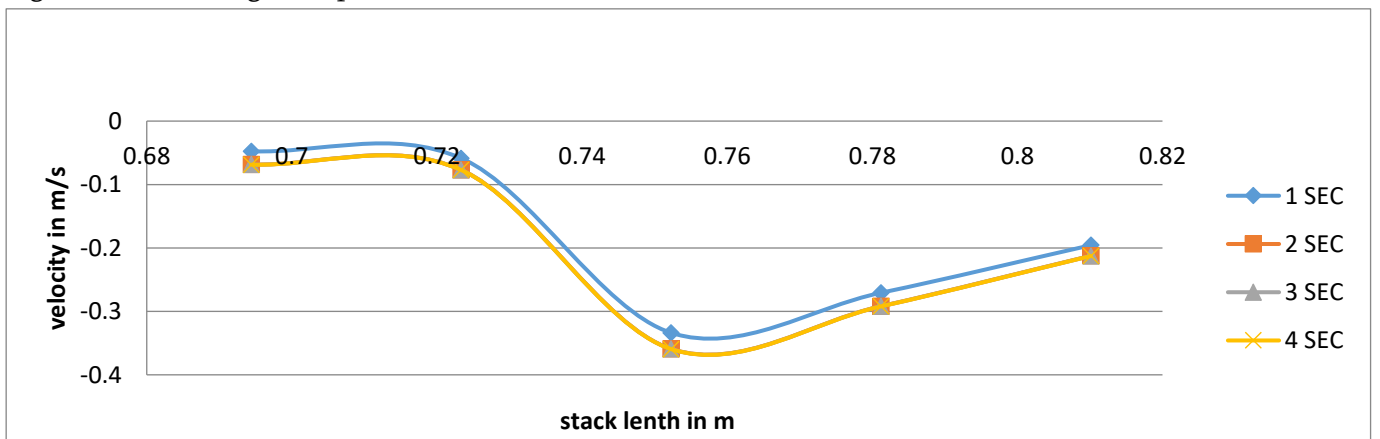


Figure 15. Stack length v/s velocity

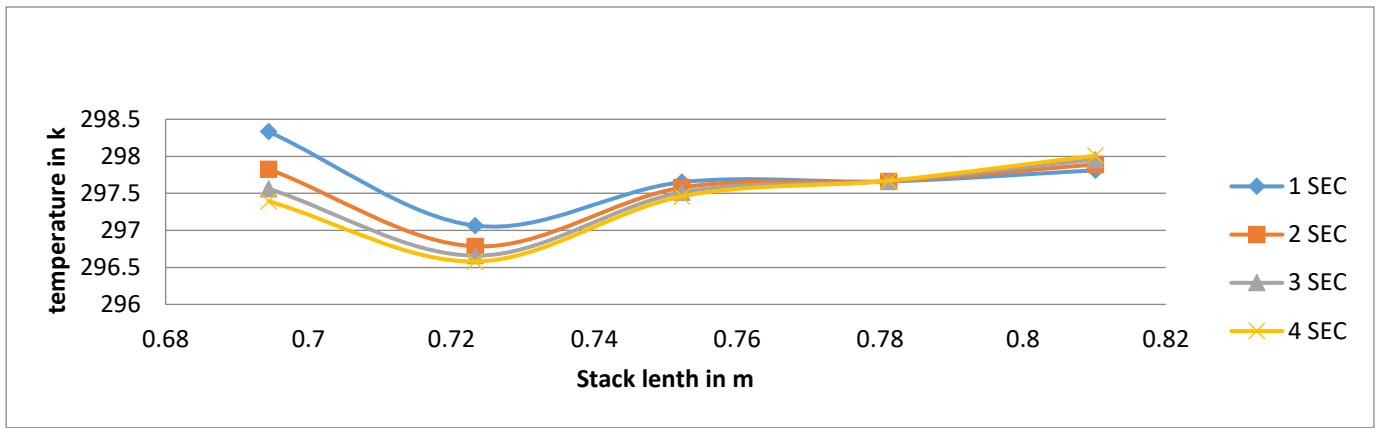


Figure 16 stack length v/s temperature

Figure 16 shows that the variation of temperature along the paper stack length. It is noticed that the temperature is in higher side at initial timings (i.e. 1 sec) compared to delay timings (i.e. 2 to 4 secs).

4.6 Different stack materials effect on thermo acoustic refrigerator performance

The graphs are also taken with combination of stack materials aluminium, copper, foam, lexan and paper. Compared the one stack material data with other stack and plots graphs as below.

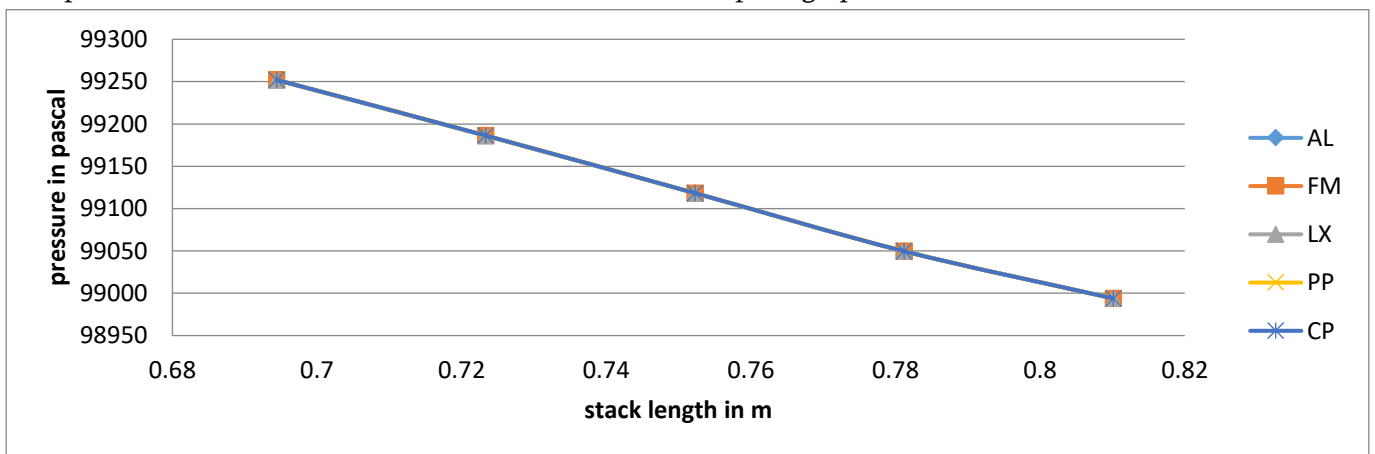


Figure 17. Stack length v/s pressure

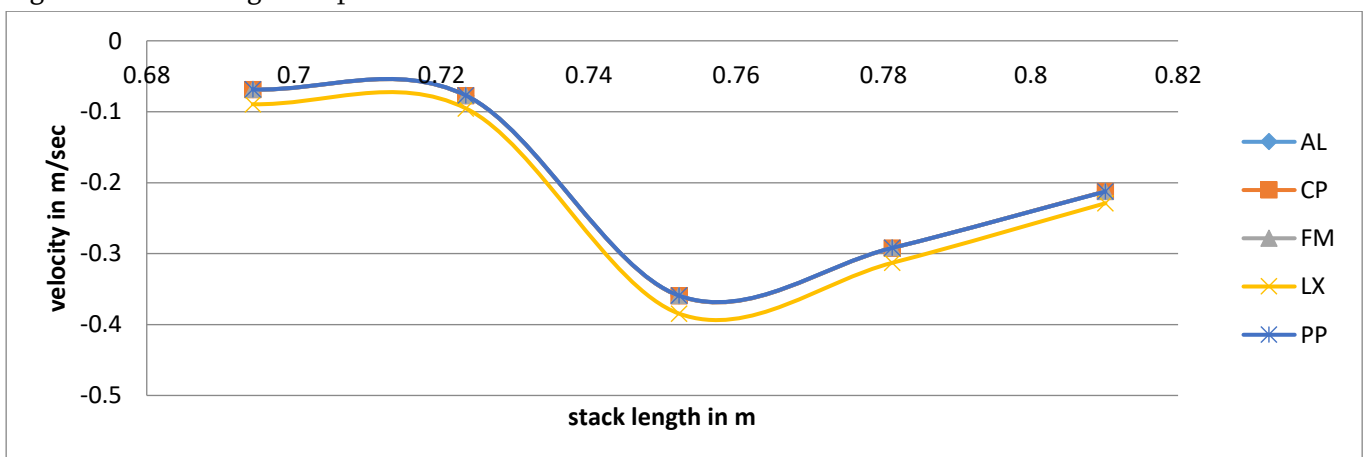


Figure 18. Stack length v/s velocity

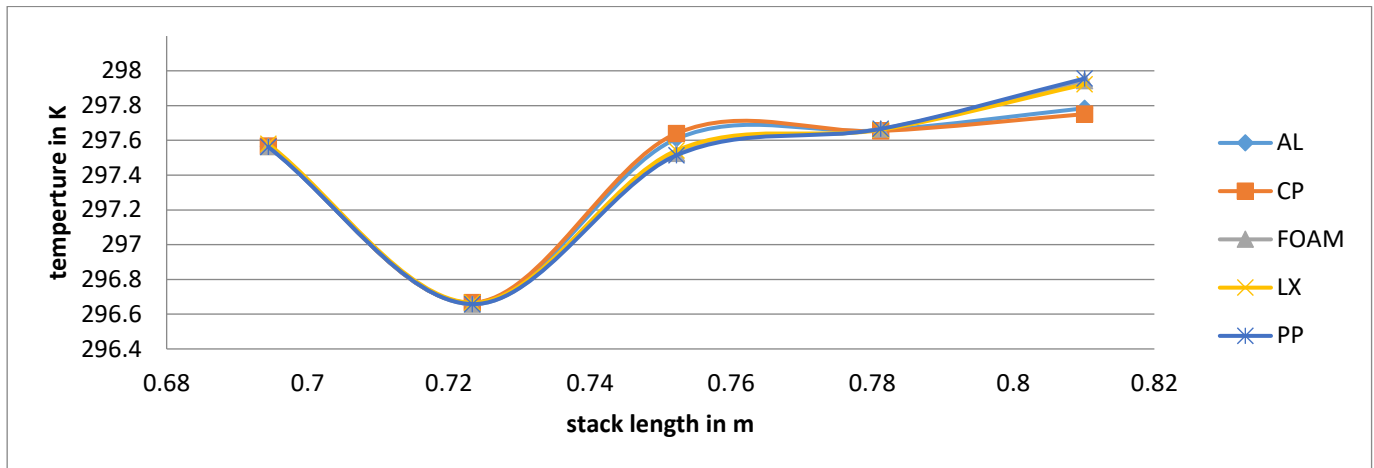


Figure 19. Stack length v/s temperature

Figures 17, 18 and 19 shows the variation of Pressure, Velocity and temperature for Aluminium, Copper, Foam, Lexan and Paper materials along stack length.

Temperature and pressure are directly proportional to stack length in thermo acoustic refrigerator the pressure is high at hot end and temperature also high but velocity is low the temperature is isothermal at both side of heat exchanger.

V. CONCLUSION

The influence of various stack materials on the velocity, pressure and temperature along the stack length is discussed and variations are plotted.

Simulation of thermo acoustic refrigerator in fluidyne software was successful using Aluminium, Copper, Foam, Lexan and Paper. Results demonstrated that these materials can be used as stack materials on thermo acoustic refrigerator.

In the future, the next obvious step is to construct an experimental unit to conduct experiments with mixture of noble gases to investigate the influence of working fluids on the performance of refrigerator. Theoretical studies to be continued with high end computers to understand the characteristics of thermo acoustic refrigerator. Experiments with different stack material and stack geometry such as honeycombs from Pyrex Glass could be tried to study the performance.

VI. REFERENCES

- [1]. Rijke, P.L., Notiz über eine neue Art die in einer an beiden Enden offenen Röhre enthaltene Luft in Schwingungen zu versetzen. *Annalen der Physik*, 1859. 107: p. 339-343.
- [2]. Swift G.W. *Thermoacoustics: A unifying perspective for some engines and refrigerators*. Condensed Matter and Thermal Physics Group, Los Alamos National Laboratory, LAUR 99-895, 2002.
- [3]. Swift G.W. and Keolian R.M. Thermoacoustic in pin-array stacks. *The Journal of the Acoustical Society of America*, 94 (1993) 941-943.

- [4]. Roh H., Raspert R., and Bass H. E. Parallel capillary-tube-based extension of thermoacoustic theory for random porous media. *The Journal of the Acoustical Society of America*, 121(3) (2007)1443-1421.
- [5]. Tasnim, Syeda Humaira. "An experimental study on heterogeneous porous stacks in a thermoacoustic heat pump." *Journal of Energy Resources Technology* 139, no. 4 (2017).
- [6]. Jensen C, Raspert R. Thermoacoustic properties of fibrous materials. *J Acoust Soc Am*. 2010 Jun;127(6):3470-84. doi: 10.1121/1.3425735. PMID: 20550247.
- [7]. Tasnim, Syeda Humaira. *Porous Media Thermoacoustic Stacks: Measurements and Models*, PhD Dissertation work, Waterloo, Ontario, Canada, 2011
- [8]. Lotton P., Blanc-Benon Ph., Bruneau M., Gusev V., Duffourd S., Mironov M., and Poignand G. Transient temperature profile inside thermoacoustic refrigerators. *International Journal of Heat and Mass Transfer*, 52 (2009) 4986-4996.
- [9]. Reid R.S. and Swift G.W. Experiments with a flow through thermoacoustic refrigerator. *The Journal of the Acoustical Society of America*, 108(6) (2000) 2835-2842.
- [10]. Worlikar A.S. and Knio O.M. Numerical study of oscillatory flow and heat transfer in a loaded thermoacoustic stack. *Numerical Heat Transfer (Part A)*, 35 (1999) 49 –65.
- [11]. Worlikar, A S., and Klein, R. "Numerical study of the effective impedance of a thermoacoustic stack." *Acta Knio, O.M., Acustica united with Acustica* 85, no. 4 (1999): 480-494.
- [12]. Worlikar, A. S., and Knio, O.M.,. "Numerical simulation of a thermoacoustic refrigerator: I. Unsteady adiabatic flow around the stack." *Journal of Computational Physics* 127, no. 2 (1996): 424-451.
- [13]. N.M. Hariharan P. Sivashanmugam S. Kasthuriengan Influence of stack geometry and resonator length on the performance of thermoacoustic engine *Applied Acoustics* 73 (2012) 1052–1058
- [14]. Ahmed, S., Rehman, A., Fareed, A., Al Haque, S.M.S. and Muhammad, A., Simulation of a Thermo-Acoustic Refrigerator. *International Journal of Mining, Metallurgy & Mechanical Engineering (IJMMME)* Volume 5, Issue 1 (2017) ISSN 2320–4060 (Online)
- [15]. Haggag, Salem, Ghaleb Ibrahim, Bader Al-Ajeel, Tasneem Suboh, and Aly Tourk. "Steady State Modelling, Experimental Validation and Performance Analysis of Thermo-Acoustic System." *Proceedings of the 5th International Conference of Fluid Flow, Heat and Mass Transfer (FFHMT'18)* Niagara Falls, Canada – June 7 – 9, 2018 Paper No. 147 DOI: 10.11159/ffhmt18.147
- [16]. Kajurek, Jakub, Artur Rusowicz, and Andrzej Grzebielec. "Design and simulation of a small capacity thermoacoustic refrigerator." *SN Applied Sciences* 1, no. 6 (2019): 1-9.
- [17]. Tartibu, L. K. "Developing more efficient travelling-wave thermo-acoustic refrigerators: A review." *Sustainable Energy Technologies and Assessments* 31 (2019): 102-114.
- [18]. Desai, A. B., K. P. Desai, H. B. Naik, and M. D. Atrey. "Experimental study and analysis of a thermoacoustically driven thermoacoustic refrigerator." *Sādhanā* 45, no. 1 (2020): 1-12.
- [19]. Shivakumara, N. V., and Bheemsha Arya. "Effect of parallel plate stack spacing on the performance of thermoacoustic refrigerator in terms of temperature difference using air as a working fluid." In *Journal of Physics: Conference Series*, vol. 1473, no. 1, p. 012051. IOP Publishing, 2020.
- [20]. Namdar, Ali, Ali Kianifar, and Ehsan Roohi. "Numerical investigation of thermoacoustic refrigerator at weak and large amplitudes considering cooling effect." *Cryogenics* 67 (2015): 36-44.



Experimental Studies on Oscillating Heat Pipe using conventional and Nano Fluids

Parashuram A K¹, K. RamaNarasimha², K. Gopalakrishna³

¹Department of Mechanical Engineering, K S Institute of Technology, Bangalore-560062, Karnataka, India

²Department of Mechanical Engineering, K S School of Engineering and Management, Bangalore -560062, Karnataka, India

³Department of Mechanical Engineering, Jyothy Institute of Technology, tataguni off kanakapura road, Bangalore - 560082, Karnataka, India

ABSTRACT

Oscillating heat pipe (OHP) cooling is the new and emerging technique in the field of thermal management of electronics. In the present work, transient and steady state experiments are conducted on a multi turn closed loop OHP. Evaporator and condenser wall temperatures are measured. Copper is used as the capillary tube material in the evaporator and condenser sections with inner diameter of 1.5 mm and outer diameter of 3 mm. The total length of the closed loop pulsating heat pipe is 2040mm. The experiments are conducted in vertical orientation for different heat loads varying from 20 W to 40 W in steps of 5W. The OHP is tested with different working fluids viz. Acetone, water, SWCNT and Graphene. The performance parameters such as temperature difference between evaporator and condenser, thermal resistance and the overall heat transfer coefficient are evaluated. The experimental results demonstrate that SWCNT& Graphene particle based Nano fluid is the better working fluid among the working fluids considered in terms of lower thermal resistance and higher heat transfer coefficient. The multi loop OHP is found to perform better for all heat loads & working fluids considered.

Keywords: Nano fluids, oscillating heat pipe, experimental studies, thermal performance

I. INTRODUCTION

Thermal management is the challenge of the day in electronic product development. Presently, the chip heat flux level ranges between 40 to 120 W/cm². It is expected to increase to 200 W/cm² in the next few decades. Several cooling methods are employed to cool the electronic devices. Heat Pipe is being explored for electronic cooling devices with promising results. Even though the conventional heat pipes are excellent heat transfer devices their application is mainly confined to transferring small amount of heat over relatively short distances.

Oscillating heat pipe (OHP) is a passive two-phase heat transfer device, which is a special category of wickless heat pipes. It has been invented by Akachi [1-3], it exhibits self-sustained oscillation of the working fluid and phase change phenomenon leading to enhanced heat transfer. Due to its simple design, light weight, low fabrication cost and very fast response at higher heat loads, OHPs have been considered as one of the compact heat transfer devices for various cooling applications such as electronics cooling, heat exchanger and space application, etc. Since the last two decades, many researchers have investigated its thermal performance experimentally and theoretically. These experiments reveal that the Closed Loop Oscillating Heat Pipe (CLOHP) performance is strongly affected by many parameters including geometrical, physical and operational parameters. Furthermore, it is mentioned that the problem of two phase flow oscillation in closed loop Oscillating heat pipe is very complicated because of many unstable variables and complexity of thermo-hydrodynamic operational characteristics. In the meantime, some visual studies have been performed using glass tube to understand the operational behaviour and considerable progress has been also achieved in these Attempts [4]. In recent years, improving thermal performance of CLOHP has become a demanding challenge and hot research topic due to rapidly increasing heat load and miniaturization of electronic devices. Based on existing experimental results the working fluid is the most important parameter in the CLOHP. At the same time, Nano fluids are viewed as advanced heat transfer fluids in heat transfer devices. In general, the nanoparticles suspended in the base fluid forming the Nano fluid are of size about less than 100 nm. The heat transfer performance of the base fluid is significantly improved due to increased surface area. In 1995, this concept was first proposed by Choi Since then, some researchers have focused on the heat transfer characteristics of Nano fluids such as thermal conductivity and viscosity in single-phase flow and also flow with phase change.

In recent years, the nanofluid, employed as a working fluid in the heat transfer device, is an emerging topic. In 2004, Tsai et al. [5] found application of nanofluids in the Conventional heat pipes using gold nanoparticle solution and there was a significant reduction noted in thermal resistance of heat pipe with nanofluid as compared to the one with DI water. In 2006, Ma et al. [6] conducted experiments under various operating temperatures and heat powers using water based diamond nanofluid in the CLOHP.

They reported that the nanofluid could effectively enhance heat transfer due to occurrence of strong oscillatory motion of flow. Lin et al. [7] observed thermal enhancement of the heat pipe with water based silver nanofluid at very low mass concentration. Visualization

Experiments are carried out on two phase flows of the CLOHP using DI water and Nano fluid [8, 9]. Ji et al. [10] found improvement in the start-up performance of CLOHP due to alumina nanofluid. Jian Qu et al. [11] pointed out improvement or deterioration of the CLOHP performance due to different nanoparticle deposition behaviour with different nanofluids. A similar deterioration of heat pipe (thermosyphon) was found by Khandekar et al.

[12]. It is noticed from relevant literatures [5–12] that the improvement/deterioration of boiling performance in the heat pipes is due to the change in surface property. The small amount of the nanoparticle suspended on the base fluid cannot largely increase the thermal conductivity of the working fluid. However, the oscillating motion of the particles in the working fluids might have additional contribution to improvement of thermal performance of the CLOHP [6]. From the literatures [13–15], it is felt that the study of Nano fluids is still

promising and the overall understanding of two phase flow heat transfer with the CLOHP is at the beginning stage. Hence, exploratory researches in both fundamental and engineering systems are needed.

Further, it is noted that very little amount of work has been carried out with use of metal nanoparticles in the CLOHP. Therefore, the present study aims at experimentally investigating the thermal performance of the device using SWCNT & Graphene Nano particle based Nano fluid, Results of the present study are expected to help us understand and design more efficient Nano fluid-charged CLPHPs operational behaviour

II. EXPERIMENTATION

2.1 Material Selection & Fabrication

The basic components used in OHP are copper tubes, glass tubes, silicon rubber tubes, a non-return valve, a Mica heater and thermocouples. Copper is used as the tube material since it is an excellent conductor of heat. The tube is bent into a multi loop U turn with a radius of 35mm. The glass tube attached between the U turn copper tubes acts as the adiabatic section and provides the flow visualisation. The glass tube is made of borosilicate, which can resist temperature up to 1200°C. Silicon tubes are used as the connectors between glass and copper tubes. They can resist temperatures up to 400° C. In order to maintain unidirectional fluid flow, a non-return valve is used. Eight 'K-type' thermocouples are used for temperature measurement. Four thermocouples each are connected in the evaporator and condenser sections at equal distances. An Eight - channel digital temperature indicator is used to record the temperatures at different locations. A coil wound heater attached to evaporator section acts as the source of heat input. The experimental setup is worked with four working fluids viz., water, acetone, SWCNT and Graphene based Nano fluids. The Working fluid is injected into the heat pipe using a syringe

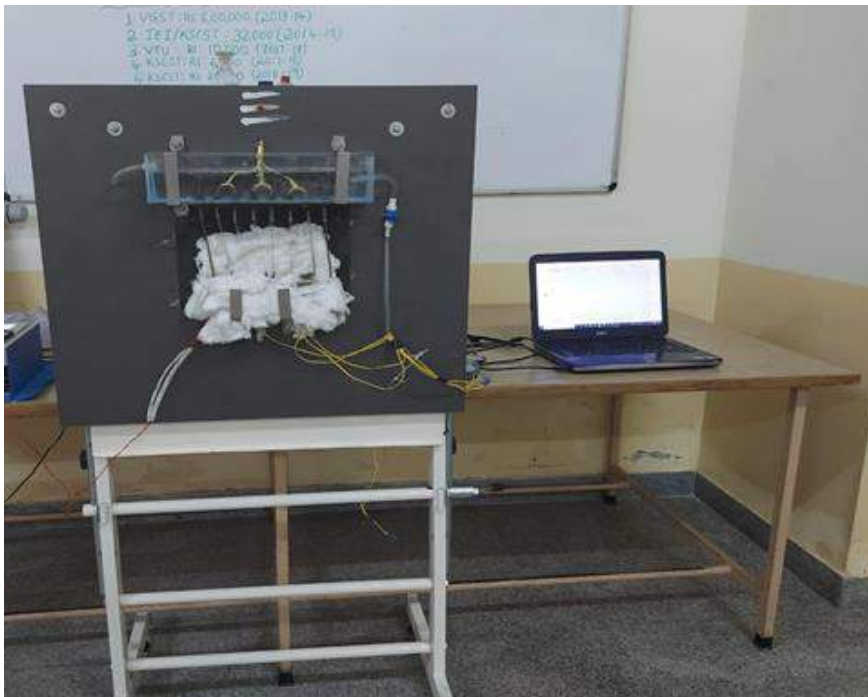


Figure. 1 OHP experimental setup

2.2 Experimental Procedure

Before conducting the experiment, it is ensured that there is no fluid inside the tubes. The required amount of working fluid is then filled through a syringe by opening one end of the non-return valve such that the fluid directly enters the evaporator section. Now the air is filled through the projection provided on the copper tube using another syringe. This is done to ensure simultaneous formation of liquid slug and vapour plug. The display unit is switched ON and the required wattage is set. A fan arrangement is used for cooling the fluid in the condenser section. The transient experiments are conducted and the various temperatures are recorded from the digital temperature indicator. The experiments are continued till SteadyState is reached.

The colloidal solution of SWCNT particle Nano fluids is prepared by using water as base fluid & graphene particle based Nano fluid is prepared by using acetone as base fluid and experimentation is carried out by varying the fill ratio as well as by varying the heat load input. The obtained values will be plotted against the graph through which the values of thermal resistance and heat transfer coefficient. The heat input and the variation of the temperature is noted with the aid of temperature data logger. The output of the temperature data logger with the help of the software is monitored in the computer. A typical output from the data acquisition system is as shown below,

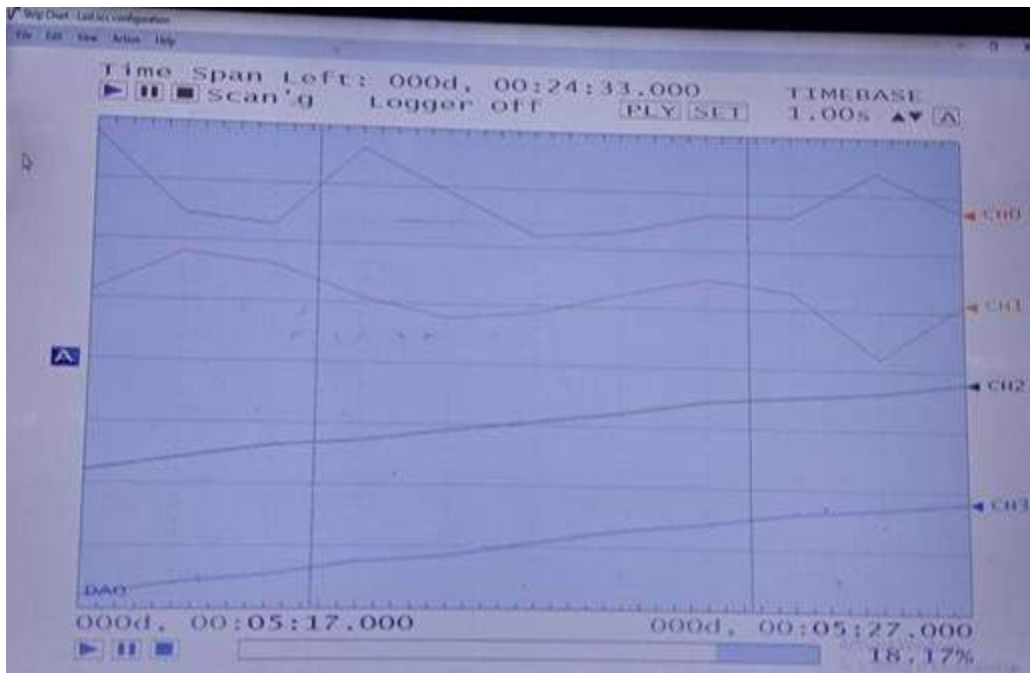


Figure 2 Output of the Data Acquisition System

III. RESULTS AND DISCUSSION

Transient experiments have been conducted with different working fluids i.e., acetone, water, SWCNT and Graphene Nano particle based Nano fluid and variations of temperature with time are recorded. The experiments are continued till steady state is reached.

Fig 3 shows the variation of temperature difference between evaporator and condenser with time at different heat inputs for water at a fill ratio of 50%. It is observed that the temperature difference between evaporator and condenser is considerably less at lower heat input of 25 W

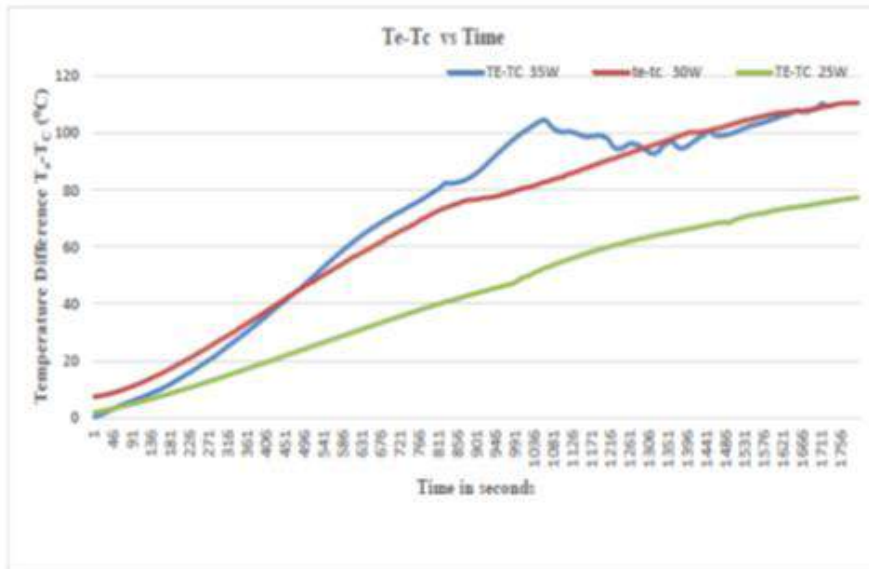


Figure 3 .Temperature Difference (Te -TC) Plot for water

Fig 4 shows the variation of temperature difference between evaporator and condenser with time at different heat inputs for SWCNT at a fill ratio of 50%. It is observed that the temperature difference between evaporator and condenser is considerably less at lower heat input of 25 W

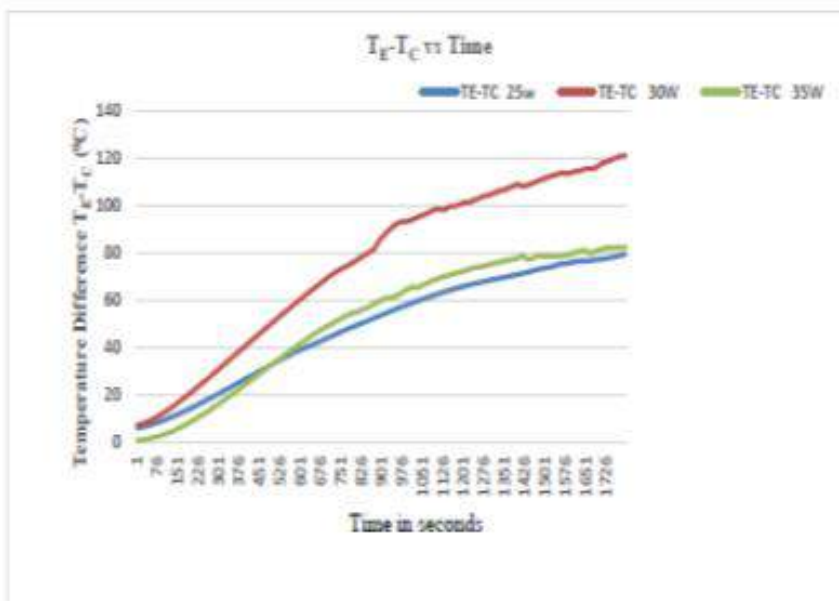


Figure 4. Temperature Difference (Te -TC) Plot for SWCNT

Fig 5 shows the variation of temperature difference between evaporator and condenser with time at different heat inputs for Graphene at a fill ratio of 50%. It is observed that the temperature difference between evaporator and condenser is considerably less at lower heat input of 25 W

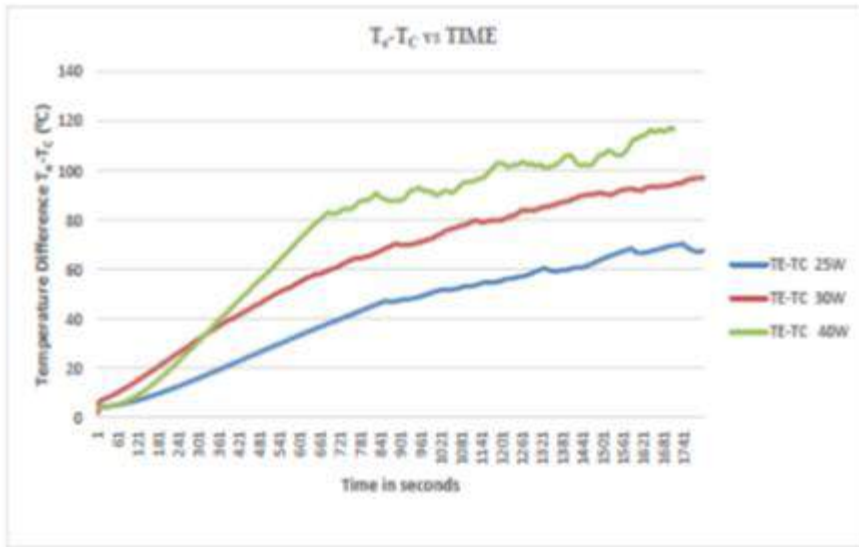


Figure 5. Temperature Difference (Te –TC Plot for Graphene

Fig 6 shows the variation of temperature difference between evaporator and condenser with time at different heat inputs for Graphene at a fill ratio of 50%. It is observed that the temperature difference between evaporator and condenser is considerably less at lower heat input of 25 W

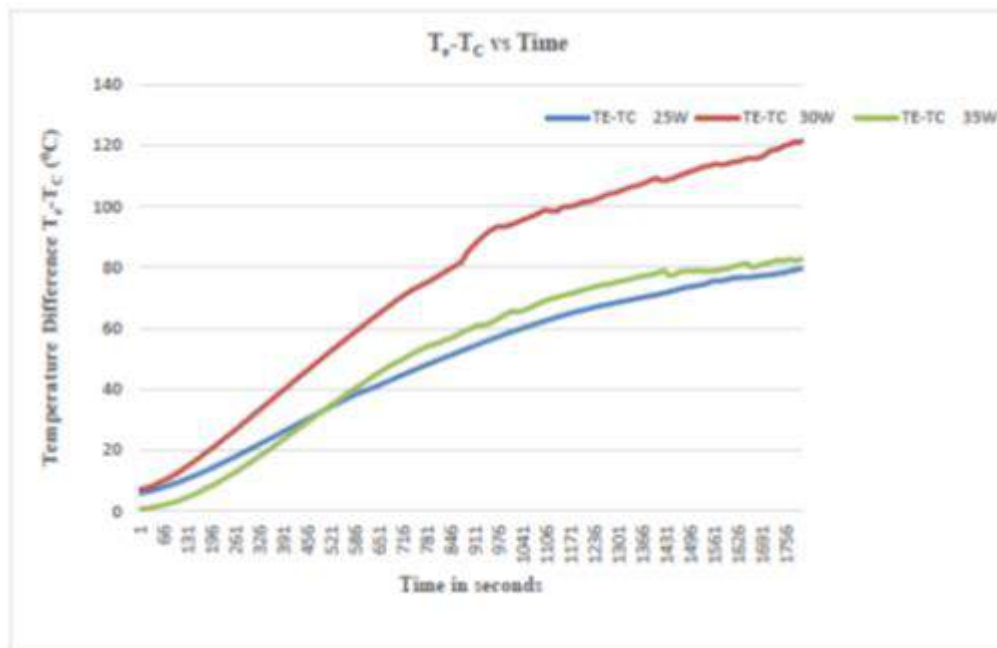


Figure 6. Temperature Difference (Te -TC) Plot for Acetone

Finally the effectiveness of the heat pipe is indirectly brought in terms of thermal resistance and convective heat transferco-efficient.

The thermal resistance is computed as,

$$R_{th} = \frac{T_e - T_c}{Q} \text{ } \text{-----}^{\circ}\text{C/W} \text{ } \text{-----} \text{ (1)}$$

Convective heat transfer co-efficient is given by

$$h = \frac{Q}{A_s (T_e - T_c)} \text{ } \text{-----} \text{ W/m}^2\text{C} \text{ } \text{-----} \text{ (2)}$$

Where T_e = Evaporator temperature in $^{\circ}\text{C}$

T_c = condenser temperature in $^{\circ}\text{C}$

A_s = surface area of the condenser section of heat pipe in m^2

h = Heat transfer coefficient $\text{W/m}^2\text{C}$

R_{th} = Thermal resistance $^{\circ}\text{C/W}$

Fig.7 &8 shows the variation of thermal resistance and heat Transfer coefficient with heat load at steady state for Water and SWCNT at a fill ratio of 50%. It is observed that the thermal resistance decreases with increase in heat load & heat Transfer coefficient increases with increase in heat load for both Water and SWCNT. However, it is clear that the magnitude of thermal resistance is lower for SWCNT compared to Water. As the temperature difference between evaporator and condenser is less for SWCNT, the thermal resistance is also

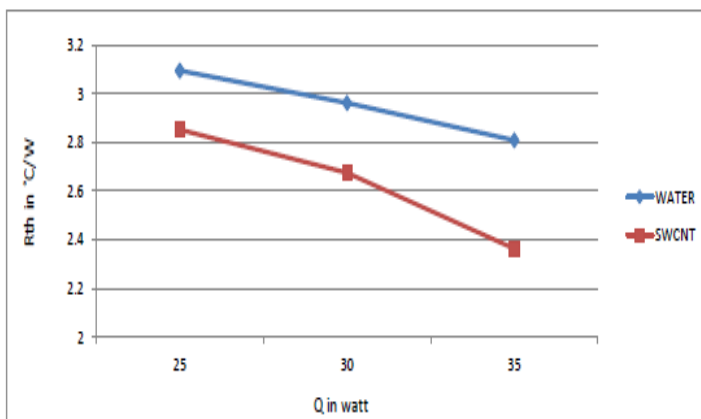


Figure 7. Thermal Resistance vs heat input

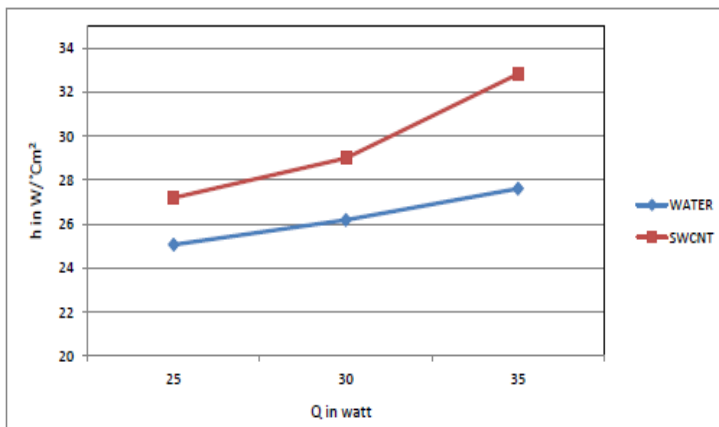


Figure 8. Heat transfer coefficient vs heat input

Fig.9 & 10 shows the variation of thermal resistance and heat Transfer coefficient with heat load at steady state for Acetone and Graphene at a fill ratio of 50%. It is observed that the thermal resistance decreases with increase in heat load & heat Transfer coefficient increases with increase in heat load for both Acetone and Graphene. However, it is clear that the magnitude of thermal resistance is lower for Graphene compared to Acetone. As the temperature difference between evaporator and condenser is less for Graphene, the thermal resistance is also less.

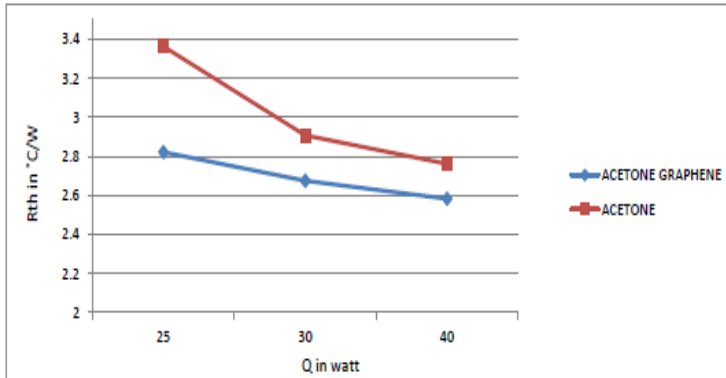


Figure 9. Thermal Resistance vs Heat input

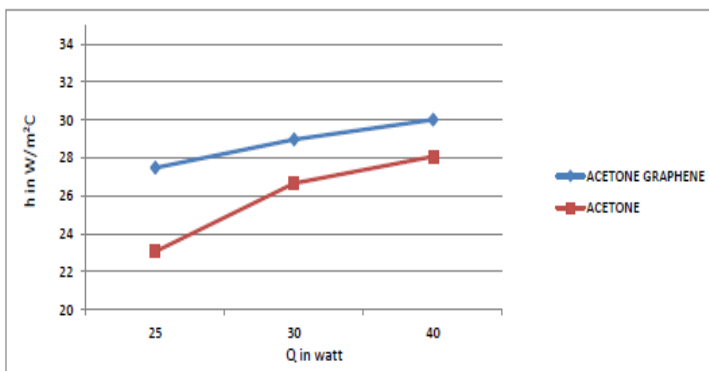


Figure10. Heat transfer coefficient vs Heat input

Figure 11. Shows the variation of thermal resistance with heat input for different working fluids at 50% fill ratio. The figure indicates that the thermal resistance decreases with increase in heat input in case of both the working fluids considered. Further it is seen that SWCNT exhibits lower values of thermal resistance compared to Water and Graphene. This is due to lower value of temperature difference between evaporator and condenser in case of SWCNT. The lower values of thermal resistance of SWCNT indicate that SWCNT has better heat Transport capability compared to Water and Graphene

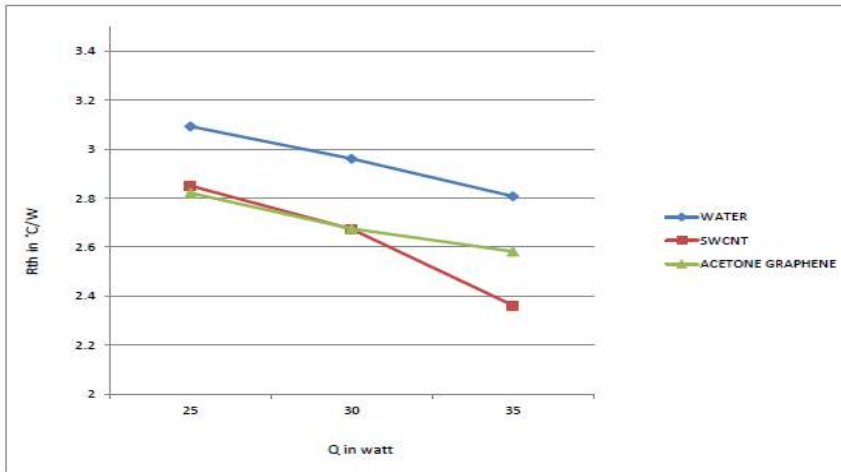


Figure 11. Thermal resistance plot for different fluids

The variation of Heat transfer coefficient with respect to heat input for different working fluids at a fill ratio of 50% is shown in Fig.12. It is seen that the Heat transfer coefficient increases with increase in heat input for the working fluids considered. SWCNT shows higher heat transfer coefficient values compared to water & Graphene. This is due to the lower values of temperature difference between evaporator and condenser for SWCNT.

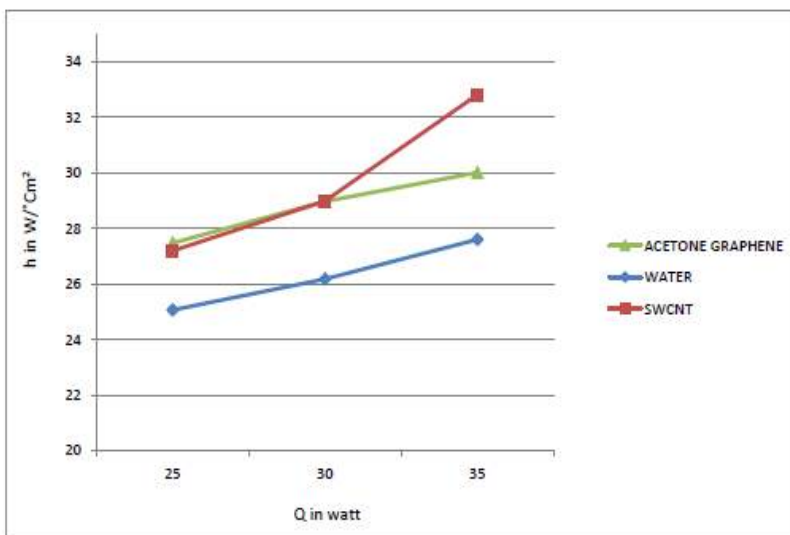


Figure 12. Heat transfer coefficient plot for different fluids

IV. CONCLUSION

In the present work, the experimental investigations are carried out on a multi turn loop OHP. The effects of heat input, working fluid and fill ratio on the performance of OHP are studied.

Following conclusions are drawn from the present experimentation:

1. The variation of temperature difference between evaporator and condenser wall with time is found to be periodic.

2. The temperature difference between evaporator and condenser at steady state is found to be less for SWCNT compared to water & Graphene.
3. SWCNT and Graphene are observed to be more suitable working fluid for OHP operation under different operating conditions.
4. The results indicate that SWCNT can transfer more heat with less temperature difference and less thermal resistance. Thus SWCNT can be considered as more suitable working fluid for OHP operation.

V. REFERENCES

- [1]. Akachi, Structure of a heat pipe, US Patent # 4991041, 1990.
- [2]. H. Akachi, Structure of micro-heat pipe, US Patent # 5219020, 1993.
- [3]. H. Akachi, F. Pola' s_ek, P.S_tulc, Pulsating heat pipes, in: Proceedings of the Fifth International Heat Pipe Symposium, Melbourne, Australia, (1996) 208–217.
- [4]. S. Khandekar, P. Charoensawan, M. Groll, P. Terdtoon, Closed loop pulsating heat pipes -Part B: visualization and semi-empirical modelling, *Appl. Therm. Eng.* 23 (2003) 2021–2033.
- [5]. C.Y. Tsai, H.T. Chien, P.P. Ding, B. Chan, T.Y. Luh, P.H. Chen, Effect of structural character of gold nanoparticles in nanofluid on heat pipe thermal performance, *Mater. Lett.* 58 (2004) 1461–1465.
- [6]. H.B. Ma, C. Wilson, Q. Yu, K. Park, S.U.S. Choi, Murli Tirumala, An experimental investigation of heat transport capability in a nanofluid oscillating heat pipe, *J.Heat Transfer* 128 (2006) 1213–1216.
- [7]. Y.-H. Lin, S.W. Kang, H.L. Chen, Effect of silver nano-fluid on pulsating heat pipe thermal performance, *Appl. Therm. Eng.* 28 (2008) 1312–1317.
- [8]. N. Bhuwakietkumjohn, S. Rittidech, Internal flow patterns on heat transfer characteristics of a closed-loop oscillating heat-pipe with check valves using ethanol and a silver nano-ethanol mixture, *Exp. Therm. Fluid Sci.* 34 (8) (2010) 1000–1007.
- [9]. Q-M. Li, Jiang Zou, Zhen Yang, Yuan-Yuan Duan, Bu-Xuan Wang, Visualization of two-phase flows in nanofluid oscillating heat pipes, *J. Heat Transfer* 133(2011). 052901-1.
- [10]. Y. Ji, H.B. Ma, Fengmin Su, Guoyou Wang, Particle size effect on heat transfer performance in an oscillating heat pipe, *Exp. Therm. Fluid Sci.* 35 (2011) 724–727.
- [11]. J. Qu, Huiying Wu, Thermal performance comparison of oscillating heat pipes with SiO₂/water and Al₂O₃/water nanofluids, *Int. J. Therm. Sci.* 50 (2011) 1954–1962.
- [12]. S. Khandekar, Yogesh M. Joshi, Balkrishna Mehta, Thermal performance of closed two-phase thermosyphon using nanofluids, *Int. J. Therm. Sci.* 47 (2008)659–667.
- [13]. Lixin. Cheng, Lei. Liu, Boiling and two phase flow phenomena of refrigerant based nanofluids: fundamentals, applications and challenges, *Int. J.Refrigeration* 36 (2013) 421–446.
- [14]. Lixin Cheng, Nanofluid heat transfer technologies, *Recent Pat. Eng.* 3 (1) (2009)1–7.
- [15]. Lixin Cheng, Enio P. Bandarra Filho, John R. Thome, Nanofluid two-phase flow and thermal physics: a new research frontier of nanotechnology and its challenges, *J. Nanosci. Nanotech.* 8 (2008) 3315–3332.



Effect of Cooling Rate on Mechanical Properties of ASTM Grade Steel

Devaraj M R¹, Mohan kumara K C¹, Niranjana Kumar V S¹, Joel Hemanth²

¹Associate Professor, Department of Mechanical Engineering, ATME college of Engineering, Mysuru -570028, Karnataka, India

²Former Principal, HMS Institute of Technology, Tumkur, Karnataka, India

ABSTRACT

The objective of the present research is to produce cryogenically treated low carbon low alloy steel which has extreme properties for that composition like high tensile strength, high hardness and wear resistance. The cryogenic treatment is given to steel during solidification, which introduces severe chilling effect in steel. The under cooling of the melt during solidification increases the number of nuclei and thereby enhance the properties of steel. Chills of different thermal conductivity are used to get chilled steel for comparison purpose. It was found from literature review that, so far no work has been done on cryogenically treated steel during solidification. Hence, the present investigation is undertaken to fill the void.

Keywords : Chilled steel, cooling rate, Microstructure, Pearlite.

I. INTRODUCTION

Steel with very low carbon content is generally not responsive for heat treatment and has nearly the same properties as iron. It can be easily formed as they are quite softer. As the carbon content increases becomes stronger and harder by gradually losing its ductility. The properties of iron and steels are linked to the chemical composition, processing path and resulting microstructure of the material. The metal alloys solidify over a range of temperature. Solidification behavior depends on parameters such as growth rate, temperature gradient and alloy constituents. Temperature gradient and growth rate influence the solidification morphology and solidification substructure respectively.

Growth rate or solidification rate is the rate of advance of the solid /liquid interface into the liquid. The rate of movement of solidification front determines solute redistribution during solidification, scale of solidification substructure and the growth under cooling. Rapid solidification (faster movement of solid/liquid interface) minimizes the tendency of segregation of elements temperature gradients both in solid and liquid are important.

II. METHODOLOGY

Preparation of wooden pattern for four cavities mold and providing gating systems like location of risers, runners and gates etc. Preparation of end chills metallic, non-metallic and metallic with

Water cooled one each. Preparation of sand mold with CO₂ process by providing end chills. Preheating and setting the mold sets. Pouring the prepared liquid melt by using induction furnace into the molds. Removing the cast blocks from the molds by knocking process. Degating cast blocks by removing risers, runners, gated, fins etc. by fettling process Shot blasting process to remove sand particles adhered on the surface of castings. Preparations of test samples as per ASTM standards from the cast blocks. Conduction of tensile and hardness tests to find mechanical properties. Tabulation and analysis of test results.

III. EXPERIMENTAL PROCEDURE

A. Preparation of Mold:

Wooden pattern was used to prepares and mold with CO₂ process and four cavities were created in a mold. In the four cavities of the mold, copper chill, silicon carbide chill and cold water circulated copper chill was provided one in each cavity and a cavity without a chill. Two risers are provided in the gating system at suitable locations to get sound cast specimens and sufficient care has been taken in the gating system to avoid defects in castings.

The end chills used were fabricated to required size and set in CO₂ molds (AFS standard of size 115* 75*25mm) with arrangements made to circulate chilled water. Molding sand mixed with sodium silicate (silica gel) and water at suitable proportions and mixed by a Muller. Four mold sets were prepared and each mold having four cavities were applied with zircon fluid for smoothness of the cavities and to avoid fusing of sand, then molds were preheated by torch burner and kept ready for pouring liquid melt.

B. Base Material:

The chemical composition of the base alloy (ASTM Grade Steel) used in this investigation and the compositions of chilled ASTM Grade steel cast separately was analyzed using an emission spectrometer. Pure carbon in the form of shell coke was used to bring the carbon content in the steel to required percentage. Table 1 below shows the chemical composition of ASTM Grade steel.

Table 1. Chemical Composition of the ASTM grades steel

Alloy Designation	C	Si	Mn	P	S	Cr	Mo	Ni	Cu
A-(Mold-1)	0.23	0.45	0.82	<0.008	<0.008	0.06	0.05	0.02	0.008
B-(Mold-2)	0.23	0.45	0.82	<0.008	<0.008	0.06	0.05	0.02	0.71
C-(Mold-3)	0.23	0.45	0.82	<0.008	<0.008	0.06	0.05	0.02	1.45
D-(Mold-4)	0.23	0.45	0.82	<0.008	<0.008	0.06	0.05	0.02	1.90

C. Molding Process:

One metallic (copper), one non-metallic (silicon carbide) and one chilled water circulated chills were used in the present research. Chills used are of size 25mm x 25mm in cross section and 150 mm in length. All the chills were made of having thickness of 25 mm. Chills of different material were placed on the match plate pattern at

desired location in order to introduce chilling effect and to achieve directional solidification during solidification process and to get sound castings. Arrangements were made to circulate cold water through one copper chill.

The mold was prepared using CO₂ molding process. The sand used for the process contains a maximum moisture content of 0.25% and free from clay. The process is basically a hardening process for molds and cores. The principle of CO₂ molding process is based on the fact that if CO₂ gas is passed through a sand mix containing sodium silicate, the sand becomes strongly bonded as the sodium silicate becomes a stiff gel and this gel is responsible for giving the necessary strength to the mold. Zircon sand coating (Trade name – Ceramal) was applied to mold to get good surface finish and also avoids fusing of sand as said above. The mold was then dried using gas torch as shown in figure3 then mold halves were closed carefully as shown in figure4. The gating system for casting (AFS standard) as well as the prepared mould is as shown in Figure 1, 2(a) and 2(b).

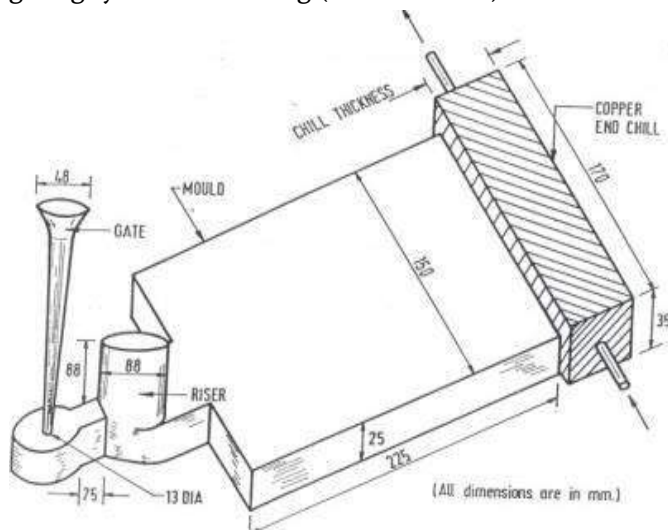


Figure 1: AFS Standard mould cavity along with an end chill



Figure 2: (a) Mold cavities with different end chills



Figure 2: (b) Mold cavities with Coated



Figure 3: Preheating the Molds



Figure 4: Mold box ready for pouring

D. Casting-Melting and Pouring of liquid metal:

The base metal composition of carbon, silicon, was melted using medium frequency induction furnace. The furnace was charged with steel scrap and melted in a 150 kg capacity induction furnace. Chemical composition was adjusted and maintained the steel having the composition of ASTM grade steel shown in table no1 at the time of pouring.

Ferro-Chrome around 950 gm was poured into the melt which may weighing approximately 80 kgs and stirred well. The melt was super-heated to 1650 °C and taken into a preheated ladle containing calcium silicide (which acts as deoxidizing agent) for pouring. Hot topping compound which is a mixture of silica, aluminum oxide, iron oxide and carbon will also be poured into the molten metal to retain the heat in the melt.

Finally, the treated molten metal from the preheated ladle was directly poured by maintaining a temperature of 1620°C into the first mold without adding copper and chilled water (5°C) circulation made through one of the chills (copper) while pouring the liquid metal into the mold. The melting furnace used in the present research is as shown in Figure 5.

Copper is added to the liquid melt [in the ladle] and poured to the second mold set similarly, for third and fourth mold sets. In all the four sets of mold chilled water circulation was made through the copper chill. Once the liquid metal cooled and solidified was taken out from the molds by knocking, then fettling and degating done. All cast specimens were cleaned by shot blasting process and these cleaned cast blocks were cut into desired size and subsequently prepared test specimens as per ASTM standards.



Figure 5: Steel melting Induction furnace

IV. TESTING OF SPECIMEN

A. Microstructural Examination

The polished specimens were then etched using 3% Nital solution to evolve grain boundaries. Micro-structural studies were conducted on all polished specimens using Nikon optical microscope LV150 with clemex image analyzer. The specimens for microstructural studies were polished according to metallurgical standards and fine polishing was done using alumina powder and diamond paste.

B. Tensile Test

Tensile tests were conducted at room temperature on computerized Instron Universal testing machine of 60t capacity in a load range of 0 – 600KN. The specimens for the test were taken at three different locations along the length of the casting from chill end. The tensile test specimens were prepared as per ASTM standards.

C. Harness Test

The Vicker's hardness number (HV) of the test samples were measured using HWMMT-X7-microhardness tester. The values reported are the average of three repetitions on the same sample.

V. RESULTS AND DISCUSSIONS

A. Microstructural Analysis

Specimens were prepared for metallographic studies. Test samples are polished by emery paper in sequence with different grades followed by polishing using nylon cloth and alumina powder of submicron size and diamond paste. After polishing samples were etched with 2% Nital solution and rinsed in distilled water to evolve grain boundaries while the microstructural features were examined under an optical microscope Nikon Microscope LV150 with Clemex Image Analyzer at X100 and X500 magnification and the micrograph presented. Equipment used is Nikon Microscope LV150 with Clemex Image Analyzer.

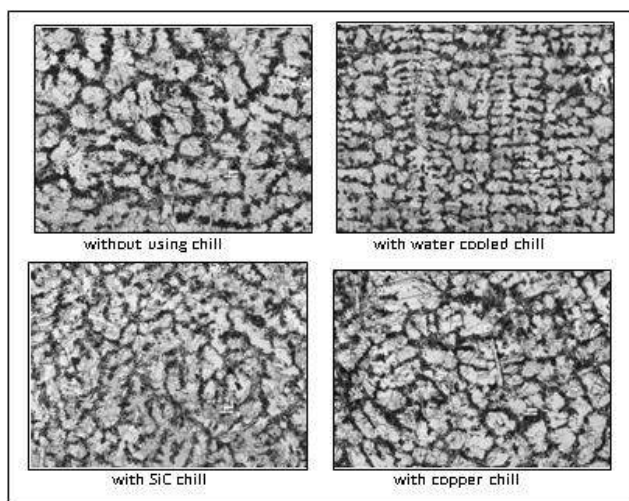


Figure 6: Effect of chilling on microstructure (Mould-1)

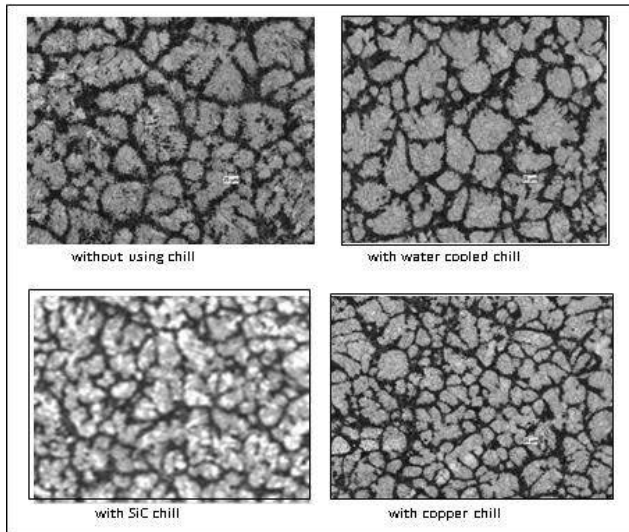


Figure 7: Effect of chilling on microstructure (Mould-2)

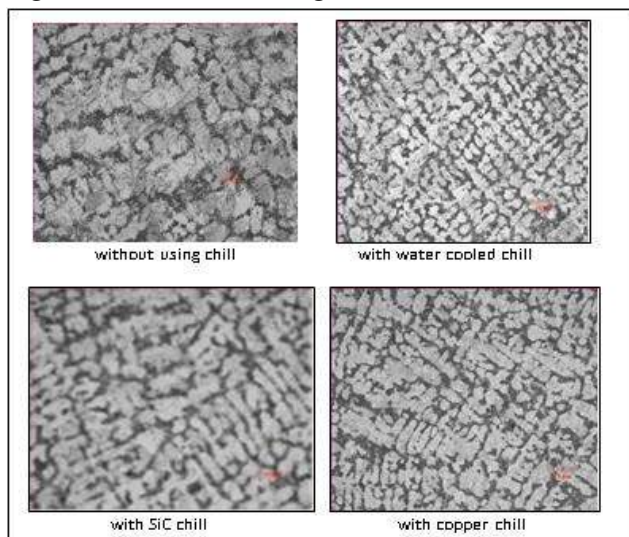


Figure 8: Effect of chilling on microstructure (Mould-3)

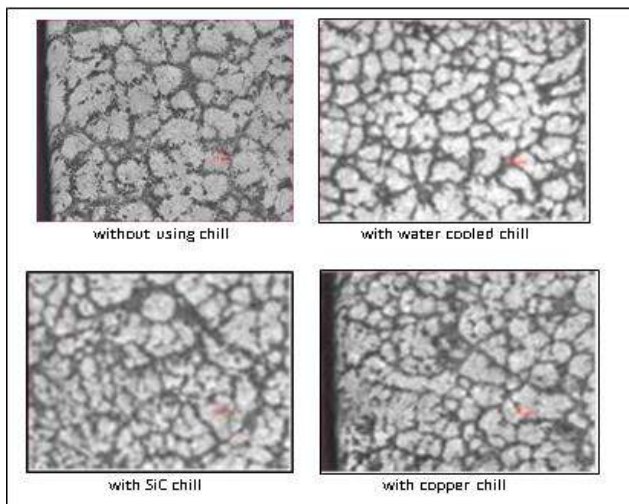


Fig.9 Effect of chilling on microstructure (Mould-4)

B. Hardness Test

The experimental results on hardness test for all test specimens conducted and tabulated in table 2. It has been observed that an increase in hardness in the test specimens used water cooled copper chills because of effective directional solidification and more chilling effect cause formation of carbide precipitation.

Noticeable improvement in hardness is also observed in test specimens produced using copper chills. The test specimens casted were shown no considerable improvement in its hardness because of the influence of progressive solidification caused by the absence of chills.

Table 2: Results of hardness test of various test samples

Alloy Designations	Without chill	Silicon carbide chill	Copper chill	Water cooled copper chill	Copper composition
A-(Mould-1)	201	208	224	250	0.008
B-(Mould-2)	217	250	268	271	0.71
C-(Mould-3)	225	262	264	265	1.45
D-(Mould-4)	213	251	262	272	1.90

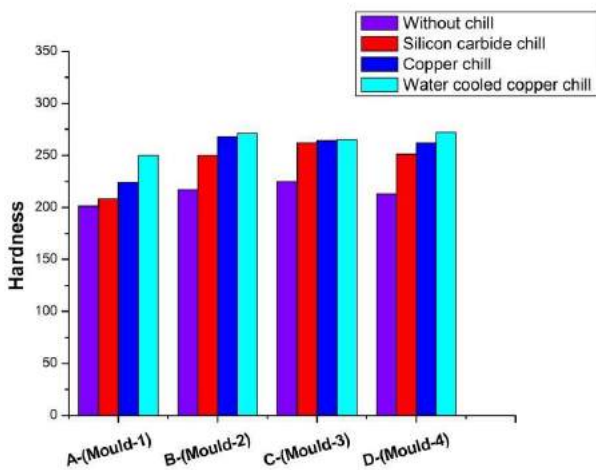


Figure 10: Hardness of un-chilled and chilled specimens

C. Strength Test

Tensile tests were conducted at room temperature on computerized Instron Universal testing machine of 60t capacity in a load range of 0 – 600KN. Three test specimens were taken from the chill end and prepared as per ASTM standards. The tensile test results revealed that the ultimate tensile strength increases with increase in copper content in the alloy composition and also it is observed that the test specimens cast with water cooled copper chills exhibit higher strength due to higher chilling effect during solidification. Further, cast specimens with copper chills shows relatively higher strength with respect to test samples produced with silicon carbide chills tabulated in table 3.

The tensile strength of the cast specimens produced without using chills shows lesser strength compared to other test samples. This is because of poor thermal conductivity and influence of progressive solidification from all sides of the cast specimens.

Table 3: Results of UTS test of various test samples

Alloy Designation	Without chill	Silicon carbide chill	Copper chill	Water cooled Copper chill	Copper composition
A-(Mold-1)	504.96	515.7	518.03	526.75	0.008
B-(Mold-2)	494.08	536.9	542.15	552.92	0.71
C-(Mold-3)	614.22	623.3	626.02	626.3	1.45
D-(Mold-4)	586.06	600.1	604.57	604.17	1.90

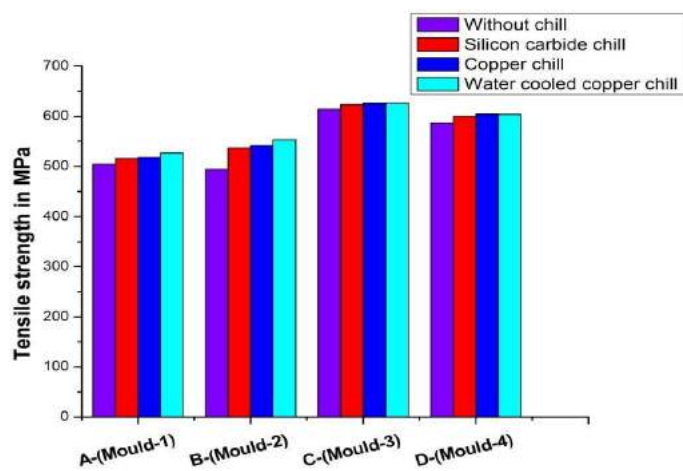


Figure 11: Tensile strengths of un-chilled and chilled specimens

VI. CONCLUSION

The rate of cooling of a solidifying metal controls the structure of the metal which in turn properties of the material. Improved mechanical properties observed in cast specimens produced using water cooled copper chill which causes more chilling effect during solidification.

The higher hardness and higher tensile strength observed in cast specimens used water cooled copper chills. Lower mechanical properties observed in cast specimens produced without using chills because of these cast specimens Figure.11 Tensile strength of un-chilled and chilled specimens influenced by progressive solidification from all the directions. Chilling effect during solidification influences on improvement in mechanical properties.

VII. REFERENCES

- [1]. J.K. Odusote, T.K. Ajiboye, A.B. Rabi, "Evaluation of Mechanical Properties of Medium Carbon Steel Quenched in Water and Oil", Journal of Minerals and Materials Characterization and Engineering, 2012.

- [2]. M. Pellizzari and A. Molinari, "Deep Cryogenic Treatment of Cold Work Tool Steel", University of Toronto, Italy.
- [3]. Joel Hemanth, "Microstructure, Mechanical Properties and wear behavior of metallic, non-metallic and deep cryogenically chilled ASTM A216 WCB Steel" journal of alloys and compounds 506 (2010) 645-652
- [4]. Rahul H. Naravade, U.N.Gujar, R.R.Kharde,"Optimization of Cryogenic Treatment on Wear Behaviour of D6 Tool Steel using DOE/RSM", International Journal of Engineering and Advanced Technology, Volume 2,2012.
- [5]. D. Das, A.K.Dutta, V.Toppo and K.K. Ray, "Effect of Deep Cryogenic Treatment on the Carbide Precipitation and Tribological Behavior of D2 Steel", Materials and Manufacturing Processes,22, 474-480,2007.
- [6]. Dr.Joel Hemanth and B.Vasudeva "Effect of Nickel addition on the mechanical properties of chilled ASTM A216 Grade WCB Steel". IJAEA, Volume 1, issue 4, pp 17-21 (2008)
- [7]. Joel Hemanth and K.L.Rathanakar, "Effect of high rate heat transfer during solidification of alloyed cast iron using water-cooled and sub-zero chills on mechanical behavior. Elsevier Materials and Design 24 (2003) 37-45.



Stiffness Variation Study of Fingers in Finger Seal

Rajesh P¹, J Sharana Basavaraja¹, V Arun Kumar¹

¹Department of Mechanical Engineering, B M S College of Engineering, Bangalore, Karnataka, India

ABSTRACT

Seals play a very important role in Gas turbines and there are more than fifty points where sealing is required. A good Sealing between the High pressure and low-pressure region improves the performance and efficiency of the gas turbine. Commonly used Seals in gas turbines are Labyrinth, Brush, and finger seal where each has its advantages and limitation. Sealing can be achieved by giving a tight clearance fit which could not be achieved in the labyrinth seal but since it is a solid seal and there is a contact with the rotor, life reduces due to wear. Brush seal also has the same problem with the stiffening of the bristles. Finger seal with hydrodynamic lift capability is used to reduce the wear and also gives efficient sealing. In this paper, an effort is made to carry out a stiffness analysis of the finger by varying the finger parameter and designing a finger for a newly conceptualized finger seal for a gas turbine application. An analysis is carried out for various parameter which affects the finger stiffness such as arc radius, length of the finger, repeat angle, and stick arc center. Geometric modeling's done using commercial software and analysis is carried out.

Keywords: Finger seal, Finger, Stiffness, Hydrodynamic lifting capability, Length, Stick arc Radius, Repeat angle

I. INTRODUCTION

Labyrinth seal which is vastly used in gas turbines has to have a certain clearance between the rotor and seal surface as it is a solid seal. Maintaining tight clearance fit in the labyrinth is not possible as rotor expansion due to operating temperature and radial displacement causes contact between the rotor and seal surface. Brush which can give a tight clearance fit and good sealing capability has the problem of stiffening of bristles due to stress and high operating temperature. With all these inputs an effort is being put in this paper to analyze the finger seal and hydrodynamic lift capability of the finger by studying the stiffness of the finger. The stiffness of the finger usually depends on its length, width, and thickness of a finger. The seal developed in this case has a fixed thickness for a particular application.

II. METHODOLOGY

Geometric Modeling of Finger

The basic model of finger seal consists of a finger and a pad where the pad is pressed against the rotor with a very tight clearance fit. Once the rotor starts rotating a pressure wedge is created below the pad which causes

hydrodynamic lift of fingers thus reducing wear of the seal and thus increasing the life of the seal. Dimension of the Finger seal and the basic parameters of the seal are summarized in the Table 1 below.

Finger Geometry	Symbols	Value(mm)
Seal Outside diameter	D_o	110
Seal inside diameter	D_i	80
Finger base diameter	D_b	92

Table 1. Geometric Details of the Finger seal

The main objective of this experiment is to analyze the stiffness variation by varying the parameters of the fingers such as Arc Radius R_s , Length of the finger L_s , Stick arc center D_{cc} and Repeat angle α . Model of this fingers were created using Catia and Analysis was done by importing the model of the finger into Ansys. Finger Models created for different Parameters are shown in the Figures 1,2,3 and 4 below.

Dcc stick arc circle center. When the diameter of the circle center (D_{cc}) of the finger stick arcs was increased, while all others dimensions remained same, the sticks became thicker and pointed more directly towards the center of the seal. Figure2. Shows the change in shape of the finger and visual comparison shows the increase in length, stick angle and stick height. Effect of this change in stiffness is discussed and summarized in results and discussion section.

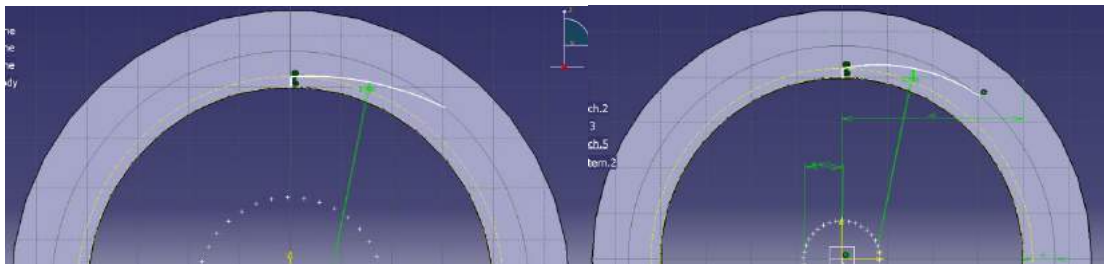


Figure 2.: CATIA model showing change of stick arc circle center(18 and 8 mm)

R_s stick arc Radius. The increase of the stick arc radius causes the stick to curve more concentric to the inside diameter of the seal and consequently made the stick much longer than the original. Figure.3 shows the 20mm and 60mm arc radius finger seals, and it shows that there is an increase in the length of the finger and height narrows down, which lowers the stiffness of the finger stick.

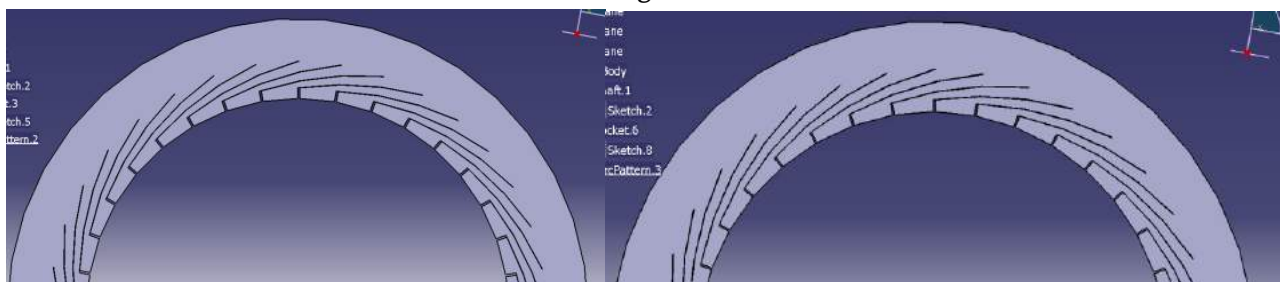


Figure 3: CATIA model showing change of stick arc Radius(20 and 80mm)

L_s Length of the finger: Increasing the length of the finger was done with four different values of 10,20,30 and 40mm approximately. The initial length of 10 mm showed a very high stiffness and the deflection was very minimum but as the length increased the stiffness reduced making the fingers more flexible. The pictures of the seals with finger length 10 and 40 is shown in Figure 4.

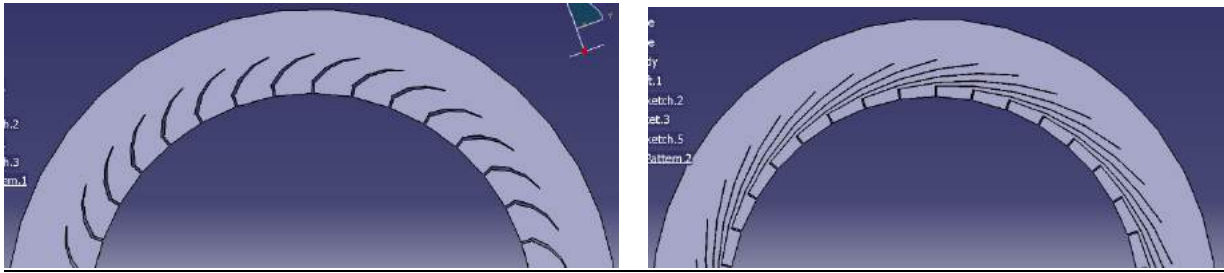


Figure 4: CATIA model showing change of length(10 and 40mm)

Finite Element Grid Generation

The goal of the discretization was to produce a finite element model that correctly demonstrated the fingers’ response to various loading cases while keeping the computer analysis run time to an acceptable amount. The mesh was automatically generated using 0.01-in as the standard length between nodes in an element. The finger seal was discretized using brick/tetrahedron finite elements. These brick elements are three-dimensional with three translational degrees-of-freedom per node. In sum, the discretized single finger with a pad finite element model consisted of approximately 1628 solid brick elements partitioned between the rim, the finger stick, and the foot/pad. The breakdown of this and other pertinent finite element information is summarized in Table below. Figure 6 shows the discretised model of two fingers with pad for different repeat angle of 5 and 10°

Materials Properties	Young’s Modulus	210 x 10 ⁵ N/mm ²
	Poisson’s Ratio	0.3
Element types	Element	Linear 8-noded brick element
Gridding Information	Material Model	Isotropic
	Element in finger and pad	1628

Table 2: Finite Element Analysis Parameters for a Single Finger

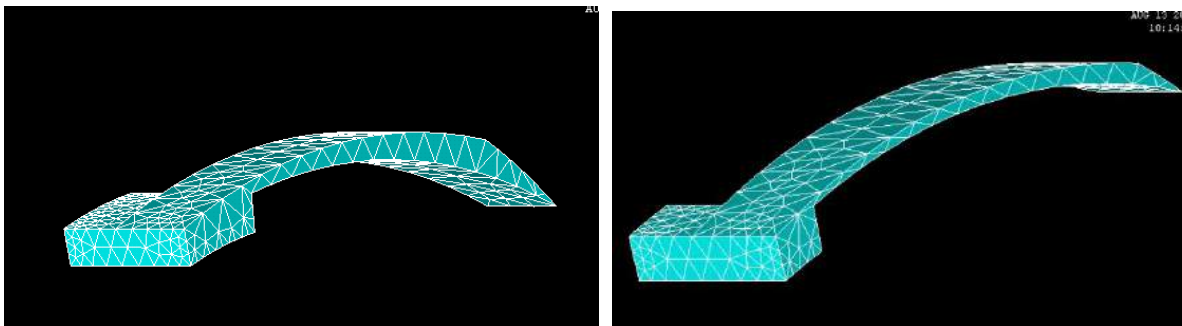


Fig 6: Discretized model of single finger considered for analysis on ANSYS (10°&5° Repeat angle)

Theoretical Stiffness Calculation

Seals are designed to minimize the level of leakage to function effectively but the life of the seal also becomes equally important when there is friction between the rotating shaft and the seal. To maintain the integrity of the seal the compliance of the finger plays a major role in radial motion of the finger. This radial motion is achieved by the hydrodynamic lift capability of the finger which is due to the compliance of the finger. The measure of this marinating the correct amount of compliance of the finger is the stiffness of the finger. The

finger here is approximated as a cantilever beam subjected to an end load, the properties that influences the change in compliance can easily be seen by examining its stiffness equation equation1 [Ref-1].

$$k_{stick} = \frac{3EI_{xx}}{L^3} \text{-----}(1)$$

Where I_{xx} is Moment of Inertia of the Seal, E is young’s Modulus, L is Length of the Finger seal

III. RESULTS AND DISCUSSION

Verification of approximated cantilever Beam model with the Discretised model:

In order to determine the straight cantilever beam would adequate model a comparative study with Discretised ansys model was carried out the maximum deflection for the cantilever beam was given equation 2. Summerised results of the comparison is showed in the Table 3. Results showed that the difference between the maximum deflections was 1% . One can conclude that the fingers behaved very similar to straight cantilever beam.

$$\Delta_{max} = \frac{Pl^3}{3EI_{xx}} \text{-----}2$$

Where P is concentrated load ,L is length of the finger, E is young’s modulus , I_{xx} is moment of Inertia

	Symbol	FEA model	Cantilever Beam
Load total	P	0.9964N	0.9964N
Elastic Modulus	E	$2.1 \times 10^5 \text{ N/mm}^2$	$2.1 \times 10^5 \text{ N/mm}^2$
Total Beam Length	L	N/A	41.88
Cross-section Base	b	4mm	4mm
Cross-section Height	h	2.4mm Approx	2.4mm
Moment of Inertia	I_{xx}	4.608 mm^2	4.608 mm^2
Maximum deflection	Δ_{max}	.783mm	.704mm

Table.3: Validation of the cantilever Beam Model for the finger Deformation Simulations

Dcc stick arc circle Centre: As Dcc increased, L decreased, and h increased; both of which, in the context of Equations 1& 2 cause an increase in the stick stiffness. The same was seen with the analysis done using Ansys for the stick arc circle centre of 8 and 18mm from the Centre. When the diameter of the circle center (Dcc) of the finger stick arcs was increased, while all others dimensions remained same, the sticks became thicker and pointed more directly towards the center of the seal. If the Dcc is kept increasing to the upper limit the finger stick becomes a post and as the Dcc is kept decreasing to the lower limit the finger radius becomes concentric to the inner circle of the seal, the finger stick lengthened, narrowed and ultimately collapsed Of the seal. and as the arc center kept moving away from the seal Centre the deflection reduced for the same load applied which can be seen on the figure 7. The increase in stiffness can be seen in the figure 8.

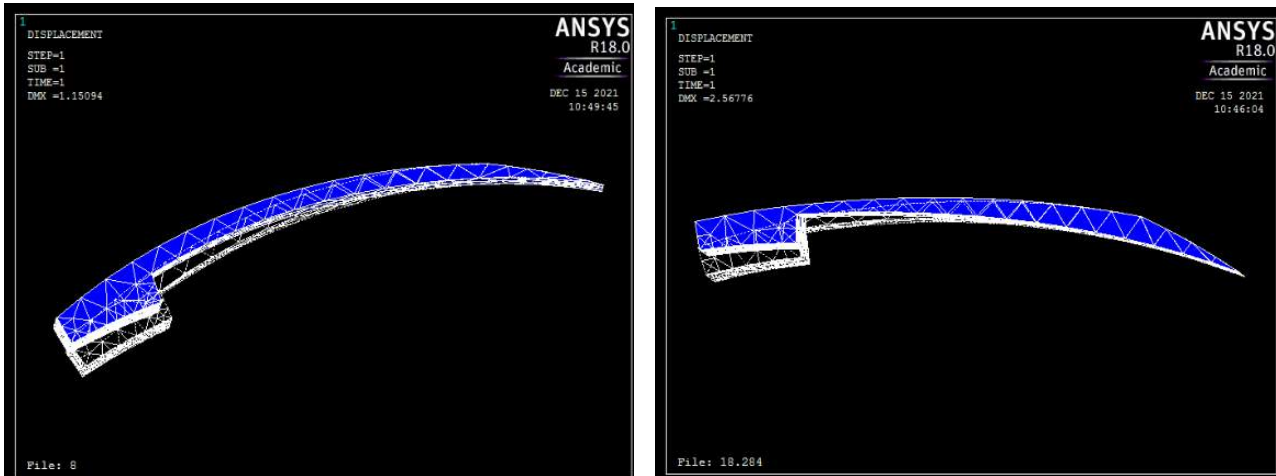


Fig 7: Deflection of finger after application of Load for (8&18mm_stick arc circle centre)

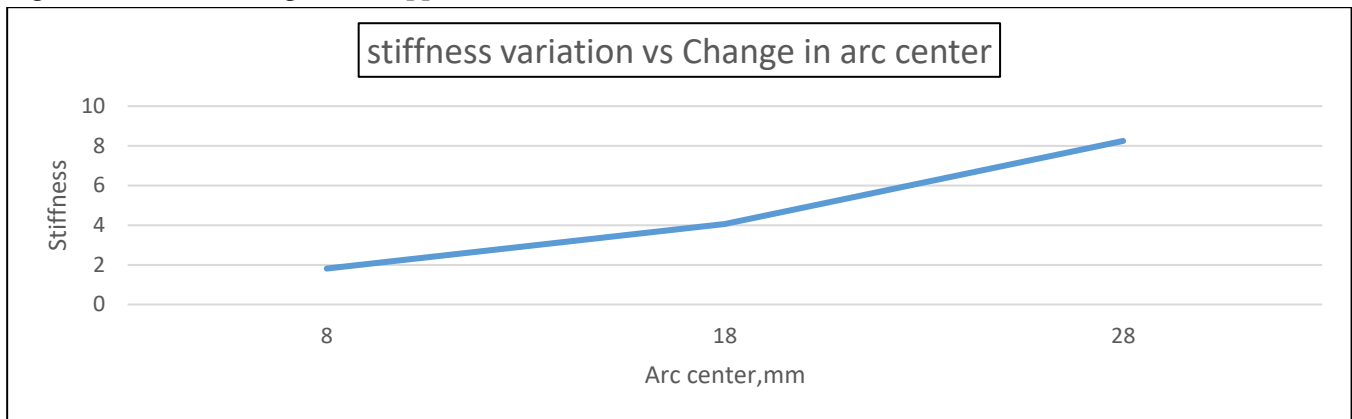


Fig 8: Stiffness VS Change in Stick arc circle centre

Rs stick arc Radius: This showed that the stick constructed from 60mm arc radii was much narrower and attached to the foot at a much shallower angle than 20mm arc radii. With the length significantly increased and the height significantly narrowed, the stiffness of the finger stick was lowered, and the analysis carried out also agreed with the same. The deflection of the fingers with arc radius 40 and 60mm shown in figure 9 and it showed that there was a considerable change in stiffness. Variation of the stiffness with the Stick arc radius can be seen in the figure 9. This shows that with the increase in radius of stick arc stiffness reduces.

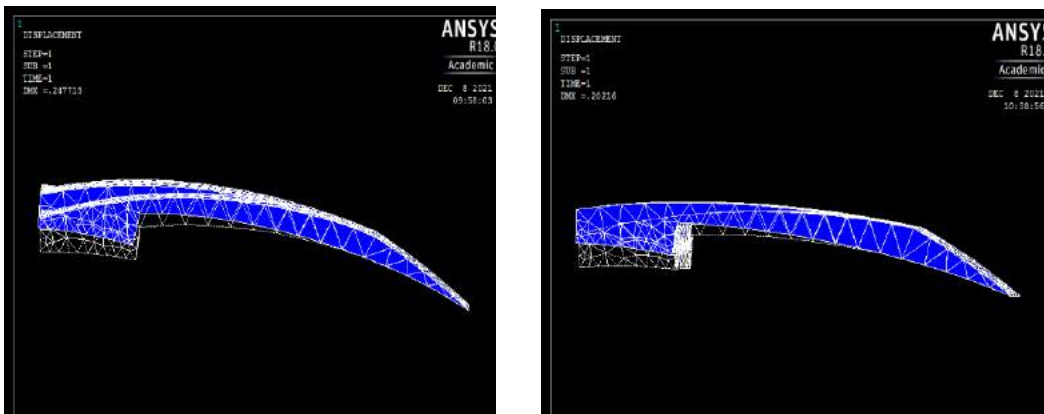


Fig 9: Deflection of finger after application of Load for (40&60 mm_stick arc radius)

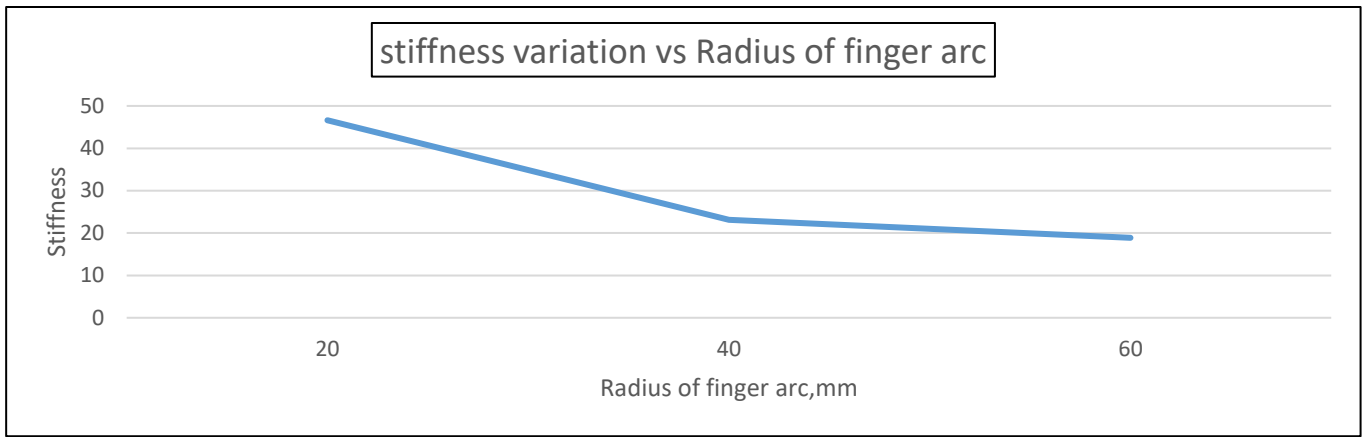


Fig 10: Stiffness VS Change in stick arc Radius

Length of the finger L: Stiffness is inversely proportional to the length of the component as the length increases stiffness reduces. Increasing length of the finger makes the finger less stiff. This is what is required to obtain the hydrodynamic lifting of the finger. The analysis carried out on the finger with different length of the finger showing deflection is seen in figure 11 and the stiffness variation is shown in the figure 12.

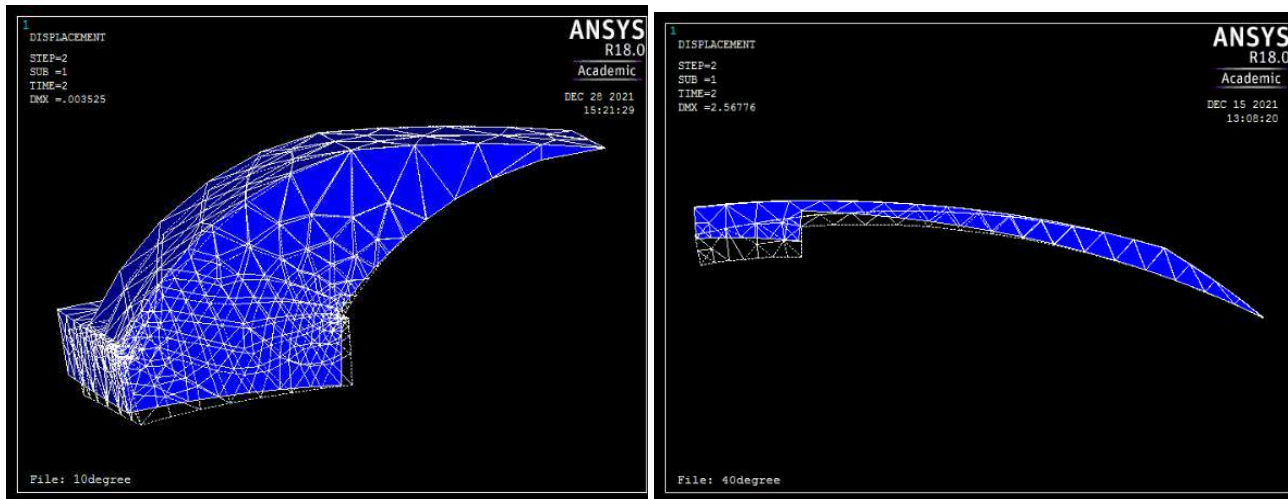


Fig 11: Deflection of finger after application of Load for (length of the finger 10 and 40 mm)

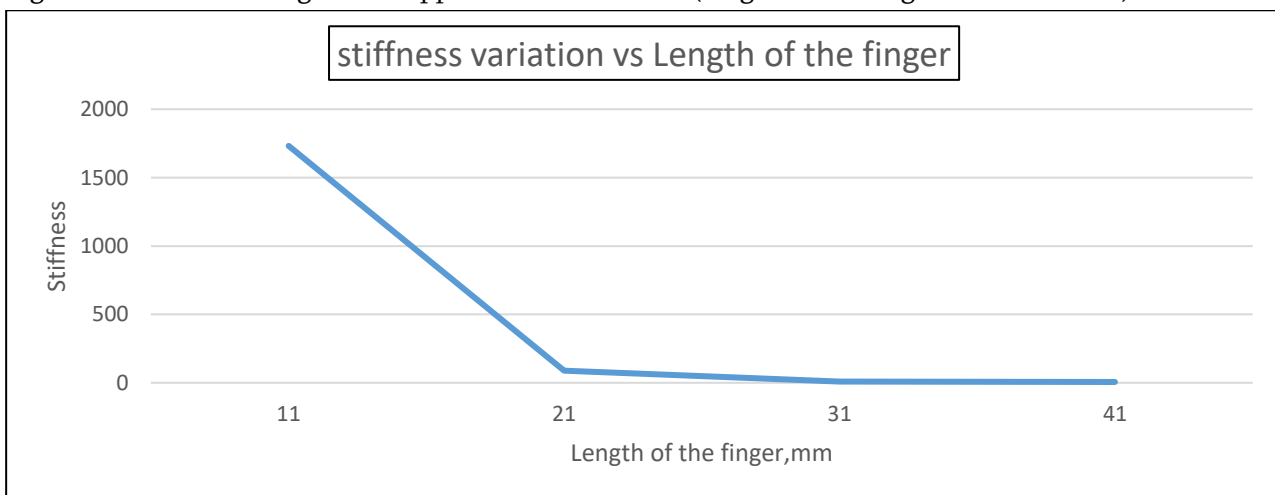


Fig 12: Stiffness VS Change in Length of the finger

IV. CONCLUSION

From the analysis carried out the following conclusions are drawn that overall Variations of Stick arc centre of circle, Finger radius and Length of fingers keeping the base radius and Inner radius constant there was considerable change in stiffness of the finger. The variations of this stiffness with the change in stick arc circle centre shows there is rise as the centre goes away,. Same way increase in the radius of arc varied the height and length of the finger which in turn effects the stiffness. The length variation has a direct effect on the stiffness as we know stiffness is inversely varying with length. Since the flexibility of the finger effects the hydrodynamic lift capability of the finger which plays a major role in reducing the wear and leakage. Considering all these parameter a conclusion over development of finger seal for a gas turbine was achived which had finger seal with the optimised stick arc radius of 60mm, arc center of 8mm and finger with a length of 41 was developed to achive good hydrodynamic lifting of finger and avoid wear.

I. REFERENCES

- [1]. Delgado, Irebert R., and Margaret P. Proctor. "Continued investigation of leakage and power loss test results for competing turbine engine seals." AIAA Paper 2006-4754, 2006.
- [2]. Delgado, Irebert R., and Margaret P. Proctor. "Leakage and power loss test results for competing turbine engine seals." AIAA Paper 2006-4754, 2006.
- [3]. Chen Guoding, Wang Li'na, Yu Qiangpeng and Su Hua. "Dynamic analysis of C/C composite finger seal." Chinese Journal of Aeronautics 2014, 27(3):745-748.
- [4]. Hazel, M. "A study of non-contacting passive-adaptive turbine finger seal performance." Ph.D. Thesis, 2007, the University of Akron, 2007.
- [5]. Proctor, Margaret P, and Irebert R. Delgado. "Preliminary test results of a non-contacting finger seal on a herringbone-grooved rotor." NASA Technical Memorandum NASA/TM-2008-215475, 2008.
- [6]. Hendricks, R. C., Bern O'Halloran, Gul K. Arora, H. E. Addy, J. Flowers, J. Carlile, and B. M. Steinetz. "Advances in Contacting Sealing." NASA CP-32821 (1994): 363-371.
- [7]. Temis, Joury, Alexey Selivanov, and Ivan Dzeva. "Fluid-structural analysis of a non-contacting finger seal." In ASME Turbo Expo 2013: Turbine Technical Conference and Exposition, pp. V03AT15A019-V03AT15A019. American Society of Mechanical Engineers, 2013.
- [8]. Proctor, Margaret P., Arun Kumar, and Irebert R. Delgado. "High-speed, high-temperature finger seal test results." Journal of propulsion and power 20, no. 2 (2004): 312-318.
- [9]. Galimutti, Peter P., Jerzy T. Sawicki, and David P. Fleming. "Analysis of finger seal lift pads." In ASME Turbo Expo 2009: Power for Land, Sea, and Air, pp. 941-950. American Society of Mechanical Engineers, 2009.
- [10]. Yucel, Ugur. "Calculation of leakage and dynamic coefficients of stepped labyrinth gas seals." Applied mathematics and computation 152, no. 2 (2004): 521-533.
- [11]. Proctor, Margaret P., and Bruce M. Steinetz. "Noncontacting finger seal." U.S. Patent 6,811,154, issued November 2, 2004.

- [12]. Arora, Gulshan K. "Noncontacting finger seal with hydrodynamic foot portion." U.S. Patent 5,755,445, issued May 26, 1998.
- [13]. Johnson, Mark C., and Eric G. Medlin. "Laminated finger seal with logarithmic curvature." U.S. Patent 5,108,116, issued April 28, 1992.
- [14]. Ludwig, L.P. and R.C. Bill. "Gas Path Sealing in Turbine Engines," ASLE Transactions, Vol. 23, No. 1, pp. 1-22, 1980.



Plain Points Picking (PPP) Algorithm- A New Method of Slicing In 3D Printing

Ashwin N¹, Anoop N¹, Dr. Raviraj M S², Dr. Muniraju M²

¹Mechanize solutions LLP, Director, Chamarajanagar -571313, Karnataka, India

²Department of Mechanical Engineering, Government Engineering College, Chamarajanagar -571313,
Karnataka, India

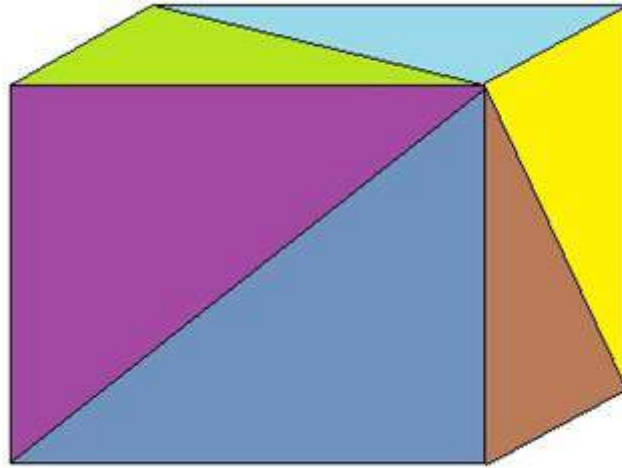
ABSTRACT

A new slicer software is developed which is light weight and yet functional, to obtain slice of any STL file without the need for conventional methods. We have been able to come-up with a solution and implement it without any errors. At the same time, we have been aiming to make the output G – code file readable by almost all the market available 3D printers with little to no modifications. This program uses a revolutionary new concept, which does not depend on conventional ray object intersection method for finding the slice points of the object. This new method is named as “**Plane points picking (PPP) algorithm**”. We have come to realize after successful implementation of the new concept that, this method of slicing will reduce the total space required by the software package required. As we all know STL file structure consists of one normal and 3 vectors in recurring manner. this software supports both ASCII and binary type of STL files. And the software is built in “mm” unit system. The new method gives much higher accuracy coordinate values when compared to conventional method.

Keywords: Plane points picking (PPP) algorithm, ASCII and binary STL file, Slicing, 3D printing, DraftCAD slicer.

I. INTRODUCTION

This new method is named as “**Plane points picking (PPP) algorithm**”, can be explained with an example so that it is easy to understand. let’s first start with the 20 mm cube as shown in the fig below. In this cube the three faces which are visible are divided into 6 triangles which can be easily identified by the different colors used for its surface.



There are six more triangles making up the other three faces which are hidden in this image. Making a total of 12 triangles with 3 points for each triangle. making a total of 36 points, this points makeup the definition of the cube for the renderer to use for rendering.

Now let us consider for the sake of understanding what is going on in the PPP algorithm consider a single triangle from that cube shown above.

Assume that at this particular point in time we are aiming to find the sliced points of that cube at a height of 10 mm from the print bed. Let's consider that triangle having three points equal to

Point 1 – (-10,10,0)

Point 2 – (-10,10,20)

Point 3 – (10,10,20)

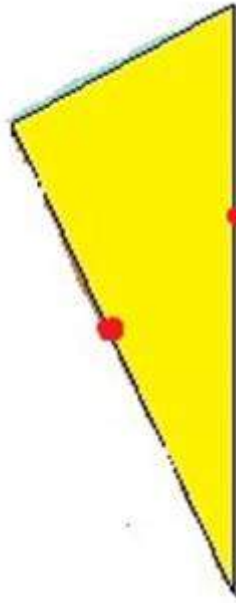
Now to the next part we have to know the height at which the sliced points are to be found out. This we have already decided to 10 mm.



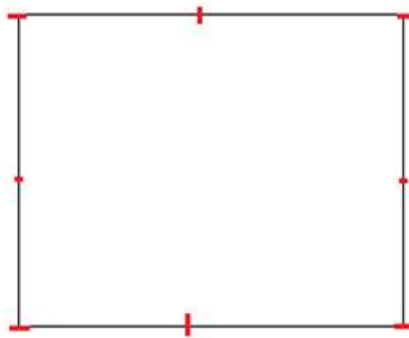
The equation for the plane is $Z = 10$ this is used in the following process. The triangle in consideration is considered as the set of three lines the points on the line at $z = 10$ is found in this condition we get two points which can be seen in the fig.

Then a line is drawn using those two points. Which results in finding all the points on that line.

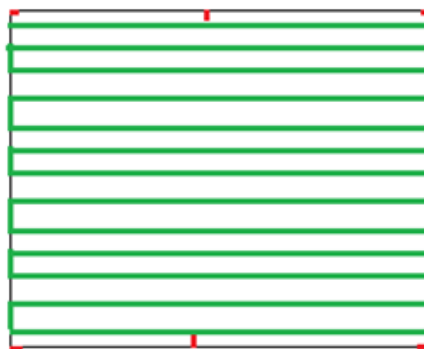
Now imagine the process repeating for all triangle then the resulting lines are used to render lines which will trace the walls of the object at that height accurately.



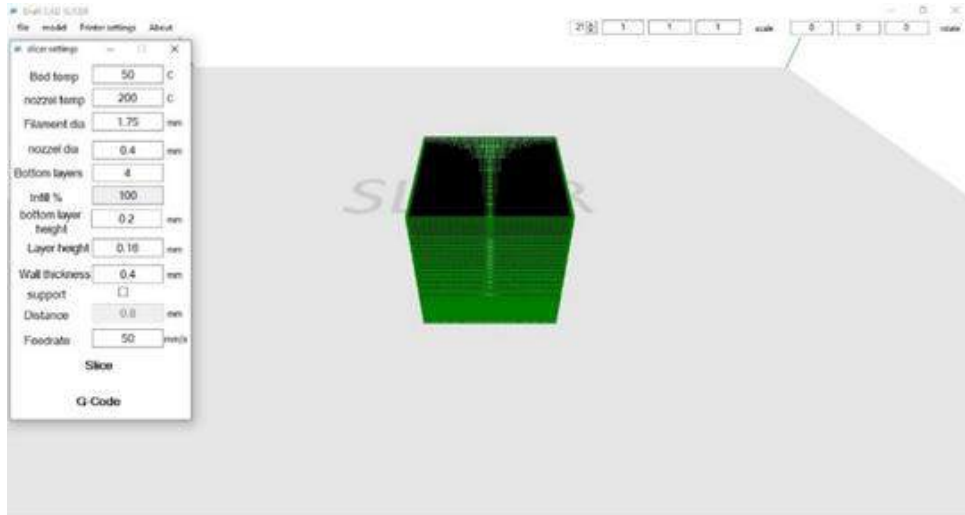
The resulting polygon generated is as shown for the cube in consideration.



The polygon is used so that infill path can be traced inside of the polygon, the infill points are also generated using the polygon intersection with the x plain, it is an implementation of PPP algorithm in x plain. The resulting path obtained is shown in the fig below.



The complete slicing operation using the PPP algorithm which is previewed in Draft CAD slicer can be seen in the image below. This concludes the use of PPP algorithm for producing slice.

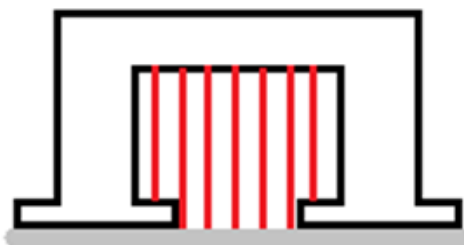


Now let us discuss the support structure generation.

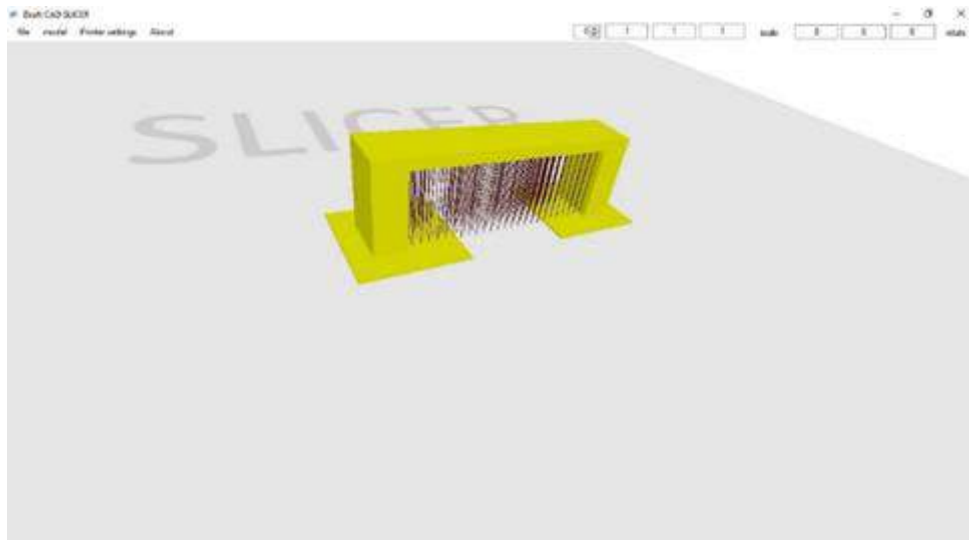
Now let us consider an object which has overhang which is shown in the fig below. The method used to generate support is similar to that of PPP algorithm used for slicing only difference is that in previous case plane z and x were considered,



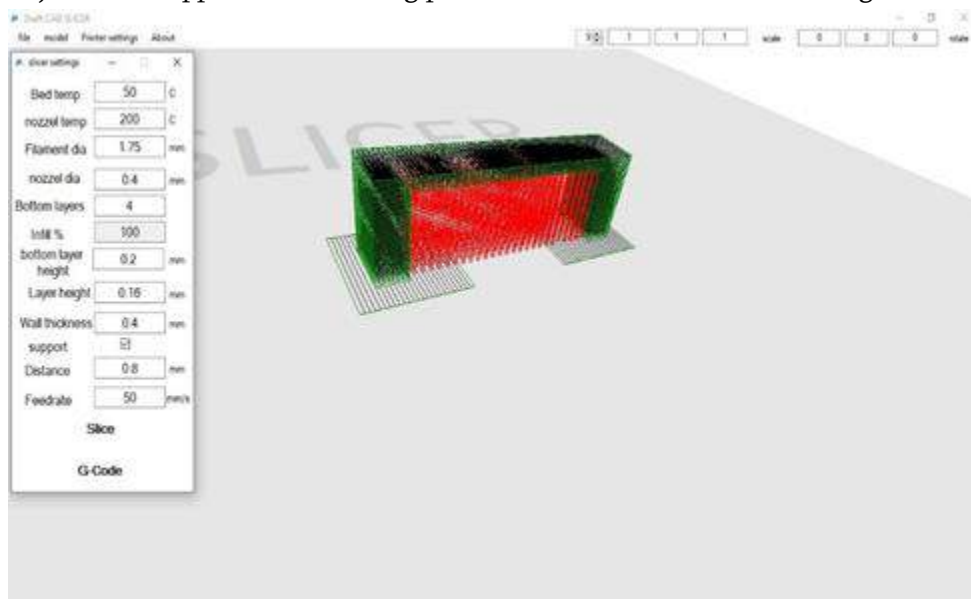
now plane x and y are considered and resulting slice at $x = 0$ is considered which results in a polygon as shown below fig. This polygon is used to produce points inside polygon in Y plane and then those points is used to build the support structure.



By expanding it to entire object the support requirement can be seen in the preview. The preview of this is shown in the fig below.



Now slicing the object with support, the resulting preview can be seen in the below fig.



II. RESULTS AND DISCUSSION

We have been able to build world's most advanced and most accurate slicing software catered specifically for FFF 3D printer technology. The G-code generated is accepted by almost all the 3D printers available in the market.

III. CONCLUSION

Software is accurate to 12 places after decimal point. And it supports both cartesian as well as delta type systems. The current software supports single extruder, and support structure generation with overhang angle greater

than 0 degree. This current software only works with fixed Infill of 100%. This program requires low run time memory. This program is currently able to load one file at a time.

Future aim

1. Support multi-extruder
2. Generate brim
3. Generate skirt
4. Variable infill
5. Multiple file load capabilities

IV.REFERENCES

- [1]. [https://en.wikipedia.org/wiki/Slicer_\(3D_printing\)](https://en.wikipedia.org/wiki/Slicer_(3D_printing))
- [2]. An Optimal Algorithm for 3D Triangle Mesh Slicing, by Rodrigo Minetto, Neri Volpato, Jorge Stolfi, Rodrigo M. M. H. Gregori and Murilo V. G. da Silva.
- [3]. Slicing and support structure generation for 3D printing directly on B-rep models Kanle Shi^{1,2,3}, Conghui Cai^{1,2,3}, Zijian Wu^{1,2,3} and Junhai Yong^{1,2,3*}



Microstructure and Mechanical Behaviour of Chromium Oxide reinforced LM26Based Metal Matrix Composites

T V Nagaraja¹, Dr Ravindra Sagar²

¹Assistant Professor, Mechanical Engineering Department, The Oxford College of Engineering, Bengaluru – 560068, Karnataka, India

²Associate Professor, Mechanical Engineering Department, Sri Siddhartha Institute of Technology, Tumakuru – 572105, Karnataka, India

ABSTRACT

This work was focused on development of LM26 composites reinforced with Chromium Oxide particles by utilizing the technique of stir casting. Percentage of chromium oxide was varied between 0 to 10wt%. A study of the mechanical properties as well as microstructure of the developed composites had been performed. With the assistance of optical microscope, the microstructural studies of LM26 alloy as well as composites have been conducted. Investigations were carried out on the LM26 alloy as well as composites for properties such as tensile strength as well as hardness. Microstructure confirms that the chromium oxide particles' distribution has been uniform. The hardness of composites was found to higher than unreinforced alloy and increases over time as weight percentage increases of Chromium Oxide particles from 0% to 10%. For LM26/10% Chromium Oxide composite showed highest yield and tensile strength compared to other composites and unreinforced LM26 alloy.

Keywords: Aluminium matrix composites, stir casting, Microstructure, Mechanical properties.

I. INTRODUCTION

Many engine components need to work for longer life in challenging conditions without comprising the mechanical properties. Most of the engine components are made up of aluminum alloys which's because of their excellent mechanical properties as well as light weight. However, aluminium alloys are known for their softness, high wear rate and high ductility which are undesirable for many applications. Keeping their disadvantages and increasing demanding working conditions in mind many researchers across the world are developing aluminium alloy based metal matrix composites [1-3]. Light weight reinforcements like TiB₂, TiC, TiO₂, SiC, Si₃N₄, B₄C, Al₂O₃ and carbon based nanomaterials are used to reinforce aluminium alloys to obtain high hardness and strength [4-8]. Most of these reinforcements are light weight, capable of withstanding high temperature, possess high hardness, high compressive and tensile strength values. After addition of these

various reinforcements in to their respective aluminium matrices resulted in significant increase in hardness and strength values. The reinforcements can be of different morphology and size but the main distinguishable criterion is aspect ratio. Based on the aspect ratio reinforcement can be termed as fiber, short fiber, particulate or whisker. Out of all most commonly used reinforcement type is particulates which are quite easily available and it terms of cost they are quite cheap as compared to whiskers and fibers. Using particulates reinforced aluminium alloy composites many material engineers were able to achieve near net shaped product with high productivity [9].

Many techniques have been adopted to develop particulate reinforced aluminium matrix composites. Primary processing techniques include liquid metallurgy, powder metallurgy and thermal spray. But majority of commercial applications are produced using liquid metallurgy techniques like reaction casting, squeeze casting and as simple as stir casting. This is mainly due to inherent advantages of liquid metallurgy like low cost of liquid metal compared to powders, easy in handling, required shape and size can be easily produced. Sanni Dev and Amit Aherwar [10] have studied the mechanical properties of composites materials made from LM26 aluminum alloy with porcelain filled percentages of 2 weight percentage, 4 weight percentage, 6 weight percentage, as well as 8 weight percentage, with the assistance of stir casting. Evaluation as well as comparison of physico-mechanical properties of fabricated composites have been conducted which includes tensile strength, void fraction, micro hardness as well as their density. To the LM26 master alloy the inclusion of 8 weight percentage porcelain results in the enhancement of microhardness by 10 percent. In addition, the inclusion of porcelain of about 6 weight percentage enhanced tensile strength by 20 percent. Comparatively to LM26 master alloy, the fabricated composites exhibited superior physical as well as mechanical properties when examined.

Ravi kuamr etal[11] As a matrix material the mechanical composites with LM6 have been investigated, and technique of stir casting has been used successfully to fabricate cenospheres with different percent's as well as red mud of two percent as reinforcement materials. Compared to the base material, the composites had a higher hardness. The composites' density is reduced as the red mud as well as cenosphere percentage increases. As the percentage of red mud as well as cenosphere percentage increase then the UTS decreases according to the outcomes of the tensile test. Eight percent reinforcement was found to result in least elongation of the composites. Increasing the reinforcement percentage results in a decrease of percent elongation.

Thirumalvalavan et al [12] In their study, manufacturers described the fabrication and evaluation of aluminum matrix composites' impact energy, tensile strength, microstructure as well as hardness etc. and the aluminum matrix composites comprises of the fused silica-SiO₂ particulates as well as aluminum alloy LM25 matrix as reinforcement (dimension 150-250µm) within matrix. In the steps of 4 percent, the reinforcements are included which are in the range of 4 to 12 weight percent. Stir casting was used to make the composites. The composites' mechanical properties are enhanced by the SiO₂ particulates reinforcement's inclusion. A study had been conducted on fabricated metal matrix composites' mechanical properties as well as microstructure. Compared to the unreinforced alloy, there's an improvement in mechanical properties such as impact resistance, hardness as well as tensile strength. Radhika etl [13] have developed LM25/SiC/Al₂O₃ metal matrix composites by adopting liquid metallurgy route. The effects of reinforcement additions on hardness, tensile strength and Wear characteristics Composites have been studied. Highest percentages of reinforcement with 30 wt.% of have exhibited greater tensile strength and hardness than LM25 base alloy.

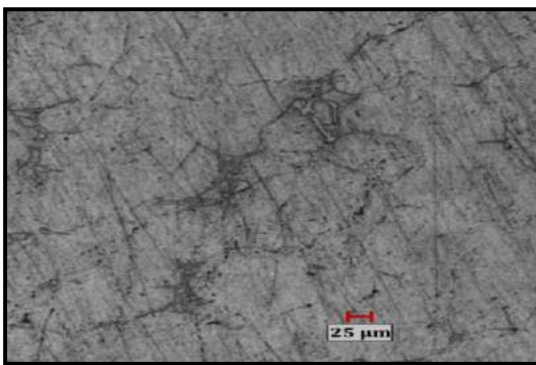


Fig.2 Photograph of Tensile test specimen

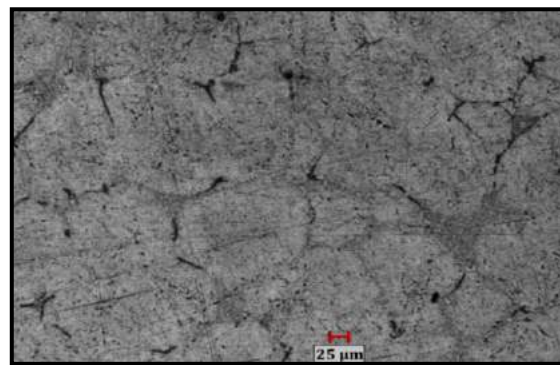
III. RESULTS AND DISCUSSION

3.1 Microstructure

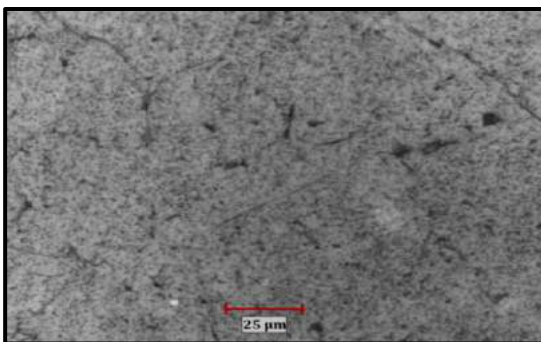
Microstructure analysis of stir cast LM26 alloy and Chromium Oxide reinforced composites were conducted using optical micrographs. Fig. 3 (a) – (d) depicts the optical images of unreinforced LM26 alloy as well as its composites with different weight percentage (2.5% to 10%) of Chromium Oxide particles. Fig. 1 (a) shows unreinforced LM26 alloy is composed of grain boundaries, pores and intermetallic compounds at the grain boundaries.



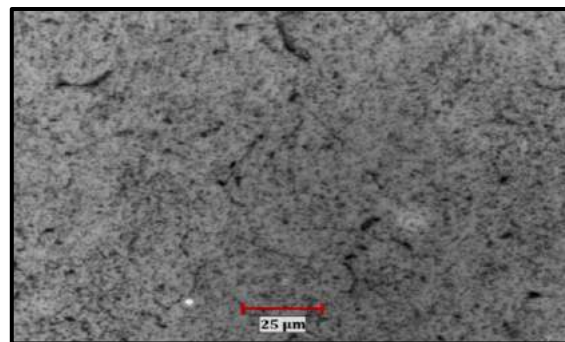
1. LM26 alloy



2. LM26+5wt%Chromium Oxide



(c) LM26+7.5wt%Chromium Oxide



(d) LM26+10wt%Chromium Oxide

Fig.3 (a-d) Optical micrographs of LM26 and its composites

According to the image, the unreinforced alloy grain size lies between 40 and 60 μm but there are few grains which has size more than 80 μm . Fig. 2 (b) to (d) depicts the optical images of LM26 composites with varying weight percentages (2.5%, 5% and 7.5%) of Chromium Oxide particles. The microstructure is composed of small size grains and Chromium Oxide particles located at the grain boundaries. Composites exhibit a gradual decrease in grain size with increasing weight percentage of Chromium Oxide particles and LM26/10% Chromium Oxide composite with highest Chromium Oxide particle weight percentage showed smaller grain sizes. Unlike in many cast alloy and composite the dendrites with columnar structure are found to form in conventional casting technique. In present case using mechanical stirring to create vortex and stirring molten metal, the dendrites are broken and equi-axed globular grains are formed in both LM26 alloy and its composites [14].

3.2 Grain size and Hardness

Effect of addition of different Chromium Oxide weight percentage on to the LM26 matrix grain size is analyzed and presented in Fig. 4. From Fig it is seen that the alloy LM26 has 59 μm of average grain size while that of composites is lesser. For composite with 2.5 and 10% Chromium Oxide particle content the average grain size is 54 μm and 44 μm respectively. The average grain size in composites is quite significantly smaller than unreinforced LM26 alloy. Reduced grain size is caused due to the existence of Chromium Oxide particles which were effective heterogeneous nucleation sites. When the weight percentage of Chromium Oxide particles increases, the number of heterogeneous nucleation sites also increases which in turn increase the number of fine size equi-axed grains. In addition to this the grain growth is hindered by the presence of Chromium Oxide particles thereby contributing to the grain refinement.

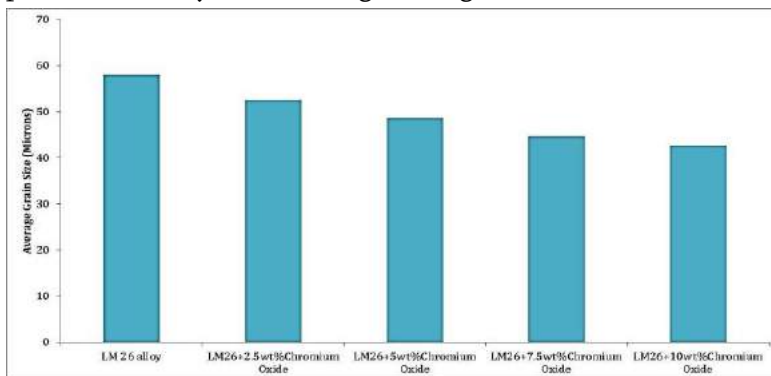


Fig.4 Graphical representation of grain size variation

Vickers hardness of LM26 and its composites with different Chromium Oxide particle weight percentage is displayed in Figure.5. The composites hardness was found to higher than unreinforced alloy and turns to rises as the rise in weight percentage of Chromium Oxide particles from 2.5% to 10%. The hardness of LM26 alloy was 59 VHN while that of composite with 2.5 and 10% Chromium Oxide particle content was 66 and 81 BHN respectively. The increment in hardness of LM26/2.5% Chromium Oxide and LM26/10% Chromium Oxide composites when compared to unreinforced LM26 alloy were 12.32% and 37.44% respectively. Chromium oxide particles cause grain refinement, which is what increases the hardness. The observed result is assisted quite well which was done by Jayakumar et al [15]. It was discovered that grain refinement had been the reason of the increase in hardness of A319/SiC composite caused by the addition of SiC particles.

Even distribution of Chromium Oxide reinforcement in matrix material is the main contributor for improved hardness. In aluminum alloy the Uniform distribution of reinforcements is critical factor in boosting composite materials' hardness, as indicated by optical images. A relatively high value of hardness was observed when evaluating the reinforced alloy in comparison to the unreinforced alloy. The enhancement of hardness is expected always because of the chromium oxide which's hard material when included in ductile as well as soft aluminum alloys. Additionally, the reinforcements of Chromium Oxide as well as aluminum matrix also have significant variation in thermal expansion coefficients. As a result, dislocations form between reinforcement-matrix at the boundary [16-17].

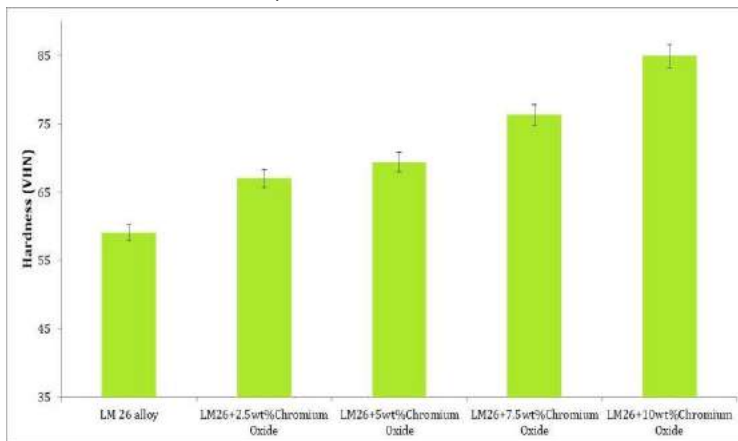


Fig.5 Graphical representation of hardness

3.3 Tensile properties

Yield and tensile strength values for LM26 and its composites with different Chromium Oxide particle weight percentage are shown in Fig. 6 and 7 respectively. It has been found that composites exhibit higher tensile as well as yield strengths compared to unreinforced alloy and generally increases in proportion to an increase in weight percentage of Chromium Oxide particles from 2.5% to 10%.

Unreinforced LM26 alloy had yield and tensile strength values of 154 MPa and 172 MPa respectively while LM26/10% Chromium Oxide composite had values 211 MPa and 254 MPa respectively. One can observe that the strength values for composites having up to 7% Chromium Oxide particle content were significantly higher than that of unreinforced LM26 alloy. However, there was marginal decrease in yield and tensile strength of composite Chromium Oxide particle content was increased from 7.5% to 10% weight percentage. The increase strength values can be because of the grain refinement as a result of the inclusion of Chromium Oxide particles. According to the equation of Hall-Petch which states that, as the size of grain decreased the yield strength tends to increase. In present case when the Chromium Oxide particle content increased, the grain size decreased. Due to the grain refinement caused by Chromium Oxide particles the strength was found to higher for composites having up to 10% Chromium Oxide particle content.

Composites' ultimate tensile strength is greatly affected by the content of reinforcement. This's due to the reinforcements' dispersion in LM26 matrix must be uniform, so no areas should be free of particles. The particles of chromium oxide dispersed uniformly in a composite can be used to enhance its strength due to their high hardness as well as other better properties. Alternatively, reinforcements clustering can cause local

weakness at the point of tensile loading, which could result in cracks developing. Furthermore, there should be strong bonding between LM26 as well as reinforcement at the same time at interface there must be free of discontinuities. Between reinforcement as well as matrix the perfect interface encourages not just wetting as well as a suitable degree of adhesion of reinforcement particles to matrix. Or else in the absence of strong interfacial bonding, reinforcement particles may detach prematurely in the course of force application. Furthermore, for effective load transfer to reinforcements from matrix, good and strong interfacial bonding is critical. The extent of load transfer will be higher as the greater the strength of interfacial bonding, and therefore the particles of reinforcement will then be subjected to their fracture stress [18-20].

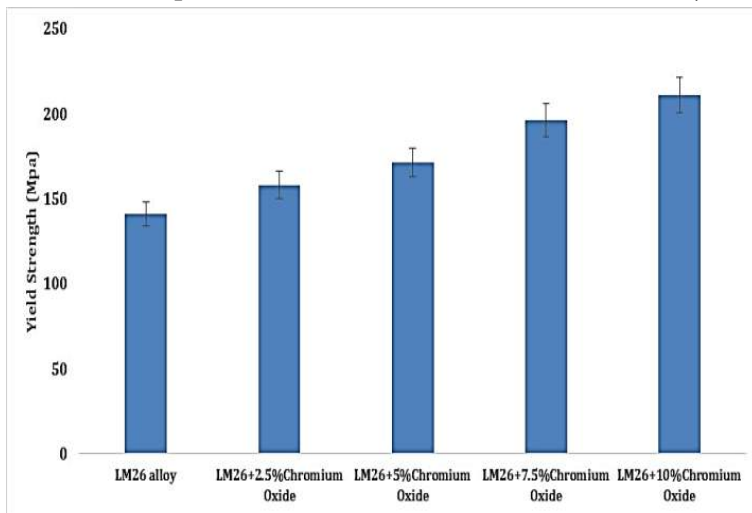


Fig.6 Graphical representation of yield strength

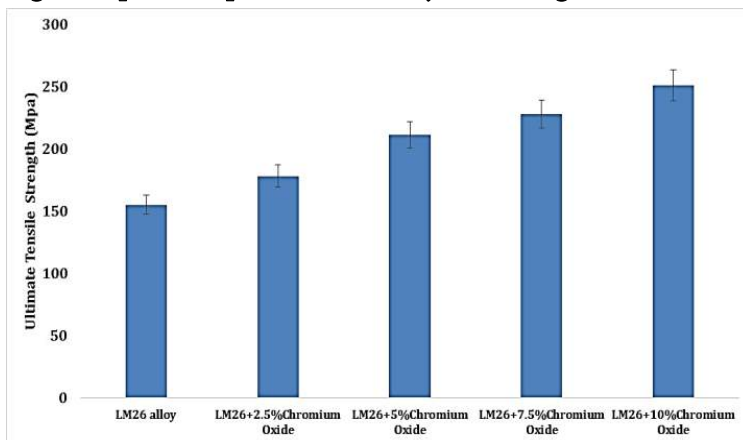


Fig.7 Graphical representation of ultimate tensile strength

Ductility of LM26 alloy as well as composites of it sare shown in Figure. 8. First the effect of reinforcement on ductility is presented in Fig. 11. It is seen that addition of Chromium Oxide particles led to decrement in the ductility of LM26 alloy composites. LM26 alloy demonstrated the highest ductility of 16.1% while LM26/10% Chromium Oxide composite showed the lowest of 11.6% value.

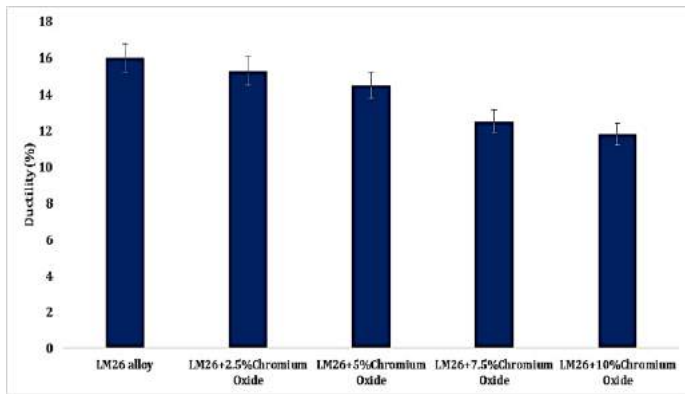
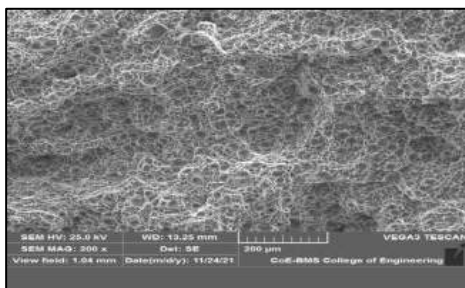


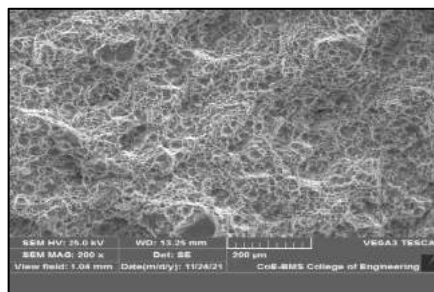
Fig.8Graphical representation of ductility

3.4 Fractured Surface Analysis

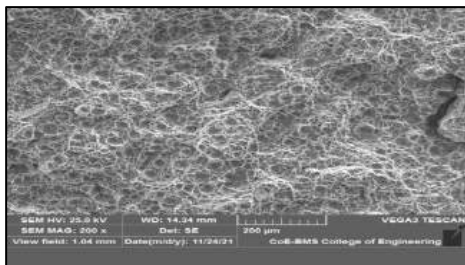
Tensile fracture surface of LM26 and its composites were studied using SEM and are displayed in Fig. 9. The fracture surfaces of both LM26 alloy as well as composites showed dimples and dendrites. The shrinkage porosity caused during processing period is preferential sites for crack initiation site and in these cases fractured surfaces showed such sites. All the samples showed dendritic structure in the fracture surface indicating failure due to formation of shrinkage porosity. During casting when the temperature of molten is very high than there is very high possibility of formation of shrinkage porosity. Apart from this gas pore formation and segregation are other two big problems which are likely to form in the molten metal held for longer time and poured at very high temperature. Cracks tend to initiate in the shrinkage porosity region and propagate along the gas pores leading to fracture of material. However in case of composites with 7.5% and 10% Chromium Oxide particle content as shown in Fig. 13 (c) and (d) there are some regions pertaining to clustered Chromium Oxide particles which are also capable of nucleating and propagating the cracks[21-22].



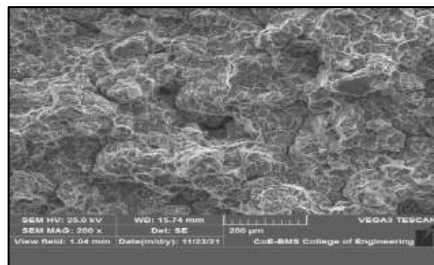
(a)LM26 alloy



(b)LM26+4wt%Chromium Oxide



(c)LM26+6wt%Chromium Oxide



(d)LM26+8wt%Chromium Oxide

Fig.9 SEM of tensile fractured surfaces

Due to high work hardening rates, LM26 matrix is most likely to exhibit high hardness values and strong values, which in turn result in lower ductility values. Or that may even be expressed as an enhancement in reinforcement content especially reinforcement the LM26 could act similar to the character of brittle that exhibits poor values of ductility after the tensile testing. There is no doubt that for composites the ductility goes along with the definite pattern because with a 10% increase in the content of chromium oxide, a noticeable improvement had been found. However, the values of ductility of 10% content of chromium oxide composites have been greater compared to 2.5% 5% 7.5% and 10% chromium oxide reinforced composites but found to be lesser compared to LM26 alloy. This is mostly due to a rise in the percentage of porosity with increasing content of reinforcement. Along with this at several regions had been found the clustering of particles that aid in the formation of voids, particularly at the interface of reinforcement as well as LM26 matrix. Particularly in composite materials, the reinforcement particles' sharp edge operates as the areas of stress concentration that may lead to low values of ductility.

IV. CONCLUSIONS

In this study effect of varying Chromium Oxide weight percentage on the mechanical behavior as well as microstructure of LM26 composites is reported. The conclusions drawn from this work are given below,

1. In LM26 matrix chromium Oxide particles dispersed uniformly, as revealed by micro structural analysis.
2. The LM26 matrix's grain size had been discovered to decrease with increased chromium Oxide particle weight percentage.
3. The hardness of composites were found to be significantly higher than that of unreinforced LM26 alloy owing to grain refinement which caused by the addition of Chromium Oxide particles.
4. Composites exhibited significantly higher yield as well as tensile strengths compared with unreinforced LM26 alloy. The increase in strength was attributed grain refinement and hardening. However, the ductility decreases with addition of chromium oxide particles.

V. REFERENCES

- [1]. A.C. Gowda, P.G. Koppad, D. Sethuram, R. Keshavamurthy, Morphology studies on mechanically milled aluminium reinforced with B4C and CNTs, Silicon, Volume 11, 2019, pages 1089-1098.
- [2]. K.V. Shivananda Murthy, D.P. Girish, R. Keshavamurthy, "Mechanical Characteristics of Hot Forged LM26-Al₂O₃ Composite" Journal of Applied Mechanics and Materials, Vol. 787, pp. 598-601, 2015.
- [3]. K.V. Shivananda Murthy, D.P. Girish and R. Keshavamurthy, "Investigation on mechanical Behavior of Hot Forged AL7075-TiO₂-flyash Hybrid Metal Matrix Composites", International Journal of Applied Engineering Research, Vol. 10 (2015), 55, pp.4105-4109.
- [4]. R Keshavamurthy, J M Sudhan, N Gowda, RA Krishna (2016), Effect of Thermo-Mechanical Processing and Heat Treatment on the Tribological Characteristics of Al Based MMC's", IOP Conference Series: Materials Science and Engineering 149 (1), 012118.

- [5]. AK Gajakosh, R Keshavamurthy, G Ugrasen, H Adarsh “Investigation on Mechanical Behavior of Hot Rolled Al7075-TiB2 In-situ Metal Matrix Composite”, *Materials Today: Proceedings* 5 (11), 25605-25614.
- [6]. G.S.P. Kumar, P.G. Koppad, R. Keshavamurthy, M. Alipour, Microstructure and mechanical behaviour of in situ fabricated LM26-TiC metal matrix composites, *Archives of Civil and Mechanical Engineering* Volume 17, 2017, Pages 535-544.
- [7]. C.S.Ramesh, R.Keshavamurthy, J.Madhusudhan “Fatigue behavior of Ni-P coated Si₃N₄ reinforced LM26 composites” *Journal of Procedia Materials Science*. Volume 6, 2014, Pages 1444-1454.
- [8]. K V Shivananda Murthy, D P Girish, R.Keshavamurthy, Praveennath Koppad, Temel Varol, “Mechanical and thermal properties of AA7075/TiO₂/Fly ash hybrid composites obtained by hot forging”, *Journal of Progress in Natural Science: Materials International* May 2017.
- [9]. G.S.PradeepKumar , R.Keshavamurthy, Prachi Kumari “Influence of Hot forging on Tribological behavior of LM26-TiB2 In-situ composites “ *IOP Conf. Series: Materials Science and Engineering* (2016) 149 (1), 012087.
- [10]. Ravi Kumar V., Suresh R., Prakash Rao C. R., Ravi Kumar D. V. and Bharat V. (2019) Effect of Heat Treatment on Tensile and Corrosion Properties of LM6 Hybrid Metal Matrix Composite Reinforced with Cenosphere and Red Mud. *Journal of Minerals and Materials Characterization and Engineering*, 7,1-17. doi: 10.4236/jmmce.2019.71001.
- [11]. S.Thirumalvalavan, N. Senthil kumar Evaluation of mechanical properties of aluminium alloy (LM25) reinforced with fused silica metal matrix composite, February 2019, *Indian Journal of Engineering and Materials Sciences* 26(1): 59-66.
- [12]. Radhika n., balaji t. V., palaniappan. S “studies on mechanical properties and Tribological behaviour of LM25/SiC/Al₂O₃ composites” *journal of engineering science and technology* vol. 10, no. 2 (2015) 134 – 144 © school of engineering, taylor’s university.
- [13]. SANNI DEV, 2AMIT AHERWAR “STUDY OF PHYSICO-MECHANICAL PROPERTIES OF PORCELAIN FILLED ALUMINIUM LM26 ALLOY FOR PISTON MATERIAL” *International Journal of Mechanical And Production Engineering*, ISSN: 2320-2092, Volume- 4, Issue-9, Sep.-2016. PP 38-41.
- [14]. D.S. MacKenzie, G.E. Totten, Analytical characterization of aluminum, steel, and superalloys, Taylor & Francis Group, LLC, 2006.
- [15]. E. Jayakumar, A.P. Praveen, T.P.D. Rajan, B.C. Pai, Studies on Tribological Characteristics of Centrifugally Cast SiCp-Reinforced Functionally graded A319 aluminium matrix composites, *Transactions of the Indian Institute of Metals* 71 (2018) 2741-2748.
- [16]. C.S. Ramesh, R. Keshavamurthy “Influence of Forging on Mechanical Properties of Ni-P coated Si₃N₄ Reinforced LM26 Composites”, *Materials Science & Engineering A*, 551, 2012, 59-66.
- [17]. G.M. Janowski, B.J. Pletka, The effect of particle size and volume fraction on the aging behavior of a liquid-phase sintered SiC/aluminum composite, *Metallurgical and Materials Transactions A* 26 (1995) 3027-3035.
- [18]. U.Cocen, K Onel, "Ductility and strength of extruded aluminum alloy Composites" *Composite Science Technology* 62(2002)275-282.

- [19]. V. Vembu, G. Ganesan, Heat treatment optimization for tensile properties of 8011 Al/15% SiCp metal matrix composite using response surface methodology, *Defence Technology* 11 (2015) 390-395.
- [20]. K H W Seah, S C Sharma, A Ramesh, Mechanical properties of cast aluminium alloy 6061-albite particulate composites, *Proceedings of the Institution of Mechanical Engineers, Part L: Journal of Materials Design and Applications* 214 (2000) 1-6.
- [21]. J. Zhou, S. Xu, Shu Huang, X. Meng, Jie Sheng, Haifeng Zhang, Jing Li, Yunhui Sun, E. A. Boateng, Tensile Properties and Microstructures of a 2024-T351 Aluminum Alloy Subjected to Cryogenic Treatment, *Metals* 2016, 6, 279.
- [22]. T. S. Srivatsan, J. Mattingly, Influence of heat treatment on the tensile properties and fracture behaviour of an aluminium alloy-ceramic particle composite, *Journal of Materials Science* 28 (1993) 611-620.



Effect of Injecting Bio-Diesel from the Used Cooking Oil and Graphene Nano Platelets on Performance, Combustion and Emission Characteristics of Diesel Engine

Nagaprasad K S¹, Rajesh Kumar Kodi², Prakash Raju S³, Madhu.D⁴

¹Associate Professor, Department of Mechanical Engineering, K.S. Institute of Technology, Bengaluru-560109, Karnataka, India

²Bioenergy Research and Quality Assurance Laboratory, Department Of Forestry and Environmental Science, University of Agricultural Sciences, Bangalore, Karnataka, India

³World of River Pvt. Ltd., Bangalore, Karnataka, India

⁴Professor & Head, Department of Mechanical Engineering, Government Engineering College, Ramanagaram, Karnataka, India

ABSTRACT

This comprehensive study mainly focuses on the production Bio-Diesel from the Used Cooking Oil (BD) by Trans-Esterification process and its usage with Graphene nano platelets(GNP) into diesel engine. Graphene Nano Platelets were chosen as the best possible nano addition for a 20% Bio-Diesel and 80% Pure-Diesel blend and various concentrations of graphene such as 25,50,75 mg/L were subjected to a constant speed engine testing at GKVK Bioenergy Research and Quality Assurance Laboratory at various Engine loads on a computerized “Variable Compression Ratio Multi Fuel Engine Test Rig” along with a top of the line computerized “AVL MDS-450 Emission Testing Equipment” with an effort to use the blend as an substitute to Pure-Diesel. The performance, combustion and emission characteristics were compared when engine is injected with various blend ratios. The results showed that BD20-75GNP had 11.5% increases in break thermal efficiency than 20BD-80D blend at 8Kg load. Also 36% of decrease in ignition delay was observed in BD20-25GNP fuel blend and 13.1% increase in peak pressure in BD20-75GNP; 55% and 51% reduction in CO and HC emission 20BD-75GNP fuel; 34% reduction in NO_x emission in 20BD-25GNP fuel. Considering the various optimization factors, the recommended GNP concentration to achieve the most significant enhancement in engine performance is 75 mg/L with BD20.

Keywords: Diesel Engine, Graphene nano platelets, Ignition Delay, Nitrogen Oxide emissions.

I. INTRODUCTION

Diesel engines have low specific fuel consumption and high thermal efficiency owing to their high compression ratio, low pumping work, and lean fuel air operating conditions. In addition, they have high reliability and low

operating and maintenance cost, enhancing their benefits in different sectors such as electricity generation, automobile sector, and agricultural machinery. However, compression ignition engines emit large quantity of emissions (NO_x, soot, CO, UHC, and particulate matter) causing serious health hazards and environmental degradation. Additionally, petroleum-derived fuels are declining and are predicted to provide our energy requirements until the middle of the 21st century because of the significant increase in energy demand and population. There are several techniques to reduce diesel exhaust emissions. These include engine design modification, combustion enhancement, and use of treatment devices for exhaust systems. The enhancement of engine combustion is the most recommended approach because it requires only few modifications of engine systems compared to the use of new designs or additional systems. This technique is achieved by adjusting the fuel properties, enhancing fuel injection, and using fuel additives.

One approach is by utilizing biodiesel as an oxygenated fuel, which is a promising alternative to the conventional diesel fuel [1]. Biodiesel is gaining more acceptance as a promising alternative energy resource because of the global fossil fuel shortage and emission issues. It is considered as an excellent choice for diesel engines because it is biodegradable, oxygenated, non-toxic, and environmentally friendly. However, graphene nanoplatelets (GNPs) can be an environmentally friendly fuel additive for promoting the combustion process of diesel biodiesel blended fuels efficiently owing to its low toxicity, high energy density, and high thermal conductivity. The ultra-thin and layered nanostructure of GNPs and the existence of different oxygen functional groups in GNPs provide a large surface area to volume ratios and chemically energetic sites for enhancing complete combustion[2,3].

Saxena and Khalife et al (2016) stated that the influence of adding nano-particle additives with diesel, biodiesel and diesel-biodiesel blends on a diesel engine performance and emission parameters was comprehensively surveyed. They concluded that the metallic-based additives and multi walled carbon nano-tubes additive have been demonstrated promising in terms of their impacts on engine performance and emission characteristics[4].

Harish Kumar Patel et al (2017) project's focussed to improve the performance of CI engine using diesel and bio-diesel by adding appropriate amount of nano-aluminium oxide (n-Al₂O₃). An experimental investigation was carried out to find out the performance of Single cylinder, 4 stroke diesel engine using Jatropha oil bio diesel and n-Al₂O₃ mixed diesel. It had been found the better results while using n-Al₂O₃ nano particle as an additive[5].

Ahmed I. EL et al (2019) paper tells about the experimental study which aims at investigating the impact of adding graphene oxide nanoparticles (GO) to neat Jatropha Methyl Ester (JME) on a single cylinder air cooled direct injection four stroke diesel engine. The nano-fuels have been prepared from 25, 50, 75 and 100 mg/l concentrations of graphene oxide with neat Jatropha biodiesel through ultrasonication process. The results indicate that the diesel engine operated by JME-GO nano-fuels enhanced the brake thermal efficiency by 17% compared to neat JME fuel. Furthermore, the peak cylinder pressure, the highest rate of pressure rise, and maximum heat release rate were also increased by 8%, 6%, and 6%, respectively. The CO and UHC emissions were decreased significantly by 60% and 50%, respectively, for JME-GO blends compared to pure JME fuel[6].

H. Suresh Babu Rao et al (2018) stated that Injection timing (IT) is a vital factor among different injection parameters which governs the emissions and performance factors of the engine. This work portrays the effect of IT on cerium oxide nanoparticle doped Waste Cooking Palm Oil biodiesel and diesel blends. The doping is

made at 30, 60 and 90 ppm. The modified fuels are introduced in reducing IT of 19° , 21° and 23° bTDC. 1500 rpm engine is made use in this study. Results revealed a significant reduction in emissions [7].

II. EXPERIMENTAL SETUP AND EXPERIMENTATION

A computerized variable compression Ratio Multi-Fuel Engine Test rig was used for the performance analysis, with technical specifications presented in Table 1. The diesel engine test rig is coupled with eddy current dynamometer as shown in figure 1. Figure 2 shows the photograph of diesel engine test rig.

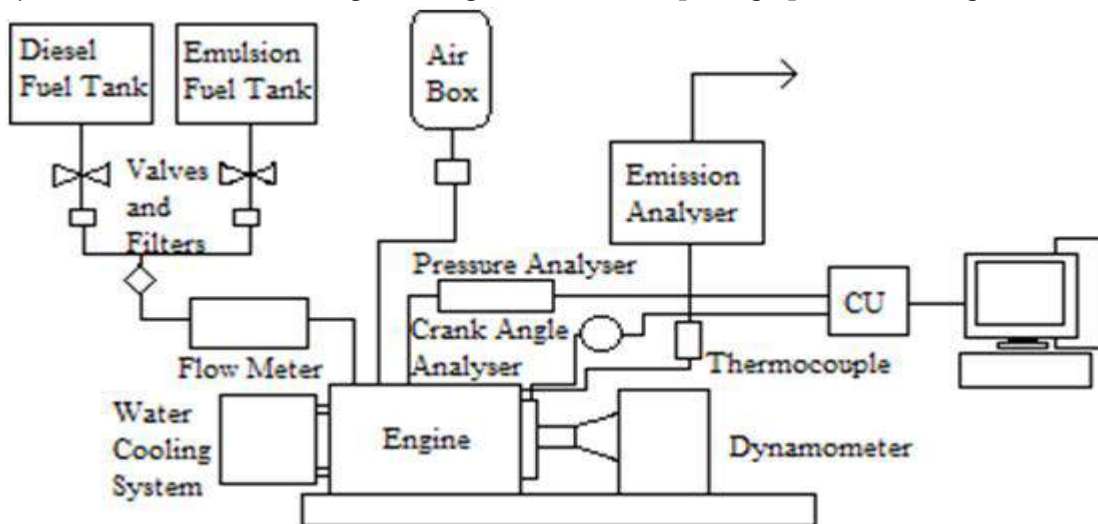


Figure 1: Diesel engine test rig



Figure 2: Photograph of Diesel engine test rig

TABLE I SPECIFICATIONS OF THE ENGINE

Engine Parameter	Specifications
Engine model	Computerized Variable Compression Ratio Multi fuel Engine Test Rig
Number of cylinders	1
Bore, mm	80
Stroke, mm	110
Displacement, cm ³	553
Compression ratio	5:1 to 20:1
Idle speed, rpm	1400-1500
Type of injection	Direct
Type of cooling	Water cooled
Starting up	Electric Start
Dynamometer	Type: EddyCurrent Capacity: 5HP
Combustion pressure sensor	Piezo-electric 0-100 bar

The exhaust gas analyser, Model “AVL-MDS 450” was utilized to measure the engine emissions of CO, UHC, NO_x, and O₂. The technical specifications of the exhaust gas analyser are presented in Table 2

TABLE III SPECIFICATIONS OF EXHAUST GAS ANALYSER

Gas	Measuring Range	Resolution	Accuracy
CO	0-4000 ppm	1 ppm	±10 ppm
CO ₂	0-20% by vol.	0.1% by vol.	0.5% of reading
UHC	0-10% by vol.	0.1% vol.	± 0.3% of reading
O ₂	0-20.9% by vol.	0.01% by vol.	± 0.3%
NO _x	0-4000 ppm	1 ppm	± 5ppm

Fuels used

The extracted UCO Bio-Diesel was blended with Pure-Diesel in the ratio of 80:20 by volume, then various quality test was carried on the extracted bio on the Blend in “Bio-Energy Research and Quality Assurance Laboratory” in Gandhi Krishi Vignan Kendra, Bangalore (GKVK), Diesel Blend was subjected to various quality testing process before its used on Engine, mainly done to protect various components of engine from any residue which may be left behind during the bio-diesel extraction process. All the properties of fuels, were measured according to ASTM standards. The values are shown in table 3. Blend’s density was measured using a “Anton Paar- DMATM 35”, it is portable specific gravity measuring kit with very high accuracy. Both pure-Diesel and Blend were subjected to Calorific value test in “Oxygen bomb calorimeter C3000 isoperibol”. The samples were tested by the Pensky-Martens Closed cup technique on a “Opti Flash - Pensky Martens Herzog” following these standards “ASTM D93 Methods A,B & C, ISO 2719 A, B & C, EN ISO 2719 A, B & C, IP 34 A,B & C, JIS K 2265 and GB/T261”.

TABLE IIIII PROPERTY OF FUELS USED

Property	Pure-Diesel	20BD80D
Density (g/cm ³)	0.8159	0.8352
Calorific Value (J/gm)	46272	44291
Flash point (°C)	41	46

GNPs-20BD80D Mixture Preparations

The GNPs-JB20 blended fuels were prepared according to the method mentioned. In, the mechanical disperser (LABSONIC M, the ultrasonic homogenizer, Volume range: 50 mL-30 L, speed range: 0 to 23,000 rpm) was used to prepare the homogeneous fuel mixtures of GNPs20BD80D and dismantle the agglomeration of nanoparticles. GNP-20BD80D blends were subjected to probe sonication for 20 mins at 30Khz thrice to enhance the stability of fuel blend. The GNPs were dispersed into the biodiesel blend using an ultrasonication pulsating frequency technique to avoid nanoparticle agglomeration in the fuel blend. The GNPs of mean outer diameter less than 2 mm, thickness of 6 to 8 nm, and width of 5 µm were prepared for testing. The Physical properties of Graphene Nano Platelets used is shown in table 4.

TABLE IV PHYSICAL PROPERTIES OF GRAPHENE NANO PLATELETS

Parameters	Measured values
Graphene nanoplatelets nano-powder	~99% purity
Average particle size	6-8 nm thick, 5 mm
Appearance	Black
Bulk Density	0.45 g/cm ³
Thermal conductivity	3000 W/m-K

The values indicates that the thermal conductivity of GNPs at room temperature is over 2000 times greater than that of pure JB20 blends. Therefore, GNPs-20BD80D blends have a higher thermal conductivity compared to pure 20BD80D blends. As a result, the evaporation rate of fuel droplets increases, yielding a shorter ignition delay. Moreover, the surface area to volume ratio of GNPs is higher than that of diesel biodiesel blends. Consequently, GNPs-20BD80D fuels will have higher heat transfer rates compared to diesel biodiesel blends.

III. RESULTS AND DISCUSSION

This section explains the performance of the diesel engine operated on diesel engine at different load by 20% biodiesel and varying the percentage of concentrations of graphene as 25,50,75 mg/L respectively.

Brake thermal Efficiency

Figure 3 shows the Break thermal efficiency against load. The thermal efficiencies at 8kg load are 22.19 %, 21.64%, 22.8%, 24.73% for 20BD80BD, 25, 50 and BD2075GNP fuels respectively. The highest of 11.5% increase in break thermal efficiency observed for 20BD80D blend compared to BD2075GNP.

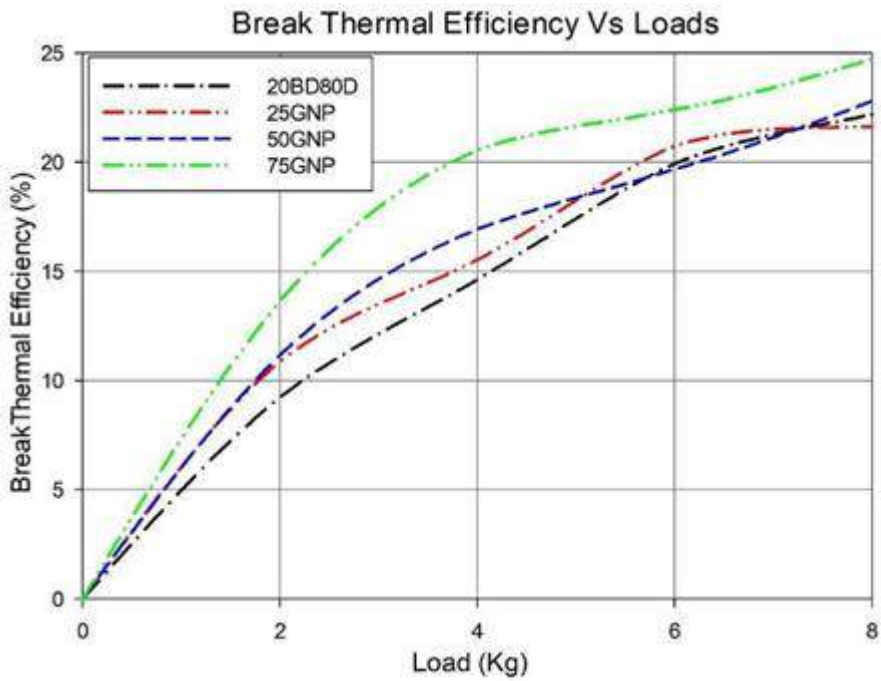


Figure 3: Effect of graphene nano platelets on Brake thermal efficiency

Combustion Characteristics

Peak pressure and Ignition delay

The P – θ history was acquired for fifty cycles and the averaged pressure v/s crank angle at when diesel injected with different graphene nano platelets is shown in Figure 6. Peak pressures were 52.55, 55.25, 55.7, 59.46 bar for 20BD80BD, 25, 50 and BD2075GNP fuels, respectively and 23.84, 15.24, 15.32 and 20.58 °CA were the respective Ignition delays of the corresponding fuel samples. Hence 36% of decrease in ignition delay was observed in BD2025GNP fuel blend and 13.1% increase in peak pressure in BD2075GNP; both at 8Kg engine loads.

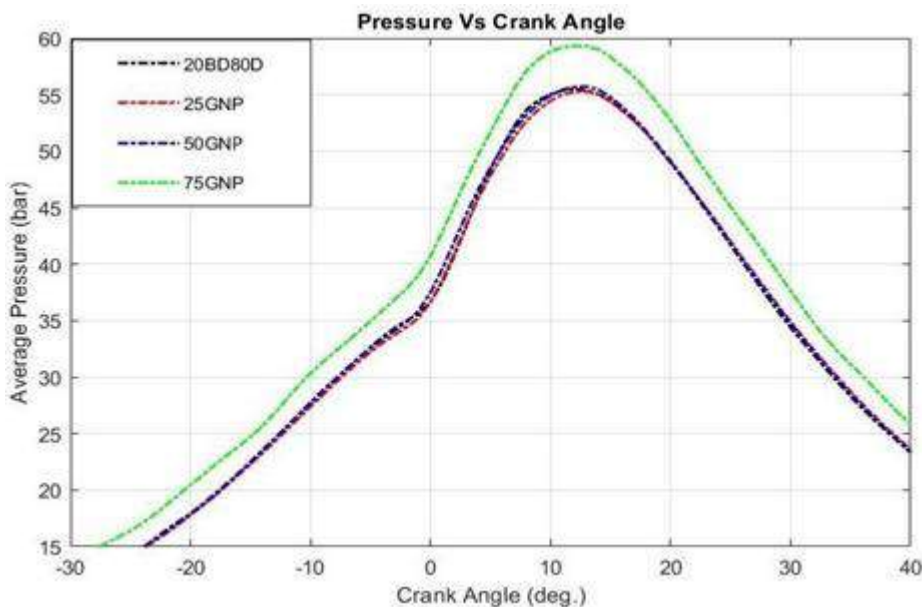


Figure 4: Variation of pressure with crank angle for graphene nano platelets

Emissions Characteristics

HC and CO emissions.

The addition of GNPs into BD20 has a significant positive effect on CO and UHC emissions. The reason for this may be due to the shortened ignition delay and the enhanced ignition characteristics of GNPs. Moreover, the high catalytic activity of GNPs is due to their higher surface area to volume ratio, which improved the fuel air mixing in the combustion process[12,13]. From figure 5 and figure 6 there has been 55% and 51% reduction in CO and HC emission at 8Kg load in 20BD75GNP fuel.

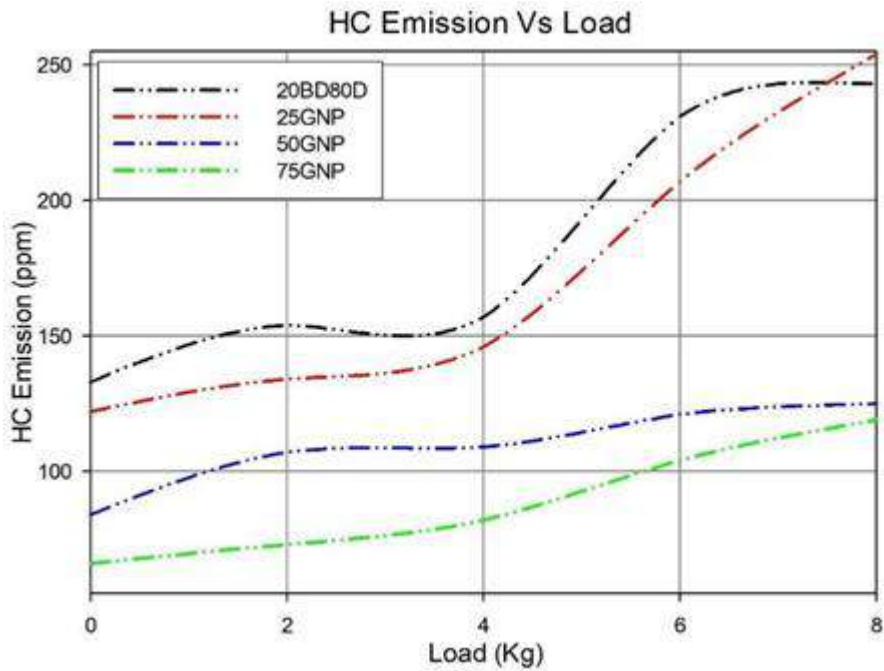


Figure 5: Effect of graphene nano platelets on HC emissions

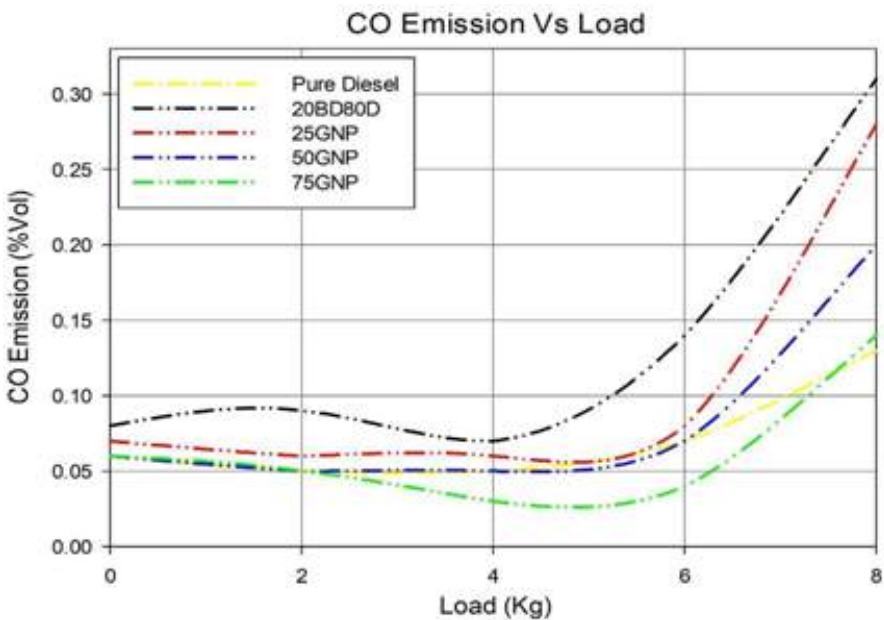


Figure 6: Effect of graphene nano platelets on CO emissions

NO_x emissions

Figure 7 shows the NO_x against load. NO_x emission reduced due to increasing the ignition delay[11] and as stated before with huge reduction in ignition delays in the 20BD25GNP and it is evident in Figure 7, it observed that 34% reduction in NO_x emission at 8kg load in 20BD25GNP fuel.

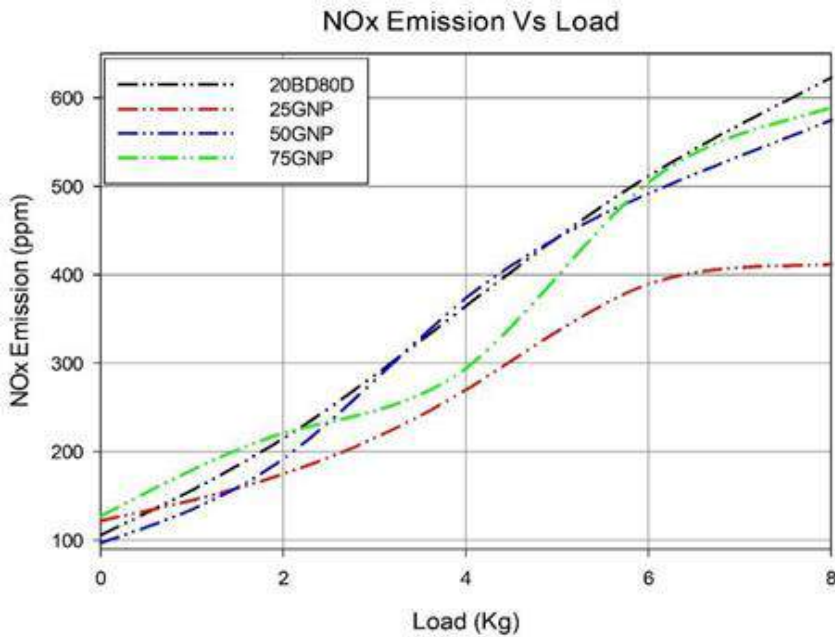


Figure 7: Effect of graphene nano platelets on NO_x emissions

Optimized Condition

In order to choose the best fuel as a substitute for Pure-Diesel, an optimization technique is used by plotting results of various Emission gasses against Brake Thermal Efficiencies at 8 kg load as shown in figure 8. It is observed that point closest to Pure-Diesel is 20BD75GNP Data points suggesting the fact that it has the best or the closest Thermal Efficiency as Pure-Diesel and least emission compared to all other fuels.

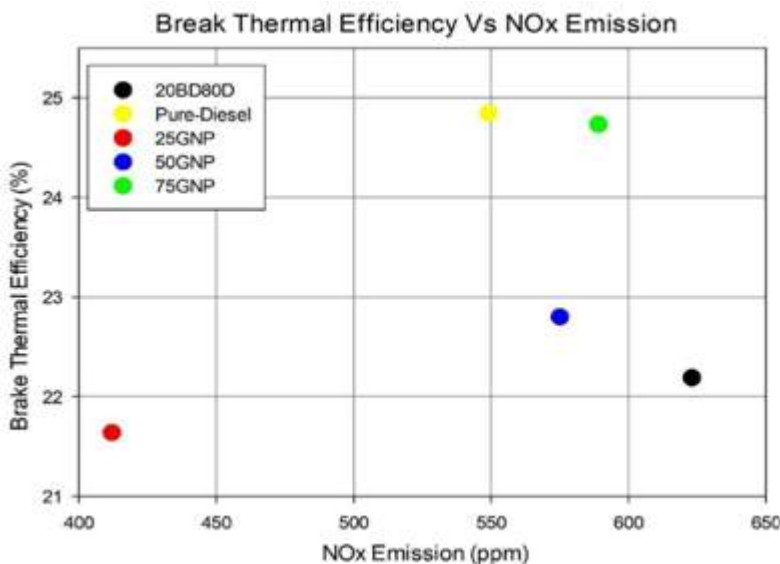


Figure 8: Brake thermal efficiency –NO_x emissions trade-off

IV. CONCLUSION

In the present experimental work, the engine was operated on diesel, 20BD80D Blend and 20BD80D emulsified with 25, 50, 75 mg/L blend at 1500 RPM Engine speed at various loads (from 0-8kg loads). BTE of BD2075GNP was higher than Pure-Diesel at 6kg Load and almost same as Pure- Diesel at 8kg Engine Load. Peak pressure of 20BD75GNP fuel was found to be 10% more than that of peak pressure of Pure-Diesel throughout various loads. 2% of reduction in Ignition Delay compared to Pure-Diesel was found when engine was operating on BD2025GNP fuel. 25% of Reduction NO_x emission was found at various engine load compared to Pure- Diesel while using BD2025GNP fuel. 7% less CO and 30% less HC emissions we recorded during BD2075GNP compared to that of Pure-Diesel at various loads. Considering the various Optimization factors considered in previous chapter of the report, The recommended GNP concentration to achieve the most significant enhancement in engine overall performance is 75 mg/L, which had the better performance and emission characteristics than that of Pure-Diesel.

V. REFERENCES

- [1]. Hasan MM, Rahman MM, "Performance and emission characteristics of biodiesel/diesel blend and environmental and economic impacts of biodiesel production: a review", *Renew Sustain Energy Rev* 2017.
- [2]. Agarwal AK. "Biofuels (alcohols and biodiesel) applications as fuels for internal combustion engines", *Energy Combustion Science* 2007.
- [3]. Atabani AE, Silitonga AS, Anjum I, Mahlia TMI, Masjuki HH, Mekhilef S. A comprehensive review on biodiesel as an alternative energy resource and its characteristics. *Renew Sustain Energy Rev* 2012.
- [4]. Amay Saxena, "Deriving a generalized, actuator position-independent expressions for the force output of scissor lift", University of California, Berkeley.
- [5]. Harish Kumar Patel and Saurabh Kumar, "Experimental Analysis on Performance of Diesel Engine using mixture of Diesel and Bio-Diesel as a Working Fuel with Aluminum Oxide Nanoparticle Additive", *Thermal Science and Engineering Progress* 4(2), September 2017, DOI:10.1016/j.tsep.2017.09.011
- [6]. Ahmed I. EL-Seesy, Ali K. Abdel-Rahman, Mahmoud Bady and S. Ookawar, "The Influence of Multi-Walled Carbon Nanotubes Additives into Non-Edible Biodiesel-Diesel Fuel Blend on Diesel Engine Performance and Emissions", 3rd International Conference on Power and Energy Systems Engineering, CPESE 2016, 8-12 September 2016, Japan.
- [7]. H. Suresh Babu Rao, T. Venkateswara Rao and K. Hemachandra Reddy, "Influence of injection timing on cerium oxide nanoparticle doped in waste cooking palm oil bio-diesel and diesel blends fuelled in diesel engine", *International Journal of Ambient Energy*, Volume 41, 2020 -Issue 4, Pages 403-408
- [8]. Jiaqiang E, Pham M, Zhao D, Deng Y, Le DH, Zuo W, Zhu H, Liu T, Peng Q, Zhang Z. Effect of different technologies on combustion and emissions of the diesel engine fueled with biodiesel: a review. *Renew Sustain Energy Rev* 2017.

- [9]. Anderson, A., Y. Devarajan, and B. Nagappan, "Effect of Injection Parameters on the Reduction of NO_x Emission in Neat Bio-diesel Fuelled Diesel Engine.", *Energy Sources, Part A: Recovery, Utilization, and Environmental Effects* 40 (2): 186–192. doi:10.1080/15567036.2017.1407844
- [10]. Devarajan, Y., D. B. Munuswamy, and A. Mahalingam. "Performance, Combustion and Emission Analysis on the Effect of Ferrofluid on Neat Biodiesel." *Process Safety and Environmental Protection* 111: 283–291.
- [11]. C. H. Lee, S. M. Sapuan, M. R. Hassan, 2017, Mechanical and Thermal Properties of Kenaf Fiber Reinforced Polypropylene/Magnesium Hydroxide Composites, *Journal of Engineered Fibers and Fabrics*, 12, 50-58
- [12]. Devarajan, Y., D. B. Munuswamy, A. Mahalingam, and B. Nagappan, "Performance, Combustion, and Emission Analysis of Neat Palm Oil Biodiesel and Higher Alcohol Blends in a Diesel Engine." *Energy & Fuels* 31 (12): 13796–13801. doi:10.1021/acs.energyfuels.7b02939
- [13]. Ramkumar S, Kirubakaran V, "Biodiesel from vegetable oil as alternate fuel for C.I engine and feasibility study of thermal cracking: a critical review", *Energy Conversion* 2016;155–69.
- [14]. Tamilselvan P, Nallusamy N, Rajkumar S. A comprehensive review on performance, combustion and emission characteristics of biodiesel fuelled diesel engines. *Renew Sustain Energy Rev* 2017; 79:1134–59.
- [15]. Khalife E, Tabatabaei M, Demirbas A, Aghbashlo M., "Impacts of additives on performance and emission characteristics of diesel engines during steady state operation", *Energy Combust Science*. 2017;59: 32–78.



Variation of Tensile, Hardness, Impact and Natural Frequency in Jute/E-Glass Epoxy Composite For Varying Fiber Loading and Addition of Shear Thickening Fluid

Dr. Abhishek M R^{1*}, Dr. Suresh P M², Dr. Mruthunjaya M³, Dr. Balaji B¹

^{1*}Department of Mechanical Engineering, K S School of Engineering & Management, Off Kanakapura Road, Bengaluru -560109, Karnataka, India

²Department of Mechanical Engineering, A C S College of Engineering, Off Mysore Road, Bengaluru -560074, Karnataka, India

³Department of Mechanical Engineering, Dr. Vishnuvardhan Road JSSATE, Bengaluru - 560060, Karnataka, India

ABSTRACT

In the recent decade composite materials plays a significant role in the manufacturing sector of many industries contributing towards the social and economic development of a country. This is because of flexibility to combine different set of materials to bring out the desired properties in developed material. Many researchers performed experimental investigation on potential use of composite in various engineering application viz. structural components of automobile and aerospace application. In this regard current investigation is intended to tailor a hybrid fiber reinforced composite material constituting Jute, E – Glass and Epoxy matrix material. Traditional hand layup technique is adopted to cast the composite based on weight fraction. Thus casted composites are tested for Mechanical properties and vibration characteristics. Also the composites are tested for the effect of addition of Shear Thickening Fluid (STF). Scanning Electron Microscope (SEM) images were captured for the composites developed to validate the test results. Mechanical and dynamic test result indicates that addition of STF to composite improved the mechanical properties and vibration characteristics and has potential to be used in automobile application.

Keywords: Hybrid composites, Shear thickening fluid, Mechanical testing, Jute, E-glass, Epoxy

I. INTRODUCTION

Hybrid composite materials are those when two or more fibers combined together with the aid of a polymer resin [1]. The purpose for combining two or more fiber in composite is to develop the desired mechanical properties so as to be used in a specific application. In this regard many researchers performed research for the true worthiness of the developed composite. Also researcher tries many natural fibers as replacement for

synthetic fiber to improve the degradability to make composites eco – friendly by not compensating with properties of material [2]–[6].

K Abdurohman et al. investigated the effect of different casting technique on the tensile properties of composites made of E – glass and epoxy. Techniques involved in the casting of composites are hand layup, vacuum bagging and vacuum infusion. American Standard for Testing Materials (ASTM) D 3039 was adopted as testing procedure. Results indicates that the composites processed using vacuum infusion with 60 wt % fiber and rest as resin possess higher tensile modulus and Ultimate Tensile Strength (UTS) of 10673.4 MPa and 346.15 MPa respectively compared to 8660 MPa and 260.986 MPa for hand layup method [7].

Abhishek et al. experimented the tensile and hardness properties of hybrid composites having jute, e-glass and epoxy resin. Composites were casted using conventional hand layup method. Composites were tested for the effect of addition of Shear Thickening Fluid (STF). Fibers and resins were maintained in the ratio of 60 wt % of fibers and 40 wt % resins. Jute fibers were varied to examine the effect of jute fiber variation. Results concluded that tensile modulus and UTS of the composite increased with the increase in the jute wt %, but the percentage elongation of the composite decreased. Addition of STF to the composite further increased the strength and UTS. The tensile modulus and UTS recorded were around 1300 MPa and 200 MPa for composites with STF [8].

Joselin et al. in their investigation attempted to improve the impact resistance in high performance Kevlar fabrics by impregnating the fabrics using STF. Results indicated that the fabric with impregnated STF exhibited better impact resistance, also the depth of penetration in the fabrics with STF was lesser compared to fabrics without STF [9].

Davoodi et al. tested composite material comprising of Kenaf – Glass fiber bonded with epoxy resin for bumper beam application in passenger car and found that above said composite has a greater potential to be used in bumper beam application since its strength was on par with the requirement, but its impact resistance was on lower side [10]. Raghavendra et al. tested hybrid composites made of Jute and glass, epoxy as polymer for mechanical properties to be used in automobile application and concluded that combination of natural and synthetic fiber hybrid composite had greater abilities to replace conventional materials in automobile application with improvement in impact strength [11].

Kunkun et al. carried out their research on effect of shear thickening fluid on energy absorption capacity and transverse impact strength in sandwich composites. Sandwich composite panels were prepared using carbon fibers facing with shear thickening fluid filled in composite. Thus prepared composite were tested for low velocity impact loading. It was found from results that composite made of shear thickening fluid as core material exhibited higher energy absorption capacity than aluminium foam as core material. Also the depth of penetration in the composite panel was less compared to aluminium foam sandwich composite panels [12].

Kejing et al. [13] evaluated the stab resistance of fiber by coating with silicon based shear thickening fluid. Glass fibers were soaked in STF and dried before fabrication. The evenly distribution of STF was established by SEM photographs. Quasi – static stab resistance test was conducted on fiber with and without STF. Fiber coated with STF indicated superior stab resistance compared to fibers without STF.

It can be summarized from the literature that the composite with the addition of STF improves the Strength and impact resistance. In the current investigation, it is intended to process a hybrid composite consisting of e-glass, jute as fibers and epoxy as resin. Also the developed composites are tested for the effect of addition of STF.

II. MATERIALS AND METHODS

As discussed in the previous section in the current investigation a hybrid composite are developed with e-glass and jute as fibers and epoxy as matrix materials. Figure 1 depicts the jute. E-glass and epoxy used in the casting of composites. Composites are fabricated using hand layup method [14]–[17]. In this method the woven fibers are placed in a flat mould and the measured quantity of matrix material is added with constant rolling to remove any trapped air gaps in the composites. Thus prepared composites are allowed to cure in the room temperature for one day. Cured composites are then processed according to ASTM standard for evaluating tensile, hardness, impact and dynamic properties. Also the composite are tested for the addition of STF, which are made of corn starch suspended in water in the ratio of 10:1. This mixture is then added to resin. Mechanical properties of the jute, e-glass and epoxy are listed in Table 1, 2 and 3 respectively.

Table 1. Mechanical properties of Jute

Density (g cm ⁻³)	Tensile strength (MPa)	Youngs modulus (GPa)
1.3	393	26.5

Table 2. Mechanical properties of E - Glass

Density (g cm ⁻³)	Tensile strength (MPa)	Youngs modulus (GPa)
2.55	1750	70

Table 3. Mechanical properties of Epoxy

Density (g cm ⁻³)	Tensile strength (MPa)	Youngs modulus (GPa)
1.2 -1.3	50-125	2.5-4.0

Hybrid composites are prepared with varying jute fiber loading viz. 5 – 20 wt % i.e. in steps of 5 wt %. Also composites are tested for the effect of addition of shear thickening fluid; the details of the composition in the composite are tabulate in Table 4 and 5.



a



b



c

Figure 1: (a) Jute (b) E-glass (c) Epoxy

Table 4. Composition of the composite without STF

Composition	Jute Wt%	E-Glass Wt%	Epoxy Wt%
C1	5	45	50
C2	10	40	50
C3	15	35	50
C4	20	30	50

Table 5. Composition of the composite with STF

Composition	Jute Wt%	E-Glass Wt%	Epoxy Wt%
CS1	5	45	50
CS2	10	40	50
CS3	15	35	50
CS4	20	30	50

Tensile Test

Material of any form, assessment of tensile properties is very important since, materials to be used in structural application requires mechanical properties, one such property is tensile strength which are assessed through tensile testing. In this test materials are subjected to axial loading. Gradually load is increased till the failure of the material. standards are adopted for testing is ASTM D638 type I [18]. Mechanical properties such as UTS and percentage elongation are determined for the composites defined in previous section.

Rockwell Hardness Test

Surface property is one of the key factors to assess the wear in materials. Here composites are tested for Rockwell hardness testing for M Scale with ASTM D785, size of the ball indenter being 6.35 mm. Composites are subjected to minor load of 10 kg and major load of 100 kg. The hardness of the materials is evaluated using Equation 1.

$$\text{Rockwell hardness number} = 130 - \frac{h}{0.02 \text{ mm}} \quad \dots \text{Equation 1}$$

Charpy Impact Test

Resistance against sudden load is as important property for structural application like in automobile/aerospace industry. This charpy impact test characterises the strength of the materials against impact. The ASTM D 256 standards are adopted for the conduction of test. Figure 2 indicates the tailored composites according to ASTM standards.

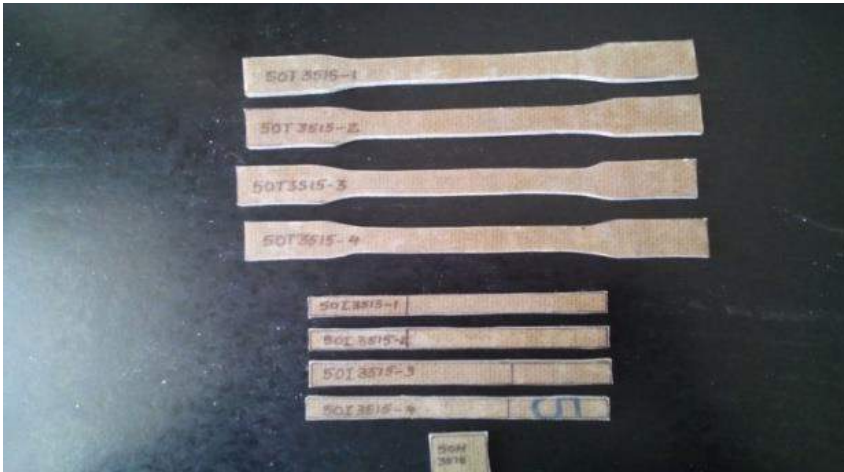


Figure 2: Composites according to ASTM standards

Dynamic Mechanical Test

Fast Fourier Transform (FFT) analysis are performed to evaluate natural frequency of the materials [19]–[23]. Dynamic vibration analysis were conducted to evaluate the natural frequencies of the passenger car components [24]–[26]. In this test a specimen of dimension 300 * 300 mm are held as cantilever beam, specimens are subjected to excitation force to record FRF variation in the material which are utilized to compute natural frequency of the components. Figure 3 illustrates arrangements made in dynamic mechanical testing to assess natural frequency of the composites for different modes.

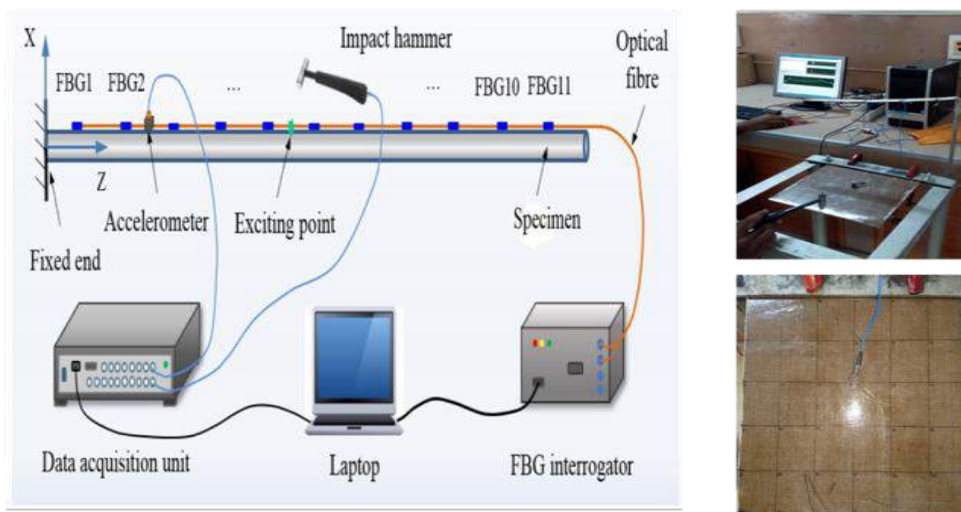


Figure 3: Dynamic mechanical testing setup

SEM Analysis

SEM photography of composites with and without STF is captured in order to validate the bonding between fibers and fiber-matrix by using Hitachi SU 3500 machine. Initially composites are subjected to Gold sputtering process as surface preparation.

III. RESULTS AND DISCUSSION

Tensile Test

Mechanical properties such as UTS and percentage elongation are recorded for the hybrid composites with and without STF and the Table 6 reveal the results.

Table 6. Results for Tension test

Composite	UTS (MPa)	% Elongation	Composite	UTS (MPa)	% Elongation
C1	96.49	2.09	CS1	211.06	4.79
C2	81.83	3.34	CS2	147.42	2.83
C3	137.89	4.31	CS3	97.74	1.87
C4	61.27	4.36	CS4	100.04	1.43

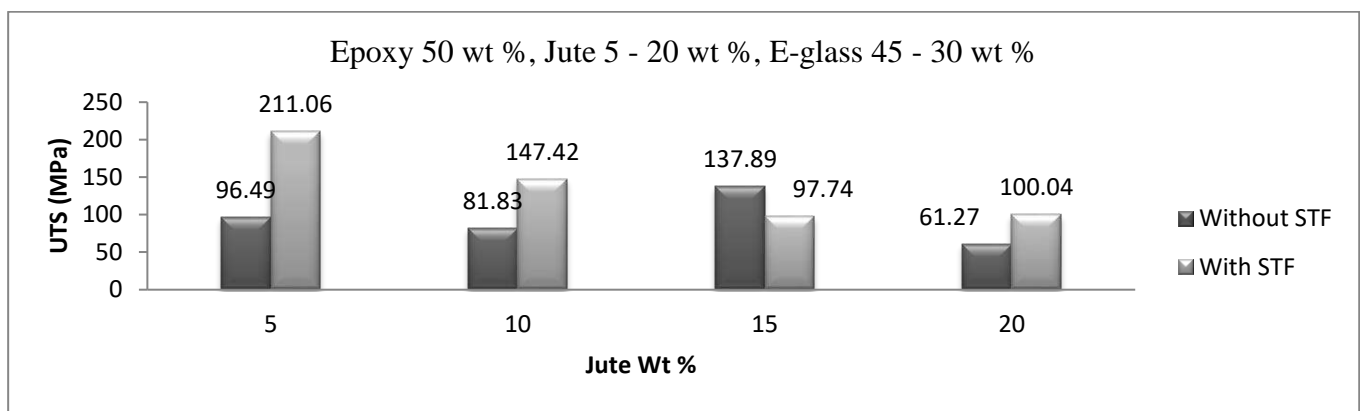


Figure 4: UTS vs jute wt % in composites with and without STF

The variation in the UTS for the change in the jute wt % in composite with and without STF is depicted in Figure 4. It indicates that the UTS in composite C3 are higher compared to composite C1, C2 and C3, but a decreasing trend is observed except in C3 composites this is argued later with the morphology images that the bonding in composite C3 is better compared to rest of composition. Similar variations are recorded for the composites with STF. This decrease in the UTS is because of increase in the jute wt % i.e. e-glass is stronger compared to jute as shown in Table 1 & 2. This is supported by the work carried out K Abdurrohman et al. in the application of alkali treated rice straw fiber composite in bumper beam application [7].

The highest UTS are recorded for the composite without STF is 137.89 MPa for C3 and for composite with STF it is 211.06 MPa in CS1. Results also indicates that the addition of STF to composites enhances the UTS in C1, C2 and C4 but in C3 it decreased as a result of poor bonding between fibers and fiber-matrix by SEM morphology.

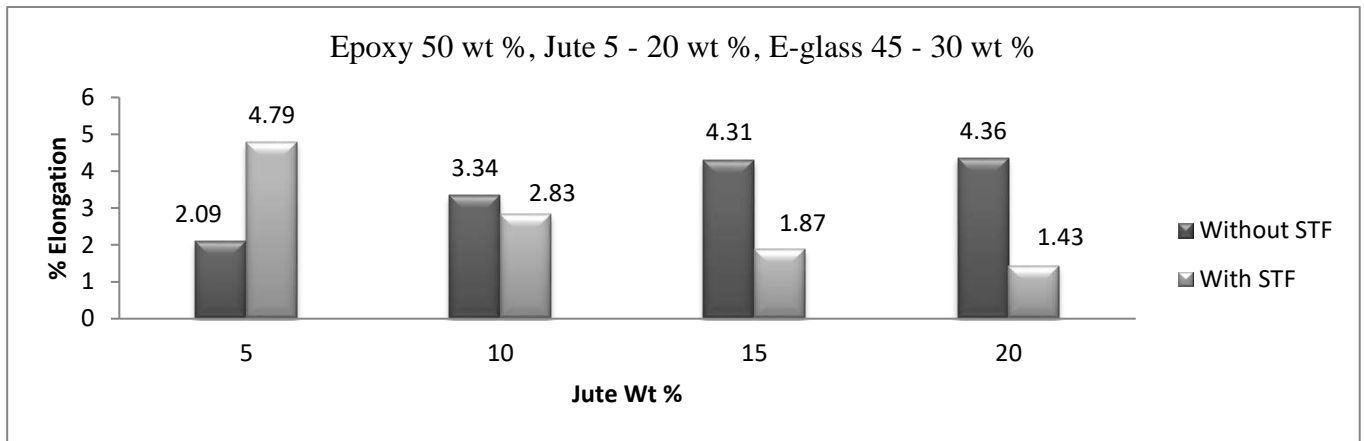


Figure 5: Percentage elongation vs jute wt % in composites with and without STF

Effect of varying fiber loading and addition of STF to composite on percentage elongation is shown in Figure 5. On comparing the stiffness of jute and e-glass as listed in Table 1 & 2, jute is less stiffer than e-glass, this is distinctly visible in the results of percentage elongation for varying jute fiber loading in composites i.e. as the jute wt % in composite increases, the percentage elongation increases. The highest percentage elongation of 4.36 % is noted for the composite C4 and lowest of 2.09 % for C1.

In composites with STF this trend is overturned, percentage elongation decreased with the increase in the jute wt %. The formation of tenacious like substance due to the addition of STF to composite is one of the reasons, which improves bonding between fibers and matrix to increase the strength and decrease in percentage elongation as revealed in SEM images.

Hardness Test

Surface hardness of the composites are measured using Rockwell hardness and test results are shown in Figure 6. It indicates that the variation in the hardness between composites has not varied significantly for varying jute wt % in both composites with and without STF this is because of the reason that the resin is kept constant and the facing layers of composites comprises of e-glass. But composites with STF revealed lower HRM compared to without STF. Highest HRM is noted in composite C1 with 82 HRM while lowest of 61 HRM in CS4.

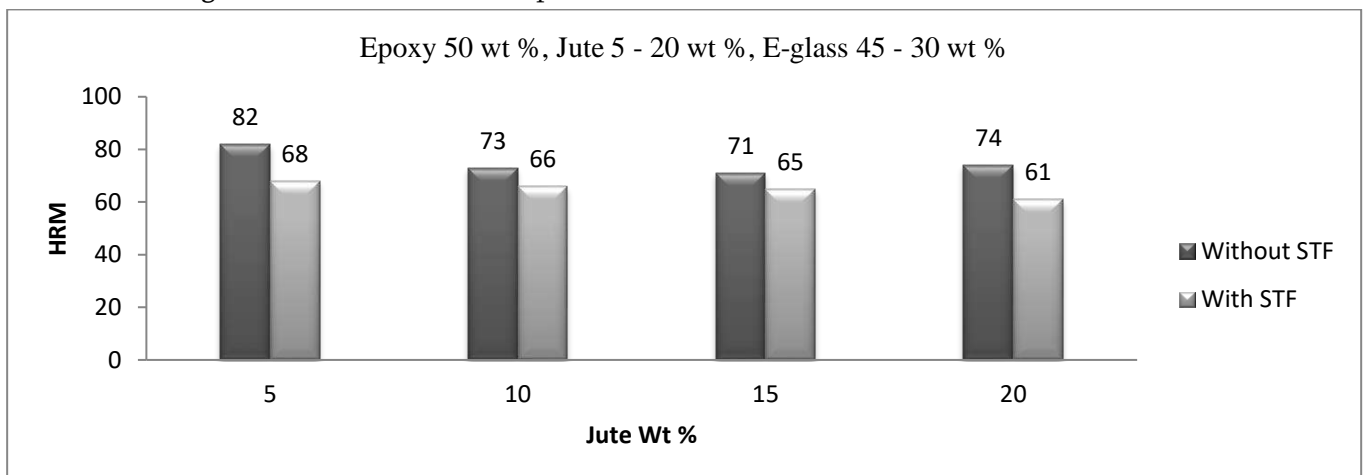


Figure 6: HRM vs jute wt % in composites with and without STF

Impact Test

Effect of Adding STF and varying fiber loading on charpy impact strength are depicted in Figure 7. Results indicated that increase in the jute wt % in composite increases the impact strength in both composites with and without STF, but the effect of increment in impact strength is not that significant for composites with STF and for 15 and 20 jute wt %. M K Gupta et al. [15] in their investigation proved that the combining jute with sisal increased the impact strength in the composites. Similar results are noticed in the composites without STF. Kejing et al.[13] in their investigation proved that the addition of STF increases the impact strength of the composite, similar observation are noticed in the current research that the addition of STF increased the impact strength in composite with STF compared to the composites without STF.

Dynamic Mechanical Test

The results for the dynamic mechanical test are illustrated in Figure 8, 9 and 10 for mode 1, 2 and 3 respectively for composites with and without STF. The effect of adding STF and varying jute wt % in the composite is not significant for the 10, 15 and 20 jute wt %. But in composite with 5 wt % jute natural frequency increased in mode 1 and decreased noticeable in mode 2 and 3. Results concluded that a range of natural frequency can be obtained by varying jute wt % and addition of STF to composite.

SEM Analysis

Surface morphology for the composites with and without STF for varying jute fiber loading is illustrated in Figure 11 and 12 with 500X magnification. Figure 11 reveals the presence of voids in composite C1, C2 which reduced the strength in the composite as seen for UTS. Also from Figure 12, it is noticed that the addition of STF transposes resin into sticky which hold the fibers and matrix to higher strength and reduced the formation of voids in the composites.

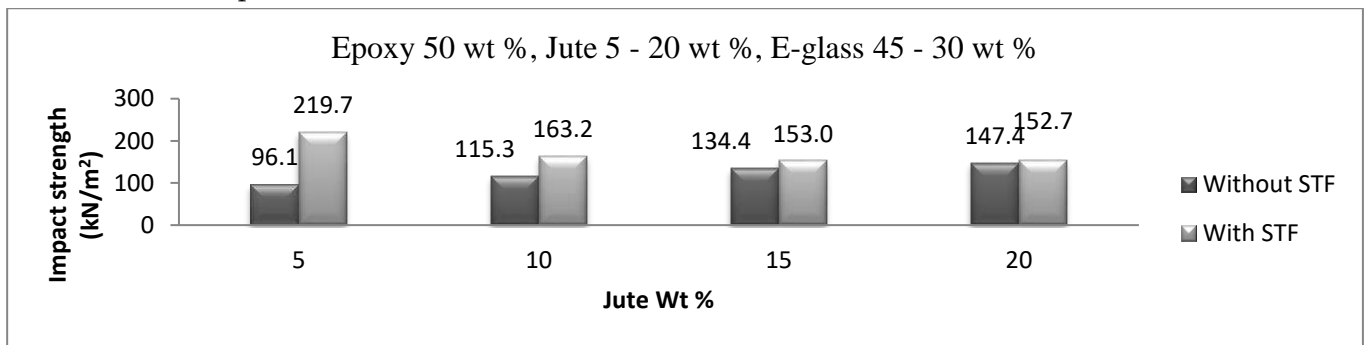


Figure 7: Impact strength vs jute wt % in composites with and without STF

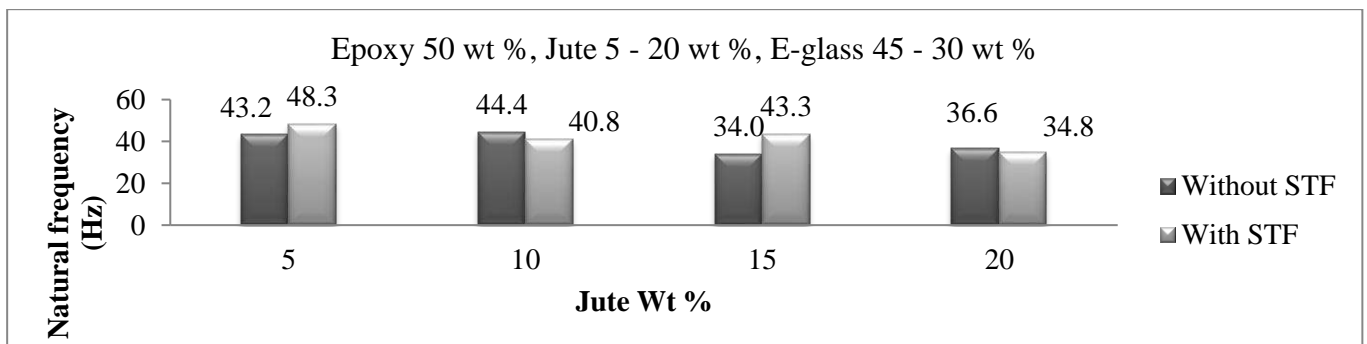


Figure 8: Natural frequency vs jute wt % in composites with and without STF for mode 1

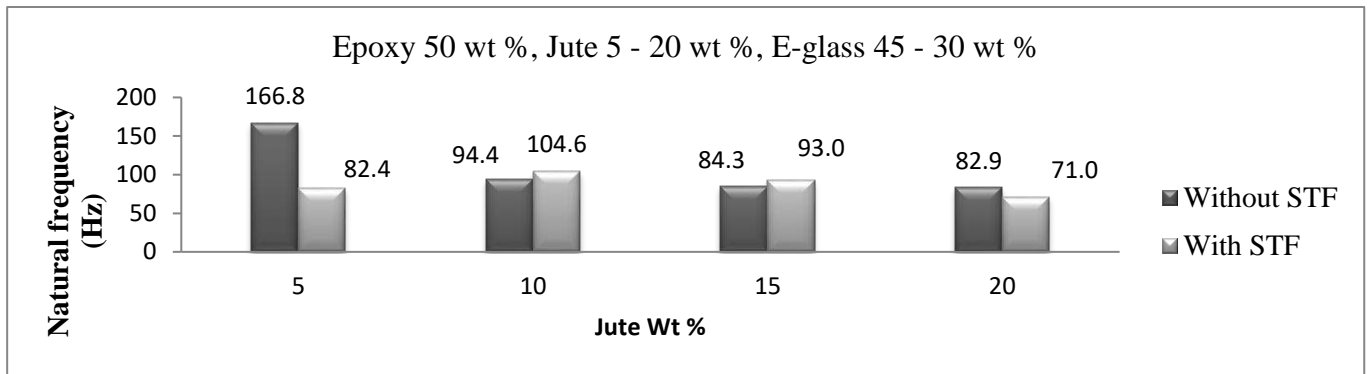


Figure 9: Natural frequency vs jute wt % in composites with and without STF for mode 2

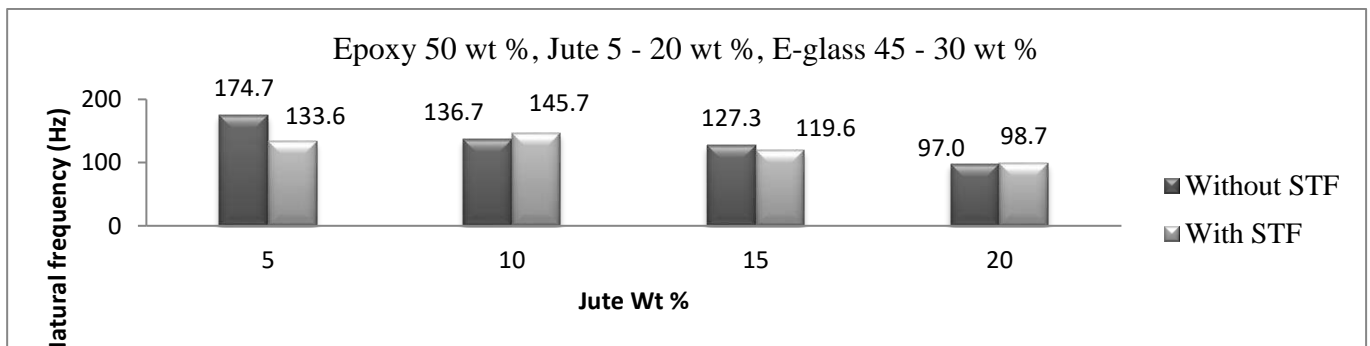


Figure 10: Natural frequency vs jute wt % in composites with and without STF for mode 3

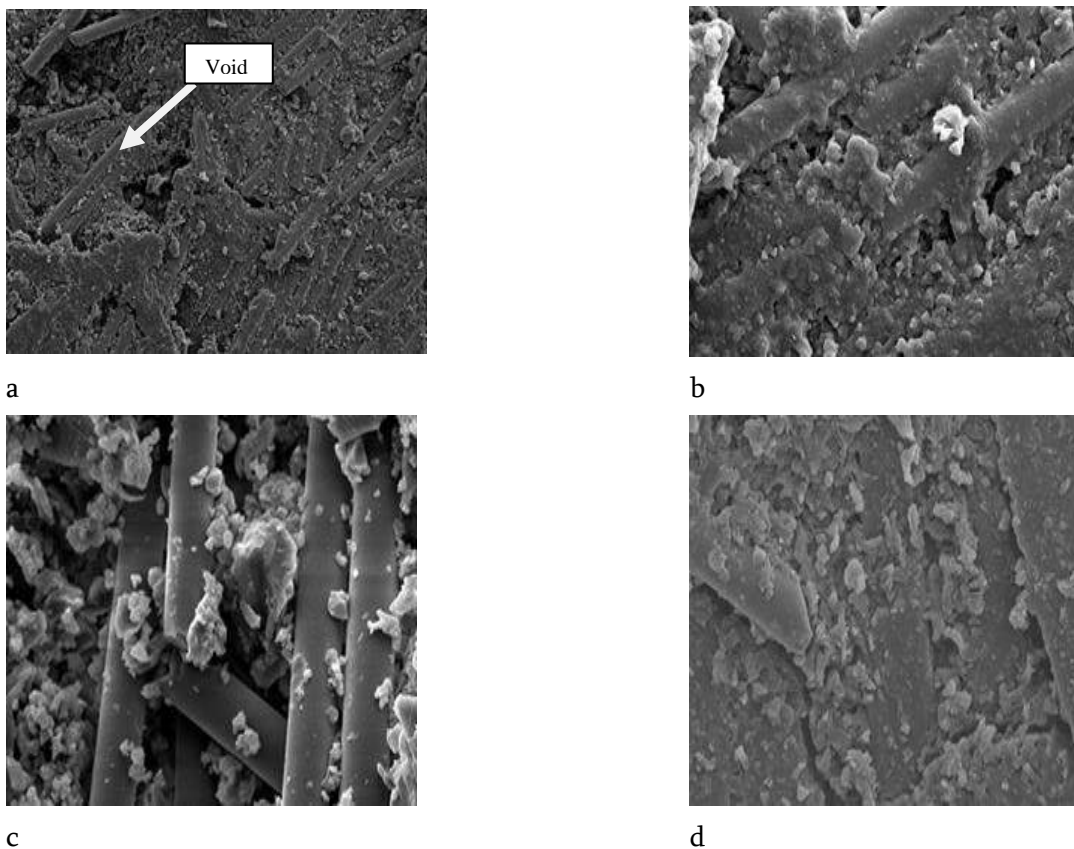


Figure 11: SEM images of composites without STF (a) C1 (b) C2 (c) C3 (d) C4

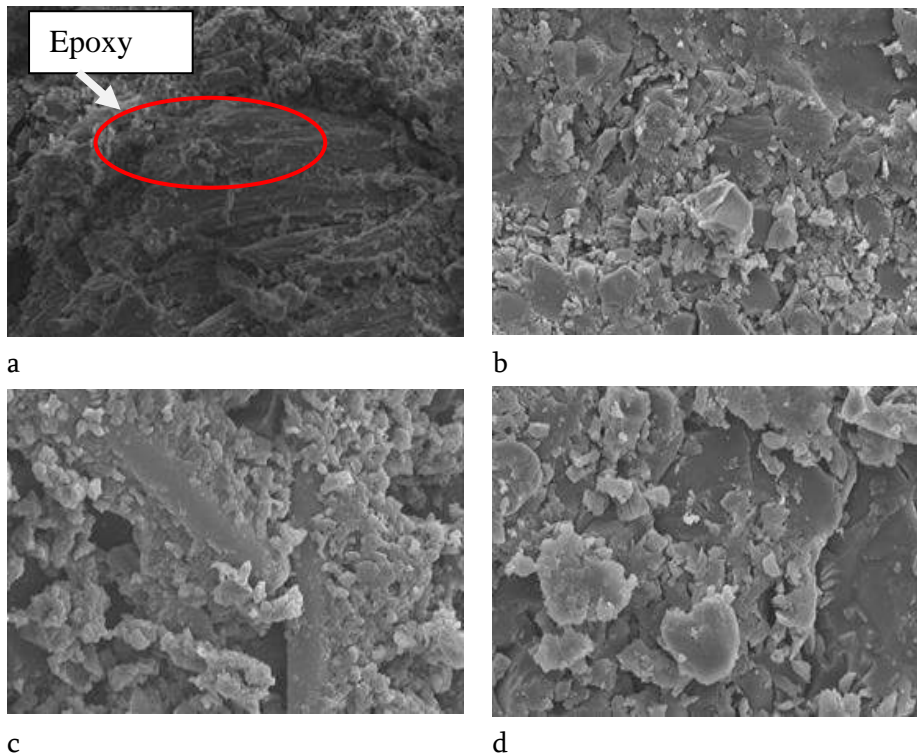


Figure 12: SEM images of composites with STF (a) CS1 (b) CS2 (c) CS3 (d) CS4

IV. CONCLUSION

Mechanical Properties such as tensile strength, percentage elongation, hardness, impact strength and Vibrational characteristic like natural frequency for the composites for varying fiber loading and effect of STF are studied and following conclusion were drawn: the hybrid composite CS1 shows better ultimate tensile strength, percentage elongation, hardness, impact strength and natural frequency in mode 1 indicating addition of STF increased mechanical properties. But the addition of higher jute wt % fiber to composites reduced the UTS, increased the impact strength making the composite potential to be used in automotives with impact application.

V. REFERENCES

- [1]. W. D. Callister, "Materials science and engineering: An introduction," Mater. Des., 1991.
- [2]. K. P. Ashik and R. S. Sharma, "A Review on Mechanical Properties of Natural Fiber Reinforced Hybrid Polymer Composites," J. Miner. Mater. Charact. Eng., vol. 03, no. 05, pp. 420–426, 2015.
- [3]. Y. Swolfs, I. Verpoest, and L. Gorbatikh, "Recent advances in fibre-hybrid composites: materials selection, opportunities and applications," Int. Mater. Rev., vol. 64, no. 4, pp. 181–215, 2019.
- [4]. P. V Senthil and A. Sirshti, "Studies on Material and Mechanical Properties of Natural Fiber Reinforced Composites," Int. J. Eng. Sci., pp. 2319–1813, 2014.

- [5]. M. Indra Reddy, U. R. Prasad Varma, I. Ajit Kumar, V. Manikanth, and P. V. Kumar Raju, "Comparative Evaluation on Mechanical Properties of Jute, Pineapple leaf fiber and Glass fiber Reinforced Composites with Polyester and Epoxy Resin Matrices," *Mater. Today Proc.*, vol. 5, no. 2, pp. 5649–5654, 2018.
- [6]. H. Raghavendra Rao, Y. Indraja, and G. Meenambika Bai, "Flexural Properties and Sem Analysis Of Bamboo And Glass Fiber Reinforced Epoxy Hybrid Composites \n," *IOSR J. Mech. Civ. Eng.*, vol. 11, no. 2, pp. 39–42, 2014.
- [7]. K. Abdurohman, T. Satrio, N. L. Muzayadah, and Teten, "A comparison process between hand lay-up, vacuum infusion and vacuum bagging method toward e-glass EW 185/lycal composites," *J. Phys. Conf. Ser.*, vol. 1130, no. 1, 2018.
- [8]. M. R. Abhishek, P. M. Suresh, and H. S. Sreedhar Murthy, "Evaluation of Mechanical Properties of Jute/E-Glass Epoxy Hybrid Composites by Varying Fibre Loading With And Without Shear Thickening Fluid," *Mater. Today Proc.*, vol. 4, no. 10, pp. 10858–10862, 2017.
- [9]. R. Joselin and W. J. Wilson, "Investigation on impact strength properties of kevlar fabric using different shear thickening fluid composition," *Def. Sci. J.*, vol. 64, no. 3, pp. 236–243, 2014.
- [10]. M. M. Davoodi, S. M. Sapuan, D. Ahmad, A. Ali, A. Khalina, and M. Jonoobi, "Mechanical properties of hybrid kenaf / glass reinforced epoxy composite for passenger car bumper beam," *Mater. Des.*, vol. 31, no. 10, pp. 4927–4932, 2020.
- [11]. R. Gujjala, S. Ojha, S. K. Acharya, and S. K. Pal, "Mechanical properties of woven jute-glass hybrid-reinforced epoxy composite," *J. Compos. Mater.*, vol. 48, no. 28, pp. 3445–3455, 2014.
- [12]. K. Fu, H. Wang, L. Chang, M. Foley, K. Friedrich, and L. Ye, "Low-velocity impact behaviour of a shear thickening fluid (STF) and STF-filled sandwich composite panels," *Compos. Sci. Technol.*, vol. 165, no. March, pp. 74–83, 2018.
- [13]. K. Yu, H. Cao, K. Qian, L. Jiang, and H. Li, "Synthesis and stab resistance of shear thickening fluid (STF) impregnated glass fabric composites," *Fibres Text. East. Eur.*, vol. 95, no. 6, pp. 126–128, 2012.
- [14]. S. Mutalikdesai, G. Sujaykumar, A. Raju, C. J. Moses, J. Jose, and V. Lakshmanan, "Mechanical Characterization of Epoxy/Basalt Fiber/Flax Fiber Hybrid Composites," *Am. J. Mater. Sci.*, vol. 7, no. 4, pp. 91–94, 2017.
- [15]. M. K. Gupta and R. K. Srivastava, "Mechanical, thermal and water absorption properties of hybrid sisal/jute fiber reinforced polymer composite," *Indian J. Eng. Mater. Sci.*, vol. 23, no. 4, pp. 231–238, 2016.
- [16]. M. R. Sanjay, G. R. Arpitha, L. Laxmana Naik, K. Gopalakrishna, and B. Yogesha, "Studies on mechanical properties of Banana/E-Glass fabrics reinforced polyester hybrid composites," *J. Mater. Environ. Sci.*, vol. 7, no. 9, pp. 3179–3192, 2016.
- [17]. M. M. Davoodi, S. M. Sapuan, A. Aidy, N. A. Abu Osman, A. A. Oshkour, and W. A. B. Wan Abas, "Development process of new bumper beam for passenger car: A review," *Mater. Des.*, vol. 40, pp. 304–313, 2012.
- [18]. ASTM D638-14, "Standard Test Method for Tensile Properties of Plastics," *ASTM Int. West Conshohocken, PA*, no. January, 2014.
- [19]. A. Zak, M. Krawczul, and W. Ostachowicz, "Vibration of a Laminated Composite Plate with Closing Delamination," *J. Intell. Mater. Syst. Struct.*, vol. 12, no. August 2001, pp. 545–551, 2001.

- [20]. S. S. Chavan and M. M. Joshi, "Study on vibration analysis of composite plate," *Int. J. Adv. Prod. Mech. Eng.*, vol. I, no. Viii, pp. 69–76, 2015.
- [21]. A. S. Bassiouni, R. M. Gad-Elrab, and T. H. Elmahdy, "Dynamic analysis for laminated composite beams," *Compos. Struct.*, vol. 44, no. 2–3, pp. 81–87, 1999.
- [22]. K. Senthil Kumar, I. Siva, P. Jeyaraj, J. T. Winowlin Jappes, S. C. Amico, and N. Rajini, "Synergy of fiber length and content on free vibration and damping behavior of natural fiber reinforced polyester composite beams," *Mater. Des.*, vol. 56, pp. 379–386, 2014.
- [23]. I. Mishra and S. K. Sahu, "An Experimental Approach to Free Vibration Response of Woven Fiber Composite Plates under Free-Free Boundary Condition," *Int. J. Adv. Technol. Civ. Eng.*, no. 2, pp. 67–72, 2012.
- [24]. B. Basanth Kumar, B. T. Chandru, P. M. Suresh, and B. H. Maruthi, "Numerical and Experimental Modal Analysis of Car Door with and without Incorporating Visco-elastic Damping," *Mater. Today Proc.*, vol. 5, no. 10, pp. 22237–22244, 2018.
- [25]. B. T. Chandru and P. M. Suresh, "Finite Element and Experimental Modal Analysis of Car Roof with and without damper," *Mater. Today Proc.*, vol. 4, no. 10, pp. 11237–11244, 2017.
- [26]. B. T. Chandru, P. M. Suresh, J. Sathya, and B. H. Maruthi, "Modal Analysis of Car Hood with Viscoelastic Damper," *Mater. Today Proc.*, vol. 5, no. 10, pp. 22293–22302, 2018.



Finite Element Analysis of Hybrid Biodegradable Composite

Praveenkumara B M¹, Vignesh Kumar R¹

¹Department of Mechanical Engineering, Vidyavardhaka College of Engineering Mysuru, Karnataka, India

ABSTRACT

Composites are defined as a mixture of two or more ingredients where one is called a matrix (larger in quantity) and the other is called reinforcement (smaller in quantity). Now a day's research is concentrated on various methods of making biodegradable composites where either reinforcement or matrix are biodegradable, or both are biodegradable. Composites have so many applications in industrial as well as commercial use due to their low weight to strength ratio that attracted the automobile manufacturers to use these materials in cars which in turn increases the efficiency as well as reduce the cost of the automobile. In this paper, an effort has been made to investigate the various process of manufacturing composites manufactured from banana fibres using different matrices preferably PLA (Polylactic Acid). The methods of improving the bonding between the reinforcement and matrix, effect of fiber orientation, size of the fibers and percentage reinforcement have been studied.

Keywords: Bio-degradable composite, Polylactic Acid, Layered solid, Deformation, FEA, Von Mises stress.

I. INTRODUCTION

In today's scenario, due to industrialization, environmental degradation is attracting people all over the globe to think about future materials that could be more sustainable and eco-friendlier in nature. These biodegradable plastics and other bio-based polymers when used as composites can replace the petroleum-based polymers in the market up to the large extent. Composites are classified as non-biodegradable and biodegradable. Biodegradable can be partially or fully depending upon the type of matrix and reinforcement[1].

During the past decades, researchers are shifting their interest to fibre-reinforced polymer composites due to many advantages such as great stability, easy fabrication method, low cost etc. by making the different compositions of fibers and polymers. The use of carbon, glass and graphite have been widely used synthetic fibers for many industries as well as domestic applications. Due to the environment, which concerns, every technology should be environment friendly. Therefore, the importance of natural fibers are increasing rapidly. Due to their environment-friendly nature, very low need of energy consumption during production of these fibers, degradable nature, renewable and low cost of these materials attracts researchers to develop new composites using natural fibers like jute, hemp etc. The use of natural fibers in the place of synthetic fiber like glass fiber can save 60% per ton of product. For fabricating biodegradable hybrid composite using hemp fiber,

bamboo fiber and jute fiber in epoxy as matrix materials, knowledge of their different characteristics is essential [2].

The full separation of natural fibers into elementary fibers is difficult to achieve and requires severe mechanical treatments of the fibers, which might introduce damages and degrade the properties of the reinforcement [3]. The amount of mechanical processing of the fibers in the separation step highly depends on how they were initially extracted from the plants. Typically, to facilitate the separation of the fiber from the stem, they are retted and then mechanically separated. However, the retting process is often not efficient enough. Therefore, the fibers should go through a harsh mechanical processing before they can be used. More recently, a more efficient extraction process, combining retting with a bacterial treatment, has been employed (e.g., flax produced by Fin flax in Finland) [4]. The bacterial treatment removes the residues of the plant more effectively and requires a less mechanical treatment afterwards to separate the fibers. This results in less damaged elementary natural fibers and with higher mechanical properties [5]. These fibers are further assembled in various types of reinforcement, such as mats, roving's, yarns, and other textile-like products (e.g. weaves, non-crimp fabrics). It should be noted that each extra processing step adds to the cost of the fibers. It also reduces the environmental friendliness aspect of these materials since they often undergo chemical treatments, in order to protect the natural fibers from moisture and to improve the compatibility with polymers [6]. Apart from the damage and defects introduced by pre-processing, natural fibers possess inherently irregular and somewhat unpredictable properties. These variations depend on the type of plant from which natural fibers are derived, the region of harvest and the annual weather conditions during the growth [7]. The variety influences not only the geometry of the fibers (diameter and length) but also the chemical composition, and consequently variability of the mechanical properties [8].

a. Problem statement

Increased use of plastic (or thermostat plastic) in day-to-day life has caused severe problems in recycling and reuse resulting the environmental pollution and has been hazardous to health.

b. Objective

The objective of this project is to fabricate the composite material using hybrid composite (bamboo sticks and pista shell) reinforced bio epoxy (Epibiox) to reduce the use of plastic and to overcome health problems & environmental pollution.

II. DESIGN AND EVALUATION

a. Flexural Test

The flexure test method measures the behaviour of materials subjected to simple beam loading. It is also called a transverse beam test with some materials. Maximum fiber stress and maximum strain are calculated for increments of load. Results are plotted in a stress-strain diagram. Flexural strength is defined as the maximum stress in the outermost fiber. This is calculated at the surface of the specimen on the convex or tension side. Flexural modulus is calculated from the slope of the stress vs. deflection curve. If the curve has no linear region,

a secant line is fitted to the curve to determine slope. The 3-point flexure test is the most common for polymers. Specimen deflection is usually measured by the crosshead position. Test results include flexural strength and flexural modulus. Flexural strength can be obtained from the following formula [9].

$$\sigma = 3PL / 2bd^3 \quad (1)$$

Where:

σ = flexural strength,

P = maximum load

L = Span length

b = Width

d =Thickness

b. Numerical Model

Geometrical model of jute composite, Indicated below are the established models. Fig.1 shows the solid model of the standard specimen Suggested by the American society for testing and materials ASTM D 790. Fig.2 shows the meshes for the E-glass fiber, the epoxy and E-waste as a filler material. Fig.3 shows the layered composite solid developed using the Ansys ACP Pre-post. In the reinforcement-matrix interface of the model, bonded contact conditions were established. The convergence of the numerical results was evaluated in terms of stress and Deformation.

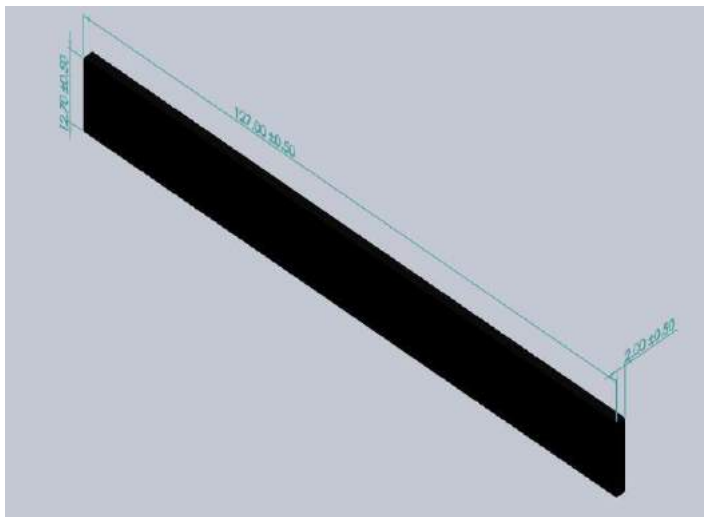


Fig:1 Solid Model(ASTM D790)

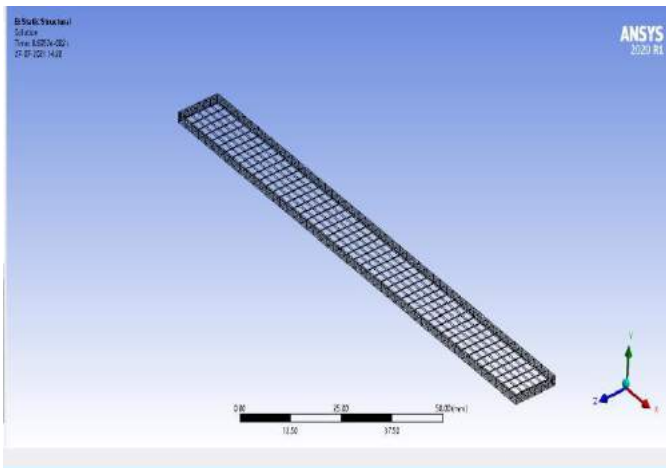


Fig:2 Meshed Model

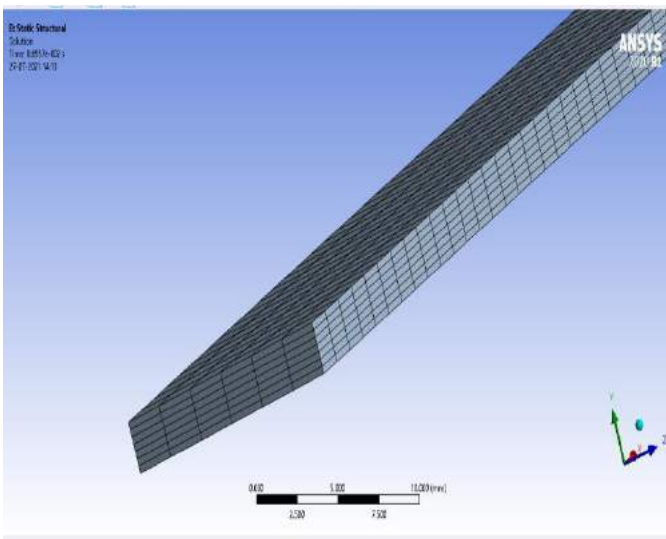


Fig: 3 Layered solid

Structural analysis was performed for stresses for all materials. So only these two parameters were considered for structural analysis. The result of this analysis evaluates the static failure condition of the specimen. In this part of structural analysis, the beam undergoes a 3 point flexural bending test, so the boundary conditions are different as compared to modal analysis of cantilever composite specimen.

c. Boundary conditions

For structural analysis 3-point flexural bending test is used for FEM analysis boundary conditions are applied in such a way in that two ends of plate are fixed and load is applied at center portion of plate.

d. Tensile Test

Tensile tests were performed to find out the in-plane tensile properties of polymer composites fabricated with matrix and reinforcements. In a broad sense, the tensile test is a measurement of the ability of a material to

withstand external forces that tend to pull apart and to what extent the material stretches before breaking. The dimensions were considered as per ASTM D638 standards.

The tensile strength of composites was calculated by using the following relation [9] .

$$\sigma = F / A \quad (2)$$

σ = tensile strength

P = maximum load

A = cross sectional area

e. Numerical Model

The geometrical model of Glass fiber, epoxy and E-waste composite materials, Indicated above are the established models. Fig.8 shows the solid model of the standard specimen Suggested by the American society for testing and materials ASTM D638. Fig.9 shows the meshed model of jute and epoxy composite material.

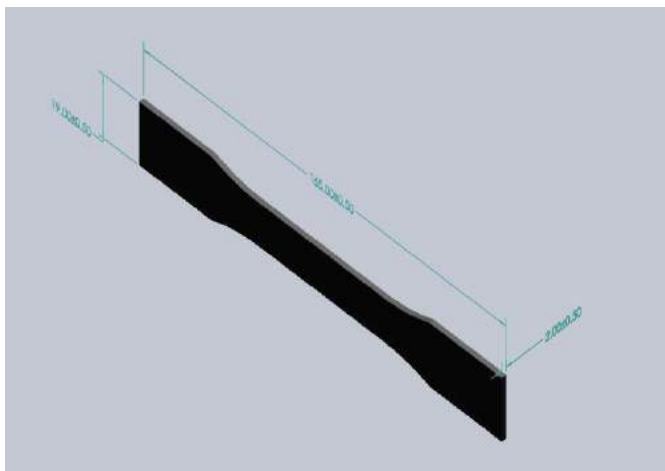


Fig: 4 Solid Model (ASTM D638)

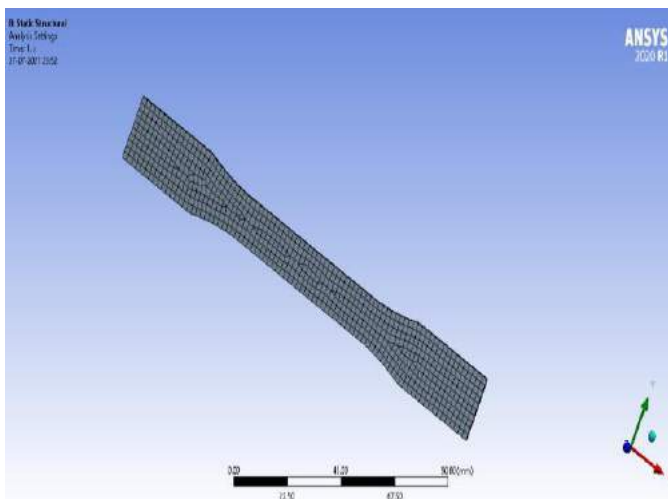


Fig:5 Meshed Model

III. RESULTS AND DISCUSSION

a. Analysis

Structural analysis was performed for stresses for all materials. So only these two parameters were considered for structural analysis. The result of this analysis evaluates the static failure condition of the specimen. In this part of structural analysis, the beam undergoes a 3-point flexural bending test, so the boundary conditions are different as compared to modal analysis of cantilever composite specimen.

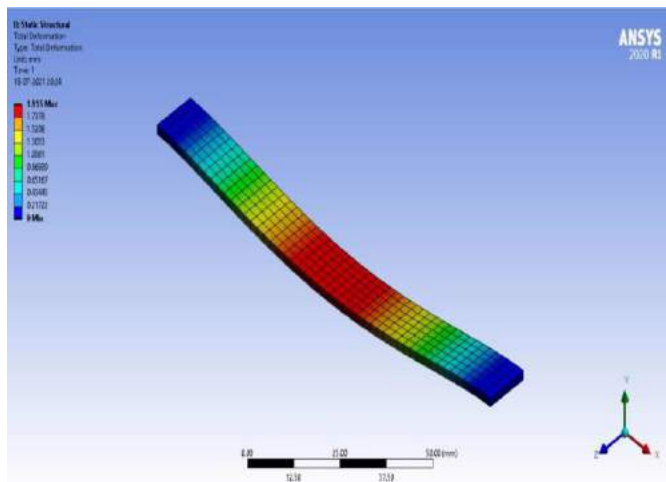


Fig: 6 Total Deformation (composite Material)

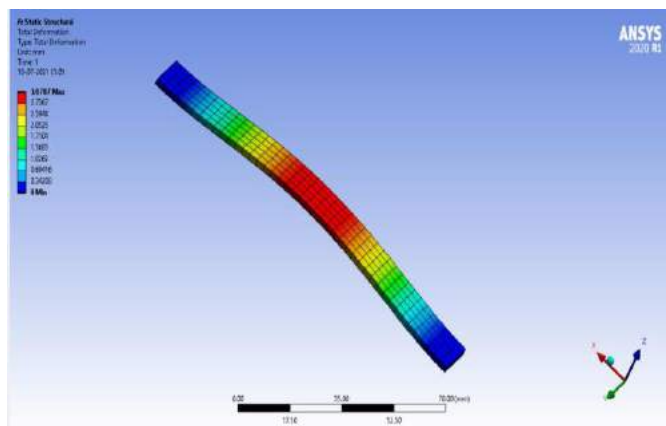


Fig: 7 Total Deformation (plastic Material)

A load of 1000 N is applied to obtain the Maximum Deformation on the composite. Fig.6 shows the maximum Deformation of composite material and Fig.7 shows the Maximum deformation in the plastic Material. As expected, composite material bears some of the stress and allows less deformation. load of the composite. The deformation is concentrated in the reinforcement-matrix interface, close to the end of the model, where the load is applied, thus, it could be expected that the material fails close to these zones. Where we observed less Deformation.

b. Equivalent Stress

Fig.8 and Fig.9 shows the von Mises stress distribution of composite and the plastic. As expected, composite material bears some of the load of the composite, since they support stresses near to 191.59 MPa, while in the absence they support average stress of 137.45 Mpa. The stresses are concentrated in the reinforcement-matrix interface, close to the end of the model, where the load is applied, thus, it could be expected that the material fails close where the boundary conditions are applied.

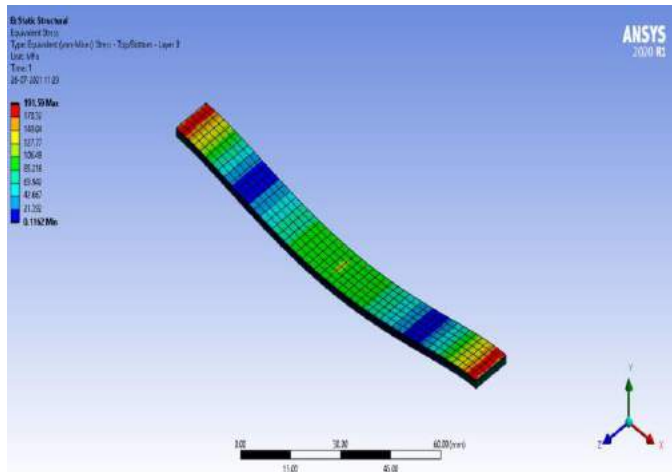


Fig:8 Equivalent Stress distribution (composite)

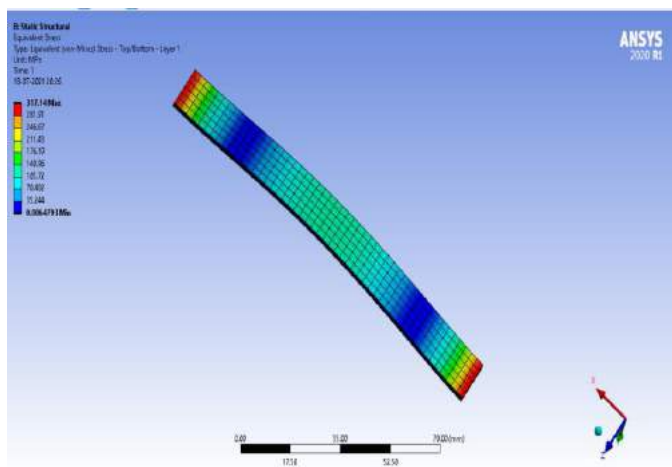


Fig:9 Equivalent stress distribution (plastic)

c. Total Deformation

A load of 1000N is applied to obtain the longitudinal deformation on the composite. Figure 10 shows the Max deformation of 0.8315 mm in composite and Figure 11 shows the Max deformation of 0.9 mm in the presence of filler material, from this we can conclude that deformation is less in the presence of filler material.

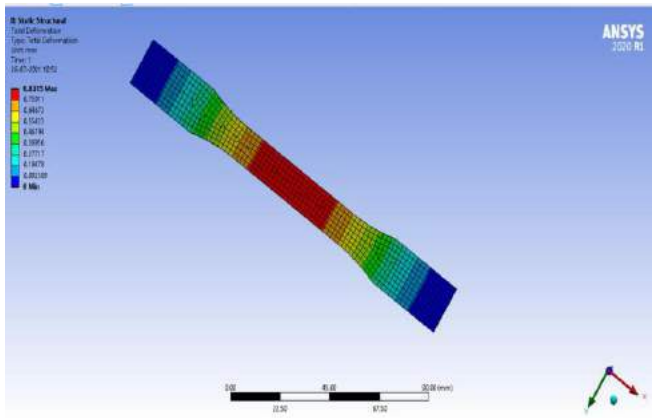


Fig: 10 Total Deformation (composite)

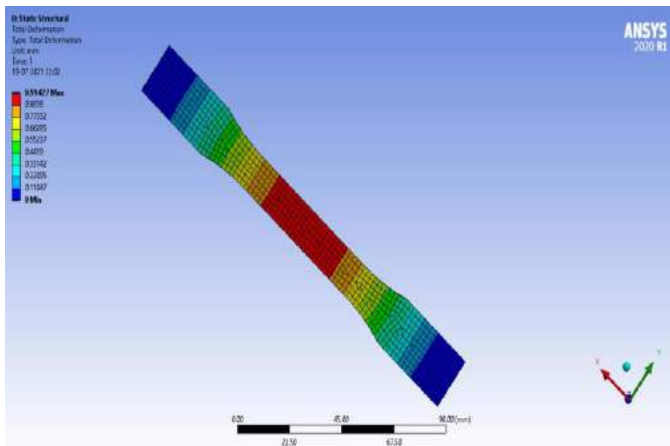


Fig: 11 Total Deformation (plastic)

d. Equivalent Stress

A load of 1000N is applied to obtain the Equivalent - stress on the composite. Figure 12 shows the Max stress of 40.3 Mpa in composite material. and Figure 13 shows the Max stress of 65.6652M pa in the plastic material , From this we can conclude that specimen can withstand more stress in the composite material than in the plastic material.

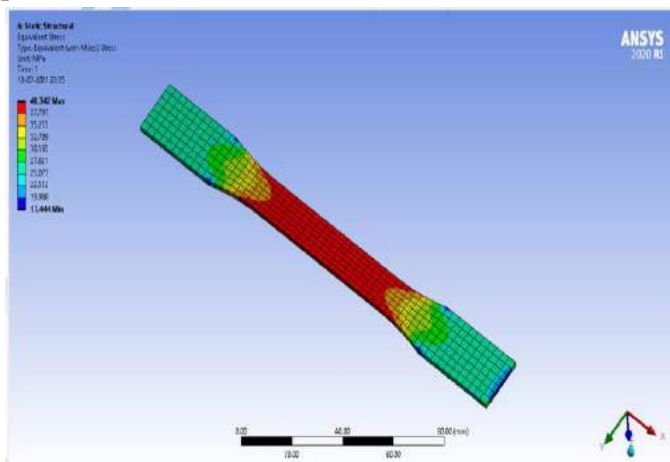


Fig:12 Equivalent Stress distribution (composite)

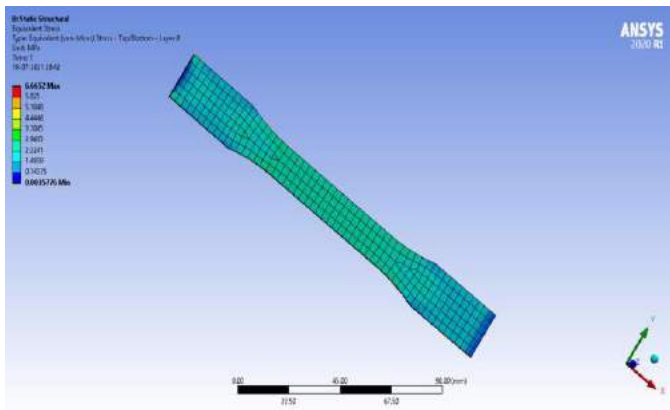


Fig:13 Equivalent stress distribution (plastic)

IV. CONCLUSION

Bio-degradable composite material using bamboo fiber is manufactured and designed according to the ASTM specimen in the solid works software and analyzed using Ansys fluent and static structural. On analysis, we can conclude that biodegradable composites are more useful than plastic material.

V. REFERENCES

- [1]. Satyanarayana KG, Arizaga GGC and Wypych F. biodegradable composite based on ligno cellulose fibres an overview.
- [2]. Masoodi R and Pillai KM. modelling the processing of natural fibre composites made using liquid composite molding.
- [3]. Shakeri A and Raghimi M. Studies on mechanical performance and water absorption of recycled newspaper/glass fibre reinforced polypropylene hybrid composites.
- [4]. Ashori A and Sheshmani S. Hybrid composites made from recycled materials.
- [5]. Chand N and Rohatghi PK. Natural fibres and their composites. Delhi.
- [6]. Hand dermatoses and contact allergic reactions in construction workers exposed to epoxy resins.
- [7]. John, M. J.; Thomas, S. Carbohydr. Polym. 2008, 71, 343.
- [8]. Javadi, A.; Srithep, Y.; Lee, J.; Pilla, S.; Clemons, C.; Gong, S.; Turng, L. Compos. Part A. 2010, 41, 982.
- [9]. Bledzki, A. K.; Jaszkievicz, A. Compos. Sci. Technol. 2010, 70, 1687.
- [10]. Pivsa-Art, S.; Srisawat, N.; O-Charoen, N. Energy Procedia. 2011, 9, 589.
- [11]. Martelli, S. M.; Sabirova, J.; Fakhoury, F. M. Food Sci. Technol. 2012, 47, 386.
- [12]. Lucchesi, C.; Ferreira, B. M. P.; Duek, E. A. R.; Santos, A. R., Jr.; Joazeiro, P. P. J. Mater. Sci Mater. Med. 2008, 19, 635.
- [13]. Hao, A.; Zhao, H.; Chen, J. Y. Compos. Part B 2013, 54, 44.
- [14]. Hao, A.; Zhao, H.; Jiang, W.; Yuan, L.; Chen, J. Y. J. Polym. Environ. 2012, 20, 959.
- [15]. Lucas, N.; Bienaime, C.; Belloy, C.; Queneudec, M.; Silvestre, F.; Nava-Saucedo, J. E. Chemosphere 2008, 73, 429.



Influence of Nano graphite based Vegetable oils as Cutting Fluids for Mild Steel Drilling

Viraja Deshpande¹, P.N. Jyothi²

¹Research Scholar VTU, R&D Mechanical Engineering, KSSEM, Bengaluru, Karnataka, India

²Professor, Department of Mechanical Engineering, KSSEM, Bengaluru, Karnataka, India

ABSTRACT

In last decades, a considerable attention is received by non-edible vegetable oils as Bio lubricant due to their eco-friendly products, increased remarkable improved tribological characteristics and as they are renewable sources. In this work, different vegetable oils namely Neem, sunflower, coconut, Karanja (Honge) and Neem oil (50% Neem & 50% Karanja) blend are used as cutting fluid for the drilling of Mild steel. The same vegetable oils with addition of Nano graphite powder are also used as Nano based bio-oils in the second stage experimentation. The effect on parameters of these cutting fluids like cutting temperature, cutting force, tool wear, chip formation, drilled hole surface roughness are studied. The results obtained are compared with petroleum based cutting fluids and at dry conditions. From the results, it is observed that the blend of 50% Neem and 50% Honge and sunflower oil is the best cutting fluid compared to other cutting fluids used in this work, more over these oils are environmentally friendly, non-hazardous, bio-degradable and economical.

Keywords: Mild Steel, Neem, sunflower, coconut, Karanja (Honge) and Neem oil (50% Neem & 50% Karanja) blend, Nano graphite powder

I. INTRODUCTION

During machining operation, relative motion between work piece and cutting tool produces the friction, resulting to generation of high temperature at the interface between tool- work piece and tool-chip. The heat generated decreases tool life, increases surface roughness and decreases the dimensional sensitiveness of work material. This case is more important when machining difficult-to-cut materials as heat would be observed. Various methods have been reported to protect cutting tool from the generated heat. Choosing coated cutting tools are an expensive alternative and generally it is a suitable approach for machining some materials such as titanium alloys, heat resistance alloys etc. The application of cutting fluids is another alternative that can be used to increase the tool life and also higher material removal rates can be achieved which is as shown in figure 1.



Figure 1. Application of cutting fluids on drilling

They are used to provide lubrication and cooling effects between cutting tool and work piece and cutting tool and chip during machining operation resulting in lesser amount of heat generation. As a result, important benefits would be achieved such longer tool life, easy chip flow and higher machining quality in the machining processes using cutting fluids. A review was carried out by Lawal [1] on Application of vegetable oil-based metalworking fluids in machining ferrous metals. In the review, the advantages and performances of metal working fluids with respect to surface finish of the work piece, tool wear, cutting force and temperature at the cutting zone have been observed. The major focus is given on the performance and environmental impact of this vegetable oil as emulsion and straight oils for various materials and machining conditions. The effects of MQL on vegetable oil based cutting fluid under turning operation of low alloy steel AISI 9310 was investigated by Khan [2]. The results of dry and wet machining in terms of chip formation mode, tool- chip interface temperature, tool wear and surface roughness were compared. The Results showed that MQL provides improved machinability characteristics and environmental friendliness. A detailed work has been carried out on metal working fluids that are widely employed to increase the machining productivity and quality of metal cutting by Vaibhav Koushik [3], but the usage poses great threat to the ecology health of workers in industry. Therefore, it is needed to identify hazard free and eco- friendly alternatives to convention mineral oil-based material working fluid. An effort has been undertaken to provide highlights of vegetable oils over petroleum-based oils in this review paper. Many research works presented that vegetable oils have capable scope of their emergence as metal working fluids. Shaikh [4], determined the material removal rate (MRR) and influence of lubricant on surface roughness on AISI D2 Steel using CNC lathe machine. to determining and optimizing operating parameters, Taguchi method was used. The above experimentation results help practitioners to compare and increase MRR, surface finish using more environmentally friendly oil as lubricant. But it was found that, cutting fluid formulation became more complex as cutting operation became more severe. Lawal [5] has carried out research work on the application of vegetable oil based cutting fluids in machining nonferrous metals. The results obtained established that vegetable oil based cutting fluids are good metal working fluid. The formulation of vegetable based cutting fluids and machining with cutting fluids was carried out by Babur Ozcelik Emel kuram [6]. The characterization of chemical and physical analyses of these formulated cutting fluids are carried out. Experimental results show that Canola based cutting fluid gives the best performance due to its higher lubricant properties with respect to other cutting fluids with constant cutting conditions. Again, Babur Ozcelik Emel kuram [7] studied the Effects of vegetable-based cutting fluids on the wear in drilling.

Performances of three VBCFs developed from crude sunflower oil, refined sunflower oil, refined canola oil and commercial semi-synthetic cutting fluid are compared in terms of thrust force, tool wear and surface roughness during drilling of AISI 304 austenitic stainless steel .the HSSE tool was used. Experimental results showed, canola based cutting fluid gives the best performance due to its higher lubricant properties at the constant cutting conditions (spindle speed of 750 rpm and feed rate of 0.1 mm/rev) with respect to other cutting fluids. It maintains the reliability of machine functions and reduces the risk of failures. Lubricants provide smooth operation between movable parts of all machines. Vegetable bio lubricants are non-toxic, degradable, and renewable also possess good lubricating properties. A review has been carried out by Suhane [8], on edible oils as cutting fluids. There are papers, in which study has been done on non-edible oils such as castor, Karanja, Mahua as cutting fluids and proved to have a great potential as lubricant for some of the machining operations.

II. MATERIALS, METHODS AND EXPERIMENTAL DETAILS

The experiments initially started in a medium duty lathe. The work piece is firmly held in a 3- jaw chuck at cutting speed of 775 rpm. The work piece is of AISI 1014 mild steel having diameter of 25mm with 70mm length. For drilling a HSS drill bit of diameter 13mm is used. Before drilling operation, the work piece was faced and turned for finishing in lathe and centring is done for all the work pieces using centre drill. The depth of the hole is 30mm with constant speed and feed. The drilling operation is carried out on a Radial drilling machine at 800 rpm at constant feed 0.1mm using blends of 50% Neem and 50%Karanja, Neem, Sunflower oil and Coconut oil with different percentages Graphite Nano power, petroleum- based oils as cutting fluids and also in dry condition.



Figure 2. Radial Drilling Machine

Cutting fluid is supplied using MQL (Minimum quantity lubrication) method. A drilling tool dynamometer is used while machining in order to find out the cutting force required for the drilling of mild steel using different cutting fluids. The specimen temperature and tool temperature are determined using Infra-Red thermometer by focusing the laser on to the specimen and tool. The chips obtained are collected and parameters are determined for those chips. The physical parameters of the chips are found using profile projector. The roughness of the machined surface is determined using surface roughness tester. The specimens are tested for hardness using Rockwell hardness tester to analyse heat transferred to the specimen during machining.

III. RESULTS AND DISCUSSIONS

A. Study of chips:

Chip formation usually depends on type of metal being machined i.e. whether brittle or ductile and temperature at the machining zone. The temperature generation is due to friction that exists between drill bit and the work piece. There may be breaking of chips due to chattering of work piece and due to overheating of work surface during the cutting process.

The chatter in the material is avoided by taking larger diameter work piece. the petroleum- based oil (SAE 20W40) lubrication is less, hence friction is more as seen in work piece temperature. Compared to all the oils, it is observed that for sunflower oil and blend of 50% Neem and 50%Honge has longer length continuous chips, indicating that temperature at machining zone is less as shown in the figure 2.

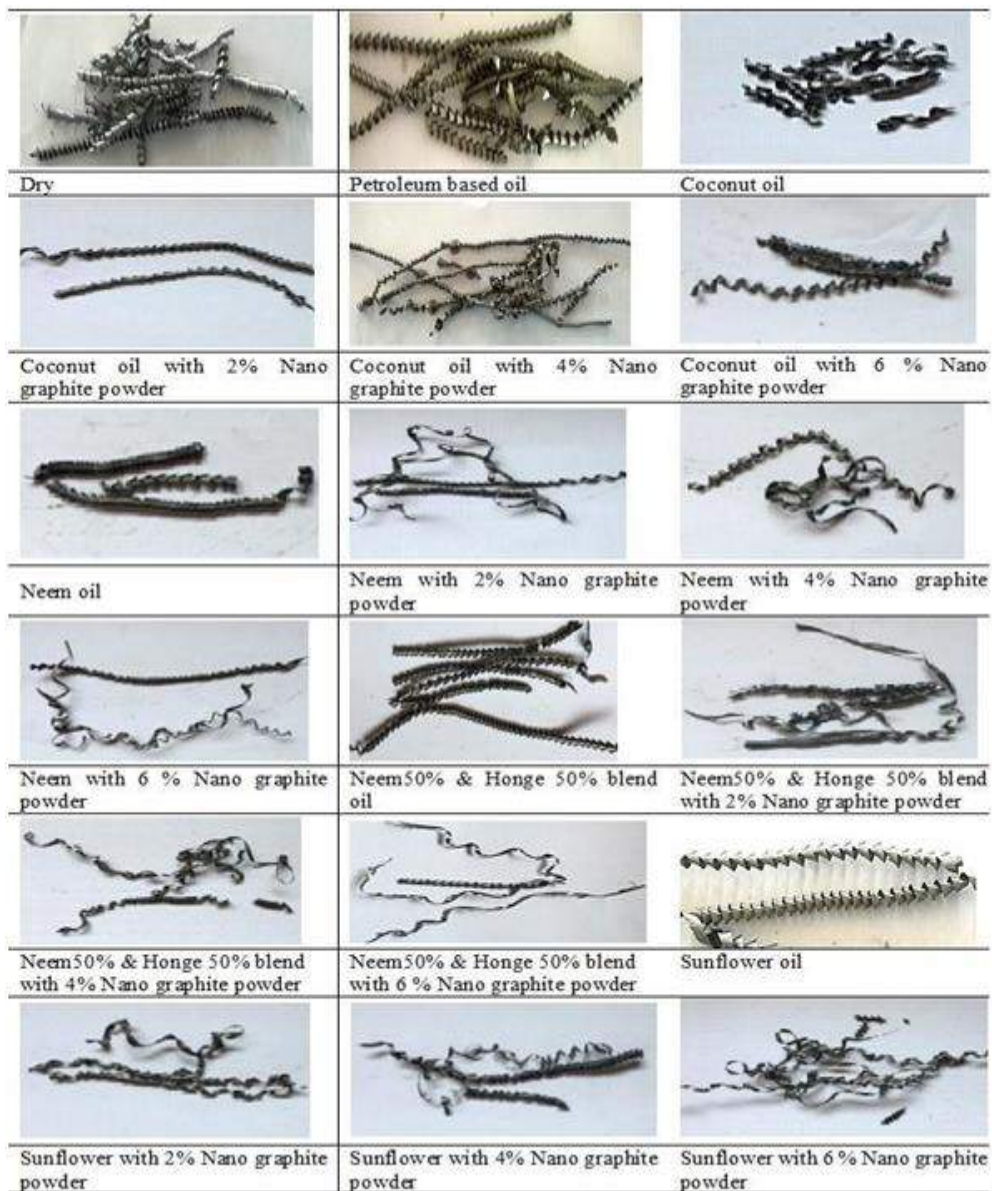


Figure 3.1: Chips formed with different colours by application of different cutting fluid and at dry condition

This can also be observed by the colour of the chip, which is not dark like obtained for other cutting fluids. The results show that sunflower oil and blends of 50% Neem and 50%Honge has good lubricating and cooling property.

During machining at dry cutting condition, the value of pitch height is too large and pitch is smaller amount, because of minimum control of the heat generated during the process. Instead of transferring heat to be the air and due to rotation; a heat zone is generated around the material surface. This has made too difficult in transferring the heat from the material to surrounding. With the use of petroleum based cutting fluids, there was increase in the value of pitch with reduction in pitch height. An improvement in surface finish was observed with this process. Increase in the pitch value and decrease in the pitch height showed that there was some improvement in the surface finish with work piece thickness. Due to excessive heat produced during the machining, surface of work piece material gets converted from ductile to brittle and the chip becomes discontinuous. This discontinues chips were observed for dry condition and when coconut oil is used as cutting fluid. With petroleum-based oil helped in reducing the heat but to a smaller extent. SAE 20W40 has better specific. The details of the chip obtained using different cutting fluids and during dry cutting condition are given in the table 1. Nano graphite powder addition increases the chip length, helps in absorbing more heat generated. Due to which metal surface becomes more soft and ductile resulting in longer continuous chip with less coil diameter and higher pitch length compared to pure oils used as cutting fluids, it is also seen that instead of coiled chip, with increase of graphite percentage from 2%,4% and 6% continuous ribbon chips are produced.

B. Colour of the chip

The colour of the chip represents the measure of the temperature obtained at the tool point. A blue temper colour on the surface of a chip formed in dry cutting represents that the tool point is hotter than chip which is obtained for cutting work piece with a fluid .the colour of the chip is uncoloured silvery. The best uncoloured silvery chip is formed when Neem50% & Honge 50% blend oil and sunflower oil are used as cutting fluid as shown in the Figure 3.1. For dry condition the chips are completely burnt i.e. dark colour indicating that maximum heat is transferred to work piece during machining. Chip details are tabulated in table 1.

C. Surface roughness of machined surface:

Surface finish usually depends on machining parameters like speed, depth of cut & feed, also on also on type of material being machined, type of cutting fluid used and also on type of tool material. In the present work all, the elements are constant but only cutting fluid used are been varied. The surface obtained after drilling using sunflower oil, coconut oil, Neem oil and Blend of 50% Neem and 50 % Honge oil and petroleum based SAE 20W40 as cutting fluids and also for dry drilling condition are shown in the Fig 3.2 (a). the effect of pure oils and addition of graphite nan powder in varying percentage of 2%, 4%, and 6 % to these oils as cutting fluid on the work surface can be observed clearly . From Fig 3.2(a) it can be seen that surface roughness obtained using pure sunflower oil and 50% Neem and 50 % Honge blend is very less with values as 1.664 and 1.663 respectively compared to other surfaces. Fig

3.2 (b) shows variation of surface roughness with application of different cutting fluids. Addition of graphite powder has not improved the surface finish even though it is soft and is been used as solid lubricant, but instead

as percentage of graphite powder is increased from 2%, 4% and 6%, the surface roughness is also increasing as compared to surface obtained using pure oil. This may be due to formation of brittle layer by the graphite powder at the cutting temperature. Therefore as graphite percentage is increased, brittle ness of the surface also increases resulting to rough surface. From the measured value and from the figure 3.2, it can be observed that surface roughness obtained for sunflower oil and 50% Neem and 50 % Honge blend is very less compared to other vegetable oil, Nano based vegetable oil and SAE 20W40 oil used as cutting fluids.

Table 1: Details of chips formed during drilling operation on Mild steel with different cutting fluids

Sl . No	Type of cutting fluid	Length (mm)	Thickness (mm)	Coil Diameter (mm)	Pitch length (mm)
1	Coconut oil	3	0.16	6.03	128
2	Coconut oil with 2% Nano graphite powder	3.97	0.3	5.68	185
3	Coconut oil with 4% Nano graphite powder	4.00	0.39	5.57	110
4	Coconut oil with 6 % Nano graphite powder	4.15	0.34	5.33	160
5	Neem oil	2.30	0.35	6.99	180
6	Neem with 2% Nano graphite powder	2.38	0.41	6.84	175
7	Neem with 4% Nano graphite powder	2.65	0.32	6.18	174
8	Neem with 6 % Nano graphite powder	3.19	0.36	6.23	123
9	Neem50% & Honge 50% blend oil	4.27	0.35	6.08	85
10	Neem50% & Honge 50% blend with 2% Nano graphite powder	4.83	0.38	6.59	120
11	Neem50% & Honge 50% blend with 4% Nano graphite powder	4.86	0.45	6.72	213
12	Neem50% & Honge 50% blend with 6 % Nano graphite powder	4.88	0.44	6.92	213
13	Sunflower oil	4.06	0.57	6.06	195
14	Sunflower with 2% Nano graphite powder	4.38	0.42	6.08	120
15	Sunflower with 4% Nano graphite powder	4.43	0.41	5.99	133
16	Sunflower with 6 % Nano graphite powder	4.27	0.35	5.95	157
17	Petroleum based oil	1.9	0.25	6.4	513
18	Dry Condition	1.1	0.21	4.45	266

		
Dry	Petroleum based oil	Coconut oil
		
Coconut oil with 2% Nano graphite powder	Coconut oil with 4% Nano graphite powder	Coconut oil with 6 % Nano graphite powder
		
Neem oil	Neem with 2% Nano graphite powder	Neem with 4% Nano graphite powder
		
Neem with 6 % Nano graphite powder	Neem50% & Honge 50% blend oil	Neem50% & Honge 50% blend with 2% Nano graphite powder
		
Neem50% & Honge 50% blend with 4% Nano graphite powder	Neem50% & Honge 50% blend with 6 % Nano graphite powder	Sunflower oil
		
Sunflower with 2% Nano graphite powder	Sunflower with 4% Nano graphite powder	Sunflower with 6 % Nano graphite powder

Figure 3.2(a): Worn surface of machined Specimen with different cutting fluids and at dry condition

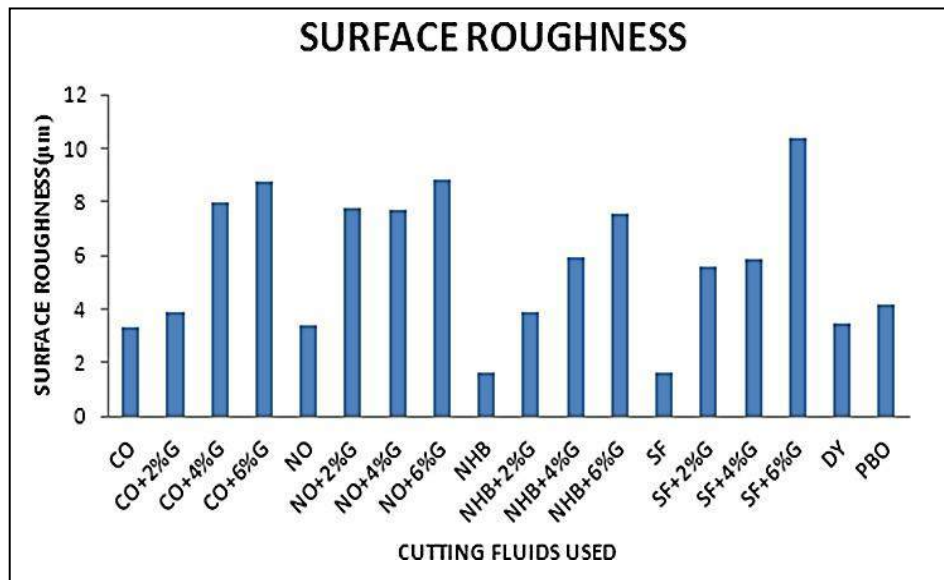


Figure 3.2 (b): Graph of surface roughness measured using different cutting fluids and at dry condition

D. Cutting Temperature

To increase tool life, there should be decrease in heat absorption by the tool. This can be achieved by use of good cutting fluid which absorbs maximum heat from the machining zone, giving very less heat to tool and the work piece. Due to heat generation, the machining accuracy will also be affected along with varying the properties of work piece. Figure 3.3 shows, Temperature measured at tool and work piece interface using different cutting fluid and at dry cutting condition. For dry condition temperature of tool and work piece is 122 °C which is very high. This is due to the transfer of heat generated to tool and work piece as no coolant is used and also due to high friction between tool and work piece as no lubricant is used. The temperature measured for both tool and the work piece for SAE 20W40 oil are 101°C, which is less compared to dry cutting but higher than non-edible oils used, this is due to its lower adhesiveness and lower dynamic viscosity. For 50%Neem, 50%Honge blend and sunflower oil, the cutting temperature is 74°C which is less compared to other measured values obtained using other vegetable and Nano graphite-based vegetable oils. This is due to high specific heat, high adhesiveness and higher dynamic viscosity. Indicating that, sunflower oil and blend of 50% Neem and 50% Honge oil has better cooling and good lubricating property. Graphite addition with varying percentage of 2%, 4% and 6% has not reduced the cutting temperature but instead it increases slightly with increasing percentage. From Fig 3.3 it can be seen that as graphite percentage increases temperature also increases slightly this may be due to properties of graphite. Graphite is a good lubricant but not a good coolant.

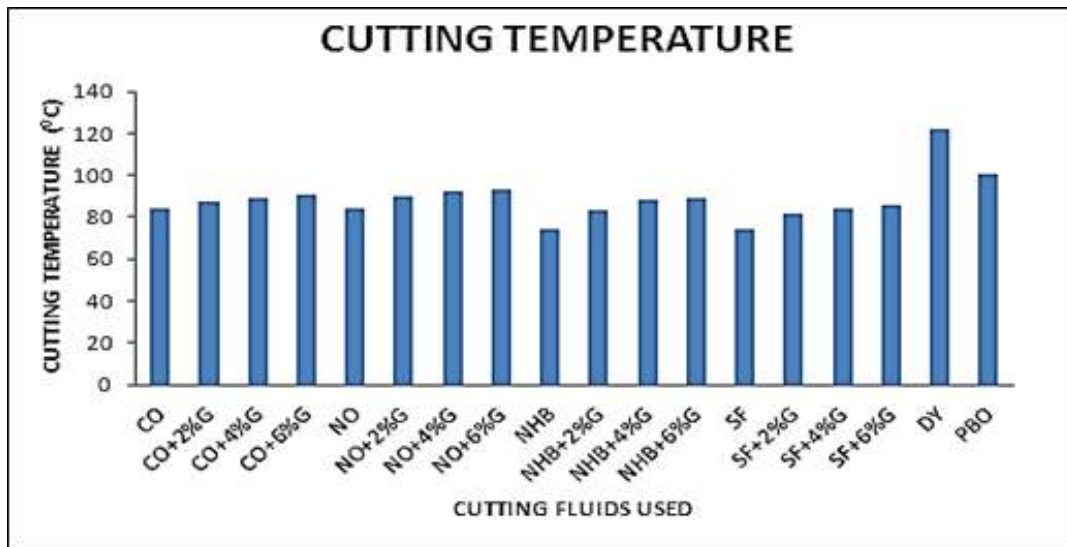


Figure 3.3: Graph of cutting temperature measured using different cutting fluids and at dry condition

E. Hardness Test

Hardness can be determined by forcing an indenter on to the surface. The resultant deformation in steel is both elastic and plastic. The hardness values of all the specimens before drilling and after drilling operation using different cutting fluids are determined using Rockwell hardness tester and the results are tabulated in the table 2.

If cutting fluid is not used, the Heat generated during drilling operation due to friction between the work piece and drill bit is given out to tool, chip and work piece. If the maximum heat is given to tool, then the tool wear is observed leading to reduction in tool life and if it is given to work piece then the mechanical properties will be affected. The function of good cutting fluid is to absorb and carry away the heat generated in the machining zone. From table 2, it can be observed that hardness measured on the work surface before drilling is 79HRB. For dry condition temperature given to work piece is more due to which after drilling hardness value measure is 84 HRB. This is very high compared to hardness value measured before drilling, which indicates that the metal surface has become very brittle increasing its hardness because it has absorbed more heat during machining. Lowest hardness value is measured for work material drilled using sunflower and Neem-Honge blend followed by coconut and Neem and petroleum based oil.

Addition of graphite powder to pure vegetable oil has slightly increased hardness. From the table 2, it can be observed that as graphite percentage is increased from 2%, 4% and 6% hardness value is slightly increased. This may be due to graphite acting as lubricant but not as coolant resulting to higher heat transfer to work-piece making surface brittle.

Table 2: The hardness values of all the specimens before drilling and after drilling operation using different cutting fluids and at dry condition

Sl.No	Type of cutting fluid	Hardness before drilling	Hardness after drilling
1	Coconut oil	79	82.5
2	Coconut oil with 2% Nano graphite powder	79	82.6
3	Coconut oil with 4% Nano graphite powder	79	82.3
4	Coconut oil with 6 % Nano graphite powder	79	83.3
5	Neem oil	79	83
6	Neem with 2% Nano graphite powder	79	83.3
7	Neem with 4% Nano graphite powder	79	83.3
8	Neem with 6 % Nano graphite powder	79	82.6
9	Neem50% & Honge 50% blend oil	79	82
10	Neem50% & Honge 50% blend with 2% Nano graphite powder	79	82.3
11	Neem50% & Honge 50% blend with 4% Nano graphite powder	79	82.6
12	Neem50% & Honge 50% blend with 6 % Nano graphite powder	79	83
13	Sunflower oil	79	82
14	Sunflower with 2% Nano graphite powder	79	82
15	Sunflower with 4% Nano graphite powder	79	83
16	Sunflower with 6 % Nano graphite powder	79	83
17	Dry	79	84
18	Petroleum Based oil	79	82.6

F. Cutting Force

In the present work different types of cutting fluid are been used keeping cutting speed, feed as constant parameters. to know the efficiency of cutting fluid used, Cutting force is considered as one of the measuring parameter. With respect to work piece, cutting force is the measure of resistance offered by the work piece during machining process. Cutting force is less if drill bit enters work-piece smoothly. Therefore a good cutting fluid should reduce the cutting force during the machining operation resulting in lesser mechanical stress in the work piece. Figure 3.5 below shows the cutting force measured during drilling of mild steel at constant speed and feed using Drill tool dynamometer.

During machining process, cutting force depends on the friction between the tool and work piece. More cutting force accumulates more heat in the work material and makes it soft for further processing. Cutting force refers to the force applied by the tool to shear the work- piece, greater the force greater will be the power consumption and lesser will be the tool life. It depends on type of material being machined, type of cutting fluid used, type of tool material and machining parameters. In the present work since all the elements are kept constant and only cutting fluid is changed, cutting force measured will be based on cutting fluid used. Figure 3.5 gives cutting force measured during drilling using sunflower oil, coconut oil, Neem oil and Blend of 50% Neem and 50 % Honge oil and petroleum based SAE 20W40 as cutting fluids and also for dry drilling condition

also with addition of graphite Nano powder in varying percentage i.e. 2,4, 6%. It is observed from Figure 3.5 that force required for shearing the work piece material in case of sunflower oil (220N) and 50% Neem and 50 % Honge blend (223N) is less compared to other vegetable oil, SAE 20W40 oil used as cutting fluids and also for dry cutting condition, next followed by Neem oil. It is being observed that, during dry machining, the cutting force was increased because oexcess of heat generation by the friction. it is observed that the cutting forces were reduced gradually during petroleum based (SAE20W40) oil based machining due to the interface of petroleum based lubricant in between tool and work piece and in this process the petroleum based oil acts as coolant but not as lubricant. Graphite powder addition to these bio oils in varying percentage of 2%, 4% and 6%, reduces the force required by the tool for shearing. This may be due to softness of graphite powder which makes the tool to move in to the work piece very smoothly and with lesser force. As the graphite powder percentages increases the cutting force required gets reduced. Hence it is used as solid lubricant.

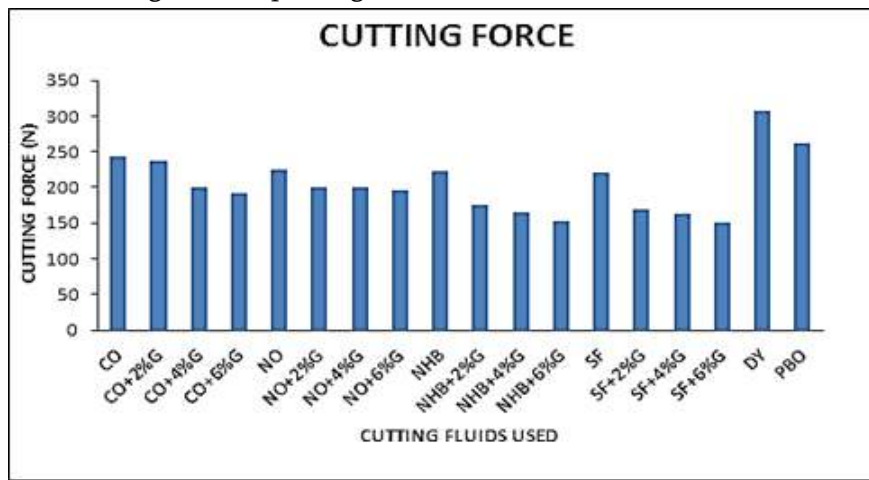


Figure 3.5: Graph of cutting force measured using different cutting fluids and at dry condition

G. Tool Wear Studies

Removal of material from the tool surface due to abrasive action is called as wear. Wear may be due to friction between two contacting surfaces of materials such as micro-ploughing, micro cutting, fracture, plastic deformation and melting, welding and chemical interaction. Various forms of tool wear on the drill tools are crater wear, flank wear, chisel edge wear and chipping. Wear on the flank of a cutting tool is caused by friction between the newly machined work material surface and the contact area on the tool flank. The width of the wear land is usually taken as a measure of the amount of wear. The wear pattern is irregular along the edge of the tool. The chipping wear leads to a catastrophic failure early in the life of the tool which masks the failure mode. Mechanical issues such as part fixture or machine spindle vibration will contribute to chipping wear. Higher loads on the tool will cause chipping.

Tool wear depends on type material machined; machining parameters like feed, speed and depth of cut; cutting fluids used, working and tool holding devices and so on. In the present work all the elements are kept constant and only the cutting fluids are changed. Wear of the drill bit depends on only the cutting fluids used as only cutting fluids are variable in the present work keeping all other elements constant. Figure 3.6 shows worn out surface of drill bit at chisel edge and drill bit point. For dry cutting condition, drill point is worn out as heat generated is high due to the friction between tool and work piece. Whereas in case of Petroleum based oil, loss

of material at drill point is less compared to dry condition. Tool wear is less when sunflower oil and 50% Honge and 50% Neem blend is used as cutting fluid and not much wear is observed when pure oils is used as cutting fluids compared to dry and petroleum based oil. From the Figure 3.6 below it can be observed that Nano graphite powder addition to these vegetable oils with varying percentage of 2%, 4% and 6% results in slight loss of tool material at drill bit chisel edge and also leads to sticking of chip to the tool.

		
Dry	Petroleum based oil	Coconut oil
		
Coconut oil with 2% Nano graphite powder	Coconut oil with 4% Nano graphite powder	Coconut oil with 6 % Nano graphite powder
		
Neem oil	Neem with 2% Nano graphite powder	Neem with 4% Nano graphite powder
		
Neem with 6 % Nano graphite powder	Neem50% & Honge 50% blend oil	Neem50% & Honge 50% blend with 2% Nano graphite powder
		
Neem50% & Honge 50% blend with 4% Nano graphite powder	Neem50% & Honge 50% blend with 6 % Nano graphite powder	Sunflower oil
		
Sunflower with 2% Nano graphite powder	Sunflower with 4% Nano graphite powder	Sunflower with 6 % Nano graphite powder

Figure 3.6 : Tool wear using different cutting fluids and at dry condition

IV. CONCLUSIONS

EXPERIMENTAL RESULTS during drilling of mild steel work piece using sunflower oil, coconut oil, Neem oil, SAE20W40 (petroleum based oil) and blend of 50% Neem- 50% Honge oil, dry cutting condition and also with addition of varying percentage of graphite powder i.e. 2%, 4% and 8% to sunflower oil, coconut oil, Neem oil and blend of 50% Neem- 50% Honge oil given following results and conclusions.

CUTTING FORCE: when sunflower oil is used as cutting fluid, the cutting force measured was 220N and for 50% Neem and 50 % Honge blend it was 223N which is less compared to cutting force measured during dry cutting condition and also using other vegetable oil and SAE 20W40 oil as cutting fluids.

CUTTING TEMPERATURE: the temperature of tool and work piece for dry condition is 1220C which is very high. the temperature measured at tool and work interface For SAE 20W40 oil is 101°C, which is less compared dry cutting but higher than non-edible oils used. Whereas for 50%Neem, 50%Honge blend and sunflower oil, the cutting temperature 74°C which is less compared to other measured values obtained using other vegetable and Nano graphite-based vegetable oils

HARDNESS: For dry cutting condition heat given to workpiece is more due to which after drilling, hardness value measure is 84 HRB which is very high compared to hardness value measured before drilling. Lowest hardness value is measured for workpieces drilled using sunflower and blend of 50% Neem and 50%Honge followed by coconut and Neem and petroleum-based oil.

STUDY OF CHIPS FORMED: when Sunflower oil and blend of 50% Neem and 50%Honge is used as cutting fluid, longer length continuous chips were produced, indicating that temperature at machining zone is less. For other oils used, heat produced during machining converts from the surface from ductile to brittle resulting to discontinuous chips

COLOR OF THE CHIPS: The best uncolored silvery chip is formed when sunflower oil and Neem50% & Honge 50% blend oil are used as cutting fluid, which indicates that sunflower oil and blends of 50% Neem and 50%Honge has good lubricating and cooling property **SURFACE ROUGHNESS:** surface roughness obtained using pure sunflower oil and 50% Neem and 50 % Honge blend is very less with values as 1.664 and 1.663 respectively compared to other surfaces. Addition of graphite powder has not improved the surface finish even though it is soft and is been used as solid lubricant, but instead as percentage of graphite powder is increased from 2%, 4% and 6%, the surface roughness is also increasing as compared to surface obtained using pure oil.

TOOL WEAR: For dry cutting condition, drill point is worn out as heat generated is high due to friction between tool and work piece. Whereas in case of Petroleum based oil, loss of material at drill point is less compared to dry condition. Tool wear is less when sunflower oil and 50% Honge and 50% Neem blend is used as cutting fluid and not much wear is observed when pure oils is used as cutting fluids compared to dry cutting conditions and when petroleum-based oil and Nano based oils used as cutting fluids.

From the above results it was found that the blend of 50% Neem and 50% Honge and sunflower oil are the best cutting fluid compared to other cutting fluids used in this work, more over it is environmentally friendly, bio-degradable, non-hazardous and economical. The addition of graphite Nano powder to these cutting fluids acts as good solid lubricant but not contributed to decrease surface finish of the work-piece

V. REFERENCES

- [1]. A. L. S., "A Review of Application of Vegetable Oil-Based Cutting Fluids in Machining Nonferrous Metals," *Indian Journal of Science and Technology*, vol. 6, no. 1, pp. 113- 118, 2013.
- [2]. M. M. A. Khan, "Effects of minimum quantity lubrication on turning AISI 9310 alloy steel using vegetable oil based cutting fluid," *Journal of Materials Processing Technology*, pp. 5573- 5583, 2009.
- [3]. V. K. A.V, "Vegetable Oil-Based Metal Working Fluids-A Review," *International Journal on Theoretical and Applied Research in Mechanical Engineering*, pp. 2319- 3182, 2012.
- [4]. J. B. Shaikh, "Experimental Investigation and Optimization of Process Parameters in Turning of AISI D2 Steel using Different Lubricant," *International Journal of Engineering and Advanced Technology*, pp. 189-197, 2014.
- [5]. I. C. S.A. Lawal, "Application of vegetable oil-based metalworking fluids in machining ferrous metals—A review," *International Journal of Machine Tools and Manufacture*, vol. 52, pp. 1- 12, 2012.
- [6]. P. E. Babur Ozcelik Emel kuram, "Effects of vegetable-based cutting fluids on the wear in drilling," *Indian Academy of Sciences*, vol. 38 , no. 4, p. 687–706, 2013.
- [7]. P. E. Babur OzcelikEmel kuram, "Effects of vegetable-based cutting fluids on the wear in," *Indian Academy of Sciences*, vol. 38, no. 4, p. 687–706, 2013.
- [8]. J. K. Suhane, "The Prospects of Vegetable Based Oil as Metal working Fluid in Manufacturing Application-A Review," *International Journal of Engineering Research and*, vol. 3, no. 5, pp. 2196-2202, 2014.



Design of Reconfigurable Manufacturing Systems : A Review

N Swamy¹, Dr. U M Daivagna², Dr. A Thimmana Gouda¹, Dr. Veerabhadrappe Algur¹

¹Department of Mechanical Engineering, Rao Bahadur Y mahabaleshwarappa Engineering College, Ballari - 583104, Karnataka, India

²Department of Mechanical Engineering, Ballari Institute of Technology and Management, Ballari-583104, Karnataka State, India

ABSTRACT

Only one thing is constant in this great world: Change. In today's environment change has also become a constant. While change is necessary, to construct and acquire it with competence by implementing excellent plans and generating attractive change by enabling agents. The global is evolving, leading in volatile market situations. The manufacturing system's act is often subjected to the potential to be soft as well as conflicting. A Reconfigurable Manufacturing System (RMS) is intended for quick adjustments in skills of production and quality as a way of improving economic conditions and periodic growth. With competitive environment consumers becoming more intensive nature, a reconfigurable production system delivers expandable flexibility in a brief span of time. This review paper is a honest effort to understand and comment on the concept of RMS. Also, RMS's primary goal in increasing performance and efficiency facilitates the implementation of reconfigurable manufacturing systems, which aim to reach cost-effective and rapid system changes required in a short period of time.

Keywords: RMS, Flexibility, Efficiency.

I. INTRODUCTION

In this competitive world only one thing is stable – Change. In today's manufacturing environment, innovation has become a permanent. While change is essential, it is important to maximize on it and make it happen effectively through sound design and planning of effective change accelerators. The current world is developing, leading to a unpredictable market condition. Manufacturing is the process of converting raw materials and input pieces into finished products by the use of resources such as machines, equipment, energy, and labour. The configurations and requirements of resources, referred known as manufacturing systems, must be constructed in order to perform efficiently and meet demands of the market. Even though today's manufacturing is facing so many challenges such as unpredictable demand, requirement of variety of products, increasing product quality, process technology, rapid development cost effectiveness and reducing lead time. Presented with the abovementioned constraints, Hendry Ford outlined moving assembly lines in 1913, opening

up in mass production processes. In the 1940's John T. Parson's worked closely with MIT and invented numerical control systems which started to support mass production with a cost effective system. Later in 1970's the era of lean manufacturing and its principles have started which helped in producing a consistent products, in late 1970's the advances in Computer Numerical Control System (CNC) machines enabled the use of a central production system to produce a wide range of components. During the era of economies of scale, the 1970s, organizations sought cost advantages gained via size. As a result, manufacturing systems incorporated some specific techniques that produced a limited range of products at a large number. This is related as a dedicated manufacturing line in the manufacturing system. Due to significant changes in the market in 1980s, the focus shifted from mass production for a single product to mass customization and greater adaptability to product changes. As an outcome, production systems were comprised of adaptive technology that satisfied medium volume and output criteria. This decade was described and labeled as economy; the facilitators for the period are numerical control, programmable logic control, robots, AGV's, and automated material handling systems this constituted Flexible Manufacturing Systems (FMS). However, FMS is still inadequate because of production losses and long production times even though machines are open source rather than specially designed. They are also a very costly approach, because FMS provides generic flexibility; Such that, an FMS system would integrate all possible functionality into the system anticipation. They are developed before the process plan has been finalized. As a response, a future era of system called as reconfigurable manufacturing system (RMS) is being established to generate as much adaptability as FMS and expandable capacity as DML as possible. RMS is a machine system that may be built by combining fundamental process modules, both hardware and software, that can be easily and precisely ordered or replaced. The secret of implementing RMS is to develop the system and its components with variable system which allows for scalability in volume and efficiency.

In RMS, Configurations are established over an increased product family and the unique adaptability needed to produce the entire specified extensive product group. In other words, commodities are first classified into subcategory; all of these need a separate software structure. The controller is programmed to generate the very initial item subcategory. When it is done, the system is revised to create the 2nd subcategory, and so on.

II. TYPE OF MANUFACTURING SYSTEM

I) Machine System

One or more cutting machine tools, along with tooling and required equipment, that works in conjunction to produce the specified volume and quality.

II) Dedicated Machining Systems

This is a manufacturing system that employs a transfer line with a static tool and automation to produce a specified item. The aim is to create one single component in big amounts but with the good standards at a low cost.

III) Flexible Manufacturing System

This is a machine system having basic components but changeable software that can modify tasks, manufacturing schedules, part programs, and tooling for multiple parts. The vision is to create parts at a

minimal cost that could vary with time, with a rapid variation, employing the same system at the required amount and quantity.

IV) Reconfigurable Manufacturing System

A reconfigurable manufacturing system (RMS) is one that has been created to enable for significant changes in its structure, including hardware as well as software, in order to ensure effective configure its rate of production and abilities within a product family in response to current changes in the market.

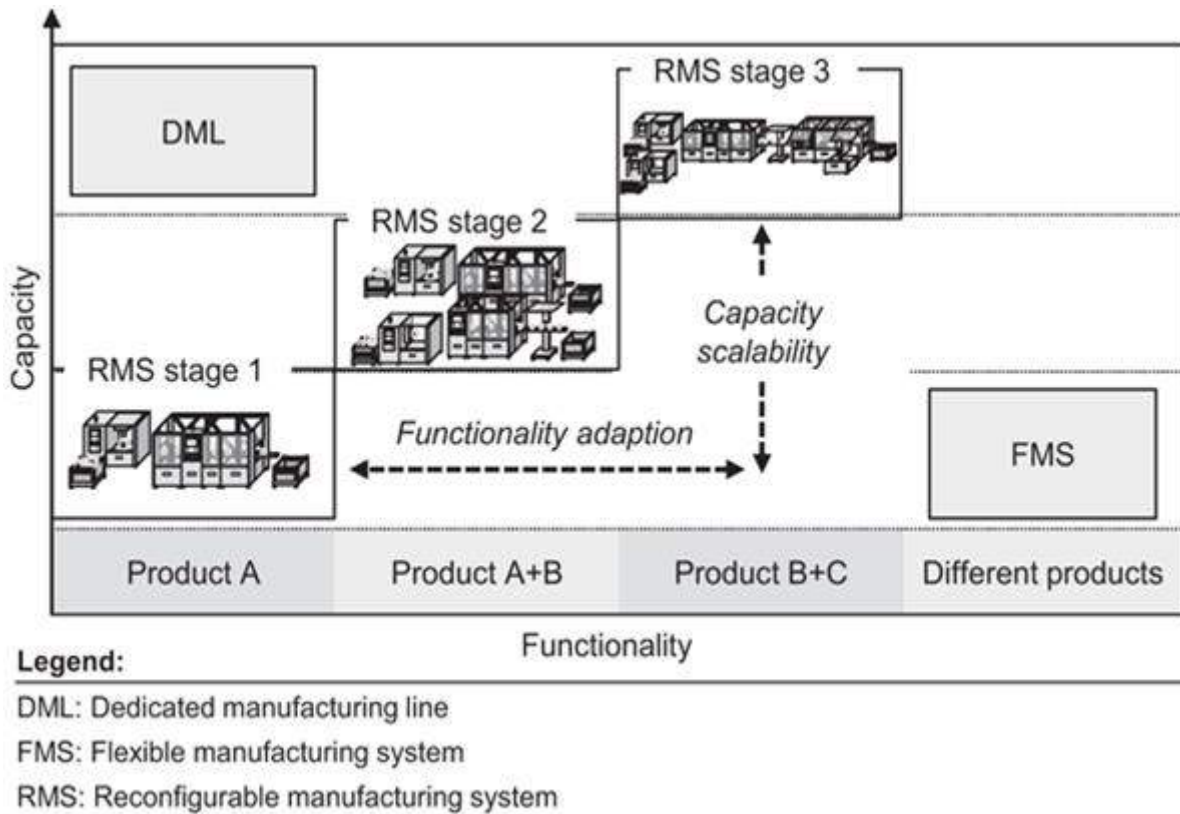


Figure 1 shows comparison of manufacturing systems

Comparison between the three manufacturing systems is shown in the table1, identifies the key limitations of all the types of the systems

	Dedicated	FMS	RMS
System arrangement	permanent	variable	variable
Machine	permanent	permanent	variable
System focus	Product	Machine	Product family
Scalability	No	Yes	Yes
Flexibility	No	universal	personalized
Simultaneously Operating Tool	Yes	No	Yes
Efficiency	High	Low	High

III. COMPONENTS OF RECONFIGURABLE MANUFACTURING SYSTEM

- **Reconfigurable machine tool:** - The reconfigurable machine tools are a key component of RMS (RMT). RMT are intended for specific specialized range of operation needs and may be instantly modified when those requirements alter. Machine tools that can be reconfigured to produce a specified set of attributes for a different range of cycle time.
The key objective of the RMT is to accommodate changes in the products or components to be designed. The various possible modifications must be evaluated.
 - Size of the Work piece
 - Geometry and complication of parts
 - Volumes and rates of production
 - Process that must be followed
 - Geometrical accuracy
 - Precision, surface characteristics
 - Type of Material,
 - Toughness etc.
- **Reconfigurable Controller:** - Any machine-specific functions are used to control a single machine. or Currently, classes must be developed and implemented into a Reconfigurable Controller. At run-time, the Reconfigurable controller becomes unchangeable for handling various computers.
- **Reconfigurable Inspection Machines** the machines which are used to carry out the inspection process and which are depend upon the type of the technology used.
- **Material transport systems** that link the devices together to build the system productivity will be affected by the different orders and designs of these equipment. The RMS Science Base is a collection of mathematical techniques that may be used to improve production efficiency with the lowest number of machines possible.

IV. CORE CHARACTERISTICS OF IDEAL RMS

Ideal Reconfigurable Manufacturing Systems possess six core RMS characteristics:

- 1) **Modularity:** - The partition of manufacturing operation and requirements into operational units that can be adjusted between alternative process to produce the desired arrangement for a given set of needs. Many components in a reconfigurable manufacturing system are often modular (e.g., machines, axes of motion, controllers, and tooling).
- 2) **Integrability:**- The capability of quickly and effectively combine modules using a combination of mechanical, informational, and operational techniques that enable integration and collaboration of Axes of motion and spindles can be combined to construct machines .
- 3) **Customized flexibility:** - To develop system/machine flexibility entirely around a product family, obtaining flexible as opposed to FMS/broad CNC's flexibility This feature distinguishes RMS from flexible manufacturing systems (FMS) and provides for a lower investment cost.

4) Scalability: - The ability to modify production capacity quickly by adjusting a current manufacturing system and/or upgrading the productivity of reconfigurable units Scalability is the coefficient property of convertibility.

5) Convertibility: - The ability to quickly adapt the accessibility systems, processes, and governs to meet new production demands there may be different levels of system convertibility.

6) Diagnosability: - The ability to recognize the current state of a system automatically in order to detect and diagnose the underlying cause of output product problems and immediately repair operational defects. Normal RMS will contain a few of these properties, but not all of them. When these features are present, RMS increases the speed with which production systems respond to unexpected occurrences, such as quick Factors such as market demand or unknown machine problems.

V. LITERATURE REVIEW

Sl.No	Name of the Author	Year of Publication	Characteristics	Results Observed
01	Y Koren	1999	Reconfigurability	Reconfigurability is an engineering approach that is both cost effective and very flexible to market changes.
02	Farshid MaghamiASI	2000	Stability	A basic simplified mathematical model, based on this analogy, was presented for the capacity and/or functionality of the manufacturing system.
03	I Batchkova	2004	Optimal Scheduling	The proposed model for integrated based on behaviours and agendas and short times is necessary to adjust RMS for another detail processing.
04	Ahmed M. Deif	2006	System Configuration	The model revealed how each design layer is regulated by different parameters that represent the reconfigurable manufacturing system's strategic objectives.
05	Kapil Kumar Goyal	2013	Responsiveness	Greater operational ability and machine values The capacity to reconfigure reduces response time. As a result, responsiveness has been calculated by taking the average of the observed variables of both parameters.
06	Shady S. Elmasry	2015	Capacity and Scalability	It was demonstrated that the criteria for choosing the optimal scaling strategy was based on reducing capacity, scalability, delay, and product cost. Kim approach has substantial costs, particularly for high target responsiveness time value.
07	Xavier	2016	Total cost &	Technique can be applied to sequences to increase

	Delorme		Time	overall operation efficiency and provide solutions based on the information rather than pure randomness.
08	Hichem Haddou-Benderbal	2016	Completion time and Robustness Index	It has been revealed that the impact generated exclusively by OP3 is 1055 time units. Spite of the fact that OP4 of F1 might be conducted on a replacement machine M4 rather than the unavailability of M6.
09	Aihua Huang	2018	Convertibility	Option B offers higher convertibility than option A, as well as outstanding quality and effectiveness, with a score of 4.23/5.22.
10	Eram Asghar	2018	Machine Capability	The suggested algorithm is durable because it finds the minimal constraints and capacities to a part's associated activities, with the least amount of production changeover time but the most machine capabilities.
11	Hichem Haddou Benderbal	2018	System Modularity	The adopted strategy yields the best process designs, improved system modularity and minimizing system completion time.
12	Bashir Salah	2019	Configuration Layout	U-shape has the highest throughput, least amount of time in the system, and the highest resource utilization rate.
13	Faycal A. Touzout	2019	Sustainability	When the probability declines, so has the gesture of the adapted NSGA-II and the adapted NSGA-II produces better the adapted AMOSA.
14	Rajeev Kant	2019	Sequencing, Total configurable time and optimal capacity	It was shown that the planned technique optimizes production system performance in different demand periods, as well as a significant reduction in synchronization error from 12 percent to 1.2 percent on average, and from 17 percent to 1.7 percent on average delay.
15	Shokraneh K. Moghaddam	2019	RMS Design, Capacity and Scalability	It is stated it's more logical in the mean time but that the approach is more acceptable when faced with an unknown future.

VI. CONCLUSION

Traditional methods are unsuitable for dealing with problems such as unpredictable demand, the need for a wide range of products, boosting product quality, process selection, continuous improvement low cost, and minimizing lead time, prompting the emergence of new innovation such as FMS in industries. FMS includes a

few restrictions such as restructuring, family resource, modification, and changing limits, which encourages the growth of more advanced innovation such as RMS. The new system should be designed out from start to be reconfigurable. This is accomplished by designing the system and its machines for customization. The manufacturing system will be developed around the product family, with the unique flexibility order to generate all of the components in the part family. The approach proposed in this research for reconfigurable manufacturing systems exhibits an effort toward analytically tending to assembly within a global roof of reconfigurability.

VII. REFERENCES

- [1]. Y.Koren, U. Heisel, F.Jovane, T.Moriwaki, Pritschow, G.Ulsoy and H Van Brussel paper Entitled "Reconfigurable Manufacturing Systems" Article in CIRP annals manufacturing technology, Vol. 48 August 1999, DOI: 10.1007/978-3-642-55776-7_19.
- [2]. Asl, Farshid Maghami, A. Galip Ulsoy, and Yoram Koren. "Dynamic modeling and stability of the reconfiguration of manufacturing systems." Proc. of Japan-USA Symp. on Flexible Automation. 2000.
- [3]. Batchkova, I., G. Popov, and G. Stambolov. "Application of Generalized Nets for optimal Scheduling of Reconfigurable Manufacturing Systems." Proceedings of the 10th ISPE International Conference on Concurrent Engineering: Research and Applications. 2003.
- [4]. Deif, Ahmed M., and Waguih H. ElMaraghy "A systematic design approach for reconfigurable manufacturing systems." Advances in Design. Springer, London, 2006. 219-228.
- [5]. Kapil Kumar Goyal, Pramod Kumar Jain, Madhu Jain "A novel methodology to measure the responsiveness of RMTs in reconfigurable manufacturing system", Journal of Manufacturing Systems 32 (2013) 724– 730.
- [6]. Shady S. Elmasry, Ayman M.A. Youssef, "A cost-based model to select best capacity scaling policy for reconfigurable manufacturing systems", Int. J. Manufacturing Research, Vol. 10, No. 2, 2015, P.No 162-183.
- [7]. Xavier Delorme, Sergey Malyutin, Alexandre Dolgui, "A multi-objective approach for design of reconfigurable transfer lines", IFAC-PapersOnLine 49-12 (2016) 509–514.
- [8]. Hichem Haddou-Benderbal, Mohammed Dahane and Lyes Benyoucef, "Hybrid Heuristic to Minimize Machine's Unavailability Impact on Reconfigurable Manufacturing System Using Reconfigurable Process Plan", IFAC-PapersOnLine 49-12 (2016) 1626–163.
- [9]. Aihua Huang, Fazleena Badurdeen, I S Jawahir, "Towards Developing Sustainable Reconfigurable Manufacturing Systems", 28th International Conference on Flexible Automation and Intelligent Manufacturing (FAIM2018), June 11-14, 2018, Columbus, OH, USA, Procedia Manufacturing 17 (2018) 1136–1143.
- [10]. Eram Asghar, Uzair Khaleeq uz Zaman, Aamer Ahmed Baqai, Lazhar Homri, "Optimum machine capabilities for reconfigurable manufacturing systems", The International Journal of Advanced Manufacturing Technology (2018) 95:4397–4417.

- [11]. Hichem Haddou-Benderbal, Mohammed Dahane and Lyes Benyoucef, "Modularity assessment in reconfigurable manufacturing system (RMS) design: an Archived Multi-Objective Simulated Annealing-based approach", *Int J Adv Manuf Technol* (2018) 94:729–749.
- [12]. Salah, Bashir. "Design and Simulation Based Validation of a Reconfigurable Manufacturing System.", *Proceedings of the International Conference on Industrial Engineering and Operations Management Bangkok, Thailand, March 5-7, 2019*.
- [13]. Faycal A. Touzout & Lyes Benyoucef, "Multi-objective sustainable process plan generation in a reconfigurable manufacturing environment: exact and adapted evolutionary approaches", *International Journal of Production Research*, 57:8, 2531-2547.
- [14]. Rajeev Kant, L. N. Pattanaik & Vijay Pandey, "Sequential optimisation of reconfigurable machine cell feeders and production sequence during lean assembly", *International Journal of Computer Integrated Manufacturing*, ISSN: 0951-192X.
- [15]. Shokraneh K. Moghaddam, Mahmoud Houshmand, Kazuhiro Saitou & Omid Fatahi Valilai, "Configuration design of scalable reconfigurable manufacturing systems for part family", *International Journal of Production Research*, ISSN: 0020-7543



Performance of Different Refrigerants in a Four-Wheeler Automobile AC Condenser

H. M. Gurudatt^{1*}, G. S. V. L. Narasimham¹, B. Sadashive Gowda²

^{1*}Department of Mechanical Engineering, Indian Institute of Science, Bangalore - 560012, Karnataka, India

²Department of Mechanical Engineering, Vidyavardhaka College of Engineering, Mysuru- 570002, Karnataka, India

ABSTRACT

Due to strict rules on Global Warming Potential (GWP) and Ozone Depletion Potential (ODP) of refrigerants, the existing automotive refrigerant R134a is to be replaced with new low GWP refrigerants by 2036 in developed nations and by 2047 in developing countries. Researchers have found that HydroFluroOlefins (HFOs) such as R1234yf and R1234ze(E) are suitable replacements for R134a due to their zero ODP and very low ODP low GWP. In this work, a comparative numerical study is reported of the performance of the refrigerants R1234yf and R1234ze(E) with R134a in an automotive condenser of flat-tube-louvered-fin type, for the same condenser inlet temperature and pressure. Results are presented for several quantities of interest, such as the heat rejection rate and pressure drop. The thermodynamic and transport properties of the refrigerants are obtained from REFPROP software and moist air properties from suitable correlations from the literature. A custom code is prepared in MATLAB to solve the governing relations of heat transfer. The objective is to compare the refrigerant passage length per unit latent heat removal. The basis of comparison is the same mass flow rate and inlet vapour temperature and either the same inlet pressure or the same saturation temperature for the refrigerants. The heat transfer performance of R1234ze(E) is the highest, followed by those of R1234yf and R134a. For all refrigerants, higher refrigerant side heat transfer coefficients are observed at relatively higher qualities. The refrigerants with increasing order of pressure drop are R1234ze(E), R1234yf and R134a.

Keywords: Numerical simulation, Minichannel, Flat-tube condenser, R1234yf, R1234ze(E), R134a, Louvered fin.

Nomenclature

A_f	:	Fin surface area corresponding to one channel (m ²)
$A_{t,i}$:	Inside surface area corresponding to one channel (m ²)
$A_{t,o}$:	Outside tube surface area corresponding to one channel (m ²)
c_{pa}	:	Specific heat of the air (J/kg/K)
f_p	:	Fin pitch (m)
L_{DS}	:	Refrigerant passage length in the superheated region (mm)

L_{TP}	:	Refrigerant passage length in the two-phase region (mm)
L_{SC}	:	Refrigerant passage length in the subcooled region (mm)
\dot{M}_a	:	Mass flow rate kg/s
N_{ch}	:	Number of channels in a unit cell
\dot{Q}	:	Heat transfer rate (W)
S	:	Conduction shape factor (W/°C)
T	:	Temperature (°C)
x	:	Dryness fraction

Greek Symbols

α	:	Heat transfer coefficient of refrigerant (W/m ² .K)
η	:	Efficiency
λ	:	Thermal conductivity (W/m.K)

Subscripts

a	:	air
f	:	fin
i	:	inside, refrigerant side
o	:	outside, air side
r	:	refrigerant
t	:	tube
uc	:	unit cell
1	:	inlet
2	:	exit

I. INTRODUCTION

Important properties of the refrigerants considered in this study, namely, R134a, R1234yf and R1234ze(E) are shown in TABLE I.

TABLE I Properties of refrigerants

Refrigerant	R134a	R1234ze(E)	R1234yf
Molecular formula	C ₂ H ₂ F ₄	C ₃ H ₂ F ₄	C ₃ H ₂ F ₄
Molar mass (kg/kmol)	102,03	114	114
Critical temperature (K)	374.21	382.52	367.85
Critical pressure (kPa)	4059.3	3636.3	3382.2
Normal boiling point (°C)	-26.3	-19	-30
Latent heat (kJ/kg) at normal boiling point.	217.12	195.45	180.51
Density of saturated vapour at -10°C in kg/m ³	10.041	8.1328	12.559
GWP	1300	7	4
ODP	0	0	0

Nair¹ reviewed thermodynamic properties, transport properties, flammability, oil compatibility, boiling and condensation heat transfer performance of HFO refrigerants and discussed the scope for future research work. In his review, he reported that POE oil is suitable for R1234yf rather than PAG oil. Babiloni et al.² conducted a review of the refrigerant R1234ze(E) and reported that under normal operation and at low humidity R1234ze(E) becomes non-flammable. HFO/HFC mixtures when used as low GWP HFC replacements, require fewer system changes. Liu et al.³ conducted an experimental investigation on heat transfer and pressure drop of propane, R1234ze(E) and R22 in circular and square horizontal minichannels and found that both propane and R1234ze(E) are good substitutes for R22 based on condensation characteristics. The refrigerants in decreasing order of pressure gradient are propane, R1234ze(E) and R22. Guo et al.⁴ conducted the experimental investigation on heat transfer coefficient and frictional pressure drop of the two-phase condensation of R1234ze(E), R290, R161 and R41 with R134a and R32 as baseline refrigerants. Their results showed that with increasing saturated temperature and heat flux the heat transfer coefficient during condensation decreases and that R161 and R1234ze(E) had the highest and lowest heat transfer coefficients at the same working conditions. By comparing experimental heat transfer coefficients with predictions from 7 models, they concluded that the model of Koyama⁵ had the better predictive capability. Diani et al.⁶ conducted the experimental investigation on heat transfer coefficient and frictional pressure drop during condensation of R1234ze(E) and R134a. They observed that for vapour quality lower than 0.7, the higher the mass velocity, the higher the heat transfer coefficient. At higher vapour quality the effect of mass velocity is not monotonic. Frictional pressure gradient increases with the mass velocity at constant vapour quality. Pabon et al.⁷ conducted the experimental investigation of void fraction in adiabatic two-phase flow of R1234yf in smooth horizontal tubes. Their results highlighted that the void fraction of R1234yf is 5% lower than that of R134a. They compared seven correlations from the literature with their experimental data and found that the Baroczy and the Hughmark correlations provided the best predictions. Mathur⁸ has developed a correlation for HFO-1234yf to predict condensation heat transfer coefficient for an automotive condenser by considering mass flow rate ranging from 180 to 475 kg/hr, maintaining the oil circulation ratio at 3% and condensation saturation temperature of 50°C. Fazelnia et al.⁹ experimentally studied condensation of R1234yf in flattened smooth tubes with internal heights of 6.2, 5.1 and 2.8 mm and with 8.2 mm ID round tubes and found that using flattened tubes increases both heat transfer coefficient and pressure drop. Based on their results they proposed two correlations to predict the pressure drop and heat transfer coefficient in flattened tubes by modifying the existing correlations in the literature. Gu et al.¹⁰ conducted the experimental investigation on the condensation characteristic of R1234ze(E) in horizontal circular, square and triangle channels. The results showed that the square tube has a higher heat transfer coefficient than the circular tube. In contrast, the triangle cross-section tube showed a similar heat transfer performance to the circular tube. Longo et al.¹¹ performed a comparative analysis of the forced convection condensation of R134a, R152a, R1234yf and R1234ze(E) inside a 4mm ID smooth tube and found that the condensing coefficient shows great sensitivity only to refrigerant mass flux and mean vapour quality. All the three GWP refrigerants considered showed condensation heat transfer and pressure drop performances similar to R134a. Bashar et al.¹² conducted experimental studies on the performance of R1234yf during condensation in a small diameter smooth tube and microfin tube. They developed condensation heat transfer correlation and claimed that their newly developed correlation successfully predicts their experimental

data and data from other sources within a mean deviation of 15%. Jeong and Yun¹³ studied condensation heat transfer characteristics of R1234ze(E) and R134a experimentally at high reduced pressure. They found that the effects of mass flux on refrigerants decreased with an increase in reduced pressure. Pham and Oh¹⁴ analyzed R1234yf in the condensation process inside two different minichannel multiport horizontal tubes and developed a new correlation for predicting heat transfer coefficient from their experimental data. They found that their correlation predicts the heat transfer coefficients in condensation with a mean deviation of 11.7%. Keniar and Garimella¹⁵ conducted an experimental investigation of refrigerants R134a, R245fa and R1234ze(E), condensation in circular and square micro and mini channels. They found that the pressure gradient and heat transfer coefficient is highest for R245fa compared to R1234ze(E) and R134a and that the mass flux has minimum effect on the heat transfer coefficient in the circular channel. In contrast, in the case of the square channel, an increase in mass flux increases the heat transfer coefficient.

The literature shows that numerous experimental studies were done on forced convection condensation of low GWP refrigerants. Relatively less work is done in comparing the performance of condensers with various refrigerants. This work compares the performance of an automotive condenser with the low GWP refrigerants R1234yf and R1234ze(E) with that of the baseline refrigerant R134a. The objective is to compare the refrigerant passage length per unit latent heat removal. The basis of comparison is the same mass flow rate and inlet vapour temperature and pressure for the various refrigerants. In addition, results are tabulated for the same inlet vapour temperature and saturation temperature of the refrigerants.

Design and development of hybrid fibrous composites is one of the important stage in materials engineering. Synthetic fibers such as glass fiber, carbon fiber, Kevlar fiber have rendered their service to greater extent in the field of structural applications [1].

An automobile condenser originally used with R134a which has louvered fins, flat tube, multi-channels which are preferred in automotive air conditioning because of their high performance and compactness, is adopted in this study.

Fig. 1 and Fig. 2 shows the front view and the channels in the flat tube of the condenser. From the exit of the compressor, the super-heated vapour refrigerant will enter pass 1 through the header, where the refrigerant will be distributed to the minichannels of all the tubes of pass 1. It will make three more passes before exiting the condenser. Through the refrigerant passage inside the condenser, the refrigerant will be condensing from vapour to liquid. As the liquid is denser than vapour and occupies less space, the number of tubes will decrease from pass to pass along the refrigerant flow direction.

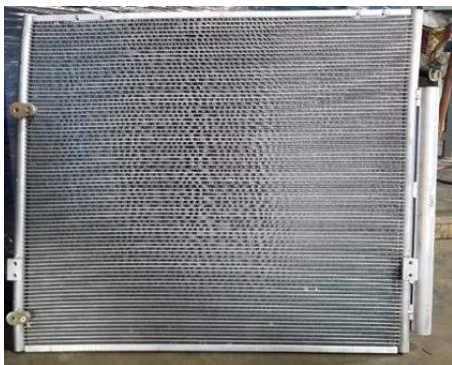


FIG. 1: FLAT-TUBE LOUVERED-FIN AUTOMOTIVE CONDENSER



FIG. 2: REFRIGERANT CHANNELS IN A TUBE.

TABLE II Details of the condenser and louvered fin

Sl. No.	Parameter	Data
1	Total number of tubes	82
2	Number of tubes in pass 1	40
3	Number of tubes in pass 2	18
4	Number of tubes in pass 3	13
5	Number of tubes in pass 4	11
6	Single tube length (mm)	630
7	Tube width (mm)	16
8	Tube thickness (mm)	1
9	Number of refrigerant channels (N_{ch}) per tube	20
10	Number of louver banks	2
11	Number of louvers per louver banks	8
12	Louver angle (deg)	30
13	Fin pitch (mm)	2
14	Louver pitch (mm)	0.9
15	Fin thickness (mm)	0.05
16	Length of one fin (mm)	6.32

II. MATHEMATICAL MODELLING

FIG. 3. shows a unit cell with 20 refrigerant channels in the direction of air flow with the tube width (dimension perpendicular to the figure) being the same as the condenser depth of 16 mm. Each unit cell has a cross-sectional area of tube pitch times fin pitch ($t_p \times f_p$). For analysis, one unit cell with one refrigerant channel is considered and the heat transfer from all the remaining channels are considered as identical. In a unit cell heat transfer takes place from the refrigerant to inside tube wall, from inside tube wall to outside tube wall through conduction and from exterior tube wall and extended surfaces to the air by convection. In the steady state, all the heat transfer rates are equal.

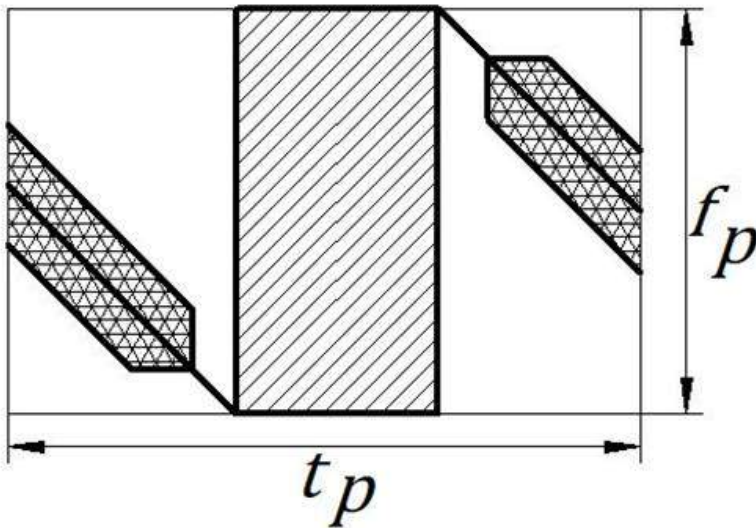


FIG. 3. UNIT CELL SHOWING THE FIN AND TUBE PORTIONS

$$\dot{Q}_{uc} = N_{ch} \alpha_i A_{t,i} (T_i - T_{t,i}) \quad (1)$$

$$\dot{Q}_{uc} = N_{ch} \lambda_t S F_p (T_{t,i} - T_{t,o}) \quad (2)$$

$$\dot{Q}_{uc} = N_{ch} \alpha_o (A_{t,o} + A_f \eta_f) (T_{t,o} - T_a) \quad (3)$$

The quantity S in “Eq. (2)” is the conduction shape factor for the channel walls and its calculation is explained in Gurudatt et al. ¹⁶. The conduction shape factor S is found to be 5.74. The various quantities appearing in the equations are presented in the nomenclature. “Eq. (1)” to “Eq. (3)” can be combined to form a relation for the overall heat transfer coefficient. The three simultaneous equations are solved for the unknowns \dot{Q}_{uc} , $T_{t,i}$ and $T_{t,o}$. For better accuracy, the logarithmic mean temperature difference (LMTD) is used in “Eq. (3)” in place of $T_{t,o} - T_a$ instead of the arithmetic mean temperature difference (AMTD).

A. Inside Nusselt number and refrigerant side pressure gradient.

To calculate the inside Nusselt number in single phase laminar flow, correlations from Refs. 17 and 18 are employed. For turbulent flow, Gnielinski¹⁹ correlation is used. In the two-phase region, the in tube condensation heat transfer coefficient is calculated from the most recent correlation of Shah²⁰ which is based on 4063 data points covering 33 fluids, and valid for conventional, mini and microchannels, a range of geometrical parameters and all orientations (horizontal, inclined, and vertical). The pressure drop in single phase is calculated using the Darcy friction factor for rectangular channels (Refs. 17 and 18), while in the case of two-phase flow, the same was determined using correlations from Refs. 21-23. The void fraction is calculated using Zivi²⁴ relation. The entry and exit refrigerant pressure drops are found using the correlations in Refs. 25-27. Details are reported in Gurudatt et al. ¹⁶.

B. Air side heat transfer coefficient and pressure loss

The air side heat transfer coefficient and pressure loss are calculated using the correlations of Park and Jacobi²⁸ as reported in Gurudatt et al. ¹⁶.

III. CALCULATION PROCEDURE

Calculations are done by marching along the passage length and solving the three simultaneous equations iteratively for each unit cell. For each unit cell, the heat transfer rate and pressure drop are determined. The property data for the refrigerants is obtained from NIST REFPROP 9.0 Version. The properties of moist air are generated from dry air and water vapour. More details of the numerical procedure and its validation are available in Gurudatt et al.¹⁶

IV. RESULTS AND DISCUSSION

In the results reported in subsections A to G, the inlet vapour temperature and pressure for all the three refrigerants are 60°C and 12 bar.

A. Refrigerant side heat transfer coefficient along the passage length

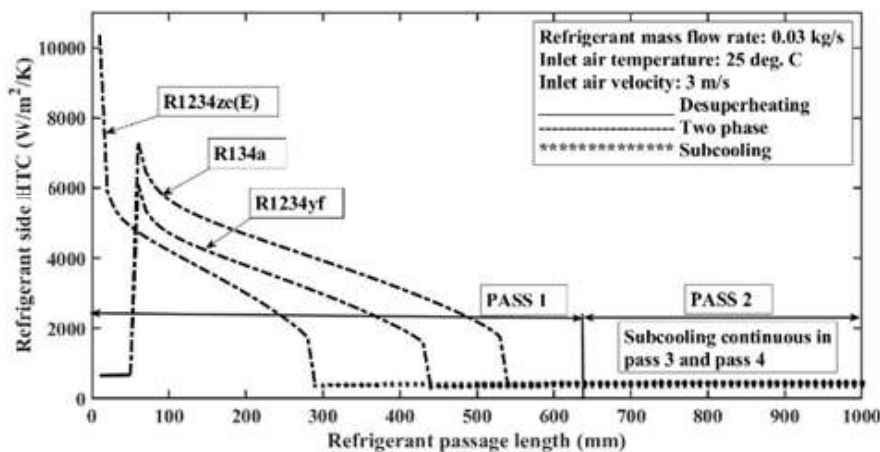


FIG. 4. VARIATION OF REFRIGERANT SIDE HEAT TRANSFER COEFFICIENT ALONG THE REFRIGERANT PASSAGE LENGTH

The refrigerant side heat transfer coefficient variation over the refrigerant passage length (4 passes \times 630 mm/pass = 2520 mm) is shown in “Fig. 4.” The refrigerant mass flow rate, inlet air temperature and inlet air velocity are kept constant as mentioned earlier. It can be observed that the heat transfer coefficient attains a maximum in the two-phase region, particularly at higher dryness fractions. For R1234ze(E), the desuperheating part is negligibly small. The highest heat transfer coefficient in the two-phase region is observed for R1234ze(E). R1234ze(E) condenses faster than R134a and R1234yf, due to its lower enthalpy of condensation.

B. Variation of quality with refrigerant passage length

The variation of dryness fraction over the span of refrigerant passage is shown in “Fig. 5”. It is observed that R134a requires a longer refrigerant passage length compared to R1234ze(E) and R1234yf, whereas R1234ze(E) requires significantly less refrigerant passage length and hence can handle higher mass flow compared to R134a.

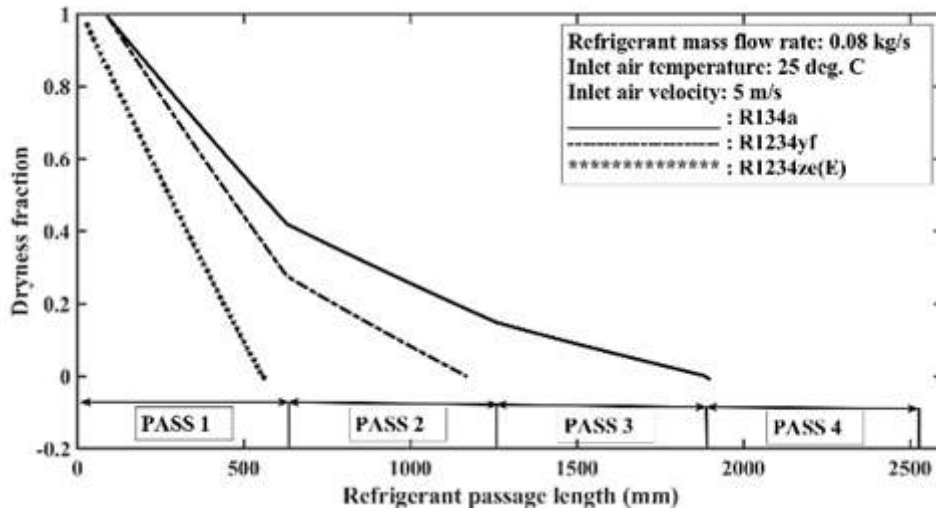


FIG. 5. VARIATION OF DRYNESS FRACTION ALONG THE REFRIGERANT PASSAGE LENGTH.

C. Variation of refrigerant side pressure along the refrigerant passage length

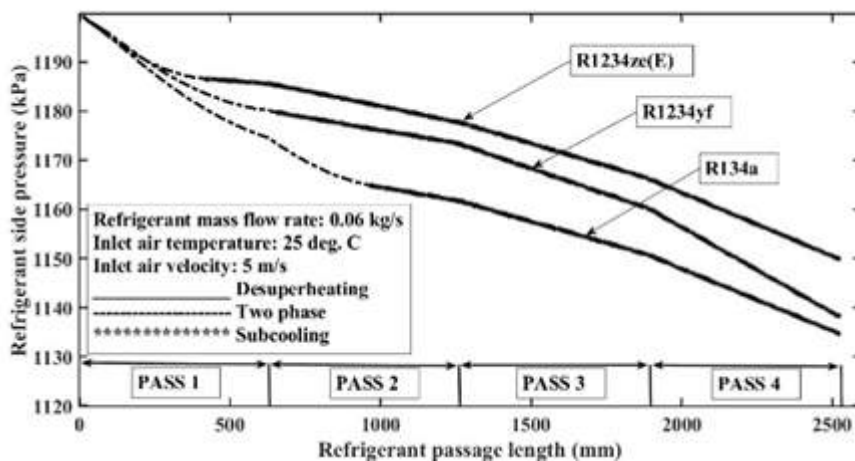


FIG. 6. VARIATION OF REFRIGERANT SIDE PRESSURE ALONG THE REFRIGERANT PASSAGE LENGTH.

The variation of refrigerant side pressure over the length of the refrigerant passage is shown in “Fig. 6”. It can be observed that R134a experiences the most significant pressure drop, while the pressure drop with R1234ze(E) is the lowest. However, the overall pressure drop on the refrigerant side is less than 100 kPa for all three refrigerants.

D. Cummulative heat transfer rate along the refrigerant passage length

“Fig. 7” depicts the cummulative heat transfer rate against the refrigerant passage length for different refrigerants. The heat transfer rate is dominant in the two-phase region and it is tiny in the subcooled part. This is due to the higher values of condensation heat transfer coefficient compared to those of single-phase. It can be seen that refrigerants R134a, R1234ze(E) and then R1234yf exhibit cummulative heat transfer rate in decreasing order.

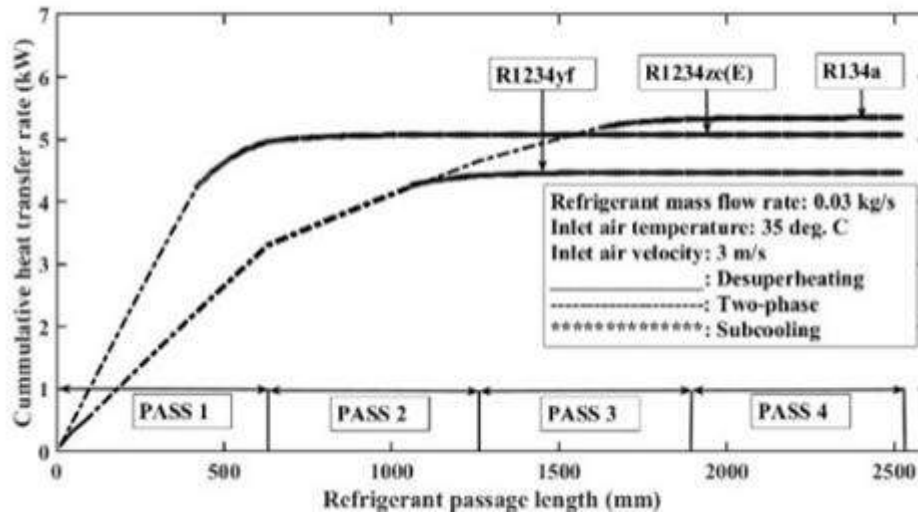


FIG.7. VARIATION OF CUMMULATIVE HEAT TRANSFER RATE ALONG THE REFRIGERANT PASSAGE LENGTH.

E. Effect of refrigerant mass flow rate on heat removal rate

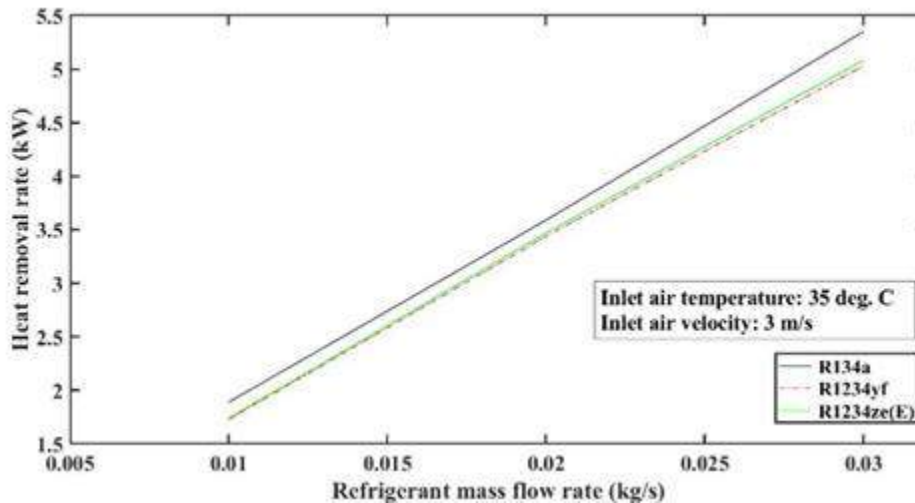


FIG. 8. EFFECT OF REFRIGERANT MASS FLOW RATE ON HEAT REMOVAL RATE.

“Fig. 8” shows the variation of heat removal rate with refrigerant mass flow rate when inlet air temperature and the inlet air velocity are kept constant. For the same mass flow rate of the refrigerant heat removal rate is maximum for R134a followed by R1234ze(E) and R1234yf. Since subcooling results in negligible heat dissipation, the condenser area will be effectively utilized if complete latent heat removal occurs when the refrigerant reaches the end of the condenser. Lowering the inlet air temperature or increasing the inlet air velocity beyond this condition does not significantly affect the heat removal rate.

F. Variation of inside side tube wall temperature with refrigerant passage length

“Fig. 9” shows the refrigerant side tube surface temperature variation along the refrigerant passage length. It can be observed that there is a slight decrease in tube wall temperature during condensation for R134a and R1234yf, while the tube wall temperature decrease for R1234ze(E) is higher. A rapid drop in wall temperature

is observed where the dryness fraction attained low values. The wall temperature for R1234yf during the major part of the condensation region is not too different from that of R134a.

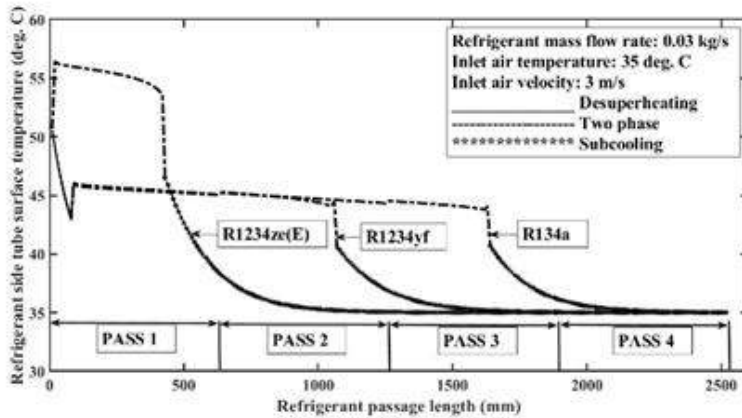


FIG. 9. VARIATION OF THE INSIDE TUBE WALL TEMPERATURE ALONG THE REFRIGERANT PASSAGE LENGTH.

G. Refrigerant passage length per unit latent heat removal

TABLE III shows the refrigerant passage length required per unit latent heat removal with both inlet temperature and inlet pressure kept constant for all the three refrigerants considered. It is observed that the passage length required per unit latent heat removal rate is in increasing order for the refrigerants R1234ze(E), R1234yf and R134. Since the inlet pressure is kept constant, the condensation temperatures of the refrigerants differ. However, to examine the case of the same condensation temperature, results are also obtained for the same inlet vapour temperature and inlet pressures corresponding to the same condensation temperature. Since the pressure drop in the desuperheating region is very less, this results in more or less the same condensing temperature for all the refrigerants. These results, tabulated in TABLE IV, are similar to the former observation.

TABLE III Refrigerant passage length per unit latent heat removal ($T_1 = 60^\circ\text{C}$ and $P_1 = 1200$ kPa, Temperatures at the beginning of condensation: R134a = 46°C , R1234yf = 46.5°C and R1234ze (E) = 57°C)

Refrigerant	Refrigerant mass flow rate (kg/s)	Latent heat removed (kJ/kg)	Refrigerant passage length for condensation (mm)	Refrigerant passage length per unit latent heat removal (mm-kg/kJ)
R134a	0.035	156	2284	14.55
R1234ze(E)		138	476	3.45
R1234yf		125	1334	10.67
R134a	0.03	156	1550	9.88
R1234ze(E)		138	408	2.96
R1234yf		125	982	7.86
R134a	0.025	156	1058	6.74
R1234ze(E)		138	342	2.48
R1234yf		125	692	5.54

TABLE IV Refrigerant passage length per unit latent heat removal ($T_1 = 60^\circ\text{C}$, Temperatures and pressures at the beginning of condensation: R134a = 46°C , 1.19 MPa; R1234yf = 46°C , 1.18 MPa; R1234ze (E) = 46°C , 0.899 MPa)

Refrigerant	Refrigerant mass flow rate (kg/s)	Latent heat removed (kJ/kg)	Refrigerant passage length for condensation (mm)	Refrigerant passage length per unit latent heat removal (mm-kg/kJ)
R134a	0.03	156	1550	9.94
R1234ze(E)		150	1282	8.55
R1234yf		125	1082	8.66
R134a	0.025	156	1058	6.78
R1234ze(E)		150	900	6.00
R1234yf		125	772	6.18
R134a	0.02	156	686	4.4
R1234ze(E)		150	594	3.96
R1234yf		125	520	4.16

H. Energy balance

TABLE V. shows the energy balance by considering the heat removed from the refrigerant and the heat abstracted by the ambient air.

Heat abstraction rate by ambient air is calculated using the formula

$$\dot{Q} = \dot{M}_a c_{pa} (T_{a,2} - T_{a,1}) \tag{4}$$

The energy balance shows that the heat transfer rates from the refrigerant and air sides agree to within 1%.

TABLE V. Energy balance

\dot{M}_r (kg/s)	Particulars	Refrigerants	$T_{a,1} = 35^\circ\text{C}$ $V = 3 \text{ m/s}$	$T_{a,1} = 25^\circ\text{C}$ $V = 3 \text{ m/s}$	$T_{a,1} = 25^\circ\text{C}$ $V = 5 \text{ m/s}$
0.01	Heat rejected by Refrigerant (kW)	R134a	1.89	2.03	2.03
		R1234ze(E)	1.74	1.88	1.88
		R1234yf	1.59	1.73	1.73
	Heat abstracted by air (kW)	R134a	1.87	2.01	2.02
		R1234ze(E)	1.72	1.85	1.85
		R1234yf	1.58	1.71	1.71
0.02	Heat rejected by Refrigerant (kW)	R134a	3.59	4.04	4.06
		R1234ze(E)	3.47	3.75	3.76
		R1234yf	3.07	3.44	3.45
	Heat abstracted by air (kW)	R134a	3.57	4.00	4.02
		R1234ze(E)	3.42	3.7	3.71

		R1234yf	3.05	3.41	3.42
0.03	Heat rejected by Refrigerant (kW)	R134a	5.35	5.83	6.02
		R1234ze(E)	5.08	5.56	5.61
		R1234yf	4.47	5.03	5.13
	Heat abstracted by air (kW)	R134a	5.31	5.78	5.96
		R1234ze(E)	5.00	5.48	5.53
		R1234yf	4.44	4.99	5.08

V. CONCLUSION

The following conclusions can be drawn from the present study:

- 1) The refrigerant passage length required per unit latent heat removal is the least for R1234ze(E) and highest for R134a whereas R1234yf lies in between.
- 2) A condenser with R134a experiences more pressure drop whereas that with R1234ze(E) experiences the lowest pressure drop for the same operating conditions.
- 3) Inside heat transfer coefficient is maximum in two-phase region, particularly when the refrigerant has a higher dryness fraction. R1234ze(E) has the highest value of two phase heat transfer coefficient among the three refrigerants considered.
- 4) The decrease in tube wall temperature during condensation for R134a and R1234yf is minimal, while the tube wall temperature decrease for R1234ze(E) is slightly larger. A rapid drop in wall temperature is observed where the dryness fraction attained low values. The wall temperature for R1234yf during the major part of the condensation region is not too different from that of R134a.

An experimental investigation to rapidly analyze the performance of an automotive condenser could be costly and time-consuming hence present simulation program can be used effectively.

VI. REFERENCES

- [1]. Vipin Nair, HFO refrigerants: A review of present status and future prospects, International Journal of Refrigeration, 122 (2021) 156-170.
- [2]. A. M.-Babiloni, J. N.-Esbri, F. Moles, A. B. Cervera, B. Peris and G. Verdu, A review of refrigerant R1234ze(E) recent investigations, Applied Thermal Engineering, 95 (2016) 211-222.
- [3]. N. Liu, H. Xiao and J. Li, Experimental investigation of condensation heat transfer and pressure drop of propane, R1234ze(E) and R22 in mini-channels, Applied Thermal Engineering, 102 (2016) 63-72
- [4]. Q. Guo, M. Li and H. Gu, Condensation heat transfer characteristics of low GWP refrigerants in a smooth horizontal mini tube, International Journal of Heat and Mass Transfer, 126 (2018) 26-38.
- [5]. S. Koyama, K. Kuwahara and K. Nakashita, Condensation of refrigerant in a multi-port channel, First international conference on microchannels and mini-channels, Rochester, NY, 2003, ICMM2003-1021.

- [6]. A. Diani, M. Campanale and L. Rossetto, Experimental study on heat transfer condensation of R1234ze(E) and R134a inside a 4mm OD horizontal microfin tube , *International Journal of Heat and Mass Transfer*, 126 (2018) 1316-1325.
- [7]. J. G. Pabon, L. C. Pereira, G Humia, A Khosravi, R Revellin, J Bonjour and L Machado, Experimental study on the void fraction during two-phase flow of R1234yf in smooth horizontal tubes, *International Journal of Refrigeration*, 104 (2019) 103-112.
- [8]. G. D. Mathur, Development of a correlation for predicting condensation heat transfer coefficients for refrigerant HFO-1234yf, SAE Technical Paper 2019-01-0150 (2019).
- [9]. H. Fazelnia, B Sajadi, S Azarhazin, M A Behabadi and S Zakeralhoseini, Experimental study of the heat transfer coefficient and pressure drop of R1234yf condensing flow in flattened smooth tubes, *International Journal of Refrigeration*, 106 (2019) 120-132.
- [10]. X. Gu, J. Wen, X. Zhang, C. Wang and S. Wang, Effect of tube shape on the condensation patterns of R1234ze(E) in horizontal mini-channels, *International journal of Heat and Mass Transfer*, 131 (2019) 121-139.
- [11]. G. A. Longo, S. Mancin, G. Righetti and C. Zilio, Saturated vapour condensation of R134a inside a 4 mm ID horizontal smooth tube: Comparison with the low GWP substitutes R152a, R1234yf and R1234ze(E), *International Journal of Heat and Mass Transfer*, 133 (2019) 461-473.
- [12]. M. K. Bashar, K. Nakamura, K. Kariya and A Miyara, Condensation heat transfer of R1234yf in a small diameter smooth and microfin tube and development of correlation, *International Journal of Refrigeration*, 120 (2020) 331-339.
- [13]. J. Jeong and R. Yun, A study on the condensation heat transfer coefficient of R1234ze(E) and R134a near the critical point, *International Journal of Refrigeration*, 128 (2021) 83-94.
- [14]. Q. V. Pham and J. -T. Oh, Condensation heat transfer characteristics of R1234yf inside multiport mini-channel tube, *International Journal of Heat and Mass Transfer*, 170 (2021) 121029.
- [15]. K. Keniar and S Garimella, Experimental investigation of refrigerant condensation in circular and square micro and mini channels, *International Journal of Heat and Mass Transfer*, 176 (2021) 121383.
- [16]. H. M. Gurudatt, G. S. V. L. Narasimhan and B. Sadashive Gowda, Performance of a flat tube louvered fin automotive condenser with R1234yf, *Int. J. Air Conditioning and Refrig.* 29 (2021) 2150002.
- [17]. W. M. Kays and M. E. Crawford, *Convective Heat and Mass Transfer*, Third Edition (McGraw-Hill, New York, 1993), pp. 80, 138.
- [18]. R. K. Shah and A. L. London, *Laminar flow forced convection in ducts: A source book for compact heat exchanger analytical data*, *Advances in Heat Transfer*, eds. T. F. Irvine, Jr. and J. P. Hartnett (Academic Press, New York, 1978), pp. 200, 216.
- [19]. V. Gnielinski, On heat transfer through tubes, *Int. J. Heat Mass Transf.* 63 (2013) 134-140.
- [20]. M. M. Shah, Comprehensive correlations for heat transfer during condensation in conventional and mini/micro channels in all orientations, *Int. J. Ref.* 67 (2016) 22-41.
- [21]. V. P. Carey, *Liquid-Vapor Phase-Change Phenomena*, Second Edition (CRC Press, Boca Raton, 2008), p. 493. K. Stephan, *Heat Transfer in Condensation and Boiling* (Springer-Verlag, Berlin, 1992), pp. 184-198.

- [22]. G. F. Hewitt, Subsection 2.3.2: Gas-liquid flow, Heat Exchanger Design Handbook, ed.-in-chief: E. U. Schlunder (VDI-Verlag GmbH, Duesseldorf / Hemisphere Publishing Corporation, Washington, 1983), pp. 2.3.2-1 to 2.3.2-33.
- [23]. M. Zhang and R. L. Webb, A correlation of two-phase friction for refrigerants in small-diameter tubes, *Exp. Therm. Fluid Sci.* 25 (2001) 131–139.
- [24]. S. M. Zivi, Estimation of steady state steam void fraction by means of principle of minimum entropy production, *Trans. ASME: J. Heat Transfer* 86 (1964) 247-251.
- [25]. W. M. Kays and A. L. London, Compact Heat Exchangers, Third Edition (McGraw Hill, New York, 1984).
- [26]. Perry's Chemical Engineers' Handbook, Fourth Edition (McGraw-Hill, New York, 1963), pp. 5-30.
- [27]. J. G. Collier and J. R. Thome, Convective Boiling and Condensation, Third Edition (Clarendon Press, Oxford, 1994).
- [28]. Y.-G. Park and A. M. Jacobi, Air side heat transfer and friction correlations for flat-tube louver fin heat exchangers, *Trans. ASME, J. Heat Transfer* 131 (2009) (0021801) 1-12.



Influence of Cerium Oxide on Wear Characteristics of GFRP Composites

Vithal Rao Chavan^{1*}, Dr. K.R. Dinesh², Dr. Veerabhadrapppa Algur³, Dr. K. Veeresh⁴

^{1*}Research Scholar, Department of Mechanical Engineering, Rao Bahadur Y Mahabaleswarappa Engineering College, Ballari-583104, Karnataka, India

²Professor & Principal, Department of Mechanical Engineering, Government of Engineering College, K.R Pet-571426 Mandya, Karnataka, India

³Associate Professor, Department of Mechanical Engineering, Rao Bahadur Y Mahabaleswarappa Engineering College, Ballari-583104, Karnataka, India

⁴Professor, Department of Mechanical Engineering, Rao Bahadur Y Mahabaleswarappa Engineering College, Ballari-583104, Karnataka, India

ABSTRACT

This study comprises the development of innovative composite materials that outperform existing composites. Cerium oxide, a rare earth material family member in the periodic table, Lapox L-12 resin, and E Glass fibre material are used to develop newer composite materials. The wear loss and surface roughness in a dry sliding wear were investigated using a combination of materials and process factors, such as % of filler material, normal load, and sliding speed. L16 orthogonal array based on taguchi design was used to plan the tests. The result reveals that the optimum process parameters for the wear loss is A3,B4,C3 similarly for surface roughness A4,B3,C4

Keywords: GFRP, Wear loss, Surface Roughness, Pin-on-disc testing machine.

I. INTRODUCTION

In recent days the polymers are replacing the metal and alloys by their promising property i.e. high strength-to-weight ratio and stiffness-to-weight ratio. As a reason, mechanical components such as gears, cams, wheels, brakes, clutches, bearings, and seals are being used consistently. The majority of these are impacted by tribological loading, when they are in service. as a result, the researchers are much interested to develop the newer material for the polymer system.

There are the two methods to get the newer material, by varying the filler material and the proportion of the filler material in the polymer-based matrix such as fillers/whiskers. Another method is by varying the type of reinforcement material and the geometry of the reinforcement such as woven/ fibrous/ unidirectional/ bidirectional/ random etc., [1,12]. B. Suresh et al.,2006 examined the wear properties by varying the three percentages of graphite filler in E-glass-epoxy composite, the comparison of wear behaviour is been carried

with and without graphite filler, and concluded that the graphite filled composite poses higher value of resistance to sliding wear when compared to unfilled.[5,6]. Gewen Yi and Fengyuan Yan,2007 Tribological and mechanical characterization is being conducted on phenolic based composite with numerous inorganic fillers. Addition of petroleum coke in phenolic composite, increases bending strength and hardness characteristics. Talcum powder (5-10%) and hexagonal boron nitride (5-15%) of volume fraction acts as friction modifier, to increase the wear resistance of phenolic composite [11]. Further addition leads to inappropriate results of wear resistance and decrease in strength. S. Basavarajppa et al., 2007 an experiment approach using DOE (taguchi) method for analyzing the wear characteristics of the composite with varying filler (SiC and Graphite) material, sliding distance, sliding speed and load with aid of pin-on-disc test rig under dry condition. The result revealed that the wear resistance increased tremendously by the inclusion of Sic and Graphite as fillers in the polymer composite [7].

Through above cited literature survey, shows an ample opportunity to conduct the experimentation on wear behavior of polymer composite by varying the filler material i.e. one of the rare earth material lanthanum oxide. Taguchi approach helps to design a plan of experiments to get a good control on the variables opted to investigate the wear characteristics of particulate filled composites [6].

II. MATERIALS, FABRICATION, METHODS AND TESTING OF COMPOSITES

A. Materials

To carry out the experimentation the random orientation E-glass fiber with density of 2.62gm/cm³, Lapox L-12 resin with density of 1.120gm/cm³ hardener with density of 0.954gm/cm³ and secondary filler material lanthanum oxide with density of 6.51gm/cm³ is been incorporated to get a newer polymer composite. The below table-I shows the proportionate used to fabricated the composites [8,9].

TABLE I PROPORTIONATE COMBINATION OF MATERIAL USED IN THE COMPOSITE

Specimen	Composition		
	Resin	Fiber	Filler Material
1	60%	40%	0%
2	60%	30%	10%
3	60%	20%	20%
4	60%	10%	30%

B. Fabrication of Composites

The composite are fabricated as per the proportionate by hand layup method and further the composites are machined as per the required ASTM D G99 standard for wear test rig some samples [8.9, 10, 13].

C. Wear Test

The whole test was carried on a "DUCOM" wear test machine at ambient conditions. The wear test was conducted for the samples without post curing and with post curing. The wear rate was monitored from the wear loss versus time plot. All the tests carried at constant track distance of 70mm [2,3,4].The below fig.1 show the picture of DUCOM test rig and table. II shows specifications of Pin On Disc.



Fig.1 Pin-on-disc wear testing apparatus.

TABLE II. SPECIFICATIONS

Sl.no	Parameters	Range
01	Load Range	Up to 200N
02	Rotational Speed	200-2000rpm
03	Frictional Force Measurement	0-200N
04	Compound Wear Measurement	0-1200 μ m
05	Wear	0-3mm
06	Disc Size	160mm (Dia)
07	Pin Size	3-10mm

D. Taguchi Approach

In this work, along all four different levels, the influence of three design variables was examined utilizing L16 experimental plan. The working conditions under which wear tests were performed are tabulated in table III.

TABLE III. LEVELS FOR VARIOUS CONTROL FACTORS

Control variables	Units	Level I	Level II	Level III	Level IV
% of filler material	Wt.%	0	10	20	30
Load	N	5	10	15	20
Sliding speed	m/s	0.25	0.5	0.75	1

III. RESULTS AND DISCUSSION

In this investigation, wear test and surface roughness were examined on modified particulate filled polymer composite and also the influence of post curing on wear behaviour. In order to obtain the optimum result prediction, the obtained results need to transform into signal/noise ratio, because the S/N ratio greatly

contribute, as objective function for optimization. The objective function for the wear loss and surface roughness obtained by the S/N ratio is smaller the better, which further can equated as a logarithmic loss function.

A. S/N ratio analysis

The test carried out as per the plan of experiment obtained by the L16 orthogonal array and wear results are been tabulated in the table.4. To estimate the quality characteristics of obtained results, then the results need to transformed into S/N ratio with the help of software MINITAB16, these ratios are been tabulated in table. IV

The main interest is to know the influence of the filler material, as it key factor for the modification of the composite. Signal/Noise ratio responsive analysis need to carry between percentage of filler and wear loss. To get the very high quality the process parameters is to set to be optimum.

The higher and lower value of mean of S/N ratios difference leads to know the strongest impact parameter among the set parameters. If the difference is greater value of the averages of S/N ratios, would be the more prominent parameter

The difference between the higher and lower values of the mean of S/N ratios was also used to determine the control parameter with the strongest recommendations. The control parameter would be more influential if the difference between the averages of S/N ratios was greater.

Within the range of control parameters, the delta value will assign rank and average value of S/N ratio, which is been tabulated in the table V & VI for the samples. The ranks to the control factors are assigned by the delta value, highest the delta value will be the 1st rank and highest delta value will be the 2nd rank and so on. The factor load is possessing highest value hence 1st rank is assigned to the load for the sample.2nd rank is given to the percentage of filler material and 3rd rank is given to the sliding distance.

The optimum process parameters level for minimum wear loss of GFRP composites are percentage of filler material is 20%, Load is 20N and sliding speed is 0.75 m/s wear loss is A3,B4,C3 similarly for surface roughness A4,B3,C4.

Fig 2 and Fig 3 shows the main effects plots of S/N ratios for composites graphically. From the figures it is evident that the average means wear loss of as of GFRP composites is 0.089844.

TABLE VI Plan of Experiment using L16 orthogonal array with and without post cured composite

Trial	% of filler material	Load (N)	Sliding speed (m/s)	Wear loss (mm ³ /m)	S/N ratio (dB)	Surface roughness (Ra)	S/N ratio (dB)
1	0	5	0.25	0.15012	16.4712	4.140	-12.3400
2	0	10	0.5	0.11745	18.6029	2.380	-7.5315
3	0	15	0.75	0.00217	53.2708	2.450	-7.7833
4	0	20	1	0.0436	27.2103	1.580	-3.9731
5	10	5	0.5	0.11947	18.4548	2.860	-9.1273
6	10	10	0.25	0.09028	20.8882	3.723	-11.4179
7	10	15	1	0.09875	20.1093	2.920	-9.3077
8	10	20	0.75	0.00602	44.4081	2.670	-8.5302

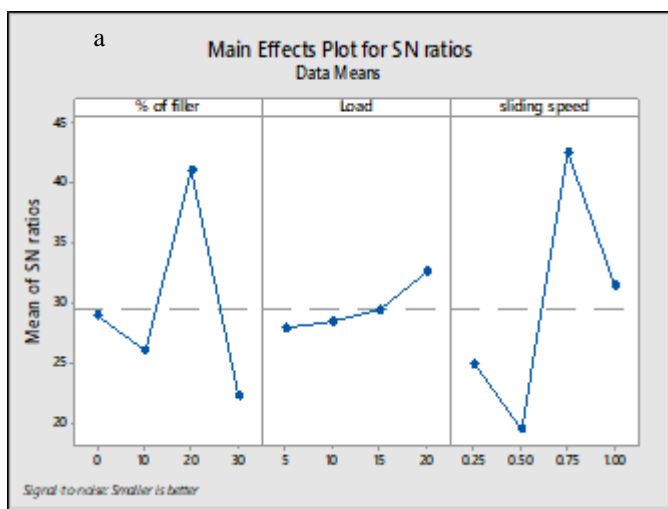
9	20	5	0.75	0.00248	52.1110	6.560	-16.3381
10	20	10	1	0.00201	53.9361	4.680	-13.4049
11	20	15	0.25	0.02925	30.6775	2.593	-8.2761
12	20	20	0.5	0.04357	27.2162	7.143	-17.0776
13	30	5	1	0.06028	24.3965	2.110	-6.4856
14	30	10	0.75	0.09985	20.0130	1.890	-5.5292
15	30	15	0.5	0.21387	13.3970	3.220	-10.1571
16	30	20	0.25	0.02718	31.3150	2.380	-7.5315

TABLE V RESPONSE TABLE FOR SIGNAL TO NOISE RATIOS –SMALLER THE BETTER (WEAR LOSS)

Level	% of filler material	Load	Siding speed
1	28.89	27.86	24.84
2	25.97	28.36	19.42
3	40.99	29.36	42.45
4	22.28	32.54	31.41
Delta	18.70	4.68	23.03
Rank	2	3	1

TABLE VI RESPONSE TABLE FOR SIGNAL TO NOISE RATIOS –SMALLER THE BETTER (SURFACE ROUGHNESS)

Level	% of filler material	Load	Siding speed
1	-7.907	-11.073	-9.891
2	-9.596	-9.471	-10.973
3	-13.774	-8.881	-9.545
4	-7.426	-9.278	-8.293
Delta	6.348	2.192	2.681
Rank	1	3	2



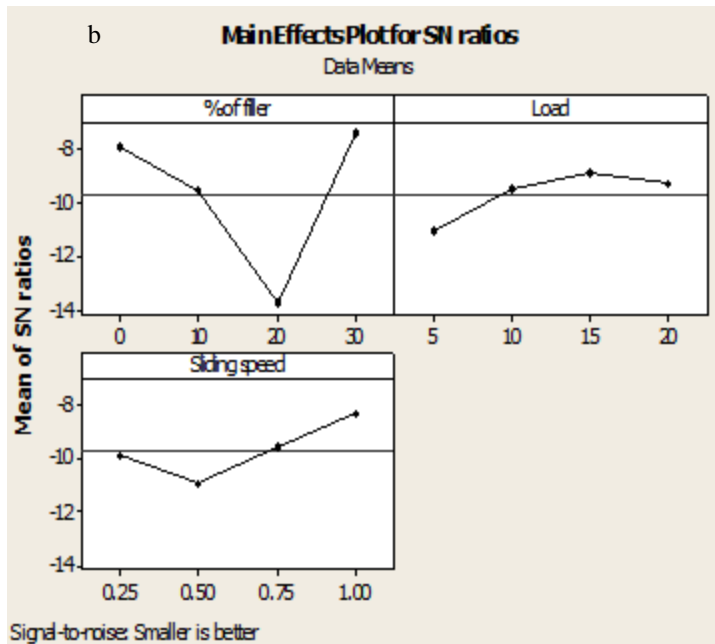


Fig.2: Main effects plot for S/N ratios- specimens (a) wear loss (b) Surface roughness

IV. CONCLUSION

The following conclusions were obtained as an outcome of the investigations:

1. The optimum process parameters level for minimum wear loss for GFRP are percentage of filler material is 20%, Load is 20N and sliding speed is 0.75 m/s wear loss (A3, B4, and C3).
2. The optimum process parameters level for minimum surface roughness GFRP composites, optimum process parameters are percentage of filler material is 30%, Load is 15N and sliding speed is 1 m/s (A4, B3, and C4).
3. As the applied stress is increased, wear loss increases.
4. Wear loss is reduced as the sliding speed is increased.
5. Surface roughness is high for without post cured specimens whereas for as post cured composites it is low.

V. REFERENCES

- [1]. ASM Hand book, 1992, Materials Park, Ohio, USA, ASM International, Volume 18.
- [2]. Algur Veerabhadrapa, Kabadi V R, Ganeshari S M, chavan rao Vithal, 2017, Effect of Mn content on tribological wear behaviour of ZA-27 alloy, Materials today: Proceedings, vol. 4, pp. 10927- 10934.
- [3]. Algur Veerabhadrapa, Kabadi V R, Ganeshari S M and Sharanabasappa, 2014, Experimental Investigation on Friction Characteristics of Modified ZA-27 Alloy Using Taguchi Technique, Int. J. Mech. Eng. & Rob. Res, vol. 3(4), pp.24-32.
- [4]. Algur Veerabhadrapa, Hulipalled Poornima, Lokesha V, Nagara Madeva, Auradi V, 2022, "Machine Learning Algorithms to Predict Wear Behavior of Modified ZA-27 Alloy Under Varying Operating Parameters", Journal of Bio-and Tribo-Corrosion, vol. 8(1), pp. 1-10.

- [5]. B .Suresha, Chandramohan, G., J. N. Prakash, Balusamy, V., Sankaranarayananasamy K., 2006, The Role of Fillers on Friction and Slide Wear Characteristics in Glass-Epoxy Composite Systems. *Journal of Minerals & Materials Characterization & Engineering*, Vol. 5, pp 87-101.
- [6]. B.Suresha, G.Chandramohan, P.Sampathkumaran and S.Sethuramu, 2007, Investigation of the friction and wear behavior of glass-epoxy composite with and without graphite filler, *J. Reinforced Plastics and Comp.*, 26:81.
- [7]. Basavarajappa.S, Chandrmohan.G, Mahadevan.A, Mukundan, Subramanian.R, Gopalakrishan.P, 2007, Influence of sliding speed on the dry sliding wear behavior and the subsurface deformation of hybrid metal matrix composite, *Wear*, Vol. 262, pp. 1007-1012.
- [8]. Chavan Rao Vithal, Dinesh .K.R, Veeresh K., Algur Veerabhadrapa, Shettar Manjunath, 2017, Taguchi's orthogonal array approach to evaluate drilling of GFRP particulate composites, *AMMMT 2016 Materials Today: Proceedings 4*, 11245–11250.
- [9]. Chavan Rao Vithal, Dinesh .K.R, Veeresh K., Algur Veerabhadrapa, Shettar Manjunath, 2018, Influence of post curing on GFRP hybrid composite " *MATEC Web of Conferences 144*, 02011..
- [10]. Chavan Rao Vithal, Algur Veerabhadrapa, Dinesh .K.R, Veeresh K., Gouda Sridhar, 2019, Effect of Post Curing On Rare Earth Particulates Filled Polymer Composite, *JETIR May 2019*, Volume 6, Issue 5 ISSN-2349-5162.
- [11]. Chavan Rao Vithal, Dinesh.K.R, Veeresh K., Algur Veerabhadrapa, Shettar Manjunath, S P Jagadish, C Madhu Mohan, 2015, Evaluating The Influence Of Fiber Orientation And Filler Content On Tensile, Hardness, And Impact Strength, *International Journal of Research in Aeronautical and Mechanical Engineering*, 3(1), 25-31.
- [12]. Gewen Yi and Fengyuan Yan. 2007, Mechanical and tribological properties of phenolic resin based friction composite filled with several inorganic fillers. *Wear*, 262, 121-129.
- [13]. Pascoe, M.W., 1973, Plain and filled plastics materials in bearing: a review. *Tribology*, Vol. 6 No. 5, pp. 184-190.



Investigations on Effect of Fill Ratio and Heat Input on Thermal Performance in Oscillating Heat Pipe using Acetone Working Fluid

M. Prashanth¹, Santhosh Gotagunaki²

¹Department of Mechanical Engineering, Government Engineering College, Hassan-573201, Karnataka, India

²Department of Mechanical Engineering, Government Engineering College, Ramanagara-562159, Karnataka, India

ABSTRACT

In the present study the effect of heat transfer performance of oscillating heat pipe (OHP) using acetone with different fill ratios and heat input. A closed loop oscillating heat pipe with four turns is fabricated and tested. The oscillating heat pipe is filled with 50%, 60%, 70% and 80% fill ratio and 15 w to 40w in steps of 5 w heat input. The variation of temperature difference of evaporator and condenser section temperatures versus Heat is studied at steady state condition. The obtained result indicated that higher fill ratio of working fluid shows the better results in terms of increased heat transfer coefficient and small temperature difference across the evaporator and condenser.

Keywords: Oscillating Heat Pipe (OHP); Acetone; Heat Performance; Fill Ratio, Thermal Resistance, Heat Transfer Coefficient.

I. INTRODUCTION

Thermal management is the challenge of the day in electronic product development. Presently the chip heat flux level range between 40 to 120 W/cm². It is expected to increase to 200 W/cm² in the next few decades. Several cooling methods are employed to cool the electronic devices. Heat pipe is being explored for electronic cooling devices with promising results. Even though the conventional heat pipes are excellent heat transfer devices but their application is mainly confined to transferring small amount of heat over relatively short distances. Oscillating Heat Pipes have proved to transport heat for longer distances, helping in placing the condenser away from compact cabinets. They also proved to be beneficial in the refrigeration applications [1-4]. Several researchers studied the effect of many factors on heat transfer performance of Oscillating Heat pipe (OHP) with traditional working fluids [5-8]. However, the working temperature of OHP with traditional working fluids is more than room temperature. It is difficult for the applications like Aerospace, Refrigeration, and electronic system.

Shafii et al. [6] studied the Thermo hydrodynamics of PHP using multi-quasi steady state, the experiments were conducted for heat input of 10 to 20 watts with Acetone as the working fluid at different fill ratios. The obtained results indicate that churn flow takes place in the evaporator and slug flow in the condenser, it is noticed that continuous heat transfer takes place in both evaporator and condenser. The effect of heat load on the performance of PHP is reported. It indicates the increase in heat load with increase in operating temperature resulting in better thermal performance. Rama narasimha et al. [7] Studied the single loop Pulsating Heat pipe (PHP) with copper tube of 2mm internal diameter in the condenser and evaporator section. They conducted the transient studies for different heat inputs, working fluids and different fill ratios [8]. The obtained results indicated acetone is the most suitable working fluid for pulsating heat pipe operations. From the above literature it reveals that the impact of fill ratio and heat input influence on the performance of oscillating heat pipe (OHP). Hence, in the present investigation, the performance parameters such as thermal resistance and heat transfer coefficient of the OHP with acetone as the working fluid for different fill ratios and heat input has been studied.

II. MATERIALS, METHODS, PROCESSING AND TESTING OF COMPOSITES

A. Experimental setup

The Experimental setup consists of copper tube OHP, power controller, data acquisition systems, steady flow cooling system and evaporator section. The OHP was made up of Copper tube and bent into the coil of 4 turns, inner diameter of the tube is 1.7 mm and outer diameter is 2.4 mm. The length of evaporator section, adiabatic section and condenser sections are 84 cm, 30 cm and 60 cm respectively. The detailed specification of the OHP is given in Table 1. The adiabatic section is insulated using glass wool insulation. In the evaporator section mica heater power of 6 w/cm² and heater temperature range of 500 °C is used to heat the OHP at the bottom, Heater carrying wire is connected to power controller. At the top continuous steady flow of water is used in the condenser section. In the experiment four k type thermocouples in the condenser and four in the evaporator section are connected to Data Logger, the operating temperature of k type thermocouple is -200 to 1260 °C. The assembly of experimental setup is mounted on the wooden board is as shown in Fig. 1.

TABLE I SPECIFICATION OF OSCILLATING HEAT PIPE (OHP)

Sl. No.	Descriptions	Dimensions
1	Number of Turns	4
2	Length of the copper tube in the Condenser	60 cm
3	Length of the copper tube in the Evaporator	84 cm
4	Inner Diameter of Copper Tube	1.7 mm
5	Inner Diameter of Glass Tube	2.4 mm
6	Volume of copper	3.268 ml lit
7	Volume of Glass	1.357 ml lit
8	Total Volume	4.625 ml lit

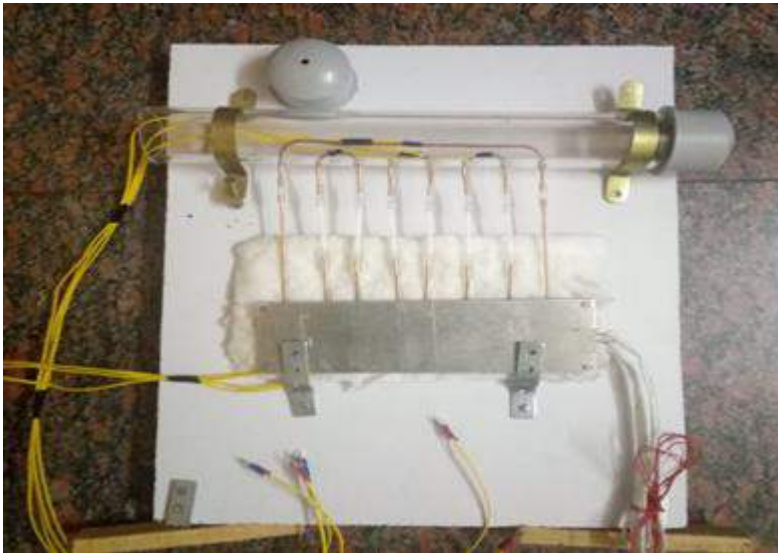


Fig.1 Experimental setup of Oscillating Heat Pipe (OHP)

B. Working Fluids

The first consideration is the identification of a suitable working fluid and the operating temperature range. Within the approximate temperature band, several possible working fluids are employed. A variety of characteristics must be examined in order to determine the most acceptable of these fluids for the application considered. In the present work based on the available literature, Acetone is used as the working fluid. The properties of these working fluid are listed in the table.

TABLE II PROPERTIES OF WORKING FLUIDS

Fluids	Acetone
Boiling Point (° C)	57
Melting Pt. (For Solid State) (° C)	-95
Specific Heat Cp (J/Kg K)	2031
Useful Temp. Range(° C)	0-120

C. Experimental Procedure

The Experiment is conducted for Four turns and working fluid used is Acetone. Before conducting the experiment, it is ensured that there is no fluid inside the tubes. The required amount of working fluid is then filled through a syringe by opening one end the silicon rubber tube and the rubber tube is closed and ensured for tightness without any leakage. Then the display unit is switched on and the thermocouples are checked. The heater plate is connected to the power controller and suitable wattage has been adjusted, it is left until steady temperature is reached and then the data logger is turned on, once the pulsation of the liquid begins and the reading have been taken until flow reaches steady state. Once the reading for a particular heat input is over, the system is kept for cooling the temperature of the copper pipes and the glass tube is monitored in the same

software. Once the pulsations of the liquid are stopped the procedure repeats the heater plate is adjusted to the suitable heat input again and the readings are tabulated.

III. RESULTS AND DISCUSSION

3.1 Effect of Fill Ratio on Temperature

Fig. 2 and Fig. 3 shows the evaporator temperature and difference between evaporator and condenser temperature versus time for different watt at fill ratio of 60% . It is observed that the temperature increases with time as the wattage is increased.

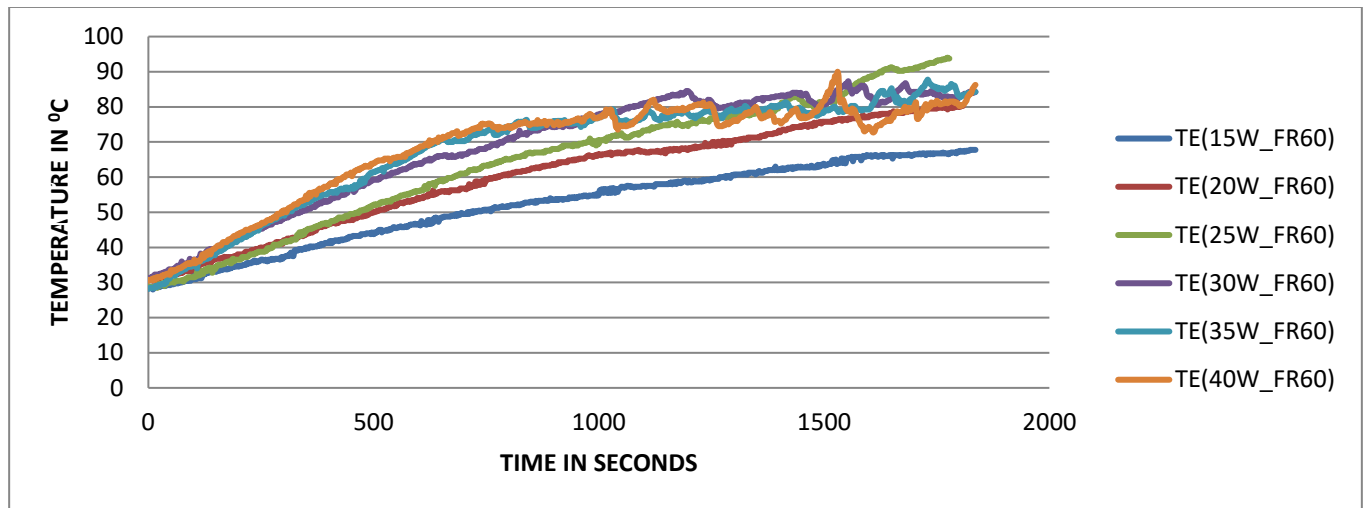


Fig.2 Evaporator temperature for 60% fill ratio (FR) and different watt

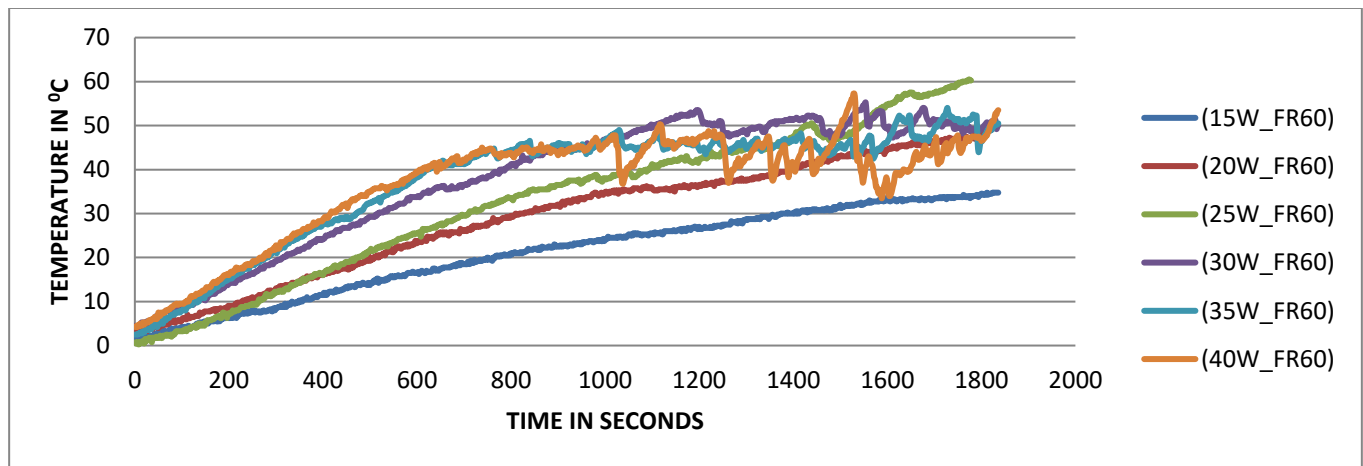


Fig.3 Difference between evaporator and condenser temperature for 60% fill ratio (FR)

Fig.4 and Fig.5 shows evaporator temperature and difference between Evaporator and Condense Temperature Vs Time for different watt at fill ratio of 80% . It is observed that the temperature increases with time as the wattage is increased.

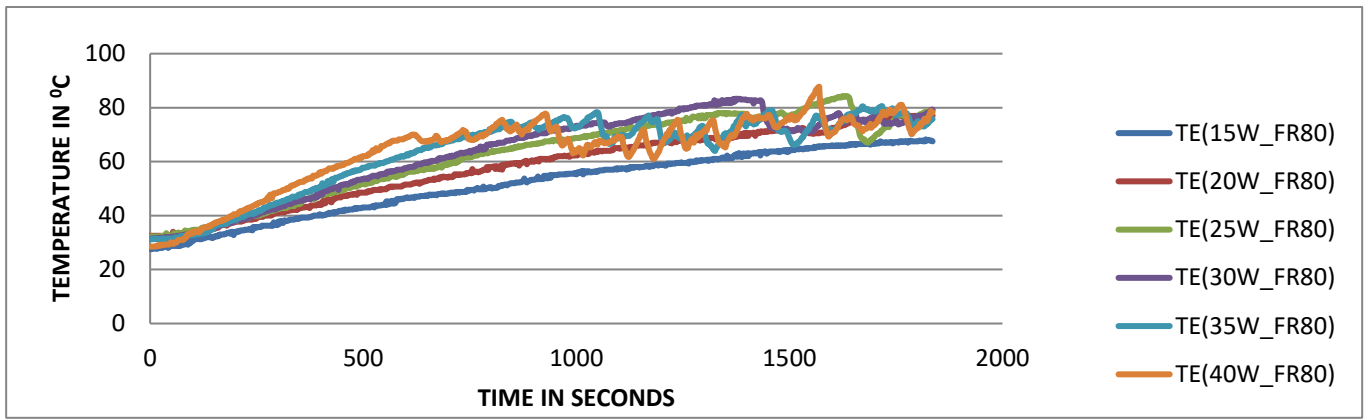


Fig.4 Evaporator temperature for 80% fr and different watt

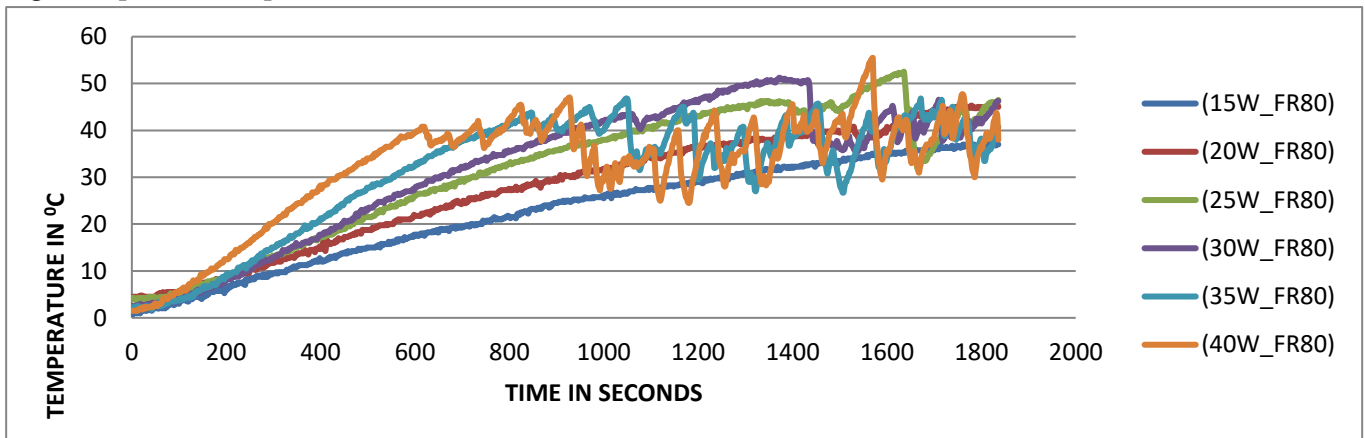


Fig.5 Difference between evaporator and condenser temperatutre for 80%fill ratio.

Fig.6 shows the variation of temperature difference of Evaporator and condenser section temperatures versus Heat for Acetone fluid at different Fill Ratio (FR). It is seen that temperature Difference is less for 15 watts and it increases for 40 watts this is because temperature difference is directly proportional to heat input, as heat input increases temperature difference increases.

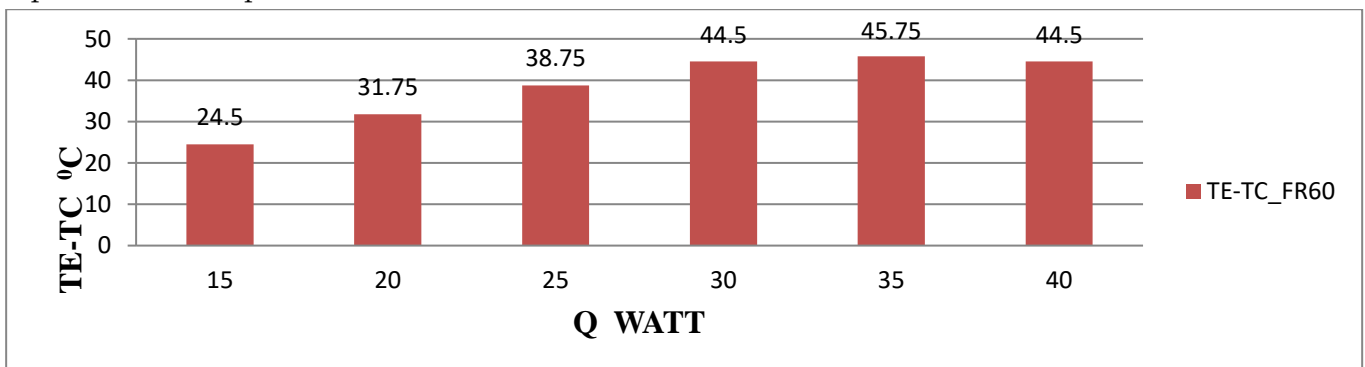


Fig.6 The variation of temperature difference of evaporator and condenser section temperatures versus Heat at steady state condition

The Figure 4.7 represents the thermal resistance versus the heat input for various fill ratios, from 50% to 80% fill ratios for Acetone fluid. The Thermal Resistance R is given by

$$R = \frac{TE - TC}{Q} \text{ K/W}$$

As we can observe from the graph the thermal resistance decreases with increase in the fill ratio, the thermal resistance is least for 80% fill ratio and the thermal resistance increases as the fill ratio decreases and it is highest for 50% ratio. This is because in 80% fill ratio there is more volume of fluid compared to 50%, 60%, 70% fill ratios and thus better transfer of heat is possible due to the presence of more volume of liquid compared to volume of vapour.

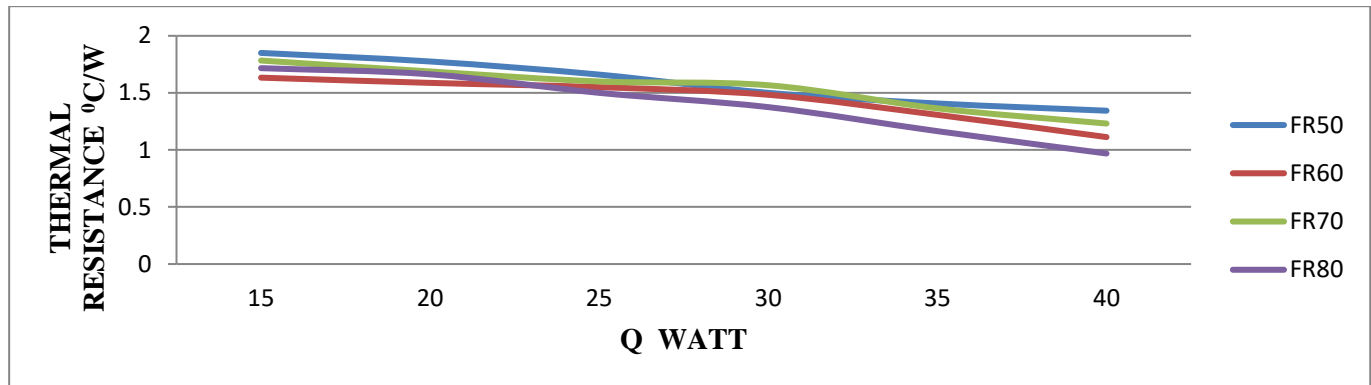


Fig.7. Thermal Resistance (R) V/s Heat (Q) for different fill ratio

Fig.8 shows the heat transfer coefficient (h) vs heat (Q) for different fill ratio for the acetone fluid. The higher fill ratios of working fluid shows better results in terms of increased heat transfer coefficient decreased thermal resistance and small temperature difference across the evaporator and condenser.

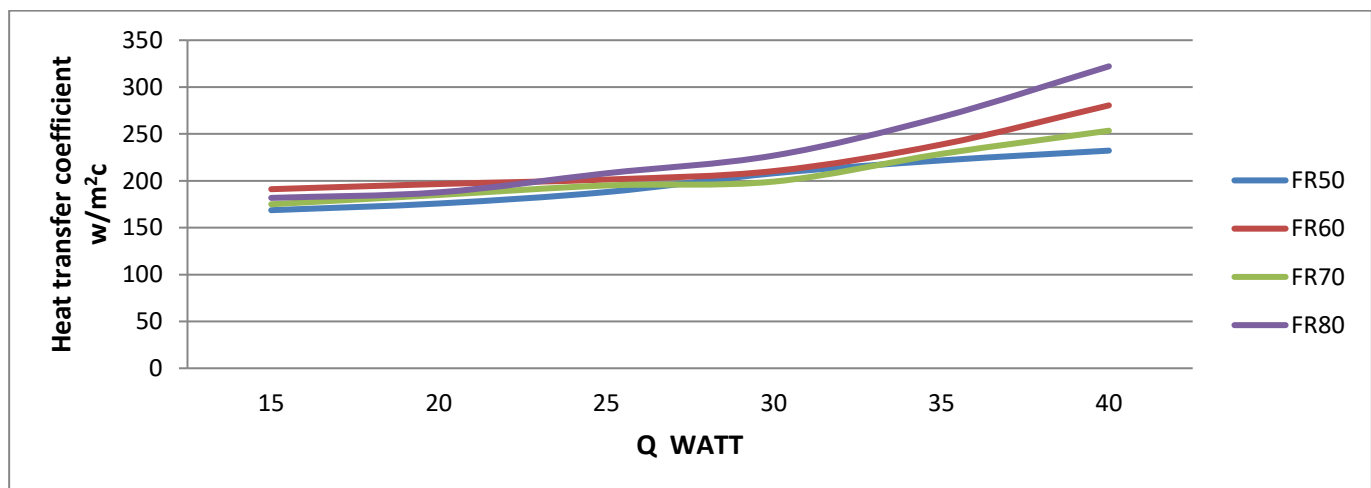


Fig.8. Heat transfer coefficient (h) vs Heat (Q) for different fill ratio

IV. CONCLUSION

This work presents the experimental investigations of a OHP. The effects of input power, time constant, heat transfer coefficients and the thermal resistance on the performance of the heat pipe are studied through experimentation. The results of the present study are summarized as follows.

- The results indicate that acetone can transfer more heat with less temperature difference and less thermal resistance. Thus acetone can be considered as more suitable working fluid for OHP operation.

- The overall heat transfer coefficient of heat pipe increases with increase in heat input, in the range of inputs tested for acetone
- In case of acetone, the temperature difference across evaporator and condenser continues to drop down with an increase in the fill ratio.
- With acetone as the working fluid, 80% fill ratio of evaporator volume shows the best result with minimum temperature difference across the evaporator and condenser.

The higher fill ratios of working fluid shows better results in terms of increased heat transfer coefficient, decreased thermal resistance and small temperature difference across the evaporator and condenser.

V. REFERENCES

- [1]. Prafull V Shahare, Jain K. K., (2012) Review of Unsolved matters related to Pulsating Heat Pipes, International Journal of Mechanical Engineering and Robotics Research, Vol. 1, No. 2, pp 220 – 228.
- [2]. Ch. Sreenivasa Rao, AVSSKS Gupta and K. Rama Narasimha, (2013) Influence of Working Fluid on the Performance of a Single Loop Pulsating Heat Pipe, International Journal of Emerging Technology and Advanced Engineering, Vol.3, Issue 4, , pp 460 – 464.
- [3]. Prafull V Shahare, Jain K. K.,(2012) Review of Unsolved matters related to Pulsating Heat Pipes, International Journal of Mechanical Engineering and Robotics Research, Vol. 1, No. 2, , pp 220 – 228.
- [4]. Rudra Naik, Venugopal Varadarajan, Pundrika G., Rama Narasimha K., (2013)Experimental Investigation and Performance Evaluation of a Closed Loop Pulsating Heat Pipe, Journal of Applied Fluid Mechanics, Vol.6, No.2, 2013, pp 267 – 275.
- [5]. Rama Narasimha K., Sridhara S.N., Rajagopal M.S., Seetharamu K.N., (2012) Influence of Heat Input, Working Fluid and Evacuation Level on the Performance of Pulsating Heat Pipe, Journal of Applied Fluid Mechanics, Vol. 5, No. 2, Issue 10, pp 33 – 42.
- [6]. Shafii, B. M. Faghri, A. Zhang, Y., (2001) Thermal modeling of looped and unlooped pulsating heat pipes”, ASME J, Heat Transfer, Vol.123 No.6, pp.1159-1172.
- [7]. Rama Narasimha K., Sridhara S.N., Rajagopal M.S., Seetharamu K.N., (2010) Parametric Studies on Pulsating Heat Pipes, International Journal of Numerical Methods for Heat and Fluid Flow, Vol.20, No.4, pp 392 – 415, Emerald Publications.
- [8]. Sreenivasa Rao, AVSSKS Gupta and K. Rama Narasimha, (2013) Effect of Design Parameters on the performance of a Closed loop Pulsating Heat Pip, International Journal of Mechanical Engineering and Technology, Vol.4, Issue 3, , pp 306 – 317.



Intelligent Autonomous Braking System for Accident Prevention

Prashanth K P¹, Amruth K U^{1*}, Chandru M K¹, Sanman S², Yashaswini T C³

¹Department of Automobile Engineering, Acharya Institute of Technology, Bengaluru, India

²Department of Mechanical Engineering, Acharya Institute of Technology, Bengaluru, India

³Department of Civil Engineering, Acharya Institute of Technology, Bengaluru, India

ABSTRACT

There exist few objects and obstructions on the roads which we concern a lot about but these might not be visible from the vehicle's cabin, such as kids playing around or pets relaxing behind the vehicle. If the driver is unaware of these objects or obstructions, both the external obstructions and the vehicle will suffer significant damage and hence it is essential to have an intelligent system that automatically engages the brakes to limit the amount of damage caused during an unexpected situation. The "Intelligent Autonomous Braking System" is an electronically controlled car slowing mechanism in which the infrared sensor, ultrasonic trigger and receiver circuit, control unit, and pneumatic slowing mechanism are all housed in a sensor operated pneumatic braking system. The ultrasonic and infrared sensors are used to identify obstacles, and if an obstruction is found, the ultrasonic or infrared sensor sends a signal to the control unit to engage the slowing mechanism, which is a pneumatic slowing mechanism for vehicle safety. In essence, the vehicle brakes without the assistance of the driver by determining the best path away from the object. The ultrasonic and infrared sensors fixed both at the front and the rear of the vehicle provides the necessary signal to the control unit to engage the braking mechanism.

Keywords : Ultrasonic trigger, Infrared sensor, Intelligent Autonomous Braking System, Obstacle.

I. INTRODUCTION

Ultron and Infrared course circuits are used to operate a pneumatic slowing mechanism, resulting in an Intelligent Autonomous Braking System. The primary goal of this task is for the vehicle to be able to turn around and perform programmed braking in an event when an obstruction is being detected by the system as well as for the vehicle to disengage the system when appropriate space is detected. The braking circuit's role is to brake the vehicle appropriately after receiving a signal from the sensor. These concepts address the use of mechanical brakes to replace human intervention [1]. While traveling at a speed of fifty kilometers per hour, the automated slowing system can stop the vehicle in 2 to 3 seconds, within a distance of 1 meter. The intelligent braking system is completely automated, allowing the driver to let the vehicle stop once the obstacle is detected. It also includes a normal mode for basic conventional operation. In addition, the framework contains a late catch that, when held, supersedes the slowing mechanism. The present stopping mechanism is

activated when the release button is depressed. This mode is activated when the night time factor is greater than the day time threshold for the sensors to detect the area ahead.

II. METHODOLOGY

This paper started with field research, in which numerous articles and papers relevant to the concept were reviewed and observed. This leads us into the next step, which was problem facing. The study explored various and common challenges/difficulties such as to overcome the limitations of the previously studied experiments that were recorded in the field study stage. Following this, auto-electronic sensors and the problems faced in their applications were studied. Finally, ideas were transformed into a physical project and the last phase, testing was carried out to evaluate the working of the model.

The ultrasonic sensor consists of transmitter and receiver units, with the ultrasonic transmitter transmitting signals that are reflected back to the ultrasonic receiver unit to detect the obstacle. The ultrasonic sensor information is then used to determine whether or not there are any objects in the vehicle's path. If an item is identified, the system can determine whether the vehicle's speed is greater than that of the object ahead of it. The computations will take done through a PIC microcontroller using an Arduino dumped C programme, based on the stated maximum distance and distance between the automatic system and the barrier. Through servomotor braking mechanism phenomena, the DC gear motor rotates consistently at a given rpm and gradually drops speed while automatically breaking the system. A large speed disparity may suggest the likelihood of a collision, in which case the system is capable of automatically applying the brakes.

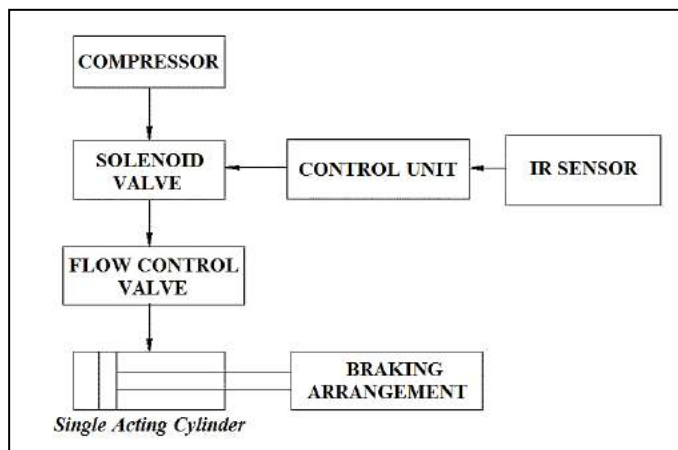


Figure 1: Primary segments canny switch stopping mechanism

Ultrasonic moving and spotting systems use high-recurrence sound waves to determine the distance and range of an object. An ultrasonic sensor often employs a transducer that generates an electrical yield signal when ultrasonic energy is applied. Fig. 1 shows the primary segments canny switch stopping mechanism. An Arduino is used to detect the pulses and apply brakes to the vehicle [2, 9]. There are two types of energy supply required, i.e. the electric supply for the functioning of the ultrasonic sensor control unit, and the air supply for the pneumatic brake to work. Different surfaces exhibit different responses. Some surfaces scatter, reflect, and absorb infrared radiation, making it difficult to interpret sensor output as a distance measurement [3]. Ultrasonic STNT is made up of an ultrasonic transmitter and a receiver. An ultrasonic transmitter sends a

constant stream of graded class waves. Ultrasonic waves are created when the vehicle gets too close to a deterrent, which are then picked up by the Ultrasonic receiver. The control unit is powered after receiving the reflected signal. This controls whether or not the solenoid valve is to be switched on. These tactics are entirely electronic, necessitating the use of computerized inventory.

III. COMPONENTS OF SYSTEM

The components and requirements for the complete operation of the pneumatic bearing press are as follows:

A. Control Unit

The main parts of the control unit are:

- 1) Arduino Uno: The ATmega328 microprocessor is used in the Arduino Uno microcontroller board (datasheet). It has 14 digital input/output pins, six analogue inputs, and a 16 MHz ceramic resonator (six of which can be used as PWM yields). A USB port, a power jack, an ICSP header, and a reset switch are also included. Everything a user needs to get started with the microcontroller is included. It merely requires a USB cable to connect to a computer, or an AC-to-DC adapter or a battery to power it.
- 2) Relay: Relays are electronic and electromechanical switches that are used to close and open circuits. It controls how connections in an electrical circuit open and close. The device is made up of a set of input terminals for a single or many control signals, as well as a set of operational contact terminals. The switch can have several contacts in any contact form, such as 'make contacts', 'break contacts' and combinations of the two [4].

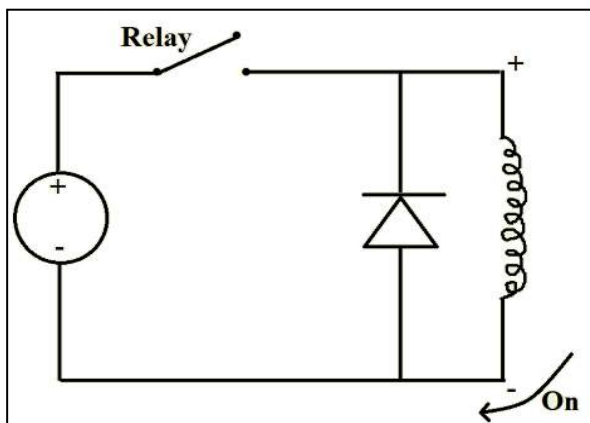


Figure 2: Snubber Diode Circuit

The switch connections on the relay are generally labelled 'COM,' 'NC,' and 'NO':

- COM stands for Common Terminal, and it is always connected to a terminal depending on the application.
- NC = Normally closed; while the relay coil is off, COM is linked to NC.
- NO = Normally open; when the relay coil is on, COM is linked to NO.

A snubber diode was used to protect the circuit from voltage spikes. Fig. 2 shows a snubber diode circuit being used.

B. Sensor Unit

The sensor unit consists of an ultrasonic transmitter for creating ultrasonic beams and an ultrasonic collector for receiving ultrasonic beams that are reflected back from obstacles. When Ultrasonic receiver receives waves reflected from the obstacle, it communicates the data to the control unit. The control unit then determines the distance between the deterrent and the vehicle, and if the distance is within a specific range, it sends a signal to the solenoid valve, which therefore engages the brake.

C. Ultrasonic Sensor

The ultrasonic sensor detects an obstruction in the path of movement and sends the signal to the microcontroller. It acts as the eyes of the control unit. The HC-SR04 Ultrasonic Sensor is a low-cost proximity or distance sensor that is primarily used for object detection in robotics applications. It simply acts as a pair of eyes for the Arduino. It comprises of 4 pins, that is: GND, Vcc, Trig (output) and Echo (input) [8].

D. Infrared sensor

An infrared sensor (IR sensor) is an electronic sensor that detects and analyses infrared radiation in its environment. Infrared detection and accuracy can outperform ultrasonic detection over long distances [5]. It accomplishes this by generating and detecting infrared radiation in numerous ways. Infrared sensors can also detect movement and measure the heat generated by an object. It has 3 pins, that is: Vcc, GND and Out [10].

E. Pneumatic cylinder

The compressor function is performed by the pneumatic cylinder. A compressor is a mechanical device that reduces the volume of a gas in order to increase its pressure [6]. When an action requires more than one movement and a device to transfer load in both directions, double acting cylinders come in handy. Double-acting air cylinders do not require a spring to inflate and retract, unlike single-acting air cylinders. Double acting cylinders have two ports via which air can flow in and out instead of a single port for providing pressured air. Few advantages of using a double acting cylinder are that they offer more control over movement since pressurized air moves both ways, they are both fast and strong and also use less energy. Double acting cylinders also feature design variations, ie. stroke and bore sizes which can be chose according to the design requirements.

F. Solenoid valve

To regulate the fluid flow automatically, solenoid valves are employed. A solenoid valve is an electrically controlled valve. The valve uses a solenoid, which is an electric coil with a moveable ferromagnetic core (plunger) at its centre. In the rest position, the plunger covers a small aperture. When a magnetic field is created by passing an electric current through the coil, the plunger is pushed higher by the magnetic field, which in turn opens the aperture. This is the basic principle which is employed to open and close the solenoid valves.

G. Flow Control valve

A flow control valve regulates the volume of air that flows in one direction alone. This valve is used to keep the compressor from being disrupted. A non-return valve and a variable throttle combine to make a flow control valve. Between the solenoid valve and the compressor, there is a flow control valve. The flow control valve, on the other hand, is usually attached to the cylinder. Because the piston moves faster when this valve is used, the time consumption is reduced.

Technical Data:

Size: 1/4th inch.

Pressure: 0 to 10 kg/cm².

Media: Air.

H. Motor

A three-phase squirrel cage induction motor is a form of electromagnetic three-phase induction motor. A squirrel cage motor's capacity to change its speed-torque characteristics is a key advantage. This can be done easily by changing the shape of the rotor's bars. Squirrel cage induction motors are commonly used in industry because they are dependable, self-starting, and easy to tune.

IV. EXPERIMENTATION

The intelligent autonomous braking system consists of an ultrasonic sensor which when detects an obstruction ahead, engages the pneumatic brakes automatically. The goal of this project is to slow down the automobile when an obstacle or a barricade is sensed with the sensors which are placed both at the front and the rear of the vehicle. Furthermore, the usage of a button to apply the brakes is preferred by the vehicle's motive force.

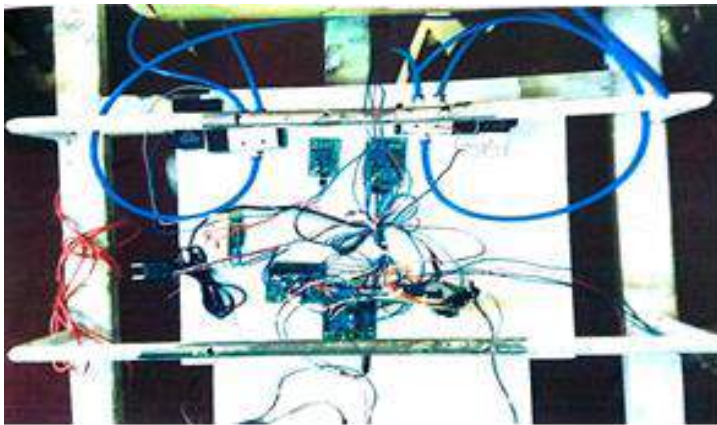


Figure 3: The circuit in application

An air storage tank, an ultrasonic sensor, a double acting pneumatic cylinder, a solenoid valve, and a control unit are all part of the system. A flow control valve is integrated in the air storage tank, which regulates the float of air pressure through the tank. The solenoid valve receives high-pressure air.

A solenoid valve is an electromechanically operated valve controlled by a solenoid that acts as an interface between the control unit and the pneumatic cylinder, with the control unit guiding the action.

The solenoid valve controls the double acting pneumatic cylinder, which generates force in a reciprocating linear motion using compressed air energy. The control unit is regarded to be the brains of the system, as it is powered from the outside and receives signals from the ultrasonic sensors.

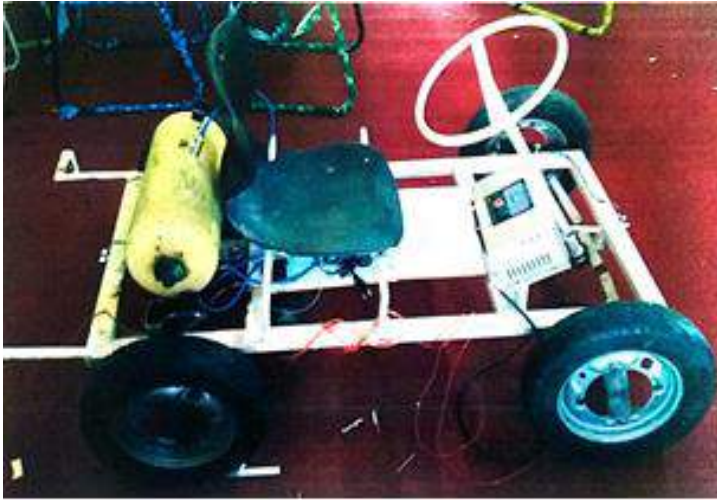


Figure 4: Side View of the test vehicle

The ultrasonic sensor consists of a trigger and a receiver. The trigger releases ultrasonic waves, which are absorbed by the receiver when the waves are obstructed by an object. If the ultrasonic wave is redeemed within the sensor's range, a response is given to the control unit, which then activates the solenoid valve, which ejects high-pressure air into the pneumatic cylinders. The shaft protruding from the cylinder now travels perpendicular to the shafts linked to each of the rear wheels [i.e. brakes]. As a result, the car is brought to a complete stop.



Figure 5: Rear View of the test vehicle

A rectifier converts AC to DC and serves as the control unit for the intelligent autonomous braking system. This system's speed controller transforms 250 V AC to 188 V DC, which drives a 1 horsepower motor. The two infrared sensors at the back of the car detect an obstruction or barrier and provide a signal to the pneumatic braking system to activate. By loosening or tightening the screw on the sensor circuit board, the infrared detection range can be manually changed. The vehicle's forward and reverse motion is controlled by pressing the corresponding switches on the velocity controller. The intensity of the brakes can be adjusted using the adjustment screw situated on each of the pneumatic cylinders. The ultrasonic sensors, which are located on both sides of the vehicle's chassis and have a detection range of up to 400cms, are mounted on both sides of the vehicle's chassis. The power is transmitted via the differential with the help of a ball joint, which eliminates the problem of meshing that can arise when gears are utilised.

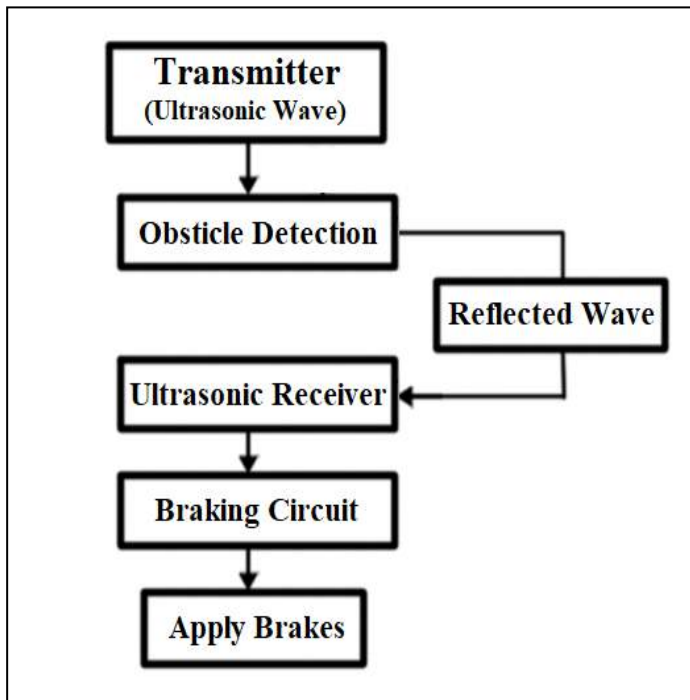


Figure 6: Sensor-Brake block diagram [7]

Also, the driver is provided with a button which can be pressed at any occasion anticipated by the driver, and when the button is pressed, a signal is sent to the control unit, which directs the solenoid valve for the application of brakes through the pneumatic cylinder, permitting for regular braking of the vehicle.

V. RESULTS AND DISCUSSION

Consider a vehicle driving through a crowded parking space at a speed of 15 Kmph. If there is an obstruction caused to the vehicles path, such as a random pedestrian getting into the path, pets moving around or a random object which is out of sight of the driver, the intelligent autonomous braking system detects these random objects present within the sensors range ie. up to 400cms and automatically applies the brakes to reduce the damage caused both for the obstructing object and for the vehicle itself.

The Fig. 7(a) and Fig. 7(b) represent the effectiveness of the intelligent autonomous braking system. When the

obstruction at point 'b' is identified within the sensors range (~150cms) at point 'a', the autonomous brakes engage, as shown by the green line between points 'a' and 'b', thus slowing the vehicle to a standstill without colliding with the obstacle. The blue line indicates the absence of the automatic braking system and hence leads to a collision with the obstacle which is out of sight from the driver's cabin.

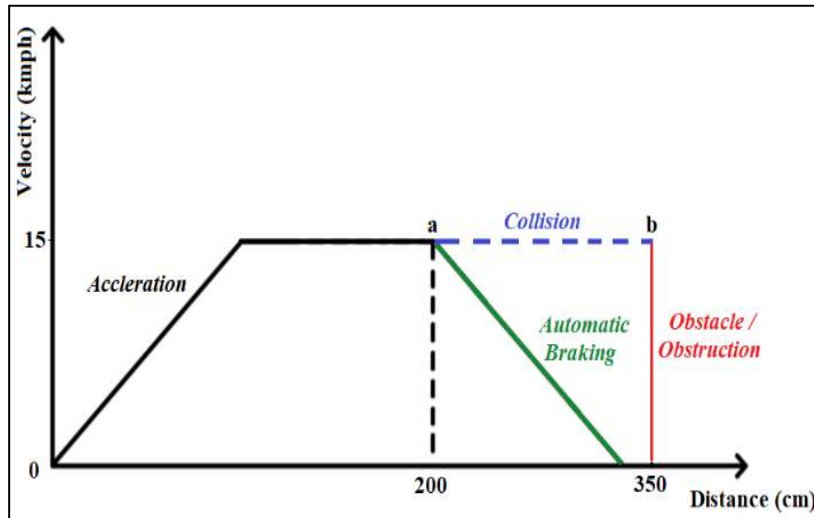


Figure 7(a): Absence of automatic braking

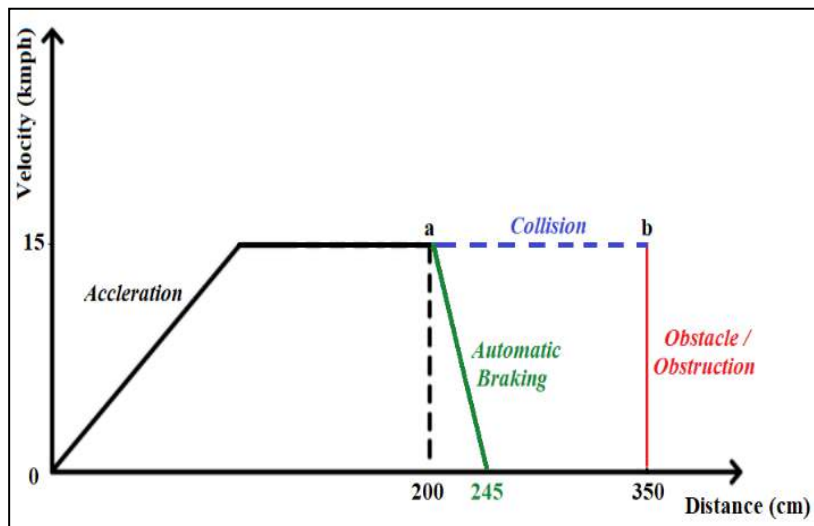


Figure 7(b): Intelligent automatic braking in action

The pneumatic cylinder in Fig.7 (a) is set at the lowest intensity and the vehicle moves up to 130cms with the brakes applied before coming to a complete stop. When the pneumatic cylinder is set to its full potential, the vehicle can reach a complete standstill within 45cms post the object detection, and this is represented in the Fig. 7(b).

VI. CONCLUSION

Every feature of each component present in the prototype test vehicle functions effectively and the whole system together reflects successful results. Once the obstruction or the obstacle is detected, the vehicle moves

till the safe distance and is braked until the path of travel is free from any kinds of obstructions. The prototype's ultrasonic sensor has a range accuracy of around 2cm to 4m and operates perfectly within the prescribed range. The functioning of the system was analysed by plugging in the system into the battery, and by controlling the braking system with a DC motor and a servo motor's assistance. This is an immature approach, and this effort is towards to reduce the damages which may occur due to poor vision or during critical driving scenarios.

VII. REFERENCES

- [1]. Prashanth, K.P., Padiyar, K., Naveen, K.P.H. and Kumar, K.S., 2014. Road accident avoiding system using drunken sensing technique. *International Journal of Engineering Research and Technology*, 3(10), pp.818-823.
- [2]. Gajanan Koli, Akshay Patil, Prasad Patil, Shubham Sokashe, "Intelligent Braking System using the IR Sensor", *International Journal of Advances in Scientific Research and Engineering (IJASRE)* ISSN: 2454-8006, Vol.03, Issue 2, March -2017
- [3]. Niveditha, P. and Gowri, S., 2014. Collision warning system using ultrasonic sensors and automatic brake system. In *Proceedings of the 5th International Conference on Recent Trends in Information, Telecommunication and Computing* (pp. 419-424).
- [4]. Prashanth, K.P., Prajwal M and Deepak J., 2020. Motorcycle headlight design for clear visibility & comfort riding. *Our Heritage Journal*, 3(22), pp.240-248.
- [5]. Hai Wang & Ronghong Xiao, "Automatic Car Braking System --Based on original reverse warning system" March 2012
- [6]. Tembhurkar, C., Jatav, V., Pande, A., Udupurkar, S., Sinha, N., Borkar, P., Thakre, A., Madankar, V. and Runghe, K., 2018. Design of Intelligence Braking System.
- [7]. G.V. Sairam, B. Suresh, CH. Sai Hemanth, K. Krishna sai, Intelligent Mechatronic Braking System, *International Journal of Emerging Technology and Advanced Engineering*, ISSN 2250-2459, Volume 3, Issue 4, April 2013
- [8]. Naveen Navudu, Aravind Ramapatruni, Jagadeesh Polaki, Jaya Surya Navagana, Srihari Palli, Automatic Breaking System Using Ultrasonic Sensor, AUG 2021, *IRE Journals*, Volume 5 Issue 2, ISSN: 2456-8880
- [9]. G.Muthu Brindha, K.K.Karishma, A. Mukhesh, K.K.Nilesh Veeramani, M.Mohamed Faizal, Dr.B.Maruthi Shankar, B.Vidhya, Accident Prevention By Automatic Braking System And Multisensors, *International Journal of Advanced Science and Technology*, Vol. 29, No. 8s, (2020), pp. 873-879
- [10]. J.V.Sai Ram, K.M.S.V.Manikanta, G.Pavanth, B.Jagadeep ,Dr. B.Raghu Kumar, Automatic Braking System Using Ultrasonic Sensor, *International Journal of Innovative Science and Research Technology*, Volume 2, Issue 4, April- 2017 ISSN No: - 2456 – 2165



Influence of Deccan Hemp Biodiesel over the Performance and Emissions of a CI Engine

N. Srujana¹, G. Bhanodaya Reddy¹, J Subramanyam²

¹Department of Mechanical Engineering, SVU College of Engineering, Sri Venkateswara University, Tirupati, Andhra Pradesh, India

²Department of Mechanical Engineering, Vemana Institute of Technology, Bengaluru, Karnataka, India

ABSTRACT

Pollution levels for two decades have risen to alarming levels due to rapid growth in transportation sector all over the world. In this regard many researchers worked on finding an alternate fuel either to replace or to blend partially with diesel. In this work, Deccan hemp oil's influence over the performance of internal combustion engine is studied experimentally. This paper presents the trials conducted by blending the diesel and the Deccan hemp oil at five different ratios. The performance and emission characteristics are elaborated. It was evident from the results that emissions improved briefly but the performance was less than the diesel engines.

Keywords: Alternate fuels, Biodiesel, Deccan Hemp oil, Emissions, Diesel.

I. INTRODUCTION

Two main outcomes of industrialization had severe impacts on the environmental aspects of the earth. These were rapidly driven by the transportation and the power generation sectors that actively employed fossil fuels. This led to the increase in pollutants and the global temperature levels. With the recent estimations in energy scarcity of fossil fuels in near future many organisations and researchers turned towards the renewable and novel energy generation and consumption approach.

Most of them are mainly focused in creating bio diesel as an alternate fuel to support or completely replace the diesel fuel. Oils that were massively accredited for their energy potential are palm oil, rice bran oil, cotton seed oil, jatropha oil, mahua oil. These were the biproducts of agricultural waste which were commonly available in many developed nations (Ravichandra, Puli, Chandramohan and Geo, 2018) [1].

India is known for its agricultural production capacity due to the vast availability of cultivable land. This agricultural advantage paves way for the abundant availability of options for bio diesel generation. Factors that influence in choosing a particular oil source is dependent on its accessibility, availability, associated costs and majorly the oil yield per kilogram (Sonar et al. 2014) [2].

Most of many lands which are not suitable for agricultural purpose can be used for processing the non-edible oil which would help in fighting the food vs fuel crises. Bio diesel production from non-edible sources will also help in tackling the socio-economic problem in backward or rural regions (Shehata2013) [3].

Utilisation of bio diesel has its own setbacks, the main problem is associated in using them is viscosity. The viscosity of most biodiesels is higher than diesel, thus making it difficult for them to flow through small places and even atomisation is affected. These are mainly responsible for reduction in thermal efficiency of the engines (Nwafor 2004) [4].

Thus, bringing down the viscosity has been the main objective when exploring alternate energy sources for the internal combustion Engine (Senthil kumar 2015) [5].

Many clogging problems like injector clogging were encountered when the raw oils were used. Thus, oils were blended with diesel and they achieved similar performance results without substantial modifications to the engine. This was even experimented with altering the inlet temperature of fuel (FIT) (Chauhan et al. 2010) [6].

II. METHODOLOGY

The oil was extracted from Deccan hemp seeds from a local dealer. The thermo-physical properties of the extracted oil were examined for its density, viscosity, flash and fire points. A bomb calorimeter was used for estimating the calorific value of the oil. The same procedure was followed for examining the properties of the oil extracted from the transesterification process.

A. Transesterification Process :

The general procedure of transesterification was followed where Ethanol and Potassium Hydroxide were used as catalysts. Dilution of these catalysts was done by mixing 200 ml and ten grams of ethanol and Potassium hydroxide, respectively. One litre of extracted oil was then mixed with the diluted catalyst solution and this entire mix was heated to 60° C for thirty minutes. After the entire solution is left undisturbed for one complete day, two layers were formed and with the influence of gravity the heaviest glycerol layer settles down. The upper layer was of ester that was washed away by water and dried later at temperatures above boiling point of water. The extracted biodiesel was blended with diesel in a volumetric fashion to obtain these compositions Dh05D95, Dh10D90, Dh15D85, Dh20D80, and Dh25D75.

TABLE I FUEL COMPOSITION TABLE

composition	Diesel (%)	Deccan hemp oil (%)
Dh05D95	95	5
Dh10D90	90	10
Dh15D85	85	15
Dh20D80	80	20
Dh25D75	75	25

The properties of the fuel samples blended are mentioned in the following table.

TABLE 2 FUEL COMPOSITION PROPERTIES

composition	Viscosity (Cst at 40°C)	Density (kg/m ³)	Calorific Value (MJ/Kg)	Fire point (°C)	Flash point (°C)
Diesel	3.04	840	45.5	62	51
Dh05D95	3.17	843.7	44.46	63	58
Dh10D90	3.24	850.5	43.26	65	61
Dh15D85	3.31	856	41.46	69	63
Dh20D80	3.34	861	39.28	72	66
Dh25D75	3.41	868	36.72	75	69

III. TESTING

The predefined compositions were tested for their pollutant formation and performance of the engine. It is to be noticed that the experiment runs were conducted with no load condition as the focus of this work is to observe the performance of fuel but as the loading is introduced into the experiment then this would hinder the performance to an extent. The motto of this work is to first of all identify the discrepancies associated in using biofuels as an alternate fuel source. The experimental setup that is employed in this scenario was of Kirloskar make single cylinder Combustion Ignition Engine.

A. Emissions Analyser:

QROTECH 401 was used as the gas analyser which has the capability to measure five pollutants. They are CO, HC, CO₂, NO_x, and O₂. The method employed to detect these pollutants is NDIR for CO, HC, CO₂ and the other two are captured using electro-chemical method.

TABLE 3 TEST RIG SPECIFICATIONS

parameter	Value
Manufacturer	Kirloskar Oil Engines Ltd
Power Output (rated)	7.5Kw@1500rpm
Bore(mm)	116
Stroke(mm)	102
Engine Volume (cc)	948
Starting type	Hand cranking
Fuel type	Diesel



Figure No.1 Test engine setup



Figure No.2 Exhaust gas analyser



Figure No.3 Hot Plate Magnetic stirrer

Hot plate magnetic stirrer was used for mixing the diesel and bio diesel into the proportionate ratios. The stirrer was run for 12 minutes at 45°C. This leads to a uniform distribution of biodiesel.

IV. RESULTS

A. Cylinder pressure:

The cylinder pressure reading of the experiments shows the results in reference with diesel run (black line). The maximum pressure of 87 bar was observed for the 100 percent diesel runs while the maximum pressure achieved by biodiesel was 80 bar for Dh5D95 fuel sample.

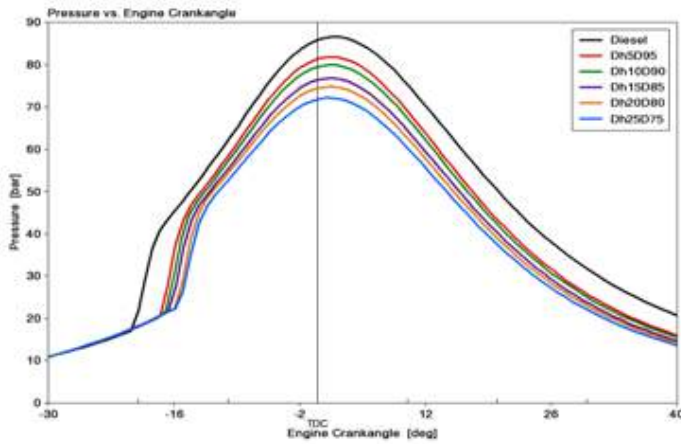


Figure No.4 Cylinder Pressure

It can be seen that there is an ignition delay of at least 4° CA for the diesel and biodiesel samples.

B. Heat release rate :

The instantaneous heat release of the diesel was maximum with 300 J/deg, while the samples with 5 and 10 percent biodiesel blends were more than 273 Joules

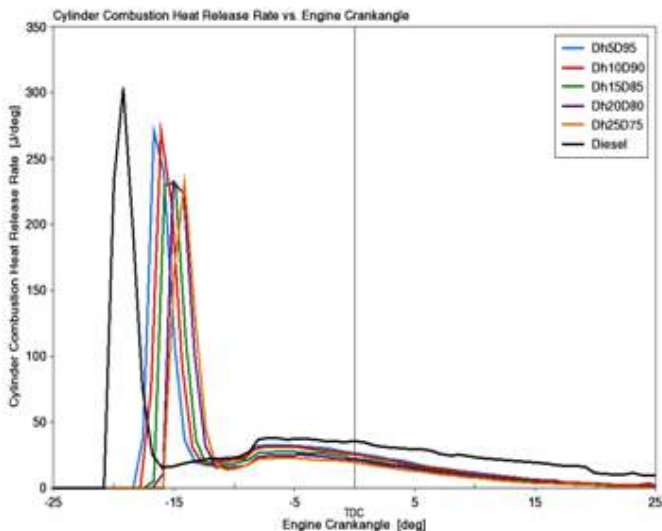


Figure No.5 Heat release rate

The fuels with further dilution of biodiesel dropped gradually in heat release with the lowest being 236 J/deg. The location of maximum heat release has a direct effect on the BTE of the engine.

C. Hydro-carbon emissions:

The hydro-carbon fuel emissions of diesel fuel were 0.158 g/kW/hr which was the lowest while the Dh5D95 fuel sample emitted the lowest of the biodiesel fuel sample which was 0.186 g/kW/hr. However, the emissions rose rapidly for the samples with more than 10 percent biodiesel fuel content. The highest emissions of 0.218 g/kW/hr were recorded when the Dh25D75 sample was run. Thus, it is evident that as the dilution increased the emissions also increased.

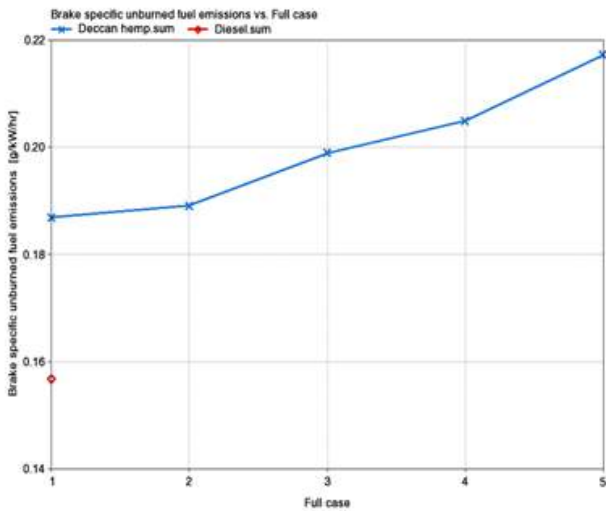


Figure No.6 Hydro-carbon (HC) emissions

D. Carbon monoxide :

The carbon monoxide depicts an inverse behaviour to the HC emissions where the diesel fuel emission was 0.16 g/kW/hr while the Dh05d95 emitted just over 0.35 g/kW/hr. The CO emissions decreased rapidly for the first three fuel samples with the least dilutions.

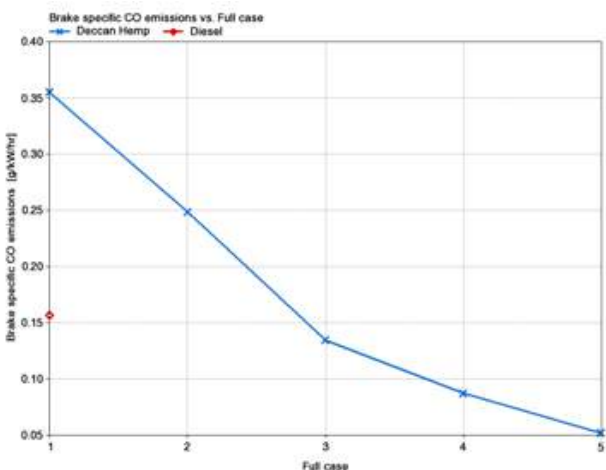


Figure No.7 Carbon monoxide (CO) emission

The Dh25D75 sample produced less CO emissions of 0.05 g/kW/hr. the emission for the samples Dh15D85, Dh20D80 and Dh25D75 were less than the diesel fuel emissions.

E. NOx emissions :

The trend of the NOx emissions was similar to that of the CO emissions. The fuel samples with less dilution generated more emissions as higher temperatures are observed. The Dh05D95 sample produced 5650 ppm which was the highest while the Dh25D75 produced the least of 4500 ppm. However, the 100 percent diesel fuel produced much lesser emissions than Dh25D75 fuel sample. The emissions of diesel run were 4400 ppm.

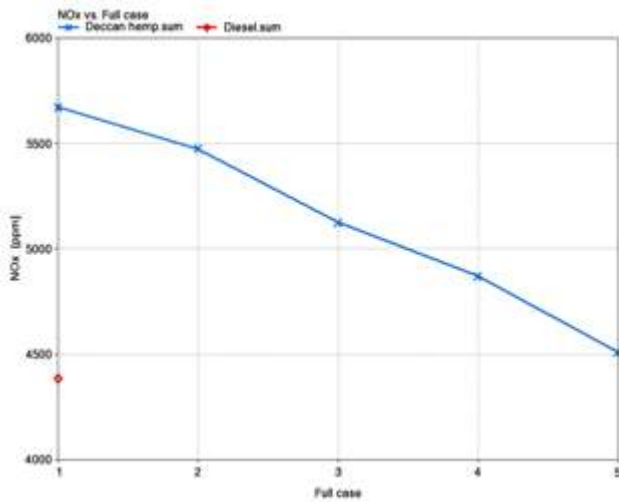


Figure No.8 Oxides of Nitrogen (NOx)

V. CONCLUSION

The main factor that influences the overall performance and emissions of the engine are the developed cylinder pressure. The cylinder pressure is in turn dependant on the ignition delay property of the fuel. As this ignition delay is more for the biodiesel blended fuel samples compared to the diesel fuel this resulted in the generation of less pressure at TDC which led to the decrease in BTE of engine with increase in biodiesel composition

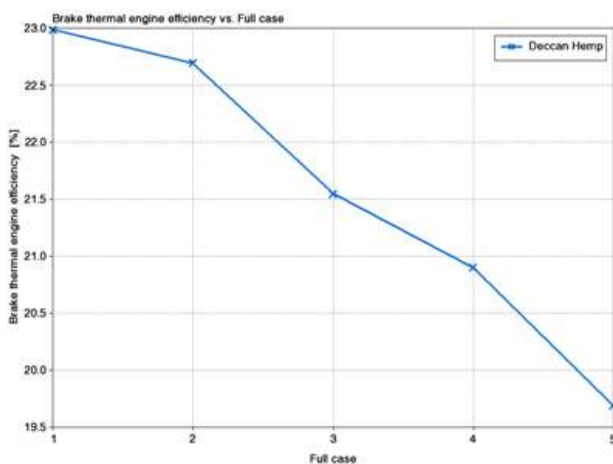


Figure No.9 Brake thermal efficiency

Since the cylinder pressure is again the ability to of the fuel to burn quickly, the heat release of the diesel is quicker than the biodiesel blends. This is primarily due to the density and the viscosity of the fuel. As the blend percentage of the biodiesel increased, the average density and viscosity of the entire fuel sample increased, resulting in faster settling of fuel droplets, much coarse atomisation of fuel. These factors led to the decrease in combustion efficiency. This in turn led to more emissions depending upon the scenario of poor and better combustion which led to formation of CO, HC and NO_x formation.

VI. REFERENCES

- [1]. Ravichandra, D., Puli, R., Chandramohan, V. and Geo, V., 2018. Experimental analysis of Deccan hemp oil as a new energy feedstock for compression ignition engine. *International Journal of Ambient Energy*, 40(6), pp.634-644.
- [2]. Sonar, D., S. L. Soni, D. Sharma, A. Srivastava, and R. Goyal. 2015. "Performance and emission characteristics of a diesel engine with varying injection pressure and fuelled with raw mahua oil (preheated and blends) and mahua oil methyl ester." *Clean Technologies and Environmental Policy* 17 (6):1499–1511.
- [3]. Shehata, M. S. 2013. "Emissions, performance and cylinder pressure of diesel engine Fuelled by biodiesel fuel." *Fuel* 112: 513–522.
- [4]. Nwafor, O. M. I. 2004. "Effect of advanced injection timing on emission characteristics of a diesel engine running on biofuel." *International Journal of Ambient Energy* 25 (3): 115-122.
- [5]. Senthilkumar, P., and G. Sankaranarayanan. 2015. "Effect of Jatropha methyl ester on waste plastic oil fueled DI diesel engine." *Journal of the Energy Institute*, article in press: 1 – 9.
- [6]. Chauhan, B. S., N. Kumar, Y. D. Jun and K. B. Lee. "Performance and emission study of preheated Jatropha oil on medium capacity diesel engine ." *Energy* 35: 2484-2492.



Nursery Monitoring System using IoT

Sanjay H S¹, Hemanth U¹, Vaidesh B¹, Harisha V R¹, Lakshmi D L², Goutham V²

¹Student, Department of Electronics and Communication Engineering, BGS Institute of Technology,
Adichunchanagiri University, BG Nagara, Karnataka, India

²Assistant Professor, Department of Electronics and Communication Engineering, BGS Institute of Technology,
Adichunchanagiri University, BG Nagara,, Karnataka, India

ABSTRACT

This paper is based on Nursery Monitoring System. In these days each and every one thinks that agriculture is just a physical work which is not at all a justified answer. There is also a way to help farmers by using advanced technology which can bring a good and big impact on agriculture.

This paper is about design of the Nursery Monitoring System using modern Technology by which we can have the best possible quality of plants for formers. This modern Technology includes all the modern and innovative technology like providing the proper sunlight, water and temperature to the plants in every climatic condition using sensors. By using this we can obtain a good yield plants and it can provides a maximum profit to the farmers.

Keywords: Nursery, plants, sensors, temperature, humidity

I. INTRODUCTION

A nursery is place where the plants are propagated and grown. Nursery may be open fields' container fields or greenhouse in which plants are grown. Shrubs and Decorative trees are grown in Open fields. Small trees and herbaceous plants, which are basically for sales in garden centres, are grown in Container fields. These nurseries have good ventilation with proper sunlight and watering time to time for the growth of plants. The grown plants are taken from roots or from shoot tips based on the type of the plants. The common method is used in nurseries is cutting of plants. With proper procedure the plants are grown in these nurseries which yield good growth.

Here we have used some of the sensors which can detect the temperature, soil moisture and light intensity. These parameters are controlled by some of the innovative techniques.

II. METHODOLOGY

Design of Nursery Monitoring System is represented with the block diagram which consists of Temperature sensor, Soil moisture sensor and Light sensor. All the sensors are connected to the microcontroller which controls the operation of Exhaust Fan, Water pump and shade net.

The block diagram representation of Nursery Monitoring System is as shown in the figure 1.

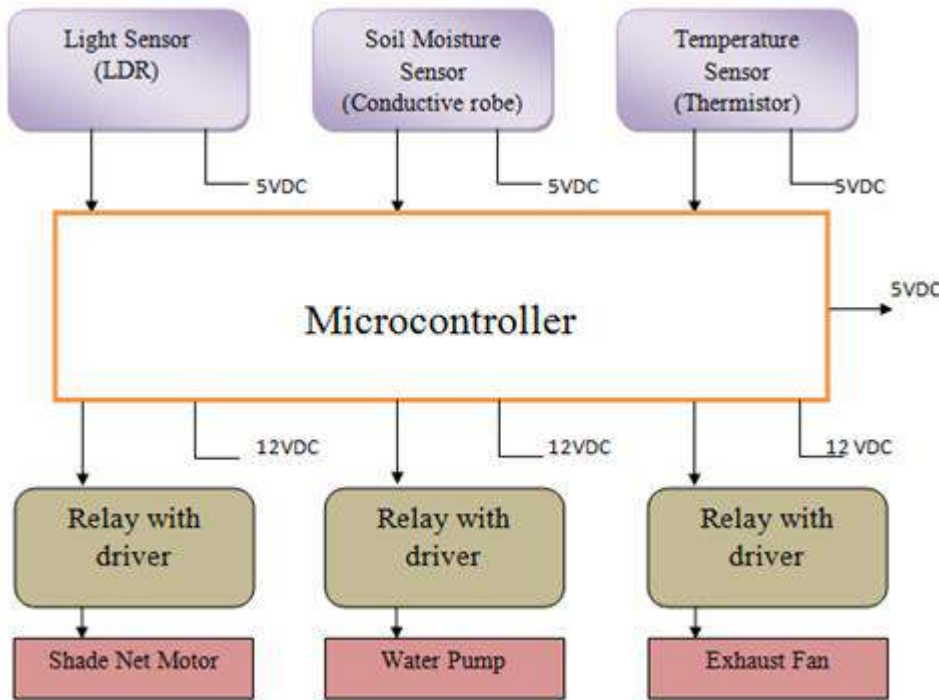


Figure 1: Block diagram representation of Hi-Tech Nursery

Temperature sensor: When the temperature changes above the set value, the fan will turn ON until the temperature will comes below the set value. When the temperature reaches the reaches below the set value the Fan will automatically turns off.

Soil Moisture: When the soil present inside the tray gets dry the Soil moisture sensor detects, the signal is passed through the microcontroller and turns ON the water pump to pour the water on the tray until the plants get the sufficient water for proper growth.

When the soil gets enough moisture, the sensor again detects the moisture level and turns OFF the water pump.

Light Sensor: The LDR circuit senses the intensity of the light. When the light intensity varies above the set value the Shade net will open to provide the sunlight to the plants.

When the light intensity is below the set value then the shade net will automatically close using the shade net motor.

By this way, the different sensors detects the parameters like temperature, soil moisture and the necessary sunlight required to the plants and fullfill the requirements controlling the exhaust fan, water pump and shade net.

III. ADVANTAGES

- Easy for Human resource
- Less effort
- Less cost
- Maximum profit
- To magnify the light of the sun while protecting plants from freezing temperatures.
- Less dependence on the owner
- Less time consumption
- Usage of smart technologies
- Plants are grown according to their climatic conditions.

IV. FIGURES AND TABLES

SENSORS CONDITIONS	STATUS OF MOTOR	STATUS OF FAN	STATUS OF WATER PUMP
Temperature > Set value	-----	ON	-----
Temperature < Set value	-----	OFF	-----
Light intensity < Set value	Turn ON the Motor [Open the shade Net]	-----	-----
Light intensity > Set value	Turn ON the Motor [Close the shade Net]	-----	-----
Soil Moisture < Set value	-----	-----	Turn ON the Water Pump
Soil Moisture > Set value	-----	-----	Turn OFF the Water Pump

TABLE: controlling of motor, fan and water pump through sensors

When the temperature value is greater than the set value the Fan Turns On and when it is less than the set value the Fan Turns Off.

Similarly, when the light intensity is lesser than the set value the Shade net opens and reverses its operation when the intensity value becomes greater than the set value.

The soil moisture value is also monitored and Turns On the water pump and when there is sufficient moisture in the soil, the water pump will be Turned Off.

These actions are given in the above Table.

The designed Nursery Monitoring System is as given in the figure 2.



Figure 2: Nursery Monitoring System

V. CONCLUSION

Even though there is a huge demand and also a challenging, there are various possibilities like creating complex connections of plants which are similar or it is also termed as “Internet of Plants”. Here, using more than one sensor indicates experimental venture. Different experimental and challenging ideas like using solar power supply and time for setting irrigation system are employed here. This system controls the amount of water released from the farm from the process of watering the plant. This IoT based monitoring system solves many problems and promotes wide range of applications to the farmers with affordable cost.

VI. REFERENCES

- [1]. https://www.researchgate.net/publication/317649753_High_Tech_Nursery_Management_in_Horticultural_Crops_A_Way_for_Enhancing_Income
- [2]. https://www.researchgate.net/publication/276417195_DESIGN_AND_DEVELOPMENT_OF_SOIL_MOISTURE_SENSOR_AND_RESPONSE_MONITORING_SYSTEM



A Review on Microstrip Patch Antennas

Imran Khan^{1*}, Vaishnavi H T¹, Kiran K B¹, Yuktha M¹, Kavya M R¹

¹Department of Electronics and Communication Engineering, Government Engineering College, Ramanagara, Karnataka, India

ABSTRACT

Antenna play a critical role in today's rapidly evolving wireless world. An antenna is a directing device that is used to receive and transmit radio waves. Because of its multiple advantages, such as high dependability, light weight and ease of manufacture, antenna designers are putting more emphasis on MSPA today. Patch antennas, despite their benefits, have certain disadvantages including low gain and limited bandwidth. These shortcomings can indeed be addressed by paying attention to a few criteria while designing antennas. This paper is a review of MSPAs based on three factors: feeding techniques, substrate type and patch shape. Existing literatures studies are also analysed in detail, highlighting the use of various feeding mechanisms, substrates and slots for multiple radio technologies.

Keywords: Feeding, Microstrip Patch Antenna, Patch Shape, Substrate, Slots, 5G

I. INTRODUCTION

In today's world the cell phone has become an indispensable element of our lives. Previously, mobile phones were only used to communicate with others. However, the use of mobile phone applications has grown to the point where they have become a necessary part of everyone's day-to-day activities such as shopping, trip planning, e-commerce and navigation. Early communication systems only allowed analogue voice, but now offer a diverse range of applications to a huge number of users. In the previous few years, we've seen the gradual evolution of mobile communications with the introduction of 1G, 2G, 3G, 4G, and wireless networks. Because of the growing number of smart phone users, wireless communication data traffic is expanding with the introduction of new Internet of Things technology.

Wireless system designers will need a new idea and design approach to meet the needs of 5th generation wireless systems, which include faster data rates, better reliability, more connectivity, more latency, and stronger security measures. In a substantial percentage of the area, researchers have been intrigued to Microstrip Patch Antennas in the past because to their many appealing properties.

Microstrip patch antenna structures are relatively simple to make, which has transformed Microstrip analysis into a major study topic. The Microstrip antennas are relatively inexpensive to manufacture and design because of the simple two-dimensional physical geometry. They are usually employed at UHF and HF because the size

of the antenna is directly tied to the wavelength at the resonant frequency [1]. The goal of this paper is to review different feeding techniques, substrates, different shapes and slots that can be used in designing of MSPA. The antenna needs to be tiny enough to fit within any new technology's compact communication equipment.

II. MICROSTRIP PATCH ANTENNA

Microstrip is a type of electrical transmission line comprises of a conductor separated from a ground plane by a dielectric layer called the substrate. Microstriplines are a type of microwave-frequency signal transmission cable. A conducting patch, a dielectric substrate, and a ground plane are the three components of a microstrip patch antenna detailed in Figure 1. On the top and bottom of the substrate, the patch and ground planes are printed in order. The patch can be any shape: rectangular, square, triangular, circular, elliptical, or any other.

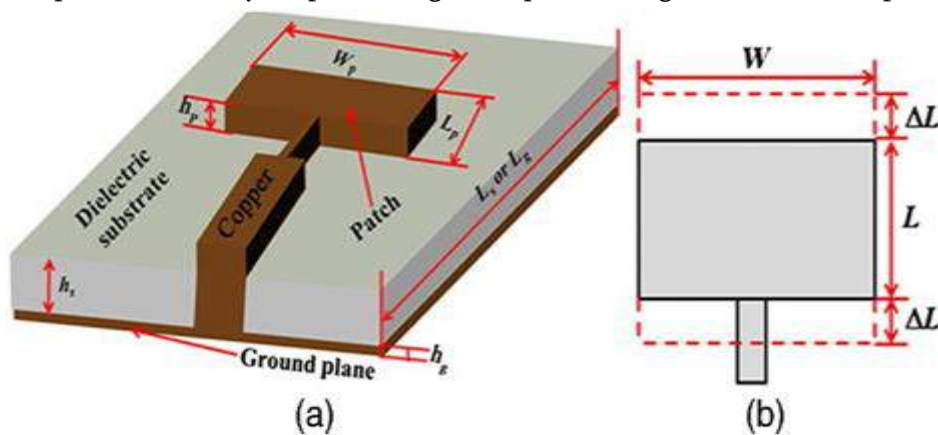


Figure1: Microstrip Patch Antenna

Based on prior research on microstrip antennas, the study reveals that the microstrip patch antenna has a number of distinct advantages, including light weight, low cost, low profile, planar configuration, superior portability, suitability for arrays, ease of fabrication, and easy integration with external circuitries, to name a few. Though standard microstrip antennas have many advantages, they also have three major drawbacks: narrow bandwidth, poor gain and relatively large size, all of which have a negative impact on antenna efficiency [2].

III. CLASSIFICATION OF MSPA BASED ON VARIOUS CRITERIA

The following classification are done depending on substrate, depending on feed, depending on shape & slots.

A. Depending on type of Feeding Techniques

A microstrip antenna can be fed in a variety of ways. The feedline is a narrower conducting strip when compared to the patch width. Radio-frequency power/energy is delivered directly to the radiating patch in contacting feed via a Microstriplines or coaxial line. Microstrip feedlines are easy to make and can be etched on

the same substrate as the feed for a planar construction. Centre feed, offset feed, and inset feed are the three types of microstrip feed lines. Coaxial feed line is also known as probe feed.

Line Feed

In this form of feed technology, a conducting strip is directly attached to the microstrip patch's edge. The conducting strip is smaller than the patch, allowing the feed to be etched on the same substrate as the patch, resulting in a planar structure. This feed mechanism as shown in Figure 2 is simple to build and emits very little unwanted radiation. The function of the inset cut in the patch is to match the impedance of the feed line to the patch without using any additional matching devices [3].

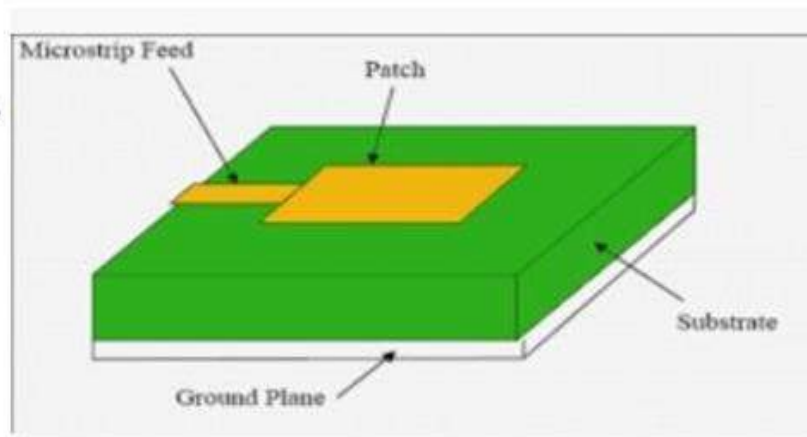


Figure 2: Line Feed

Co-axial Feed

The co-axial feed as given in Figure 3, is a non-planar feeding technique that uses a co-axial cable to feed the patch. The probe is positioned at the 50 ohms antenna input point and is in direct contact with the antenna. This feed mechanism is easy to build and emits very little unwanted radiation [3].

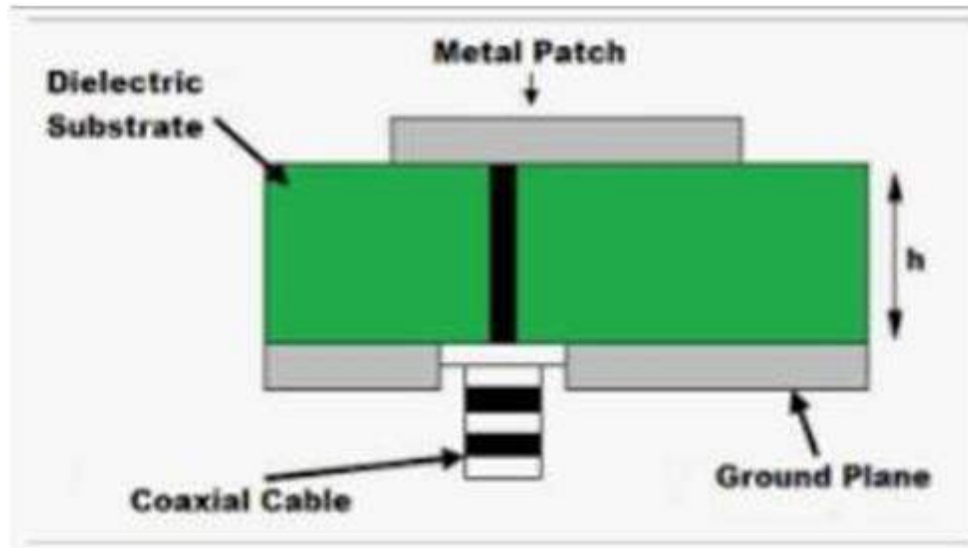


Figure 3: co-axial feed

Aperture Coupled Feed

Antenna and feed dielectric substrates are used in the aperture feed technique as given in Figure 4. These dielectric substrates are separated by a ground plane with a slit in the middle. The ground plane is positioned on the opposite side of the antenna dielectric. The feed dielectric and feed line are placed on the opposite side of the ground plane, which provides isolation. The bandwidth of an aperture-fed antenna is greater [3].

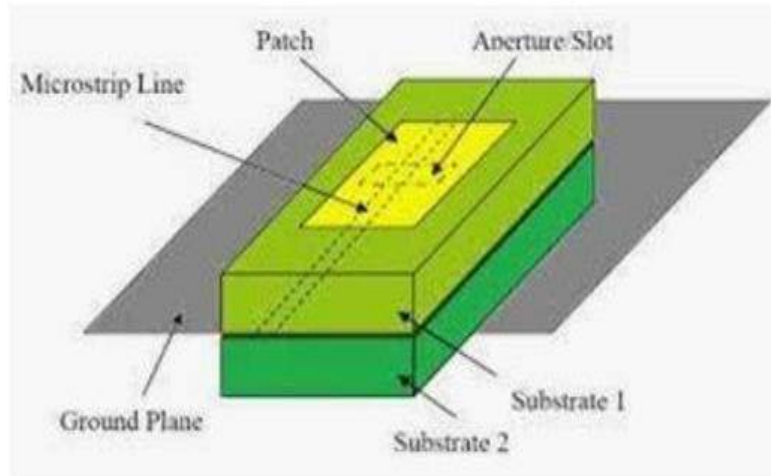


Figure 4: Aperture Coupled feed

Proximity Feed

In proximity feeding, this feed line is sandwiched between two dielectric surfaces as indicated in Figure 5. In the edge feed approach, picking a 50 ohms feed point is impractical due to the high impedance at the edges. Electromagnetic field coupling is used to transmit electricity from the feed to the patch. The radiation from the feed line has been greatly reduced as a result of the feed line being lowered to a lower level, and this technology also allows for planar feeding. In comparison to the other approaches, it also has a higher bandwidth efficiency [3].

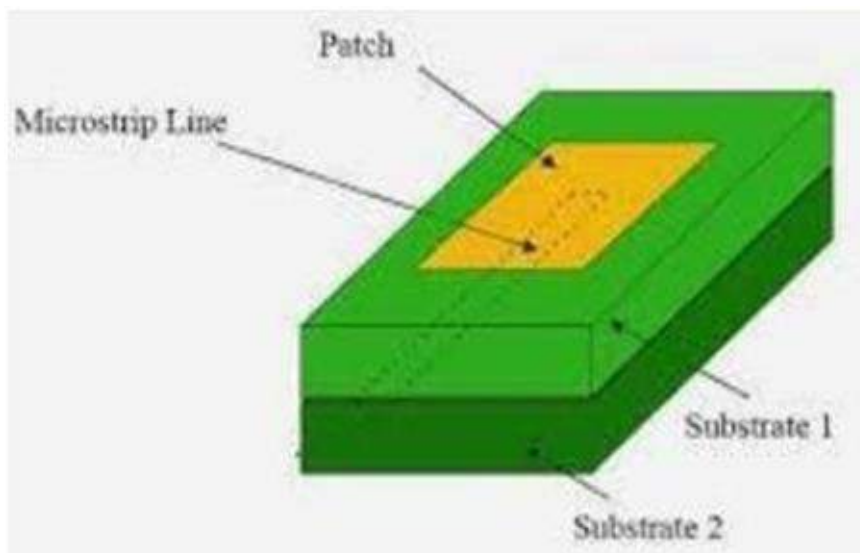


Figure 5: Proximity feed

B. Depending on Substrates

The dielectric substrate material selection is one of the most essential elements in the microstrip antenna design process. Thickness, permittivity and loss tangent are all important criteria to consider while designing an antenna. In order to obtain the design antenna size and performance, these factors must be chosen carefully. Surface waves are generated when the substrate material is thicker, which influences the antenna's radiating characteristics [4]. As a result, the dielectric substrate has a considerable impact on the overall performance of a microstrip patch antenna. To build a Microstrip patch antenna, one must be aware of the various substrate options and their characteristics that are indicated in Table I. Various types of substrate are reviewed which includes FR4 Epoxy, RT Duroid, LCP, Bakelite, TLC, and R04003.

The FR4 substrate is widely available and inexpensive with a high dielectric constant of 4.4 that improves its electrical properties. It can also be used as an insulator in electrical systems. The MSPA will be built using a FR4 substrate, which will save time and money. It has a dielectric constant of 4.4 [3].

Roger Corporation manufactures RT Duroid, a glass microfiber reinforced polytetrafluorethylene (PTFE) composite. RT duroid offers the lowest electrical loss of any reinforced polytetrafluorethylene (PTFE) material, as well as isotropic and homogenous electrical properties and low moisture content [5].

Liquid Crystal Polymer (LCP) are actually inspiring thermoplastic natural materials made up of particles with unbending and adaptable monomeric units. High mechanical qualities are provided by the rigid monomer. LCP is substantially less expensive than other dielectric materials, making it interesting for low-cost high- frequency design. It also has a lower dielectric constant. The LCP substrate is a good contender for improving gain in the lower band [6].

Bakelite, also known as poly oxybenzyl methylene glycol anhydride, is a primitive plastic. It's a thermosetting phenol formaldehyde resin made by combining phenol and formaldehyde in an elimination reaction. The most typical application is as an electrical component. It is mechanically strong insulator [7].

TLC is designed to be a versatile microwave substrate. Compared to thermostats (Fr-4, PPO, BT, polyimide and cyanate ester), TLC offers better electrical execution [5].

The R04003 hydrocarbon earthenware manufacturing overlays are designed to provide unrivalled high recurrence execution and circuit fabrication with minimal effort. The end result is a low-failure material that can be made with ordinary epoxy/glass (Fr-4) forms that are available at high targeted costs [5].

TABLE I Substrate property comparisons

Different substrates	Loss tangent	Dielectric Constant	Tensile strength	Break Down Voltage	Density	Surface resistivity
RT Duroid	0.0009	2.2	450MPa	> 60Kv	2200kg/m	3×10^7 moh mm
LCP	0.004	2.8 – 3.0	200MPa	37Kv	1.76g/cm ³	NA
Bakelite	0.002	4.8	60 MPa	2 – 28Kv	1810kg/m	5×10^{10} moh m
TLC	0.003	3.2	NA	NA	NA	1×10^7 moh m
R04003	0.0027	3.55	141MPa	NA	1790kg/m	4.2×10^9 moh m
FR4	0.02	4.4	< 310MPa	55Kv	1850kg/m	2×10^5 moh mm

C. Depending on Shape of the Patch

Microstrip patch antennas exist in a number of shapes, but the most common are rectangular, circular, triangular, and elliptical. Few shapes are shown in Figure 6. The radiating patch and feed lines are typically photo-etched on the dielectric substrate. Antennas come in a range of designs depending on the pattern or direction required for transmission.

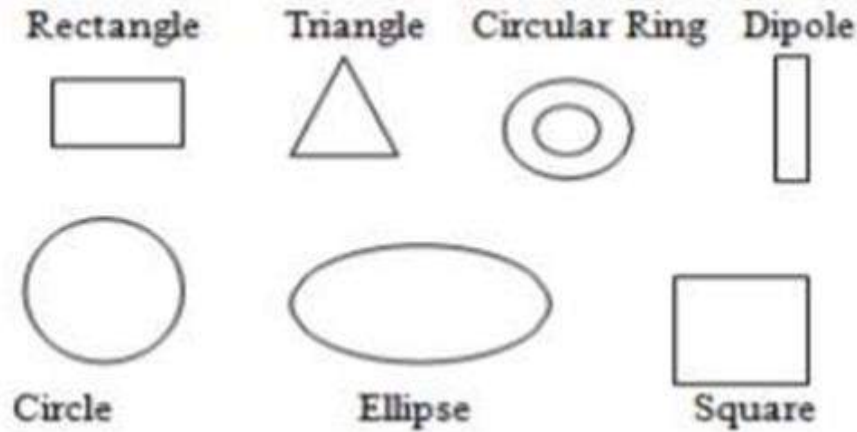


Figure 6: Patch Shapes

Types of Slots

On the relevant shapes, different types of slots can be engraved. Few are indicated in Figure 7. Slot antennas are utilized in the frequency range of 300MHz to 25GHz. When a high-frequency field crosses a slot in a metallic sheet, energy is emitted, according to slot antennas. This is why, when an electromagnetic wave is emitted through a slot etched onto the surface of a copper plate, the slot acts as an antenna. They are often used in navigation radar usually as an array fed by a waveguide.

U-slot: A U-shaped slot in a probe-fed microstrip patch antenna on a low permittivity (foam) substrate greatly improved the otherwise narrow impedance bandwidth (BW). The presence of two resonances—one of the patch and the other of the U-shaped slot—was thought to be the cause of the higher impedance bandwidth at the time.

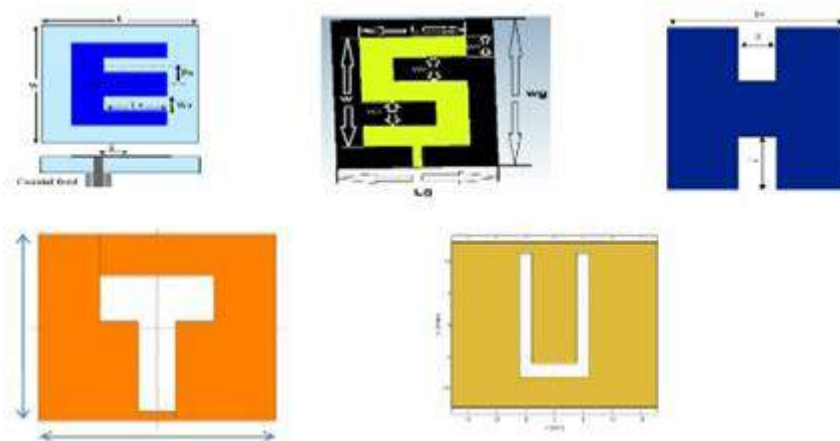


Figure 7: Different Slots

E-slot: The e-shaped slot antenna is a novel shape that will be used and managed for dual frequency operation with matching resonant frequency. The E-slot microstrip patch antenna was then constructed using a microstrip line feed arrangement, and its S11 and VSWR values were calculated using a vector network analyzer (VNA).

S-slot: In the ground, an S-shaped slot is used, consisting of a circular aperture with a radius of mm, a corner with a size of implanted on one side of the feedline, and a corner with a size of embedded on the other side.

H-slot: The antenna's H-shaped patch increases surface current and efficiency, while the etching grooves reduce return loss. As a result, the H-shaped antenna outperforms conventional antennas in terms of efficiency. As a result, the reflection loss will be minimised, and the user will be able to employ the radiation pattern effectively and distortion-free.

T-slot: The properties of a Microstriplines-fed printed slot antenna with a T shape are discussed. The antenna's bandwidth was found to be significantly dependent on the design parameters. The properties of a T-shaped microstrip feeding a ground plane slot antenna were investigated using the finite difference time domain (FDTD) method. The suggested antenna's impedance and bandwidth are largely reliant on the design parameters. The radiation resistance is low. The measured bandwidth for $|S_{11}| > 10$ dB is approximately 39.6 percent.

IV. REVIEW OF MSPA USING VARIOUS SUBSTRATES, SIZE & SLOTS

A review on patch antennas for 5G applications is done as outline in Table II, considering the shape of the patch, size of the antenna, slot shapes, frequency of oscillation, return loss, bandwidth and tool used for simulation. RT duroid and Rogers's outshined the remaining substrates considered under the review for 5G applications.

TABLE II Different Patch shapes and its comparisons

Ref.]	Shape	Size	Subs.	Freq.	S ₁₁	BW	Tool
[1]	Elliptical	55 × 40mm ²	FR4	3.5Ghz	-41.31db	1.133Ghz	CST
[2]	Rectangular	2.02 × 2.38 × 0.149mm ³	RT duroid	83Ghz	55.79db	3.12Ghz	HFSS
[4]	Rectangular	8.6 × 9.2 × 0.6mm ³	FR4	23.8Ghz	31.51db	1.466Ghz	HFSS
[9]	Rectangular	2.5mm × 1.8mm	FR4	28Ghz	-31.5db	64Ghz	HFSS
[10]	Elliptical	6.72mm × 4.2mm	Rogers RT5880	27.74Ghz	NA	56.9Ghz	NA
[11]	H slot Rectangular	14.53 × 19.19mm	FR4,RT duroid	4.8Ghz	-25.4db	NA	CST
[12]	Circular	NA	RT duroid	28.5Ghz	-32.8db	1.6369Ghz	FEKO
[13]	Rectangular	52 × 41 × 1.6mm ²	FR4	3.43Ghz	-29.7db	400kHz	CST
[14]	Elliptical	25.2 × 48mm ²	FR4	3.5Ghz	-30db	NA	CST
[15]	Rectangular	6.285 × 7.35 × 0.5mm	RT Duroid	28Ghz	-13.48db	84.7Mhz	CST

V. LITERATURE REVIEW

The authors Osama Y.A.Saeed presents the design and implementation of a unique mm-wave multiband microstrip patch antenna for 5G wireless communication. The design and implementation of a novel mm-Wave multiband microstrip patch antenna for 5G wireless communication is presented in this work. An H-shaped radiating patch with an inset feed and a rectangular slit on the upper side as shown in Figure 8 makes up the proposed design. The maximum bandwidth of the 5G mm-Wave antenna is 1.1, 2.8, 18.1, 7.7, and 10.7 GHz, and it resonates at 23.2, 40.3, 59.3, 86.9, and 104.3 GHz. The antenna represented in Figure 8 has enough realised gains of 6.4882, 7.1198, 7.9062, 8.1804, and 9.8156 dBi at the resonant frequencies [16].

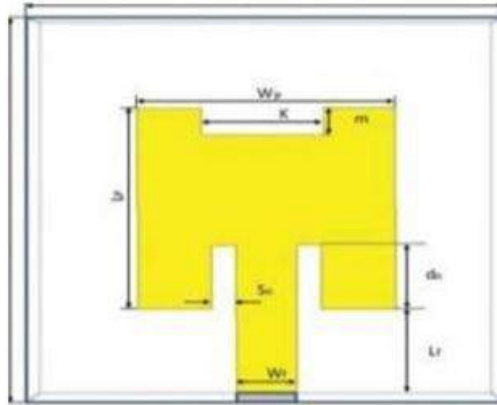


Figure 8: Proposed multiband MSPA [16]

The author Akashmodi proposed a slotted microstrip patch antenna as shown in Figure 9 for 5G applications in cellular networks, namely in the Ka-band, that is created and simulated with the use of a high-frequency structure simulator (HFSS). (26-40) GHz is the Ka-band frequency range. With a dielectric constant of 2.2, the dielectric substrate ROGERS RT/DUROID-5880(tm) was employed. The lowest return loss of the antenna is -33.02dB. The effect of slots increases the antenna's peak gain to 7.17dB and its VSWR to 1.04 at the resonant frequency of 29.8090GHz. The lowest return loss of the antenna represented in Figure 9 is -33.02dB. The effect of slots increases the antenna's peak gain to 7.17dB and its VSWR to 1.04 at the resonant frequency of 29.8090GHz [17].

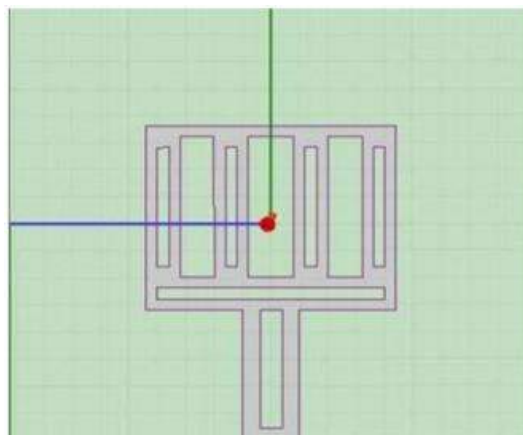


Figure. 9: Proposed Design of Antenna [17]

The author Yu Qing Guo presents a single-port, single-layer, dual-band antenna shown in Figure 10 with a high frequency ratio to accommodate the MW and MMW applications. We offer a single-port, single-layer, dual-band antenna for wireless communication that operates at 4.85 GHz MW and 26 GHz MMW in this research. The prototype has a 10-dB impedance bandwidth of 3.1 percent and a peak gain of 8.93 dBi at 4.85 GHz MW, and a peak gain of 13.57 dBi at 26 GHz MMW [18].

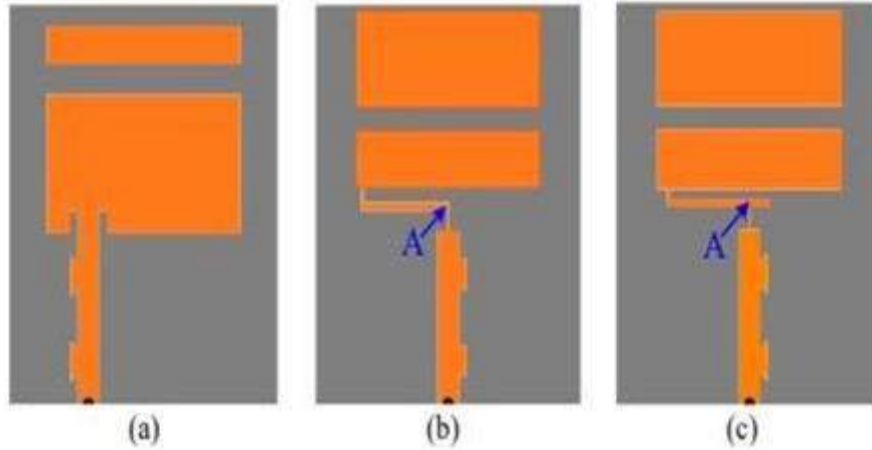


Figure 10: (a) Reference Antenna (b) Reference Antenna (c) The proposed antenna [18]

According to the author, Vinoth M, the first design represented in Figure 11 is a simple Rectangular Patch Antenna (RPA) that runs at 3.13 GHz and is modelled using Feko software. It uses an Fr4 substrate with a dielectric constant of 4.4. The fundamental construction is examined and improved by adding a Metamaterial (MTM) ground. The enhanced RPA with MTM ground displays resonance at 3.27 GHz, 3.78 GHz, and 3.92 GHz [19].

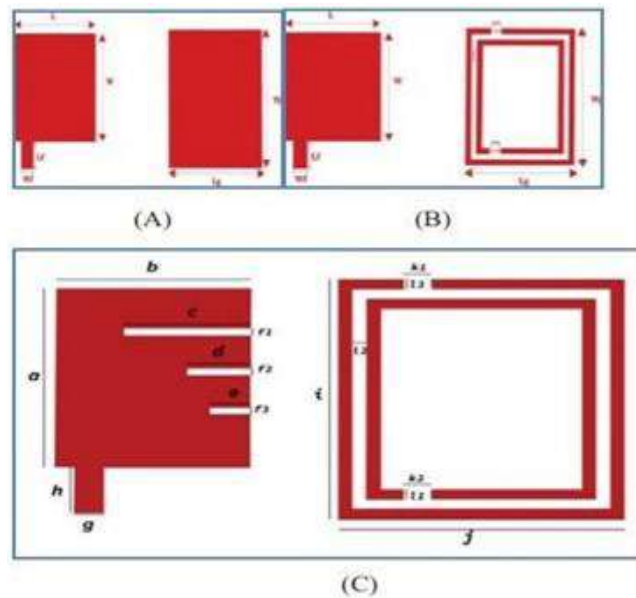


Figure 11: (a) RPA, (b) RPA with MTM ground (c) TSRMPA with MTM ground [19]

Zheng Gan and Zhi Hong Tu proposed an antenna shown in Figure 12, in which the 10 dB impedance bandwidth is roughly 23.7 percent (23.8–30.2 GHz), which is wide enough to span the 26 and 28 GHz bands at the same time. Rogers’s 5880 sub-1 substrate with a thickness of 0.127 mm, a relative permittivity of 2.2, and a loss tangent of 0.0009 was used. Two semicircular ends are loaded to the connecting strip piece of Roger 4003 substrate (sub-3) with a relative permittivity of 3.55 and loss tangent of 0.0027, as well as a 50 input microstrip feedline, to configure the two vias [20].

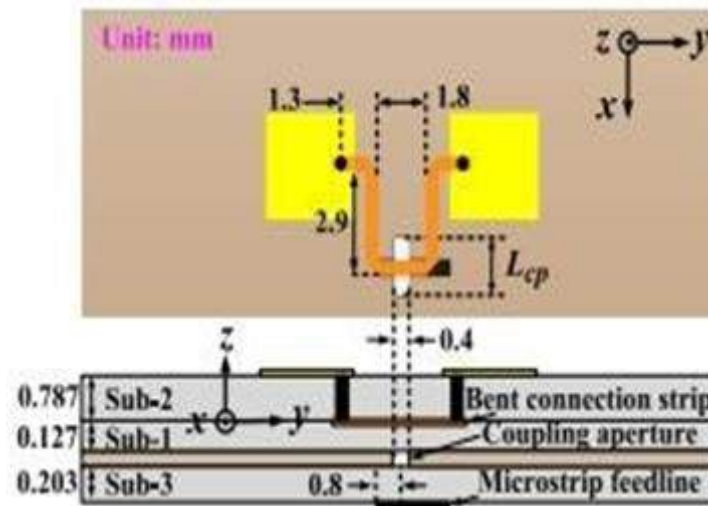


Figure 12: Configuration of the proposed dual-mode 1 × 2 patch antenna subarray [20]

Abdulaziz M. Al-hetar designed a microstrip patch antenna with a rectangular patch and a resonance frequency of 93 GHz, shown in Figure 13. The proposed microstrip antenna achieved a gain of 8.2 dB, a bandwidth of 5 GHz. $S_{11} = -41$ is the return loss. At 93 GHz, the VSWR is 1.01 [21].

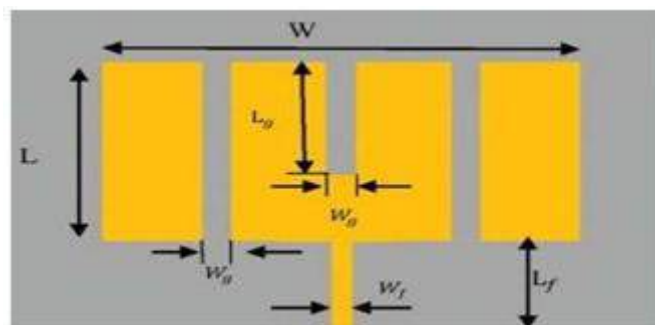


Figure 13: Designed Patch Antenna [21]

Hongxin Ai proposed two types of patch antennas for the 5G millimetre wave n258 band. Coaxial back feed and microstrip side feed methods are used to feed them, respectively. It was built with a Rogers 5880 with a dielectric constant of 2.2, and it was simulated at a central frequency of 26 GHz using CST software. Microstrip line patch antennas have a bandwidth of 25.20-26.81 GHz, while coaxial patch antennas have a bandwidth of 24.71-27.32 GHz [22].

In the work proposed by Mohammad Lutful Hakim a deflected ground structure (DGS) and stub slot design were used as shown in Figure 14 to achieve broad bandwidth and dual-band performance. The antenna is 8.25 x

9.69 x 0.45 mm³ in total. A 2x2 MIMO antenna with less than -20 dB isolation between ports has also been built, which is a critical requirement for 5G wireless communication for high-speed data rates and excellent performance, as well as enhancing the MIMO antenna's transmission rate. The suggested antenna has a -10-dB impedance bandwidth of 5.13 GHz and 11.63 GHz, gains of 8.31 dB and 6.38 dB, and a 98 percent efficiency for both the 28 and 38.5 GHz resonant frequencies [23].

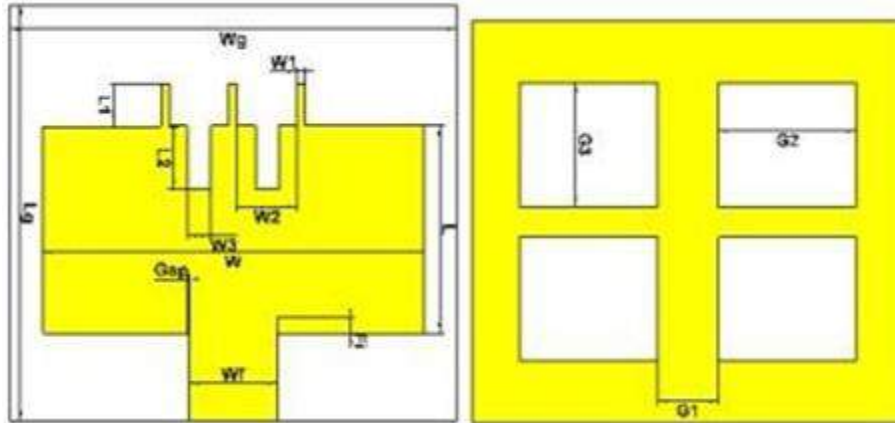


Figure 14: Front and Backside view of designed antenna [23]

Prateek Patel, using an RT duroid 5880 substrate, developed a 28 GHz millimetre wave rectangular microstrip patch antenna shown in Figure 15 and simulated it with HFFS Software. The antenna has a resonance frequency of 28 GHz and a -26.40 dB return loss. The antenna features a 1.102 GHz bandwidth and a gain of 7.4 dB, as well as improved radiation pattern, return loss, and VSWR [24].

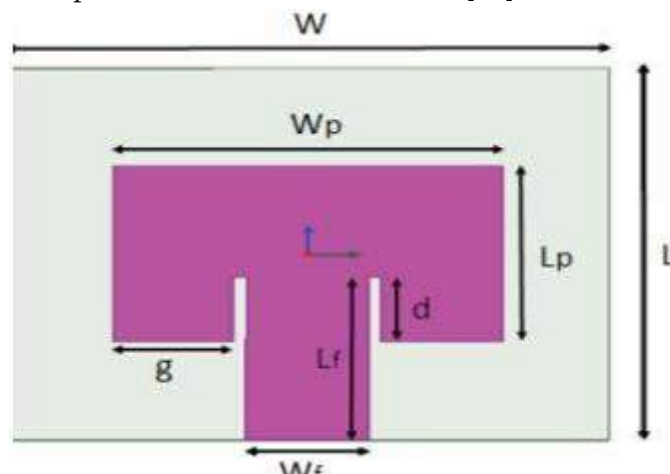


Figure 15: View of design antenna [24]

VI. CONCLUSION

This review paper brings out a detailed study about MSPA, its classification based on substrate, feed, shape and the frequency and different types of slots that can be etched on the radiating part or the ground part to get the desired results. Analysis is done taking different criteria focusing on 5G applications and as far as the literature

review in this paper is concerned RT duroid substrate with patch shapes of Rectangular, Circular and Elliptical produces good results with the required frequency and bandwidth for 5G applications.

VII. REFERENCES

- [1]. Hasan, Md Mahady, et al. "Design and Analysis of Elliptical Microstrip Patch Antenna at 3.5 GHz for 5G Applications." 2020 IEEE Region 10 Symposium (TENSymp). IEEE, 2020.
- [2]. Gaid, Abdulguddoos SA, et al. "83 GHz Microstrip Patch Antenna for Millimeter Wave Applications." 2021 International Conference of Technology, Science and Administration (ICTSA). IEEE, 2021.
- [3]. Nagarjun J et al. "Design and Analysis of E and F shaped Microstrip Patch Antenna (MSPA) for 5G Applications" International Journal of Science, Engineering and Management (IJSEM), June 2021
- [4]. Saeed, Ahmed AA, et al. "A low Profile Multiband Microstrip Patch Antenna For 5G Mm-Wave Wireless Applications." 2021 International Conference of Technology, Science and Administration (ICTSA). IEEE, 2021.
- [5]. Khan, Imran, and Raksha Gunjal. "Review of MSP Antenna Design for Various Substrates." (2018).
- [6]. Khan, Imran, et al. "LCP substrate based micro strip patch antenna." 2016 International Conference on Electrical, Electronics, Communication, Computer and Optimization Techniques (ICEECOT). IEEE, 2016.
- [7]. Khan, Anzar, and Rajesh Nema. "Analysis of five different dielectric substrates on microstrip patch antenna." International journal of computer applications 55.14 (2012).
- [8]. Patidar, Praveen Kumar. "A Review Paper on Microstrip Patch Antenna (MPA) for 5G Wireless Technology." Turkish Journal of Computer and Mathematics Education (TURCOMAT) 12.13 (2021)
- [9]. Ling, Zimeng, Chuanhao Liu, and Hui Li. "Wideband Patch Antenna Array for 5G Terminal Devices." 2020 IEEE 3rd International Conference on Electronic Information and Communication Technology (ICEICT). IEEE, 2020.
- [10]. Madankar, Abhishek, Vijay Chakole, and Sachin Khade. "H-slot Microstrip Patch Antenna for 5G WLAN Application." 2020 3rd International Conference on Intelligent Sustainable Systems (ICISS). IEEE, 2020.
- [11]. Colaco, John, and Rajesh Lohani. "Design and Implementation of Microstrip Circular Patch Antenna for 5G Applications." 2020 International Conference on Electrical, Communication, and Computer Engineering (ICECCE). IEEE, 2020.
- [12]. Hanaoui, Mohamed, and Mounir Rifi. "Elliptical slot rectangular patch antenna array with dual band behaviour for future 5G wireless communication networks." 2019 7th Mediterranean Congress of Telecommunications (CMT). IEEE, 2019.
- [13]. Ferdous, Nayla, et al. "Design of a small patch antenna at 3.5 GHz for 5G application." IOP Conference Series: Earth and Environmental Science. Vol. 268. No. 1. IOP Publishing, 2019.
- [14]. Gameda, Mulugeta Tegegn, et al. "Design and Analysis of a 28 GHz Microstrip Patch Antenna for 5G Communication Systems." International Research Journal of Engineering and Technology (IRJET) 8.02 (2021): 881-886.

- [15]. Darboe, Omar, Dominic Bernard Onyango Konditi, and Franklin Manene. "A 28 GHz rectangular microstrip patch antenna for 5G applications." *Int. J. Eng. Res. Technol* 12.6 (2019): 854.
- [16]. Saeed, Osama YA, et al. "Multiband Microstrip Patch Antenna Operating at Five Distinct 5G mm-Wave Bands." 2021 International Conference of Technology, Science and Administration (ICTSA). IEEE, 2021.
- [17]. Modi, Akash, Vanshul Sharma, and Abhishek Rawat. "Compact Design of Ka-Band antenna for 5G Applications." 2021 3rd International Conference on Signal Processing and Communication (ICPSC). IEEE, 2021.
- [18]. Guo, Yu Qing, et al. "A Singly-Fed Dual-Band Microstrip Antenna for Microwave and Millimeter-wave Applications in 5G Wireless Communication." *IEEE Transactions on Vehicular Technology* (2021).
- [19]. Vinoth, M., and R. Vallikannu. "A compact triple slotted Rectangular Microstrip Patch Antenna with Metamaterial ground for Sub-6 GHz/5G communication." 2020 Fifth International Conference on Research in Computational Intelligence and Communication Networks (ICRCICN). IEEE, 2020.
- [20]. Gan, Zheng, and Zhi-Hong Tu. "Dual-Mode Conjoint Patch-Pair for 5G Wideband Patch Antenna Array Application." *IEEE Antennas and Wireless Propagation Letters* 20.2 (2020): 244- 248.
- [21]. Al-hetar, Abdulaziz M., and Esmat AM Aqlan. "High performance & Compact Size Of Microstrip Antenna For 5G applications." 2021 International Conference of Technology, Science and Administration (ICTSA). IEEE, 2021.
- [22]. Ai, Hongxin, Chenwei Wu, and Suhang Zhou. "Design and Simulation of Rectangular Microstrip Patch Antenna with 5Gmm-wave Coaxial Line Back-Feed and Microstrip Line Side- Feeds." 2020 5th International Conference on Information Science, Computer Technology and Transportation (ISCTT). IEEE, 2020.
- [23]. Hakim, Mohammad Lutful, Mohammed Jashim Uddin, and MD Jiabul Hoque. "28/38 GHz Dual-Band Microstrip Patch Antenna with DGS and Stub-Slot Configurations and Its 2x 2 MIMO Antenna Design for 5G Wireless Communication." 2020 IEEE Region 10 Symposium (TENSYP). IEEE, 2020.
- [24]. Patel, Prateek, and Devendra Kumar Meda. "28GHz Millimeter Wave Rectangular Microstrip Patch Antenna for 5G Communication." 2020 International Conference on Recent Trends on Electronics, Information, Communication & Technology (RTEICT). IEEE, 2020.



Minimizing of Latency in Cognitive Radio Based IoT Systems for SDR Applications

Prathibha. S

Assistant Professor, Department of ECE, Govt. Engineering College, Ramanagar, Karnataka, India

ABSTRACT

The Finite impulse response (FIR) filter is prominently employed in many digital signal processing (DSP) systems for various applications. In this paper, we present a high-performance RNS based FIR filter design for filtration in SDR applications. In general, the residue number system (RNS) gives significant metrics over FIR implementation with its inherent parallelism and data partitioning mechanism. But with increased bit width cause considerable performance trade-off due to both residue computation and reverse conversion. In this paper optimized Residue Number System (RNS) arithmetic is proposed which includes distributed arithmetic based residue computation during RNS multiplication followed by speculative delay optimized reverse computation to mitigate the FIR filter trade-off characteristics with filter length. The proposed RNS design utilizes built-in RAMs block present in the devices of FPGA to accomplish the process of reverse conversion and to store pre-computational values. A distinctive feature of the proposed FIR filter implementation with core optimized RNS is to minimize hardware complexity overhead with the improved operating speed. Initially, fetal audio signal detection is carried out to validate the functionality of FIR filter core and FPGA hardware synthesis is carried out for various input word size and FIR length. From the experimental, it is proved that the trade-off exists in conventional RNS FIR over filter length is narrow down along with considerable complexity reduction with our proposed optimized RNS system.

Keywords: DA arithmetic, PPA, FIR filter; RNS system; Speculation, Low Energy-power product, area-power product, FPGA.

I. INTRODUCTION

The most vital element of the residue number system (RNS) that has drawn significant interest is known as the Modulo multiplier and this multiplier is based on the circuit computation. For the first time, the detailed analysis of the architecture of modulo $2n-1$ multipliers is presented in this research work. With help of VLSI modules that are memoryless and look-up-table i.e. through Read-only memory the implementation of modulo multipliers is carried out. On the other hand, the concept is initially used for the word length of low size, and later it can be used for the larger length of the word. To enhance the efficiency of multipliers that are

memoryless, the features of residue number systems such as parallel and modular are utilized, and to accelerate multipliers, an algorithm such as Booth-encoding is employed. Additionally, for extremely high range, a highly developed $2n-1$ modulo multiplier is been selected which is dependent on the redundant residue number system (RRNS). Therefore, with the application of the synopsis design compiler tool, the concepts of $2n-1$ modulo multipliers have been successfully analyzed and examined for the latest modulo multipliers advancements. For various applications of signal processing namely image processing, finite impulse response (FIR) filters, communication, cryptography, discrete cosine transform, and for various applications of the digital signal processor (DSP), the $2n-1$ modulo multipliers which are based on Residue number system are widely recognized as a quicker and more convenient arithmetic circuit. When compared to the typical 2's complement system, the Residue number system is more beneficial as it is a number system that is carry-free and non-weighted. The co-prime integer moduli $\{m_1, m_2, m_3, \dots, m_k\}$ that is comparative is characterized by RNS, such that whichever arbitrary integer i.e $X=\{x_1, x_2, x_3, \dots, x_k\}$, is referred to as residues of X and $x_i = X \text{ modulo } m_i$ ($x_i = |X|/m_i$). Forward and reverse converter, inter modulo operations, and arithmetic channels are considered as the four major components of the RNS block diagram and are represented in Figure 1. Here the forward converters and reverse converters are regarded as inter modulo operations. The conversion of residue numbers into weighted numbers is done by reverse converters and vice versa i.e. conversion of weighted numbers into residue numbers are carried out by forward converters. The arithmetic channels carry out operations such as multiplication and addition. However, the operations performed by the arithmetic channels are intra-modulo operations.

Particularly, for modulo multiplication of shorter word-length, modulo multiplier which is based on look-up-table was employed previously [12]. Since the ROM size rises dramatically with the modulus size thus, it is undesirable for relatively large moduli and this technique turns out to be unachievable. In [13] a $2n-1$ modulo multiplier that is based on cost-effective hardware look-up-table is suggested and this technique makes use of cyclic convolution to carry out multiplication operations among two numbers that are decomposed and thus, reducing the size of the ROM. However, for modulus of relatively small size, the technique that is based on look-up-table is quite appropriate. In [14], a $2n-1$ modulo multiplier that is memoryless is presented for the moduli which are significantly larger and medium in size and are carried out through various logic gates, adder, and multiplier. A significantly larger area is required by the Binary multiplier and correspondingly reduces the speed. In [15] a $2n-1$ modulo multiplier that is non-encoded and operates at high speed is suggested and is implemented without the application of binary multiplier. When compared to the exiting technique the suggested work in [15] has relatively less complexity in the circuit. Thus, to accelerate the multiplier Booth algorithm is employed and, in the work, presented in [16] a radix-2 Booth encoded multiplier is presented. On the other hand, the bits in the operands are the same as that of the number of partial products (PPs) presented in [15] and [16]. Depending on the number of added PPs, the speed of the multiplier is computed. In [17-20] a $2n-1$ modulo multiplier that is based on the Booth algorithm was proposed to minimize the number of PPs. The partial products that are required for the computation of $2n-1$ modulo multiplication are reduced to $[(n+1)/2]$ and $n/2$ for the radix-4 Booth encoded multiplier suggested in [17-18]. But in the case of radix-8 Booth encoded multiplier the total number of partial products are lowered to $[(n-2)/3] + 1$ and is presented in the work

proposed in [19-20] and one of the disadvantages of this work is the enhanced delay because of hard multiple existing in the Booth encoding multiplier of radix-8. In

[19] the hard-multiple generators were implemented with the application of an improved structure of parallel prefix and ripple carry adders. The intra-carry propagation in the RNS [38] is avoided with the development of a redundant residual number system (RRNS) that is proposed for a high range.

II. RELATED WORK

Residue Number System (RNS) Applications: Over the past fifty years in computer arithmetic, the RNS is considered as a substitute for the weighted two's complement number system and this system is one of the most confronting and desirable number systems. For the application of rapid computer arithmetic many aspects of residue number systems that are appropriate are considered. Some of the applications of residue number systems are cryptography and digital signal processing [5-8] where subtraction, multiplication, and addition are considered as the most important arithmetic operations and other than these applications the residue number system can detect and correct errors with the help of fault-tolerant and redundant RNS facilities presented in [3,4]. The residue number system can additionally be utilized for the transfer of data securely and without any error in the system of communication and the information is transmitted in the form of residues. As these residues present in the system are not dependent on one another as a result it can minimize the error by itself in their channel of moduli from which the information is transmitted. Therefore, for many wireless sensor networks application, these features of the residue number system are very much appropriate. For the detection and correction of an error in the system of communication, the Redundant RNS (RRNS) can be utilized by the addition of redundant moduli with an existing set of moduli.

RNS in digital signal processing: In the case of processing of digital signal applications, the Finite impulse response (FIR) filter is taken into account as one of the frequently utilized building blocks. Typically, with the application of a binary number system that experiences a significantly high propagation delay, the implementation of FIR filters is carried out. However, a large delay is introduced in the FIR filters of higher-order due to n number of multiplications and additions. As a result, the speed of the DSP also reduces. Thus, with the help of the Residue Number System, the FIR filter speed can be enhanced as it can execute addition and multiplication without any carry propagation. In this framework, we examine the model of FIR filters that is of low complexity and linear phase. The design suggested in this work are generally employed for the applications of digital communication. One of the important and efficient techniques is dividing the filters into two sub filters namely cosine and comb filters to attain low complexity. The advantages of comb and cosine filters are that it requires fewer hardware resources and the cost required for the computation is also less but one of the disadvantages is that these filters possess reduced magnitude features. Thus, with the help of these two filters, a novel structure has been presented in this research work. When compared to the earlier system, the novel structure developed achieves improved area, power, speed, and also enhanced magnitude features which are particularly employed for sampling rate conversion of low-pass narrowband filtering. The coefficients of filters are defined with no multipliers as these components are costly in terms of power, speed, and the area thus, an appropriate technique for achieving filters with low complexity for constant coefficients

filters is realized. Therefore, the work proposed in this thesis mainly concentrates on the constant multiplication's implementation as the network of shifts as well as addition. A new conceptual lower bound has been developed in this work with the factor that every arithmetic operation i.e. subtraction and addition can possess n inputs for a set of pipelined operations which are required in the Multiple Constant Multiplication (MCM) and Single Constant Multiplication (SCM) blocks and the expense of both pipelined operation and single pipelined register is same. The above requirement is vitally useful as it exists in the latest Field Programmable Gate Arrays (FPGAs) families and is considered as the most effective platform for digital signal processing algorithms implementation.

Audio processing, instrumentation or image processing, mobile communications, and many others [1]-[4] are the applications of DSP. Therefore, digital signal processing has been greatly recognized due to its applications in recent years. Approximately 7 billion subscribers to mobile communication were estimated in 2016 alone which signifies 96% of the world's population [5]. Some of the digitally transmitted systems that are used for the communications are Global Navigation Satellite System (GNSS), Digital Subscriber Line (DSL), Cell phones, satellite television, hard drives [6]-[8]. Digital filters are essentially utilized and play an important part in the above-mentioned communication systems. One of the primary functions of the digital filter is to enhance the signal quality, split the components of the signal which are initially combined, or to obtain the signal information. Therefore, because of these functions, digital signal processing is considered an important block [6],[9]-[10]. Nowadays, as the usage of battery-driven mobile devices is rapidly rising so it is necessary to maintain the battery backup for a long time [6],[10]. The number of hardware components that are required is limited due to the increased competition in portable devices for less power consumption. Therefore, to comply with the above features such as less utilization of hardware resources and power [11], the present work mainly concentrates on the advancement of novel digital filter methods. The data rates and bandwidth has been enhanced for the succeeding generations in the wireless communication system. The data rates and bandwidth links achieved by the existing method are 100 M-bit/sec and 20 MHz respectively whereas the upcoming generations are predicted to achieve the bandwidth links of 500MHz and data rates of 1 G-bit/sec [12]. However, the processing of the signal in the digital field is required to be carried out in the future where digital filters are considered as an essential feature of digital signal processing. However, the hardware processing capability is saturated by the process of filtering and the functioning of the system is considered at high rates. Moreover, the lifespan of the batteries is reduced as the digital filters are prohibitively costly (for the necessary arithmetic operations to be executed). Therefore, it is essential to develop algorithms and structures for digital filters with high performance. The digital filters must consume less power and a relatively low number of arithmetic operations, and it should be able to function at higher sampling rates so that these digital filters can be used in the system of communication. When compared to Infinite Impulse Response (IIR) filters, the Finite Impulse Response (FIR) filters possess higher-order for the same conditions of magnitude response. Hence, FIR filters are generally chosen in communications because of their assured stability, linear phase and can execute arithmetic operations in multivariate blocks because of their easy and straightforward decomposition of polyphase.

The data rates and bandwidth has been enhanced for the succeeding generations in the wireless communication system. The data rates and bandwidth links achieved by the existing method are 100 M-bit/sec and 20 MHz

respectively whereas the upcoming generations are predicted to achieve the bandwidth links of 500MHz and data rates of 1 G-bit/sec [12]. However, the processing of the signal in the digital field is required to be carried out in the future where digital filters are considered as an essential feature of digital signal processing. However, the hardware processing capability is saturated by the process of filtering and the functioning of the system is considered at high rates. Moreover, the lifespan of the batteries is reduced as the digital filters are prohibitively costly (for the necessary arithmetic operations to be executed). Therefore, it is essential to develop algorithms and structures for digital filters with high performance. The digital filters must consume less power and a relatively low number of arithmetic operations, and it should be able to function at higher sampling rates so that these digital filters can be used in the system of communication. When compared to Infinite Impulse Response (IIR) filters, the Finite Impulse Response (FIR) filters possess higher-order for the same conditions of magnitude response. Hence, FIR filters are generally chosen in communications because of their assured stability, linear phase and can execute arithmetic operations in multivariate blocks because of their easy and straightforward decomposition of polyphase.

III. PROPOSED METHODOLOGY

3.1 RRNS system for FIR filter design:

Some of the applications of residue number systems are cryptography and digital signal processing where subtraction, multiplication, and addition are considered as the most important arithmetic operations, and other than these applications the residue number system can detect and correct errors with the help of fault-tolerant and redundant RNS facilities. The residue number system can additionally be utilized for the transfer of data securely and without any error in the system of communication and the messages are transmitted in the form of residues. As these residues present in the system are not dependent on one another as a result it can minimize the error by itself in their channel of moduli from which the information is transmitted. Therefore, for many wireless sensor networks application, these features of the residue number system are very much appropriate. For the detection and correction of an error in the system of communication, the Redundant RNS (RRNS) can be utilized by the addition of redundant moduli with an existing set of moduli.

In the case of digital signal processing applications, the Finite impulse response (FIR) filter is considered as one of the most frequently utilized building blocks. Typically, with the application of a binary number system that experiences a significantly high propagation delay, the implementation of FIR filters is carried out. However, a large delay is introduced in the FIR filters of higher-order due to n number of multiplications and additions. As a result, the speed of the DSP also reduces. Thus, with the help of the Residue Number System, the FIR filter speed can be enhanced as it can execute addition and multiplication without any carry propagation. Intra-modulo is the operation performed by modulo multiplication. Therefore, propagation of carry does not take place between modulo channels. A redundant encoding has been developed to avoid intra- carry propagation from arithmetic operations in residue number systems as it is suitable for significantly high dynamic range. Thus, to achieve an effective modulo multiplier in the application of digital signal processing, the redundant residue number system (RRNS) can be studied.

Contributions: The contributions that are illustrated in this research work is explained as follows:

- The feature of Minimum Phase (MP) is considered as one of the mathematical proofs for the filter that is designed in the technique of sharpening which is based on Chebyshev polynomials along with the cascaded cosine sub-filters. The presentation of expanded and cascaded Chebyshev-sharpened cosine filters, as well as MP filters, are carried out and these filters possess lower group delay for the same features of magnitude to that compared with the conventional cascaded cosine filters. The group delay can be enhanced with the increase in the utilization of hardware resources. However, the designed technique utilizes fewer hardware resources and it exhibits low computational complexity for the application of a low-delay decimation filter.
- A decimator that is based on the comb is made up of a structure that is efficient in the area and is driven by a generalized embedded Chebyshev-sharpened unit. The suggested system enhances comb filters' least desirable aliasing rejection and retains a structure with low computational complexity and also consumes significantly less power and very fewer hardware resources. Regularity is considered as one of the unique and necessary features observed in the designed methodology and is not seen in any other techniques that are based on the comb.
- The decimation filter that is based on the comb is introduced to enhance the features of magnitude response by employing the technique of Hartnett-Boudreaux sharpening. This technique is also referred to as improved sharpening and is used to enhance the least desirable attenuation and modify the droop in the region of the passband. The polynomials of sharpening coefficients are defined as the Sum of Power of Two (SPT) and result in the implementation without a multiplier.
- Whenever the down sampling factor is of two's power then the decimation structure that is based on the comb and which is non-recursive is used. The structure of decimation that is based on the comb is divided into various phases and is based on Harnett-Boudreaux sharpening. The non-recursive comb-based decimation architecture is employed when the down sampling factor is a power of two, whereas two and three stages are employed for another composite down sampling factors, with the non-recursive structure in the first stage and recursive structure in subsequent stages.
- In the case of several operators that are required in the blocks of constant multiplication with fixed points, a novel theoretical lower limit is carried out. With the help of the shift-and-add technique, the constant multipliers are generated and here every individual operation is pipelined, as well as with the application of this simplified structure, the pipelined subtractions or additions with n inputs are permitted with the application of pipelining registers that are pure. The above requirement is vitally useful as it exists in the latest Field Programmable Gate Arrays (FPGAs) families and is considered as the most effective platform for digital signal processing algorithms implementation as it requires less hardware resource and low-cost constant multiplication blocks.
- Several research works proved that the residue number system (RNS) can give a notable hardware utilization rate as compare to all other optimization models.

In this paper, we propose DA based speculative RNS MAC unit for FIR filter design which has metrics as follows:

- DA based residue computation unit will offer considerable complexity reduction over a wide range of moduli set.

- It can be used for higher-order FIR design to solve tradeoff constraints related to the conventional RNS system.
- Speculative reverse conversion at the final stage can enhance the accumulation speed with direct RAM-based data accessibility.

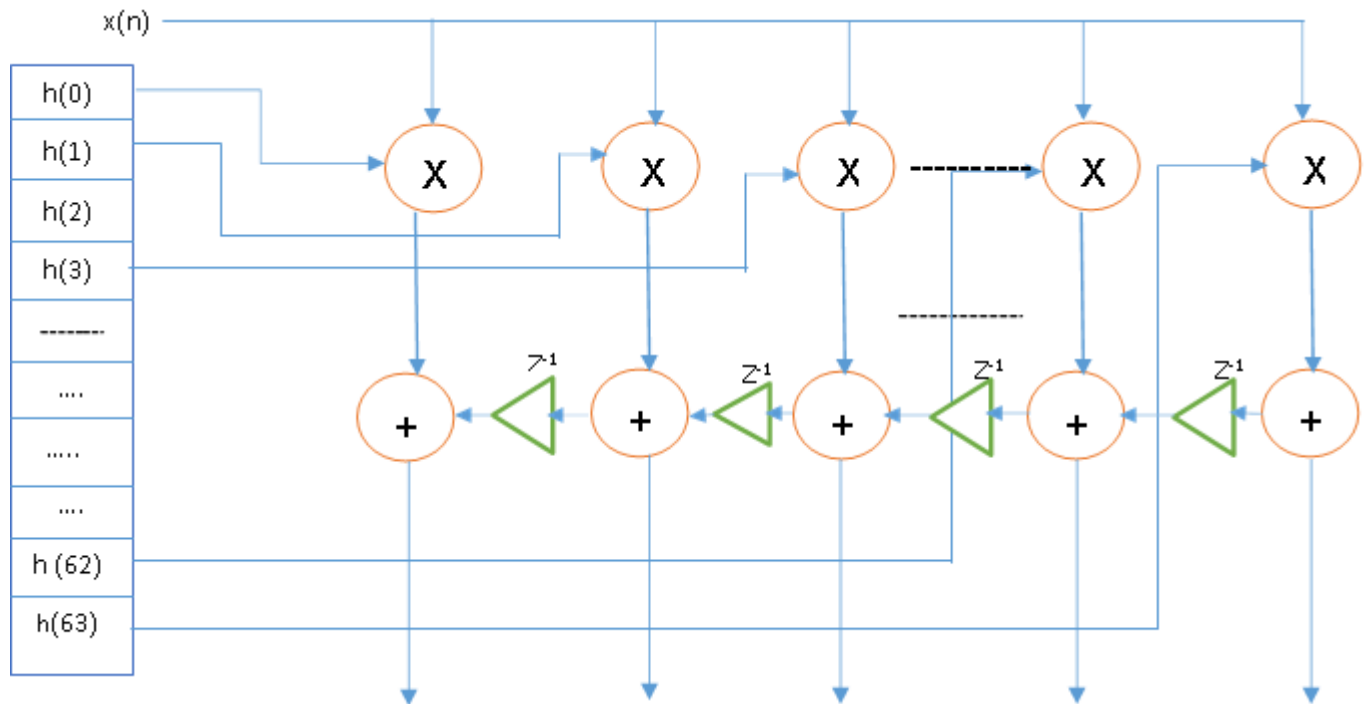


Fig.3. Internal Architecture of Proposed sub-band RFIR filter for module $n1$

The basic FIR filter function is given by $y(z) = \sum_{j=0}^{M-1} x(j)h-j = \sum_{j=0}^{M-1} x(n)h(n-k) \dots \dots (1)$

Where k is length of filter, in this design, the k is 0 to 63. Equation (1) proposes FIR filter operation with direct structure which requires less number of registers and its internal architecture is shown in Fig.2. The Fig.2. is a sub part in the RNS based RFIR which is shown in Fig.1. In FIR filter is most commonly used in DSP applications, the traditional FIR filter design uses binary number system for design of adders and multipliers which leads to larger propagation & net delays and it limits the speed of operations. To address these limitations, the proposed RNS based FIR filter given in equation (1) which uses faster modified Parallel Prefix Adder (PPA) where carry bit propagation is avoided, the results of existing PPA and modified PPA are shown in Table.1.

3.2 Memory efficient post computation

After residue computation which follows conventional arithmetic operation reverse conversion is performed as post computation to convert the residue number to an integer value. This process involves numbers with a maximum range of values depends on the size of each moduli. Here all possible results are pre-computed and stored in memory as readily available blocks to perform the reverse conversion process. It will reduce the hardware complexity of the reverse conversion unit since all these memory units are transformed into dedicated onboard block RAMs during hardware synthesis. As compared to other computations this on-chip

memory access not only minimize the computation cost the access time is also minimized with the least critical path.

Algorithm: Proposed Ternary-RNS based FIR filter

Input: Sampled Audio Signal, Moduli sets ($m_1, m_2, m_3, \dots \dots m_n$)

Output: Filtered sampled audio signal $y(n-k)$

Start:

Process 1: RNS Computation

////Define the moduli sets Module set (7,8,9)

Input operands: $A=14$; and $B=20$; /////for RNS multiplier Input to FIR filter: Sampled Audio Signal (x)

Process 2: Forward Conversion for RNS computation

Let Ar_1 is modulo operation between one of the operand and moduli set $Ar_1=(A) \bmod (m_1)$;

$Ar_2=(A) \bmod (m_2)$;

$Ar_3=(A) \bmod (m_3)$;

$Br_1=(B) \bmod (m_1)$;

$Br_2=(B) \bmod (m_2)$;

$Br_3=(B) \bmod (m_3)$;

Compute above $Ar_1 \dots \dots Ar_3$ to get Input Residual 1= (0, 6, 5) and $Br_1 \dots \dots Br_3$ to get Input Residual 2 = (6, 4, 2).

Process 3: Residue Computation for Multiplication, where * is RNS based multiplier

Compute $r_1 = (Ar_1 * Br_1) \bmod (m_1)=0$ Compute $r_2 = (Ar_2 * Br_2) \bmod (m_2)=0$ Compute $r_3 = (Ar_3 * Br_3) \bmod (m_3)=1$

Output of the process 3 i.e Residue Components are (0,0,1)

Process 4: Residue Computation for Adder (+) where + is Ternary-RNS based adder

Compute $r_1 = (Ar_1 + Br_1) \bmod (m_1)=6$ Compute $r_2 = (Ar_2 + Br_2) \bmod (m_2)=2$ Compute $r_3 = (Ar_3 + Br_3) \bmod (m_3)=7$

Output of the process 4 i.e Residue Components are (6,2,7)

Process 5: Reverse Conversion for RNS computation Inputs: Moduli set and $invM_1, invM_2, invM_3$ Outputs: ROM_1, ROM_2 and ROM_3

Where ROM_1 stores computational of $(M_1 * invM_1) \bmod (m_1)=1$ Where ROM_2 stores computational of $(M_2 * invM_2) \bmod (m_2)=1$ Where ROM_3 stores computational of $(M_3 * invM_3) \bmod (m_3)=1$ Compute $M_1 = m_2 * m_3$

Compute $M_2 = m_1 * m_3$

Compute $M_3 = m_1 * m_2$

Compute do iterative process till to get $(M_n * invM_n) \bmod (m_n)=1$

$|M_1 * invM_1| \bmod (m_1)=1$

$|M_2 * invM_2| \bmod (m_2)=1$

$|M_3 * invM_3| \bmod (m_3)=1$

At $M_1 = 72, M_2 = 63$ and $M_3 = 56$ we will get above three equations output is 1

Process 6: Final Reverse Conversion for RNS computation

$$\text{RNS output} = (|M1 * \text{inv}M1 * r1| + |M2 * \text{inv}M2 * r2| + |M3 * \text{inv}M3 * r3|) \bmod (m1 * m2 * m3)$$

$$\text{RNS output} = |280| \bmod 504 = 280$$

i.e $14 * 20 = 280$ hence it is proved end:

First Micro architecture for C0

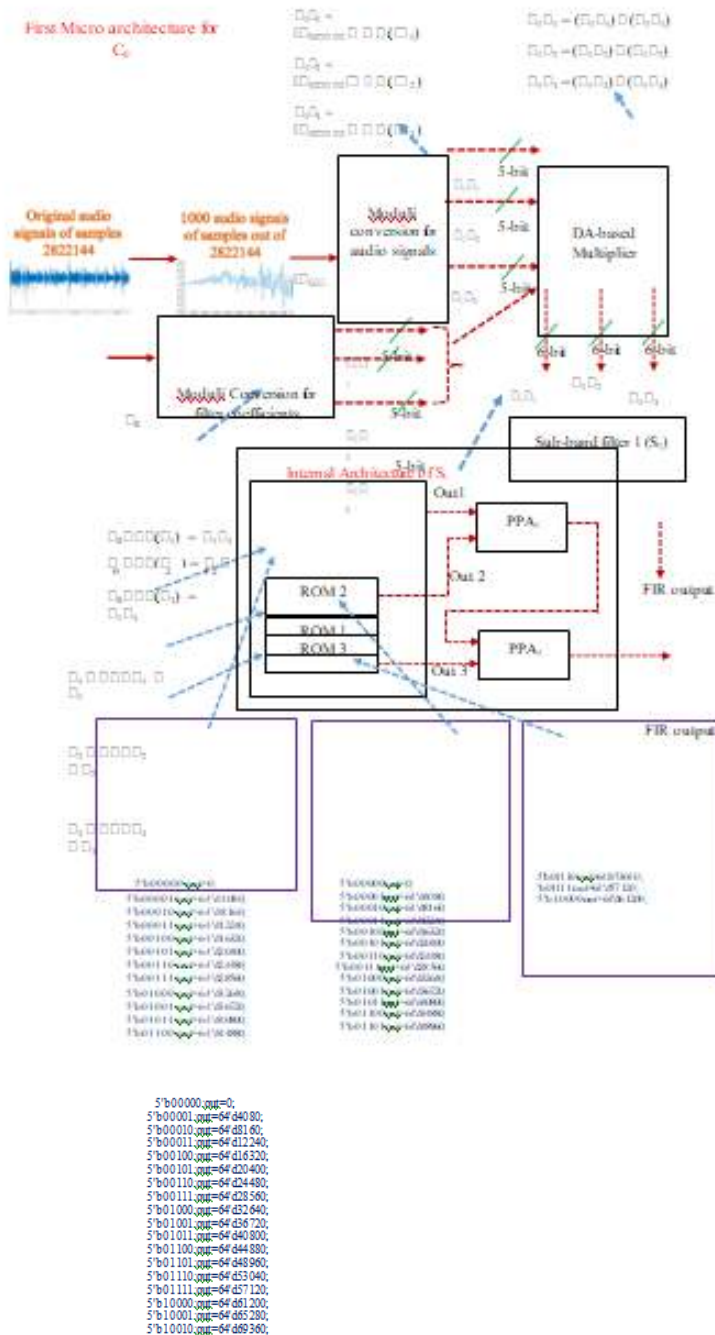
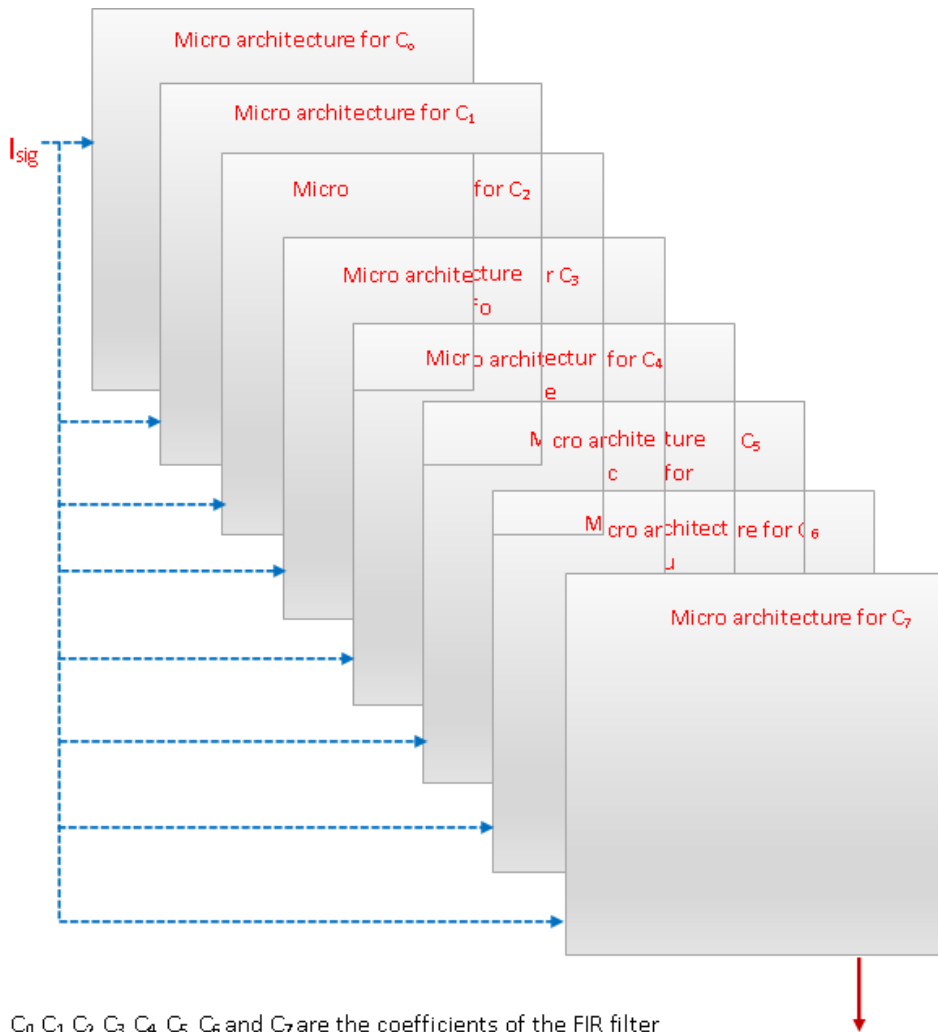


Fig.4. Proposed Internal micro-architecture of one coefficient and audio signal of RNS-Ternary PPA based RFIR filter for high speed and low energy consumption in SDR application.



$C_0, C_1, C_2, C_3, C_4, C_5, C_6$ and C_7 are the coefficients of the FIR filter

Fig. 5. Combined architectural blocks of proposed R FIR filter with given audio signal and filter coefficients for SDR applications.

Table 3. Performance analyzes of speculative DA based RNS FIR design in terms of energy, power and product of area, delay and power

Multiplier	Slices (area)	LUT	Delay (ns)	Power (mW)	Area* delay	Time* power	Area*time *power
Two speed Radix-4 Serial-Parallel multiplier for 32 bit [19]	1590	-	26.820	86.6	7186×10^{-6}	143.27×10^{-9}	22.852×10^{-9}

Booth Serial-Parallel Multiplier for 16 bits[19]	1200	-	27.2	0.85	19.06×10^{-6}	23.13×10^{-9}	16.19×10^{-6}
Modified Shift-Add Multiplier for 16 its [19,23]	2107		20.51	0.1	21.07	25.1	52.8
Bawooley1 multiplier	10475		10.25	22.62	1.07368×10^{-4}	1.691×10^{-10}	2.42×10^{-6}
Wallace tree multiplier	111		8.51ns	16.5	9.4461×10^{-7}	1.40×10^{-10}	1.55×10^{-8}
Proposed Ternary-RNS based FIR design for SDR	174	249	4.771	0.088	8.30×10^{-6}	41.9×10^{-9}	7.3×10^{-6}

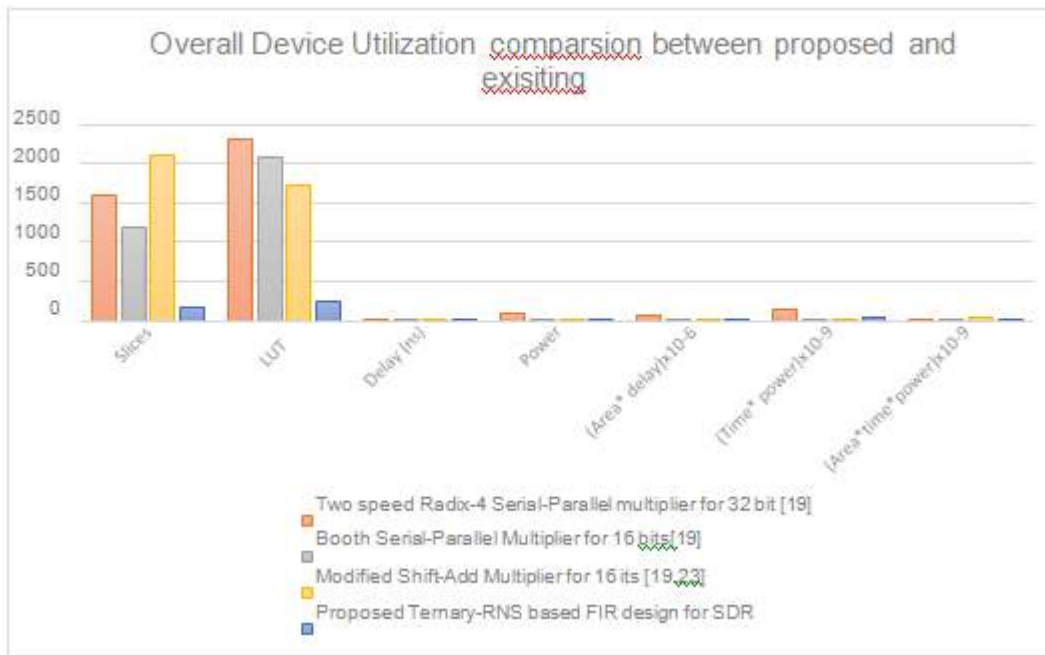


Fig.6. Overall Device utilization comparison between proposed ternary-RNS based FIR filter design for SDR applications

Figure.7. Simulated results for Audio samples and after filtering reconstructed output

V. REFERENCES

- [1]. Oscar T C. Chen, Sandy Wang and Yi-Wen Wu, Minimization of switching activities of partial products for designing low-power multipliers, *IEEE Trans. Very Large Scale Integration (VLSI) Systems*. 11 (2003) 418–433
- [2]. Jinn-Shyan Wang, Chien-Nan Kuo, and Tsung-Han Yang. Low-power fixed-width array multipliers, in *Proc. IEEE Int. Symp. Low Power Electronics and Design (ISLPED04)*, 2004, pp. 307–312.
- [3]. Huang Zhijun and Milos D. Ercegovac, High-performance low-power left-to-right array multiplier design, *IEEE Trans. Computers*. 54 (2005) 272–283
- [4]. Kuan Hung Chen and Yuan Sun Chu, A low-power multiplier with the spurious power suppression technique, *IEEE Trans. Very Large Scale Integration (VLSI) Systems*. 15 (2007) 846–850
- [5]. Hasan Krad and Aws Yousif Al Taie, Performance analysis of a 32-bit multiplier with a carry look ahead adder and a 32-bit multiplier with a ripple adder using VHDL, *J. Computer Science*. 4(4) (2008) 305–308
- [6]. M. Mottaghi-Dastjerdi, A. Afzali-Kusha, and M. Pedram, BZ-FAD: A low-power low area multiplier based on shift-and-add architecture, *IEEE Trans. Very Large Scale Integration (VLSI) Systems*. 17 (2009) 302–306
- [7]. Alope Saha, Dipankar Pal and Mahesh Chandra, Low-power 6-GHz wave-pipelined $8b \times 8b$ multiplier, *IET Circuits, Devices & Systems*. 7(3) (2013) 124–140.
- [8]. Cong Liu, Jie Han and Fabrizio Lombardi, A low-power, high-performance approximate multiplier with configurable partial error recovery, in *Proc. IEEE Design, Automation and Test in Europe Conf. and Exhibition (DATE)*, (2014), pp. 1–4.
- [9]. Basant K. Mohanty and Vikas Tiwari, Modified PEB formulation for hardware efficient fixed-width Booth multiplier, *J. Circuits Syst. Signal Process*. 33 (2014) 3981– 3994.
- [10]. Botang Shao and Peng Li, Array-based approximate arithmetic computing: A general model and applications to multiplier and squarer design, *IEEE Trans. Circuits and Systems-I: Regular Papers*. 62 (2015) 1081–1090
- [11]. When-Quan He, Yuan-Ho Chen and Shyh-Jye Jou, Dynamic error compensated fixed width Booth multiplier based on conditional-probability of input series, *J. Circuits Syst. Signal Process*. 35 (2016) 2972–2991.
- [12]. Zain Shabbir, Anas Razzaq Ghumman and Shabbir Majeed Chaudhry, A reduced-sp D3Lsum adder based high frequency 4×4 bit multiplier using Dadda algorithm, *J. Circuits Syst. Signal Process*. 35 (2016) 3113–3134.
- [13]. Ahmad Hiasat.et.al, “A Scaler Design for the RNS Three-Moduli Set $\{2n+1-1, 2n, 2n- 1\}$ Based on Mixed-Radix Conversion”, *Journal of Circuits, Systems, and Computers*, Vol. 29, No. 3 (2020) 2050041 (12 pages), World Scientific Publishing Company, DOI: 10.1142/S0218126620500413.
- [14]. Raj Kumar.et.al, “Perspective and Opportunities of Modulo $2n-1$ Multipliers in Residue Number System: A Review”, *Journal of Circuits, Systems, and Computers* Vol. 29, No. 11 (2020) 2030008 (24 pages), World Scientific Publishing Company, DOI: 10.1142/S0218126620300081.

- [15]. Grande Naga Jyothi.et.al, "ASIC implementation of distributed arithmetic based FIR filter using RNS for high speed DSP systems", International Journal of Speech Technology, Springer, 2020, <https://doi.org/10.1007/s10772-020-09683-1>.
- [16]. Rami Akeela.at.al, "Software-defined Radios: Architecture, State-of-the-art, and Challenges", INTERNET OF THINGS RESEARCH LAB, DEPARTMENT OF COMPUTER ENGINEERING, SANTA CLARA UNIVERSITY, USA — MARCH 2018.Lamjed Touil.et.al, "Design of Low-Power Structural FIR Filter Using Data Driven Clock Gating and Multibit Flip-Flops", Hindawi, Journal of Electrical and Computer Engineering Volume 2020, Article ID 8108591, 9 pages, <https://doi.org/10.1155/2020/8108591>.
- [17]. Lamjed Touil,et.al, "Design of Low-Power Structural FIR Filter Using Data-Driven Clock Gating and Multibit Flip-Flops", Hindawi Journal of Electrical and Computer Engineering Volume 2020, Article ID 8108591, 9 pages, <https://doi.org/10.1155/2020/8108591>
- [18]. C. Efstathiou.et.al, Modified Booth modulo $2n - 1$ multipliers, IEEE Trans. Comput. 53 (2004) 370–374.
- [19]. R. Muralidharan.et.al, Radix-8 booth encoded modulo $2n - 1$ multipliers with adaptive delay for high dynamic range residue number system, IEEE Transactions Circuit Systems. International Regular. Pap. 58 (2011) 982–993.
- [20]. R. Muralidharan.et.al, Area-power efficient modulo $2n - 1$ and modulo $2n + 1$ multipliers for $2n - 1$, $2n$, $2n+1$ based RNS, IEEE Trans. Circuits Syst. I Regul.Pap. 59 (2012) 2263–2274.
- [21]. R. Muralidharan.et.al., Radix-4 and Radix-8 booth encoded multi-modulus multipliers, IEEE Trans. Circuits Syst. I Regul. Pap. 60 (2013) 2940–2952.
- [22]. H. Pettenghi.et.al, Efficient method for designing modulo $\{2n+k\}$ multipliers, J. Circ. Syst.Comp. 23 (2014) 1450001.
- [23]. Romero, D.E.T. "High velocity multiplierless Frequency Response Masking (FRM) FIR channels with diminished use of equipment assets," IEEE International Midwest Symposium on Circuits and Systems (MWSCAS), pp. 1-4, 2015.
- [24]. Lu, W.- S. what's more, Takao H., "A bound together way to deal with the plan of added and recurrence reaction concealing FIR channels," IEEE Transactions on Circuits and Systems I – Reg. Papers, 2016.
- [25]. Demirtas, S. what's more, Oppenheim A. V., "A useful sythesis way to deal with channel honing and secluded channel plan," IEEE Transactions on Signal Processing, 2016. (in press)
- [26]. Candan, C. "Ideal Sharpening of CIC channels and a proficient usage through Saramaki- Ritoniemi obliteration channel structure," 2011. http://www.eee.metu.edu.tr/~ccandan/bar_dir/pick_honed_CIC_filt_broadened_new.pdf. (keep going access on February 2017)
- [27]. Molnar G., Dudarin A. what's more, Vucic M. "Minimax plan of multiplier less honed CIC channels dependent on span examination," IEEE Internat. Show on Information and Communication Technology, Electronics and Microelectronics (MIPRO), May 2016.
- [28]. Aksoy, L., Costa, E., Flores, P. and Monteiro, J. Multiplierless design of linear DSP transforms, in VLSI-SoC: Advanced Research for Systems on Chip, Springer, Chap. 5, pp. 73–93, 2012.
- [29]. Meyer-Baese, U. Digital Signal Processing with Field Programmable Gate Arrays, Springer, 2014.



Touch less Touch Screen Using Gesture Processing

Komala K V¹, Deepa V P²

¹Department of Computer Science and Engineering, Government Engineering College, Ramanagara -562159,
Karnataka, India

²Department of Electronics and Communication, Government Engineering College, Ramanagara -562159,
Karnataka, India

ABSTRACT

With the technological era there is always an intention to fit the whole world into a small screen. Living in the technology era where it attempts to fit the whole world into a small screen. Gadgets have become part of human life. Touch screen interface between the gadgets and the human begins for interaction and also to use them. Touch screen also known as human machine interface (HMI) have wiped out the use of keypads. Due to many issues caused by touch screen an evolution of touch less touch screen has occurred. Here the machine learning method is used for the implementation of the touchless touch screen. The action such as swipe left, swipe right so on are recognized and then Semi-supervised method is used to implement these actions by comparing them with the trained dataset.

Keywords: Gadgets, Human Machine Interface (HMI), Touch Screen, Machine Learning, Semi-supervised method.

I. INTRODUCTION

Data science otherwise called data driven science is an interdisciplinary field of logical techniques, procedures, calculations and framework to separate learning or experiences from information in different structures. It's an idea to bring together machine learning, data examination and their related strategy.

Machine learning is a field of software engineering that enables PC frameworks to learn with information, without being expressly modified. Machine learning was instituted in 1959 by Arthur Samuel. It investigates the examination and development of algorithms that can learn from and make predictions on data.

In machine learning focus is essentially on prepared dataset, with the assistance of these prepared dataset the machine can learn and play out the activities individually with no outside obstruction. It is a subfield of artificial intelligence, its primary objective is to comprehend the structure of information and after that fit the information into the models which can be used and comprehended by the general population. In spite of the fact that machine learning is a field of software engineering it is entirely different from the conventional computational methodologies.

In old processing strategies the calculation are the arrangements of unequivocally customized directions utilized by the PCs to take care of the issue. Machine learning calculations rather enable the PC to prepare on the information data sources and utilize measurable investigation keeping in mind the end goal to get the coveted yield. In machine learning, undertakings are broadly ordered in light of how learning is done or how input on learning is given to the framework to create. The most broadly utilized machine learning strategies are supervised learning and unsupervised learning. Supervised learning method trains the algorithms based on labeled data whereas the unsupervised learning trains on unlabeled data. The blend of the two techniques offer ascent to another strategy known as Semi-supervised learning strategy which prepares the calculation in light of labeled and unlabeled data.

II. LITERATURE SURVEY

In literary survey, we analyze critically and concisely earlier research and literature related to a particular research problem, and utilize them for their own research purposes. It helps in understanding the significance of new research and its connections to earlier work. The survey may display an insufficiency in the literature, which a new research can correct. In such case, the survey focuses on what is known about the topic and what is not known.

Nilofar E. chanda in his research work, "Study of touch less touch screen technology"[1] explains the mechanism of touch less touch screen technology uses finger motions without touching a screen. It simply uses hand wave in certain direction, or a flick of the hand in one area. In the touch screen display if the screen is cracked then we cannot operate the device by simply touching a display. The purpose of this touch less technology is to make life simple and more convenient. This system requires a sensor but the sensor is neither hand mounted nor present on the screen. The sensor can be placed either on the table or near the screen. The hardware setup is so compact that it can be fitted into a device like a mobile phone or laptop screen. It recognizes the position of an object from 5 feet Touch less touch screen technology means without using a finger or without touching a device we can easily operate the system. It is also called as "Don't touch me" technology. In this technology we have to simply draw a pattern for selecting tool or deleting a tool. This pattern we have to store in the database and the currently shown pattern is compared with the already stored images if pattern matches then the system work properly. Touch less display doesn't require any special sensors that we wear on our finger or either on our hand. We have to just point at the screen (from as far as 5 feet away), and we can easily operate the system Microsoft Company rebranded the technology as Pixel Sense once Microsoft introduced its unrelated Surface tablet to consumers. The name "Pixel Sense" refers to the way the technology actually works: a touch-sensitive protection glass is placed on top of an infrared backlight. As it hits the glass, the light is reflected back to integrated sensors, which convert that light into an electrical signal. That signal is referred to as a "value," and those values create a picture of what's on the display. The picture is then analyzed using image processing techniques, and that output is sent to the connected computer. In this paper the working of touch less displays and its applications is mentioned.

Aditi Obol, Suman Govdar, Sukita Shettigar, Shubhum Anand in their research work, "Touch Less Touch Screen User Interface" [2] demonstrates how touch screens were responsible for creating a great future to the

technology at an alarming rate. We have to face many problems while working with the touch screen and end scratching up on the screen. The result, by frequently touching a touch screen display with the help of a touching device is that it depicts that there is a gradual dullness or de-sensitization of the touch screen to the input. This could result in a failure of the touch screen. To avoid this problem a simple user interface is being developed for Touch less control of electrically operated equipment is being developed. Elliptic Labs innovative technology lets us to control our gadgets like computers, MP3 players or mobile phones without touching them. A simple user interface for Touchless Control of electrically operated equipment. Unlike other system which gradually depends on the distance from the sensor or this system depends on the hand, finger motion, a hand wave in a certain direction, or a flick of the hand in one area, and holding the hand in one area towards which we are pointing with one finger for example, The device is based on optical pattern recognition using a solid state optical sensor with a lens to detect hand motion. This sensor is then connected to a digital image processing; this interprets the patterns of motion and output the result as signal to control fixtures, applications, machineries, or on any other device which is controllable through electrical signal. In this paper, we are introducing about various touchless touch screen technology methods and its various types and discussed about one of the implemented touchless touch screen technology i.e. leap motion Controller is a device that connects with a user's interface to Manipulate digital objects with hand motions. Working with other hardware the controller adds a new way to interact with the world.

Mona M. Moussa, Elsayed Hamayed, Magda B. Fayek, Heba A. El Nemr in their work "An enhanced method for human action recognition" [3] explains about human action recognition is an active area of research due to the wide applications depending on it as detecting certain activities in surveillance video, automatic video indexing and retrieval, and content based video retrieval. Action representation can be categorized as: flow based approaches, spatio-temporal shape template based approaches, tracking based approaches and interest points based approaches. In flow based approaches optical flow computation is used to describe motion, it is sensitive to noise and cannot reveal the true motions. Spatio-temporal shape template based approaches treat the action recognition problem as a 3D object recognition problem and extracts features from the 3D volume. The extracted features are very huge so the computational cost is unacceptable for real-time applications. Tracking based approaches suffer from the same problems. Interest points based approaches have the advantage of short feature vectors; hence low computational cost. They are widely used and are adopted in this work. One of the widely used techniques in the action recognition task is Bag of Video Words (BoVW); which is inspired from bag of words model in natural language processing, where videos are treated as documents and visual features as words. This approach proved its robustness to location changes and to noise. Usually the system consists of four main steps: interest-points detection, features description, vector quantization and normalization of the features to construct histogram representation. Finally, the histograms are used for classification. In this work SIFT is used for detecting interest points where the extracted features are invariant to scale, location and orientation changes. 2D SIFT has another advantage which is the limited size of the features vectors; which consumes less computation time than other techniques such as 3D descriptors. In addition, the accuracy is better than all (to our knowledge) previous work in this field. This paper presents a fast and simple method for human action recognition. The proposed technique relies on detecting interest points using SIFT (scale invariant feature transform) from each frame of the video. A fine-tuning step is used here to limit the number of interesting

points according to the amount of details. Then the popular approach Bag of Video Words is applied with a new normalization technique. This normalization technique remarkably improves the results. Finally a multi class linear Support Vector Machine (SVM) is utilized for classification. Experiments were conducted on the KTH and Weizmann datasets. The results demonstrate that our approach outperforms most existing methods, achieving accuracy of 97.89% for KTH and 96.66% for Weizmann.

L. Liu, L. Shao, X. Li, and K. Lu, "Learning spatio-temporal representations for action recognition: A genetic programming approach," [4] carries out work on fusing information extracted from multiple layers of a convolutional neural network has been proven effective in several domains. Common fusion techniques include feature concatenation and Fisher embedding. In this work, we propose to fuse multilayer information by genetic programming (GP). With the evolutionary strategy, we iteratively fuse multilayer information in a systematic manner. In the evaluation, we verify the effectiveness of discovered GP-based representations on three image classification datasets, and discuss characteristics of the GP process. This study is one of the few works to fuse multilayer information based on an evolutionary strategy. The reported preliminary results not only demonstrate the potential of the GP fusion scheme, but also inspire future study in several aspects.

Darshana Ministry and Asim Banerjee, "Comparison of Feature detection Approaches: SIFT AND SURF" [5] research work explains on Image representation of complex information in easy way. In today world, image and video are used in every way. Feature represent information of an image. Features can be point, line, edges, and blob of an image etc. There are areas as image registration, object tracking, and object retrieval etc. where require to detect and match correct features. Therefore, features are found such way which invariant to rotation, scale, translation, illumination, noisy and blur images. The search of interest points from one object image to corresponding images is very challenging work. It should be such that same physical interest points has found in different views. There are many algorithms are used to detect and match features as SIFT (Scale Invariant Feature Transform), SURF (Speeded up Robust Feature), FAST, ORB etc. SIFT and SURF are most robust and used method for feature detection and matching. Features are matched based on finding minimum threshold distance. Distance can be found using Euclidean distance, Manhattan distance etc. If distances of two points are less than minimum threshold distance, that key points are known as matching pairs. Feature points are applied to find homographic transformation matrix which are found using RANSAC. Feature detection and matching are used in image registration, object tracking, object retrieval etc. There are number of approaches used to detect and matching of features as SIFT (Scale Invariant Feature Transform), SURF (Speeded up Robust Feature), FAST, ORB etc. SIFT and SURF are most useful approaches to detect and matching of features because of it is invariant to scale, rotate, translation, illumination, and blur. In this paper, there is comparison between SIFT and SURF approaches are discussed. SURF is better than SIFT in rotation invariant, blur and warp transform. SIFT is better than SURF in different scale images. SURF is 3 times faster than SIFT because using of integral image and box filter. SIFT and SURF are good in illumination changes images.

Qing Lei, Zhang et al., "Multi Surface Analysis for Human Action Recognition in Video", [6] research work explains the majority of methods for recognizing human actions are based on single-view video or multi-camera data. In this paper, we propose a novel multi-surface video analysis strategy. The video can be expressed as three-surface motion feature (3SMF) and spatio-temporal interest feature. 3SMF is extracted from the motion history image in three different video surfaces: horizontal-vertical, horizontal- and vertical-time surface. In

contrast to several previous studies, the prior probability is estimated by 3SMF rather than using a uniform distribution. Finally, we model the relationship score between each video and action as a probability inference to bridge the feature descriptors and action categories. We demonstrate our methods by comparing them to several state-of-the-arts action recognition benchmarks.

III. PROBLEM STATEMENT

Touch less touch screen technology uses finger motions without touching a screen. It simply uses hand wave in certain direction, or a flick of the hand in one area. In the touch screen display if the screen is cracked then we cannot operate the device by simply touching a display. The purpose of this touch less technology is to make life simple and more convenient. This paper demonstrates the implementation of image processing and gesture control for touchless screen.

Present State and its drawbacks

Touch screen displays found everywhere in the world. The touch screen display provides a greater flexibility to user but after some year's touch screen display becomes less sensitive which causes failure of touch on touch screen display. If we use a screen protector still dirty marks present on the display to avoid this problem a simple user interface for touch less control of electrically operated equipment is being developed. This project overcomes the drawback of touch screen display by providing touch less display.

Advantage of Proposed System

The proposed system will help in the implementing machine learning, image processing technology. Proposed system will help in the monitoring the gesture controls using image.

IV. METHODOLOGY

In this we are proposing a semi-supervised action recognition for the touch less touch screen. Here the system is trained with the datasets. The trained dataset contains various labeled and unlabeled videos of various actions, action such as like open PDF, open applications and action to recognize the alphabets or keystrokes of the keyboard.

The Gesture is recognized by the camera attached to the laptop. The laptop will process without any one touching the keyboard according to the gesture motion given by the user. The gesture recognition is recognized by the method of CNN algorithm through open CV.

A. WORKING

Sensors are mounted around the screen that is being used, by interacting with the line-of-sight of these sensors the motion is detected and interpreted into on-screen movements. There is a stop unintentional gestures being used as input that are not completely clear, but it looks promising nonetheless. The system is capable of detecting movements in 3-dimensions without ever having to put your fingers on the screen. Touch less

interface does not require that we have to wear any special sensors on our hand for navigation control. We have to point fingers at the screen and manipulate object in 3D. The best part of Touch less touch screen is that the technology will be easily small enough to be implemented into mobile and everywhere as shown in Figure 1.

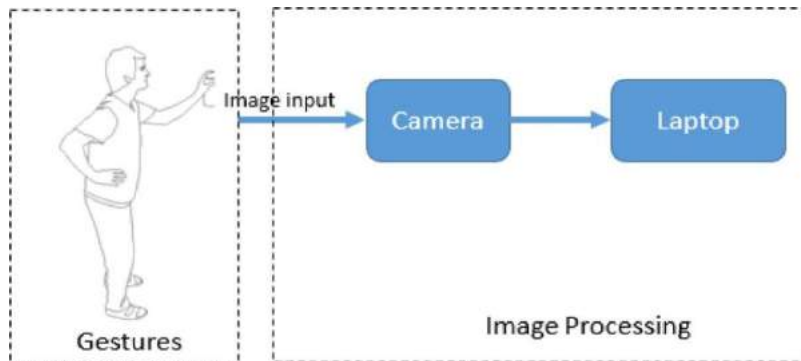


Figure 1: Block diagram of Touchless Touch Screen using Gesture Processing.

Block Diagram of Convolutional Neural Networks applied in processing of touchless touch screen using different gestures as shown in Figure 2.

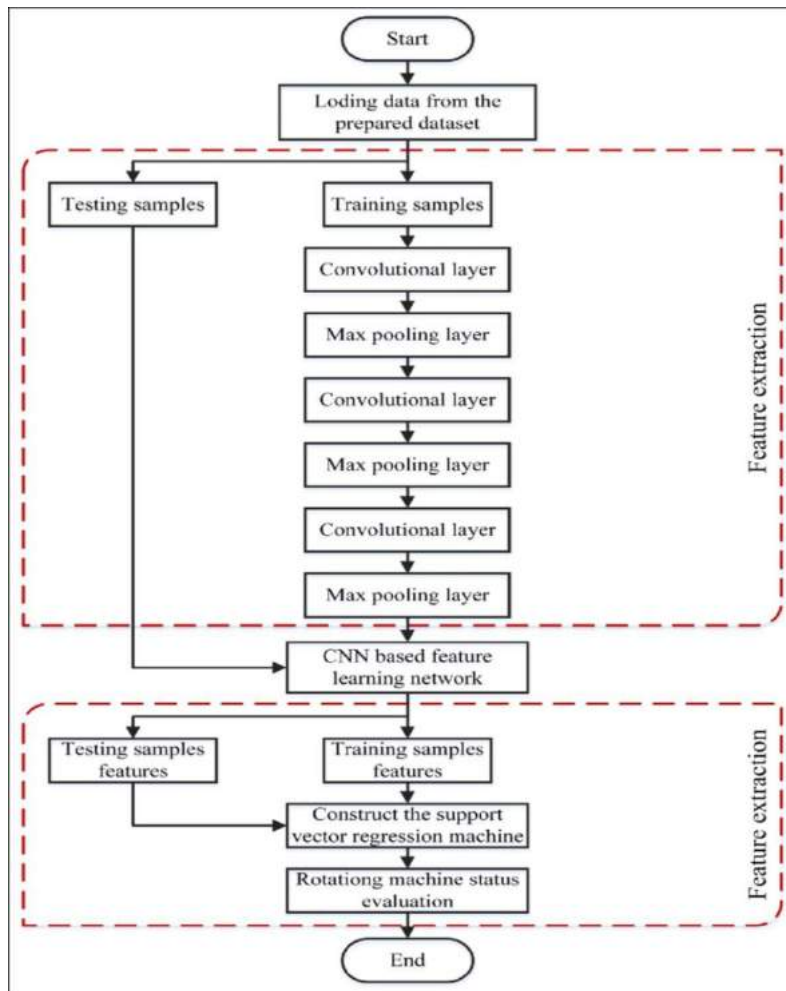


Figure 2: Block Diagram of Convolutional Neural Networks (CNN) Algorithm.

Figure 3 explains the flow of the touchless touch screen using gesture processing.

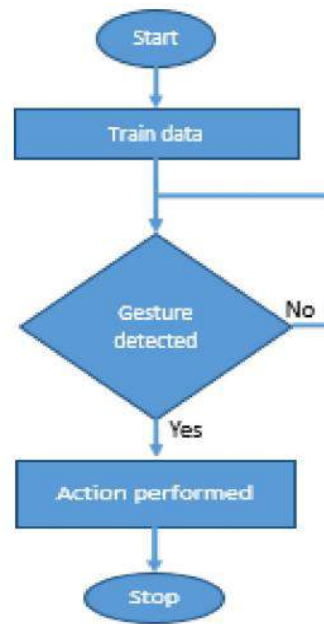


Figure 3: Flowchart of Touchless Touch Screen using Gesture Processing.

B. System Architecture Diagram

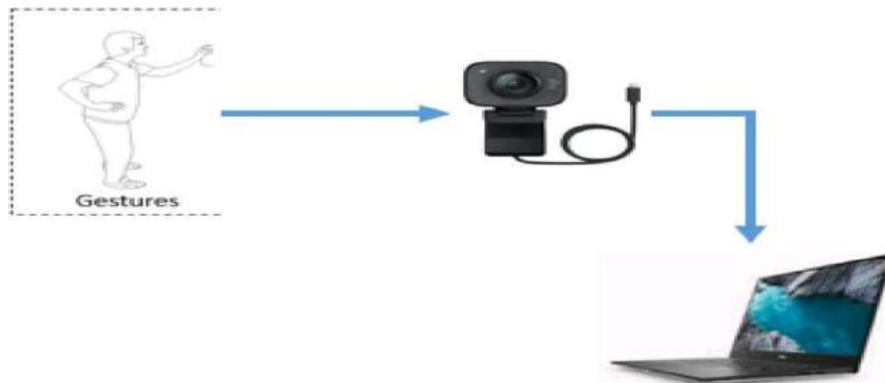


Figure 4: System Architecture Diagram of Touchless Touch Screen using Gesture Processing.

C. Functional Requirement

Functional Requirements are those requirements which show the working and functionality of a system and the expected behaviour of a system based on certain situations and inputs. It defines specific functionality of a system.

Functional requirements of system are:

1. Collecting data set
2. Uploading data set.
3. Clustering data set.

D. Non-functional Requirement

Non-functional requirements is not about functionality or behaviour of system, but rather are used to specify the capacity of a system. They are more related to properties of system such as quality, reliability and quick response time. Nonfunctional requirements come up via customer needs, because of budget, interoperability need such as software and hardware requirement, organizational policies or due to some external factors such as:

1. Basic Operational Requirement.
2. Organizational Requirement.
3. Product Requirement.
4. User Requirement.

V. ALGORITHM

The touch screen display provides a greater flexibility to user but after some year's touch screen display becomes less sensitive which causes failure of touch on touch screen display. If we use a screen protector still dirty marks present on the display to avoid this problem a simple user interface for touch less control of electrically operated equipment is being developed. The Gesture is recognized by the camera attached to the laptop. The laptop will process without any one touching the keyboard according to the gesture motion given by the user. The gesture recognition is recognized by the method of CNN algorithm through open CV. Semi-supervised action recognition for the touch less touch screen. Here the system is trained with the datasets. The trained dataset contains various labeled and unlabeled videos of various actions, action such as like open PDF, open applications and action to recognize the alphabets or keystrokes of the keyboard.

In the process of fruit sorting and grading to work system efficiently proper image acquisition is very important. The image is captured with camera that image is with noise and its features are not clearly seen so image pre-processing is done on that image. In this project the features required are colour, texture and size. To get exact feature pre-processing is done on acquired image. The main aim of image processing is an improvement of image so that unwanted distortions are suppressed and enhance image features which are important for further processing.

The basic steps of pre-processing are first convert RGB image to grey scale image. Then image histogram equalization is applied on grey image. This helps in adjusting image intensities in order to enhance contrast. Remove noise with filter, here we use median filter for removing noise here laplacian is used for edge detection as it highlights the region with rapid intensity change. So this enhanced, noise free, filtered image is ready for further processing.

VI. EXPERIMENTAL RESULTS

Screenshots of the results obtained is shown below:

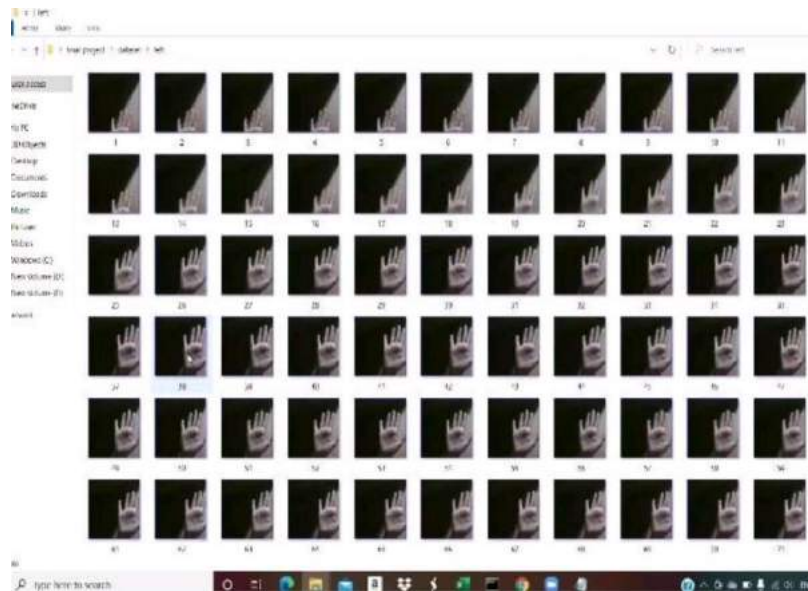


Figure 6c: Storing hand gestures: Hand showing Five Fingers in database and performing hand recognition task.

VII. CONCLUSION AND FUTURE WORK

Consumers around the world are worried about the safety and cleanliness of public touchscreens, such as self-service kiosks, and would be very open to trying new ways of interacting if they are available. Prior to this, technologies that could help to mitigate the spread of bacteria and viruses were a developing trend. Customers will consider these types of risks more intently in the future and are likely to expect devices, which are of a shared use nature, to be designed to mitigate any risks that might be created by touch surfaces which are potentially shared by many different people."

With this in mind, it should come as no surprise that interest is growing in touchless interfaces.

VIII. REFERENCES

- [1]. Nilofar E. chanda, "Study of touch less touch screen technology," International Journal of current engineering and scientific research, Vol. No. 04, pp. 48-52, 2017.
- [2]. Aditi Obol, Suman Govdar, Sukita Shettigar, Shubhum Anand, "Touch Less Touch Screen User Interface," International Journal of Technical Research and Applications, Vol. No. 42, pp. 59-63, Aug 2017.
- [3]. Mona M. Moussa, Elsayed Hamayed, Magda B. Fayek, Heba A. El Nemr, "An enhanced method for human action recognition," Journal of Advanced Research, Vol. No. 36, pp. 163-169, Jan 2015.
- [4]. L. Liu, L. Shao, X. Li, and K. Lu, " Learning spatio -temporal representations for action recognition: A genetic programming approach," IEEE trans. Cyber, Vol. No. 46, pp. 158-170, Jan. 2016.
- [5]. Darshana Minstry and Asim Banerjee, "Comparision of Feature detection Approaches: SIFTAND SURF," Vol. No. 01, pp 1-7, Nov (2017).
- [6]. Qing Lei, Zhang et al., "Multi Surface Analysis for Human Action Recognition in Video," SpringPlus, Vol. No. 05, 2016.



Face Recognition Based Attendance Marking System

Prathibha S

Department of Electronics and Communication Engineering -562159, Karnataka, India

ABSTRACT

Automatic face recognition (AFR) technologies have seen dramatic improvements in performance over the past years, and such systems are now widely used for security and commercial applications. An automated system for human face recognition in a real time background for a college to mark the attendance of their employees. So Smart Attendance using Real Time Face Recognition is a real world solution which comes with day to day activities of handling employees. The task is very difficult as the real time background subtraction in an image is still a challenge (6). To detect real time human face are used and a simple fast Principal Component Analysis has used to recognize the faces detected with a high accuracy rate. The matched face is used to mark attendance of the employee. Our system maintains the attendance records of employees automatically. Manual entering of attendance in logbooks becomes a difficult task and it also wastes the time. So we designed an efficient module that comprises of face recognition to manage the attendance records of employees.

Our module enrolls the staff's face (3). This enrolling is a one time process and their face will be stored in the database. During enrolling of face we require a system since it is a one time process. You can have your own roll number as your employee id which will be unique for each employee. The presence of each employee will be updated in a database. The results showed improved performance over manual attendance management system. Attendance is marked after employee identification. This product gives much more solutions with accurate results in user interactive manner rather than existing attendance and leave management systems.

Keywords: AFR (Automatic face recognition), attendance, identification, interactive, intervention

I. INTRODUCTION

Maintaining the attendance is very important in all the institutes for checking the performance of employees (4). Every institute has its own method in this regard. Some are taking attendance manually using the old paper or file based approach and some have adopted methods of automatic attendance using some biometric techniques. But in these methods employee has to wait for long time in making a queue at the time they enter the office. Many biometric systems are available but the key authentication is same in all the techniques. Every biometric system consists of enrollment process in which unique features of a person is stored in the database and then there are processes of identification and verification. These two processes compare the biometric feature of a person with previously stored template captured at the time of enrollment. Biometric templates can be of many

types like Fingerprints, Eye Iris, Face, Hand Geometry, Signature, Gait and voice. Our system uses the face recognition approach for the automatic attendance of employees in the office room environment without employees' intervention (2).

Face recognition consists of two steps, in first step faces are detected in the image and then these detected faces are compared with the database for verification. Our system utilized this algorithm for the detection of faces in the office room image.

A facial recognition system is a technology capable of matching a human face from a digital image or a video frame against a database of faces, typically employed to authenticate users through ID verification services, works by pinpointing and measuring facial features from a given image.

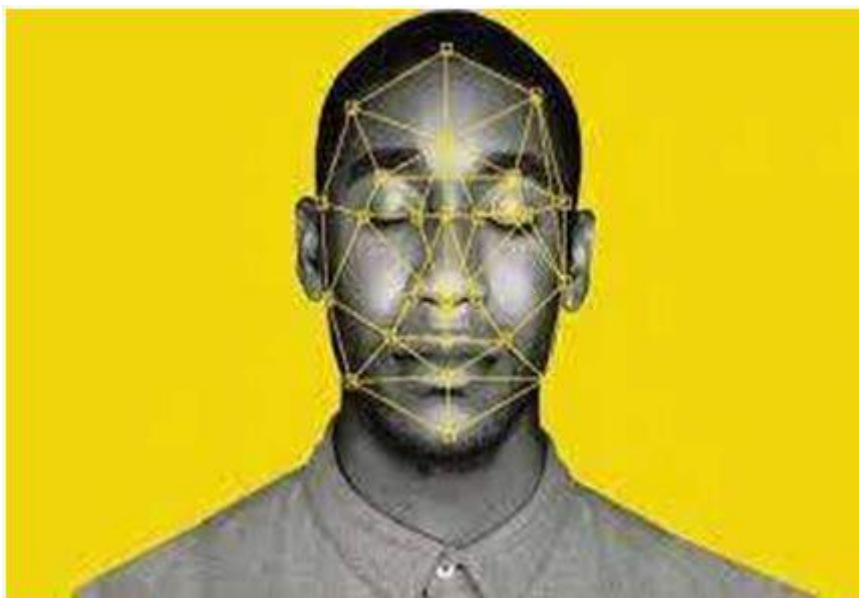


FIG1.1 HUMANFACE PATTERN

While initially a form of computer application, facial recognition systems have seen wider uses in recent times on smart phones and in other forms of technology, such as robotics. Because computerized facial recognition involves the measurement of

a human's physiological characteristics, facial recognition systems are categorized as biometrics. Although the accuracy of facial recognition systems as a biometric technology is lower than iris recognition and fingerprint recognition, it is widely adopted due to its contactless process. [1] Facial recognition systems have been deployed in advanced human-computer interaction, video surveillance and automatic indexing of images. [2] They are also used widely by law enforcement agencies.

II. LITERATURE SURVEY

Automated facial recognition was pioneered in the 1960s. Woody Bledsoe, Helen Chan Wolf, and Charles Bisson worked on using the computer to recognize human faces. Their early facial recognition project was dubbed "man-machine" because the coordinates of the facial features in a photograph had to be established by a human before they could be used by the computer for recognition. On a graphic tablet a human had to pinpoint the coordinates of facial features such as the pupil centers, the inside and outside corner of eyes, and the widow's peak in the hairline.

The coordinates were used to calculate 20 distances, including the width of the mouth and of the eyes. A human could process about 40 pictures an hour in this manner and so build a database of the computed distances. A computer would then automatically compare the distances for each photograph, calculate the difference between the distances and return the closest records as a possible match. [3]

In 1970, Takeo Kanade publicly demonstrated a face matching system that located anatomical features such as the chin and calculated the distance ratio between facial features without human intervention. Later tests revealed that the system could not always reliably identify facial features. Nonetheless, interest in the subject grew and in 1977 Kanade published the first detailed book on facial recognition technology. [4]

In 1993, the Defense Advanced Research Project Agency (DARPA) and the Army Research Laboratory (ARL) established the face recognition technology program FERET to develop "automatic face recognition capabilities" that could be employed in a

productive real life environment "to assist security, intelligence, and law enforcement personnel in the performance of their duties." Face recognition systems that had been trialed in research labs were reevaluated and the FERET tests found that while the performance of existing automated facial recognition systems varied, a handful of existing methods could be used to recognize faces in still images taken in a controlled environment. [5] The FERET tests spawned three US companies that sold automated facial recognition systems. Vision Corporation and Miros Inc were both founded in 1994, by researchers who used the results of the FERET tests as a selling point. Viisage Technology was established by an identification card defense contractor in 1996 to commercially exploit the rights to the facial recognition algorithm developed by Alex Pentland at MIT. [6]

III. TECHNIQUES FOR FACE RECOGNITION, METHODOLOGY, SYSTEM ALGORITHM, FACE RECOGNITION PROCESS & SOFTWARE REQUIREMENT

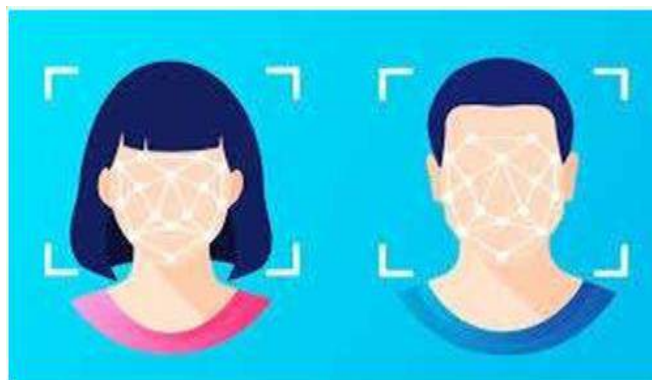


FIG1.2 FACE RECOGNITION PATTERN

Automatic face detection with OpenCV.

While humans can recognize faces without much effort, [20] facial recognition is a challenging pattern recognition problem in computing. Facial recognition systems attempt to identify a human face, which is three-

dimensional and changes in appearance with lighting and facial expression, based on its two-dimensional image. To accomplish this computational task, facial recognition systems perform four steps. First face detection is used to segment the face from the image background. In the second step the segmented face image is aligned to account for face pose, image size and photographic properties, such as illumination and grayscale. The purpose of the alignment process is to enable the accurate localization of facial features in the third step, the facial feature extraction. Features such as eyes, nose and mouth are pinpointed and measured in the image to represent the face. The so established feature vector of the face is then, in the fourth step, matched against a database of faces. [21]

IV. METHODOLOGY

The system consists of a camera that captures the images of the employee and sends it to the image enhancement module. After enhancement the image comes in the Face Detection and Recognition modules and then the attendance is marked on the database server. At the time of enrolment, templates of face images of individual employees are stored in the Face database.

Here all the faces are detected from the input image and the algorithm compares them one by one with the face database. If any face is recognized the attendance is marked on the server from where anyone can access and use it for different purposes. In this way a lot of time is saved and this is highly securing process no one can mark the attendance of other. Attendance is maintained on the servers so anyone can access it for purposes like administration, employees themselves (7). Using this technique enhances the efficiency and accuracy of the detection process two databases are displayed in the experimental setup. Face

Database is the collection of face images and extracted features at the time of enrolment process and the second attendance database contains the information about the employees and also uses to mark attendance.

Face recognition are often passively refrained from many specific action or participation on the part of the users since face pictures are often acquired from a distance by a camera. This can be significantly useful for security and surveillance functions. Face could be an advanced multidimensional structure and needs smart computing techniques for recognition. There could also be variations in faces because of aging and distractions like beard, modification of hair styles or glasses etc. Features extracted from a face are processed and compared with the equally processed faces that are present within the info. If a face is recognized it's best

known or the system might show an analogous face existing in info else it's unknown. In general, face recognition techniques are often divided into 2 teams supported the face illustration they use appearance-based, that uses holistic texture options and is applied to either whole of the face or specific regions during a face image and feature-

based, that uses geometric facial expression like mouth, eyes, brows, cheeks etc.. The student needs to be a head of a camera at a minimum distance. The system can find the image of the student consistent with the Eigen face and OpenCV algorithm. A program converts it into a grayscale and stores it in a very

file. Once the student reappears before the camera, faces are recognized by comparison the Eigen faces of current and keep images. Then the names of the detected faces are kept in info. This project effectively defines the automatic attendance system based on face recognition to implement on schools/colleges. The system takes attendance for particular quantity of yo

urtimeandwhenthe time expires the system mechanically closes the attendance. The results of the experiments show improved performance within the estimation of attending compared to ancient pen and paper kind attending system. The present work is principally focused on face detection and extraction by OpenCV within the picture exploitation wireless mode Wi-

Fi. In any work we are going to be supposed to enhance face recognition's limitations and additionally by comparing 3D face pictures with second face pictures (Realtime). Also we have a tendency to be supposed to enhance on multiple face recognition as a similar time in order that the effectiveness of your time will still be managed and take a look at to enhance on the portability of the system

V. SYSTEM ALGORITHM

This section describes the software algorithm for the system. The algorithm consists of the following steps

- Image acquisition
- Face detection
- Face recognition
- Attendance

The proposed attendance system chiefly consists of 3 phases; Image acquisition, Face Detection, Face Recognition. The operating of the system is represented as follows:

Image Acquisition:

The system consists of a camera that captures the pictures of the school room and sends it to the image pre-processing. Then that image is sent for face detection.

Face Detection:

This method separates the facial space from the remainder of the background image. The face area unit keeps within the information and detected, when that Face extraction is additionally administered.

Face Recognition:

The face image is then compared with the kept image. If the face image is matched with the stored image then the face is recognized. Then for that individual student the attending is recorded.

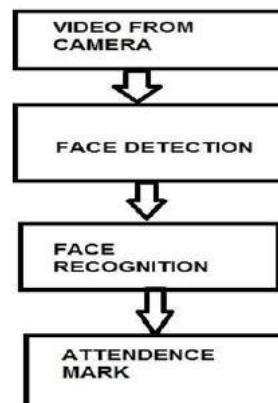


FIG2.1 FACERECOGNITIONALGORITHM

In the first step image is captured from the camera. There are illumination effects in the captured image because of different lighting conditions and some noise which is to be removed before going to the next steps

(1). Histogram normalization is used for contrast enhancement in the spatial domain. Median filter is used for removal of noise in the image. There are other techniques like FFT and low pass filter for noise removal and smoothing of the images but median filter gives good results.

Student Management: This constitutes the primary section of our project module. This section consists of the following parameters: 1. Student Registration type, the student seems as a brand new candidate for registration. Registration consists of adding every candidate's personal details. 2. Student Face detection: The freshly registered candidate's face gets detected for the very 1st time and hold on within the info.

Attendance System:

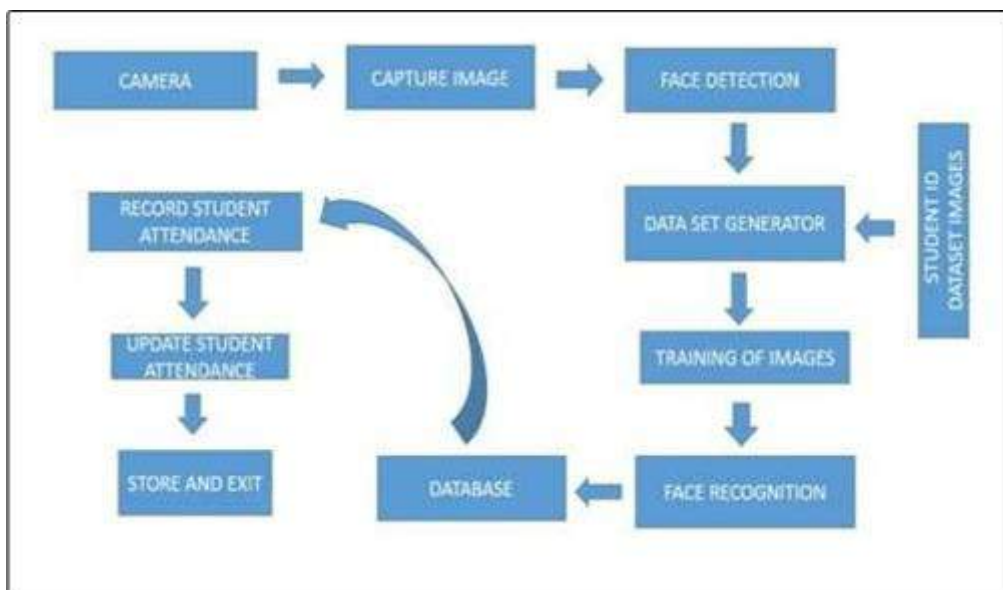


Fig.2.2 Flow Chart of Attendance system

This constitutes the second section of our project module. The popularity of every individual student takes place by extracting the common options of every individual by exploitation of image integral technique. Then the face image is matched with the image hold on within the info and therefore the attendance is marked for the candidate providing the facial feature of the freshly captured image matches with the already hold on image.

Exit: It takes the system out of the module.

FACE RECOGNITION PROCESS

Face Count Algorithm:

- The detect MultiScale function is a general function that detects objects. Since we are calling it on the face cascade, that's what it detects.
- The first option is the grayscale image.

- Thesecondisthescale Factor.Sincesomefaces maybe closeto the camera,they would appear bigger than the faces in the back.The scale factor compensates for this.
- The detection algorithm uses a moving window to detect objects. Min Neighbors defines how many objects are detected near the current one before it declares the face found. Min Size, meanwhile, gives the size of each window.

Template Matching:

Template Matching is a method for searching and finding

the location of a template image in a larger image. OpenCV comes with a function `cv2.Match`

`Template()` for this purpose. It simply slides the template image over the input image (as in 2D convolution) and compares the template and patch of input image under the template image. Several comparison methods are implemented in OpenCV. It returns a grayscale image, where each pixel denotes how much does the neighbourhood of that pixel match with template.

If input image is of size $(W \times H)$ and template image is of size $(w \times h)$, output image will have a size of $(W-w+1, H-h+1)$. Once you got the result, you can use `cv2.minMaxLoc()` function to find where is the maximum/minimum value. Take it as the top-left corner of rectangle and take (w, h) as width and height of the rectangle. That rectangle is your region of template.

It has two primary components-

Source image (I): The image in which we expect to find a match to the template image.

Template image (T): The patch image which will be compared to the template image.

Approach to Solve Template Matching:

There have been two approaches to solve template matching problem:

- **Full Search (FS):** This algorithm computes the distance between q and all template-sized sub-windows in the image and returns either the patch with the smallest distance or all the patches with distance below a threshold T .
- **Fast Fourier Transform (FFT) approach:** This algorithm has been traditionally used for accelerating pattern matching in the L_2 norm (vector norm) especially for large pattern sizes where the idea is based on L_2 norm observations between two M pixels-sized sub-windows.

Working of Template matching:

- The template image simply slides over the input image (as in 2D convolution)
- The template and patch of input image under the template image are compared.
- The result obtained is compared with the threshold.
- If the result is greater than the threshold, the portion will be marked as detected.
- In the function `cv2.matchTemplate(imagegray, template, cv2.TM_CCOEFF_NORMED)`
- the first parameter is the main image, second The Matching Methods Available in OpenCV:

- Parameteristhetemplatetobematchedandthirdparameteristhemethodusedformatching.

OpenCVimplementsTemplatematchinginthefunctionmatchTemplate.Theavailable methods are 6:

- method=CV_TM_SQDIFF
- method=CV_TM_SQDIFF_NORMED
- method=CV_TM_CCORR_NORMED
- method=CV_TM_CCOEFF
- method=CV_TM_CCOEFF_NORMED

FaceRecognition:

To make a face recognition program, initially we need to coach the recognizer with a dataset of antecedently captured faces along with their IDs. To illustrate we've 2 persons then each person can have an ID. In order that all the photographs of a person within the dataset can have an ID and every one of the photographs of the 2nd person within the dataset can have an ID2, then we are going to use those dataset pictures to coach the recognizer to predict the one of the associated degrees freshly conferred face from the live video frame.

Algorithm for Face Recognition:

1. DatasetCreator.
 2. Trainer.
 3. Detector.
- Starts capturing frames from the camera object
 - Convert it to GrayScale
 - Detect and extract faces from the images
 - Use the recognizer to recognize the ID of the user
 - Put predicted ID/Name and Rectangle on detected face

Database Using SQLITE:

Database Using SQLITE: Here we have created a python program that connects to a sqlite database.

Sqlite database does not require any preinstallation and saves database as a file in the current working directory. So the database.py consists of three functions: init, update, select. init() -

> it takes one argument: a list of names and it creates a database with names and time periods 1, 2, 3, 4 with all the time periods available (absent). Once the database is created and values are inserted, it displays the database. You can pass any length of list of names; it will create the database with that many records

```
ex: from database import *
init(['hello', 'hi', 'how'])
('hello', 'N', 'N', 'N', 'N')
('hi', 'N', 'N', 'N', 'N')
('how', 'N', 'N', 'N', 'N')
```

Update()-

>ittakestwoargumentsfirstislistofnamesofstudentswhoarepresentandsecondiswhichhourininteger.itwillupdateth edatabaseandmakethosenamespresentforthathourwhichyou have passed.

ex:update(['hi','hello'],1)

select()->ittakesoneargumenti.eiswhichhoursdatauwanttosee.onceyougivetheargumentit willdisplaythe dataofallthenames forthathour.

ex: select(1)

('hello','P')

('hi','P')('how','N')select(2)

('hello','N')

('hi','N')

('how','N')

SOFTWARE REQUIREMENT

1. PYTHON
2. CMAKE
3. DLIB
4. FACERECOGNITIONLIBRARY

VI. IMPLEMENTATION AND RESULT ANALYSIS

COMMANDSTORUNINCOMMAND PROMPT

FollowingCommandhastobeenteredwhileexecutionoftheprogramincmdline

STEP1

cdC:\Users\MaheshkumarU\Desktop\faceReco\myvenvpy\Scripts

STEP2

.\activate

STEP3

cd..

STEP4

cd..

STEP5

cdC:\Users\Maheshkumar U\Desktop\faceReco\project\Face_Recognition_Project-main(1)

\Face_Recognition_Project-main

STEP2

.\activate

STEP3

```
cd..
STEP4
cd..
STEP5
cdC:\Users\Maheshkumar          U\Desktop\faceReco\project\Face_Recognition_Project-
main(1)\Face_Recognition_Project-main
STEP6
pythonattendance.py
Here
Step1:ismovingtovirtualenvironmentfolder
Step2:activatingthevirtualenvironment
Step3: Going back tomyevenpy folder
Step4: Going back tofaceReco folder
Step5: MovingintoFace_Recognition_project-mainfolder
Step6-Running attendance.pyprogramfile
```

PROGRAM

```
importcv2
importnumpyasnp
importface_recognition
importosfromdatetimeimportdatetime
importface_recognitionimportosfromdatetimeimportdatetimepath='images'

images=[]

personNames= []

myList=os.listdir(path)

print(myList)

forcu_imginmyList:
current_Img=cv2.imread(f'{path}/{cu_img}')

images.append(current_Img)
personNames.append(os.path.splitext(cu_img)[0])

print(personNames)
```

```
deffaceEncodings(images) :  
  
    encodeList=[]  
  
    forimginimages:  
  
        img = cv2.cvtColor(img, cv2.COLOR_BGR2RGB)  
  
        encode = face_recognition.face_encodings(img)[0]  
  
        encodeList.append(encode)  
  
    returnencodeList  
defattendance(name):  
  
    withopen('Attendance.csv','r+')asf:  
  
        myDataList=f.readlines()  
  
        nameList= []  
  
        forlineinmyDataList:entry=line.split(',')  
  
        nameList.append(entry[0])  
  
        ifnamenot innameList:  
  
            time_now=datetime.now()  
            tStr = time_now.strftime('%H:%M:%S')  
  
            dStr = time_now.strftime('%d/%m/%Y')  
  
            f.writelines(f'\n{name},{tStr},{dStr}')  
  
        encodeListKnown=faceEncodings(images)  
  
    print('AllEncodings Complete!!!')  
    cap=cv2.VideoCapture(0)  
    whileTrue:
```



```

ret,frame=cap.read()
faces=cv2.resize(frame,(0,0),None,0.25,0.25)

faces=cv2.cvtColor(faces,cv2.COLOR_BGR2RGB)

facesCurrentFrame=face_recognition.face_locations(faces)
encodesCurrentFrame=face_recognition.face_encodings(faces,facesCurrentFrame)
forencodeFace,faceLocinzip(encodesCurrentFrame,facesCurrentFrame):

matches=face_recognition.compare_faces(encodeListKnown,encodeFace)

faceDis=face_recognition.face_distance(encodeListKnown,encodeFace)

#print(faceDis)

matchIndex=np.argmin(faceDis)
ifmatches[matchIndex]:
name=personNames[matchIndex].upper()

#print(name)

y1,x2,y2,x1=faceLoc
y1,x2,y2,x1=y1*4,x2*4,y2*4,x1* 4
cv2.rectangle(frame,(x1,y1),(x2,y2),(0,255,0),2)
cv2.rectangle(frame,(x1,y2-35),(x2,y2),(0,255,0),cv2.FILLED)
cv2.putText(frame,name,(x1+6,y2-6),cv2.FONT_HERSHEY_COMPLEX,1,(255,255,
255),2)
attendance(name)

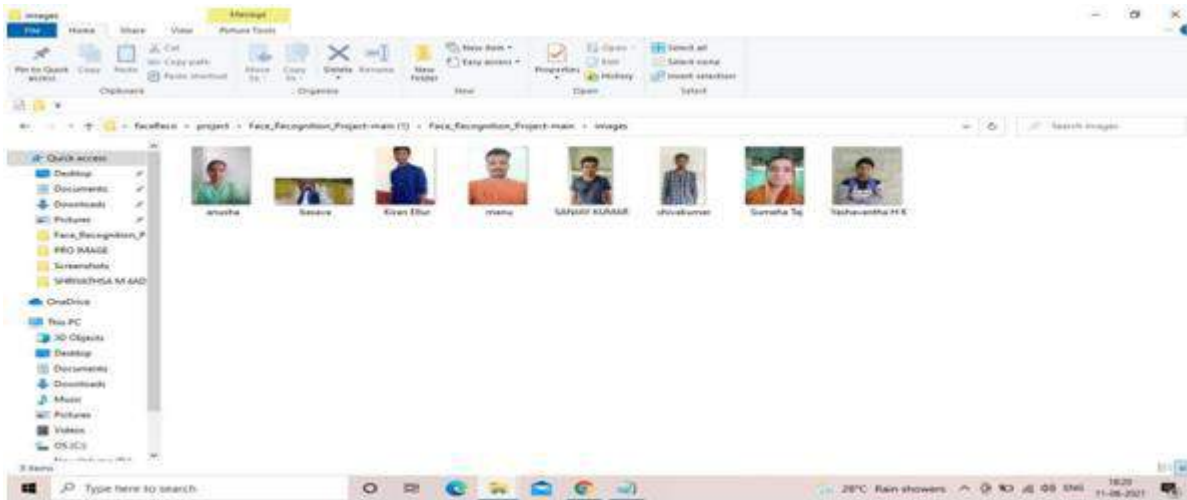
cv2.imshow('Webcam',frame)

ifcv2.waitKey(1)==13:

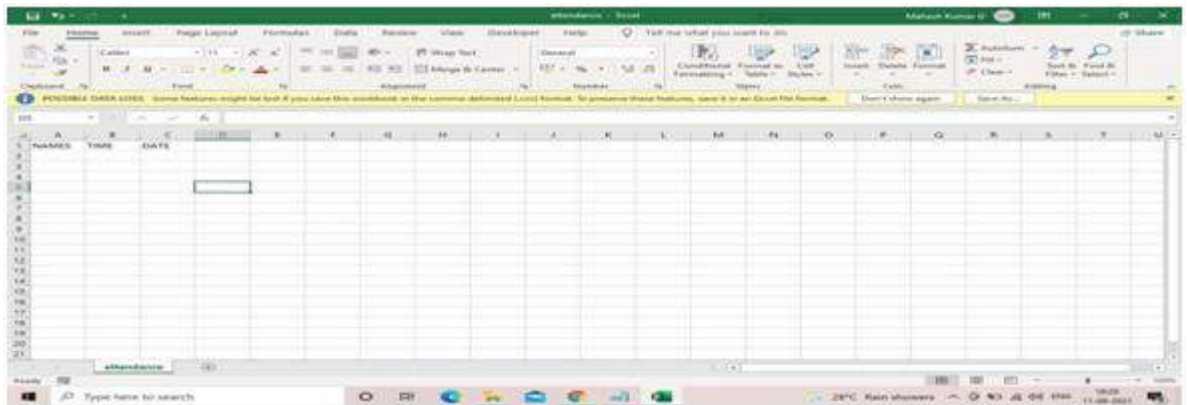
break
cap.release()cv2.destroyAllWindows()

```

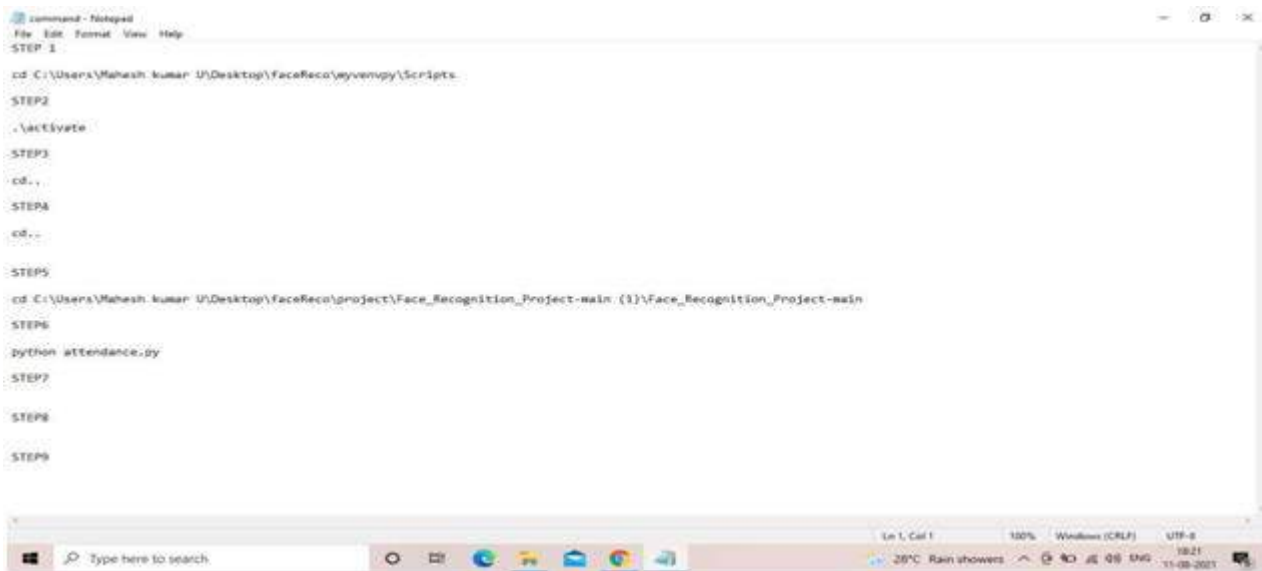
RESULTANALYSIS



STEP1FIG4.1 Feeding of Image to selected folder



STEP2FIG4.2 CLEARING THE DATA SHEET OF THE ATTENDANCE



STEP3 FIG4.3(a) COMMAND TO BE EXECUTED ON THE CMD SCREEN

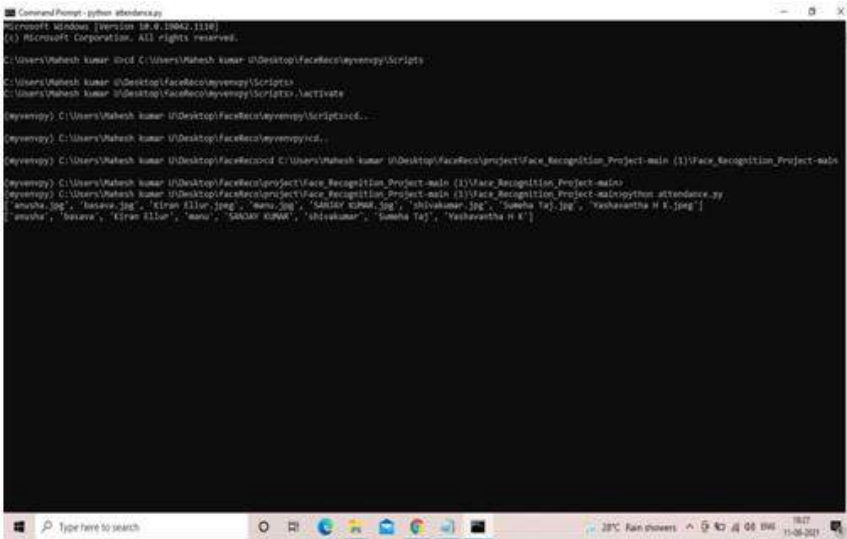
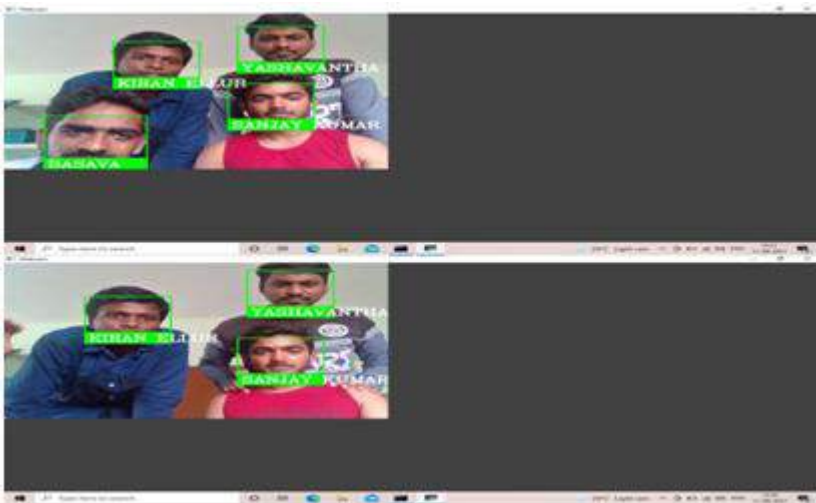
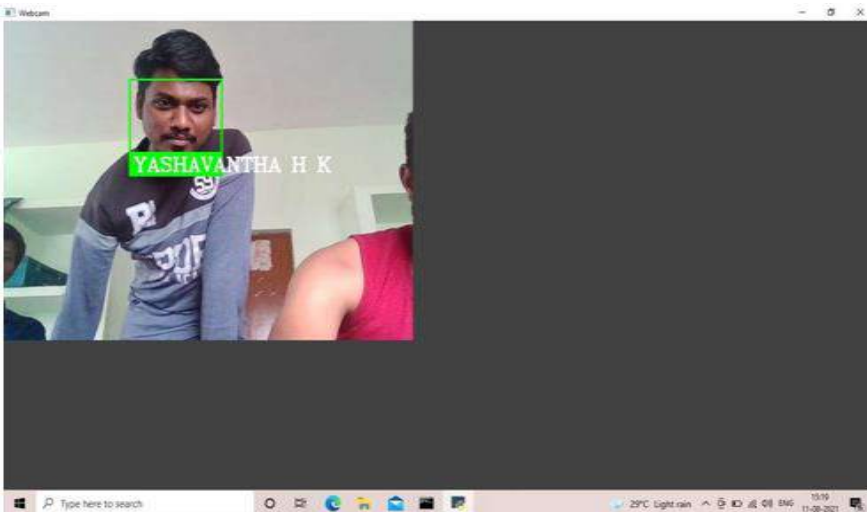


FIG4.3(b)COMMANDEXECUTEDONTHECMDSCREEN



STEP4 FIG4.4(a)FACERECOGNITIONOFMULTIPLEPERSONUSINGCAMERA



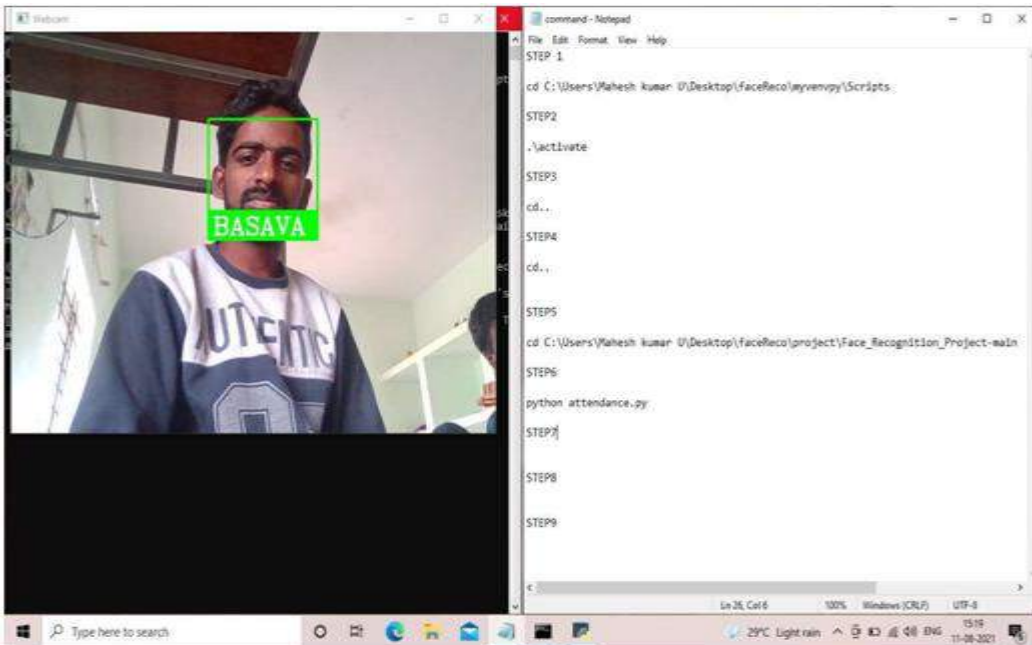
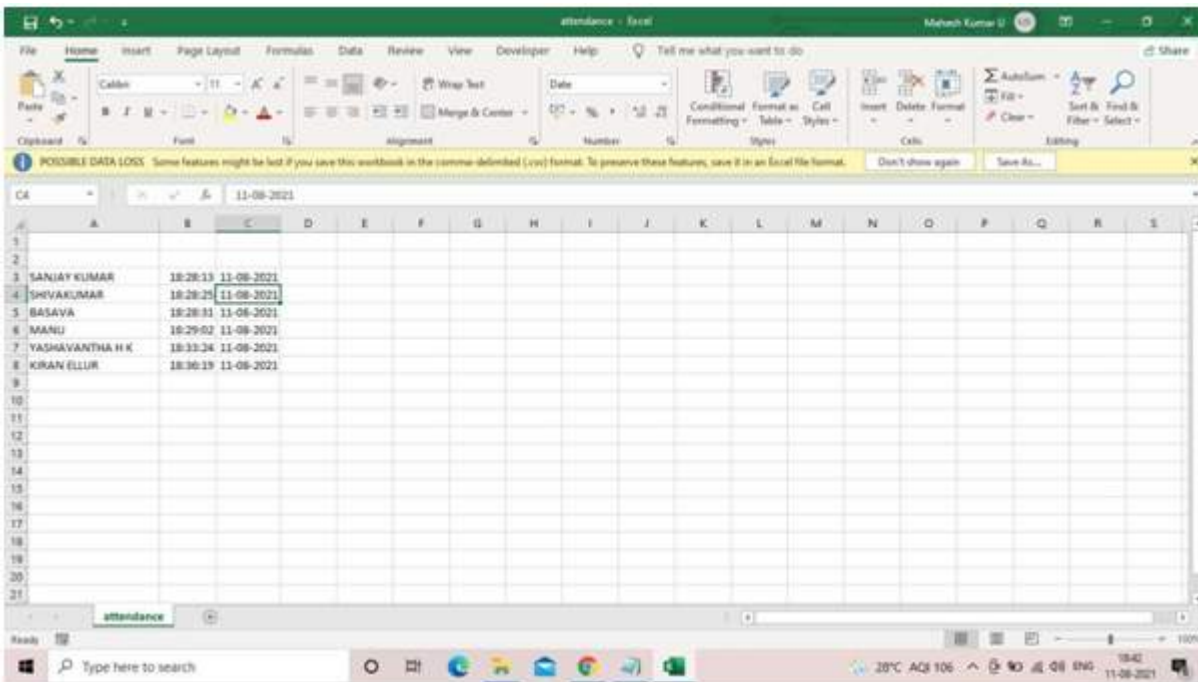


FIG4.4(b)FACERECOGNITIONOFSINGLEPERSONBYCAMERA



Step 5 FIG4.5AUTOMATICATTENDANCEMARKINGDATASHEET

VII. ADVANTAGES AND APPLICATION

Faster processing

The process of recognizing a face takes a second or less—and this is incredibly beneficial for the companies. In the era of constant cyberattacks and advanced hacking tools, companies need a technology that would be both

secure and fast. Considering that facial recognition is almost instant, it grants a quick and efficient verification of a person. In addition, it's hard to fool this technology so this is another bonus.

Seamless integration

This is probably one of the biggest benefits for companies. The facial recognition technology is quite easily integrated so it's a perfect choice. It does not require spending additional money on its integration and most facial recognition solutions are compatible with the majority of security software. A 100% win-win.

Automation of identification

Before, security guards had to perform manual identification of a person that took too much time and did not boast high accuracy. But today, facial recognition is completely independent in the identification process and not only takes seconds but is also incredibly accurate.

The 3D facial recognition technology and the use of infrared cameras significantly boosted the level of accuracy of facial recognition and made it really hard to fool.

APPLICATION:

- It can be used in schools and colleges to maintain a transparent education system
- It can be used in examination halls to achieve a fair examination by avoiding proxy candidates to write the exams of the other.
- It can also be used in security systems to avoid interruption of a known person to a specified system by feeding raw images of an authorized person.
- It can be used in election voting halls to achieve a fair process.

VIII. CONCLUSION

Automated Attendance System has been envisioned for the purpose of reducing the error that occurs in the traditional (manual) attendance taking system. The aim is to automate and make a system that is useful to organizations such as an institute. The efficient and accurate method of attendance in the office environment that can replace the old manual methods. This method is secure enough, reliable and available for use. No need for specialized hardware for installing the system in the office. It can be constructed using a camera and computer.

IX. REFERENCES

- [1]. W. Zhao, R. Chellappa, P. J. Phillips, and A. Rosenfeld, "Face recognition: A literature survey," *ACM Computing Surveys*, 2003, vol. 35, no. 4, pp. 399-458.
- [2]. Herbert Bay, Andreas Ess, Tinne Tuytelaars, and Luc Van Gool. Surf: Speeded up robust features. *Computer Vision and Image Understanding (CVIU)*, 110(3):346-359.
- [3]. H. K. Ekenel and R. Stiefelhagen, Analysis of local appearance based face recognition: Effects of feature selection and feature normalization. In *CVPR Biometrics Workshop*, New York, USA, 2006
- [4]. *IJCSI International Journal of Computer Science Issues*, Vol. 9, Issue 4, No 1, July 2012 ISSN (Online): 1694-0814



Study on Paper Making Process Using Agricultural Waste as Raw Material

Vinay J S¹, Vinay K R¹, Ekanthappa², H S Shivashankar³

¹UG Student, Department of Mechanical Engineering, Siddaganga Institute of Technology, Tumakuru -573103, Karnataka, India

²Assistant professor, Department of Mechanical Engineering, Siddaganga Institute of Technology, Tumakuru - 573103, Karnataka, India

³Associate professor, Department of Mechanical Engineering, Siddaganga Institute of Technology, Tumakuru - 573103, Karnataka, India

ABSTRACT

Since paper industries are heavily dependent on trees for paper making process which impacts the environment, an alternative substance agricultural waste such as tender coconut coir which is abundantly available resource which goes unused can reduce the primary dependence on wood for paper making process. This research was focused on making paper from agricultural waste such as dry grass, husks, coconut shell, sugar cane waste etc as primary raw material along with secondary material as waste paper. With Literature survey we selected kraft process (sulphate process) of pulp and paper making due to its environmentally friendly and high chemical recovery along with good mechanical properties imparted into the paper. This process is widely used in almost all paper industries hence gives flexibility of readily adapting it. During the study of process different proportions of coir-wastepaper ratios were tested and graph of transmittance vs nanometer was tested in UV Spectrometer. Properties suitable for different application can be compared.

Keywords: Paper making, environmentally friendly paper.

I. INTRODUCTION

Paper is a thin sheet material produced by mechanically or chemically processing cellulose fibres derived from wood, rags, grasses or other vegetable sources the pulp from these is mixed in water, draining the water through fine mesh leaving the fibre evenly distributed on the surface, followed by pressing and drying.

There are 2 main problems involved 1.) As M suraj, Akram Khan [1] States that 93% of raw material for the production of paper comes from trees. Of an average tree, we get 8000 white pages after production, it also involves cutting down trees. Deforestation is one of the main environmental problems we're facing in these times. 42% of all global wood harvest is used to make paper. Although recycling reduces use of raw material to some extent but it is very difficult to produce tree at a pace at which they are cut down every day. 2.) According to Kalidas Kalimuthu, RaghaviMd[2]

72% of worlds total coconut production is from India. In India, Tamil Nadu tops the list in the productivity of coconut, but production is high in Karnataka and Kerala as well. [3] Increased consumption of coconut water and green coconut fruit pulp has increased the generation of coconut shells which in some regions tends to become waste, generating negative social, economic and environmental impacts Due to the lack of management. Coconut shell accounts for around 85 % of the weight of the fruit and has an assumed composition of 33.30 % lignin, 30.58 % cellulose, 43 26.70 % hemicellulose, 8.86 % water and 0.56 % ash.

To account for these problems the process of making paper using coconut coir as potential substitute for wood is studied.

Paper making process using agricultural waste such as tender coconut shell, sugarcane, dry grass etc.theseshare common process which can be divided into 2 process as follows: (1) Pulp making process, (2) Paper making process. Pulp making process include chopping, Beating, Sun drying, cooking, grinding and mixing the obtained substance is a pulp.Paper making includes conversion of pulp to paper which includes screening, finishing.

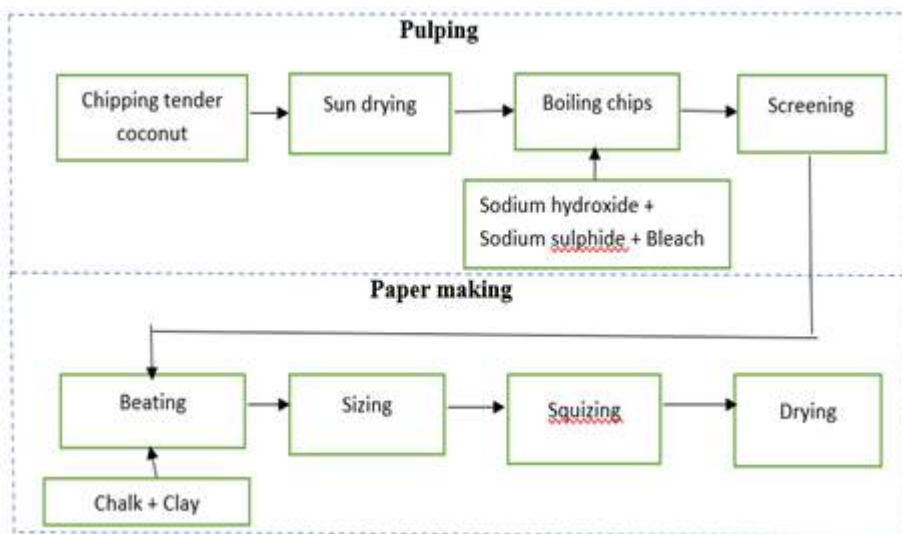


Fig 1: Paper making process.

II. LITERATURE REVIEW

Types of pulping include mechanical pulping and chemical pulping Pratima Bajpai in her paper [4] Mechanical pulp is pulp produced by using only mechanical attrition to pulp lignocellulosic materials; no chemicals (other than water or steam) are used. Light-coloured, no resinous softwoods and some hardwoods are often the fiber source. The total yield is about 90%–98%. Lignin is retained in the pulp; therefore, high yields of pulp are obtained from wood. Mechanical pulps are characterized by high yield, high bulk, high stiffness, and low cost. They have low strength because the lignin interferes with hydrogen bonding between fibers when paper is made. The lignin also causes the pulp to turn yellow with exposure to air and light.

Raymond A. Young, ... David A. Tillman in [5] Chemical pulping has been performed or proposed with a wide variety of reactants. Today the dominant chemicals used in pulping are sulfur based, although numerous sulfur-free processes have been proposed. The processes available currently include sulfate or Kraft pulping, acid and alkaline sulfite pulping, neutral sulfite semichemical (NSSC) pulping, and soda pulping. Of these the Kraft

process has become dominant and for the following reasons: (1) it can produce useful pulps from all wood species; (2) it readily permits chemical and energy recovery from the spent pulping liquor and was the first pulping process to do so; and (3) it regularly produces the highest-strength pulps.

Honghi Tran, Esa k. Vakkilainen's research [6] Kraft pulping process is the most dominant lignocellulose pulping process producing about 130 million tons of pulp annually. Lignin obtained from kraft pulping process has a complex and recalcitrant structure. The success of kraft pulping is attributed to the recovery of inorganic reactants. The black liquor obtained after pulping contains a mixture of fragmented lignin and Na_2SO_4 , which upon incineration provides Na_2S and CO_2 . Energy released from incineration of the carbonaceous lignin is used to generate steam in a high-pressure boiler. Therefore, the residual lignin acts a fuel to power the pulping process. The critical role of lignin in the kraft process prohibits diverting the lignin stream for alternative application and catalytic upgrading to valuable chemicals. Furthermore, the presence of sulfur, a known catalyst poison, is also detrimental for downstream catalytic processes. Nevertheless, the abundance of kraft lignin provides options for utilizing excess lignin residue for catalytic upgrading.

Kraft process is most widely used process for wood pulp and can be used for other raw materials like tender coconut shell without change in machineries and chemicals used to readily adapt to current industries. Kraft break down lignin and hemicellulose and due to its high chemical recovery rate this process is considered for research.

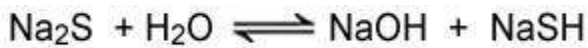
There have been studies to make paper using raw materials such as sugarcane as in [10], Pineapple leaves [11], Elephant grass [12], Elephant Dung [13], Rice Husk [14] etc..

Testing of paper as mentioned by Shabir Ahmad Mir ... in [9] includes 1.) Thickness: The thickness is the perpendicular distance between the two outer surfaces of material. The method for determining the thickness is given in TAPPI T411. Generally, thickness is measured at different locations of the sample, and the mean is calculated. 2.) Bursting Strength: Bursting strength is measured by the pressure developed behind a circular rubber diaphragm when it is forced through the paper so as to burst it. The maximum pressure sustained by the specimen is recorded. The burst test is the most common evaluation test used for paper and corrugated fiberboard. The TAPPI method is T81. The test is conducted using a bursting tester and, in essence, consists of forcing a rubber diaphragm through a hole approximately 25 mm in size using hydraulic pressure. The resultant upward bulge of the diaphragm causes it to puncture the specimen. The hydraulic force required to burst the specimen is recorded on a dial or an electronic digital readout device. 3.) Tensile Strength Tensile strength The most common strength test for paper is that of tensile strength. The limiting resistance of a test piece of paper or board is submitted to a breaking force applied to each of its ends under the conditions defined in the standard method of test. The tensile strength is generally expressed as breaking length. The most common method is to use gripping devices that are attached to a testing machine. 4.) Density: Density is an important parameter for paper and paperboard. Density is defined as the mass per unit volume of the tested material

III. CHEMICAL REACTIONS INVOLVED

In Kraft pulping process, cooking liquor chemicals are NaOH and Na_2S . Although the high percentages of sodium sulfide darken the pulp color but it has huge benefits; it increases penetration of the wood, uniform

cooking, low cooking time, high yield and strength. The Na₂S hydrolyzed in presence of water and gives hydroxide and hydrosulfide. The reaction is reversible and can be described as below:



In kraft pulping process NaOH is the key chemicals for completed the cooking process. Temperature also plays a significant rule. The main chemical reactions in the kraft cooking process can be expressed as:



Here the wood represents various organic compounds as like: Cellulose, Hemi-cellulose, Lignin, fats, and Resins.

The average wood chemical compositions are:

Cellulose: 40-45 %

Lignin 18-32 %

Rest are Hemicelluloses, fat, Resins

After the karft cooking process the chemical composition of the pulp are:

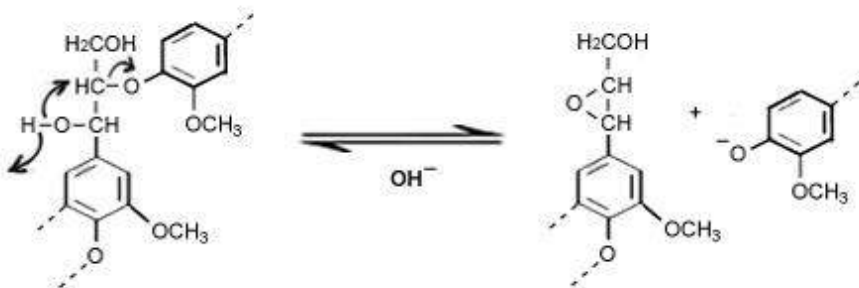
Cellulose: 70-75 %

Lignin 2-5 %

Rest are Hemicelluloses and others organic compounds.

At first step of the karft pulping process the white liquor penetration and diffusion into the interior of the wood chip.

When the wood chips are heated the delignification reactions starts, but the reaction rate is very slow. The specific kraft cooking temperature is generally 135-175°C in which the lignin structure and others organic compounds are broken down into small fragments and solubilized into the alkaline solution.



Courtesy: <http://www.pulppapermill.com/wp-content/uploads/reaction-of-lignin.jpg>

IV. STEPS INVOLVED IN PAPER MAKING PROCESS

Procedure involves:

Chopping:

1.5 kg of Tender coconut was chopped to expose fibres.

In industries this process can be compared to crushing.

Drying

The chopped coconut was sun dried to remove moisture content, chopping in addition increases the rate of drying. The weight obtained at this stage was 800 gms. Which is dry weight.



Fig 2: Sun drying

Cooking:

It involves Kraft process of pulp making as mentioned earlier, this is the most important part of the process and results of final product depends on it. After lignin and hemicellulose which get dissolved in water was washed the weight reduced to 350 gms

$$W\% = (W_f/W_i) \times 100$$

% of weight reduced = final weight of substrate after cooking / dry weight before cooking.

$$W\% = (350/800) \times 100$$

$$W\% = 43.75\%$$



Fig 3: Cooking

Bleaching:

It is process of removing impurities and make the final product light colour. This is done by cooking the substrate with 8% of hydrogen peroxide.

Grinding:

Grinding of coir to make the fibres as smooth as possible and to remove left out impurities.

Mixing

Mixing was done in various proportions of coir to paper ratio, paper includes waste newspaper which represents reused papers. Addition of starch increases strength of paper and hence 10 % of starch was used per sample.

Table no. 1: %of coir and waste paper

SL.No	Coir %	Waste paper %
1	20	80
2	30	70
3	40	60
4	50	50
5	60	40
6	70	30
7	80	20

Screening:

Screening was done by manual method by using 0.5 mm grade screening material.



Fig 4: Screening



Fig 5: After screening

Drying:

Sun drying of substrate after pressing to get uniform paper thickness.

V. RESULTS AND DISCUSSION

The products obtained at different proportions are of size 210:297 mm



Fig 6: Sample paper of 80% coir: 20% Paper (Left) and 20%coir : 80% paper (right)

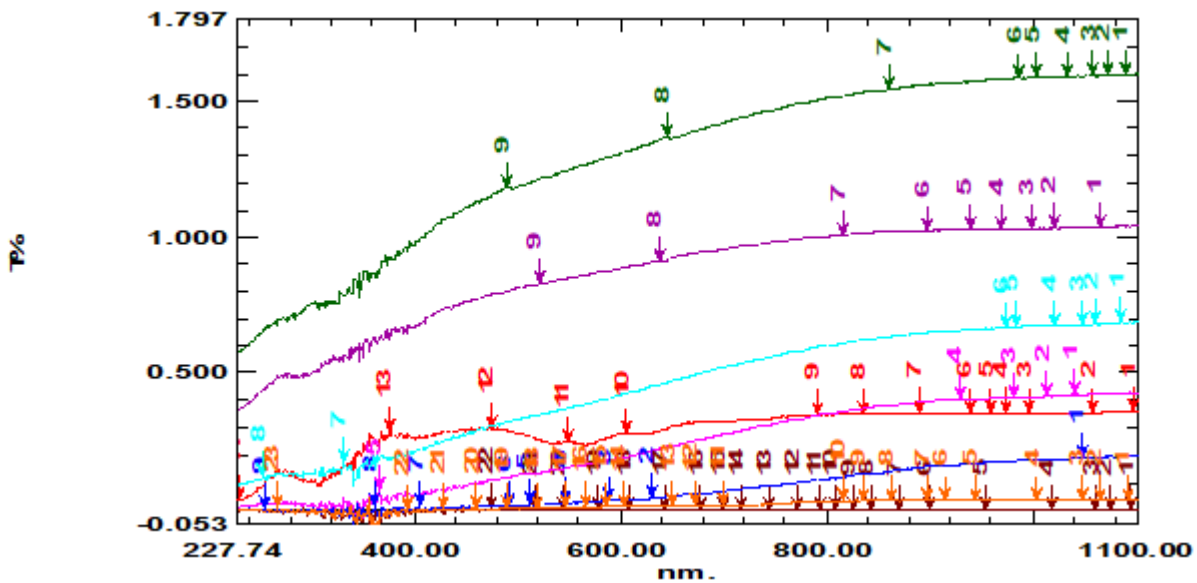


Fig 7:Graph of Transmittance vs wavelength in nm.

In UV Spectrometer model SHIMADZUEUROP A GmbH.

As the coir% increases the transmittance of substrate decreases.

VI. CONCLUSIONS

Though this product is far to replace writing paper as application but can be used for packaging, binding, paper bags and for different texture papers where writability and smoothness is compromised. The potential use of tender coconut fiber for making diversified products by an ecofriendly process could be confirmed. A simple unconventional paper making process can lead to efficient change in waste and resource management. Reduction of impact on environment through a much ecofriendly process, governed by reducing pollutants into environment as well as reducing wastage of much potential substance alongside restricting deforestation, avoiding expenditure on transport of wood. Even achieving 30% of coir-compost could lead to preserving resources and cut down of unnecessary costs.

VII. REFERENCES

- [1]. M suraj, Akram Khan. (2015). Environmental Impact of Paper Industry. ISSN: 2278-0181 ISNCESR-2015 Conference Proceedings IJEDR, 03(20).
- [2]. Kalimuthu, Kalidas&Md, Raghavi. (2019). Review on area, production and productivity of coconut in india. Researchgate1-6.
- [3]. Nunes, Luane A.; Silva, Maria L.S.; Gerber, Juliano Z.; de A. Kalid, Ricardo (2020). Waste green coconut shells: Diagnosis of the disposal and applications for use in other products. Journal of Cleaner Production.
- [4]. Pratima Bajpai,(2018) in Biermann's Handbook of Pulp and Paper (Third Edition), Science direct.
- [5]. Raymond A. Young, ... David A. Tillman, (2003) in Encyclopedia of Physical Science and Technology (Third Edition), Science direct.
- [6]. Honghi Tran, Esa k. Vakkilainen .(2015), Increasing Energy and Chemical Recovery Efficiency in Kraft Process, Natural Sciences and Engineering Research Council of Canada (NSERC).
- [7]. Presley, J.R., R.T. Hill. 1996. The Technology of Mechanical Pulp Bleaching. In: Peroxide Bleaching of Chemical Pulps, Pulp Bleaching: Principles and Practice.
- [8]. Mitra B.C., R.K. Basak, and M. Sarkar 1998.Studies on jute-reinforced composites, its limitations and some solutions through chemical modification of fibers.Journal of Applied Polymer Science.
- [9]. Shabir Ahmad Mir, HaroonMaqboolWani, Idrees Ahmed Wani, Preeti Singh, and Ali Abas Wani 2016, Food packaging material (Chapter 8) 1st Edition, ISBN.
- [10]. Al-Sulaimani, Khalsa&Dwivedi, Priy. (2017). Production Of Handmade Papers From Sugar Cane Bagasse And Banana Fibers In Oman.International Journal of Students' Research in Technology & Management. 5. 16. 10.18510/ijstrtm.2017.534.
- [11]. Yusof, Yusri& Ahmad, Mohd&Wahab, MdSaidin&Mustapa, Mohammad Sukri&Tahar, Mohd. (2012). Producing Paper Using Pineapple Leaf Fiber. Advanced Materials Research. 383. 3382-3386. 10.4028/www.scientific.net/AMR.383-390.3382.
- [12]. Madakadze, I. &Masamvu, Tariro&Radiotis, T & Li, Jian& Smith, Donald. (2010). Evaluation of pulp and paper making characteristics of elephant grass (*PennisetumpurpureumSchum*) and switchgrass (*Panicumvirgatum L.*).African Journal of Environmental Science and Technology. 4. 465-470.

- [13].Nadeem Farah, MoazzamAmna, YaqoobNaila and RehmanIshtiaq (2014), Processing of Elephant Dung and its Utilization as a Raw Material for Making Exotic Paper, Research Journal of Chemical Sciences, 03(08).
- [14].Khadoo-Jeetah, Pratima&Golaup, Nisha&Buddynauth, Karishma. (2015). Production of cardboard from waste rice husk.Journal of Environmental Chemical Engineering.3. 10.1016/j.jece.2014.11.013.
- [15].Main, Nor Mazlana& A. Talib, Rosnita& Ibrahim, Rushdan& Abdul Rahman, Russly& Mohamed, AinunZuriyati. (2014). Suitability of Coir Fibers as Pulp and Paper.Agriculture and Agricultural Science Procedia. 2. 304-311. 10.1016/j.aaspro.2014.11.043.
- [16].MohdHilmi Othman, Nor Mazlana Main, SitiZaharahKunchi Mon and ZalehaMohamad, 2013.Development of Paper Using Coir Fibers as a Packaging Product. Asian Journal of Scientific Research, 6: 207-216.



Smart Multipurpose Surveillance Robot

Deepak H A¹, Deepak R¹, Sharath S², Sowmyashree²

¹Assistant Professor, Department of ECE, Navkis College of Engineering, Hassan, Karnataka, India

²Assistant Professor, Department of ECE, GEC, K R Pet, Mandya, Karnataka, India

ABSTRACT

The various sensors, mechanical arms, wheel system, wireless communication mechanism and remote controlling mechanism are used to design the proposed robot that can be used in military and civil fields. The coordination of smart robot various parts to perform different fields are discussed in this project. Our project deals with a multi-purpose robot that has been designed in such a way that it can fulfil the needs of the military, police, spy teams and armed forces. It has numerous applications and can be used in different environments and for different situations. This robotic vehicle uses a specific set of sensors for performing various tasks such as the PIR (passive infrared) sensor that detect the alive humans by emitting the infrared rays, as an alive human (body) emits thermal radiation, this thermal radiation is detected by the PIR sensor in order to detect alive humans, the bomb (metal) sensor is used for the detection of bombs, the fire or flame sensor is used for fire detection and the gas sensor, which is used to detect harmful gases. The robot is designed in such a way that it can perform multiple operations which is achieved by embedding different features into a single prototype.

Keywords: Robot, mechanical arm, wheel system, gas, PIR sensor.

I. INTRODUCTION

Robotics is the branch of technology that deals with the design, construction, operation, and application of robots. Robots have become a subject of great interest nowadays. Robots are, in fact, defined as man-made mechanical devices that can move by themselves, whose motion must be modeled, planned, sensed, actuated and controlled, and whose motion behavior can be influenced by “programming”.

Advancing the economy of many countries around the world is maybe due to mining/extracting the minerals and geological materials that are valuable from the core of the earth. It is estimated that mining industry is employing one million people and worth 70 billion dollars. Many countries contribute an average of 20% approximately to their GDP. There are various health issues. The metals and metalloids that are generated as a waste during mining are highly toxic for human health.

In modern technology, autonomous robotic system is an excellent novelty. It helps mankind in performing laborious task and where humans cannot perform or when it is difficult for humans to go into war fields. In

such cases a robotic vehicle can be deployed, where existing tools cannot be employed. With the availability on various sensors in the market building up of robots has become an easy task. The various sensors available are Para Infrared (PIR) sensor, IR sensor, metal (bomb) sensor, fire sensor etc. Based on the application and necessity of situation we can embed various sensors according to the need. Many areas of the world get affected by natural calamities. Disasters like earthquake, floods, etc. are unstoppable and leave behind a great loss of life. Large area becomes a hurdle for rescue workers. Hence, we are proposing a Multi-purpose robot.

The robot is equipped with a PIR sensor to detect live human, a robotic arm to remove any obstacles in its way, a camera to send images to control unit. The robot has a fire sensor or a gas sensor that detects the fire explosion or any gases released in the area and extinguish it. It has a bomb detector that detects the bomb in the area and sends an alert to control office/room.

All objects emit what is known as black body radiation. It is usually infrared radiation that is invisible to the human eye but can be detected by electronic devices designed for such a purpose. The term passive in this instance means that the PIR device does not emit an infrared beam but merely passively accepts incoming infrared radiation. There are a variety of robotic systems being developed to support firefighters due to the wide range of fire events including fires involving structures, vehicles, aircrafts, ships, and wild lands. These robots which we used for detect and extinguish fire by means of various sensors

II. PREVIOUS ROBOTIC SYSTEM

There is much progression in the field of engineering, robotics in particular. Many robotic systems have been advanced for various purposes. Some robotic systems are used for automatic motion of vehicles on road and wheel chairs, which can help disabled. There are also other robotic systems, which can be used for defense purposes. Along these innovations there are also robotic systems, which can combat in war times. One of the robots is named "Security Warrior", which consists of five features including vision, motion, robot arms and power estimation.

One more robot that autonomously detects and extinguish fire, which is known as a "Fire Fighter robot". It uses thermal sensor for fire or flame detection and extinguish it. Some robotic systems are designed and constructed particularly for bomb detection. They achieve this by sending the robot to the respective place. In case of disaster-prone areas, detection by rescue workers becomes time consuming and due to the vast area, that gets affected it becomes more difficult. So, a robot is sent to the disastrous area for identifying the live people and rescue operations. There are various robotic systems invented with different applications, which are currently available and in use.

III. PROBLEM DEFINITION

During the tragedy, many people will die because they will not get the aid at the right moment, and many people will also be harmed by the unintentional events, at which moment there will not be too much human resources to locate and rescue them. In our study, we found robots are developed for various applications like detecting fire incidents, military applications, detecting live humans, detecting atmospheric gases, etc. But we

didn't find a single robot which can be used for various applications, this motivated us to design and build a cost-effective robot that can be incorporated with features such as fire detection, live human detection, audio and video transmission, obstacle detection, etc.

- For each operation there are different robots are constructed
- There is only text reply coming from the robot
- Robot design is not perfect so it cannot run in odd surface
- In present system DTMF is used to control the robot, Network is major drawback in this robot

IV. PROPOSED SYSTEM

Our project deals with a multi-purpose robot that has been designed in such a way that it can fulfill the needs of the military, police, spy teams and armed forces. It has numerous applications and can be used in different environments and for different situations. This robotic vehicle uses a specific set of sensors for performing various tasks such as the PIR (passive infrared) sensor emits the infrared rays in order to detect the alive humans, as an alive human (body) emits thermal radiation, this thermal radiation is detected by the PIR sensor in order to detect alive humans, the bomb (metal) sensor is used for the detection of bombs, the fire or flame sensor is used for fire detection and the gas sensor, which is a type of chemical sensor is used for the detection of harmful gases. The robot is designed in such a way that it can perform multiple operations which is achieved by embedding different features into a single prototype.

V. WORKING PRINCIPLE COMPONENTS USED

1. Arduino Mega

The Arduino mega also have advanced features like an inbuilt temperature sensor, the real-time clock, external and software interrupts, analog comparator. The output of this micro controller is LCD and communication between multiple devices by using wires and input devices are various sensor which has the capabilities to sense from the surroundings or environment when there is any fault/problem.

2. Fire sensor:

A fire sensor is a type of sensor specifically designed to identify and react to the presence of a fire or flame. The flame sensors response may depend on its appealing. It includes a warning system, oil and gas pipe, propane and a fire control system. This sensor uses the infrared blaze flare system that enables the detector to function through a layer oil, dust, water vapor, and indicator.

3. Gas sensor:

A gas detector is a device that detects the presence of gases in an area, often as part of a safety system. This sensor is used to detect a gas leak or other emissions and can interface with a control system so a process can be automatically shut down. A gas detector is a sensor that senses the emission or intensity of atmospheric gases.

4. Wireless Camera

Wireless cameras work by transmitting the camera's video through a radio (RF) transmitter.

5. DC Motor

A simple DC motor has a coil of wire that can rotate in a magnetic field. The current in the coil is supplied via two brushes that make moving contact with a split ring. The coil lies in a steady magnetic field. The forces exerted on the current-carrying wires create a torque on the coil.

6. Bluetooth Model

HC-05 Bluetooth device is a convenient to use Bluetooth SPP (serial port protocol) device built to provide clear serial radio communications. Its connectivity is through serial connectivity which makes it very easy for controller or computer to connect.

7. PIR Sensor

The term PIR is a shortened version of the Passive Infra- Red. The word " passive" implies that the detector does not participate in the operation, indicating that it does not release the related IR signals themselves, but instead passively senses the human body's infrared emissions in the region.

The radiations detected are switched into an electric current which is equivalent to the contamination intensity observed. This charge is then further enhanced by an integrated FET and loaded into the output pin of the system which becomes important to an additional circuitry to further trigger and intensify the alarm phases. The PIR detector spectrum is up to 10 m at angle of 15°.

8. Metal Sensor

The precious metal scanner used to detect mines; tests interference of the electrical current produced by the existence of pieces of metal in the soil. The common, simple metal detectors are easy to use, and it has an excellent rate of success. Metal detector operates by emitting an electric current into the surface from the scanning coil. Some metallic objects inside the EMF become energized and will rebroadcast their own energy field.

9. L293 DRIVER

The L293 is an integrated circuit motor driver that can be used for simultaneous bidirectional control of two small motors, which allows the motor to drive on any direction. It means by using L293D IC we can control two motors with a single L293D IC. Motor driver act as an interface between Arduino and the motors. Two servos will act as entry and exit gate and rotate to open or close the gate.

VI. METHODOLOGY

The block diagram of multipurpose robot mainly consists of arduino, to which multiple sensors are connected like the PIR (Passive-infrared) sensor which is used for the detection of alive human being, metal (bomb)

sensor that is used for bomb detection, fire sensor which is used for detecting fire explosion and gas sensor which detects harmful gases in the war field. When all the actions mentioned above are sensed by sensors, an LED blinks as an indication and the buzzer sound indicates that there is a problem and checks further in PC to find whether it is fire explosion or bomb is detected etc., then further intimation is sent to respective teams to rescue. It also includes a Bluetooth module, which is designed for clear wireless serial connection setup. Two DC motors are used for the movement of robot-like forward, left, right and reverse. A Wi-Fi camera is used to capture live video and send to the control unit.

A Passive Infrared sensor (PIR sensor) is an electronic device that Measures infrared (IR) light radiating from objects in its field of view. PIR sensors are often used in the construction of PIR-based motion detectors (see below). By using android technology, we can control the movement of vehicle in the Specified direction. A metal detector is implemented in the system which will inform about any explosives are detected in suspected areas. We can use this robot as fire fighter robot. We will use fire sensor to detect the fire and we have fire extinguisher to control the fire. We can use this robot as mining robot. We will use gas sensor to measure the hazardous gasses like CO₂, CO, LPG, etc and upload the values into cloud. We have Wi-Fi camera, so we can use this robot for surveillance and security. Thingspeak.com is the cloud where we will store all measured data.

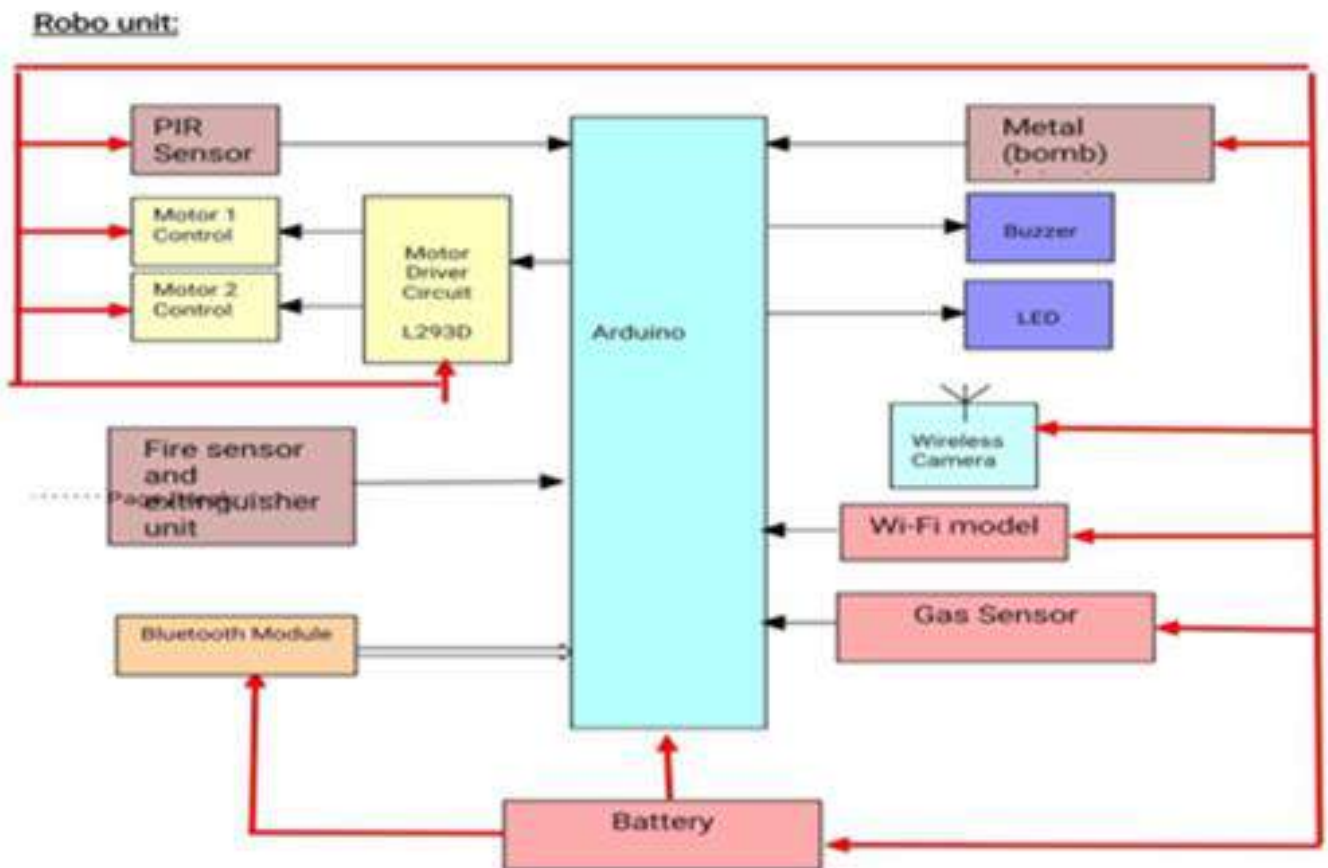


Figure 1: Block diagram

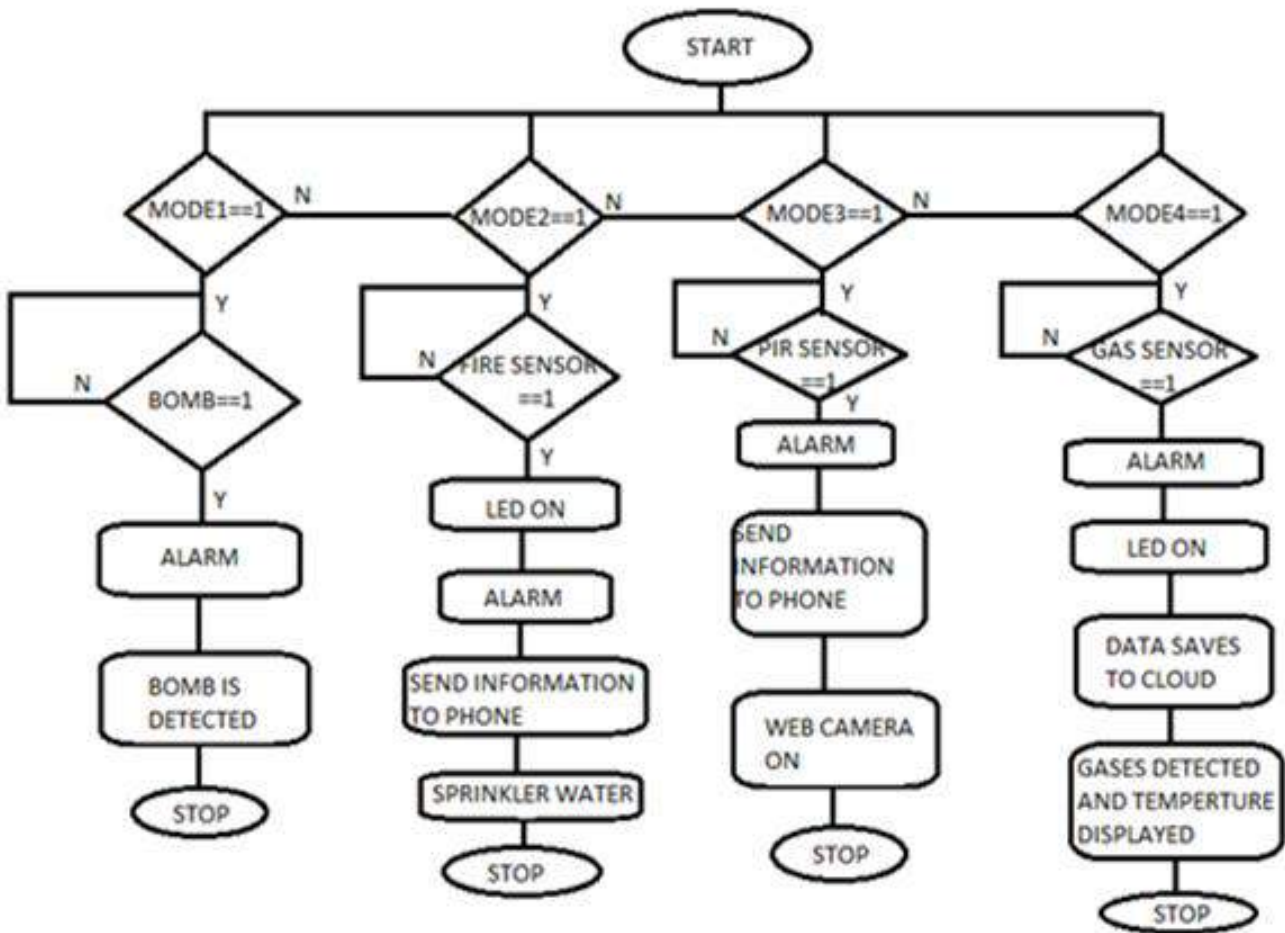


Figure 2: Flow Chart

VII. TEST RUN PROCEDURES AND RESULTS

A. Live Human Detection:

In case of disaster-prone areas, it is very difficult and time consuming for rescue workers in the vast area. So, a robot is sent to the disastrous area for identifying the live people and rescue operations. The PIR (Passive Infra-Red) Sensor placed on a robot detects motion by measuring changes in the infrared levels emitted by surrounding objects.

B. Bomb Detection:

In the present-day scenario, we are facing many threats by bomb blasts, in such cases detection of bombs by sending the robot to a respective place can save the lives of human at risk. A metal detector is implemented in our robotic system which detects the bomb in the area and sends an alert to the control unit.

C. Fire detection:

Fire fighters always cannot get into dangerous regions and rescue victims. The proposed robotic vehicle can reach in to such dangerous positions like petrochemical complexes and huge warehouse fire. A fire sensor placed in a robot that detect flame or fire. The range of detection is up to 10m. The water tank with capacity of 2 liters is placed on the robot which can be used to shut down the fire by spraying the water. Once the fire is detected the pump motor automatically spray water and it is controlled through motor driver circuit.

D. Harmful Gases detection:

The Gas sensor placed on a robot is used to detect hazardous gas. By using an audible alarm, alert can be given to people whenever a dangerous gas is detected.

E. Obstacle detection:

When the obstacle comes in path of robot an IR (infrared) sensor detects the obstacle and decides to avoid the obstacle by taking left or right turn.

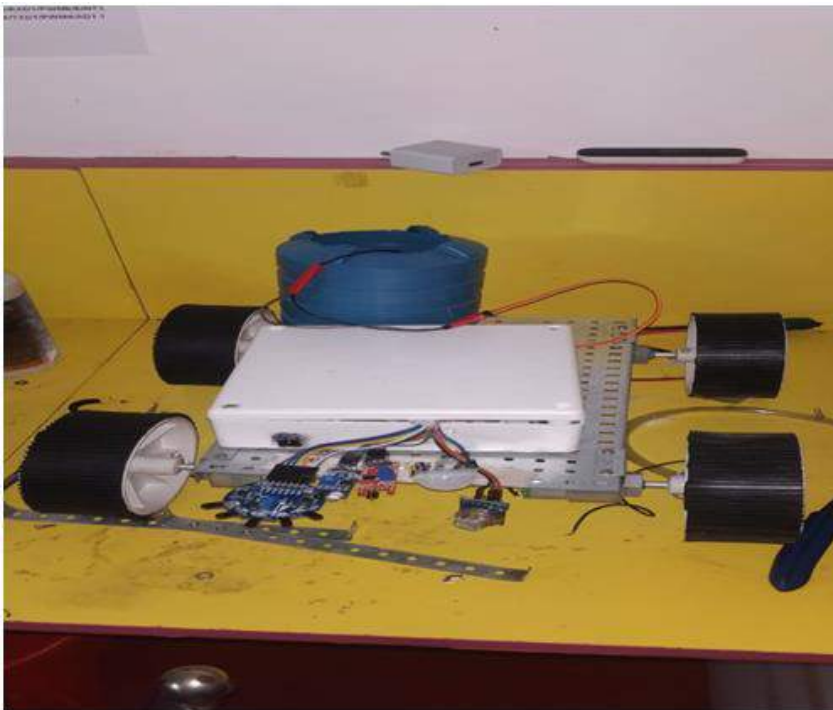


Figure 3: smart multipurpose surveillance robot

Future work of the Project

1. Automatic pick and drop of blocks or humans with robotic arm can be implemented which can future reduce the time consumption.
2. Laser gun: To make robot self-defense we give the robot a laser gun that can shoot.
3. We can implement the detection of faces of terrorist using image processing using open CV.

VIII. CONCLUSION

The purpose of the proposed system is to provide a robotic vehicle, which plays a vital role in war field, where the disaster takes place like bomb explosion, fire accident and release of harmful gases. This proposed system is superior to other existing system due to use of different sensors like Metal sensor(works similar to bomb sensor) which is used for bomb detection, similarly Fire sensor for fire detection, Gas sensor for detection of harmful gases and PIR sensor(which detects the thermal radiation emitted by the alive human body) for alive human detection. After each detection the buzzer gets ON and the message is sent to control room. The robotic vehicle can perform multiple operations at a time in comparison with the existing robotics systems. Many disasters can be detected by using this autonomous vehicle which can be done in a limited period of time. It can be done without affecting any humans and affected if done manually. The robot is manually controlled. Hence, our system is sure to create a revolution in its own field.

IX. REFERENCES

- [1]. Sivasoundari,S.Kalaimani,M.Balamurugan“Wireless Surveillance Robot with Motion Detection and Live Video Transmission”,” International Journal of Emerging Science and Engineering (IJESE)” ISSN: 2319–6378, Volume-I, Issue-6 April 2017.
- [2]. Trupti B. Bhondve, Prof.R.Satyanarayan, Prof. Moresh Mukhedkar: “Mobile Rescue Robot for Human Body Detection in Rescue Operation of Disaster”,” International Journal of Advanced Research in Electrical, Electronics and Instrumentation Engineering”, Vol. 3, Issue 6, June 2017.
- [3]. Mr. S.P Vijayaragavan, Hardeep Pal Sharma,Guna sekar.C.H, S.Adithya Kumar: “Live Human Detecting Robot for Earthquake Rescue Operation”,” International Journal of Business Intelligents” Vol 02, Issue 01, June 2017.
- [4]. B.Ramesh G.Shivakumar J.R. Manjunath C, Mnaveen Kumar Android Based Autonomous Intelligent Robot for Outdoor Security vol.1 pp.2348-7968 July 2014
- [5]. L.Iocchi F.M, Deller Fave S Multi-objective Multi Robot Surceillance pp. 978-989 Feb 2009.
- [6]. PratimaBhagat,KishoriBidawadc, Komal Amel;“Rescue robot for hazardous coal mines”, International journal of technology and science.
- [7]. Issue-2, vol.1,may 2014 M. Thamrin N., Rosman R, and SATMEGA 8Aawi D.S, “Design and analysis of wireless controller panel using RF module’s for Robotic



The Effect of Heat Treatment Process on the Microstructure and Micro Hardness of AlSi10Mg Alloy Samples Fabricated by Additive Manufacturing

Manjunath Prasad R^{1*}, U N Kempaiah², Santhosh N³

^{1*}Research Scholar, Department of Mechanical Engineering, University Visvesvaraya College of Engineering, Bangalore University, Bangalore, Karnataka, India

²Professor, Department of Mechanical Engineering, University Visvesvaraya College of Engineering, Bangalore University, Bangalore, Karnataka, India

³Associate Professor, Department of Mechanical Engineering, MVJ College of Engineering, Near ITPB, Whitefield, Bangalore – 560 067, Karnataka, India

ABSTRACT

Additive manufacturing (AM), also known as 3D printing is becoming an industry standard for manufacturing components. The AM processes can produce complex metal parts with potential applications in aerospace, automobile, medical and fashion domains. Direct Metal Laser Sintering (DMLS) is a commonly used laser powder bed fusion (LPBF) type of AM technique for processing widely used aluminum alloys due to its light weight, high strength, and corrosion resistance properties. This paper presents an experimental work of the latest research carried out in understanding the Hardness and Microstructure of the Aluminium alloys processed by DMLS before and after heat treatment conditions with the aim of identifying research gaps and future research directions. The present research has effectively utilized the established characterization techniques like optical microscopy (OM), scanning electron microscopy (SEM), and X-ray diffraction (XRD), and the effects of Heat treatment on Microstructure and Hardness are investigated and the inferences are reported.

Keywords: Additive Manufacturing; Laser Powder Bed Fusion; Direct Metal Laser Sintering; Metal powder; Characterization; Hardness; Heat treatment.

I. INTRODUCTION

The ASTM definition for Additive Manufacturing is “process of joining materials to make objects from 3D model data, usually layer upon layer, as opposed to subtractive manufacturing methodologies” [1]. The Additive Manufacturing (AM) is a class of layer-by-layer manufacturing techniques that can fabricate highly complex components from CAD model. This CAD model is sliced into 2D slices with a certain layer thickness, and subsequently each layer is built up by adding material. There are different types of Metal Additive

Manufacturing (AM) Methods, namely Selective Laser Sintering (SLS), Selective Laser Melting (SLM), Direct Metal Laser Sintering (DMLS), Laser Engineered Net Shaping (LENS), and Direct Metal Deposition (DMD). Among these Metal AM methods, the Direct Metal Laser Sintering (DMLS) process can be used for Aerospace parts, customized medical parts, tooling with conformal cooling channels and functional components with high geometrical complexity. Direct Metal Laser Sintering is an additive freeform manufacturing process which creates 3-D parts through the application of laser energy to powder beds [2]. The manufacturers are focusing on the potential cost reduction, fewer steps in the production process and design-freedom and these are achievable through Additive Manufacturing (AM) technologies. There has been number of studies on Additive Manufacturing of AlSi10Mg alloys, because of the demand from the industrial field for lightweight structures with complex geometries [3]. The AlSi10Mg alloy has been widely used in the aerospace and automotive industry, because of its neat eutectic composition of Al and Si; further, it has good weldability. However, the Aluminium alloy powder is very easy to be oxidized, and the formation of oxide film is one of the challenges when exposed to laser during the fabrication of samples. There are many recent studies, which have reported the microstructure and mechanical properties of DMLS / SLM fabricated AlSi10Mg alloys. Kempen et al. [4] studied the mechanical properties of AlSi10Mg produced by SLM and found that the SLM-fabricated AlSi10Mg parts exhibited higher tensile strength and hardness than the casted parts; these parts have exhibited anisotropic behavior at rupture under different build directions. Brandi et al. [5] studied the microstructure and fatigue performance of SLM-fabricated AlSi10Mg under different directions (0°, 45°, and 90°). The researchers found that the heat treatment had the noteworthy effect on fatigue resistance and least effect on the building direction. Read et al. [6] studied the influence of process parameters on porosity development in the SLM of AlSi10Mg alloys using a DOE. The reviewers found that the laser power, scanning speed, and the interaction between the scanning speed and hatch spacing had a pronounced effect on porosity development. From, the literature review, it is evident, that this paper focuses on the Microstructure and Hardness properties of fabricated samples both in “as fabricated” and post “Heat treatment” condition. The effects of Heat treatment on Microstructure and Hardness are investigated.

II. MATERIALS, METHODS, PROCESSING AND CHARACTERIZATION TECHNIQUES

The chemical composition of AlSi10Mg powder as provided by the powder manufactures (EOS GmbH) is given in Table 1, and has been ascertained through powder Particle Elemental Composition studies by the Energy Dispersive X-Ray Analysis (EDAX). The Microtrac Bluewave Particle Size Analyzer are used to analyze three powder samples Particle Size Distribution (PSD) and the average D10, D50 and D90 values are 30.29 μm , 43.60 μm and 63.61 μm respectively. Figure 2 shows a Scanning Electron Microscope (SEM) micrograph of the powder; it is obvious that the powder particles are not spherical. The particle shows irregular morphology, with small irregular satellite particles attached to the bigger particles (Fig. 1). The specimens are manufactured by EOSINT M280 system (EOS GmbH - Electro Optical Systems, Germany). The EOS EOSINT M 280 is based on the DMLS (Direct Metal Laser Sintering) 3D printing technology developed by EOS, equipped with Ytterbium fibre laser with 400W power, and a Scan speed of 7 (m/s), and a minimum re coater time of 8 sec, and build rate of 5-20 ($\text{cm}^3 / \text{hr.}$) The process takes place in an inert environment in a working space with 250 \times 250 mm

dimensions on the horizontal plane and a maximum height of 290 mm. The layer thickness was set to 60 μm and a parallel scan strategy with alternating scan direction was adopted. In the current study, the samples are produced using the process parameters of LASER Power of 240 W, Scan speed of 1180 mm/s, Hatch spacing of 0.12 mm, and Laser Spot Size of 0.1mm. The DMLS process parameters are listed in Table 2 and these are the optimum setting parameters from previous studies. The test samples with dimensions of 10mm \times 10mm \times 10mm have been fabricated to examine the Microstructure and Hardness as per the dimensions given in figure 2.

TABLE 1 CHEMICAL COMPOSITION OF AlSi10Mg ALLOY POWDER (Wt. %)

Element	% Composition
Si	9.5-10.5
Mg	0.15-0.45
Fe	0.45-0.55
Cu	0.05-0.1
Pb	0.05-0.1
Ti	0.1-0.15
Zn	0.1-0.15
Mn	0.4-0.45
Sn	0.15-0.2
Ni	0.05-0.1
Al	Rem.

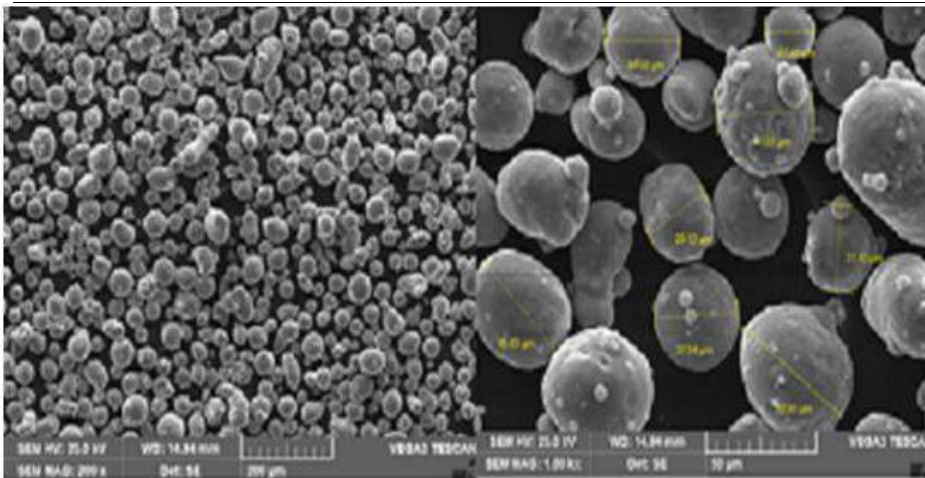


Figure 1: The morphology of AlSi10Mg powder

TABLE 2 DMLS PROCESS PARAMETERS

Sl. No.	Parameter	Value
1	Power	240 W
2	Scan Speed	1180 mm/s
3	Layer Thickness	60 μm
4	Hatch Spacing	0.12 mm
5	Laser Spot Size	0.1 mm

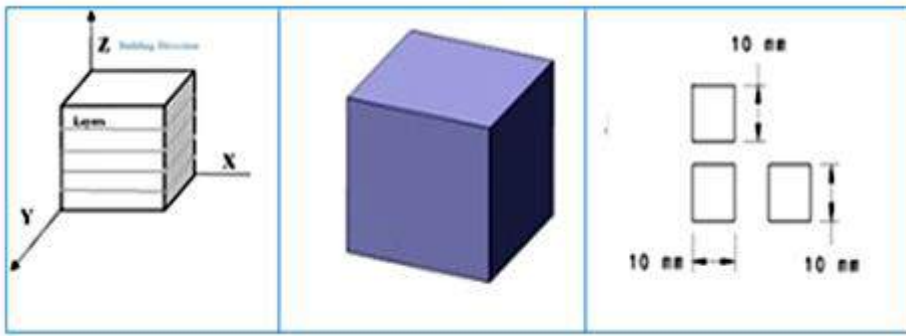


Figure 2: Build Orientation and Test samples dimensions

The microstructure of both “as fabricated” and “Heat Treated” AlSi10Mg samples are characterized with Optical Microscopy (OM), Scanning Electron Microscope (SEM), and X-ray diffraction (XRD) measurements. A Nikon optical microscope LV100 with Clemex Image Analyzer is used to evaluate the microstructure of the etched parts. The polishing and etching procedures are performed according to the ASM Metal Handbook recommendations. The samples are etched using Keller’s reagent (190 ml distilled water, 5 ml HNO₃, 3 ml HCl, 2 ml HF) for 20 seconds to reveal the microstructure. The Micro Vickers Hardness Tester (MMT-X7, Matsuzawa, Japan) is used for measuring the hardness with Vickers scale (0,5 kg load). A TESCAN- VEGA3 LMU Scanning Electron Microscope and EDAX – AMETEK is used to investigate the grain size, structure observations, and elemental analysis (Energy-dispersive X-ray spectroscopy). For X-ray diffraction analysis, the Malvern Panalytical's X-ray diffractometer is used.

The Post-processing operations like Heat treatment is required in order to enhance the mechanical properties [7]. For the Heat treatment study, the samples are fabricated by DMLS process in accordance with the dimensions shown in figure 2. This study is to explore the effect of a T6 heat treatment on the DMLS fabricated samples, and understand its influence on the microstructure. The Tensile, Compression and Impact samples are solution heat treated at 540 °C and 1.5 h soaking time for solution heat treatment, followed by water quenching, and artificial ageing (AA) at 200°C for a duration of 8 hours.

III. RESULTS AND DISCUSSIONS

A. Microstructure

The Optical microscope analysis is performed using the “as fabricated” and “Heat-Treated” samples along the building direction that is perpendicular to the printed layers (Z-direction) and parallel to the printed layers (XY direction). The Figure 3 shows OM images showing the microstructure of “as fabricated” and “Heat-treated” samples. The microstructure has resulted from the high cooling rate experienced by the material during the layer wise printing operation. The as-fabricated sample is shown in Figure 3 (a and b). The characteristic cellular microstructure, supersaturated α -Al matrix and continuous network of eutectic Si particles are characterized from the morphological features. The resulting microstructures are non-homogenous. The Al cells usually appear finer when viewed perpendicular to the build direction. And the Al cells appear elongated when viewed parallel to the build direction, After the Heat treatment; the microstructure changes noticeably.

Figure 3 (c and d) establishes microstructure of T6 Heat treated AlSi10Mg alloy. The Si particles have grown and are uniformly dispersed in α -Al matrix owing to solution heat treatment and aging.

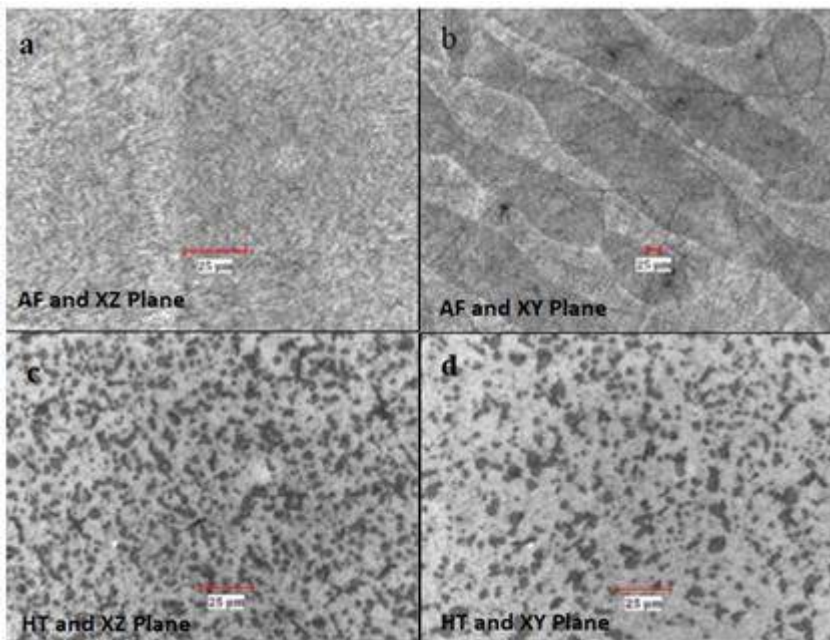


Figure 3: OM images showing the microstructure of as-fabricated samples (a and b) Heat-Treated samples (c and d).

The scanning electron microscope (SEM) analysis is performed using the “as fabricated” and “Heat-treated” samples along the build direction that is perpendicular to the printed layers (Z-direction) and parallel to the printed layers (XY direction). The Figure 4 (a and b) shows SEM images depicting the microstructure of as fabricated and the Heat-treated samples [Figure 4 (c and d)].

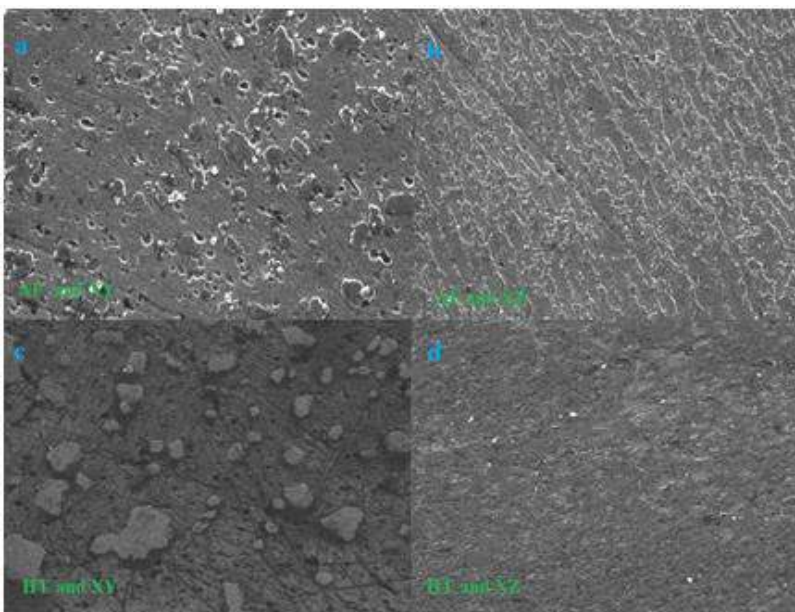


Figure 4: SEM images showing the microstructure of “as-fabricated” samples (a and b) and “Heat Treated” samples (c and d)

B. Microhardness

Hardness is well known as a preliminary indication for mechanical properties. The microhardness measurement is performed according to ASTM E384 (The standard test method for Knoop and Vickers Hardness Testing of Materials). The average values of the samples of microhardness are obtained along all the three (X, Y, and Z) directions. Each recorded value was an average of 3-5 indentations along the tested area of a 500-gf load applied over a period of 15 to 20 seconds dwell time. The Vickers microhardness of the “as built” DMLS samples is much higher (almost 45 Hv) than the microhardness of the T6 heat treatment samples due to the softening the material, fine distribution of the Si phase and attributable to the grain growth, which has reduced the grain boundaries. The microhardness of the “as fabricated” DMLS material is always higher than the heat-treated material. The anisotropy is not observed in the material after heat treatment since the hardness in all planes is found to be an average of 132 ± 4 HV for as fabricated samples and 87 ± 4 for Heat treated samples. This is possibly due to the homogenized microstructure and evolution of the crystallographic texture. This significant drop in hardness for the DMLS alloy is clearly due to the microstructural changes related to the treatment itself. The table 3 gives the hardness values for as fabricated specimens, while the table 4 gives the hardness values for heat treated specimens. The figure 5 gives the hardness values for both, “As Fabricated” (AF) and “Heat Treated” (HT) specimens.

TABLE 3 HARDNESS VALUES FOR (AS FABRICATED) SPECIMENS

As Fabricated		Hardness (HV 0.5)		
Orientation		X avg	Y avg	Z avg
XYZ	TC1	128.70	132.70	130.00
	TC2	131.00	134.30	137.70
	TC3	133.00	132.00	134.70

TABLE 4 HARDNESS VALUES FOR (HEAT TREATED) SPECIMENS

After T6		Hardness (HV 0.5)		
Orientation		X avg	Y avg	Z avg
XYZ	TC1	84.00	84.10	85.70
	TC2	90.30	91.10	91.70
	TC3	84.70	85.40	86.00

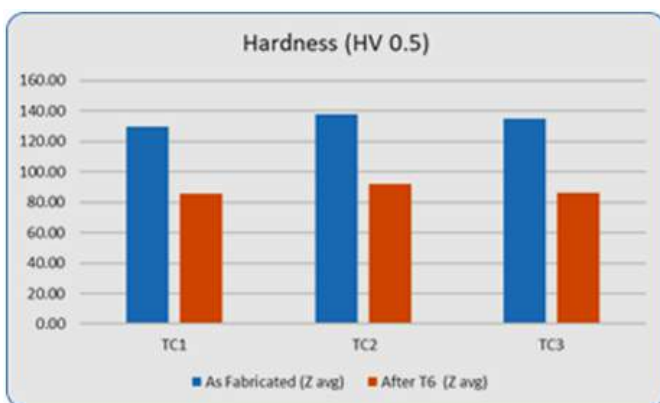


Figure 5: Hardness Values Graphs (Both AF and HT)

C. XRD Analysis

XRD analysis is carried out to investigate the different phases, present in the samples in both “as fabricated” and post “heat treatment” conditions [8]. The XRD analysis are performed on cross sections of polished un-etched samples and there is no specific preparation for XRD, since the size of the “as built specimen” is suitable and can be easily fitted onto the mounting plate available [9]. The XRD patterns of “as-built” sample is depicted in Figure 6. It mainly consists of α -Al and Si phases and the intensity of Si peaks is relatively lower than that of Al peaks. The XRD spectra has not revealed Mg_2Si peak although the alloy has ability to precipitate it. This study reveals that sample is a two-phase material and that Si is not completely dissolved within the Al phase.

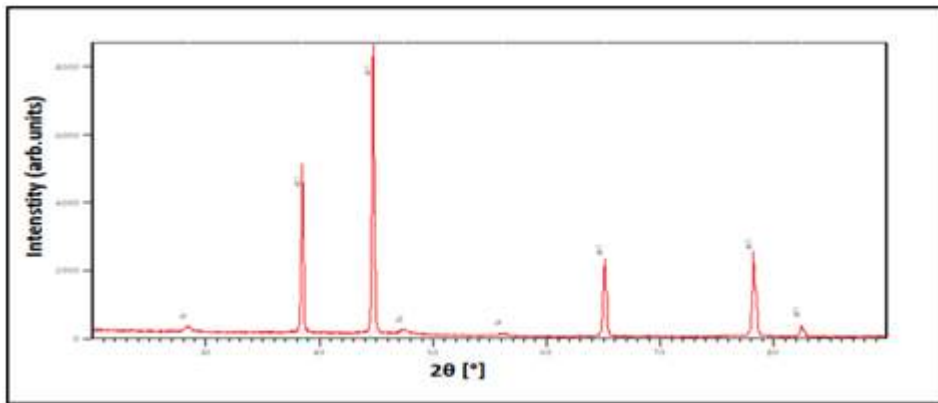


Figure 6: Diffraction pattern of XRD peaks of AlSi10Mg as-built samples

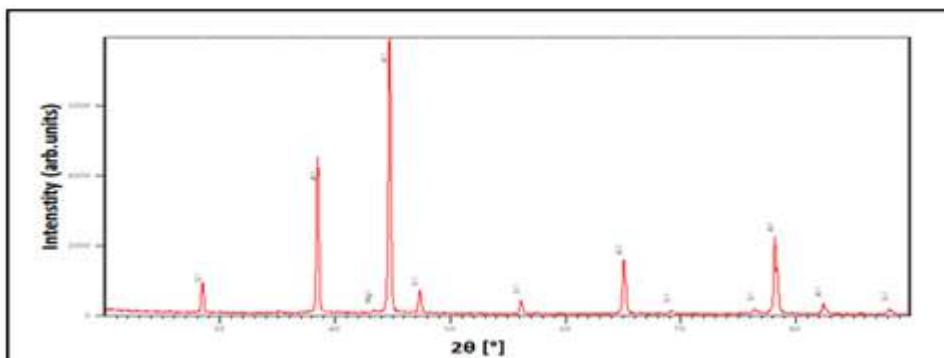


Figure 7: Diffraction pattern of XRD peaks of AlSi10Mg after Heat treated condition

The T6 heat treated sample is subjected to the XRD analysis in order to evaluate the effect of the heat treatment on the microstructure, focusing the attention on the Al, Si and Mg_2Si peaks. The XRD patterns of the heat-treated sample is shown in Figure 7. The breadth of the Si peaks transforms to the peaks as that of α -Al, confirming that crystals are coarsened. The results reveal that the crystallite sizes of Al and Si increases for heat treated samples as compared to the “as fabricated” samples.

IV. SUMMARY AND CONCLUSIONS

The current study focused on the influence of Heat Treatment on the microstructure and Hardness of the “as fabricated” and “Heat treated” AlSi10Mg samples. The key results are as follows:

- In comparison with “as-built” samples, T6 Heat treatment results in a decrease of the hardness by 65%.

- The Post-processing of the samples using T6 Heat treatment creates a homogenous microstructure with Si particles in an Al matrix.
- The T6 Heat treated sample shows the α -Al phase and with coarse dispersed particles of silicon. The Si particles are larger and more widely spaced.
- This study reveals that sample is a two-phase material and that Si is not completely dissolved within the Al phase.
- After Heat treatment the crystallite sizes of Al and Si increased compared to as built samples.

V. REFERENCES

- [1]. ASTM International. (2015). Standard Terminology for Additive Manufacturing – General Principles – Terminology (ISO/ASTM 52900:2015(E)). Online.
- [2]. Louvis, E., Fox, P. and Sutcliffe, J. "Selective laser melting of Aluminium components," *Journal of Materials Processing Technology*, pp. 275–284, 2011.
- [3]. Dadbakhsh S, Hao L, "Effect of Al alloys on selective laser melting behavior and microstructure and mechanical of in situ formed particle reinforced composites", *J Alloy Compd*, pp. 328–334, 2012.
- [4]. Kempen K, Thijs L, Van Humbeeck J, Kruth J-P (2012) Mechanical properties of AlSi10Mg produced by selective laser melting. *Phys Procedia* 39:439–446.
- [5]. Brandl E, Heckenberger U, Holzinger V, Buchbinder D (2012) Additive manufactured AlSi10Mg samples using selective laser melting (SLM): microstructure, high cycle fatigue, and fracture behavior. *Mater Des* 34:159–169.
- [6]. Read N, Wang W, Essa K, Attallah MM (2015) Selective laser melting of AlSi10Mg alloy: process optimization and mechanical properties development. *Mater Des* 65:417–424. <https://doi.org/10.1016/j.matdes.2014.09.044>.
- [7]. Santhosh Nagaraja, Ramesha Kodanda, Khalid Ansari, Mohamed S. Kuruniyan, Asif Afzal, Abdul R. Kaladgi, Navid Aslfattahi, C. A. Saleel, Ashwin C. Gowda, and Praveena Bindiganavile Anand. (2021). "Influence of Heat Treatment and Reinforcements on Tensile Characteristics of Aluminium AA 5083/Silicon Carbide/Fly Ash Composites" *Materials* 14, no. 18: 5261. <https://doi.org/10.3390/ma14185261>.
- [8]. Santhosh Nagaraja, Kempaiah Ujjaini Nagegowda, Anand Kumar V, Sagr Alamri, Asif Afzal, Deepak Thakur, Abdul Razak Kaladgi, Satyam Panchal and Ahamed Saleel C, (2021). "Influence of the Fly Ash Material Inoculants on the Tensile and Impact Characteristics of the Aluminum AA 5083/7.5SiC Composites" *Materials* 14, no. 9: 2452. <https://doi.org/10.3390/ma14092452>.
- [9]. Manjunath Prasad R., U. N. Kempaiah, Santhosh N., (2019). A Review on Metal Additive Manufacturing Techniques and its Applications, *Journal of Polymer & Composites*, 7(3): 24 – 31. <http://engineeringjournals.stmjournals.in/index.php/JoPC/article/view/3413>



IOT Based Industrial Pollution Monitoring and Controlling System

Rajani¹, Lakshmi D L², Hamsashree M K³, Shama Firdose U¹

¹Lecturer, Department of ECE, SJBGS Polytechnic College, BG Nagara, Karnataka, India

²Assistant Professor, Department of ECE, BGS Institute of Technology, Adichunchanagiri University, Karnataka, India

³Assistant Professor, Department of CSE, BGS Institute of Technology, Adichunchanagiri University, Karnataka, India

ABSTRACT

The level of pollution is increasing rapidly due to factors like industries, urbanization and modernization, which effect the human health. The proposed system IOT based industrial pollution monitoring and controlling system is used to monitor and control the air quality and water quality over the web server using the internet of things [IOT]. It will be triggering an alarm called voice Message, when air and water quality goes down below certain level and update data in IOT.

I. INTRODUCTION

The Internet of Things is a vision which is under development and there can be many stake holders in this development depending upon their interests and usage. It is still in nascent stages where everybody is trying to interpret IOT in with respect to their needs. Sensor based data collection, data management, data mining and World Wide Web is involved in the present vision. Of course, sensor-based hardware is also involved. A simple and broad definition of the internet of things and the basic idea of this concept is the pervasive presence around us of a variety of things or objects – such as Radio-Frequency Identification (RFID) tags, sensors, actuators, mobile phones, etc. Fig. 1 has been discussion on three particular visions given by.

They are:

- Things Oriented Vision
- Internet Oriented Vision
- Semantic Oriented Vision

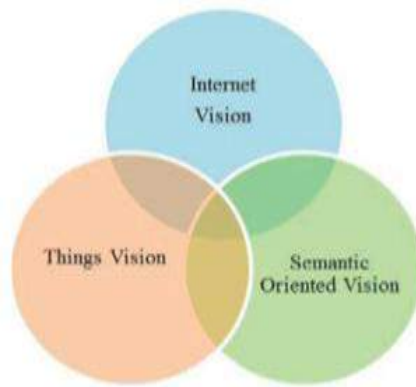


Figure 1 : Three main vision of Internet of things.

II. BLOCK DIAGRAM

The above figure shows that the block diagram of existing system. Here NODE MCU acts as heart of the system. It connects following devices are MQ5 sensors it monitors and detect the H₂, LPG, CH₄, CO. gases. The ODOUR sensor is detecting and monitor the LPG, Alcohol, Propane harmful gases. The PH sensor is detected the water pollution in the industry. And the relay and air filter circuit are used to controlling the air pollution. When the exceed gases released it sensed and automatically turned on. The APR kit and speaker is giving the alert message to the workers and labors in the industry. Here we used 16x2 LCD display for displaying the alert messages. We use cloud for the data storing purpose and monitoring purpose through using IOT and machine learning.

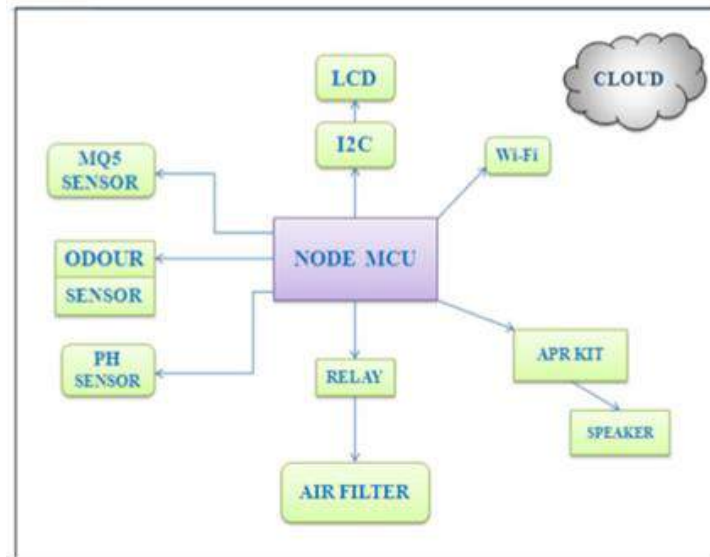


Figure 2 : Block diagram of existing system.

Use case diagram is the primary form of system/software requirements for a new software program underdeveloped. Use cases specify the expected behavior, and not the exact method of making it happen. Use cases once specified can be denoted both textual and visual representation. A key concept of use case modeling

is that it helps us design a system from the end user's perspective. It is an effective technique for communicating system behavior in the user's terms by specifying all externally visible system.

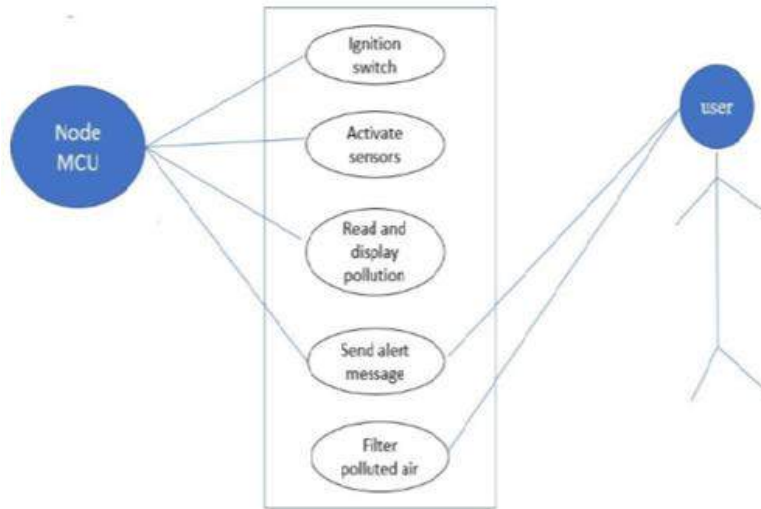


Figure 3 : Use case diagram.

III. FLOWCHART

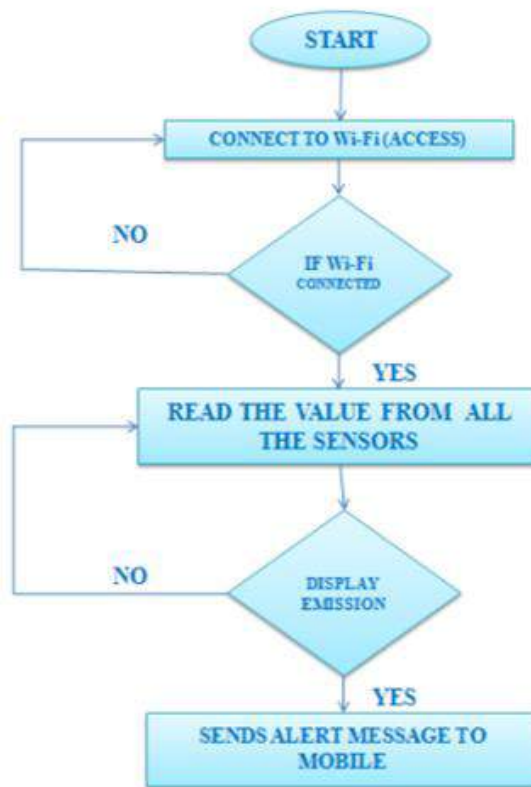


Figure 4 : Flow chart.

A flow chart is a visual representation of the sequence of steps and decisions needed to perform a process. Each step in the sequence is noted within a diagram shape. Steps are linked by connecting lines and directional arrows. This allows anyone to view the flowchart and logically follow the process from beginning to end.

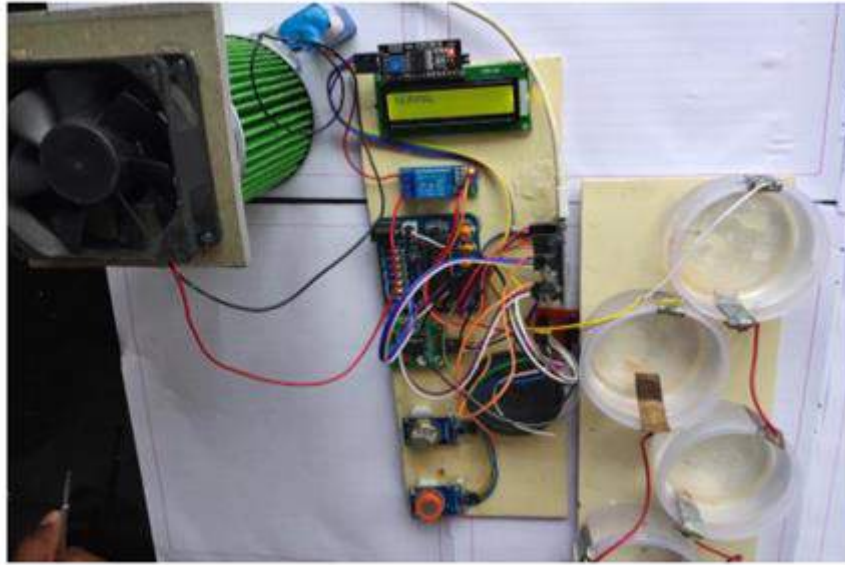
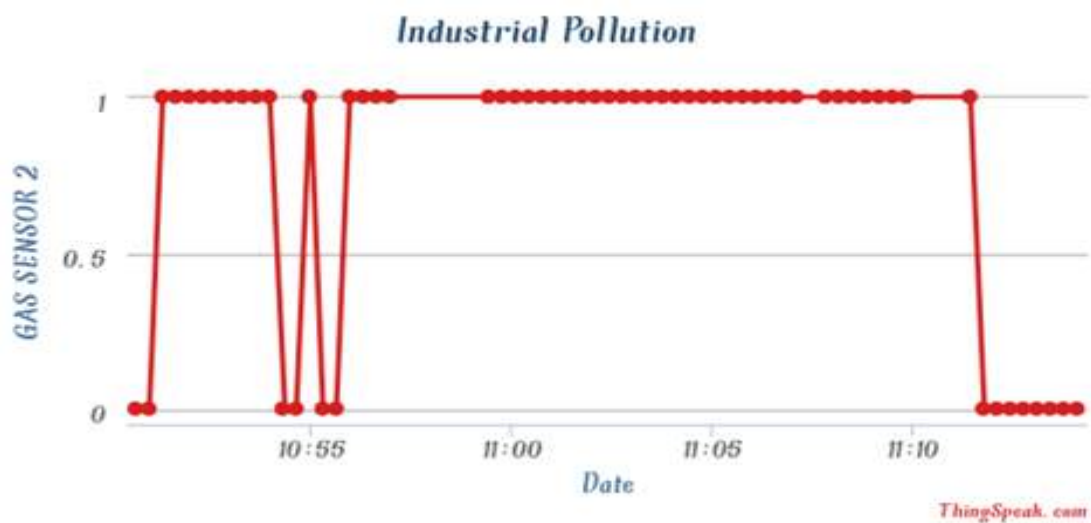


Figure 5 : Circuit connection.

IV. RESULTS



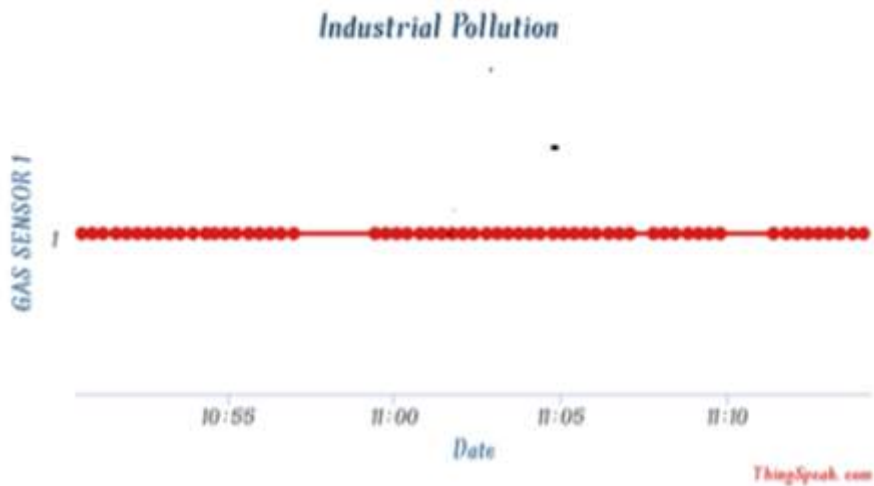


Figure 7 : Monitoring of CO2 gas during the MQ5 will be turned on.

The above figure 7 shows that the monitoring of the co2 using MQ5 sensor. When CO2 gases [Alcohol, CO2] are increased in industry. Then automatically graph will be raised to level low (0). When no gas will be increased in the industry the sensor will be off to level high (1).

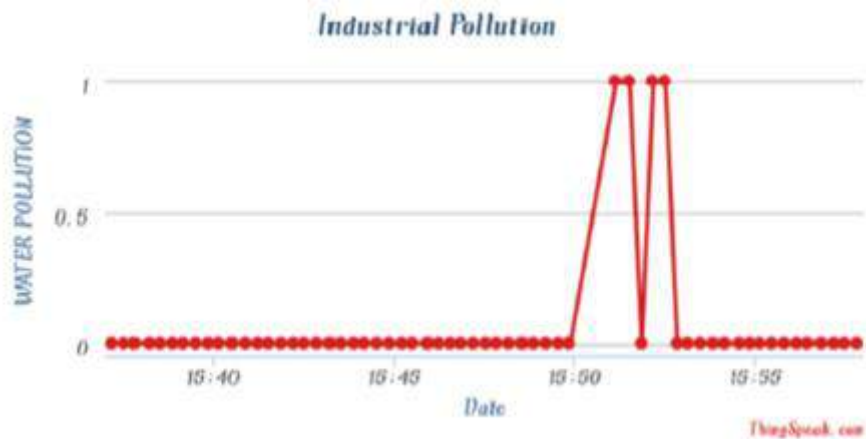
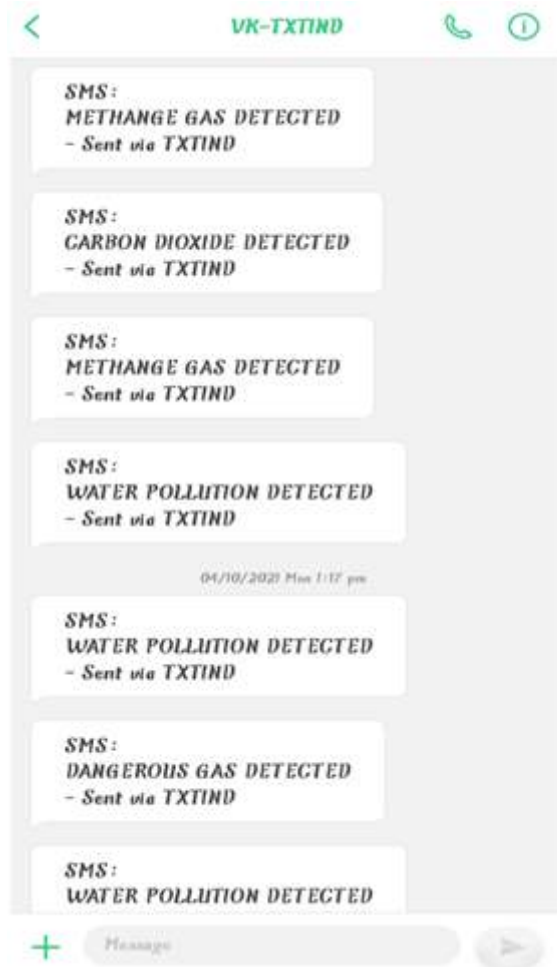


Figure 8: Monitoring of water PH level during the PH sensor will be turned on.

The above figure 8 shows that the monitoring of the Water pollution using PH sensor. When water pollution is occurred in the industry. Then automatically graph will be raised to high (1). In normal condition graph will be low state (0).



ENTRY ID	TIME	MQ2 GAS SENSOR	MQ 5 ODOUR SENSOR	PH SENSOR	IGNITION STATUS
1	2021-10-04 13:19:50 IST	1	0	0	ON
2	2021-10-04 13:22:09 IST	0	1	0	ON
3	2021-10-04 13:24:09 IST	0	0	1	ON
4	2021-10-04 13:27:49 IST	0	0	0	OFF

Applications:

- Industrial perimeter monitory and controlling.
- Hospital perimeter monitory and controlling.
- Indoor air quality monitoring and controlling.
- Public sector monitoring and controlling.

V. CONCLUSION

The system to monitor and control the air and water in industrial area, Technology enhance the process of monitoring and various aspects of environment issues proposed in this paper. Here, using MQ2, MQ5 gas sensors and PH water sensor, since different types of dangerous element in environment. NODE MCU is the heart of project which controls the entire process. WI-FI module connects the whole process to internet to store the value in cloud. And LCD is used for the visual outputs.

I. REFERENCES

- [1]. Li Da Zu” Internet of Things in Industries: A Survey” IEEE Transactions on Industrial Informatics, vol. 10, no. 4, November 2014
- [2]. Geetesh Chaudhari, Sudarshan Jadhav, Sandeep Batule, Sandeep Helkar, “Industrial Automation Using sensing-based application for Internet of Things”, IARJSET, Vol.3, Issue 3, March 2016.
- [3]. Rujiroj Leelaruji et.all, “Power system protective relaying, fundamental concepts, industrial-grade tools, and communication mechanisms”
- [4]. Vilem Srovnal et.all, [1] “Embedded System Design for Health Supervisory Systems”



Effect of Graphene Loading on The Thermal Behaviour of Glass Epoxy Nano Composites

M.S. Aswathnarayan¹, Munirju.M², Reddappa H N³, B M. Rudresh⁴

¹Research scholar VTU Belagavi, Karnataka, India

²Department of Mechanical Engineering, Government Engineering College, Chamrajanagara -571440, Karnataka, India

³Department of Mechanical Engineering, Bangalore Institute of Technology, Bangalore - 560002, Karnataka State, India

⁴Department of Mechanical Engineering, Government Engineering College, K R pet, Karnataka State, India

ABSTRACT

The thermal behavior glass epoxy composites reinforced with nano graphene has been studied. The hybrid fiber reinforcement of glass epoxy with 1wt% and 2wt% of nano graphene. These composites were processed and developed using vacuum bag technique the test results reveal that addition of glass fabric and nano graphene has improved the thermal behaviour of formulated composites the thermal properties such as glass transition temperature, degradation time, degradation temperature recrystallization temperature etc has improved

Keywords: Epoxy, graphene, thermal behavior, vacuum bag method, DSC, TGA.

I. INTRODUCTION

Need for newer materials with improved properties is the present requirement in today's world. The engineers and researchers always in search of materials with enhanced mechanical tribological and thermal properties. Polymer based composites are class of materials which finds their applications in various engineering disciplines like automotive aerospace and electronics industries, the polymer based composites have less structural ability hence they are used as secondary loading members, epoxy is one of the important matrix material used in the fabrication of composites. These matrix materials have lower melting temperature, hence the composites prepared from these matrix degrades when they are exposed to higher temperatures, hence a composite should possess a good thermal behavior, the thermal behavior is evaluated by conducting Differential scanning thermometry(DSC) and thermo gravimetric analysis(TGA).The thermal properties define the suitability of polymer composites to the specific applications, the limitation of polymer composites in structural applications is due to lower melting temperature, therefore, the performance of polymers under different thermal conditions and their weight loss must be critically studied to evaluate the thermal behaviour of polymers. Graphene has excellent thermal properties; the graphene addition improves both the electrical and thermal properties of

epoxy. Karpipal et al. [11] has investigated that the presence of nano clay at 2 wt% in the composites enhanced the glass transition temperature of epoxy nano composites. but higher loading of nano clay in to composite system declined the glass transition temperature Florian H.Gojny et al. [12] evaluated the effect of carbon nano tubes(CNT)on Physical -Mechanical and thermal characteristics of epoxy based composites. They concluded that the thermo mechanical properties of polymer composites (epoxy) is influenced by functionalization of nano fillers and their weight percentage. It is observed that glass transition temperature was increased with increase in wt% of reinforcement. The addition of multi walled carbon nano tube (MWCNT) in to epoxy. This gain in thermal stability can be ascertained to the reduction of mobility of epoxy around carbon nano tubes by interfacial interactions Lico et al.[12] in their investigation on the mechanical and thermal behaviour of Polyamide reinforced amino propyl trimethoxysilane (APTME) and reduced graphene oxide This couple of reinforcement shows better dispersion of fillers. The glass transition and thermal decomposition temperature was increased by 21.7°C and 44°C respectively. Ismadi et al, has investigated the thermal conductivity of graphene reinforced epoxy composites, they compare the same results with the theoretical values using Maxwell model. They found from their research work that the dispersion of graphene into epoxy matrix has improved the thermal conductivity up to 17.5% with 1.5 wt % of graphene content They found that the thermal conductivity, higher stirring speeds break down Vander walls forces and lead to agglomeration of graphene in matrix.

II. MATERIALS, METHODS, PROCESSING AND TESTING OF COMPOSITES

The technical data of the materials used in processing and development of composites is shown in the table 1. The suppliers data used in the development of these epoxy based hybrid composites is detailed in the table 1.

TABLE1: TECHNICAL DATA OF THE MATERIALS USED IN PROCESS

Materials	Designa-tion	Form and size	Density (gm/cc)
Epoxy L-12	EP	Liquid	1.202
Hardener K-6	H	Liquid	1.202
Glass fabric 360 GSM		Fabric	2.58
Graphene		Powder	0.45

The weight fraction formulation of the materials system used for the investigation is shown in the Table 2

A. Processing of Hybrid Epoxy composites

The steps involved in processing and fabricating of composite is as follows

1. Drying of fibers and fillers
2. Cleaning of mould surface
3. Applying relief agent and wax pol
4. Making up plate thickness by placing layers of glass fabric and resin
5. Apply preparatory breeze for vacuum bagging
6. Apply vacuum bagging
7. Place the plates in oven for required period

TABLE2 WEIGHT % OF MATERIALS IN PROCESSING OF COMPOSITES

Material system	Material Id	Weight %	Weight of matrix	Weight of glass fabric	Weight of reinforcement
Neat epoxy	EP	100	100	----	----
Glass epoxy	GE	100	67	33	----
Glass epoxy with 1 wt% graphene	GE1	100	66	33	1
Glass epoxy with 2 wt% graphene	GE2	100	65	33	2

B. Testing of Hybrid Epoxy composites

The thermal properties of glass epoxy hybrid composites have been tested using DSC and TGA setup STM D 256. TGA and DSC tests were carried out according to ASTM E-1131 and ASTM E-1356 standards



Figure1.1: Set up for DSC Test



Figure1.2: Setup for TGA Test

III. RESULTS AND DISCUSSION

The addition of micro and nano fillers improves the thermal behaviour of polymer based composites. The different thermal properties such as glass transition temperature, thermal degradation, re-crystallization temperature, heating and cooling cycle,

A. Differential Scanning Calorimetry:

the DSC is carried out in nitrogen atmosphere at a constant flow rate in given temperature range with a scanning rate of 10°C.min, the samples with weight of 5-10 mg is heated in ceramic pans the Figure 1.3 shows thermo grams for different composites formulated and influence of addition of nano fillers on thermal behaviour is studied. The cross linking structure of epoxy is effected by addition of nano fillers, the endothermic and exothermic peaks exits at around 95°C, 190°C for neat epoxy corresponding to melting and decomposition of epoxy. For epoxy filled with glass fabric shows a clear peaks around 95°C and 130°C corresponding to melting of epoxy and formation of crystals with glass reinforcement, with reinforcement of nano graphene into glass epoxy will decreases the re-crystallization temperature of the glass epoxy system to 85°C. these results are on par with the claims of many researchers [10][6][8]. It is interesting to know that degree of crystallinity in cooling cycles are similar to second heating cycle indicating that most of the crystals are formed during solidification and few crystals are formed during heating cycle, The difference of crystals formed between pure epoxy and glass epoxy filled with nano graphene is due to the lower rate of crystallization in epoxy [10] Increased crystallization rate in nano composites is due to crystallization effect, with the addition of graphene.

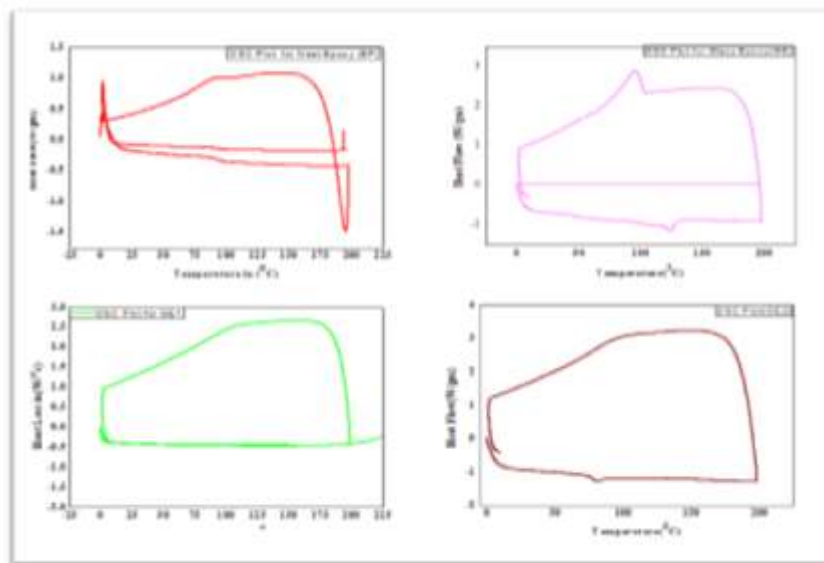


Figure 1.3 Thermo grams for a) Epoxy b) glass epoxy c) glass epoxy filled with 1 wt% graphene d) glass epoxy c) glass epoxy filled with 2 wt% graphene

B. Thermo gravimetric analysis:

Figure 1.4 shows TGA plots for composite/polymeric material with raise in temperature in nitrogen atmosphere. The curves shows two stage weight loss which indicates the same degradation pattern for all composites, the first

weight loss occurs from 300°C to 430°C and second weight loss occurs from 430°C to 580°C. The glass epoxy with 1wt% and 2 wt% graphene shows better degradation rate which shows better thermal stability[12] due to the fact that the graphene addition has affected the cross linking structure of epoxy. In this work 33wt % of glass fiber was used which was tested under nitrogen atmosphere The TGA curves shows addition of glass fiber has improved the initial thermal stability of epoxy composites and graphene decomposes after leaving volatile mixture and residues around 38 wt%

Results of TGA curves for Epoxy and formulated composites under Nitrogen atmosphere shows an onset degradation temperature of 284°C (2% weight loss) for neat epoxy and completely degrades at 600°C with leaving ash content of 2 wt% with wider degradation window(350°C-645°C), the degradation of epoxy and epoxy based composites is shown in Figure1.3(a-d) the thermal degradation has improved with addition of graphene in small wt%, neat epoxy shows an on set temperature of 320°C after complete degradation around 630°C, glass filled epoxy exhibits better thermal stability[13] compared to epoxy with onset temperature 280°C and complete degradation at 630°C with 38% residues glass transition temperature of glass epoxy is 490°C with 1wt% addition of graphene Tg is increased to 520°C, further addition of graphene about 2wt% improves Tg about 535°C after leaving ash content about 38%, the residues in these composites may be due to incomplete burning of glass fiber and other volatilities, further the improvement of thermal stability may be due to shielding effect of graphene flakes there by obstructing the diffusion of volatile decomposition products with in composite.

Table 1.2 TGA temperature at which 10, 20 and 50 % reduction in weight occurs in initial polymer content of nano composites

Sample	T _{10%} (°C)	T _{20%} (°C)	T _{50%} (°C)
EP	352	360	372
GE	360	396	562
GE1	363	407	798
GE2	362	402	594

Neat epoxy shows an onset temperature of 284°C and completely degrades at 600°C and leaves 2 wt% ash content Glass filled epoxy shows onset temperature of 280°C and complete degradation at 630°C with 38% residue due to incomplete burning of fibers and other components further lower and higher loading of graphene will enhance the degradation time of composites, degradation time for epoxy for 1 wt% loss lies between 9.7 minutes to 13.76 minutes, for glass epoxy it lies between 9.7 minutes 14.75 minutes and graphene addition improves the degradation time from 9.7 minutes to 17.87 minutes. Complete degradation of epoxy occurs at 800°C leaving 2wt% residue other systems degrade at same temperature leaving 38% residue.

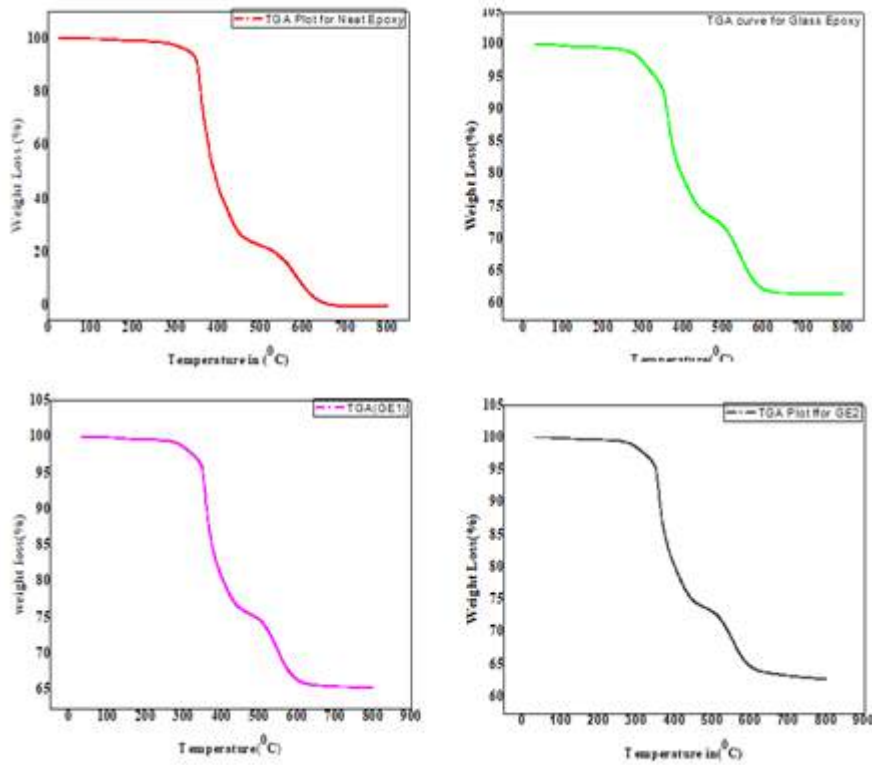


Figure 1.4(a-d) TGA Curves for a) neat epoxy b) glass epoxy c) glass epoxy filled with 1 wt% graphene d) glass epoxy filled with 2 wt% graphene

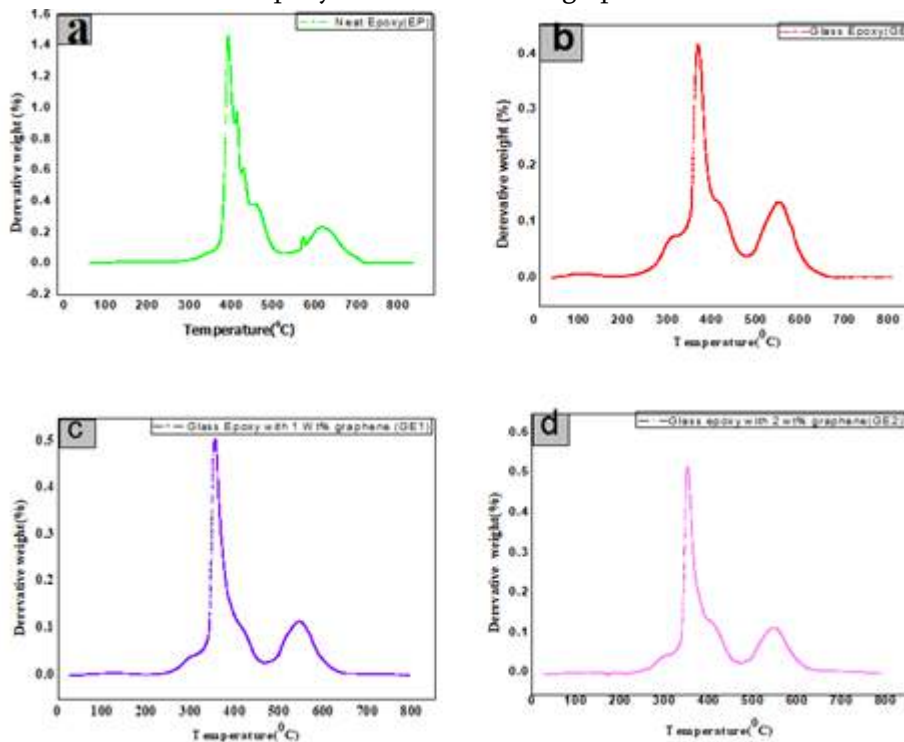


Figure 1.5(a-d) plots for variation of Derivative Weight (%) V/s Temperature in °C a) neat epoxy b) glass epoxy c) glass epoxy filled with 1 wt% graphene d) glass epoxy filled with 2 wt% graphene

IV. CONCLUSION

The influence of loading of both fibers and fillers on the thermal behaviour of epoxy-based hybrid composites was investigated. It is found that the thermal properties have improved with graphene reinforcement.

1. Glass transition temperature of epoxy has increased with addition of graphene nano filler. T_g for GE is 490°C , GE1 it's around 300°C to 430°C and second weight loss occurs from 430°C to 580°C . and for GE2 it is about 535°C
2. The first and second weight loss of glass epoxy is between 300°C to 430°C and 430°C to 580°C , due to addition of glass fabric,
3. the time for 1 wt% loss of Epoxy is 9.7 minutes to 13.76 minutes with addition of glass fabric it increased from 9.7 minute
4. GE1 Composites shows better degradation properties compared to other material systems

V. REFERENCES

- [1]. Hong Ruan, Qui zhang, Weiqiang, Liao, Yuqi Li, Xiaohua Haung, Xu Xu, Shaorong Lu. Enhancing tribological, mechanical and thermal properties of polyamide composites by synergistic effect between graphene and ionic liquid, *Materials and Design* vol 189 (2020).108527
- [2]. Rudresh B.M, Ravikumar B.N and Madhu.D. Synergistic Effect of micro and nano fillers on mechanical and thermal behaviour of Glass hybrid nano composites. *International Journal of Surface Engineering and Interdisciplinary Material Science*, 7(1) (2016), pp. 20-36
- [3]. Rudresh B.M, Ravikumar B.N, and Madhu.D. combined effect of micro and nano fillers on mechanical thermal and morphological behaviour of glass-carbon PA66/PTFE hybrid composite. *Advanced composites and hybrid Materials*. <http://doi.org/10.1007/s42114-019-00089-5>
- [4]. Florian H.Gojny, Karl Schulte. Functionalisation Effect on the thermo-mechanical Behavior of multi wall carbon nanotube/Epoxy composites. *Composite Science and Technology* 64(2004) 2303-2308.
- [5]. S.G.Prolongo, M.R.Gude, A.Urefia, Improving the flexural and Thermo-mechanical properties of amino functionalised carbon nano tube/epoxy composites by using a pre curing treatment, *composite science and technology* 71(2011) 675-771.
- [6]. Weikang Li, Anthony Dichiara, Junwei Zha, Zhongqing Su, Jinbo Bai, An Improvement of mechanical and thermo-mechanical properties of glass fabric/epoxy composites by incorporating CNT-Al₂O₃/hybrids *Composites Science and Technology* 103 (2014) 36-43.
- [7]. Sachin Kumar Chaturvedi, Satendra Kumar. Evaluation of Thermal Properties of E-Glass/Epoxy Composites filled by Different Filler materials. *International Journal of Advances in Engineering & Scientific Research (IJAESR)* vol 1 issue 3(2014).pp 01-07
- [8]. M Wasim Aktar, Yun seon Lee, Dong Jin Yoo, Jong seok Kim, Alumina-Graphene hybrid filled composites: Quantitative Validation and enhanced thermal conductivity, *Composites Part B: Engineering*, vol 131, (2017), pp.184-195.

- [9]. V.Dastuk, S. Trotsenko, G Trakakis,A .Boden,K.Vyzas-Asimakopulos, J.Parthenios, C.Gliotis,S.Reich, K.Papagelis. Thermal properties enhancement of epoxy resins by incorporating polybenzimidazole nanofibers filled with graphene and carbon nanotubes as reinforcing material, Polymer Testing. (2020),vol 82, 106317,
- [10].K.Devendra and T.Rangaswamy Evaluation of Thermal Properties of E-Glass/Epoxy Composites Filled By Diffrent Filler Materials. International Journal of Computational Engineering Research Vol2 issue5 (2012) 1708-1714
- [11]. Karippal.J, NarasimhaMurthy,H.N, Rapi.K.S,Sreejith. M,Krishna.M, Study of mechanical properties of Epoxy/Glass/Nanoclay hybrid composites, Journal of Composite Materials(2011) 45(8) 1893-1899.
- [12].Florian H.Gojny, Karl Schulte. Functionalisation Effect on the themo-mechanical Behavior of multi wall carbon nanotube/Epoxy composites. Composite Science and Technolgy 64(2004) 2303-2308



Effect of Sliding Pressure on Wear Behaviour of Polypropylene Natural Composites

Mahesha A¹, Rudresh B M^{2*}, Reddappa H N³, Madhu D¹

¹Department of Mechanical Engineering, Government Engineering College, Ramanagara, Karnataka, India

^{2*}Department of Mechanical Engineering, Government Engineering College, K R Pet, Karnataka, India

³Department of Mechanical Engineering, Bangalore Institute of Technology, Bangalore, Karnataka, India

ABSTRACT

The influence of sliding pressure on Ramie and Sisal fiber reinforced Polypropylene based hybrid thermoplastic composites were studied. Four Material systems were considered for the investigation: Polypropylene (PP), PP/5 wt. % Ramie fiber/5 wt. % Sisal fiber (PP/10), and PP/10 wt. % Ramie fiber/10 wt. % Sisal fiber (PP/20), PP/15 wt. % Ramie fiber/15 wt. % Sisal fiber (PP/30). These hybrid thermoplastic composites were developed using melt mix method with the help of twin screw extrusion followed by injection molding. The dry sliding wear behavior was studied as an effect of sliding pressure as per ASTM G99 method. The load considered for the experimentation was 25, 50, 75 and 100 N through a sliding distance of 1000 m at a velocity of 0.5 m/s. It was found that PP/30 composites exhibited better sliding wear resistance. The interaction of natural fibers with the hard surface reduced the plastic deformation due to less interfacial temperature. This may lead to exhibit lower frictional effect at the surface. The worn surfaces were studied using SEM images.

Keywords: Research Paper, Technical Writing, Science, Engineering and Technology

I. INTRODUCTION

The role of polymers in modern industry is very important. The light weight and self lubrication of polymers are the credits to their usage in the industrial applications. Further, it is observed that wear of polymer is one of the critical issues in industrial applications. The applications like clutches, brake shoes, liners, sliding valves etc. were subjected to severe wear and fail to resist the application load [1]. Therefore, it is not possible by a homopolymer to support both tribological and mechanical load simultaneously. Due to this, failure of polymers is common. Many research studies suggested that the tribological response of composites can be improved through polymer modification using fillers and or fibers. Further, reinforcing fibers in to polymers has promising results in wear resistance [2]. The hybridization of fibers is the best method for the modification of polymer composites. But the optimum volume fraction of fibers is the issue for the production. Therefore, the best formulations of composites should be designed and their tribological response related to different process parameter has to be reported. High specific modulus and strength are good with fiber reinforced polymers.

Short fibers made of glass (SGF), carbon (SCF), basalt (SBF) and kevlar (SKF) are some of the potential fibers used for the structural applications. Their mechanical and tribological behaviours are very much significant for the structural applications. Many research studies are focusing their attention towards the behaviour of FRPs particularly on thermoplastics. Usage of the synthetic fibers is very common and their processing seems to be tough job. But the use of environment friendly fibers like natural fibers such as sisal fibers, jute fibers, banana fibers, sugarcane fibers are exhibiting their strength in the structural applications. But the critical study is required in their processing and enhancing the resistance of these natural fibre reinforced composites. The processing of natural fibers using epoxy resin was easy, but the reinforcing these natural fibers with the thermoplastic is challenging one.

The mechanical and wear behavior of three different natural fiber composites (NFCs) were analysed BY Venkateshwara Reddy et al [3]. Natural fibers like prosopis juliflora (PJ), abuliton indicum (AI), and tapsi (T) fibers in the form of straws were considered. Composites were fabricated for three different fibers with 20 wt. % by hand layup method. They studied the effect of lsdng load on the waer behaviour of natural composites. Among all the NFCs, prosopis juliflora fiber attained an improved mechanical and wear behaviours when contrasted to the other two NFCs. Yallew et al [4] studied the tribological behaviour of Jute-reinforced polypropylene composites. The effect of Jute fabric reinforcement on the resulting composite's behaviour under friction was investigated. The tribological behaviour was assessed with a computerized pin-on-disc wear and friction tester at an operating dry condition and different working parameters of sliding speed (1–3 m/s), applied load (10–30 N), and sliding distance (1000–3000 m). The results revealed that, the addition of woven Jute fabric into PP matrix increases the wear resistance properties of polypropylene based composites as there was 3.5 - 45% reduction in coefficient of friction values and a decrease by 65% in the specific wear rate on account of incorporation of Jute fabric as reinforcement. Parikh et al [5] studied the tribological characteristics of hybrid natural fiber reinforced composites. They explored the effect of hybrid basalt - banana reinforced epoxy composite and their effectiveness in substituting few conventional materials in terms of their mechanical properties, wear resistance and water absorption rate. The test results reveal that the hybrid basalt banana epoxy composite is a good substitute over various conventional materials. Jia et al [6] worked on carbon reinforced polymer composite in which they studied the comparative wear behaviour of dry sliding and water lubrication. There are marked differences in the response of wear materials when water lubrication was added in the sliding of polymer composites/stainless steel contact. The four polymer composites in this study hold the lowered friction coefficient and showed much better wear resistance under water lubricated sliding against stainless steel than under dry sliding. It could be concluded that the easier of the composite transfer onto the counterpart steel surface accounted for the larger wear rate of the polymer composite under dry sliding, its hindered transfer onto the steel surface and the boundary lubricating action of water accounted for the much smaller wear rate under water lubrication . Goriparthi et al [7] paying attention to improve the adhesion of jute fibre with polylactide (PLA). For this intention, surface of the jute fibre was modified by alkali, permanganate, peroxide and silane treatments. The surface tailored fibres were characterized by FTIR spectroscopy. Unidirectional composites were prepared with treated jute fibres and PLA matrix by hot pressing of solvent impregnated prepregs. Experimental results on abrasive wear tests revealed that the wear resistance of composite is sensitive to fibre/matrix adhesion. Chand et al [8] conducted the study to investigate the abrasive

wear behaviour of jute fibre-reinforced polypropylene composites. Effect of addition of maleic anhydride-grafted polypropylene (MA-g-PP)-coupling agent by two different approach, sliding distance and load on abrasive wear performance of jute fibre-PP composites has been determined by using a SUGA abrasion tester. Use of coupling agent gives better wear resistance as compared to without the use of coupling agent. It has also been found that addition of MA-g PP coupling agent during melt mixing gives better wear resistance as compared to the jute PP composites having MA-g -PP solution-treated jute fibres. Hashmi et al [9] studied for sliding and friction wear behavior at different applied loads and graphite concentrations on the developed graphite modified polyester-cotton composites. With cotton reinforcement specific wear rate of polyester reduced, which further decreased on addition of graphite. In case of cotton reinforcement the coefficient of friction of polyester resin increased and reduced significantly on addition of graphite in cotton-polyester composite. The influence of SGF on mechanical and tribological behavior of Nylon 66/PPS blend was investigated by Chen et al. [10]. The composition of 70/30 vol. % PA66/PPS has been used for the matrix and is loaded with varying percentage of glass fiber. The volumetric loss of blend has been lowered with higher volume of SGF reinforcement. The frictional constant (0.35) of composites was lowered for 20 vol. % of short glass fibers in composites. Influence of SCFs on wear mechanisms of Polyamide 66/ Polyphenylene sulphide blend composites was revealed by Chen et al. [11]. The frictional coefficient of blend declined through rise in content of SCF. The wear rate of PA66/PPS blend has been lowered for a content of SCF less than 30 vol. %. The 30 vol. % SCF in blend exhibits the minimum frictional factor and volumetric loss with 70/30 vol. % PA66/PPS blend. The influence of reinforcement effect of fibers on wear mechanisms of PA66 in rolling – sliding has been reported by Kukureka and others [12]. The short fibers such as aramid fiber, glass fiber and carbon fiber were used for the investigation. It is shown that the aramid fiber is not a good fiber for the frictional factor. Both glass fiber and carbon fiber reduced the frictional constant substantially. The frictional effects and tribological behavior as an effect of applied pressure and speed of some of the engineering polymers such as PA66, POM, UHMWPE, 30% glass fiber filled PPS, 30% SGF filled PA46 and 30% SGF reinforced PPS were studied and results are analyzed [13, 14]. The experimental results revealed that the frictional constant of composite deteriorated with increase in applied pressure. The material removal rate showed very little sensitivity towards the applied pressure. The influence of short carbon fibers loading on mechanical and wear mechanisms of Polyoxymethylene has been reported by Yuquin and Junlong [15]. The frictional constant of pure POM and carbon fiber filled POM composites has been promoted with raise in load and lowered with increase with speed.

The investigation on the role of SCF in improvement of mechanical and tribological mechanisms of SCF filled PA6 studied by Li and Xia [16]. The carbon fiber reinforcement was varied from 0 to 30 vol. %. The composites with 20 vol. % of SCF in PA6 exhibits the least wear rate. The frictional effects and volumetric loss of SCF and Polyamide 6 filled Polypropylene has been studied by Jian and Waiter [17]. The good wear behavior of CF/PP composites have been improved by the reinforcing effect of SCF. The tests were performed up to 20 vol. % SCF. The friction and wear behavior of composites showed an improvement over unfilled polymer. The individual effect of SCF and SGF reinforcement on strength and sliding wear behavior of Nylon 66 composites was reported by Srinath and Gnanamoorthy [18]. The design and improvement of thin transfer film on counter surface is responsible for the enhancement of wear resistance of filled composites. Further, the material

removal rate of SGF/PA 66 composites was the least among the composites studied. Reinforcing Nylon 66 with carbon fiber or SGF decreased the volumetric loss and frictional constant of composites. The frictional and tribological characteristics of SCF loaded PA6 composites has been reported by Nie and Li [19]. The SCF addition into PA6 polymer may result in decreasing or increasing frictional coefficient. The best wear resistance was obtained for 20 vol. % SCF in composite. The influence of sliding speed and pressure on adhesive wear behavior of aramid fiber filled PA1010 composite was studied by Xu et al. [20]. They reinforced PA1010 polymer with 5 to 15% aramid fiber and their tribological behavior was studied. The frictional coefficient of PA1010 polymer found to be reduced as an effect of fiber loading. Further, the addition of aramid fiber decreased the volumetric loss of composites. The best tribo-performance of PA1010/ aramid fiber composites is obtained for 15% of aramid fiber in composite. The wear properties of SGF reinforced PP has been reported by Hufenbach et al. [21]. They revealed that the effect of fiber reinforcement was significantly influenced the adhesive wear behavior of composites. Also, they stated that the wear behavior of composites has been promoted by the loading of glass fibers. The effect of SCF reinforcement on frictional and strength behaviour of PPS/PTFE blend was studied by Luo et al. [22]. The SCF from 0 to 15 vol. % was reinforced into the blend PPS/Teflon and their tribological behaviour was studied. The material removal rate and the frictional constant of the blend reinforced with 15 vol. % CF exhibited 5.2×10^{-6} mm³/ N-m and 0.085 respectively. This is 88% and 47% lower than the neat blend PPS/Teflon. The wear behaviour of fiber- filled polyimide composites has been reported by Zhao and others [23]. Three different fibers are used for the composites. They are SGF, SCF and short aramid fibers. 15 vol.% of each fiber individually was reinforced into PI composites. It was demonstrated that the fiber reinforcement in to PI composites greatly affected the tribological properties. The best performance under test condition was exhibited by inorganic fibers reinforced composites due to the significant sharing of load between the contact surfaces.

From the above literature observations, it is clear that potential of natural fibers in tribology has to be explored. Further, no work has been reported on Ramie fiber. Further, the Sisal fiber proved to be the best fiber in structural applications. On the other hand, the hybrid combination of Ramie- Sisal fiber with Polypropylene thermoplastic is not reported. Keeping this in view, the effect of experimental parameters such as load (Sliding pressure) on the sliding wear behaviour of Ramie –Sisal reinforced Polypropylene hybrid composites have been reported effectively.

II. METHODS AND MATERIAL

The polymer materials and natural fibers used for the development of hybrid natural composites are shown in table 1. The physical data of the materials as supplied are in the same table. The weight fraction formulation of the materials used for the production of composites and their evaluation is shown in the table 2.

TABLE 1. THE SUPPLIER'S DATA OF THE MATERIAL

Material	Designation	Form and Size (µm)	Suppliers	Melting Temperature (0C)	Density (g/cc)
Polypropylene	PP	Granules (10 to 12)	CIPET Mysore	160	0.9
Maleic grafted	MagH	Powder (10 to 12)	GLS Polymers	53	1.5

anhydride			Bangalore		
Ramie fiber	RF	5 to 10 mm	GLS Polymers Bangalore	---	1.5

Material	Designation	Weight fraction percentage			
		PP	MagH	SF	RF
Polypropylene	PP	97	3	---	---
Polypropylene/5 wt.% sisal fiber/ 5 wt.% Ramie fiber	PP/10	87	3	5	5
Polypropylene/20 wt.% sisal fiber / 10 wt.% Ramie fiber	PP/20	77	3	10	10
Polypropylene/15 wt.% sisal fiber / 15 wt.% Ramie fiber	PP/30	67	3	15	15
Sisal fiber	SF	5 to 10 mm	GLS Polymers Bangalore	----	1.5

TABLE 2. WEIGHT FRACTION FORMULATION OF POLYPROPYLENE BASED HYBRID NATURAL COMPOSITES

A. Processing of Composites

The materials used for the process (Table 1 and Table 2) were dried at a temperature 48 °C for about 24 hours to free up them from moisture and plasticizing effects. The materials Polypropylene, Ramie fiber and Sisal fibers were mixed thoroughly using mixer and subjected to melting process through the extruder chamber. The temperature controlled in the zones of heating chamber in the extruder was 220, 230, 245, 260 and 267 °C respectively. The melt mix of composites has been extruded in the cylindrical form through quenching followed by pelletization [11, 12]. These pellets were once again heated in the chamber and then subjected to injection molding process. The injection molding machine produces the specimens as per ASTM method [12]. All the inspected specimens were subjected to testing and defective ones were rejected

B. Testing of Composites

The Pin on disc machine supplied by Ducom Bangalore has been used to conduct the sliding wear experiment as per ASTM G99 method (Fig.1). The samples used for the test were prepared using cutting machine and were cut into proper dimensions prescribed by ASTM. The generally used dimensions as per the standards are 6 mm x 6 mm x 3.2 mm. The prepared specimens were rubbed against smooth abrasives of 600 Grit in order to prepare the perfect sliding surface against the counter steel disc. The samples to be tested were attached to the steel pins of 8 mm diameter with a length of 27 mm. The weight of the specimen is measured before subjecting them to sliding process along with the pin. The counter surface has been cleaned with the help of soft material using acetone before sliding process to ensure no polymer substrate of previous stroke was present. The details of the experimentation and the process parameters used for the test as per ASTM G99 have been depicted in the Table 3.

TABLE 3. EXPERIMENTAL PARAMETERS USED FOR SLIDING WEAR TEST (ASTM G99)

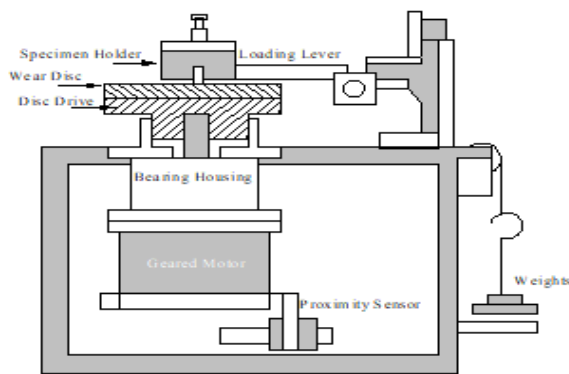
Process Parameters	
Sliding load (N)	25, 50, 75 and 100
Sliding velocity (m/s)	0.5 m/s
Sliding distance (m)	1000

The experimental parameter such as normal load, total travelling distance and velocity of sliding were inputted by setting the time and speed of the disc. When the predefined time is reached, the timer mechanism equipped in the machine stops the machine automatically. The weight of the sample along with the pin after the sliding process has been measured. The experimentation has been conducted for different load, velocity and distance and loss in weight is recorded in every trial. The three samples were tested for the same conditions and the average value of the same is considered to represent the data. The wear volume loss of composites has been obtained through the weight loss (W) using the density d (ρ) which is determined experimentally. The wear volume (ΔV) and specific wear rate (K_s) have been calculated using the wear volume loss from the experimentation. The wear volume loss ' ΔV ' and specific wear rate ' K_s ' polymer composites are calculated using the following formulas:

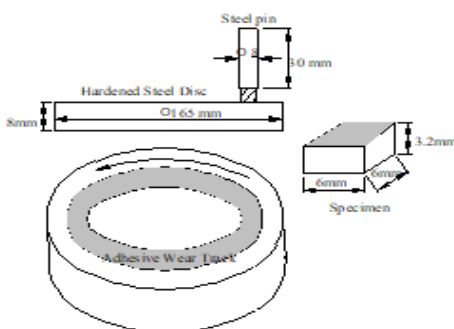
$$\text{Wear volume} = \Delta V = W/\rho \text{ mm}^3 \quad (1)$$

$$\text{Sp. wear rate} = K_s = (\Delta V / (F \cdot D)) \text{ mm}^3/\text{N-m} \quad (2)$$

Where ρ = density in gr/cc, F, the experimentally applied load in N and D, the sliding distance (m)



(a)



(b)

Figure. 1. Sliding wear system for ASTM G99: a) Experimental set up and b) specimen details

III. RESULTS AND DISCUSSION

The tribological response for varying experimental sliding load as a result of hybrid fiber reinforcement effect on volumetric loss of Polypropylene (PP) composites is shown in fig. 2(a - b). The sliding velocity of 0.5 m/s has been maintained for a period of time (33.33 Mins.). The graph demonstrated that the volumetric loss has been promoted with increase in normal load. The tribological behaviour of natural fiber reinforced composites was studied against varying sliding load and also with the dry sliding wear behaviour of Neat PP composites. The highest wear volume loss is experienced by Neat PP among the composites studied. The experimental range of load is 25 N to 100 N. The wear volume loss of neat PP at lower load was 4.7 mm³. As the sliding pressure increases, the wear volume loss is found to increase linearly exhibiting the highest wear volume loss of 9.32 mm³ which is 98% increase. The rise in frictional shear force at the surface interface promoted the higher wear volume loss [11, 12]. The frictional and tribological behaviour of Neat PP was significantly influenced by the capability to form a transfer substrate on the steel counter face [22-23]. During low load conditions, crystalline PP forms a straight, parallel, unvarying and continuous polymer substrate on the counter surface of steel [20].

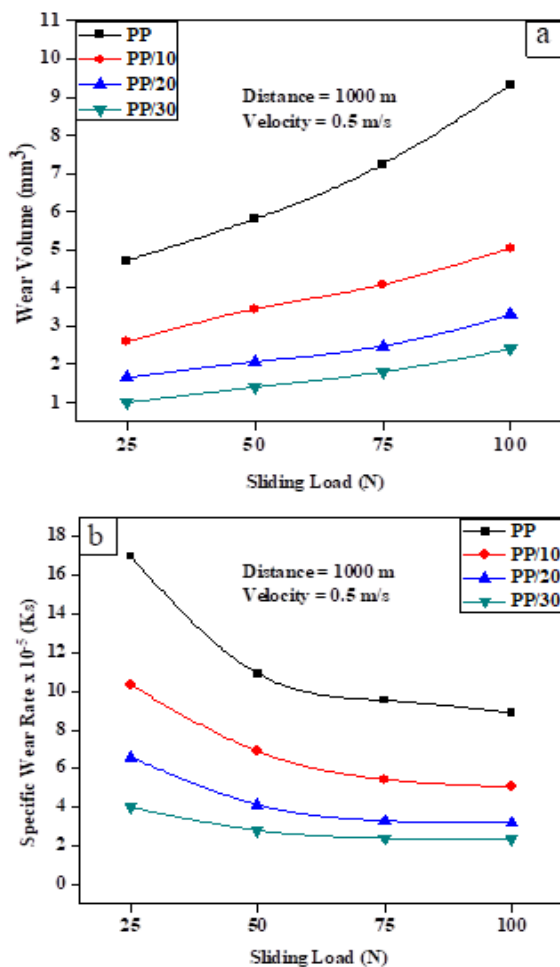


Figure. 2. Effect of sliding load on the sliding wear behaviour of PP natural composites: a) Wear volume and b) specific wear rate

The low shear strength interfacial layer formed by melting PP on sliding surface acts as lubricant [20]. Furthermore, PP is a crystalline polymer which can be easily detachable from the steel surface. Further, this transfer layer disconnects the actual contact of polymer specimen with counter steel surface. This result in friction between surfaces of polymer resulting low wear volume loss. With increase in load, the high frictional shear force breaks the transfer film. In this condition, plastic deformation of PP and its melting occurs due to the generation of heat by the resultant shear and applied force during sliding against steel.

Similar observations were made with PP/10 composites. Here also, increase in wear volume loss as a result of increase in the application of sliding pressure was noticed. From the graph, it is observed that 98% wear volume loss has been exhibited as an effect of PP/10 composites (5 wt. % of each Ramie and Sisal fiber) reinforcement at lower and higher sliding load over the blend. Addition of 10 wt. % of these fibers could effectively resist the sliding load compared to neat PP. During lower load, the fibre filled composites offered resistance against the shearing force. During this process, fiber sliding wear is more prominent than matrix wear [11, 12]. Therefore, less wear volume loss. But at higher load, sliding was accompanied by matrix melting. The combined action of frictional force and sliding load results in rupturing of short fibbers' into fibrils which were bounded by matrix. Hence, more wear volume loss. These 10 wt.% of natural fibers raised the thermal resistance of PP and greatly controlled the promotion of melting wear. At this stage, the exposed fibers supported a part of applied load there by avoiding the entry of steel asperities into polymer surface deteriorating the intensity of micro cutting and micro ploughing actions [12]. High modulus, good mechanical behavior, superior hardness and excellent thermal capacity of fibers defined the wear rate of composites. The superior wear resistance of PP/20 composites has been submitted to addition of more weight fraction of short natural fibers. The wear volume loss at lower load is small as other composites but the significant effect of wear resistance is observed at higher load. As a hybrid effect of friction and normal load, the plastic deformation of PP/20 composites was more due to matrix wear. During this process, fibers will not ruptured by these actions instead sliding of fibers occurs [21]. Therefore, the wear volume loss of composites at higher thermal conditions was controlled by fibers in composites. Therefore, increase in the inclusion of fibres has improved the wear resistance of PP/20 composites. The combined effect of Ramie and Sisal fibers with high weight fraction of 15% each has effectively supported the sliding wear resistance of PP/30 composites. The wear volume loss of 1 mm³ to 2.4 mm³ has been exhibited by these composites during the range of sliding pressure studied. Reinforcement of hybrid fibers significantly enhanced the wear resistance of composites. The increase in wear resistance is due to: i) The surface of natural fibers were rough and they could make good mechanical interlocking with the thermoplastic, ii) The high strength Ramie fiber can sustain the frictional load, iii) The hybridization effect of both the fibers offers good compatibility and also the interfacial bonding strength to uphold the mechanical locking for long time. The investigated results match with others works [11, 12, 21].

The specific wear rate of PP natural composites is show in the figure 2 (b). It is responded from the figure that the specific wear rate, K_s , of composite studied tends to decrease with increase in applied sliding pressure. This is due to increase in frictional force due to abrasivity of the surface as and when the natural fibers worn out during interaction. The hard natural fibers tends to offer good resistance against the thermal softening of the matrix which may lead to size the fibers resulting less wear volume loss per sliding load. The over breakage of these fibers they themselves acts as abrasives to resist against the sliding load offered by external pressure. It is

observed that the K_s of the composite studied was in the range of 16.98×10^{-5} to 8.89×10^{-5} , 10.32×10^{-5} to 5.05×10^{-5} , 6.59×10^{-5} to 3.2×10^{-5} and 4.01×10^{-5} to 2.34×10^{-5} $\text{mm}^3/\text{N}\cdot\text{m}$ respectively of PP, PP/10, PP/20 and PP/30 composites.

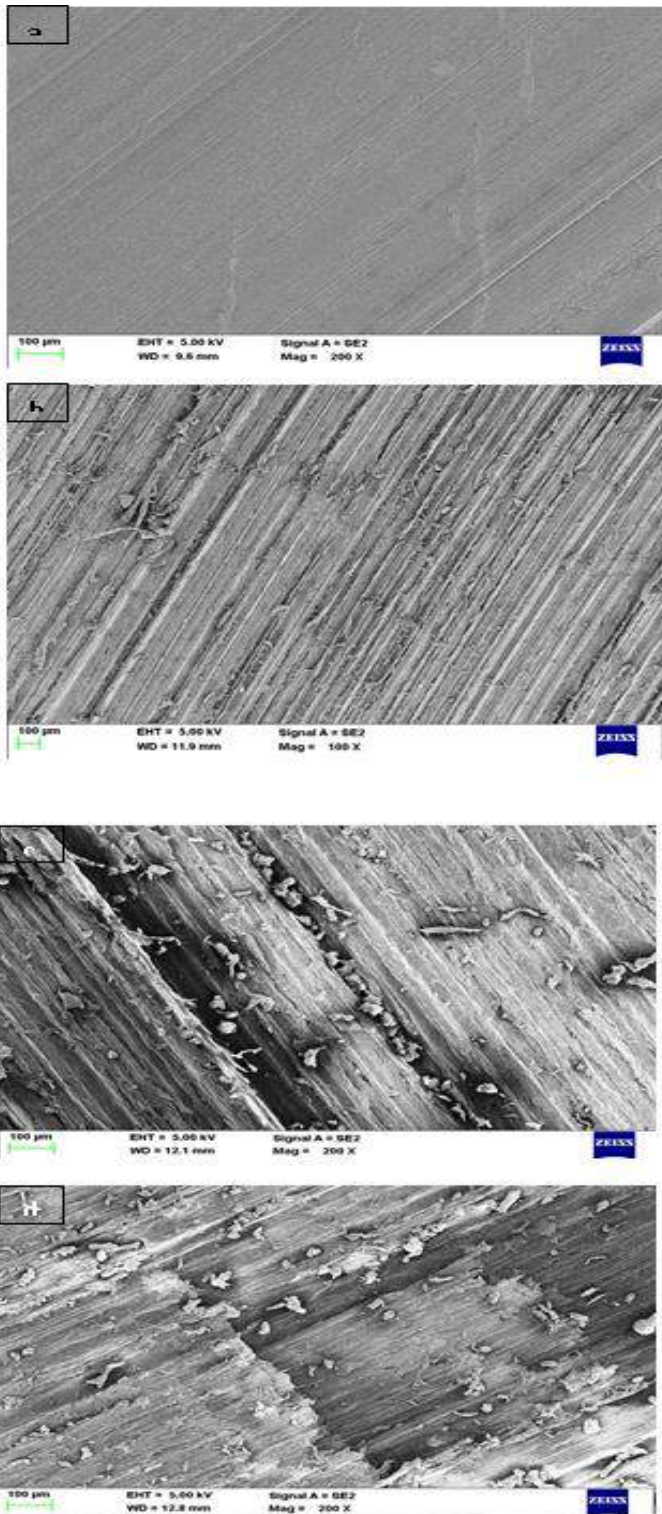


Figure.3. SEM images of PP natural composites under the action of higher sliding pressure of 100 N : a) Neat PP, b) PP/10 composites, c) PP/20 composites and d) PP/30 composites

Figure 3 (a – d) shows the SEM images of the worn surfaces of PP natural composites under the action of higher sliding pressure of 100 N. Figure 3(a) exhibits the worn surface of Neat PP composites under severe sliding pressure. Basically, PP is semicrystalline in nature. Due to sliding action, the smooth and varying surface is shown in the figure. This shows the slight plastic deformation has been exhibited by the worn surface. Further, figure 3(b) indicates the slight uniform wear tracks parallel to each other. This may due to nature of natural fibers. At higher pressure, these hybrid fibers which were not uniform rub against the hard surface resulting in heavy shear. But the detaching of fibers from the specimen surface is very less in figure. This indicates less wear volume loss than neat PP. Similar observation was noticed in the figure 3(c) and 3(d) respectively. It is concluded from both the figure that adhesion was good between fibres and matrix surface. The interface strength across the interaction of fibers and matrix is seemed to be good. This has avoided the pull out of fibers from the surface. Further, the severe matrix surmounts the fibers which may lead to matrix wear rather than fibers. This tends to decline the wear volume loss of PP/20 and PP/30 composites respectively.

IV. CONCLUSION

The effect of varying sliding pressure on the dry sliding wear behaviour of PP natural composites was studied. Further, the effect of hybrid fibers in equal proportions was also explored to study the potential of natural fibers (Ramie and Sisal fibers) to wear behaviour of natural composites. It is observed that the wear volume loss of composites increases linearly with increase in sliding pressure. The specific wear rate of composite decreases with increase in sliding pressure. Neat Polypropylene exhibited the least wear resistance whereas PP/30 composites found to be the best wear resistance material among the composites studied. This may due to the excellent thermal adhesion of natural fibers with matrix PP. Plastic deformation, thermal adhesion and fiber wear were some of the mechanisms observed. PP/10 and PP/20 exhibited the better wear resistance than neat PP comparatively lesser wear resistance than PP/30 composites. The study indicates that higher volume fraction, good adhesion and excellent mechanical properties of both matrix and fibers enhanced the wear resistance.

V. REFERENCES

- [1]. Y Yamaguchi, Tribology of plastic material(1990), Tribology series16, Elsevier, New york
- [2]. N V Klaas , K Marcus, C Kellock , 2005, The tribological behavior of glass filled polytetrafluoroethylene, Tribology international , 38, 824-833
- [3]. P. Venkateshwar Reddy, R. V. Saikumar Reddy, P. Rajendra Prasad, D. Mohana Krishnudu, R. Meenakshi Reddy, H. Raghavendra Rao, 2020, Evaluation of Mechanical and Wear Performances of Natural Fiber Reinforced Epoxy Composites, Journal of Natural fibers, 21, 52-58
- [4]. Temesgen Berhanu Yallewa , Pradeep Kumara , Inderdeep Singh,2014, Sliding Wear Properties of Jute Fabric Reinforced Polypropylene Composites, Procedia Engineering 97, 402 – 411
- [5]. Hiral H. Parikh, Harshit P. Soni , Deval A. Suthar and Dhruv H. Patel, 2019, Mechanical and Tribological characterization of Hybrid Natural Fiber Reinforced Composites, 12 (2), DOI: 10.2174/1874464812666190919091045

- [6]. J. Jia, J. Chen, H. Zhou, L. Hu, L. Chen, 2005, Comparative investigation on the wear and transfer behaviours of carbon fibre reinforced polymer composites under dry sliding and water lubrication, *Composites Science and Technology*, 65, 1139– 1147
- [7]. B. K. Goriparthi, K.N.S. S. N. M. Rao, “Effect of fibre surface treatments on mechanical and abrasive wear performance of polylactide/jute composites” *Composites: Part A*, 43 (2012) 1800–1808
- [8]. N. Chand, U. K. Dwivedi, “Effect of coupling agent on abrasive wear behaviour of chopped jute fibre-reinforced polypropylene composites” *Wear*(2006)10571063.
- [9]. S. A. R. Hashmi, U. K. Dwivedi, N. Chand, “Graphite modified cotton fibre reinforced polyester composites under sliding wear conditions” *Wear*, 262 (2007) 1426 –1432.
- [10]. Zhaobin Chen, Xujun Liu, Renguo Lu and Tongsheng Li, (2006) Mechanical and tribological properties of PA66/PPS blend - III reinforced with glass fiber, *Journal of Applied Polymer Science*, vol. 102, pp. 523-529, 2006
- [11]. Zhaobin Chen, Xujun Liu, Renguo Lu and Tongsheng Li, (2007), Mechanical and tribological properties of PA66/PPS blend reinforced with carbon fiber, *Journal of Applied Polymer Science*, vol. 105, pp. 602-608, 2007
- [12]. S. N. Kukureka, C. J. Hooke, M. Rao, P. Liao, Y. K. Chen, (1999) The effect of fiber reinforcement on the friction and wear of polyamide 66 under dry rolling – sliding contact, *Tribology International*, vol. 32, pp. 107-116
- [13]. H. Unal, U. Sen and A. Mimaroglu, (2004) Dry sliding wear characteristics of some industrial polymers against steel counter face, *Tribology International*, vol. 37, pp. 727-732
- [14]. A. Mimaroglu, H. Unal, A. Oztel, N. Filiz, K. Ozkan, C. Karadeniz and I. Kayo, (2008), Friction and wear behavior of engineering polymers against polymer, 2nd international conference on advanced tribology, iCAT, pp. 103-105
- [15]. Tian Yuqin and Huo Junlong, (2012), The mechanical and tribological properties of carbon fiber reinforced POM composites, *Applied Mechanics and Materials*, vol. 182-183, pp. 135-138,
- [16]. J. Li and Y.C. Xia, (2009), The reinforcement effect of carbon fiber on the friction and wear properties of carbon fiber reinforced PA6 composites, *Fibers and Polymers*, vol.10 (4), pp. 519-525
- [17]. Li Jian and Sharon Kao-Walter, (2010) The friction and wear properties of polypropylene composite filled with carbon fiber and polyamide 6, *Journal of Thermoplastic Composites*, vol.10, pp. 1-8,
- [18]. G. Srinath and Gnanamoorthy, (2005), Effect of short fiber reinforcement on the friction and wear behavior of Nylon 66, *Applied Composite Materials*, vol.12, pp.369-383
- [19]. W.Z. Nie and J. Li, (2010), Effect of carbon fiber content on friction and wear properties of carbon fiber reinforced PA6 composites, *Plastics, Rubber and Composites*, vol.39 (1), pp.10-15
- [20]. Lei Xu, Zhencai Zhu, Guoan Chen and Chao Qu, (2010) Effect of load and sliding velocity on tribological behaviors of aramid fiber reinforced PA1010 composites, *Industrial Lubrication Tribology*, vol. 62(1), pp. 46-51
- [21]. Werner A. Hufenbach, Alesksander Stelmakh, Klus Kunze, Robert Bohm and Robert Kupfer, (2012), Tribo-mechanical properties of glass fiber reinforced polypropylene composites, *Tribology International*, vol. 49, pp.8-16

- [22].Wei Luo, Qi Liu, Yi Li, Shengtai Zhou, Huawei Zou and Mei Liang, (2016)Enhanced mechanical and tribological properties in polyphenylenesulfide /polytetrafluroethylene composites reinforced by short carbon fiber, Composites: Part B, vol. 91, pp. 579-588
- [23].Gia Zhao, Irina Hussainova, Maksim Antonov, Qihua Wang and Tingmei Wang, (2013), Friction and wear of fiber reinforced polyimide composites, Wear, vol.301, pp. 122-129,



3D Design Model of Miniature Sugarcane Harvesting Machine

Irappa Hunagund¹, Sadananda Megeri², Deepak S Gasthi³, Kiran R P³, Bharath B M³

¹Assistant Professor, Department of Mechanical Engineering, Government Engineering College Ramanagar,
Ramanagar- 562159, Karnataka, India

²Assistant Professor, Department of Mechanical Engineering, Government Engineering College Ramanagar,
Ramanagar- 562159, Karnataka, India

³Under Graduate Students, Department of Mechanical Engineering, Government Engineering College
Ramanagar, Ramanagar- 562159, Karnataka, India

ABSTRACT

Agriculture is the backbone of human society. In India, most of the farmers face problems of labour shortage. Sugarcane is one of the labour-intensive agriculture products. Presently there is a huge demand for agriculture labours and because of this, the wages of the labour are very high. The Labour cost is the major cost in the production of sugarcane. This project aims to design and develop a 3D design model of a sugarcane harvesting machine to reduce farmers' effort. The proposed machine model has the capacity to cut canes at a faster rate compared to manual harvesting. This machine is economically viable for small and big farmers.

Keywords: Sugarcane, Mechanization, Model, Harvesting machine

I. INTRODUCTION

Nowadays agriculture is facing serious challenges like scarcity of agricultural labour, not only in peak working seasons but also in normal times. This is mainly for increased nonfarm job opportunities having a higher wage, migration of labour force to cities, and low status of agriculture labors in the society. Sugarcane is the world's largest crop 2010 Food Agricultural Organization (FAO) estimates it was cultivated on about 23.8 million hectares in more than 90 countries, with a worldwide harvest of 1.69 billion tons. India is the largest producer of sugarcane in the world and Brazil in the second position.

Sugarcane harvesting is agricultural machinery used to harvest and process sugarcane. Sugar cane is a hardy crop that is cultivated in tropical and sub-tropical regions for its sucrose content and by-products such as molasses and bagasse (the waste fibrous residue). The plant grows in clumps of cylindrical stalks measuring from 1.25 to 7.25 cm in diameter and reaching 6 to 7 m in height. The cane stalks grow straight upward until the stalk becomes too heavy to hold itself up. It then lies on its side and continues to grow upward. This results in a mature cane field lying on top of itself in a mesh pattern.

There are two main methods of sugarcane harvesting

1. Sugarcane harvesting by manual
2. Mechanical harvesting by sugarcane harvester

1. Manual Harvesting:

In manual harvesting, Sugarcane is harvested mostly by Hand knives, cutting blades or hand axes are used for manual harvesting. In manual harvesting, workers usually become fatigued after manually cutting the cane for a few hours. They need frequent pauses for rest, and they experience sustained injuries from excessive stress on the joints and muscles of the body. The cutting tool and motion involved directly influence the stresses created. A cutting tool that has not been designed by taking into consideration occupational biomechanics can lead to unnecessary strains in the body's muscle system, resulting in injuries. Manual harvesting skilled labors as the improper harvest of cane lead to loss of cane and sugar yield, poor juice quality, and problems in milling due to extraneous matter. Hand harvesting accounts for more than half of production and is dominant in the developing world. In hand harvesting, the field is first set on fire. The fire burns dry leaves, and kills any lurking venomous snakes, without harming the stalks and roots. Harvesters then cut the cane just above ground level using cane knives or machetes. A skilled harvester can cut 500 kilograms (1,100 lb) of sugarcane per hour. But manually sugarcane harvesting is more labour intensive and as compare to machine harvesting the cutting speed is very slow. Steps to be taken in Cut and Windrow methods. Some of the merits of manual harvesting are Low cost, Low soil compaction, Low damage to cane roots mostly for use in relatively large cane fields.

2. Mechanical harvesting

The various factors that cause sugar cane harvesting done mechanically are Difficulties in obtaining sugar cane cutters. Labor can only work for 8 hours during the day while the sugar cane harvesting machine can work for 24 hours. The capacity of sugarcane harvesting machines is much greater than manual cane cutting. The maximum time for sugarcane harvest is relatively short, especially in areas with limited manpower, will be able to resolve the harvest activities at a given time, so that losses can be reduced.

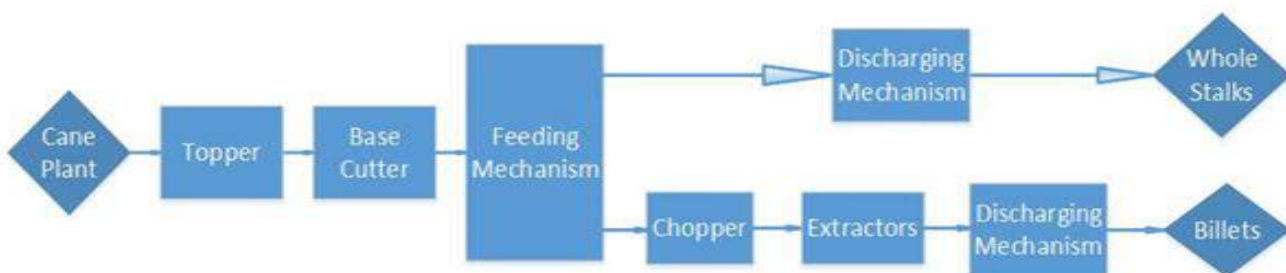


Figure 1. Cane flow in typical sugarcane whole stalk harvesters and chopper harvesters.

Mechanical harvesting of sugar cane can be done in two ways:

Whole stalk Harvester: In this process, the cutting of the sugar cane is done at the base of the stem near the soil surface. Then sugar cane is brought back and arranged into a windrow for subsequent loading.

Chopper Harvester: In this process, the sugar cane is cut at the base and then it is fed into the harvester where the cane is cut again into shorter pieces called billets with a size 20-40 cm. Each cane harvester has some

advantages and disadvantages. Harvesting using a Chopper Harvester will be more profitable than whole stalk Harvester under certain conditions. Figure 1 gives the cane flow chart for the whole stack and chopper harvesters.

Some of the limitations of large scale sugar cane harvesting machines are soil compaction, High initial cost i.e. Rent of this machine is also not affordable in small farmers, High operating cost, Area required is more for application i.e. it requires more space at starting of cutting and also it doesn't work in a small area of the farm, Size of the machine is very big.

In the present work, the 3D model design of the miniature machine is carried out to meet the following criteria:

1. The machine should cut the sugarcane stem at ground level. It is the basic need of cutting as the sugar content in the cane is more at its base.
2. The cane must be cut quickly and very sharply.
3. The eye should remain below ground level and it should operate without damage to the blade.
4. The cane should not squeeze while it is being cut.
5. The cost of a machine should be such that it should be affordable to a middle-class farmer.
6. Space occupied by the machine should not be too large.
7. The machine should have optimum weight so that a single man can operate it very easily.

The paper is organized as follows: in Section 2, gives the literature review; in Section 3, 3D design parameters for developing presented; in Section 4, 3D models are developed in the software; and finally in Section 5, the conclusions of this study are drawn.

II. LITERATURE REVIEW

Salass and Champagne [1] developed a spreadsheet-based cost model for sugarcane harvesting systems. The model is capable of estimating equipment requirements and costs for one-row and two-row wholestalk sugarcane harvesters as well as for combine, or billet, sugarcane harvesters. Costs of hauling harvested sugarcane to mills are estimated for both direct haul systems (tractor and wagons) and transfer haul systems (trucks and trailers). Ma et al. [2] presented the overview of sugarcane harvester technology. Authors gave insights of various harvesting practices such as burnt cane harvesting and green cane harvesting. Authors also presented the two harvesting modes i.e., whole stalk harvesting and chopper harvesting. Also reviewed the two core technologies of a sugarcane harvester, cutting, and feeding mechanisms. Shelke et al. [3] presented the design of a sugarcane harvesting machine. This research was carried out to determine the effect of loading rate and internode position on shearing characteristics of the sugar cane stalk. The experiments were conducted at three loading rates of 5, 10, and 15 mm min⁻¹ and at ten internode positions down from the flower. Siddaling and Ravaikiran [4] presented the design and fabrication of small-scale Sugarcane harvesting machine. Santoro et al. [5] presented the route optimization technique in mechanized sugarcane harvesting. This optimization technique help to reduce the costs. The work proposes a mathematical model to the Route Planning Problem for Mechanized Harvesting. This mathematical model minimizes the time of maneuvering the harvesting machine and, consequently, reduces fuel and labor costs, among others. Authors

performed the computer tests using data supplied by a company from the sugarcane energy sector located in the state of São Paulo, Brazil. Corredo et al [6] acquired data, such as yield, losses, and quality that would provide valuable information for site-specific management of sugarcane. This research work describes the current instrumentation used by sugarcane harvesters to map yield with the current technologies that have the highest potential applications for losses and quality mapping. The authors provide some information regarding the automation of the machines and the operational improvements, such as logistics planning and machine performance. Inkane et al. [7] presented a design calculation of a solar power operated sugarcane harvesting machine. Aliano Filho et al. [8] proposed a bi-objective mathematical model for integrated planning of sugarcane harvesting and transport operations. Authors addresses the integrated planning of harvesting and transport operations over a multi-period planning horizon. In this research authors developed a tactical plan for the deployment of harvesting and transport equipment that sets the periods for the execution of the harvesting operations on the sugarcane fields and the type of harvesting machines and road haulage vehicles to be operated.

This paper contributes to the literature by proposing a 3D Design Model of Miniature Sugarcane Harvesting Machine for Mechanized Harvesting with aiming to minimize the harvesting time reduce the fuel and labour costs.

III. DESIGN PARAMETERS FOR MODEL DEVELOPING

In this section, the various design data required for the development of the miniature sugar cane model is established and the details of these design data are as under.

Force required for cutting the sugar cane by shearing

Shearing strength of sugarcane: 3.03 to 4.43 MPa (AVG 3.64 MPa)

Area of sugarcane stalk cutting at a time = Diameter of stalk \times length of serration

$$= 40\text{mm} \times 1\text{mm}$$

$$= 40 \text{ mm}^2$$

Shearing force required = Shear strength \times Cutting area

$$= 4.43 \times 40 \text{ (Taking maximum shear strength)}$$

$$= 177\text{N}$$

Power required to cut the sugarcane

The optimal combination of parameters was: blade cutting velocity of 13.8 m/s, oblique

The angle of $\sim 35^\circ$ and disc tilt angle of $\sim 27^\circ$.

Diameter of Cutting Disc = 200mm

Optimal rpm for cutting sugarcane = Blade cutting velocity $\times 60 / \text{Radius} \times 2\pi$

Optimal rpm for cutting sugarcane = Blade cutting velocity $\times 60 / \text{Radius} \times 2\pi$

$$13.5 \times 60 / 0.1 \times 2 \times 3.14$$

$$= 1318.47 \sim 1320 \text{ rpm}$$

= Cutting Force \times Radius $\times 2\pi N / 60$

$$= 172 \times 0.1 \times 2\pi \times 1320 / 60$$

= 2376.35 ~2380W

Engine power

15 hp diesel engine is used for both driving system and sugar cane cutting mechanism

- Diesel engine provides high torque and high load-carrying capacity which satisfy the objectives of the machine design.
- The designed power capacity for the machine is 15 HP.
- The designed engine speed is 2300rpm Single cylinder.

Gear Box :

- Gear box is used to vary or manipulate the speed of the engine.
- The gearbox is connected between engine and drive shaft and transmit the desired rpm to the drive shaft.
- Helical gear box is used

Drive Shaft :

- Driveshaft is one of the main component of the driving mechanism.
- Driveshaft receives the desired rotational motion from the gearbox and transmits it to the wheels which eventually moves the vehicle.
- The designed material for the fabrication of the shaft is SM45C.

Driver Cabin :

- Drivers cabin provides comfort and controlling access to the driver.
- All the components control unit is provided inside the driver's cabin.
- The desired and objectified operations will be controlled by the driver inside the cabin.

Other Components:

● **Steering :**

Steering is used to provide Particular direction to the machine. Our machine is designed to have mechanical steering.

Steering used is mechanical type (rack and pinion type)

● **Braking System:**

Braking system is used to reduce the speed or either to stop the machine,.

- The braking action is carried out by pressing the brake peddle which transmits this power to the brake pads.
- Brakes used is hydraulic brake

● **Cooling System:**

The machine is designed with water cooling system which removes the heat from the engine and other components.

A. Design of V Belt:

Rated power of Engine, $P_R = 6.25 \text{ HP} = 4.6 \text{ kw}$

Speed of Engine, $N_1 = 5500 \text{ rpm}$

Design Power $P_D = P_R * K_1$

$K_1 = \text{loading factor} = 1.45$

$P_D = 6.67 \text{ kw}$

Now select designation from design power,

Designation is 'B'

From this we can get

$D_1 = \text{diameter of smaller pulley} = 135 \text{ mm}$

$W = 17 \text{ mm}$, $t = 11 \text{ mm}$, centrifugal tension factor $K_c = 4.34$

Pitch line velocity $= v_p = \frac{\pi D N}{60 * 1000}$, m/s

$= 2332.63 \text{ m/min} = 38.87 \text{ m/s}$

Assume V.R. = 2:1

Therefore $D_2 = 270 \text{ mm}$

$N_2 = 2750 \text{ rpm}$

Various tension acting

$$F_1 - F_2 = \frac{P_d}{v_p} = 171.6 \text{ N} \dots\dots\dots(a)$$

$$F_1 / F_2 = e^{\mu \theta \operatorname{cosec}(\frac{\alpha}{2})}$$

$\mu = \text{friction of coef.} = 0.3$

$$\theta = \pi \pm \frac{D_2 - D_1}{C} \text{ approx.}$$

$\alpha = \text{groove angle} = 38^\circ$

$C = \text{centre distance in mm}$

$$C = D_1 + D_2 = 405 \text{ mm}$$

$$\theta = 2.8$$

Therefore,

$$F_1 / F_2 = 13.2 \text{ N} \dots\dots\dots(b)$$

From (a) and (b)

$$F_1 = 185.665 \text{ N}$$

$$F_2 = 14.065 \text{ N}$$

$$\text{Power Rating per Belt} = (F_w - F_c) \frac{e^{\mu \theta \operatorname{cosec}(\frac{\alpha}{2})} - 1}{e^{\mu \theta \operatorname{cosec}(\frac{\alpha}{2})}} * V_p$$

$$F_w = w^2 = \text{working load} = 289 \text{ N}$$

$$F_c = k_c (V_p / 5)^2 = 262.288 \text{ N}$$

$$\text{Power Rating per Belt} = 959.63 \text{ W / Belt}$$

$$\text{No. of Belts} = P_D / \text{Power Rating per Belt}$$

$$= 6.95 = 7 \text{ belts}$$

$$L_p = 14 \text{ mm}, b = 4.2 \text{ mm}, h = 10.8 \text{ mm}, e = 19 \text{ mm}, f = 12.9 \text{ mm}$$

$$\text{Width of pulley rim} = L_p = (\text{no. of belts} - 1) * e + 2f = 139.8 \text{ mm}$$

$$\text{Length of Belt} = \frac{\pi(D_1 + D_2)}{2} + 2C + (D_1 - D_2)^2 / 4C$$

$$L = 1457.42 \text{ mm} = 1.457 \text{ m}$$

Design of larger pulley,

$D_2 = 270$ mm
 Arm construction
 No. of arms = 4 , no. of sets = 1
 Face width = $W = 1.1 * b = 4.62$ mm

B. Design of Shaft:

Design Torque, N-m
 $T_d = (60 P * K_1) / 2\pi N$
 And we also have
 $T_d = \pi / 16 * d^3 * \tau_{max}$
 Where, d = diameter of shaft
 τ_{max} = maximum shear stress = $< 0.18 S_{ut}$ or $< 0.3 S_{yt}$
 Selecting material I.S. C-30 (SAE 1030)
 S_{ut} = ultimate stress = 527 Mpa
 S_{yt} = yield strength = 296 Mpa
 From this we get
 $\tau_{max} = 88.8$ Mpa or 94.86 Mpa
 Selecting lower value
 $\tau_{max} = 88.8$ Mpa
 If we used key then we can reduced the stress
 $\tau_{max} = .75 * 88.8 = 66.6$ Mpa
 Design Torque, $T_d = 11.58$ N-m
 Therefore we get
 $d = 9.6$ mm
 Increase the diameter by 50% to sustaining the various load
 Then , $d = 9.6 * 1.5 = 14.4$ mm
 Selecting standard value
 $d_s = 20$ mm
 Moment on each arm
 $M = ((F_1 - F_2)(D - D_h)) / n$
 D_h = hub diameter = $1.5 * d_s + 25$ mm
 = 49 mm

σ_b = allowable stresses = 8 Mpa for cast iron and sudden load
 Commonly used section for arms is elliptical
 $Z = \pi / 64 h^3$
 h = major axis of elliptical arm
 $\sigma_b = M / Z$
 From this we get
 $h = 28.9$ mm
 Now for space accommodation
 Space required should be less than space available
 $nh < \pi D_h$
 115.6 mm < 159.93 mm
 Therefore no beading is required.

C. Key Design:

From d_s
 Key cross section, $b = 6$ mm , $h = 6$ mm
 Length of key = 14 mm to 71 mm

D. Design of Bevel Gear:

Design power $P_D = P_R * K_1$
 $K_1 = 1.25$ for steady and continuous work
 P_R = rated power = 4.6 kw
 $P_D = 5.75$ kw
 $N_p = 2750$ rpm

Assume velocity ratio = 1
 Therefore $t_g = t_p = 18$ teeth
 $N_g = 2750$ rpm
 Pitch angles, γ
 For acute angles gears
 For pinion, $\tan \gamma = \sin \theta / (T_g / T_p + \cos \theta)$
 $\theta =$ angle between axes of shafts = 90°
 $\gamma = 45^\circ$ for pinion
 Now
 For gear,
 $\tan \gamma = \sin \theta / (T_p / T_g + \cos \theta)$
 $\gamma = 45^\circ$ for gear
 Cone distance, L
 $L = 0.5 \sqrt{[(D_g)]^2 + [(D_p)]^2}$
 Consider module 'm'
 $m = D / T$
 Therefore
 $L = 12.72m$ mm
 Now formative no. of teeth
 T_r for pinion = $1 / \cos \gamma = 25.45 = 26$ teeth
 T_r for gear = $1 / \cos \gamma = 25.45 = 26$ teeth
 Now for tooth load
 $F_t = P_d / V_p$
 $V_p = \pi D N / (60 * 1000)$, m/s
 $V_p = 2.592m$ m/s
 $F_t = 2218.364 / m$ N
 Beam strength, F_B
 $F_B = S_o * C_v * Y * m * b * (1 - b/L)$
 $S_o =$ basic stress
 Selecting cast steel 0.20% carbon, heat treated
 $S_o = 196$ Mpa
 Assume 20° full depth tooth profile
 $Y =$ form factor
 $Y_p = 0.485 - 2.87 / T_p$
 $Y_g = 0.485 - 2.87 / T_g$
 Where formative no. of teeth is used.

$$Y_p = 0.375$$

$$Y_g = 0.375$$

$C_v =$ velocity factor

Assume 0.3

$b =$ face width

Assume from 6m to 7m

$$F_B = 69.894 m^2 N$$

Comparing F_B and F_T

We get module 'm'

$$m = 3.166$$
 mm

standard module $m = 5$ mm

Actual Parameter

$$D_g = 90$$
 mm

$$D_p = 90$$
 mm

$$V_p = 12.96$$
 m/s

$$F_B = 1747.35$$
 N

$$F_T = 443.67$$
 N

$$L = 63.6$$
 mm

Now C_v actual

$$C_v = 4.5 / (4.5 + V_p)$$

$$C_v = 0.258$$

For actual value of b_{min}

$$F_B = S_o * C_v * Y * m * b * (1 - b/L)$$

By putting value we get

$$F_B = 94.815b - 1.49 b^2$$

Comparing this value to F_T we get

$$b = 58.548 \text{ mm}$$

but range of b min is 30mm to 35 mm

so selecting $b_{\min} = 35 \text{ mm}$

From new value of b we get

$$F_{B \text{ actual}} = 1492.29 \text{ N}$$

So $F_{B \text{ actual}} > F_T$

Hence design is safe and feasible.

Dynamic load

$$F_d = F_T + (21V_p (C_{eb} + F_T)) / (21V_p + \sqrt{(C_{eb} + F_T)})$$

Where

C = deformation factor = 11800 for steel and steel & 20o full depth

e = error = 0.025 mm

$$F_d = 8239.75 \text{ N}$$

Now for limiting wear strength, F_w

$$F_w = (K \cdot b \cdot D_p \cdot Q) / (\cos \gamma_p)$$

Where

$$Q = \text{size factor} = 2T_g / (T_g + T_p)$$

$$Q = 1$$

$$F_w = 4454.77 \cdot K_{\min} \text{ N}$$

Again using limiting condition and comparing $F_w \gg F_d$

$$K_{\min} = 1.84$$

So standard $K = 1.920$

$$\text{BHN}_p = 350$$

$$\text{BHN}_g = 350$$

$$F_{w \text{ actual}} = 4454.77 \cdot K_{\text{act}} = 8553.15 \text{ N}$$

So $F_{w \text{ actual}} > F_d$

Hence our design is safe and feasible.

E. Gear Blank Design:

Select type of construction

For pinion

Consider solid construction

$$D_p \leq 15m + 60 \text{ mm}$$

$$90 \leq 135 \text{ mm}$$

So condition is satisfied

Hence we select solid construction for pinion.

For gear

Consider solid construction

$$D_g \leq 15m + 60 \text{ mm}$$

$$90 \leq 135 \text{ mm}$$

So condition is satisfied. Hence we select solid construction for gear.

F. Design of Cutter:

Torque = Force * Radius

$$= 11.58 \text{ N-m}$$

Cutting Force = 106.5 N

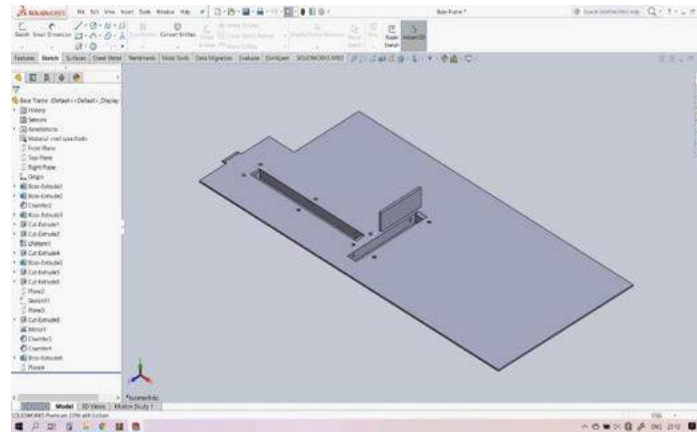
Hence, Cutter Radius = 108.73 mm

IV. 3D DESIGN MODELS FOR VARIOUS PARTS AND ASSEMBLY OF MINIATURE SUGAR CANE MACHINE

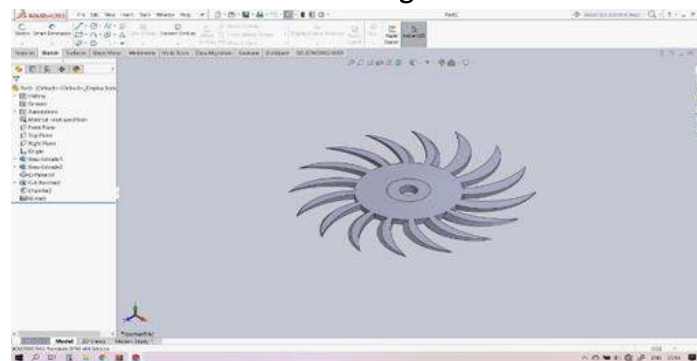
MACHINE

In this section, the various parts and assembly model of miniature sugar cane machine developed in the software is presented and the details of these models are as under.

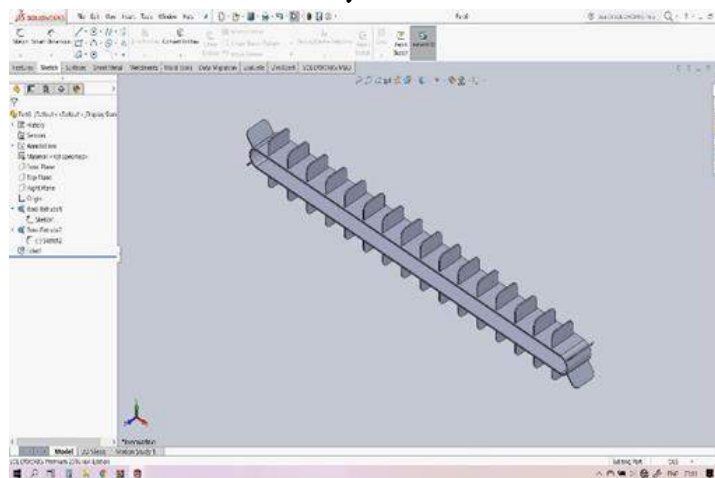
Base Frame:



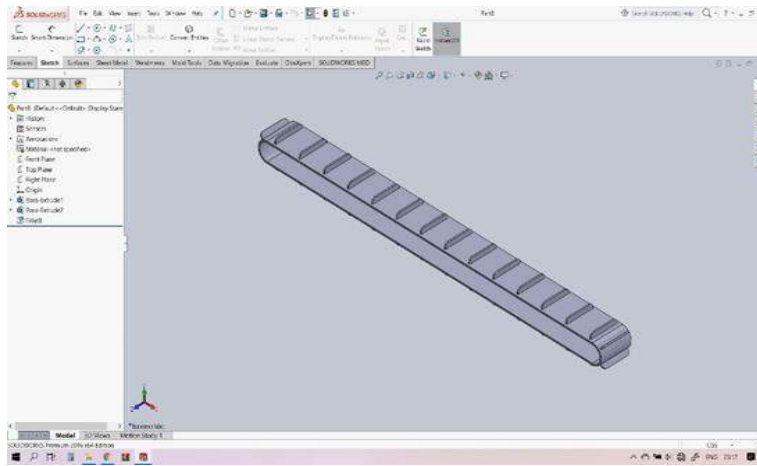
Bottom Cutting Blade:



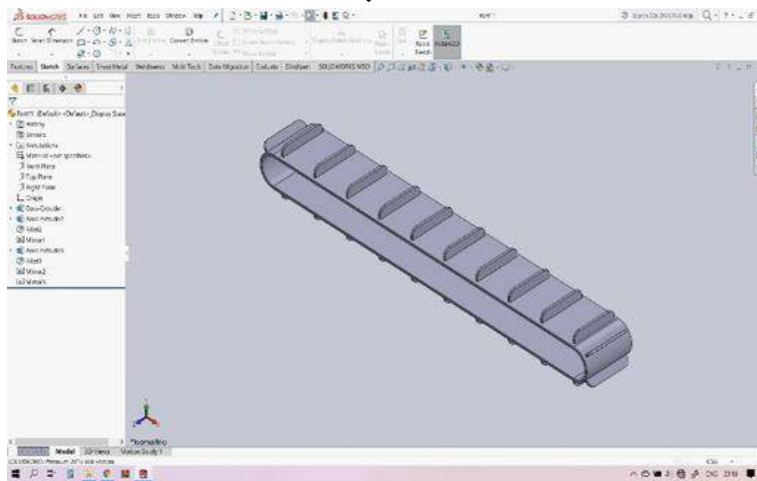
Conveyer Belt-1



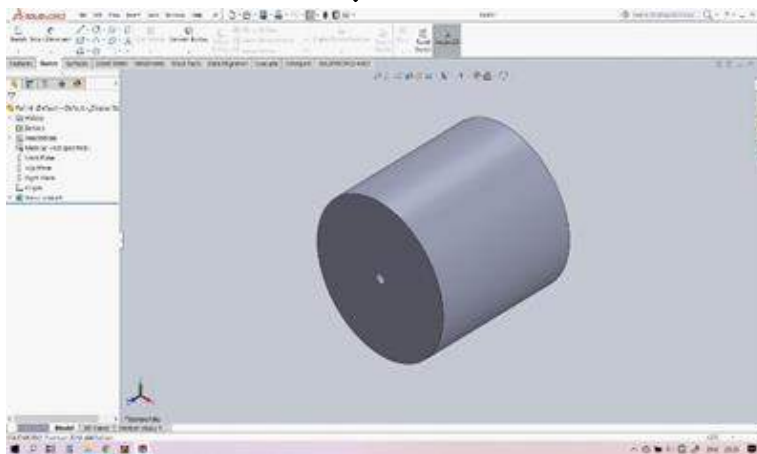
Conveyer Belt-2



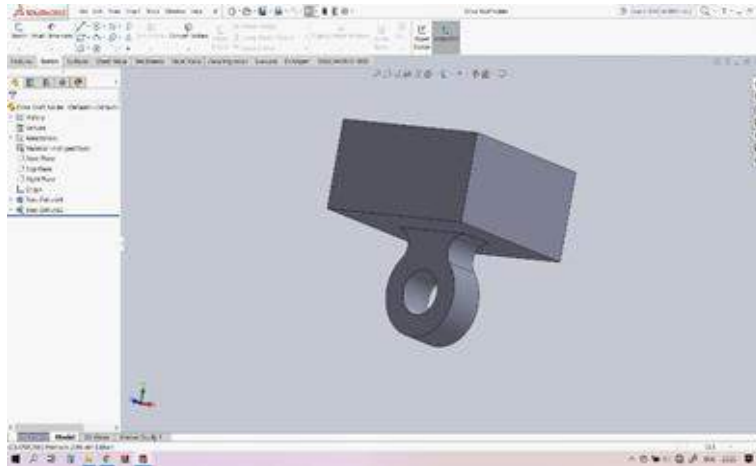
Conveyer Belt-3



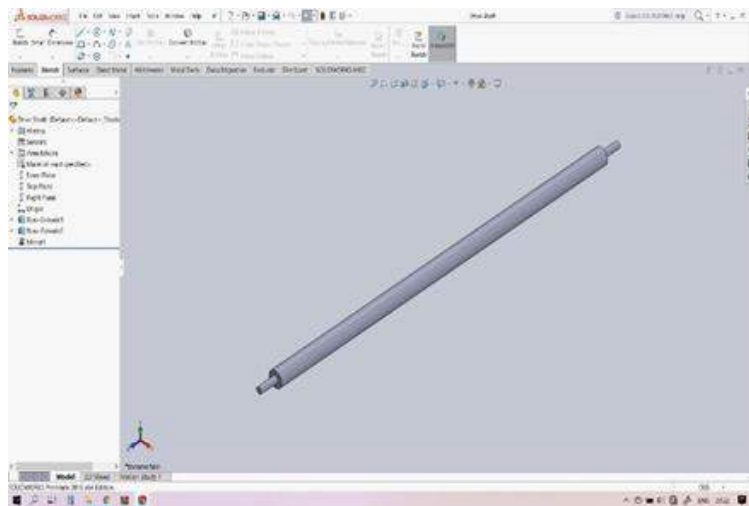
Cylinder



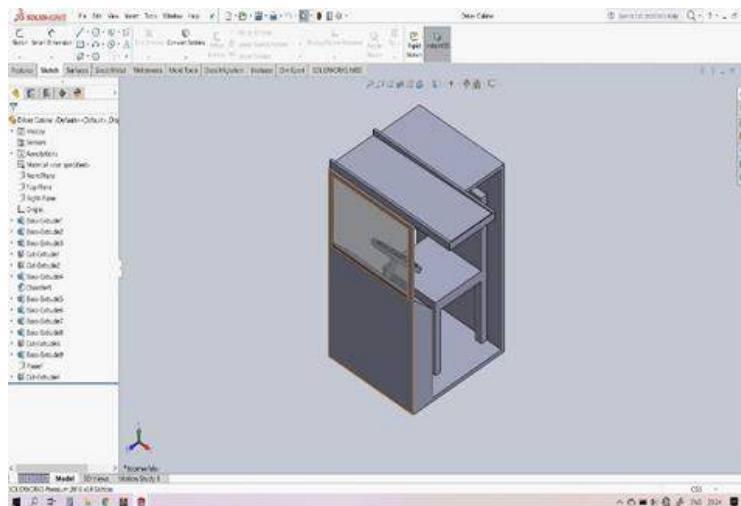
Driving Shaft holder



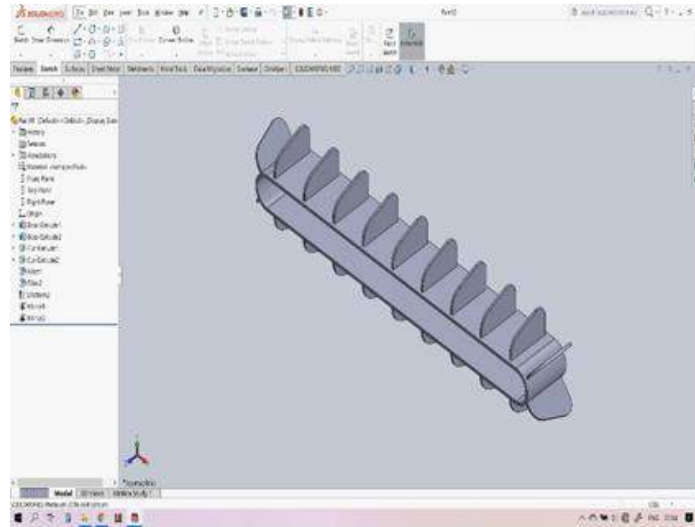
Drive Shaft



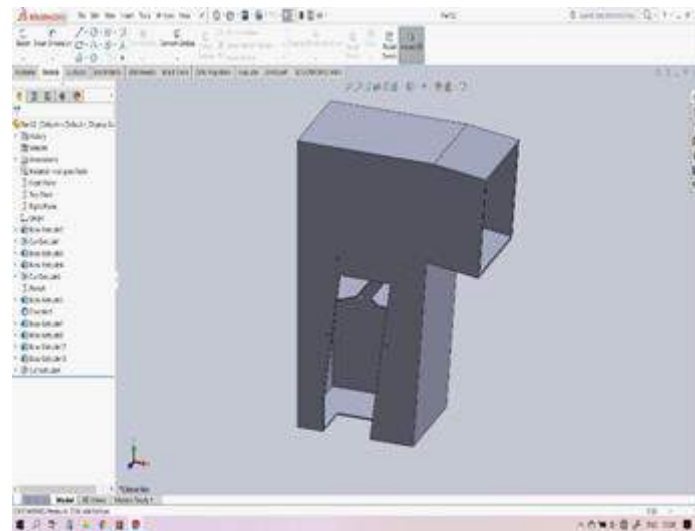
Driver Cabin



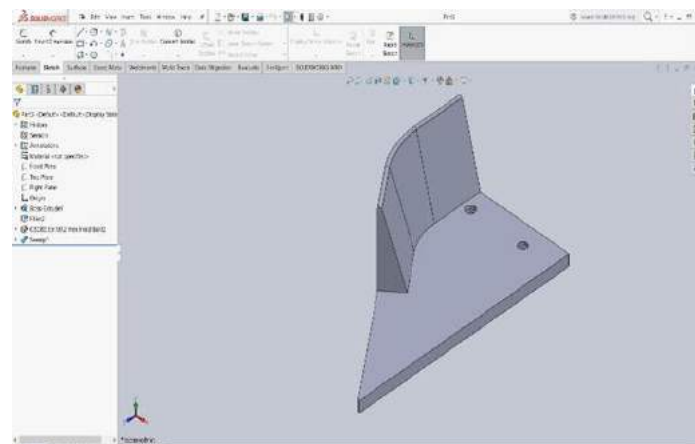
Inclined Conveyer Belt



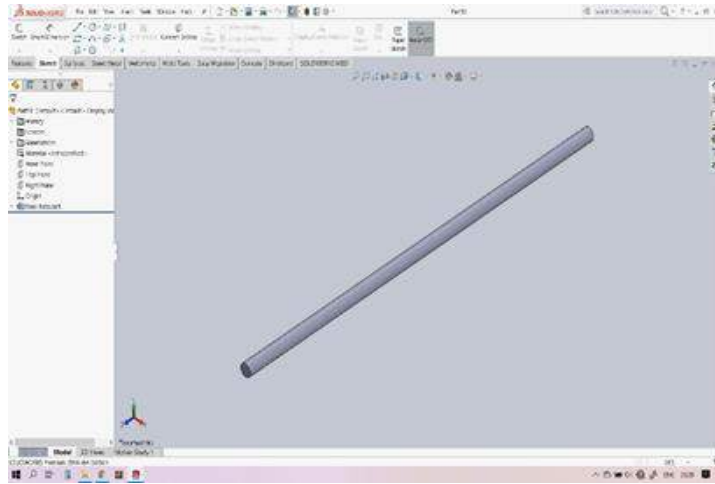
Liver remover Frame



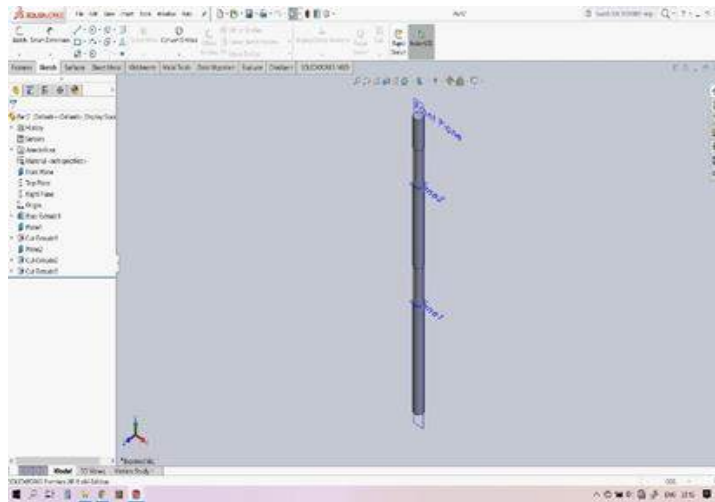
Row Driver



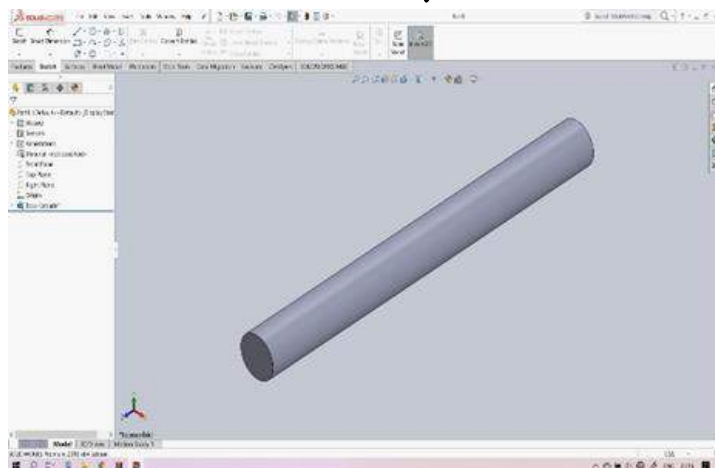
Shaft-3



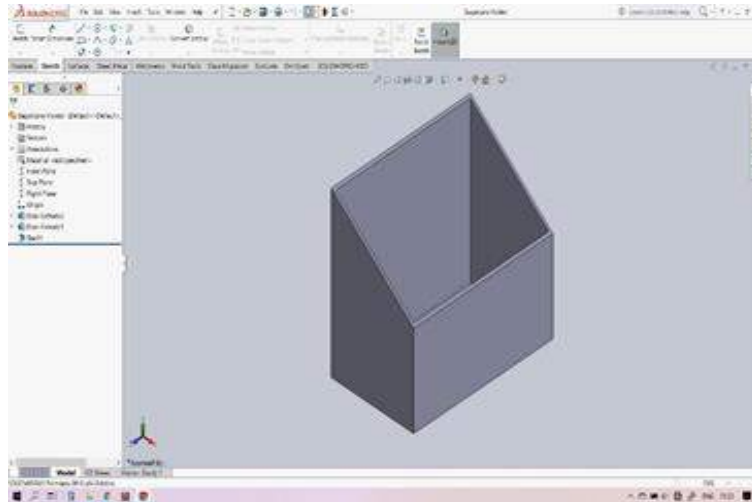
Shaft-1 for Conveyer belt



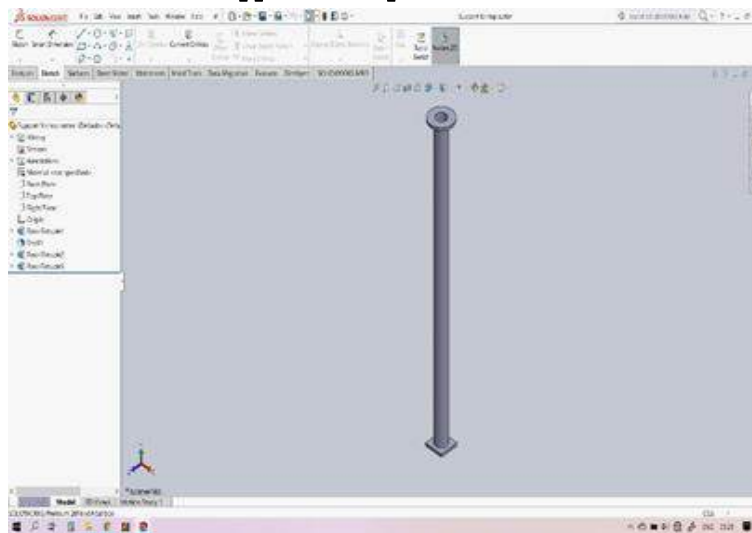
Shaft-2 for conveyer belt



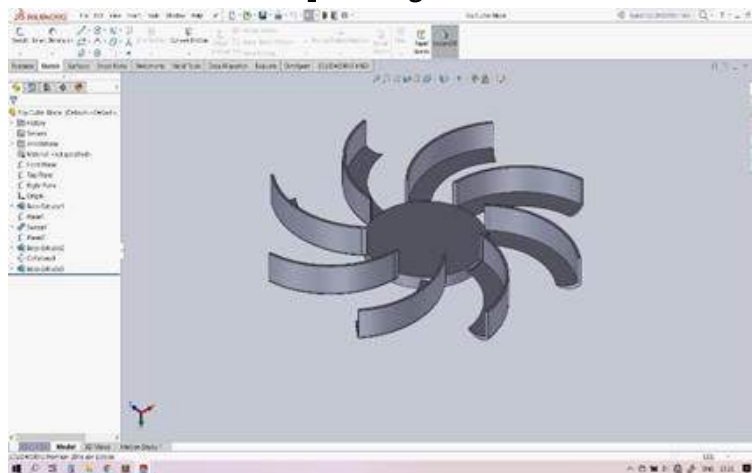
Sugar Cane Holder



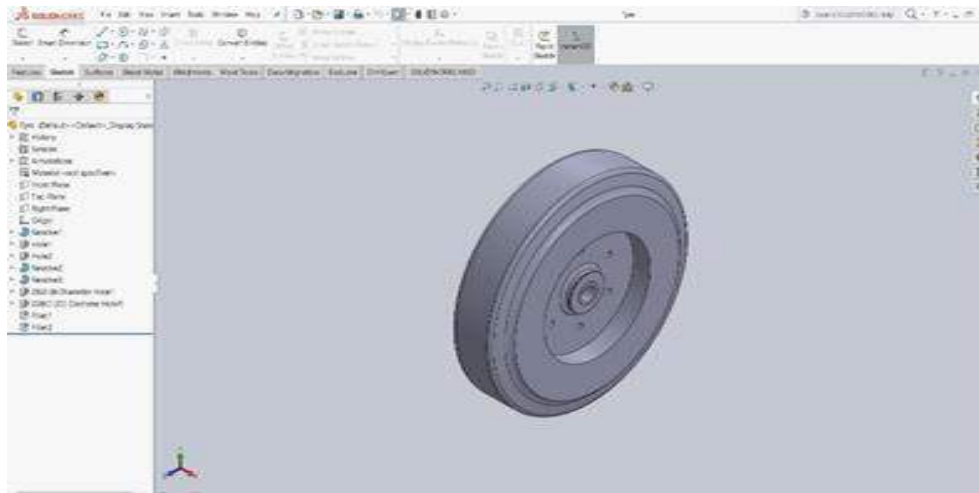
Support for Top Cutter Blade



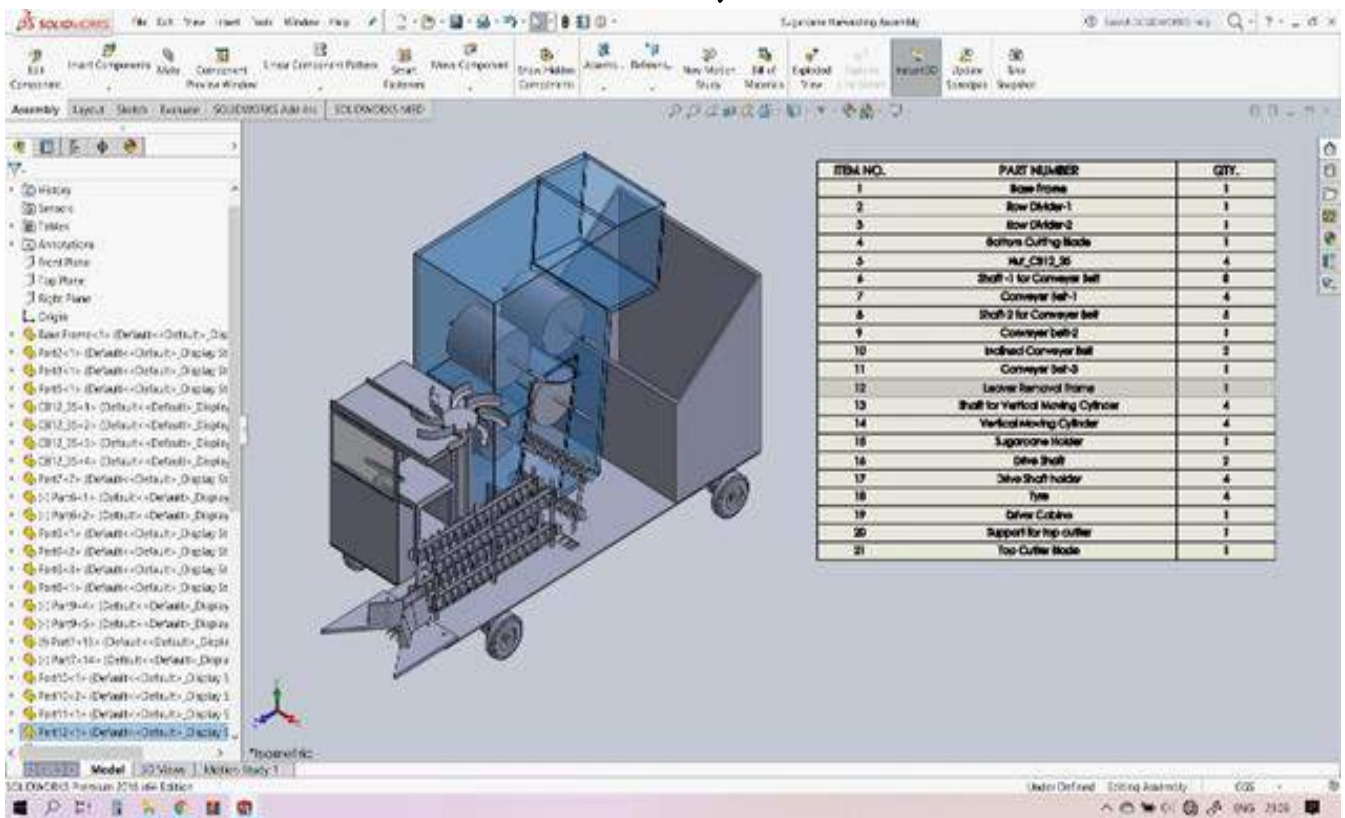
Top Cutting Blade



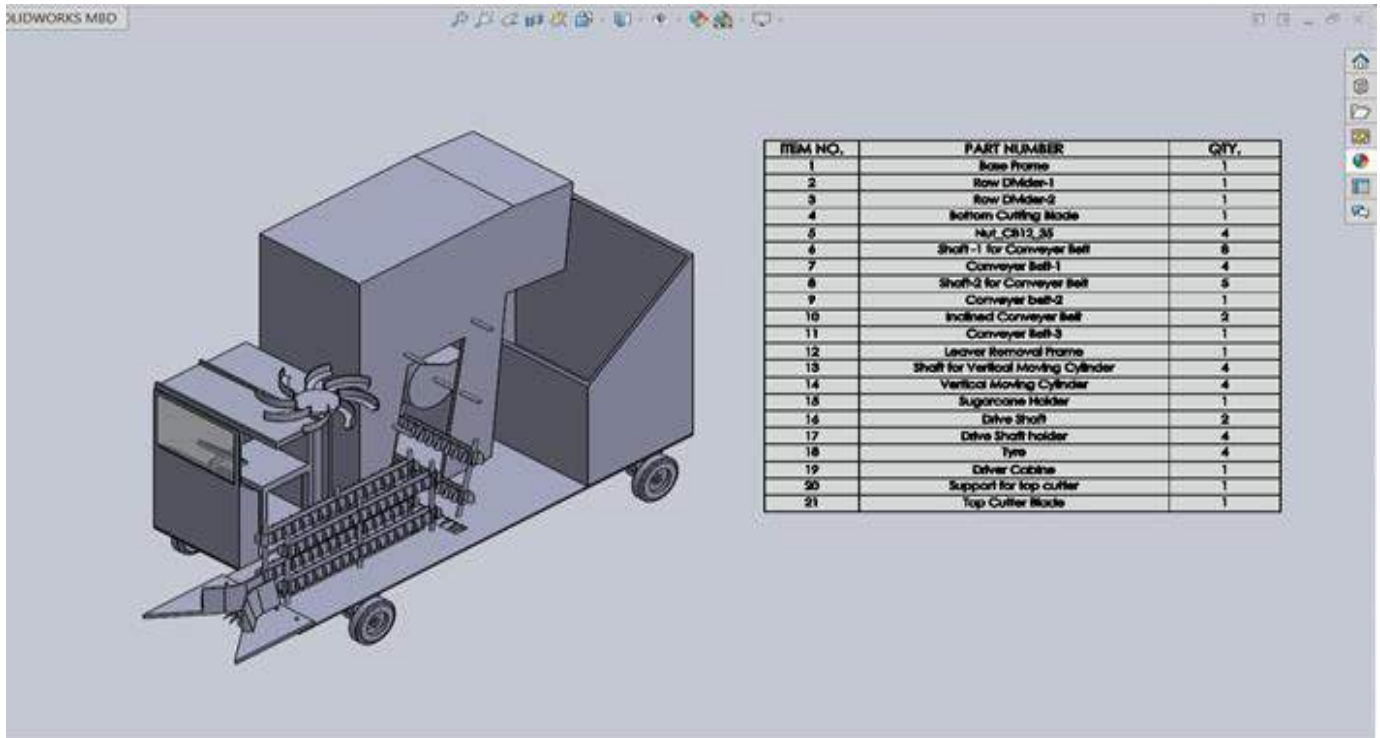
Tyre



Assembly



Final 3D Model of Miniature Sugar Cane Machine



V. CONCLUSION AND SCOPE FOR FUTURE WORK

In this project, design and development of 3D model of a sugarcane harvesting machine is established. This model helps to reduce farmers' effort. The proposed machine model has the capacity to cut canes at a faster rate compared to manual harvesting. This machine is economically viable for small and big farmers. The model cuts the sugarcane at ground level compared to manual labor who cut sugarcane above the ground level with a distance 6" to avoid the strike of the knife with soil. So in case of manual harvesting it is required to cut the remaining sugarcane stem after harvesting/cutting manually which requires extra labor and it is very much required to cutting off the remaining sugarcane stem otherwise it affects the next crop generation.

Future work can be extended in the following direction:

Automation: The machine can be updated to automatic operation by including electronics and programming.

Power: The diesel for the power can be replaced with dc motor which can be powered with solar energy.

Wheels: The tyre and rim Wheel system can be replaced with continuous track wheel system which can operate easily in all conditions.

Steering: The mechanical steering can be replaced with power steering

VI. REFERENCES

- [1]. Salassi, M. E., & Champagne, L. P. "A spreadsheet-based cost model for sugarcane harvesting systems". Computers and electronics in agriculture, (1998), 20(3), 215-227

- [2]. Ma, S., Karkee, M., Scharf, P. A., & Zhang, Q. "Sugarcane harvester technology: a critical overview". *Applied engineering in agriculture*, (2014), 30(5), 727-739.
- [3]. Shelke, G. D., Borikar, S. S., Awathale, M. P., Khante, A. P., & Zode, P. M. "Design of Sugarcane Harvesting Machine". *International Journal of innovative research science in science and technology*. (2015), Volume I issue II April, 122, 127.
- [4]. Siddaling, S., & Ravaikiran, B. S. "Design and fabrication of small scale Sugarcane harvesting machine". *International journal of Engineering Research and General science*, (2015), 2091-2730.
- [5]. Santoro, E., Soler, E. M., & Cherri, A. C. "Route optimization in mechanized sugarcane harvesting". *Computers and Electronics in Agriculture*, (2017), 141, 140-146.
- [6]. Corredo, L. D. P., Canata, T. F., Maldaner, L. F., de Lima, J. D. J. A., & Molin, J. P. "Sugarcane Harvester for In-field Data Collection: State of the Art, Its Applicability and Future Perspectives". *Sugar Tech*, (2021), 23(1), 1-14.
- [7]. Inkane, P., Burati, Y., Bhendarkar, H., & Gondane, R. "Design and Calculation Of Solar Power Operated Sugarcane Harvesting Machine". *International Research Journal of Engineering and Technology (IRJET)*, (2017), 4(03).
- [8]. Aliano Filho, A., Melo, T., & Pato, M. V. "A bi-objective mathematical model for integrated planning of sugarcane harvesting and transport operations". *Computers & Operations Research*, (2021), 134, 105419.



Study, Optimization of Cutting Parameters of Non-Ferrous Metal by Turning Operation in Lathe Machine

Nagesha N¹, B S Praveen Kumar²

¹Research scholar, Department of Mechanical Engineering, Visvesvaraya Technological University, Belagavi, Karnataka, India

²Associate professor, Department of Mechanical Engineering, Govt. Engineering College, K R Pet, (Affiliated to VTU, Belgaum) Karnataka, India

ABSTRACT

A collective method to manufacture parts to a precise dimension involves the removal of excess material by machining operation with the help of cutting tool. In any machining process, it is most important to determine the optimal settings of machining parameters take aim at reduction of production costs and achieving the desired product quality. we were conducting different experiments with varying one parameter and keeping other two fixed so maximum value of each parameter was obtained. Vibrations not only increase the surface roughness of work piece but also affect the tool life and noise during the machining operation

Operating range is found by investigating with spindle speed and taking the four levels of other parameters. Every day scientists are developing new materials and for each new material, have need economical and efficient machining. It is also predicted that Taguchi method is a adoptable method for optimization of various machining parameters. In this work the relation between change in hardness caused on the material surface due the turning operation with respect to different machining parameters like spindle speed, feed and depth of cut have been investigated. Taguchi method has been employed to plan the experiment where the material used is aluminium. The main effects have been calculated and percentage contribution of various process parameters affecting hardness also determined.

Key words - Lathe Machine, Tool Dynamometer Cutting Speed, Feed, Depth of Cut and Surface tester etc.

I. INTRODUCTION

Present manufacturing industries are facing difficulties due to vibrations induced in machine tools like lathe, milling, grinding, etc. during machining. Vibrations produced in machine tools like lathe, milling and grinding, etc. during machining operation are one of the primary concern in manufacturing industries. These vibrations not only increase the surface roughness of work piece but also affect the tool life and noise during the machining operation [1,2]. Machining practice under conventional dry condition of hardened work material has been a usual practice in metal machining industries, but it has its drawbacks. In addition, the improved

relationship between input and output factors is established considering suitability and potential approach with appropriate selection of working environment for effective utilization in turning practice [3]. In the current scenario, there is a greater demand for increased productivity with smaller tolerances. It paved way for increased material removal per unit time and higher spindle speeds, increased feed rate, and greater depth of cut. Certain combinations of machining parameters, cause process instabilities causing vibrations which in turn result in a decrease in accuracy, inferior surface finish, reduced tool life time, a decrease of the metal removal and in certain extreme cases, it can even cause spindle failure and decline in the life of the machine tool. Vibration amplitude modelling forms the basis for realizing the cutting process which has to be maintained at the least in order to reduce tool deflection, vibration, tool wear, improve surface finish quality, augment tool life time, enhance of the metal removal, provide a long life of a machine tool and to maintain the process parameters at an optimum level so that it ensures the delivery of a premium product with the minimum machining time [4]

If there be any relative vibratory motion present between the cutting tool and the job, it is obvious that the performance of the machine tool not be satisfactory. Moreover machine tool vibration has detrimental effect on the tool life, which in turn, lowers down the productivity and increase cost of production.

Machining is the most wide spread metal machining process in mechanical manufacturing industry. The goal of changing the geometry of raw material in order to form mechanical parts can be met by putting material together. Conventional machining is the one of the most important material method. Machining is a part of the manufacturing all most all metals

products. In order to perform cutting operations, different machining tools such as lathes, drilling machine, horizontal and vertical milling machines etc. are utilizing. Out of this machining process, shape metal, because in turning the condition of operation are most varied. Increasing productivity and reducing manufacturing cost has always been the primary object of successful business.

Turning operation is very important material removal process in modern industry. The study on the influence of hardness during machining has been going back to change.

II. LITERATURE SURVEY

Many eminent researchers from India such as, . A. G. Yuvaraju, Ritesh Upase, Samarjit Swain, M. Subramanian, Siamak Ghorbani, Prof. A. M. Patil, Siamak Ghorbani, A. Palanisamy, Khalid Ahmed Al-Dolaimy, Amal S. Siju, S.S. Sarjana, Ramneek Singh F. S. Sabirov Dr. C. J. Rao A. Fouathiya, 2021 Amal S. Siju and Prabhakaran, showed significant improvement in conventional Turning process optimization by using various non-conventional optimization techniques. They compared their results with the results obtained from hand books. The goal of optimization in all the cases is to reduce vibration and determine the minimum surface roughness by considering various cutting parameters. Some researchers tried various combinations of cutting process parameters and non-traditional optimization techniques.

[1] It has been found that there is a reduction in surface roughness as well as vibration amplitude with an increase in the number of composite plates placed under the tool. [2] In this study, tool wear is monitored by

measuring vibration signals when turning hardened steel.[3]analysis of the correlation of input machining parameters and vibration signal on machining features like tool wear, surface roughness and cutting temperature under MQL environment.[4]investigation on the direct and interactive effect of the process parameter with vibration amplitude was carried out for the selection of process parameter so that the vibration amplitude was maintained at the minimum which ensures the stability of end milling process.[5]The present paper outlines an experimental study while turning unreinforced and Al/SiC/RHA hybrid composite with varying reinforcements in equal proportions at different turning conditions. Cutting forces, surface roughness, power consumption, metal removal rate are analyzed through graphical representations[6].Vibration influence on tool wear is assessed, which considers the phase shift of vibration in different coordinates and forces on rake and rear faces of the tool. Tool life is predicted based on fatigue strength of tool material and parameters of tool vibrations[7].To attain quality of the turned components, Ra was minimized and MRR was maximized via Taguchi - based Grey Relational Analysis (GRA).[8] To measure the vibrations of HSS single point cutting tool. To measure the vibrations of Carbide tipped single point cutting tool. To find the better tool with cutting parameters for maintaining good surface finish. [9]The intention on finding the alternative tool material to support the usage of Coated Cemented Carbide for increasing the productivity in turning of hardened steel is the rationality of this study. Study on the mechanical properties of hard metals and the advantages of modern Cermet cutting tools lead to nominate this tool to be applied for turning of hardened steel.[10]The main objective is to evaluate the variations in the tool–chip contact length, tool wear, chip morphology, and cutting forces whenever textured inserts with various surface textures are used

III. MATERIALS AND METHODOLOGY

A. Work Piece Material

An aluminium (AL6065) 32 mm dia and 120 mm length rod is used for the machining operation. Its composition is given in Table 1

cu	Fe	Mg	Si	Zn	Ti	Bi	Zr	Cr	Mn	Al
0.274	0.4	1.028	0.609	0.06	0.06	1.25	0.12	0.03	0.05	96.11

After iron, aluminium is now the second most widely used metal in the world. This is because aluminium has a unique combination of attractive properties Low weight, high strength, superior malleability, easy machining, excellent corrosion resistance and good thermal and electrical conductivity are amongst aluminium's most important properties. Aluminium is also very easy to recycle. 6065-T6 aluminium is 6065 aluminium in the T6 temper. To achieve this temper, the metal is solution heat-treated and artificially aged until it meets standard mechanical property requirements. It has the lowest strength and highest ductility compared to the other variants of 6065 aluminium

B. Tool material

High-speed steel (HSS) is used as the cutting tool material. It is a subset of tool steels, commonly used in tool bits and cutting tools. It is often used in power-saw blades and drill bits. It is superior to the older high-carbon

steel tools used extensively through the 1940s in that it can withstand higher temperatures without losing its temper (hardness). This property allows HSS to cut faster than high carbon steel, hence the name high-speed steel. At room temperature, in their generally recommended heat treatment, HSS grades generally display high hardness (above IIRC60) and abrasion resistance (generally linked to tungsten and vanadium content often used in HSS) compared with common carbon and tool steels.

C. Machining Process

The experiments were conducted as per the orthogonal array and the spindle speed, depth of cut, feed is measured and the surface roughness is measured with the help of SJ210 Surf test. A SJ210 Surf test is a device used to measure the roughness of a surface. A diamond tip is run over a sample of a material. The stylus records the grooves as a wave pattern and sends the information back to a computer. By the time the process is done, the system has an accurate model of every location measured.



Fig: SJ210 Surf test

IV. EXPERIMENTAL DETAILS



Fig.2: Lathe machine

Lathe Name	Turbo LX175 Lathe
Type of bed	Induction Hardened, Straight Gap bed
Distance between centers (mm)	2000
Surface finish Max. :	0.8 micron Surface roughness Ra value
Speed Range	Standard -from 40-2040 forward
from 60-1430 reverse	
Feed range	longitudinal (mm/rev) from 0.04-2.24

The experimental setup includes Lathe machine, cutting tool, sensor, Vibrometer and Data acquisition system. In this setup an experimental study to investigate the effects of cutting parameters like Cutting speed, feed and depth of cut on surface finish. Aluminium, mild steel , cast-iron & hard steel in the form of round bar $\varnothing 32\text{mm}$ and 120mm length was used to carry out for machining operation on Lathe machine



Fig: Al Machining work pieces

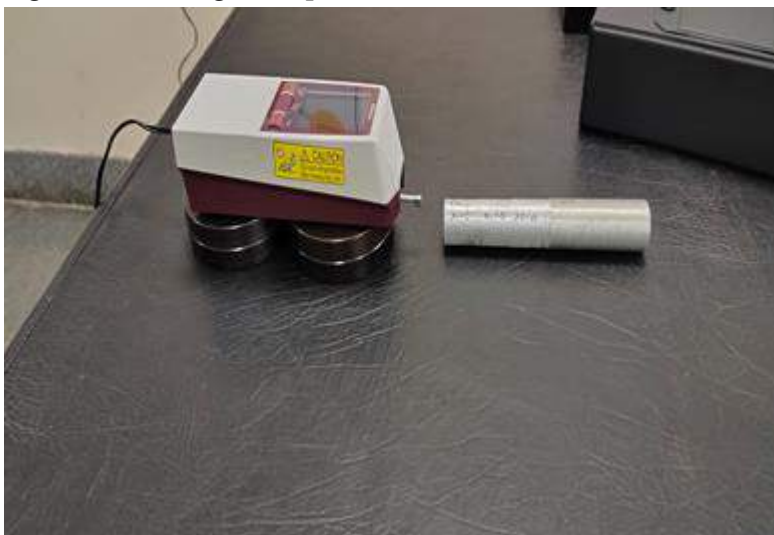


Fig : Surface tester

Table 1: Tabulated values

Sl No	Cutting speed mm/min	Feed mm/rev	Depth of cut mm	Surface roughness (Ra)
1	245	0.45	1.5	0.82
2	245	0.45	1.0	0.56
3	245	0.45	0.5	0.60
4	545	0.35	1.5	0.48
5	545	0.35	1.0	0.64
6	545	0.35	0.5	0.72
7	745	0.25	1.5	0.52
8	745	0.25	1.0	0.66
9	745	0.25	0.5	0.53

Table2: Factors that affect Turning operation

CONTROL FACTORS	NOISE FACTORS
Cutting Speed	Vibration
Depth of cut	Raw material variation
Feed rate	Machine Condition
Nose radius	Temperature
Coolant	Operator Skill

After listing the control and the noise factors, decisions on the factors that significantly affect the performance will have to be ascertained and only those factors must be taken in to consideration in constructing the matrix for experimentation. All other factors are considered as Noise Factors.

Table 3: testing conditions quality characteristics to be observed:

Quality characteristic	Surface finish
Work piece material	Aluminium
Cutting tool	Tungsten Carbide Tripped tool
Operating Machine	Lathe machine
Testing Equipment	Portable surface tester

A. Identifying the Objective Function

S/N Ratio for this function:

$SNl = -10 \log \frac{1}{N} \sum_{i=1}^N \frac{1}{y_i^2}$ Type equation here.

Where,

N=Sample Size, and y= Surface Roughness in that run

B. Identifying the control factors and their levels:

The factors and their levels were decided for conducting the experiment, based on a “brain storming session”. The factors and their levels are shown in table .

Table 4: Selected Factors and their Levels

FACTOR	LEVELS		
	1	2	3
Cutting speed(v, rpm)	245	545	745
Depth of cut(t, mm)	1.5	1.0	0.5
Feed rate(f, mm/min)	0.45	0.35	0.25

C. Selection of Orthogonal Array

To select an appropriate orthogonal array for conducting the experiments, the degrees of freedom are to be computed. The same is given below: Degree of Freedom: 1 for Mean Value and $8 = (2 \times 4)$, two each for the remaining factors Total Degree of Freedom: 9 the most suitable orthogonal array for experimentation is L9 array as shown in Table . Therefore, a total nine experiments are to be carried out.

Experiment No.	Control Factors		
	1	2	3
1	1	1	1
2	1	2	2
3	1	3	3
4	2	1	3
5	2	2	1
6	2	3	2
7	3	1	2
8	3	2	1
9	3	3	3

D. Conducting the Matrix Experiment:

In accordance with the above OA, experiments were conducted with their factors and their levels as mentioned in table . The experimental layout with the selected values of the factors is shown in table . Each of the above 9 experiments were conducted 5 times (45 experiments in all) to account for the variations that may occur due to the noise factors.

Table 4 : OA with Control Factors

Experiment No.	Control Factors		
	V(m/min)	D(mm)	F(mm/rev)
1	245	1.5	0.45
2	245	1.0	0.35

3	245	0.5	0.25
4	545	1.5	0.45
5	545	1.0	0.35
6	545	0.5	0.25
7	745	1.5	0.45
8	745	1.0	0.35
9	745	0.5	0.25

E. Examination of Data:

The Following are the experimental results of the work carried out. Since the objective function (surface finish) is smaller-the-better type of control function, was used in calculating the S/N ratio. The S/N ratios of all the experiments were calculated and tabulated as shown in table 5

Table 5 : Tabulated S/N ratios

Experiment No.	S/N Ratio
1	-8.9702
2	-6.2568
3	-9.4539
4	-10.9196
5	-10.0971
6	-13.101
7	-9.2385
8	-11.4642
9	-10.2941

Average S/N ratio corresponding to Cutting Speed at level 1 = $Ss1/3$ Average S/N ratio corresponding to Cutting Speed level 2 = $Ss2/3$ Average S/N ratio corresponding level each factor. Similarly $Sf1$ and $St1$ are calculated for feed and depth of cut .The average of the signal to noise ratios is shown in table 8. Similarly S/N ratios can be calculated for other factors.

Table 6: Average S/N Ratio for each factor

Level	Speed		Feed		Depth of cut	
	Sum	Avg. S/N ratio	Sum	Avg. S/N ratio	Sum	Avg. S/N ratio
1	-27.69	-9.23	-28.46	-9.39	-28.22	-9.55
2	-34.11	-11.38	30.59	-10.28	-30.81	-10.23
3	-28.91	-9.69	-31.83	-10.61	-31.84	-10.66

F. Anova & Its Significance

the result of the ANOVA analysis for the surface roughness of turning and facing process respectively. This analysis was carried out for a significance level of $\alpha=0.05$, i.e., for confidence level of 95%. the probability level that is realized significance levels, associated with the F-tests for each source of variation. The sources with a Probability level less than 0.05 are considered to have a statistically significance with the variation surface roughness generation in the work piece. From the Table 9 none of the factors having either statistical or physical significance on the flank wear obtained. Notice that the error associated in the ANOVA analysis for the surface roughness was 25.79 %(turning) and 13.21% (facing) and for the flank wear was approximately 9.98%(turning) and 31.8%(facing). If the error percentage was greater amount the linear model developed by using factor and their interactions may not give precise prediction results.

Table 7:- ANOVA for surface roughness of turning process

Source	Sum of Squares	Mean Square	F-Ratio	Probability level	% of contribution
V	0.07062	0.0353	1.1	0.379	7.09
F	0.00511	0.0025	0.08	0.926	0.51
A	0.03605	0.001823	0.57	0.589	3.65
V×f	0.14355	0.03599	1.12	0.412	14.43
V×a	0.3179	0.08198	2.52	0.121	32.88
f×a	0.14617	0.03904	1.21	0.376	15.67
Error	0.25721	0.03215			25.78
Total	0.9973				100

Table8: Optimum values of factors and their levels

Parameters	Optimum value
Cutting speed(m/min)	35
Feed(mm/rev)	0.15
Depth of cut(mm)	1.25

V. RESULTS AND CONCLUSION

The harder work material, the slower the cutting speed. The softer work material the faster the recommended cutting speed Steel. The harder the cutting tool material, the faster the cutting speed. The softer the cutting tool material the slower the recommended cutting speed. If the cutting speed is too slow than a lot of time is wasted during the machine process but if the cutting is too fast than also time is wasted in replacing or regrinding the cutters so the process should be carried out with an optimum cutting speed.

The speed of the cutting tool's movement relative to the work piece as the tool makes a cut. The feed rate is measured in inches per minute. As the feed increases the cutting force also increases but in accordance with this the tool life decreases. If the fees is too slow than time is wasted and the cutter also chatters but if the

cutter speed is too fast than the cutter teeth can broke so the process should be carried out with a optimum value of feed.

The depth of the tool along its axis in the work piece as it makes a cut. As the depth of cut increases feed rate increases the load on tool increases and the combined effect of this is that the tool life decreases. There are several shallow cuts that waste time so this should be eliminated.

VI. REFERENCES

- [1]. "Analysis of the surface roughness and cutting tool wear using a vapor compression assisted cooling system to cool the cutting fluid in turning operation" Rogério Pontes Araújo* , Tiago L Rolim, Carlos A Oliveira, Alex E Moura, José Carlos A Silva Federal University of Pernambuco, Recife 50670-901, Brazil.
- [2]. Prof. R. L KEGG Research Supervisor, Product Development Department, The Cincinnati Milling Machine Company, Cincinnati, Ohio. Assoc. Mem. ASME "Cutting Dynamics in Machine Tool Chatter Contribution to Machine-Tool Chatter".
- [3]. Thomas M. Beauchamp Y, Youssef A. Y. Masounave J. "Effect of tool vibrations on surface roughness during lathe dry turning process"
- [4]. M. Postel a , D. Aslan b , K. Wegener (1)a , Y. Altintas (1)b, Monitoring of vibrations and cutting forces with spindle mounted vibration sensors" Manufacturing Automation Laboratory, Department of Mechanical Engineering, The University of British Columbia, Vancouver, BC, V6T 1Z4, Canada.
- [5]. "Experimental Investigation and Estimation of Spindle Bearing Vibration in Turning Process" Dr. K.M.Sathish Kumar & Dr. H.V. Ravindra International Journal of Engineering Research & Technology (IJERT) Vol. 1 Issue 4, June – 2012
- [6]. "The spindle defect evaluation using a three-dimensional vibration analysis" Claudiu-Florinel bisu1, alinavintilescu, raynaldlaheurte, philippe darnis, miron zapciu, proceedings in Manufacturing Systems, Volume 6, Issue 4, 2011 ISSN 2067-9238
- [7]. "Numerical Investigation of Orthogonal Cutting Processes with Tool Vibration of Ti6Al4V Alloy" a Institute of Mechanics, Chinese Academy of Sciences, Beijing 100190, China b Department of mechanical and Aerospace Engineering, University of Florida, Gainesville, FL 32611-6250, USA



Effect of Nano and Hybrid Micro fillers on Two Body abrasive wear Behaviour of Polyamide 66 and Polyamide 6 (PA66/PA6) Blend Based Composites

Umesh G L¹, Rudresh B M², Krishna Prasad N J³, Madhu D⁴

¹Department of Mechanical Engineering, Bangalore Institute of Technology, Bangalore- 560004, Karnataka, India

²Department of Mechanical Engineering, Government Engineering College, Krishnarajapet- 571426, Karnataka, India

³Department of Industrial Engineering and Management, Bangalore Institute of Technology, Bangalore- 560004, Karnataka, India

⁴Department of Mechanical Engineering, Government Engineering College, Ramangaram- 571426, Karnataka, India

ABSTRACT

The effect of nano and hybrid micro fillers on two body abrasive wear of PA66/PA6 blend based composites is studied. Three composites Blend (PA66/PA6) (80/20 wt.%)/10 wt.% PTFE, Blend/10 wt.% PTFE/5 wt.% MoS₂/ 2.5 wt.% TiO₂ and Blend/10 wt.% PTFE/5 wt.% MoS₂/ 2.5 wt.% TiO₂/2.5 wt.% Nano graphene were considered for the investigation. These Nano and hybrid micro composites were prepared using melt mix method by twin screw extrusion technique. The Two body abrasive wear behavior was studied by considering the experimental parameters such as abrading load (2.5,5,7.5,10 N), Water proof SiC abrasive paper 180 Grit Size, abrading velocity 0.5 m/s as per ASTM G99 method. It is found from the experimentation that the volumetric wear loss is totally depends on the abrading load, abrading velocity and abrasive grit size. Micro ploughing and micro cutting were noticed during the morphological study through SEM images. Among the studied nano and hybrid micro composites, Blend (PA66/PA6) (80/20 wt.%)/10 wt.% PTFE exhibited better abrasive wear behavior compared to other composites.

Keywords: PA66/PA6, Abrasive wear, nano fillers, micro fillers, two body

I. INTRODUCTION

Mechanical industries are constantly under pressure to come up with new materials that are both mechanically strong and tribologically efficient. Polymers and composites are increasingly being used in a variety of industrial applications, including bearings, rollers, gears, cams, wheels, and clutches. The usage of polymers and polymer-based composites with good mechanical and tribological properties can only be beneficial. It is often

found that such a property cannot be achieved with a homopolymer. As a result, polymer blends have been developed. Various reinforcements and fillers are incorporated into the polymer blend to improve tribology, mechanical and thermal behavior [1]. The abrasion properties of PA66/graphite composites in two body mode were studied by Nomula et al. [2]. The wear characteristics were studied by varying the graphite percentage. The best results were obtained for PA 66/10 wt. % Graphite and PA 66/20 wt. % Graphite.

The two-body wear behaviour of glass-basalt composites under the impact of different abrasive particle size was investigated by Rudresh et al. [3]. The synergism between matrix and fibres improved the wear resistance of composites. The 2-BAW behaviour of SGF loaded Vinyl ester resin and particulate UHMWPE filled Vinyl ester composites were studied [4]. The solid fillers used for the abrasion test were granular form coal and mineral ignimbrite. The UHMWPE filled resin showed the better wear resistance both for hard and soft abrasives. The SGF reinforced composites exhibited the complicated behaviour. When coal as abrasive, the SGF filled composites exhibits good wear resistance whereas with harder ignimbrite, it showed negative trend on abrasive wear resistance. This showed that the abrasive wear behaviour is a function of abrasive particle size. The mechanical and abrasive wear properties of PA66/PP microcomposites was studied by Suresha and Ravi Kumar [5]. They found from their study that the sole effect of nanoclay was not favourable to improve the 2-BAW resistance. But the synergism between SCF and nanoclay proved to be the best combination for the abrasion resistance. The abrasive wear behaviour was affected by distance, load and grit size. Microcutting and micro ploughing are the failure mechanisms noticed during SEM analysis.

The synergism effect between fibers and fillers in improving the abrasion wear properties of polymers was reported by Bijwe et al. [6]. They studied the effect of inclusion of carbon filler, graphite, PTFE and MoS₂ filler on PEI/SGF, Polyimide (PI)/SGF, Nylon 6/SGF and PTFE/SGF composites. They found that the specific wear rate decreases with increase in load. The wear behaviour of bronze filled ones was better compared to all other composites. Further, it is concluded that the reinforcement greatly reduced the ultimate elongation to fracture which is the main factor for the abrasion behaviour. It was showed that the inclusion of SCF into the blend was detrimental to abrasion resistance of composites. The blend PA66/PP exhibited the better abrasive wear resistance. Matrix damage and debonding were some of the mechanisms observed through SEM. The wear behaviour of PA6 and its composites under two body abrasion was reported [7]. They used 25 wt. % glass beads, 20 wt. % talc and 30 wt. % wollastonite fillers for the composites. It is found from the study that the composites with glass bead fillers found to exhibit the better abrasion wear resistance. The abrasive wear behaviour of PTFE/SCF composites has been presented [8]. The composites were developed using SCF varying from 0 to 40% and PTFE from 0 to 15%. The hybrid effect of SCF and PTFE found to be detrimental to abrasive wear resistance. Load, velocity and fiber geometry affected the wear behaviour.

From the above literature review, it is clear that the blend of PA66 and PA6 was not reported. Both PTFE, MoS₂, TiO₂ and Nano graphene are known for their effective tribological resistance behaviour when combined with thermoplastics. Further, the hybrid effect of micro fillers such as PTFE, MoS₂, TiO₂ and Nano fillers such as Nano graphene on two body abrasive wear behaviour of PA66/PA6 blend based composites was not investigated. The individual effect of PTFE, MoS₂, TiO₂ and Nano graphene and their combined effect are very much required for the structural applications. Therefore, an attempt has been made to study the effect of

varying abrasion pressure on the two body abrasive wear behaviour of PA66/PA6 blend based composites. Further, the morphological study of abraded surfaces has been presented in the form SEM images.

II. EXPERIMENTAL

2.1. Materials and their formulations

Materials used in the present investigation and formulation of composite blend PA66/PA6 in different weight percentage are tabulated in table 1 and table 2 respectively.

Table 1: The details of supplier's physical data of materials

Material	Designation	Supplier's Name	Form	Size (μm)	Melting Temperature ($^{\circ}\text{C}$)	Density (g/cm^3)
Polyamide 66	PA66	GLS Polymers,Bangalore	Granules	----	256	1.14
Polyamide 6	PA6	GLS Polymers, Bangalore	Granules	----	215	1.14
Polytetrafluoroethylene	PTFE	GLS Polymers, Bangalore	Powder	12	327	2.2
Molybdenum Disulphide	MoS ₂	GLS Polymers, Bangalore	Powder	10- 20	1185	5.06
Titanium Dioxide	TiO ₂	GLS Polymers,Bangalore	Powder	10- 20	1843	3.78
Nano Graphene	--	United Innovation Ltd. Bangalore	Powder	5	4125	0.17

Table 2: Formulations of polymer composites

Composition	Mat. ID	Weight fraction percentage					
		PA66	PA6	PTFE	MoS ₂	TiO ₂	Nano Graphene
Blend (PA66/PA6)/PTFE	U1	80	20	10	----	----	----
Blend/PTFE/ MoS ₂ / TiO ₂	U2	80	20	10	5	2.5	----
Blend/PTFE/ MoS ₂ / TiO ₂ /Nanographene	U3	80	20	10	5	2.5	2.5

2.2. Fabrication of blends and micro fillers

For the fabrication of these composites, two steps are required. In the initial stage, a blend of PA66 and PA6 is weighed in the desired proportion based on the formulation. Compositions are heated separately in a separate

chamber, and then the mixture is made to pass through a Barbender co-rotating twin-screw extruder (Make: CMEI, Model: 16CME, SPL, chamber size 70cm³). A five-zone extruder chamber was designed with temperatures of 220°C, 235°C, 240°C, 265°C, and 270°C for heating the mixture to form fine melts, respectively. In order to keep the feed rate of 5 kg/h, the screw speed of the extruder is maintained at 100 RPM at a temperature of 220 °C. The extrudates which were in cylindrical form were quenched in cold water and pelletized using a pelletizing machine. The quenched pellets of PA66/PA6 blend were once again subjected to heating before subjected to any other process.

During the second step, the preheated micro and nano fillers were mixed with the polyamide 66 and polyamide 6 pellets. The compounding process has to take place before the pellets can be extruded. The uniform melting process is then repeated in the heating chamber in order to obtain uniform blended melt. This blended melt was then made to pass through the necessary diametrical nozzles where these pellets were projected in the form of cylindrical wires. Using a cold bath chamber, the extruded pellets were water quenched and then pelletized. The resulting composite pellets were dried in a vacuum oven at 100°C for 24 hours. As per ASTM, heated pellets were injected into an injection molding machine to generate the test specimens. For injection molding the temperature maintained in zone 1 and zone 2 is 265°C and 290 °C further mold temperature of 65°C was maintained and also screw speed of 10-15rpm and injection pressure of 700-800 bar was maintained. Injection time of 10 s, cooling time of 35 s and ejection time of 2 s have been maintained in injection molding. The molded specimens for mechanical and tribological testing as per ASTM standards were carefully inspected, visually tested and defective ones were rejected.

2.3. Two Body Abrasive Wear test (ASTM G99)

As per ASTM G99 method with the help of wear testing machine (Fig. 1) (Ducom, Bangalore) two body abrasive wear behaviour of the samples was conducted. Table 3 shows the details of the experimentation parameters used in the test. The standard dimensions of 8 mm x 8 mm x 3.2 mm test specimens were used and they were rubbed against 600 grit SiC abrasive paper to ensure the uniform specimen surface contact. These prepared samples were glued using suitable adhesive to the steel pins of diameter 8 mm and length 27 mm. The initial weight of specimen including the pin was measured using an electronic weighing balance with an accuracy of 0.0001 grams (Metler Toledo).

Table 3. Experimental test parameters for two body abrasive wear test (ASTM G99)

Experimental parameters	
Abrading load (N)	2.5, 5, 7.5 and 10
Abrading velocity (m/s)	0.5
Abrading distance (m)	100
Abrasive Grit size	180

Based on the experimental conditions 180 Grade of SiC abrasive paper were glued on to the steel surface of the disc of diameter 165 mm. For each trial fresh abrasive paper was used. After fixing abrasive paper and pin with the sample attached in the perfect position, a normal load is applied to the pin through pivoted loading lever which is shown in fig. 1. The machine stops automatically when the pre-set time is reached. The final weight of

the polymer composite sample along with the pin was measured. The tests were conducted for different experimental conditions by varying load, varying abrading velocity, abrasive grit size and distance. In all the cases, the samples initial weight is measured before and after conducting experiment. The weight loss of the composites is recorded. To obtain the average value for the purpose of data representation, minimum three samples were tested. The weight loss of specimen (W) gives the abrasive wear volume loss using experimentally determined density (ρ). The wear volume loss and specific wear rate are calculated using the equations 1 and equation 2 respectively.

Wear volume = $\Delta V = W / \rho \text{ mm}^3$ Eq. (1)

Specific wear rate = $K_s = \Delta V / (F * D) \text{ mm}^3 / \text{N-m}$ Eq. (2)

Where ρ = density (g/cm^3), F, the applied normal load (N) and D, the sliding distance (m)

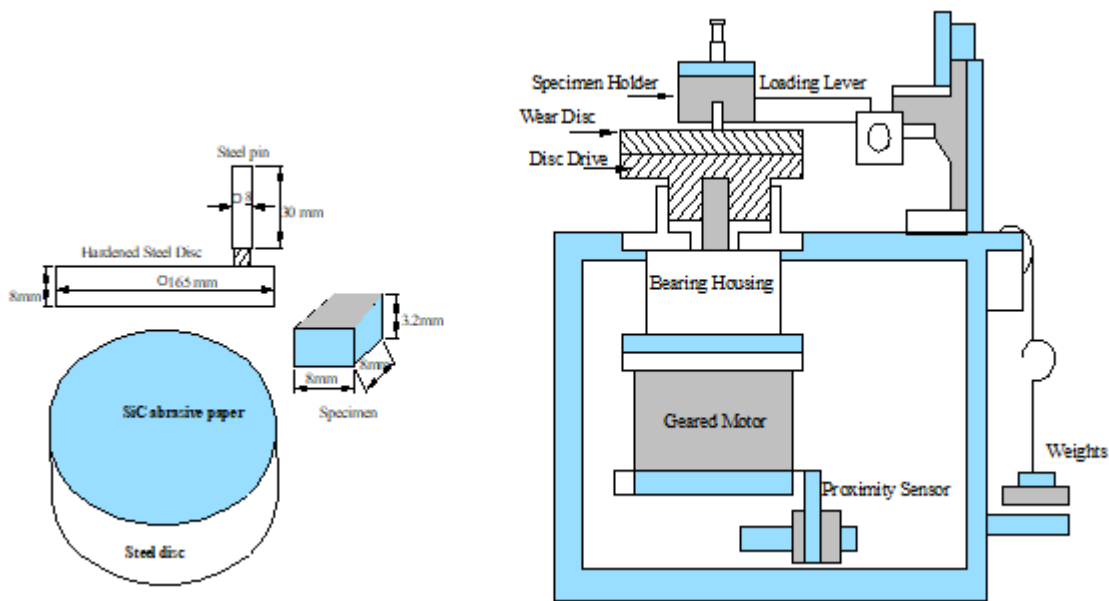


Fig. 1. Set up used for two body abrasive wear system: Pin on disc machine and specimen dimensions

III. RESULTS AND DISCUSSION

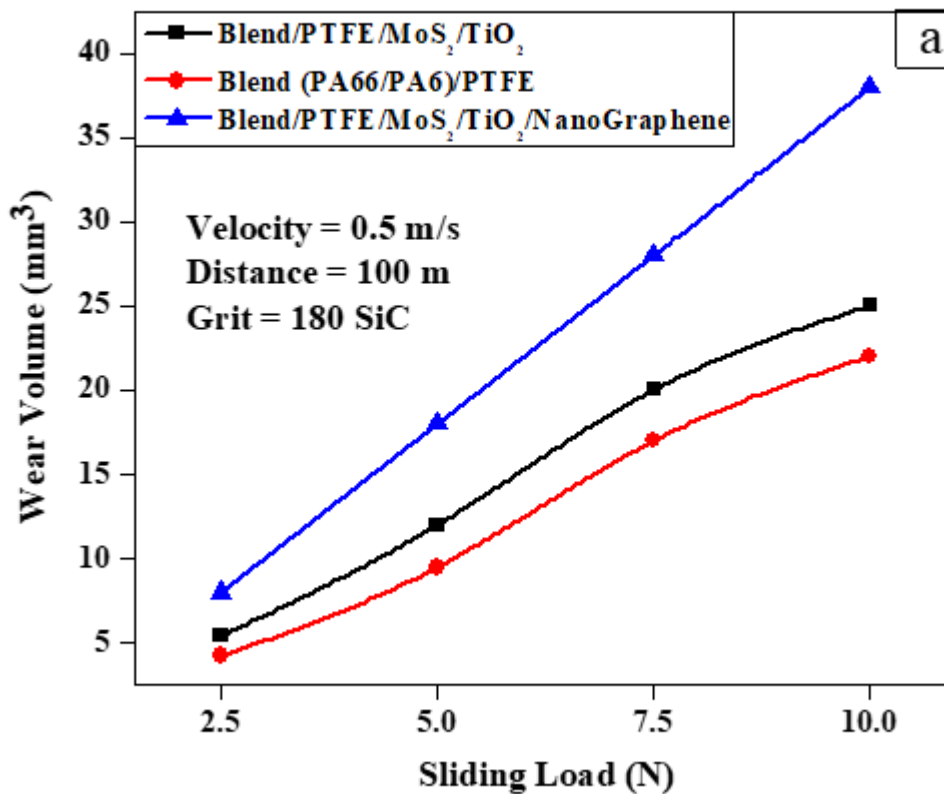
3.1. Two Body Abrasive Wear Behaviour of (PA66/PA6) based Micro and Nano Composites: Effect of abrading load

Figure 2 (a and b) shows the effect of abrading load on 2-BAW behaviour of (PA66/PA6) composites. The abrasion wear behaviour is presented through wear volume loss and specific wear rate (K_s). The two-body abrasion wear behavior was studied for an abrading load ranging from 2.7 to 10 N through an abrading velocity of 0.5 m/s under the action of second body 180 grit size SiC abrasive paper for a distance of 100 m.

The study showed that wear loss of composites increases with abrading load and purely a function of type of fillers used in the development of composites. Figure 2(a) presents the impact of varying abrading load on the abrasion wear volume loss of composites. It is concluded through the figure that nanographene filled composites (U3) has exhibited the highest volumetric wear loss whereas PTFE filled composites (U1) showed the least among the composites tested.

Table 4. Factors affecting 2-BAW behavior of (PA66/PA6) blend composites

Particulars	(PA66/PA6) blend based composites		
	Blend (PA66/PA6) /PTFE (U1)	Blend/PTFE/ MoS ₂ / TiO ₂ (U2)	Blend/PTFE/ TiO ₂ /Nanographene (U3)
Ultimate tensile strength (σ) (MPa)	61.7	61.5	50
% elongation (ϵ)	27.07	16.36	11.47
Factor ($\sigma\epsilon$)	16.702	10.064	5.737
Hardness (H)	76	68	73
$1/\sigma\epsilon$	0.059	0.099	0.174
$1/H\sigma\epsilon$	0.78×10^{-3}	1.46×10^{-3}	2.38×10^{-3}



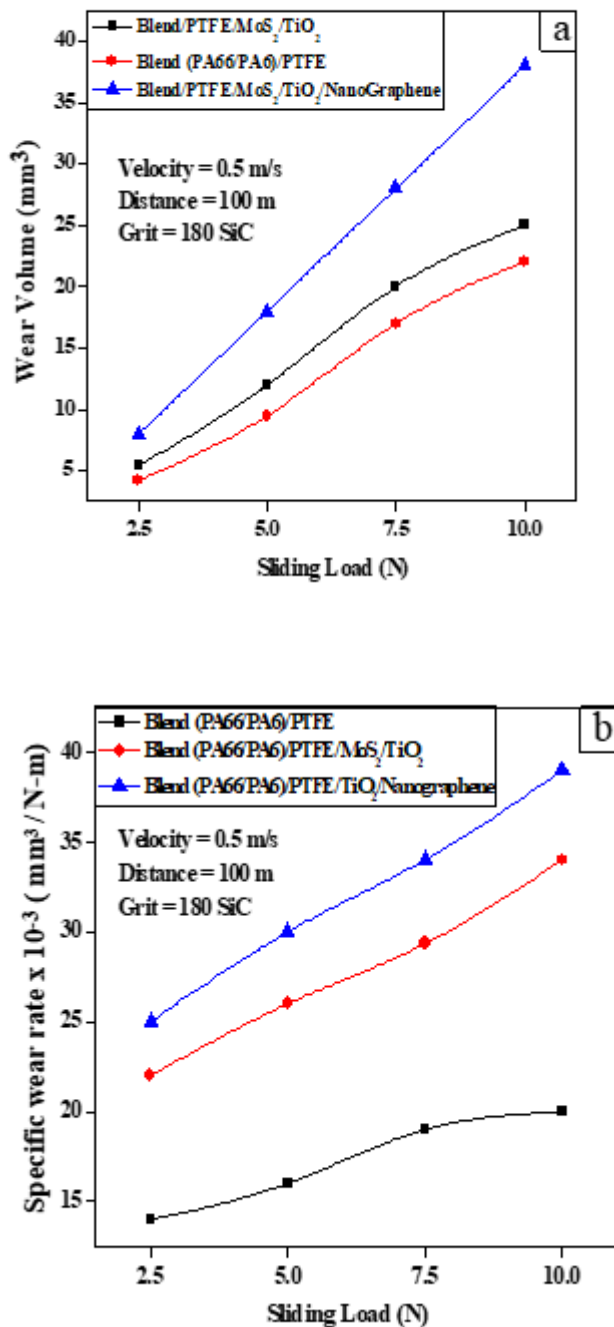


Fig 2: 2-BAW behavior of (PA66/PA6) based composites under the action of varying abrading load through 180 grit SiC: a) Wear volume and b) Specific wear rate (Ks)

The blend (PA66/PA6) /PTFE exhibits the wear loss of 3.5 mm³ under the impact of lesser load of 2.5 N. But at higher abrading load of 10 N, the wear volume loss was 18 mm³. The remaining composites exhibited the same trend under the impact of varying abrasion load. The volumetric loss of 6.5 to 30 mm³ and 8 to 38 mm³ was experienced by U2 and U3 composites respectively between the range of abrading load applied. The study suggested that PTFE filled composites (U1) exhibited the better abrasive wear resistance.

The abrasive wear response of the blend (PA66/PA6)/PTFE as a linear function of abrading load is shown in figure 2 (a). The intensity of SiC abrasive particles was very much effective due to lesser interaction as an effect of lesser abrasion pressure. The minimum contact stresses exist between polymer surface and abrasion particles during interaction. It has been proved at this stage that surface fracture energy of polymers is greater than the fracture energy required by the abrasive grits [9]. The thin polymer film has been spread out across all the abrasive grains on abrasive paper as result of sliding. This action has weakened the abrasion intensity of abrasion grains.

The abrasion wear behaviour of U1 and U2 composites has exhibited the abrasion wear resistance in the order of $U1 > U2$. The abrasion wear behaviour of PTFE filled composites (U1) is seemed to be very appreciable because of the presence of PTFE in composites. At lesser abrasion pressure, the effective wear resistance was shown by the blend. The abrasion effect at this condition has been compensated by the matrix wear. The filler volume fraction is found to be the one of the significant factors to enhance the abrasion wear resistance [10,7]. The lesser abrasive pressure leads to repetitive matrix deformation in the same wear track. These results in accumulation of wear debris in the gap between the abrasive grains as a result of clogging [11]. These clogged wear debris completely nullify the intensity of abrasive grains which may lead to exhibit lesser volumetric wear loss. This is due to the fact that sharp abrasive particles have ploughed PTFE and dragged it in the form of fibrils on to SiC abrasive surface. The microploughing of deformed matrix has transferred the polymer substance on to the abrasive paper. Therefore, the effect of abrasives reduces and hence the penetration effect decreases which results in poor material loss. Further, the fracture energy ($\sigma\epsilon$) of "U1" composites is greater compared to other composites [12,13]. Therefore, high abrasion wear resistance.

TiO₂ filled composites (U2) showed poor abrasion resistance due to brittle phase. Adding TiO₂ in to 'U1' composites significantly reduced the ductility of "U2" composites which is the abrasion resistance promoting parameter. At lesser abrasion pressure, deformation and micro ploughing of matrix has been resulted because of sharp abrasive SiC particles. But the material loss was less due to effective synergism between micro fillers. But as the load increases, the penetration of abrasive particles with high pressure increases wear of composites. The clogging process was completely eliminated due to the presence of hard fillers. These hard fillers supported the abrasive surface to improve the effect of penetration. High abrasive load further removed the material resulting in high wear volume loss. The fracture energy required to pull out the abrasives from the abrasive surface was less and therefore, high wear volume loss. Agglomeration of fillers has further supported the microploughing and cutting action to promote abrasive wear volume loss [13]. Among the filled composites studied, the abrasive wear resistance was exhibited in the order of $U1 > U2$.

The abrasion wear behaviour of nanographene filled composites (U3) seemed to be worse compared to all other composites studied. Nanocomposites have experienced high volumetric loss because of increase in deep penetration and tough contact stresses due to increased abrasion pressure. This condition may result in more loss. At lower pressure, high frictional force between the interacting surfaces has created high temperature and results in severe plastic deformation [14,15]. These micro and nano fillers which were transferred to abrasive surface improve the abrasive action of SiC paper. This may promote the wear volume loss. Initially the process of clogging has controlled the wear volume loss. But as the penetration pressure increases, the sharp abrasive particles along with agglomerated micro and nano fillers further removed the material from the polymer

surface [16,17]. Therefore, higher wear volume loss. The abrasivity action of fillers was improved due to micro and nano fillers inclusion. This has impaired the abrasion wear resistance of nanocomposites [18,19]. Among the composites studied, nanocomposites have exhibited the least abrasion wear resistance.

The 'Ks' of (PA66/PA6) blend based composites under the impact of varying abrasion load is depicted in figure 2 (b). The study reports that 'Ks' of (PA66/PA6) based composites enhances with increase in abrasion pressure. This is because of increase in abrasion effect with the addition of hard fillers. When the load increases, the abrasion efficiency of the grains decreases due to repetitive contact stresses. The wear rate increases due to disintegration extended by these fillers. When the abrasion pressure was less, wear rate impairs due to weakened abrasive grains as a result of clogging. The behaviour of the composites matches with similar work [5,6,20]. The specific wear rate of U1 varied from $14 \times 10^{-3} \text{ mm}^3 / \text{N-m}$ to $20 \times 10^{-3} \text{ mm}^3 / \text{N-m}$ increases as abrading load increases. Similar observations are made with other filled composites. The wear rate ranges from $22 \times 10^{-3} \text{ mm}^3 / \text{N-m}$ to $34 \times 10^{-3} \text{ mm}^3 / \text{N-m}$ and $25 \times 10^{-3} \text{ mm}^3 / \text{N-m}$ to $39 \times 10^{-3} \text{ mm}^3 / \text{N-m}$ respectively for U2 and U3 composites. The reinforced fillers made the materials to exhibit high wear rate. The fracture energy ($\sigma\epsilon$) of "U1" composites is high because of the presence of ductile PTFE (Table 4). From the study, it is clear that 'U1' composites exhibit least wear rate.

3.2. Worn surface analysis using SEM

Figure 3 (a – c) shows the SEM images of failure surfaces abraded against 180 grit SiC abrasive paper under high abrasion pressure. The abrasive wear behaviour indicates that microploughing, microcutting and microcracking phenomenon were held responsible for poor abrasion wear resistance. The combined action of aforesaid mechanisms tends the material to experience more wear loss.

The worn surface of PTFE filled composites is shown in the figure 3 (a). The plastic deformation is seemed to be small. Further, the fibrils of PTFE were projected out of deep wear track showing microploughing process. Figure shows microploughing process is dominant over micro cutting. This is because of the ductile nature of PTFE. The sharp penetration of abrasives is not seen in the figure. The plastic deformation along with the frictional effects are seen in the picture.

The SEM image of the abraded surface of TiO_2 filled composites (U2) is shown in the figure 3 (b). Here the deep penetration of the abrasives has ploughed the matrix deeply and deep micro cutting action is noticed. The surface exhibits the abrasive nature and micro cutting action is dominant. The feathery like debris are projected out of the wear track as result of deep ploughing. The matrix deformation is severe due to heavy penetration of the abrasives along with the micro fillers. The surface exhibits the pure abrasive nature as a result of disintegration of micro fillers. The SEM image of the nano graphene filled nano composites (U3) is shown in the figure 3 (c). Here the deep wider wear track is seen as a result of microploughing.

The matrix deformation is seemed to be severe due to heavy abrasion action [20]. The agglomerated fillers have avoided the projection of wear debris from the wear surface. Microploughing and micro cutting are found to be dominant mechanisms. Further, fatigue is one among the failure mechanisms. It is witnessed because of deeper deformation of the matrix. Micro cutting action has left the wear debris across the surface. The deep ploughing action is noticed as a result of combined action of abrasion both by fillers and abrasives. Among the

SEM images studied, nano composites have exhibited the severe abrasion surface with micro cut wear debris [12,13].

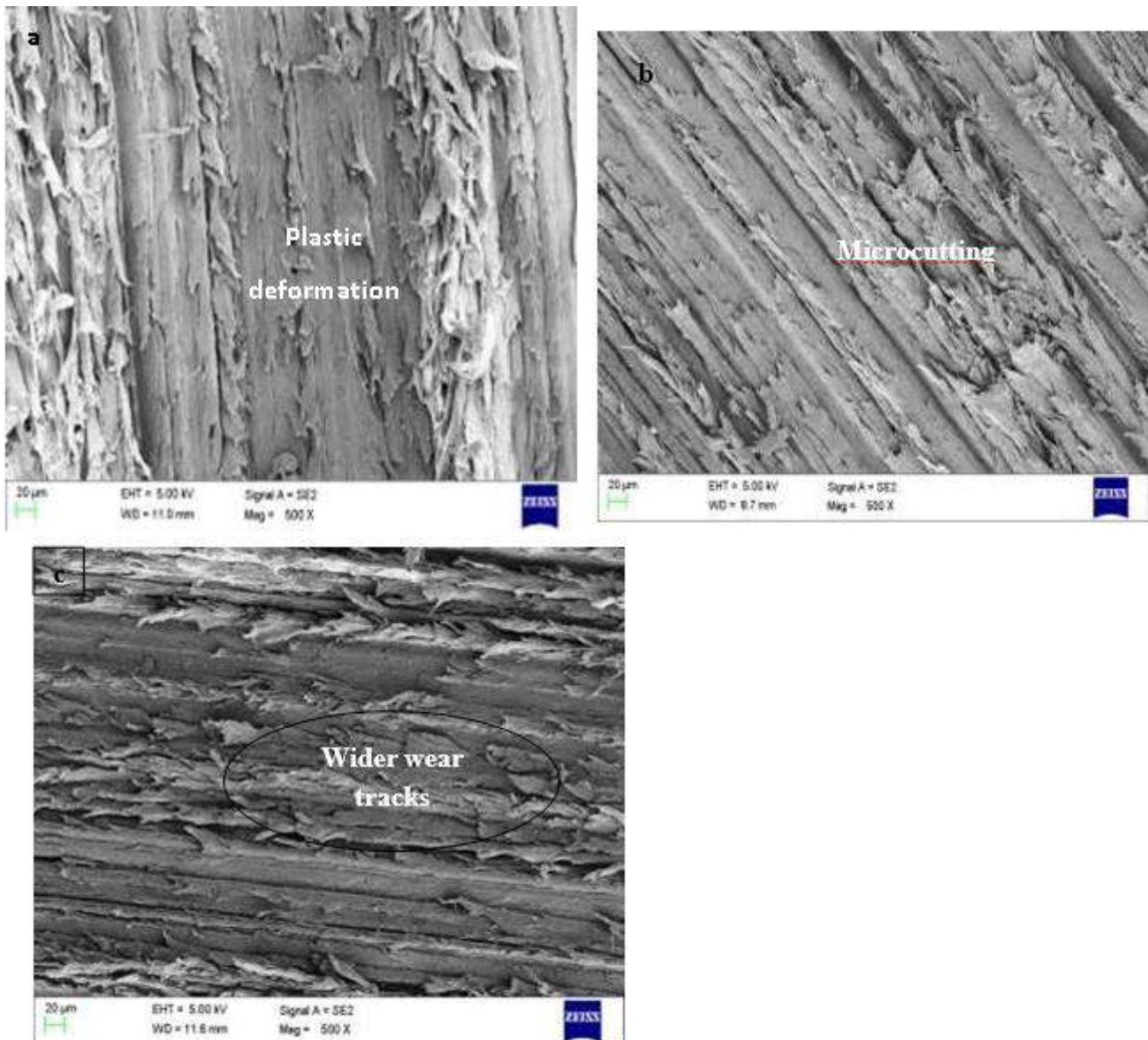


Figure 3: 2 - BAW behaviour of (PA66/PA6) blend composites under the action of 180 grit size abrasives at higher abrading load of 10N: a) Blend (PA66/PA6)/PTFE, b) Blend/PTFE/MoS₂/TiO₂ and c) Blend/PTFE/MoS₂/TiO₂/Nanographene

IV. CONCLUSION

The tribological behaviour of (PA66/PA6) micro and nano composites was studied using 2-BAW behaviour. The specific wear rate of composites tested increases with increase in sliding load. The 2-BAW behaviour of blend (PA66/PA6)/PTFE composites was improved by the addition of PTFE under all the conditions of abrasion test parameters. Blend (PA66/PA6)/PTFE composites exhibits better 2-BAW resistance among all the

composites tested. Addition of MoS₂, TiO₂ and Nanographene slightly impaired the abrasion wear behavior of blend (PA66/PA6)/PTFE /MoS₂/ TiO₂ and blend (PA66/PA6)/PTFE /MoS₂/ TiO₂/Nanographene composites. Among composites studied, blend (PA66/PA6)/PTFE /MoS₂/ TiO₂/Nanographene composites exhibit the least abrasion wear resistance in all the test conditions. It is proved that the synergistic effect of micro fillers is detrimental to 2-BAW behavior of composites tested. The SEM micrographs observations revealed that micro cutting, micro ploughing, fatigue was some of the failure mechanisms observed during the morphological study of the worn surfaces.

V. REFERENCES

- [1]. Nirmal N D, Belkar S B, Tajane K P, "Tribological behavior of Polyamide 66 Blend with GF, PTFE and CNT in Journal bearing Application", IJRASET, vol. 8, pp. 595-600, 2020.
- [2]. Mani Deep. Nomula, Shaik Himan Saheb, U Sandeep Prasanth, "Investigation of Abrasive Wear Properties of Graphite Reinforced PA66 Polymer Composites", International Journal of Recent Scientific Research, Vol.6, Issue 4, pp 3272-3279, 2015.
- [3]. Rudresh B M, Ravikumar B N, Madhu D, "Impact of Grit Geometry on the Abrasion Wear Behavior of Glass-Basalt Hybrid Thermoplastic Composites", International Research Journal of Engineering and Technology, 7 (2020) 280-287.
- [4]. A. A. Cenna, J. Doyle, N. W. Page, A. Beehag and P. Dastoor, Wear mechanism in polymer matrix composites abraded by bulk solids, *Wear*, 240 (2000) 207-214
- [5]. B. Suresha and B. N. Ravi Kumar, Two body abrasive wear behavior of particulate filled polyamide66 and polypropylene nano composites, *Journal of Applied Polymer Science*, 119 (2011) 2292-2301
- [6]. J. Bijwe, C. M. Logani and U. S. Tewari, Influence of fillers and fiber reinforcement on abrasive wear resistance of some polymeric composites, *Wear*, 138 (1990) 77-92
- [7]. A. Mimaroglu, U. Sen and H. Unal, Abrasive wear volume maps for PA6 and PA6 composites under dry working conditions, *Applied Composite Materials*, 15 (2008) 13-25
- [8]. U. S. Tewari, J. Bijwe, J. N. Mathur and Indusharma, Studies on abrasive wear behavior of carbon fiber reinforced polyamide composites, *Tribology International* 25(1) (1992) 53-60
- [9]. B V Lingesh, B N Ravi Kumar, B M Rudresh, "Investigation on the effect of grit size on two body abrasive wear behavior of Polyamide66/Polypropylene (PA66/PP) blends", *Materials Today Proceedings*, 5(2018) 2444-2452
- [10]. B. N. Ravi Kumar, B. Suresha, and M. Venkataramareddy, Effect of particulate fillers on mechanical and abrasive wear behavior of PA66/PP nano composites, *Materials and Design*, 30 (2009) 3852-3858
- [11]. A. P Harsha, An investigation on low stress abrasive wear characteristics of high performance engineering thermoplastic polymers, *Wear*, 271 (2011) 942-951.
- [12]. Navin Chand, Ajay Naik and Somit Neogi, Three- body abrasive wear of short glass fiber polyester composite, *Wear*, 242 (2000) 38-46
- [13]. Sudhirkumar and Pannerselvam, Two-Body abrasive wear behavior of Nylon 6 and glass fiber reinforced nylon 6 composite, *Procedia Technology*, 25 (2016) 1129- 1136

- [14].J. K. Lancaster, Polymer based bearing materials: The role of fillers and fiber reinforcement, *Tribology*, 5 (6) (1972) 249-255
- [15].N. Mohan, S. Natarajan, S. P. Kumaresh Babu and Siddaramaiah, Investigation on two body abrasive wear behavior of silicon carbide filled glass – fabric epoxy composites, *Journal of Minerals and Material Characterization*, 9(3) (2010) 231-246
- [16].N. S. M EI-Tayeb, Two-body abrasive behavior of unsaturated SC and R-G fibers polyester composites, *Wear*, 266 (2009) 220-232
- [17].Horst Czichos, Influence of adhesive and abrasive mechanisms on the tribological behavior of thermoplastic polymers, *Wear*, 88 (1983) 27-43.
- [18].A. A. Torrance, The effect of grit size and asperity blunting on abrasive wear, *Wear*, 253 (2002) 813-819
- [19].S. Bose and P.A. Mahanwar, Effect of particle size of filler on properties of nylon- 6, *Journal of Minerals and Materials Characterization*, 3(1) (2004) 23-31.
- [20].H. Sin, N. Saka and N.P. Suh, Abrasive wear mechanism and the grit size effect, *Wear*, 55 (1979) 163-190



Determination of Optimum Pressure Loss Coefficient and Flow Distribution at Unsymmetrical Pipe Trifurcation Using Experimental and Numerical Technique

Basappa Meti¹, Nagaraj Sitaram²

¹Assistant Professor, Govt. Engineering College, Haveri 581110, Karnataka, India

²Professor, Department of Civil Engineering, East Point College of Engineering, Bangalore, Karnataka, India

ABSTRACT

The branching of pipes is common in water distribution system and penstocks of hydroelectric power plants. Hydraulic analysis is needed to optimize the head losses occurring pipe junctions. Junction introduces extra energy losses due to changes in the flow direction and magnitude of velocity and flow rate and separation the flow at the sharp corner.

The flow prediction at pipe trifurcation due to combining streamlines, curvature, turbulence, anisotropy and recalculating region at high Reynolds number is complex. An attempt is made to study experimentally and numerically, the pressure loss ($K = \Delta P$) for unsymmetrical (15o-45o, 30o-15o and 35o-20o) pipe trifurcation, by controlling of line pressure from 50 KPa. to 300 KPa. at inlet. It is found that the turbulence and unequal angle of trifurcation are the main reasons for losses and separation of flow. The combined trifurcation loss coefficient (K) and branch loss coefficients (K₁₂, K₁₃, K₁₄) have been correlated between split flow ratios (Q₂/Q₁), (Q₃/Q₁), (Q₄/Q₁) and energy ratio (E₂/E₁, E₃/E₁, E₄/E₁, E_{out}/E₁). The experimental findings suggest, the overall trifurcation loss coefficient (K) is more for higher angle of the trifurcation and the head loss will be optimum, when the rate of flow in branches is nearly equal.

Keywords: Trifurcation, split flow ratio, optimum loss co-efficient.

I. INTRODUCTION

Pipe networks are very common in industries, water supply schemes where fluid or gases to be transported from source to the receiver. The trifurcation junction is a part of the hydroelectric plant, which together with other parts and equipment has the purpose to produce electricity using the hydraulic potential. The losses must be reduced to obtain the best operating condition, with stable flow. These conditions can be known from tests in preliminary models to obtain appropriate geometries, with controlled load losses and variations of flow supplying the turbines.

The pressure loss may vary depending on the type of components in the network, material of the pipe, fluid that is being transported through the network, pipe fittings, and placement of valves, pumps, turbines and geometry pipe fittings. Minor loss is a term used to describe losses that occur in fittings, expansions, contractions etc. Fittings commonly used in the industry include bends, tees, elbows, unions, valves and branching. The branching of flow in to streams of different velocities in turbulent region with high Reynolds number results in the exchanges of fluid momentum, energy transfer from low to high velocity. There is a need for flow parameter to account for the distribution of flow between the junction legs.

Albert (2003) presented that, in the power plant sever power oscillations were encountered at the outer turbine in the range of +/-10% of nominal power. Vortex instability forming in the sphere starting at the top and extending in to the side branch after a certain period it changes it behavior and extends to the opposite side branch and after some time jumps back, this unpredicted movement of the vortex causes power fluctuations and head loss in the branch. These losses reduce the head of the turbine and consequently the power output. Further he has recommended that an adaptive turbulence model based on the extended K- ϵ model instead of RANS methods for VLES in pipe trifurcation.

Buntic(2005) presents that the turbulent flows are characterized by transport of the large quantities of mass, momentum and energy. Malik (2009) has carried out 3D flow modeling of the trifurcation to find out the most efficient profile of the trifurcation in the given constraints of pressure, velocity and layout.

Bohuslav, has presented the calculation methods of pressure drop in pipe line components such as elbow, tube fittings and various valves etc. The methods are equivalent length method, Crane method loss, coefficient method, Idelchik method and Blevins method and considering the diameter ratio Reynolds Number, he has recommended the Blevins method for wide range of hydraulic parameters. Aguirre has analyzed the CFD tool to determine the loss coefficient in the adduction system type Symmetrical trifurcation, by dividing the geometry in to structure and unstructured volumetric elements, and concluded that hexahedral (structured) mesh is more sensitive to quantify the head losses mean while the tetrahedral (unstructured) mesh shows similar behavior comparing its results with reduced model tests.

II. METHODOLOGY

The experiments were carried out in the closed loop test rig as shown in the Fig.1. The test trifurcation junction was made by GI pipe of 25.4mm diameter main pipe and 19.6mm diameters GI branching with different angle of trifurcation. The branching pipes are carefully joined for required angle of trifurcation. The flow meters are installed at downstream of the pressure gauges in each of the branching to quantify the flow. Valves are installed to control the flow distribution in each of the pipe. The flow was continuous and driven by a volumetric pump of 2HP capacity, supplied by constant head tank. The temperature of the re circulated water is also noted. The water temperature variation during each test run was within +/-0.5°C because of large volume of water in the test rig tank. The pressure gauges, in the main pipe and each of the three branching are installed at 400mm away from the trifurcation junction. The pressure measurements were noted for each leg of the branching pipes to obtain the flow parameters.

III. EXPERIMENTAL RESULTS AND DISCUSSION

The pressure at the trifurcation is reduced due to recirculation at this zone, but there is a small region near the junction where negative pressure is developed due to change in direction of flow resulting in the pressure drop at downstream and increase in the velocity at the outlet.

Figure 3(a): The combined loss coefficient (k) with the split flow ratio (Q_3/Q_1) reaches a common optimum value of 0.35 ($Q_3/Q_1 = 0.4$) and all curves converge at a common optimum split flow ratio of 1.00 with loss coefficient value as 0.6. For unsymmetrical trifurcations the value of loss coefficient is 0.8 in the low Reynolds number region and converges to 0.6 at split flow ratio ($Q_3/Q_1 = 1.0$).

Figure 3(c): The combined loss coefficient (k) with the split flow ratio (Q_4/Q_1) attains a minimum optimum value of 0.45 ($Q_4/Q_1 = 0.4$).

Figure 3(d): Shows that for fully developed flow inlet Reynolds Number (Re_1) is more than 8000, the loss coefficient is independent from the Reynolds Number (Re_1).

Figure 3(e): The branch loss coefficient varies linearly as the velocity in the branch pipe no 3 increases and attains the maximum value of 0.6 when the flow is fully diverted to pipe 3.

The loss coefficient for the branch No 4 for 30 to 40 % of the flow through it varies from 0.4 to 0.86 for symmetrical and unsymmetrical trifurcations. The loss coefficient for the branch No 2 for 30 to 40 % of the flow through it varies from 0.3 to 0.70 for symmetrical and unsymmetrical trifurcations branch angle. It shows that as the angle of trifurcation increases the loss coefficient also increases in parabolic order. The loss coefficient for the branch No 3 for 60 to 70 % of the flow through it varies linearly and is independent of the branch angle and flow ratios.

The numerical model is created using GAMBIT2.4.6 with tetrahedral unstructured mesh of 4 mm size for the standard $K-\epsilon$ model. The boundary conditions were set as the velocity at inlet and the outlet parameters are static pressure, mass flow rate, turbulence, pressure coefficient and mean velocity. The model is run through the commercial software ANSYS FLUENT 15, the predicted loss coefficient is validated with the experimental results.

The CFD output is validated with the experimental results. For the standard $K-\epsilon$ models, the simple algorithm is adapted to couple pressure and momentum equations. The solutions were considered to be converged when the sum of the normalized residuals for all the cells became less than 10^{-5} for the variables.

IV. CONCLUSIONS

The distribution of flow in the pipes has been studied in pipe unsymmetrical trifurcation with different line pressures and flow rates for unsymmetrical trifurcation angles. The experimental results show that the pressure loss coefficient increases with trifurcation angles, and its optimum value is obtained, at 30% split flow ratio in each outer branch and 60 % in the middle branch. The loss coefficient is more in case of unsymmetrical trifurcation when compared with symmetrical trifurcation for same value of flow rate. The loss coefficient is independent for high Reynolds number. The CFD analysis for total pressure, velocity, loss coefficient is validated with the experimental results.

Nomenclature:

Energy Equations: ρ : Density of water 1000 kg/m³, Q_1 : Discharge in main pipe, γ_w : Unit weight of water 9810 N/m³, Q_2, Q_3, Q_4 Discharge in Branching, U_1, U_2, U_3, U_4 : Velocities in main pipe, Velocities in branching, P : Static pressure, $Q_2/Q_1, Q_3/Q_1, Q_4/Q_1$: Split flow ratio, K_{12}, K_{13}, K_{14} , and K : branch loss coefficient and combined loss coefficient, Re_1, Re_2, Re_3, Re_4 : Reynolds Number in main, branching. E_1, E_2, E_3, E_4 : Total Energy in main, branching, θ_1, θ_2 branch angle in degree

V. REFERENCES

- [1]. Albert Ruprecht, Thomas Helmrich, Ivana Buntic, (2003) "Very large eddy simulation for the prediction of unsteady vortex motion ,Conference on Modeling Fluid Flow" (CMFF'03) The 12th International Conference on Fluid Flow Technologies Budapest, Hungary,
- [2]. Blevins RD 1984 Applied fluid Dynamics Hand book Reprint Krieger Publishing Co. USA Bureau of Indian Standards (2009) Guide lines for design of branching in penstocks for Hydro electric project Doc WRD 14(496) C Indian standard criteria for Hydraulic design of Penstocks IS 11625- 1988
- [3]. Bohuslav Kilkovsky Zdenek Jegla, Petr stehlik "Comparison of Different methods for pressure drop calculation in 90o and 180 Elbow" ,Institute of process and Environmental Engineering, Faculty of Mechanical Engineering Brno University of Technology Technicka Brno Czech Republic
- [4]. Buntic I. Helmrich T. Ruprecht A. (2005) "Very large eddy simulation for swirling flows with application in hydraulic machinery" scientific bulletin of the politehnica University of Timisoara Transactions on Mechanics special issue Timisoara Romania.
- [5]. Hoffmann H Roswara RR Egger A (2000) Rectification of Marsyandi Trifurcation, Hydro version, Charlotte.
- [6]. Hyoung Woo Oh Applied Computational Fluid Dynamics published by In tech Janeza 9, Rijeka Croatia .
- [7]. LiuW Long Z, and Chen Q, (2012) Procedure for predicting pressure loss coefficient of duct fitting using CFD (RP 1493) HVAC & R Research 18(6) 1168-1181
- [8]. Malik R K & Paras Paudel (2009) "3D flow modeling of the first trifurcation made in Nepal" (Hydro Nepal Issue)
- [9]. Mays LW(1997) Hydraulic Design hand book Editorial Mc Graw Hills Education New yark USA Miller DS Internal Flow systems 2nd Edition published by BHRA Information services

Equations:

The computation is based on the principle of conservation of mass, momentum and energy.

Expected discharge through each nozzle = $Q/3$.

The inlet energy per unit time = Work done by Pressure per unit time + Kinetic Energy

$$\text{Inlet Energy/ Time} = P_1 Q_1 + \frac{\rho Q_1 U_1^2}{2} \quad (1)$$

$$Outlet\ Energy/Time = \frac{\rho Q_2 U_2^2}{2} + \frac{\rho Q_3 U_3^2}{2} + \frac{\rho Q_4 U_4^2}{2} \tag{2}$$

Blevins (1984)

$$K_{ij} = 0.96 \sin^2 \theta_j + \alpha_j (\cos \theta_j / U_1)^2 + \beta_j U_j / U_1 \tag{3}$$

$$\alpha_j = 0.22 \theta_j \cos \theta_j + 1.2 \sin \theta_j \cdot \sin(60 - \theta_j)$$

$$\beta_j = \{0.00698(45 - \theta_j) + 0.075 A_j / A_1 + 0.0262 \theta_j\} \sin(75 - \theta_j), \theta \text{ in degree}$$

Combined loss coefficient:

$$K = (Q_2/Q_1) \times K_{12} + (Q_3/Q_1) \times K_{13} + (Q_4/Q_1) \times K_{14} \tag{4}$$

Table No 1. Split flow Ratio and Total Energy.

θ ₁ Deg	θ ₂ Deg	Q ₂ / Q ₁	Q ₃ / Q ₁	Q ₄ / Q ₁	E ₁ (Joul)	E _{out} (Joul)	E _{1-out} (Joul)	% los	inle t hea d (m)	hea d loss (m)	E _o ut/ E _{in}	E ₂ (jou l)	E ₃ (j oul)	E ₄ (jou l)	E ₂ /E ₁	E ₃ / E ₁	E ₄ /E ₁
35	20	0.30	0.32	0.38	243.94	101.33	142.61	0.58	11.62	6.79	0.42	21.17	56.77	23.39	0.09	0.23	0.10
35	20	0.32	0.30	0.37	261.26	102.26	159.00	0.61	12.17	7.40	0.39	23.47	55.16	23.63	0.09	0.21	0.09
35	20	0.32	0.30	0.38	243.56	98.24	145.32	0.60	12.06	7.19	0.40	25.16	50.83	22.25	0.10	0.21	0.09
35	20	0.31	0.31	0.38	246.52	96.03	150.48	0.61	12.52	7.65	0.39	23.21	50.83	21.99	0.09	0.21	0.09
35	20	0.33	0.41	0.26	265.20	132.00	133.20	0.50	13.08	6.57	0.50	32.80	79.28	19.91	0.12	0.30	0.08
30	15	0.36	0.34	0.30	255.95	88.94	167.01	0.65	12.58	8.21	0.35	47.33	33.33	7.71	0.18	0.13	0.03

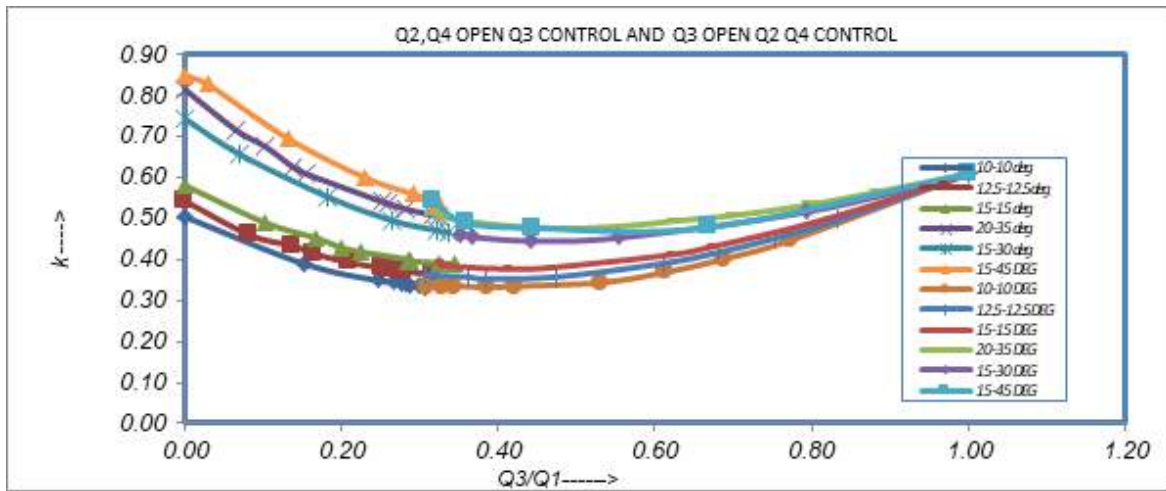
													8 9				
30	15	0.3 6	0.3 4	0.2 9	257.2 5	97. 51	159 .74	0.6 2	12.5 9	7.82	0.3 8	52.0 9	3 7. 9 3	7.49	0.20	0. 15	0.03
30	15	0.3 8	0.3 6	0.2 7	261.2 9	104 .42	156 .86	0.6 0	13.0 6	7.84	0.4 0	56.6 5	3 8. 6 1	9.17	0.22	0. 15	0.04
30	15	0.4 2	0.3 9	0.2 0	260.7 8	129 .32	131 .46	0.5 0	13.5 1	6.81	0.5 0	68.9 0	4 8. 5 0	11.9 2	0.26	0. 19	0.05
30	15	0.4 8	0.4 5	0.0 7	255.6 7	152 .48	103 .19	0.4 0	14.4 1	5.82	0.6 0	86.2 5	6 0. 6 0	5.63	0.34	0. 24	0.02
15	45	0.3 9	0.4 0	0.2 1	117.8 0	50. 85	66. 95	0.5 7	7.63	4.34	0.4 3	4.52	3 6. 3 7	9.96	0.04	0. 31	0.08
15	45	0.4 6	0.4 7	0.0 7	123.2 7	59. 55	63. 72	0.5 2	8.58	4.44	0.4 8	8.66	4 7. 0 6	3.83	0.07	0. 38	0.03
15	45	0.4 7	0.4 8	0.0 5	118.5 9	64. 05	54. 55	0.4 6	8.55	3.93	0.5 4	11.8 4	4 9. 5 9	2.61	0.10	0. 42	0.02
15	45	0.4 7	0.4 8	0.0 4	118.5 5	64. 53	54. 02	0.4 6	8.55	3.90	0.5 4	11.8 0	4 9. 9 2	2.81	0.10	0. 42	0.02
15	45	0.4 9	0.5 1	0.0 0	121.4 8	66. 60	54. 87	0.4 5	9.04	4.08	0.5 5	15.1 2	5 1. 4 8	0.00	0.12	0. 42	0.00

Table No 2. Loss Coefficient and Reynolds Number.

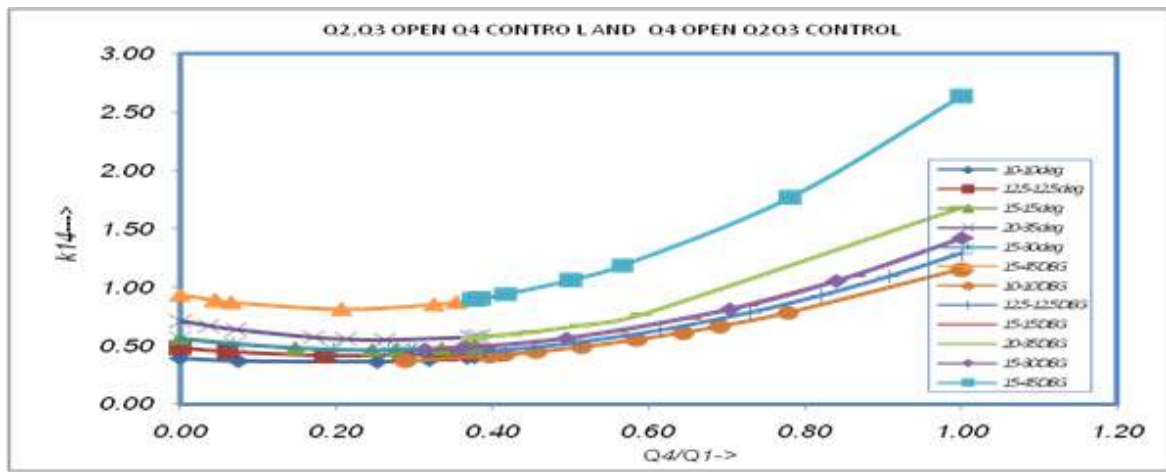
		Blevins formula				Reynolds Number			
θ_1 Deg.	θ_2 Deg.	k_{14}	k_{13}	k_{12}	k	Re_1	Re_2	Re_3	Re_4
35	20	0.57	0.20	0.75	0.51	10745	4465	4710	5546
35	20	0.57	0.19	0.76	0.52	10987	4877	4584	5591
35	20	0.57	0.18	0.76	0.52	10336	4584	4245	5331
35	20	0.58	0.19	0.75	0.51	10071	4271	4245	5282
35	20	0.55	0.25	0.76	0.50	10372	4710	5779	3721
30	15	0.47	0.21	0.71	0.47	10411	5132	4849	4282
30	15	0.47	0.21	0.72	0.47	10458	5225	4908	4193
30	15	0.46	0.22	0.72	0.47	10237	5290	4987	3747
30	15	0.47	0.24	0.75	0.50	9875	5632	5245	2651
30	15	0.52	0.28	0.81	0.55	9077	5954	5623	858
15	45	0.88	0.20	0.47	0.53	8878	3820	4045	4298
15	45	0.86	0.21	0.47	0.51	8548	3820	4088	3801
15	45	0.82	0.25	0.50	0.46	7901	4237	4352	2235
15	45	0.87	0.29	0.54	0.44	7349	4649	4762	657
15	45	0.89	0.29	0.55	0.44	7095	4590	4681	448



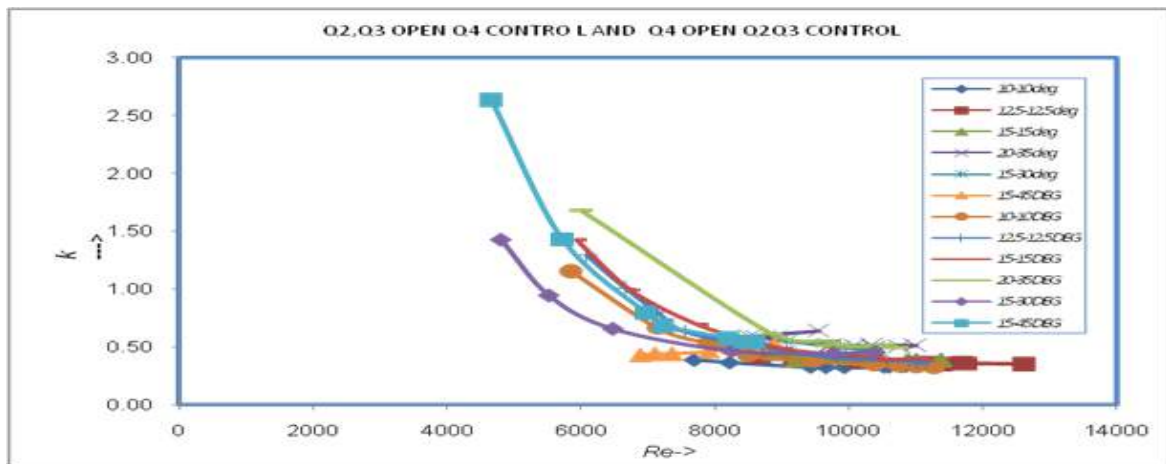
Figure1. Experimental Setup.



2 (a)



2 (b)



2 (c)

Figure 2: (a) Combined loss Coefficient (k) with Split flow ratio (Q_3/Q_1); (b) branch loss coefficient (k_{14}) with split flow ratio (Q_4/Q_1); (c) combined loss coefficient vs. Reynolds Number

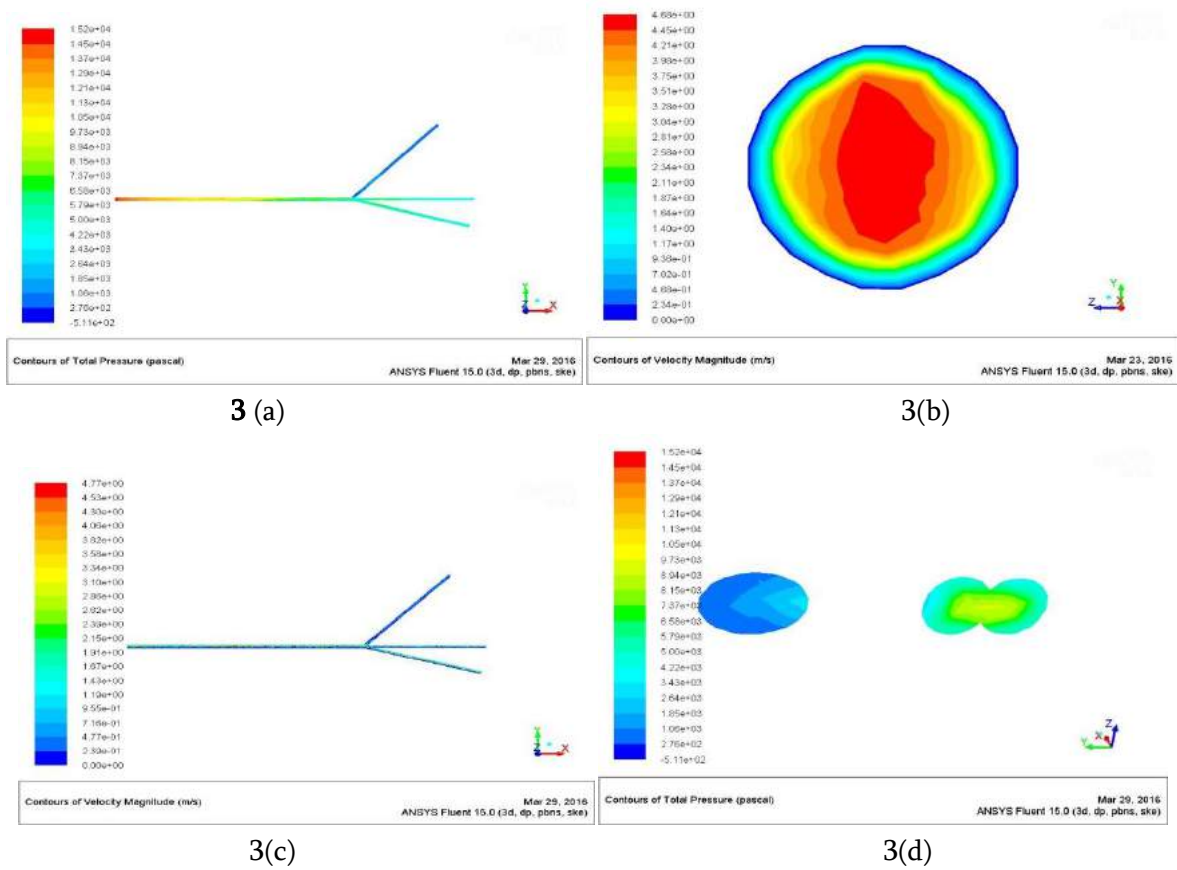


Figure 3: (a) Output total pressure for unsymmetrical trifurcation; (b) Velocity magnitude at inlet of the trifurcation; (c) velocity magnitude at unsymmetrical trifurcation; (d) Total pressure at plane 100mm from the junction for unsymmetrical trifurcation.



Investigation of Various Mg Alloy and Nano Composite for Enhancing Mechanical Properties, Corrosion Protection for Light Weight Component for The Application of Automobile Industry

Amit Tiwari¹, Dr. Neeraj Kumar²

¹Ph.D. Scholar, Department of Mechanical Engineering, Suresh Gyan Vihar University, Jaipur, Rajasthan, India

²Professor & HOD, Department of Mechanical Engineering, Suresh Gyan Vihar University, Jaipur, Rajasthan, India

ABSTRACT

The demand of utilization of Mg alloy and Mg matrix composite in railway and automobile industry. With the rapidly growth of vehicle the fuel consumption increased respectively to solve such issues required light weight material for fuel/energy saving, The aim of this research paper is to identify the possibility of light weight material for railway and automobile components fabrication by using magnesium material. This paper is to summarized the importance of magnesium with the influences of various reinforcement material and Nano composite on the mechanical properties of pure Mg is reviewed.

Keywords: Magnesium alloy, Magnesium matrix Nano composite, Mechanical Properties, Corrosion nature of magnesium alloy, uses of Mg in railway and automobile sector.

I. INTRODUCTION

The aim of this paper is to highlights best suitable material for to provide research direction such as influences of various alloying element on pure magnesium, for the application of magnesium alloy in railway and automobile sector and last but not the least for understanding Magnesium corrosion mechanism. Magnesium is the lightweight of all the elements used as the base material for constructional alloys. [1]Currently automobile manufactures to exchange light material not only steel, cast iron, copper based alloy but aluminum alloy by magnesium composite or magnesium alloy because of its low density. [2]The demand of reducing weight of railway car body and automobile car body has been a major problem in manufacturing industry. Currently lightweight composite material and alloys are trends in world wide of transportation section. It is requirement for pollution and reducing fuel consumption. [3]Due to this industries are now mainly focused on developing light weight material where magnesium demand is so high due to their ultimate properties like low density only two third that of aluminum alloys. Most of the railway car bodies and automobile car bodies are generally

fabricated by aluminum alloys and steel alloy. [4]Weight reduction challenge is the major concern for the researcher who works in the field of aluminum alloy and magnesium alloy or their composites.

Uses of strength and light weight material for the car body of railway and automobile industry can both improve the stress bearing capability during impact or sudden load act on the rail car body. Lots of Aluminum alloy has been developed in some past years for weight reducing purpose but we required advance material which is lighter than aluminum i.e. magnesium alloy and magnesium composite is present demand. The design of reducing weigh of train body or car body needs high strength material with light weight in nature. However the light weight vehicle body is play an important role for enhancing the speed of vehicle. [2]The selection of magnesium as a weigh reducing because of its low density metal (1.8 g/m^3) and its alloy or composite show valuable impact for application in the development in the new light weight high speed rail or automobile car components. [6]The major advantages of magnesium alloy or composite include energy saving, less fuel consumption, better heat distribution and good damping properties. With easy of recycling defend more research and development of Mg alloy and Mg based composites [7,8].

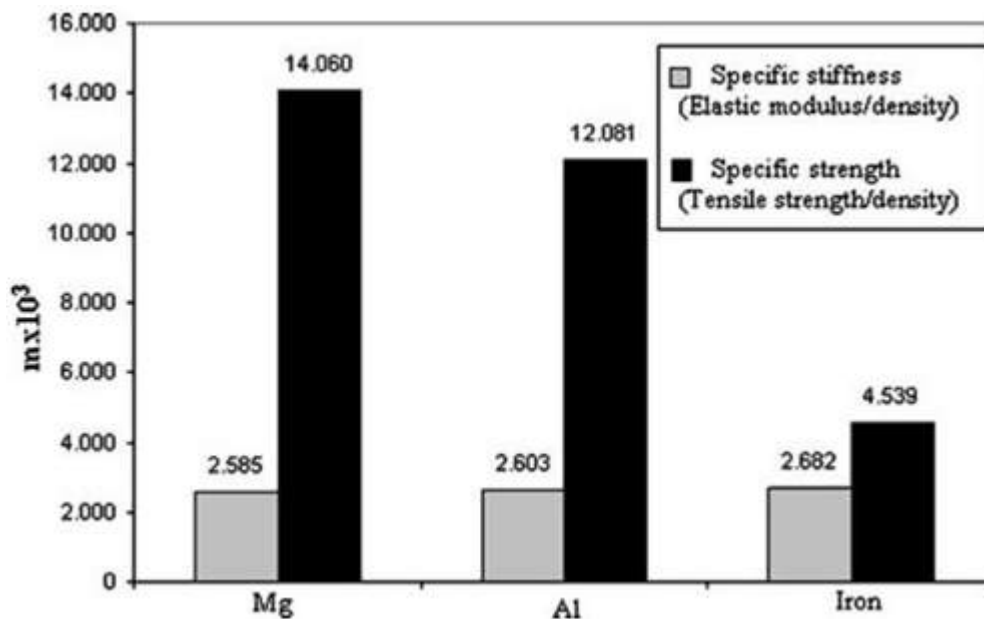


Figure.1: Discussion on general element properties of Mg with Aluminum and Fe.

Composite having reduce weight and good potency would have enhanced performance by various testing [9]. The light weight material in railway and automated application are an excellent substitute as they can enrich the capability of the railway and automobile and also reducing CO_2 emission. [7]The good quality of light weight material having capability to minized the fuel consumption issue. Physical properties of Mg, Aluminum and Fe and mechanical properties of pure Mg are shown in Table1 and Table 2.

Table 1: Physical properties of Mg, Al, and Fe [10,11]

Property	Mg	Al	Fe
----------	----	----	----

Crystal structure	hcp	FCC	Bcc
ρ , at 20°C (g/cm ³)	1.74	2.70	7.86
α , 20–100°C	25.2	23.6	11.7
E, (MPa)	44.126	68.947	206.842
UTS (MPa)	240 (for AZ91D)	320 (for A380)	350
Melting point (°C)	650	660	1536

Table 2: Mechanical Properties of pure Mg at room temperature [6,12,13]

Mechanical Property	Annealed Sheet	Hand Rolled	Sand	Extruded
		Sheet		
Compressive Yield Strength (MPa)	69 to 83	105 to 115	21	34 to 55
Tensile Yield Strength (MPa)	90 to 105	115 to 140	21	69 to 105
UTS (MPa)	160 to 195	180 to 220	90	165 to 205
Hardness (HB)	40 to 41	45 to 47	90	35

Weight reducing of railway and automobile car body can be achieved in many ways like selecting light weight material, design modification by using optimization methods and decreasing numbers of components by exploiting by their multi functionality. [4,14] Currently Mg material have received lot of focused from railway and automobile industries because of low density and more potency than aluminum. Mg alloys and Mg composites are going to utilized in manufacture of railway train car and automobile car. This is dynamic changes of invention in cars body design, material fabrication.

1.1. Problem Statement

Reducing the components weight of railway and automobile industry has been a important problem, minimizing rail body maintenance costs and energy consumption required to drive vehicle, to identify the possibility of light weight material for design a new rail parts and automobile component, so in this research paper we discussed various alloy and Nano particles on the basis of their mechanical strength and corrosion resistance properties for understand the impact of various reinforcement material and Nano particle to help to reducing weight and enhance mechanical strength of the vehicle components.

II. MATERIAL AND METHODS

In this section we discussed on types of magnesium alloys and magnesium composite used in the field of railway and automobile sector for the purpose of reduction in weight of vehicle. The current scenario in the area of railway the magnesium alloy and its composites show their potential for fabricate car body due to good mechanical strength [4,15,16]. The continuous innovation of the high speed railway and demand of light

weight material with good microstructure property can be applied to enhance the quality of rail. Welding is major problem that should be point out in the manufacturing process and repair rail train materials. Manufacturing and welding method provide impact in design of light weight. Figure 2, shows mechanical strength of well manner formed by applying MIG, TIG and friction stir welding and it's proof that the mechanical strength of magnesium alloy and magnesium composite [17]. Mg alloys have two major drawbacks for the application in railway and automobile industry which they having low high temperature strength and comparatively poor corrosion protection. [18] The most important step for enhancing the corrosion obstruction to Mg alloy.

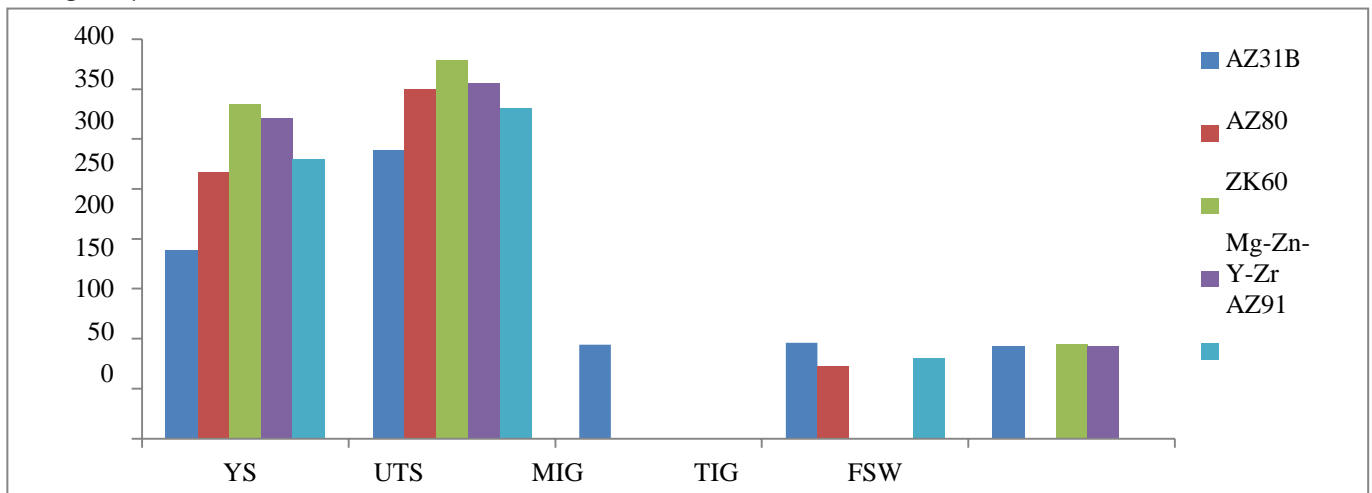


Figure 2: Mechanical Strength and welding techniques give impact in design of light weight Mg Alloy.

Mg-Al alloy one of the most important group among Mg based alloy [17]. The potency of the alloy is enhanced by addition of reinforcement elements in pure form of Mg. [19] With the addition of reinforcement element the composition in (wt%) of each element play an important role for improving strength of base material. [20] As we know that magnesium is reactive material above 650°C magnesium will start to boil or may be burn during casting more it is very tough to handle the situation. There are many form of magnesium alloys has been developed in past year for reducing weight of automobile components. The mechanical potency of Magnesium alloy is also be governed by on at the time of casting the uniform distribution of elements in bases material and the grain size of elements. [13, 15, 21] Some general Mg alloy and their uses are exposed in figure 3. Due to low mechanical potency of pure Mg must be alloyed with other elements to enhance their strength. The Magnesium-Aluminum-Zinc groups of alloy are general alloying elements uses for room temperature. Thorium, Cerium and Zirconium (in absence of Al) are used for dignified temperature form the Mg- Zn-Zr group [22]. Th and Ce is added to enhance mechanical potency at the temperature of 270 °C to 354°C. Al is the most emphatic elements in enhancing results. A small amount of 3% to 9% of Al with minor addition of Zn and Mn enhanced potency and hardness. [23].

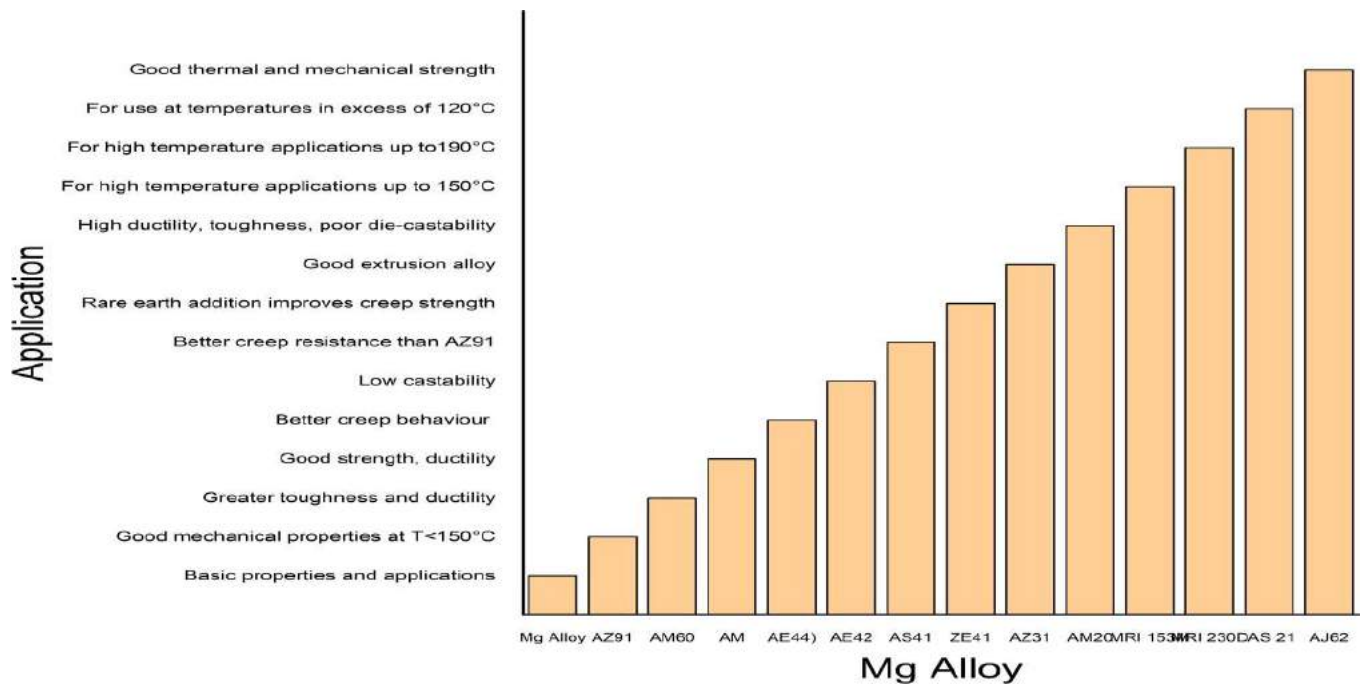


Figure 3: Some common magnesium alloy and their application

In order to reduce the disadvantage of flux additions and to reducing the percentage weight of Fe content in the melt to much lower level [25][26]. The effect of different melt temperature and the arrangement with Mn/Zr addition on the Fe content in the melt of magnesium and its alloy were examined. During 2018-19, heat resistance cast magnesium alloy focused on rare earth containing alloy, mainly Gd covering alloys, [27,28]The mechanical properties of high temperature resistant cast alloy designed are shown in figure 3. The UTS of Mg-Gd-Y-Zr reached 351 MPa at 210°C and 366 MPa at 129°C. On the other hand to increasing the elements of Gd results in high cost which limits its railway and automobile industry [29].

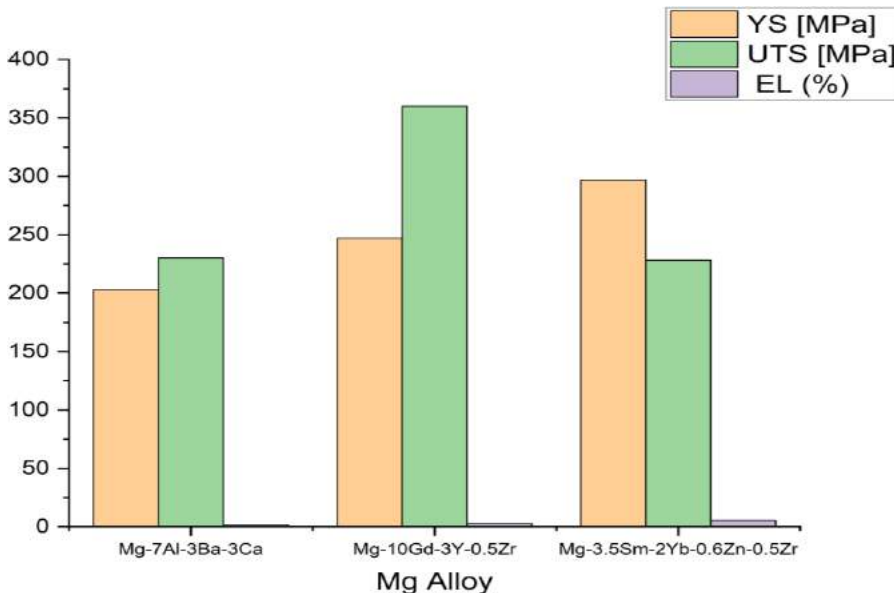


Figure 4: Mechanical Properties of Heat Resistant Cast Alloy

Mingting Chang group fabricated a Mg-3Gd-2Ca (wt %) with a excellent creep properties. During tested they found at 213°C/103MPa for 100h. Diemag633 alloy has excellent strength. Wencai Liu et.al developed Mg- 10 Gd-3Y-0.5Zr with good potency at high and tom temperature which has outstanding heat obstruction property. UTS are 363 MPa, YS 243 MPa and 2.7% elongation respectively. Mg-3.5Sm-2Yb-0.6Zn- 0.5Zr (wt%) alloy was developed by Jian Mang group with enhanced mechanical potency and ductility at elevated temperature, where yield strength 178 ± 3 MPa, a UTS of 274 ± 4 MPa and an EL (%) of 16.8 ± 2 %. In various cast magnesium alloy with high potency were also discussed in Table 3.

Table 3: Mechanical properties of high performance cast Mg alloys at room temperature [11,23,30,31].

Alloy (wt%)	UTS (MPa)	YS (MPa)	EL (%)
Mg-10Gd-1Zn-0.5Zr	315	201	7.6
Mg-10Gd-2Y-1Zn-0.5Zr	359	247	12.3
Mg-12Gd-0.8Zn-0.4Zr	354	-	4.6
Mg-10Gd-3Y-0.5Zr	335	-	4
Mg-2Zn-0.2Y-0.5Nd-0.4Zr	219	95	43

The improvement of low cost Magnesium alloy a cost gives impact in the economical point of view with high potency is requirement of automobile and railway industry to fabricate component but due to addition of some reinforcement alloy the cost will provide impact on manufacturer industry [32]. Some low cost high strength cast magnesium alloy was discussed in Table 4. For this reason the vehicle components price rapidly increased with increasing the labor charges. [33] With the addition of Y, Zn, Nd, Ce, Al, La and Mn all such elements enhanced strength, creep resistance and corrosion resistance also, but most important factor is on how much percentage of elements adding with pure Mg.

Table 4: Mechanical strength of low cost high strength cast Magnesium alloys [34] [13,35].

Alloy (wt%)	UTS (MPa)	YS (MPa)	EL (%)
Mg-5Y	-	-	-
Mg-10Zn-5Al	248	193	6.8
Mg-3.5Al-4.2La-0.3Mn	-	-	-
Mg-1Nd-1Ce-0.5Zn-Zr	231	143	13.5

2.1. Environmental Corrosion of Mg alloy.

A various investigation has been done on corrosion magnesium alloy for enhancing corrosion protection from the environment. [36] One disadvantage of pure form of magnesium is poor corrosion resistance due to this reason a lot of Mg corrosion resistance alloy has been investigated by researchers to find out which alloying elements give high efficient performance to protect material by Mg alloy. [37] Corrosion formation in pure

magnesium was optimized by microstructure with surface roughness occur through Image J software the detail description of microstructure were discussed in result section.

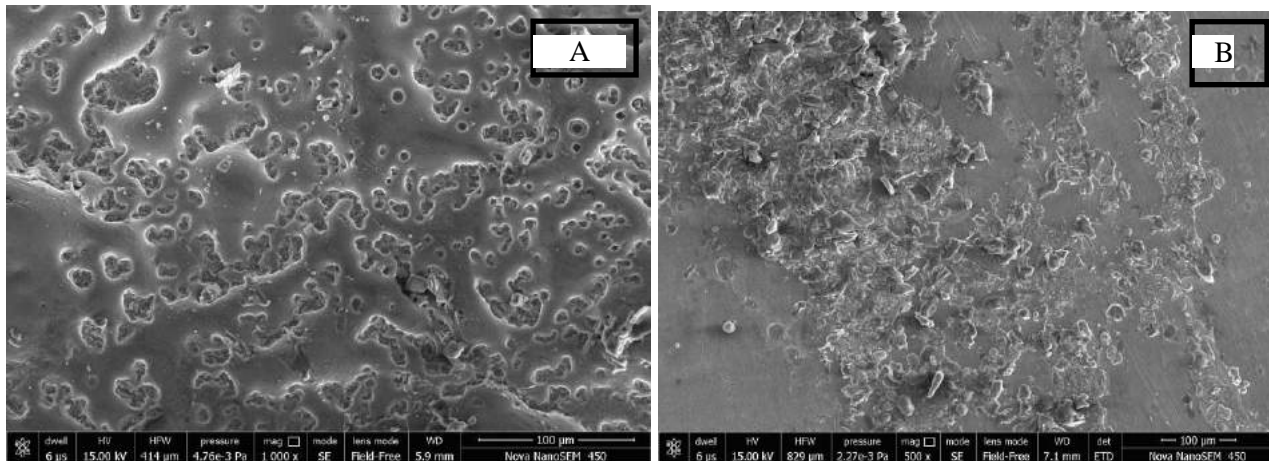


Figure 5: Typical corrosion phase for high purity Mg.

The general form of corrosion in rail is atmospheric corrosion. The holding time of moisture on the surface and the rate of recurrence of wetting and drying determine the severity of atmospheric corrosion.[38] The good feature of atmospheric corrosion is that the resulting corrosion is generally uniform in nature. However economic loss due to corrosion problem is still a major problem world wide. A huge quantity of rail was replacement by new rail due to corrosion problem. Many alloying elements are present in earth which have capability to solve magnesium corrosion problem but toxicity is a major issue of each elements which is discussed the range of toxicity of elements in magnesium by figure 6.

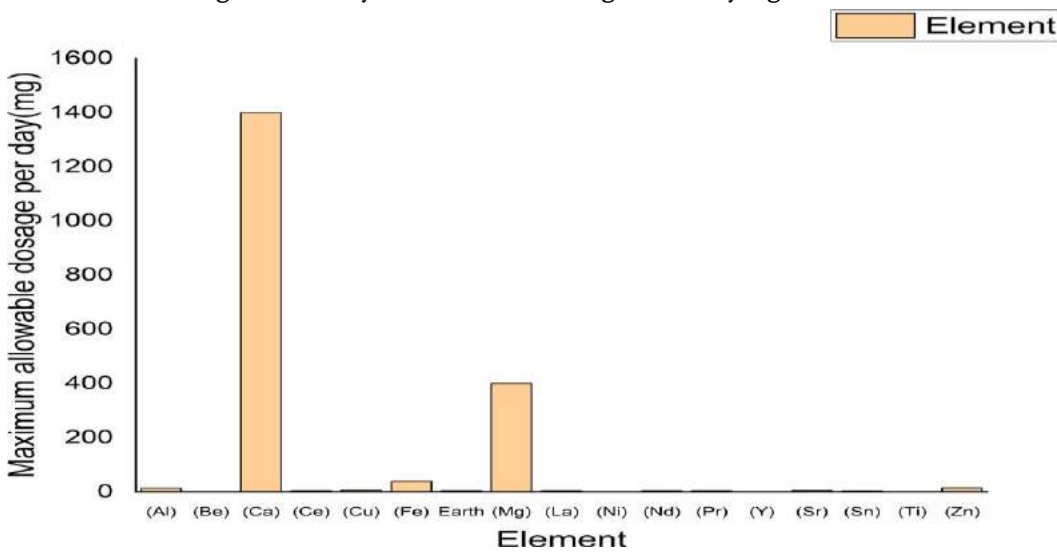


Figure 6: Toxicity of elements for Mg.

The cast Mg has poor mechanical strength and exorbitant degradation rate. The material properties hence, can be improved by mixing correct combination of reinforcement elements and processing technique. [39] Mechanical property of magnesium alloy will also have improved by annealing, rolling and other heat treatment methods with different temperature region. During mixing of alloying elements most important factor to be

considered that each elements having own temperature region where appropriate combination come out with good mechanical strength. The popular elements and their influence of Mg alloy are discussed in figure 7.

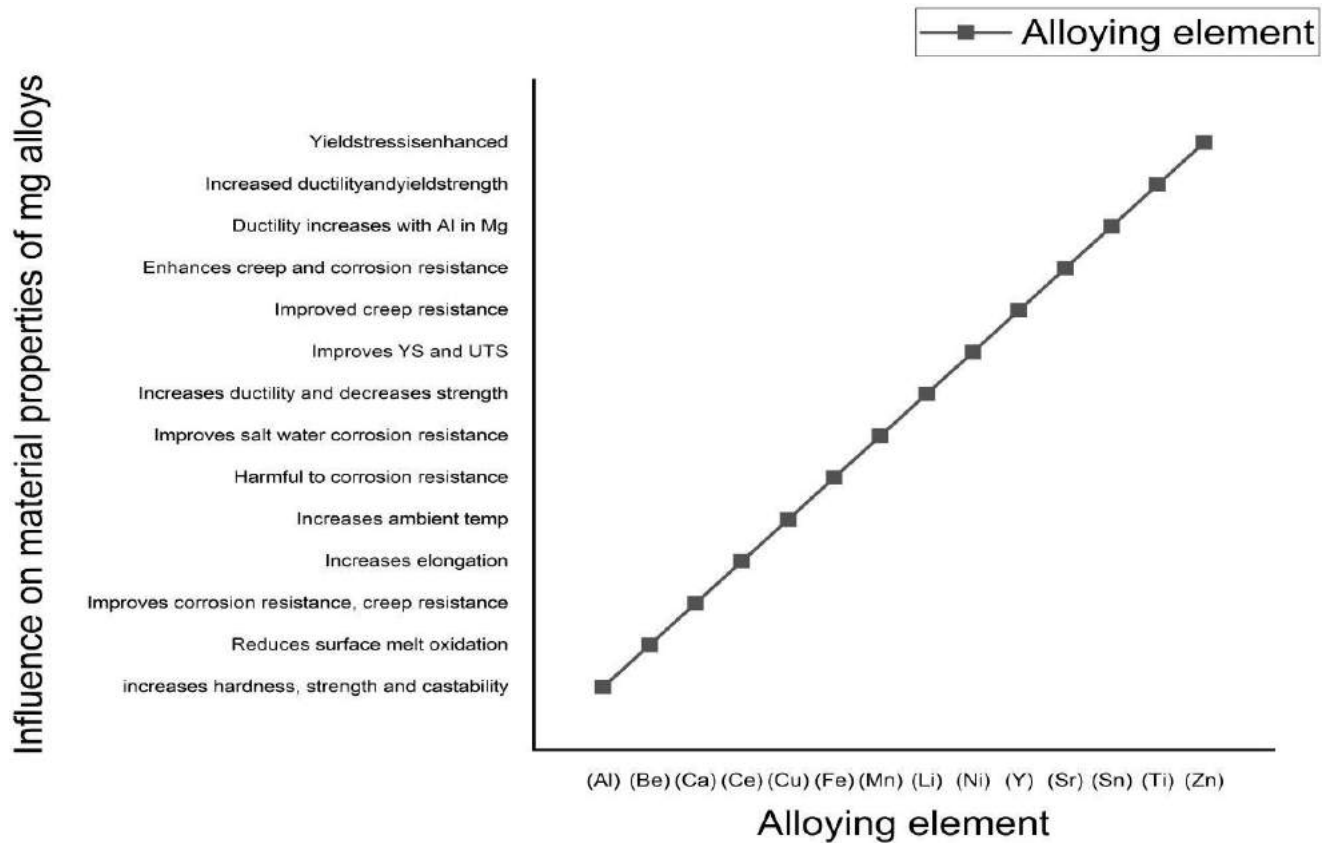


Figure 7: Some Reinforcement elements and their influences on Mg

2.2. Medium Strength Wrought Magnesium Alloy

The deformation mechanism of magnesium alloy depends on a combination of grain size and crystallographic structure. For this reason, to enhance ductility of magnesium alloy, it is not only needs to create a structure containing a mixture of large grain and fine grains but also require weakening the texture of the alloy. [40] Enhancing the ductility at room temperature has been a vital demand for ultrafined grain magnesium alloy. Railway and automobile car body work under the heavy stress due to this material structure should be more powerful to avoid undesirable stresses. A part of enhance material structure internally with combination of correct reinforcement elements with pure magnesium, so some medium strength wrought magnesium alloys are discussed in Table 5. [41] To enhance the strength of Mg alloy some methods should be required i.e. rolling, extraction, annealing etc.

Table 5: The mechanical properties of medium strength wrought Mg alloys.

Alloy (wt%)	Process	UTS (MPa)	TYS (MPa)	EL (%)	Ref.
Mg-2Ca	Hot extrusion	389	375	2.8.0	[43]

Mg-7Zn-0.7Zr-0.7Cu-0.7Ce	Hot extrusion	341	313	22	[44]
Mg-6Al-2.9Sn-1.0Ca	Hot extrusion+ aging	304	234	8.5	[45]
Mg-2.5Zn-3Sm-1Zr	Hot extrusion	289	229	24.1	[46]
Mg-1.6Zn-0.30Zr-0.19Nd	Hot rolling	236	171	26.0	[47]
Mg-3.5Sn-6Zn-0.8Sc	Hot extrusion	279	168	21.5	[16]
Mg-0.6Sn-0.5Y-0.8Zn	Hot extrusion	257	183	30.1	[8]
Mg-6Sn-3Al-2Zn	Hot extrusion	346	230	18.1	[48]
Mg-1.0Sn-0.5Zn-0.5Ca	Hot extrusion	334	109	36.5	[49]
Mg-1.0Sn-0.5Zn-2.0Ca	Hot extrusion	300	184	15.9	[50]
Mg-8Sn-2Zn-0.5Cu	Hot extrusion	390	367	7.8	[9]
Mg-1.1Al-0.33Ca-0.44Mn	Hot rolling	289	276	13.2	[51]

2.3. High Strength wrought magnesium alloy.

The growth of high potency wrought Magnesium alloys with 0.3% proof strength above 310 MPa by grain modification and toughness has acknowledged advanced attention because of high demand to decrease the weight of railway and automobile parts [53]. Currently the yield strength of rare earth alloy sequence has extended 520 MPa and the rare earth alloy sequence has reached 464 MPa.

Table 6: The mechanical properties of typical medium strength wrought Mg alloys at room temperature in 2018–2019.

Alloy (wt%)	UTS (MPa)	TYS (MPa)	EL (%)	Ref.
Mg-8.1Gd-4Y-1Zn	369	300	10.0	[54]
Mg-12Dy-11Ni	328	272	14.7	[20]
Mg-8Gd-3Yb-1.2Zn-0.5Zr	429	410	6.5	[4]
Mg-9.2Gd-3.3Y-1.2Zn-0.9Mn	411	340	7.8	[55]
Mg-8.3Gd-4.2Y-1.4Zn-1.1Mn	392	278	17.4	[11]
Mg-15Gd-1Zn-0.4Zr	520	452	6.0	[56]
Mg-8Gd-1Er-0.5Zr	448	420	5.2	[58]
Mg-7.2Gd-3.9Y-1.5Zn-0.6Zr	438	389	18	[5]
Mg-6Er-3Y-1.5Zn-0.4Mn	334	282	13.7	[10]
Mg-3.6Zn-0.6Y-0.2Ca	351	312	7.4	[60]
Mg-5Al-3.5Ca-1Mn	365	320	14	[61]
Mg-2Sn-2Ca	462	446	1.8	[18]
Mg-5Zn-3.5Sn-1Mn-0.5Ca-0.5Cu	409	390	9	[64]

III. RESULT

3.1. Microstructure Analysis

In the assessment of Magnesium corrosion behavior of magnesium alloy is very limited compared with that of other conventional engineering metals. The contents of hydrogen melt in the Magnesium during corrosion. A corrosion level minor than that of major purity Magnesium is only possible for such a Mg alloy having two phases. If the quantity of second phase is continuous an alloying having a second phase can have a steady state corrosion rate which is below than that of high purity magnesium. Such corrosion is illustrated in Figure 8 and Figure 9.

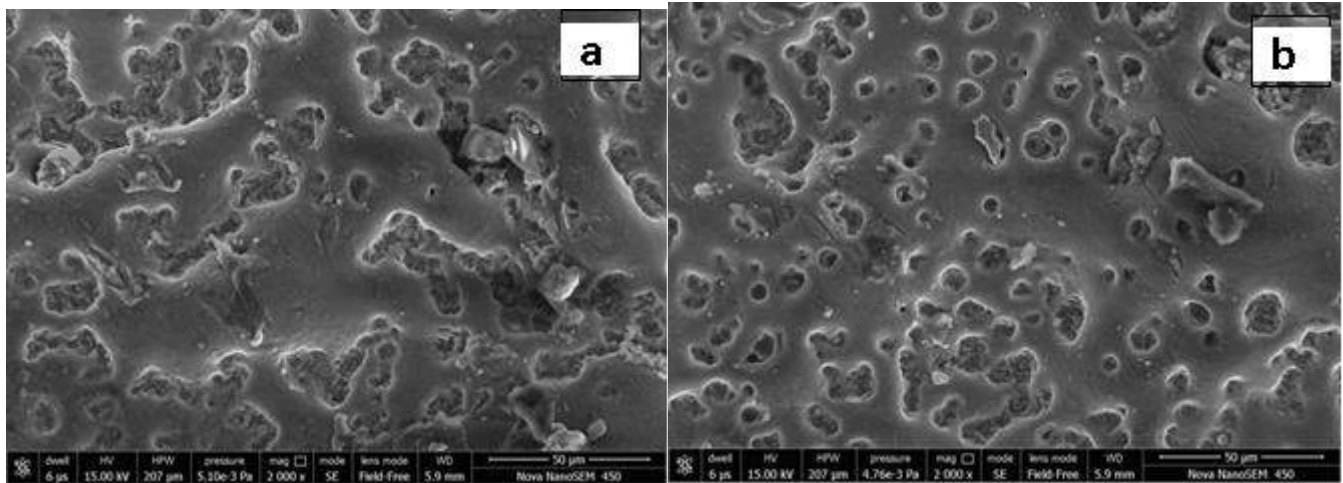


Figure 8: Typical corrosion phase for high purity Mg.

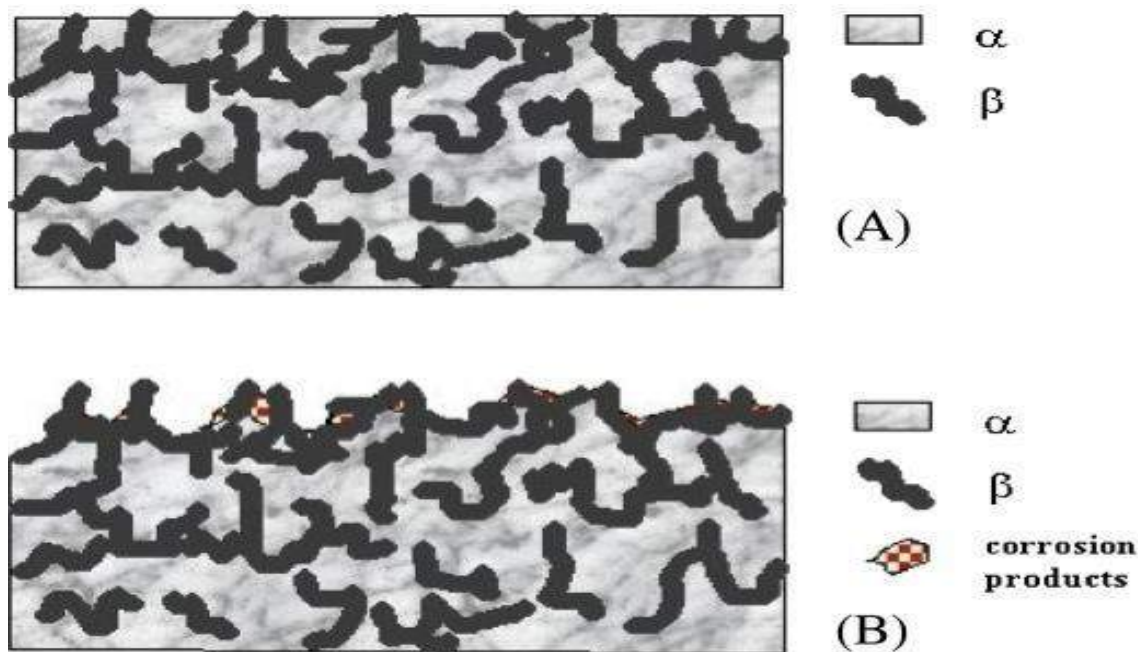


Figure 9. (A) A cross section of Mg alloy containing a continuous second phase (beta) [5]. (B) illustrate the steady state.

In generally, the potency of the magnesium alloy is highly affected by the normal grain size from the Hall Pitch relationship. Figure (10, 11, 12) shows a comparison of the reported value of the extruded commercial magnesium alloys.

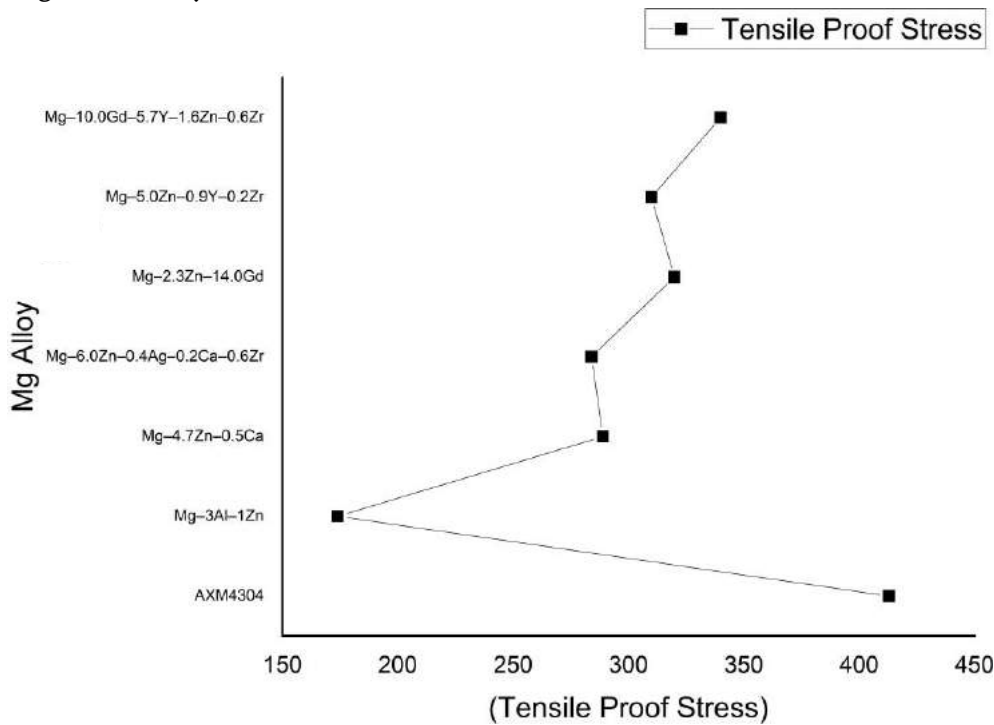


Figure 10: Tensile Proof Stress in [MPa] of Magnesium Alloy

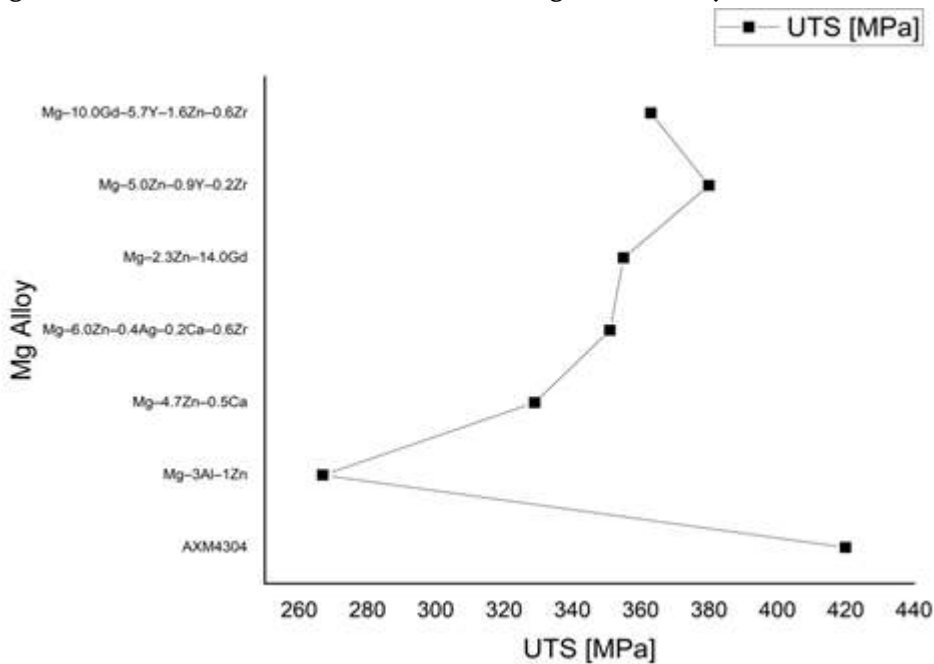


Figure 11: Ultimate Tensile Strength [MPa] of Magnesium Alloy

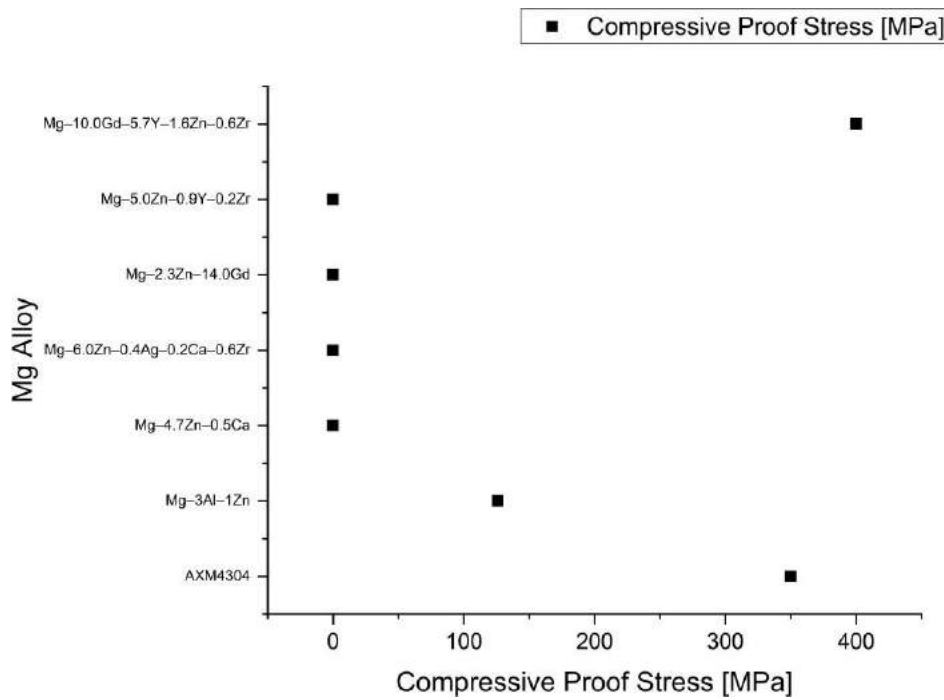


Figure 12: Compressive Proof Stress in [MPa] of Magnesium Alloy

3.2. Magnesium Composite Trends

With the addition of Titanium Oxide (TiO₂) nanoparticles the effect shown to enhance ductility and hardness of pure magnesium. Graphene (GNP) nanoparticles is used for stress enhancement and good corrosion protection with the percentage of 1% (wt), 3 % (wt) and 4% (wt), but above 5% (wt) its increase carbon particles in alloy due to this corrosion properties will be decreasing as increasing GNP particles. In pure form of Mg addition of Manganese Oxide Nano particles it enhancing salt water corrosion protection of alloy, magnesium have tendency to oxidized fast and its high reactive elements, it is required to maintain the temperature of furnace otherwise it will burn with nanoparticles. Tin Oxide Nano particles (SnO₂) enhanced ductility of magnesium and aluminum with increasing compressive strength or corrosion resistance properties. Yttrium Oxide Nano particles give their effect to enhancing creep strength and high temperature resistance, magnesium having low melting point 650°C for fabricate automobile components such as engine block, piston assembly, cooling pipes etc, magnesium alloy or composite should be higher temperature resistance otherwise melting of alloy will be start after reach 650°C. The utilization of Calcium Oxide (CaO) nanoparticles for enhancing corrosion, creep with addition of pure Mg.

Table 7: The mechanical properties of Magnesium matrix composite reinforcement by nanoparticles.

Alloy (wt%)	UTS (MPa)	0.2% YS (MPa)	EL (%)	Ref.
1 vol% nano-SiCp/AZ91	220	83	7.1	[3]
12 vol% SiCp/Mg-4 Zn	-	710	-	[44]
0.7 wt%TiC p /Mg-3Zn-0.7Ca	380	345	10.2	[45]

11 μm M-SiCp/Mg-5Zn-0.7Ca	327	245	6.7	[46]
S-0.4 + M -9 μm SiCp/AZ91	356	320	1.80	[47]
10 μm M-SiCp/AZ91	342	286	1.19	[16]
30-50 nm TiCp/Mg	189	123	19	[8]
50 nm TiCp/ ZK60A	311	182	10.6	[48]

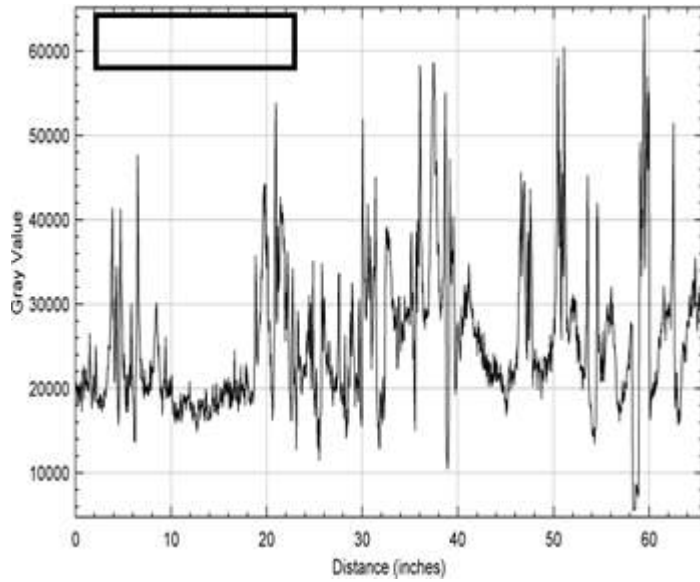


Figure 5: A

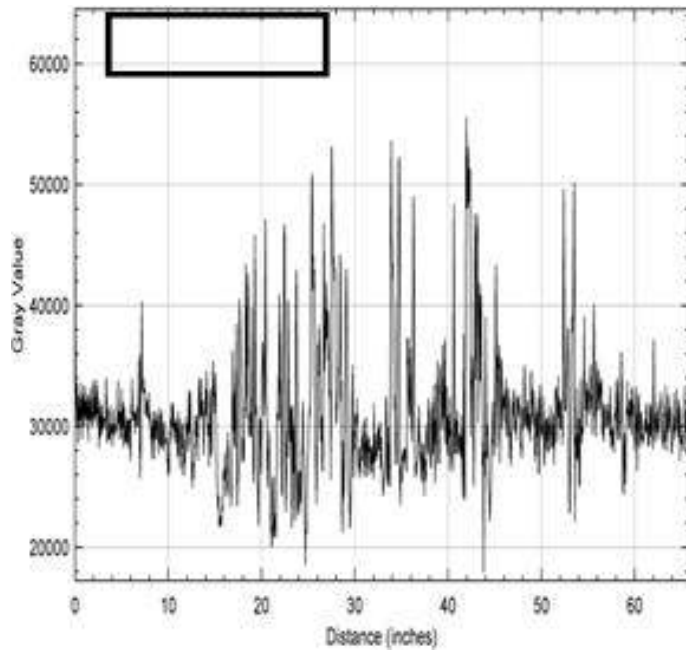


Figure 5: B

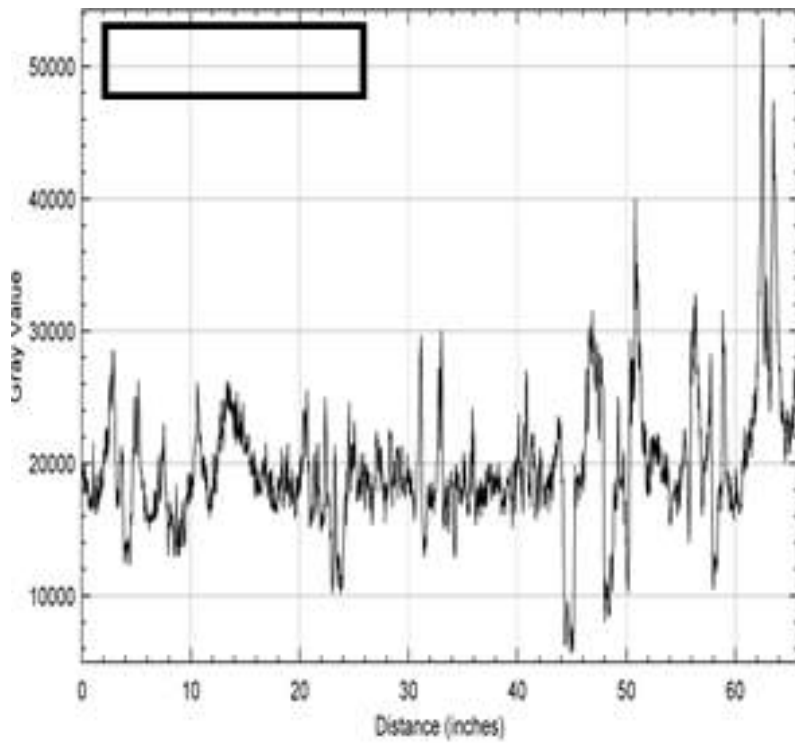


Figure 8: A

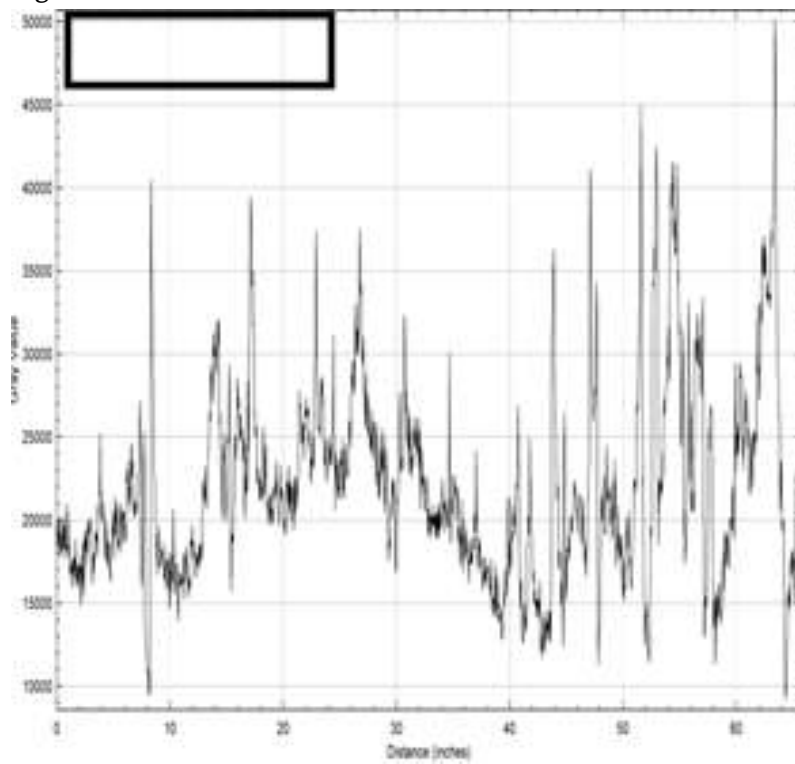


Figure 8: B

Plot 1: Analysis of Profile plot of figure 5 and 8

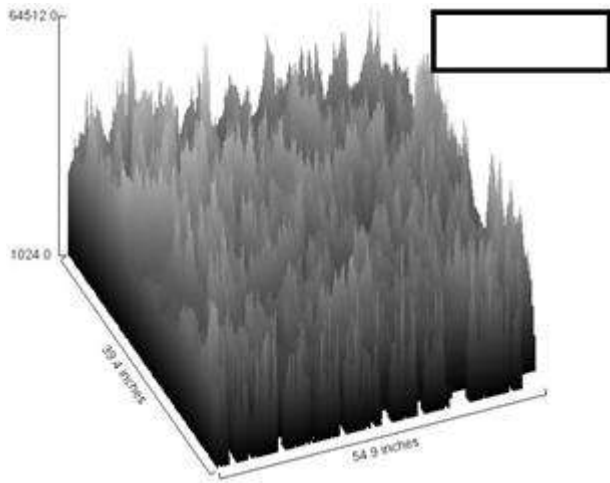


Figure 5: A

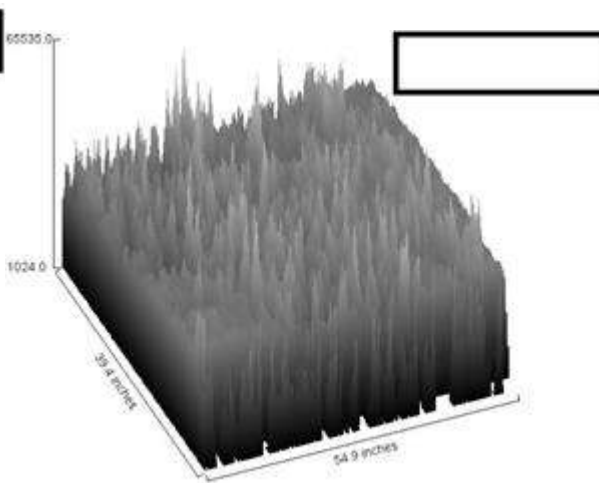


Figure 5: B

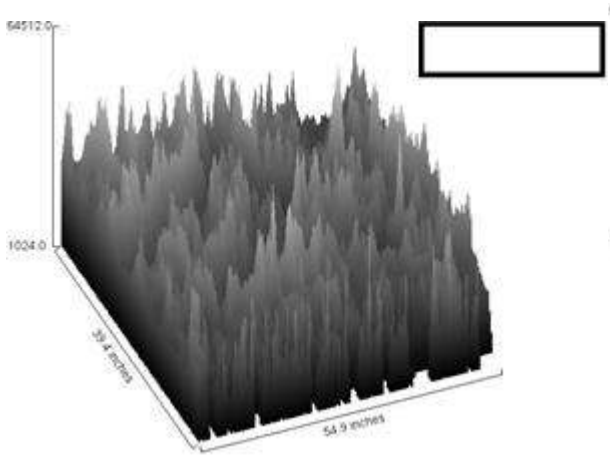


Figure 8: A

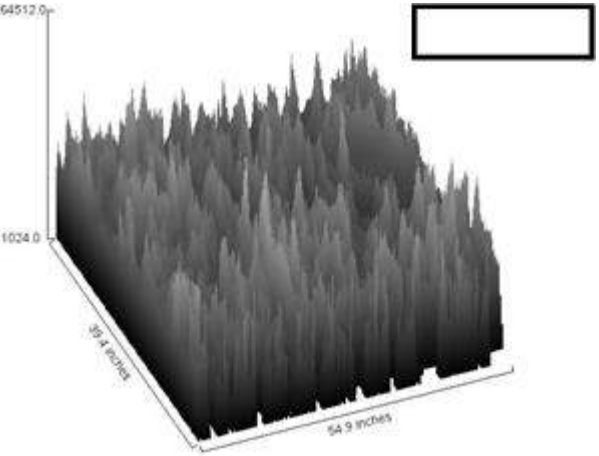
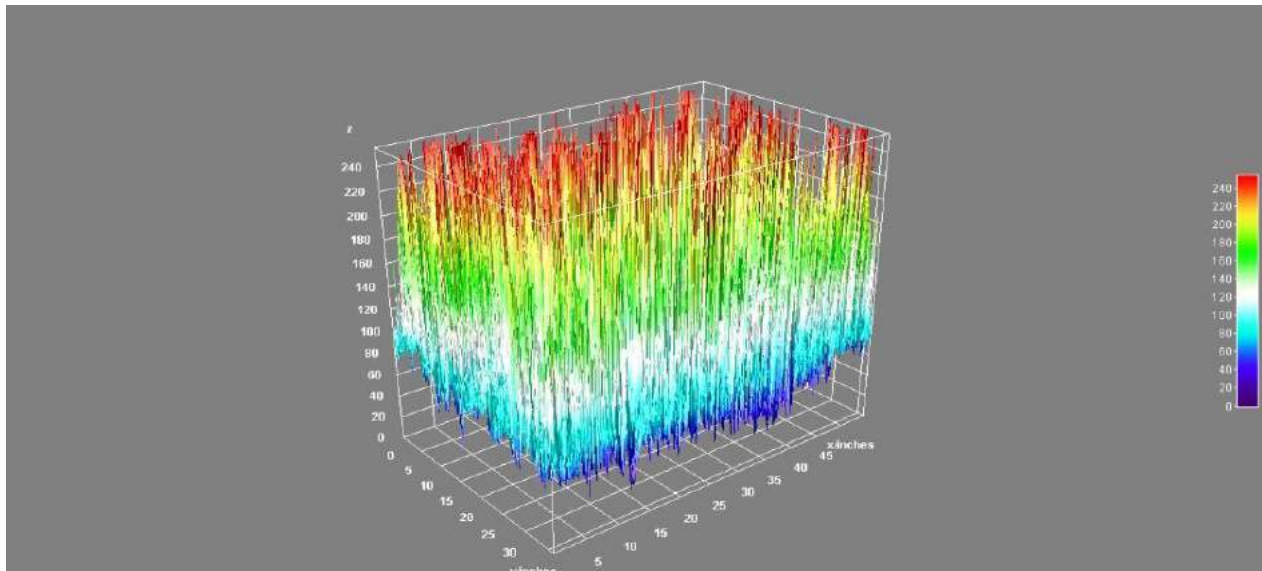
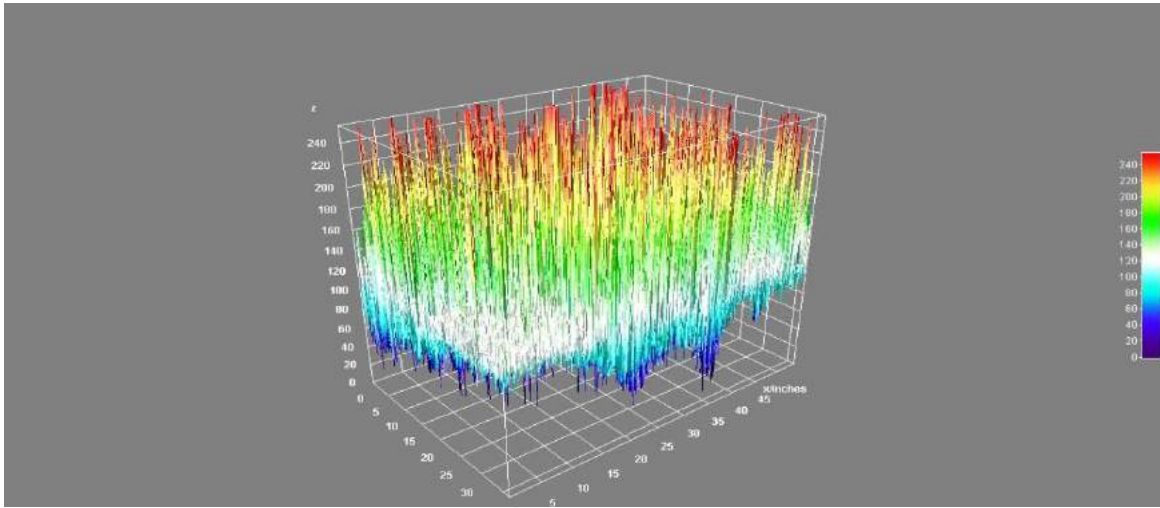


Figure 8: B

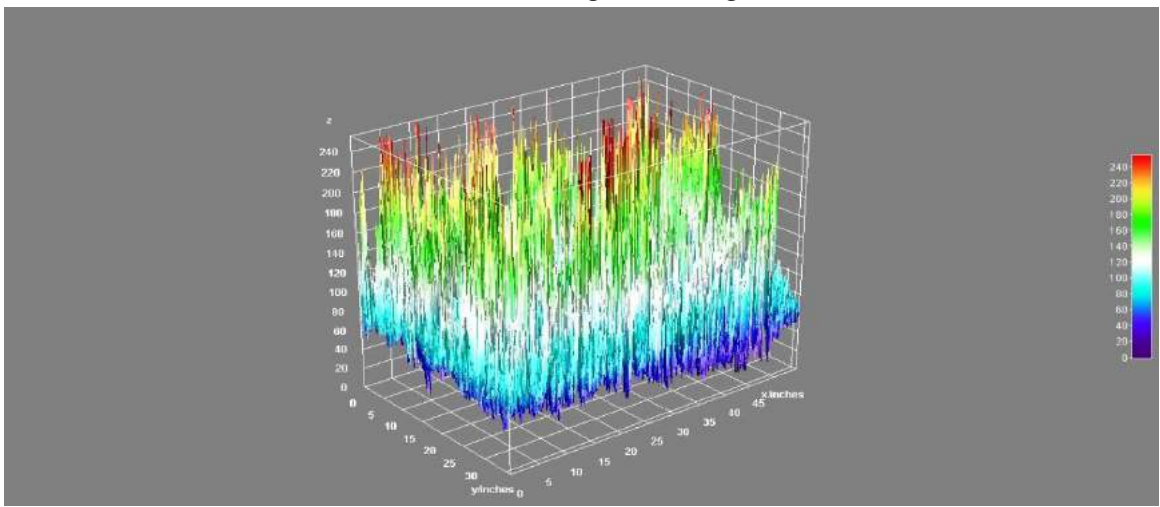
Plot 2: Analysis of Surface roughness plot of figure 5 and 8



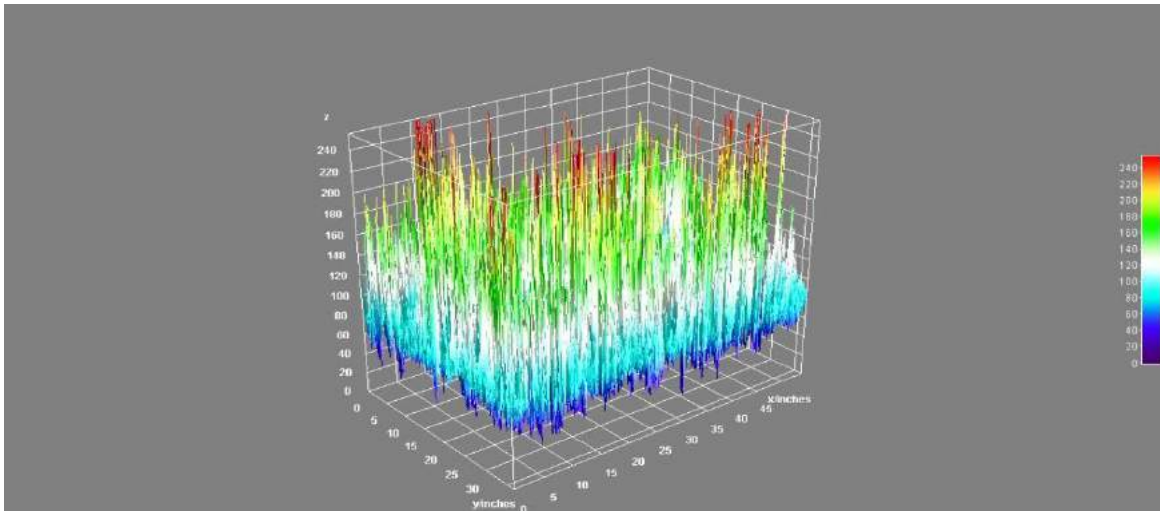
Plot 3: Thermal Simulate Profile of Surface Roughness of figure 5 (A)



Plot 4: Thermal Simulate Profile of Surface Roughness of figure 5 (B)



Plot 5: Thermal Simulate Profile of Surface Roughness of figure 8 (A)



Plot 6: Thermal Simulate Profile of Surface Roughness of figure 8 (B)

IV. DISCUSSION

By nature magnesium is a reactive metal and so corrosion obstruction is a problem of the poor corrosion obstruction of magnesium alloy is essential with Magnesium having low electrochemical efficient of any metals used in railway and automobile structure. The lower creep of Mg alloy limits the applications of magnesium alloy to be used for critical parts the major problem that require high focused to enhance creep resistance of Mg alloy. In figure number 5 (a &b) all these profile plot, surface plot and thermal simulate curve shows that major irregulaties are shown. The curve wavelength is too large and thermal simulate properties red color indicated that maximum corrosion resistance occur in that region where surface roughness as high as increasing corrosion on magnesium alloy, where as in figure 8 (a & b) cover less amount of corrosion on surface with less roughness. So there are many magnesium alloy has been developed by researchers all having their unique properties to make alloy attractive as compare to pure magnesium. To enhance strength of magnesium various alloying elements and nanoparticle play an important role to increasing mechanical properties and good corrosion protection.

V. CONCLUSION

Due to the demand of light weight material a Mg is best choice as compared to Aluminum. It has a lower density with high potency. This alloy property has focused on enhancing in the utilization of Mg and its alloy in application to railway and automobile sector. Meanwhile Mg is highly reactive metal. Thus it is important to identify the corrosion nature of Mg and its alloy in its applications. Likewise magnesium also owns drawback and its tremendously low protection to corrosion being the most important to them. Some of the important alloys and composite are Mg-Ca, Mg-Al, Mg-Zn, Mg-RE, Mg-Li , Mg/TiO₂ ,Mg/CaO, Mg/SnO₂, Mg/GNP etc. Some research papers related to different types of magnesium alloys and composite and their behaviour characteristics has been collected and mentioned in detail. The results of the study concluded that suitable price and enhanced the properties of magnesium alloy and composite will lead to vast use of magnesium.

Declaration of Competing Interest

The authors declare that they have no known competing financial interests or personal relationships that could have appeared to influence the work reported in this paper.

Funding

This research did not receive any specific grant from funding agencies in the public, commercial, or not-for-profit sectors.

Acknowledgments

I am extremely obliged and thankful to Dr. Neeraj Kumar (Professor & HOD of Department of Mechanical Engineering), Suresh Gyan Vihar University Jaipur for his guidance, support and encouragement. It has been an extremely constructive and pleasant experience working with him. I learnt a lot from his patience and encouraging attitude. He provided me a platform to work on challenging areas of Fabrication of Composite Material. His profound insights and attention to details have been true inspirations to my research.

My special thanks go to Dr. M.K. Banerjee (Chair Professor, Suresh Gyan Vihar University, Jaipur) for giving me the valuable suggestion to do work in the field of magnesium alloy.

VI. REFERENCES

- [1]. D. Wang , P.H. Fu , L.M. Peng , Y.X. Wang , W.J. Ding , Mater. Charact. 153 (2019) 157– 168 ., (n.d.).
- [2]. X. Wu , Study on Microstructure and Mechanical Properties of Cast Mg–Gd–Zn Serial Alloys, Chongqing University, 2018 ., (n.d.).
- [3]. H.C. Pan , C.L. Yang , Y.T. Yang , Y.Q. Dai , D.S. Zhou , L.J. Chai , Q.Y. Huang , Q.S. Yang , S.M. Liu , Y.P. Ren , G.W. Qin , Mater. Lett. 237 (2019) 65–68 ., (n.d.).
- [4]. B.S. Li , K. Guan , Q. Yang , X.D. Niu , D.D. Zhang , S.H. Lv , F.Z. Meng , Y.D. Huang , N. Hort , J. Meng , J. Alloy Compd. 776 (2019) 666–678 ., (n.d.).
- [5]. C. Xu , G.H. Fan , T. Nakata , X. Liang , Y.Q. Chi , X.G. Qiao , G.J. Cao , T.T. Zhang , M. Huang , K.S. Miao , M.Y. Zheng , S. Kamado , H.L. Xie , Metall. Mater. Trans. A 49A (2018) 1931–1947 ., (n.d.).
- [6]. M.I. Jamesh , G.S. Wu , Y. Zhao , D.R. McKenzie , M.M.M. Bilek , P.K. Chu , Corros. Sci. 91 (2015) 160–184 ., (n.d.). <https://www.sciencedirect.com/science/article/abs/pii/S0143974X2100403X> (accessed September 16, 2021).
- [7]. P.H. Fu , L.M. Peng , H.Y. Jiang , W.J. Ding , C.Q. Zhai , China Foundry 11 (2014) 277– 286 ., (n.d.).
- [8]. Q. Wang , B. Jiang , A. Tang , C. He , D. Zhang , J. Song , T. Yang , (n.d.). [9] Y. Wang , J. Peng , L. Zhong , J. Alloy Compd. 744 (2018) 234–242 ., (n.d.).
- [9]. M. Zhang , Y. Feng , J. Zhang , S. Liu , Q. Yang , Z. Liu , R. Li , J. Meng , R. Wu , J. Mater. Sci. Technol. 35 (2019) 2365–2374 ., (n.d.).
- [10]. S.J. Liu , K. Wang , J.F. Wang , S. Huang , S.Q. Gao , X. Peng , H. Hu , F.S. Pan , Mater. Sci. Eng. A –Struct. 758 (2019) 96–98 ., (n.d.).
- [11]. A novel approach to melt purification of magnesium alloys, (n.d.).
- [12]. D.D. Zhang , Q. Yang , K. Guan , B.S. Li , N. Wang , P.F. Qin , B. Jiang , C. Sun , X. Qin , Z. Tian , Z.Y. Cao , J. Meng , J. Alloy Compd. (2019) 810 ., (n.d.).
- [13]. M.-A. Assily Alegre , R. Tremblay, Experimental program on the flexural response of steel joist top chord extensions, Journal of Constructional Steel Research. 186 (2021) 106890. <https://doi.org/10.1016/j.jcsr.2021.106890>.
- [14]. X.W. Heng , Y. Zhang , W. Rong , Y.J. Wu , L.M. Peng , Mater. Des. (2019) 169 ., (n.d.).
- [15]. P. Wang , E. Guo , X. Wang , H. Kang , Z. Chen , Z. Cao , T. Wang , J. Magnes. Alloy 7 (2019) 456–465 ., (n.d.).
- [16]. Substitution of Ni for Zn on microstructure and mechanical properties of Mg–Gd–Y–Zn– Mn alloy, (n.d.).
- [17]. A.Y. Zhang , R. Kang , L. Wu , H.C. Pan , H.B. Xie , Q.Y. Huang , Y.J. Liu , Z.R. Ai , L.F. Ma , Y.P. Ren , G.W. Qin , Mater. Sci. Eng. A –Struct. 754 (2019) 269–274 ., (n.d.).
- [18]. Chennakesava Reddy and Essa Zitoun “Matrix Al-alloys for silicon carbide particle reinforced metal matrix composites” Indian Journal of Science and Technology, Vol. 3 No. 12 (Dec 2010) ISSN: 0974- 6846., (n.d.).

- [19]. G.L. Bi, Y.X. Han, J. Jiang, Y.D. Li, D.Y. Zhang, D. Qiu, M. Easton, *Mater. Sci. Eng. A –Struct.* 760 (2019) 246–257., (n.d.).
- [20]. I. Asiltürk, H. Akkus, Determining the effect of cutting parameters on surface roughness in hard turning using the Taguchi method, *Measurement* 44 (2011) 1697–1704., (n.d.).
- [21]. Z. Ding, H. Li, L. Shaw, New Insights into the Solid-State Hydrogen Storage of Nanostructured LiBH₄-MgH₂ System, *Chem. Eng. J.* 385 (2019) 123856 p, doi: 10.1016/j.cej.2019.123856., (n.d.).
- [22]. Z. Ding, L. Shaw, Enhancement of hydrogen desorption from nanocomposite prepared by ball milling MgH₂ with in situ aerosol spraying LiBH₄, *ACS Sustain. Chem. Eng.* 7 (17) (2019) 15064–15072, doi: 10.1021/acssuschemeng.9b03724., (n.d.).
- [23]. Y.H. Sun, C.Q. Shen, Q.W. Lai, W. Liu, D.W. Wang, K.F. Aguey Zinsou, Tailoring magnesium based materials for hydrogen storage through synthesis: current state of the art, *Energy Storage Mater* 10 (2018) 168–198, doi: 10.1016/j.ensm.2017.01.010., (n.d.).
- [24]. J. long Su, J. Teng, Z. li Xu, Y. Li, Biodegradable magnesium-matrix composites: a review, *Int. J. Miner., Metall. Mater.* 27 (6) (2020) 724–744, doi: 10.1007/s12613-020-1987-2., (n.d.).
- [25]. J. Song, J. She, D. Chen, F. Pan, Latest research advances on magnesium and magnesium alloys worldwide, *Journal of Magnesium and Alloys* 8 (1) (2020) 1–41, doi: 10.1016/j.jma.2020.02.003., (n.d.).
- [26]. T. Mandai, Critical Issues of Fluorinated Alkoxyborate-Based Electrolytes in Magnesium Battery Applications, *ACS Appl. Mater. Interfaces* 12 (35) (2020) 39135–39144, doi: 10.1021/acsmi.0c09948., (n.d.).
- [27]. T.W. Cain, M.A. Melia, J.M. Fitz-Gerald, J.R. Scully, Evaluation of the Potential Range for Sacrificial Mg Anodes for the Cathodic Protection of Mg Alloy AZ31B-H24, *Corrosion* 73 (5) (2017) 544–562, doi: 10.5006/2356., (n.d.).
- [28]. V.A. Yartys, M.V. Lototsky, E. Akiba, R. Albert, V.E. Antonov, J.R. Ares, M. Baricco, N. Bourgeois, C.E. Buckley, J.B. von Colbe, J.C. Crivello, Magnesium based materials for hydrogen based energy storage: past, present and future, *Int. J. Hydrog. Energy* 44 (15) (2019) 7809–7859, doi: 10.1016/j.ijhydene.2018.12.212., (n.d.).
- [29]. A. Çiçek, T. Kivak, E. Ekici, Optimization of drilling parameters using Taguchi technique and response surface methodology (RSM) in drilling of AISI 304 steel with cryogenically treated HSS drills, *J. Intell. Manuf.* (2015), (n.d.).
- [30]. L. Ouyang, K. Chen, J. Jiang, X.S. Yang, M. Zhu, Hydrogen storage in light-metal based systems: a review, *J Alloys Compd* 829 (2020) 154597, doi: 10.1016/j.jallcom.2020.154597., (n.d.).
- [31]. K. Kumar, R.S. Gill, U. Batra, Challenges and opportunities for biodegradable magnesium alloy implants, *Mater. Technol.* 33 (2) (2018) 153–172, doi: 10.1080/10667857.2017.1377973., (n.d.).
- [32]. A. Mahajan, S.S. Sidhu, Surface modification of metallic biomaterials for enhanced functionality: a review, *Mater. Technol.* 33 (2) (2018) 93–105, doi: 10.1080/10667857.2017.1377971., (n.d.).
- [33]. K. Saptaji, M.A. Gebremariam, M.A. Azhari, Machining of biocompatible materials: a review, *Int. J. Adv. Manuf. Technol.* 97 (5) (2018) 2255–2292, doi: 10.1007/s00170-018-1973-2., (n.d.).

- [34]. B.R. Sunil, K.V. Ganesh, P. Pavan, G. Vadapalli, C. Swarnalatha, P. Swapna, P. Bindukumar, G.P.K. Reddy, Effect of aluminum content on machining characteristics of AZ31 and AZ91 magnesium alloys during drilling, *Journal of Magnesium and Alloys* 4 (1) (2016) 15–21, doi: 10.1016/j.jma.2015.10.003 ., (n.d.).
- [35]. E. Zhang, L. Yang, J. Xu, H. Chen, Microstructure, mechanical properties and bio-corrosion properties of Mg-Si(-Ca, Zn) alloy for biomedical application, *Acta Biomater* 6 (2010) 1756–1762, doi: 10.1016/j.actbio.2009.11.024., (n.d.).
- [36]. F. Witte, J. Fischer, J. Nellesen, C. Vogt, J. Vogt, T. Donath, F. Beckmann, In vivo corrosion and corrosion protection of magnesium alloy LAE442A, *Acta Biomater* 6 (5) (2010) 1792–1799, doi: 10.1016/j.actbio.2009.10.012., (n.d.).
- [37]. T. Huehnerschulte, J. Reifenrath, B. von Rechenberg, D. Dziuba, J. Seitz, D. Bormann, H. Windhagen, A. Meyer-Lindenberg, In vivo assessment of the host reactions to the biodegradation of the two novel magnesium alloys ZEK100 and AX30 in an animal model, *Biomed Eng Online* 11 (1) (2012) 14–14, doi: 10.1186/1475-925x-11-14., (n.d.).
- [38]. F. Feyerabend, J. Fischer, J. Holtz, F. Witte, R. Willumeit, H. Drücker, C. Vogt, N. Hort, Evaluation of short-term effects of rare earth and other elements used in magnesium alloys on primary cells and cell lines, *Acta Biomater* 6 (5) (2010) 1834–1842, doi: 10.1016/j.actbio.2009.09.024., (n.d.).
- [39]. L. Yang, Y. Huang, Q. Peng, F. Feyerabend, K.U. Kainer, R. Willumeit, N. Hort, Mechanical and corrosion properties of binary Mg–Dy alloys for medical applications, *Mater. Sci. Eng.: B* 176 (20) (2011) 1827–1834, doi: 10.1016/j.mseb.2011.02.025 ., (n.d.).
- [40]. E. Willbold, X. Gu, D. Albert, K. Kalla, K. Bobe, M. Brauneis, C. Janning, J. Nellesen, W. Czayka, W. Tillmann, Y. Zheng, F. Witte, Effect of the addition of low rare earth elements (lanthanum, neodymium, cerium) on the biodegradation and biocompatibility of magnesium, *Acta Biomater.* 11 (2015) 554–562, doi: 10.1016/j.actbio.2014.09.041 ., (n.d.).
- [41]. L.N. Zhang, Z.T. Hou, X. Ye, Z. Xu, X.L. Bai Bin, P. Shang, The effect of selected alloying element additions on properties of Mg-based alloy as bioimplants: a literature review, *Front Mater Sci* (2013), doi: 10.1007/s11706-013-0210-z., (n.d.).
- [42]. C.A. Grillo, F. Alvarez, M.A.F.L. de Mele, Degradation of bioabsorbable Mg-based alloys: assessment of the effects of insoluble corrosion products and joint effects of alloying components on mammalian cells, *Materials Science and Engineering: C* 58 (2016) 372–380, doi: 10.1016/j.msec.2015.08.043 ., (n.d.).
- [43]. M.L. He, T.J. Luo, Y.T. Liu, T. Lin, J.X. Zhou, Y.S. Yang, *J. Alloy Compd.* 767 (2018) 1216–1224 ., (n.d.).
- [44]. Q. Huang, Y. Liu, A. Zhang, H. Jiang, H. Pan, X. Feng, C. Yang, T. Luo, Y. Li, Y. Yang, *J. Mater. Sci. Technol.* 38 (2020) 39–46 ., (n.d.).
- [45]. T. Zhang, H. Cui, X. Cui, E. Zhao, Y. Pan, R. Feng, Q. Jia, J. Zhao, *J. Alloy Compd.* 784 (2019) 1130–1138 ., (n.d.).
- [46]. A. Javaid, F. Czerwinski, *J. Magnes. Alloy* 7 (2019) 27–37 ., (n.d.). [48] S.-H. Kim, S.H. Park, *Mater. Sci. Eng.: A* 733 (2018) 285–290 ., (n.d.).
- [47]. Y. Chai, B. Jiang, J. Song, B. Liu, G. Huang, D. Zhang, F. Pan, *Mater. Sci. Eng.: A* 746 (2019) 82–93 ., (n.d.).

- [48]. Y. Chai , B. Jiang , J. Song , Q. Wang , H. Gao , B. Liu , G. Huang , D. Zhang , F. Pan , J. Alloy Compd. 782 (2019) 1076–1086 ., (n.d.).
- [49]. T. Nakata , C. Xu , R. Ajima , Y. Matsumoto , K. Shimizu , T.T. Sasaki , K. Hono , S. Kamado , Mater. Sci. Eng.: A 712 (2018) 12–19 ., (n.d.).
- [50]. J. Wang , F. Wei , B. Shi , Y. Ding , P. Jin , Mater. Sci. Eng.: A 765 (2019) 138288 ., (n.d.).
- [51]. X. Xia, J.F. Nie, C.H.J. Davies, W.N. Tang, S.W. Xu, N. Birbilis, The Influence of Low Levels of Zinc, Calcium, Gadolinium, Strontium, and Zirconium on the Corrosion of Magnesium for Wrought Applications, CORROSION 71 (11) (2015) 1370–1386, doi: 10.5006/1802., (n.d.).
- [52]. Y. Yao , Z.H. Huang , H. Ma , H. Zhang , Z.M. Zhang , C.J. Xu , N. Zhou , M. Kuang , J.C. Huang , Mater. Sci. Eng. A –Struct. 747 (2019) 17–26 ., (n.d.).
- [53]. K. Wang , J.F. Wan , S. Huang , S.Q. Gao , S.F. Guo , S.J. Liu , X.H. Chen , F.S. Pan , Mater. Sci. Eng. A –Struct. 733 (2018) 267–275 ., (n.d.).
- [54]. W. Rong , Y. Zhang , Y.J. Wu , Y.L. Chen , M. Sun , J. Chen , L.M. Peng , Mater. Sci. Eng. A –Struct. 740 (2019) 262–273 ., (n.d.).
- [55]. C. You , C.M. Liu , Y.C. Wan , B. Tang , B.Z. Wang , Y.H. Gao , X.Z. Han , J. Magnes. Alloy 7 (2019) 414–418 ., (n.d.).
- [56]. X.B. Zheng , W.B. Du , Z.H. Wang , S.B. Li , K. Liu , X. Du , Mater Lett. 212 (2018) 155– 158 ., (n.d.).
- [57]. Y. Feng , J.H. Zhang , P.F. Qin , S.J. Liu , Q. Yang , J. Meng , R.Z. Wu , J.S. Xie , Mater. Charact. 155 (2019) ., (n.d.).
- [58]. X.K. Kang , K.B. Nie , K.K. Deng , Y.C. Guo , Mater. Charact. 151 (2019) 137–145 ., (n.d.).
- [59]. S.S. Nene , S. Zellner , B. Mondal , M. Komarasamy , R.S. Mishra , R.E. Brennan , K.C. Cho , Mater. Sci. Eng. A –Struct. 729 (2018) 294–299 ., (n.d.).
- [60]. L.P. Zhong , Y.J. Wang , Y.C. Dou , J. Magnes. Alloy 7 (2019) 637–647 ., (n.d.).
- [61]. C. Wang , T. Luo , Y. Liu , T. Lin , Y. Yang , Mater. Charact. 147 (2019) 406–413 ., (n.d.).
- [62]. S. Aliyari , S.M. Fatemi , S.M. Miresmaeili , Trans. Nonferrous Metals Soc. China 29 (2019) 1842–1853 ., (n.d.).
- [63]. S. J. Splinter, N. S. McIntyre, The initial interaction of wa- ter vapour with MgAl alloy surfaces at room temperature, Surface Science 314 (2) (1994) 157–171. Doi: 10.1016/0039- 6028(94)90003-5. [https://dx.doi.org/10.1016/0039-6028\(94\)90003-5](https://dx.doi.org/10.1016/0039-6028(94)90003-5). Refson, R. A. Wogelius, D. G. Fraser, M. C. Payne, M. H. Lee, V. Milman, Water chemisorption and reconstruction of the MgO surface, Physical Review B 52 (15) (1995) 10823–10826. <https://dx.doi.org/10.1103/physrevb.52.10823>, (n.d.).
- [64]. H. Pan, Y. Ren, H. Fu, H. Zhao, L. Wang, X. Meng, Recent de- velopments in rare-earth free wrought magnesium alloys having high strength: a review, J. Alloys Compd. 663 (2016) 321–352, doi: 10.1016/j.jallcom.2015.12.057 ., (n.d.).



An Experimental Study on Mechanical Characterization of Fiber Based Hybrid Polymer Composites

Pradeepkumar G R¹, Paraveej shirahatti², H K Shivanand³, Sadashiva M⁴

¹Lecturer, Department of Mechanical Engineering, Govt Polytechnic Chitradurga, Karnataka, India

²Research scholar, Department of Mechanical Engineering, UVCE, Bangalore, Karnataka, India

³Professor, Department of Mechanical Engineering, UVCE, Bangalore, Karnataka, India

⁴Assistant Professor, Department of Mechanical Engineering, PESCE, Mandya, Karnataka, India

ABSTRACT

Composites materials those special in modern materials era due to its nature of taylor made properties. Their most attractiveness lies in high Strength- to weight ratio and high stiffness-to- weight ratio. Recent development of the polymer composites with synthetic fibres and natural fillers as a sustainable alternative material for some engineering applications, particularly in aerospace applications and automobile application. In this way artificial fibre composites such as glass, carbon, and kelper polymer composites appear more attractive. In this paper extensively use glass fibre as the major reinforcement long with silicon particles and epoxy resin as the base material to prepared hybrid composite material by hand layup process. ASTM standard test samples were prepared with different weight fractions of glass fibre and silicon. Tensile and flexural test were conducted to enhance mechanical properties of the hybrid composite materials, results were compared and tabulated.

Keywords: Hybrid composite, Glass fiber, Epoxy, Flexural strength

I. INTRODUCTION

Composite materials are nowadays employed in many engineering structures, such as helicopter and wind turbine rotor blades, boat hulls, and buildings, implying the application of variable loadings for long time spans[1]. This raises the question of their fatigue behaviour, whose importance is increasingly appreciated also in the fixed-wing aircraft industry, where fatigue life has not been a major issue in the past, due to the low working strains used in practical components. Significant efforts have been devoted toward the use of lightweight structures to increase energy efficiencies in various industrial and commercial sectors[2]. Fiber-reinforced composites have found numerous applications in aerospace industry for their high specific strength and specific stiffness[3]. However, the cost of traditional composite materials is also considerable. Random chopped fiber-reinforced composites (RFCs) have emerged as promising alternative materials for lightweight structures due to their low cost and mass production capabilities[4]. Their potential application in, for example,

automotive industry has been documented. In order to expand their use, accurate material characterization is required[5]. The main difficulty in fully exploring the capabilities of the RFCs lies in the apparent impediment to effectively model their geometry at the micro-level for high fiber volume ratios (35-40%). This difficulty becomes even more obvious at high aspect ratio fibers[6].

Glass-fiber-reinforced composites (or glass-fiber reinforced plastics, GFRP) have seen limited use in the building and construction industry for decades. Because of the need to repair and retrofit rapidly deteriorating infrastructure in recent years, the potential for using fiber-reinforced composites for a wider range of applications is now being realized[7].

A study on numerical generation of a random chopped fiber composite RVE and its elastic properties has been done by research study on theory of fabrication-induced anisotropy of chopped-fibre/resin panels martin has been done by Martin[8]. A study on chopped glass and recycled newspaper as reinforcement fibers in injection molded poly (lactic acid) (PLA) composites has been done[9]. Although a great deal of work has been reported in the literature which discuss the mechanical behavior of fiber reinforced polymer composites, however, very limited work has been done on effect of fiber loading on mechanical behaviour of chopped glass fiber reinforced epoxy composites[10].

Against this background, the present research work has been undertaken, with an objective to explore the potential of chopped glass fiber as a reinforcing material in polymer composites and to investigate its effect on the mechanical behaviour of the resulting composites[11],[12]. The present work thus aims to develop this new class of polymer composites with different fiber loading and to analyse their mechanical behaviour by experimentation.

Tensile and flexural characteristics of the epoxy based metal matrix hybrid composites plates fabricated with hand layup was the main focus of the present research work.

1.1. Objectives:

An experimental study of mechanical characterization of glass fiber and silicon Reinforced epoxy composite is our main objective of this research. The study included following tasks.

- Fabrication of glass fiber, silicon / epoxy composite using hand layup technique.
- Mechanical characterization such as tensile strength, flexural strength, impact strength, different weight percentage of fiber loadings.
- Compatibility of unmodified of glass fiber and silicon fiber with epoxy matrix material.

II. MATERIALS USED



Fig.1 Microspheres, Chopped or Woven.

Fig. 2 Silicon powder Fiberglass is a strong lightweight material

and is used for many products. Although it is not as strong and stiff as composites based on carbon fiber, it is less brittle, and its raw materials are much cheaper. Its bulk strength and weight are also better than many metals, and it can be more readily molded into complex shapes[13]. Applications of fiberglass include aircraft, boats, automobiles, bath tubs and enclosures, swimming pools, hot tubs, septic tanks, water tanks, roofing, pipes, cladding, casts, surfboards, and external door skins.

2.1. Properties of Epoxy resin

Epoxy resins are low molecular weight pre-polymers or higher molecular weight polymers which normally contain at least two epoxide groups. The epoxide group is also sometimes referred to as a glycidyl or oxirane group. a wide range of epoxy resins are produced industrially[14], [15].

The raw materials for epoxy resin production are today largely petroleum derived, although some plant derived sources are now becoming commercially available Epoxy resins are polymeric or semi-polymeric materials, and as such rarely exist as pure substances, since variable chain length results from the polymerization reaction used to produce them[16].

High purity grades can be produced for certain applications, e.g. using a distillation purification process[17]. One downside of high purity liquid grades is their tendency to form crystalline solids due to their highly regular structure, which require melting to enable processing[18].

III. EXPERIMENTATION AND PROCESS

3.1. Processing Technique: Hand Layup

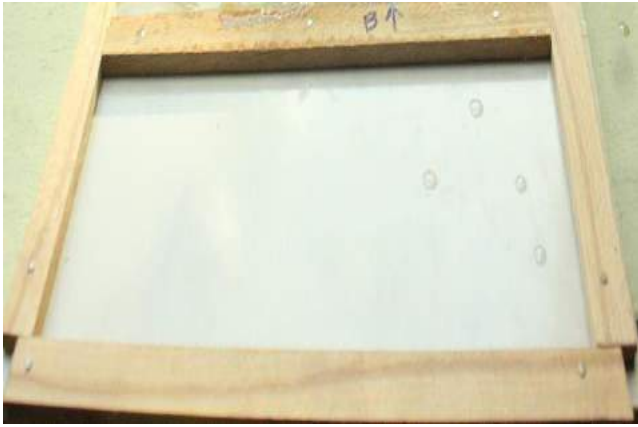


Fig.3 Mould



Fig.4 Weighing machine



Fig.5 Materials used



Fig.6 Mixing of resin and silicon



Fig.7 Molding process



Fig.8 Curing process

3.2. Fabrication Procedure

3.2.1. Pre-Preparations

- Safety Hand Glows (latex hand glows).
- Brushes -Small and Medium sized.
- Steel plates-Small sized to overlay mixer.

- 0Steel sticks- for stirring of resin and reinforcements mixed in a mug.
- Hand rollers- to apply pressure.
- Mylar sheets.
- Chemicals-Hardeners.
- Weighing machine.

3.2.2. Processing Procedure of Glass Fiber / Epoxy

- Cut the Mylar sheet according to Mold size and place it on the Mold.
- According to calculation pour the resin into the mug.
- According to the percentage of volume required the calculated amount of rice husk is mixed into the weighted resin.
- Stir well for about two minute in clockwise and alternatively anticlockwise to mix the content thoroughly.
- Then add hardeners i.e. 1.10 ratio depending of volume fraction
- Once it is mixed thoroughly now it is ready to lay on the mold.
- Before layup clean the Mylar sheet with little amount of resin.
- Pour the mixer continuously over the mold apply little pressure using plates to fill the mixer all along the mold.
- Wait for a minute and apply pressure using hand rollers to remove air bubbles and to maintain uniqueness in the laminate.
- Once the layup is over put Mylar sheet on it to avoid sticking of specimen onto the male portion of the mold.
- And put heavy weight on the specimen and leave it for curing.
- Approximately after 24 hour at room temperature the laminate is ready for cutting operation.
- The specimen is cut to the desired size and taken for testing.

3.3. Sample Preparation

Composite laminate of 300 mm X 200 mm X 5 mm were fabricated according to ASTM standards for mechanical tests.

IV. TESTING AND DISCUSSION

4.1. Tensile and Flexural Specimen



Fig.9 Tensile test specimen 100% epoxy resin Tensile specimen 250mmX25mmX5mm



Fig.10 Flexural test specimen 100% epoxy resin Flexural specimen 200mmX15mmX5mm

4.2. Ultimate Tensile Strength (UTS)

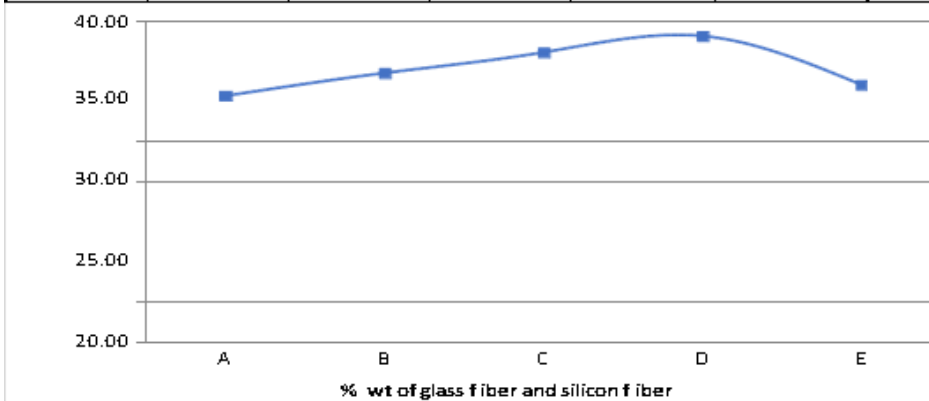
Ultimate tensile strength, often referred to tensile strength is the maximum stress that a material can withstand while being stretched or pulled before fracture. The tensile test for the specimens was conducted according to ASTM D3039. The specimens of size 250 mm x 25 mm x 10 mm were tested with a span length of 100 mm in tensile mode at a cross head speed of 1 mm / min. The fixtures used for the tensile testing is shown in Figure 5.1.



Fig.11 Specimens loaded in tension

Table 1. Ultimate tensile strength of glass fiber/ silicon / Epoxy resin composite

Samples	Glass fiber(%)	Silicon (%)	Ultimate Tensile Strength (MPa)			Avg UTS Mpa
A	15	0	32.36	31.28	28.42	30.69
B	15	3	32.88	33.8	33.78	33.49
C	15	5	35.28	35.98	36.82	36.03
D	15	7	38.08	37.78	38.22	38.03
E	15	9	31.08	32.22	32.8	32.03



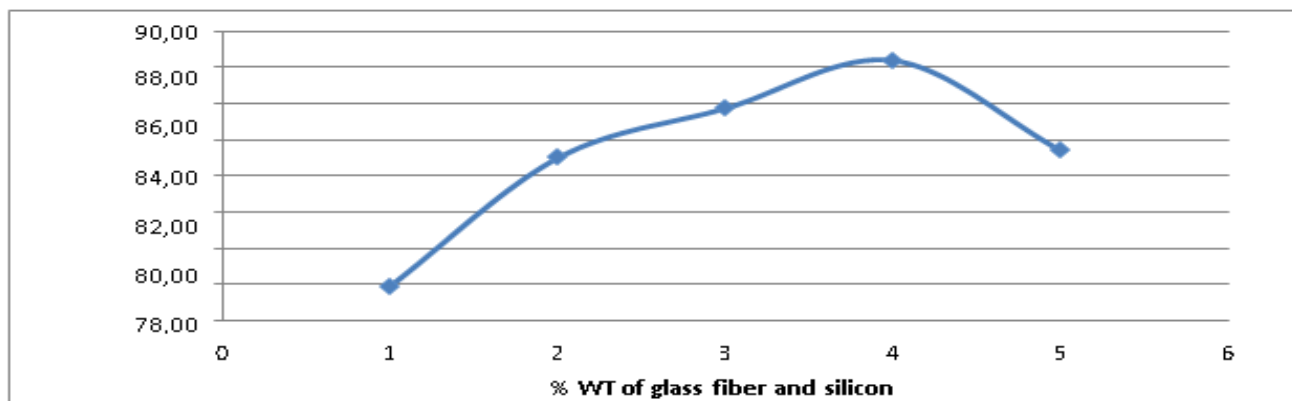
Graph 1. UTS of glass fiber / silicon different percentage loadings

4.3. Flexural Strength

The use of flexural tests to determine the mechanical properties of polymeric composites is widely prevalent because of the relative simplicity of the test method, instrumentation and testing equipment required. The flexural strengths of the specimens were determined for specimens using the three-point bending test as per ASTM-D790. The specimens of dimensions 200 mm x 15 mm x 5 mm tested with a span length 50 mm. Figure 5.6 shows the flexural test setup used in the experiment.

Table 2. ultimate flexural strength of glass fiber / silicon / Epoxy.

Samples	Glass fiber(%)	Silicon (%)	Ultimate flexural Strength (MPa)			Avg flexural Mpa
			75	76.4	76.4	
A	15	0	75	76.4	76.4	75.93
B	15	1	82	83	84	83.00
C	15	3	85.6	86.4	85.2	85.73
D	15	5	87.8	88.6	88.7	88.37
E	15	7	82.88	83.48	83.8	83.39



Graph 2. Ultimate flexural Strength of glass fiber / silicon composite at different percentage loading.

V. CONCLUSION

Mechanical Properties of Glass Fiber and Silicon / Epoxy Resin

Table 3. Results of UTS of composite material

SAMPLES	ULTIMATE TENSILE STRENGTH			RESULTS
	Glass fiber, %	Silicon	Av g.UTS, MPa	
A	0	0	30.69	
B	15	1	33.49	Tensile strength increases by 8.36%
C	15	3	36.03	Tensile strength increases by 7.04%
D	15	5	38.03	Tensile strength increases by 5.25 %
E	15	7	32.03	Tensile strength decreases by 18.34%

Table 4. Results of flexural strength of composite material

SAMPLES	ULTIMATE TENSILE STRENGTH			RESULTS
	Glass fiber, %	Silicon Av	g.UTS, MPa	
A	0	0	75.93	
B	15	1	83.00	Flexural strength increased by 8.51%
C	15	3	85.73	Flexural strength increased by 3.18%
D	15	5	88.37	Flexural strength increased by 2.98%
E	15	7	83.39	Flexural strength decreases by 5.97%

The conclusion of the study of glass fiber & silicon reinforced epoxy resin composite is that there is significant increase in the tensile and flexural strength of the composite.

Table 5. Results of Mechanical tests

Samples	Tensile strength in MPa	Flexural strength in MPa
A	30.69	75.93
B	33.49	83.00
C	36.03	85.73
D	38.03	88.37
E	32.03	83.39

1. Tensile strength increased by 19.30% gradually with more percentage of loading of Silicon composite and hybrid composite
2. The flexural Strength increased by 14.22 gradually with the more percentage silicon composite hybrid composite
3. To have better mechanical properties at higher silicon content, the bonding between glass fiber/ silicon and epoxy resin must improved
4. To increase the mechanical properties of the composite there must be homogenous mixture of the silicon and matrix to have the property of the composite.
5. Hybridization has been successfully found to be better option to have better mechanical property which alone a glass fiber fails.

VI. SCOPE OF FUTURE WORK

From the conclusion of the study it clearly states that improvement/implementing following will yield composite of enhanced strength.

- Glass fiber reinforcement resulted in a increase in tensile strength for different loading proportion that can be compared with the treated /modified silicon to know which one gives improved strength value.
- Glass fiber shown poor interfacial bonding with epoxy resin which can be made better for bonding strength by treating the silicon with the (10% NaOH) solution for optimal result.

- Micro cracks and voids are present in the matrix material which is due to inhomogeneous mixing of silicon with epoxy resin is avoided by mixing thoroughly in mechanical means.
- The composite is to also be tested for hardness to conclude the right application of material developed

VII. REFERENCES

- [1]. Prof. M. Sadashiva, J. V. Abhishek, "Characteristic evaluation of tensile properties of hybrid bio composites with different orientation of fibers", AIP Proceedings, <https://doi.org/10.1063/5.0027005>, ISBN: 978-0-7354-4004-3, pp: 030041-1–030041-5, 2020.
- [2]. Sadashiva M, Praveen Kumar S, M K Yathish, Satish V T, Srinivasa M R, Sharanraj V, "Experimental investigation of bending characteristics of hybrid composites fabricated by hand layup method" Journal of Physics: Conference Series, volume 2089, 012033, AMSE, IOP Publishing, doi:10.1088/1742-6596/2089/1/012033, page 1-7, 2021.
- [3]. V. Sharanraj ,C. M. Ramesha ,K. Kavya , Vasantha Kumar ,M. Sadashiva, B. R. Chandan& M. Naveen Kumar, "Zirconia: as a biocompatible biomaterial used in dental implants", Advances in Applied Ceramics, Published by Taylor & Francis, ISSN: 1743-6753, DOI: 10.1080/17436753.2020.1865094 ,Volume 119, Issue 8,PP :1-6, 2020.
- [4]. Sadashiva.M, H.K.Shivanand and H.N.Vidyasagar, "Characteristic Evaluation of Process Parameters of Friction Stir Welding of Aluminium 2024 Hybrid Composites", AIP Conference Proceedings, Volume 1943, 020054-1–020054-10; ISBN:9780735416383, <https://doi.org/10.1063/1.5029630>, pp. 020054 (1-10), 2018.
- [5]. J. Zhou et al., "Tensile Properties and Microstructures of a 2024-T351 Aluminum Alloy Subjected to Cryogenic Treatment," 2016, doi: 10.3390/met6110279.
- [6]. V.Sharanraj, C.M.Ramesha, V.Kumar, Sadashiva.M, "Finite Element Analysis of Zirconia Ceramic Biomaterials Used in Medical Dental Implants", SPRINGER-INTERCERAM, International ceramic review, ISSN: 0020-5214, Volume 68, Issue 3, pp. 24-31, 2019.
- [7]. S. V. Prasad and R. Asthana, "Aluminum metal-matrix composites for automotive applications: Tribological considerations," Tribol. Lett., vol. 17, no. 3, pp. 445–453, 2004, doi: 10.1023/B:TRIL.0000044492.91991.f3.
- [8]. F. Nturanabo, L. Masu, and J. Baptist Kirabira, "Novel Applications of Aluminium Metal Matrix Composites," Alum.Alloy.Compos., 2020, doi: 10.5772/intechopen.86225.
- [9]. J. M. Torralba, C. E. Da Costa, and F. Velasco, "P/M aluminum matrix composites: An overview," J. Mater. Process. Technol., vol. 133, no. 1–2, pp. 203–206, 2003, doi: 10.1016/S0924-0136(02)00234-0.
- [10]. I. A. Kartsonakis, E. P. Koumoulos, and C. A. Charitidis, "Advancement in corrosion resistance of AA 2024-T3 through sol-gel coatings including nanocontainers," Manuf. Rev., vol. 4, 2017, doi: 10.1051/mfreview/2017001.
- [11]. T. Technique, "Hardness improvement of aluminum alloy 2024 T3 after artificial aging treatment Hardness improvement of aluminum alloy 2024 T3 after artificial aging treatment," 2019, doi: 10.1088/1757-899X/539/1/012004.

- [12]. M. Maurya, N. K. Maurya, and V. Bajpai, "Effect of SiC Reinforced Particle Parameters in the Development of Aluminium Based Metal Matrix Composite," no. September, 2019, doi: 10.5109/2349295.
- [13]. Gujjala Anil Babu, M. Sadashiva, Ranjith R. Hombal, D. Aravinda, (2022). Fabrication and working of portable PPE kit sterilizer using UV Ozone Sanitization process, *Materials Today: Proceedings*, Elsevier, ISBN 2214-7853, <https://doi.org/10.1016/j.matpr.2022.01.021>.
- [14]. H. M. Zakaria, "Microstructural and corrosion behavior of Al / SiC metal matrix composites," *AIN SHAMS Eng. J.*, 2014, doi: 10.1016/j.asej.2014.03.003.
- [15]. M.R. Srinivasa, Y. S. Rammohan, M. Sadashiva, "Analysis of mechanical properties of graphene reinforced aluminum composites treated with shock waves", <https://doi.org/10.1063/5.0027005>, ISBN: 978-0-7354-4004-3, pp: 030040-1–030040-7, 2020.
- [16]. Sadashiva.M, H.K.Shivanand, "Characteristic Investigation on Impact Strength of Aluminium Based Hybrid Composite Plates Weld by FSW", *International Journal of Engineering and Technology (IJET)*, e-ISSN:2227-524X, doi : 10.14419/ijet.v7i3.12.15891, volume 7 (3.12) pp. 120-127, 2018.
- [17]. N.M. Siddesh Kumar, Dhruthi G.K, Pramod, P. Samrat, M. Sadashiva, (2022). A Critical Review on Heat Treatment of Aluminium Alloys, *Materials Today: Proceedings*, Elsevier, ISBN 2214- 7853, <https://doi.org/10.1016/j.matpr.2021.12.586>.
- [18]. H.K.Shivanand, M. Sadashiva, Paraveej, Shirahatti, S.ShivaPrakash, (2022). Comparative study on tensile characteristics of friction stir welded aluminium hybrid composite plates, *Materials Today: Proceedings*, Elsevier, ISBN 2214-7853, <https://doi.org/10.1016/j.matpr.2022.01.016>.



Tribological Studies of Structural Steels - A comprehensive Study

Hemaraju¹, Santosh Kumar TC¹, Sharath N¹, Sudesha Shetty M²

¹BGSIT, BG Nagara-571448 Nagamangala, Mandya, Karnataka, India

²YIT, Thodar, Moodbidri, Mangalore-574225 Karnataka, India

ABSTRACT

Tribology is the science of two rubbing bodies. Machin elements during their operations transfer either force or motion from one location to other locations. Transfer of load and displacement causes friction between one among them results with progressive failure ending with breakdown of the machineries. Wear is the process of material removal due to micro fracture, chemically dissolutions or melting at contact surfaces. Understanding wear mechanisms and describing wear phenomena is difficult due to complex changes during friction. The displacements involved in contacting surfaces loading wear are; elastic deformation & inelastic deformation. Plastic deformation and fracture are the sub-groups of inelastic deformation. It is required to understand these deformations by conducting the experiments in the lab which simulates the wear conditions in the field. Keeping this in our mind the comprehensive study has been discussed with the review on the failure of steel category materials subjected to two body and three body wear abrasion. Influence parameters mechanisms of wear to cause the failure was discussed.

I. INTRODUCTION

The dependency of specific wear rates in case of metallic materials in different lubricating conditions are summarized in figure number 1.1.

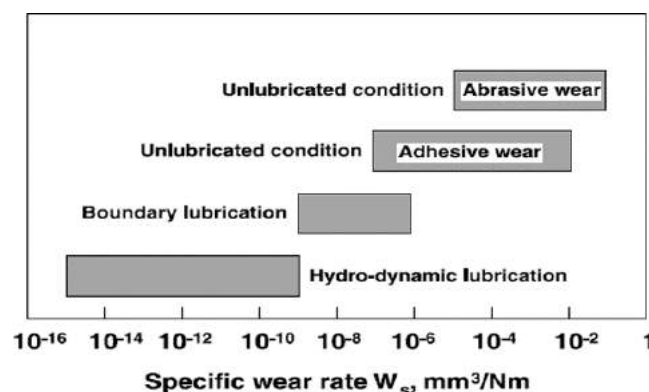


Fig: 1.1 Distribution of specific wear rate of metallic materials in sliding contact under different lubrication conditions. (Courtesy: Koji-Kato & Koshi Adachi (2000) Modren Tribology Hand book, CRC Press, Vol-1, 273-300)

The specific wear rates were found vary over a wide range of 10^{-15} to 10^{-1} $\text{mm}^3/\text{N}\cdot\text{m}$. Attempts are also made in relating specific wear rate with prevailing friction conditions. Figure 1.2 shows the dependency of specific wear rates with friction coefficients. The specific wear rate was found to change over a range from 10^{-1} to 10^{-2} $\text{mm}^3/\text{N}\cdot\text{m}$ for a similar material pair depending on materials and friction conditions.

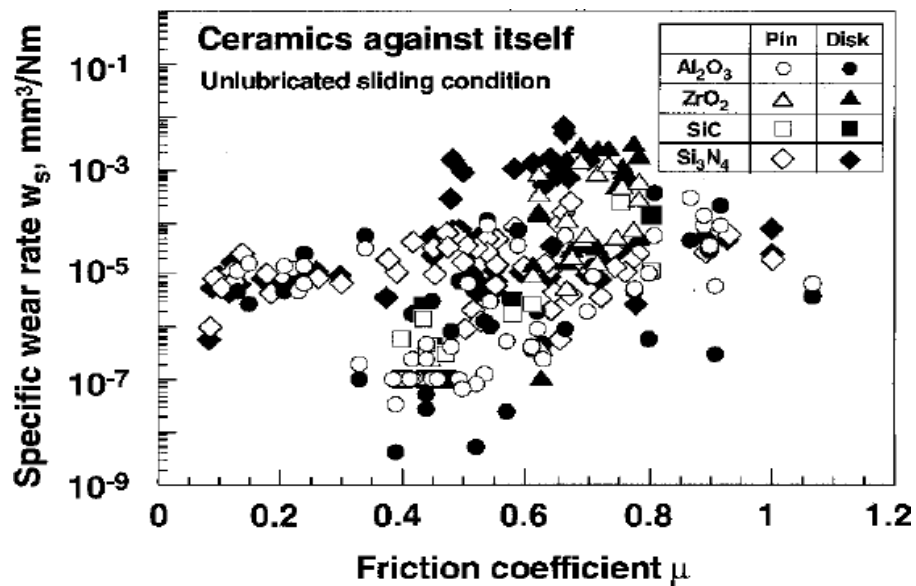


Fig: 1.2 Distribution of specific wear rates and friction coefficients of ceramics in unlubricated sliding against themselves. ((Courtesy: Koji-Kato & Koshi Adachi (2000) Modern Tribology Hand book, CRC Press, Vol-1, 273-300)

It was found from different scientists all over the world who conducted experiments simulating field conditions that the wear rate was drastically changed in the range of 10^{-15} to 10^{-1} $\text{mm}^3/\text{N}\cdot\text{m}$. These wear rates were found to depend on operating conditions and material pairs involved [1-7]. The design engineer should be able to know in advance the operating conditions and materials for a given machine element pairs. The wear phenomenon and its stages were defined by the various parameters like wear modes and wear rates [8 & 9]. It was believed that wear map is most convenient and suitable for selection of material under a wide range of operating conditions. Designing a tribo-system and selecting material pairs based on wear maps further requires the understanding of wear rates, different wear modes and mechanisms involved. The experimental results show that wear a consequence of displacement is not a metal property but a system dependent. Wear drastically changes with a relatively small change in tribo system which has parameters like dynamic conditions, environmental conditions and materials state [10 & 11]. In the present study it was found that wear volume, wear surface roughness and wear particle shape gave important information on wear mechanisms. In general, three types of dependency of wear with time were found. In first type wear was found to be constant with change in time. In the second type, a transitions of wear rate from a very large initial rate followed by steady state with time, was found. This type of wear behavior was found in case of metals [10]. In the third type, a catastrophic transition from initial lower wear rate to a very high wear failure, was found. This type of wear was observed in ceramics [11]. A crack initiation which depends on surface finish, material properties and frictional conditions precedes the catastrophic failure. There are many types of wear; adhesive, abrasive, fatigue

and corrosive. In any situations all the above- mentioned types of wears individually or in combination could occur due to change in material surface properties and dynamic surface responses due to frictional heating, chemical film formation [12].

II. TRIBOLOGICAL BEHAVIOR OF STEELS

Stanisla Verichev et al [13] tried to understand the impact of hydrostatic pressure on wear behavior of structural materials. Tests were conducted in a custom-made pressure vessel where very high level of hydrostatic pressure could be realized. Hydrostatic pressures of the order of 250 atm were realized. The target materials used are steel and tungsten carbide. From the study they found that the weight loss of steel increases to 1.6 times and twice increases to tungsten carbide alloy shown in the figure 2.1 & 2.2. The target materials used were steel and tungsten carbide. The worn surface was studied in SEM. The results showed increased wear rate with increase in hydrostatic pressure. The SEM study revealed the peeling of layers and chipping of hot particles. A reasonable co-relation was obtained for wear data with a deformation factor that incorporated the friction of the abrasive on plastic and a term related to energy observed for plastic deformation. Improved abrasion resistance was observed for materials which were easily deformed plastically. The study reveals that hydrostatic pressure also influences the actual wear rates in structural components.

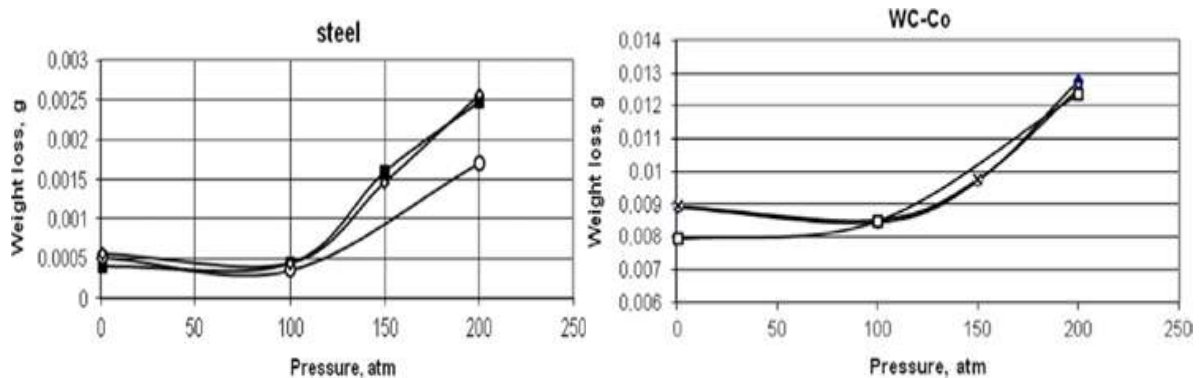


Figure: 2.1. weight loss of steel & tungsten carbide samples subjected to hydrostatic pressure. (Courtesy: Stanislav N. Verichev et al, (2015), Experimental study of abrasive wear of structural materials under high hydrostatic pressure, Ocean Engg, Wear, 99, 9-13.)

Juri Pirso et al [13] tried to understand the wear characteristics of TiC-NiMo cermet's. The author conducted test using a block on ring test according to ASTM B611-85 procedure. Silica sand was used as an abrasive. The abrasive was fed in to the test rig as slurry in the ratio 1:1.5 along with water. The abrasive grit size varied from 0.1 to 0.3 mm. The normal loads of 40 N and 200N were used. The linear speed was 2.2 m/s. Series of target specimen with different percentage of nickel molybdenum binder were tested. The results showed that a wear resistance depends on the type of composite and its binder with respect to the varying loads and the mechanisms of the wear found was similar shown in fig 2.2. The decrease in wear rate was found increase in titanium carbide and molybdenum. Wear track was studied in SEM. Material removal process such as extrusion, removal of binder, fracture of carbide grain and carbide networks were found.

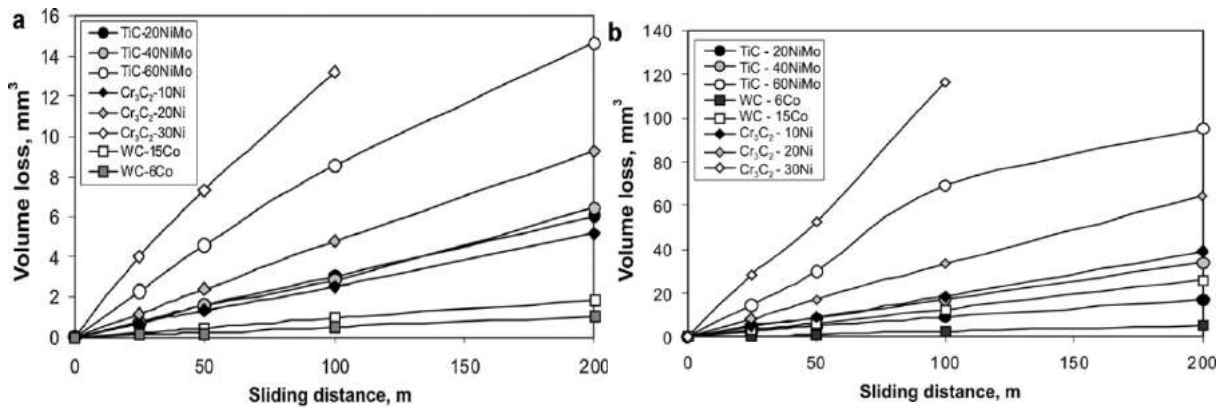


Figure 2.2. Volume loss of cermet's vs sliding distance P= 40 N (a) & P = 20 N (b) (Courtesy: Juri Pirso et al, (2015), Three body abrasive wear of cermet steel, *Wear*, 271, 2868-2878)

Penagos et al [14] investigate the refinement of structure in case of high chromium cast iron on wear loss. Castings were done employing different cooling rates for obtaining refinement of structure. Pin on garnet paper tester was used for two body abrasion and tests were conducted according ASTM G132 standards. Three body abrasive wear tests were conducted using dry sand rubber wheel abrasion tester and test were conducted according ASTM G65. The wear coefficient was observed to be depending on grain refinement instead of bulk material hardness shown in fig 2.3. M7C3 carbide was found to show cracking and fracture in case of fine grain structure whereas sub critical cracking of M7C3 is observed in case of coarse grain castings.

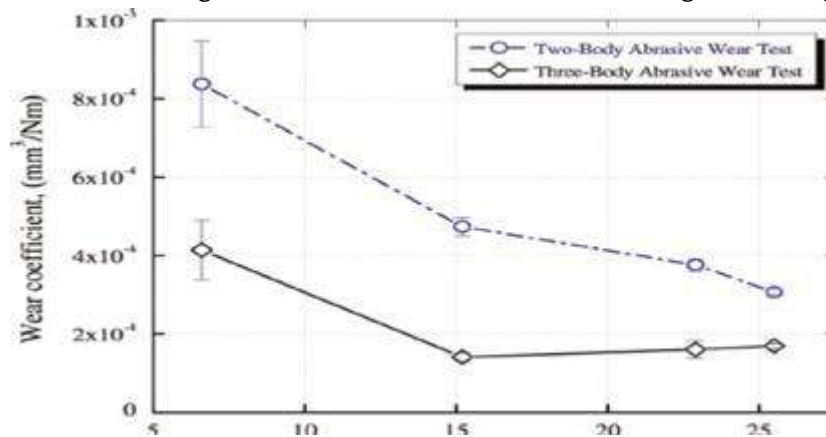


Figure 2.3. Wear coefficient vs mean free path for two body & three body abrasion tests. (Courtesy: J. J Penagos et al, (2015), Structure refinement effect on two and three body abrasion resistance of high chromium cast irons, *Wear*, 340-341, 19-24)

Kritika singh et al [15] attempted to understand the effect of heat treatment on micro structure and wear behavior of D2 steel. Tests were conducted using pin on plate abrasive wear test rig. The test samples were hardened and multiple tempered. The abrasive material was silicon carbide. The test parameters were systematically and simultaneously varied. The worn-out surface, subsurface and debris were examined in SEM, EDS and XRD. Random variation of abrasive particle size and load increased the volume loss along with temperature shown in fig 2.4. The wear results were analyzed with respect to micro-structure and operating wear mechanism which were influenced by wear parameters.

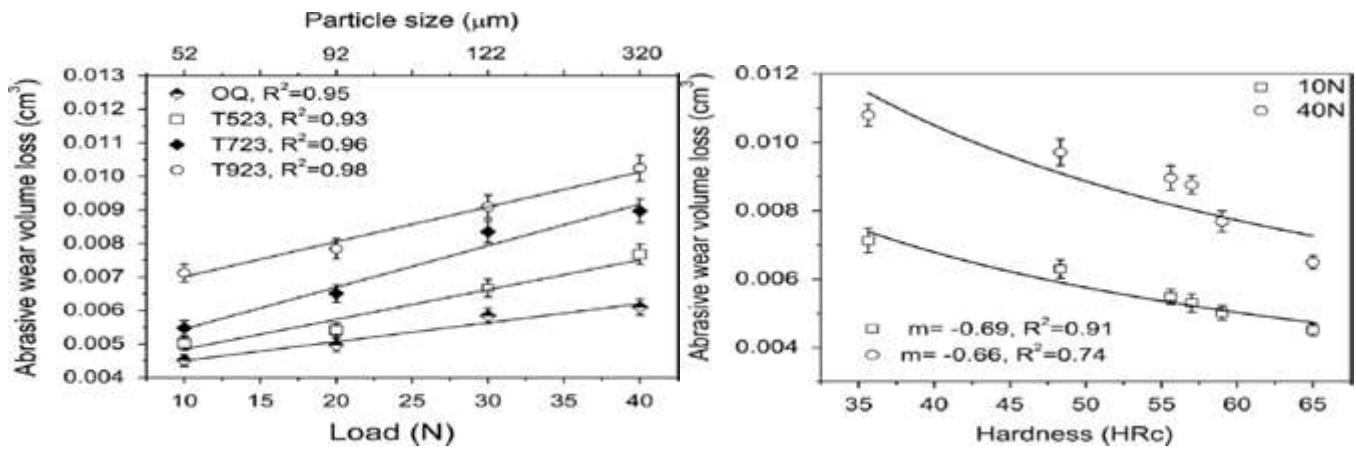


Figure 2.4. Variation of abrasive wear volume loss (cm³) as a function of hardness at a load of 10 N and 40 N. (Courtesy: Kritika Singh et al, (2015), Microstructure evolution and abrasive wear behavior of D2 steel, Wear, 328-329, 206-216)

Das Bakshi et al [16] attempted to understand the influence of micro-structure on wear behavior of graded steel. The tests were conducted using standard rubber wheel abrader test. The test samples were of three metallurgical structures and different hardness for the same steel. It was found that the abrasive particles were slide and cause pitting. Fragmentation of the surface in untampered martensite was found. Plastic deformation was found in active bainite. Depth and width of grooves was plotted and shown in the fig 2.4. The test results did not show any major deviations in wear co-efficient and wear loss for three different micro structured steels studied. The study in scanning electron microscopy of wear track identified different wear mechanism.

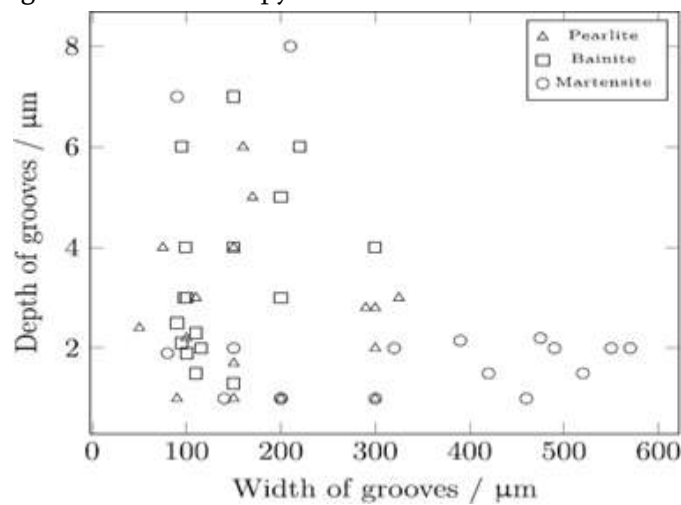


Figure 2.5. Groove characteristics for the three kinds of abraded samples. (Courtesy: S Das Bakshi et al, (2013), Three-body abrasive wear of fine pearlite, nanostructured bainite and martensite, Wear, 308, 46-53)

Nikola Ojala et al [17] attempted to understand the effect of compositions and micro-structure on the abrasive performance of quenched wear resistance steels. Experiments were conducted using crushing pin on wear testing rig. Experiments were conducted using 15 varieties of commercially available quenched wear resistance steel materials. The abrader was granite gravels and tests were conducted under high state of stresses. Wear loss of the order of 50 percent of variations was observed. The observed variations in wear loss were attributed to

prevailing micro-structure in different grade steels. The steels show different wear rates due to manufacturing conditions. 400 HB grades steels show better wear life compared with commercially available steels.

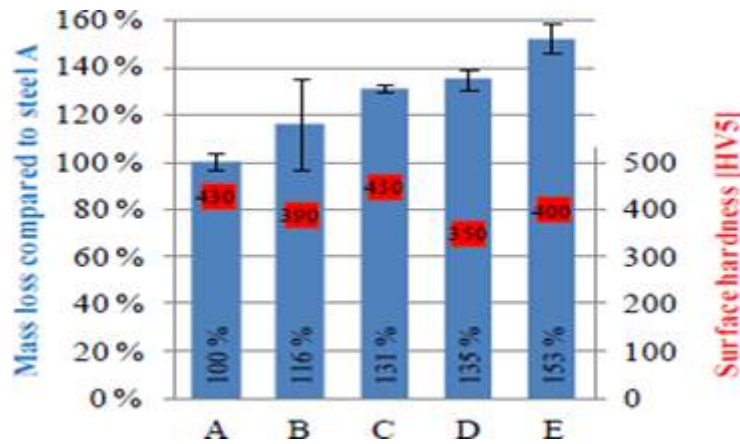


Figure: 2.6. Average mass loss for steel for 5 grades of steel. (Courtesy: Niko Ojala et al, (2014), Effects of composition and microstructure on the abrasive wear performance of quenched wear resistant steels, *Wear*, 317, 225-232)

Woldman et al [18] studied the influence of size of the abrader on single asperity wear. Tests were conducted using pin on flat machine which facilitated scratching along a straight line and under active load control. The abrasive body was a single crystal SiO₂ tip and the substrate was Din St-52 steel. The radius of the tip varied to understand the effect of size of the abrader and normal load changed to understand its influence. They found that the amount of wear and mechanisms involved in the wear varied with a given load shown in the fig.2.6. Microscopic studies were carried out on scratches to study the wear mechanism. The results showed that an increase in wear rate for increased load. The wear rate was found to be dependent on size of the abrader. Contrary to normal observation, the author observed increased wear rate for smaller sized abrader. Within the experimental range of abrader size and load, the author identified a regime of limited plastic deformation.

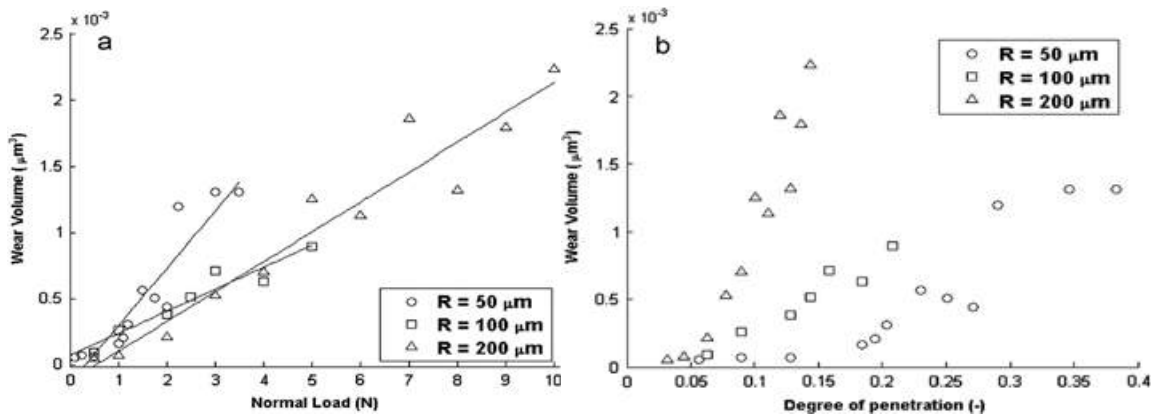


Figure: 2.7. Wear loss vs normal load and wear loss vs DOP for the different tip radius. (Courtesy: Niko Ojala et al, (2014), Effects of composition and microstructure on the abrasive wear performance of quenched wear resistant steels, *Wear*, 317, 225-232)

Vytenis jankauskas et al [19] made an attempt to characterize wear behaviour of manually arc welded hard facings with low carbon and stainless-steel matrix. Experiments were conducted using dry sand wheel abrader according ASTM G65 specifications. The authors, in the experiments, tried to address the effect of binder material, tungsten carbide grain size and contents of tungsten carbide in an electrode used for hard facings of agricultural implements. The resistance of wear and hardness was increased by addition of WC. The hard facings by WC grain size of 135 micrometre. A lower wear rate of factor of 9 was found. The experimental results also showed an improvement in wear resistance when tungsten carbide content was an order of 42 to 48%. Attempt was also made to find the wear mechanism in the hard facings.

Hernandez et al [20] made an attempt to understand role of temperature on abrasive of boron steel and hot forming tool steels. Experiments have been conducted using a high temperature continuous abrasion machine. Tests were conducted over a temperature 20° to 800°c with a constant normal load of 45N and sliding speed of 1m/s. The wear results were co-related with hardness obtained by hot hardness tester. The worn surface studied in scanning electron microscope. The target materials used were boron steel and two different pre-hardened tools steels. The hot hardness test results indicated a gradual decrease in hardness up to 600°C and above 600°C hardness dropped at a much faster rate. The rate of wear was found to remain constant and improved up to 400°C. The improvement in wear performance was attributed to increased toughness and wear protective tribo-layers. The wear rate was found to increase with increase in temperature above 400°C. This trend was attributed to decrease in hardness and re-crystallization.

III. CONCLUSIONS

From the study carried out from various researchers it was concluded that, the quantum of the abrasive wear is grater in extent may takes place than the excepted. Abrasive wear was influenced by hard particles on the surface of the material. Abrasive wear does not only depend on the hardness of the particles also on size of the abrasive and nature of contact. Microscopic study of abraded area reveals various mechanisms of wear like cutting mode, wedge mode, ploughing mode and so on. Various mechanisms were found by the observers from the influence of abrasive wear. Influence of wear was also depending on the type of materials subjected to abrasion also on temperature that influence the area of abrasion

IV. REFERENCES

- [1]. Archard, J.F, J. Appl. Phys., 1953, 24, 981-988.
- [2]. Bhansali, K.J, wear control hand book, Peterson M.B and Winer, W.O, (Eds), 1980, ASME, 373-383
- [3]. Johnson, K.L., Wear, 1994, 190, 162-170.
- [4]. Hokkarigawa, K., Bulletin of the ceramic society of japan, 1997 1, 19-24.
- [5]. Holm, R., Electric contact, Almquist and Wiksells, Stockholm, 1946, section 40.
- [6]. Lancaster, J.K., Trans. Inst. Metal Finish. 1978, 56, 4, 145.
- [7]. Rabinowicz, E., Wear control hand book, Peterson M.B and Winer, W.O, (Eds), ASME, 1980, 475.
- [8]. Lim, S.C. and Ashby, M.F., Acta Metallurgica, 1987, 35, 1, 1-24.

- [9]. Hokkarigawa, K and Kato, K., *Tribology Int.*, 1988, 21, 1, 51-57.
- [10]. Chiou, Y.C., Kato, K., and Kayaba, T. *ASME, J. Tribology*, (1985), 107, 491-495.
- [11]. Cho, S.J., Hockey, B.J., and Lawn, B.R. (), *J. am .Ceram, Soc.*, 1989, 72, 7, 1949- 1952.
- [12]. Stanislav N. Verichev, Vasily V. Mishakin, Dmitry A. Nuzhdin, Evgeny N. Razov, *Ocean Engineering*, 99 (2015) 9-13.
- [13]. Juri Pirso, Mart Vijijs, Sergei Letunovits, kristjan, Renee Joost *Wear* 271 (2011) 2868-2878.
- [14]. J.J. Penagos, F.Ono, E. Albertin, A. Sinatora, *Wear*, 340-341(2015) 19-24.
- [15]. Kritika Singh, Rajesh K. Khatikar, Sanjay G. Sapate, *Wear*, 328-329 (2015) 206-216.
- [16]. S. Das Bakshi, P.H. Shipway, H.K.D.H. Bhadeshia, *Wear*, 308 (2013) 46-53.
- [17]. Nikola Ojala, Kati Valtonen, Vuokko Heino, Marke Kallio, Jonas Aaltonen, *Wear*, 317 (2014) 225-232.
- [18]. M Woldman, E, Van Der Heide, T.Tinga, M.A,Masen, *Wear* 301 (2013) 76-81.
- [19]. Vytenis Jancauskas, askim Antonov, Valentinas Varnauskas, Remigijus Skirkus., *Wear* 328-329 (2015) 378-390.
- [20]. S. Hernandez, J. Hardel, H. Winkelmann, M.Rodriguez Ripoll, B. Prakash, *Wear* 338- 339 (2015) 27-35.



Energy Efficient Automated Hydraulic Power Unit

Nikhil Kumar K¹, Paraveej Shirahatti², S. ShivaPrakash³, Gujjala Anil Babu⁴, H.K. Shivanand⁵

¹M.tech Student, Department of Mechanical Engineering, UVCE, Bangalore, Karnataka, India

²Research scholar, Department of Mechanical Engineering, UVCE, Bangalore, Karnataka, India

³Assistant Professor, Department of Mechanical Engineering New Horizon College of Engineering, Bangalore, Karnataka, India

⁴Senior Manager, Hindustan Aeronautics Limited, Bangalore, Karnataka, India

⁵Professor, Department of Mechanical Engineering, UVCE, Bangalore, Karnataka, India

ABSTRACT

The variable frequency drive (VFD) industry is growing rapidly and it is now more important than ever for technicians and maintenance personnel to keep VFD installations running smoothly. Variable frequency drives (VFD) change the speed of motor by changing voltage and frequency of the power supplied to the motor. In order to maintain proper power factor and reduce excessive heating of the motor, the name plate volts/hertz ratio must be maintained. This is the main task of variable frequency drive. Implementation of Variable Frequency Drive to the present system to run motor at different speeds. Test the performance of the developed system for clamping operation. Integration of Programmable Logic Controller to achieve automation. Energy usage is reduced and hence system becomes economical. The flow rate of the hydraulic fluid can be controlled and reduces the cooling time. It reduce the process cost. The most dominating parameter is determine the actual amount of saving was ratio of idle time to total cycle time and also observed that at idle time there is less usage of hydraulic oil. This increase the life hydraulic oil and hence its components.

Keywords: programmable logic controller, variable frequency drive, hydraulic oil

I. INTRODUCTION

The word “hydraulics” generally refers to power produced by moving liquids. Modern hydraulics is defined as the use of confined liquid to transmit power, multiply force, or produce motion. This force and motion maybe in the form of pushing, pulling, rotating, regulating and driving. Though hydraulic power in the form of water wheels and other simple devices has been in use for centuries, the principles of hydraulics weren't formulated into scientific law until the 17th century. It was then that French philosopher Blaise Pascal discovered that liquids cannot be compressed. He discovered a law which states “Pressure applied on a confined fluid is transmitted in all directions with equal force on equal areas”.

MOTIVATION

Most of the machines tools in use today utilize a complex hydraulic system to perform the necessary work required for the process. The pressure and flow rate demands on the hydraulic system vary significantly throughout the cycle. Many older systems are greatly oversized so that they are able to meet the peak hydraulic demand at any point. These systems operate inefficiently because there is typically no way to limit the hydraulic capacity during periods of low demand. As a result, fluid is throttled to lower pressures and excess fluid flow is routed directly back to the system reservoir, wasting motor energy and increasing the thermal load on the cooling system. There is unnecessary power consumption in system.

There is a need to change how hydraulic system works.

II. SCOPE OF WORK

Consisting mainly of a motor, a reservoir and a hydraulic pump, these units can generate a tremendous amount of power to drive most any kind of hydraulic ram. Hydraulic Power Units are based on Pascal's law of physics, drawing their power from ratios of area and pressure. Hydraulic Power Units are used in a wide range of applications:

- Machine Tool
- Mobile Equipment
- Paper Mill Machinery
- Rolling Mill Machinery
- Material Handling

The energy can be saved for the systems which have idle time.

III. OBJECTIVE

The objectives of the study titled “Energy Efficient Automated Hydraulic Power Unit” are as follows

- Implementation of Variable Frequency Drive to the present system to run motor at different speeds.
- Test the performance of the developed system for clamping operation.
- Integration of Programmable Logic Controller to achieve automation.

IV. METHODOLOGY

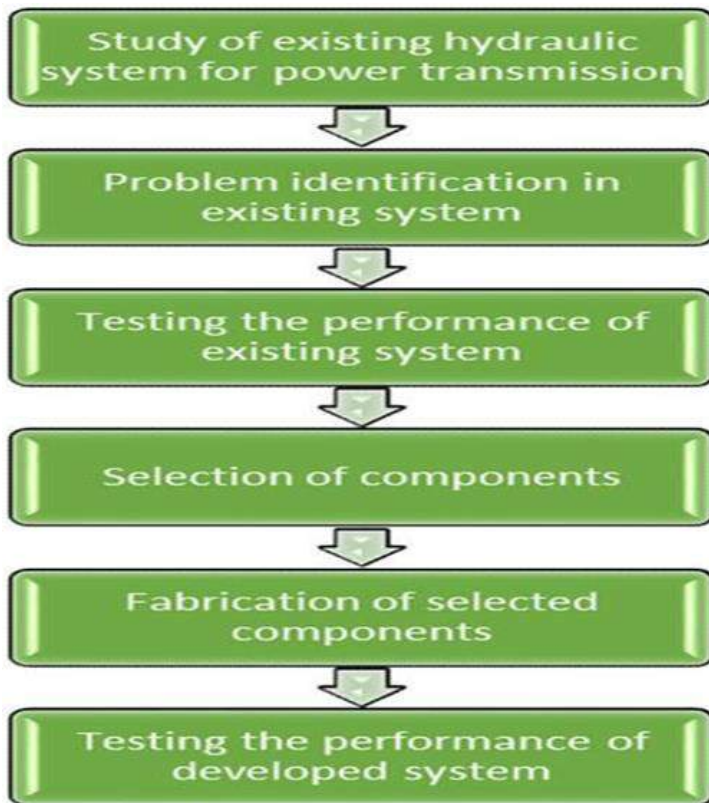


Fig.1 Flow Chart

V. PRESENT SCENARIO

SERIAL NUMBER	PARAMETER	SPECIFICATIONS
1	DIMENSIONS	W=540 x H =650 x D=625 mm
2	WEIGHT	107.5 Kg
3	PAINT COATING	BLUE RAL 5010
4	PRESSURE	55 BAR
5	OIL TANK	40 L
6	FLOW	8lpm
7	VOLTAGE	415 VAC
8	FREQUENCY	50 HZ
9	POWER	1.5 KW

Table 5: Specifications of Present System

CYLINDER IS IN MOTION

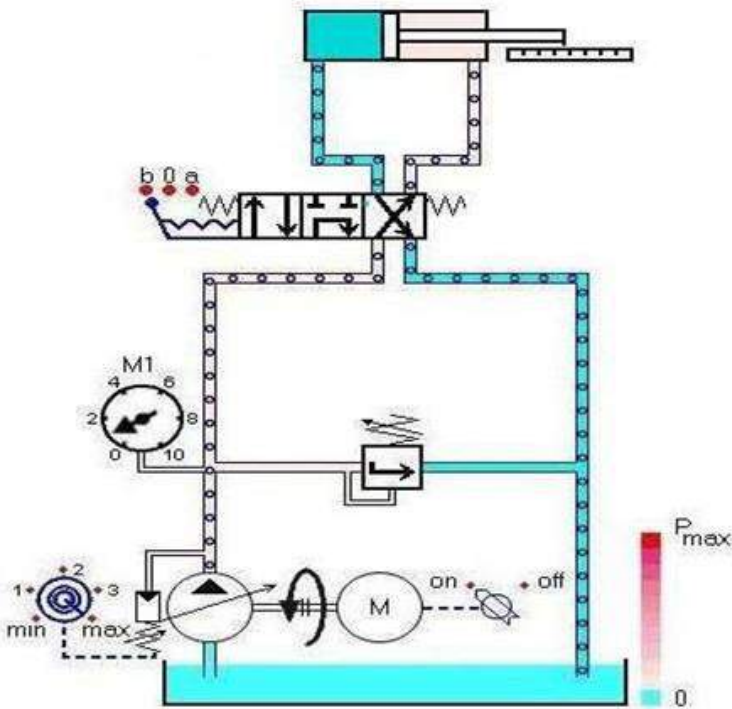


Fig.2 Cylinder in transition

CYLINDER IS AT THE DEAD END POSITION (CLAMPED POSITIONS)

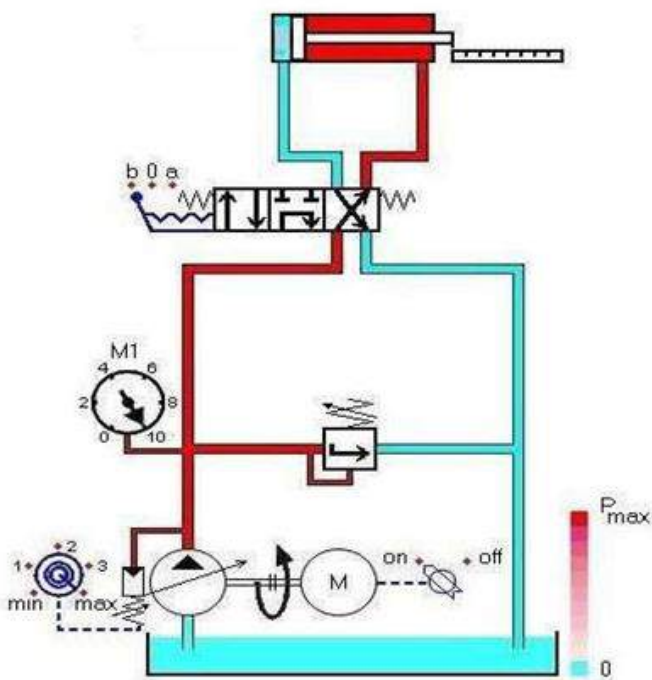


Fig.3 Cylinder in clamped position

VI. RESULTS OF DEVELOPED SYSTEM

POWER CALCULATIONS

Frequency-1 = 10 Hz Pressure = 50 bar Speed= 300 rpm.

Displacement of the pump(v)= $8\text{cc/rev}=8 \times 10^{-3}$ liters /revolution

Discharge (Q) = $v \times N$ lpm

= 2.4 lpm

Power Consumed (P_w)= 0.1936 KW

Frequency-2 = 50 Hz Pressure < 50 bar Speed= 1500 rpm

Displacement of the pump(v)= $8\text{cc/rev}=8 \times 10^{-3}$ liters /revolution

Discharge (Q) = $v \times N$ lpm

= 12 lpm

Power Consumed (P_w)= 0.4841 KW

TOTAL POWER CONSUMED

Using a 25 % loading cycle: 45 min clamped and 15 min loading

Total Power = $[(P_{w1} \times 75\%) + (P_{w2} \times 25\%)]$

= 0.2662 KW

Heat dissipation in a tank:

$EL = 0.6438 Q P (1 - \mu)W$

$EL = 51.504 W$

$TD = EL / (\sum KA)$

TD = temperature over ambient K $TD = T_{oil} - T_{air}$

= $(60+273) - (27+273) = 33 K$

The surface area of our tank, $A = 0.351 m^2$

$\therefore 33 = (51.504) / (205 \times A)$

$A = 0.00761 m^2$.

The designed surface area of the tank $0.351 m^2$ is larger than the required surface area

$A = 0.00761 m^2$ for the natural heat dissipation of oil in the tank

\therefore We conclude that design of the tank is safe.

VII. POWER CIRCUIT

PRESENT SYSTEM

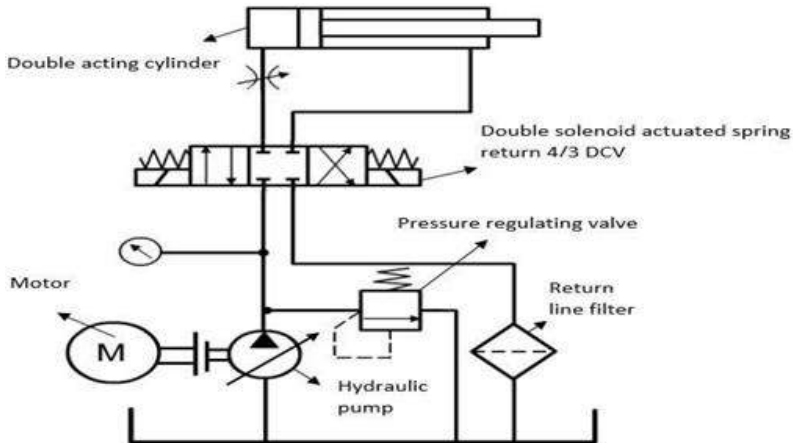


Fig.4 present working circuit

Developed System circuit.

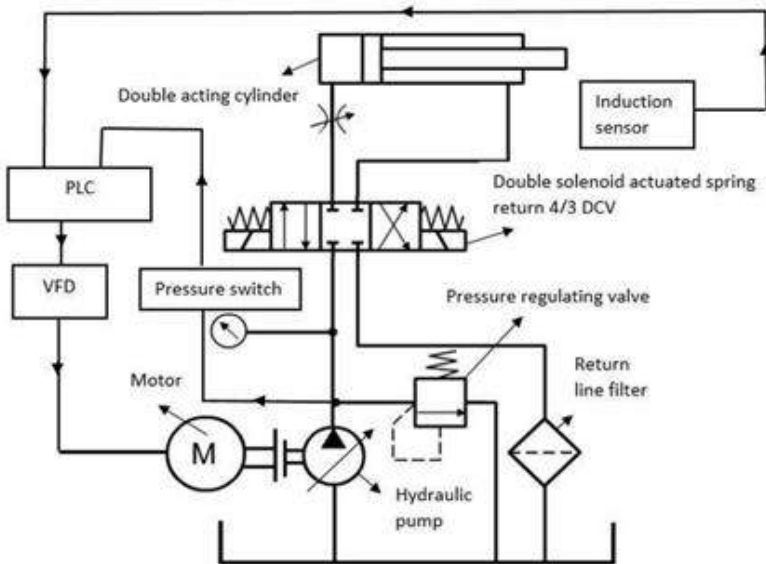
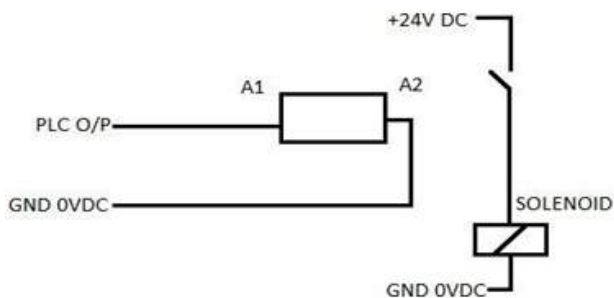


Fig.5 Developed System circuit

WIRING DIAGRAM



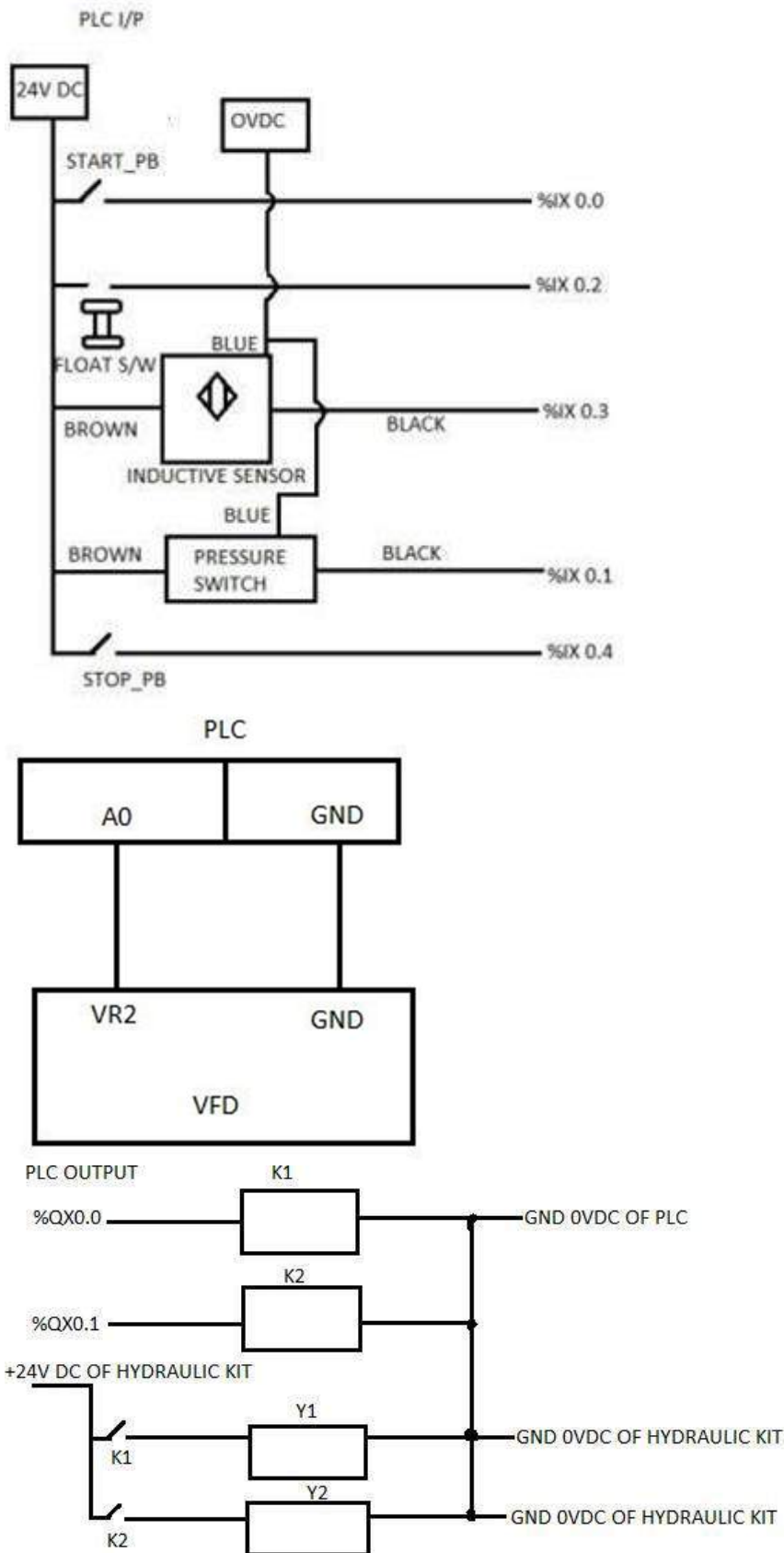


Fig.6 wiring diagram

PLC PROGRAM

Fig 7.4 shows PLC program, developed using, Indra Works Engineering 12.8.301.0 software, which is developed by BOSCH REXROTH.

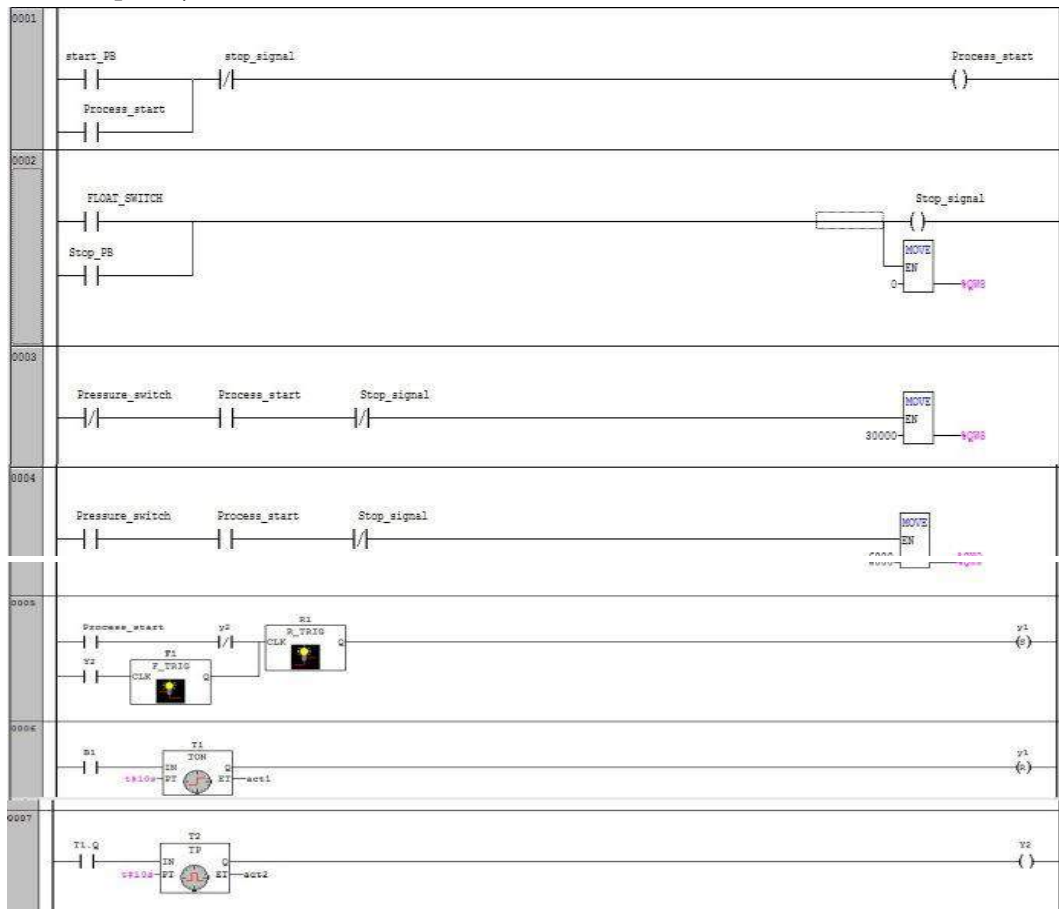


Fig.7 PLC program

PROGRAM PLC_PRG

start_PB AT %IX0.0: BOOL;
 Pressure_switch AT %IX0.1: BOOL; FLOAT_SWITCH AT %IX0.2: BOOL; B1 AT %IX0.3: BOOL;
 Stop_PB AT %IX0.4: BOOL; y1 AT %QX0.0: BOOL;
 Y2 AT %QX0.1: BOOL;
 Process_start: BOOL; stop_signal: BOOL; F1: F_TRIG;
 R1: R_TRIG; T1: TON;
 act1: TIME; T2: TP; act2: TIME;

VIII. BILL OF MATERIAL FOR POWER UNIT

Table 1

SL.NO	DESCRIPTION	QUANTITY	MODEL CODE	ID CODE
1	OIL RESERVOIR	1	40LTRS (ALUMINUM)	R983020305
2	AIR FILTER	1	AIR BREATHER	R983029536
3	OIL GAUGE	1	LG6-05-M12	R983027465
4	STRAINER-TYPE FILTER	1	SE-05 F-58L-250 1/2"BSPP	R983028532
5	PUMP STATION	1	1.5KW,B35/V7- 6/10	R983015045
6	DISTRIBUTION BLOCK ASSLY (BARE)	1		R983008274
7	RETURN FILTER	1	FIF-04-B-025	R983020315
8	CLOGGING INDICATOR	1	VISUAL INDICATOR ""GR50""	R983027464
9	HY-CHECK VALVE	1	S10 A 1.0	R983030666
10	TOP PLATE	1	40L- DRG:343116464	R983016271
11	OIL COLLECTING PAN	1	40L AL TANK- DIDACTIC	R983017547
12	THREADED TUBE	1	1/2" BSP- 344107224/1	R983016747
13	ELECTRIC EQUPT MOUNTING DIDACTICS POWER PACK	1		R983051228
14	VANE PUMP	1	8cc/rev	R983057626
15	FREQUENCY CONVERTOR	1	1.2HP KVFC- 407GR	R983016857
16	TEMPARATURE INDICATOR	1	LCD DIGITAL TEMPERATURE INDICATOR	
17	PRESSURE SWITCH	1	EVC002	R983056189

IX. COMPONENTS USED FOR EFFICIENT SYSTEM

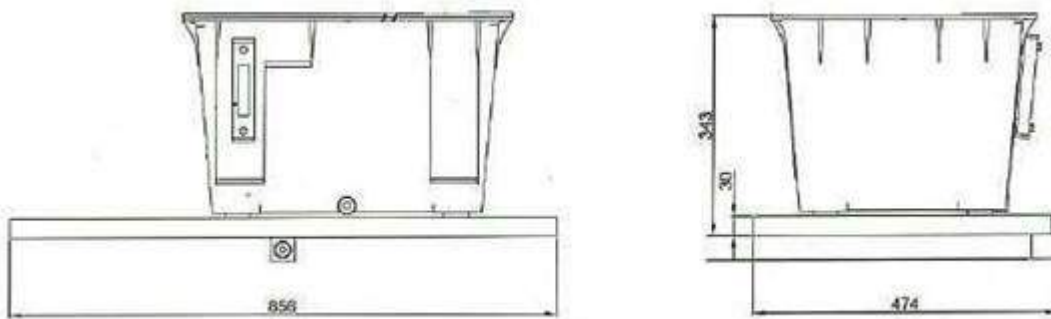


Fig.8 oil reservoir



Fig.9 Pressure Compensated Vane Pump



Fig.10 Breather



Fig.11 oil level indicator Fig.12 Electric Motor

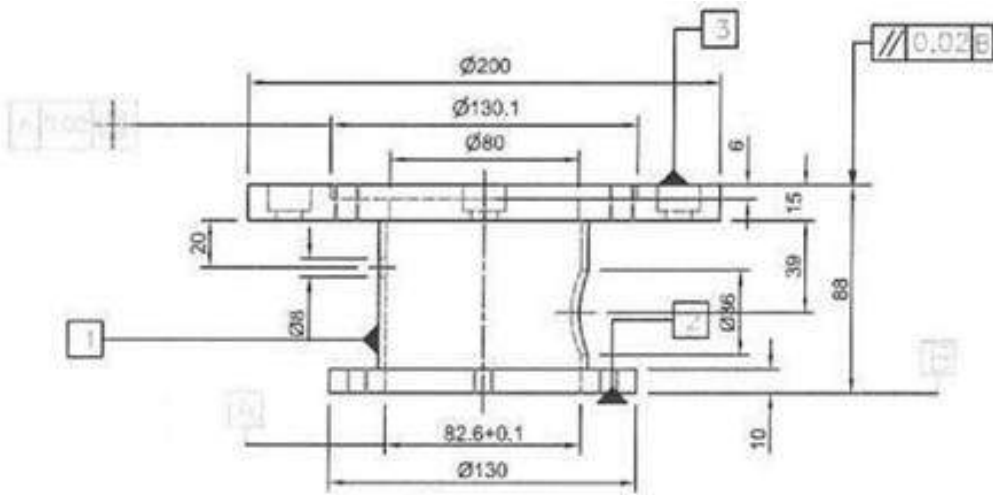


Fig.13 Bell Housing

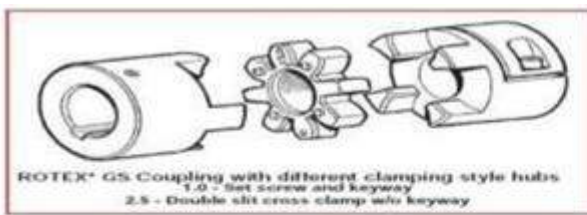


Fig.14 Coupling



Fig.15 Frequency Convertor Fig9.9Check Valve



Fig.15 Pressure Gauge Fig.16 Temperature Indicator

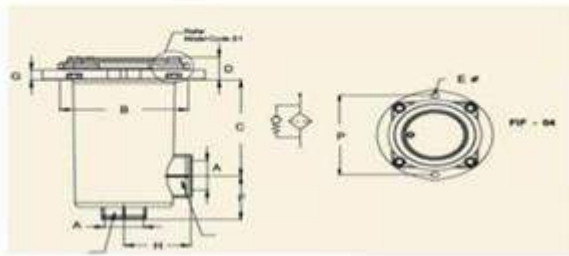


Fig.17 Return Line Filter



Fig.18 Clogging Indicator Fig.19 Quick Disconnect Coupling

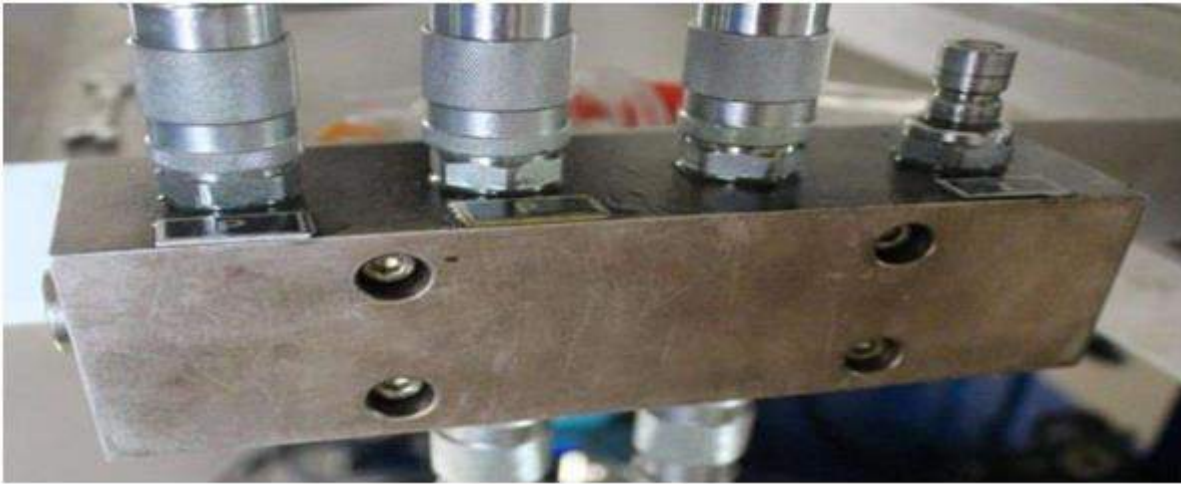


Fig.20 P/T Distributor



Fig.21 Pressure Switch

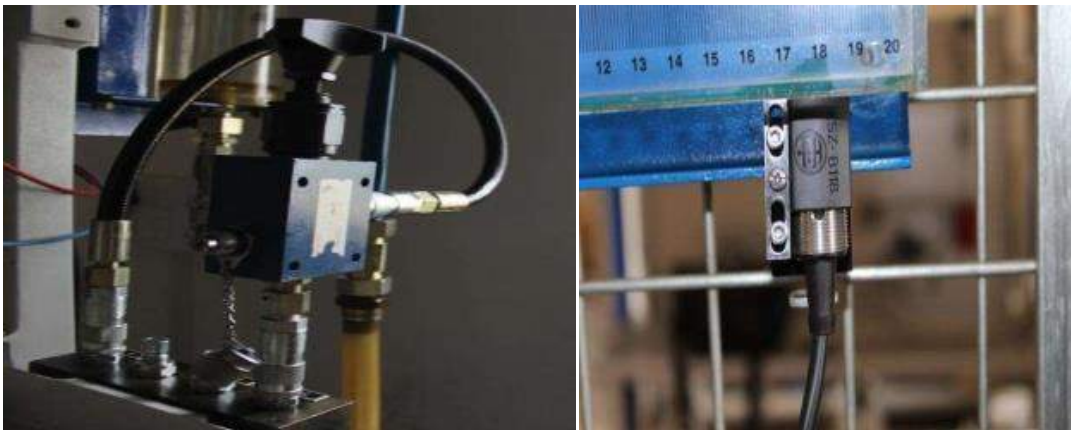


Fig.22 Pressure Relief Fig.23 Inductive Sensor Valve

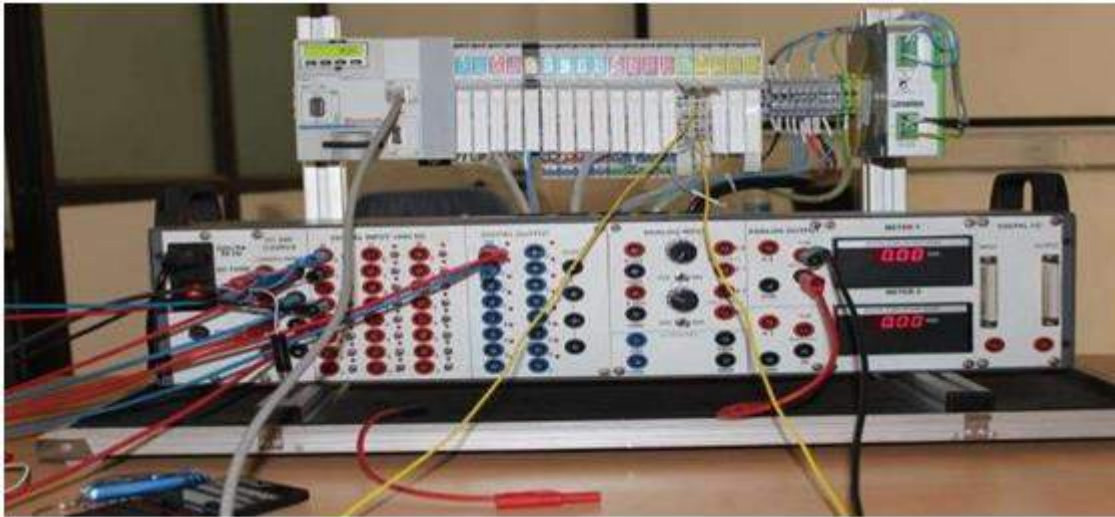


Fig.24 Programmable Logic Controller

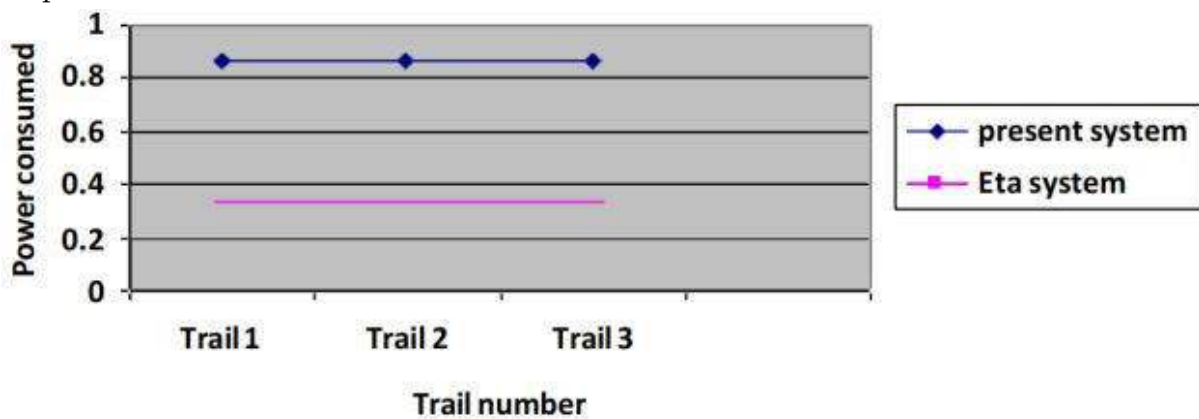
X. COMPARISONS

POWER CONSUMED

Table.2 Comparison of Power Consumed

TRAIL	PRESENT SYSTEM(kW)	Eta SYSTEM(kW)
I	0.8625	0.345
II	0.8625	0.345
III	0.8625	0.345

Graph.1 Power consumed vs Trail number

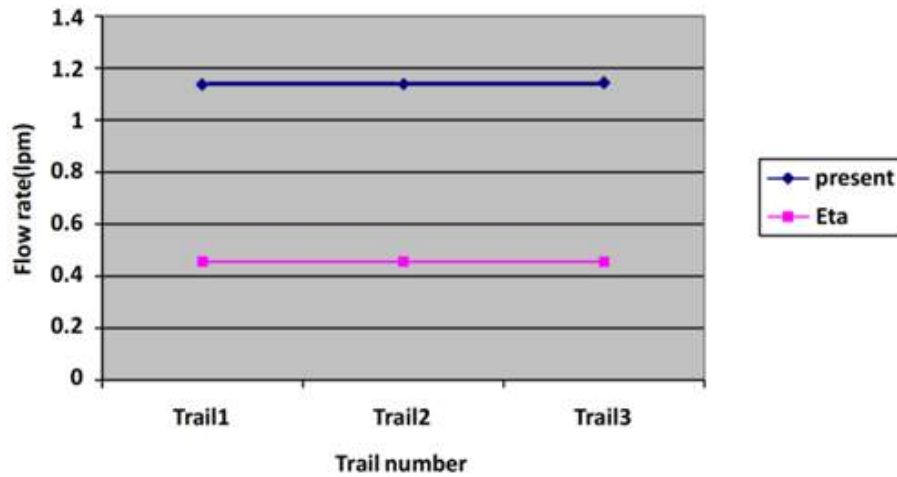


FLOW OF OIL THROUGH PRV DURING CLAMPED POSITION

Table.3 Flow of oil during clamped position

TRAIL	PRESENT SYSTEM(lpm)	Eta SYSTEM(lpm)
I	1.137	0.4555
II	1.139	0.4557
III	1.143	0.4552

Graph.2 Flow rate(lpm) v/s Trail

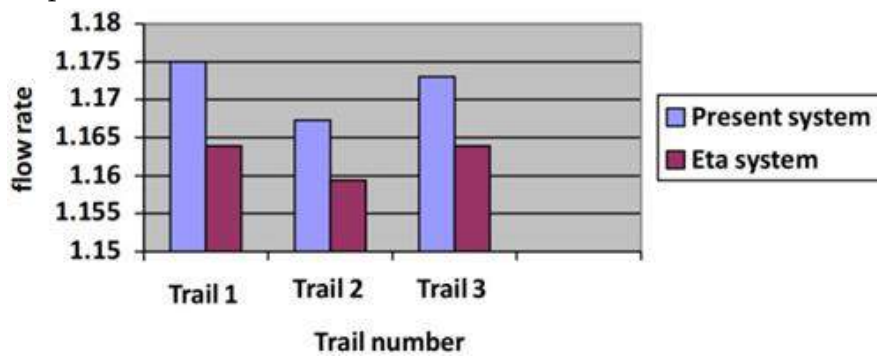


TOTAL FLOW OF OIL THROUGH THE SYSTEM DURING LOADING

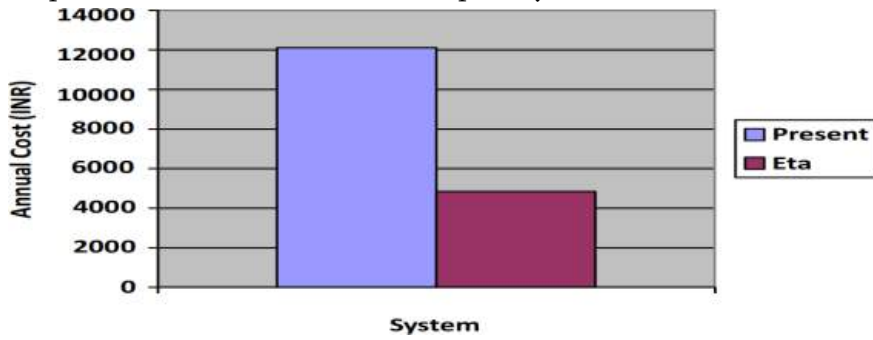
Table.4 Flow of oil during loading

TRAIL	PRESENT SYSTEM	Eta SYSTEM
I	1.175	1.1639
II	1.1673	1.1594
III	1.173	1.1639

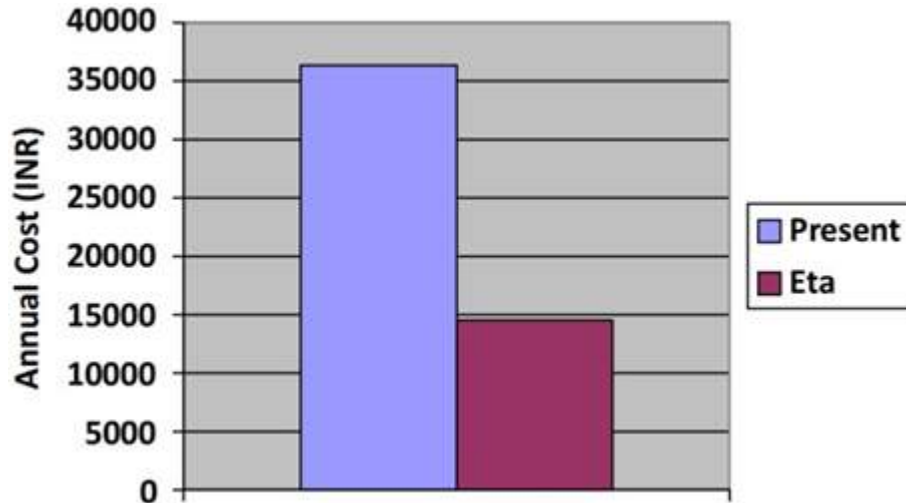
Graph.3 Flow rate vs Trail number



Graph.4 Annual cost in INR for 8hrs per day



Graph.5 Annual cost in INR for 24hrs per day



COMPARISON TABLE OF BOTH THE SYSTEMS

Table.5 Comparison of present system with Eta system

PARAMETER	PRESENT SYSTEM	Eta SYSTEM
Power consumed	0.8625 kW-hr	0.345kW-hr
Flow of oil through PRV during clamped position	1.139 lpm	0.4554 lpm
Flow of oil through PRV during Loading cycle	1.171 lpm	1.1624 lpm
Cost to run for 8 hrs. a day	Rs.12,109	Rs.4,843
Cost to run for 24 hrs. a day	Rs.36,328	Rs.14,531

XI. CONCLUSION

- Energy saving potential of machine tool running by hydraulic systems with variable frequency drive.
- It is found that the energy usage by present system is 0.8625kW and Eta system is 0.345kW respectively. Energy usage is reduced by 61% and hence system becomes economical.
- The most dominating parameter in determining the actual amount of saving was ratio of idle time to total cycle time and also observed that at idle time there is less usage of hydraulic oil.
- As there is less circulation of fluid during idle cycle, oil will not get heated up easily as compared to loading cycle. So that oil temperature slightly reduces and viscosity of oil will remain almost same.

This increases life of hydraulic oil and hence the components.

- The entire system is automated with the help of programmable logic controller, so that actuation as well as frequency controlling can be done simultaneously without human intervention.

XII. REFERENCES

- [1]. Srinivasan M, Sheng P (1999) Feature- Based Process Planning for Environmentally Conscious Machining – Part 1: Microplanning. *Robotics and Computer-Integrated Manufacturing* 15(3):257–270.
- [2]. Toenissen S (2009) Power Consumption of Precision Machine Tools Under Varied Cutting Conditions, LMAS Report. University of California, Berkeley.
- [3]. Devoldere T, Dewulf W, Deprez W, Willems B, Duflou JR (2007) Improvement Potential for Energy Consumption in Discrete Part Production Machines. *Proceedings of 14th CIRP Conference on LCE*, 311–316.
- [4]. Herrman C, Bergmann L, Thiede S, Zein A (2007) Energy Labels for Production Machines– An Approach to Facilitate Energy Efficiency in Production Systems.
- [5]. boschrexroth.com/ics
- [6]. boschrexroth.com/spc
- [7]. Efficient energy management is variable frequency drives the solution *Procedia - Social and Behavioral Sciences* 145 (2014) 371 – 376, Nasir Khalid.
- [8]. *CIRP Annals - Manufacturing Technology* 59 (2010) 21–24.



Effect of Heat Flux on Free Convection Heat Transfer in Porous Trapezoidal Enclosures

Vijaya Kumara V M^{1*}, Aswatha¹, Hemanth Kumar C B¹

¹Department of Mechanical Engineering, Bangalore Institute of Technology, K R Road, Bangaluru -560004, Karnataka, India

ABSTRACT

The current work is undertaken to investigate the buoyant circulation in a porous non-square cavity with heat flux is determine using finite element based mathematical procedure. The cavity is used for fluid flow, analysis of fluid flow and heat transfer has bottom wall subjected to heat flux and constant thermal effect at top and inclined walls The bottom wall subjected to uniformly and non-uniformly heat fluxes. The numerical simulations has been studied for Rayleigh number $101 \leq Ra \leq 103$ with respect to uniform and non-uniform heated wall and top cold walls. The fact inside the enclosure with centrally located porous media and analyzed through isotherm pattern, streamline pattern, local and mean Nusselt number. It is found that the average Nu more for linearly varied heat flux boundary condition at bottom wall.

Keywords: Trapezoidal cavity, Natural convection, Porous medium, Heat flux and Nusselt number.

I. INTRODUCTION

The paper deals with fluid and heat transfer has occupied the centre stage in many industrial and engineering applications. However, from one decade, awareness on free convection in a closed porous cavity with Heat function boundary condition is increased very rapidly. Most of the commonly used cavities in industries are triangle, square, circular and non-square cavity.

Different cavities with various boundary conditions with porous media have been considered extensively by different researchers. However cavities with bottom wall heating have received less consideration. There are many engineering applications where the buoyant energy through a fluid region contained in a cavity is to be controlled.

Saranya et al.[1] presented the effect of heat flux on porous square cavity. They observed that, uniformly varying heat flux along bottom wall, the maximum rate of heat transfer at middle of the heated wall due to increased fluid flow rate at center region of the cavity.

Prasad [2] studied buoyant thermal effect in a regular porous cavity with constant heat flux on one vertical wall. Peter Vadasz [3] derived analytical solutions to confirm radical and differential data disclose a wide spread

dispersion of heat flux data in buoyant heat transfer in porous media. The buoyant circulation was higher when the strong fluid flows at the midpoint of the enclosure.

Bader Alazmi et al. [4] have studied initial conditions for constant wall heat flux in the absence of local thermal boundary. Outcome of changing porosity and buoyant heat transfer were analyzed. Results were found in terms of streamlines and heat lines.

Mahapatra et al. [5], have conducted a numerical simulations on mixed convection with radiation effect. The work reveals that radiation has substantial bearing on buoyant heat transfer and it is managed to flow turnaround in the middle of the enclosure. After thorough literature, the authors feel to outline a few prior research works identifying the phenomenon of natural convection in divided cavities.

Numerical simulations on laminar natural convection in a 2D air filled regular enclosure with a vertical partition of finite thickness carried out by Mezrhab and Bchir [6]. The computational model is bounded by adiabatic horizontal end walls, and vertical surfaces at different temperature. Calculations including shadow effects have been carried out using finite volume based computational procedure. It is noticed that there is no significant modifications on heat transfer through the enclosure, especially at Ra.

Aparna et al.[7] studied simulations using finite element method with triangular elements to investigate the heat flux effect in a trapezoidal cavity .Numerical study has been carried out different number of Rayleigh number. Nusselt numbers and stream functions. The heat transfer is maximum for sinusoidal varying Ra and heat flux.

Varol et al. [8] numerically performed fluid motion and buoyant energy in a porous cavity with constant isotherms and non-isothermally bottom wall heated a triangular cavity is analyzed using finite difference method. Darcy governing law was used to generate the codes of porous medium filled inside a cavity.

From the above literature scan, it can be seen that there is lack of information regarding buoyant thermal flux in enclosures with bottom wall subjected to heat flux boundary conditions. The of the present work is to numerically estimate the heat transfer and fluid flow in a 2D porous non-square enclosure with thermal flux initial conditions along the bottom wall.

II. POROUS GEOMETRY

A physical domain of a Non-Square Porous region is depicted in Figure 1. Notice that, bottom wall with uniformly and sinusoidal varying boundary conditions, left and right side walls are well insulated and top wall is cold.

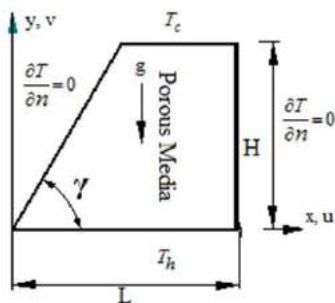


Fig. 1: Physical domain

A. PROBLEM FORMULATION

In order to obtain the governing equations for above working model following assumptions are adopted,

- The Radiation heat exchange is negligible.
- The fluid flow with small Reynolds's numbers.
- The working medium is Newtonian and the Boussinesq approximation.
- Thermal equilibrium obtained between fluid and porous medium.
- For the flow prediction inside the porous cavity, Darcy's governing equation is used.

For buoyant energy transfer, the dimensionless variables as

$$X = \frac{x}{L}, Y = \frac{y}{L}, \psi = \frac{\psi}{\alpha}, \theta = \left(\frac{T - T_C}{T_h - T_C} \right) \quad (1)$$

$$\text{Modified Rayleigh number} \quad Ra = \frac{g\beta_T \nabla T K L}{\nu \alpha} \quad (2)$$

$$\frac{\partial u}{\partial x} + \frac{\partial v}{\partial y} = 0 \quad (3)$$

The velocity in X- direction can be described by

$$u = \frac{-K}{\mu} \frac{\partial p}{\partial x} \quad (4)$$

Velocity in vertical direction is given by

$$v = \frac{-K}{\mu} \left(\frac{\partial p}{\partial y} + \rho g \right) \quad (5)$$

The permeability K of porous medium is given by

$$K = \frac{D_p^2 \phi^3}{180(1-\phi)^2} \quad (6)$$

The buoyant parameter variation within the porous cavity is given by

$$\rho = \rho_\infty [1 - \beta_T (T - T_\infty)] \quad (7)$$

Momentum equation:

$$\frac{\partial v}{\partial x} - \frac{\partial u}{\partial y} = \frac{K g \beta_T}{\gamma} \frac{\partial T}{\partial x} \quad (8)$$

Energy equation;

$$u \frac{\partial T}{\partial x} + v \frac{\partial T}{\partial y} = \alpha \left(\frac{\partial^2 T}{\partial x^2} + \frac{\partial^2 T}{\partial y^2} \right) \quad (9)$$

The continuity equation follows following stream functions such as

$$u = \frac{\partial \psi}{\partial y} \quad (10)$$

$$v = -\frac{\partial \psi}{\partial x} \quad (11)$$

Non-dimensional equations for porous cavities are

$$\left(\frac{\partial^2 \psi}{\partial X^2} + \frac{\partial^2 \psi}{\partial Y^2} \right) = -Ra \frac{\partial \theta}{\partial X} \quad (12)$$

B. BOUNDARY CONDITIONS

The boundary conditions for temperature with case (see Fig 1) are

$$\theta_h = 1 \text{ (Uniform heating, bottom wall)}$$

$$\theta_c = 0 \text{ (Top cold wall)} \quad (13)$$

$$\frac{\partial \theta}{\partial Y} = 0 \text{ (adiabatic inclined walls)}$$

$$\frac{\partial H}{\partial Y} = U\theta - \frac{\partial \theta}{\partial X} \text{ (Heat function)}$$

C. SOLUTION METHODOLOGY

The computations are undertaken for 41 X 41 grid based on a grid refinement study. A Galerikin's Residual finite element method is used for solution of the dimensionless governing equations. In order to determine the buoyant heat transfer parameters in the non square cavity, Eqn. (12) is to be solved.

D. SIMULATION RESULTS

The grid independency against for various mesh size of 11×11, 21×21, 31×31, 41×41, 51×51 and 61× 61 of a porous square cavity for regular mesh with triangular element have been investigated using Finite Element Method. Table shows grid independence study of the average Nusselt numbers with Ra =500 for left side is wall uniform heating. Average nusselt number is increases from 11 X 11 to 31 X 31 and constant at 41 X 41,51 X 51,61 X 61 Grid size , hence 41 X 41grid is used for all further computations.

Grid independence Test	
Grid Dimension	Average Nusselt No(\overline{Nu})
11 X 11	10.3212
21 X 21	8.5325
31 X 31	7.1023
41 X 41	6.4456
51 X 51	6.4435
61 X 61	6.4401

Table. 1: Mesh convergence study.

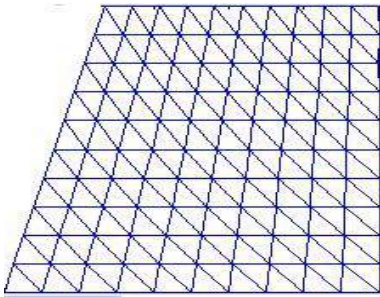


Fig. 2: Triangular Mesh for trapezoidal cavity

Local parameters such as heat functions and stream functions have been comparing to the reference Aparna and Seetharamu [7] for linear heating. A code is developed to generate isotherms and streamlines for 2D free convection problems in trapezoidal cavities using MATLAB.

Local parameters such as heat functions and stream functions have been comparing to the reference Aparna and Seetharamu [7] for linear heating. A code is developed to generate isotherms and streamlines for 2D free convection problems in trapezoidal cavities using MATLAB.

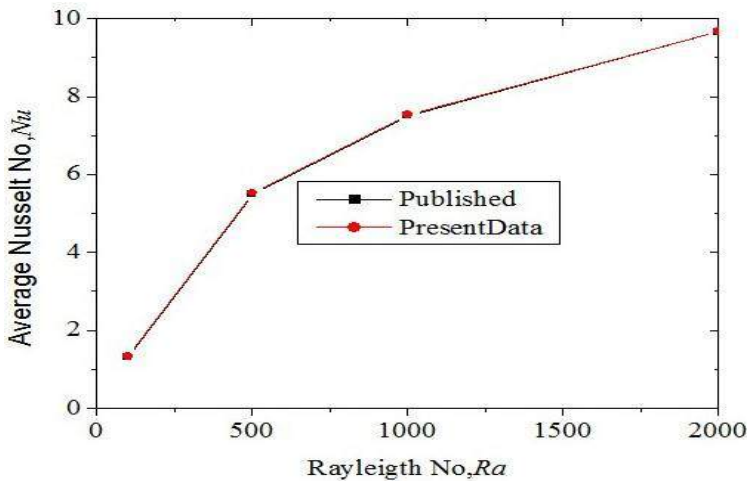


Fig. 3: Assessment of the present work with other published data for Non square enclosure at Ra = 500

A 2D non-square enclosure filled with saturated water is considered to validate the current study. The work has been investigated for Ra = 500 and data is calculated in terms of average Nusselt Numbers. It is found that the excellent agreement between Published data [7] and present study with sidewall inclinations of 550 for non-square cavity.

Ra	\overline{Nu}		Discrepancy in %
	Present Study	Published Data [7]	
100	1.325	1.302	0.876
500	5.526	5.499	0.576
1000	7.525	7.505	0.306
2000	9.662	9.655	0.099
2000	9.662	9.655	0.099

Table 2 Validation of Average Nu with uniform heating is carried out with Published data of Aparna and Seetharamu [7].

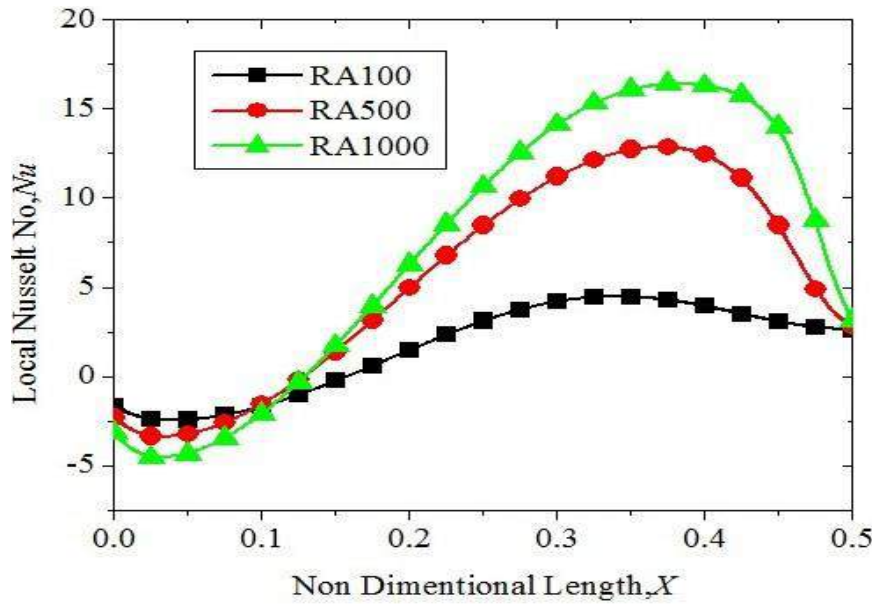


Fig. 4: Variation in local Nu with distance X for different Rayleigh Numbers with Sinusoidal temperature

Fig. 4 displays non-uniform heating curve like variation but asymmetry trend is found for the heated wall. The local Nu begins with -ve coefficients and increases to positive.

The effect of Ra on skin friction coefficient along the warm wall for sinusoidal case is plotted in Fig. 4 and 5. At Rayleigh number, Ra = 102, the heat transfer is primarily by conduction dominated mode. In contrast, the magnitudes of stream function curves are very small and the stratification of temperature contours are around the enclosure. Hence, the local heat transfer is almost straight line. The significant of convection occurs at Ra > 1 x 103. The magnitude of the fluid flow is very small near the corners. The increasing and decreasing behaviour is observed at the beginning and end of the local heat transfer along the warmed and chilled surfaces.

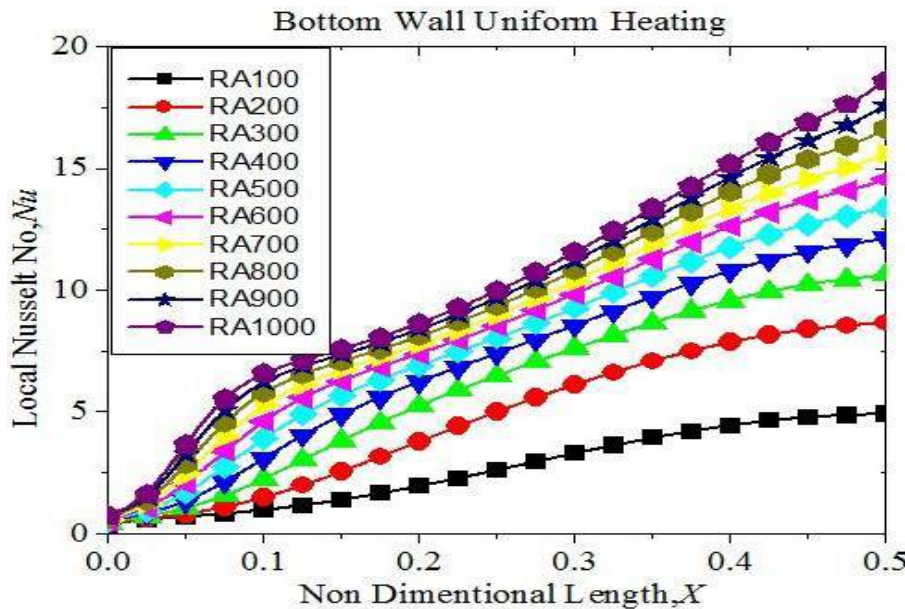


Fig. 5: Variation in local Nu with distance X for different Rayleigh Numbers with Uniform temperature condition

III. RESULTS AND DISCUSSION

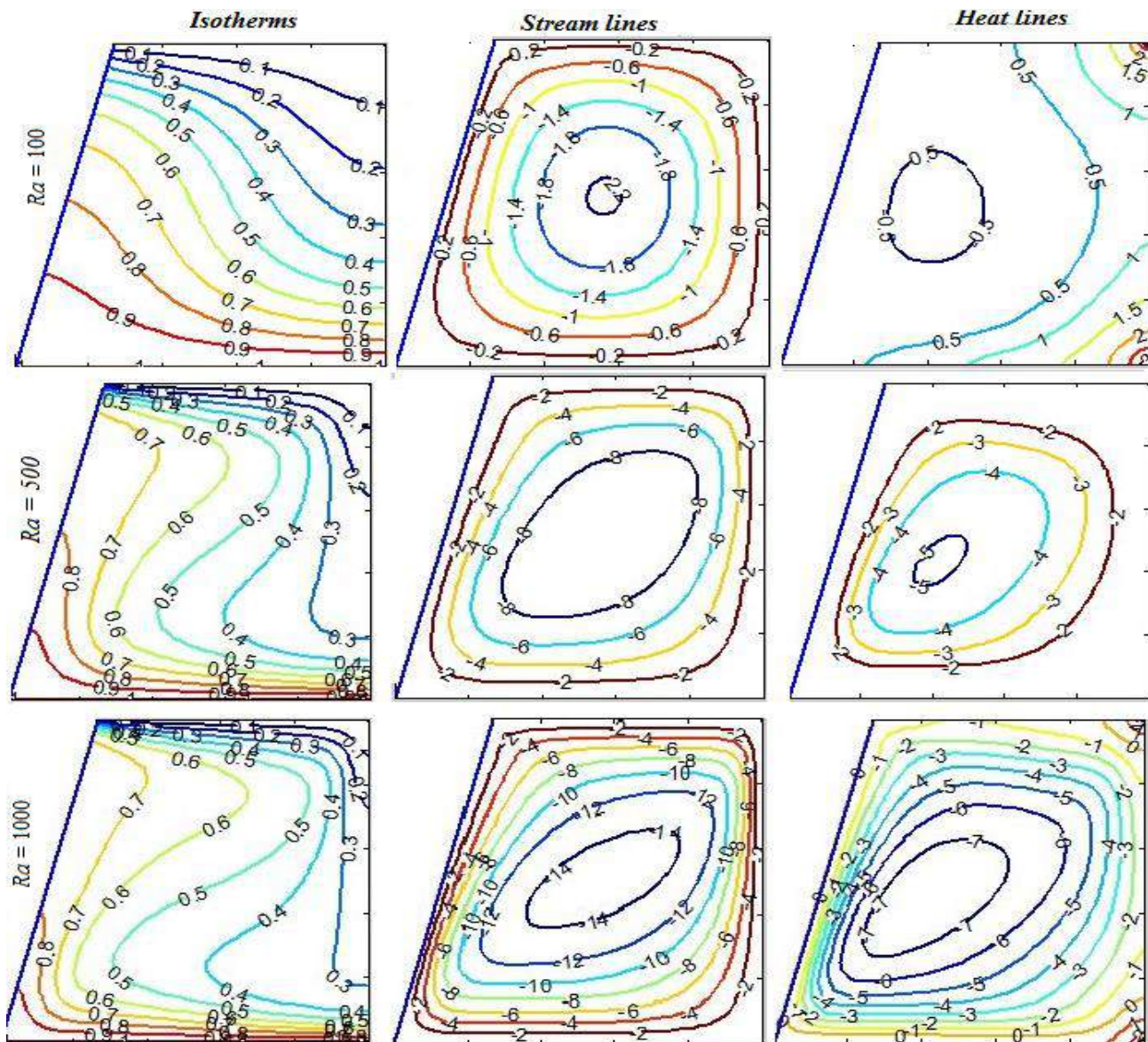


Figure.6 Isotherms, Streamlines and Heat lines of bottom wall for $Ra = 100$, $Ra = 500$ and $Ra = 1000$ (Uniform Heating).

Fig. 6 shows the temperature contours, stream lines and heat lines for $Ra = 100$ to 1000 with the bottom wall exposed to uniformly varying heat flux boundary condition. The aspect ratio is considered as 1. The temperature difference between the top and bottom walls induced raising fluid from the left face. As a result, fluid rises from the middle portion of the left sidewall and the fluid flows towards the right side wall. The buoyant energy travels from the left sidewall is higher than that from the right side wall. Because of this magnitude of the isotherms for different Ra is almost invariant but flow pattern is increase from low Ra to higher Ra . The isotherm contours which are very close to the hot wall ($\theta = 0.9$) and cold surface ($\theta = 0.1$) are almost curved to the inclined wall. However, the isotherm contours, θ ($0.8 \geq \theta \geq 0.2$) are smooth curves and surround the heat flux walls.

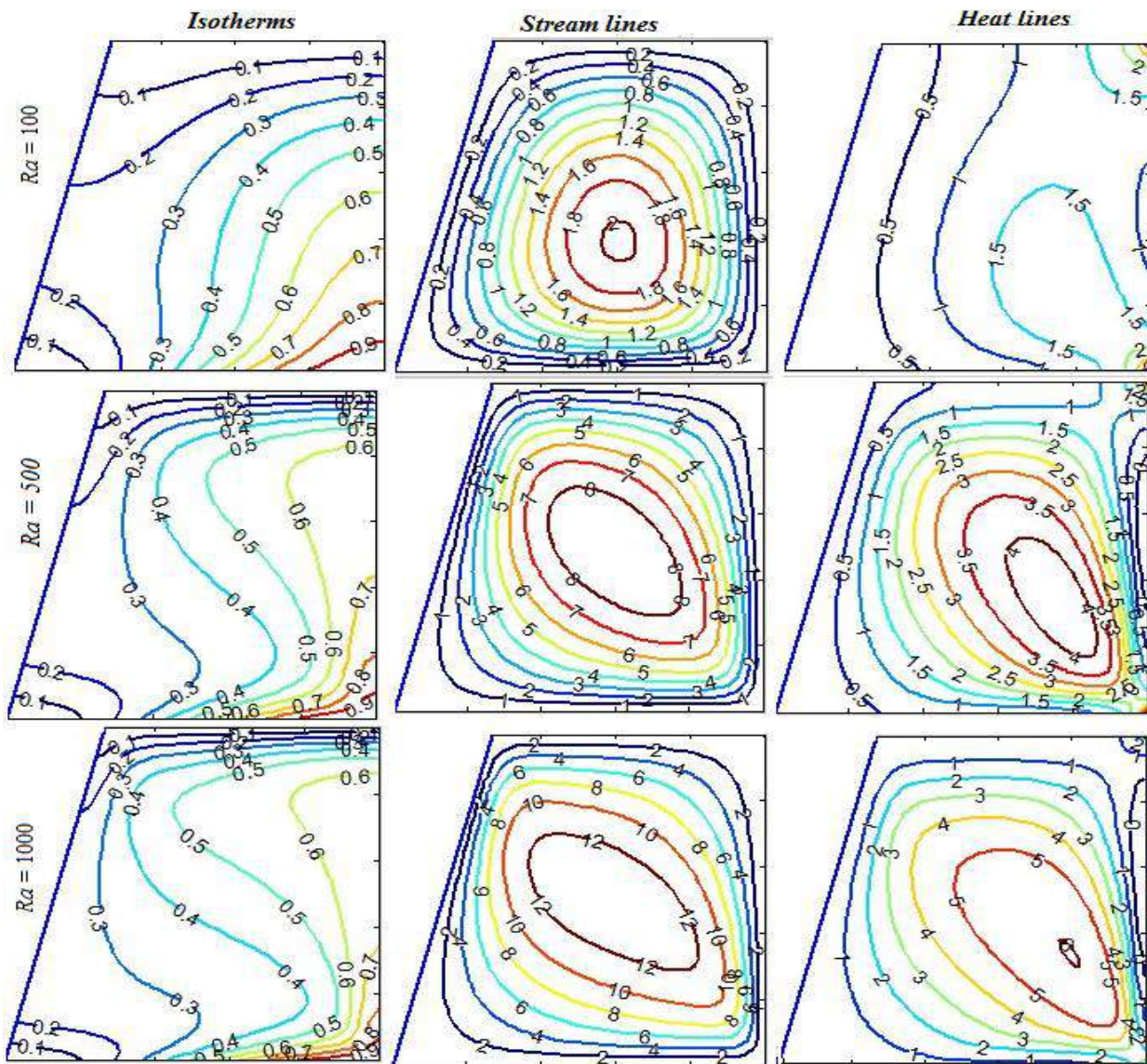


Figure.7: Isotherms, Streamlines and Heat lines of bottom wall for $Ra = 100$, $Ra = 500$ and $Ra = 1000$, (Sinusoidal heating).

Figure.7 The stream function corresponding to $\Psi=12$ stretches more at the centre for $Ra=1000$ compare to $Ra=100,500$. With respect to streamlines, number of elliptical loops formed varies with higher value of magnitude $\Psi=12$ and centre egg-shaped loop of larger size obtained compare to lower Ra values in non square cavity

IV. CONCLUSION

The above addressed to numerically investigate the fluid flow and buoyant heat transfer characteristics in a porous non square cavity with uniformly and sinusoidal heat flux on bottom wall.

The current work highlights the effect of Ra on bottom wall heating in porous cavity. The FEM is used to predict the problem under consideration. For this study, it can be concluded that:

- In the case of linearly varying heat flux on bottom wall, the maximum thermal effect occurs at the bottom edge of the cooled left wall.
- The average Nu increases monotonically with higher values of modified Rayleigh numbers.
- The value of velocity field increases as higher Ra as a result conduction region becomes buoyant heat region.
- The average Nu is more for linearly varied heat flux for bottom wall.
- The average Nu increase consistently with increase of Ra for right side heating wall for square and non-square cavity and is more for uniform temperature than linearly varying temperature case for the walls.

V. REFERENCES

- [1]. I Saranya “Numerical study on Natural Convection in a Square Cavity with linearly varying heat flux on side Wall” Universal Journal of Fluid Mechanics 1 (2016), pp 24-36.
- [2]. V.Prasad, “Heat and fluid flow in porous medium”, Int. Journal of Heat and Mass Transfer, Vol 29, 1986, pp 841-853.
- [3]. V.Prasad, “Free convection heat transfer in porous square cavity”, IJHMT, 1984
- [4]. Prasanth Anand Kumar Lam, K.Arul Prakash, “A numerical study on natural convection and entropy generation in a porous enclosure with heat sources”, Int. Journal of Heat and Mass Transfer, Vol 69, 2014, pp 390-407.
- [5]. S. K. Mahapatra, P. Nanda, A. Sarkar, “Interaction of mixed convection in two-sided lid driven differentially heated square enclosure with radiation in presence of participating medium”, Heat Mass Transfer, 42, pp. 739 - 757, 2006.
- [6]. A. Mezrhab, L. Bchir, “Radiation-natural convection interactions in partitioned cavities”, Int. J of Numer. Methods Heat and Fluid flow, 8, pp. 781 – 799, 1998.
- [7]. Aparna and Seetharamu “FEM Analysis of natural convection flows in porous trapezoidal Enclosure” International Journal of innovative Research (2017).
- [8]. Yasin Varol, Hakan F.Oztop, Asaf Varol, “Free convection in porous media filled right-angle triangular enclosures”, Int. communications in Heat and Mass Transfer, Vol. 33, 2006, pp 1190-1197.



A Review on Mechanical and Tribological Properties of Natural Fiber Reinforced Polymer Composites

Prashanth N¹, Dr. Ranganatha Swamy L², Dr. Hemaraju²

¹Department of Mechanical Engineering, Adichunchanagiri Institute of Technology, Chikkamagaluru, Karnataka, India

²Department of Mechanical Engineering, BGSIT, B.G. NAGARA, Karnataka, India

ABSTRACT

Conventional materials fail to provide a good combination of strength, stiffness, toughness, wear resistance, and density. In order to overcome these shortcomings and to meet the ever-increasing demands of modern technology, composites have emerged as the most promising materials of recent interest. Composite materials are macroscopic combinations of two or more distinct materials that have a recognizable interface.

The outstanding mechanical properties of composite materials make them useful in engineering. viz. high stiffness, strength and wear resistance. Natural fiber reinforced polymer composites are considered a cost effective option for synthetic fiber reinforced composites due to heightened environmental awareness today. Extensive research was conducted on the manufacturing and qualities of polymer matrix composite (PMC) with natural fibres such as jute, sisal, pineapple, bamboo, kenaf, and bagasse replacing synthetic fibres. Development of natural fiber reinforced polymer composites has become an important area of research interest in Material Science. Engineering and agricultural components are now subjected to machine abrasive wear caused by abrasive particles. If abrasive wear rates are to be reduced/controlled, an understanding of the effects of all system variables must be gained during the design of the machinery and the selection of materials. The need for new materials to combat wear situations has led to the development of polymer-based systems.

The present research is aimed at studying the abrasive wear behavior of jute fiber reinforced polymer composites at the mechanical, physical, and three-body levels. The morphology of abraded surfaces is examined by using scanning electron microscopy (SEM) and possible wear mechanisms are discussed.

Keywords: Natural Fibers, Polymer Matrix, SEM, Tribological Properties, Mechanical Properties.

I. INTRODUCTION

Human development is defined by the advancement of materials, i.e. the Stone Age, the Bronze Age, and the Iron Age. Today's material era belongs to composite materials due to their lighter weight, higher strength, corrosion resistance, and ease of shaping. The selection of a material system that meets not only industrial requirements but also this wider definition of eco-materials, as described above, is an urgent necessity.

The most appropriate concept for material selection is composite materials. Composite materials contain natural fibers for reinforcement. In terms of their industrial applications and fundamental research, natural fiber reinforced composites are gaining rapidly in popularity. Their availability, renewability, low density and price as well as satisfactory mechanical properties, they offer an appealing ecological alternative to glass, carbon and other man-made fibers used in composites.

Composites are materials made up of two or more chemically different elements with a distinct interface separating them on a macro-scale. To make a composite, one or more discontinuous phases are inserted in a continuous phase. The reinforcement refers to the discontinuous phase, which is usually harder and stronger than the continuous phase, whereas the matrix refers to the continuous phase. Metals, polymers, and even ceramics can be used as matrix materials. The composite is known as a polymer matrix composite when the matrix is a polymer (PMC).

Many traditional metals/materials have been replaced by polymers in diverse applications over the last few decades. This is achievable due to benefits such as simplicity of processing, productivity, and cost savings, offered by polymers over conventional materials.

The characteristics of polymers are modified in most of these applications by employing fibres to meet the high strength/high modulus criteria. Fiber reinforced composite materials have discrete interfaces (boundaries) between fibres embedded in or bonded to a matrix.

Both fibres and matrix retain their physical and chemical identities in this state, but they provide a unique combination of qualities that neither of the constituents could attain on their own.

Fibers are the primary load-bearing elements, with the surrounding matrix ensuring that they remain in the proper placement and orientation. The matrix also serves as a load transfer medium between them and protects the fibres from damage caused by high temperatures, humidity, and other environmental factors.

While the fibres offer reinforcement for the matrix, the matrix also serves a variety of roles in a composite material. Many fibre reinforced polymers (FRPs) have a strength-to-modulus ratio that is comparable to or better than that of many traditional metallic materials.

II. LITERATURE REVIEW

S Velumani, et.al., [1] investigated mechanical properties of non-woven short sisal fiber reinforced vinyl ester composite using factorial design and genetic algorithm (GA) method. Untreated short sisal fiber reinforced vinyl ester polymer based composite developed by hand lay – up techniques with varying fiber percentages (10, 30 and 45 wt%) and different combination of fiber length (10,30 and 50 mm)(Table 2.1). The results show that the fiber length plays a prominent role in deciding the mechanical properties of sisal composite compared with fiber content. From the result of optimization, the best combination of fiber parameter (length = 50 mm and 34.05 wt%) are determined to attain maximum value of tensile, flexural and impact strength. The average tensile strength ranges between 27.1 to 43.9 MPa (Figure 2.1), the flexural strength ranged between 26.9 to 49.5 MPa (Figure 2.2) and the impact strength ranges between 16 to 93 J/m (Figure 2.3).

Identification	f_1	f_2	t_s	f_s	i_s
A1	10	15	27.1	26.9	16
A2	30	15	37.7	41.1	64
A3	50	15	42.8	47.5	89
A4	10	30	31.0	33.1	34.7
A5	30	30	41.0	44.5	75
A6	50	30	45.1	49.5	91.7
A7	10	45	34.5	38.7	47.5
A8	30	45	42.0	46.3	85
A9	50	45	43.9	47.8	93

Table 2.1 Mechanical properties of composite sheets

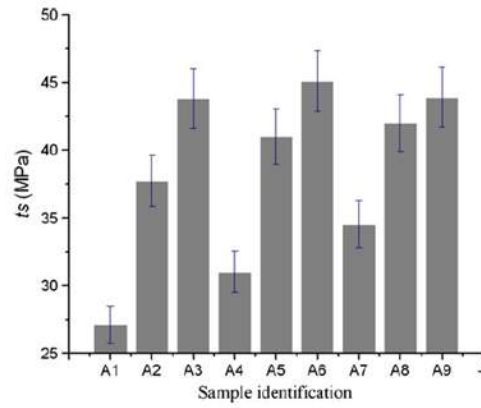


Figure 2.1 Effect of fiber parameter on tensile strength

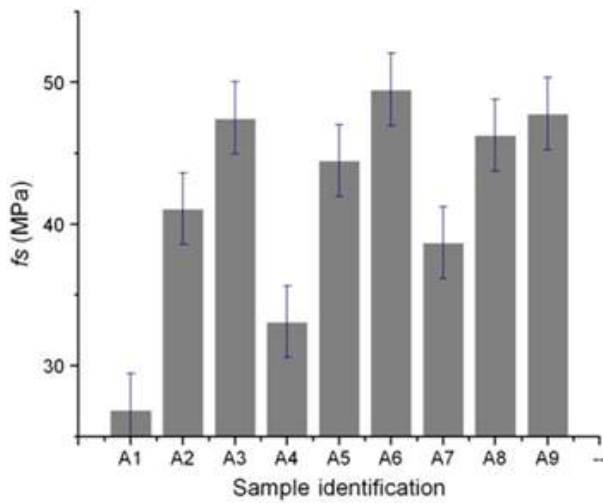


Figure 2.2 Effect of fiber parameter on flexure strength

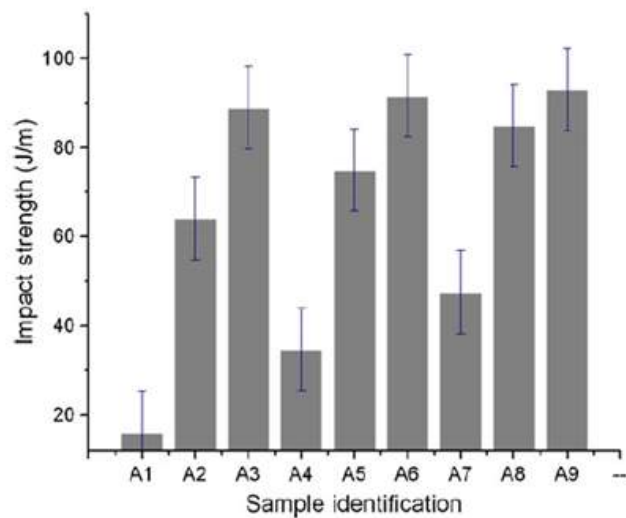


Figure 2.3 Effect of fiber parameter on impact strength

Dayakar Penumadu, et.al., [2] authors focused on the effect of confined and one sided sea water confinement on the cyclic fatigue behavior of carbon fiber reinforced VE composites that serve as facing material for naval sandwich structure. They observed that the fatigue life of polymeric composites shortened dramatically up to 85 %, when cyclic loading was applied under immersed conditions shows every significant loss of mechanical strength under cyclic loading due to sea water exposure while the stress cycle were applied. Also, voids between matrix and fiber rapidly grows and lead to the early fatigue failure mode while fatigued under sea water confined. They concluded that water confinement or exposure while cyclic or dynamic loading is applied plays an important role on degrading the cyclic fatigue life of carbon fiber/vinyl ester composites for marine applications and sea water induced degradation considered carefully for novel structures.

The percentage of stiffness reduction ratio of dry sample in air was observed 500 % higher than that of wet one side immersed, also reported that average number of cycle to failure of dry sample in air was higher than that of wet one side immersed.

R.J. Brambleby, et.al., [3] studied the influence of loading rate on the mode II damage behavior of vinyl ester GRP composite. Load displacement rate ranging from 1 to 6000 mm/min. to determine its effects on four point bending end notched flexure test (4ENF) mode II damage behavior (G_{IIC}) of glass fiber reinforcement vinyl ester (GFRVEP) specimens. The specimens were tested at normal loading rates of 50 mm/min, 750 mm/min and 6000

mm/min respectively. During the 4ENF tests, the length of the crack propagating was measured using the digital image correlation (DIC) technique. It was concluded that the loading rate effect on the initial GIIC of Derakane 510A-40 VE GFRP. Loading rate effect on G_{IIC} is a significant contributing factor to the higher tensile strength of perforated double lap joints tested at higher rate of loading.

Sathishkumar. S, et.al., [4] have evaluated the effect of alkaline treatment on properties of jute fiber mat and its vinyl ester composites. The untreated and treated jute fiber mat were used as reinforcing agent of VE resin composites fabricated by vacuum bag method with a number of 4 piles laminate prepared in the ratio of 60:40. Alkaline treatment on the static mechanical properties are evaluated shows that the higher moduli in comparison to the neat resin. The addition composite reinforced with unidirectional layers show higher strength than the resin. It was observed from SEM analysis an untreated a very poor dispersion of the fiber and exhibited fiber agglomeration, poor adhesion between fiber and matrix. Thus lower strength is occurred. The fibers treating with NaOH (Table 2.2). Binder lignin and fatty substances that hold the unit cells firmly in a fiber and have a better fiber – matrix interaction. At different exposure times 0,1,2,3,4,5,6 and 7 hours dried in hot 30°C. the results shows that the better fiber matrix interface adhesion caused due to the fiber surface treatment by alkali (Figure 2.4).

Time of exposure 5% NaOH	Untreated jute fiber W_1 (GM)	Treated jute fiber W_2 (GM)	% W loss = $[(W_1-W_2) / W_1] * 100$
0	0	0	0
1	22.64	19.0	16.1
2	24.07	20.0	16.1
3	23.54	20	17.1
4	23.28	19	19.1
5	24.28	19.2	21.1
6	24.87	19.4	22.1
7	25.12	19.3	23.1

Table 2.2 Time of exposure to treated jute fiber mat

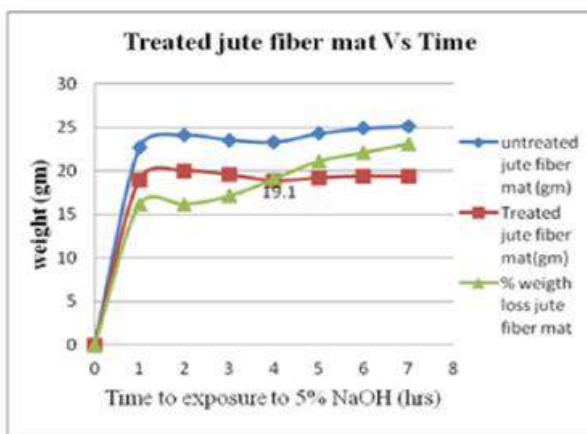


Figure 2.4 Time exposure jute mat in 5 % NaOH

Essi Sarlin, et.al., [5] have studied effect of matrix type on aging of thick vinyl ester glass fiber reinforce laminates. Composite laminate samples were manufactured with filament winding technique using four

different VE resin systems to study. The manufactured laminate samples were conditioned in an environmental cabinet (70°C , 95 RH%), water immersion (95°C) and in sulphuric acid solution immersion under pressure (5 % H_2SO_4 95°C , 15 bar), after 6 and 12 months of conditioning, the samples were tensile tested. In their study four different VE resins were used as the matrix material in the composites: Derakane 441-400, Atlac E-Nova FW 1045, Dian 9400 and Derakane 455-400. The main goal of their studies correlate with the long term properties of the composite laminates. The authors found that the Derakane 455-400 shows the best values of hardness, tensile strength and tensile modulus.

Carlos Eduardo Correa, et.al., [6] conducted wear performance of vinyl ester reinforced with musaceae fiber bundles sliding against different metallic surfaces. Composite were characterized by different fiber content (0 - 60 wt%). The result shows that 30 wt% fibers loading exhibited the better wear mechanism and surface damage characteristics, also cracks are increased with increase of fiber loading. They concluded that wear severity is dependent on the counter body's surface roughness in neat resin and composites with low and medium fiber content, but independent for high fiber content samples.

F.A. Almansour, et.al., [7] discussed the influence of water absorption on the mode I inter laminar damage behavior of flax and basalt fiber reinforced vinyl ester hybrid composite, three types of composite laminates, flax fiber reinforced vinyl ester (FVE), flax fiber hybridized basalt unstitched (FBVEu) and flax fiber hybridized basalt stitched (FBVEs) fabricated by vacuum infusion technique are investigated. They found from the experimental result that the mode I damage behavior initiated propagation of water immersed FVE composites were decreased by an average of 27 % and 10 % respectively compared to the dry specimen. Whereas the damage behavior propagation of water immersed FBVEu and FBVEs composites were improved by approximately 15 % and 17% compared to dry specimen. The results shown that basalt fiber hybridization has positive effects on durability and the moisture resistance of natural fiber composites.

G. Anand, et.al., [8] studied dynamic mechanical, thermal stability and wear properties of neat GF reinforced, nickel phosphorus coated glass fiber/ Al_2O_3 nanowire reinforced vinyl ester composite. It observed that 44 wt% Ni-P/GF and 0.75 wt% Al_2O_3 nanowire reinforced VE composite exhibited higher properties than neat GF reinforced VE Composites, different composites with different concentration of Al_2O_3 nanowire and Ni-P coated GF prepared by hand lay up process. The experimental results revealed that the maximum storage modulus and glass transition temperature value of $6.16 \times 10^3 \text{ MPa}$ and $106 - 87^{\circ}\text{C}$ is obtained for the 44 wt% Ni-P/GF and 0.75 wt% Al_2O_3 nanowire reinforced VE composite. In their paper optical microscope images aid a support to the specific wear resistance value to conclude the wear behavior of the hybrid composite.

Khubbab Shaker, et.al., [9] evaluated the enhancement in the properties of glass/vinyl ester composites by incorporating silica micro particles composite materials were fabricated without particles and with 2 % and 5 wt% particle loadings, using UD glass fabric reinforcement. They found substantial increase in the matrix strength and interfacial adhesion and considerable enhancement in tensile strength, tensile modulus, flexural strength and flexural modulus by addition of 5 % silica particles. The tensile modulus and tensile strength were enhanced by 13.88 % and 15.39 % respectively (Figure 2.5), flexural modulus and strength were enhanced by 42.73 % and 36.37 % respectively by the addition of 5% silica particles (Figure 2.6). The same particle loading also enhanced the hardness, impact and short beam shear strength by 13.89 %, 25.12 % and 16.40 % respectively (Figure 2.7).

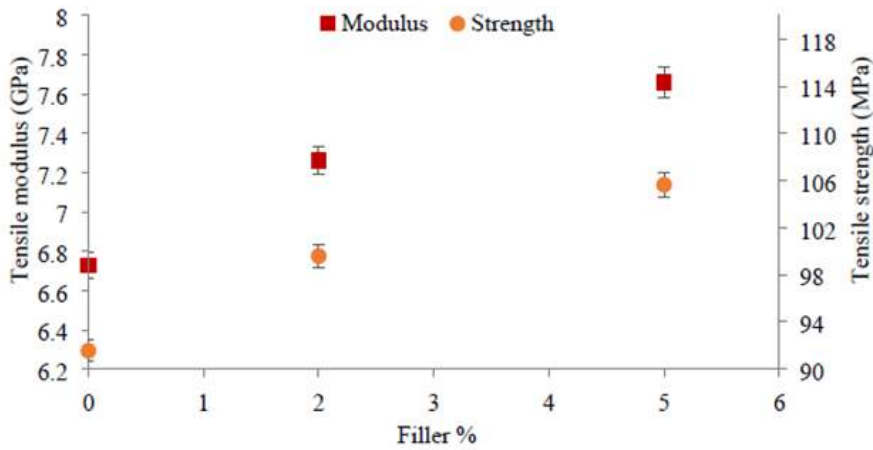


Figure 2.5 Tensile properties of composite with different particle concentrations

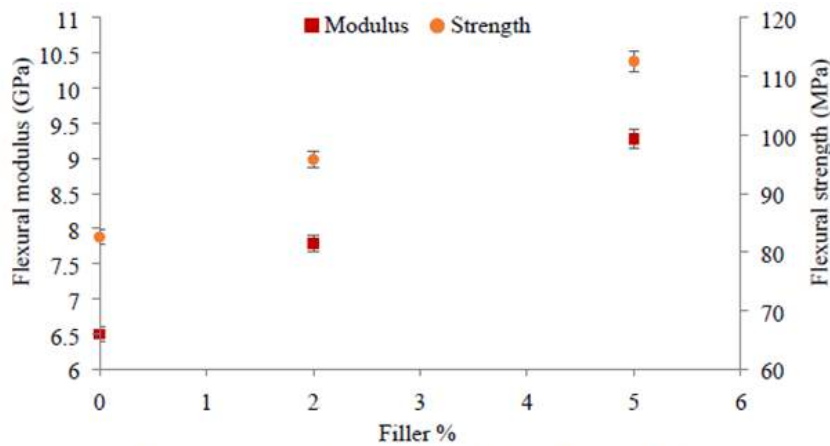


Figure 2.6 Flexural properties of composite with different particle concentrations

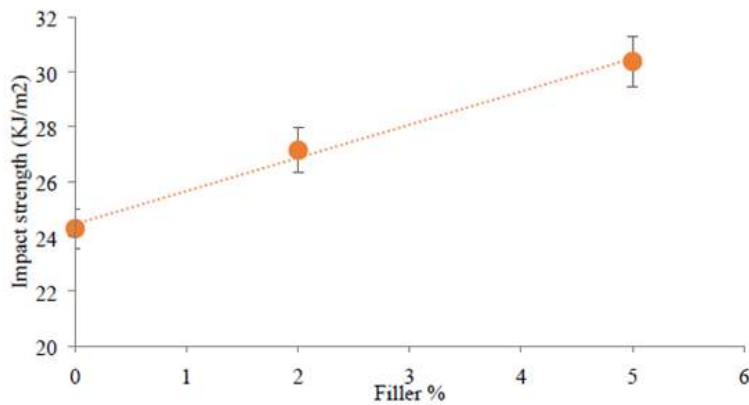


Figure 2.7 Impact properties of composites with different particle

Nagaraj Nagaprasad, et.al., [10] investigated ob tensile, flexural, impact and hardness properties of date seed filler reinforced vinyl ester (DSF-VE) composites experimentally. DSF-VE composite were prepared by using conventional compression molding technique with varying fillers loadings from 5 % to 50 wt%. SEM characterization of the fracture surface used to identify the interfacial strength and to reveal the mechanism of failure. The major finding in their work is the attainment of high mechanical properties of composite specimens

with 30 wt% fiber loading. The heat deflection temperatures of DSF – VE composites increased by 58.49 % were compared with the neat pure vinyl ester resin. The authors found that tensile, flexural, impact and hardness properties of pure vinyl ester resin addition of DSF loading of 30 % increased it by 64.5 %, 91 %, 44 % and 93.67 % respectively (Figure 2.8 & Figure 2.9), compared with the neat, pure vinyl ester resin. They concluded that the DSF-VE composite which can be considered for many automobile and structural application.

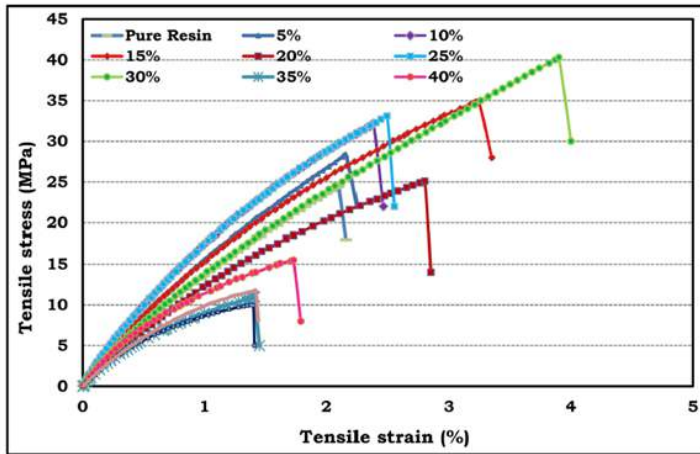


Figure 2.8 Effect of filler loadings on tensile stress and tensile strain of the DSF-VE composites.

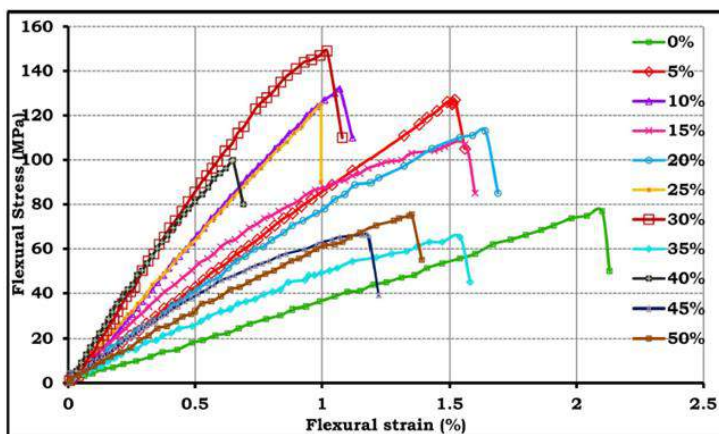


Figure 2.9 Effect of filler loadings on flexural stress and flexural strain of the DSF-VE composites.

B. Suresha, et.al., [11] have reported that carbon fiber (CV) with graphite reinforced vinyl ester composite compete with and even out perform SiC/ carbon fiber reinforced vinyl ester composite. In term of tensile and flexural properties. CV hybrid composite developed by hand lay up technique with varying SiC/Graphite fillers percentage (2 to 6 wt%). The results shows the a mechanical properties increases with increases in filler percentage. The author concluded that 6 wt% of graphite reinforcement CV composite showed improved mechanical properties, the tensile strength improved by 16 % and flexural strength by 7 %.

S. Anilkumar Global, et.al., [12] while studying the mechanical strength behavior of egg shell/termite mound filler coir fiber vinyl ester composite found that tensile strength, impact strength and flexural strength increased with increase of egg shell/ termite filler, composites developed by the compression molding machine. An overall comparison between the properties of all the testing samples revealed that the termite mound filler composite performed better in tensile strength (28.6 MPa , 30 mm), impact strength ($46.2 \frac{\text{kJ}}{\text{m}^2}$, 30 mm) and

flexural strength (28.4 MPa, 50 mm). Test results indicated that the incorporation of termite mound with egg shell filler coir fiber vinyl ester filler coir fiber vinyl ester composite.

B.N.V.S Ganesh Gupta K, et.al., [13] tried to improve tensile, flexural and inter laminar shear properties of the glass fiber reinforced polymer blend of epoxy and vinyl ester. Three different types of composites, i.e., GE, GVE and GEVIPN hybrid composites developed by the hand lay - up techniques, in the case of epoxy matrix preparation, 10 wt% of curing agent TETA were mixed in the epoxy polymer, 15 wt% of free radical MEKP mixed in vinyl ester. They studied role of curing temperature (140, 170, 200 and 230^o C) on the flexural properties of the glass fiber reinforced epoxy vinyl ester interpenetrate polymer network composite (GEVIPNC). 21.83 %, 22.54% and 13.45% improvement in inter laminar shear strength (ILSS), tensile and flexural strength respectively. From scanning electron microscopy (SEM), it was concluded that strong interfacial bonding between the matrix and fiber mode GEVIPN composite exhibits better mechanical property. Cuong Manh Vu, et.al., [14] studied the mechanical and flame retardant properties of phenyl/vinyl polysilsesquioxane based ladder polymer as navel additive for vinyl ester resin. Composites were characterized by different fiber loading (0-20 wt%). The experimental investigation revealed the VER with presence of 20 wt% of navel ladder polymer (NLP) (S3 Sample) exhibits superior flexural strength, flexural modulus increased by 195.5%, 260.6% respectively, also test samples exhibits the decreasing in total smoke release (TSR) and peak heat release rate (PHRR) was about 20.7% and 52.2% respectively. They concluded that the NLP is the good candidate for simultaneous improvement of mechanical properties and flame retardant of VER.

Chang Su, et.al., [15] they found that enhancement of tensile strength and toughness of fiber reinforced polymer composites by incorporation of multi wall carbon nanotubes. Mechanical properties, damage behavior and stiffness of impregnated basalt, carbon and glass fiber ravings were systematically examined. In their study, MWCNTs were used for dispersion epoxy and vinyl ester resins. The MWCNTs with an average diameter and length of 15 nm and 20 μm, respectively. The results shows that as compared to pure epoxy resin, the 0.3 wt% MWCNT-modified epoxy resin exhibited elevated K_{IC} , tensile strength (σ_t), flexure strength (σ_f) and impact strength, also similar improvements were discovered for the MWCNTs modified vinyl ester resin. It were identified the combined action of restricted crack propagation and the promoted co stress of fibers and σ_t of the basalt, carbon and glass ravings increased with the addition of MWCNTs. The results indicated that modified methods significantly increased the mechanical properties, damage behavior and design strength of FRP.

Ashis Kumar Samanta ,et.al., [16] authors provided detail information on Processing of jute fibres and its Applications. They reported chemical aspects and effects of chemical treatments of jute fibers. Different chemical treatments such as treatment of jute with caustic soda (NaOH), treatment of jute with meatl salt and complexes, Bleaching/Oxidation of jute fibers, ohoto yellowing or colour reversion of bleaching jute. Staboilized bleaching of jute, treatment with glycols. Enzyme treatment, treatment with silicone (antifriiction agent), treatment of jute fibers with jute batching oil. They also reported chemical finishing and allied processes for jute fibers, to improve abrasion resistance and fiber shedding, to softening, to improve crease resistant property, to improve rot resistant property, to improve water repellent property, to improve fire retardant property. They concluded that jute based composite materials wide applications in different fields. Specially designed and developed Jute fabric reinforced bio-degradable geo membrane or medical disposable bags and

wipes, Jute fabric based combined/multi-layered Tar Felt can also be used for potential applications in civil engineering for roof treatment in particular, Use of Jute based composites for awning, false ceiling board, cover wall of railway coaches and even door panel for cars, bioengineering measure for soil and water conservation and fertility enhancement of the Barren & Baid Lands , development of jute-based substitute of mastic asphalt by designing and manufacturing Bituminized Jute Paving Fabric, with polymerized special grade a bitumen coated multi-layered composite of jute woven and nonwoven fabric composites.

B.S. Raju, et.al., [17] authors research work is concerned with the fabrication and evaluation of the physical and mechanical properties of a new polymer hybrid epoxy composite consisting of glass fiber, jute fiber mat, ZnS microparticles and LY556 Epoxy resin with HY951 Hardener. The specimens were prepared using hand lay-up technique as per ASTM standard & were tested for Tensile, Flexural, Interlaminar Shear Strength, Impact, Water Absorption Test, Density, Micro Hardness and the microstructure was evaluated by SEM analysis. The hybrid polymer composites with micro ZnS fillers are prepared with five different microparticle weights (0, 3, 6, 9 and 12%). They observed that in flexure test, the flexure strength was found to increase as compared to C1 (0%ZnS) which is because of increase in ZnS micro particulate content, significantly increases up to C3 (6% ZnS) but decreases thereafter due to increase in the brittleness, hence flexure strength decreases. In impact test, the impact strength decreases as compared to base composite C1 (0% ZnS). It is because of increase in % of ZnS reinforcement. Micro graph shows better bonding between matrixes, ZnS reinforcement. It was concluded that Overall composition C3 (6% ZnS) can be considered as suitable composition for the development of ZnS, jute mat, glass fiber and epoxy based composites by hand lap-up process. Carlos Eduardo Correa , et.al., [18] the aim of there work was to compare the effect of vinyl ester reinforced with Musaceae fiber bundles on tribological behavior while varying the composite 's fiber content and the counter-body's material and surface roughness. The composite fabrication process using the bulk moulding compound (BMC) fabrication techniques with varying fiber percentages (10, 20, 30, 40, 50, 60 wt%). Pin-on-disc test equipment was used to slide composites while keeping the test parameters fixed and the variation in the counter-body's material. The counter-bodies used were discs of carbon steel AISI 1045 with a hardness of 10 HRC and aluminum alloy 6061-T6 with a hardness of 31 HRB. SEM images were used to identify the wear mechanisms and surface topography in the friction and wear. The experimental results reveled that the COF for almost all the composites tested falls between 0.2 and 0.4. The composite with 30 wt% fiber content has the most stable behavior in the COF, having the same COF value of approximately 0.29, no matter the counter-body material or the surface roughness. samples tested against carbon steel generally exhibit lower specific wear than the samples tested against aluminum alloy. Test results indicated that The severity of the wear depends of the counter-body's surface roughness for the samples of the neat resin and composites with low and medium fiber content. In the case of composites with high fiber content, no dependence is observed.

Chandra Prakash Singh, et.al., [19] tried to characterize the jute and coir fibers composites and develop a better understanding of these composites, the physical and mechanical properties of these composites are evaluated to find hardness, flexural and tensile properties of the jute/coconut coir reinforced polymer matrix composite. Three different types of composites, ie., 50% jute and 50% coconut coir fiber, 85% jute and 15%coconut coir fiber, 15%jute and 85% coconut coir fiber composites developed by the hand lay - up techniques, Epoxy and resin are used to bind, hold and provide strength to the fiber matrix. The experimental investigation revealed

that the composite with the composition of 85% jute and 15% coconut provides higher tensile strength ($16.6\text{MPa}[B] > 10.91\text{MPa}[A]$) because of the higher wt % of the jute fiber. The composite with a composition of 50% jute and 50% coconut coir fiber behaves like semi brittle and ductile as it contains 50/50% jute and coconut fiber ($1.93\% [A] > 1.6[B]$). They concluded that composite specimens are fundamentally more durable than pure coir specimens. creating hybrid composite by the blend of two natural fibers gives them the advantage to replace synthetic fibers, this work likewise shows the capability of the hybrid natural fiber composites can be viewed as a useful material in lightweight applications.

G. Bharathiraja, et.al., [20] they found that significant improvement in fracture toughness value for the increase in volume fraction of algae filler in vinyl ester material. The materials used for there study are vinyl ester resin (matrix), methyl ethyl ketone peroxide (catalyst), cobalt naphthenate (accelerator), and algae filler (natural filler) as a reinforcement agent. Five different volume fractions of algae fillers (5%, 10%, 15%, 20%, 25%). Composite plates were prepared by hand layup method. Compact testing (CT) specimens are used extensively to determine material strength values in the field of mechanical fracture and corrosion testing. The results shows that The increase of fracture strength shows uniform dispersion of algae filler with vinyl ester matrix material. The composite exhibited high fracture strength at 25% volume fraction of algae filler. It was due to strong interfacial bonding between algae filler and vinyl ester material. They concluded that this kind of natural filler reinforced polymer composite can be used in low load bearing structural applications.

J. Sai Revanth, et.al., [21] studied Thermal gravimetric analysis (TGA) and Differential scanning calorimetry (DSC) analyses to determine physical properties of respective materials. DSC analysis provides information regarding Transition temperatures, glass transitions, Polymorphic transformation. TGA provides information regarding physical properties such as vaporization, sublimation, absorption, adsorption and chemical properties like chemisorptions, desolvation, decomposition. The materials used for there study are Polyvinyl ester (matrix) 66 %, *Vetiveria Zizanioides*, (10 to 17 %), Glass (0 – 14 %), and Jute (natural filler) (10 to 17 %). The results shows that of Thermo gravimetric analysis: Sample 1 procuring residual mass of about 11 percent at a temperature of about 599.50 centigrade seem promoting than the other samples having residual masses at 11.33 and 9.22 percentages at temperatures 599.50 and 599.60 respectively. Further increase in percentages of natural fibre i.e. above 11.33 shows inferior thermal stability. Differential scanning calorimetry: the Transition temperature of sample 1 is superior to sample 2 and 3, and sample 2 has Tg that is superior to sample 3. Adding synthetic fibres to the already existing composites (while synthesis) decreases the transition temperature but increases the recrystallization temperature.

Jeetendra Mohan Khare, et.al., [22] studied the influence of different resin on physico-mechanical properties of hybrid fiber reinforced polymer composites. Three type of polymer matrix (Epoxy, Vinyl ester and Polyester) and Three type of reinforcement (Glass fiber , Jute fiber and Graviaoptiva fibre) were used in the fabrication of composite. Glass, *Grewiaoptiva* and Jute fibers were reinforced in epoxy, vinylester and polyester resin in four different proportions. Conventional hand layup process was used for the fabrication of prosthetic composite. The weight fraction of the fiber in the composite was varied from 5% to 20%, in which the percentage of glass fiber was fixed (i.e. 5%) and the percentage of other two fibers (jute & *Grewiaoptiva*) was varied as 5%, 10%, 15% in equal proportion respectively. They found from the experimental result that the epoxy-based composite at 5 wt% jute fiber and 5 wt% *Grewiaoptiva* gives the maximum value of hardness i.e. 76 HRL. the maximum value

of tensile strength was found to be 72 MPa for epoxy-based composite (at 7.5 wt% jute and 7.5 wt% grewiaoptiva). In case of vinyl ester, the maximum value of tensile strength was found to be 69 MPa (at 7.5 wt% jute and 7.5 wt% grewiaoptiva). For the case of polyester, maximum value of tensile strength was observed as 60 MPa (at 7.5 wt% jute and 7.5 wt% grewiaoptiva). Maximum value of flexural strength obtained was 42 MPa, 48 MPa and 35 MPa for epoxy based, vinyl ester based and polyester based composite respectively (at 5 wt% jute and 5 wt% grewiaoptiva) for all the matrix composites. The impact energy increases as the natural fiber loading increases. The percentage increases in impact energy was 17% in epoxy based, 9% in vinyl ester based and 16% in polyester based composite at 10 wt% of natural fiber. Test results indicated that the composition E2 is the best optimized samples among all.

Levente Ferenc Toth, et.al., [23] investigated tribological behaviour of advanced unsaturated polyester/vinyl ester based thermoset composites reinforced by inorganic (mineral-based) or organic (vegetal) fibres such as basalt and jute. polyester/vinyl ester based basalt/jute fibre reinforced composites with PTFE/POM/MoS₂ tribo-fillers developed by hand lay – up techniques with varying tribo-fillers percentages (2 and 4 wt%) and different combination of basalt (40 to 45 wt%) and jute (25 to 30 wt%). They observed that the Jute fibre reinforced composites had slightly lower hardness compared to basalt composites with the same 2 wt% tribo-filler content. The highest strength values were reached with the vinyl ester matrix ((332.4 ± 15 MPa). Specimens with vinyl ester matrix had higher lifetime (1367 Cycles) compared to the same composites based on unsaturated polyester. Transfer layer formation generated from PTFE/POM/MoS₂ tribo-fillers was clearly observed for steel counterfaces both in micro-and macrographs.

M. Arun, et.al., [24] developed Cellulose Reinforced Polymer Composite (CRPC) using cellulose from jute and sisal fibers as reinforcement and epoxy L-12 as matrix. The composite with Lapox L-12 matrix and cellulose as the constituent elements, were prepared with the proportions of 85%–15%, 80%–20% and 70%–30% using compression moulding technique. The experimental investigation revealed the maximum value of impact strength obtained was 7.02 kJ/m², E70JC30 sample, An average tensile strength of 35.52 MPa was observed for samples E85SC15 sample, ultimate tensile strength of 35.52 MPa has been observed for sample E85SC15 which is far more superior than the reported values of jute fiber reinforced polymer composite in both epoxy and polyester matrix, they reported that flexural strength for jute fiber reinforced composite in epoxy and polyester matrix was 44.71 MPa. They concluded that Among all the samples tested E85SC15 and E85JC15 shows increased in tensile strength with low cellulose concentration. Tensile, impact flexural strengths of cellulose-epoxy composite was found to be better than that of jute fiber reinforced polymer composites in epoxy as well as polyester matrixes, cellulose–epoxy composites have a good potential to replace natural fiber based polymer composites for the manufacturing of many automotive parts which do not require high load bearing capability.

M. Rajesh, et.al., [25] studied the effect of reinforcing natural fiber in the form of woven fabric on dynamic mechanical and thermogravimetric analysis were investigated. Further the influence of water molecule interaction on dynamic mechanical analysis of natural fiber composite were studied. In their study, jute and banana fibers were used as a reinforcement in the woven form. Unsaturated polyester resin, methyl ethyl ketone peroxide (MEKP), and cobalt naphthenate were used as the matrix, catalyst, and accelerator, respectively. Composite were prepared by using hand lay up technique with varying fillers loadings from 10 % to 80 wt% and weaving pattern (plain, basket and her-ringbone) and intra-ply hybrid woven fabric. The Results revealed

that basket and intra-ply hybrid composite shown higher storage and loss modulus compared to herringbone and plain-woven composites. sandwich composite enhanced the dynamic properties and glass transition temperature of the composites.

P. Deepak, et.al., [26] investigated wear and mechanical properties of Molybdenum disulphide Modified Epoxy based composites reinforced by organic fibres such as banana and jute. Epoxy based banana/jute fibre reinforced composites with Molybdenum disulphide tribo-fillers developed by hand lay – up techniques with varying tribo-fillers percentages (5,10 and 15 wt%) and The epoxy resin and amine hardener were mixed in the ratio of 2:1. The results shows the a S15 composite had shown the least abrasion loss of 0.2729g among all the form of composites, which is 31.62% less than that of SN composite. The tensile strength and tensile modulus of S15 composite was found to be 32.47MPa and 1623MPa, respectively. The flexural strength of the S15 composites was 21.9% more than that of SN composites. experimental results indicated that the composition S15 is the best optimized samples among all.

Sahas Bansal, et.al., [27] evaluated the comparative analysis of bamboo using jute and coir fiber reinforced polymeric composites. The paper deals with the study of bamboo fiber, jute fiber and coir fiber cut into 2-4 mm of length with epoxy resin having random orientations. Various tests like Impact test (IZOD test and CHARPY test), Fourier Transform Infra-Red (FTIR) test and Rockwell Hardness test were conducted on bamboo epoxy resin composite, bamboo-jute epoxy resin composite and bamboo-coir epoxy resin composite developed by hand lay – up techniques. For sample A, B and C, the combinations taken are in the ratio 90:10 (epoxy resin: bamboo fiber), 90:5:5 (epoxy resin: bamboo fiber: jute fiber), 90:5:5 (epoxy resin: bamboo fiber: coir fiber) respectively. the Impact results, bamboo-coir epoxy resin composite showed the highest value of 4 Joules and 5 Joules while bamboo epoxy resin composite showed the lowest value of 2 Joules and 3 Joules for IZOD test and CHARPY test respectively. the hardness results, bamboo-coir epoxy resin composite had the highest Rockwell hardness test value of 38 RHN , bamboo epoxy resin composite had the lowest Rockwell hardness test value of 20 RHN.

Srinivas Shenoy Heckadka, et.al., [28] studied the mechanical characterization of Flax/Jute/Ultra high molecular weight polyethylene reinforced phenol formaldehyde (PF) composites. research work compares the flexural and Interlaminar Shear Strength (ILSS) of three varieties of fiber reinforced phenol formaldehyde composites. Composites were fabricated with hand layup and compression molding technique with eight layers of same fabric. Thickness of 4 mm was maintained for all the composite panels. Composite were characterized by different fiber content UHMWPE – 78 wt%, Jute – 71 wt% and Flax – 75 wt%. They found from the experimental result that among the three varieties of composites, Flax fiber reinforced composites displayed superior flexural strength (46 MPa) and inter-laminar shear strength (4.4 MPa). Second best being jute fiber composites. Least flexural strength (19 MPa); inter-laminar shear strength (1.4 MPa) was observed for UHMWPE composites.

A complete study on literature survey shows that the reinforcement have better mechanical and tribological properties such as hardness, tensile strength, yield strength, density, compression test, % of elongation, wear resistance and coefficient of friction compared to unreinforcement composite materials. These are carried out through fabrication process of reinforcement using different kind of fabrication technique. As mentioned above hand layup technique have implemented more for composite materials. This literature survey also revealed that

polymer material reinforced with natural fibres also might show good mechanical and tribological properties with different weight percentage ratios.

III. CONCLUSION

Polymer base material reinforced with different kind of composite material is fabricated using hand layup technique shows good mechanical and tribological properties. In this review, I conclude that using polymer (vinyl ester) reinforced with natural fibres (Jute, Banana and Coir) will show the better properties and further work has to done on these materials.

The conclusions drawn from the previous investigations are as follows:

1. The jute and coir natural fibers can successfully be used as reinforcing agent to fabricate composite by suitably bonding with resin for the development of value added products.
2. There is a good dispersibility of jute and coir in the matrix, which improves the hardness, strength, and modulus and work fracture of the composite.
3. The abrasive wear resistance of neat polymers is appreciably enhanced by incorporation of natural fibers. The specific wear rate of the composite also decreases with addition of fiber.
4. The abrasive wear rate of the natural fibers polymer composite is influenced by several parameters e.g. sliding velocity, sliding distance and normal load. The wear rate of the composite is found to be more sensitive to normal load in comparison to sliding velocity. The coefficient friction of the composites decreases with addition of fibers which confirms that the addition of this fiber is beneficial in reducing the wear of neat resin.

IV. REFERENCES

- [1]. S Velumani, P Navaneethakrishnan, S Jayabal, D S Robinson Smart, "Optimization of mechanical properties of non-woven short sisal fibre-reinforced vinyl ester composite using factorial desiand Ggn A method", Bull. Mater. Sci., Indian Academy of Sciences, Vol. 36, No. 4, August 2013, pp. 575–583.
- [2]. Dayakar Penumadu, Akawut Siriruk, "Degradation in fatigue behavior of carbon fiber–vinyl ester based composites due to sea environment", Composites Part B: Engineering, Volume 61, May 2014, Pages 94-98.
- [3]. R.J. Brambleby, L.A. Louca, S.E. Mouring, "Influence of loading rate on the mode II Damage behavior of vinyl ester GRP", Composites Part A: Applied Science and Manufacturing, Volume 93, February 2017, Pages 153-162.
- [4]. Sathishkumar. S, A. V. Suresh, Nagamadhu. M, M. Krishna, "The effect of alkaline treatment on their properties of Jute fiber mat and its vinyl ester composites", 5th International Conference of Materials Processing and Characterization (ICMPC 2016), Materials Today: Proceedings 4 (2017) 3371–3379.
- [5]. Essi Sarlin, Reija Sironen, Tuomas Pärnänen, Mari Lindgren, Mikko Kanerva, Jyrki Vuorinen, "The effect of matrix type on ageing of thick vinyl ester glass-fibrereinforced Laminates", Composite Structures, Volume 168, 15 May 2017, Pages 840-850.

- [6]. Carlos Eduardo Correa, Santiago Betancourt, Analía Vázquez, Piedad Gañan, "Wear performance of vinyl ester reinforced with Musaceae fiber bundles sliding against different metallic surfaces", *Tribology International* Volume 109, May 2017, Pages 447-459.
- [7]. F.A. Almansour, H.N. Dhakal, Z.Y. Zhang, "Effect of water absorption on Mode I interlaminar Damage behavior of flax/basalt reinforced vinyl ester hybrid composites", *Composite Structures*, Volume 168, 15 May 2017, Pages 813-825.
- [8]. G. Anand, N. Alagumurthi, R. Elansezhian, N. Venkateshwaran, "Dynamic mechanical, thermal and wear analysis of Ni-P coated glass fiber/Al₂O₃ nanowire reinforced vinyl ester composite", *Alexandria Engineering Journal*, Volume 57, Issue 2, June 2018, Pages 621-631.
- [9]. Khubab Shaker, Yasir Nawab, Abdelghani Saouab, "Influence of silica fillers on failure modes of glass/vinyl ester composites under different mechanical loadings", Volume 218, September 2019, 106605.
- [10]. Nagaraj, N., Balasubramaniam, S., Venkataraman, V., Manickam, R., Nagarajan, R., Sikiru Oluwarotimi, "Effect of cellulosic filler loading on mechanical and thermal properties of date palm seed/vinyl ester composites", *International Journal of Biological Macromolecules*, Volume 147, 15 March 2020, Pages 53-66
- [11]. B.Suresha, E.Ganesh, "Influence of fillers on mechanical behaviour of carbon fiber/vinyl ester hybrid composites", *Materials Today: Proceedings*, 21 October 2020.
- [12]. S. Anilkumar, K. Arumugam, Venkata Ramarao Mutyala, K. Kodanda Ramc, T.S. Krishna Kumar, "Investigation on mechanical properties of natural fiber-polymer composite materials", *Materials Today: Proceedings* 9 December 2020.
- [13]. B.N.V.S.Ganesh Gupta K, Mritunjay Maharudrayya Hiremath, Bankim ChandraRay, Rajesh Kumar Prusty, "Improved mechanical responses of GFRP composites with epoxy-vinyl ester interpenetrating polymer network".
- [14]. Cuong Manh Vu, Van-Huy Nguyen, Tuyen Nguyen Van, "Phenyl/vinyl polysilsesquioxane based ladder polymer as novel additive for vinyl ester resin: Fabrication, mechanical and flame retardant properties", Volume 93, January 2021, 106987.
- [15]. Chang Su, Xin Wang, Lining Ding, Pancheng Yu, "Enhancement of mechanical behavior of resin matrices and fiber reinforced polymer composites by incorporation of multiwall carbon nanotubes", Volume 96, April 2021, 107077.
- [16]. Ashis Kumar Samanta, Asis Mukhopadhyay, Swapan Kumar Ghosh, "Processing of jute fibres and its applications" *Handbook of Natural Fibres (Second Edition)*, Volume 2: Processing and applications, Pages 49-120, 2020.
- [17]. B.S. Raju, L.H. Manjunatha, Santosh, N. Jagadeeswaran, "Fabrication & characterization of ZnS micro particulate filled glass and jute fibre reinforced hybrid polymer composites" *Materials Today: Proceedings*, Volume 20, Part 2, Pages 125-133, 2020.
- [18]. Carlos Eduardo Correa, Santiago Betancourt, Analía Vázquez, Piedad Gañan, "Wear performance of vinyl ester reinforced with Musaceae fiber bundles sliding against different metallic surfaces", *Tribology International*, Volume 109, Pages 447-459, May 2017.
- [19]. Chandra Prakash Singh, Raj Vardhan Patelb, Mohd Faizul Hasanc, Anshul Yadav, Virendra Kumar, Anil Kumar, "Fabrication and evaluation of physical and mechanical properties of jute and coconut coir

- reinforced polymer matrix composite” *Materials Today: Proceedings*, Volume 38, Part 5, , Pages 2572-2577, May 2021.
- [20].G. Bharathiraja , N. Karunakaran , V. Jayakumar, Saran Ganesh, “Investigation on fracture toughness of algae filler vinyl ester composite, *Materials Today: Proceedings*, Volume 22, Part 3, Pages 1233-1235, Feb 2020.
- [21].J. Sai Revanth, V. Sai Madhav, Y. Kalyan Sai, D. Vineeth Krishna, K. Srividya, C.H. Mohan Sumanth, “TGA and DSC analysis of vinyl ester reinforced by *Vetiveria zizanioides*, jute and glass fiber”, Volume 26, Part 2, Pages 460-465, June 2020.
- [22].Jeetendra Mohan Khare, Sanjeev Dahiya, Brijesh Gangil, Lalit Ranakoti, “Influence of different resins on Physico-Mechanical properties of hybrid fiber reinforced polymer composites used in human prosthetics”, *Materials Today: Proceedings*, Volume 38, Part 1, Pages 345-349, July 2021.
- [23].Levente Ferenc Toth, Jacob Sukumaran, Gabor Szebenyi , Adam Kalacska, Dieter Fauconnier, Rajini Nagarajan, Patrick De Baets, “Large-scale tribological characterisation of eco-friendly basalt and jute fibre reinforced thermoset composites”, *wear* , Volumes 450–451, 203274, 15 June 2020.
- [24].M. Arun, S. Vincent, R. Karthikeyan,“ Development and characterization of sisal and jute cellulose reinforced polymer composite”, *Materials Today: Proceedings*, Volume 28, Part 2, Pages 556-561, 2020.
- [25].M. Rajes, K. Jayakrishna, M.T.H. Sultan, M. Manikandan, V. Mugeshkannan, A.U.M. Shah, S.N.A. Safri, “The hygroscopic effect on dynamic and thermal properties of woven jute, banana, and intra-ply hybrid natural fiber composites”, *JMR&T, Journal of Materials Research and Technology* Volume 9, Issue 5, Pages 10305-10315, September–October 2020
- [26].P. Deepak, H. Sivaraman, R. Vimal, S. Badrinarayanan , R. Vignesh Kumar, “Study of Wear Properties of Jute/Banana Fibres Reinforced Molybdenum disulphide Modified Epoxy Composites”,5th International Conference on Materials Processing and Characterization (ICMPC 2016), *Materials Today: Proceedings* 4 (2017) 2910–2919, Dec 2018.
- [27].Sahas Bansal, M. Ramachandran, Pramod Raichurkar, “Comparative Analysis of Bamboo using Jute and Coir Fiber Reinforced Polymeric Composites”, 5th International Conference of Materials Processing and Characterization (ICMPC 2016), *Materials Today: Proceedings* 4, 3182–3187, Feb 2018.
- [28].Srinivas Shenoy Heckadka, Raghuvir Pai Ballambat , Vijaya Kini Manjeshwar, Vineetha Ravindranath,Pranav Hegde, Ajith Kamath, “Cone beam computed tomography for mechanical characterization of Flax/Jute/Ultra high molecular weight polyethylene reinforced phenol formaldehyde composites: A comparative assessment”, Volume 47, Part 19, Pages 6740-6745, July 2021.



Mechanical Characterization of Coconut Spathe and Bast Papaya Fiber Reinforced Epoxy Polymer Composite

Pradeepkumar G R¹, Shiva Prakash S², Paraveej Shirahatti³, Gujjala Anil Babu⁴, Sampathkumar R¹

¹Lecturer, Department of Mechanical Engineering, Govt Polytechnic Chitra Durga, Karnataka, India

²Assistant Professor, Department of Mechanical Engineering New Horizon College of Engineering, Bangalore, Karnataka, India

³Research Scholar, Department of Mechanical Engineering, UVCE, Bangalore, Karnataka, India

⁴Senior Manager, Hindustan Aeronautics Limited, Bangalore, Karnataka, India

ABSTRACT

The present work involves in fabricating “Coconut Spathe and Bast Papaya Fibre Reinforced Epoxy Polymer Composites. The reinforcements used are Coconut spathe and papaya in different weight fraction. The mechanical properties are compared for these polymer composites. The main objective is to enhance the properties of Epoxy based polymer by adding reinforcements like Coconut spathe and bast papaya. The reinforcement increases the mechanical properties of a polymer. Epoxy is a Copolymer and is formed from two different chemicals, Resin and Hardener. Epoxy has very large application. In general epoxy is known for their excellent adhesion, chemical and Heat resistant, excellent Mechanical properties and very good insulating properties. But these properties can be modified by adding materials to it. Natural fibres have been used to reinforce materials for over 3,000 years. More recently they have been employed in combination with plastics. Many types of natural fibres have been investigated for use in plastics including Flax, hemp, jute, straw, wood fibre, rice husks, wheat, barley, oats, cane (sugar and bamboo), grass reeds, kenaf, ramie, oil palm empty fruit bunch, sisal, coir, water hyacinth, pennywort, kapok, paper- mulberry, raphia, banana fibre, pineapple leaf fiber and papyrus.

Natural fibres have the advantage that they are renewable resources and have marketing appeal. The Asian markets have been using natural fibres for many years e.g., jute is a common reinforcement in India. Natural fibres are increasingly used in automotive and packaging materials. Polymer matrix composites are gaining more importance compare to monolithically materials as being more reliable and cheaply available. Polymer matrix composites finding application from household to engineering approach. With the advancement of PMC’s their properties have been increased by addition of one more fibre made as hybrid composite which boosts the property of PMC where a single fibre composite lag. We have chosen coconut spathe, papaya bast fibre as reinforcement and Epoxy resin as the base material, composite material prepared by hand layup process according to ASTM. Tests were conducted and the improvement in mechanical properties (tensile strength and flexural strength, impact strength. hardness test.) of the composite material is observed. The result on this study

indicate the coconut spathe composite shows better mechanical properties compare than papaya best fibre and hybrid composite

Keywords: Coconut Spathe, Bast Papaya, Epoxyresin, Hand lay-up process tensile strength, flexural strength, impact strength and hardness.

I. INTRODUCTION

In the current quest for improved performance, which may be specified by Numerous criteria comprising less weight, more strength and lower cost, currently used materials frequently reach the limit of their utility. Thus, material researchers, engineers and scientists are always determined to produce either improved traditional materials or completely novel materials. Composites are an example of the second category. Over the last thirty years composite materials, plastics and ceramics have been the prevailing emerging materials. The volume and numbers of applications of composite materials have developed steadily, penetrating and conquering new markets persistently. Modern composite materials establish a significant proportion of the engineered materials market ranging from everyday products to sophisticated niche applications.

Composites have already proven their worth as weight-saving materials; the current challenge is to make them cost effective. The hard work to produce economically attractive composite components has resulted in several innovative manufacturing techniques currently being used in the composites industry. The composites industry has begun to recognize that the commercial applications of composites promise to offer much larger business opportunities than the aerospace sector due to the sheer size of transportation industry.

India endowed with an ample availability of natural fiber such as Bamboo, Ramie, Jute, Sisal, Pineapple, Coir, Banana etc. has focused on the improvement of natural fiber composites mainly to explore value-added application avenues. Such natural fiber composites are well matched as wood substitutes in the housing and building sector. The development of natural fiber composites in India is based on two cleft strategy of preventing depletion of forest resources as well as ensuring good economic returns for the cultivation of natural fibers.

The developments in composite material after meeting the challenges of aerospace industry have poured down for catering to domestic and industrial applications. Composites, the spectacle material with light-weight; high strength-to-weight ratio and stiffness properties have come a long way in replacing the conventional materials like wood, metals etc. The material experts all over the world focused their attention on natural composites to cut down the cost of raw materials.

II. OBJECTIVES

Keeping in view of the current status of research the following objectives are set in the scope of the present research work.

- Fabrication of coconut spathe / papaya bast fiber reinforced epoxy composites using hand lay-up process.

- Test specimens are 2 layer of coconut spathe with epoxy composite, 2 layer of papaya bast fiber with epoxy composite and 1 layer coconut spathe + 1 layer papaya bast fiber with epoxy composite.
- Material used in this composite are lighter in weight, lesser density and more strength.
- Epoxy resins used in the composite are low viscosity, higher heat resistance and corrosion resistance.
- To study the Mechanical characterization. Such as tensile strength, flexural strength, impact strength and hardness of composite.

III. MATERIALS USED

3.1. Matrix Material

Among different types of matrix materials, polymer matrices are the most commonly used because of many advantages such as cost effectiveness, ease of fabrication with less tooling rate and they also have outstanding room temperature properties. Polymer matrices can be either thermoplastic or thermosetting. The most commonly used thermosetting resins are epoxy, polyester, vinyl ester, Polyurethanes and phenolics. Among them the epoxy resins are generally used for many superior composites due to their many advantages such as tremendous adhesion to wide variety of fibers, superior mechanical and electrical properties and good performance at elevated temperatures. In addition to that they have low shrinkage upon curing and good chemical resistance. Due to numerous advantages over other thermoset polymers, epoxy is chosen as the matrix material for the present research work. It chemically belongs to the 'epoxide' family and its common name of epoxy is Bisphenol-A-Diglycidyl Ether.

3.2. Epoxy

The epoxy resin i.e., diglycidyl ether of biphenyl-A (LY 556) with hardener i.e., triethylenetetramine (HY 951) is used as polymer matrix in this study. The typical properties of the epoxy resin (C₁₈H₂₁ClO₃) used in this study are given in Table 3.2.1

Table 1. Specifications of the Materials Used In the Research

Properties of Epoxy resin	
Density at 25 °C (g/cm ³)	1.15 – 1.20
Weight per epoxide (g)	188.68 g (LY556) & 187.57 g (Lapox L-12)
Viscosity at 25 °C (mPas)	10000 – 12000
Molecular weight (g/mol)	320.8483



Fig.1 Epoxy resin with hardener

3.3. FIBER MATERIALS

3.3.1. COCONUT SPATHE

Coconut spathe, the covering of the coconut inflorescence, is an under-exploited material with considerable potential in this respect. Although substantial research has been carried out on other tissue-types of the coconut palm (*Cocos nucifera*), e.g., leaf bud sheath reports on the use of coconut spathe as a source of fiber in composite materials are scarce. Furthermore, production of fiber reinforced composite materials strengthens the bonding between fiber and matrix, so that it could resist the applied load. Hence coconut spathe-fiber and fiber-reinforced epoxy composites were tested in this study to determine the tensile and flexural strengths

3.3.2. PAPAYA BAST FIBER

Papaya is interesting resource of natural fibers, have not been studied yet. Papayas plants may reach an age of 20 years and do usually not branch. Characteristically, the secondary xylem remains completely parenchymatous. Despite the lack of wood, individual plants grow up to nine metres; hence papaya is called a giant herb. Lignified fibers occurring in the bark (secondary phloem) are the only reinforcing structures interacting with the turgor pressure. The fibers form a complex lattice like mesh, which again is filled with parenchyma. The small amount of fibers compared to the total weight of the stem arouses interest as a model for light-weight applications and structures. Papaya plants were cultivated primarily due to the palatable fruits. Main producers in 2012 have been India (5.16 million ton), Brazil (1.52 million ton) and Indonesia (0.91 million ton). The world's total yield in 2012 accounted for ca. 12.4 million ton. Papaya may therefore be source for

fibers as by-product after have been harvested, such as pineapple, palm and coir. Since the papaya fruit maximum in the first three years, replaced mostly after 3 - 5 years. Fiber material is available in a large usually discarded. Further processing material in composites could be source of income for the producer. Only idea for an application was the use papaya fibers as bio sorbent to remove metals from water.

Coconut and papaya fibers are selected as reinforcements, which is extracted mechanically and they are cleaned manually and then the specimens are prepared as per the ASTM standards are used for this study.

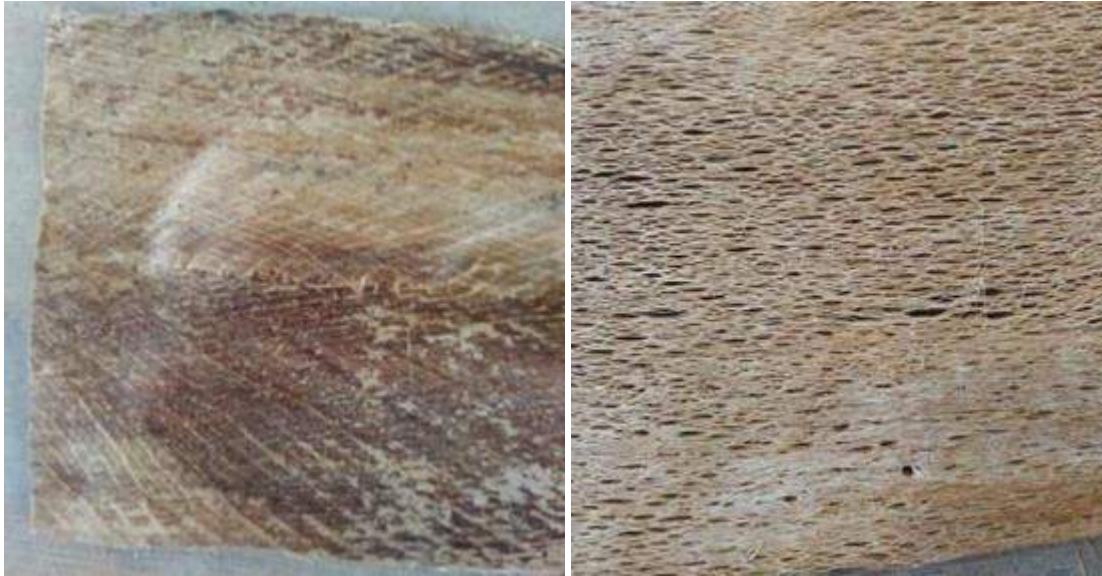


Fig.2 Coconut spathe and papaya bast fiber.

3.4. PROCESSING REQUIREMENTS

Table 2. Materials Used In the Fabrication of Composite.

Sl. No	Materials	Sample Dimensions (mm)
1	Mould made of Wooden pattern	250×150×6
2	Mylar sheet	260 X 150
3	Epoxy	4 lit
4	Coconut/Papaya fiber	250*150*2
5	Hardener	50 gm
6	Polish Wax	250gm
7	Weighing machine	0.2g to 3kg capacity
8	Concrete block	30 kg weight

IV. EXPERIMENTATION AND PROCESS

4.1. PROCESSING TECHNIQUE: HAND LAYUP



Fig.3 Mould



Fig.4 Weighing machine



Fig.5 Epoxy and Harder



Fig.6 Pouring of resin Mixing



Fig.7 Fabrication process



Fig.8 Coconut spathe composite

4.2. FABRICATION PROCEDURE

4.2.1. PRE-PREPARATIONS

- Safety Hand Glows (latex hand gloves).
- Brushes Small and Medium sized...
- Glass sticks- for stirring of resin and reinforcements mixed in a mug.
- Hand rollers- to apply pressure.
- Mylar sheets.
- Chemicals-Hardeners.
- Weighing machine.

4.2.2. PROCESSING PROCEDURE OF COCONUT SPATHE &PAPAYA BAST FIBER / EPOXY

- Cut the Mylar sheet according to Mold size and place it on the Mold.
- According to calculation pour the resin into the mug.
- Stir well for about two minutes in clockwise and alternatively anticlockwise to mix the content thoroughly.
- Then add hardeners
- Once it is mixed thoroughly now it is ready to lay on the mold.
- Before layup clean the Mylar sheet with little amount of resin.
- Before pour the mixed resin in to the mould place one layer of coconut spathe.
- Pour the mixer continuously over the mold apply little pressure using plates to fill the mixer all along the mold.
- Wait for a minute and apply pressure using hand rollers to remove air bubbles and to maintain uniqueness in the laminate.
- And In top of the mould, place one more layer of coconut spathe.
- Put Mylar sheet on it to avoid sticking of specimen onto the mold.
- The cast of each composite is preserved under a load of about 30kg for 24 hours before it removed from the mould cavity.
- Then this cast is post cured in the air for another 24 hours after removing out of the mould.
- Specimens of ASTM standards dimension are cut for physical and mechanical tests.

4.2.3. ASTM STANDARDS FOR TESTING OF SPECIMEN

Table 3. ASTM standard list for testing of samples

Tensile	
• Tensile of Composite Materials	ASTM D3039
• Tensile of Reinforced Thermosetting Resins	ASTM D5083
• Tensile of Sandwich Core Materials	ASTM C297
• Open-Hole Tensile Strength of Composite Laminates	ASTM D5766
• Tensile of Plastics	ASTM D638
Flexural	
• Flexural Properties of Matrix Composites	ASTM D7264
• Flexural Properties by Four-Point Bending	ASTM D6272
• Flexural Properties of Plastics	ASTM D790



Fig.9 Shows specimen before testing

The above figure shows the specimen of tensile, flexural, impact and hardness before testing. The specimen prepared with according to ASTM standard.

- Tensile specimen size 250 X25X 5mm
- Flexural specimen 200 X15 X 5mm
- Impact specimen 64mm x 12.6 X 5mm
- Hardness specimen 25 X25 X 5mm

V. TESTING AND DISCUSSION

5.1. ULTIMATE TENSILE STRENGTH (UTS)

Ultimate tensile strength, often referred to tensile strength is the maximum stress that a Material can withstand while being stretched or pulled before fracture. The tensile test for the specimens was conducted according to ASTM D3039. The specimens of size 250 mm x 25 mm x 5mm were tested with a span length of 100 mm in tensile mode at a cross head speed of 1 mm / min. The fixtures used for the tensile testing is shown in Figure 5.10.



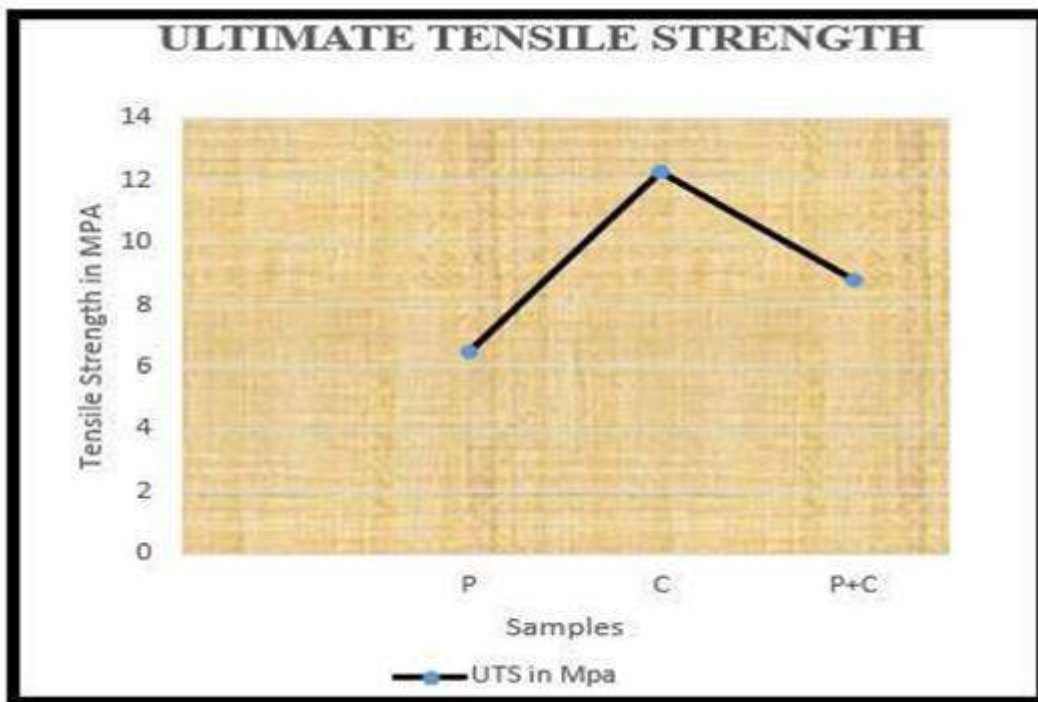
Fig.10 Tensile fixture

Tensile test was conducted for coconut spathe / papaya bast fiber / epoxy specimens using 10 tonne capacity Universal testing machine.

Table 4. The UTS of coconut spathe / papaya bast fiber / epoxy resin

SL.NO	SAMPLE	UTS in Mpa
P	2 Layer of papaya bast fiber	6.47
C	2 Layer of coconut spathe	12.25
P+C	1 Layer papaya + 1 layer of spathe	8.804

Table 4. Shows the variation of UTS of coconut spathe / papaya bast fiber / epoxy composite. The tensile strength is maximum in case of coconut spathe composite is 12.25Mpa and minimum in case of papaya composite 6.47Mpa, and this can be seen in the following graph 1.



Graph 1. Ultimate Tensile Strength Test

5.2. FLEXURAL STRENGTH

The use of flexural tests to determine the mechanical properties of polymeric composites is widely prevalent because of the relative simplicity of the test method, instrumentation and testing equipment required. The flexural strengths of the specimens were determined for specimens using the three-point bending test as per ASTM-D790. The specimens of dimensions 200 mm x 15 mm x 5 mm tested with a span length 50 mm. Figure 5.4 shows the flexural test setup used in the experiment.

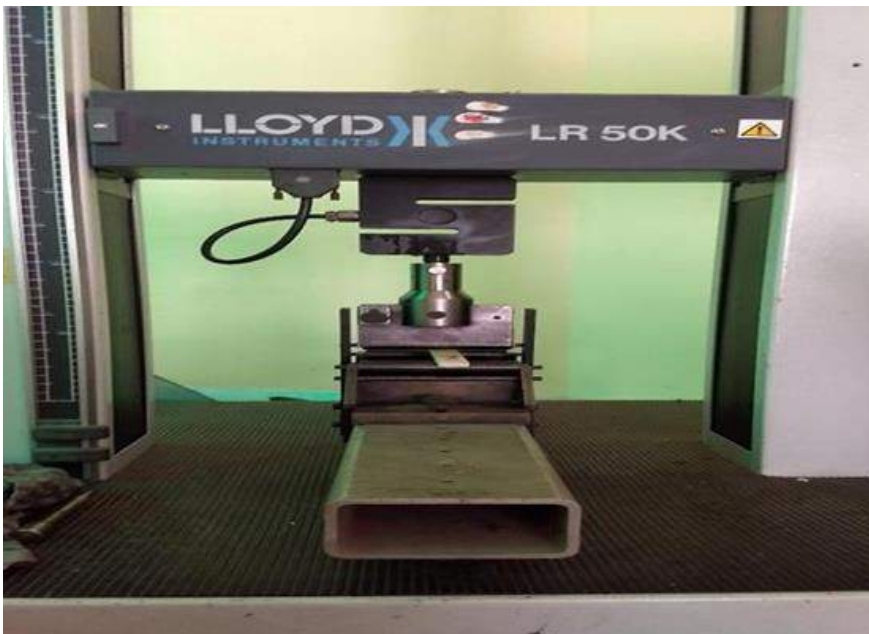


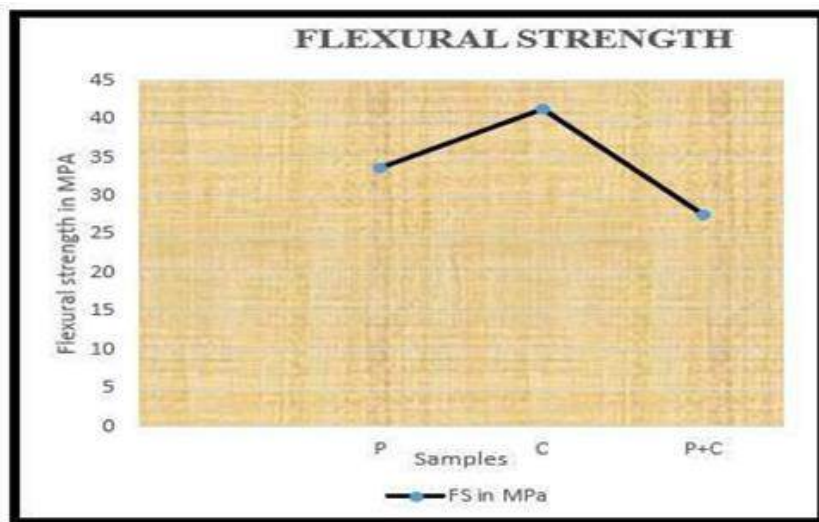
Fig.11 Flexural test setup

The use of flexural tests to determine the mechanical properties of polymeric composites is widely prevalent because of the relative simplicity of the test method, instrumentation and testing equipment required

Table 5. The flexural strength of coconut spathe / papaya bast fiber / epoxy resin

SL.NO	SAMPLE	FS in MPa
P	2 Layer of papaya bast fiber	33.60
C	2 Layer of coconut spathe	41.29
P+C	1 Layer papaya + 1 layer of spathe	27.62

Table 5. Shows the variation of flexural strength of coconut spathe / papaya bast fiber / epoxy composite. The ultimate flexural strength is maximum in case of coconut spathe composite is 41.29 Mpa and minimum in case of papa composite 27.62Mpa, and this can be seen in the following graph 2.



Graph 2. Flexural strength Test

5.3. SHORE D HARDNESS TEST ASTM D2240

Shore hardness is a measure of the resistance of a material to penetration of a spring load needle-like indenter. Hardness of Polymers (rubbers, plastics) is usually measured by Shore scales. Shore A scale is used for testing soft Elastomers (rubbers) and other soft polymers. Hardness of hard elastomers and most other polymer materials (Thermoplastics, Thermosets) is measured by Shore D scale. Shore hardness is tested with an instrument called Durometer. Durometer utilizes an indenter loaded by a calibrated spring. The measured hardness is determined by the penetration depth of the indenter under the load. Two different indenter shapes (see the picture below) and two different spring loads are used for two Shore scales (A and D). The loading forces of Shore A: 1.812 lb (822 g), Shore D: 10 lb (4536 g). Shore hardness value may vary in the range from 0 to 100. Maximum penetration for each scale is 0.097-0.1 inch (2.5-2.54 mm). This value corresponds to minimum Shore hardness: 0. Maximum hardness value 100 corresponds to zero penetration

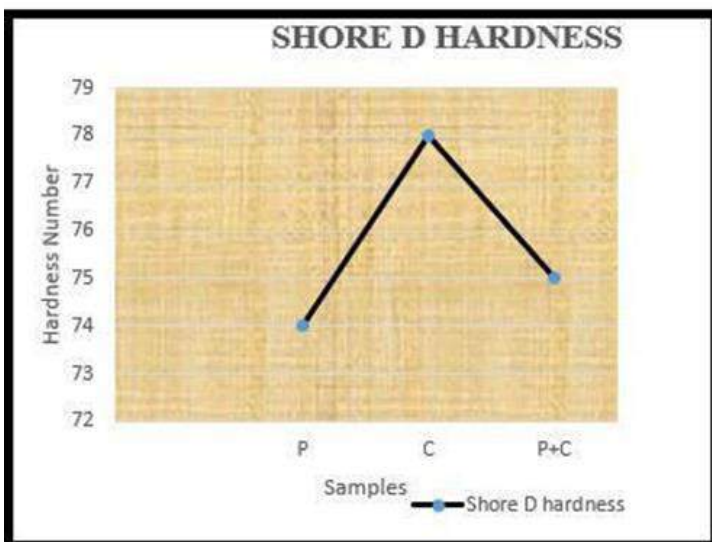


Fig.12 shore D Hardness testing machine

Table 6. The hardness of coconut spathe / papaya bast fiber / epoxy resin

SL.NO	SAMPLE	Shore D hardness
P	2 Layer of papaya bast fiber	74
C	2 Layer of coconut spathe	78
P+C	1 Layer papaya + 1 layer of spathe	75

Table 6. shows the shore D hardness of coconut spathe / papaya bast fiber / epoxy composite. The shore D hardness number is maximum in case of coconut spathe composite is 78 and minimum in case of papa composite 74, and this can be seen in the following graph 3.



Graph 3. Shore D Hardness Test.

5.4. IMPACT TEST

The Izod impact strength of composite samples were evaluated as per ASTM D256, using testing equipment (internal equipment, Mumbai. Capacity up to 25J, release angle of pendulum:1500) the specimen dimension was 64x12.6x6

The impact strength of coir composite samples was evaluated as per ASTM D256, the RI scale was used as the impact load which is having a range of (0-2.71) J, the obtained impact energy was divided by the thickness of the specimen to get impact strength.

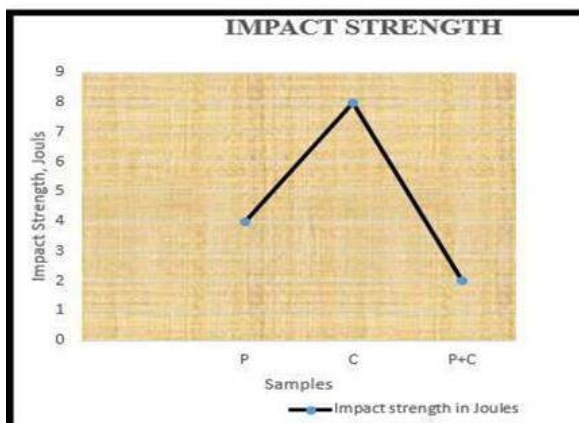


Fig.13 Impact test machine

Table 7. The impact strength of coconut spathe / papaya bast fiber / epoxy resin

SL.NO	SAMPLE	Impact strength in Joules
P	2 Layer of papaya bast fiber	4
C	2 Layer of coconut spathe	8
P+C	1 Layer papaya + 1 layer of spathe	2

Table 7. shows the impact strength of coconut spathe / papaya bast fiber / epoxy composite. The impact strength is maximum in case of coconut spathe composite is 8 and minimum in case of papa composite 2, and this can be seen in the following graph 4.



Graph 4. Impact Strength Test

5.5. TEST SAMPLES AFTER TESTING



Fig.14 Tensile specimen after testing



Fig.15 Flexural specimen after testing



Fig.16 Impact specimens after testing

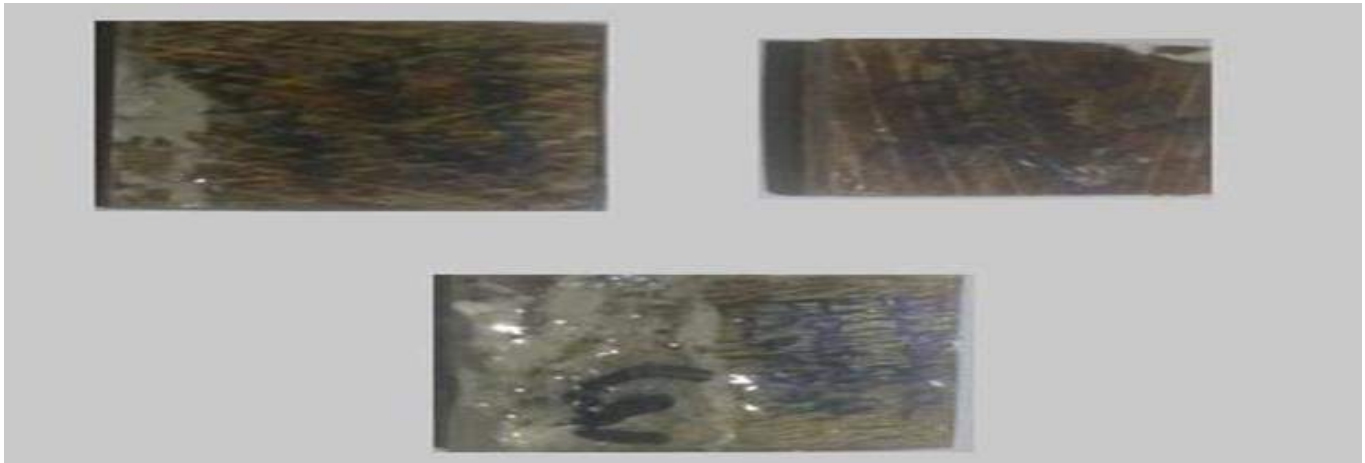


Fig.17 hardness specimen after testing

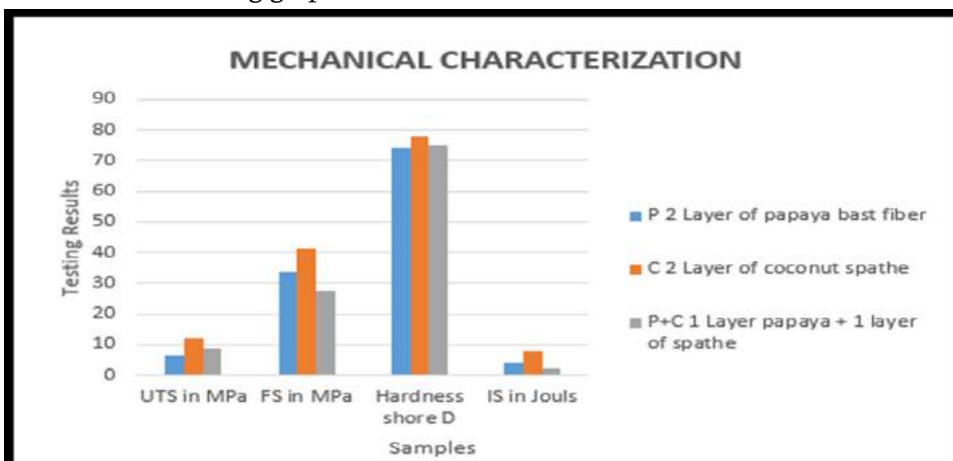
5.6. COMBINED RESULTS

The results of mechanical behaviour of coconut spathe /papaya bast fiber reinforced epoxy- based hybrid composites.

Table 8.

SL.NO	SAMPLE	UTS in MPa	FS in MPa	Hardness shore D	IS in Jouls
P	2 Layer of papaya bast fiber	6.47	33.60	74	4
C	2 Layer of coconut spathe	12.25	41.29	78	8
P+C	1 Layer papaya + 1 layer of spathe	8.80	27.62	75	2

Table 8. Shows the result of coconut Spathe /Papaya bast fiber reinforced with epoxy composite, and this can be seen in the following graph 5.



Graph 5. Combined Results

VI. CONCLUSION

In recent years, the plant based natural cellulose fiber-reinforced polymer composites have attracted the attention of many researchers and material engineers due to their advantages of specific properties over synthetic fibers. The proper selection of the materials and fabrication methods for the preparation of natural fiber polymer composites is necessary to achieve the application of composites. In the present work the coconut and Papaya fibers as reinforcing agents to epoxy matrix composites are prepared by hand layup followed by compression moulding technique. The mechanical characteristics of the coconut and papaya fiber reinforced with epoxy composites are studied.

The experimental investigation on the physical, mechanical behaviour of coconut spathe /papaya bast fiber reinforced epoxy composites lead to the following conclusions.

- Successful fabrication of coconut spathe /papaya bast fiber reinforced epoxy composites by simple hand lay- up technique.
- Tensile strength is maximum in case of coconut spathe composite is 12.25 Mpa , minimum in case of papaya bast fiber is 6.47 and tensile strength of hybrid composite is 8.80Mpa. it clearly shows that hybrid composite lags in tensile strength compare to coconut spathe composite.
- Flexural strength is maximum in case of coconut spathe is 41.29 Mpa and minimum in case of hybrid composite and papaya composite flexural strength is 33.60 Mpa.
- Hardness no is maximum in case of coconut spathe composite is 78 and minimum in case of papaya bast fiber composite is 74 and hybrid composite is 75.
- Impact strength is maximum in case of coconut spathe composite is 8J, minimum in case of hybrid composite is 2J. and impact strength of in case of papaya bast composite is 4J.
- It has been noticed that the various properties of the composites is maximum at coconut spathe fiber loading.
- It has been noticed that the varies properties of the composite is minimum at hybrid composite
- With increasing the fiber content to coconut spathe fiber composite the mechanical properties increased.

VII. SCOPE FOR FUTURE WORK

From the conclusion of the study it clearly states that improvement/implementing following will yield composite of enhanced strength.

- Papaya bast fiber shown poor interfacial bonding with epoxy which can be made better for bonding strength by treating the papaya bast fiber with the solution for optimal result.
- Micro cracks and voids are present in the matrix material which is due to inhomogeneous mixing of epoxy/hardener is avoided by mixing thoroughly in mechanical means.
- The composite is to also be tested for ballistic to conclude the right application of material developed.
- The experiment is tested for temperature variation to know the behaviour of composite under environmental changes.

- The mechanical properties and the machinability behavior can be optimized and predicted using soft computing techniques such as Artificial Neural Network, Neuro Fuzzy and Genetic Algorithm for future work.

VIII. REFERENCES

- [1]. D. Verma, P.C. Gope², A. Shandilya, A. Gupta¹, M.K. Maheshwari. Coir Fiber Reinforcement and Application in Polymer Composites. *J. Mater. Environ. Sci.* 4 (2) (2013) 263-276.
- [2]. D. NABI SAHEB and J. P. JOG. Natural fiber reinforced composites. *Adv in Polymer Techn: Vol. 18, No. 4,* 351–363.
- [3]. Romildo D. Toledo Filho, Karen Scrivener, George L. England, Khosrow Ghavami, Durability of alkali-sensitive sisal and coconut fibres in cement mortar composites. *Cement & Concrete Composites* 22 (2000) 127±143.
- [4]. Mohammad Hajmohammadian Baghban and Reza Mahjoub. Natural Kenaf Fiber and LC3 Binder for Sustainable Fiber-Reinforced Cementitious Composite: *Appl. Sci.* 2020, 10, 357.
- [5]. Manoj kumar, Rakesh Rathee. Determination of Avg. Barcol Hardness by Varying Percentage of EGlass Fiber in Epoxy Composites. (*IJSRD/Vol. 2/Issue 06/2014/057*).
- [6]. S. A.Dhar, D.Roy, M.A. Gafur and M.S.Khatun. STUDY OF THE MECHANICAL, PHYSICAL AND THERMAL PROPERTIES OF COCONUT SPATHE FIBER REINFORCED UNSATURATED POLYESTER COMPOSITE. *Mech. Eng. Res. Journal*, Vol. 10 (2016).
- [7]. Dr. S. VijayaKumar, K. Ashwin Vishwanath, T. Nilavarasan, S. Prabhakar, R. Usharani. STUDY OF MECHANICAL PROPERTIES OF COCONUT-SPATHE FIBERS AND KENAF BAST FIBER REINFORCED EPOXY POLYMER MATRIX COMPOSITES. 3rd International Conference On Recent Advances in Material Processing Technology (RAMPT'13).
- [8]. S.Karthik, V.P.ArunachalamDry. Sliding Wear Behavior of Coconut Spathe Fiber Reinforced Epoxy Composites. *International Journal of Pure and Applied Mathematics* Volume 119 No. 12 2018, 2251-2258.
- [9]. Girisha.C, Sanjeevamurthy, Gunti Rangasrinivas. TENSILE PROPERTIES OF NATURAL FIBER-REINFORCED EPOXY-HYBRID COMPOSITES (*IJMER*) Vol.2, Issue.2, Mar-Apr 2012 pp-471-474
- [10].Abdulla Tamseef D A, Shreehari H R, Harinarayana Mayya B, Praneeth R, Amit Kumar H. Potential of Coconut SPATHE in Composites: *IJIRT | Volume 5 Issue 1*.
- [11].S.M. Sapuan, M.N.M. Zan, E.S. Zainudin and Prithvi Raj Arora. Tensile and flexural strengths of coconut spathe-fiber reinforced epoxy composites. *Journal of Tropical Agriculture* 43 (1-2): 63-65, 2005.
- [12].Senthilkumaran Jagadeesh J, and Shalini N. An Overview of Carica papaya and its Medicinal Uses. *RJPBCS* 5(2) Page No. 641-650.
- [13].Agnivesh Kumar Sinha, Harendra K. Narang and Somnath Bhattacharya. Mechanical properties of natural fiber polymer composites. *J Polym Eng* 2017; 37(9): 879–895.
- [14].Gabriela Luiza Cota Coura , Rodrigo Teixeira Santos Freire, Júlio César dos Santos, Lívia Ávila de Oliveira, Fabrizio Scarpa, Túlio Hallak Panzera a. Tensile and flexural properties of epoxy laminates with natural papaya bast fiber cellular layers. *Composites Part C: Open Access* 2 (2020) 100017, UFSJ, 36307-344.

- [15]. Andreas Kempe, Anne Göhre, Thea Lautenschläger, André Rudolf, Michaela Eder and Christoph Neinhuis. Evaluation of Bast Fibers of the Stem of *Carica papaya*. for Application as Reinforcing Material in Green Composites. Kempe et al.; ARRB, 6(4): 245-252, 2015; Article no.ARRB.2015.082.
- [16]. Md.Fayaz.K, P.Mohamad Zameer, S.M. Hifzaan Sharieff, Syed Mohammed Nizamuddin, Gulbaz Afridi.N. Fabrication and Testing of Composite Materials using Natural Fibers (IJRSI) | Volume VI, Issue V, May 2019 | ISSN 2321–2705.
- [17]. Anjali pal and Avijit mazumdar. CARICA PAPAYA, A MAGIC HERBAL REMEDY. Int. J. Adv. Res. 5(1), 2626-2635.
- [18]. Chanchal Divya, Puri Lakhvinder Kaur. EVALUATION OF THE SENSORY CHARACTERISTICS OF NAMKEEN PREPARED FROM COMPOSITE PAPAYA SEED FLOUR. International Journal of Engineering, Science and Mathematics Vol. 7, issue 4, April 2018.



The Effect of Heat Treatment Process on the Microstructure and Micro Hardness of AlSi10Mg Alloy Samples Fabricated by Additive Manufacturing

Manjunath Prasad R^{1*}, U N Kempaiah², Santhosh N³

^{1*}Research Scholar, Department of Mechanical Engineering, University Visvesvaraya College of Engineering, Bangalore University, Karnataka, India

²Professor, Department of Mechanical Engineering, University Visvesvaraya College of Engineering, Bangalore University, Karnataka, India

³Associate Professor, Department of Mechanical Engineering, MVJ College of Engineering, Near ITPB, Whitefield, Bangalore – 560 067, Karnataka, India

ABSTRACT

Additive manufacturing (AM), also known as 3D printing is becoming an industry standard for manufacturing components. The AM processes can produce complex metal parts with potential applications in aerospace, automobile, medical and fashion domains. Direct Metal Laser Sintering (DMLS) is a commonly used laser powder bed fusion (LPBF) type of AM technique for processing widely used aluminum alloys due to its light weight, high strength, and corrosion resistance properties. This paper presents an experimental work of the latest research carried out in understanding the Hardness and Microstructure of the Aluminium alloys processed by DMLS before and after heat treatment conditions with the aim of identifying research gaps and future research directions. The present research has effectively utilized the established characterization techniques like optical microscopy (OM), scanning electron microscopy (SEM), and X-ray diffraction (XRD), and the effects of Heat treatment on Microstructure and Hardness are investigated and the inferences are reported.

Keywords: Additive Manufacturing; Laser Powder Bed Fusion; Direct Metal Laser Sintering; Metal powder; Characterization; Hardness; Heat treatment.

I. INTRODUCTION

The ASTM definition for Additive Manufacturing is “process of joining materials to make objects from 3D model data, usually layer upon layer, as opposed to subtractive manufacturing methodologies” [1]. The Additive Manufacturing (AM) is a class of layer-by-layer manufacturing techniques that can fabricate highly complex components from CAD model. This CAD model is sliced into 2D slices with a certain layer thickness, and subsequently each layer is built up by adding material. There are different types of Metal Additive

Manufacturing (AM) Methods, namely Selective Laser Sintering (SLS), Selective Laser Melting (SLM), Direct Metal Laser Sintering (DMLS), Laser Engineered Net Shaping (LENS), and Direct Metal Deposition (DMD). Among these Metal AM methods, the Direct Metal Laser Sintering (DMLS) process can be used for Aerospace parts, customized medical parts, tooling with conformal cooling channels and functional components with high geometrical complexity. Direct Metal Laser Sintering is an additive freeform manufacturing process which creates 3-D parts through the application of laser energy to powder beds [2]. The manufacturers are focusing on the potential cost reduction, fewer steps in the production process and design-freedom and these are achievable through Additive Manufacturing (AM) technologies. There has been number of studies on Additive Manufacturing of AlSi10Mg alloys, because of the demand from the industrial field for lightweight structures with complex geometries [3]. The AlSi10Mg alloy has been widely used in the aerospace and automotive industry, because of its neat eutectic composition of Al and Si; further, it has good weldability. However, the Aluminium alloy powder is very easy to be oxidized, and the formation of oxide film is one of the challenges when exposed to laser during the fabrication of samples. There are many recent studies, which have reported the microstructure and mechanical properties of DMLS / SLM fabricated AlSi10Mg alloys. Kempen et al. [4] studied the mechanical properties of AlSi10Mg produced by SLM and found that the SLM-fabricated AlSi10Mg parts exhibited higher tensile strength and hardness than the casted parts; these parts have exhibited anisotropic behavior at rupture under different build directions. Brandi et al. [5] studied the microstructure and fatigue performance of SLM-fabricated AlSi10Mg under different directions (0°, 45°, and 90°). The researchers found that the heat treatment had the noteworthy effect on fatigue resistance and least effect on the building direction. Read et al. [6] studied the influence of process parameters on porosity development in the SLM of AlSi10Mg alloys using a DOE. The reviewers found that the laser power, scanning speed, and the interaction between the scanning speed and hatch spacing had a pronounced effect on porosity development. From, the literature review, it is evident, that this paper focuses on the Microstructure and Hardness properties of fabricated samples both in “as fabricated” and post “Heat treatment” condition. The effects of Heat treatment on Microstructure and Hardness are investigated.

II. MATERIALS, METHODS, PROCESSING AND CHARACTERIZATION TECHNIQUES

The chemical composition of AlSi10Mg powder as provided by the powder manufactures (EOS GmbH) is given in Table 1, and has been ascertained through powder Particle Elemental Composition studies by the Energy Dispersive X-Ray Analysis (EDAX). The Microtrac Bluewave Particle Size Analyzer are used to analyze three powder samples Particle Size Distribution (PSD) and the average D10, D50 and D90 values are 30.29 μm , 43.60 μm and 63.61 μm respectively. Figure 2 shows a Scanning Electron Microscope (SEM) micrograph of the powder; it is obvious that the powder particles are not spherical. The particle shows irregular morphology, with small irregular satellite particles attached to the bigger particles (Fig. 1). The specimens are manufactured by EOSINT M280 system (EOS GmbH - Electro Optical Systems, Germany). The EOS EOSINT M 280 is based on the DMLS (Direct Metal Laser Sintering) 3D printing technology developed by EOS, equipped with Ytterbium fibre laser with 400W power, and a Scan speed of 7 (m/s), and a minimum re coater time of 8 sec, and build rate of 5-20 ($\text{cm}^3 / \text{hr.}$) The process takes place in an inert environment in a working space with 250 \times 250 mm

dimensions on the horizontal plane and a maximum height of 290 μm . The layer thickness was set to 60 μm and a parallel scan strategy with alternating scan direction was adopted. In the current study, the samples are produced using the process parameters of LASER Power of 240 W, Scan speed of 1180 mm/s, Hatch spacing of 0.12 mm, and Laser Spot Size of 0.1mm. The DMLS process parameters are listed in Table 2 and these are the optimum setting parameters from previous studies. The test samples with dimensions of 10mm \times 10mm \times 10mm have been fabricated to examine the Microstructure and Hardness as per the dimensions given in figure 2.

TABLE 1 CHEMICAL COMPOSITION OF AlSi10Mg ALLOY POWDER (Wt. %)

Element	% Composition
Si	9.5-10.5
Mg	0.15-0.45
Fe	0.45-0.55
Cu	0.05-0.1
Pb	0.05-0.1
Ti	0.1-0.15
Zn	0.1-0.15
Mn	0.4-0.45
Sn	0.15-0.2
Ni	0.05-0.1
Al	Rem.

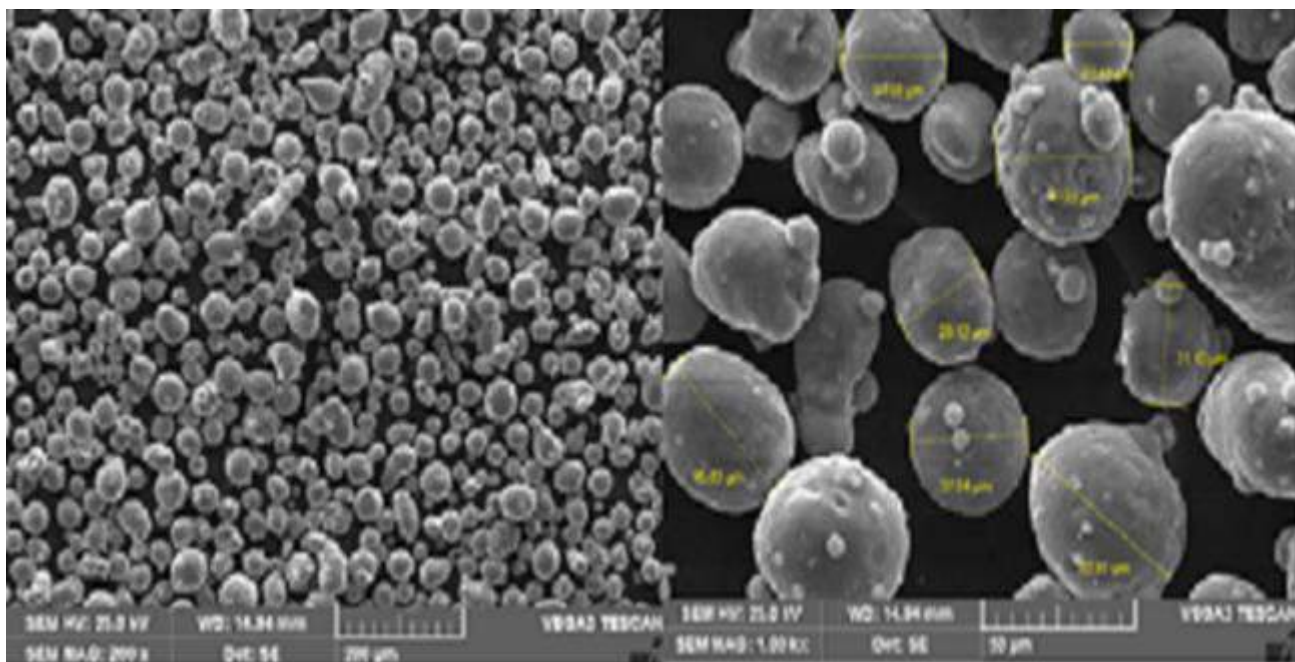


Figure 1: The morphology of AlSi10Mg powder

TABLE 2 DMLS PROCESS PARAMETERS

Sl. No.	Parameter	Value
1	Power	240 W
2	Scan Speed	1180 mm/s
3	Layer Thickness	60 μm
4	Hatch Spacing	0.12 mm
5	Laser Spot Size	0.1 mm

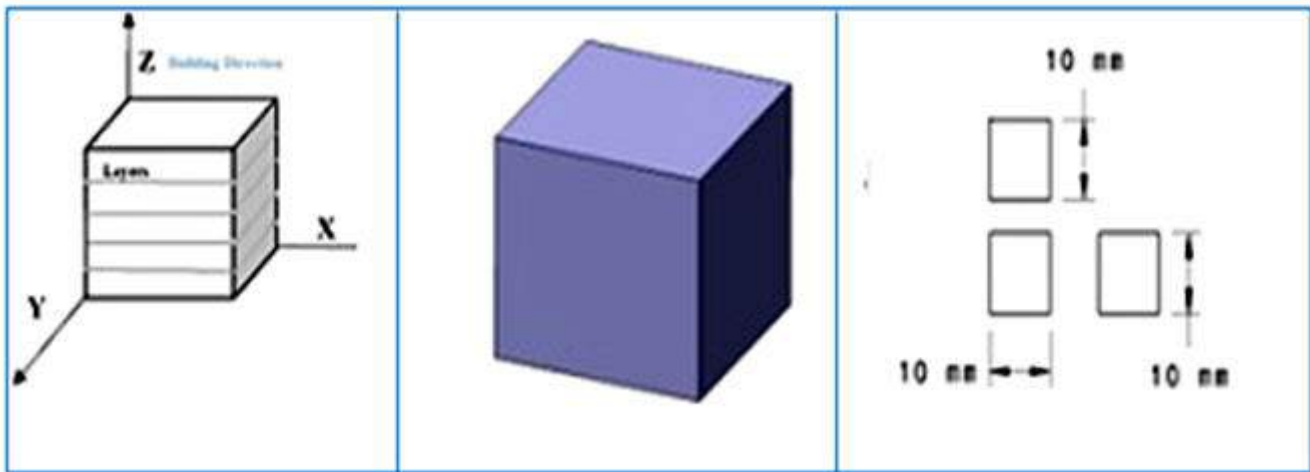


Figure 2: Build Orientation and Test samples dimensions

The microstructure of both “as fabricated” and “Heat Treated” AlSi10Mg samples are characterized with Optical Microscopy (OM), Scanning Electron Microscope (SEM), and X-ray diffraction (XRD) measurements. A Nikon optical microscope LV100 with Clemex Image Analyzer is used to evaluate the microstructure of the etched parts. The polishing and etching procedures are performed according to the ASM Metal Handbook recommendations. The samples are etched using Keller’s reagent (190 ml distilled water, 5 ml HNO₃, 3 ml HCl, 2 ml HF) for 20 seconds to reveal the microstructure. The Micro Vickers Hardness Tester (MMT-X7, Matsuzawa, Japan) is used for measuring the hardness with Vickers scale (0,5 kg load). A TESCAN- VEGA3 LMU Scanning Electron Microscope and EDAX – AMETEK is used to investigate the grain size, structure observations, and elemental analysis (Energy-dispersive X-ray spectroscopy). For X-ray diffraction analysis, the Malvern Panalytical's X-ray diffractometer is used.

The Post-processing operations like Heat treatment is required in order to enhance the mechanical properties [7]. For the Heat treatment study, the samples are fabricated by DMLS process in accordance with the dimensions shown in figure 2. This study is to explore the effect of a T6 heat treatment on the DMLS fabricated samples, and understand its influence on the microstructure. The Tensile, Compression and Impact samples are solution heat treated at 540 °C and 1.5 h soaking time for solution heat treatment, followed by water quenching, and artificial ageing (AA) at 200°C for a duration of 8 hours.

III. RESULTS AND DISCUSSIONS

A. Microstructure

The Optical microscope analysis is performed using the “as fabricated” and “Heat-Treated” samples along the building direction that is perpendicular to the printed layers (Z-direction) and parallel to the printed layers (XY direction). The Figure 3 shows OM images showing the microstructure of “as fabricated” and “Heat-treated” samples. The microstructure has resulted from the high cooling rate experienced by the material during the layer wise printing operation. The as-fabricated sample is shown in Figure 3 (a and b). The characteristic cellular microstructure, supersaturated α -Al matrix and continuous network of eutectic Si particles are characterized from the morphological features. The resulting microstructures are non-homogenous. The Al cells usually appear finer when viewed perpendicular to the build direction. And the Al cells appear elongated when viewed parallel to the build direction, After the Heat treatment; the microstructure changes noticeably. Figure 3 (c and d) establishes microstructure of T6 Heat treated AlSi10Mg alloy. The Si particles have grown and are uniformly dispersed in α -Al matrix owing to solution heat treatment and aging.

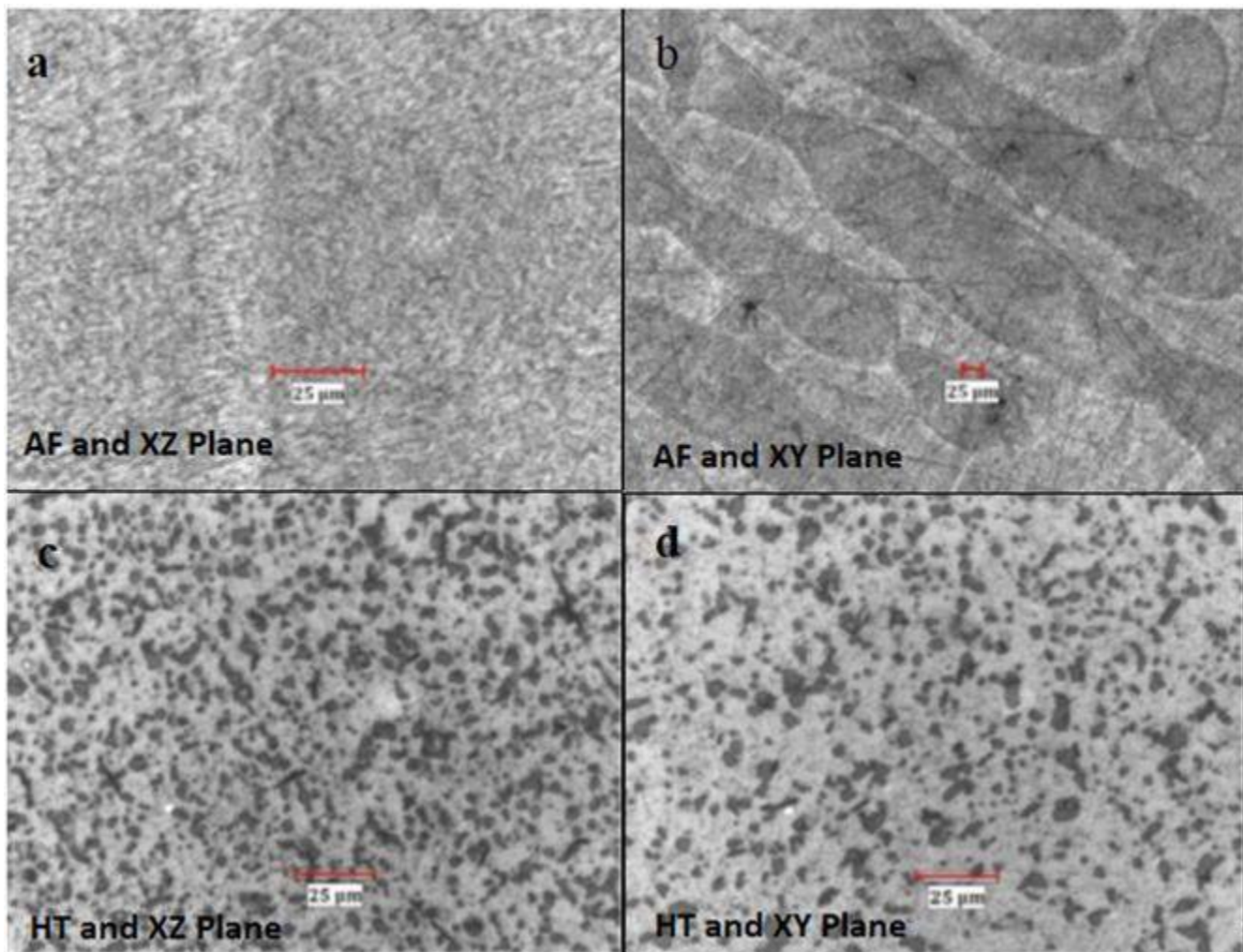


Figure 3: OM images showing the microstructure of as-fabricated samples (a and b) Heat-Treated samples (c and d).

The scanning electron microscope (SEM) analysis is performed using the “as fabricated” and “Heat-treated” samples along the build direction that is perpendicular to the printed layers (Z-direction) and parallel to the printed layers (XY direction). The Figure 4 (a and b) shows SEM images depicting the microstructure of as fabricated and the Heat-treated samples [Figure 4 (c and d)].

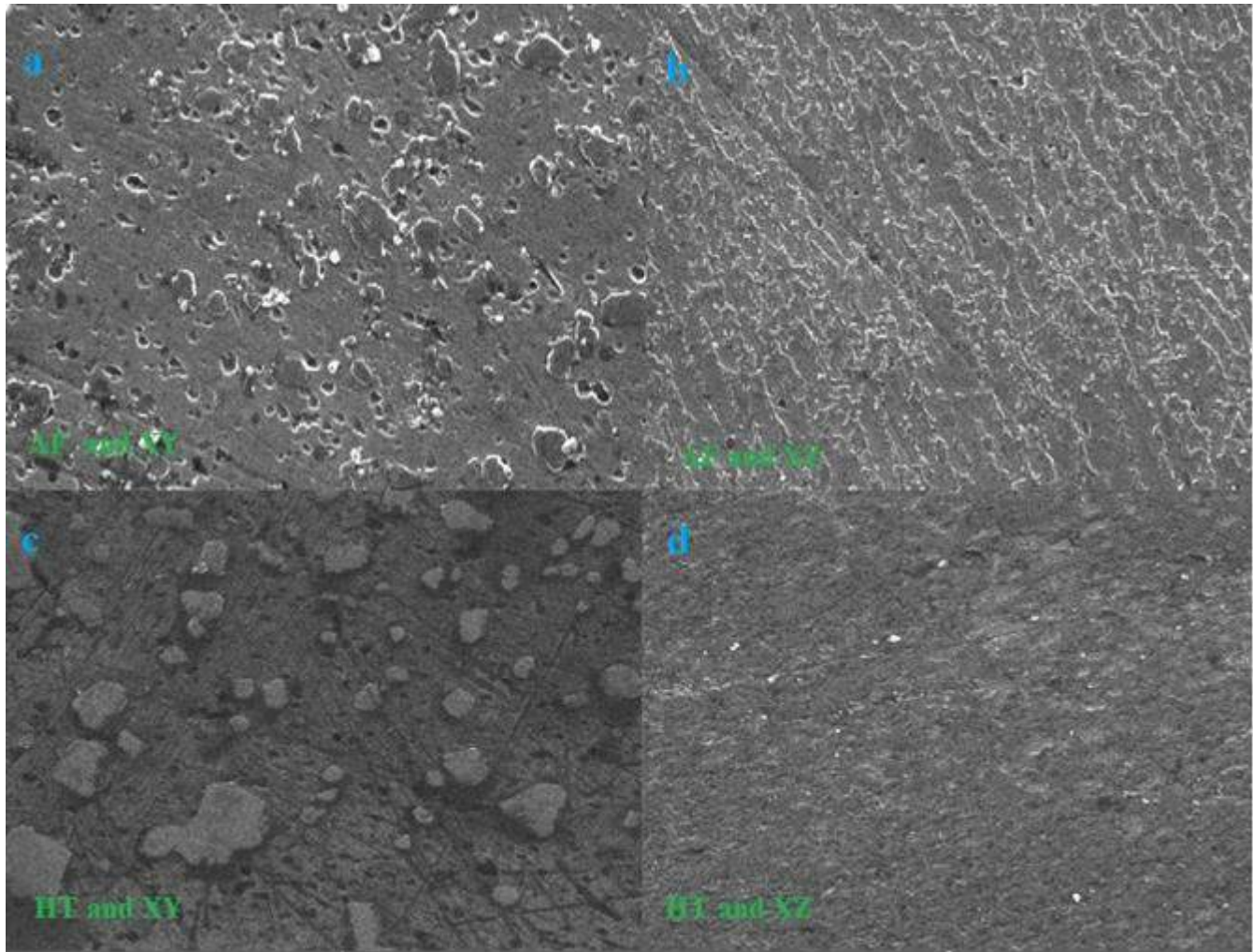


Figure 4: SEM images showing the microstructure of “as-fabricated” samples (a and b) and “Heat Treated” samples (c and d)

B. Microhardness

Hardness is well known as a preliminary indication for mechanical properties. The microhardness measurement is performed according to ASTM E384 (The standard test method for Knoop and Vickers Hardness Testing of Materials). The average values of the samples of microhardness are obtained along all the three (X, Y, and Z) directions. Each recorded value was an average of 3-5 indentations along the tested area of a 500-gf load applied over a period of 15 to 20 seconds dwell time. The Vickers microhardness of the “as built” DMLS samples is much higher (almost 45 Hv) than the microhardness of the T6 heat treatment samples due to the softening the material, fine distribution of the Si phase and attributable to the grain growth, which has reduced the grain boundaries. The microhardness of the “as fabricated” DMLS material is always higher than

the heat-treated material. The anisotropy is not observed in the material after heat treatment since the hardness in all planes is found to be an average of 132 ± 4 HV for as fabricated samples and 87 ± 4 for Heat treated samples. This is possibly due to the homogenized microstructure and evolution of the crystallographic texture. This significant drop in hardness for the DMLS alloy is clearly due to the microstructural changes related to the treatment itself. The table 3 gives the hardness values for as fabricated specimens, while the table 4 gives the hardness values for heat treated specimens. The figure 5 gives the hardness values for both, "As Fabricated" (AF) and "Heat Treated" (HT) specimens.

TABLE 3 HARDNESS VALUES FOR (AS FABRICATED) SPECIMENS

As Fabricated		Hardness (HV 0.5)		
Orientation		X avg	Y avg	Z avg
XYZ	TC1	128.70	132.70	130.00
	TC2	131.00	134.30	137.70
	TC3	133.00	132.00	134.70

TABLE 4 HARDNESS VALUES FOR (HEAT TREATED) SPECIMENS

After T6		Hardness (HV 0.5)		
Orientation		X avg	Y avg	Z avg
XYZ	TC1	84.00	84.10	85.70
	TC2	90.30	91.10	91.70
	TC3	84.70	85.40	86.00

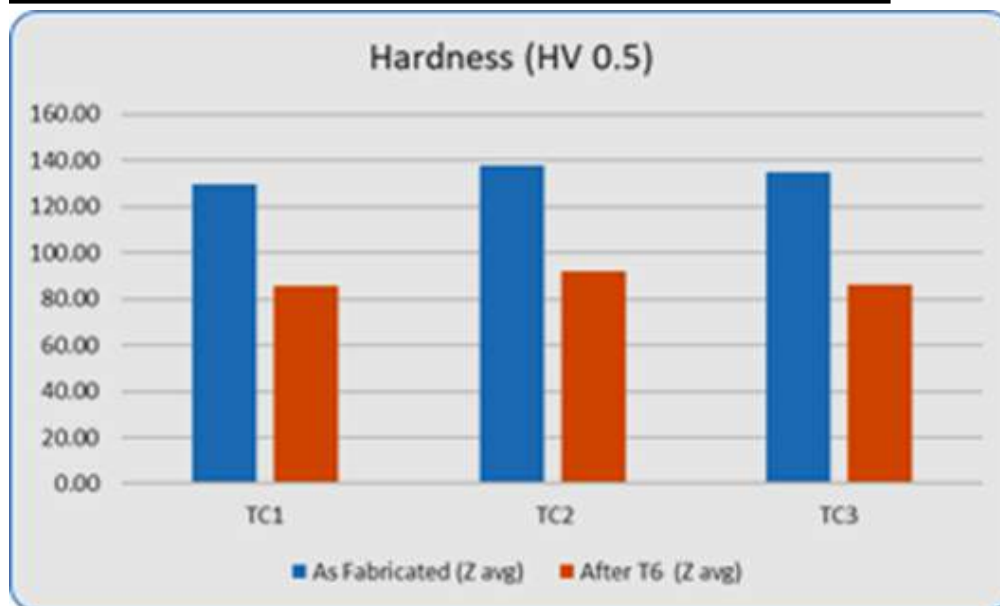


Figure 5: Hardness Values Graphs (Both AF and HT)

C. XRD Analysis

XRD analysis is carried out to investigate the different phases, present in the samples in both "as fabricated" and post "heat treatment" conditions [8]. The XRD analysis are performed on cross sections of polished un-etched samples and there is no specific preparation for XRD, since the size of the "as built specimen" is suitable and can

be easily fitted onto the mounting plate available [9]. The XRD patterns of “as-built” sample is depicted in Figure 6. It mainly consists of α -Al and Si phases and the intensity of Si peaks is relatively lower than that of Al peaks. The XRD spectra has not revealed Mg_2Si peak although the alloy has ability to precipitate it. This study reveals that sample is a two-phase material and that Si is not completely dissolved within the Al phase.

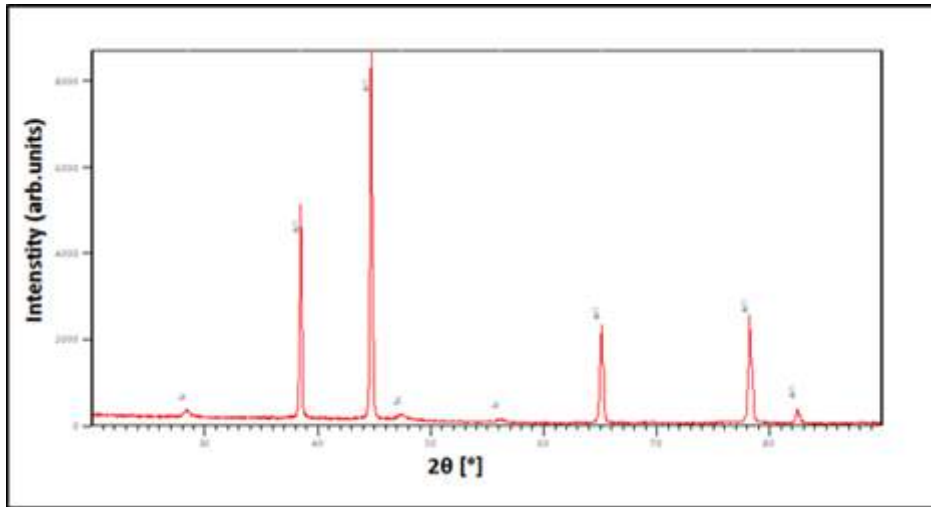


Figure 6: Diffraction pattern of XRD peaks of AlSi10Mg as-built samples

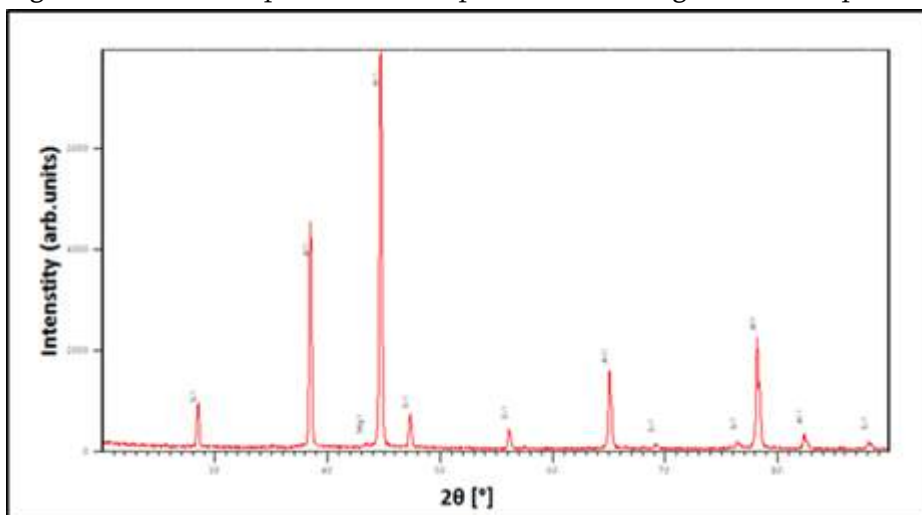


Figure 7: Diffraction pattern of XRD peaks of AlSi10Mg after Heat treated condition

The T6 heat treated sample is subjected to the XRD analysis in order to evaluate the effect of the heat treatment on the microstructure, focusing the attention on the Al, Si and Mg_2Si peaks. The XRD patterns of the heat-treated sample is shown in Figure 7. The breadth of the Si peaks transforms to the peaks as that of α -Al, confirming that crystals are coarsened. The results reveal that the crystallite sizes of Al and Si increases for heat treated samples as compared to the “as fabricated” samples.

IV. SUMMARY AND CONCLUSIONS

The current study focused on the influence of Heat Treatment on the microstructure and Hardness of the “as fabricated” and “Heat treated” AlSi10Mg samples. The key results are as follows:

- In comparison with “as-built” samples, T6 Heat treatment results in a decrease of the hardness by 65%.
- The Post-processing of the samples using T6 Heat treatment creates a homogenous microstructure with Si particles in an Al matrix.
- The T6 Heat treated sample shows the α -Al phase and with coarse dispersed particles of silicon. The Si particles are larger and more widely spaced.
- This study reveals that sample is a two-phase material and that Si is not completely dissolved within the Al phase.
- After Heat treatment the crystallite sizes of Al and Si increased compared to as built samples.

V. REFERENCES

- [1]. ASTM International. (2015). Standard Terminology for Additive Manufacturing – General Principles – Terminology (ISO/ASTM 52900:2015(E)). Online.
- [2]. Louvis, E., Fox, P. and Sutcliffe, J. “Selective laser melting of Aluminium components,” *Journal of Materials Processing Technology*, pp. 275–284, 2011.
- [3]. Dadbakhsh S, Hao L, “Effect of Al alloys on selective laser melting behavior and microstructure and mechanical of in situ formed particle reinforced composites”, *J Alloy Compd*, pp. 328–334, 2012.
- [4]. Kempen K, Thijs L, Van Humbeeck J, Kruth J-P (2012) Mechanical properties of AlSi10Mg produced by selective laser melting. *Phys Procedia* 39:439–446.
- [5]. Brandl E, Heckenberger U, Holzinger V, Buchbinder D (2012) Additive manufactured AlSi10Mg samples using selective laser melting (SLM): microstructure, high cycle fatigue, and fracture behavior. *Mater Des* 34:159–169.
- [6]. Read N, Wang W, Essa K, Attallah MM (2015) Selective laser melting of AlSi10Mg alloy: process optimization and mechanical properties development. *Mater Des* 65:417–424. <https://doi.org/10.1016/j.matdes.2014.09.044>.
- [7]. Santhosh Nagaraja, Ramesha Kodanda, Khalid Ansari, Mohamed S. Kuruniyan, Asif Afzal, Abdul R. Kaladgi, Navid Aslfattahi, C. A. Saleel, Ashwin C. Gowda, and Praveena Bindiganavile Anand. (2021). "Influence of Heat Treatment and Reinforcements on Tensile Characteristics of Aluminium AA 5083/Silicon Carbide/Fly Ash Composites" *Materials* 14, no. 18: 5261. <https://doi.org/10.3390/ma14185261>.
- [8]. Santhosh Nagaraja, Kempaiah Ujjaini Nagegowda, Anand Kumar V, Sagr Alamri, Asif Afzal, Deepak Thakur, Abdul Razak Kaladgi, Satyam Panchal and Ahamed Saleel C, (2021). "Influence of the Fly Ash Material Inoculants on the Tensile and Impact Characteristics of the Aluminum AA 5083/7.5SiC Composites" *Materials* 14, no. 9: 2452. <https://doi.org/10.3390/ma14092452>.
- [9]. Manjunath Prasad R., U. N. Kempaiah, Santhosh N., (2019). A Review on Metal Additive Manufacturing Techniques and its Applications, *Journal of Polymer & Composites*, 7(3): 24 – 31. <http://engineeringjournals.stmjournals.in/index.php/JoPC/article/view/3413>.



Effect of Heat Treatment on Dry Sliding Wear Behaviour of AA6061-Gr Metal Matrix Composites by Taguchi Techniques

Lokesh T*, Rudresh B M

Department of Mechanical Engineering, Government Engineering College, K R Pet -571426, Karnataka, India

ABSTRACT

In the present study, metal matrix composites of Al6061 matrix with varying composition of 2%, 4% and 6wt. % Gr were prepared by liquid metallurgy route. The cast composites have been subjected to solutionizing heat treatment at a temperature of $5300 \pm 20\text{C}$ for 6 hours followed by ageing at a temperature of $1750 \pm 20\text{C}$ for 4 hours. The wear and frictional properties of metal matrix composites were studied by conducting dry sliding wear test using Pin on Disc machine as per ASTM G-99 standard. The wear tests were carried out by using Taguchi technique. The L9 orthogonal array and analysis of variance approach was employed to study the effect of wear parameters such as load, percentage reinforcement and sliding distance on wear rate of the composites. The effect of wear parameters on wear rate of the composites was studied. The experimental results revealed that applied load had the most significant effect on wear rate of composites than the reinforcement and sliding distance load. The worn surfaces of samples were examined by using Scanning Electron Microscope (SEM) photographs to analyze the nature of wear mechanism.

Keywords: Taguchi technique; Wear; MMC; AA6061; Graphite

I. INTRODUCTION

It is well known that aluminium and its alloys being lightweight materials have huge applications in the area of automotive and aerospace applications. Taking a cue from their low density and moderate strength properties, many researchers across the world have developed composite materials using organic and ceramic based materials as reinforcement [1]. Among the various series of aluminium alloys, the Al6061 is better choice for a matrix material because it has excellent mechanical properties, good formability and the strength of this material can be altered by doing the heat treatment [2]. Most commonly used reinforcements are SiC, Al₂O₃, graphite, TiB₂, TiC, B₄C and carbon nanotubes. The stir casting method is found to be easier and the low cost production method when compared to other processing methods, particularly when discontinuous reinforcements are used [3, 4].

Devis et.al [5] reported the influence of volume fraction and particle size on the wear behaviour of aluminium composites. They concluded that the most significant parameter on the wear rate was sliding distance and applied load. Radhika et.al [6] reported that the Taguchi technique is a better technique to deal with responses

influenced by multivariable. Basavarajappa et.al [7] found that addition of graphite particles into the aluminium matrix increases wear resistance of the composite. Mahdavi and Akhlaghi [8] studied the dry sliding wear behaviour of SiC and graphite particles reinforced Al6061 composites. Most of the studies have been carried out on Al-Gr [9, 10] and Al-SiC [11, 12] composites individually. From the literature survey, not much work has been reported on the effect of heat treatment, applied load, % reinforcement and sliding distance on the dry sliding wear behaviour of AA6061-Gr composites. In view of the above, an attempt was made to study the effect of these parameters on AA6061-Gr composites using Taguchi design of experiments.

II. TAGUCHI TECHNIQUE

Taguchi technique is a powerful tool for designing high quality systems based on orthogonal array (OA). It is a reliable and systematic approach to optimize designs for performance, quality and cost [13]. There are several orthogonal arrays based on the process Parameters and their levels. The suitable Orthogonal Array is selected and the experiments are conducted as per the OA specifies. The experimental results are analyzed by signal to noise ratio (S/N) values. The S/N ratios are categorized into three types i.e. lower the better (LB), higher the better (HB) and nominal the best (NB). This will be selected based on the response of the process, since here the response is the wear rate and we have to minimize the value of the response so LB characteristics needs to be applied here. The Mathematical equation for smaller is better S/N ratio is represented in equation 1. Furthermore Analysis of Variance (ANOVA) was performed to find out which parameter is significant over the other and to find the percentage of contribution of each parameter on the wear rate. With the help of the S/N ratio and ANOVA analysis, the optimal combination of process parameters can be obtained. At last a confirmation test was performed to verify the optimal process parameters.

$$\frac{S}{N} = -10 \log_{10}^2 (y_1^2 + y_2^2 + y_3^2 + \dots + y_n^2) \quad (1)$$

Where $y_1, y_2, y_3, \dots, y_n$, are the response of sliding wear, n is the number of observations.

III. MATERIALS, METHODS, PROCESSING AND TESTING OF COMPOSITES

A. MATERIALS AND METHODS

The matrix material selected for the present research study is AA6061. The reinforcing material selected were Gr particles of 10 to 30 μm size. The chemical composition of AA6061 alloy by weight percent Si = 0.72, Mg = 0.89, Cu = 0.21, Fe = 0.23, Cr = 0.22, Zn = 0.10, Ti = 0.01 and Al = Balance. The amount of Gr particles are varied from 2 to 6 wt. % in steps of 2wt. %. Stir casting technique has been used to prepare the AA6061-Gr composite. The detailed procedure adopted during composite preparation has been explained in our earlier paper [5].

B. PROCESSING OF COMPOSITES

The cast composites have been subjected to solutionizing heat treatment at a temperature of $530^\circ \pm 2^\circ\text{C}$ for 6 hours, followed by ageing at a temperature of $175^\circ \pm 2^\circ\text{C}$ for 4 hours. The microstructural study revealed that, the distributions of reinforcements in the matrix are fairly uniform. The detailed microstructural analysis and hardness of composites have been explained in our earlier paper [5].

C. PLAN OF EXPERIMENTS

The L9 orthogonal array was used to conduct the experiment. The wear parameters chosen in this experimental study were (i) Applied Load, (ii) Sliding Distance and (iii) Percentage Reinforcement and the response studied was the wear rate. Table 1, indicates the level and their factors. The experiment consists of 9 tests and each parameter was varied for three levels.

Table 1: process parameters and levels

Level	% Reinforcement	Sliding Distance, D (m)	Applied load, L (N)
1	2	500	9.81
2	4	1000	19.62
3	6	1500	29.43

D. DRY SLIDING WEAR TEST

Dry sliding wear test were conducted by using a pin on disc wear test machine. Test specimens as per ASTM G-99 standard of size 8mm diameter and 30mm length were cut from the cast samples. The surface of the specimen was polished by fine emery paper. A single pan digital weighing machine with the least count of 0.0001gram was used for measuring the initial weight of the specimen. The wear test was conducted at room temperature. During the test the track diameter was set for 100 mm the specimen was mounted in between the grippers and pressed against a rotating EN 32 steel disc of hardness 65 HRC by applying the load. After the test, the specimen was removed and cleaned with acetone. The final weight of the specimen was measured. The difference in the weight of specimen before and after the test gives the amount of material removed from the surface of the composite.

IV. RESULTS AND DISCUSSION

A. STATISTICAL ANALYSIS OF EXPERIMENTS

The experiments were conducted as per L9 orthogonal array and the obtained results of wear rate and S/N ratio for various combinations of parameters are shown in the Table 2

Table 2: Taguchi orthogonal array Result of AA6061-Gr composites for wear rate

S D (m)	L (N)	R P	As Cast		Heat Treated	
			WR(mm ³ /m)	SNR	WR(mm ³ /m)	SNR
500	9.81	2	0.003335	49.5381	0.002756	51.1944
500	19.62	4	0.003786	48.4364	0.003236	49.7998
500	29.43	6	0.003947	48.0747	0.003381	49.4191
1000	9.81	4	0.002605	51.6838	0.002153	53.3391
1000	19.62	6	0.002779	51.1222	0.002296	52.7806
1000	29.43	2	0.004263	47.4057	0.003828	48.3406
1500	9.81	6	0.001779	54.9965	0.001470	56.6537
1500	19.62	2	0.003480	49.1684	0.002875	50.8272

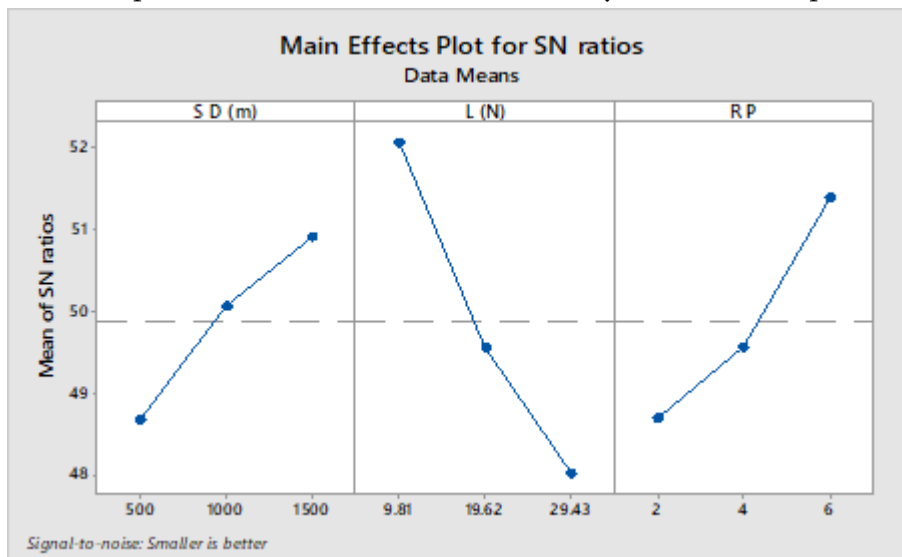
1500	29.43	4	0.003722	48.5845	0.003076	50.2403
------	-------	---	----------	---------	----------	---------

Table 2 shows the wear rate of AA6061-Gr composites for two processing conditions. It can be observed that the as cast composites displayed highest wear rate than the heat treated ones. The reason behind this is the presence of as cast defects like porosity can lead low hardness values when compared to heat treatment processing conditions. So in such conditions the AA6061 matrix doesn't offer any resistance to plastic deformation caused by hard asperities of counter surface. The penetration of hard asperities can lead to high wear of as cast composites. While in case of heat treated composites, due to high hardness attributed to the presence of precipitates like MgZn₂ and Al₂Cu strengthen the matrix material for heat treated composites. Further the uniformly dispersed Gr can help by distributing the load applied on the composite pin during sliding test and lubricating nature of graphite.

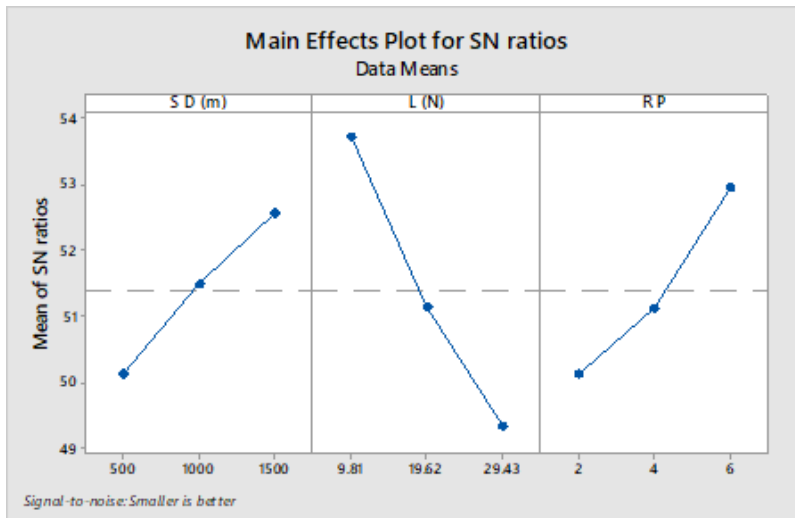
Table 3: Response table for signal to noise ratios of AA6061-Gr composites for wear rate (smaller is better)

Level	As Cast			Heat Treated		
	S D (m)	L (N)	R P	S D (m)	L (N)	R P
1	48.68	52.07	48.70	50.14	53.73	50.12
2	50.07	49.58	49.57	51.49	51.14	51.13
3	50.92	48.02	51.40	52.57	49.33	52.95
Delta	2.23	4.05	2.69	2.44	4.40	2.83
Rank	3	1	2	3	1	2

The response table obtained for this process is shown in the Table 3. The rank values provide the level of influence of input factors on response variable. This table is clearly indicating that the applied load is a dominant parameter on the wear rate followed by reinforcement percentage and sliding distance.



(a) Main effects plot for S/N ratios –wear rate (As Cast)



(b) Main effects plot for S/N ratios –wear rate (Heat Treated)

Fig.1 Main effects plot for S/N ratios of AA6061-Gr composites - Wear Rate

Figure 1 shows the influence of process parameters on wear rate graphically. The optimum condition for wear rate which is shown in Figure1 is D3, L1 and R3. Fig.1(a, b) depicts main effect plot for S/N ratio. It shows that S/N ratio increases with the increase in sliding distance. Applied Load has inverse relation with wear rate. Since it is desirable to have maximum S/N ratio, as per lower the better option, SN ratio graph depicts that minimum wear rate is achieved at 1500m of sliding distance, 9.81N of applied Load and 6% of Reinforcement Percent same for all categories.

B. ANALYSIS OF VARIANCE (ANOVA) RESULTS

Table 4(a): Analysis of Variance of Al6061-Gr composites for wear rate (As Cast)

Source	DF	Adj SS	Adj MS	F-Value	P-Value	P (%)
S D (m)	1	0.000001	0.000001	48.89	0.001	14.93
L (N)	1	0.000003	0.000003	199.22	0.000	60.85
R P	1	0.000001	0.000001	74.31	0.000	22.69
Error	5	0.000000	0.000000			01.53
Total	8	0.000005				100

Table 4(b): Analysis of Variance of Al6061-Gr composites for wear rate (Heat Treated)

Source	DF	Adj SS	Adj MS	F-Value	P-Value	P (%)
S D (m)	1	0.000001	0.000001	81.19	0.000	15.45
L (N)	1	0.000003	0.000003	325.11	0.000	61.92
R P	1	0.000001	0.000001	113.91	0.000	21.68
Error	5	0.000000	0.000000			00.95
Total	8	0.000004				100

The ANOVA results shown in Tables 4(a) and 4(b) is clearly indicating that the applied load is a dominant parameter on the wear rate followed by reinforcement percentage and sliding distance. Same is presented in terms of percentage in the last column of ANOVA results shown in Table 4(a) and 4(b). P-value in the ANOVA table tells which factors are significant on wear rate. Applied Load, Reinforcement Percent and Sliding Distance are significant factors affecting wear rate because their P-values are less than 0.05.

Table 5: Model Summary of Al6061-Gr composites for wear rate

As Cast		Heat Treated	
R-sq	R-sq(adj)	R-sq	R-sq(adj)
98.47%	97.56%	99.05%	98.48%

R²-value measures degree of fit, 98.47%, 99.05% of variability in data can be explained by present R² value for all categories As Cast and Heat Treated respectively. As R² value approaches unity, fitted model fits the actual data better. It also tells how much performance characteristics are affected by unaccountable factors. Thus it confirms that present model presents fairly good explanation of relationship between input factors and the response variable.

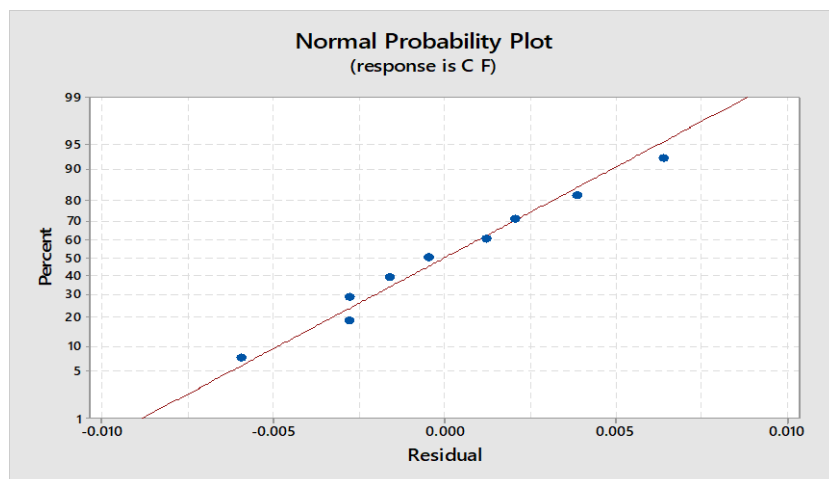
C. MULTIPLE LINEAR REGRESSION MODELS (MLRM)

The statistical tool MINITAB 17 was used to develop the MLRM. The relation between independent variable and the response variable from the observed data in the form of linear equation was obtained by this model.

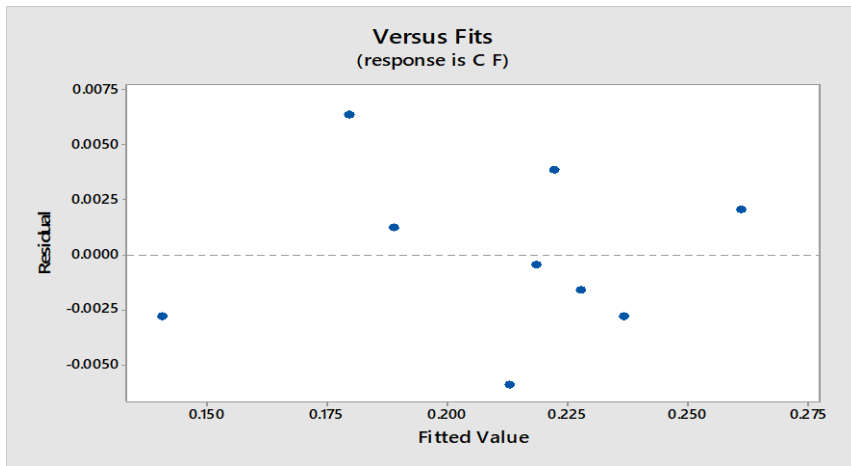
The regression equation developed for wear rate is

$$W R_{(As\ Cast)} (mm^3/m) = 0.003449 - 0.000001 S D (m) + 0.000072 L (N) - 0.000214 R P \quad (5.8)$$

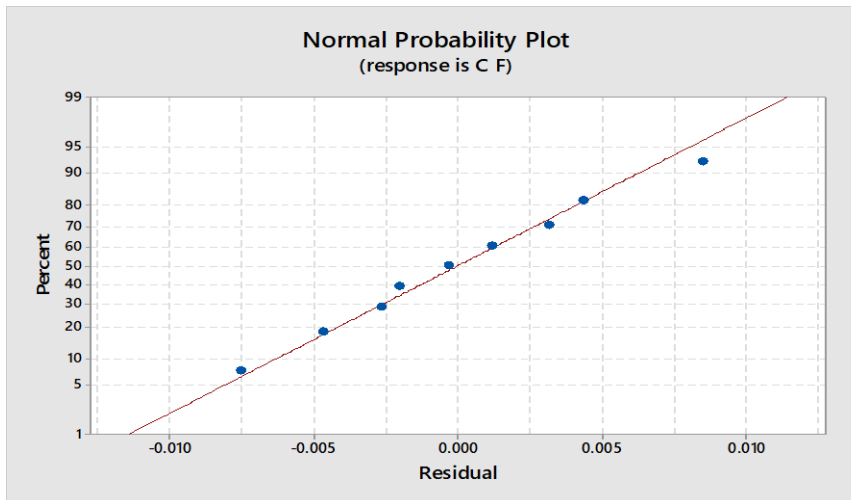
$$W R_{(Heat\ Treated)} (mm^3/m) = 0.002905 - 0.000001 S D (m) + 0.000066 L (N) - 0.000193 R P \quad (5.9)$$



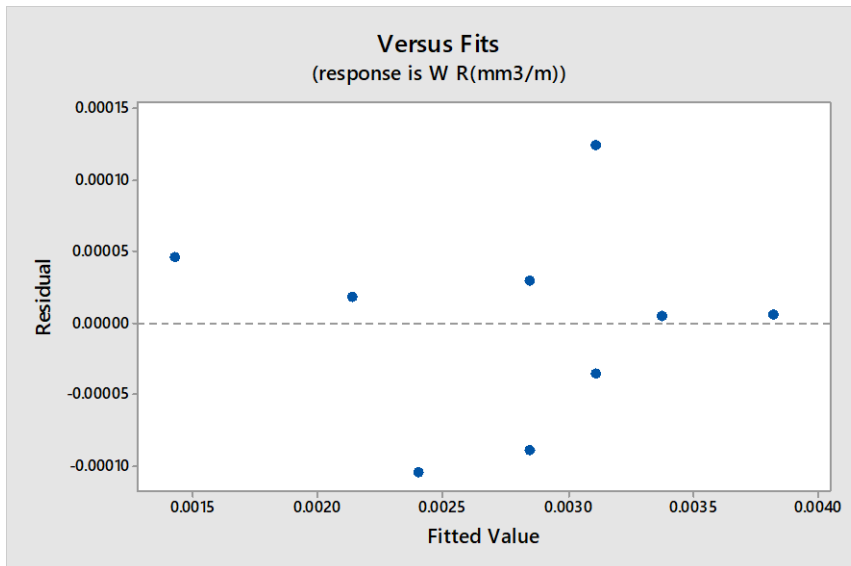
(a) Normal probability plot of Residuals-As Cast



(b) Plot of Residuals v/s fitted values- As Cast



(c) Normal probability plot of Residuals-Heat treated



(d) Plot of Residuals v/s fitted values- Heat Treated

Fig.2 Normal probability plot of Residuals and Fits of AA6061-Gr composites for Wear Rate

Figure 2 shows the normal probability plot of residuals and Fits for wear rate. From the figure it is observed that the data points are close to the normal probability line. It shows that the residuals are normally distributed over the line and the model is best fit to forecast the wear.

D. CONFIRMATION TEST

The obtained results were confirmed by conducting the confirmation test. The experimental parameters used for the test was shown in the Table 6(a).

Table 6(a): Confirmation Experiment of AA6061-Gr composites for wear rate

Expt. No	Sliding Distance, S D (m)	Applied load, L (N)	% Reinforcement Percentage
1	900	22	2
2	1200	28	4
3	1500	36	6

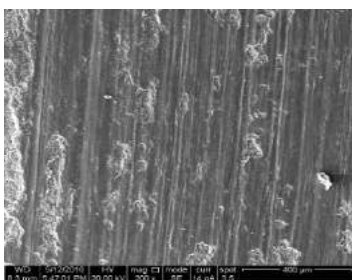
The results of confirmation test and comparison between the experimental values and computed values developed from the regression model is recorded in the Table 6(b). The experimental value of wear rate is found to vary from the regression equation in the range of 1.08% to 4.58%. The wear rate obtained from the regression model and the experimentation was found to match with least error.

Table 6(b): Result of Confirmation Experiment of AA6061-Gr composites for wear rate and their comparison with regression model

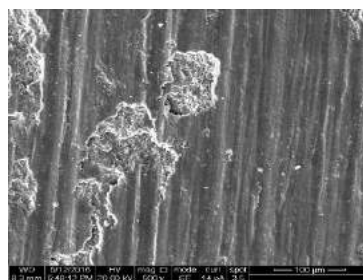
Expt. No	Expt. WR (mm ³ /m)	Reg. model W R (mm ³ /m)	%Error
1	0.002442	0.002352	3.68
2	0.002486	0.002372	4.58
3	0.002493	0.002466	1.08

E. SEM ANALYSIS OF WORN SURFACES OF AA6061-GR COMPOSITES

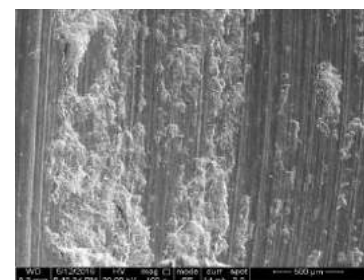
As Cast



a) Distance=500, Load=29.43N,
Al606-2wt.%Gr

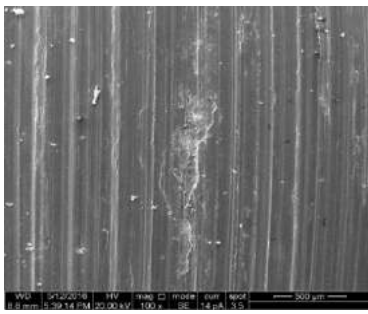


b) Distance=1000, Load=29.43N,
Al6061-2wt.%Gr

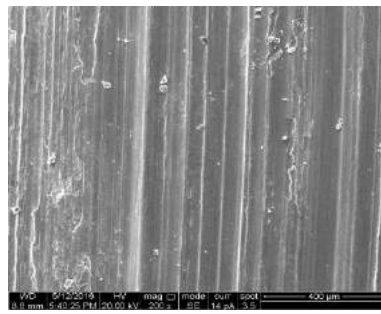


c) Distance=1500, Load= 29.43 N,
Al6061-2wt.%Gr

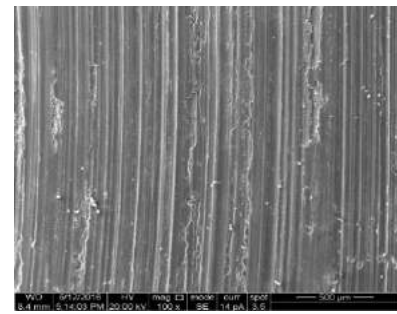
Heat treated



a) Load=9.81N, Distance=1000,
Al6061-4wt.%Gr



b) Load=19.62N, Distance=1000
Al6061-4wt.%Gr



c) Load= 29.43 N, Distance=1000,
Al6061-4wt.%Gr

Fig.3 SEM wear tracks of Al6061-Gr composites

During testing the uniformly distributed graphite smears way layer by layer and forms a lubricating layer [14]. This layer formed in between the contact surface and composite pin effectively avoid the wear. This phenomenon is well reflected in the SEM analysis of worn surfaces of these materials as shown in Fig.3 In case of as cast composites we can see peeling off large lumps from the surface. This was further increased with the increase in load during test due to deep penetration of hard asperities of counter surface. Further comparatively large grain sizes of AA6061 matrix in case of as cast composite systems are ineffective in resisting the plastic deformation and lead to high wear rate. So the SEM micrographs of as cast composite systems show the features like peeling off matrix along with scratches due to penetration of hard asperities of counter surface disc. [15]. On the other hand heat treated composite surfaces do exhibit the scratches but the depth or width is not as high as that of as cast ones.

V. CONCLUSION

The following conclusions are drawn from the present investigation:

1. Liquid metallurgy route was successfully adopted in the preparation of AA6061- (2-6wt. %) Gr composites.
2. The load (61.92%) has the highest influence on specific wear rate of the composite followed by percentage reinforcement (21.68%) and sliding distance (15.45%).
3. Incorporation of Graphite particulates into the AA6061 matrix increases the wear resistance of the composite by forming a protective lubricating layer between the pin and counter face.
4. Regression equation generated for AA6061- (2-6 wt. %) Gr composite has been used to predict the specific wear rate for the intermediate conditions with good accuracy.
5. The confirmation test results showed least error. Thus, design of experiments by Taguchi technique was successfully used to study the tribological behaviour of AA6061- (2-6 wt. %) Gr composites.

VI. REFERENCES

- [1]. ASM Handbook Volume 21: 2001, Composites. ASM International, 21, 1029-1032, 2001
- [2]. M K Surappa, Sadhana, 28, 319-334. 2003

- [3]. Lokesh T, U. S. Mallik, 2018, Effect of ECAP process on the Microstructure and Mechanical Properties of Al6061-Gr Composites, *Materials today Proceedings*, Elsevier, 5, 2453-2461, 2018
- [4]. M.A. Taha, Practicalization of cast metal matrix composites (MMCCs), *Materials and Design* 22, 431-441, 2001
- [5]. R.L. Deuis, C. Subramanian and J.M. Yellup, Abrasive wear of aluminium composites--a review ,*Wear* 63, 132-139, 1996
- [6]. N. Radhika, R. Subramanian, S. Venkat Prasad, "Tribological Behaviour of Aluminium/Alumina/Graphite Hybrid Metal Matrix Composite Using Taguchi's Techniques," *Journal of Minerals & Material Characterization & Engg.* 10(2011) 427-443
- [7]. S. Basavarajappa, G. Chandramohan, A. Mahadevan, M. Thangavelu, R. Subramanian, P. Gopalakrishnan, 2007, Influence of sliding speed on the dry sliding wear behaviour and the subsurface deformation on hybrid metal matrix composite, *Wear* 262, 1007-1012, 2007
- [8]. S. Mahdavi, F. Akhlaghi, 2011, Effect of the SiC particle size on the dry sliding wear behaviour of SiC and SiC-Gr-reinforced Al6061 composites, *Journal of Materials Science*, 46, 7883-7894, 2011
- [9]. S. Suresha, B.K. Sridhara, 2010, Effect of addition of graphite particulates on the wear behaviour in aluminium-silicon carbide-graphite composites, *Materials and Design* 31 1804-1812, 2010
- [10]. A. Baradeswaran & A. Elaya Perumal, 2015, Effect of Graphite on Tribological and Mechanical Properties of AA7075 Composites, *Tribology Transactions*, 58, 1-6, 2015
- [11]. J. Guo, X. Yuan, The aging behavior of SiC/Gr/6013Al composite in T4 and T6 treatments, *Materials Science and Engineering A* 499 (2009) 212-214.
- [12]. A. Vencel, I. Bobic, S. Arostegui, B. Bobic, A. Marinkovic, M. Babic, Structural, mechanical and tribological properties of A356 aluminium alloy reinforced with Al₂O₃, SiC and SiC + graphite particles, *Journal of Alloys and Compounds* 506 (2010) 631-639.
- [13]. F. Akhlaghi, A. Zare-Bidaki, Influence of Graphite Content on the Dry Sliding and Oil Impregnated Sliding wear Behavior of Aluminium 2024-Graphite Composites Produced by in situ Powder Metallurgy Method, *Wear* 266 (2009) 37-45.
- [14]. Y.B.Liu, S.C.Lim, S.Ray, P.K.Rohatgi, 1992, Friction and wear of aluminium-graphite composites: the smearing process of graphite during sliding, *Wear* 159, 201-205, 1992
- [15]. A. Baradeswaran & A. Elaya Perumal, Effect of Graphite on Tribological and Mechanical Properties of AA7075 Composites, *Tribology Transactions*, 58, 1-6, 2015



Study of Corrosion of Aluminium 6061 Based Metal Matrix Composite

Sunitha V¹, Girisha H N¹, Madhu D¹

¹Department of Mechanical & Smart Manufacturing Engineering, Government Engineering College,
Ramanagar-562159, Karnataka, India

ABSTRACT

Aluminium 6061 alloys have been widely used in the field of the application of aerospace, sports equipment's manufacturing and automobiles industries and there have been distinct cases of experimental implementation. It has been investigated with various ceramic reinforcements to enhance the usability of the material. Feasibility of different constituent depends on the compatibility of the properties.

In the present investigation, efforts are made to study the corrosion properties of Al6061 alloy reinforced with alumina particulate and zircon sand in different compositions. The vortex method of stir casting was employed in which the reinforcements were introduced into vortex created by the molten metal by mechanical stirrer. Castings were machined to the ASTM standards on a highly sophisticated lathe. The alloy exhibit improved corrosion resistance with increased weight percentage of alumina and zircon sand.

Keywords: Aluminium 6061, Alumina, Zircon sand, corrosion.

I. INTRODUCTION

Composite metals have an unique advantage of low weight to strength ratio, better mechanical properties like hardness, wear resistance and fatigue properties which is of high importance.

Das et al [1] Basavarajappa and Chandramohan et al [2] have demonstrated dry sliding wear behaviour, aluminium alloy reinforced with reinforced with SiCp-Graphite. The un-lubricated pins on disc wear test were conducted, to examine the wear behaviour of aluminium alloy and its composites. They reported that wear rate of graphite composites is lower than that of matrix alloy and SiCp reinforced composite. Sharma et al [3] have studied liquid metallurgical technique. A pin on disc wear testing machine was used to carry out the tribological tests on both composites and matrix alloy over a load range of 10–50N and sliding velocities of 1.25–3.05 m/s for various sliding instances of 0.5–3 km. The wear resistances of Al6061 matrix, garnet particulate reinforced composites are superior to that of unreinforced matrix alloy. Olivier Beffort et al [4] alloying effects on microstructure and mechanical properties of high volume fraction SiC-particle reinforced Al-MMCs made by squeeze casting infiltration. Suresh et al [5] have observed that one of the important limitations in fabrication of aluminium matrix composites is the compatibility of reinforcement in the matrix. This is of prime importance in case of Al composites; as Al is covered with a thin layer of oxide which blocks the surface wetting and reacts with some ceramics to form inter metallic phases which tend to influence the

final properties of composites. The tribological behaviour of self-lubricated aluminium/SiC/graphite hybrid composites with various amount of graphite addition synthesized by the semi-solid powder densification method [6]. In the case of particle-filled MMCs, the mechanical properties are not significantly altered, but tribological properties show marked improvements. Soft solid lubricant particles such as graphite and mica improve anticizing properties of Al alloys whereas hard particles like SiC, alumina, WC, TiC, zircon, silica, and boron Carbide greatly improves the resistance to abrasion of Al alloys. [7]

Based on the literature survey, it is observed that very minimal work was reported based upon Al6061/Al₂O₃/Zircon sand, hence the present investigation is to fabricate a Aluminium 6061/Zircon sand and Al₂O₃. Aluminium is a light metal whose alloys already are widely used in aircraft industries such as aircrafts whereas Zircon has high wear resistant and hardness properties. Therefore, Aluminium MMCs have the potential to further improve the application characteristics. In the present investigation, Zircon sand and Al₂O₃ was dispersed in molten Al6061, where in Al₂O₃ wt% and Zircon sand wt% was varied

II. MATERIALS, METHODS, PROCESSING AND TESTING OF COMPOSITES

The materials used for processing and development of Aluminium alloy metal matrix composite are Aluminium 6061 alloy, Zircon sand and their properties are shown in the Table 1.

TABLE 1 PROPERTIES OF ALUMINIUM 6061 ALUMINA AND ZIRCON SAND

Chemicals	Density	Melting point	Thermal Conductivity
Al6061	207 g/cm ³	580°C	173 W/mK
Alumina	3.95 gm/cm ³	2072 ^o C	40 W/mK
Zircon sand	3.95 g/cm ³	2072 ^o C	40 W/mK

A. Composite Preparation

Composite materials were prepared using Liquid metallurgy technique where Zircon sand particles and Al₂O₃ were introduced into the molten metal pool through a vortex created in the melt by the use of a zirconium coated stainless steel stirrer. Stirring was carried out by means of a mechanical stirrer which rotates at a speed of 150 rpm. The Aluminium composite material reaches to a complete liquid state at the temperature of about 800^o C as the melting point of Aluminium is 700^o C as shown in Figure 1. Thus, the completely melted Aluminium Metal matrix composite was poured into the permanent moulds as shown in Figure 2. The specimen was prepared for different percentage composition of Al6061, Alumina and Zircon sand. Castings are prepared by pouring the melt into preheated moulds of cylindrical shapes. Zircon sand and Al₂O₃ was dispersed in molten Al6061, where in Al₂O₃ wt% and Zircon sand wt% was varied. The specimen with varied reinforcement composition was prepared as shown in Table 2. Then these specimens were tested for corrosion characteristics to be compared with pure Al 6061



Figure 1: The specimen with varied reinforcement composition before being poured into molds

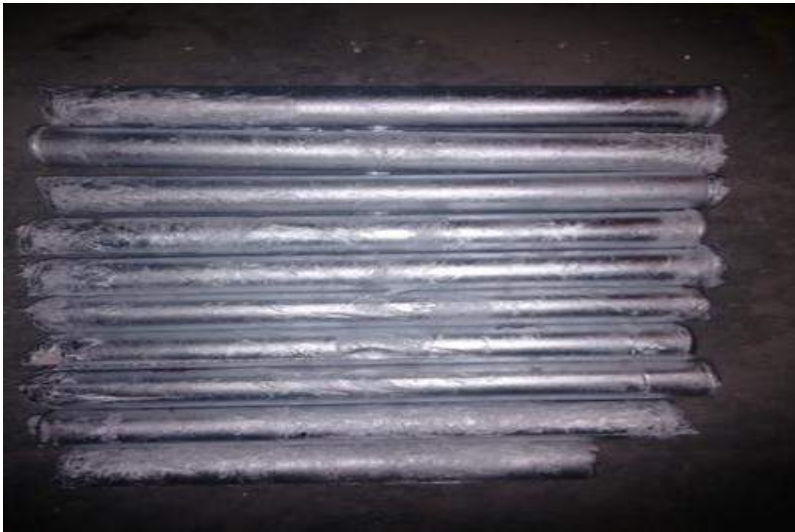


Figure 2: Specimen after casting

TABLE 2 AL 6061 MMC WITH VARIED REINFORCEMENT COMPOSITION

Specimen No.	Al6061	Alumina	Zircon sand
1	97%	1%	2%
2	95%	3%	2%
3	93%	5%	2%
4	95%	1%	4%
5	93%	3%	4%
6	91%	5%	4%
7	93%	1%	6%
8	91%	3%	6%
9	89%	5%	6%

B. Testing of composites

The corrosion behaviour of the composite material was carried out by immersion corrosion test at room temperature by placing the composite sample in 1 Normality of NaCl solution as shown in Figure 3. The solution contained 58.44 gms of NaCl which was dissolved in 1 litre of distilled water. Weight loss was calculated for 10, 20 and 30 days respectively. The corroded specimen were thoroughly cleaned as per ASTM standard G1. The cleaning solution contained 20 gms of chromium oxide and 50 ml of phosphoric acid which was dissolved in 1 litre of distilled water. The weight loss due to corrosion was measured for 10 days, 20 days and 30 days duration



Figure 3: Corrosion test set-up

III. RESULTS AND DISCUSSION

Table 3 shows the weight loss as a function of immersion time in number of days in 1Normality NaCl solution. It is seen that at in the beginning the weight loss decreases with increment in immersion time, a drop in weight loss is seen for both Al6061 matrix and its composites up to 30 days. It is additionally noticed that the weight loss of composites is lesser after 20 days. The saturation of solution with anodic ions and also presence of relatively more stable passive oxide layer, a steady state condition is arrived after few days irrespective of fact that if unreinforced matrix alloy or hybrid composite. When evaluated with matrix material can be ascribed to the large quantity of porosity in composites.

TABLE 3 WEIGHT LOSS DUE TO CORROSION

Alumina	Zircon	Weight loss in 10 days (mg)	Weight loss in 20 days (mg)	Weight loss in 30 days (mg)
1%	2%	3	6	12
3%	2%	4	7	11
5%	2%	2	5	10
1%	4%	3	6	12

3%	4%	2	5	10
5%	4%	3	6	8
1%	6%	2	6	10
3%	6%	2	4	9
5%	6%	4	8	8

From the Figure 4 we observe that the corrosion weight loss decreases as the percentage of Alumina is increased, but it is also observed that with the increase in the addition of zircon sand also decreases corrosion rate. From this graph, it is observed that for a smaller duration of time period there is a smaller decrement in weight loss. As the process continuous for 30 days, there is a slight decrement in the weight loss. For increase in reinforcement from 1% to 3% alumina in the base matrix there is a decrease in weight loss about 20%. Further increase in 3% to 5% alumina in base matrix will decrease weight loss by about 41.6%. Similarly, weight loss decreases as the percentage of alumina increases.

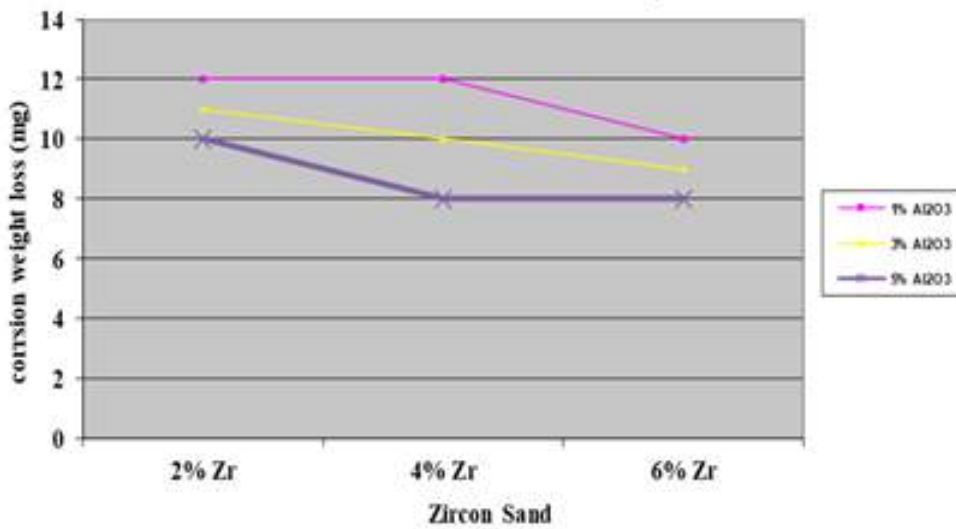


Figure 4: Variation of corrosion weight loss for 30 days in aluminium 6061 for different % of Zircon Sand and Alumina

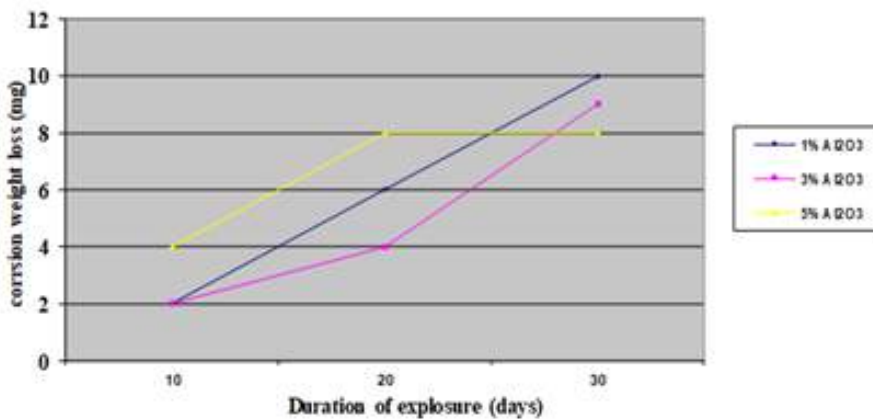


Figure 5: Variation of corrosion weight loss for 6% of Zircon Sand with varying Alumina and time duration

Figure 5 shows the weight loss of specimens due to corrosion for different composition of composites. For increase in reinforcement from 1% to 3% alumina in the base matrix, the decrease of weight loss is about 15%. Further increase in 3% to 5% alumina in base matrix will decrease the weight loss by about 14%. Therefore, the weight loss decreases as the percentage of alumina increases. For increase in reinforcement from 2% to 4% zircon sand in the base matrix there will be decrease in weight loss about 33%. Further increase in 4% to 6% zircon sand in base matrix, will decrease it about 20%. Therefore, weight loss decreases as the percentage of alumina increases. For the increase in reinforcement from 2% to 4% zircon sand in the base matrix, this will decrease weight loss about 33%. Further increase in 4% to 6% zircon sand in base matrix will decrease weight loss about 20%. Therefore, weight loss decreases as the percentage of zircon sand increases.

IV. CONCLUSION

Aluminium 6061 based metal matrix composite reinforced with different weight percentage of Zircon sand and Alumina were successfully synthesized by stir casting technique. The corrosion test conducted based on ASTM standards shows the improved mechanical properties. The weight loss of alloy decreases with the increased percent weight of alumina and zircon sand. This can be ascribed to the fact that there is a presence of steady oxide layer, which is framed over the Al 6061 composite, development of such oxides reduces the corrosion rate response over period of time

V. REFERENCES

- [1]. Das, D., Pattanaik, S., Routara, B. C., Mishra, P. C., & Samal, C. (2017). Dry sliding wear behaviour of SiCp reinforced Zn-Mg-Cu based aluminium matrix composite. *Materials Today: Proceedings*, 4(2), 2965-2974.
- [2]. Basavarajappa, S., Chandramohan, G., & Davim, J. P. (2007). Application of Taguchi techniques to study dry sliding wear behaviour of metal matrix composites. *Materials & design*, 28(4), 1393-1398.
- [3]. Sharma, S. C. (2001). The sliding wear behavior of Al6061-garnet particulate composites. *Wear*, 249(12), 1036-1045.
- [4]. Beffort, O., Long, S., Cayron, C., Kuebler, J., & Buffat, P. A. (2007). Alloying effects on microstructure and mechanical properties of high volume fraction SiC-particle reinforced Al-MMCs made by squeeze casting infiltration. *Composites Science and Technology*, 67(3-4), 737-745.
- [5]. Suresh, R., & Kumar, M. P. (2013). Investigation of tribological behavior and its relation with processing and microstructures of Al 6061 metal matrix composites. *International Journal of Research in Engineering & Technology*, 1(2), 91-104.
- [6]. Guo, M. T., & Tsao, C. Y. (2000). Tribological behavior of self-lubricating aluminium/SiC/graphite hybrid composites synthesized by the semi-solid powder-densification method. *Composites science and technology*, 60(1), 65-74.
- [7]. Nagaral, M., Auradi, V., & Ravishankar, M. K. (2013). mechanical behaviour of aluminium 6061 alloy reinforced with Al_2O_3 & graphite particulate hybrid metal matrix composites. *International Journal of Research in Engineering & Technology (IJRET)*, 1(2), 193-198.

- [8]. Ahmed, S. S., Girisha, H. N., & Keshavamurthy, R. (2022). Impact of Hot Rolling on Mechanical Characteristics of AA7075/TiB₂/Graphite Hybrid Composites. *Journal of The Institution of Engineers (India): Series D*, 1-11.
- [9]. Ahmed, S. S., Girisha, H. N., & Keshavamurthy, R. (2022). Impact of Hot Rolling on Mechanical Characteristics of AA7075/TiB₂/Graphite Hybrid Composites. *Journal of The Institution of Engineers (India): Series D*, 1-11.
- [10]. Chandrashekhar, K. G., Girish, D. P., & Girisha, H. N. (2016). Effect of granite particulate on Tensile Properties & Hardness of Aluminium 6061 based Metal Matrix Composite.
- [11]. HN, G., & Sharma, K. V. Effect of magnesium on strength and microstructure of Aluminium Copper Magnesium Alloy.
- [12]. Talikoti, B. H., & Girisha, H. N. Assessment of UTS and Yield Strength of Aluminium 6061 alloy-based Metal Matrix Composites.
- [13]. HN, G., & SHARMA, K. INFLUENCE OF PROCESS PARAMETERS ON THE MECHANICAL PROPERTIES OF HEAT-TREATED ALUMINIUM COPPER MAGNESIUM ALLOY.
- [14]. Talikoti, B. H., Girisha, H. N., & Bharath, L. (2021). Validation of hardness and tensile strength of Al-Mg alloy reinforced with silicon carbide and graphite hybrid composite by regression equation. *Materials Today: Proceedings*.
- [15]. Ramesh, C. S., & Safiulla, M. (2007). Wear behavior of hot extruded Al6061 based composites. *Wear*, 263(1-6), 629-635.
- [16]. Ezatpour, H. R., Sajjadi, S. A., Sabzevar, M. H., & Huang, Y. (2014). Investigation of microstructure and mechanical properties of Al6061-nanocomposite fabricated by stir casting. *Materials & Design*, 55, 921-928.



Study of Mechanical Properties of Aluminium 7075 Alloy Reinforced with Cenosphere and E-Glass Fibres

Sunitha.V¹, Girisha H N¹, Dr. Girish D P², Suhael Ahmed S³

¹Department of Mechanical & Smart Manufacturing Engineering, Government Engineering College, Ramanagar-562159, Karnataka, India.

²Department of Mechanical Engineering, Government Engineering College, Mosalehosahally, Hassan, Karnataka, India

³Department of Mechanical Engineering, Government Engineering College, K R Pete, Karnataka, India

ABSTRACT

The Aluminum alloy has excellent properties such as high thermal conductivity and low density. These properties make its application wide in the field of automotive, aerospace and mineral processing industries to make their products. In spite of these properties the main drawback of aluminum alloys are low hardness and strength. To overcome this drawback, these types of alloys are reinforced with some other materials so that its hardness, Young's modulus and ultimate tensile strength and yield strength can be increased to the desired limit. In the present investigation, Al 7075 alloy as matrix cenosphere as reinforcement has been identified since it has potential applications in aircraft and space industries because of lower weight to strength ratio. Among various reinforced materials used, cenosphere (a small proportion of the pulverised fuel ash (PFA) produced from the combustion of coal in power stations) is one of the most inexpensive and low density reinforcement available in large quantities as waste product during combustion of coal in thermal power plants. Hence, composites of Al 7075 with cenosphere and e glass as reinforcement are likely to overcome the cost barrier as well as the different physical and mechanical properties for wide use in the today's world & serve a wide range of applications.

Keywords: Aluminium 7075, cenosphere, e-glass, mechanical properties.

I. INTRODUCTION

Conventional monolithic materials have limitations in achieving good combination of strength, stiffness, toughness and density. To overcome these shortcomings and to meet the ever increasing demand of modern day technology, composites are most promising materials of recent interest. Metal composites possess significantly improved properties including high specific strength, specific modulus, damping capacity, good

wear resistance and corrosion resistance compared to unreinforced alloys. There has been an increasing interest in composites containing low density and low cost reinforcements.

A composite material can be defined as a combination of a matrix and reinforcement, which when combined gives properties superior to the properties of the individual components. The constituent which Present in the greater quantity in the composite is termed as matrix. The second constituent is referred to as the reinforcing phase or reinforcement. In the present work Al7075 is used as a matrix and tungsten carbide is used as reinforcement. Olivier Beffort et al [4] alloying effects on microstructure and mechanical properties of high volume fraction SiC-particle reinforced Al-MMCs made by squeeze casting infiltration. Suresh et al [5] have observed that one of the important limitations in fabrication of aluminium matrix composites is the compatibility of reinforcement in the matrix. This is of prime importance in case of Al composites; as Al is covered with a thin layer of oxide which blocks the surface wetting and reacts with some ceramics to form inter metallic phases which tend to influence the final properties of composites. The tribological behaviour of self-lubricated aluminium/SiC/graphite hybrid composites with various amount of graphite addition synthesized by the semi-solid powder densification method [6]. In the case of particle-filled MMCs, the mechanical properties are not significantly altered, but tribological properties show marked improvements. Soft solid lubricant particles such as graphite and mica improve anticizing properties of Alalloys whereas hard particles like SiC, alumina, WC, TiC, zircon, silica, and boron Carbide greatly improves the resistance to abrasion of Al alloys. [7]

Based on the literature survey, it is observed that very minimal work was reported based upon Al7075/cenosphere/ e-glass, hence the present investigation deals is about the fabrication of Aluminium 7075, Cenosphere and E-glass fibres. Aluminium is a light metal whose alloys already are widely used in aircraft industries such as aircrafts whereas Cenosphere is a low density material with high compression strength having its application in automotive components, biomedical applications and other industrial materials. Therefore, Aluminium MMCs have the potential to further improve the application characteristics. In the present investigation, Cenosphere and E-glass fibres were dispersed in molten Al 7075, where in Cenosphere wt% and E-glass fibres wt% was varied.

II. MATERIALS, METHODS, PROCESSING AND TESTING OF COMPOSITES

The materials used for processing and development of Aluminium alloy metal matrix composite are Alumiunium 7075 alloy and their properties are shown in the Table 1.

TABLE 1 PROPERTIES OF ALUMINIUM 7075

Property	Tensile Strength (MPa)	Yield Strength (MPa)	Elongation (%)
Casting	248	138	1-3

A. Composite Preparation

The Al 7075-Cenosphere and E-Glass composite was prepared by using stir-casting technique. This approach involves mixing of the reinforcement particulate into a molten metal bath as shown in figure 1 and transferring the mixture directly into a cylindrical shaped die, as shown in Figure 2, to complete solidification. In this

technique aluminum alloy 7075 ingot pieces were heated in the furnace to its molten state and the temperature was maintained between 800-850° C. A vortex was created using a mechanical stirrer. Cenosphere and E-Glass particles were preheated in the furnace. The temperature of the furnace was maintained between 825-850° C. Preheated Cenosphere and E-Glass particles were added with different weight percentages to the melt with continuous stirring. Different weight percentage of the reinforcement is as shown in Table 1. Stirring was carried out for about 15 min after the addition of Cenosphere and E-Glass particles for uniform distribution in the melt. Castings were prepared by pouring the melt into preheated molds of cylindrical shapes as shown in Figure 3. Prepared specimens as shown in Figure 4 were tested for tensile properties & hardness characteristics and was compared with pure Al 7075.

Heat treatment:-

Heat treatment process called aging was carried out for the as processed specimens. First then specimens are subjected to solution treatment for 12 hours 530°C, then quenched in water at 80° c .Then after stabilizing for 3 hours ,the aging is carried out at 1750c for different intervals of time ranging from 1hr,3hr,5hr.



Figure 1: MMC Molten metal bath in furnace



Figure 2: Cylindrical shaped Die



Figure 3: Casting process



Figure 4: Specimen after casting

TABLE 1 PERCENTAGE COMPOSITION OF REINFORCEMENTS

Specimen No.	Al7075	CENOSPHERE	E-GLASS
1	97%	2	1
2	95%	2	3
3	93%	2	5
4	95%	4	1
5	93%	4	3
6	91%	4	5
7	93%	6	1
8	91%	6	3
9	89%	6	5

B. Testing of composites

a. BRINELL HARDNESS TEST

Brinell hardness is determined by forcing a hard steel or carbide sphere of a specified diameter under a specified load into the surface of a material and measuring the diameter of the indentation left after the test. The Brinell hardness number, or simply the Brinell number, is obtained by dividing the load used, in kilograms, by the actual surface area of the indentation, in square millimeters. The result is a pressure measurement, but the units are rarely stated.

The BHN is calculated according to the following formula:

$$BHN = \frac{F}{\frac{\pi}{2} D \cdot (D - \sqrt{D^2 - Di^2})}$$

Where

BHN = the Brinell hardness number

F = the imposed load in kg

D = the diameter of the spherical indenter in mm

Di = diameter of the resulting indenter impression in mm

b. Tensile Test

The tensile test was conducted using a computerized universal testing machine as per the ASTM E8 standard. The test uses specimens of 20 mm grip diameter, 30 mm grip length, 62.5 mm gauge length, 75 mm length of reduced cross section, inner diameter of 12.5 mm and total length 155 mm machined from the cast specimens of various compositions mentioned earlier. Tensile test helps to calculate tensile strength, yield strength, percentage of elongation. The apparatus consists of loading unit and control unit. The tensile properties of reinforce alloy were evaluated using UTM machine as per the ASTM E8 standard at Advanced Metallurgical Laboratory, Peenya, Bangalore, India. Yield strength, Ultimate tensile strength and ductility were evaluated. An average of three results was taken as strength of each material. Tensile test specimens are as shown in the figure

5



Figure 5: Tensile test specimen

III. RESULTS AND DISCUSSION

Hardness test

Brinell hardness test was conducted for different specimen and BHN is calculated as shown in the table 2. As the addition of cenosphere and E-glass reinforcement increases the hardness of aluminium 7075 alloy. Hardness of the as-cast alloy produced in this work is lower at 2% of cenosphere when compared to 4% and 6%. after heat treatment the water quenched specimens exhibit higher hardness . From the graphs drawn it is evident that hardness number increases with increased percentage of cenosphere and e glass. With increase in E glass and cenosphere in base metal 19.56% of hardness increases.

TABLE 2 BHN VALUES FOR DIFFERENT COMPOSITIONS OF COMPOSITE MATERIALS

SPECIMEN NUMBER	ALLUMINIUM7075 alloy+ CENOSPHERE+ E GLASS	Brinell Hardness Number, (As cast)	Brinell Hardness Number, (BHN) ONE HOUR HT	Brinell Hardness Number (BHN) Three HOUR HT
1	97%+2%+1%	64.85	66.89	74.10
2	95% +2%+3%	69.37	71.5	79.61
3	93% +2%+5%	70.21	72.5	75.60
4	95% +4%+1%	68.56	69.70	71.62
5	93% +4%+3%	74.10	75.6	79.5
6	91% +4%+5%	76.10	78.14	87.5
7	93%+6%+1%	70.74	71.92	76.85
8	93%+6%+3%	78.62	73.92	79.61
9	89% +6%+5	87.95	89.62	96.53

Figure 6-10 shows the graph of variation of hardness with respect to different reinforcement with varied weight percentage

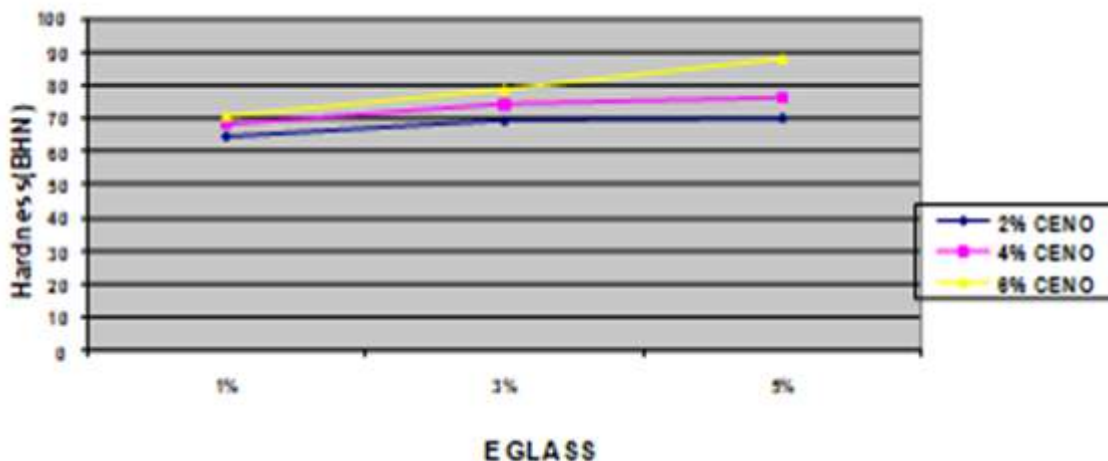


Figure 6: Variation of hardness with respect to E GLASS for as cast specimens

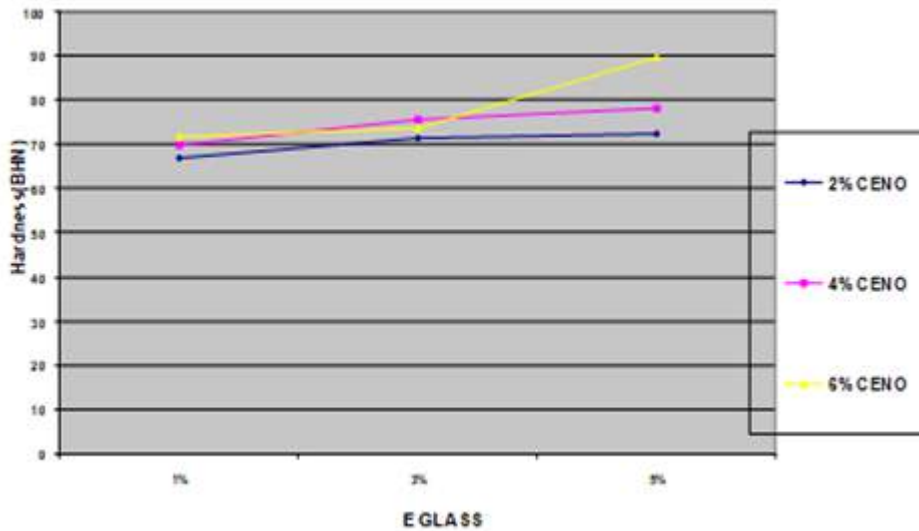


Figure 7 Variation of BHN with respect to E GLASS for ONE HOUR heat treated specimens

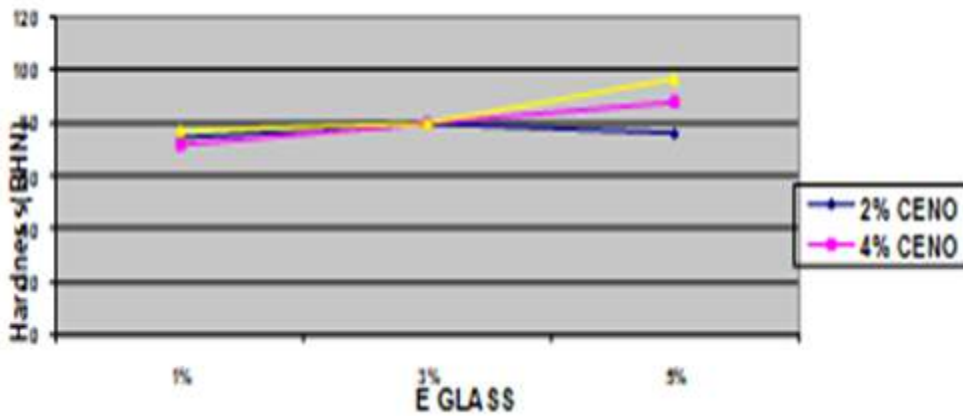


Figure 8 variation of BHN with respect to E GLASS for three HOUR heat treated specimens

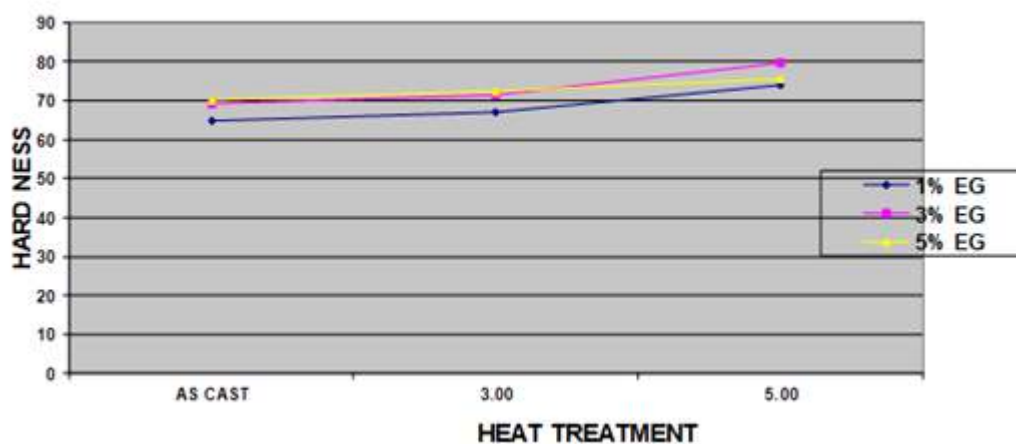


Figure 9 variation of BHN with respect to HEAT TREATMENT 2% ceno constant

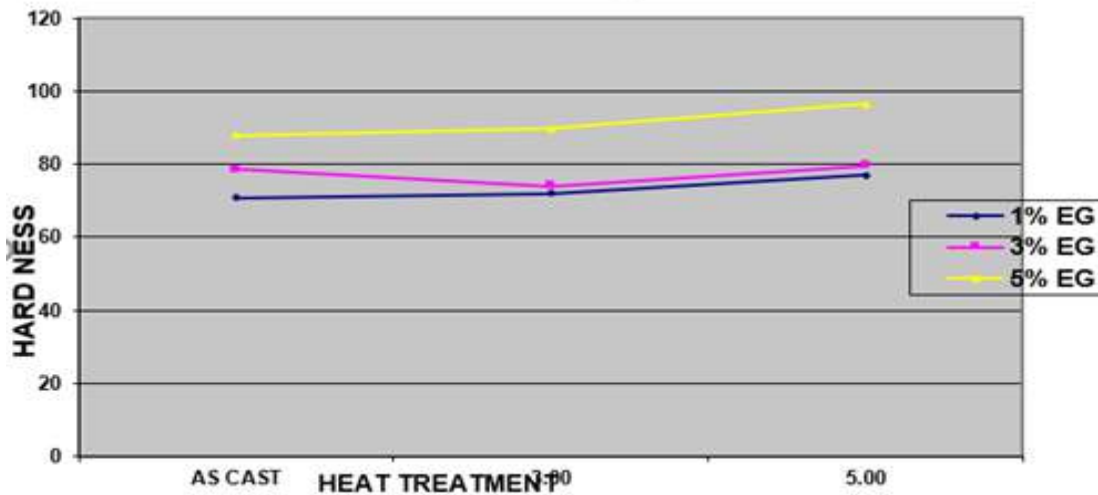


Figure 10 variation of BHN with respect to HEAT TREATMENT 6% cenosphere constant

TENSILE TEST:

Tensile test was conducted for different specimen and percentage elongation is calculated as shown in the table 3

There is a predominant decrease of ductility (% of elongation) of aluminium 7075 alloy, due to the addition of mica and E-glass reinforcement.

With increase in e glass and cenosphere in base metal 34 % of hardness increases.

Figure 11-13 show the graph of percentage elongation of different composition.

TABLE 3 PERCENTAGE ELONGATION FOR DIFFERENT COMPOSITION OF REINFORCEMENTS

SPECIMEN NUMBER	ALLUMINIUM+ CENOSPHERE+ E GLASS	0 HOUR (As cast) , %	ONE HOUR HT, %	Three HOUR HT , %
1	97+2+1	14.64	12.2	10.2
2	95 +2+3	8.34	7.4	7.2
3	93 +2+5	4.78	5.2	4.9
4	95 +4+1	15.02	14.2	12.2
5	93 +4+3	8.78	7.9	7.1
6	91 +4+5	6.44	5.7	4.8
7	93+6+1	10.34	9.7	8.9
8	93+6+3	7.4	5.3	5
9	89 +6+5	6.48	4.9	4.9

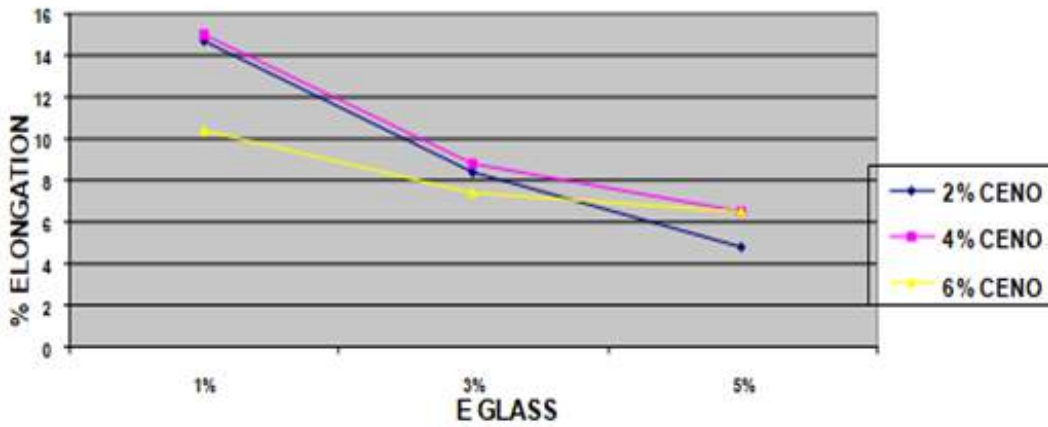


Figure 11 variation of % ELONGATION with respect to E GLASS for AS CASTspecimens

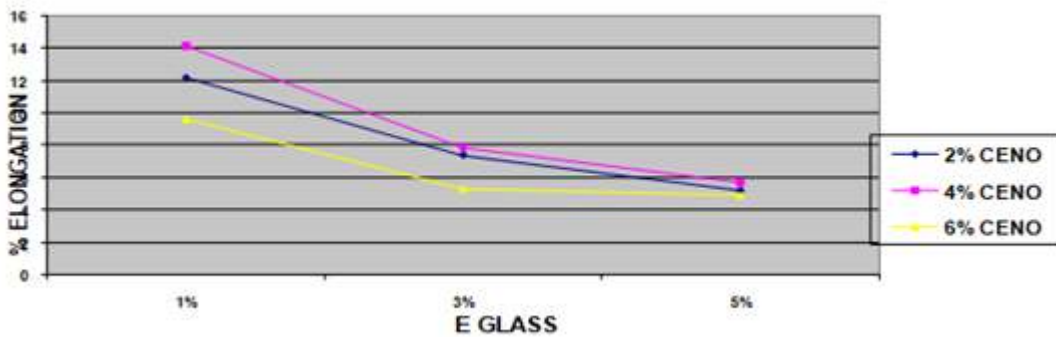


Figure 12 variation of % ELONGATION with respect to E GLASS for ONE HOUR HEAT TREATED specimens

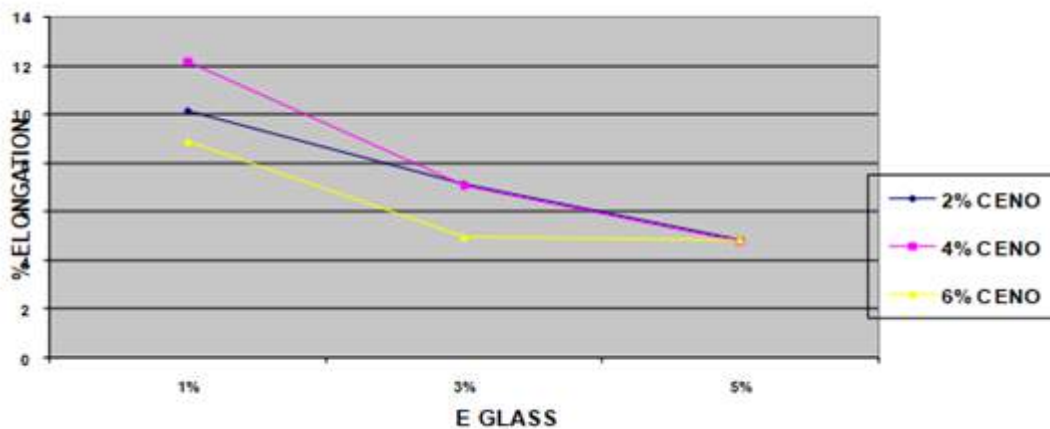


Figure 13 variation of % ELONGATION with respect to E GLASS for THREE HOUR HEAT TREATED specimens

IV. CONCLUSION

The present investigation on the effect of CENOSPHERE and E-glass reinforcements with Al-7075 metal matrix composites are led to the following conclusions

- As the addition of CENOSPHERE and E-glass reinforcement increases the UTS of aluminium 7075 alloy.
- As the addition of CENOSPHERE and E-glass reinforcement in aluminium 7075 alloy, there increase hardness, due to the presence of silica content in both reinforcement. The tensile strength (UTS) has increased in heat treated condition

V. REFERENCES

- [1]. Das, D., Pattanaik, S., Routara, B. C., Mishra, P. C., & Samal, C. (2017). Dry sliding wear behaviour of SiCp reinforced Zn-Mg-Cu based aluminium matrix composite. *Materials Today: Proceedings*, 4(2), 2965-2974.
- [2]. Basavarajappa, S., Chandramohan, G., & Davim, J. P. (2007). Application of Taguchi techniques to study dry sliding wear behaviour of metal matrix composites. *Materials & design*, 28(4), 1393-1398.
- [3]. Sharma, S. C. (2001). The sliding wear behavior of Al6061–garnet particulate composites. *Wear*, 249(12), 1036-1045.
- [4]. Beffort, O., Long, S., Cayron, C., Kuebler, J., & Buffat, P. A. (2007). Alloying effects on microstructure and mechanical properties of high volume fraction SiC-particle reinforced Al-MMCs made by squeeze casting infiltration. *Composites Science and Technology*, 67(3-4), 737-745.
- [5]. Suresh, R., & Kumar, M. P. (2013). Investigation of tribological behavior and its relation with processing and microstructures of Al 6061 metal matrix composites. *International Journal of Research in Engineering & Technology*, 1(2), 91-104.
- [6]. Guo, M. T., & Tsao, C. Y. (2000). Tribological behavior of self-lubricating aluminium/SiC/graphite hybrid composites synthesized by the semi-solid powder-densification method. *Composites science and technology*, 60(1), 65-74.
- [7]. Nagaral, M., Auradi, V., & Ravishankar, M. K. (2013). mechanical behaviour of aluminium 6061 alloy reinforced with al₂o₃ & graphite particulate hybrid metal matrix composites. *International Journal of Research in Engineering & Technology (IJRET)*, 1(2), 193-198.
- [8]. Ahmed, S. S., Girisha, H. N., & Keshavamurthy, R. (2022). Impact of Hot Rolling on Mechanical Characteristics of AA7075/TiB₂/Graphite Hybrid Composites. *Journal of The Institution of Engineers (India): Series D*, 1-11.
- [9]. Ahmed, S. S., Girisha, H. N., & Keshavamurthy, R. (2022). Impact of Hot Rolling on Mechanical Characteristics of AA7075/TiB₂/Graphite Hybrid Composites. *Journal of The Institution of Engineers (India): Series D*, 1-11.
- [10]. Chandrashekhar, K. G., Girish, D. P., & Girisha, H. N. (2016). Effect of granite particulate on Tensile Properties & Hardness of Aluminium 6061 based Metal Matrix Composite.
- [11]. HN, G., & Sharma, K. V. Effect of magnesium on strength and microstructure of Aluminium Copper Magnesium Alloy.

- [12]. Talikoti, B. H., & Girisha, H. N. Assessment of UTS and Yield Strength of Aluminium 6061 alloy-based Metal Matrix Composites.
- [13]. HN, G., & SHARMA, K. INFLUENCE OF PROCESS PARAMETERS ON THE MECHANICAL PROPERTIES OF HEAT-TREATED ALUMINIUM COPPER MAGNESIUM ALLOY.
- [14]. Talikoti, B. H., Girisha, H. N., & Bharath, L. (2021). Validation of hardness and tensile strength of Al-Mg alloy reinforced with silicon carbide and graphite hybrid composite by regression equation. *Materials Today: Proceedings*.
- [15]. Ramesh, C. S., & Safiulla, M. (2007). Wear behavior of hot extruded Al6061 based composites. *Wear*, 263(1-6), 629-635.
- [16]. Ezatpour, H. R., Sajjadi, S. A., Sabzevar, M. H., & Huang, Y. (2014). Investigation of microstructure and mechanical properties of Al6061-nanocomposite fabricated by stir casting. *Materials & Design*, 55, 921-928.



Numerical Study of Heat Flux Variation Around A Re-Entry Module at High Altitude

K. S. Santhosh^{1*}, Siddharth G²

¹Assistant Professor, Department of Mechanical Engineering, College of Engineering Trivandrum, Kerala, India

²PG Student, Department of Mechanical Engineering, College of Engineering Trivandrum, Kerala, India

ABSTRACT

A finite volume based on unstructured cell-centered Navier - Stokes solver is used to predict the heat flux variations for a scaled version of a typical re-entry module at various altitudes. The solver is validated with available experimental data and then used to predict heat flow for a typical re-entry module at various operational altitudes. The predicted heat flux is compared to the measured data

Keywords : CFD, Re-Entry, Heat Flux.

I. INTRODUCTION

During atmospheric-entry maneuvers, re-entry modules experience high thermal loads due to the shock-heated gases around the vehicle. The heat transfer to the vehicle surface comes from frictional convective heating, catalytic effects, ablation, and radiative heating. The convective heating is due to the flow past the blunt-body and scales with the nose radius, R , as $1/\sqrt{R}$, i.e. as the nose radius decreases, the heating becomes more severe. Hence re-entry modules are designed with blunted configuration (larger radius), particularly for those vehicles subject to severe convective loads. Given the mass constraints in the design of an atmospheric-entry module, there is strong demand for an optimal heat shield design, thick enough to protect the payload during descent. An optimal heat shield design relies on accurate estimates for the heating rates and heating loads during atmospheric entry. Analytical tools make oversimplifying assumptions and can be used only for simple geometries. Hence it can be used only for the preliminary phase of simple geometries. The Fay and Riddell [1] correlation, for instance, can be used to estimate convective heat transfer at a blunt body's stagnation point. Experiments are accurate but difficult[2]. In this paper, the results of CFD simulations of a re-entry module are presented.

II. GOVERNING EQUATIONS

The governing equations corresponding to two- dimensional/axisymmetric laminar flow are shown below.

$$\frac{\partial U}{\partial t} + \frac{\partial F}{\partial x} + \frac{1}{r^m} \frac{\partial (r^m G)}{\partial y} = S \quad (1)$$

By choosing proper values for m (0,1) the problem can be 2-D or axisymmetric problems. m=1 and for 2-D problems.

$$U = \begin{bmatrix} \rho \\ \rho u \\ \rho v \\ \rho E \end{bmatrix} \quad F = \begin{bmatrix} \rho u \\ \rho u^2 + \sigma_{xx} \\ \rho uv + \sigma_{xy} \\ (\rho E + p)u - \left(u\sigma_{xx} + v\sigma_{xy} + K_{eff} \frac{\partial T}{\partial x} \right) \end{bmatrix}$$

$$G = \begin{bmatrix} \rho v \\ \rho uv + \sigma_{yx} \\ \rho v^2 + \sigma_{yy} \\ (\rho E + p)v - \left(u\sigma_{xy} + v\sigma_{yy} + K_{eff} \frac{\partial T}{\partial y} \right) \end{bmatrix} \quad S = \begin{bmatrix} 0 \\ 0 \\ m(p + \sigma_{\theta\theta}) \\ 0 \end{bmatrix}$$

III. NUMERICAL METHOD

The discretization of governing equations using cell centered schemes and the procedure is given below [7]

$$\frac{\partial U}{\partial t} + \nabla \cdot H - S = 0 \quad (2)$$

$$\int_{\Omega} \left(\frac{\partial U}{\partial t} + \nabla \cdot H - S \right) = 0 \quad (3)$$

$$\int_{\Omega} \frac{\partial U}{\partial t} d\Omega + \int_{\Omega} \nabla \cdot H d\Omega - \int_{\Omega} S d\Omega = 0 \quad (4)$$

$$\int_{\Omega} \frac{\partial U}{\partial t} d\Omega + \int_{\Gamma} H \cdot nd\Gamma - \int_{\Omega} S d\Omega = 0 \quad (5)$$

$$\frac{dU_i}{dt} V_i + \sum_{faces} H ds - S_i V_i = 0 \quad (6)$$

Runge- Kutta method is used for time integration.

$$U_i^{(0)} = U_i^{(n)}$$

$$U_i^{(1)} = U_i^{(0)} - \alpha \frac{\Delta t}{V_i} (R_i^{(0)})$$

$$U_i^{(2)} = U_i^{(0)} - \alpha \frac{\Delta t}{V_i} (R_i^{(1)})$$

$$U_i^{(3)} = U_i^{(0)} - \alpha \frac{\Delta t}{V_i} (R_i^{(2)})$$

$$U_i^{n+1} = U_i^n + U_i^{(3)} \quad (7)$$

$\alpha_1 = 0.6$, $\alpha_2 = 0.6$ and $\alpha_3 = 1.0$ are the coefficients used in the Runge-Kutta integration. The stability criterion is as follows

$$\Delta t_i \leq \left(\frac{\Delta l_i}{q_i + c_i} \right) \quad (8)$$

$$q_i = \sqrt{u_i^2 + v_i^2}$$

$$c = \sqrt{\gamma RT} \quad (9)$$

As a result, the explicit solution time step can now be expressed as:

$$\Delta t_i = CFL \times \left(\frac{\Delta l_i}{q_i + c_i} \right) \quad (10)$$

Flux evaluations are based on [5,6].

IV. RESULTS AND DISCUSSIONS

A. Blunted cone-flare in hypersonic flow

Flow field around a blunted cone-flare is of particular interest since it features most of the aspects of the hypersonic flow around re-entry vehicles. The region between the cone and the flare is critical with respect to the evaluation of the surface heat flux. Flow separation is induced by the shock wave-boundary layer interactions with subsequent flow reattachment that can dramatically enhance the surface heat transfer. The experiment was carried out in H3 hypersonic wind tunnel and the chamber conditions ensure that the flow is purely laminar. Air at 580 K and 10 bar is passed through an axisymmetric nozzle where it expands to a nominal Mach number of 6 and enters the test section. This results in free stream values of $P_\infty = 673.67$ Pa, $T_\infty = 67$ K and $M_\infty = 6$ which were set as inlet conditions for our numerical model. At the solid wall adiabatic no slip conditions were imposed ($u=v=0$). The geometry and boundary conditions for the blunted cone-flare are shown in Fig. 1

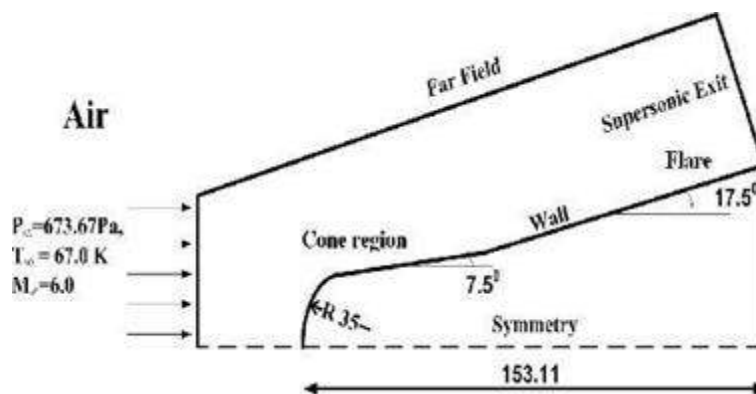


Figure 1 Validation geometry.

Numerical results of pressure and temperature variation have been shown in Figure 2 and Figure 3. Flow field separation has also been highlighted. This separation occurs at the cone-flare junction where the Mach number drops to 0.

The pressure variation occurs from 0.002 to 0.03MPa and the temperature variation occurs from 100 to 500K. Vector plot is shown in Figure 4. Validation of heat flux with experimental data is given in Figure 5.



Figure 2 Variation of Pressure

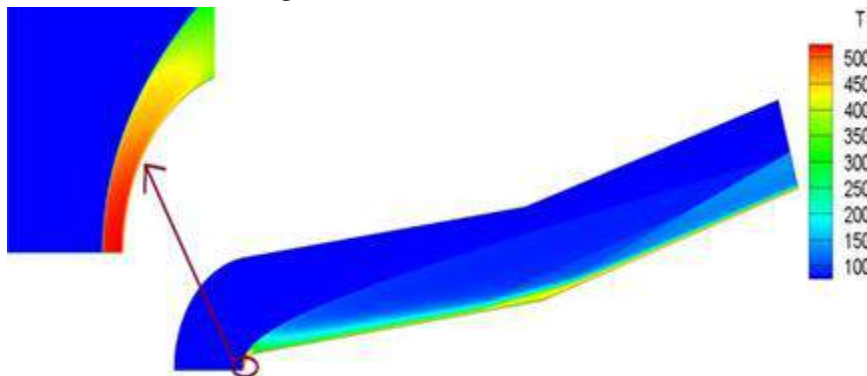


Figure 3 Variation of Temperature

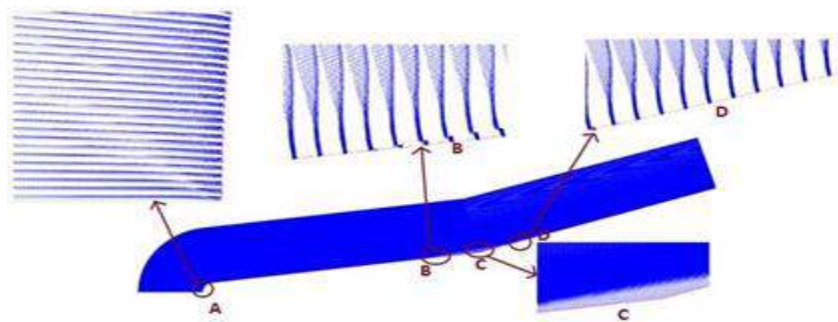


Figure 4 Vector plot

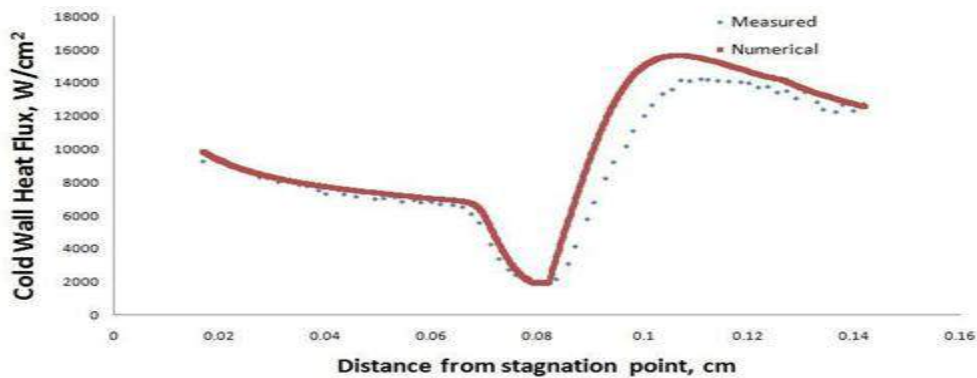


Figure 5 Validation of of heat flux with experimental data

B. Aerodynamic Heating Reduction due to Opposing Flow

Next, we consider numerical simulation of counter flow cooling for a reentry module. This simulation has been carried out for a simple axisymmetric re-entry module with and without counter flow cooling. The schematic diagram of a typical re-entry configuration and supersonic flow fields with opposing jet injected at the nose of a blunt body is shown in Fig. 6 and 7.

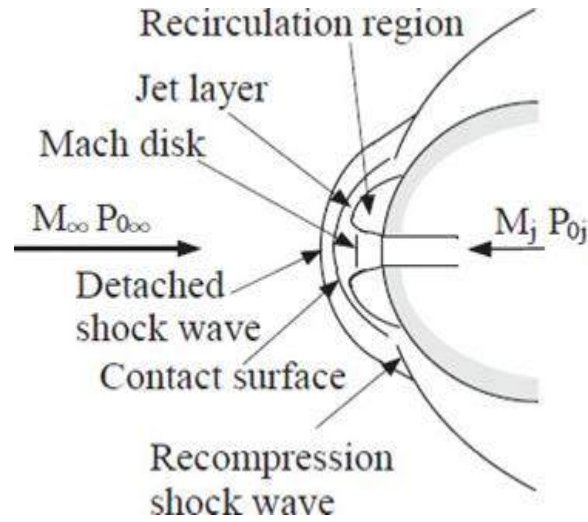


Figure 6 Schematic of counter flow

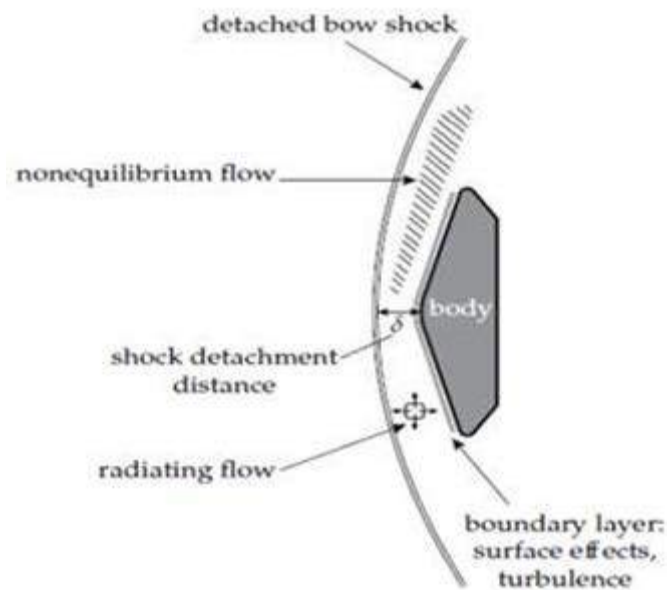


Figure 7 Schematic of re-entry vehicle.

Numerous researches on counter flow jet have been conducted in order to discover the pattern of flow. While considering counter flow jet in a supersonic flow, complexity arises, because of bow shock, contact surface of main flow and opposing jet, Mach disk, re-circulation region and re-compressed shock wave. Secondly, self-induced oscillations occur due to interaction between supersonic opposing jet and supersonic free stream in the supersonic free stream.

Our model is characterized by a spherical body of radius 25, on the end of a cylinder. Coolant is housed in a smaller cylinder of 11 mm diameter and is ejected out through a 4 mm nozzle at a pressure of 0.37 MPa and temperature of 300K under conditions of Mach number 1. The computational domain has been represented in figure 8

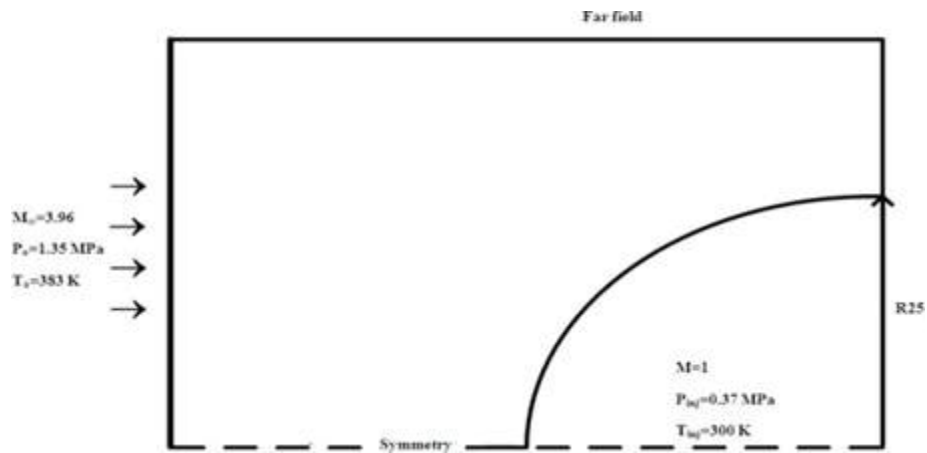


Figure 8 Test conditions and computational domain (All dimensions in mm)

Temperature variation

As seen clearly in below images, heat flux at stagnation point is at its peak in the case when there is no counter flow injection. But in the second image, where coolant injection takes place, we find that the temperature in the regions of stagnation point lies between 180K and 260K which is considerably lower than 360K. (Fig 9 (a,b))

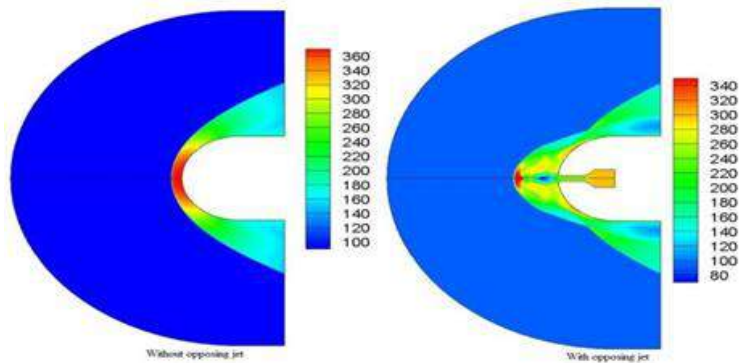


Figure 9 (a) Temperature variations in without and with counter flow cases

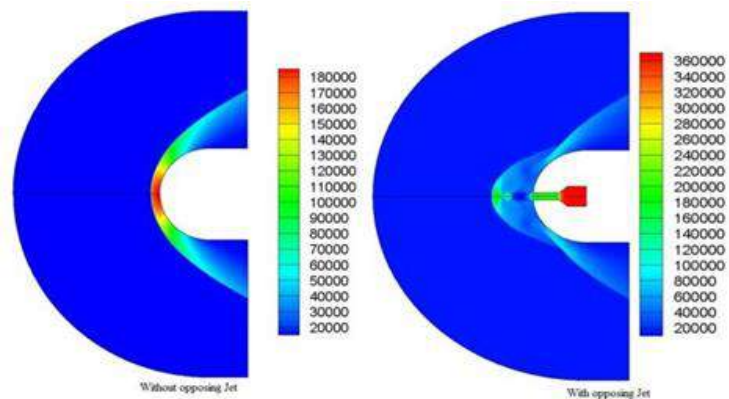


Figure 9(b) Pressure variation in without and with counter flow cases.

Pressure variation

In figure 10 and 11 normalized pressure along the surface of the blunt body is plotted and compared with experimental results of Azo’s work for without counter flow and with counter flow cases. It can be seen that for both the cases the numerical results agree very well with the experimental data. We can also observe that pressures are lower than when coolant is not used. This is an indication of effectiveness of counter flow coolant injection.

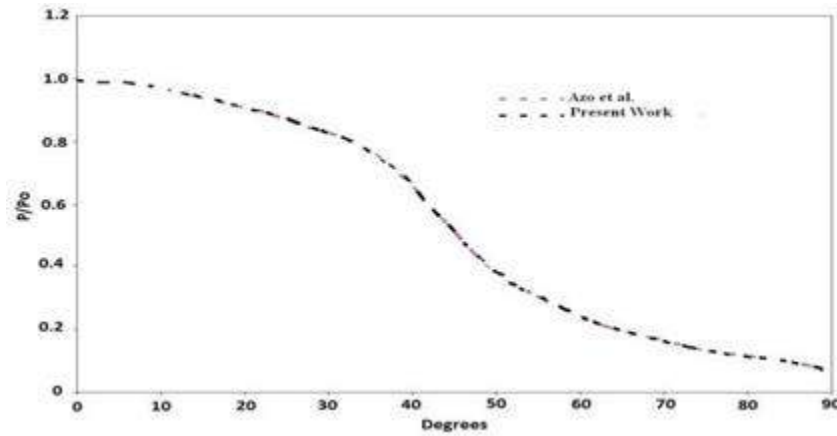


Figure 10 Pressure vs angular variation from stagnation point (Without Counter Flow)

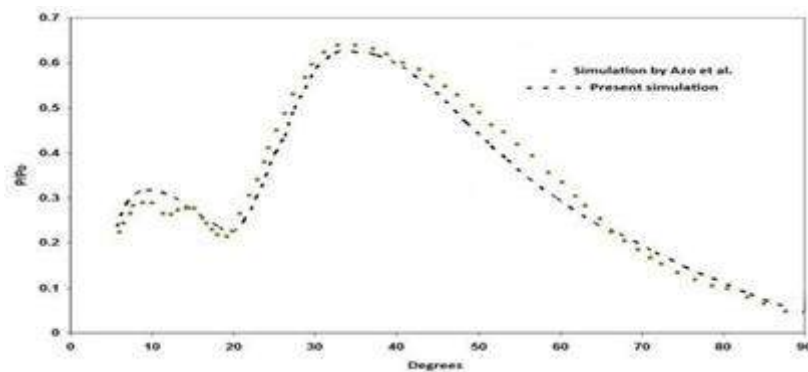


Figure 11 Pressure vs angular variation from stagnation point (With Counter Flow)

Mach number Variation

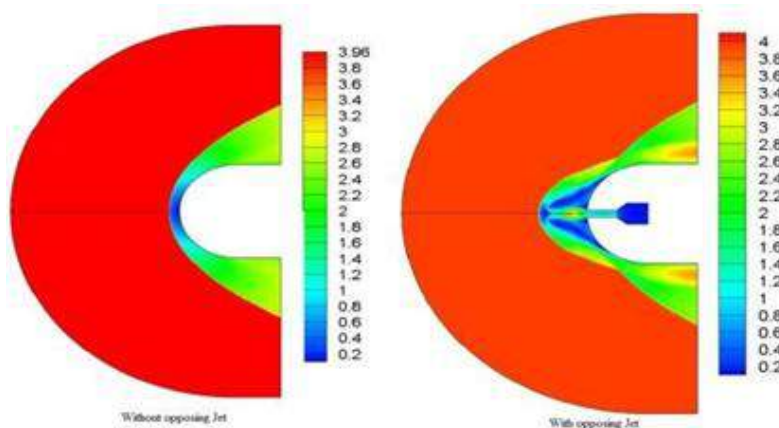


Figure 12 Mach number variation in without and with counter flow cases.

While coolant is injected at Mach no of 1, Mach no at infinity is taken as 3.96. We get to see how Mach no varies from 0 at stagnation point to 3.96 when there is no coolant. However, when a counter flow coolant is used, there is significant variation in Mach no compared to the former case.

Coolant at sonic velocity is injected through nose of the body in direction opposite to that of flow, following which the flow increases to Mach 2 while being enveloped in a region of lower Mach No. Further, the entire variation is covered in a region where Mach no is 2 to 3. This region penetrates more into the infinity region where Mach No. is 3.96.

C. Simulation of flow over re-entry module

Flow over re-entry modules are similar to supersonic flows over blunt bodies carrying some additional complexities such as reaction chemistry, flow turbulence, ablation, shock-shock interaction, entropy layer and viscous interactions, etc. Some prominent features of flow includes bow shock, flow expansion at the corners, shear layer and recirculation bubble. Detached bow shock formed ahead of the forebody decelerates the flow to a subsonic Mach number and causes sudden rise of temperature at the shock. Flow expansion around the shoulder accelerates the gas to supersonic Mach numbers. As the Mach number increases, the shock comes closer to the vehicle body and can interact with the boundary layer. High temperature prevails in the hypersonic boundary layer due to viscous dissipation, which transfers the kinetic energy of the fluid to thermal energy.

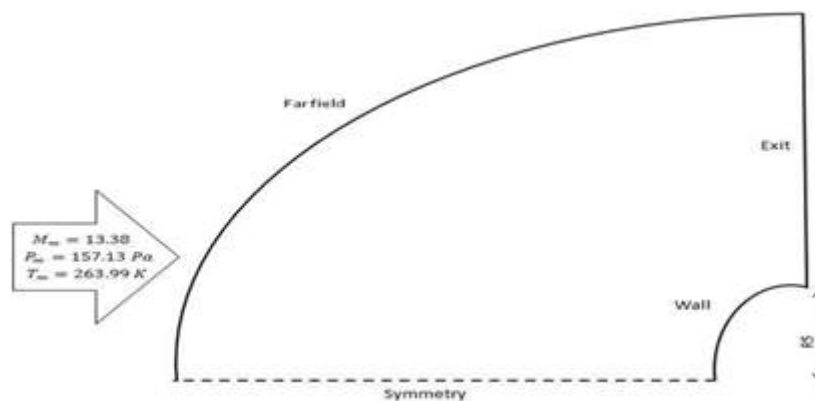


Figure 13 Computational domain (All dimensions in mm).

Boundary conditions

Supersonic inflow: Flow enters the computational domain through left boundary in the form of a supersonic jet. Static pressure P_∞ , static temperature T_∞ and free stream Mach number M_∞ were specified at this boundary.

No slip conditions: $u=v=0$ and are used at solid wall.

Isothermal wall temperature of 300K is specified on the wall.

Far field: Flow in this boundary is generally supersonic outflow and the properties (static pressure, static temperature and velocities) are linearly interpolated at the exit nodes.

Symmetry: All simulations were carried out using axisymmetric flow assumptions. Axisymmetric boundary condition can be expressed as $u=0$ and $v=0$ on the symmetry axis.

The data corresponding to various altitude through which re- entry vehicle travelling is given as the input to the code. Figure 14 (a-c) represents the Mach contours in front the vehicle while the vehicle is travelling at various speed.

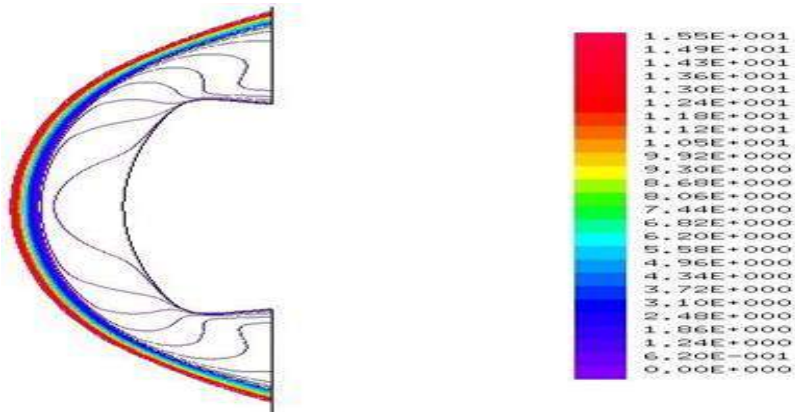


Figure 14(a) Mach contour at altitude 57.65 km Mach No.15.5

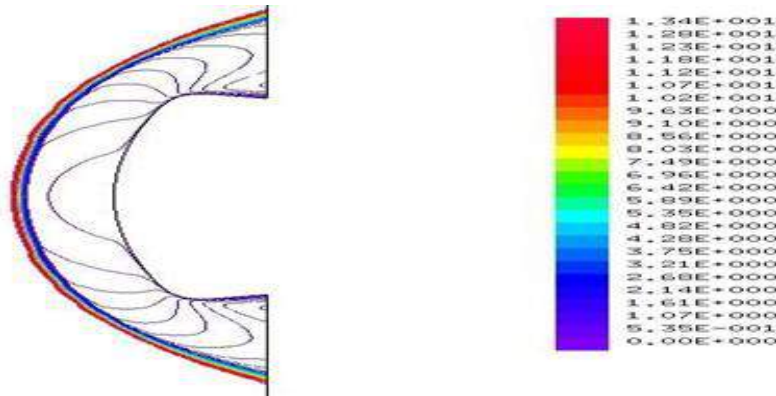


Figure 14(b) Mach contour at altitude 45.32 km Time 505s Mach No.13.38

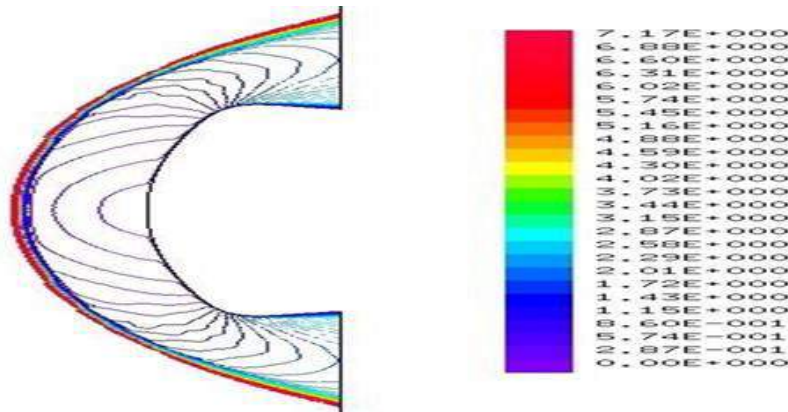


Figure 14(c) Mach contour at altitude 37.71 km Time 525s Mach No.7.17

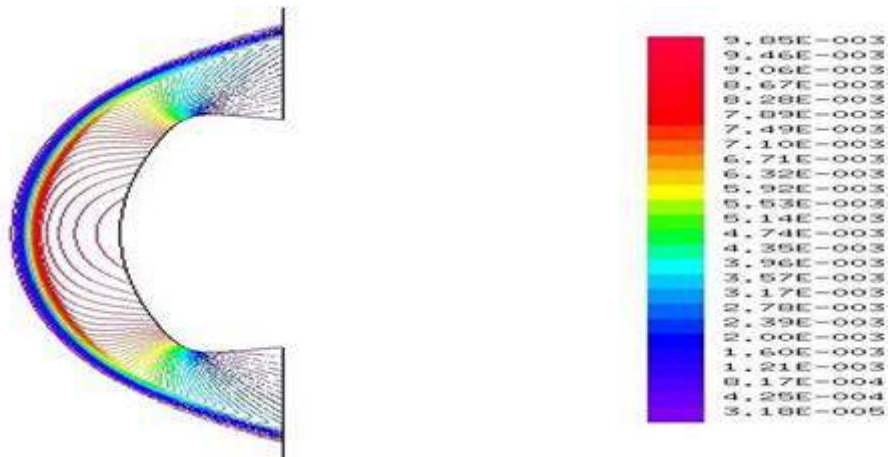


Figure 15(a) Pressure at altitude 57.65 km Mach No.15.5

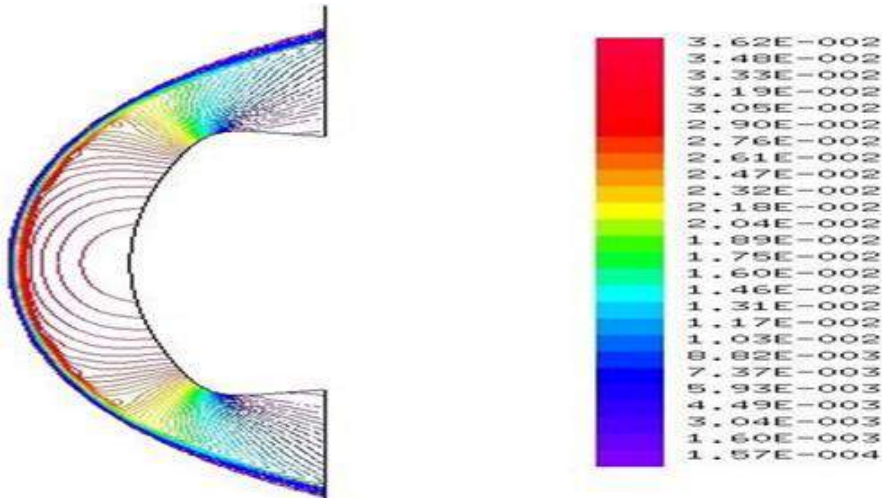


Figure 15(b) Pressure at altitude 45.32 km Mach No.13.38

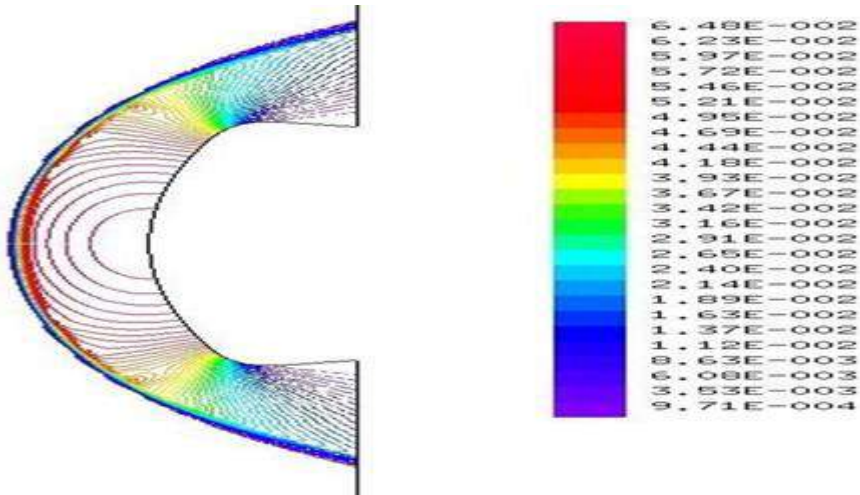


Figure 15(c) Pressure at altitude 37.71 km Mach No.7.17

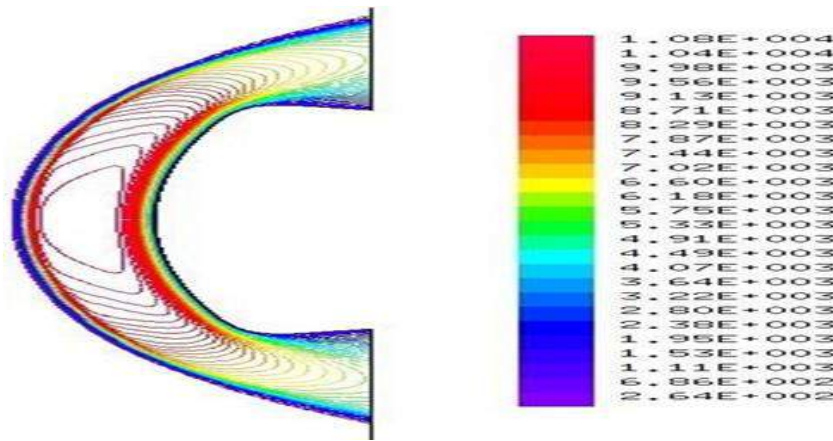


Figure 16(a) Temperature at altitude 49.4 km Time 500s Mach No.14.18

The Mach number corresponding to the vehicle speed is ranging from $M = 15.5$ to 7.17 . The vehicle is descending from an altitude 57.65 km to 37.31 km. The corresponding pressure distribution is given in Fig (15 a-c). The temperature distribution at two altitude is given in Fig 16 (a-b). The temperature distribution corresponds to 49.4 km altitude and 45.32 km respectively.

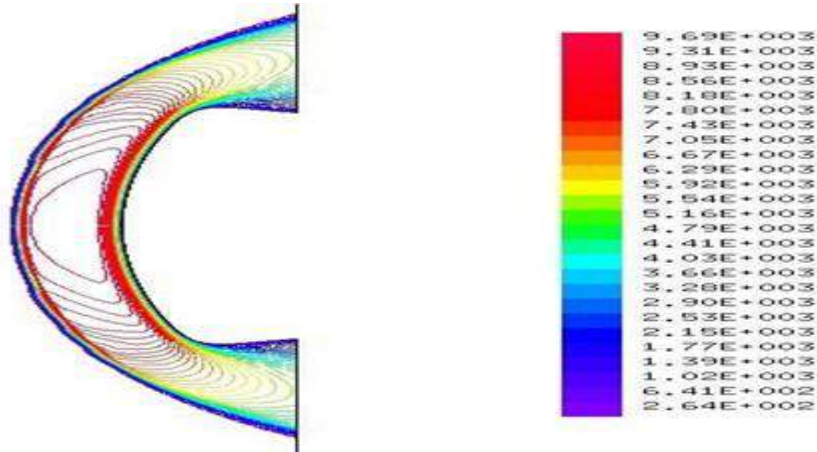


Figure 16(b) Temperature at altitude 45.32 km Time 505s Mach No.13.38

V. CONCLUSION

The finite volume solver is used to hypersonic flows after validating few test cases. Thereafter, a series of numerical experiments are carried out for flow past a scaled version of a typical re-entry module. The heat flux distribution for a range of operating conditions obtained using numerical computations matches well with the trend shown by measured values. A slightly higher value in heat flux is observed near shoulder region of the module in comparison to the stagnation region indicating that a slight transition may occur in this region. A more detailed analysis in this region may help to identify the real cause of the discrepancy. It is also observed in the numerical experiments that the first order and second order reconstruction schemes generates almost identical results as grid cell size decreases implying a decline in the influence of higher order reconstruction schemes on simulated results with refinement of grid cell size.

VI. REFERENCES

- [1]. Fay, J.A., and Riddell, F.R., "Theory of Stagnation Point Heat Transfer in Dissociated Air," *Journal of the Aeronautical Sciences*, Vol. 25, No. 2, February 1958, pp. 73-85.
- [2]. Bertin, J. J., Cummings, R. M., "Critical hypersonic aerothermodynamics phenomena.," *Annual Review of Fluid Mechanics*, Vol.38, 2006, pp. 29-157.
- [3]. R. Savino, D. Paterna, "Blunted cone-flare in hypersonic flow, Vol. 34, pp. 859-875, 2005.
- [4]. Goldberg U., "Hypersonic Flow Heat Transfer Prediction Using Single Equation Turbulence Models," *ASME Journal of Heat Transfer*, Vol.123, pp.65-69, 2001.
- [5]. Meng-Sing Liou "A Sequel to AUSM, Part II: AUSM+-UP for All Speeds", *Journal of Computational Physics* Vol.214, pp.137-170, 2006.
- [6]. Munikrishna N., Balakrishnan N., "On Viscous Flux Discretization Procedure for Finite Volume and Meshless Solver", Ph.D. Thesis, No. G21648, Indian Institute of Science, 2009.
- [7]. Nair P., Jayachandran T., Deepu M., Puranik B.P., Bhandarkar U.V., Numerical simulation of interaction of sonic jet with high speed flow over a blunt body using solution mapped higher order accurate AUSM+-UP based flow solver, *Journal of Applied Fluid Mechanics*, 3,1,2010,15.



Effect of Crosshead Speed on Mechanical Behavior of Bagasse Reinforced Polymer Composites

Sandesh S Nayak¹, Muniraju M², Rudresh B M³

¹Research Scholar, Department of Mechanical Engineering, GEC, Chamarajanagar, Karnataka, India

²Department of Mechanical Engineering, Government Engineering College, Chamarajanagar, Karnataka, India

³Department of Mechanical Engineering, Government Engineering College, K R Pet -571426, Karnataka, India

ABSTRACT

The effect of different cross head speed on the tensile and flexural behavior of sugarcane bagasse reinforced epoxy composites has been studied. The epoxy based composites with 5 wt. % varying reinforcement (5, 10 and 15) was developed using hand layup technique. The tensile behavior of these composites has been studied using different cross head speed (5, 25 and 50 mm/min) as per ASTM D3039 method. The flexural behavior of same composites has been reported using different cross head speeds (1, 1.5 and 2 mm/min) as per ASTM D790 method. It is observed from the experimented results that mechanical behavior is a function of cross head speeds. The tensile strength and the flexural strength have been improved with increase in cross head speed. This may be due to uniform stress distribution across the matrix – fiber interface and also the compatibility between both matrix and fiber. Further, higher reinforcement of bagasse fiber results in decrease of tensile strength but significant increase in flexural strength of composites. This may be due to generation of voids and non-resin section due to improper impregnation of fiber and matrix. The ductility of composites also followed the same trend as that of strength behavior.

Keywords: Polymer composite, Sugarcane Bagasse, Crosshead Speed, Tensile and Flexural Strength

I. INTRODUCTION

Engineers have access to at least 50,000 different materials. Rather than being lost by the opponent, a specific kind of welded commercial ship suffered huge losses during World War II because the steel and, in particular, the welds were not fracture resistant enough [1]. Engineers now have access to a wide variety of materials, including thousands. Timber, stone and clay goods, cast iron and copper alloys are just a few of the materials that have been used in building for ages. While high-temperature super alloys, industrial ceramics, and fiber-reinforced composites have been around for decades, other materials with great potential for use are still in the research and development stages, such as new alloy compositions, new polymers, metallic glasses, and metal-matrix composites. In addition to the development of new and better materials, casting, new moulding processes for polymers, ceramics, and composites, and novel joining technologies have been developed [2].

Research into natural fibre reinforced polymer composites as a low-cost alternative to synthetic fibre reinforced composites is being spurred on by a growing global concern for the environment. Jute, Sisal, Coir, Pineapple, Bamboo, Ramie, and Banana are just few of the natural fibres available in abundance in India, which has fueled the creation of natural fibre and particle composites. Such natural fibre and particle composites are ideal for use as wood alternatives in the housing and construction industries. For the development of natural fibre and particle composites in India, it is important to ensure that forest resources do not become depleted and that the cultivation of natural fibres is financially rewarding [3]. In terms of mechanical, thermal, and acoustic characteristics, natural fibres may compete with manufactured glass fibres. The biodegradability and recyclability of natural fibres makes them ideal for circular economy and sustainable development [4]. They are also environmentally beneficial. Due to their low cost of production and the fact that they are gentle on mixing and moulding equipment, natural fibres are a promising alternative to synthetics. Natural fibres have so many advantages that they may be employed in a wide range of industries, including construction, automobile, home appliances, and more.

II. LITERATURE REVIEW

In fiber-reinforced plastics, reinforcing materials including glass, carbon, Kevlar, and boron fibres have been extensively acknowledged as materials for structural and nonstructural uses [5]. These materials, on the other hand, are difficult to degrade and pose environmental concerns. It is well known that natural fibres from plants like jute, bamboo and coir may be used in many applications that need a high degree of weight bearing capacity. Biodegradability and plenty of supply are two of the advantages of using natural fibres over synthetic fibres. Natural fibres, on the other hand, are hydrophilic in nature and have a high moisture content, which makes the fiber-to-hydrophobic matrix interaction difficult. The interface of natural fibre composites may be improved using a variety of treatment approaches [6]. In fact, these fibres are already being employed in the automobile sector in place of glass and carbon in places where mechanical characteristics and weight are important trade-offs. VP Arthanarieswaran and his colleagues [7] studied the mechanical characteristics of epoxy composites using banana and sisal fibre. In their research, the mechanical characteristics of glass-banana, sisal, and glass-banana-sisal hybrids were examined. The tensile strength may be increased by a factor of 2.34 and 4.13 if two and three layers of glass fibre are added. Flexural characteristics on banana-sisal fibre were improved by using two glass fibres instead of three, and the laminate with sisal and three glass ply provides greater impact strength. Sugarcane bagasse fibres were employed by RupaPatil et colleagues [8] to create a polymer matrix composite and test its mechanical properties under external stresses. Sugarcane bagasse volume fraction ratio was researched by authors to illustrate the influence of fibre volume on the mechanical characteristics of composites and to examine the feasibility of processing this agro-residue with thermoplastics. Carbon nanotube (CNT) incorporation in glass fibre reinforced polymer (GFRP) composites was explored by K K Mahato et al [9]. Crosshead speeds of 1, 10, and 100 mm/min were used to evaluate the control GFRP composites and CNT-modified composites. Multi-walled carbon nanotube (MWCNT) was used as a filler with various MWCNT content in the CNT modified matrix (i.e. 0.1, 0.3 and 0.5 wt. percent). In comparison to the GFRP composite, the tensile strength increased for all crosshead speeds when the CNT content was increased by up to 0.3 percent.

According to the results, adding 0.1% CNT and 0.3% CNT increased the tensile strength of the composite by 6.11 percent and 9.28 percent correspondingly. The tensile modulus of GFRP composites with an optimal CNT content is shown to be largely impacted. Using polypropylene as the matrix and rice-husk flour as the reinforcing filler, Han-Seung Yang et al [10] prepared a particle-reinforced composite to test the physical, mechanical, and morphological properties of the composite in relation to filler loading in the thermoplastic polymer composite. Test temperatures ranged from -30 to 110°C and crosshead speeds ranged from 2 to 1500 millimetres per second in the tensile test. Filler loading enhanced the tensile strength of the composites. Increased filler loading resulted in an increase in tensile modulus. At greater crosshead speeds, the composite became brittle, and plastic deformation was seen as the test temperature rose. Multi-wall carbon nanotubes (CNTs) were incorporated into epoxy resin in the present experimental work to increase tensile strength above standard glass fibre reinforced plastics. There were three distinct crosshead speeds and three different levels of modification for the epoxy of Sugarcane Bagasse (SCB) composite in this investigation. Laminate fabrications were made. SCB composite's tensile and flexural strengths are also examined.

III. MATERIALS SELECTION

The present experimental work included the manufacture of SCB composites and the use of an epoxy resin based on Diglycidyl Ether of Bisphenol A (DGEBA) as matrix. The hardener NNO-bis (2aminoethyl ethane-1,2diamin) was employed in conjunction with the epoxy HY 951. Fresh bagasse fibres are procured from Sakti Sugar Industries in Mandya. Yuje Enterprises, Bengaluru, provided the epoxy resin and hardener under the trade names Lapox L-12 and K-6, respectively. The epoxy to hardener weight ratio was set at 10:1, as advised by the supplier.

IV. COMPOSITE PREPARATION

The composite sheet was cast using a wooden mould with dimensions of (120x100x6) mm. The samples were made with a volume percentage of fibers of 5, 10, and 15%. The samples were prepared using the standard hand lay-up process. A determined quantity of epoxy resin and hardener (ratio of 10:1 by weight) was completely mixed in a glass jar and put in a vacuum chamber to eliminate air bubbles that were introduced for varied volume fractions of fibres. This process took 10 minutes to complete. To facilitate the removal of composite sheets, a mould release sheet was placed over the glass plate and a mould release spray was sprayed to the mold's inner surface. After placing the mould on a glass sheet, a thin layer of the mixture (2 mm thickness) was poured. The needed number of fibres were then scattered on the mixture. After that, the remaining of the mixture was poured into the mould. The mould was then pressed from the top and left to cure at room temperature for 72 hours. After the allotted time, samples were removed from the mould. Figure 1 depicted the stages involved in the manufacturing of a laminated composite created by hand layup method in accordance with ASTM standards. Figure 1 shows the materials used for the fabrication of composites.

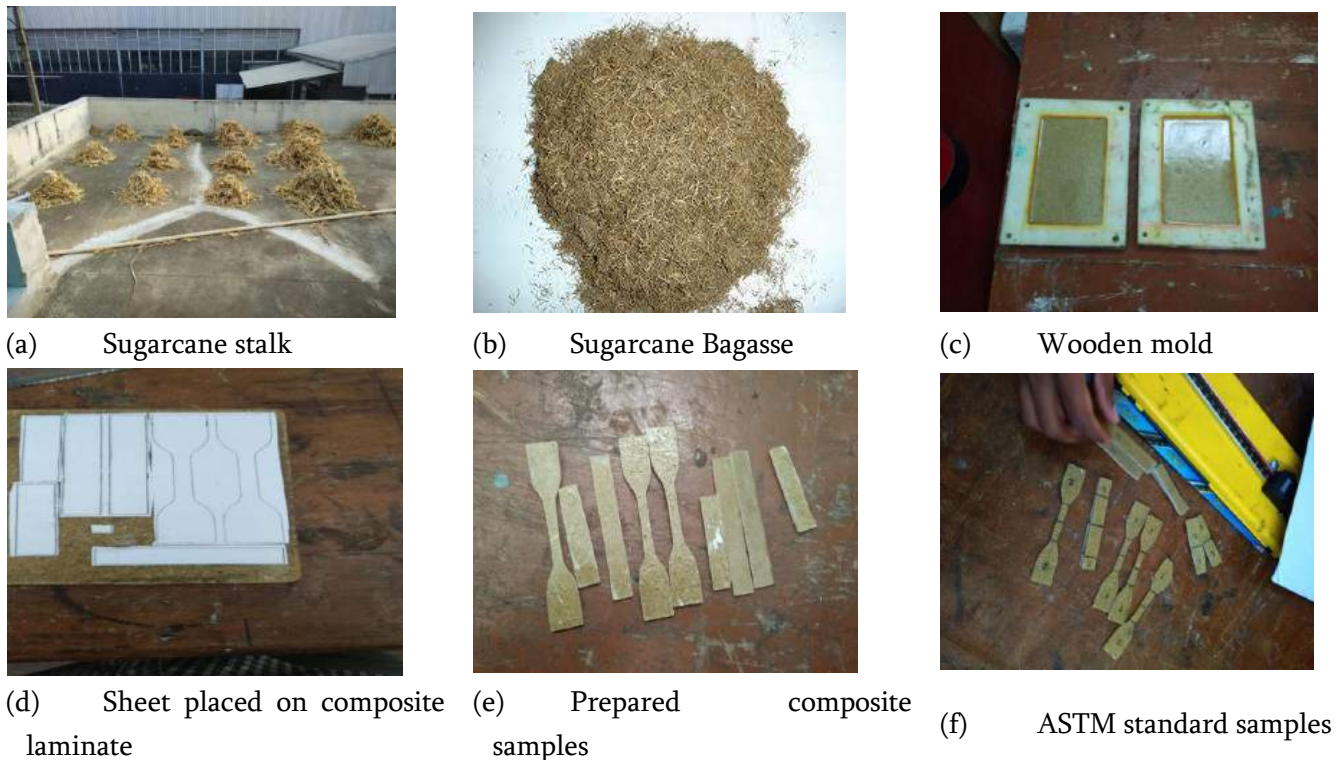


Figure 1 (a) – (f): Steps involved in fabrication of laminated composite as per ASTM standards

V. RESULT AND DISCUSSION

5.1. Tensile Test

The test was performed with tension fixture in Universal testing machine (UTM) as per ASTM D3039 standard samples to evaluate the tensile properties. The tensile test was performed in universal testing machine INSTRON H10KS. Test specimens were cut from the prepared mould with the help of cutting machine, width of 25 mm, thickness of 2, 3 & 4 mm and length of 220mm. The specimens were prepared using hand layup method exhibits similar behavior for 0° and 90° directions, only one direction is tested. The samples were tested at room temperature with different crosshead speeds viz. 5, 25 and 50 mm/min. The conditioned specimens were also tested in the tension mode with the aforesaid crosshead speeds. Figure 2 shows the tensile and flexural tested SCB composite samples of varied compositions (5%, 10% and 15%). Figure 3 signified the results obtained from tensile test conducted on UTM.

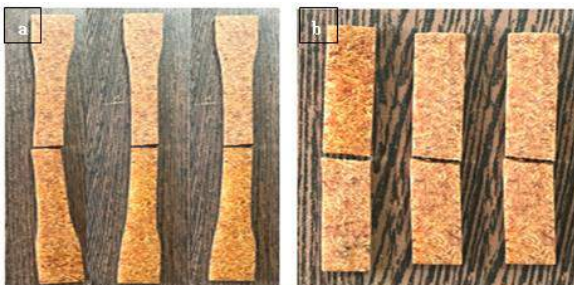


Figure 2: Tensile tested composite specimens

It is evident from all these figures that the tensile properties of the composites increases with increase in crosshead speed. Figure 3 (a) shows the tensile behavior of Bagasse reinforced epoxy composites. It was identified that 10 wt. % of SCB composite has shown more elongation at crosshead speeds of 5, 25 and 50 mm/min, respectively. Lesser percentage of elongation has seen with 5% wt. of SCB composite indicating safe deformation at three crosshead speeds. The tensile strength has shown significant increase at 10 wt. % of composite with maximum crosshead speed. Similar increase in strength values are present in the investigated PMCs which may be caused by the induced thermal stresses in the polymer phase. The induced thermal stresses in the fiber/matrix interface and/or, at polymer matrix may possibly generate micro cracks without blunting at a stable state. Few micro cracks transfers to potential cracks at lower crosshead speeds and cause substantial decrease in tensile strength of the composites, while as the crosshead speed increases the response required to propagate the micro cracks is less. Also, at lower crosshead speed the stress transfer from the matrix to the fiber through fiber/matrix interface occurred slow and steady. But as crosshead speed increases the stress transfer may not that much efficient through micro cracks in the polymer matrix composite. This can be attributed to higher strength at higher crosshead speeds [11].

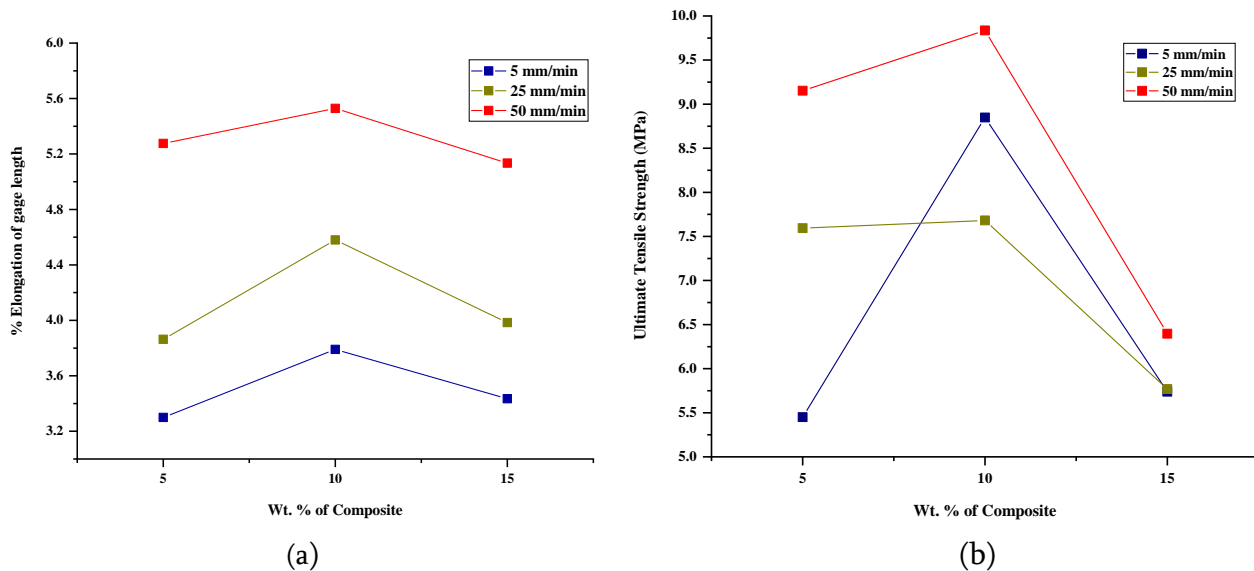


Figure 3: Tensile Properties of SCB composite (a) % Elongation of gage length (b) Ultimate Tensile Strength

5.2. Flexural Test

Three point bend tests were performed in accordance with ASTM D 790M to measure flexural properties. The specimens were 125 mm long, 12.7 mm wide and 3 mm thick. The samples were tested at room temperature with different crosshead speeds viz. 1, 1.5 and 2 mm/min. Flexural tested specimens of 5%, 10% and 15% wt. SCB composite are shown in figure 2. The flexural behavior of SCB fiber reinforced composite is presented in Figure 5. Figure 5 exhibits similar trend observed for tensile properties. The flexural strength for 15wt. % reinforcement is about 22.77MPa with highest crosshead speed of 2 mm/min [12]. The flexural strength increases with increase in fiber loading which was in agreement with the findings of other researchers [13-15]. This may be due to the favorable entanglement of the polymer chain with the filler which has overcome the weak filler matrix adhesion with increasing filler content [16].

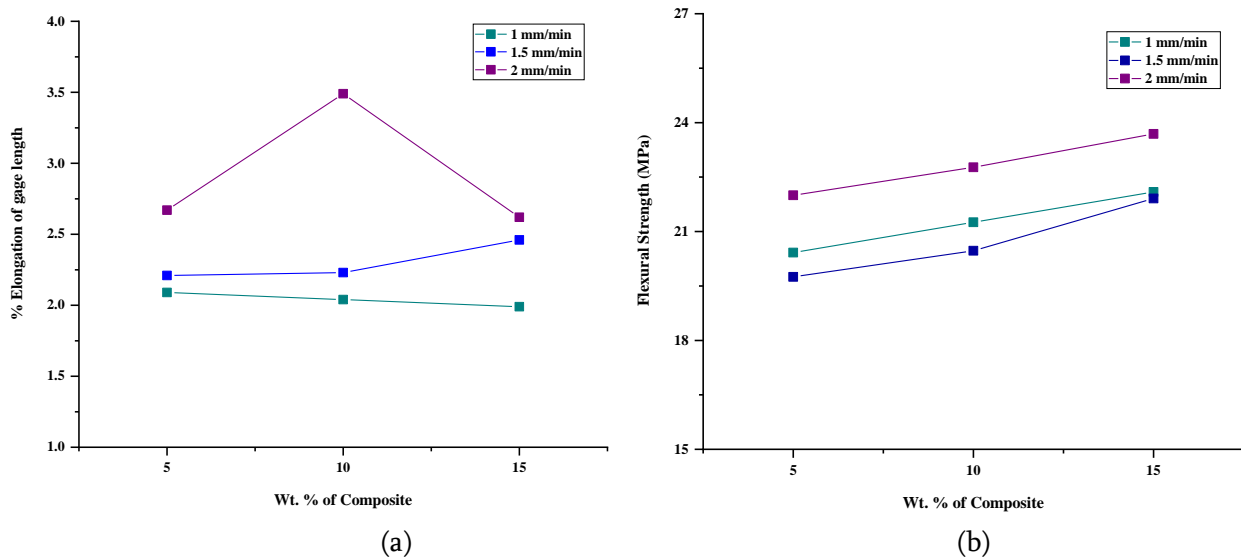


Figure 5: Flexural Properties of SCB composite (a) % Elongation of gage length (b) Flexural Strength

VI. CONCLUSION

The sugarcane bagasse (SCB) reinforced epoxy composites were fabricated by hand layup technique. The mechanical properties such as tensile and flexural strength of SCB composites at different crosshead speeds were studied as per ASTM standards. The inclusion of sugarcane bagasse reinforced natural fiber polymer composite significantly enhanced the tensile strength and flexural strength at different crosshead speeds. Flexural strength has shown significant results with crosshead speeds of 1, 1.5 and 2 mm/min due to entanglement of polymer chain with the filler content by improving the matrix adhesion. But 10 wt. % reinforcement favored both tensile and flexural behavior of composites studied.

VII. ACKNOWLEDGMENTS

The authors express their respect to the administration of Government Engineering College, Chamarajanagara. Additionally, they like to express their gratitude to Dr Muniraju M, Research Supervisor and Head of the Department for their encouragement and assistance during this research study.

VIII. REFERENCES

- [1]. Robert J. Young, Peter A. Lovell, "Introduction to Polymers", Third Edition, CRC Press, Taylor and Francis Group, LLC, ISBN-13: 978-1-4398-9415-6.
- [2]. Shaw, A., Sriramula, S., Gosling, P.D., and Chryssanthopoulo, M.K. (2010) Composites Part B, 41, 446–453.
- [3]. Sabu Thomas, Kuruvilla Joseph, Sant Kumar Malhotra, Koichi Goda, and Meyyarappallil Sadasivan Sreekala, "Polymer Composites", Volume 1, 2012 Wiley-VCH Verlag & Co. KGaA, Boschstr. 12, 69469 Weinheim, Germany, ISBN - 978-3-527-32624-2.

- [4]. Avila, A.F., Paulo, C.M., Santos, D.B., and Fari, C.A. (2003) *Materials Characterization*, 50, 281–291.
- [5]. Liu, D., McDaid, A.D., and Xie, D.Q. (2011) *Mechatronics*, 21, 315–328.
- [6]. Geethamma, V.G., Thomas Mathew, K., Lakshminarayanan, R., and Thomas, S. (1998) *Polymer*, 39, 1483–1491.
- [7]. V.P. Arthanarieswaran, A. Kumaravel, M. Kathirselvam, “Evaluation of mechanical properties of banana and sisal fiber reinforced epoxy composites: Influence of glass fiber hybridization”, doi.org/10.1016/j.matdes.2014.07.058, 27 July 2014.
- [8]. RupaPatil, ShubhangiJadhav, VishvamPanchariya, Dr. Kamlesh Kulkarni, “Investigation on Mechanical Behaviour of Sugarcane Bagasse Fiber Reinforcement in Polymer Matrix Composites”, *International Research Journal of Engineering and Technology (IRJET)*, e-ISSN: 2395-0056, p-ISSN: 2395-0072, Volume: 06 Issue: 10 Oct 2019.
- [9]. K K Mahato, D K Rathore, R K Prusty, K Dutta, B C Ray, “Tensile behavior of MWCNT enhanced glass fiber reinforced polymeric composites at various crosshead speeds”, *National Conference on Processing and Characterization of Materials*, IOP Conf. Series: Materials Science and Engineering 178 (2017) 012006 doi:10.1088/1757-899X/178/1/012006.
- [10]. Han-Seung Yang, Hyun-Joong Kim, Jungil Son, Hee-Jun Park, Bum-Jae Lee, Taek-Sung Hwang, “Rice-husk flour filled polypropylene composites; mechanical and morphological study”, *Composite Structures* 63 (2004) 305–312, doi:10.1016/S0263-8223(03)00179-X.
- [11]. Kishore Kumar Mahato, Krishna Dutta, Bankim Chandra Ray, “High-temperature tensile behavior at different crosshead speeds during loading of glass fiber-reinforced polymer composites”, *Journal of Applied Polymer Science*, 2017, DOI: 10.1002/APP.44715.
- [12]. M. Indra Reddy, M. Anil Kumar, Ch. Rama Bhadri Raju, “Tensile and Flexural properties of Jute, Pineapple leaf and Glass Fiber Reinforced Polymer Matrix Hybrid Composites”, *Materials Today: Proceedings* 5 (2018) 458–462, https://doi.org/10.1002/app.44715.
- [13]. Gujjala, R., Ojha, S., Acharya, S.K. and Pal, S.K. (2013) *Mechanical Properties of Woven Jute-Glass Hybrid Reinforced Epoxy Composite*. *Journal of Composite Materials*.
- [14]. Pujari, S., Ramakrishna, A. and Suresh Kumar, M. (2014) *Comparison of Jute and Banana Fiber Composites: A Review*. *International Journal of Current Engineering and Technology*.
- [15]. Bledzki AK, Jaszkiwicz A, Scherzer D. Mechanical properties of PLA composites with man-made cellulose and abaca fibres. *Compos Part A: Appl Sci Manuf* 2009;40:404–12.
- [16]. Mwaikambo LY. Review of the history, properties and application of plant fibres. *Afr J Sci Technol: Sci Eng Ser* 2006;7(2):120–33.



Green Synthesis of Silver Nanoparticles Using Leaf Extract of *Hyptis Capitata* and Evaluation of their Catalytic Efficiency

Revathy R¹, Jebin Joseph², Sajini T^{1*}, Cyril Augustine¹, Beena Mathew³

¹Research & Post Graduate, Department of Chemistry, St. Berchmans College (Autonomous), Affiliated to Mahatma Gandhi University, Changanassery-686101, Kerala, India

²Research & Post Graduate, Department of Botany, St. Berchmans College (Autonomous), Affiliated to Mahatma Gandhi University, Changanassery-686101, Kerala, India

³School of Chemical Sciences, Mahatma Gandhi University, Priyadarsini Hills P O, Kottayam -686560, Kerala, India

ABSTRACT

Several metal nanoparticles with numerous properties have been prepared based on plant extracts. We report in this article, an environment friendly method for the preparation of silver nanoparticles (AgNPs) using leaf extract of *Hyptis capitata*, and the evaluation of their catalytic efficiency. *Hyptis capitata* is a species of erect annual shrubs, of the plant family Lamiaceae. Extract was prepared with water using distillation technique. AgNPs were prepared by irradiating the mixture of silver nitrate and leaf extract with microwave radiation. The synthesized AgNPs were characterized by UV-visible spectroscopy, HR-TEM, SAED, EDX, XRD, DLS, Zeta Potential, and FT-IR techniques. The synthesized AgNPs exhibited good catalytic efficiency.

Keywords: *Hyptis capitata*, Silver nanoparticles, green synthesis, catalytic efficiency.

I. INTRODUCTION

Many effective physical and chemical methods such as arc discharge, vapor deposition, pyrolysis [1], micro emulsion, photo reduction [2] and chemical reduction of silver nitrate have been employed in the synthesis of silver nanoparticles. Green synthetic methods are non-toxic, cost-effective and eco-friendly. Numerous studies have been focused on the synthesis of silver nanoparticles with antimicrobial, anti-inflammatory and catalytic properties using plant materials as reducing agents [3-6]. Silver nanoparticles are used in bio sensing, antibiotics, catalysis, food industry, agriculture, microelectronics etc. [7-15]. We report in this article, the microwave assisted green synthesis of silver nanoparticles using the leaf extract of *Hyptis capitata* as reducing and capping agent and evaluated the catalytic efficiency.

II. MATERIALS AND METHODS

Silver nitrate, methyl orange and sodium borohydride of analytical grade were purchased from Merck(India) and used as such without further purification. Hyptis capitata plants were identified and collected from Changanacherry, Kerala, India. Fresh leaves were washed thoroughly with distilled water, sliced into small pieces and dried in hot air oven. Dried sample (5 g) was taken in a round bottom flask fitted with condenser and boiled for 20 min with 100 mL of distilled water. Extract was filtered through whatman paper. Stored in refrigerator for further experiments.

A. Synthesis of silver nanoparticles

In a 250ml beaker, 90ml 1mM silver nitrate aqueous solution and 10ml leaf extract were mixed and placed in domestic microwave oven [Sharp R219T (W)] for 3minutes.

B. Characterization of synthesized silver nanoparticles

Using UV-visible spectrophotometry (Shimadzu UV-2450) the formation of silver nanoparticles was monitored at 30 minutes' intervals and characterized with FT-IR (Perkin Elmer-400), HR-TEM (JEOL JEM-2100), EDX and XRD (XPERT- PRO X-ray spectrometer) analyses.

C. Catalytic activity

The reduction reaction of methyl orange by sodium borohydride in presence of silver nanoparticles was conducted to examine the catalytic action of nanoparticles.

III. RESULTS AND DISCUSSION

By irradiating the mixture of 90ml 1mM silver nitrate aqueous solution and 10ml Hyptis capitata leaf extract with microwave radiation, the silver nanoparticles were synthesized. The color change was obtained from colorless to yellowish brown which indicated the formation of nanoparticles.

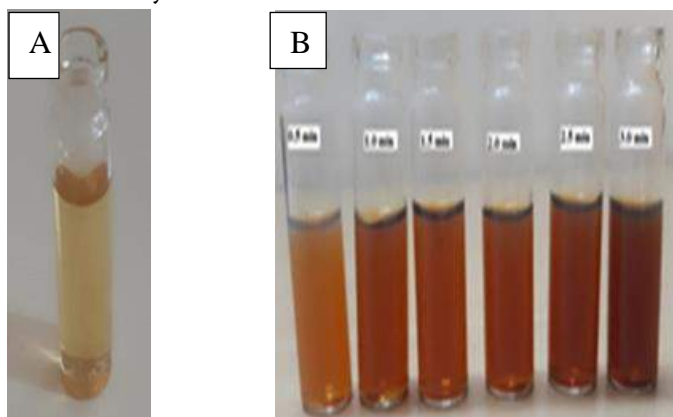


Figure1:A) Hyptis capitata leaf extract. B) Color change with microwave irradiation of mixture of silver nitrate and Hyptis capitata leaf extract.

UV-vis spectrum was taken in the range 200-800nm at 30 sec intervals and typical SPR band of silver nanoparticles was obtained.

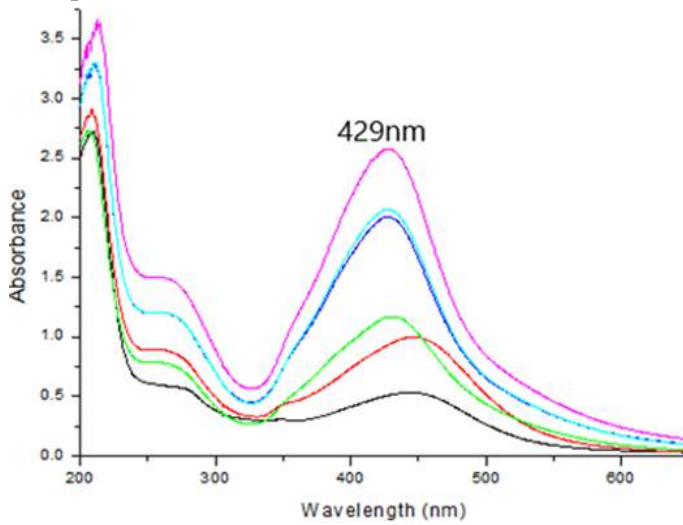


Figure2: UV-visible spectrum of synthesized silver nanoparticles.

-53.3mV zeta potential and 104.4 nm hydrodynamic size were obtained for the synthesized silver nanoparticles.

The presence of elemental silver was confirmed with the EDX spectrum.

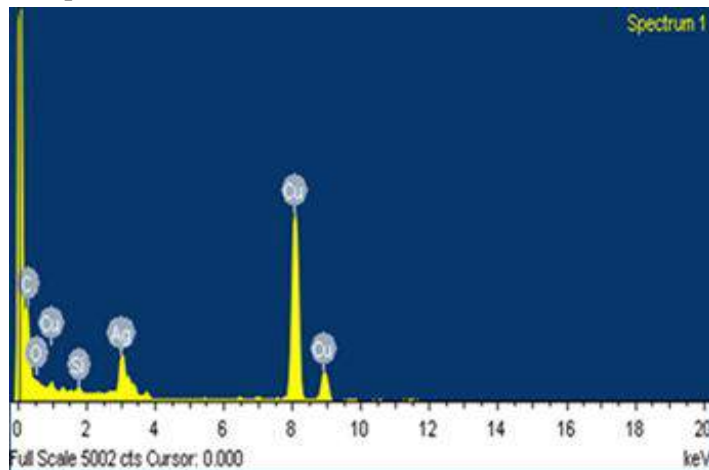
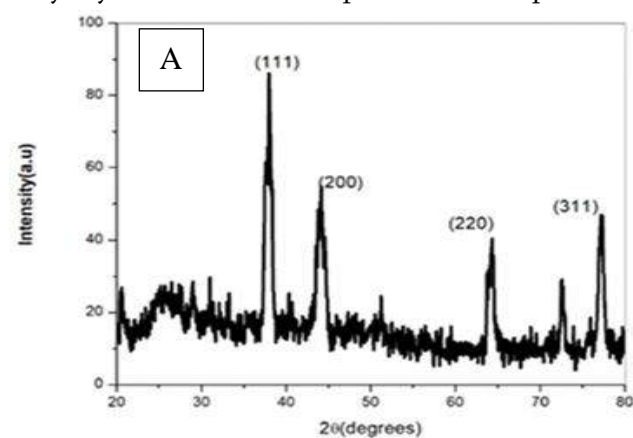


Figure3: EDX spectrum of synthesized silver nanoparticles.

Poly crystalline silver nanoparticles were spherical and oval in shape and have face centred cubic structure.



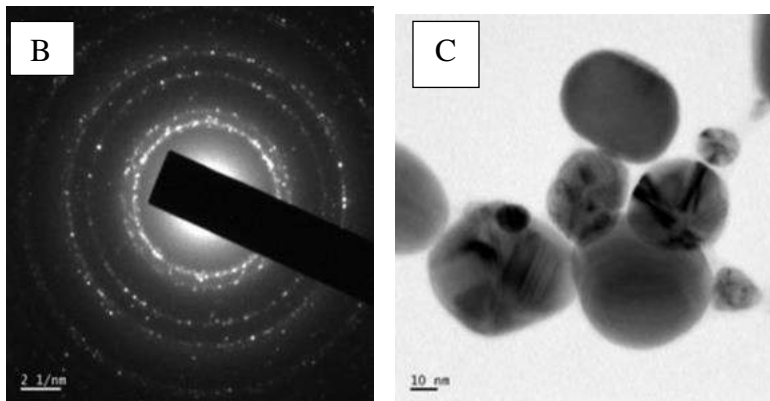


Figure4: Images of quality and morphology of synthesized silver nanoparticles. A) XRD pattern B) SAED pattern C) HR-TEM image

The various phytochemicals present in the plant extract help in capping the surface of nanoparticles. The functional groups were found in the FT-IR spectrum.

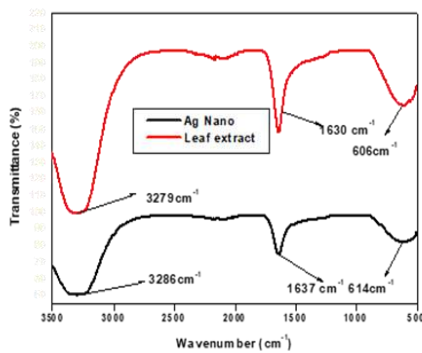


Figure5: FT-IR spectrum of silver nanoparticles.

The reduction of methyl orange by sodium borohydride in presence of silver nanoparticles was analyzed by taking UV-vis spectrum at 30 minutes' intervals. The fall in absorbance shows decrease in concentration of methyl orange in the solution. Reaction was found to be completed in 3hours with the help of the silver nanocatalyst.

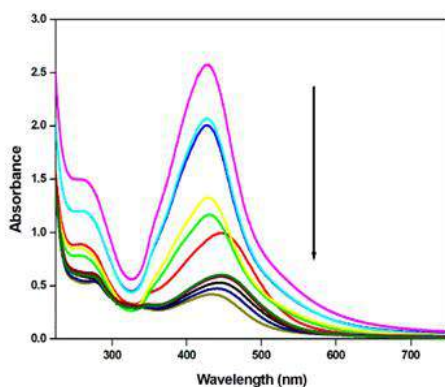


Figure6: UV-vis spectrum of catalytic reduction of methyl orange by sodium borohydride in presence of silver nanoparticles.

IV. CONCLUSION

Microwave assisted green synthesis from *Hyptis capitata* leaf extract is a rapid and simple method. Typical SPR band was obtained in the UV vis spectrum. Polyphenols and flavonoids in this leaf extract helped in this biosynthesis. Polycrystalline silver nanoparticles with spherical and oval shapes were obtained with great stability. In the EDX spectrum the presence of elemental silver was confirmed. Good catalytic efficiency was exhibited by these nanoparticles.

V. REFERENCES

- [1]. M. Yusuf, Silver Nanoparticles: Synthesis and Applications, (2019) 2343–2356.
- [2]. K.M.M. Abou El-Nour, A. Eftaiha, A. Al-Warthan, R.A.A. Ammar, Synthesis and applications of silver nanoparticles, Arab. J. Chem. 3 (2010) 135–140. <https://doi.org/10.1016/j.arabjc.2010.04.008>.
- [3]. F. Okafor, A. Janen, T. Kukhtareva, V. Edwards, M. Curley, Green synthesis of silver nanoparticles, their characterization, application and antibacterial activity, Int. J. Environ. Res. Public Health. 10 (2013) 5221–5238. <https://doi.org/10.3390/ijerph10105221>.
- [4]. S. Saha, M.M. Malik, M.S. Qureshi, Microwave Synthesis of Silver Nanoparticles, Nano Hybrids. 4 (2013) 99–112. <https://doi.org/10.4028/www.scientific.net/nh.4.99>.
- [5]. Yangqing He, A Fenfei Wei, a Zhanying Ma, b Hao Zhang, c Qian Yang, a Binghua Yao, a Zhengrui Huang, a Jie Li, a Cun Zenga and Qian Zhang, a Green synthesis of silver nanoparticles using seed extract of *Alpinia katsumadai*, and their antioxidant cytotoxicity, and antibacterial activities†
- [6]. D. Singh, D. Rawat, Isha, Microwave-assisted synthesis of silver nanoparticles from *Origanum majorana* and *Citrus sinensis* leaf and their antibacterial activity: a green chemistry approach, Bioresour. Bioprocess. 3 (2016). <https://doi.org/10.1186/s40643-016-0090-z>.
- [7]. K.M.M. Abou El-Nour, A. Eftaiha, A. Al-Warthan, R.A.A. Ammar, Synthesis and applications of silver nanoparticles, Arab. J. Chem. 3 (2010) 135–140. <https://doi.org/10.1016/j.arabjc.2010.04.008>.
- [8]. S.H. Lee, B.H. Jun, Silver nanoparticles: Synthesis and application for nanomedicine, Int. J. Mol. Sci. 20 (2019). <https://doi.org/10.3390/ijms20040865>.
- [9]. A.C. Burduşel, O. Gherasim, A.M. Grumezescu, L. Mogoantă, A. Fikai, E. Andronescu, Biomedical applications of silver nanoparticles: An up-to-date overview, Nanomaterials. 8 (2018) 1–25. <https://doi.org/10.3390/nano8090681>.
- [10]. M. Murphy, K. Ting, X. Zhang, C. Soo, Z. Zheng, Current Development of Silver Nanoparticle Preparation, Investigation, and Application in the Field of Medicine, J. Nanomater. 2015 (2015) 12. <http://dx.doi.org/10.1155/2015/696918>.
- [11]. B. Khodashenas, H.R. Ghorbani, Synthesis of silver nanoparticles with different shapes, Arab. J. Chem. 12 (2019) 1823–1838. <https://doi.org/10.1016/j.arabjc.2014.12.014>.
- [12]. K.S. Siddiqi, A. Husen, R.A.K. Rao, A review on biosynthesis of silver nanoparticles and their biocidal properties, J. Nanobiotechnology. 16 (2018). <https://doi.org/10.1186/s12951-018-0334-5>.

- [13].K. Seku, B.R. Gangapuram, B. Pejjai, K.K. Kadimpati, N. Golla, Microwave-assisted synthesis of silver nanoparticles and their application in catalytic, antibacterial and antioxidant activities, *J. Nanostructure Chem.* 8 (2018) 179–188. <https://doi.org/10.1007/s40097-018-0264-7>.
- [14].S. Joseph, B. Mathew, Microwave Assisted Biosynthesis of Silver Nanoparticles Using the Rhizome Extract of *Alpinia galanga* and Evaluation of Their Catalytic and Antimicrobial Activities, *J. Nanoparticles.* 2014 (2014) 1–9. <https://doi.org/10.1155/2014/967802>.
- [15].Y. He, X. Li, Y. Zheng, Z. Wang, Z. Ma, Q. Yang, B. Yao, Y. Zhao, H. Zhang, A green approach for synthesizing silver nanoparticles, and their antibacterial and cytotoxic activities, *New J. Chem.* 42 (2018) 2882–2888. <https://doi.org/10.1039/c7nj04224h>.



Propulsion Option for Deep Space Travel

Lakshmi Prasad L¹, Amrutha. G¹, Bharath B H¹, Divya H S¹, Kousik S²

¹U G Students of Department of Mechanical Engineering, JSS Academy of Technical Education-Bengaluru,
Karnataka, India

²Assistant Professor of Department of Mechanical Engineering, JSS Academy of Technical Education-Bengaluru,
Karnataka, India

ABSTRACT

For more than 50 years, we have been manufacturing propulsion systems for various international satellites and spacecraft. For deep-space missions, significant improvements in propulsion will be needed in the future. NASA's Deep Space 1 spacecraft technology is the mainstream option for deep-space missions; ion propulsion is considered a viable option. The purpose of this paper is to demonstrate different propulsion options and technologies needed to survive a deep space environment that can enable a spacecraft to travel into deep space.

Keywords: -Chemical propulsion, Ion propulsion, Deep space travel, etc.

I. INTRODUCTION

Physicist Stephen Hawking is one of the greatest in history. From the Big Bang to black holes, his work revolutionized the understanding of the origin and structure of the universe. Humanity has a deadline to save itself, which he set earlier this year. He warned that Mars and other planets need to be colonized within 100 years. Our future may be threatened by climate change, disease, and different kinds of doom we are likely to bring on ourselves in the coming decades. We need a propulsion option for traveling in space and migrating to another planet to achieve this goal. This must be reached within a limited period using better propulsion options.

The most significant factor contributing to aerospace vehicles' success is their engines in the past, present, and future. Among these activities are design, manufacturing, testing, production and flight operations support. This design is responsible for every aspect of the vehicle: the wing shape and size, the installation of the propulsion systems, logistics for crew and payload, the handling of propellants, and life support. In the design of hypersonic vehicles in the future, air intakes will be incorporated almost entirely into the wing-body. As the engine speed ranges from subsonic to hypersonic, it must channel and condition the airflow in an adroit manner to operate efficiently. The choice of propulsion system should be made as early as possible in the project. Propulsion systems affect the cost and lifecycle of a project. Only if we continue to make access to space reliable, safe and relatively inexpensive will technologists, experimenters, and innovators be able to take full advantage of space.

1.1 Historical Perspective

It has been centuries since propulsion systems have been developed, going back as far as the early 20th century. Early pioneers, including Jules Verne (French) and Konstantin Tsiolkovsky (Russian), first proved the improvement of Rocket-powered flight; however, the famed aerospace corporation NASA later proved it commercially. The first rockets were flown and built in the 20th century when the American Robert H. Goddard came along. The Germans were the ones who perfected Goddard's liquid missiles during World War II and flew the first operational rockets.

All rockets prior to the 1950s had a single stage and could not reach the earth's orbit. German rocket team members left Germany after the war and moved to the United States, developing the V-2 technologies for better rockets. In World War II, German soldiers assisted the Soviet rocket men. Russian cosmonaut Yuri Gagarin was the first man to orbit the earth in space. From 1960 to 2000, John Glenn became the first American to orbit the Earth on Feb. 20, 1962. In 1961, John F. Kennedy set the goal of landing a man on the moon and returning him safely to earth within that decade. American astronaut Neil Armstrong stepped onto the moon on July 20, 1969. During the 1970s, a satellite was used to broadcast television programs over the air. In the 1980s, the first interplanetary missions were launched into space. The Chernobyl nuclear disaster was seen on satellite images in 1986. A hole in the atmosphere was discovered over Antarctica, and forest fires were located using satellites. New stars have been found, and satellites reveal the centre of our galaxy. Modern space exploration has reached areas only dreamed of before. NASA is exploring the possibility of human-crewed missions to mars as part of its long-term goal to explore the Red Planet. NASA is on a mission to Mars, and its purpose is to send humans there in the 2030s.

The Indian space research organization (ISRO) has launched 79 rockets and conducted 111 spacecraft missions. Several missions are planned, including Gaganyaan, Aditya and MOM 2.

II. ROCKET PROPULSION SYSTEMS

The propulsion systems on vehicles are the ones that move the vehicle. The propulsion systems we use in walking, running, swimming, and so on are many and diverse, starting with our muscles using which we propel ourselves. As rocket propulsion systems do not utilize air from the atmosphere, it is evident that both fuel and oxidizer are to be carried by the rocket. Essentially, rocket propulsion systems can generate and store their working fluid within themselves. Due to the working fluid being generated from or contained within the rocket propulsion system, the thrust generated can be independent of the surrounding environment. Because rocket propellant is not drawn from the atmosphere free, they are more expensive to use in the atmosphere than air-breathing propulsion systems. However, rocket propulsion systems can be designed to operate regardless of the atmosphere.

Rocket propulsion is classified as

- (1) Chemical rocket,
- (2) Electric rocket, and
- (3) Nuclear rocket.

Rocket motors are classified according to the source of energy used for propulsion. Chemical rocket motors, for example, release both working fluid and thermal energy upon combustion. By expanding the combustion products through a nozzle, the hot fluid acquires high kinetic energy by transforming thermal energy into kinetic energy. Because the fluid expands through a conventional nozzle, thermal energy is converted into kinetic energy. The working fluid is accelerated by kinetic energy added by the electric energy. Solar cells can be used to convert solar energy into electricity. A photovoltaic cell converts solar energy into electricity in an electric rocket propulsion system. Nuclear-fusion reactions release thermal energy that is transferred to the working fluid during nuclear rocket propulsion, in contrast with radioactive decay or nuclear fission that can be directly converted into electricity via thermionic materials.

2.1. Chemical Rocket Propulsion

Chemical rocket propulsion is classified as follows:

- (1) Solid rocket motor,
- (2) Liquid rocket engine,
- (3) Cryogenic engine and
- (4) Hybrid rocket engine.

Combustion or exothermic reactions release heat through chemical rocket propulsion, known as propellants. The chemical is either a liquid propellant or solid propellant, depending on its phase. By burning the propellant and releasing heat, combustion products are also produced. Solid propellant rockets are generally called motors, and liquid propellant rockets are called engines.

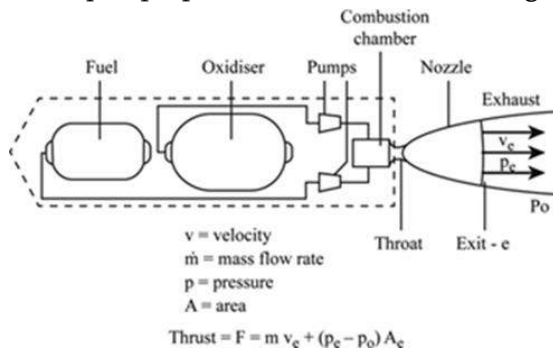


Fig. 1.1 Schematic sketch of a chemical rocket.

2.2. Solid Rocket Motor

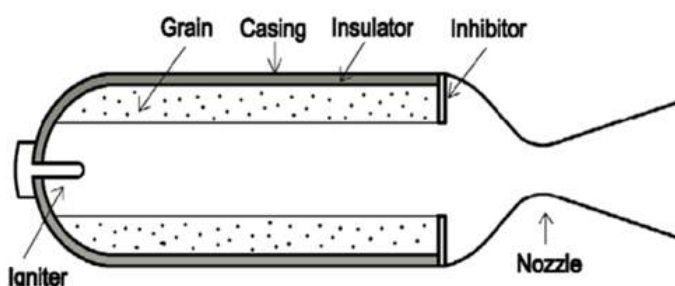


Fig. 1.2. Schematic sketch of a solid propellant

Here is a schematic representation of a solid rocket motor Fig.1.2. There are three major components: (1) Igniter, (2) Grain, and (3) Nozzle. By the name grain, we mean the solid block of propellant contained within the casing. Essentially, the grain contains an oxidizer and fuel.

A combustion chamber is typically found in the central cavity in the grain, as shown in the figure. After being ignited, the propellant grain burns. Gaseous products are produced when the grain burns.

The hot gases expand rapidly as they exit the nozzle. The nozzle is generally a convergent-divergent type. The working fluid is generated in the combustion chamber, so there is no incoming momentum rate. A high momentum rate of the exiting combustion products during combustion opposes a zero momentum rate of the incoming combustion products. The propellant grain is sandwiched between a liner and insulator in so that hot combustion products are kept out of the casing walls. For the desired thrust variation with time, certain parts may be necessary to protect certain parts of the grain from burning. This is accomplished by covering them with an inhibitor. A drawing of Fig.1.2 illustrates the insulator between the casing wall and the propellant grain, as well as the inhibitors on either side of the grain. Convergence-divergence nozzle handles high-temperature combustion gases; its walls should also be properly insulated and made of high-temperature-resistant materials.

The solid rocket engine is the simplest chemical propulsion system since fuel and oxidizer are found in the grain. One of the chief disadvantages of solid rocket motors is that their thrust is delivered based on the configuration of the grain and may not be altered at will. Furthermore, solid rocket motors cannot be easily stopped and restarted. In warfare missiles, solid rocket propulsion systems are used because they are simple and are always ready to fire. They have lower energy content per unit mass of propellant than liquid motors. Despite this, satellite launch vehicles are always powered by huge solid rocket motors to overcome the enormous gravitational pull experienced during launch due to the system's simplicity.

As an example of the type of thrust generated by a solid rocket booster, Fig. 1.3.and 1.4, show the twin solid rocket boosters of the Space Shuttle. The SRBs have a combined thrust of over 11520 KN, around 38m long and 3.7m in diameter.

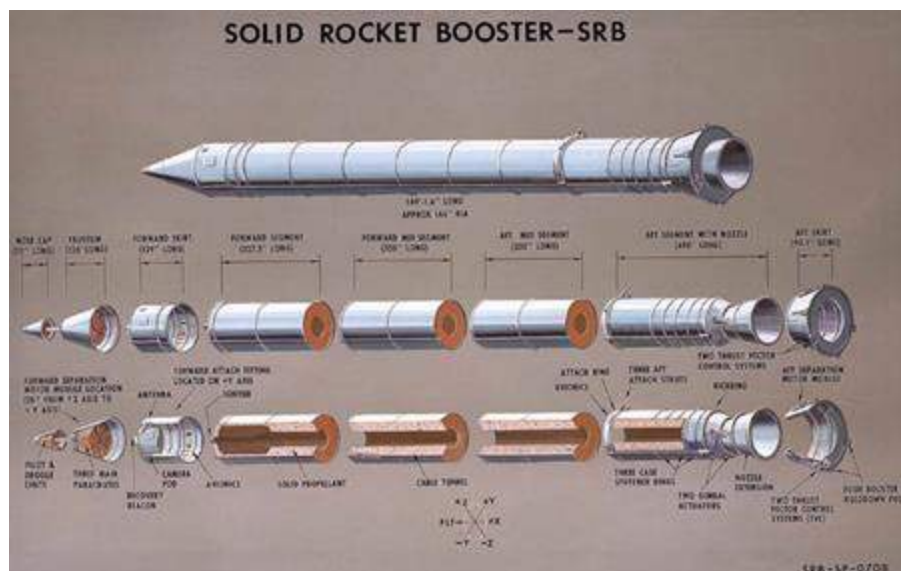


Fig. 1.3.Solid rocket boosters of the Space Shuttle CREDIT-NASA



Fig.1.4. Space Shuttle solid rocket booster. Credit-NASA

2.3. Liquid Rocket Engine

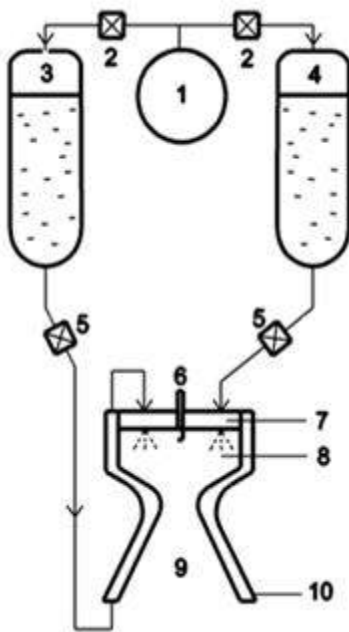


Fig. 1.5. Schematic sketch of a gas pressurized liquid rocket engine 1. High pressure inert gas, 2. Pressurization control valves, 3. Fuel tank, 4. Oxidizer tank, 5. Propellant-flow control valves, 6. Igniter, 7. Injector plate, 8. Combustion chamber, 9. Convergent divergent nozzle and 10. Regenerative cooling jacket.

As shown in Fig.1.5, a liquid rocket propulsion system consists of the propellant feed system and the engine. For cooling, one of the propellants, fuel, circulates around the nozzle and the combustion chamber.

In addition to the igniter, injector, combustion chamber, and nozzle, the engine is made up of a feed system. Liquid rockets can be classified according to which feed system is used for the propellant flow. Pressure-fed

liquid rockets and turbo-pump-fed liquid rockets have similar engine components. The pressure-fed liquid rocket shown in Fig. 1.5 is designed with an inert gas pressurizing the propellants and injecting them into a combustion chamber through flow control valves.

The engines of liquid rockets commonly operate for a long period, a few minutes or more. Therefore, they require a cooling system. Usually, the fuel has better cooling properties than the others.

Additionally, the oxidizer may corrode the metallic surfaces of the coolant passages, causing premature engine failure. Figures 1.5 and 1.6 show how the fuel circulates between the nozzle and combustion chamber, cooling them, and preventing them from oxidizing.

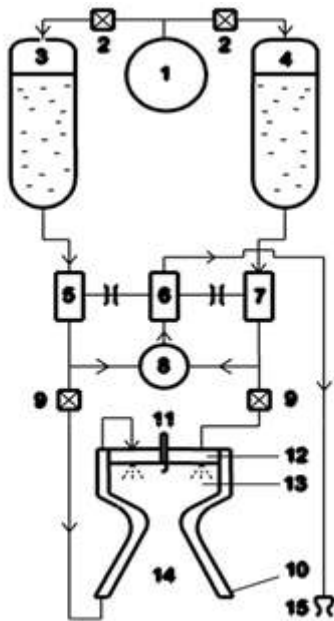


Fig.1.6. Schematic sketch of a turbo-pump fed liquid rocket engine 1. Low-pressure inert gas tank, 2. Pressurization control valves, 3. Fuel tank, 4. Oxidizer tank, 5. Fuel pump, 6. Turbine, 7. Oxidizer pump, 8. Gas generator, 9. Propellant-flow control valves, 10. Regenerative cooling jacket, 11. Igniter, 12. Injector plate, 13. Combustion chamber, 14. Convergent divergent nozzle and 15. Control thruster).

As a result, the cooling system adopted is known as regenerative cooling. Small liquid rocket engines, which can operate in pulsed operation or for short durations, are referred to as liquid thrusters, and they are used as control devices. The main cooling method used for these thrusters is radiated cooling. Liquid rocket engines are not as simple as solid rocket motors, as they require systems to supply, inject, and cool propellant. However, they offer many advantages over solid rocket motors. A characteristic of liquid propellant engines is that the thrust can be easily controlled by adjusting the propellant flow rate as well as the ability to stop and restart them. As the propellants exist in a liquid phase, one of the propellants, as discussed previously, can be used to cool the liquid engines, which can operate longer than solid motors. The propellants are kept outside of the combustion chamber for liquid engines, so the thrust chamber and nozzle assembly are not as heavy as for solid motors, and gimbals for thrust vectoring can be easily adjusted. In the case of solid motors, the propellant ingredients must be compatible with each other, as they must remain mixed and stable in the grain for a long time.

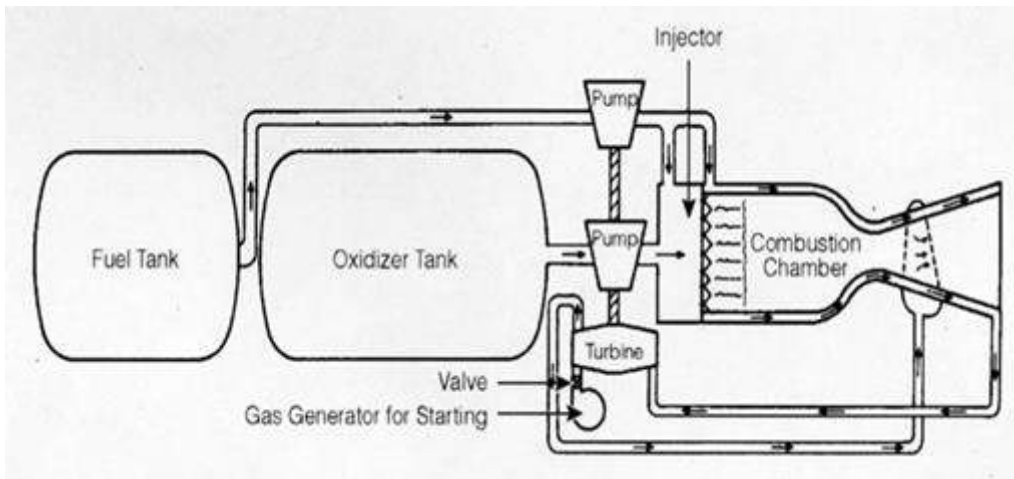


Fig. 1.7. Schematic sketch of a Liquid rocket Engine

2.4. Hybrid Rocket Engine

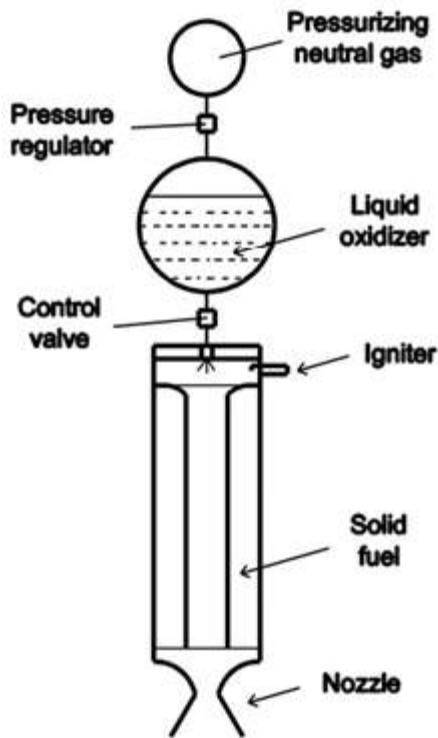


Fig. 1.8. Schematic sketch of a hybrid rocket propulsion system.

An illustration of a hybrid rocket engine is shown in Fig. 1.8. Usually the oxidizer, has a feed system similar to that of a liquid rocket engine. A solid propellant, the fuel, is housed in a casing similar to that of a solid rocket engine. They are simpler than liquid rocket engines but not as simple as solid rocket motors. Hybrid rocket engines leverage the advantages of both solid rocket motors and liquid rocket motors. The current generation of hybrid rocket engines has a short operation duration, largely due to the limited thickness of the fuel web that can be used. They can be stopped and restarted and have thrust control through the regulation of oxidizer flow

rate. Therefore, these engines do not require active cooling. However, the liquid propellant can always be used in a hybrid engine as active cooling. Based on preliminary studies, hybrid rocket engines are predicted to achieve specific impulses comparable to liquid rocket engines using earth-stored propellant or semi-cryogenic propellant combinations while utilizing lower overall systems mass. There are far fewer flight-proven hybrid rocket engines than solid rocket motors and liquid rocket engines. However, several research and development activities on hybrid rocket engines have been reported in recent years.

In order to motivate this, there is an increasing interest in (1) lower development and operation costs with little loss in specific impulse and density specific impulse, (2) safer operation characteristics, and (3) better environmentally friendly exhaust.

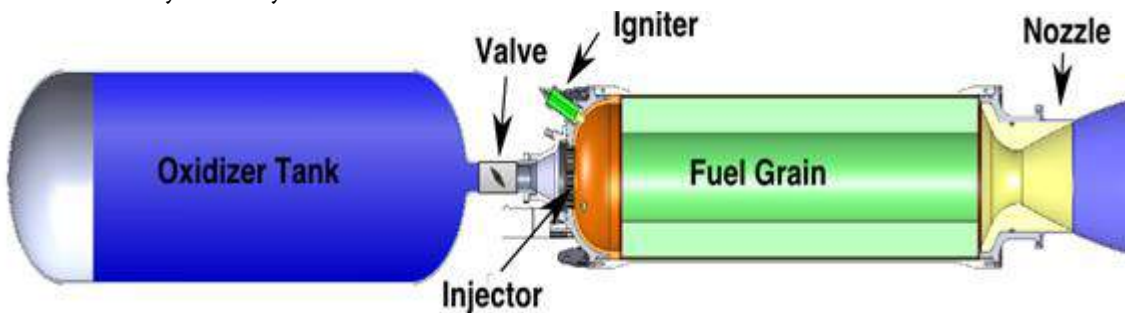


Fig. 1.9. Schematic sketch of a hybrid rocket propulsion system.

III. DEEP SPACE TRAVEL PROPULSION

In order for a vehicle to remain on course on its journey, its propulsion systems must provide precision and ensure the crew can return safely to earth the farther into space it ventures. For humans to travel farther from earth on longer missions, the systems that keep them alive must be highly reliable while taking up minimal volume and mass. A long distance from earth creates a stressful and potentially hostile living environment. Higher doses of damaging radiation and altered gravity fields are among the health hazards of space exploration.

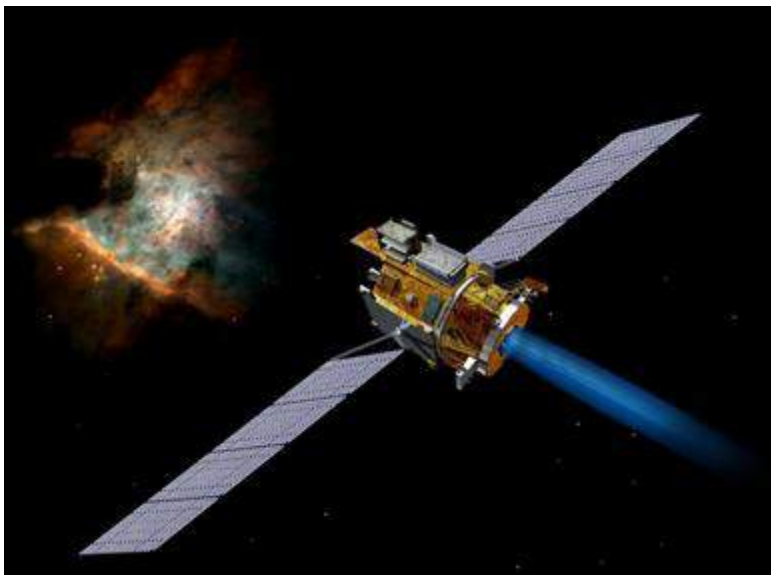


Fig. 1.10. NASA's Deep Space 1. Credit: NASA

On NASA's Deep Space 1, twelve new technologies were tested, such as highly-efficient ion engines and autonomous navigation software. As a result of the mission, ion engines were proved to be effective in long-duration spaceflight and navigational requirements were improved. Humans have occupied the ISS for more than ten years now. Likewise, some dreamers are promising consumers that commercial space travel will be available soon. As compared to earth, deep space offers a number of advantages. Additionally, based on recent events, space exploration efforts seem promising. What will deep space look like in the future and who will reach their missions first?

Though several technologies pursue deep space travel and have some slight advantages, ion and electric propulsion is on the way to space exploration, which is further, fastest, and cheaper.

3.1. ION PROPUSLION

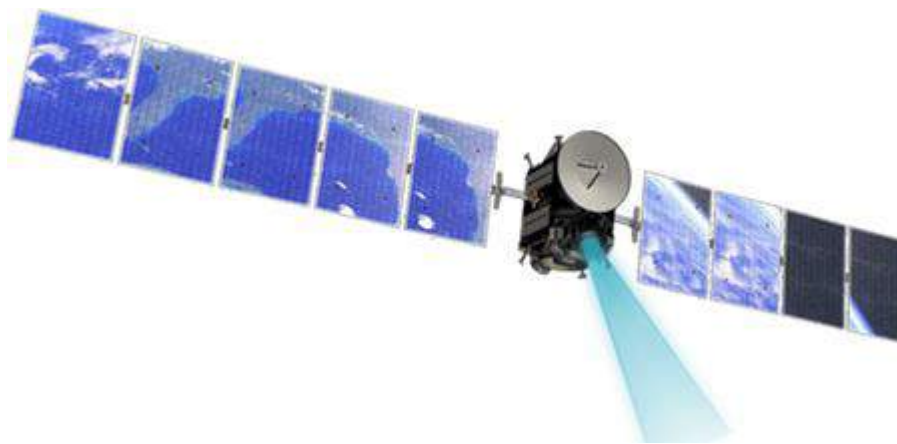


Fig.1.11.Ion-beam-propelled Dawn spacecraft

As scientists and engineers at NASA, ion thrusters have become the propulsion of choice for science fiction writers. Fuel and electrical power are efficiently used for ion propulsion, enabling modern spacecraft to travel farther, faster and cheaper than any other propulsion technology. The fuel efficiency of chemical rockets has been up to 35 percent, but the fuel efficiency of ion thrusters has been over 90 percent. As of today, ion thrusters are used to keep communication satellites on course with respect to earth, as well as to drive deep space probes. A spacecraft can have several thrusters, but they are usually used one at a time.

These thrusters can propel spacecraft up to 90.00 kilometre per hour The Space Shuttle, on the other hand, can reach 18, 00 kph. Currently, ion thrusters have a low thrust (or low acceleration) trade-off for their high top speeds. One ion thruster can deliver only 0.05098 kiloNewton of thrust, which is equal to the force that would be felt by holding ten quarters. They cannot be used to put spacecraft into orbit because large amounts of thrust are required to escape earth's gravity and atmosphere. These thrusters must be used in a vacuum to operate at their maximum power levels.

During the flight, acceleration continues continuously, so tiny amounts of thrust over a long period contribute to shorter travel times and less noise. Ion thrusters must be operated for a long time to compensate for low thrust. In over 16,000 thrusting hours, Deep Space 1 used less than 72.1212 kilogram of fuel. As a result, smaller, lower-cost space vehicles are possible.

3.2. Propulsion

Sir Isaac Newton's third law states that any action will lead to an equal and opposite reaction. For example, a balloon will be propelled forward when air escapes from its end. Conventional chemical rockets make gas propellant by burning fuel along with an oxidizer.

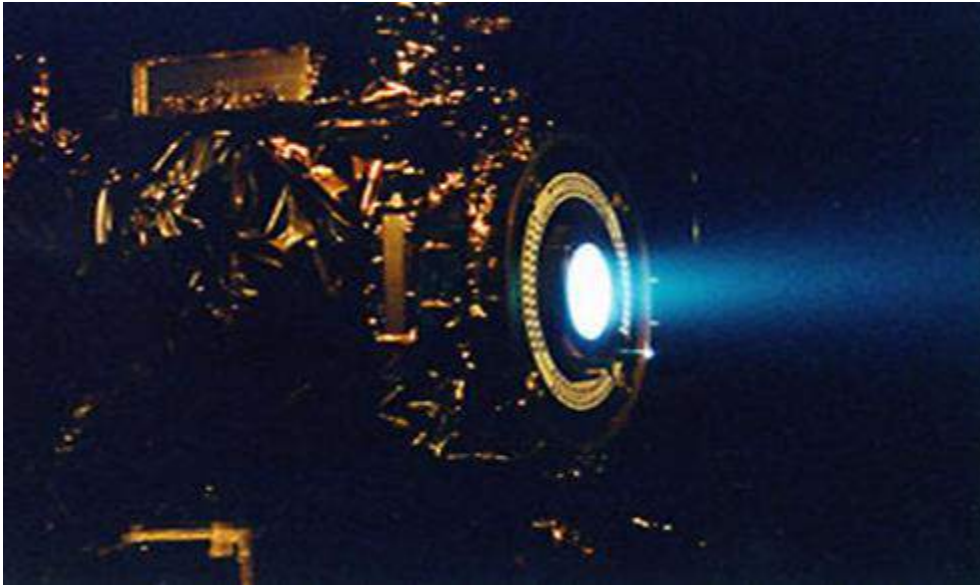


Fig.1.12. Ion thruster of Deep Space 1,

Credit: NASA

Since modern ion thrusters use inert gases as propellant, there is no risk of explosion as there is with chemical propellant. Most thrusters use xenon, which is colourless, odourless, and tasteless.

In the Deep Space 1 probe, ions were ejected at 146,000 kilometres per hour compared to other inert gases, including krypton and argon. Only relatively small amounts of ions are ejected, but they are traveling at very high speeds. Space crafts can be accelerated to close to light speed with ion and or electric rockets.

3.3. Making Ions and Plasma

As an alternative to combustion gases, ion thruster engines emit ions to create thrust, the force that propels a spacecraft forward because an ion is just an atom or with an electrical charge from losing or gaining an electron. During ion propulsion, the ions lose electrons, so they are positively ionized. Whenever some or all of the atoms or molecules in a gas are converted into ions, it is said to be ionized. All positive and negative charges--from inert gases, negatively charged electrons, and positively charged ions--add up to zero in plasma. There are plasmas everywhere in nature (for instance, in lightning and fluorescent light bulbs), and they are designated as the fourth state of matter (the others being solids, liquids, gases). Electricity can easily pass through it since it is a good conductor and has some features of a gas. Electric propulsion means accelerating electrically charged ions and electrons with an electric or magnetic field to provide thrust through plasma. The plasma in an ion thruster is composed of positive ions and electrons in equal amounts. In order to produce ions, NASA uses an electron bombardment technique. Propellant is injected into the thruster ionization chamber and flows upstream. Because of this injection method, the propellant remains in the chamber for longer time. In such ion thrusters, electrons are generated by a hollow cathode, called the discharge cathode, located at the center of the

thruster on the upstream end. The electrons flow out of the discharge cathode and are attracted (like hot socks pulled out of a dryer on a cold day) to the discharge chamber walls, which are charged highly positive by the thruster power supply. The release of a second electron occurs when an electron from the discharge cathode hits a propellant atom (neutral charge) and is accelerated into a high-energies electron (negative charge). Magnets into the discharge chamber redirect electrons approaching the walls of the discharge chamber as they approach the walls.

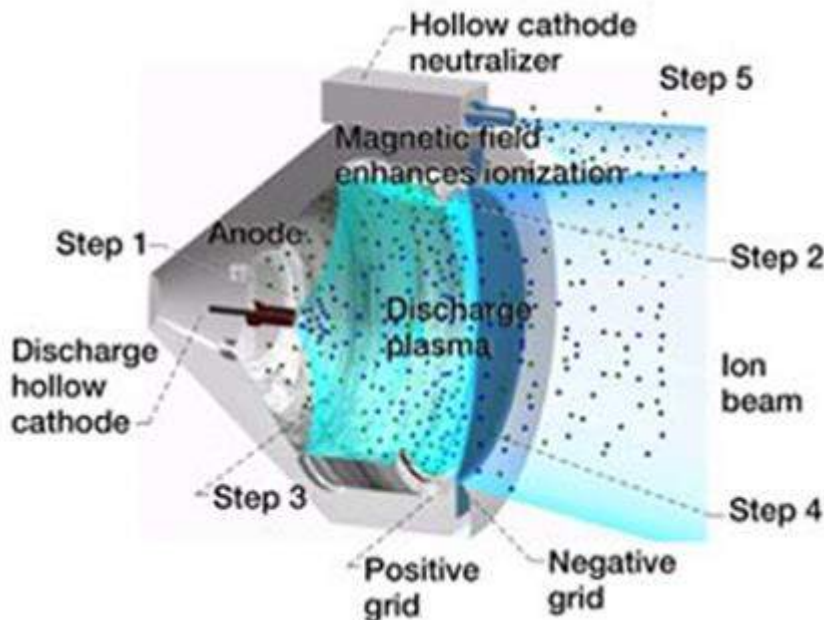


Fig1.13. Ion thruster operation: 1. Electrons (shown as small, pale green spheres) is emitted by hollow discharge cathode, traverse discharge chamber, are collected by the anode walls. 2. Propellant (shown in green) is injected from the plenum and travels toward the discharge cathode. 3. Electrons affect the propellant atoms to create ions (shown in blue). 4. Ions is pulled out of the discharge chamber by ion optics. 5. Electrons is injected into the beam for neutralization. Credit: NASA.

In order to maintain the exhaust beam's total charge neutral, an equal amount of negative charge must be ejected. Otherwise, the ions would attract the spacecraft itself. By enabling the use of much smaller, lower-cost launch vehicles as well as reducing flight times, ion propulsion systems reduce mission costs and make missions far more appealing scientifically.

IV. RESULTS AND DISCUSSION

Because of its known long-term adverse effects, space radiation can also pose health risks to astronauts on long-duration missions such as those to the Moon, Mars and beyond, but it can also become deadly in short periods. When a spacecraft leaves Earth orbit, it can use its engines. However, this is not always necessary because the rocket, gravity slingshot, and monopropellant/bi-propellant attitude control systems provide sufficient initial boost.

We provide an overview of one of the important research topics such as the search for alternative propellants based on this discussion. The technology of ion thrusters, a prominent member of the gridded ion engine family, is the focus of our discussion. Neutralizer concepts from novel insert materials and neutralizer-free propulsion concepts are examined, in addition to aspects of thruster modelling. We also talk about the development of highly efficient electronic components as well as issues relating to electromagnetic compatibility and radiation hardness in relation to space electronics.

V. CONCLUSION

Today's ion propulsion technology enables deep-space science missions to operate. Future planetary missions and beyond will highly depend on board propulsion systems. This will reduce the cost of planning while benefiting science. Deep Space technology has made ion propulsion a legitimate option for deep-space science missions. Future missions to scientifically interesting planets will place significantly greater demands on the propulsion systems onboard than in the past. It is possible to reduce the cost of planetary missions and beyond by using ion propulsion systems.

VI. REFERENCES

- [1]. Prof. K. Holste, P. Dietz, 2020 "Ion thrusters for electric propulsion: Scientific issues developing a niche technology into a game changer" <https://doi.org/10.1063/5.0010134>
- [2]. D. Sagath, A. Papadimitriou, M. Adriaensen, and C. Giannopapa, "Space strategy and governance of ESA small member states," *Acta Astronaut.* 142, 112–120 (2018) Ion thrusters for electric propulsion: Scientific issues developing a niche technology into a game changer: Review of Scientific Instruments: Vol 91, No 6 (scitation.org)
- [3]. Ivan Tchalakov (Department of Applied and Institutional Sociology, Plovdiv University "Paisii Hilendarski", Plovdiv, Bulgaria & Center for Policy Analysis and Studies of Technology, Tomsk State University, Tomsk, Russia) <https://doi.org/10.4018/ijantti.2015010104>
- [4]. GODDARD, R. A Method of Reaching Extreme Altitudes. *Nature* 105, 809811(1920).<https://doi.org/10.1038/105809a0>
- [5]. The technological and commercial expansion of electric propulsion DanLeva Roger M.Myersb Kristina.M.Lemmerc JonathanKolbeckd HiroyukiKoizumie KurtPolzinf in July 2019 <https://doi.org/10.1016/j.actaastro.2019.03.058>
- [6]. Marc.D.RaymanPhilipVargheseDavid H.LehmanLeslie L.Livesay Volume 47, Issues 2–9, July–November(2000), [https://doi.org/10.1016/s0094-5765\(00\)00087-4](https://doi.org/10.1016/s0094-5765(00)00087-4)
- [7]. Jahn, Robert G. (1968). *Physics of Electric Propulsion* (1st ed.). McGraw Hill Book Company. ISBN 978-0070322448. Reprint: Jahn, Robert G. (2006). *Physics of Electric Propulsion*. Dover Publications. ISBN 978-0486450407. Ion thruster - Wikipedia

- [8]. Jahn, Robert G. (1968). *Physics of Electric Propulsion* (1st ed.). McGraw Hill Book Company. ISBN 978-0070322448. Reprint: Jahn, Robert G. (2006). *Physics of Electric Propulsion*. Dover Publications. ISBN 978-0486450407. Ion thruster - Wikipedia
- [9]. Hitoshi kuninaka, Ikko Funaki 2007, powered flight of electron cyclotron resonance ion engine.
- [10]. Kristina M. Lemmer, Jonathan Kolbeck, 2019, the technological and commercial expansion of electric propulsion.
- [11]. David J. Anderson, ohn Dankanich, The NASA In-Space Propulsion Technology Project's Current Products&Future,Directions.<https://www.nasa.gov/centers/glenn/about/fs21grc.html>
- [12]. Sharman, s Holste, 2020, Ion thrusters for electric propulsion: Scientific issues developing a niche technology into a game changer <https://aip.scitation.org/doi/10.1063/5.0010134>
- [13]. Dan M. Goebel's, John K Ziemer, John R Brophy, 2005, *Electric Propulsion Research and Development at JPL* (PDF) *Electric Propulsion Research and Development at JPL* (researchgate.net)
- [14]. Dr. Richard E. Wirz, Aerospace | Special Issue: Electric Propulsion (mdpi.com).
- [15]. Michael G. Houts, Tony Kim, William J. Emrich, Robert R. Hickman, Jeramie Broadway, Harold P. Gerrish, Anthony Belvin, Stanley K. Borowski and John H. Scott the Nuclear Cryogenic Propulsion Stage 25 Jul 2014 <https://doi.org/10.2514/6.2014-3724>.
- [16]. S.Palerma C.Bonhommea Y.Gueloua J.N.Chopineta P.Danousb The future of cryogenic propulsion , (2015), <https://www.sciencedirect.com/science/article/abs/pii/S0094576515000685>.
- [17]. M. Martinez-Sanchez and J. E. Pollard (2012) <https://doi.org/10.2514/2.5331>.
- [18]. Sigma Xi, The Scientific Research Honor Society ELECTRIC PROPULSION (1964) <https://www.jstor.org/stable/27838991>.
- [19]. Stéphane Mazouffre Electric propulsion for satellites and spacecraft: established technologies and novel approaches (2016) <https://iopscience.iop.org/article/10.1088/0963-0252/25/3/033002>
- [20]. Michael Keidar¹, Taisen Zhuang¹, Electric propulsion for small satellites (2014) <https://iopscience.iop.org/article/10.1088/0741-3335/57/1/014005>
- [21]. J.Chem. Phys.Absolute partial cross sections for electron-impact ionization of CO₂ from threshold to 1000 eV. (1996), <https://doi.org/10.1063/1.472275>
- [22]. Patrick Dietz¹, Waldemar Gärtner¹, Quirin Koch¹, Peter E Köhler.Molecular propellants for ion thrusters.6 August 2019, <https://iopscience.iop.org/journal/0963-0252>
- [23]. R F Boivin and S K Srivastava,Electron-impact ionization of Mg, 1998, <https://iopscience.iop.org/journal/0953-4075>
- [24]. P. Chabert,J. Arancibia Monreal,J. Bredin,Global model of a gridded-ion thruster powered by a radiofrequency inductive coil,(2012),<https://doi.org/10.1063/1.4737114>
- [25]. Moscovitch, M. and Winocur, G., Frontal Lobes, Memory, and Aging. *Annals of the New York Academy of Sciences*, 769: 119–150. <https://doi.org/10.1111/j.1749-6632.1995.tb38135.x> (1995)
- [26]. J. Wang, J. Polk, J. Brophy, and I. Katz,Three-Dimensional Particle Simulations of Ion-Optics Plasma Flow and Grid Erosion, (2003), <https://doi.org/10.2514/2.6939>
- [27]. C. A. Barry Stoute and Brendan M.(2015),Design and testing of low-cost miniature ion thruster for nanosatellites <https://doi.org/10.5589/q15-009>

- [28]. Sidhant Singh Solid Rocket Motor for Experimental Sounding Rockets Number 3 (2013) http://www.ripublication.com/aasa/aasav3n3spl_11.pdf
- [29]. T. Miyasaka, T. Kobayashi, and K. Asato, Characteristics of ions impacting grid surfaces in an ion engine, 9 November 2010, <https://doi.org/10.1016/j.vacuum.2010.08.016>
- [30]. Ali Kamran Liang Guozhu March 2012 An integrated approach for optimization of solid rocket motor <https://www.sciencedirect.com/science/article/abs/pii/S1270963811000447>
- [31]. Levchenko, M. Keidar, S. Xu (2018), Recent progress and perspectives of space electric propulsion systems based on smart nanomaterials <https://www.nature.com/articles/s41467-017-02269-7>
- [32]. J. S. Sovey, V. K. Rawlin, and M. J. Patterson, "Ion propulsion development projects in U.S.: Space electric rocket test I too deep space 1," 23 May 2012, <https://doi.org/10.2514/2.5806>
- [33]. K. Nakamura, Y. Nakagawa, H. Koizumi, and Y. Takao, "Numerical analysis of a miniature microwave-discharge ion thruster using water as the propellant," (2018), <https://doi.org/10.2322/tjsass.61.152>
- [34]. Djalal Trache, ORCID logo, Thomas M. Klapötke, ORCID log, Lotfi Maiz, ORCID, Mohamed Abd-Elghany new oxidizers for solid rocket propulsion <https://pubs.rsc.org/en/content/articlelanding/2017/gc/c7gc01928a/unauth>
- [35]. Michael J. Patterson, Matthew T. Domonkos, John E. Foster, Ion Propulsion Development Activities at the NASA Glenn Research Center*†
- [36]. H. C. Straub, P. Renault, B. G. Lindsay, K. A. Smith, and R. F. Stebbings, "Absolute partial and total cross sections for electron-impact ionization of argon from threshold to 1000 eV," (1995), <https://doi.org/10.1103/physreva.52.1115>
- [37]. A. Hemant Kumar Yadav¹, V.V.S. Nikhil Bharadwaj, Kundanam Saikiran, (2014). A Study and Brief Research On Electric propulsion Of Spacecraft and Rockets
- [38]. T. Miyasaka, T. Kobayashi, and K. Asato, "Characteristics of ions impacting grid surfaces in an ion engine," (2010), <https://doi.org/10.1016/j.vacuum.2010.08.016>
- [39]. A. S. Koroteev, A. S. Lovtsov, V. A. Muravlev, M. Y. Selivanov, and A. A. Shagayda, "Development of ion thruster IT-500," (2017), <https://doi.org/10.1140/epjd/e2017-70644-6>
- [40]. I S Vavilov¹, V V Fedynin¹, P S Yachmenev¹, (2020) Review of electric thrusters with low consumption power for corrective propulsion system of small space vehicles <https://iopscience.iop.org/article/10.1088/1742-6596/1546/1/012071>
- [41]. C. Bombardelli, H. Urrutxua, M. Merino, J. Peláez, and E. Ahedo, "The ion beam shepherd: A new concept for asteroid deflection," (2013), <https://doi.org/10.1016/j.actaastro.2012.10.019>
- [42]. R. Killinger, R. Kukies, M. Surauer, A. Tomasetto, and L. van Holtz, "ARTEMIS orbit raising inflight experience with ion propulsion," (2003), [https://doi.org/10.1016/s0094-5765\(03\)80022-x](https://doi.org/10.1016/s0094-5765(03)80022-x)
- [43]. D. Lev, R. M. Myers, K. M. Lemmer, J. Kolbeck, H. Koizumi, and K. Polzin, "The technological and commercial expansion of electric propulsion," (2019), <https://doi.org/10.1016/j.actaastro.2019.03.058>
- [44]. McGraw-Hill, 1964 Ion propulsion for space flight https://scholar.google.co.in/scholar?q=ion+propulsion+research+paper&hl=en&as_sdt=0&as_vis=1&oi=scholar#d=gs_qabs&u=%23p%3DOG4L6YchorUJ

- [45].A. W. Bett, F. Dimroth, G. Stollwerck, and O. V. Sulima, "III-V compounds for solar cell applications," (1999) <https://doi.org/10.1007/s003390050983>
- [46].H. R. Kaufman, "Origin of the electron-bombardment ion thruster," J. Spacecr. Rockets, (1981), <https://doi.org/10.2514/3.28058>
- [47].E. Y. Choueiri, "A critical history of electric propulsion: The first 50 years (1906-1956)," (2004) <https://doi.org/10.2514/1.9245>
- [48].A.Hemant Kumar Yadav¹,V.V.S.Nikhil Bharadwaj² ,Kundanam Saikiran³, (2014)A Study and Brief Research On Electric propulsion Of Spacecraft and Rockets
- [49].Y. Ding, H. Fan, D. Ma et al., "Extending service life of hall thrusters: Recent progress and future challenges," (2019), <https://doi.org/10.1007/s41614-019-0036-y>
- [50].D. J. Kessler, "Collisional cascading: The limits of population growth in low earth orbit," (1991), [https://doi.org/10.1016/0273-1177\(91\)90543-s](https://doi.org/10.1016/0273-1177(91)90543-s)



Detection of Cyber Threats Using Machine Learning

Naveen T. H¹, Sudhakar K. N²

¹Department of Computer Science & Engineering, Government Engineering College, K R Pet, Mandya,
Karnataka, India

²Department of Information Science & Engineering, CMR Institute of Technology, Bengaluru, Karnataka, India

ABSTRACT

Explosive growth of digital transactions, usage of social media and weak human psychology of getting attracted to false news leading invites a huge threat to humanity effecting financially and mentally. To counter these effects on humanity, cyber security is a need of the time. Its necessary to counter the frauds. When ever a security breach is planted, study of threat patterns helps us to identify the possible breach. Countering the treats is time bound, hence physical systems may fail if the patterns are missed while analyzing. Hence, Machine Learning has a wider landscape with advance features. In our work, we propose a method to classify the traces of malware to predict the possible cyber threat.

Keywords: Machine Learning, cyber security, k- means, Random Forest, SVM.

I. INTRODUCTION

The data is generated in abundance by various platforms. Numerous mechanisms are derived to extract Information and on classification, time critical information can be mined. Such mined information can be misused effecting modern society also effecting trust on the existing system. Due to various reasons, companies are adopting cloud based work culture where the complete company assets are over Internet. Internet being public platform, securing these services from public becomes a mission critical agenda for cloud service providers. Evolution of Internet of Things (IoT) and the dependance of public over these applications are growing day by day. As the devices utilized in IoT are small in size, they are manufactured with numerous security flaws which act as exploits. These exploits pose a threats and misused by miscreants. Identifying these exploits itself is critical tasks. Some of the exploits are know only when its been breached or misused for self benefit causing unexpected lows to the society. Finding exploits, tracing the fingerprints of the breached exploits are the current research problem. Most of the solutions derived to tackle exploits are reactive derived over known attack signatures. In this process many new exploits whose signatures does not match with existing go unnoticed. By the time it is identified, damage would have been registered. To address the unnoticed threats, the signature patterns of malware and malicious software behavior is considering to build semi supervised environment. To achieve this process in the existing condition, machine learning (ML) methods are the need of

the day. ML methods can adopt supervised and unsupervised learning for detecting unnoticed threats and adopt the new findings in the future threat prediction.

II. LITERATURE SURVEY

Kozil, et.al [12] has proposed a method to balanced self learning method to detect cyber attacks. The proposed method addresses the problem of data imbalance. In the proposed framework malware behavior is monitored throughout and its influence in data manipulation is observed.

Ployphan, et.al [13] in his research, considered feature similarity correlation of malware behaviour as a constrain and proposed a hybrid method using Machine learning based on adoptive boosting. Multiple classifiers are considered to identify the irrelevant features to narrowing down to relevant features causing threat.

Javier Martinez Torres, et.al [14] in their work elaborated on using ML techniques in the domain of cyber security for find the threat signatures. As ML is based on mathematical models, it can solve wide spectrum of complex problems which include classification, predicting correlation between certain derived patterns and many more.

Thangavel M et.al [15] have elaborated over the effective usage of ML and Deep Learning (DL) mathematical models in the field of Cyber Security. Models elaborated can be utilized to process the threat signatures and predict the possible patterns which may signify a possible pattern for cyber threat.

III. METHODOLOGY

To work on, we are in need of Network Traffic data for analysis. For the said purpose, we can get the network traffic data form know institutions or organisations having signs of cyber attack and filter network flows for study. To achieve the same we can opt for public domain datasets to training the system. Popular datasets like CTU-13 (CTU University 2011), KDDCUP993 and CIC-IDS-20174 can be used for the said purpose. In our study, we have opted fo CTU-13 dataset for various reasons in which one of them being wider acceptance of it by research community working in similar problem domains. Dataset usage process is depicted in Figure 01. From the dataset, we filter common features and pattern frequencies for statistical analysis. The attribute in the NetFlow include, StartTime, Duration, Protocol, Source Address, Destination Address and many more These attributes signify the purpose and helps us in classification.

Once we have selected a dataset, the very important part of our project is to identify and extract the features. We then pre-process to extract categorical and numerical characteristics from the bidirectional NetFlow dataset within the given time window. To reduce the training matrix dimension, we use the feature selection techniques. We need to use three different types of machine learning algorithms (like Logistic Regression, Support Vector Machine (SVM), Random Forest Classifier) for comparison. Three different machine learning models created and compare to get accuracy of each. After completion of training the model is tested with test dataset. After successful training and testing our system would be ready for prediction. We have designed a GUI with help of Streamlit module for better user understanding. Complete process can be visualized in the same

platform. When user gives the input our GUI will pass the data to back-end python code and data will be processed. After pre-processing data will be compared with trained model and output will be predicted. This predicted output includes (time, attackers ip, and attack details) will be shown on the user interface.

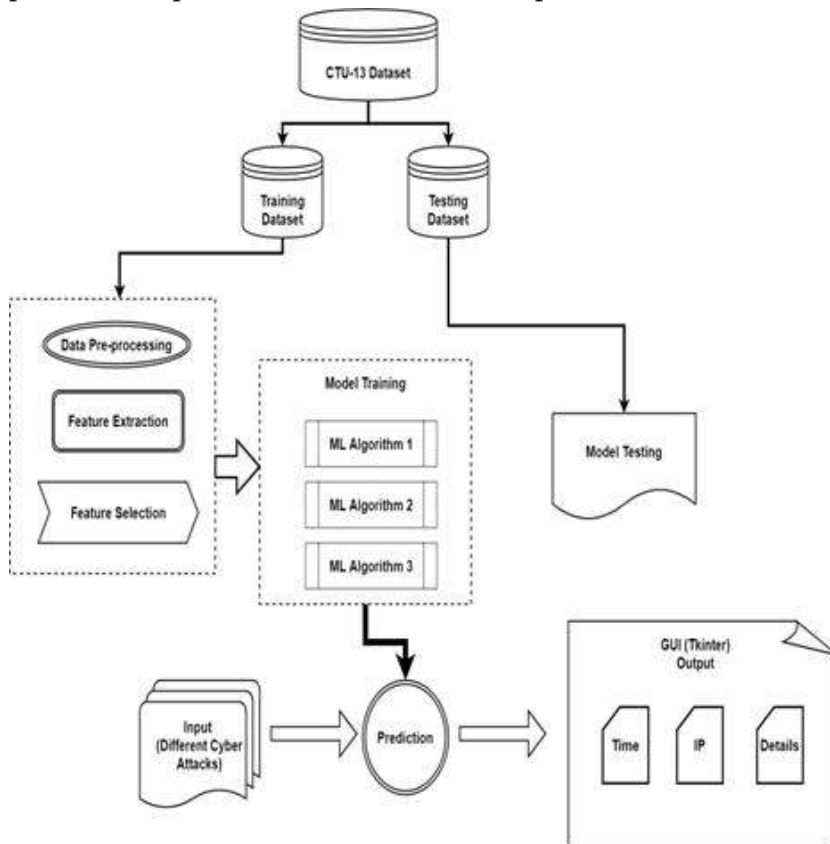


Figure 01: Dataset refinement process and feature extraction

IV. ARCHITECTURE

SYSTEM DESIGN

Figure 02 depicts the system architecture and flow used in the threat prediction process.

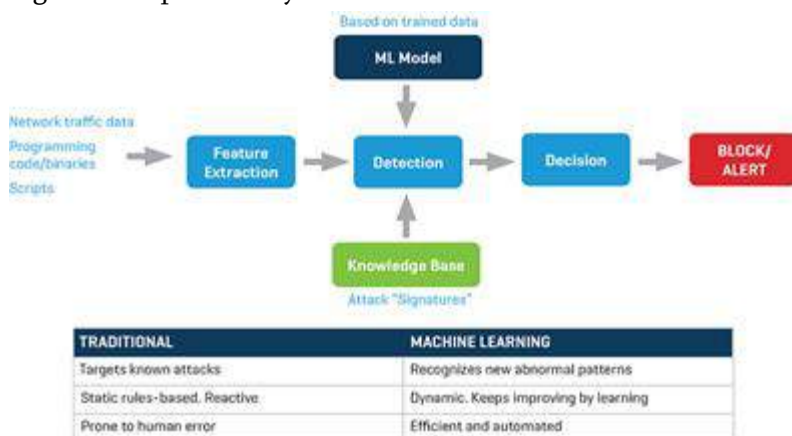


Figure 02: System architecture

V. RESULTS

We have tested our project with different aspects in the built platform. Data is process at the backend by python code. GUI frontend and python backend provides a visual platform for threat analysis and prediction. The predictions can be visualized on the front-end which includes attack types, time and ip address. In the current implementation, system detects threats based on used datasets that it is trained upon. Currently the system detects DDOS, Phishing by known constraints with 96- 98% accuracy. Same is displayed as graphical representation over the front-end.

VI. CONCLUSION

In our work, we were able to extract relevant features which match signatures of botnet from the NetFlow dataset. We used Logistic Regression, Support Vector Machine, Random Forest, Gradient Boosting and a Dense Neural Network ML models in our analysis in which found Random forest classifier was out performing in detecting botnets in all the possible scenarios. For the opted test cases, Random forest classifier had a detection accuracy near to 95%. As our work is limited to test dataset with limited parameter. In our further work we are planning to extend in the size of parameters signifying different attack scenarios and also test on the real time network traffic to check if the prediction is justifiable.

VII. REFERENCES

- [1]. I. S. Consortium. ISC Internet Domain Survey.2017.url: <tps://www.isc.org/network/survey> (visited on 22/12/2017) (cit. on p. 1).
- [2]. A. Nordrum. Popular Internet of Things Forecast of 50 Billion Devices by 2020 Is Outdated.2016 url: <https://spectrum.ieee.org/tech-talk/telecom/internet/popular-internet-of-things-forecast-of-50-billion-devices-by-2020-is-outdated> (visited on 22/12/2017) (cit. on p. 1).
- [3]. E. de Argaez. Internet World Stats. 2017. url: <http://www.internetworldstats.com> (visited on 22/12/2017) (cit. on p. 1).
- [4]. Statista. Global number of cyber security incidents from 2009 to 2015 (in millions). 2015. url: <https://www.statista.com/statistics/387857/number-cyber-security-incidents-worldwide> (visited on 22/12/2017) (cit. on p. 1).
- [5]. J. Mchugh. "Intrusion and Intrusion Detection". In: Int. J. Inf. Secur. 1.1 (Aug. 2001), pp. 14–35. issn: 1615-5262 (cit. on pp. 1, 2).
- [6]. J. Mirkovic et al. Internet Denial of Service: Attack and Defense Mechanisms (Radia Perlman Computer Networking and Security). Upper Saddle River, NJ, USA: Prentice Hall PTR, 2004. isbn: 0131475738 (cit. on p. 1).
- [7]. T. Holz. "A Short Visit to the Bot Zoo". In: IEEE Security and Privacy 3.3 (May 2005), pp. 76–79. issn: 1540-7993 (cit. on p. 1).

- [8]. NIST. NIST Information Technology Laboratory - National Vulnerability Database. 2017. url: <https://nvd.nist.gov> (visited on 22/10/2017) (cit. on p. 1).
- [9]. G. Wurster and P. C. van Oorschot. "The Developer is the Enemy". In: Proceedings of the 2008 New Security Paradigms Workshop. NSPW '08. Lake Tahoe, California, USA: ACM, 2008, pp. 89–97. isbn: 978-1-60558-341-9 (cit. on p. 2).
- [10]. Symantec. ISTR - Living the land and fileless attack techniques. 2017. url: <https://www.symantec.com/content/dam/symantec/docs/security-center/white-papers/istr-living-off-the-land-and-fileless-attack-techniques-en.pdf> (visited on 22/10/2017) (cit. on p. 2).
- [11]. B. Bashari R., M. Masrom and S. Ibrahim. "Camouflage In Malware: From Encryption To Metamorphism". In: International Journal of Computer Science And Network Security.
- [12]. Kozik Rafal, Michal Choras, and Jorg Keller, "Balanced Efficient Lifelong Learning (B-ELLA) for Cyber Attack Detection" Journal of Universal Computer Science 25 (2019)
- [13]. Ployphan Sornsuwit, Saichon Jaiyen, "A New Hybrid Machine Learning for Cybersecurity Threat Detection Based on Adaptive Boosting" Applied Artificial Intelligence, An International Journal Volume 33, 2019 - Issue 5
- [14]. Javier Martinez Torres, Carla Iglesias Comesafia, Paulino J Garcia-Nieto, [103]" International Journal of Machine Learning and Cybernetics, 2019, 10:2823-2836 <https://doi.org/10.1007/s13042-018-00906-1>
- [15]. Thangavel M, Abiramie Shree T. G, Priyadarshini P, Saranya T, Book chapter "Review on Machine and Deep Learning Applications for Cyber Security", 2020, DOI: 10.4018/978-1-5225-9611-0.ch003



Review of Cloud Computing Security on Amazon Web Service

Monika B A¹, Jeethendra S R¹, Prof. Annaiah H²

¹Student, Department of CSE, GEC, Hassan, Karnataka, India

²Department of CSE, Government Engineering College, Hassan, Karnataka, India

ABSTRACT

Cloud Computing is a recently emerged model which is becoming popular among almost all enterprises. It involves the concept of on demand services which means using the cloud resources on demand and we can scale the resources as per demand. Cloud computing undoubtedly provides unending benefits and is a cost-effective model.

The major concern in this model is Security in cloud. This is the reason of many enterprises of not preferring the cloud computing. This paper provides the review of security research in the field of cloud security. After security research we have presented the working of AWS (Amazon Web Service) cloud computing.

AWS is the most trusted provider of cloud computing which not only provides the excellent cloud security but also provides excellent cloud services. The main aim of this paper is to make cloud computing security as a core operation and not an add on operation.

Keywords: Cloud Computing, Trusted Computing, Information Centric Security, Amazon Web Service.

I. INTRODUCTION

The word “cloud” was used by Google’s CEO Eric Schmidt to describe the business model of providing services across the internet in 2006. To state various ideas the term cloud was used as marketing term. Classification of clouds is done as public, private and hybrid. Services of three types are offered by cloud providers are Platform as a Service (PaaS), Software as a Service (SaaS) and Infrastructure as a Service (IaaS) Cloud computing has a focus on maximizing effectiveness of the shared assets.

Cloud computing have certain features like they are agile, have reduced cost, easier maintenance, reliable, secure, scalable, etc Cloud computing involves communication over a loose coupling mechanism which involves multiple cloud components.

Certain security issues faced by cloud computing include sensitive data access, data segregation, privacy, authentication, bug exploitation, recovery, accountability, account control

II. CLOUD COMPUTING

It is one of the approaching IT industry murmured words- the users move their applications and data to the remote cloud so that they can have a simple and pervasive way of accessing. Clouds are categorized in two ways:

1. On the basis of location of cloud computing.
 - 1) On the basis of location of cloud computing.
 - a) **Private Cloud:** These are allocated to a particular organization and are not divided among any specific firm. Private clouds have higher cost and security in comparison to public clouds. Further types of private clouds are private clouds and externally hosted private clouds.
 - b) **Public Cloud:** In public cloud, at the vendor's premises the computing infrastructure is hosted by the traders of the cloud. The user has no clarity and control hosted by the computing framework. The computing foundation is shared between with some companies
 - c) **Hybrid Cloud:** This type of clouds is cost-effective and scalable. When we combine the use of public and private clouds together it is called as hybrid cloud. This aims in minimizing change.
 - 2) On the basis of type of services offered.
 - a) **Infrastructure as a Service (IaaS):** Using the principles of cloud computing, services related to hardware are offered. These include storage services or virtual servers.
 - b) **Platform as a Service (PaaS):** Development platform on the cloud is offered by them. Distinct vendors provide platform that are not consistent.
 - c) **Software as a Service (SaaS):** Complete software services are offered on the cloud. Software application can be accessed by the users hosted by the cloud vendor on the basis of paying as per use. The nomenclature of cloud computing consists of a part which is known as Software as a favour.

III. SECURITY IN CLOUD COMPUTING

Cloud computing undoubtedly provides very good service to the user but still many organizations do not support cloud computing because of the security issues. The main security issues are data security and privacy protection. These security issues hinders the managers or customer to support the services provided by cloud computing. This is the reason why cloud computing not gaining the expected market size. Cloud security is the responsibility of both the cloud provider and cloud consumer. There should be the relationship of trust between them before availing any cloud service.

It is the responsibility of management to take care of security risk so as to protect data. There are many risks associated with the cloud computing. Some of them are: Security, service providers, Management and Control, Laws and regulation, virtualization risks, lack of standards and auditing, uncontrolled viable cost etc. The risk which is of most concern is Security.

Cloud computing is the just the virtual environment for the customer who are using the cloud services in which he will give its data to the cloud without knowing even the location of the data. The data can be there with thousands of other data on the cloud. So the most important facilities that storage provider should provide is Confidentiality, Integrity and Availability (CIA). A model should be developed that promotes CIA. CIA can be provided by –encrypting the data, access control to prevent unauthorized user to access data and scheduled back up should be there to ensure availability.

IV. SECURITY RESEARCH

In order to tackle the security issues in cloud there is a need of some research in this area so as to provide security in the cloud computing and attracting more number of users so as to save the resources and time.

The models of security research are:

- a) **Trusted computing**
- b) **Information Centric Security [ICS].**

a) **Trusted computing:**

TC system was considered to be very important because data security is considered to be the core operation and not the add-on operation. TC system encrypts the data and application and gives the decryption key to the trusted program and information. Nowadays manufacturers provide the TC services in the computers by adding some new hardware to the computers.

b) **Information Centric Security [ICS].**

ICS architecture is made of 4 services arranged horizontally and not vertically.

The 4 services are.

- a) **Storage infrastructure services**
- b) **Data services**
- c) **Management services**
- d) **Access services**

The architecture of Information centric security protects the information by monitoring and enforcing the policies of security or privacy. The individuals who are dispersed all over can now share their documents securely. The documents now contain security rules with them so that whenever there are logs capture activities then the security policies are enforced. ICS architecture is responsible for controlling, monitoring and enforcing thesecurity over the confidential documents.

1. Access Service	a. Authentication b. Authorization
2. Management Service	a. Key Management b. Policy Management c. Monitoring d. Reporting
3. Data Service	a. Discovery b. Classification c. Data Modeling d. Data Mapping e. Meta data repository
4. Storage Infrastructure Service	a. Secure Storage Network b. Secure Storage Partitioning c. Cryptographic Processing d. ILM Services e. Infrastructure services

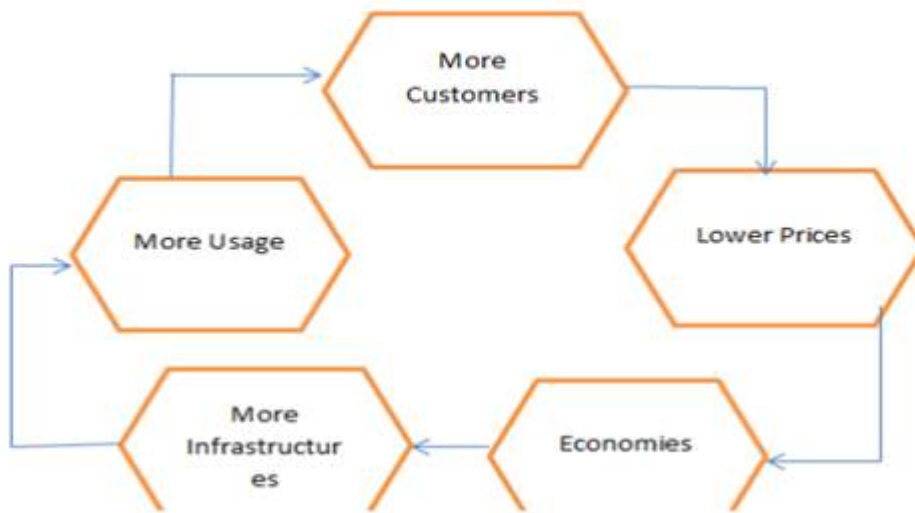
V. AWS (AMAZON WEB SERVICE)

AWS is the cloud computing provider. This service is a perfect example of true cloud computing which not only provides excellent cloud services but also provides confidentiality; integrity and availability of the customer's data. AWS give the ondemand services. The IT resources are available at cheap prices and no upfront investment is required for the resources. The customer just has to pay for the resources that he consumes on variable basis.

Another benefit of AWS is it makes the work easier and faster. With traditional architecture it was difficult to develop the application as it takes lot of time to get a server. But with AWS cloud computing one can deploy hundreds or thousands of servers without any delay. Hence AWS allows quick development and deployment of an application and hence it allows the team to experiment more frequently.

AWS not only provide resources to develop an application but also helps in deploying the application globally at minimum cost. Traditionally it was difficult for a company to provide performance to the distributed users so they concentrate on only single geographical region at a time. But with the help of AWS this problem was solved and now one can deploy its application all around the world and provide better experience for customers. AWS provides wide range of cloud computing services that helps in development of a sophisticated application.

AMAZON'S STRATEGY



VI. AWS SECURITY PROCESS

For AWS, Confidentiality, Integrity, and Availability (CIA) of the user's data is most important task. The aim of AWS is to maintain the customer confidence and trust.

a) AWS infrastructure:

AWS infrastructure contains hardware, operational software, security standards, network and other important facilities. High level security is there during the physical access of AWS data centers. Professional security staff is hired for data security. Visitors or contractors have to present their identification which is signed by authorized staff and are allowed to access if they have business needs

The environment of the data centers is controlled

- a) Automatic fire detection and suppression equipment to reduce risk.
- b) 24*7 Uninterrupted Power Supply.
- c) Climate control is there in order to maintain the temperature for working of servers and other hardware
- d) All equipment is managed, so if any issue is raised then it should be immediately identified.

b) Network Security:

AWS has an outstanding network security which is properly controlled and managed. Following are the reasons for the world class network architecture of AWS:

a) Secure Network Architecture

Secure Network Architecture is attained by the network devices such as firewall which manages and controls the boundary of network. Traffic flow policies, access control list (ACL), is generated to control the flow of informational is approved by Amazon Information Security

b) Secure Access Points

Secure Access Point indicates that AWS has limited number of access points so as to perform proper monitoring of communication. The access points of customers are called API endpoints.

c) Transmission Protection

One can make connection to the AWS access point via HTTPS using SSL (Secure Socket Layer) protocol. This protocol provides many security services like protection against message forgery, tampering etc

d) Amazon Corporate Segregation

The developer or manager cannot directly access the network devices even for maintenance. They need to access through AWS ticketing system.

e) Fault Tolerant Design

AWS has provision of storing data with multiple geographical regions with each region having independent failure zone

f) Network monitoring and Protection

AWS has a world class monitoring and control system as it has automated monitoring system which automatically detects the defects; any unauthorized access or any unusual activity.

VII. CONCLUSION

Cloud Computing undoubtedly provides many services and has uncounted advantages but still there are many problems that still exists and need to be solved to increase the market of such a world class technology. The concern in the cloud computing is SECURITY around data, access and privacy protection. Cloud computing should be secure and robust and should mitigate the risks. According to the analysis of cloud computing it was found that security should be the core operation rather than an add on operation. AWS (Amazon Web Service) has an outstanding performance in cloud computing because of its excellent work in the area of Security of data. Some of work of the AWS is a) Providing network security b) Build real time sliding window dashboard over streaming data c) AWS for Disaster Recovery (DR). d) Security at scale: logging in AWS. e) Securing data with encryption f) Backup and Recovery approach These security services provided by AWS are the reason that customers have faith in its services. So building trust by providing security services should be the main aim of cloud computing

VIII. REFERENCES

- [1]. Qi Zhang, Lu Cheng, Raouf Boutaba. Cloud Computing: State-of-the-art and research challenges. J Internet Serv Appl (2010).
- [2]. Rabi Prasad Padhy, Manas Ranjan Patra, Suresh Chandra Satyapathy. Cloud Computing: Security Issues and Research Challenges. IJCSITS Vol. 1, No. 2, December 2011.
- [3]. Meiko Jensen, Jorg Sehwenk et al. "On Technical Security Issues in Cloud Computing". IEEE International Conference on Cloud Computing, pp 109-116, October 2009.

- [4]. Shubhashis Sengupta, Vikrant Kaulgud, VibhuSaujanya Sharma. Cloud Computing SecurityTrends and Research Directions. 2011 IEEE World Congree on Services.
- [5]. Mariana Carroll, Alta van der Merwe, Paula Kotze. Secure Cloud Computing. Benefits, Risks and Controls. 2011 IEEE.
- [6]. Deyan Chen, Hong Zhao. Data Security and Privacy Protection Issues in Cloud Computing. 2012 International Conference on Computer Science and Electronics Engineering. 2012 IEEE.
- [7]. Akhil Behl, Kanika Behl. An analysis of Cloud Computing Security Issues. 2012 IEEE
- [8]. Amreen Khan and KamalKantAhirwar. Mobile Cloud Computing as a Future of Mobile Multimedia Database. IJCSC, Vol. 2,No. 1, January-June 2011, pp. 219-221.
- [9]. John Harauz, Lori M. Kaufman, Bruce Potter. Data Security in the World of Cloud Computing. IEEE July/August 2009.



Review on RDPC : Secure Cloud Storage with Duplication Technique

Ashwathnarayan¹, Rachitha M¹, Prof. Annaiah H²

¹Student, Department of CSE, GEC, Hassan, Karnataka, India

²Department of CSE, Government Engineering College, Hassan, Karnataka, India

ABSTRACT

Cloud storage offers user scalable, flexible and high quality data storage and computation services. The meaning of cloud storage is "the storage of data online in the cloud". Different companies store their data access data from many different and connected resources that comprise a cloud. Once the owner of the data transfers the data to the cloud storage server, he removes its copy from local machine, thereafter owner will not be able to access the data locally. In this situation, primary issues are integrity and confidentiality of the data transferred. The regular issue is Data Loss Leakage, cloud providers are not trustworthy. Hence for enhancing service RDPC protocol was proposed by Chen et al. Third party auditor checks the user's data correctness and also verifies the accuracy of the data that is stored in the cloud server and this reduces the burden of cloud user. RDPC supplies a method for data owner to efficiently verify whether cloud service provider faithfully stores the original files without retrieving it. And Deduplication technique is stored in cloud storage is already exist at cloud server or not. This framework is effective and secure.

I. INTRODUCTION

to MHT is used to find the location of each data operation in RDPC protocol, it allow the third party auditor (TPA) to check the integrity of outsourced data. The scheme allows unlimited times verification and also verifies accuracy of the data that is stored in the cloud server and this reduces the burden of cloud server.

A data compression technique which eliminates duplicate copies of data blocks or files in storage is known as Data deduplication. No need to check whether the content or file is stored previously in cloud. The system will check duplicate data available and notify to the user.

The review paper discussed about the working of RDPC protocol on cloud domain for securing the data.

II. REFERENCES

- [1]. M amdaqa, M., & Tahvildari, L. (2012). Cloud Computing Uncovered: A Research Landscape. H. Ali & M. Atif (Eds.), Advances in Computers Elsevier. 41–85.
- [2]. Wang W., Zeng, G., Yao, J. (2012). Cloud-DLS: Dynamic trusted scheduling for cloud computing original research article. Expert Systems with Applications, 39(3), 2321-2329

- [3]. Chen, L., Zhou, S., Huang, X., Xu, L. (2013). Data dynamics for remote data possession checking in cloud storage. *Computers and Electrical Engineering*, 39, 2413-2424.
- [4]. Secure auditing and deduplication for encrypted cloud data supporting ownership modification. *Soft Comput.*, 1–18 Bellare,
- [5]. Novel Efficient Remote Data Possession Checking Protocol in Cloud Storage P. PAVANI1 , DR. E. KESAVULU REDDY2
- [6]. R. Buyya, C. S. Yeo, S. Venugopal, J. Broberg, and I. Brandic, "Cloud computing and emerging IT platforms: Vision, hype, and reality for delivering computing as the 5th utility," *Future Gener. Comp. Sy.*, vol. 25, no. 6, pp. 599 – 616, 2009.



A Smart Stick : Senior Citizen's Friend

Dr. Shivashankara S¹

¹Department of Computer Science & Engineering, Government Engineering College, Krishnarajapet, Karnataka, India

ABSTRACT

From the beginning of human history, people are suffering from many kinds of disabilities. One of the major disabilities is senior citizen's mobility problem. This leads many severe problems to the senior citizens to carryout daily regular activities. Many senior citizens uses the walking stick as their helping tool / device for avoiding several problems like weakness in legs and loss in balance. These problems causes them to fall incidents, which increases the various elderly injuries, and sometime leads to death. Despite awareness of these, there is a scarcity of information on effective and acceptable mediation in India. Many victims depends on a walking stick (cane) for support the senior citizens in their walking. There can be decrease in the severity of injury by being ready with medical aid quicker for the senior citizens who might fall in several cases. In modern era where mobiles, laptops and many other electronics have become an important factor in everyone's life, one might indulge too much into it such that they forget to take care of senior citizens. Even in earlier generations there were cases where the senior citizens were ignored. For this major reason, In this paper, author has proposed a smart walking stick which is helpful for senior citizens for walking and also at the same time one can monitor senior citizen's health condition. Unlike visually impaired people's electronic walking stick, can detect the obstacles and alerts the user with the many features embedded in the smart stick. The proposed smart stick can monitors the pulse rate, measures the body temperature, detect if the people using it takes a fall, user's location. This smart stick alerts the family members or caretakers by sending alert messages related to the person's health issue or any other emergency. In case of emergency situations, it is also provided with an emergency button. The proposed smart stick yields an accuracy of 92.5%.

Keywords: Fall Detection, Health Monitoring, IOT, Location Tracking, Smart Stick, Walking Stick

I. INTRODUCTION

In most of the countries of the world, the life anticipation has increased dramatically in last decades. Due to the advancements in the medical science, diagnostic technology and increase in awareness of diseases, an improvement may be achieved in the health of human beings. With the speeded-up population, a huge interest in development of resolutions to the senior citizens assistance. IOT is a recent technology, which fully modifying our day-to-day life and it prospects to overturn current health care by sanctioning a much

individualized, preventative and cooperative form of care. The concept of IOT has a achievable for giving growth to most of the health check applications like health monitoring remotely, personal fitness and health, also paediatric and senior citizen care. With these comprehensive range of applications, the senior citizens health care, called Ambient Assisted Living (AAL), is appealing special attraction, because of the unexpected speedup of world population. These kinds of solutions will be very helpful in village places, in which the count and existence of exigency group with right response is poor sometimes. For senior citizens, walking stick is used for help in walk, also guide for maintaining balance and reduces the fall risk. For helping the senior citizens, an appropriate tool/device is necessary for walking in both indoor and outdoor without taking the help from others with more confidence.

With the intention of helping senior citizens for better living, a concept of wireless IOT based solution, which is capable of monitoring and collecting crucial data of the user, making it obtainable for the concerned well-wishers / caretaker is implemented. Also, this smart stick reads the various health parameters of walking stick owner. These collected information is sent to the monitor system of the well-wishers / caretaker. It triggers the alerts in exigency conditions like falling suddenly, heart rate abnormal, temperature of the body. The smart stick is much effective to the people suffering from Alzheimer's sickness. This is because of the GPS is compartment in the walking stick and caretakers can monitor the accurate locality. Also, this smart stick is incorporated with exigency buttons for lighting torch, alert the caretaker. This device is unique as its easy fundamental interaction and segregation with networks which are IOT-enabled, low-cost and provides most essential services for other related devices.

The organization of this article is as follows. Section 2 provides the methodology of the proposed work. In Section 3, presents the modelling and analysis of the work. Section 4 provides the results and discussion of the proposed work. Finally conclusive remarks and the future perspective of the proposed work is presented in section 5.

II. METHODOLOGY

The proposed smart stick development system consists of many components which are illustrated in the architecture shown in figure 1. This employs the user interface of the sensor with the patient which is in turn integrated with the Walking stick. It is attached to NodeMCU module and Arduino device. The collected information from the sensor is displayed in "Blynk" mobile app and the same can be accessed by the well-wishers/caretakers.

A. Smart Health Monitoring:

The smart health monitoring system consists of Arduino, 'Blynk' mobile application, NodeMCU module and physiological sensors., Arduino device is used as controller and NodeMCU module is used for communication. The pulse sensor is using for collecting the various physiological signals and also the sensitive temperature sensor is using to measure the body temperature. From all the various sensors described below, the various data reading are collected and the same are displayed on the Blynk mobile app by using Arduino device and ESP8266 module.

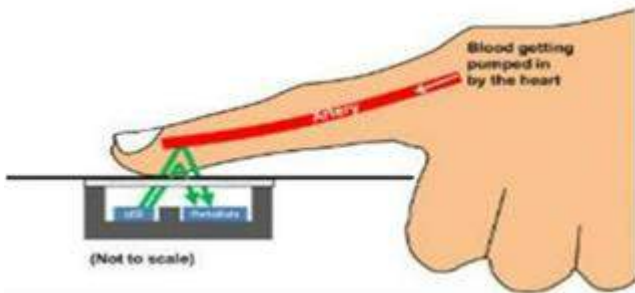
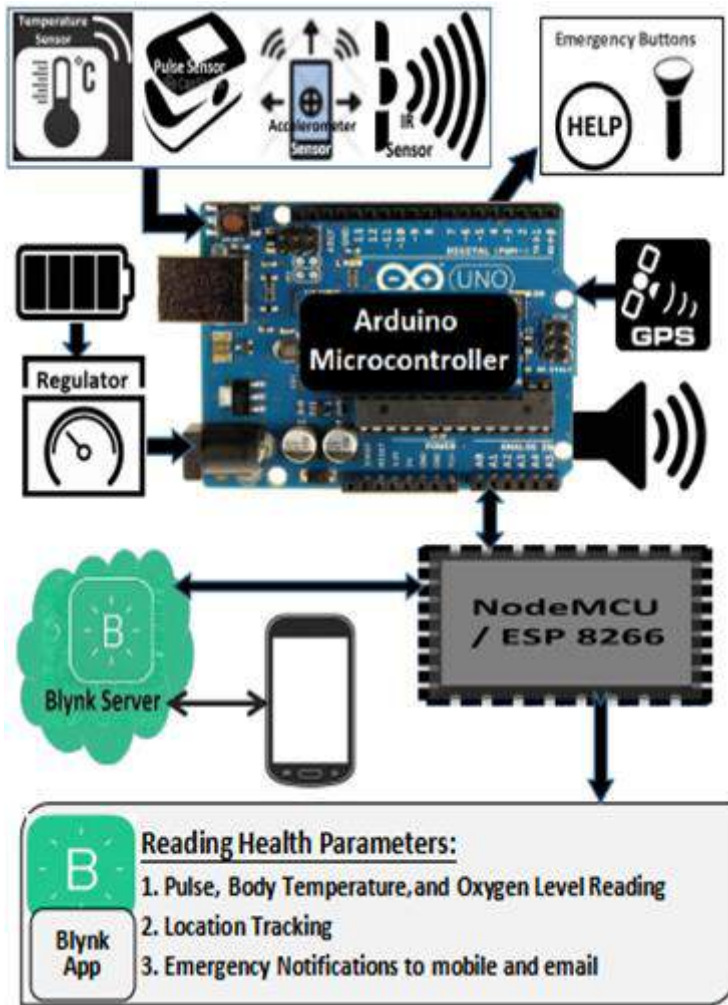


Figure 1: Block Diagram of Proposed System

B. Pulse Rate Monitoring:

Pulse Rate Monitoring System consists of a basic pulse rate sensor, which has a Light-Emitting Diode (LED) and a photo-diode or a light detecting resistor. The heart-beat pulses drives variance in the blood flow and indifferent parts of the human body. This is taken as an analog input in the monitoring system. Figure 2 shows the working of pulse sensor of the system

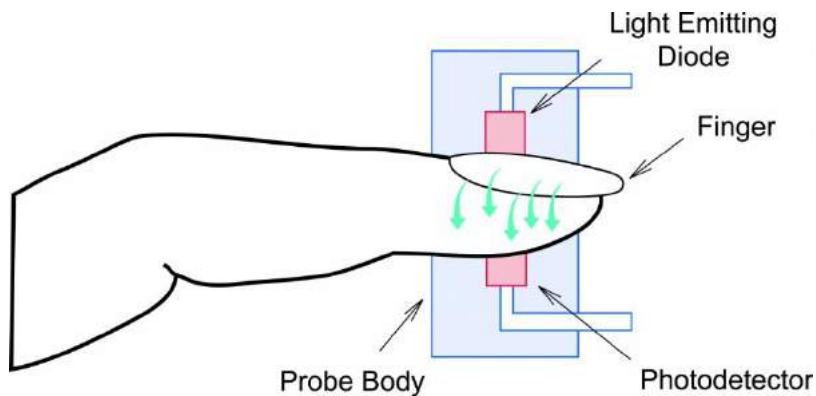


Figure 2. Working of Pulse Sensor

C. Body Temperature Measurement System:

The human body Temperature can be measured using Negative Temperature Coefficient (NTC) temperature sensor. The NTC thermistors are the resistors with a Negative Temperature Coefficient. Here, if the body temperature increases, then the resistance decreases. The sensitivity coefficient of the temperature is around 5X (five times) higher than the Silicon Temperature Sensors (STs) and 10X (ten times) higher than the Resistance Temperature Detectors (RTDs).

D. Fall Detection Sensor:

Accelerometer is a sensor, which can be used for detecting sudden fall. As this sensor provides the acceleration in three axes and an amplified output is produced from these three acceleration values in x, y and z axes. This amplified output value is compared with the threshold value. If the amplified output value crosses this threshold value, then the fall detection is produced. Finally the fall alert message will be send to the well-wishers/caretakers.

E. Location Tracking System:

Global Positioning System (GPS) module is used for tracking the live location of the user. This GPS feature is very much necessary in the system and same has been added because there is a chance that the senior citizens may get lost sometimes somewhere. So that, this location tracking system will be very helpful for the well-wishers/caretakers to know the exact live location of user through the mobile phone.

F. Giving Alert Messages:

There may be an emergency situation/condition like sudden fall or there is a disruption in heart rate or any such related situations. In such kind of situations, the well-wishers/caretakers will receive the alert message or notification to the their registered mobile phone on both 'Blynk' mobile app and to their registered email.

III. MODELLING AND ANALYSIS

The proposed system consists of both various hardware and software parts. In hardware category, the proposed system has various sensors and in software category, it has two softwares such as Arduino and 'Blynk' app. The proposed smart stick system consists of various components which are discussed in the following sub-sections.

A. Arduino Mega 2560:

Arduino is a kind of microcontroller, which is used for collecting the data/information read by the various sensors. These data/information is processed and carryout the appropriate actions based on the processed data. These collected data is also transferred serially to the NodeMCU where further processing of data will be carriedout.

B. NodeMCU:

It is a wireless module, integrated with the Arduino for transferring the data which is received from the microcontroller to 'Blynk' server. This data will be displayed in 'Blynk' app and it also generates the distinctive alert messages based on if any processed data crosses any of the threshold as already set.

C. Pulse Oxymeter:

Pulse Oxymeter one of the sensor, which is used for measuring the heart rate and the oxygen level in blood. It is one of the important and very usefull device in the proposed system. The working of pulse oxymeter is shown in Figure 3.

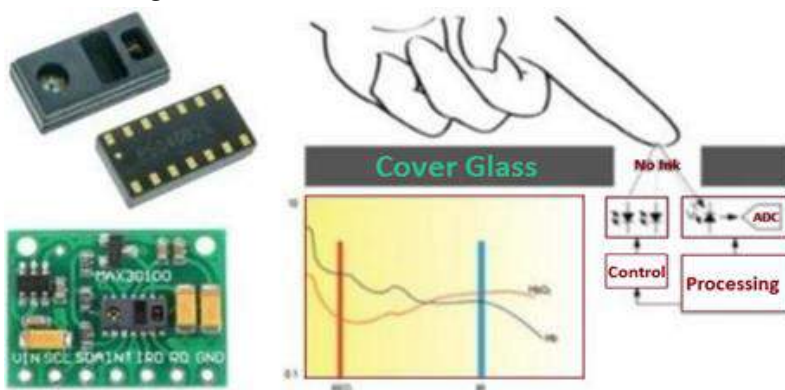


Figure 3: Pulse Oxymeter Working

D. Accelerometer:

Accelerometer is an another kind of sensor, which can be used to the fall detection. The feature fall detection needs the data from accelerometer sensor which gives acceleration in all the three axes x, y and z. From this acceleration, an amplified output value will be generated which will be compared with the threshold value for detecting sudden fall of the person and finally alert messages will be sent to the concerned person.

E. NTC Thermistor:

The NTC Thermistor is a sensor, used for measuring the body temperature. The temperature sensitivity coefficient is approximately 5X (five times) higher compared to STs and also about 10X (ten times) higher compared to RTDs. These NTC thermistor sensors are generally using between the -55°C to 200°C range.

F. GPS Module:

GPS is used to track or record the accurate live location of the person. In this Smart Stick system, by using **ublox NEO-6M GPS module** to track the live location of the user. This module acts as a receiver and the received data from satellite is sent to the 'Blynk' app through the 'NodeMCU' wireless module. The working of GPS is based on the principle of Triangulation, which is shown in figure 4. The GPS satellites communicates minimum of two low-power radio signals.

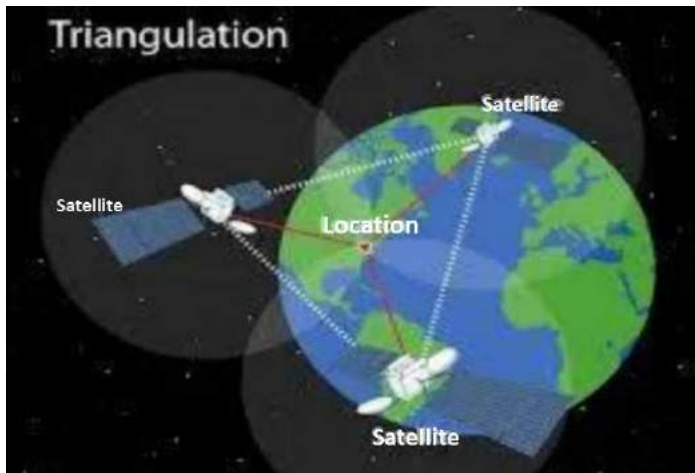


Figure 4: Location Tracking using GPS satellites

G. 'Blynk' app and Arduino Software:

The Arduino software coding is used for microcontrollers where reading data and processing of data is carried out. The collected data is successfully transmitted serially to the NodeMCU module for further processing. This NodeMCU module data is later transmitted to the 'Blynk' Server from where the data will be displayed in 'Blynk' mobile app as per the Graphical Use Interface (GUI) set by the user in the mobile app.

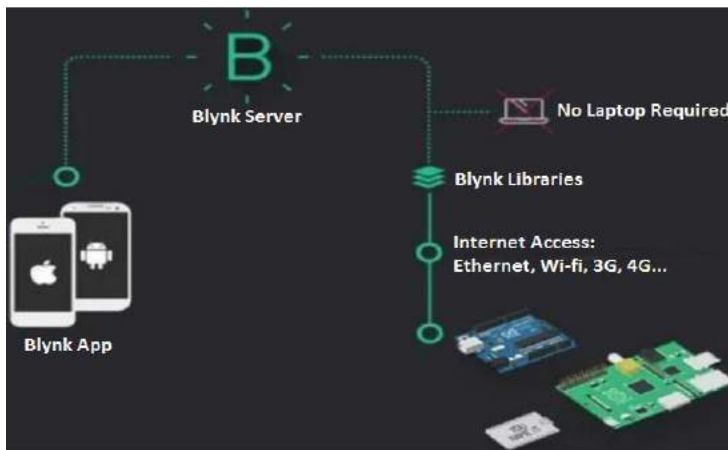


Figure 5: Blynk Working

IV. RESULTS AND DISCUSSION

In every research work, after carried out, it is very much necessary for evaluating and discussing the results of the research work. Following paragraph describes the results and discussion of this proposed work.

The simple and precise circuit of the the proposed work is illustrated in figure 6. This includes the various sensors for measuring various health parameters of the senior citizens discussed in the earlier sections. All the sensors of the circuits will collect the data, process it and send the relevant alert messages to the 'Blynk' mobile app whenever the concerned sensors sense and process the same.

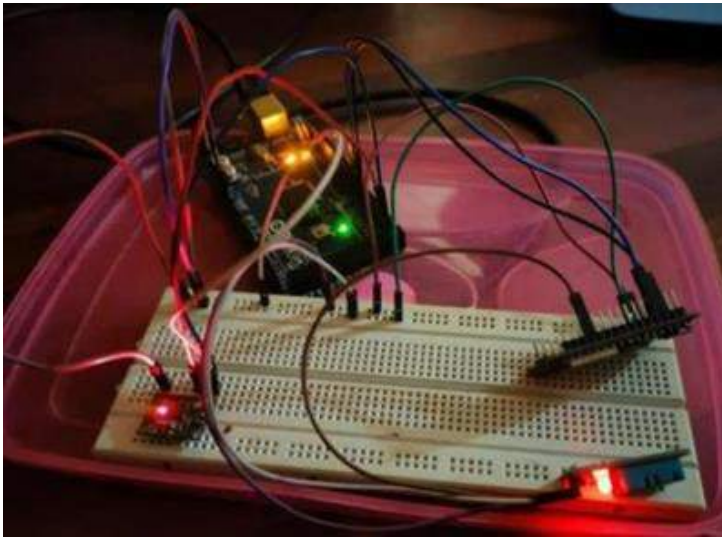


Figure 6: Smart Stick Circuit

Figure 7 shows the various readings of the health parameters such as heart rate, body temperature and oxygen level of the person, which are received from the smart stick and displayed on the 'Blynk' mobile app. In figure 7, the app shows the three readings of the person such as body temperature 37, pulse 106, and oxygen level is 95.



Figure 7: Various readings of the Person

As discussed in the earlier sections, whenever the body temperature, pulse rate, and oxygen level crosses actual set limit, then alert messages are sent to the tare takers mobile phone. The two sample alert messages (i.e., Oxygen Concentration is low and Heart Rate is High) displayed on the mobile phone is shown in Figure 8 and 9 respectively.

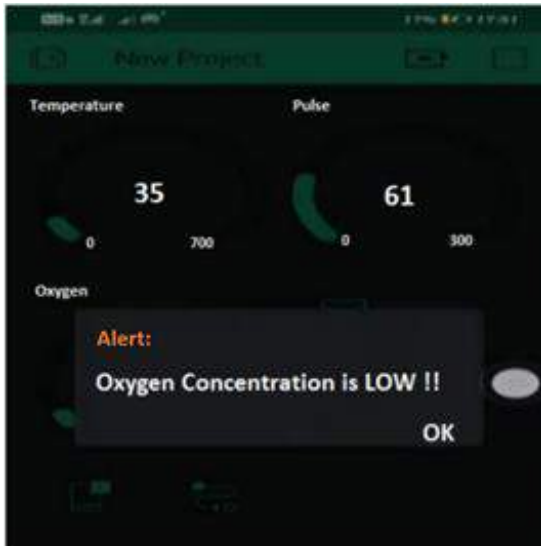


Figure 8: Sample alert message (Oxygen Concentration is Low)

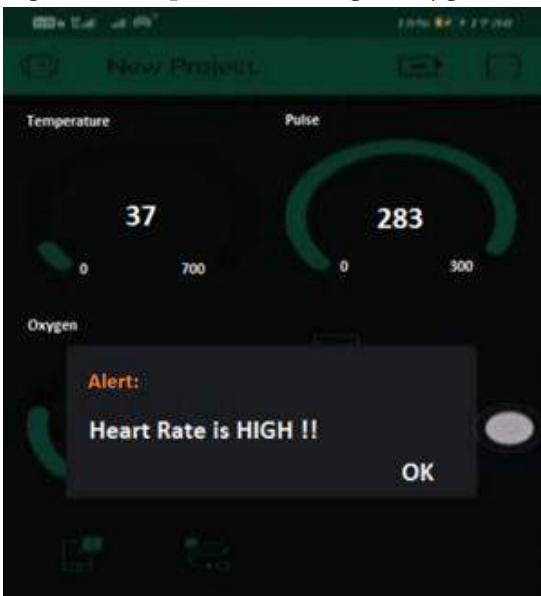


Figure 9: Sample alert message (Heart Rate is High)

In case of Location Tracking, the Latitude and Longitude values will be displayed in the 'Blynk' mobile app along with the live location position on the google map. The same has been shown in Figure 10.

Sudden Fall detection feature is integrated to know whether the person faced any fall. If in case, is there any fall of the person, the proposed stick sends an alert message immediately to the 'Blynk' mobile app as shown in the Figure 11.

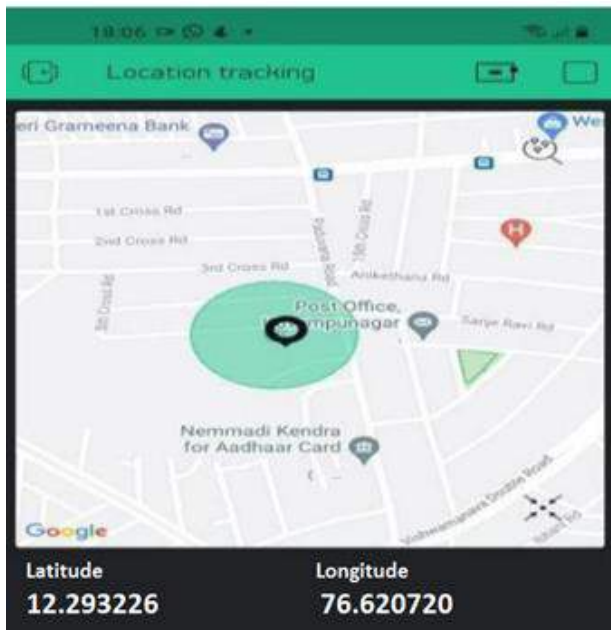


Figure 10: Sample alert message (Location Tracking)

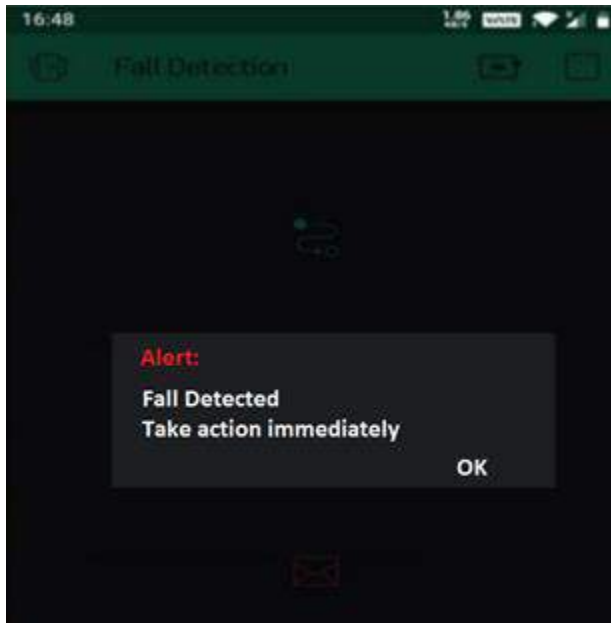


Figure 11: Sample alert message (Fall Detection)

The proposed Smart Stick system has been experimented with 14 people with 10 senior citizens (5 male and 5 female) of 61 to 68 years old and 4 middle age people (2 male and 2 female) of 35 to 44 years old.

This experimentation is carried out in various time intervals of day and night time in both indoor and outdoor locations. Here, the smart stick experimentation was carried out for body temperature, oxygen level, pulse rate, location tracking, and fall detection. There are 4 different experimentation was carried out on all the 14 people for all the 5 parameters. With the detailed experimentation, the proposed system provides an overall excellent average accuracy of 92.5%.

The detailed average accuracy of the experimentation is illustrated from Table I to Table IV .

Table I. Experiment 1 - Between 8.30 AM and 10:15 AM

Age	G	BT	PR	OL	FD	LT	AA
35	F	Y	Y	Y	Y	Y	100
38	F	Y	Y	Y	Y	Y	100
42	M	Y	Y	Y	Y	Y	100
45	M	Y	Y	Y	Y	Y	100
60	M	Y	Y	Y	Y	Y	100
60	F	Y	Y	Y	Y	Y	100
61	F	Y	Y	Y	Y	Y	100
62	F	Y	Y	Y	Y	Y	100
63	M	Y	Y	N	Y	Y	80
63	F	Y	N	Y	Y	Y	80
65	M	Y	Y	Y	Y	Y	100
67	M	Y	Y	Y	Y	Y	100
68	F	Y	Y	Y	Y	Y	100
68	M	Y	N	Y	Y	Y	80
AA		100	85.7	92.8	100	100	95.7

Note: Abbreviations in table I - IV, G - Gender, BT - Body Temperature, PR - Pulse Rate, OL - Oxygen Level, FD - Fall Detection, LT - Location Tracking, Y - Yes Matched, N - Not Matched, and AA - Average Accuracy.

Table II. Experiment 1 - Between 12 Noon and 1:50 PM

Age	G	BT	PR	OL	FD	LT	AA
35	F	Y	Y	Y	Y	Y	100
38	F	Y	Y	Y	Y	Y	100
42	M	Y	Y	Y	Y	Y	100
45	M	Y	Y	Y	Y	Y	100
60	M	Y	Y	Y	Y	Y	100
60	F	Y	Y	Y	Y	Y	100
61	F	Y	Y	Y	Y	Y	100
62	F	Y	Y	Y	Y	Y	100
63	M	Y	N	N	Y	Y	60
63	F	Y	N	Y	Y	Y	80
65	M	Y	Y	Y	Y	Y	100
67	M	Y	Y	N	Y	Y	80
68	F	N	Y	Y	Y	Y	80
68	M	Y	N	N	Y	Y	60
AA		92.8	78.6	78.6	100	100	90

Table III. Experiment 1 - Between 4.15PM and 6 PM

Age	G	BT	PR	OL	FD	LT	AA
35	F	Y	Y	Y	Y	Y	100
38	F	Y	Y	Y	Y	Y	100
42	M	Y	Y	Y	Y	Y	100
45	M	Y	Y	Y	Y	Y	100
60	M	Y	Y	Y	Y	Y	100
60	F	Y	Y	Y	Y	Y	100
61	F	Y	Y	Y	Y	Y	100
62	F	Y	Y	N	Y	Y	80
63	M	Y	N	N	Y	Y	60
63	F	Y	Y	Y	Y	Y	100
65	M	Y	Y	N	Y	Y	80
67	M	Y	Y	N	Y	Y	80
68	F	Y	Y	Y	Y	Y	100
68	M	Y	N	N	Y	Y	60
AA		100	85.7	64.3	100	100	90

Table IV. Experiment 1 - Between 7PM and 8.15 PM

Age	G	BT	PR	OL	FD	LT	AA
35	F	Y	Y	Y	Y	Y	100
38	F	Y	Y	Y	Y	Y	100
42	M	Y	Y	Y	Y	Y	100
45	M	Y	Y	Y	Y	Y	100
60	M	Y	Y	Y	Y	Y	100
60	F	Y	Y	Y	Y	Y	100
61	F	Y	Y	Y	Y	Y	100
62	F	Y	Y	Y	Y	Y	100
63	M	Y	N	Y	Y	Y	80
63	F	Y	Y	Y	Y	Y	100
65	M	Y	Y	N	Y	Y	80
67	M	Y	Y	N	Y	Y	80
68	F	Y	Y	Y	Y	Y	100
68	M	Y	Y	N	Y	Y	80
AA		100	92.8	78.6	100	100	94.3

In Table I to IV, N is nothing but the proposed system experimentation result is Not Matched with the cross verified manual results.

For verification of the experimentation results, we have used the regular classic glass thermometer and modern digital thermometer for body temperature measurement. The pulse rate experimentation result is verified with the manual wrist holding with two fingers method. Also, the oxygen level results of the experimentation is verified by using the regular pulse oximeter, which are available at the market. Experimentation results of the Location Tracking is verified with the mobile phone GPS system.

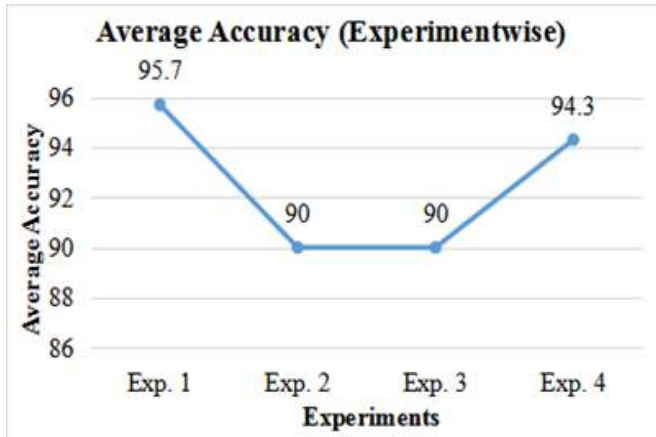


Figure 12. Average Accuracy (Experiment-wise)

Figure 12 shows the experiment-wise average accuracy of all the experiments. This average accuracy achieved by utilizing senior citizens and middle age people for experimentation.

In this proposed work experimentation, by considering only senior citizens, an average accuracy of 89.5% is achieved for experiment 1 to 4.

V. CONCLUSION

The proposed work is mainly concerned about monitoring health condition of the senior citizens and taking care of them. The proposed system is combination of many individual applications.

The proposed system, a Smart stick is a walking stick, which has pulse rate monitoring, body temperature reading, location tracking and also sudden fall detection system. The smart stick system also sends emergency alert messages to the 'Blynk' mobile application or to the registered email of the caretakers. The Smart Stick system is mainly implemented using Arduino Microcontroller and nodeMCU module which is integrated along with various sensors such as Pulse Oxymeter, Body Temperature Sensor, GPS Module, Accelerometer Sensor and etc. With the various parameters of the system, an average accuracy of 92.5% has been achieved and specifically for senior citizens, an average accuracy of 89.5% has been obtained.

As part of the future perspective, this work can extended by adding Voice Assistance System so that the proposed system can helps both the senior citizens and visually impaired people.

VI. REFERENCES

- [1]. Islam, M. M., Rahaman, A., and Islam, M. R. 2020. Development of Smart Healthcare Monitoring System in IoT Environment, SN Computer Science. 1, 185, (May 2020). <https://doi.org/10.1007/s42979-020-00195-y>

- [2]. Rahul Krishnan Pathinarupothi, P Durga and Ekanath Srihari Rangan. 2019. Iot-based Smart Edge For Global Health: Remote Monitoring With Severity Detection And Alerts Transmission, IEEE Internet of Things Journal. 2449 - 2462,(Apr 2019), Volume: 6, Issue: 2. DOI: 10.1109/JIOT.2018.2870068
- [3]. Kadhim, K. T., Alsahlany, A. M., Wadi, S. M., and Kadhum, H. T. 2020. An Overview of Patient's Health Status Monitoring System Based on Internet of Things (IoT). Wireless Personal Communications. 114, 2235–2262 (May 2020). <https://doi.org/10.1007/s11277-020-07474-0>
- [4]. Hosseinzadeh, M., Koohpayehzadeh, J., Ghafour, M. Y., Ahmed, A. M., Asghari, P., Sour, A., Rezapour, A. 2020. An elderly health monitoring system based on biological and behavioral indicators in internet of things. Journal of Ambient Intelligence and Humanized Computing. (Oct 2020). <https://doi.org/10.1007/s12652-020-02579-7>
- [5]. Mahmud, M. S., Wang, H., Esfar-E-Alam, A. M., and Fang, H. 2017. A Wireless Health Monitoring System Using Mobile Phone Accessories. IEEE Internet Of Things Journals. 2009 - 2018. (Dec. 2017). DOI: 10.1109/JIOT.2016.2645125
- [6]. Duraisamy Sathya and Pugalendhi Ganesh Kumar. 2017. Secured remote health monitoring system. Healthcare Technology Letters. 228-232. (Dec 2017). DOI: 10.1049/htl.2017.0033
- [7]. Kai Guan, Minggang Shao, Shuicai Wu. 2017. A Remote Health Monitoring System for the Elderly Based on Smart Home Gateway. College of Life Science and Bioengineering, Beijing University of Technology, Beijing, China. (Oct 2017). doi: 10.1155/2017/5843504



Electrical Conductivity (dS/m) Study for Agricultural Benefits after Optimization of Bio-Methanated High TDS Spent wash from Distilleries

Lalitha D1, Sathish Ns2, Ramesh N3, Manju B4

^{1*}Department of Chemistry, Government Engineering College, KRPet-571426, Karnataka, India

²Department of Civil Engineering, Government Engineering College, KRPet-571426, Karnataka, India

³Department of Civil Engineering, Government Engineering College, KRPet-571426, Karnataka, India

⁴Department of Chemistry, Maharaja Institute of Technology, Mysore, Mandya, Karnataka, India

ABSTRACT

The Spent wash is a beneficial by product produced from distilleries after extraction of ethyl alcohol from molasses. Being a plant extract, which is derived from sugar cane and contains nutrients and easily oxidisable organic matters. Spent wash is a rich source of organic matters and nutrients like N, P, K, Ca, and S. in addition to that sufficient amount of micro-nutrients such as Fe, Zn, Cu, Mn, B, Mb etc. It does not contain any toxic heavy metals and Hazardous constituents therefore it increases the soil fertility to increase the yield. Salinity of Soil, its structure and texture along with water availability can be studied by electrical conductivity.

Index Terms— Ethyl alcohol, Molasses, Spent wash, Anaerobic, Bio-methanation, Salinity, Electrical Conductivity.

I. INTRODUCTION

Sugar Industries globally gives lot off inputs like food items(Jagger y, sugar), Beverages, spirits, organic solutions and even waste water known as Spent wash. This Spent wash is a waste product and can be discarded to water resources or neighbouring lands but, if industries do so means it creates lot of Environmental pollution, so it is necessary to all the industries to follow treatment methodologies to avoid unnecessary harm to the environment, the treated spent wash if optimized thoroughly gives duel benefits to the mankind in the form of methane gas (bio gas) and as a fertilizer, to enrich soil fertility.

The Spent wash is a beneficial By product produced from distilleries after extraction of ethyl alcohol from molasses. Being a plant extract which is derived from sugar cane and contains nutrients and easily oxidisable organic matters. Spent wash is a rich source of organic matters and nutrients like N, P, K, Ca, and S. in addition to that sufficient amount of micro-nutrients such as Fe, Zn, Cu, Mn, B, Mb etc. It does not contain any toxic heavy metals and Hazardous constituents therefore it increases the soil fertility to increase the yield. Salinity of Soil, its structure and texture along with water availability can be studied by electrical conductivity.

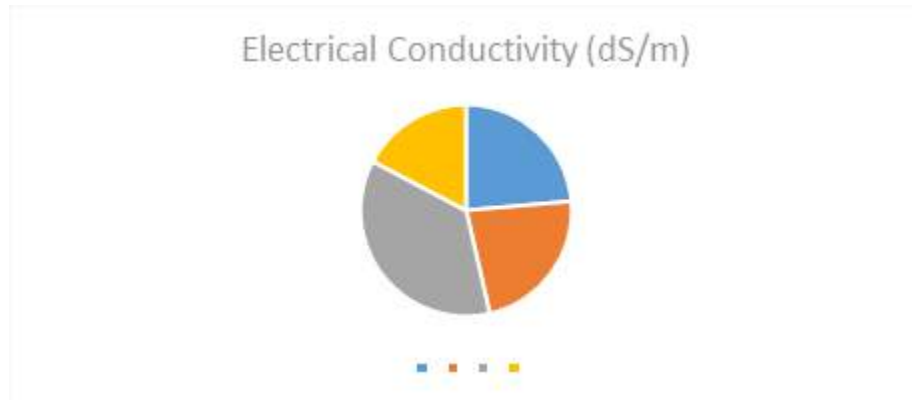
II. METHODOLOGY

Based upon UASB method Anaerobic Biomethanation process is carried and also Physical, Chemical characteristic parameters were studied along with microbial culture, pH study, and obtained optimized Spent wash is added to mud in the following order for two days and dried, subjected to determination of Electrical conductivity of soil the following results were obtained.

Table

S.N	Electrical Conductivity (dS/m)	Spent wash in ml/Soil in kg	Result
1	0.56	40ml/kg- type-1 soil	It is observed that depending upon the soil type salinity is moderate in all.
2	0.54	60ml/kg-type-2 soil	
3.	0.86	30ml/kg-type-3 soil	
4.	0.41	50ml/kg-type-4 soil	

Graphical study



Blue- 0.56 dS/m, Grey - 0.86 dS/m, orange-0.54 dS/m and yellow - 0.41 dS/m



Electrical Conductivity meter used



soil type-1

III. RESULTS AND DISCUSSION

According to obtained data the result is It is observed that depending upon the soil type salinity is moderate in all, and from that it is not much hazardous to the soil with respect to the above-mentioned ratio and spent wash

added in milliliter to soil type in kilogram. So fertility is not affecting much as the spent wash sprayed on soil in the form of press mud.

IV. CONCLUSION

Spent wash obtained from distillery as waste product can be used in dual mode as a biogas generation and also as manure to spray on the mud especially for agricultural purposes based upon the proper ratio along with mud as press mud.

V. REFERENCES

- [1]. PDISTILLERY WASTE WATER TREATMENT AND DISPOSAL BY Lt Col Mantha Nagaraj*, Dr Arvind Kumar
- [2]. Methan Emission by Gut Symbiont of Termites V. Gomathi, K. Ramasamy, M. R.V.P. Reddy, A. Ramalakshmi and A. Ramanathan
- [3]. Acid resistance of methanogenic bacteria in a two-stage anaerobic process treating high concentration methanol wastewater. ZHOU Xuefei (d), REN Nanqi
- [4]. Dr. S. Manjappa and research promotion scheme students. "Design and Optimization of Biomethanation for high TDS spent wash from Oil Resin extraction of Agrobiochem industries for the year 2007-2008.
- [5]. Chandraju, S., H. C. Basavaraju & C. S. Chidankumar, 2008. Investigation of impact of irrigation of Distillery spent wash on the nutrients of cabbage and mint leaf. Indian sugar. 39:19-28.
- [6]. Global warming methane could be far more potent than carbon dioxide new media explorer.org. Retrieved 17.08.07.
- [7]. National Non Food Crops Center. Economic Assessment of an Anaerobic Digestion Technology & its Suitability to UK Farming and Waste Systems (Report, 2nd Edition), NNF CC10-010.
- [8]. Smt. Lalitha D, Dr. N S Sathisha, Dr B Manju, Dr. B M Kiran. Optimization of biomethanation process for high TDS spent wash from distilleries IJSRR Volume 10 (2018).



Mechanical Characterization of Aluminium Based Hybrid Composites Reinforced with Boron Carbide and Alumina

Paraveej Shirahatti¹, H.K Shivanand², Ranjth R Hombal¹, Ajeet Shivaji Mankani⁴, Sadashiva M⁵

¹Research scholar, Department of Mechanical Engineering, UVCE, Bangalore, Karnataka, India

²Professor, Department of ME Department of Mechanical Engineering, UVCE, Bangalore, Karnataka, India

³M. Tech, Department of Mechanical Engineering, UVCE, Bangalore, Karnataka, India

⁴Assistant Professor, Department of Mechanical Engineering, PESCE, Mandya, Karnataka, India

ABSTRACT

Metal Matrix Composites (MMC's) have wide range of applications in aerospace, automotive, military and industrial applications due to their superior mechanical properties, light weight, electrical and thermal conductivity. Though synthesizing a hybrid composite is a challenging task due to the lack of wettability of particulates, it has a greater demand due to their attractive mechanical properties. In the present work, a hybrid composite material was synthesized with 2024 Aluminium alloy as a matrix material and the combination of Boron Carbide (B₄Cp) and Alumina (Al₂O₃) particulates as reinforcement with traditional stir casting process and also investigated the mechanical properties of composites such as tensile, compression, impact and hardness were determined. The comparative study of different parameters and variable achieved successfully and concluded that Tensile strength, Compressive strength and Hardness progressively increases up to 5% wt. to 6% wt. of Alumina (Al₂O₃), further cross the optimum range noticed that reduction in mechanical properties like tensile, compression, impact strength and even hardness too.

Keywords: 2024 Aluminium alloy, Boron carbide, Alumina, Stir casting.

I. INTRODUCTION

The globalization of modern world has sparked countries and regions to open their gates for allowing the entry of global players into their markets. Because of this scenario, thus competition situation is arising in marketing field. So the organizations are supplying the products to the customers on time in a less cost and with quality materials. So as per the subject concern to materials, lot of research works are going in engineering field to bring new materials to the market. After all the research we found the materials which are in light weight, low density and also cost is plus point.

The applications what we see in all the fields are of composite materials. The composite materials occupied more space in almost all the areas. So the design, manufacturing of materials also important as material, design

and manufacturing are interrelated to each other and we are also seeing lot of developments in material science and design field. So let's see about composite materials which are a major part in engineering field.

A composite material is a non-uniform solid consisting of two or more different materials that are mechanically or metallurgical bonded together. Each of the various composites retains its identity in the composite and maintains its characteristic properties such as stiffness, strength, weight, high temperature, corrosion resistance, hardness, and conductivity, which are not possible with the individual components by themselves. Example of the traditional composite is brick which consists of clay that mix up with grass and concrete that have mixture of cement and sand. In this example, clay and cement are matrix component while grass and sand are the reinforcement

Generally, one component acts as a matrix in which the reinforcing phase is distributed. The matrix component is, thus the continuous phase. When the matrix component is metal, we call such a composite a metal matrix composite (MMC). The reinforcement can be in the form of particles, whiskers, short fibers, or continuous fiber. There are three entities that determine the characteristics of a composite which are reinforcement, matrix and interface. The role of matrix was considered to be that of a medium or binder to hold the strong and stiff fibers or other types of reinforcement. Over the years, however, it has been realized that the matrix microstructure and consequently its mechanical properties have a considerable influence on the overall performance of a composite. This is particularly true of the MMC's because the very act of incorporating a reinforcement can result in change(s) in the microstructure of the metallic matrix and, consequently in their structure-sensitive properties such as a strength and toughness. While composites have already proven their worth as weight-saving materials, the current challenge is to make them cost effective. The efforts to produce economically attractive composite components have resulted in several innovative manufacturing techniques currently being used in the composites industry. It is obvious, especially for composites, that the improvement in manufacturing technology alone is not enough to overcome the cost hurdle. It is essential that there be an integrated effort in design, material, process, tooling, quality assurance, manufacturing, and even program management for composites to become competitive with metals.

Unlike conventional materials (e.g., steel), the properties of the composite material can be designed considering the structural aspects. The design of a structural component using composites involves both material and structural design. Composite properties (e.g. stiffness, thermal expansion etc.) can be varied continuously over a broad range of values under the control of the designer. Careful selection of reinforcement type enables finished product characteristics to be tailored to almost any specific engineering requirement

II. OBJECTIVES

In the present work an attempt will be made to prepare and evaluate the Mechanical Properties Of Aluminium 2024 Reinforced with boron carbide and Alumina particulates by novel two stage stir casting method. Some of the specific objectives are

1. Synthesis of B₄Cp -Al₂O₃ reinforced Aluminium 2024 hybrid metal matrix composite by novel two stage stir casting route for weight fraction of 7% of B₄C particulates and varying fraction of Alumina.

2. Evaluation of mechanical properties like tensile strength, compressive strength by using computerized universal testing machines respectively.
3. Evaluation of impact strength by using computerized Charpy test machine.
4. Evaluation of the Rockwell Hardness Number (RHN) by using manual Rockwell hardness testig machine.

III. MATERIALS USED

There are many interdependent variables to consider in designing an effective MMC material. Since the upper bound on MMC properties is established by the properties of the matrix and reinforcement material, careful selection of these components is necessary.

Reinforcements: Boron carbide (B₄C) and Alumina (Al₂O₃).

Matrix material: Aluminium alloy (Al2024T6).

3.1. Aluminium (2024-Al)

Aluminium alloy 2024 is an aluminium alloy, the primary alloying element being copper. Its main use is in applications that require high strength to weight ratio and good resistance to fatigue. It has the property to be welded but only through friction welding. Aluminium alloy 2024 is annealed from a heat-treated condition between 399 and 427 degrees Celsius for approximately 2 hours, after which it is slowly cooled in the furnace. Alternatively, aluminium alloy 2024 can be annealed between cold working operations at 343 degrees Celsius for 2 hours and cooled in air.

3.2. Boron Carbide –B₄Cp

Boron carbide is one of the hardest materials known, ranking third behind diamond and cubic boron carbide .Originally discovered in the mid- 19th century as a by-product in the production of metal borides. Boron carbide powder is mainly produced by reacting carbon with B₂O₃ in an electric arc furnace, through Carbothermic reduction or by gas phase reactions. Boric acid as a source of boron, and carbon active and petroleum coke as reducing agents were used. Mixtures of boric acid and carbon bearing material with a particle size of less than 44 µm were placed in a graphite crucible and heated under a flow of argon atmosphere in a tube furnace to 1400–1550 °C for 1–5 h. This resulted in the formation of boron carbide powder with or without un-reacted starting raw materials. For commercial use B₄C powders usually need to be milled and purified to remove metallic impurities.

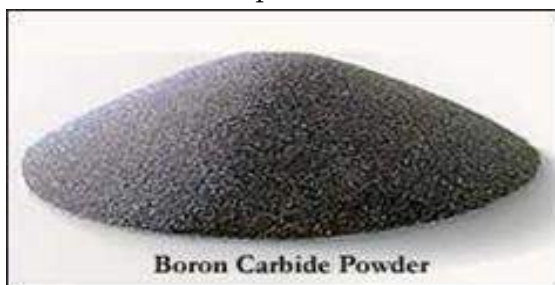
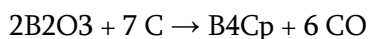


Fig.1 Showing the photograph of Boron carbide powder.

3.3. Alumina (Al₂O₃)

Al₂O₃ nanoparticles were synthesized using laser ablation of an aluminium (Al) target in deionized water. Nd:YAG laser, emitted the light at a wavelength of 1064 nm, was used as a light source. The laser ablation was carried out at different energies of 1, 3, and 5 J. Furthermore, it was observed that the particle size increased with increasing the laser energy.

Al₂O₃ or alumina generally refers to corundum. It is a white oxide. Alumina has several phases such as gamma, delta, theta, and alpha. However, the alpha alumina phase is the most thermodynamically stable phase. In general, alumina has many interesting properties, for example high hardness, high stability, high insulation, and transparency. Alumina is also widely used in the fire retard, catalyst, insulator, surface protective coating, and composite materials.

Al₂O₃ nanoparticles can be synthesized by many techniques including ball milling, sol-gel, pyrolysis, sputtering, hydrothermal, and laser ablation. Among them, the laser ablation is a widely used technique for the synthesis of nanoparticles since it can be synthesized in gas, vacuum or liquid. This technique offers several advantages such as rapid and high purity process compared with other methods



Fig.2 Showing the photograph of Alumina powder

IV. EXPERIMENTATION AND PROCESS

4.1. Steps Involved In Casting Process



Fig.3 Electrical resistance



Fig.4 Degassifier furnace for melting Al2024 Hexachloro ethane



Fig.5 Degasifier is mixed in crucible



Fig.6 B4Cp, K2TiF6 (Halide salt) and Al2O3 mixture.



Fig.7 mixing of Constituent material



Fig.8 Stirring.



Fig.9 ASTM Casting Dies



Fig.10 Hot liquid molten metal is pouring.



Fig.11 Final Castings

- First of all, 500 gm of commercially aluminium 2024-T6 was melted to 1023K temperature in resistance heated muffle furnace having clay graphite crucible
- It was degasified by pouring hexachloro ethane tablets in the clay graphite crucible. Degasification is the removal of dissolved gases from liquids, especially water or aqueous solutions, in the fields of science and engineering.
- B₄C_p, K₂TiF₆ (Halide salt) and Al₂O₃ are mixed according to the required % by mass and poured in crucible having the molten red hot Al 2024-T6 with continuous stirring in two steps with 10 to 20 second time lag, the technique is called as two stage stir casting method and here all the composites are well stirred such that all the constituent material get mixed homogeniously with the base metal that is Al 2024.
- Later the red hot liquid mixture is poured in to ASTM casting dies and allowed it for solidification for ½ hour
- Then the casting dies are separated and the casting is sent for machining for required dimension.

4.2. Composition of Test Specimens Prepared By Casting

Casting is obtained by mixing B₄C_p in composition of 7% and Al₂O₃ of 3% in red hot liquid condition of Al 2024 in composition of 90%. Similarly all different casting are obtained as the data provided in the table.

Table 1. Different casting composition.

Samples	Al 2024	Al ₂ O ₃	B ₄ C _p
Castig 1	100	0	0
Castig 2	93	0	7
Castig 3	90	3	7
Castig 4	89	4	7

NOTE- All the figures are given in percentage

V. TESTING AND DISCUSSION

5.1. Hardness Test



Fig.12 Rockwell Hardness Testing Machine

5.1.1. Procedure:

- The specimen is placed on the table. Hand wheel rotated so that the specimen along with the table moves up and just touches the ball indenter, applying an initial load of 10kgs.
- A Load of 100kg is applied on the specimen for a period of 30 seconds, during which the indenter presses onto the specimen.
- The Load is removed after 30 seconds and Rockwell hardness number (RHN) is noted from the Dial

Hardness specimen (ASTM-E18-17e1): All dimensions are in mm

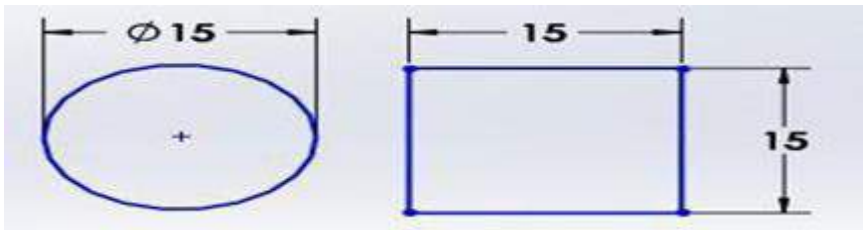


Fig.13 Hardness specimen



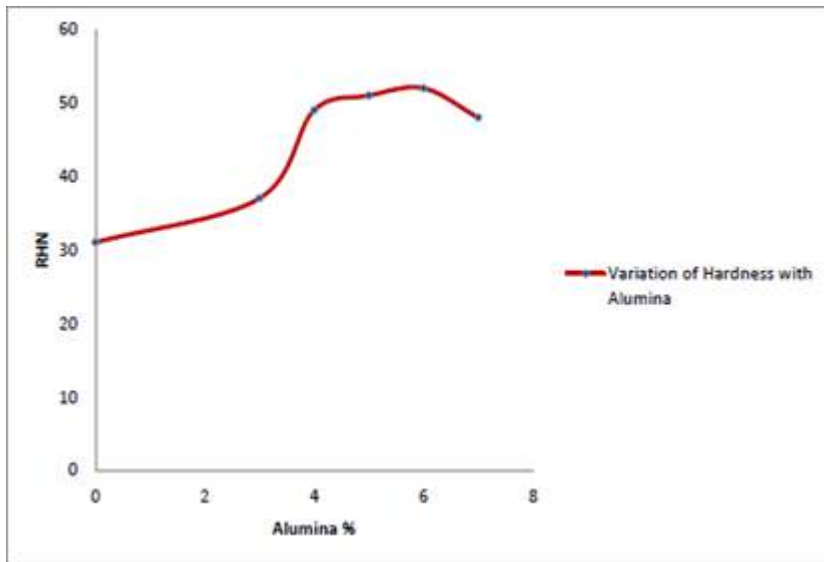
Fig.14 Hardness testing specimens

5.1.2. Hardness Test results

Test 1: Load: 100Kg, Time 20 seconds

Table 2. Hardness test Results

Samples	Al 2024	Al2O3	B4Cp	Rockwell Hardness Number (RHN)
A	100	0	0	31
B	93	0	7	34
C	90	3	7	37
D	89	4	7	49

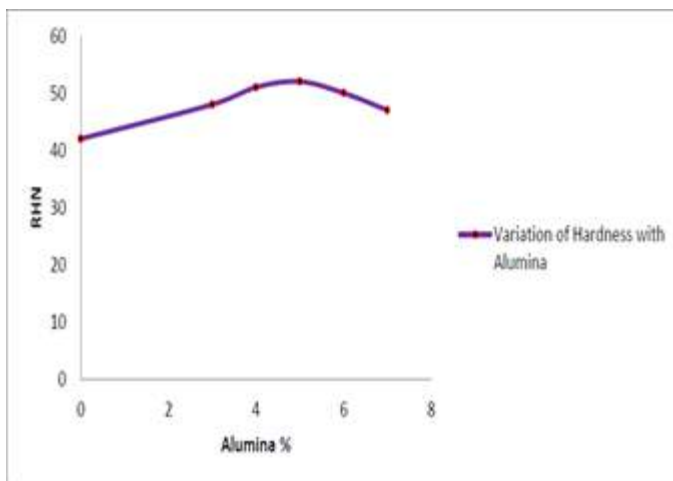


Graph 1. Hardness V/S Alumina % Curve

Test 2: Load: 120Kg, Time 20 seconds

Table 3. Hardness test Results

Samples	Al 2024	Al2O3	B4Cp	Rockwell Hardness Number (RHN)
A	100	0	0	33
B	93	0	7	42
C	90	3	7	48
D	89	4	7	51



Graph 2. Hardness V/S Alumina % Curve

It is observed from the table 3. and graph 2. that with varying Percentage of Alumina, Hardness Number (RHN) increases till 6% after that increase in the Alumina Reduces the Hardness. Decrease in hardness is mainly due to porosity as volume fraction increases and non-uniform distribution of reinforcements due to different density. Hence use of alumina up to 5% to 6% gives better results.

5.2. Tensile Test



Fig.15 Universal testing machine Apparatus

The tensile testing is carried out to get tensile strength by applying longitudinal or axial load at a specific extension rate to a standard tensile specimen with known dimensions (gauge length and cross sectional area perpendicular to the load direction) till failure. The applied tensile load and extension are recorded during the test for the calculation of stress and strain. A range of universal standards provided by Professional societies such as American Society of Testing and Materials (ASTM), British standard, JIS standard and DIN standard provides testing are selected based on preferential uses. Each standard may contain a variety of test standards suitable for different materials, dimensions and fabrication history. We have used ASTM E8M specimen for tension testing

Tensile Specimens (ASTM-E8M): All dimensions are in mm

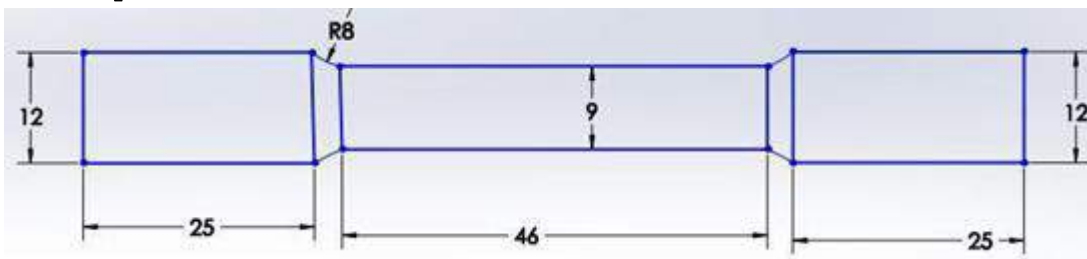
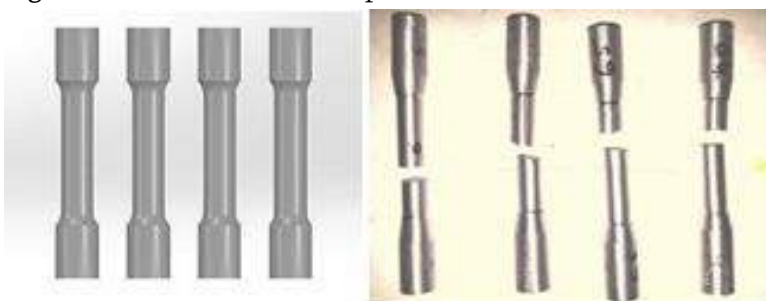


Fig.16 ASTM-E8M standard specimen for tensile test



Before testing

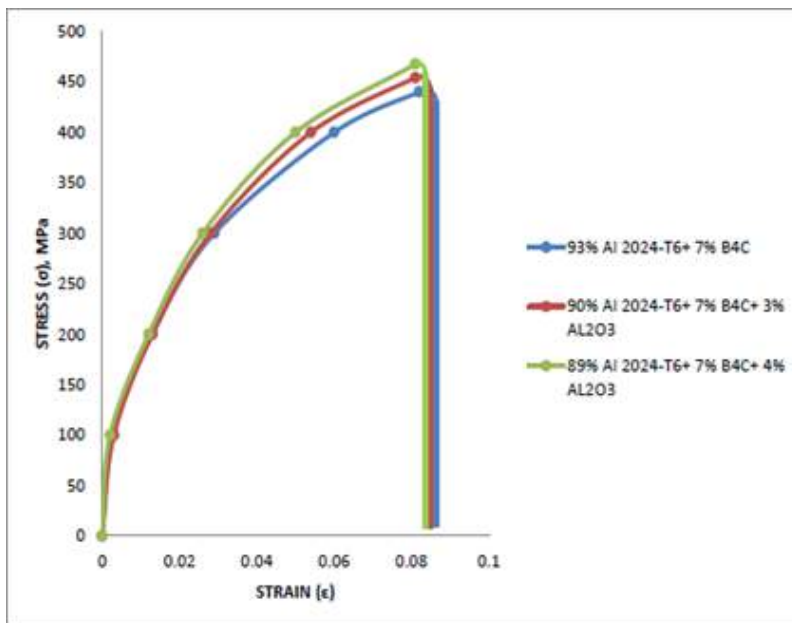
After testing

Fig.17 Tensile Specimens

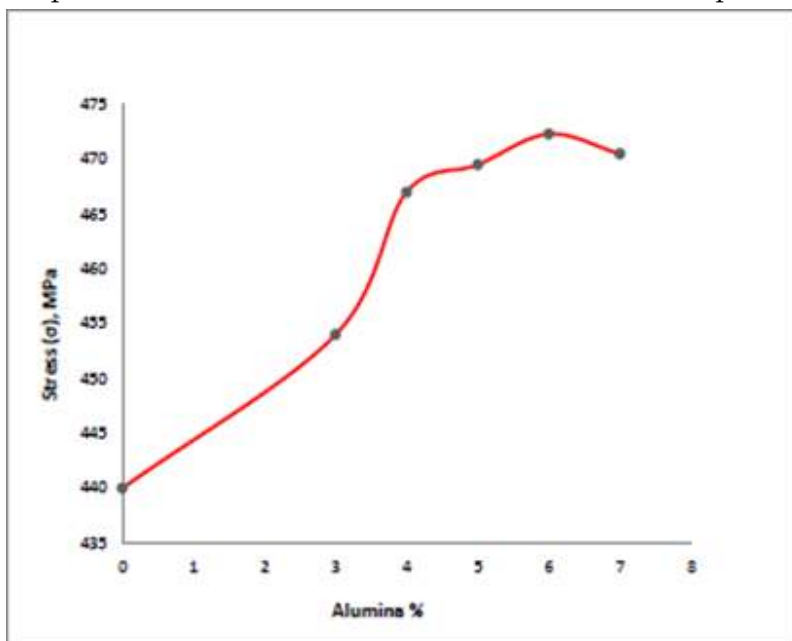
5.2.1. Tensile Test results

Table 4. Tensile test Results

Samples	Al 2024	Al ₂ O ₃	B ₄ Cp	Tensile Strength (MPa)
A	100	0	0	426.8
B	93	0	7	440.08
C	90	3	7	454.3
D	89	4	7	467.7



Graph 3. Tensile Stress V/S Strain Curve for different composition of Alumina



Graph 4. Tensile Stress V/S Alumina % Curve

It is observed from the table 4. and graph 4. that with varying Percentage of Alumina Tensile Strength increases from 440MPa to 470 MPa after that increase in the Alumina decreases the Tensile strength. Decrease in tensile strength is due to many reasons like increase in the volume fraction of reinforcement leads to porosity during the casting, improper distribution of reinforcements due to different density, and decreases the wettability, gasification etc. Hence use of alumina up to 6% gives good results.

5.3. Compression Test



Fig.18 Universal Testing Machine

A Universal Testing machine, also known as a universal tester, materials testing machine is used to test the tensile strength and compressive strength of materials. It is named after the fact that it can perform many standard tensile and compression tests on materials, components, and structures. Operation of the universal testing machine is by hydraulic transmission of load from the test specimen to a separately housed load indicator. The system is ideal since it replaces transmission of load: through levers and knife edges, which are prone to wear and damage due to shock on rupture of test pieces. Load is applied by a hydrostatically lubricated ram Main cylinder pressure is transmitted to the cylinder of the pendulum dynamometer system housed in the control panel. The cylinder of the dynamometer is also of self - lubricating design. The load transmitted to the cylinder of the dynamometer is transferred through leverage to the pendulum. Displacement of the pendulum actuates the rack and pinion mechanism which operates the load indicator pointer and the autographic recorder. The deflections of the pendulum represent the absolute load applied on the test specimen. Return movement of the pendulum is effectively damped to absorb energy in the event of sudden breakage of the specimen

Compression specimens (ASTM-E9): All dimensions are in mm

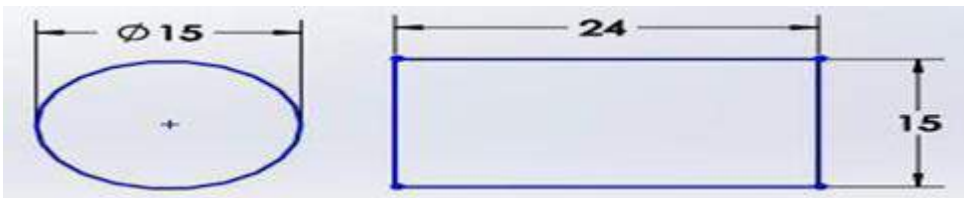


Fig.19 ASTM-E9 standard specimen for compression test



Before testing

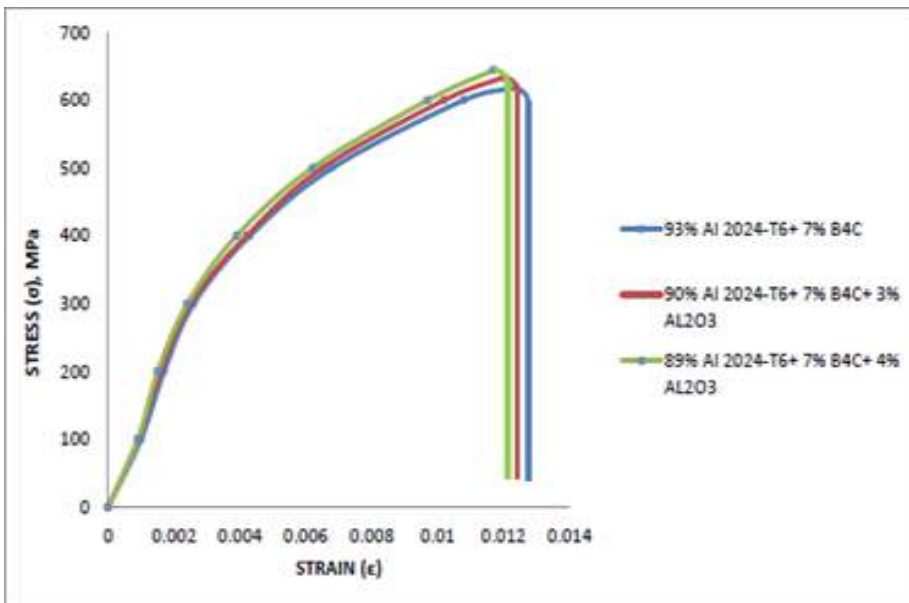
After testing

Fig.20 Compression Test Specimens

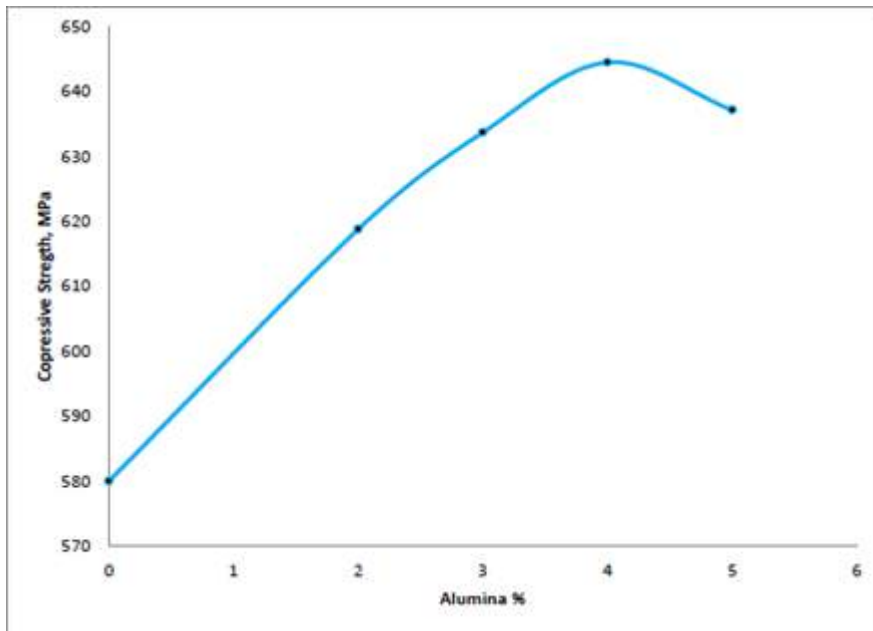
5.3.1. Compressive Test results

Table 5. Compressive Stress Results

Samples	Al 2024	Al ₂ O ₃	B ₄ Cp	Compressive Stress (MPa)
A	100	0	0	590
B	93	0	7	618.84
C	90	3	7	633.753
D	89	4	7	644.55



Graph 5. Compressive Stress V/S Strain Curve for different composition of Alumina



Graph 6. Compressive Stress V/S Alumina % Curve

It is observed from the table 5. and graph 6. that with varying Percentage of Alumina compressive Strength increases from 580MPa to 645 MPa after that increase in the Alumina decreases the compressive strength. Decrease in compression strength is due to many reasons like increase in the volume fraction of reinforcement leads to porosity during the casting, improper distribution of reinforcements due to different density, and decreases the wettability, gasification etc. Hence use of alumina up to 4% gives good results.

5.4. Impact test



Fig.21 Charpy impact Testing Machine

Charpy impact testing involves striking a standard notched specimen with a controlled weight pendulum swung from a set height. The standard Charpy-V notch specimen is 55mm long, 10mm square and has a 2mm deep notch with a tip radius of 0.25mm machined on one face. The specimen is supported at its two ends on an anvil and struck on the opposite face to the notch by the pendulum. The amount of energy absorbed in fracturing the test- piece is measured and this gives an indication of the notch toughness of the test material.

The pendulum swings through during the test, the height of the swing being a measure of the amount of energy absorbed in fracturing the specimen. Conventionally, three specimens are tested at any one temperature and the results averaged. Charpy tests show whether a metal can be classified as being either brittle or ductile. A brittle metal will absorb a small amount of energy when impact tested; a tough ductile metal absorbs a large amount of energy

Impact test specimens (ASTM-E23): All dimensions are in mm

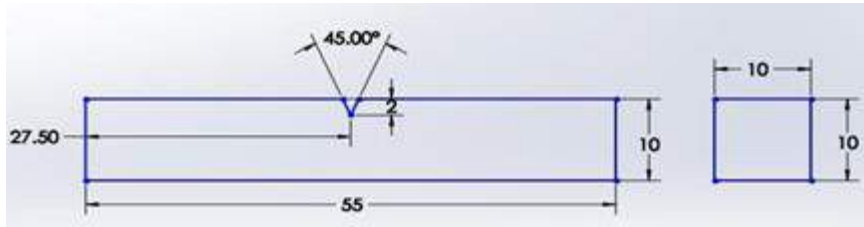
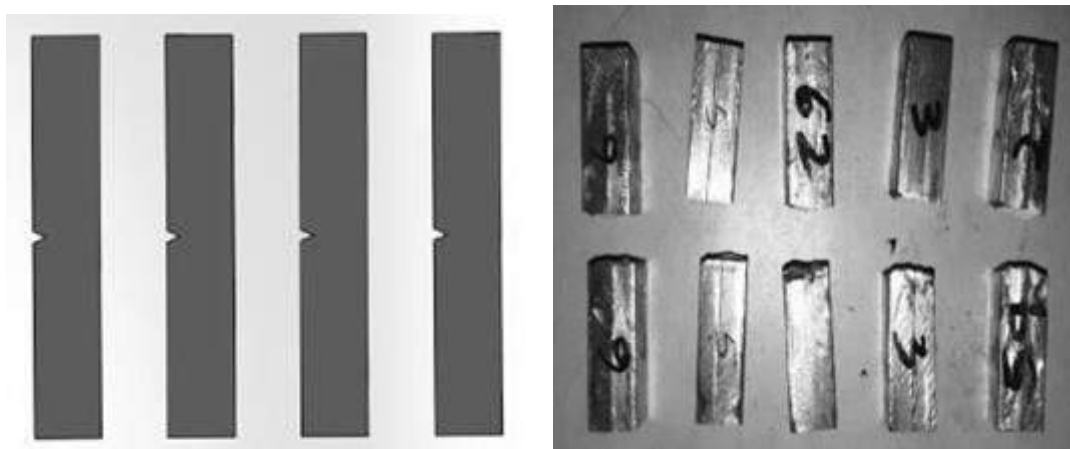


Fig.22 ASTM-E23 standard Impact test specimen



Before testing

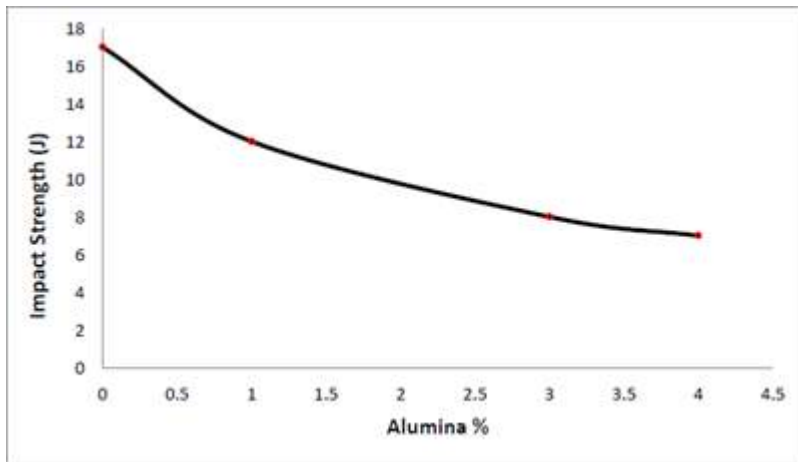
After testing

Fig.23 Impact Test Specimens

5.4.1. Impact Test results

Table 6. Impact Test Results

Samples	Al 2024	Al2O3	B4Cp	Impact Strength (J), KV300/10
A	100	0	0	17
B	93	0	7	12
C	90	3	7	8
D	89	4	7	6



Graph 7. Impact Strength V/S Alumina % Curve

It is observed from the table 6. and graph 7. that with varying Percentage of Alumina, Impact strength decreases with increases in the Alumina as brittleness increases due to this amount of energy absorbed due impact decreases. Increase in reinforcement decreases the ductility, since the ductility is directly proportional to impact strength, due to decrease in ductility impact strength decreases.

VI. CONCLUSION

New MMC's can be synthesized by liquid metallurgy technique successfully with enhanced properties using Boron carbide and Alumina particulate reinforcement.

- It is clear that ultimate tensile strength increases with increase in percentage composition of constituent material with Aluminium 2024. The increase in ultimate tensile strength is due to the addition of Boron carbide and Alumina gives strength to the matrix alloy there by enhanced resistance to tensile stresses, there is a reduction in the inter-spatial distance between the particles this leads to restriction to plastic flow due to the random distribution of the particulate in the matrix.
- It is seen that the compressive strength of the hybrid composites increases monotonically as reinforcement contents are increased. The increase in compressive strength is mainly due to the decrease in the inter-particle spacing between the particulates since Boron carbide and Alumina are much harder than Al2024 alloy. The presence of Boron carbide and Alumina resists deforming stresses and thus enhancing the compressive strength of the composite material.
- It is seen that the Hardness of the hybrid composites increases by about 20% monotonically as reinforcement contents are increased.
- It is observed that with increase in reinforcement, Impact strength decreases. It is due to increases in the Boron carbide and Alumina reinforcement increase brittleness of hybrid composite, due to this amount of energy absorbed by impact decreases. And also Increase in reinforcement decreases the ductility which reduces impact strength.

VII. SCOPE FOR FUTURE WORK

Currently few Mechanical Properties of Alluminium-2024 with different compositions are studied.

- Further studies can also be done on Tribological Properties like Corrosion properties, Bending Strength, Shear Strength, wear resistance Analysis with varying the Reinforcement material and Matrix material.
- Further studies can also be done on heat treated Aluminium reinforcement hybrid composite.
- Bonding strength between the Aluminium 2024 matrix, Alumina and boron carbide reinforcement can be analyzed by using the Nano indentation test.

VIII. REFERENCES

- [1]. Shyong J.H et al, Materials Science & Engineering A: Structural Materials; properties, Microstructure and processing, Vol.A197, N 1, Jun 30 1995, pp 11-18.
- [2]. Gomes E.G and Rossi, Key Engg. Material , Vol.189-191, Sept 2001, pp.496-502. Scolians et al, Materials Science & Engineering A: structural Materials;Properties, Microstructure and processing Vol. A210, N1-2, Jun 15 1996, pp.2269-2276
- [3]. Shakesheff A.J. et al, journal of material science Vol.30, N9, May 1 1995, pp.2269-2276.
- [4]. P.K. Rohatgi, JOM 46 (11) (1994) 55-59.
- [5]. T.P.D. Rajan, R.M. Pillai, B.C. Pai, K.G. Satyanarayana, P.K. Rohatgi, Proceedings of National Conference on: Recent Advances in Materials Processing (RAMP-2001), India, 2001, pp. 327-334
- [6]. E.A. Feest, Composites 25 (1994) 75-86.
- [7]. L. Cao, Y. Wang, C.K. Yao, The wear properties of an SiC-whisker reinforced aluminium composite, Wear 140 (1990) 273-277.
- [8]. B.N. Pramila Bai, B.S. Ramashesh, M.K. Surappa, Dry sliding wear of A356-Al-SiCp composites, Wear 157 (1992) 295-304.
- [9]. Manish Narayan, M.K. Surappa, B.N. Pramila Bai, Dry sliding wear of Al alloy 3102-Al₂O₃ particle metal matrix composites, Wear 181-183 (1995) 563-570.
- [10]. T.W.Clyne, (2001), Metal Matrix Composites: Matrices and Processing, Encyclopedia of Materials: Science and Technology ,p- 8
- [11]. E.C. Barber, Reduce Part Weight and Cast with Hollow Microspheres for Plastics, 3M Company, Technical Report, St. Paul, 1999
- [12]. Dr.H.K.Shivanand, M.M.Benal Effects of reinforcements content and ageing durations on Wear Characteristics of Aluminium based hybrid composites, Elsevier Wear Journal, Wear 262(2007) PP 759-763.
- [13]. Dr.H.K.Shivanand, Shantharaja, Effect of reinforcements On the Mech. Properties of aged Al (7075) Based Hybrid Composites, Accepted for publication in Indian Foundry Journal, Volume: 53 No.1 Jan 2007.



A Study on Parametric Optimization of Co₂ Welding Process by Taguchi Method on Structural Steel Plates

Praveen Math¹, Dr B S Praveen Kumar²

¹Research Scholar, Department of Mechanical Engineering, Government Engineering College, Ramanagara, Karnataka, India

²Associate Professor, Government Engineering College, K R Pete, Karnataka, India

ABSTRACT

Welding of metals such as steel is still a hotly debated research area. The effect of process parameters on AISI1040 steel welding using Shielded Metal Gas Welding techniques has been qualitatively examined (MIG and TIG). The Taguchi method is critical for creating the experimental layout. Arc voltage, arc current, welding speed, nozzle to work distance, and gas pressure all have an impact on weld quality, according to a thorough analysis. The thickness of the plate and the backing plate have an effect as well. A design of trials based on an orthogonal array is used to produce weldments. A set of tests are performed on the weldments in order to determine their quality. The data is tested for appropriateness using ANOVA. The computed result is in the form of a contribution from each parameter, which is used to find the best values for fault minimization. Weldments are evaluated using an angle beam technique and the findings are measured using ultrasonic testing (UT). The presence of faults such as LOP, LOF, Blowhole, and Cracks in the specimens that were tested.

Keywords: Gas Metal Arc Welding (GMAW), Weld Dilution, Regression Analysis

I. INTRODUCTION

The weldability of ferrous metals is inversely proportional to the hardenability of steel, which determines the possibility of martensite formation during welding. Ferrous metals, such as AISI1040, are prone to distortion due to their high coefficient of thermal expansion. Some of these alloys are prone to cracking and have low corrosion resistance. Hot cracking can occur if the amount of ferrite in the weld is not controlled. When an electrode is employed for deposition, a small amount of ferrite is deposited in the weld metal, which solves the problem. TIG welding (gas tungsten arc welding) is commonly used to join non-ferrous metals, but it may be used on nearly any metal. Its carbon steel applications are constrained by the availability of more cost-effective steel welding methods such as gas metal arc welding (MIG) and shielded metal arc welding (SMAW). This approach can provide corrosion-resistant welds that are robust and ductile. AISI1040 steel was employed in this work, with the following composition: C 0.37-0.44; Mn 0.60-0.90; P 0.040(max); S 0.050. (max). This material is

used to make axles, shafts, minimally stressed gears, and other components for agricultural, earth moving, and material handling equipment.

Ultrasonic testing is used in this study to assess weld flaws without destroying them. Ultrasonic flaw detection has long been the preferred method of non-destructive testing in welding applications. Because of its safety, accuracy, and simplicity, ultrasonic inspection has climbed to the forefront of inspection technology. Using ultrasonics, on-line weld pool monitoring for various flaws such as lack of fusion (LOF), porosity, undercutting, and inclusion, which are produced by in proper TIG and MIG settings, is emphasised; however, Stares [1] conducted this work on mild steel and stainless steel. Jung [2] describes the selection of process parameters for optimum weld pool geometry in stainless steel. Tarnng [3] uses Taguchi methods to detect TIG welding process parameters, and this study is done on mild steels to forecast the best setting for each welding process parameter. Giridharan [4] optimised the bead geometry of pulsed TIG welding on 304L stainless steel, constructed mathematical models, and tested them. Ross [5] provided a clear explanation of the Taguchi approach, which served as the foundation for our study. Many investigators have worked on stainless steel utilising various gas shielded arc welding processes, however there is a dearth of study on AISI 1040 steel using the Taguchi methodology and fault detection using ultrasound testing, according to the literature.

II. EXPERIMENTATION

The study's foundation materials are 2mm and 4mm thick AISI 1040 steel plates linked utilising DCSP and TIG and MIG welding methods. 100mm x 55mm x 2mm and 100mm x 55mm x 4mm are the dimensions of the specimens. The investigation's process parameters are arc voltage, arc current, welding speed, nozzle to work distance, gas pressure, plate thickness, and backing plate thickness. Optimal parameter ranges are chosen from well-known welding publications [7, 8], and values in between the ranges are chosen, i.e. two values are required.

For testing, a L8 orthogonal array was chosen. Because there are seven total variables, a perfect analysis requires two experiments. Performing such a large number of tests, however, is impractical, time-consuming, and expensive. The research is conducted using a L8 orthogonal array, which necessitates a set of 16 tests, therefore a total of 16 trials are carried out to evaluate TIG welding. Similarly, 16 tests for MIG welding assessment were conducted.

For the provided experimentation, two levels of process variable selection are required for TIG welding of AISI 1040, and welding of the coupons is performed by selecting these limits using standard data available in the literature (Table-1).

Table.1:Parameters

Thickness	02mm	04mm
Type of Groove	sq	v
Electrodesize	03mm	03mm
Size of Filler rod	01.3mm	03.4mm
Nozzledimension	09.1 mm	09.1 mm

flow rate of Gas	08l/min	011 l/min
Shielded gas	Ar	Ar
Current	056 A	075 A
No of passes	01	01

Responses are obtained using the NDT method (ultrasound testing). On the test portions, the test is carried out. The equipment is calibrated first, then the Distance Amplitude Curve is formed using a Notch plate made of the same material, with the DAC drawn at an echo level of 80%, 40%, and lastly 20%. If the echo crosses the curve, it means there's a problem that has to be looked into. To acquire echo and determine the presence of a defect, the angle probe must be positioned so that the crystal faces the weld zone. On both the RHS and LHS sides of the weld, the probe is moved in a zig-zag pattern from the weld centre line to the heat impacted zone (HAZ). The depth (D), surface distance (SD), and beam path (BP/SP) are all determined. The data relating to the defect(s) is checked for adequacy using ANOVA, and the impacts of parameters are known in the form of contribution, as shown in Tables 2 and 3.

Table.2: Lack of penetration in welding

Ranges	Sum of squares (SS _{xi})	DOF (n-1)	Mean of SS _{xi} M.SS _{xi} = SS _{xi} /D.O.F	Fisher ratio F=M. SS _{xi} / M.SSE	Contri- bution(%)
x1	105.6	1	105.6	21.0425	-
x2	45.36	1	45.36	9.1420	0.2451
x3	2673.06	1	2673.06	535.1125	-
x4	7.5625	1	7.5625	1.5125	-
x5	1785.06	1	1785.06	357.0125	9.63
x6	13398.06	1	13398.06	2679.6125	72
x7	473.06	1	473.06	94.6125	2.55
/SSE=39.5025		8	SSE/8=5		Total =84.42
iSST=18527.77					Others = 16.58

Table.3:Under fill

Para- meters	SOS (SS _{xi})		Mean of SS _{xi} M.SS _{xi}	Fisher Ratio F=M. SS _{xi} / M. SSE	Contri- bution(%)
x1	60.36	1	60.36	134.5026	-
x2	187.36	1	187.36	426.6275	45.50
x3	39.76	1	39.76	88.3184	-
x4	16.36	1	16.36	44.0411	-
x5	11.06	1	11.06	24.4656	2.54

x6	97.06	1	97.06	213.0711	22.88
x7	0.062	1	0.062	0.1420	0.015
SSE=3.7		8	SSE/8 =0.489		Total= 70.22
SST=419.4375					Other =29.99

Figures 1 and 2 show the distribution of lack of penetration (LOP) and underfill for various L7 orthogonal array settings.

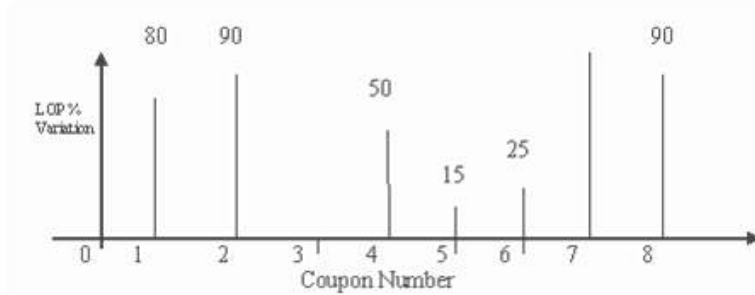


Figure.1:LOP Distribution

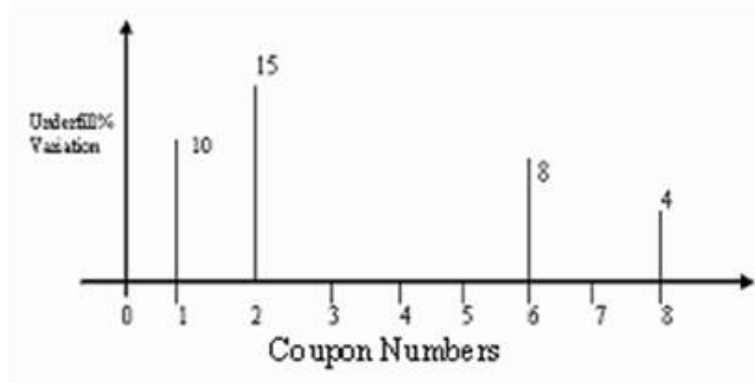


Figure-2. Distribution under fill for different conditions



Figure.3:With overlap and porosity, a typical TIG welded coupon.

A typical ultra sound scan of TIG welded coupons of 5mm AISI1040 steel plate is shown below. In TIG welding, echo signalling at a distance of 32mm from the work piece's edge.

Figures 1 and 2 show the distribution of L7 orthogonal array lack of penetration (LOP) and underfill for various situations.

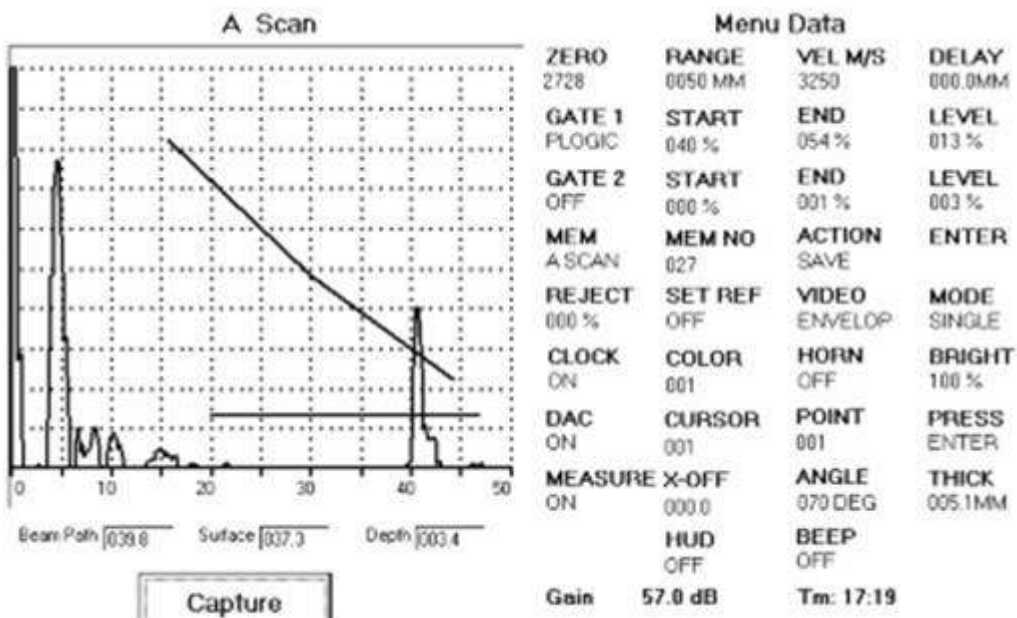
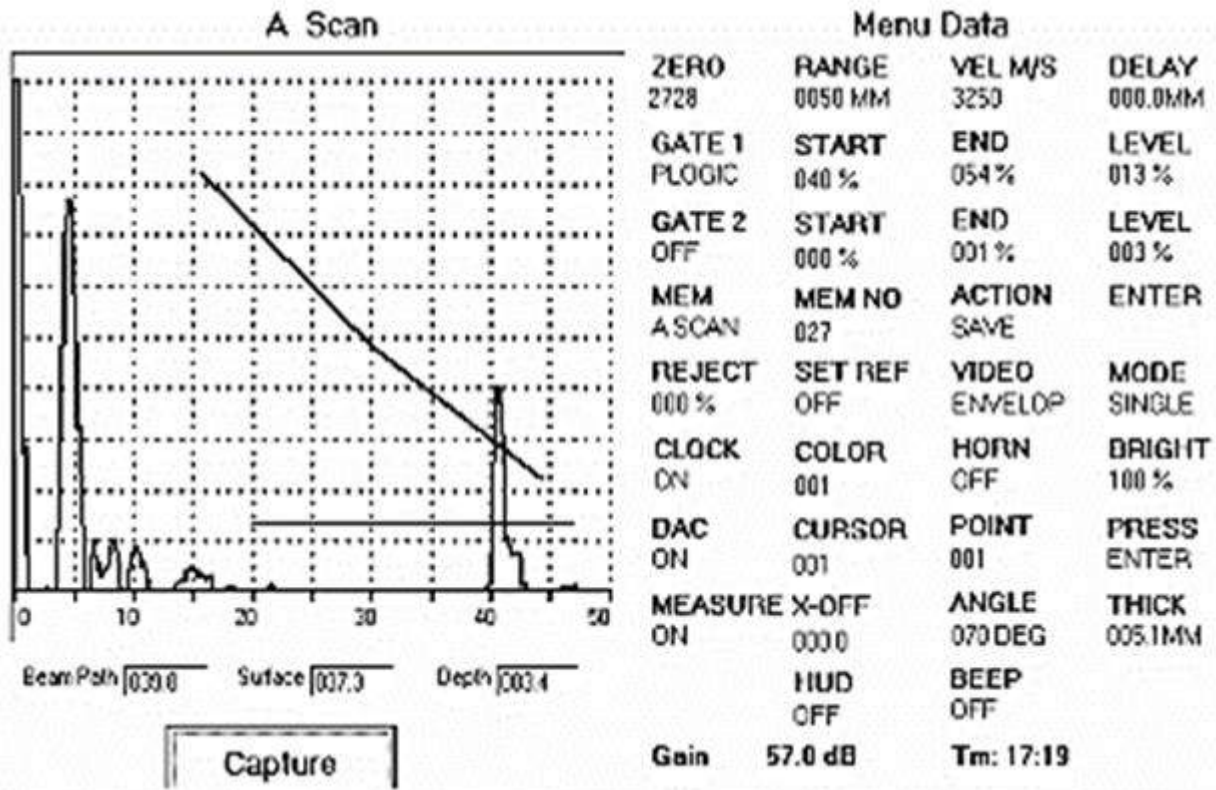


Fig.4:At a distance of 41mm from the edge of the work piece, there is a lack of penetration in TIG welding.

III. RESULTS AND DISCUSSIONS

The experimentation and welding of the coupons are accomplished at two levels. These limits were chosen using standard data from the literature (Table-4).

Table.4: Level selection.

Thickness	2mm	4mm
Type of Groove	Square	V-type
dimension of Electrode	0.97mm	0.97mm
Range of Voltage	023 V	028 V
flow rate of gas	09l/min	010 l/min
Shielded gas	CO2	CO2
Current range	123 A	147 A
Passes	01	01
Travelspeed	020 ipm	014 ipm
Distance between Nozzle and work distance	014	019

The findings of LOP and under fill are shown in Tables 5 and 6, and ANOVA is performed on MIG welded coupons in the same way that it is on TIG welded coupons.

Table.5: Lack of penetration

Values	S.O.S.(SSxi)	D.O.F.	Mean value of SSxi M.SSxi= SSxi/ D.O.F	Fisher ratio F= M. SSxi/ M.SSE	Contribution (%)
x1	45.56	1	45.56	22.0876	0.17
x2	8602.5	1	8602.5	4170.3315	32.47
x3	68.06	1	68.06	32.9952	0.25
x4	1.56	1	1.56	0.7574	0.006
x5	9168.06	1	9168.06	4444.4747	34.6
x6	264.06	1	264.06	128.0116	0.99
x7	8326.56	1	8326.56	4036.5340	31.43
S.S.E.=16.5885		8.2	SSE/8 =2.106		Total=99.913
SST=26493					Others=0.09

Table-6.under fill

Process Para- meters	S.O.S. (SSxi)	D.O.F.	Mean range of SSxi M.SSxi =	Fisher Ratio F=M.	Contribution
x1	11.73	1	11.73	316.5991	20.65
x2	5.4056	1	5.4056	145.9001	9.50
x3	2.8056	1	2.8056	75.7246	4.93
x4	2.8056	1	2.8056	75.7246	4.93
x5	5.4056	1	5.4056	145.9001	9.50
x6	11.73	1	11.73	316.5991	20.65
x7	16.6056	1	16.6056	448.1943	29.23
SSE=0.23964		8	SSE/8 =0.093705		Total=99.963
SST=56.7844					Others=0.661

The distribution of lake of penetration (LOP) and underfill for various L7 orthogonal array settings is shown in Figures 4 and 5.

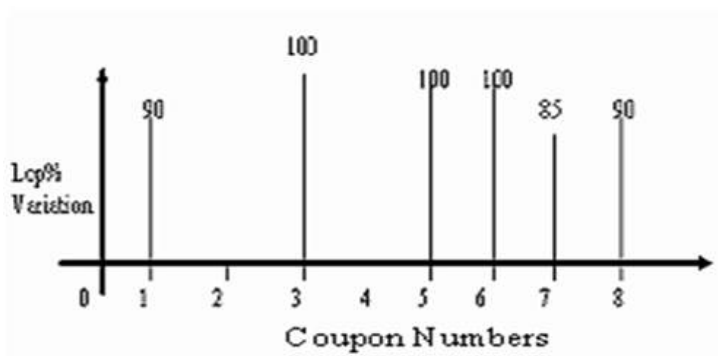
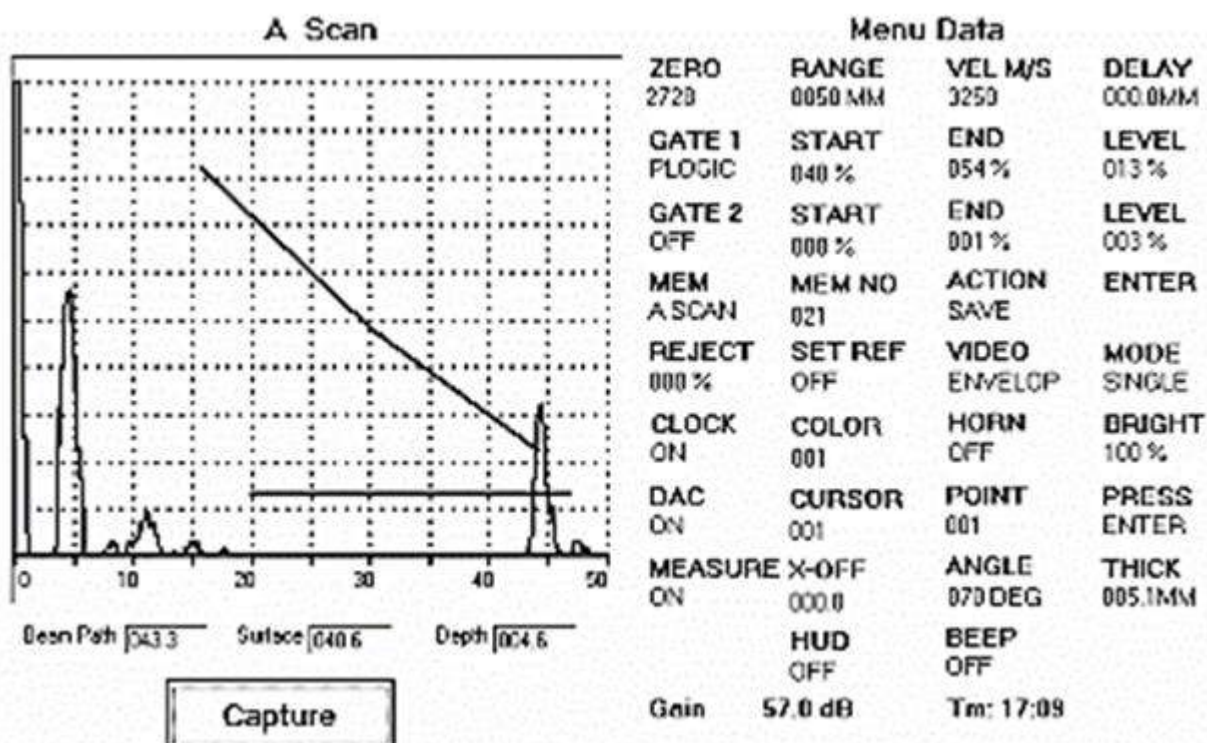
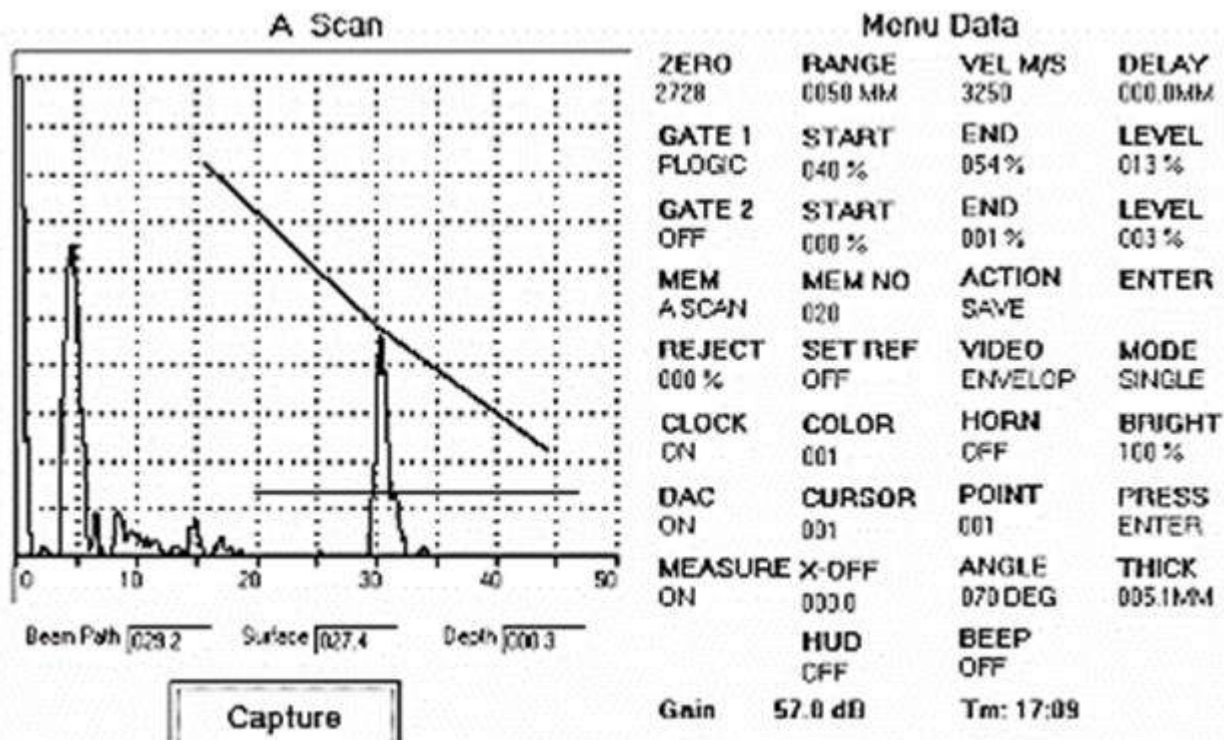


Figure.5:In MIG welding, the lack of penetration is distributed.



Figure.6:porosity and underfill.

The following is an example of a typical ultra sound scan of MIG welded coupons on 5mm AISI1040 steel plate. At a distance of 30mm from the edge of the work piece, echo indicating in MIG welding.



Echo indicating a lack of penetration in MIG welding at a distance of 45mm from the work piece's edge.

IV. TEST RESULTS ANALYSIS

In both TIG and MIG welding, low current trials increased the percent of variance of LOP; high welding speed induced underfill, which can be as large as 8mm² in TIG welding. Experiments in MIG welding with a short nozzle tip distance also demonstrated a lack of penetration. At low speeds and low current levels, over lap relative to blow holes and porosity can be identified in MIG welding; however, under fill is not visible in all studies with high current values. Weldability of AISI 1040 is excellent for both TIG and MIG welding procedures; nevertheless, in TIG welding, operator competence is shown to be more important than process parameters.

With a gas flow rate of 9-10 l/min, perfect shielding may be achieved; in TIG welding, plate thickness has a big influence on lack of penetration, and current has a 45 percent influence on under fill. In MIG welding, gas pressure is responsible for up to 35% of the lack of penetration, and current is responsible for 31% of the LOP.

V. CONCLUSION

To avoid LOP during MIG welding 3mm and 5mm plate, the recommended current values are 150A and 180A, respectively. TIG values for 3mm and 5mm plates are now 65A and 80A, respectively. In MIG welding, the weld speed should be less than 0.45 m/min for 3mm plate and less than 0.35 m/min for 5mm plate. For 3mm plates, the nozzle tip distance should be around 10mm, and for 5mm plates, it should be around 12mm. The Taguchi technique has proven to be reliable in the design of experiments for quality evaluation. You can save money on your experiments by selecting the appropriate orthogonal array.

Conflict of interest

Author declares that he has no conflict of interest.

VI. REFERENCES

- [1]. D. Frunzaverde, C.V. Câmpian, V. Cojocaru, G. Marginean, M. Baran, R. Ciubotariu, Influence of welded layers thickness on the cavitation erosion resistance, Proceedings of 6th WSEAS International Conference on Energy, Environment, Ecosystems and Sustainable Development - EEESD '10 (2010) 316-320.
- [2]. M. Zheng, J.H. Luo, X.W. Zhao, Z.Q. Bai, R. Wang, Effect of pre-deformation on the fatigue crack initiation life of X60 pipeline steel, Int. J. Pressure Vessels Pip. 82 (2005) 546-552.
- [3]. I. Bordeasu, C. Patrascioiu, V. Badarau, O. Sucitu, M. Popoviciu, New contribution to cavitation erosion curve modeling, FME TRANSACTION, University of Belgrade Faculty of Mechanical Engineering, New Series 34 (2006) 39-43.
- [4]. K.H. Lo, C.H. Shek, J.K.L. Lai, Recent developments in stainless steels, Mater. Sci. Eng. R 65 (2009) 39-104.
- [5]. C. H. Lee, K. H. Chang, Comparative study on girth weld-induced residual stresses between austenitic and duplex stainless steel pipe welds, Applied Thermal Engineering, 63(2014) 140-150.

- [6]. R.O. Rihan, Electrochemical Corrosion Behavior of X52 and X60 Steels in CarbonDioxide Containing Saltwater Solution, *Mater. Sci.* 16 (2013) 227-236.
- [7]. M. Aissani, S. Guessasma, A. Zitouni, R. Hamzaoui, D. Bassir, Y. Benkedda, Experimental and numerical analyses of residual stress distributions in TIG welding process for 304L stainless steel, *Applied Thermal Engineering*, 89 (2015) 822-832.
- [8]. J.M. Dowden, *The mathematics of thermal modeling*. USA: Taylor & Francis Group;2001.
- [9]. I.Tatucu, *Modeling electromagnetic field and thermal field*. Resita: Editor "EftimieMurgu" of University. 2002.
- [10]. M. Le Bellac, *Thermal field theory*. Cambridge monographs on mathematical physics;2000.
- [11]. Y. Han, E. Yu, H. Zhang, D. Huang, Numerical analysis on the medium-frequency induction heat treatment of welded pipe, *Applied Thermal Engineering*, 51 (2013) 212217.
- [12]. D. Gery, H. Long, P. Maropoulos, Effects of welding speed, energy input and heat sourcedistribution on temperature variations in butt joint welding, *J. Mater. Process. Technol.* 167(2005) 393-401.
- [13]. W. Piekarska, M. Kubiak, Theoretical investigations into heat transfer in laser-weldedsteel Sheets, *J. Therm. Anal. Calorim.* 110 (2012) 159-166.
- [14]. W.S. Chang, S.J. Na, A study on the prediction of the laser weld shape with varying heatsource equations and the thermal distortion of a small structure in micro-joining, *J. Mater.Process Technol.* 120 (2002) 208-214.
- [15]. A.Tokar, A. Negoitescu, L. Mihon, Studies regarding the CO₂ recovery from theatmosphere, *Annals of DAAAM and Proceedings*, 20 (2009) 349-350.
- [16]. W. Piekarska, M. Kubiak, Three-dimensional model for numerical analysis of thermalphenomena in laser-arc hybrid welding process, *Int. J. Heat. Mass. Transf.* 54 (2011) 4966-4974.
- [17]. T. Fuji, A new method for thermal analysis, *J. Therm. Anal. Calorim.* 110 (2012) 17-25.
- [18]. J.J. del Coz Díaz, P. Menéndez Rodríguez, P.J. García Nieto, D. Castro-Fresno,Comparative analysis of TIG welding distortions between austenitic and duplex stainless steelsby FEM, *Applied Thermal Engineering*, 30 (2010) 2448-2459.
- [19]. Rusu C.C. *Thermophysical modeling of arc*. Gala_i, 2011, Thesis.
- [20]. S.H. Atapek, E. Erisir, S. Gümüs, Modeling and thermal analysis of solidification in a low alloy steel *J. Therm. Anal. Calorim.* 114 (2013) 179-183.
- [21]. C. H. Lee, K. H. Chang, Temperature fields and residual stress distributions in dissimilarsteel butt welds between carbon and stainless steels, *Applied Thermal Engineering*, 45-46 (2012)33-41.
- [22]. J. Goldak, A. Chakravarti, M. Bibby, A new finite element model for welding heat sources, *Metall. Trans. B* 15 (1984) 299-305.
- [23]. B. G. Zhang, J. Zhao, X. P. Li, G. Q. Chen, Effects of filler wire on residual stress in electron beam welded QCr0.8 copper alloy to 304 stainless steel joints, *Applied Thermal Engineering*, 80 (2015) 261-268.
- [24]. V. Strezov, J.A. Lucas, L. Strezov, Computer aided thermal analysis, *J. Therm. Anal. Calorim.* 72 (2003) 907-918.
- [25]. H. Saari, D.Y. Seo, J. Blumm, J. Beddoes, Thermo physical property determination of high temperature alloys by thermal analysis, *J. Therm. Anal. Calorim.* 73 (2003) 381-388.



Design and Development of Regeneration of Electricity

Ranjith R Hombal¹, Pavan Kumar D², Paraveej Shirahatti¹, Kiran G K¹, H.K. Shivanand³

¹Research Scholar, Department of Mechanical Engineering, UVCE, Bangalore, Karnataka, India

²Assistant Professor, Department of Mechanical Engineering, HKBK College of Engineering, Bangalore, Karnataka, India

³Professor, Department of Mechanical Engineering, UVCE, Bangalore, Karnataka, India

ABSTRACT

The term "REGENERATIVE" describes processes that restore their own sources of energy and materials. RE-GENERATOR-It's a conceptual device, where we are trying to generate free electricity by means of mechanical parts. This will be used as creating sustainable systems that integrate the needs of society with the integrity of nature. The basic is derived from systems ecology with a closed loop input-output model or a model in which the output is greater than the input with all outputs variable and all inputs accounted for regenerative design is the biomimicry of ecosystems that provide for all human systems to function as a closed viable ecological economics system for all industry. It parallels ecosystems in that organic (biotic) and synthetic (a biotic) material is not just metabolized but metamorphosed into new viable materials. Ecosystems and Regenerative designed systems are holistic frameworks that seek to create systems that are absolutely waste free. The model is meant to be applied to many different aspects of human habitation such as urban environments, buildings, economics, industry and social systems. Simply put, it is the design of ecosystems and human behavior, or culture that function as human habitats.

Whereas the highest aim of sustainable development is to satisfy fundamental human needs today without compromising the possibility of future generations to satisfy theirs, the end- goal of regenerator design is to redevelop systems with absolute effectiveness, that allows for the generation to use this free electricity for further development possible for their habitat the goa of study is To produce electricity without using any fuel at the lowest possible cost,Conventional way of producing electricity, Saving fossil fuels,Pollution free production, Low maintenance requirement, Easy to operate and repair.



Influence of Server Density in Racks on Data Centre Thermal Management: A Numerical Study

Chethana G D^{*1}, Dr. Sadashive Gowda B²

^{*1}Department of Mechanical Engineering, Maharaja Institute of Technology, 571477, Mysore, Karnataka, India

²Department of Mechanical Engineering, Vidyavardhaka College of Engineering, 570002, Mysore, Karnataka, India

ABSTRACT

This work presents a numerical study of data centres' thermal performance with varying server densities inside the rack. The effects of hot-air recirculation and cold-air bypass on the temperature distribution are predicted and analysed in the data centre room using thermal performance measures such as supply/return heat index (SHI/RHI), return temperature index (RTI), and rack cooling index (RCI).

Keywords: Data Centre, Thermal Management, CFD Modeling, Energy Efficiency

I. INTRODUCTION

A Data Centre (DC) is a building that houses a collection of networked computer servers that are often used by businesses to store, process, and distribute massive amounts of data remotely[1],[2]. The rising demand for digital services has resulted in a massive increase in data centres and as a result, their electrical power consumption. Most of the energy consumed by the server is dissipated as heat which has to be removed by the cooling system for trouble-free operation of a data centre.[3]. The cooling systems in data centres require a substantial amount of data centre electricity. In most DCs, cooling consumes 30–40% of the overall energy. Fig.1 shows the typical layout of a data centre. Heat is removed from the server rack by the cold air pumped from Computer Room Air Conditioner (CRAC) units through the plenum. Perforated tiles facilitate the cold air into the cold aisle. Cold air is expected to pass through the server by absorbing heat and entering the hot aisle behind the server rack. The hot air will be carried to CRAC units through outlets in the hot aisle[3]. The facility's operating parameters must adhere to the thermal guidelines for data processing provided by the American Society of Heating and Refrigeration Engineers (ASHRAE)[4]. The main concerns with the data centre's reliability and energy usage are hot air recirculation and cold air bypass around the server racks.[5],[9],[10]. Hot air recirculation occurs when hot air circulates in the cold aisle without reaching the hot aisle. Cold air bypass occurs when cold air reaches the hot aisle without making contact with the server rack.[8] Data centres' energy usage can be lowered by enhancing their cooling systems.[5], [8]–[12].

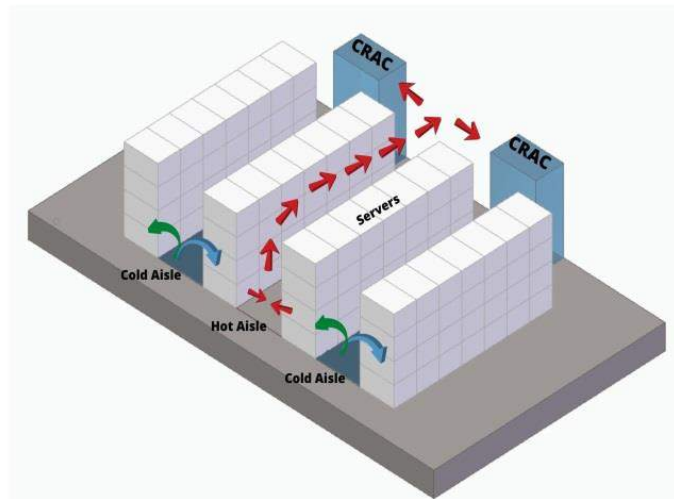


Figure1: Typical layout of a DataCentre

Experiments and field measurements at data centres are challenging, expensive and time-consuming to carry out. Without the use of a modelling tool, it is difficult to establish a plan for augmenting airflow management [13]. Computational Fluid Dynamics (CFD) is an efficient technique for examining the airflow distribution within the data centre because of the complicated nature of flow inside the data centre. CFD has enabled easy-to-use, accurate, and low-cost computational design and analysis techniques to tackle complicated and sometimes competing thermal requirements. [2],[14]–[16].

A. Data Centre Performance Parameters Indices

Thermal metrics are used in the design and operational stages to evaluate DC airflow performance and thermal managementsuch as supply/return heat index (SHI/RHI), return temperature index (RTI), and rack cooling index (RCI) [17], [18].

The ratio of the heat gained by the cold air supply in the cold aisle before entering the racks to the heat taken away from the servers is known as SHI.

$$SHI = \frac{T_{intake} - T_{supply}}{T_{exit} - T_{supply}}$$

The SHI depicts the level of recirculation in the cold aisles.

The RHI is the ratio of total heat extracted by CRAC units to sensible heat gained at the servers' exhaust.

$$RHI = \frac{T_{return} - T_{supply}}{T_{exit} - T_{supply}}$$

RHI is a measure of how much cold air mixes with hot air, and it's another indicator of recirculation.

SHI and RHI work in tandem. Thus

$$SHI + RHI = 1$$

RTI is defined as the ratio of return and supply temperature difference at the CRAC unit to the temperature difference across the IT equipment.

$$RTI = \frac{T_{return} - T_{supply}}{\Delta T_{sever}} \times 100 \%$$

The ideal value for RTI is 100 per cent. RTI values greater than 100% imply recirculation and lesser than 100% specifies cold air bypass.

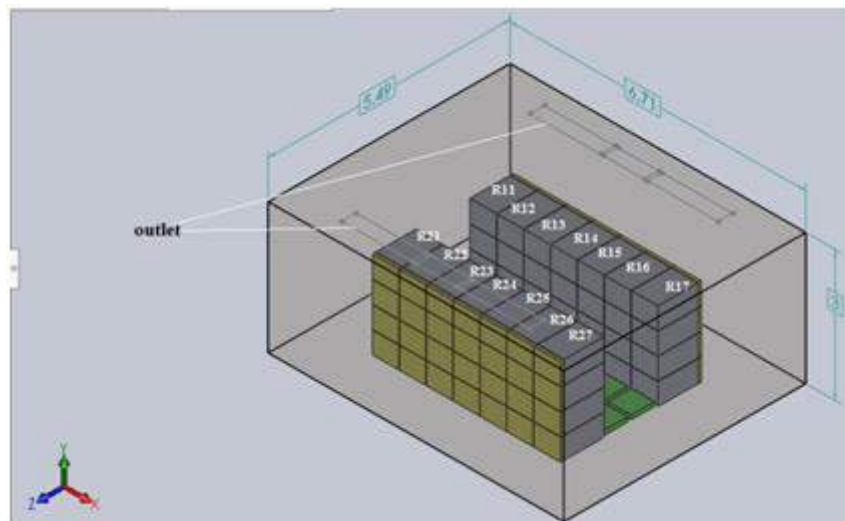
$$RCI_{HI} = \left[1 - \frac{\sum (T_{intake} - T_{max-rec})_{T_{intake} > T_{max-rec}}}{(T_{max-all} - T_{max-rec})n} \right] \times 100\%$$

$$RCI_{LO} = \left[1 - \frac{\sum (T_{min-rec} - T_{intake})_{T_{intake} < T_{min-rec}}}{(T_{min-rec} - T_{min-all})n} \right] \times 100\%$$

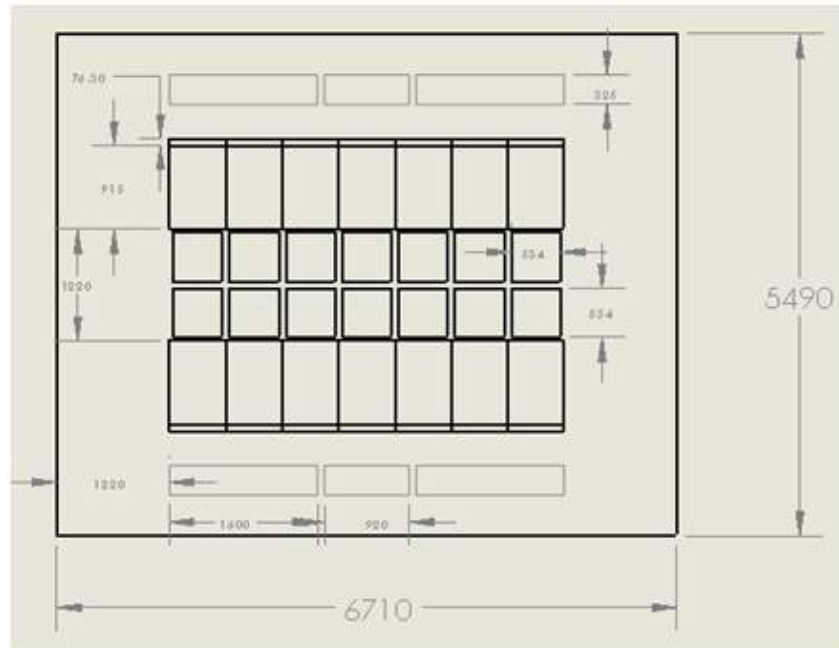
II. PHYSICAL MODEL

Fig. 2 shows the physical model for the current investigation in a data centre room with dimensions of 6.71 × 5.49 × 3.0 m.[19], [20].Nada et al.[6]Has numerically investigated the influence of CRAC unit's location inside the data centre. CRAC units placed in line with the rack row and perpendicular to the rack row are investigated.The findings revealed that placing the CRAC units perpendicular to the racks row improves the uniformity of airflow from the perforated tiles along the rack row, reduces hot air recirculation at the ends of the row and increases cold air bypass in the middle and improve the data centre's overall performance parameters RTI, SHI, and RHI.

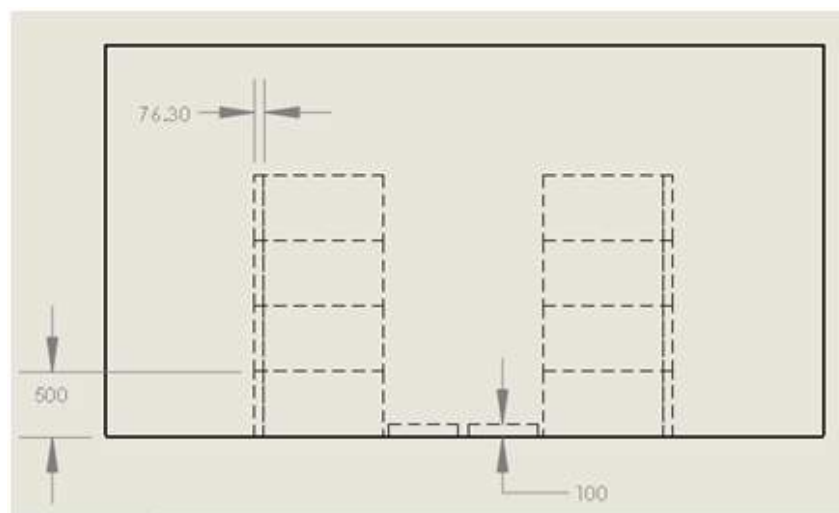
Sheth et al. [19]Have conducted a numerical investigation of data centres' thermal performance by a porous media approach.Rack servers with cooling fans installed on the backside of the servers are modelled as a momentum source. The variables considered are porosity of server, outlet locationand volumetric heat generation.For the present study geometrical model similar toSheth et al. [19] is considered. Racks with dimensions of 0.61 × 0.915 × 2 m, organised in two rows of seven racks each and separated by 1.22 mare considered.14 perforated tiles with dimensions of 0.534 × 0.534 × 0.1 m and cooling fans of size 0.61 × 0.5 × 0.0763 mare modelled behind each server.CRAC unit is neglected to reduce the computational time.The density of servers is represented by porosity. Lower porosity represents higher density, while higher porosity represents lower density.



(a) All dimensions are in m



(b) All dimensions are in mm



(c) All dimensions are in mm

Figure 2: Schematic diagram of (a) a data centre, (b) top view (c) side view

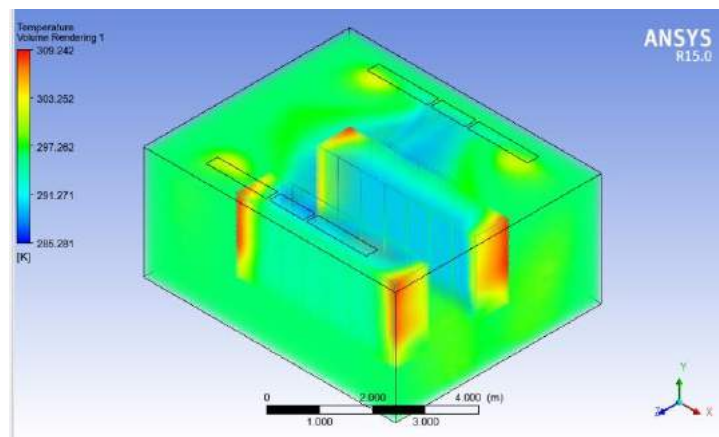
III. BOUNDARY CONDITIONS

The servers in this study have porosities of 0.35, 0.55 and 0.75, with volumetric heat generation of 3136.29, 2171.278 and 1206.265 W/m³ respectively. The porosity of the tiles considered as 0.25. Inlet velocity tile is considered as 1m/s at a temperature 12.3^o C. The outlet placed at the ceiling is considered. The thermal conductivity of the porous server is considered as 9.607 W/m K. The fan momentum considered as 150 N/m³ ANSYS Design Modeler 15.0 is used to create the physical model. The mesh package included with ANSYS Workbench 15 is used for meshing. The commercial CFD solver tool ANSYS FLUENT 15 is used for numerical

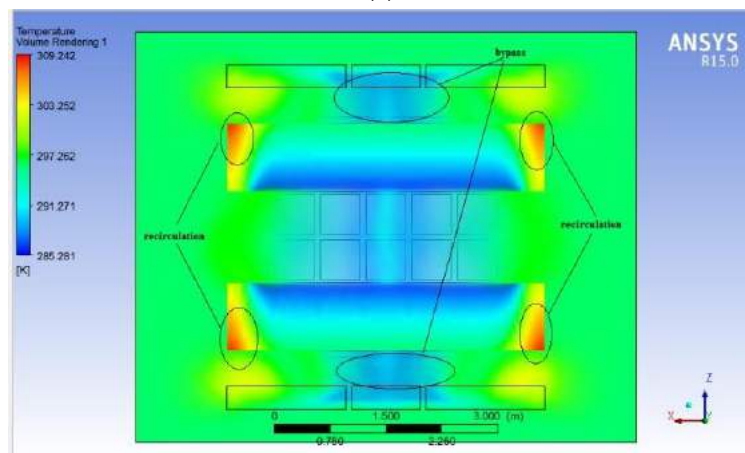
simulations. “The solution method included SIMPLE scheme for pressure-velocity coupling and the spatial discretization for gradient, pressure, momentum, k- ϵ and energy equations are achieved using least squares cell based, second order, second order upwind, first order upwind, and second order upwind methods, respectively. The convergence criteria for equations of continuity, momentum, kinetic energy and dissipation are set to 10^{-3} , whereas the same for energy is set to 10^{-6} . The convergence criterion for continuity, momentum, kinetic energy, and dissipation are set to 10^{-3} , whereas the same is set to 10^{-6} for energy”[19].

IV. RESULTS AND DISCUSSION

Figure 3 shows the temperature contours and Figure 4 shows the streamlines in the data centre room for a case with a porosity of 0.75 and a fan momentum source of 150 N/m^3 . It is evident from the figure that a few streamlines in the middle bypasses and enter directly into return vent. Servers at the top near to wall observe high-temperature zones due to hot air recirculation.



(a)



(b)

Figure 3: Temperature contours (a) and (b) showing bypass and recirculation

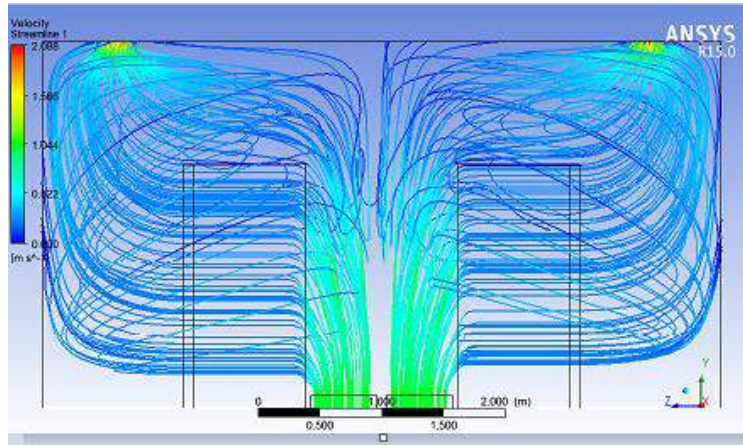
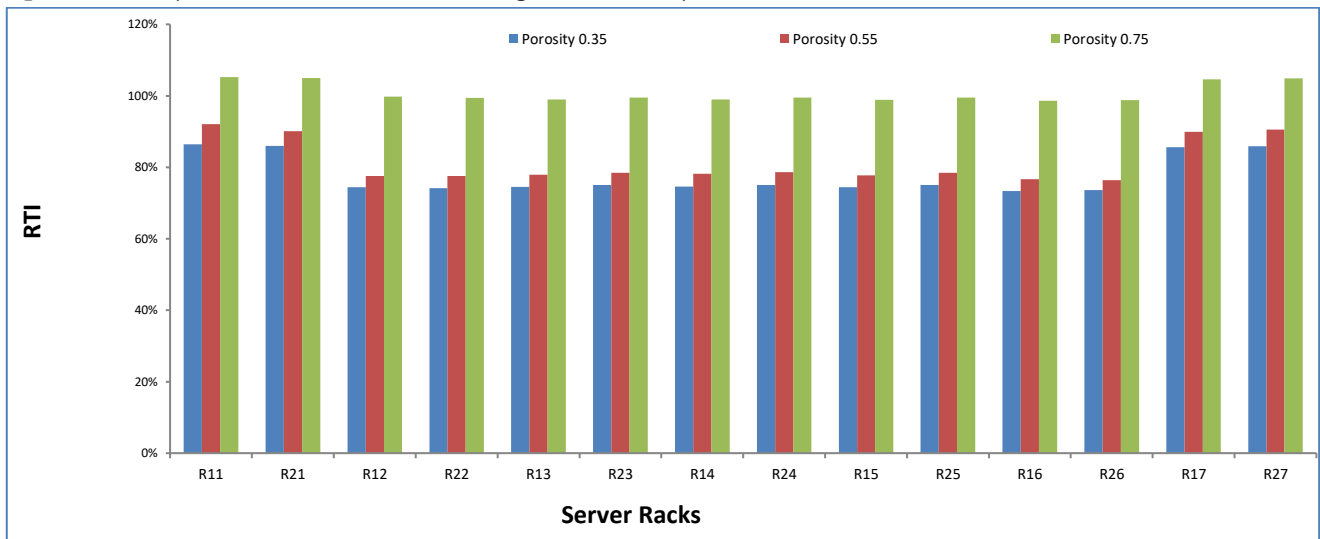
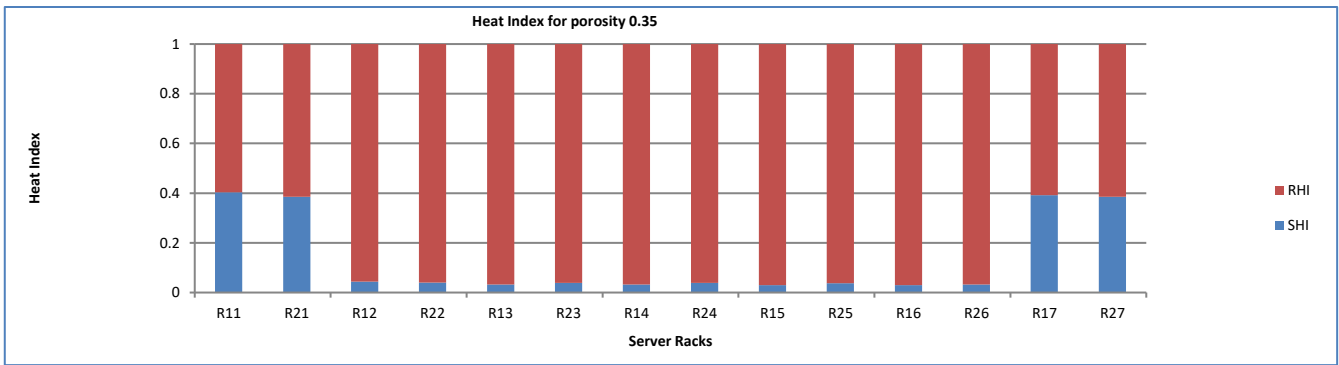


Figure4:Streamlines (velocity in m/s) for the cold airflow

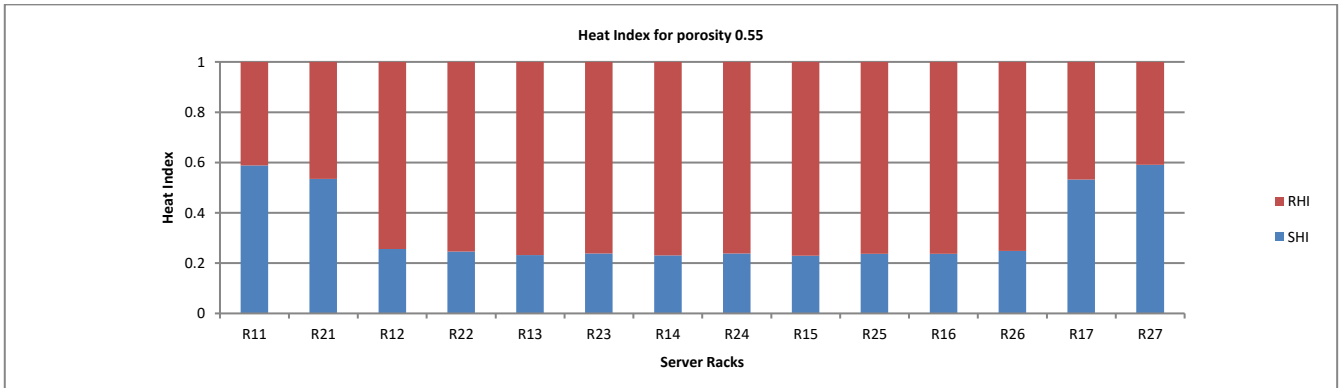
Figure 5 (a) shows RTI values for varying porosities. The target for RTI is to achieve a value of 100 percent. Recirculation is indicated by RTI values greater than 100 percent, while cold air bypass is indicated by RTI values less than 100 percent. RTI values that are significantly off from the desired value of 100 percent indicate an inadequate thermal management system. An analysis is performed for server rack with porosity of 0.35, 0.55 and 0.75. It is observed that RTI value is high at porosity 0.75 which indicates a considerable amount of recirculation. When compared to middle racks, servers closer to the wall have a greater RTI, indicating recirculation near the wall. The bypass phenomenon is observed in racks with RTI values less than 100%. From figure 5 (b), (c) and (d) it can be seen that the presence of recirculation affects the values of heat index as a result, higher SHI value and lower RHI value. From figure 5 (e) and (f) RCILO readings are within acceptable limits. Few numbers are less than 100%, indicating that temperatures in some areas are below the minimum necessary temperature of 13 degrees Celsius. All the values of RCIHI are near to 100 percent, indicating that rack inlet temperatures beyond the recommended range are unlikely.



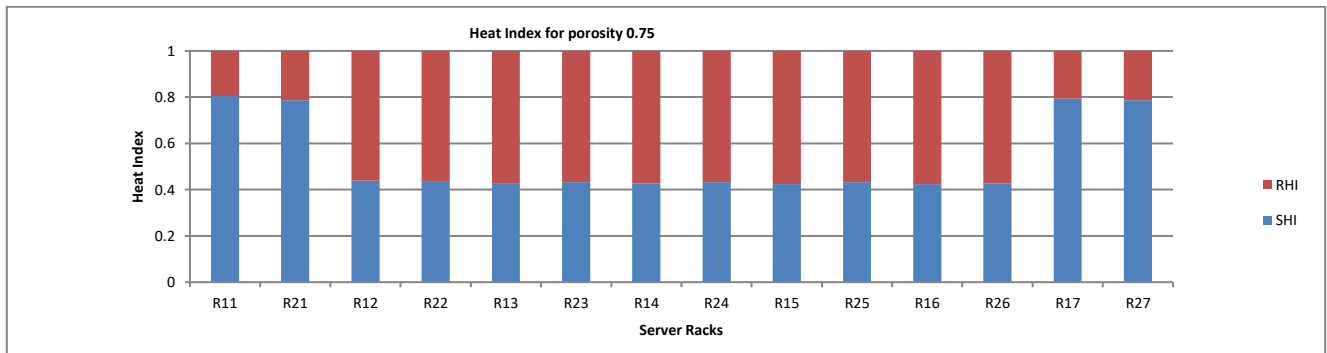
(a)



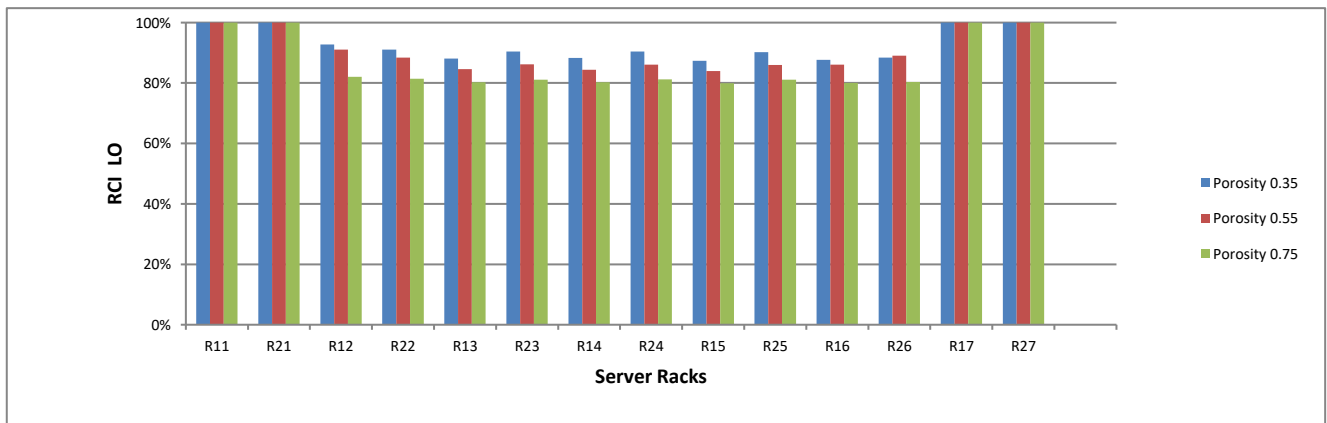
(b)



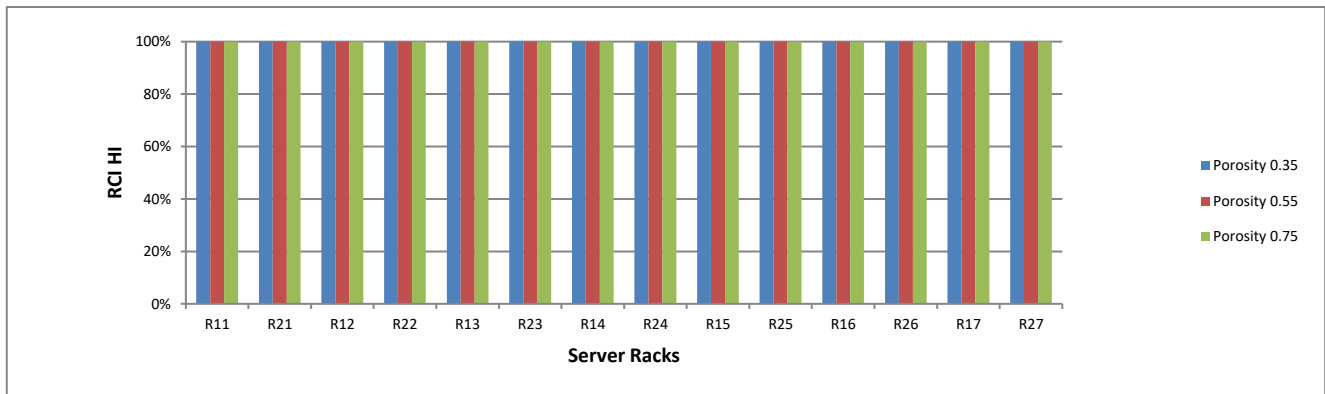
(c)



(d)



(e)



(f)

Figure5: Effect of server density on thermal metrics (a) RTI (b), (c), (d) SHI/RHI, (e) RCILO and (f) RCIHI.

V. CONCLUSION

Low server density racks have a higher barrier to air movement than higher density racks, resulting in more recirculation as a result the RTI value raises as porosity raises. As a result of recirculation, the value of SHI was observed to increase and on the other hand, results in lower RHI values. It is observed that RCILO values are decreasing with higher server density indicating lower inlet temperature at higher porosities. RCIHI values are within the recommended range. The maximum temperature observed within the server rack is 36.09°C for porosity 0.35, 27.16°C for porosity 0.55 and 23.81°C for porosity 0.75.

I. REFERENCES

- [1]. A. Habibi Khalaj and S. K. Halgamuge, "A Review on efficient thermal management of air- and liquid-cooled data centers: From chip to the cooling system," *Applied Energy*, vol. 205, pp. 1165–1188, Nov. 2017, doi: 10.1016/j.apenergy.2017.08.037.
- [2]. B. Watson and V. K. Venkiteswaran, "Universal Cooling of Data Centres: A CFD Analysis," *Energy Procedia*, vol. 142, pp. 2711–2720, Dec. 2017, doi: 10.1016/j.egypro.2017.12.215.
- [3]. S. V. Patankar, "Airflow and Cooling in a Data Center," *Journal of Heat Transfer*, vol. 132, no. 7, p. 073001, Jul. 2010, doi: 10.1115/1.4000703.
- [4]. R. A. Steinbrecher, "ASHRAE's Evolving Thermal Guidelines," *ASHRAE Journal*, p. 7, 2011.
- [5]. H. Moazamigoodarzi, P. J. Tsai, S. Pal, S. Ghosh, and I. K. Puri, "Influence of cooling architecture on data center power consumption," *Energy*, vol. 183, pp. 525–535, Sep. 2019, doi: 10.1016/j.energy.2019.06.140.
- [6]. S. A. Nada and M. A. Said, "Effect of CRAC units layout on thermal management of data center," *Applied Thermal Engineering*, vol. 118, pp. 339–344, May 2017, doi: 10.1016/j.applthermaleng.2017.03.003.
- [7]. E. Oró, A. Garcia, and J. Salom, "Experimental and numerical analysis of the air management in a data centre in Spain," *Energy and Buildings*, vol. 116, pp. 553–561, Mar. 2016, doi: 10.1016/j.enbuild.2016.01.037.

- [8]. G. D. Chethana and B. S. Gowda, "Thermal management of air and liquid cooled data centres: A review," *Materials Today: Proceedings*, vol. 45, pp. 145–149, 2021, doi: <https://doi.org/10.1016/j.matpr.2020.10.396>.
- [9]. A. R. I. Mukaffi, R. S. Arief, W. Hendradjit, and R. Romadhon, "Optimization of Cooling System for Data Center Case Study: PAU ITB Data Center," *Procedia Engineering*, vol. 170, pp. 552–557, 2017, doi: [10.1016/j.proeng.2017.03.088](https://doi.org/10.1016/j.proeng.2017.03.088).
- [10]. C. Nadjahi, H. Louahlia, and S. Lemasson, "A review of thermal management and innovative cooling strategies for data center," *Sustainable Computing: Informatics and Systems*, vol. 19, pp. 14–28, Sep. 2018, doi: [10.1016/j.suscom.2018.05.002](https://doi.org/10.1016/j.suscom.2018.05.002).
- [11]. I. W. Kuncoro, N. A. Pambudi, M. K. Biddinika, I. Widiastuti, M. Hijriawan, and K. M. Wibowo, "Immersion cooling as the next technology for data center cooling: A review," *J. Phys.: Conf. Ser.*, vol. 1402, p. 044057, Dec. 2019, doi: [10.1088/1742-6596/1402/4/044057](https://doi.org/10.1088/1742-6596/1402/4/044057).
- [12]. J. Cho and J. Woo, "Development and experimental study of an independent row-based cooling system for improving thermal performance of a data center," *Applied Thermal Engineering*, vol. 169, p. 114857, Mar. 2020, doi: [10.1016/j.applthermaleng.2019.114857](https://doi.org/10.1016/j.applthermaleng.2019.114857).
- [13]. N. M. S. Hassan, M. M. K. Khan, M. G. Rasul, and A. Oo, "Thermal Performance Modelling of Data Centre- A Case Study," p. 7.
- [14]. V. E. Ahmadi and H. S. Erden, "A parametric CFD study of computer room air handling bypass in air-cooled data centers," *Applied Thermal Engineering*, vol. 166, p. 114685, Feb. 2020, doi: [10.1016/j.applthermaleng.2019.114685](https://doi.org/10.1016/j.applthermaleng.2019.114685).
- [15]. Z. Huang, K. Dong, Q. Sun, L. Su, and T. Liu, "Numerical Simulation and Comparative Analysis of Different Airflow Distributions in Data Centers," *Procedia Engineering*, vol. 205, pp. 2378–2385, 2017, doi: [10.1016/j.proeng.2017.09.854](https://doi.org/10.1016/j.proeng.2017.09.854).
- [16]. Chaoqiang Jin, X. Bai, and C. Yang, "Effects of airflow on the thermal environment and energy efficiency in raised-floor data centers: A review," *Science of The Total Environment*, vol. 695, p. 133801, Dec. 2019, doi: [10.1016/j.scitotenv.2019.133801](https://doi.org/10.1016/j.scitotenv.2019.133801).
- [17]. A. Capozzoli, G. Serale, L. Liuzzo, and M. Chinnici, "Thermal Metrics for Data Centers: A Critical Review," *Energy Procedia*, vol. 62, pp. 391–400, 2014, doi: [10.1016/j.egypro.2014.12.401](https://doi.org/10.1016/j.egypro.2014.12.401).
- [18]. Y. Fulpagare and A. Bhargav, "Advances in data center thermal management," *Renewable and Sustainable Energy Reviews*, vol. 43, pp. 981–996, Mar. 2015, doi: [10.1016/j.rser.2014.11.056](https://doi.org/10.1016/j.rser.2014.11.056).
- [19]. D. V. Sheth and S. K. Saha, "Numerical study of thermal management of data centre using porous medium approach," *Journal of Building Engineering*, vol. 22, pp. 200–215, Mar. 2019, doi: [10.1016/j.jobe.2018.12.012](https://doi.org/10.1016/j.jobe.2018.12.012).
- [20]. S. A. Nada, M. A. Said, and M. A. Rady, "CFD investigations of data centers' thermal performance for different configurations of CRACs units and aisles separation," *Alexandria Engineering Journal*, vol. 55, no. 2, pp. 959–971, Jun. 2016, doi: [10.1016/j.aej.2016.02.025](https://doi.org/10.1016/j.aej.2016.02.025).



NVH Analysis of Acoustic Materials by Using Aluminium, Steel and Carbon Fiber

Vijaykumar¹, Dr. Vinay V. Kuppast²

¹Research scholar, Department of Mechanical Engineering, BEC, Bagalkot, Karnataka, India

²Professor, Department of Mechanical Engineering, BEC, Bagalkot, Karnataka, India

ABSTRACT

The vehicle acoustic execution advancement in an undertaking to decide the issue of sound strategies was made the clamor inside the lodge. In this paper to review the progressions up until this point did in the field of enhancement contemplates on reduction of commotion in the truck lodges by utilizing acoustic materials. Considering this, it is to examine the chance of acoustic materials as aluminum, steel metal and carbon fiber with plan to further develop the lodge commotion by NVH investigation can be done by utilizing ansys and hypermesh programming's. By observing the investigation upsides of recurrence, sound and weighted sound can be finished up the acoustic materials are great for calmer applications.

Keywords: Noise, vibration, harshness, acoustic materials.

I. INTRODUCTION

It is apparent that the quieter automotive cabin design plays a major role in meeting the statutory guidelines in minimizing the health hazards due to Noise, vibration, and harshness (NVH) of automobile vehicles. Many studies have been carried out in minimizing the noise of the automotive cabin. Still researches are going on to find out the new methods and techniques to reduce the noise of the cabin. The NVH analysis of acoustic materials will give the insight of a possibility of reduction of noise and vibration for quieter automotive cabin. The following paragraphs discuss some of the acoustic materials of design importance which will be considered for the analysis. [1,2]

Acoustic Materials

Acoustic materials are used in recording studios, the home and in offices to manipulate, deaden sound and noise. Noise can be reduced in energy, absorbed to stop resonance and echoes and reduced in pressure level using these materials. An acoustic material is a material designed to control, direct, and manipulate sound waves. Acoustic materials are often placed over interior wall surface in order to prevent reverberation of the sound waves. [3]

The objectives of the present work is to determine the best combination of acoustic materials which exhibit the minimum values of vibration and noise, better mechanical strength and higher absorptivity from the simulation.[4]

II. METHODOLOGY

- Determination of acoustic materials for clamor and vibration portrayal to set up the example for the review.
- Doing the investigation by considering these examples utilizing CAE approaches.
- Examination for the best blend of vibrio-acoustic example for low clamor and vibration weakening in light of CAE investigation.

A. Specimen of vibro-acoustic Materials

In this phase, the modeling of the specimen and the vibro-acoustic analysis (FSI-Fluid Structure Interface analysis) is carried out. The following cases have been considered for the analysis to find the amplitude of vibration in MPa and sound pressure level (SPL) in dB and weighted sound pressure in dBA.

Case 1: Base metal + Damper (Standard Aluminum-6061+ Carbon Fiber)

Case 2: Base metal + Damper (Standard Aluminum-7075+ Carbon Fiber)

Case 3: Base metal + Damper (Standard Steel-316+ Carbon Fiber)

Case 4: Base metal + Damper (Standard Steel -304+ Carbon Fiber)

III. RESULTS AND DISCUSSION

The frequency up to 5000HZ are applied and acoustic pressure will default in fluid region and no need to apply acoustic pressure, for obtaining sound pressure level and amplitudes.

The amplitude of vibration in MPa and sound pressure level (SPL) in dB and weighted sound pressure in dBA for the different cases considered are discussed. The frequency plots have been given in the following Figures.

Case 1: Aluminum 6061 + Carbon Fiber

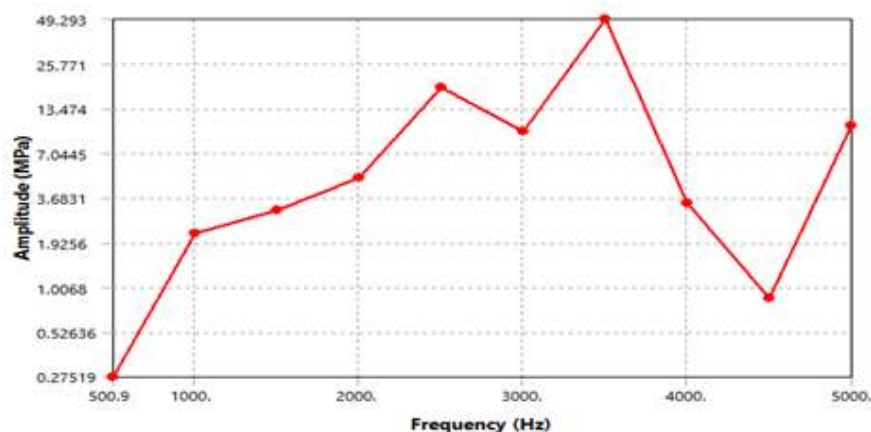


Figure 1: Amplitude Vs Frequency Response

The figure 1 shows the amplitude Vs frequency graph of aluminum 6061 and carbon fiber and amplitude is in MPa and frequency in Hz. And the maximum amplitude is ranges between 3000 Hz -4000 Hz.

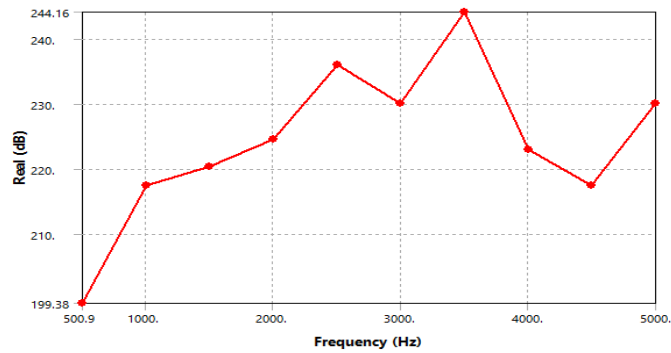


Figure 2: Real (Sound) Vs Frequency Response

The figure 2 shows the Sound pressure level (SPL) Vs frequency graph of aluminum 6061, carbon fiber and SPL in dB and frequency in Hz. And the maximum SPL is ranges between 3000 Hz -4000 Hz.

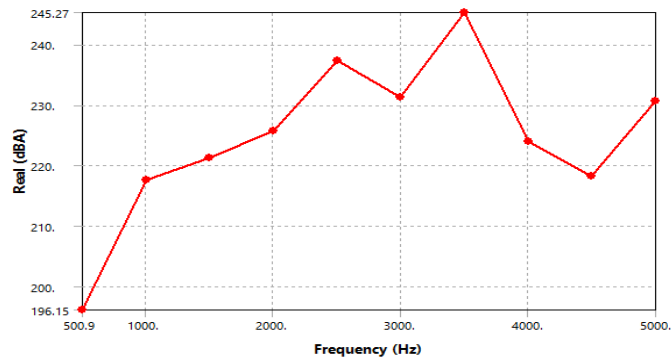


Figure 3: Real (Weighted Sound) Vs Frequency Response

The figure 3 shows the weighted SPL Vs frequency graph of aluminum 6061, carbon fiber and amplitude is in MPa and frequency in Hz. And the maximum weighted SPL is ranges between 3000 Hz -4000 Hz.

Case 2: Aluminum 7075 + Carbon Fiber

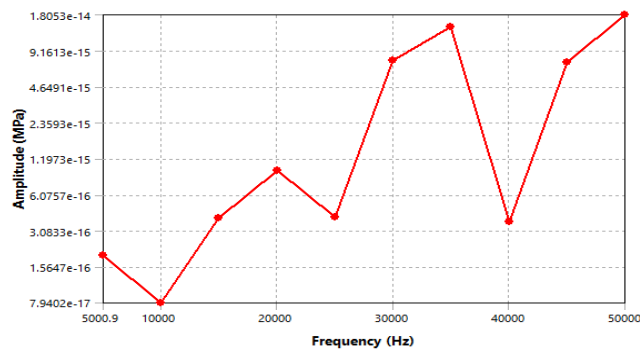


Figure 4: Amplitude Vs Frequency Response

The figure 4 shows the amplitude Vs frequency graph of aluminum 7075 and carbon fiber and amplitude is in MPa and frequency in Hz. And the maximum amplitude is ranges between 3000 Hz -5000 Hz.

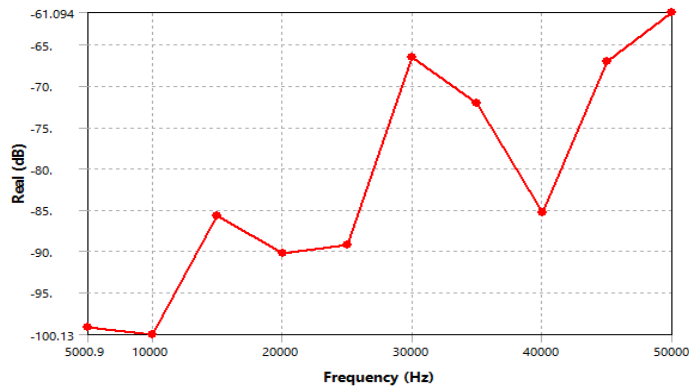


Figure 5: Real (Sound) Vs Frequency Response

The figure 5 shows the Sound pressure level (SPL) Vs frequency graph of aluminum 7075, carbon fiber and SPL in dB and frequency in Hz. And the maximum SPL is ranges between 3000 Hz -5000 Hz.

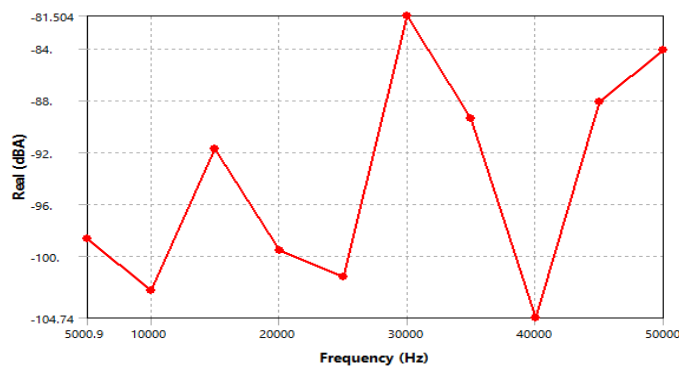


Figure 6: Real (Weighted Sound) Vs Frequency Response

The figure 6 shows the weighted SPL Vs frequency graph of aluminum 7075, carbon fiber and amplitude is in MPa and frequency in Hz. And the maximum weighted SPL is ranges between 3000 Hz -5000 Hz.

Case 3: Steel 304 + Carbon Fiber

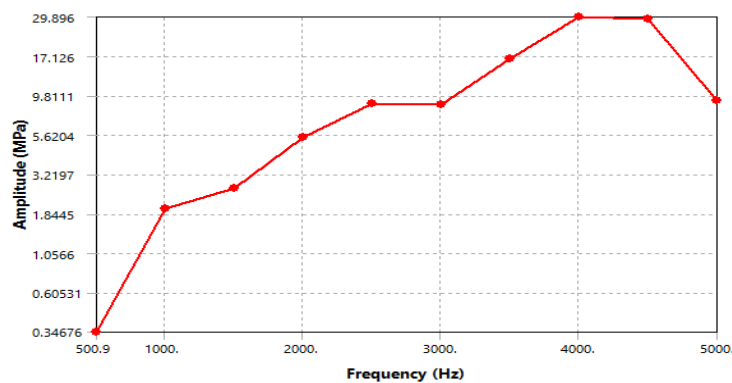


Figure 7: Amplitude Vs Frequency Response

The figure 7 shows the amplitude Vs frequency graph of steel 304 and carbon fiber and amplitude is in MPa and frequency in Hz. And the maximum amplitude is ranges between 4000 Hz -4500 Hz.

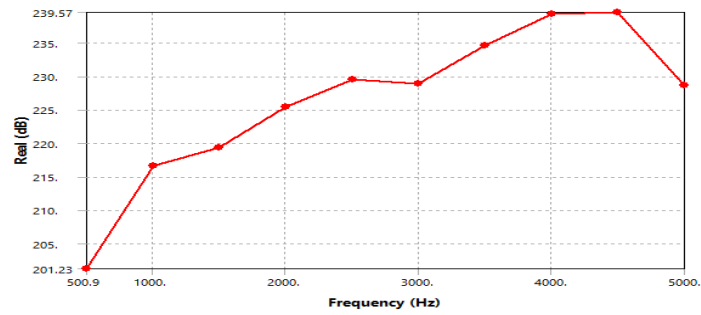


Figure 8: Real (Sound) Vs Frequency Response

The figure 8 shows the Sound pressure level (SPL) Vs frequency graph of Steel 304, carbon fiber and SPL in dB and frequency in Hz. And the maximum SPL is ranges between 4000 Hz -4500 Hz.

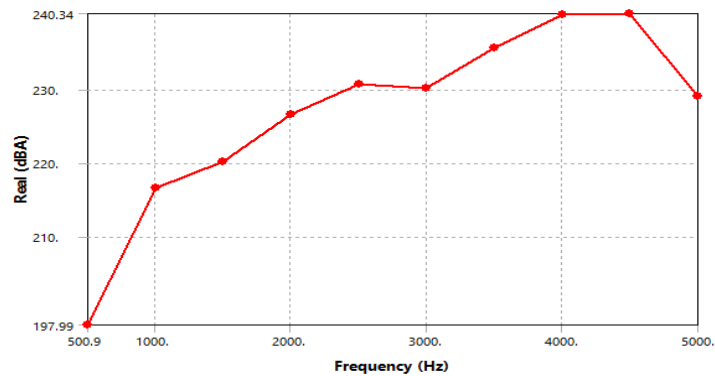


Figure 9: Real (Weighted Sound) Vs Frequency Response

The figure 9 shows the weighted SPL Vs frequency graph of Steel 304, carbon fiber and amplitude is in MPa and frequency in Hz. And the maximum weighted SPL is ranges between 4000 Hz -5000 Hz.

Case 4: Steel 316 + Carbon Fiber

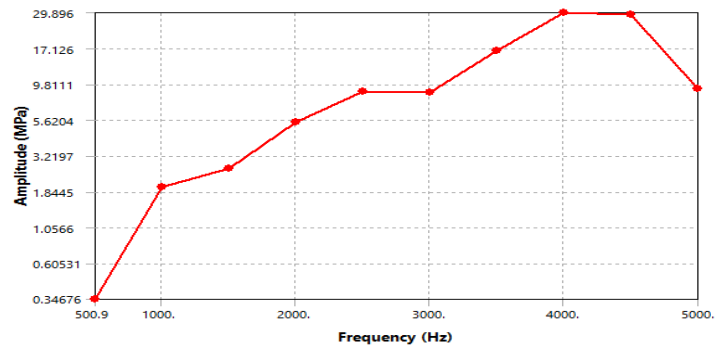


Figure 10: Amplitude Vs Frequency Response

The figure 10 shows the amplitude Vs frequency graph of Steel 316, carbon fiber and amplitude is in MPa and frequency in Hz. And the maximum amplitude is ranges between 4000 Hz -4500 Hz.

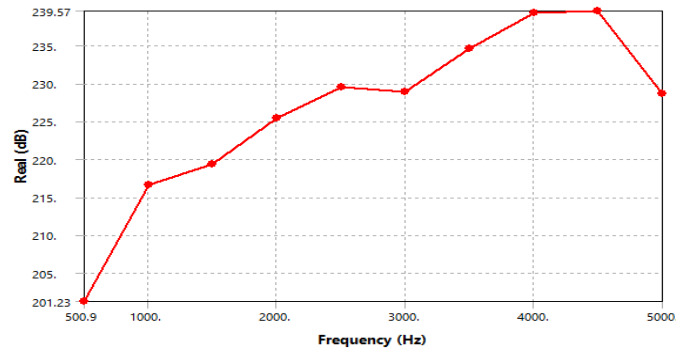


Figure 11: Real (Sound) Vs Frequency Response

The figure 11 shows the Sound pressure level (SPL) Vs frequency graph of Steel 316 and carbon fiber and SPL in dB and frequency in Hz. And the maximum SPL is ranges between 4000 Hz -4500 Hz.

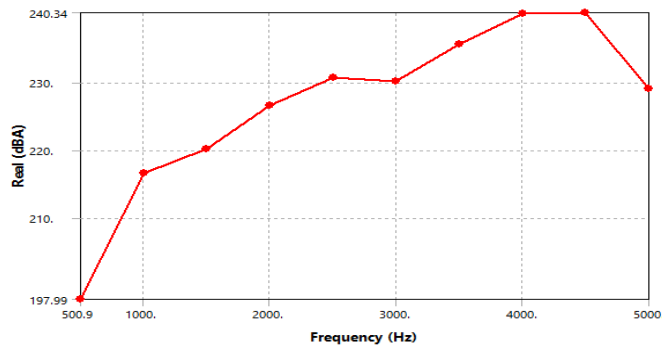


Figure 12: Real (Weighted Sound) Vs Frequency Response

The figure 12 shows the weighted SPL Vs frequency graph of Steel 316, carbon fiber and amplitude is in MPa and frequency in Hz. And the maximum weighted SPL is ranges between 4000 Hz -5000 Hz.

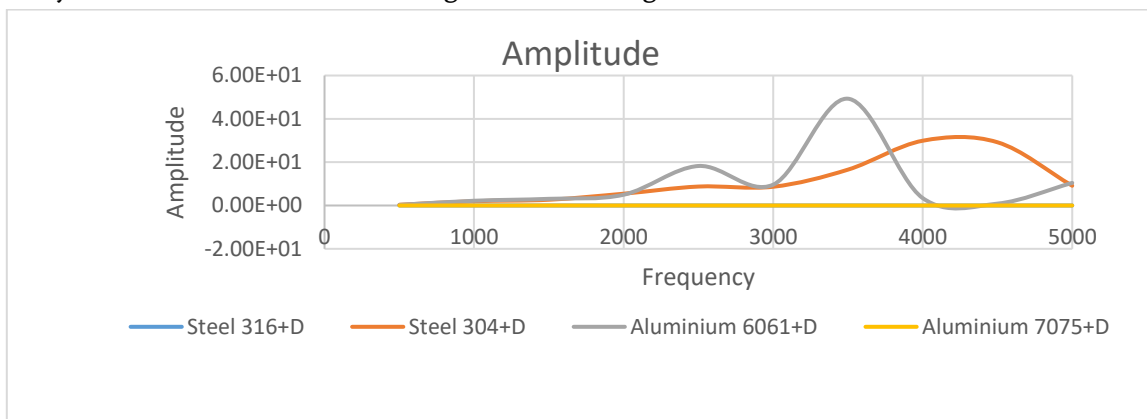


Figure 12.1 shows the analogy data comparison for Amplitude vs. frequency responses

The Figure 12.1 shows the different colour for different material, the blue line for Steel 316 and carbon fiber composition, orange line for steel 304 and carbon fiber and purple for aluminium 6061 and carbon fiber and yellow for aluminium 7075 and carbon fiber they shows the characteristics of the amplitude and frequency ranges. It can be attracted for achieving the results from 3000-4000Hz and maximum amplitude territories are less than 500mpa are achieved and are shown in figure.

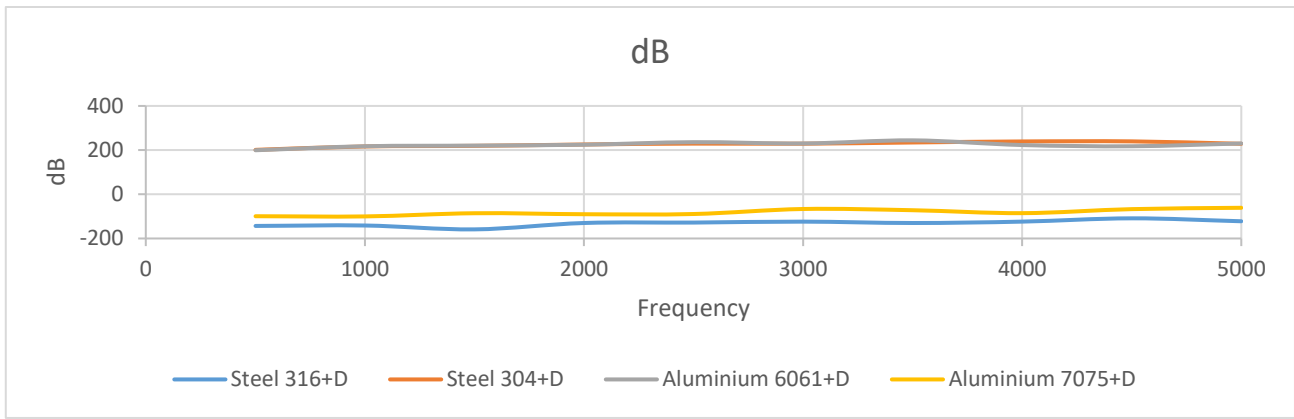


Figure 12.2 shows the analogy data comparison for SPL vs. frequency responses. The Fig 12.2 shows the different colour for different material, the blue line for Steel 316 and carbon fiber composition, orange line for steel 304 and carbon fiber and purple for aluminium 6061 and carbon fiber and yellow for aluminium 7075 and carbon fiber they shows the characteristics of the SPL and frequency ranges. It can be attracted for achieving the results from 1000-4000Hz and maximum amplitude territories are less than 300mpa are achieved and are shown in figure.

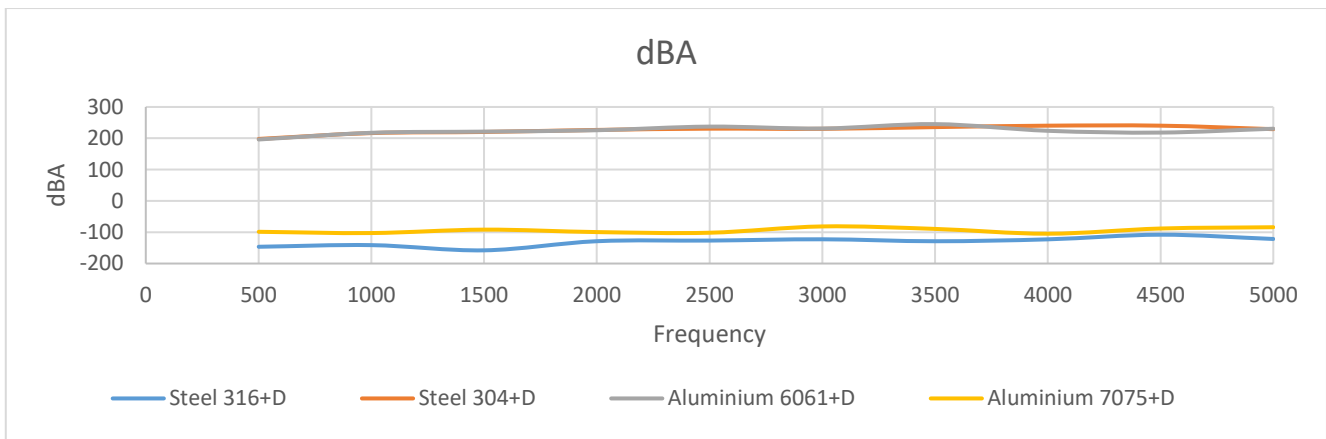


Figure 12.3 shows the analogy data comparison for weighted SPL vs. frequency responses. The Figure 12.3 shows the different colour for different material, the blue line for Steel 316 and carbon fiber composition, orange line for steel 304 and carbon fiber and purple for aluminium 6061 and carbon fiber and yellow for aluminium 7075 and carbon fiber they shows the characteristics of the weighted SPL and frequency ranges. It can be attracted for achieving the results from 0-5000Hz and maximum amplitude territories are less than 500mpa are achieved and are shown in figure.

IV. CONCLUSION

The straight portrayal shows that the ranges of explored characters for damping angle and Absorption co-efficient which are seen from beginning to 5000Hz territory. We can accomplish the last end for vibro-acoustic examination by concentrating on all the liner attributes of decided upsides of all the successful material.

The yellow line addresses the Steel-316, carbon fiber which is generally proficient than different materials accounts, the other blend of materials are slacking in damping perspective and ingestion co-effective by looking at a few qualities in our review recurrence ranges. What's more Aluminum-7075, carbon fiber, is the adjoining worth to the Steel-316, carbon fiber, and besides Aluminum-7075, carbon fiber is the closer worth than other acoustic materials. At last we wrap up that the Steel-316; carbon fiber material is gigantic in the picked material.

V. REFERENCES

- [1]. Vijaykumar , Dr. Vinay V. Kuppast, A survey on acoustic materials for noise and Vibration control in automotive cabin, International Journal of Research, ISSN NO:2236-6124, Volume VIII, Issue VI, Page No:5869. (UGC Approved) , June 2019
- [2]. Vijaykumar , Dr. Vinay V. Kuppast, NVH analysis of acoustic materials by using aluminium and steel , Journal of Advancements in Material Engineering, Volume VI, Issue 2, and eISSN NO: 2582-0036, May-Aug 2021, <https://doi.org/10.46610/JoAME.2021.v06i02.005>.
- [3]. Vijaykumar , Dr. Vinay V. Kuppast, NVH analysis of acoustic materials, Elsevier, SSRN, Materials science eJournal, Vol 4, Issue 165, November 01, 2021. Available at <http://dx.doi.org/10.2139/ssrn.3924050>.
- [4]. Vijaykumar , Dr. Vinay V. Kuppast, NVH analysis of acoustic materials by using aluminum, steel and carbon fiber for vehicle design, Authorea, Wiley Publishers, Hoboken, New Jersey, United states, October 11, 2021. DOI: 10.22541/au.163398426.60707278/v1.
- [5]. Roshan Kumar Gopal, Remin V, Richard Sen, Aero Acoustics Analysis of Car's ORVM, International Journal of Science and Engineering Investigations vol. 4, issue 38, March 2015.
- [6]. Satya Prasad Mavuri, Simon Watkins, Xu Wang, Simon St. Hill, David Weymouth, An Investigation and Bench Marking of Vehicle HVAC Cabin Noise, in 2008 SAE World Congress, Detroit, United States, 14-17 April, 2008.
- [7]. Yang Zhendong, Gu Zhengqi, Tu Jiyuan ,Dong Guangping,Wang Yiping , Numerical analysis and passive control of a car side window buffeting noise based on Scale-Adaptive Simulation, Z. Yang et al. / Applied Acoustics 79 (2014) 23–34.
- [8]. Huifang Ding, Yunxia Zhang, Hejiang Sun, Lianyuan Feng, Analysis of PM2.5 Distribution and transfer characteristics in a car Cabin, Energy and Buildings 127 (2016) 252–258.
- [9]. Semiha Türkay, Hüseyin Akçay, Multi-objective control design for a truck cabin, 19th IFAC World Congress Cape Town, South Africa. August 24-29, 2014.
- [10]. Nicholas D. Cottrell & Benjamin K. Barton, The impact of artificial vehicle sounds for Pedestrians on driver stress, Ergonomics Vol. 55, No. 12, December 2012, 1476–1486.
- [11]. Jerkin asutay, Sound sources contributing to the interior sound environment in truck cabins, erkin asutay, 2007, Master's thesis 2007:119.
- [12]. Zhengqing Liu, Mohammad Fard, Reza Jazar, Development of an Acoustic Material Database for Vehicle Interior Trims, Conference Paper in SAE Technical Papers March 2015.
- [13]. K.Gulyas, G.Pinte, F.Augusztinovicz, W.Desmet, P.Sas, Active noise control in agricultural machines, proceedings of ISMA 2002 - volume i.

- [14]. Damon W. K. Wong, Member, IEEE, and George Chen, Optical Design and Multipath Analysis for Broadband Optical Wireless in an Aircraft Passenger Cabin Application, IEEE transactions on vehicular technology, vol. 57, no. 6, November 2008.
- [15]. Vishalagoud. S. Patil , Dr. S. N. Kurbet, A survey on Recent Design Optimizations of Truck Cabin to Reduce Interior Noise, IJRSET, Vol. 6, Issue 12, December 2017.
- [16]. Peter davidsson, Structure-acoustic examination limited component displaying and decrease techniques, Structural Mechanics ISRN LUTVDG/TVSM- - 04/1018- - SE (1-180) ISBN 91-628-6176-X ISSN 0281-6679.
- [17]. Linus Yinn Leng Ang, Yong Khiang Koh and Heow Pueh Lee, Acoustic Metamaterials: A Potential for Cabin Noise Control in Automobiles and Armored Vehicles, International Journal of Applied Mechanics Vol. 8, No. 5 (2016) 1650072 (35 pages), The Author(s) DOI: 10.1142/S1758825116500721
- [18]. Prof. Deulgaonkar V.R, Prof.Dr.Kallurkar S.P, Prof.Dr. Mattani A.G, Review and Diagnostics of noise and vibrations in Automobiles, IJMERE, Vol.1, Issue2, pp-242-246 ISSN: 2249-6645
- [19]. K.D.Wang, LUK Incorporated, Kalyan Bairavarasu LUK Incorporated, Noise and Vibration Analysis by Finite Elements.
- [20]. E. Lijzzato and c. Lecointre, some straightforward and powerful techniques for sound source recognizable proof with geometrical acoustic models, diary of sound and vibration (1986) 105 (3), 473-490.
- [21]. Zbigniew Dąbrowski and Bartosz Stankiewicz, Methodology of Selecting the Reference Source for an Active Noise Control System in a Car, International Journal of Occupational Safety and Ergonomics, International Journal of Occupational Safety and Ergonomics (JOSE) 2013, Vol. 19, No. 1, 117–125.
- [22]. S.B. Bealko, Mining takes truck taxi noise: An assessment of three acoustical conditions.
- [23]. The car explore relationship of India, P.b. no. 832, Pune 412 004, Automotive Vehicles – Interior Noise – Method of Measurement and Requirements, December 2004.
- [24]. Harijono Djojodihardjo, Vibro-acoustic examination of the acoustic-structure Interaction of adaptable structure because of acoustic excitation, Pii: s0094-5765(14)00460-3, Reference: AA5278, Accepted date: 16 November 2014.
- [25]. RogérioPirk, StijnJonckheere, BertPluymers, WimDesmet, Vibro-acoustic displaying and approval utilizing viscoelastic material, C. R. Mecanique 345 (2017) 208–220.
- [26]. Andrea Santoni , Paolo Bonfiglio, Francesco Mollica, Patrizio Fausti, Francesco Pompoli,Valentina Mazzanti, Vibro-acoustic streamlining of Wood Plastic Composite frameworks, Construction and Building Materials 174 (2018) 730–740.
- [27]. A. Author, B. Author, and C. Author “Name of paper,” Title of Journal, vol. x, no. x, Month (abbreviated), year, Art. no. xxx. [in case article numbers are used]



Enhancing Surface Layer Properties of Al6061-B4C Composite by Controlled Shot Peening

Dr. Suresh Kumar. S¹, Rathan Kumar K²

¹Associate Professor, Department of Mechanical Engineering, ATME College of Engineering- Mysuru, Karnataka, India

²Assistant Professor, Department of Mechanical Engineering, Government Engineering College, Chamarajanagar, Karnataka, India

ABSTRACT

In recent days Surface treatment processes are gaining much importance because it enhances the mechanical properties. It is required to enhance surface layer properties of aerospace and automobile components to avoid early failure. Shot peening process is most commonly used surface treatment process to improve surface properties. In shot peening process Spherical shots are blasted with controlled parameters on the surface which induces compressive residual stresses by causing plastic deformation. In the present work Al 6061 with 5, 10 and 15 wt. % of B₄C reinforcements were synthesized by stir casting route and conducted shot peening process. It is observed that peened specimens exhibited improved hardness, compressive residual stresses (CRS), and fatigue life with refinement in microstructure.

Keywords: Shot Peening process, Al6061-B₄C composite, Compressive Residual stress

I. INTRODUCTION

Al-6061 alloy is extensively used 6xxx series which offers a range of good properties [1]. Al-6061 based composites are highly corrosion resistant, light weight, ductile, tough and easily extractable in nature. It exhibits moderate strength with a suitable wear resistance. Being stiff and strong material it finds many applications in different engineering fields [2, 3].

Boron Carbide (B₄C) ceramics is an exceptional physical and mechanical characteristic such as high impact and wear strength and is capable of absorbing high neutron [4, 5].

As a good ceramic material, boron carbide (B₄C) has attracted attention in a wide variety of applications especially as a neutron absorption material.

Various mechanical methods such as rolling and peening methods are used to induce residual stresses. Residual stresses play a significant role in preventing failure of components [6-10]. In rolling process material is passed between one or more rollers which rotate in opposite direction causes plastic deformation in turn induces the compressive residual stresses. Shot peening is surface strengthening process where spherical shots are blasted on

the specimen which causes plastic deformation by introducing compressive residual stresses. Cast steel shots are directed through suction type shot peening machine with suitable parameters. Shot peening process is intended to mechanical components such as coiled springs, turbine blades, connecting rods, crankshafts, gearwheels and leaf springs to enhance surface properties and fatigue life.

Most frequently used peening techniques are laser peening, cavitation peening and shot peening [11-13]. In laser peening process high energy laser beam is passed on the surface which creates shock waves that causes plastic deformation on the surface which in turn induce deeper compressive stresses. In cavitation peening low pressure high velocity water jet made to strike on the surface which creates bubbles when these bubbles impinges creates impact force which indeed creates residual stresses.

The present work focuses on the effect of shot peening on surface properties of B₄C composite material. Air blast peening was conducted to study its effect on Hardness, CRS, fatigue life cycles and microstructure.

II. METHODS AND MATERIAL

2.1 Material selection and Fabrication

Matrix material used is Al-6061 and 5, 10 and 15 wt. % of B₄C reinforced particulates are casted by using stir casting method. **Table 1&2** illustrates chemical composition of Al-6061 and B₄C material. Stir casting process is an extensively used method to fabricate MMC's in liquid state in which molten metal is mixed in the furnace by means of mechanical stirring [14-16]. Correct mixing of matrix and reinforcement takes place with the help of mechanical stirring during stir casting process. Stir casting setup along with stirrer and casted specimens are as shown in **Fig.1&2**.

Table: 1 Chemical Composition of Al 6061

Elements	Mg	Si	Ti	V	Mn	Cu	Fe	Al
Wt. %	1.08	0.63	0.02	0.01	0.52	0.32	0.17	Remainder

Table: 2 Chemical Composition of B₄C

Elements	B+C	B	C	B ₂ O ₃	Fe	Si
Wt. %	98.5	74-79	17-24	0.1-1.0	0.2-0.5	0.1-0.3



Figure 1: Stir casting process Set-Up



Figure 2: Casted specimens

2.2 Air blast shot peening process

Shot peening process was conducted on machined specimens by using Air blast shot peening machine illustrated in **Fig.3** Suitable parameters such as angle of striking nozzle is 90° , Almen intensity 4A (A-for common application of peening), standoff distance 150mm and S170 spherical cast steel shots of 0.43mm was selected **Fig.4**. Shots are made to strike in all around the specimens by moving the working table and rotating the round specimens held in attachment [17]. Shots are re-circulated with suitable air pressure from collector to tube rod then it passed through nozzle. Shot peened specimens are illustrated in **Fig.5**.



Figure 3: Air Blast shot Peening Machine



Figure 4: Cast Steel Shots

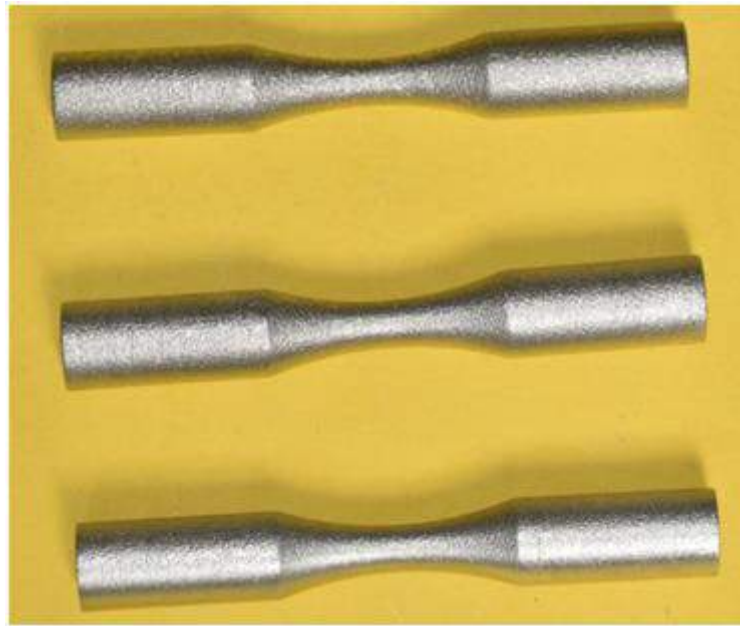


Figure 5: Shot peened specimens

III. RESULTS AND DISCUSSION

A. Effect of Shot peening on Hardness (VHN)

Shot peening improves the surface hardness [18] of B₄C Composites of 5, 10, 15 Wt. % . Hence, in this present work shot peening was carried out on different wt.% of B₄C specimens. **Fig.5** shows the Vickers Hardness value among these 5% B₄C composite exhibited hardness value 72VHN compared base metal. Increase in percentage reinforcement, specimens become hard hence shot impact causes less deformation therefore 15% Reinforced composite exhibited 77 VHN.

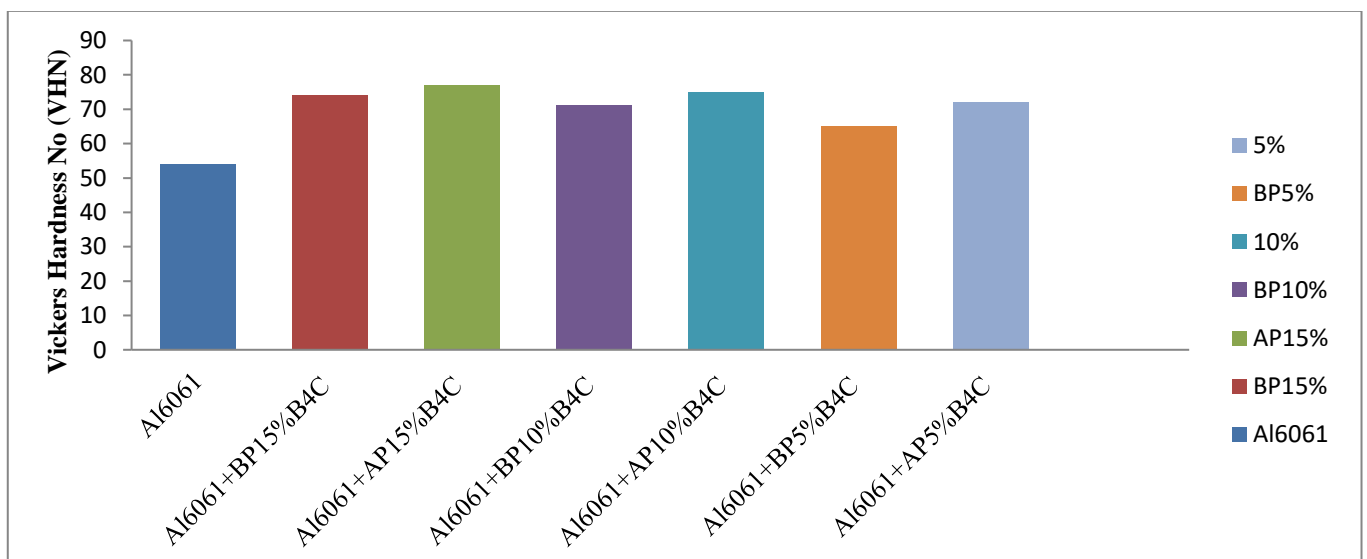


Figure 5: VHN for different wt% Before and after peening

B. Influence of Shot Peening on Compressive residual stresses (CRS)

The main advantage of SP is to create CRS which helps to enhance the life of components. [19] In the present context, shot peening process was carried out and CRS was measured by X-ray diffraction equipment. CRS calculated based on lattice spacing and is determined precisely at two extreme values of θ typically 0° and 45° CRS is calculated. **Fig.6** shows the variation CRS for specimens. For 15wt. % specimen CRS measured value is -125MPa whereas for 5 wt. % -209MPa.

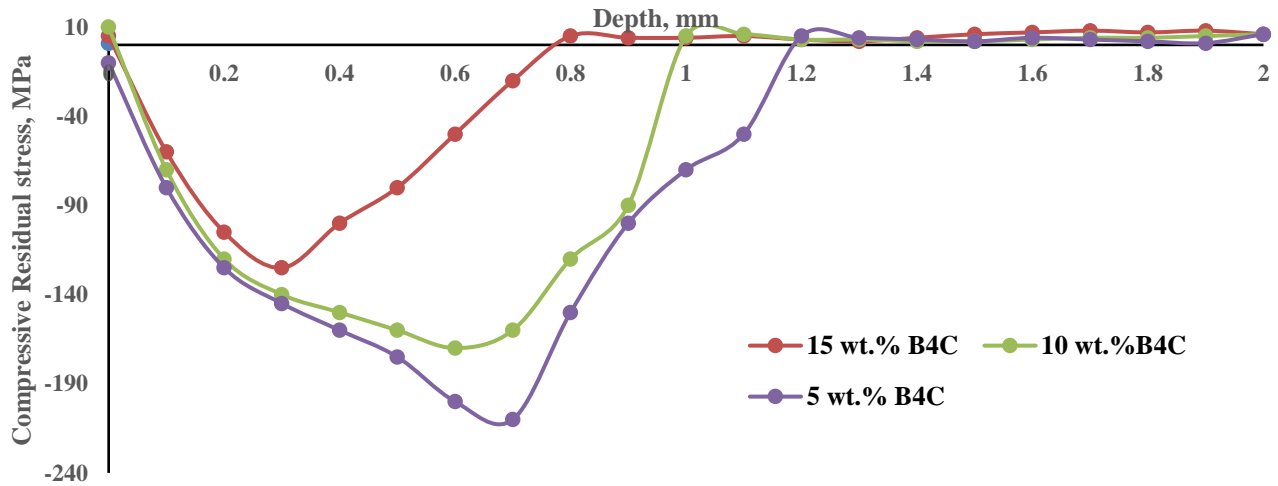


Figure 6: Compressive residual stress distribution

C. Microstructure

Microstructure unpeened and peened specimens are presented in SEM images **fig.7&8** several shots impact created dimples on the surface. On account of dimples, below the surface compression is created which reduces lattice spacing by refining the crystalline structure which indeed induces CRS [20]. In Unpeened specimen surface is free from dimples and smooth in surface consequently peened had dimples and craters.

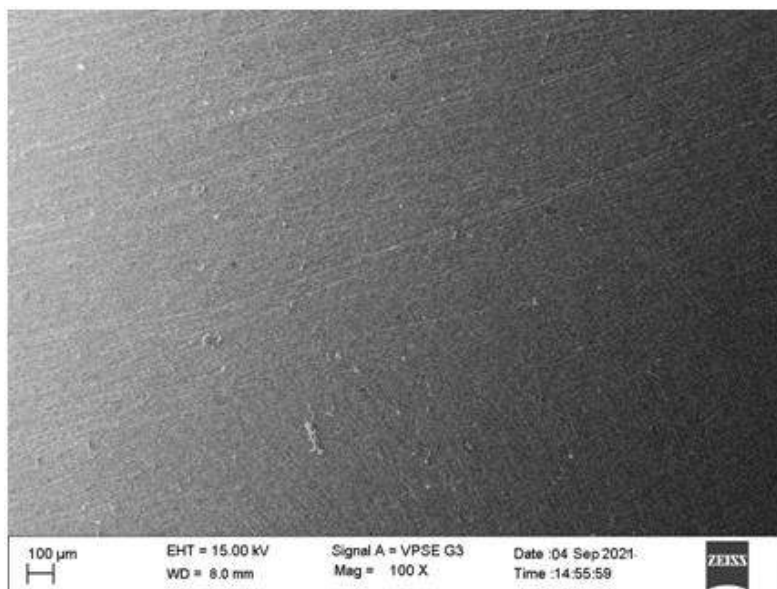


Figure 7: Al 6061-5 wt.% B₄C Unpeened

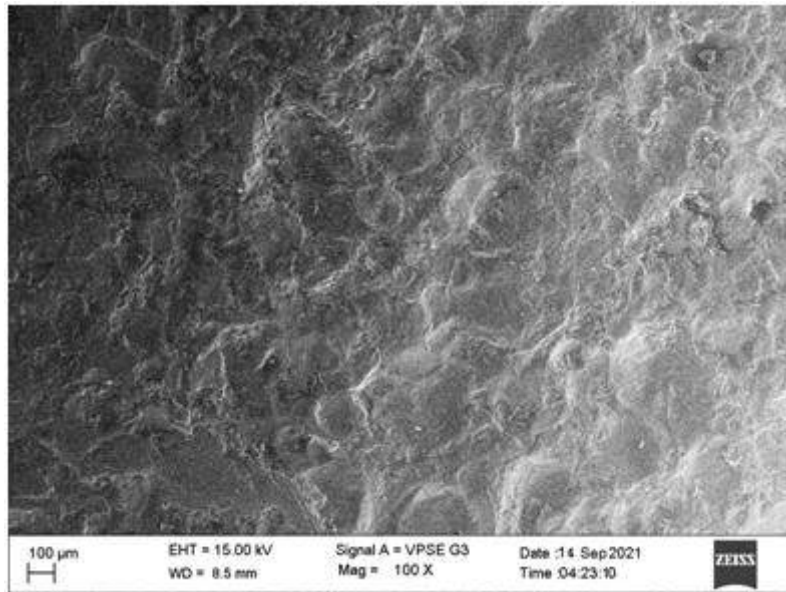


Figure 8: Al 6061-5 wt.% B₄C Shot peened

D. Fatigue Life

Fatigue life cycles of Al-6061 with 5, 10 and 15 wt.% B₄C reinforcements before and after peening is shown in **Table 3** . It is noticed that after shot peening fatigue life of all the specimens increased due to induced CRS [21&22].

Table: 3 No. of cycles to failure

wt.% of reinforcement	No. of cycles to failure	
	un peened	Shot peened with polish
5 wt.% B ₄ C	1,65,352	1,84,823
10 wt.% B ₄ C	1,43,513	1,52,531
15 wt.% B ₄ C	1,21,465	1,32,914

IV. CONCLUSION

Shot peening conducted on Al-6061 with 5, 10 and 15 wt. % of B₄C specimens using, S170 grade cast steel shots as per SAE J444 standards by using 4A Almen Intensity, standoff distance of 150 mm, 90° impingement angle with full coverage. The following conclusions are achieved:

- Stir casting method is one of the cost economical processes to obtain defect free casting and composites are successfully fabricated.
- Peening is done successfully with suitable parameters on the composites specimens.
- After Shot peening surface hardness increased up to 10.7 % due to strain hardening effect.

- Compressive residual stress (CRS) introduced up to -209MPa which indeed helped to increase fatigue life of the specimens.
- With the impact of shots Microstructure refinement taken place and lattice space is reduced.
- Fatigue life is enhanced in shot peened specimens because of induced CRS.

V. REFERENCES

- [1]. Ramesh, C. S., S. Pramod, and R. Keshavamurthy. "A study on microstructure and mechanical properties of Al 6061–TiB₂ in-situ composites." *Materials Science and Engineering: A* 528, no. 12 (2011): 4125-4132.
- [2]. Kumar, G B Veeresh, C. S. P. Rao, and N. Selvaraj. "Studies on mechanical and dry sliding wear of Al6061–SiC composites." *Composites Part B: Engineering* 43, no. 3 (2012): 1185-1191.
- [3]. El-Sabbagh, A., M. Soliman, M. Taha, and H. Palkowski. "Hot rolling behavior of stir-cast Al 6061 and Al 6082 alloys–SiC fine particulates reinforced composites." *Journal of Materials Processing Technology* 212, no. 2 (2012): 497-508.
- [4]. Suresh, S., N. Shenbag, and Vinayaga Moorthi. "Aluminium-titanium diboride (Al-TiB₂) metal matrix composites: challenges and opportunities." *Procedia Engineering* 38 (2012): 89-97.
- [5]. Xiaozhou, Cao, Wang Chao, Xue Xiangxin, and Cheng Gongjin. "Effect of ti addition on the residual aluminium content and mechanical properties of the B₄C-Al composites produced by vacuum infiltration." *Archives of Metallurgy and Materials* 60 (2015).
- [6]. Trško, Libor, Stanislava Fintová, František Nový, Otakar Bokůvka, Michal Jambor, Filip Pastorek, Zuzana Florková, and Monika Oravcová. "Study of relation between shot peening parameters and fatigue fracture surface character of an AW 7075 aluminium alloy." *Metals* 8, no. 2 (2018): 111.
- [7]. Al-Fattal, Dhafir Sadik, Samir Ali Amin Al-Rabii, and Ibrahim Mousa Al-Sudani. "Study the effect of shot peening with anodizing process on the mechanical properties and fatigue life of aluminum alloy 2024-T3." *Advances in Natural and Applied Sciences* 10, no. 15 (2016): 43-52.
- [8]. Nam, Yong-Seog, Yoo-In Jeong, Byung-Cheol Shin, and Jai-Hyun Byun. "Enhancing surface layer properties of an aircraft aluminum alloy by shot peening using response surface methodology." *Materials & Design* 83 (2015): 566-576.
- [9]. Benedetti, M., V. Fontanari, P. Scardi, CL Azanza Ricardo, and M. Bandini. "Reverse bending fatigue of shot peened 7075-T651 aluminium alloy: The role of residual stress relaxation." *International Journal of Fatigue* 31, no. 8-9 (2009): 1225-1236
- [10]. Suresh Kumar. S, Dr. G. Mallesh "Design and Development of Air Blast Shot Peening Machine to Study the Effect of Shot Peening Process On Microstructure and Residual Stress in Al-2024 Aluminum Alloy" *International Conference on Recent Trends in Science & Technology-2020 (ICRTST - 2020)*, April 8th & 9th, 2020, E-ISSN: 2395-0056.
- [11]. Bagheri, S., and Mario Guagliano. "Review of shot peening processes to obtain nanocrystalline surfaces in metal alloys." *Surface Engineering* 25, no. 1 (2009): 3-14.
- [12]. Gujba, Abdullahi K., and Mamoun Medraj. "Laser peening process and its impact on materials properties in comparison with shot peening and ultrasonic impact peening." *Materials* 7, no. 12 (2014): 7925-7974.

- [13]. Takahashi, Koji, Hiroko Osedo, Takaya Suzuki, and Shinsaku Fukuda. "Fatigue strength improvement of aluminum alloy with a crack-like surface defect using shot peening and cavitation peening." *Engineering Fracture Mechanics* 193 (2018): 151-161.
- [14]. M.K. Surappa: Microstructure evolution during solidification of DRMMCs: state of art, *Journal of Materials Processing Technology*, Vol. 63, 1997, pp. 325-333.
- [15]. Mason, J. J., and R. O. Ritchie. "Fatigue crack growth resistance in SiC particulate and whisker reinforced P/M 2124 aluminium matrix composites. " *Materials Science and Engineering: A* 231, no. 1 (1997): 170-182
- [16]. Hashim J, Looney L, Hashmi M. Metal matrix composites: production by the stir casting method. *J Mater Process Technol.* 1999; 92-93:1.
- [17]. Suresh Kumar. S , Dr. G. Mallesh "Influence of controlled shot peening on Mechanical properties and Compressive residual stress of Al6061-TiB2 Composite, *Journal of The Institution of Engineers (India): Series C.* 10.1007/s40032-022-00823-x.
- [18]. Ramos, R., N. Ferreira, J. A. M. Ferreira, C. Capela, and A. C. Batista. "Improvement in fatigue life of Al 7475-T7351 alloy specimens by applying ultrasonic and microshot peening." *International Journal of Fatigue* 92 (2016): 87-95.
- [19]. Carvalho, A. L. M., and H. J. C. Voorwald. "Influence of shot peening and hard chromium electroplating on the fatigue strength of 7050-T7451 aluminum alloy." *International Journal of Fatigue* 29, no. 7 (2007): 1282-1291.
- [20]. Lee, Hyukjae, and Robert F. Speyer. "Hardness and fracture toughness of pressure less-sintered boron carbide (B4C)." *Journal of the American Ceramic Society* 85, no. 5 (2002): 1291-1293.
- [21]. Ferreira, N., J. S. Jesus, J. A. M. Ferreira, C. Capela, J. M. Costa, and A. C. Batista. "Effect of bead characteristics on the fatigue life of shot peened Al 7475-T7351 specimens." *International Journal of Fatigue* 134 (2020): 105521.
- [22]. Goçer, Abdullah, and Mehmet Baki Karamiş. "Fatigue and Compression Characteristics of Al 6061-B4C Composite Materials." *Powder Metallurgy and Metal Ceramics* (2020): 1-9.



Friction Reduction Using Electrical Water Pump in I C Gasoline Engine

Danesh Warad¹, A P Singh²

¹Research Scholar, Department of Mechanical Engineering, SIRT, Sage University, Indore – 452020, Madhya Pradesh, India

²Associate Professor, Department of Mechanical Engineering, SIRT, Sage University, Indore – 452020, Madhya Pradesh, India

ABSTRACT

This paper illustrates the differences between mechanical and electrical water pumps of internal combustion engine. Literature have been studied regarding engine cooling with the water pumps. Main design features of the mechanical and electrical water pumps have been illustrated.

The traditional cooling system is not suitable for a high efficiency performance in terms of fuel economy and exhaust emission. Therefore, it is necessary to develop a new technology for engine cooling systems. These days, the electronic water pump is spotlighted as the new cooling system of an engine. The new cooling system can provide more flexible control of the coolant flow rate and the engine temperature, which used to be strongly relied on the engine driving conditions such as load and speed.

Keywords: Power; Torque; Electrical Water Pump; Mechanical Water Pump; Oil Temperature; Water Temperature, Cylinder Wall Temperature,

I. INTRODUCTION

Since the invention of internal combustion engine in 1883, the process of combustion unfortunately produces an abundance of waste heat energy which needs to be removed in a systematic manner via a cooling system to prevent damage to any mechanical components. The output of the energy as a percentage of the energy generated by the fuel in the combustion process is shown in Figure 1 for a modern passenger car engine when tested through a “NEDC ECE 15 EUDC” European drive cycle. Specifically, the energy generated has 33% exhaust heat losses to the wall and wall heat losses which needs to be removed by a transfer mechanism to lower the engine’s temperature. Hence in this case the heat transfer medium is the coolant fluid circulated by a water pump in the engine’s cooling system. When the engine power output is substantially increased, the large amount of heat generated needs to be removed in a timely manner to prevent damage to the engine components.

To comply with these laws the emissions control systems are rapidly developing in the market aimed at providing products that meet future emissions standards, but savings in fuel consumption and greater durability

and competitiveness in international markets, improving cost-benefit ratio. In this context, it is performed a design and analysis of a control system for cooling the diesel engine, aiming to control the engine water temperature accurately, to save fuel and reduce emissions. The system under study consists of an electric water pump, electronic controller a control algorithm. This system is intended to provide precise control in water temperature of the diesel engine, thereby reducing pollutant emissions and fuel consumption, allowing also a rapid response to heating in cold start.

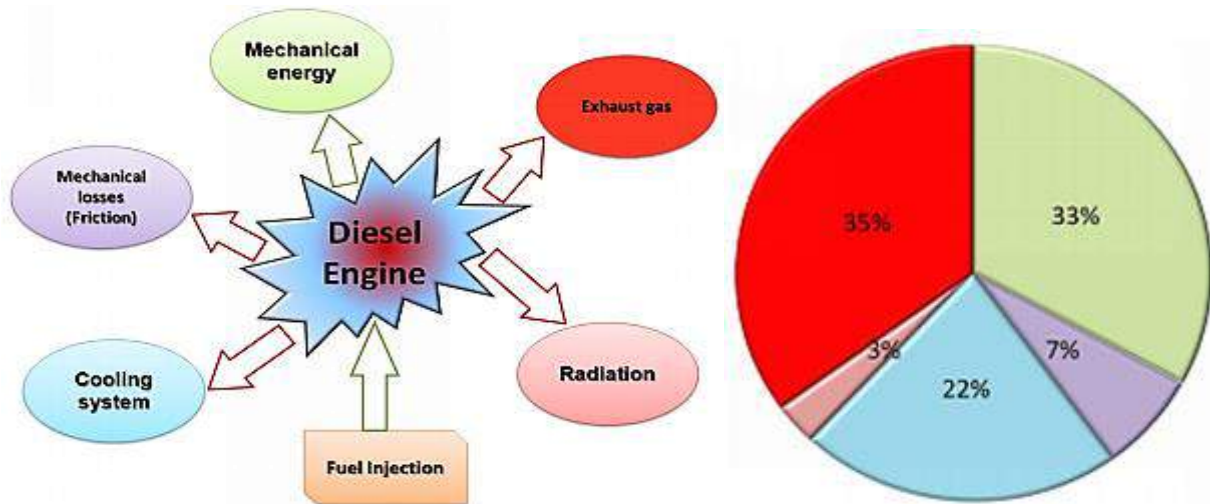


Figure 1: The heat generated by burning fuel is converted into mechanical energy

The coolant fluid, marked in a blue color as shown in Figure 2, is required to circulate around an engine to sufficiently carry the heat away, not only from the combustion chamber but also other critical areas of the engine such as the engine block, the cylinder head, the radiator and the heater core. It is this movement and circulation of the coolant fluid that is studied in this paper. Hence, the water pump can be either mechanically or electrically driven to circulate the coolant fluid around the engine in this cooling system. Instead of use of water, the coolant is often mixed with water in modern vehicle engines, which prevents the coolant fluid from either freezing or boiling, because the freezing or boiling water will significantly reduce the effectiveness of heat removal.

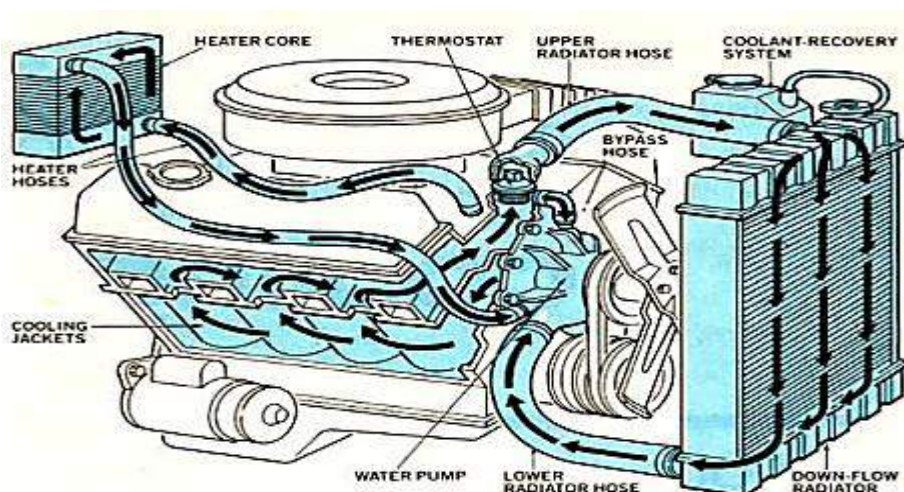


Figure 2: Coolant circulation in diesel engine

Conventional systems for cooling the engine are simply designed to keep the engine temperature acceptable for a wide range of operation and operating conditions. With the introduction of mechatronic technology conventional mechanical systems are being replaced by electronically controlled systems. A cooling system of electronically controlled diesel engine should provide improvements in performance through their effects on the engine, improved friction loss, improvement in fuel economy, reduced emissions and increased durability. The basic design of automotive cooling system has remained essentially unchanged for a long time; for example, drive the pump water from the cooling system of the motor is accomplished by rotating the engine. Thus, the coolant flow rate is determined by engine speed, which is not ideal for most cases. A conventional, mechanically driven water pump can cause unnecessary and parasitic losses. A water pump with electronic control would control the flow of water from the cooling system regardless of engine speed, providing a further reduction of parasitic losses. Another potential advantage of the electric pump is the possibility of reducing the size of the radiator, which is an important issue in the development of engine cooling systems. Increasing control possibilities provides a better choice of operating points of the diesel engine.

II. COMPONENTS OF ENGINE COOLINGSYSTEM

The purpose of the Engine Cooling System is to prevent the overheating of your vehicle's engine. With engine combustion reaching extremely high temperatures, the resulting heat needs to be dissipated. An efficient cooling system is essential to prevent the engine from burning!! Another function of the cooling system is to regulate the temperature inside the passenger compartment, insuring your comfort and that of your passengers.

- Main Components of the Engine Cooling System
- Radiator and radiator cap
- Cooling Fluid - Coolant
- Radiator Fan & Hoses
- Water Pump
- Heater Core & fan
- Temperature Knob, valves, Thermostat & sensors
- Reservoir or Reserve Tank

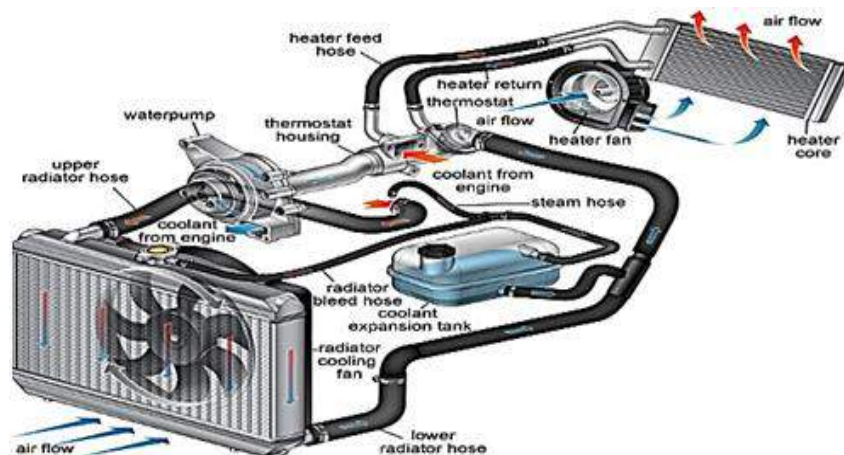


Figure 3: Main components of engine cooling system

A. Mechanical Water pump:

As shown in figure 4, a typical mechanical water pump consists of an impeller located inside spiral housing and sealed via an axial face seal. The spiral housing is mounted against the engine block with channels leading in and out of the coolant fluid channels within the engine block. The mechanical power arrives via the hub with pulley. The channels on the pulley indicate the interface for the guides on the serpentine belt which transmits power from the crankshaft. Either driven by an accessory drive belt or meshing gears, the mechanical water pump is designed to circulate the coolant fluid through the engine based on the engine speeds.

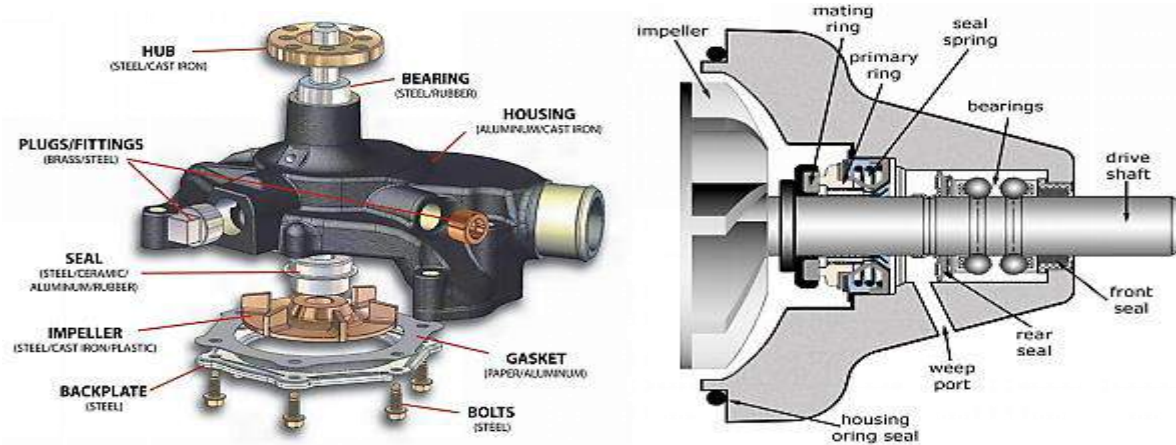


Figure 4 : Conventional(Mechanical) water circulation pump used in engines

B. Electronic Water pump

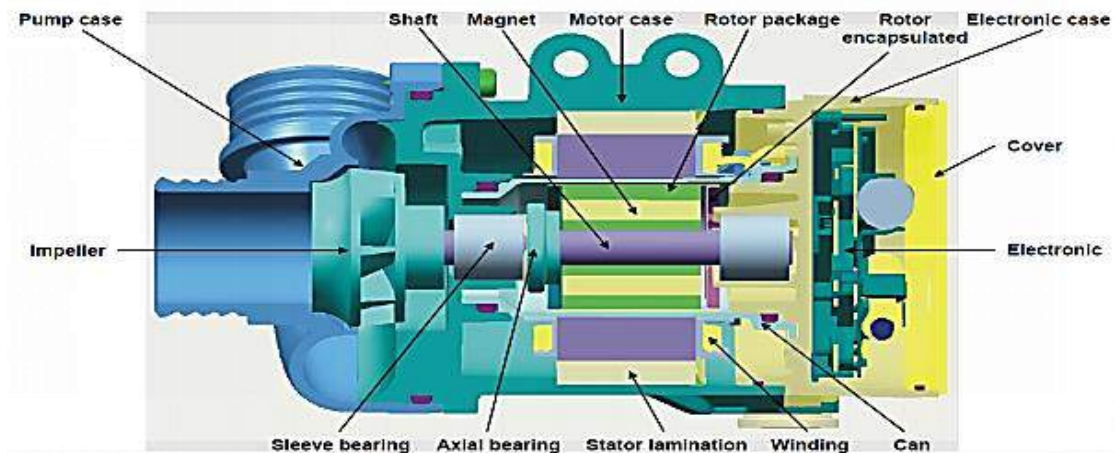


Fig 5 : Cross section view of electrical water pump

As the automotive industry strives to develop cleaner burning and more fuel-efficient engines, an electric water pump is becoming a sensible alternative to its mechanical counterpart. Modern vehicles the hybrid electric vehicles, have adopted advanced electronically control systems and sensors which have impacts on the engine cooling system, because negative aspects of the mechanically driven water pump is possible to be avoided. Since the coolant flow rates of the mechanical water pumps are elated to the engine speeds the thermal control using the mechanical water pumps is generally not effective in electric water pump shall be a good alternative to the current mechanical water pump, as the electric water pump may have an opportunity to remove a source of parasitic loss from the internal combustion engine and provide a better control of the engine temperature

according to the engine heating and cooling requirements. Since an electric pump offers an effective flow control capability which is totally independent of engine speeds, this can lower the system operating requirement with a reduced pump flow rate at high engine speeds. This allows the engine to run at a steadier temperature, as there is no sudden fluctuation in the coolant flow rate. Some advantages of an electric water pump used in internal combustion engines are discussed as below

Design Losses – mechanical water pumps must be mounted where the power to drive them is available. The power is usually at the front of the engine where belts or gear-train can be used to provide the drive power. In some instances, this package constraint can limit the ability to design a pump system and result in a reduced head flow. Furthermore, the mechanical pump design has performance limiting characteristics such as fluid cavitation and. An electric pump can be remotely mounted, allowing the flow characteristics to be hydraulically optimized while not impacting on the design constraint of both the overall engine installation package and the cooling system effectiveness

Drive Losses – the gear drives of the mechanical water pump place large accelerations into the pump shaft due to the gear teeth mesh which generates high cyclic side loads on the pump bearings. The belt driven water pumps do not have the same accelerations as the gear driven ones, but the belt driven water pumps can experience larger side loads due to the drive belt tension. Both ‘driving’ factors require the mechanical water pumps to have large bearings and the physical design to support the bearing loads.

Operating Losses - mechanical water pumps deliver the coolant flow and pressure directly proportionally to engine speed, the only means of adjusting the coolant flow rate and pressure is through use of the restriction valves. On the other hand, an electric pump can operate as a function of the engine cooling requirement(s) which can adjust coolant flow rate based on ‘need’, not engine speed

Eliminate Hot Soak after Shutdown - an electric pump can circulate coolant fluid throughout the engine post shutdown which enables one to control the engine’s thermal mass to prevent the overheat of critical components. This feature may also allow for design of engines operating at higher temperatures considering that the hot soak design limits will be eliminated

III. COMPARISON OF ELECTRICAL AND MECHANICAL WATER PUMPS

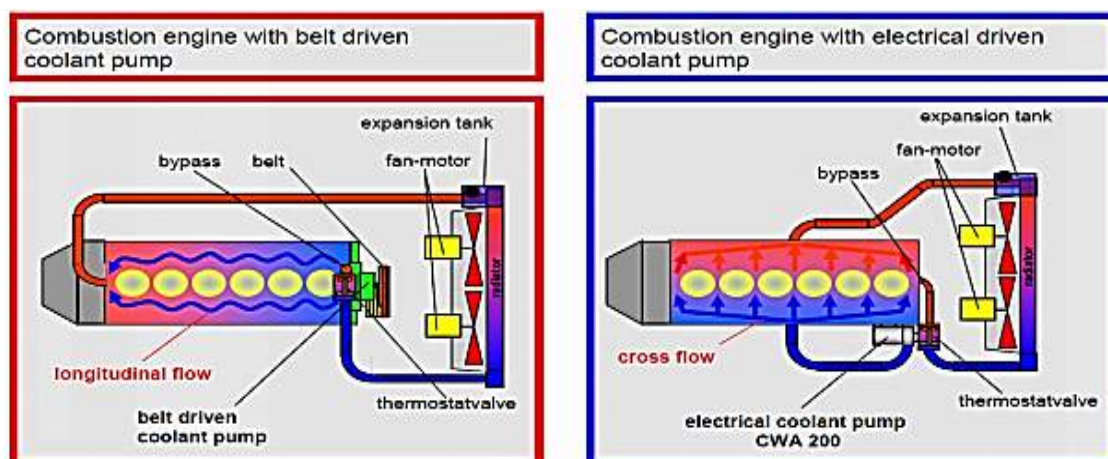


Figure 6 : Layout and energy conservation of electrical water pump

Feature	mechanical waterpump	clutched mech. waterpump	variable mech waterpump	electrical waterpump
zero flow at cold start	no	yes	no	yes
variable speed of pump	no	no	limited	yes
after running function	no	no	no	yes
compatible for start / stop	no	no	no	yes
compatible for hybrid appl.	no	no	no	yes
maintenance free	no	no	no	yes
improved efficiency	possible	possible	possible	yes
high coolant flow at low engine speed	no	no	no	yes

There are many benefits of the EWP:

- Increased Power and Torque
- Increased cooling capability
- Eliminating Heat Soak
- Better control of engine temperature
- Flexible options for pump control

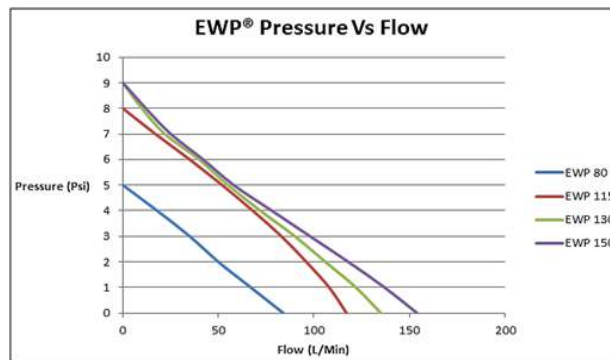
IV. SELECTION OF SUITABLE ELECTRIC WATER PUMP FOR ENGINE

Pump performance maps were used in order to calculate pump power consumption. Pump performance maps consist of pressure rise, flow rate, pump speeds, and efficiency. Based on these map data, the pump power consumption was calculated using the following equation.

$$P_{\text{pump}} = Q_p \times \Delta P \times \eta$$

Where: P: pump power consumption, η : pump efficiency, Q_p : Volumetric flow rate, ΔP : pressure rise across the pump.

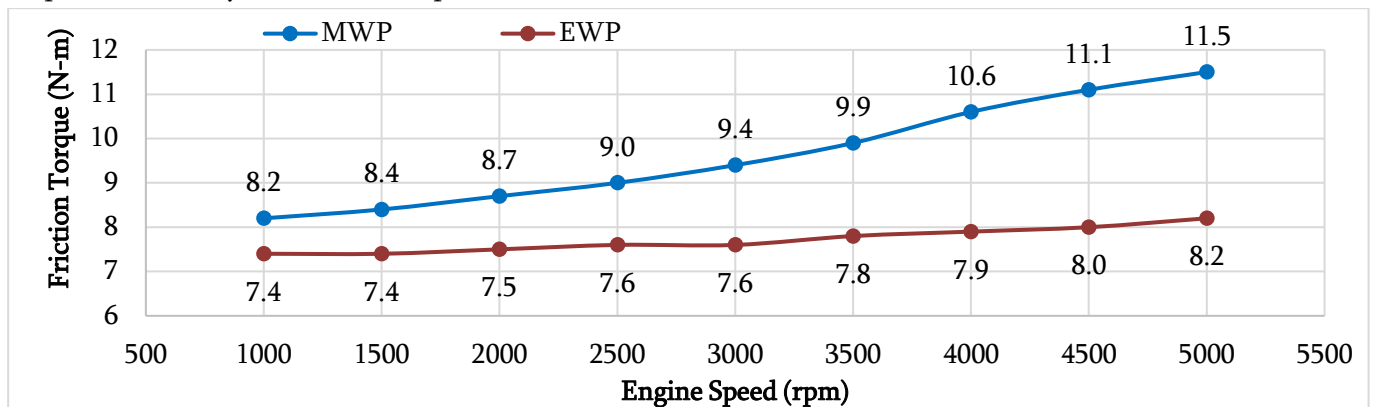
The coolant mass flow rate for a centrifugal water pump depends on the coolant density, shaft speed, system geometry, and pump configuration, the mass flow rate may be computed as: $m_c = \rho_c \times (2\pi \times r_p \times b \times v)$ mass flow rate = density of fluid X volume of flow region X velocity of pump as $v = \omega_p \times r_p \times \tan\alpha$, Velocity of pump is a function of blade speed, blade radius and blade angle.



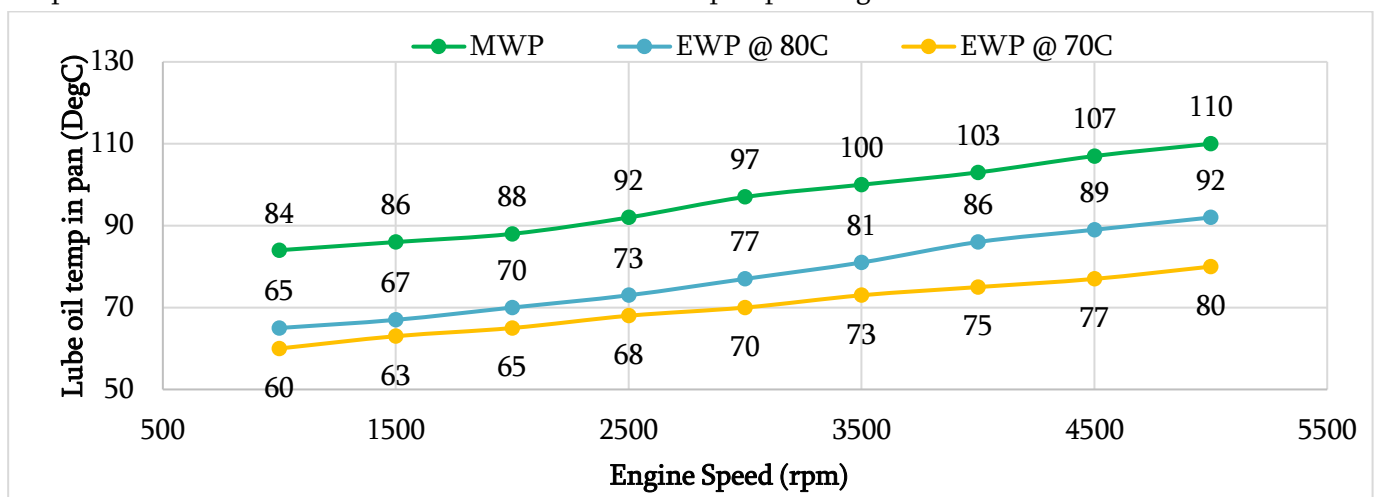
V. TESTING OF ENGINE USING ELECTRICAL WATER PUMP

In order to verify the effectiveness of an electrical pump over a standard mechanical pump, engine dynamometer tests have been conducted where the engine fitted with the mechanical and electric water pumps was run back-to-back. In order to verify if the benefits are available for use of the electric water pump, it is necessary to adequately size the electric water pump and control its use via a proper understanding of the engine's optimum operation temperatures and then implement an ECU to manage the water pump switching to adequately control the engine temperature.

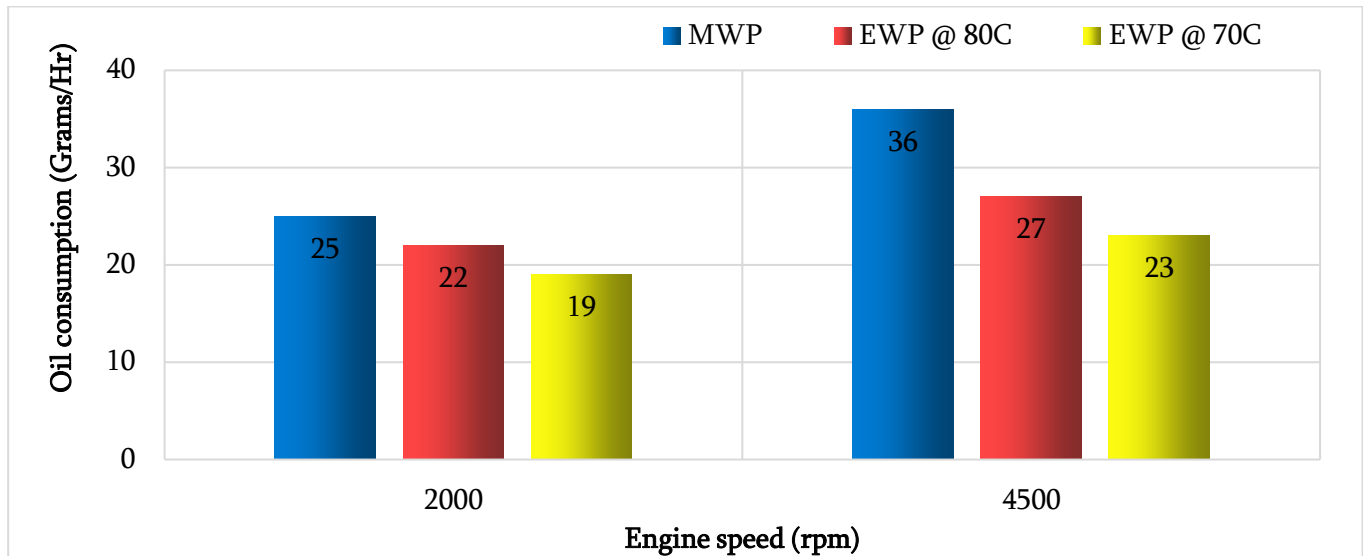
Following graph shows the details of engine torque with mechanical water pump (MWP) and electrical water pump tested under different engine rpm ranging from 1000 to 5000. As mechanical water pump is driven by the belt attached to the crankshaft pulley the power consumption (frictional torque) is higher from the engine compared to the electrical water pump (EWP) which is nowhere connected to running parts of the engine as it is mounted independently on the test bed. This non dependency of the drive saves the engine power for better output drive ability (used as useful power to the wheels)



To evaluate the oil temperature engine is tested with mechanical water pump with thermostat and electrical water pump without thermostat (Thermostat is not necessary for electrical water pump). The water limiting temperature is set at 80C and 70C for the electrical water pump through the ECU.



As shown in the above plots lube oil temperature can be controlled, we within the limits as per the design standards with electrical water pump by setting the engine water outlet temperature limit. Controlling oil temperature with mechanical water pump is limited by the thermostat of the engine which is difficult to control over the long duration running. Electrical water pump is beneficial compared to mechanical water pump in regulating oil temperature by setting water temperature rise limit. Rise in oil temperature over period during engine running will lead to evaporation of oil through the crankcases and reduces the viscosity of oil which in turn will affect the lubrication property of engine parts. To evaluate the effect of oil temperature on lubrication oil consumption engine is tested at 2000 rpm and 4500 rpm for about 8 hours in each rpm and based on the result obtained following bar chart is created to show the comparison of mechanical water pump and electrical water pump.



VI. CONCLUSIONS

1. Elimination of mechanical commutation system leaves the durability of the rotor bearings as practically the only limiting factor of service life of engine. Using electrical water pump will improve the overall engine life as well as reduces periodic maintenance problems.
2. Reducing the number of rotating parts significantly reduces the engine noise as well as frictional losses in the engine as shown in the test results. The reduction in frictional torque is 3.3 N-m at 5000 rpm which constitutes about 1.7 kW of power in engine, which is very significant when we are using small power engines. Reducing frictional power improves the fuel efficiency of the engine.
3. Matching the electrical coolant pump output to the actual cooling requirements of the engine can reduce the fuel consumption and exhaust emissions. Instead of the approximately 6.0 kW rated input for conventional mechanical pumps, an electric pump with 4.2 kW electric water pump can be used to automotive engines up to 55 kW rating engine. So effective power saving using electrical water pump is around 1.8 kW
4. It is possible to run the electrical water pump (EWP) after switching off the engines to avoid hot spots (localized overheating of parts) but this is not possible in mechanical water pump (MWP). With electrical

water pump we can keep circulating the hot water through the engine because the EWP is independent of the engine operation as it is controlled by the battery of the vehicle

5. The use of the electrically driven water pump is a design of future, such as those using hybrid or fuel technology is inevitable and most of the vehicles will use this technology in upcoming days in India. As hybrid technology uses most of the battery power so, the electrical water pump can be operated through battery in all speeds of the engine running
6. As the emission norms are getting stringent, in upcoming years with BS6 and above the particulate matter emission reduction is one of the biggest challenges. Lubrication oil consumption contributes a considerably amount in particulate matter formation. With the use of electrical water pump the oil consumption can be reduced by properly controlling the oil temperature by setting the engine out water temperature at the desired limit using electrical water pump. The experimental result shows there will be around 35% oil consumption reduction using electrical water pump in 8 hours testing.

VII. REFERENCES

- [1]. Wang, X., Liang, X., Hao, Z. and Chen, R.(2017)'Comparison of electrical and mechanical water pump performance in internal combustion engine', *Int. J. Vehicle Systems Modelling and Testing* , Vol. 10, No. 3,pp.205-223
- [2]. *Journal of Mechanical Science and Technology* 23 (2016) 1866~1870. Department of Mechanical Engineering, Haiyang University, Seoul, 133-791, Korea
- [3]. Wagner JR, Paradis L, Marotta EE, Dawson D. Enhanced automotive engine cooling systems – a mechatronics approach. *International Journal of Vehicle Design*. 2016;28(1/2/3):214-240.
- [4]. Krappel, M.; Heidecker, C.; Streng, S.; Elsaßer, A.: Electrical 48V coolant pump for highest thermal management requirements. 15th Stuttgart International Symposium, 2015
- [5]. Morita, A., Hosoi, A., Harada, T., Uchida, M., Kodama, Y. and Maegawa, H. Study of the vehicle thermal management focused on the engine lubricant oil. *VTMS* 11,pp 3-13. 2015.
- [6]. Roberto Cipollini, Davide Di Battista, sliding vane rotary pump in engine cooling system for automotive sector, *Applied Thermal Engineering*, Volume 76, 5 February 2015, Pages 157-166,
- [7]. Hyungmook Kang, Yinchuan, Kyoungdoug Min, Smart cooling system of the double loop coolant structure with engine thermal management modelling, *Applied Thermal Engineering*, Volume 79, 25 March 2015, Pages 124-131, ISSN 1359-4311,
- [8]. Ribeiro, E. G., Filho, A. and Meira, J. (2017). Electric water pump for engine cooling. *SAE Paper No. 2007-01-2785*.
- [9]. Lim, D.H., Kim, S.C. & Kim, M.S. Thermal analysis of an electric water pump for internal combustion engine vehicles. *Inc. Automot. Technol.* 14, 579–585 (2013).
- [10]. Zoz, S., Thelen, W., Alcenius, T. and Wiseman, M. (2001) Validation of Methods for Rapid Design and Performance Prediction of Water Pumps, *SAE 2001-01-1715*.



Anti-Friction Coatings for I C Engine Piston

Danesh Warad¹, A P Singh²

¹Research Scholar, Department of Mechanical Engineering, SIRT, Sage University, Indore – 452020, Madhya Pradesh, India

²Associate Professor, Department of Mechanical Engineering, SIRT, Sage University, Indore – 452020, Madhya Pradesh, India

ABSTRACT

In this paper we study different types of coatings on piston skirt and crown area, the focus will be on the anti-frictions coatings and their benefits with respect to fuel consumption, power output as well as wear rate (long durability study). Study will be focused on friction coefficient, durability and its effect on piston skirt friction with respect to Molybdenum base mixture, Graphite base mixture, Polytetra fluoroethylene (PTFE) a resin-based antifriction coating, Dimond like coating (DLC).

Keywords: Low friction coatings, Piston skirt, dry lubricant, PTFE, DLC

I. INTRODUCTION

Stricter demands on emission norms, fuel economy and performance require internal combustion engines to be optimized with respect to their frictional losses and wear. While engines ran for the last 100 years without coatings of any type, modern technology has drastically improved the science of piston coatings. While the piston appears to be a relatively simple, stable, solid component on the surface, during operation the piston expands and flexes under combustion temperature and pressure. This movement and stress in the piston absolutely require 100% proper piston prep to avoid delimitating the coating. Many manufacturers have been using piston coatings for decades, but as the benefits of piston coatings have proven themselves throughout the years. Many OEM's have used skirt coatings since the early 2000's because of the undeniable efficacy in modern diesel engines.

Approaches for reducing engine friction include low friction lubricants, reduction of engine friction through design modifications, turbocharged and downsized engines, cylinder deactivation, and hybridization. Transmissions with a higher number of gears also provide the opportunity to reduce engine speed to reduce friction work. Engine friction losses comprise approximately 8 percent of the fuel energy. If friction could be reduced by 25 percent, a 5.6 percent reduction in fuel consumption could be achieved. Advanced low-friction coatings and surface texturing are potentially new methods for reducing friction in reciprocating engines. The design of the piston skirt is one of the key features to be considered in controlling the performance of friction, oil consumption and noise. The piston skirt contributes to around 25 - 47% in piston-cylinder system losses due

to engine friction. Along with the characteristics of coatings, which decrease friction coefficient and, consequently, decrease fuel consumption, their ability to avoid increased wear and seizure of friction surfaces under operating conditions is of particular interest. The contribution of the piston assembly to overall engine frictional losses is well documented and has been the subject of a lot of research over several decades.

II. NEED OF ANTI-FRICTION COATINGS

About 7-10% of the total energy input in a vehicle is lost due to mechanical friction, and in an engine, about 50% of the total frictional losses occur at the interface between the cylinder and pistons and piston rings. Therefore, this interface offers great opportunities for friction reduction. In terms of improving the performance of the engine components and forming very demanding, high strength materials, the contact surfaces must show reduced friction, anti-adhesive properties and increased wear resistance. Robust anti-friction coatings become necessary whenever components are continuously subjected to frictional forces. When properly coated, however, the material remains intact and protected for a long time. Lubricity or lubrication's objective is to reduce friction between two mating surfaces to extend the wear life of the components. If the objective is to have a wear in period for the parts to size together then a thicker coating solution is required. If the application is an item with close tolerances or preload factors such as a bearing, then a very thin coating would be best to reduce friction.

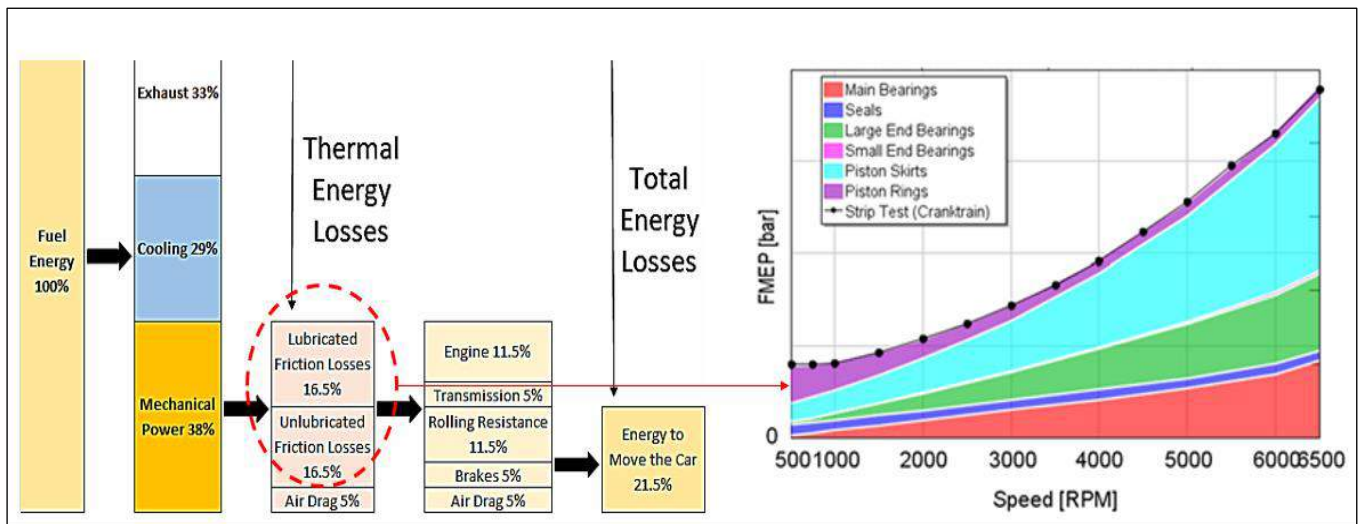


Fig 1. Mechanical losses (Frictional losses) in engine

Low friction coatings provide improved performance and service life while eliminating the need for wet lubricants in operating environments that require resistance to heat, chemicals, or clean room conditions. Coatings enhanced thermal control, improved lubrication, and oil-shedding. Depending on the type of coating and the area in which the coating is applied, the benefits can include increased power, component durability, or both.

III. TYPES OF PISTON COATINGS

Coating the tops of pistons protects and increases the life of the rings on the piston which reduces radial tension loss. Not a lot of people realize this, but the coating helps shield the rings from heat caused by improper burn of the fuel which creates hot spots. Heat kills performance so we want to get rid of it as fast as we can. Coating the tops of pistons helps with scavenging heat out of the motor. The thermal barrier coating on top of the piston helps to push the heat out of the motor. There are basically two types of piston coatings are applied viz thermal barrier coatings to reduce heat loss and anti-friction coatings to reduce the dynamic friction between moving parts



Fig 2. Different types of piston coatings

A. Thermal Barrier Coatings

Also called ceramic coatings, they act as a shield to prevent heat from passing into a part. For instance, a thermal barrier coating on a piston dome prevents combustion heat from being lost beyond the dome. This prevents heat from dissipating through the dome, causing the piston to expand. If there is a barrier coating, combustion heat is greatly reduced, and does not sink into the piston and cause expansion. Since the piston doesn't expand as much you can then run a tighter piston-to-wall clearance. Some of the advantages of thermal barrier coatings are

- High Temperature ceramic-based coatings that can withstand temperatures up to 1,800°
- Coatings that withstand thermal cycling as well as thermal shock
- Performance coatings that are simply unmatched in corrosion and chemical resistance
- A distinct, high-end look and feel
- Cost effective, single coat (straight to substrate), easy to apply products
- Ceramic coating replaces the other coating process like Anodizing, Zinc plating, Nickle plating, Chromate conversions, Powder Coating, Paint

B. Anti-Friction

Anti-Friction-Coatings are touch-dry lubricant solutions which, in their formulation, resemble common industrial varnishes. They contain solid lubricants, resins as bonding agents, as well as solvents. Solid lubricant components are mainly molybdenum desulphated, graphite and PTFE. The individual raw materials and

additives, as well as the concentration of solid lubricants are decisive for lubricating efficiency and corrosion protection. Anti-friction coatings also known as solid-film or dry-film lubricants are recommended for applications where extreme operating conditions of very high or low temperatures and significantly high pressures are preventative. Anti-friction coatings provide a low coefficient of friction between two moving surfaces and serve to retain surface oil between moving parts. Anti friction coatings are also able to avoid noises. The Anti-friction coating's true benefit is reduction of friction, which prolongs part life and reduces operating friction, and it naturally frees available horsepower. A moly skirt coating is not specifically designed to reduce heat, but because it reduces friction, heat is potentially reduced as a direct by-product. Anti-friction skirt coating improves cold-engine startups; the AFC prevents skirt scuffing that might otherwise repeatedly occur in that situation.

C. Dry film or wet film coating

Dry film lubricants are advantageous over wet (oil and grease) when adhesion, lifetime lubrication and appearance, are crucial requirements of the application. Dry lubricants perform exceedingly well at elevated high temperatures extreme pressures and in vacuum. Also, dry film lubricants are environmentally friendlier as there is no after use disposal involved as with wet lubricants. Dry film coatings provide following advantages

- Frees up horsepower normally lost to friction.
- Provides back-up lubrication if the primary lubrication has gone
- Reduces wear which increases engine life
- Reduces heat that can cause galling and seizing
- Produces tighter piston-to-wall clearance
- In majority of applications, lifetime lubrication is feasible
- Hard, durable abrasion resistant finish
- Low Surface Energy
- Dry, clean lubrication unaffected by dust, dirt and moisture
- Controlled film thickness for exact load-bearing capabilities

IV. PISTON COATING PROCESS

Anti-Friction Coatings can be economically applied by hand or drum spraying, dipping, centrifuging (dip-spinning), brushing, roll coating and printing. The size, shape, weight and quantity of the parts being coated are factors in selecting a certain application method. Film-thickness and sliding-surface requirements are other factors. Some of the most used application methods for dry/ solid lubricants are:

- Immersing/ Dipping the Object in Lubricant: This method is common for large batches of fasteners, small ID components and situations where spraying is not possible or desirable. Dip-Spin equipment is often used in these type of applications
- Spraying Technique: This is the most common application method for most dry/solid film lubricants. This is a line-of-sight application method and is only restricted by either small diameter, internal bends, long lengths, etc. Equipment utilized will be dependent on the type of lubricant being applied.

- **Burnishing:** This method is not very common and typically the least effective regarding bonding. This process utilizes the lubricant, typically in powder form and either a prepared surface or a carrier such as Isopropyl Alcohol, which is then manually rubbed onto the part until a coating is obtained

Anti-Friction-Coatings are preferably applied by immersion or by spraying onto carefully degreased surfaces. Other methods are possible as well, such as immersion centrifuges, electrostatic or automatic spraying methods, application by pressure or roller as well as the various methods for drying and hardening processes which are well-known within industry. The typical steps in applying antifriction coatings are as follow.

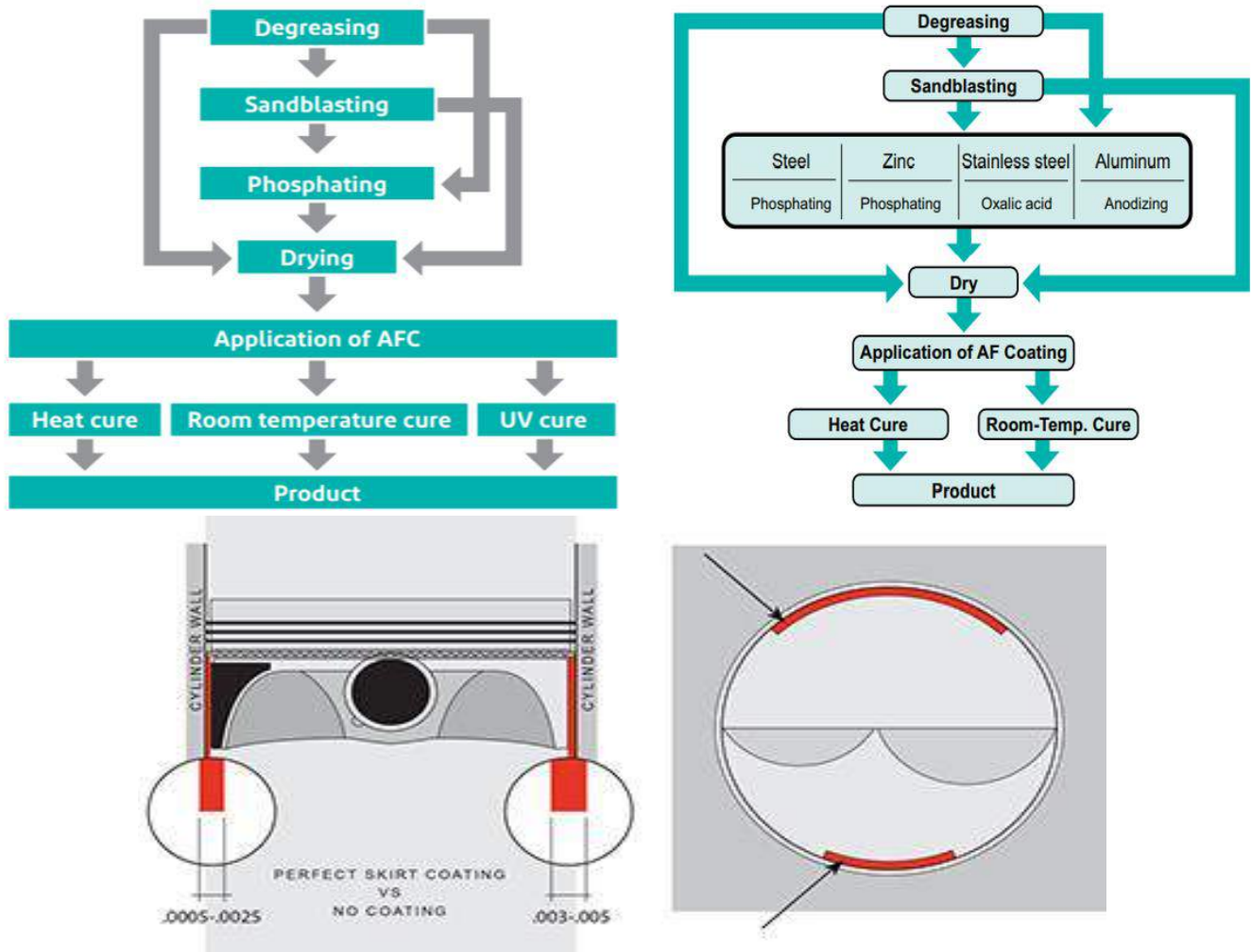


Fig 3: Typical coating process of AF material on piston skirt

Different application methods provide excellent, good or limited results, depending on the anti-friction product. Each method has certain selection parameters, advantages and disadvantages, as shown in the Coating Methods Comparison Chart. Application specialists can help make the right choice based on base material and field of working.

Sr No	Method Selection	Parameters	Advantages	Disadvantages
1	Spraying	• Speed • Quantity of material • Distance • Air pressure • Viscosity of coating	• Good appearance • Even film thickness	• Not so economical • Over-spray waste • Exhaust cabinet needed
2	Dipping	• Long, flat parts • Viscosity of coating • Withdrawal speed	• Good appearance • Even film thickness	• Batch economical • Stirring equipment
3	Dip-Spinning (Centrifuging)	• Form/quantity of parts • Rotational speed • Viscosity of coating	• Good for bulk volume • Economical	• Poor appearance • Two layers • Poor batch control
4	Roll Coating	• Long, flat parts • Viscosity of coating • Withdrawal speed	• Good appearance • Economical • Large surface areas	• Expensive equipment • Large space required
5	Printing	• Mesh size/film thickness • High-viscosity coating • Low-evaporation solvents	• Exact design coverage • Economical	• Special coatings • Viscosity, evaporation

Table 1: Coating Methods Comparison Chart

V. TRIALS WITH DIFFERENT DRY FILM ANTI FRICTION COATINGS

To conclude the benefits of the friction reduction in gasoline engine, following activities has been carried out to compare coefficient of friction for different materials of dry lubricant. Total four solid anti friction lubricants have been tried on the engine piston. i.e., Molybdenum based material, graphite based, Teflon based (PTFE) and Tungsten disulfide. Comparison study of anti-friction dry lubricants is shown in the below table related to the physical properties.

A. Comparison of physical properties of different coatings

Parameter	Molybdenum Disulfide (MoS ₂)	Tungsten Disulfide (Ws ₂)	Graphite
Co-efficiency of Friction	0.05	0.03	0.12
Thermal Stability	600 Deg F	1100 Deg F	800 Def F
Load Bearing Capacity	250,000 psi	400,000 Psi	150000 Psi
Temperature Range	-273 Deg C to +650 Deg C	-185 Deg C to +350 Deg C	- 94 Deg F to +700 Deg C
Molecular Weight	160.08	248	12.01
Density	5060 Kg.m ⁻³	7500 Kg.m ⁻³	1800 Kg.m ³

Remarks	Low friction, fuel and oil resistance, suitable for high temperature use, moderate load carrying capacity, useful for drive shafts, valve trains etc.	Low friction, fuel and oil resistance, suitable for high temperature use, high load carrying capacity, useful for bearings.Coating process is costly	Low friction, fuel and oil resistance, suitable for high temperature use, easy to apply and low cost, renewable and non-hazardous.
---------	---	--	--

Table 2: Physical property comparison of dry anti friction lubricants

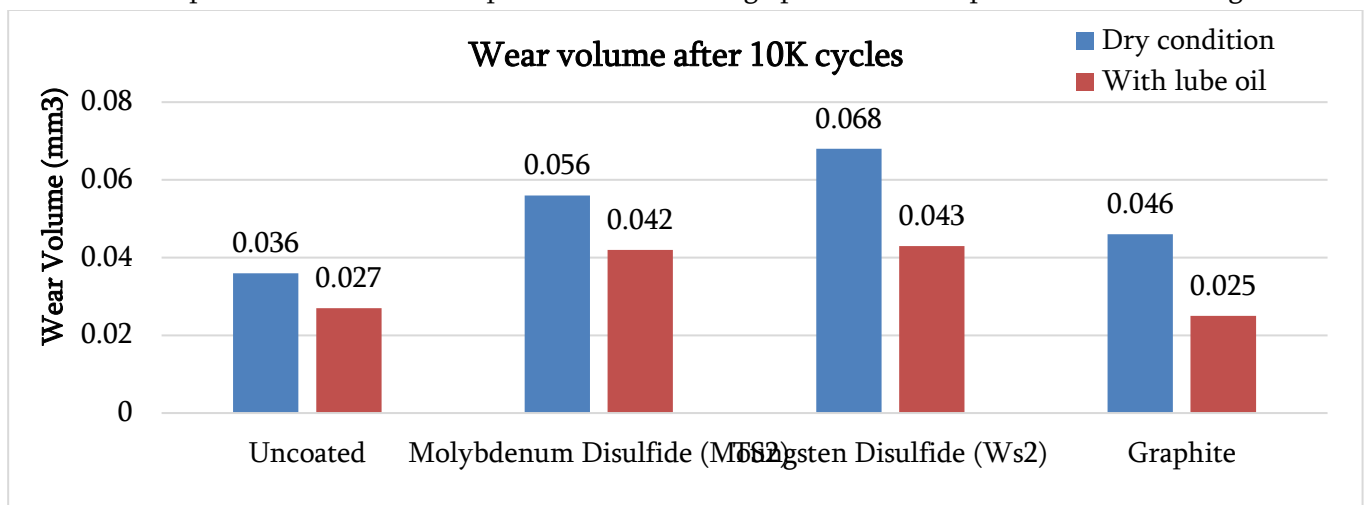
VI. EXPERIMENTAL STUDY

Three different types of coatings have been studied on the gasoline engine piston skirt. The experimental study is carried out with motoring dyno on 1.8 L naturally aspirated BS3 engine with MPFI injection. Engine testing carried out with varying rpm speed and load (automotive application) as well as constant speed with varying load (Generator application). Following graphs are plotted to understand the behavior of the engine under various conditions.

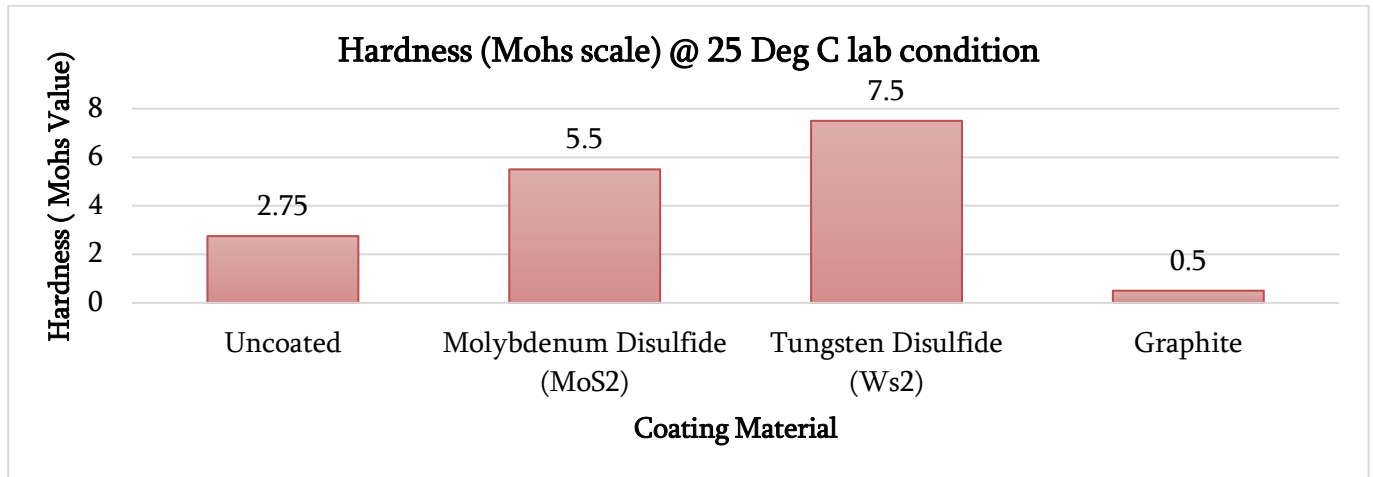
- Wear rate of different coatings over 10,000 cycles of operation under dry condition
- Hardness variation with respect to operating temperature
- Friction power comparison in four strokes of an engine

VII. FRICTION COATING WEAR STUDY

Wear resistance refers to a material's ability to resist material loss by some mechanical action. Wear volume of the material is directly related to hardness and coating thickness. Higher the thickness of coating, more is the wear rate due to low clearance in between parts. Hardness also plays vital role because harder material wears at lower rate, but the coefficient of friction will be higher due to the low micro scoping pores to retain the lubricating oils. Another important factor is about the presence of lubrication oil during operation, as a fact the softer material performs better with respect to friction during operation in the presenceof lubricating media.

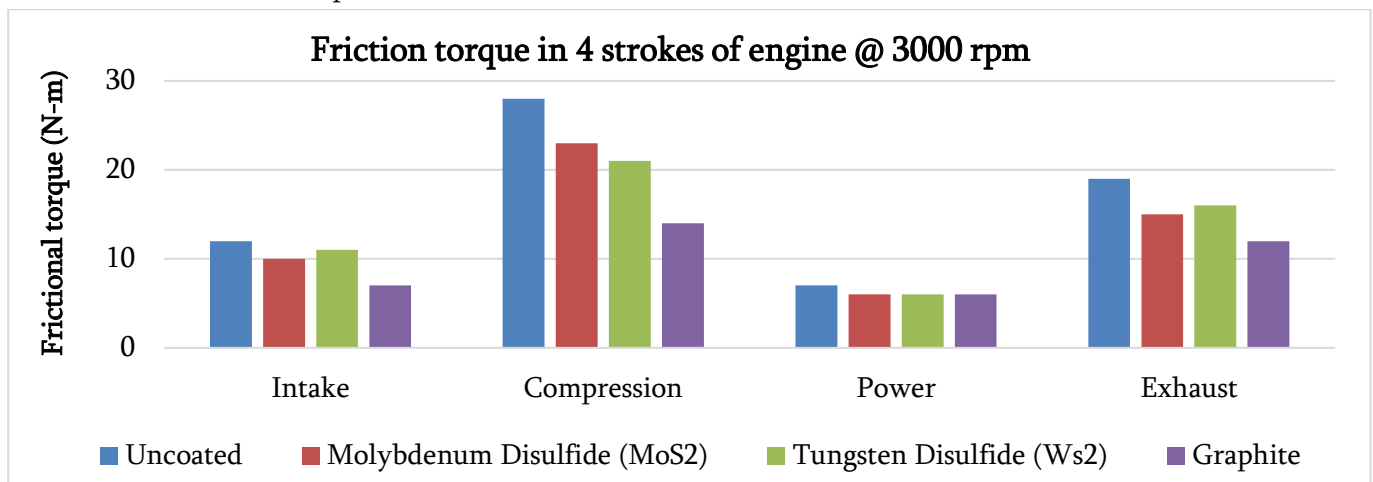


The following figure shows the details of harness measured in Mohs value. The Mohs scale is the hardness of a material is measured against the scale by finding the hardest material that the given material can scratch, or the softest material that can scratch the given material. The Mohs scale is a purely ordinal scale, and it ranges from 1 (For talc) to 1500 (for Dimond). Even though harness is directly related to the wear rate, but the friction coefficient reduction is also of equal importance in this study. Low hardness material with micropores for retention of lube oil is the focus in this study to reduce the engine friction.



A. Frictional power in different strokes of an engine

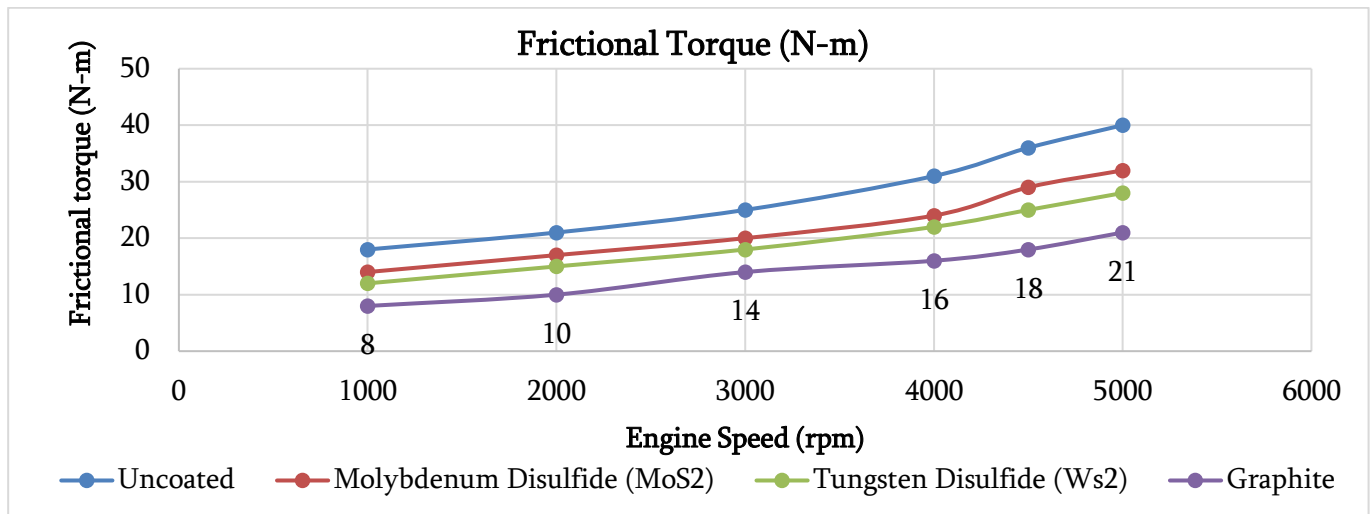
As we are aware the friction will be higher on the engine during the compression stroke because of the rubbing of parts when there is a load against the piston. This friction is not only because of the piston skirt but the presence of smooth gliders with oil retain makes piston move faster and extract useful energy by reducing friction between liner and piston skirt.



B. Frictional torque of an engine

Present research work is focused on the investigation of friction power as a function of engine speed, load, and oil viscosity, and engine components operating predominantly in hydrodynamic regime (piston ring assembly and bearings) are considered as major contributors towards engine friction power loss. Engine load also plays a

vital role in engine friction to eliminate this effect we have used motored dyno to measure the torque based on the rpm factor. As a basic principle the frictional power will be higher in case increased rpm. To analyze the effect of friction with different coatings experiments has done and results are plotted with graph as shown below



VIII. RESULTS AND DISCUSSION

The coatings have been experimentally studied without lubricating material in order to study friction and scoring resistance of the coating materials, which are employed in a piston skirt of high-force diesel, which is usually exposed to short-term boundary and even dry friction. This study has demonstrated that the friction coefficient of the specimens with a solid lubricating coating is lower, and the seizure load is higher than those of the specimens without a coating. A five-fold decrease in friction losses and an increase in the service life of piston skirt of high-forced petrol can be achieved in the coatings. A brief analysis indicates that possible benefits should be closer to 3% at high engine loads. To establish coating effectiveness, carefully controlled fuel economy testing of engines was performed on a Eddy current dynamometer at one engine speed and two output torque levels (50% load & 100% load) and also on different rpm load.

- Friction power reduction using graphite coatings shows positive results in conjunction with liquid lubrication. Graphite being soft material has more anti friction property even though it has low hardness and high wear volume percentage.
- With higher speeds the friction power reduction in engine due to application of graphite is nearly 45% under motoring condition.

IX. FUTURE WORK

To improve the wear rate as well as long duration operation, antifriction coatings with different additives like molybdenum and tungsten can be applied with low-cost production. The combination of coatings benefits in case liners are also coated with antifriction with better oil retention capacity on the surface. Wear capacity

improvement on the graphite with different additives or combination with molybdenum or tungsten will provide an added advantage.

X. REFERENCES

- [1]. Richardson D. E. ,(2017), “Review of Power Cylinder Friction for Diesel Engines” Trans. ASME: J. Eng. Gas Turbines Power 0742-4795, 122, pp. 506–519.
- [2]. Lin, J. and Wei, R. (2018), “A Comparative Study of Thick TiSiCN Nanocomposite Coatings Deposited by dcMS and HiPIMS with and Without PEMS Assistance,” Surface and Coatings Technology, 338, pp. 84-95.
- [3]. Delacorte, C. and Edmonds, B. (2019), “NASA PS400: A new high temperature solid lubricant coating for high temperature wear applications,” NASA/TM-2009-215678.
- [4]. Moughon L, and Wong, V.W. ,2015, “Effects of Lubricant and Piston Design on Reciprocating Engine Friction,” ASME-ICED Fall Technical Conference, ASME Paper No. ICEF2005-1343.
- [5]. Takiguchi, M., Machida, K., and Furuhashi, S., 2008, “Piston Friction Forces of a Small High Speed Gasoline Engine,” ASME J. Tribol. 0742-4787, 110, pp. 112–118.
- [6]. Kim, M., Kiehne, T., and Matthews, R. D. ,2015, “Friction Force Measurements Using the Instantaneous IMEP Method and Comparison with RINGPAK Simulations,” ASME-ICED Fall Technical Conference, ASME Paper No. ICEF2015-1300.
- [7]. Ye, Z., Zhang, C., Wang, Y., Cheng, H.S., Tung, S., Wang, Q.J., and He, X., An experimental investigation of piston skirt scuffing: a piston scuffing apparatus, experiments, and scuffing mechanism analyses, Wear, 2004, vol. 257, nos. 1–2, pp. 8–31.
- [8]. Min H C, Jeong J, Seong J K, Ho J 2016 Tribological properties of solid lubricants (graphite, Sb₂S₃, MoS₂) for automotive brake friction materials, Wear, 260: 855–860
- [9]. Steinmann A M, Meerkamm H 2014 A new type of tribological coating for machine elements based on carbon, molybdenum disulphide and titanium diboride, Tribol. Int. 37(11–12): 879–885
- [10]. Milojević, S., Pešić, R., Davinić, A., and Taranović, D., Coated al piston as technological solution to lowering of friction losses inside IC engine, Proc. 12th Int. Conf. on Accomplishments in Electrical and Mechanical Engineering and Information Technology, Banja Luka, 2015, pp. 741–746.
- [11]. Buyukkaya, E., Thermal analysis of functionally graded coating AlSi alloy and steel pistons, Surf. Coat. Technol., 2008, vol. 202, pp. 3856–3865.
- [12]. Cho DH, Lee SA and Lee YZ. The effects of surface roughness and coatings on the tribological behavior of the surfaces of a piston skirt. Tribol Trans 2009; 53(1): 137–144



Lowering Friction Torque Using AFC on Engine Bearings

Danesh Warad¹, A P Singh²

¹Research Scholar, Department of Mechanical Engineering, SIRT, Sage University, Indore – 452020, Madhya Pradesh, India

²Associate Professor, Department of Mechanical Engineering, SIRT, Sage University, Indore – 452020, Madhya Pradesh, India

ABSTRACT

Anti-friction coatings (AFCs) are used in a wide range of technical areas, whether for small parts in precision engineering, in electrical engineering or in the automotive industry. With a range of flexible system concepts for anti-friction coating, Sprimag is ideally equipped to meet specific requirements' -friction coatings serve a purely functional purpose. On gear parts, pistons and bearing shells, for instance, anti-friction coatings both prevent wear and optimize friction behavior. Anti-friction coatings offer a number of advantages compared to oil and grease lubricants: Only a single, one-off application of an anti-friction layer is required to separate contact surfaces, and the dry, clean lubricating film provided by the anti-friction coatings eliminates unwanted and troublesome impurities. When applying anti-friction coatings to bearing shells, the compact Sprimag automatic round-table coating machine is often used. This machine can be adapted to specific customer requirements. Different cycle operations, the coating of rotating parts, and the coating of stationary parts with a rotating extension.

Keywords: Surface coatings and textures; friction; wear; Low-friction coatings; anti friction coatings

I. INTRODUCTION

FUNCTIONS OF BEARINGS IN INTERNAL COMBUSTION ENGINES

Bearing is a device supporting a mechanical element and providing its movement relatively to another element with minimum power loss. The rotating components of internal combustion engines are equipped with sleeve type sliding bearings. The reciprocating engines are characterized by cycling loading of their parts including bearings. Such character of the loads is a result of alternating pressure of combustion gases in the cylinders. Rolling bearings, in which a load is transmitted by rolls (balls) to a relatively small area of the ring surface, cannot withstand under the loading conditions of internal combustion engines. Only sliding bearings providing a distribution of the applied load over a relatively wide area may work in internal combustion engines. A bearing is a component used to reduce friction and to maintain clearance between stationary and rotating

components of the engine. Bearings, or bearing surfaces, are located on the crankshaft, connecting rod, and camshaft, and in the cylinder block.

The sliding bearings used in internal combustion engines are:

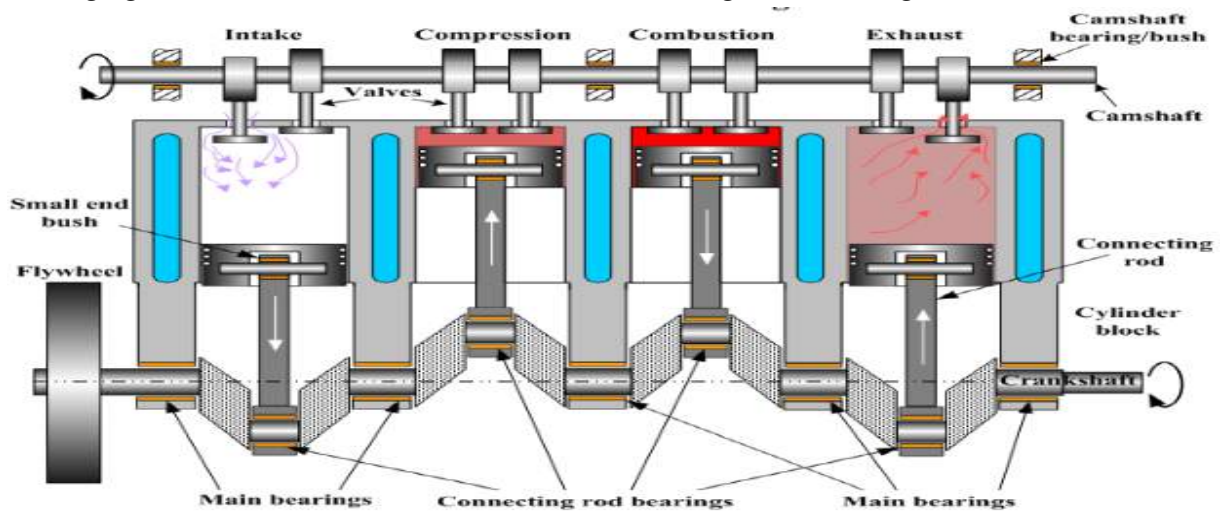
Main crankshaft bearings support crankshaft providing its rotation under inertia forces generated by the parts of the shaft and oscillating forces transmitted by the connecting rods. Main bearings are mounted in the crankcase. A main bearing consists of two parts: upper and lower. The upper part of a main bearing commonly has an oil groove on the inner surface. A main bearing has a hole for passing oil to the feed holes in the crankshaft. Some of main bearings may have thrust bearing elements supporting axial loads and preventing movements along the crankshaft axis. Main bearings of such type are called flange main bearings.

Connecting rod bearings provide rotating motion of the crank pin within the connecting rod, which transmits cycling loads applied to the piston. Connecting rod bearings are mounted in the big end of the connecting rod. A bearing consists of two parts (commonly interchangeable). Small end bushes provide relative motion of the piston relatively to the connecting rod joined to the piston by the piston pin (gudgeon pin). End bushes are mounted in the small end of the connecting rod. Small end bushes are cycling loaded by the piston pushed by the alternating pressure of the combustion gases.

Camshaft Bearings support camshaft and provide its rotation. camshaft bearings are manufactured as a "Full Round" design. Bearings are produced from extruded steel tubes with a centrifugally cast Babbitt lining. Several different grades of Babbitt are used depending on applications. Engines with inherent OE problems of bearing wiping and/or fatiguing utilize a high-grade ASTM-14 material.



The following figure shows the locations of different shell bearings in an I C Engine



A. Construction and properties of thin shell bearings

In 1839 Isaac Babbitt of Massachusetts developed a unique metal alloy that is highly resistant to galling (the sticking and pulling of two metal surfaces in contact with each other). His babbitt material became the “go-to” material for plain bearings used in a variety of applications. The material had great conformability (ability to work around the limits of the production machinery of the era) and great embeddability (ability to embed harder particles in the bearing surface instead of damaging the pin). The super alloy did have a weakness. The “soft” material would wear. In fact, early rods and main caps would be fitted with shims that would be removed to tighten up the clearance. This was a time when engine’s lacked oil filters too. Over time, it was learned that the thinner the layer of soft Babbitt material, the longer it would take to wear. The realization led to the development of bearings with an intermediate layer between the steel backing shell and a thin Babbitt top layer

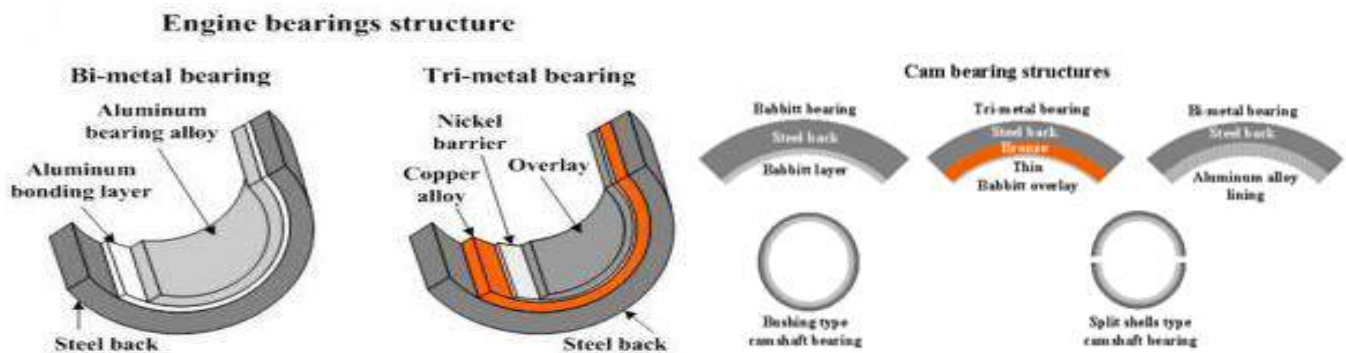


Fig 1: Engine bearing structure

II. INTRODUCTION TO BEARING COATINGS

Dry lubrication is advantageous over wet (oil and grease) when adhesion, lifetime lubrication and appearance, are crucial requirements of the application. Dry lubricants perform exceedingly well at elevated high temperatures extreme pressures and in vacuum. Also, dry lubricants are environmentally friendlier as there is no after use disposal involved as with wet lubricants. Application of the coating to the work component plays a critical role in the performance of the anti-friction coating. Dry film lubricant with good adhesion and corrosion protection properties for metal-to-metal material pairings. Coating is a layer of a substance applied to the substrate surface. Coating is also a process of applying a layer to the substrate surface. Coating material is different from the substrate material, and it permits achieving special surface properties of the part without changing its bulk properties. Coatings may improve the following surface properties:

- Anti-friction properties (wear resistance, low coefficient of friction, score resistance).
- Hardness of the material
- Corrosion and oxidation resistance
- Cosmetic appearance.

A. Coatings for improving Anti-friction properties

Low-friction coatings are used on bearings for two reasons. The first is as a backup lubricant if the primary (fluid) lubricant fails or is insufficient to prevent surface-to-surface contact. Lubricant failure occurs when new equipment is in its break-in period, during machinery start-up, or during reversing operations. Occasionally, lubrication fails when a conventional hydrodynamic bearing is momentarily overloaded, and the film of oil is partially pressed aside. In these conditions, there is mixed lubrication or, worse, boundary lubrication. Boundary lubrication refers to lubrication failure between two rubbing surfaces that don't have a full-fluid lubricating film between them. The second reason for using low-friction coatings is to handle applications that can't use fluid as the primary lubricant. Examples include nonmetallic bearings made from fiber, plastic, composites, or paper in instrument and aircraft applications. The coating also reduces friction in the bearing, which in turn reduces the heat and wear on the coating. Reduction of friction and support of bearing loads are both key for any coating used in a bearing. Coating formulators develop coatings based on tough resins, into which they add dry lubricants such as polytetrafluoroethylene (PTFE), molybdenum disulfide (MoS₂), and graphite is the premier low-friction constituent, with a coefficient of friction of 0.02. Coefficient of friction values for coatings with PTFE range from 0.02 to about 0.10, depending on PTFE loading. This corresponds favorably with the friction coefficients of bearings operating in the mixed and boundary layer conditions. But coatings with low coefficients of friction have relatively high PTFE loadings which makes the coating soft and less wear resistant. MoS₂ provides a coefficient of friction of approximately 0.12. The advantage of MoS₂ is its ability to bear high loads. Under low slip velocities, MoS₂ coatings can carry extreme loads. Graphite is perhaps the oldest known dry lubricant. It has a coefficient of friction of about 0.12 to 0.16. In a coating, it's primarily used where ambient temperatures are high or where PTFE and MoS₂ can't be used. For example, graphite is the coating of choice on tobacco processing equipment. This is because it won't leave residue that would subsequently burn and be inhaled by humans. Graphite also performs well in applications where water is present.

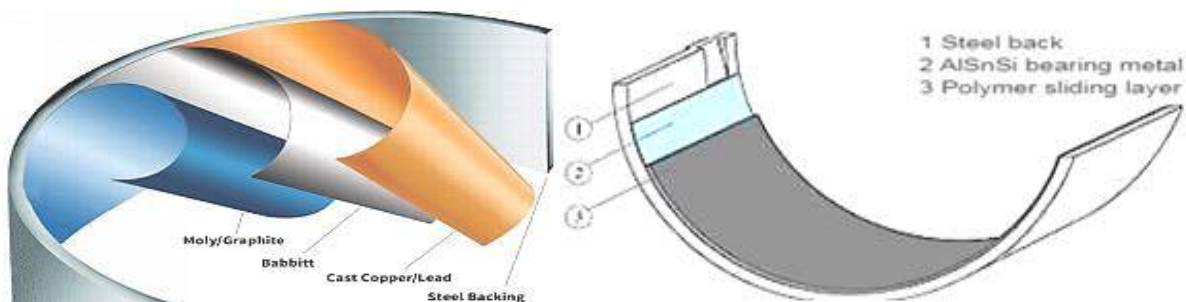


Fig 2: Bearing coatings and construction

The new engine bearings have an additional polymer sliding layer, so the bearing metal and the polymer coating can perform different tasks. After all, adaptability, wear resistance and load capacity all place extremely different demands on the system. A specially developed aluminum alloy containing silicon is used as the bearing metal; this is both extremely tough and wear resistant. Using a complicated application process, a polymer coating is applied to this aluminum alloy. The coating consists of a temperature and dirt-resistant poly amide resin that contains a high level of friction and wear-reducing bulking agents. Thanks to the combination

of metal and polymer components, the new product is 20% stronger than conventional dual-material bearings while also ensuring greater wear resistance and less friction. Using a complicated application process, a polymer coating is applied to this aluminum alloy. The coating consists of a temperature- and dirt-resistant polyamide resin that contains a high level of friction and wear-reducing bulking agents. By combining metal and polymer components, the new product is 20% stronger than conventional two-material bearings while also ensuring greater wear-resistance and less friction.

III. TECHNOLOGY USED IN APPLYING AFC ON BEARINGS

Coatings containing PTFE, MoS₂, or graphite are available as one-coat products. They can be applied to almost any bearing material except high nickel alloys and polyolefin resins. Depending on the formulation, continuous use temperatures are as high as 500°F, or 550°F for short periods of time. Suitable metal substrates include steel (carbon and stainless), aluminum (wrought and cast), copper and its alloys, and titanium. Special precautions must be taken when coating powdered metal (P/M) parts. Many P/M parts are treated with resinous impregnates that get trapped in the porosity of the parts. P/M parts need pre-baking at a temperature higher than the anticipated cure temperature for the coating. Contaminants that bleed to the surface during the pre-bake must be removed before coating. Coated plastic parts must cure at temperatures well below the softening temperature of the substrate to avoid distortion and polymer degradation. Most elastomeric parts that are not expected to elongate more than 30% in service can be coated. Woven and non-woven materials are increasingly used as bearings. Coatings adhere well to the porosity of the fabric.

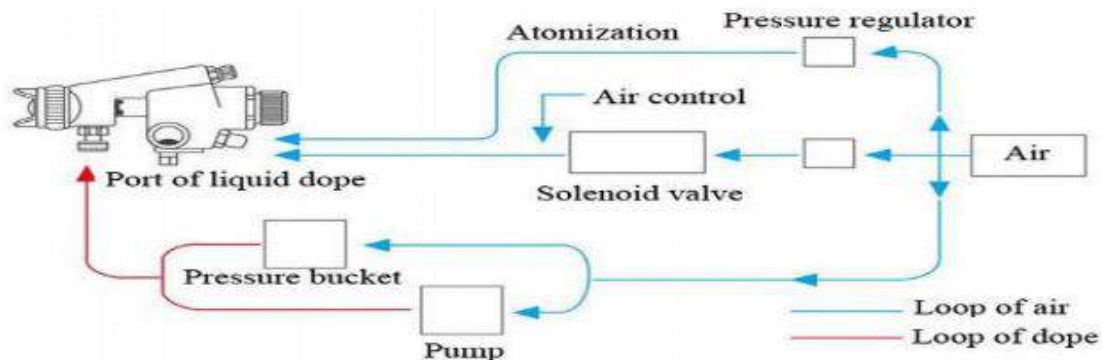


Fig 3: Example for working principle of coat spraying process

The technology for coating parts has improved recently. One result is that permanent bearing surfaces now get coated much more accurately than with conventional spray application systems. Known as the Dimension Bond process, the new technique uses computer-controlled systems that measure each part at several points during the application process to ensure consistent accuracy. The technique varies the thickness of the material being bonded to each part as necessary.

Many bearing designs use two dissimilar materials. In such situations, coat the softer of the two materials because it suffers the most damage from boundary lubrication. The roughness of a mating surface also affects coating wear. The optimum surface has a roughness of 8 to 12- inch rms. Surprisingly, hyper-smooth surfaces of less than 4 inch produce higher wear rates than those from the optimum range to the machined surface range

of 15 to 30 inch. The reason is that hyper-smooth surfaces permit less PTFE transfer to mating surfaces, which increases friction. Surfaces that are rougher than 30 inches. have higher wear rates.

IV. TESTING ENGINE WITH ANTI-FRICTION COATED BEARINGS

Friction testing is used to measure engine friction as a method of evaluating and improving fuel efficiency and component performance. Friction and wear are typically measured in engines, and mechanical systems to evaluate lubricant geochemistry, component design, and surface coatings. Coefficient of friction (COF) laboratory testing is used for a wide variety of materials and lubricants to determine their friction behavior and overall system performance. The COF is a dimensionless ratio of the tangential friction force between interacting materials, and the normal force pressing them together. COF is a system property which depends on many factors such as material type, surface finish, temperature, and contact geometry.

The experimental investigations were carried out for a modern in-line four-cylinder, four-stroke, naturally aspirated, passenger-car petrol engine with a nominal volume displacement of 1.8 L and at nominal power of 55 kW.

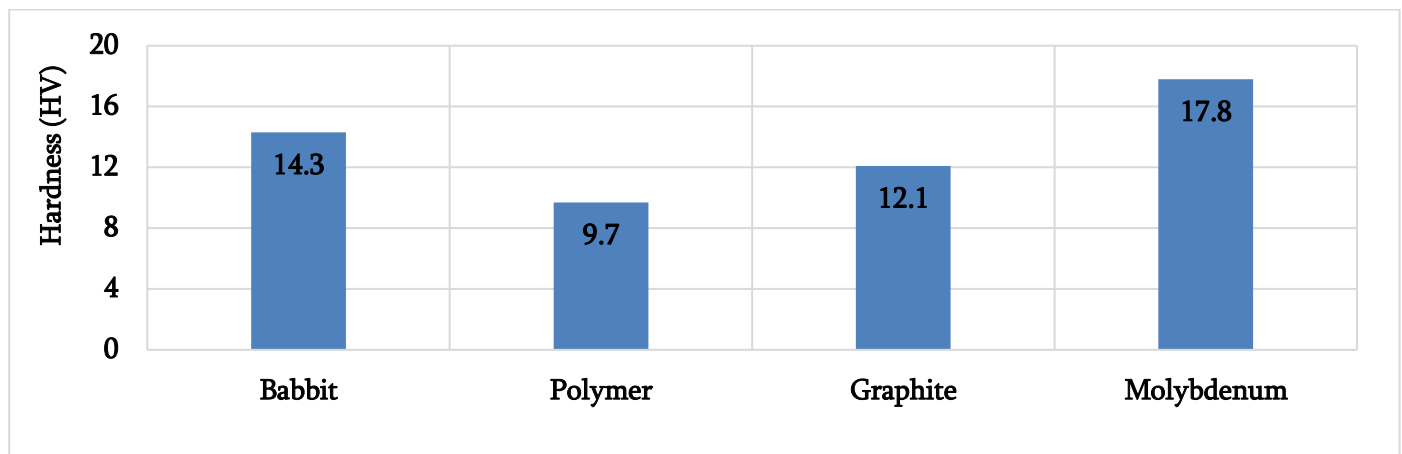


Fig 4: Vickers hardness values of different materials

Above graph shows the bearing overlay layer hardness value measured in Vickers hardness units. The bearings were coated with different overlay material composition as mentioned in the above graph. The thickness of the overlay material is kept uniform and constant for the bearings to assess the harness under standard condition. The graph shows the molybdenum base material with higher copper content will have better hardness compared to other materials. Higher copper content along with molybdenum also increases the fatigue strength of the overlay alloy. The surface condition of a material is crucial to its fatigue strength. Fatigue cracks form on the surface and then propagate into the material bulk. The higher the hardness of the surface layer, the greater the load must be for cracks to initialize.

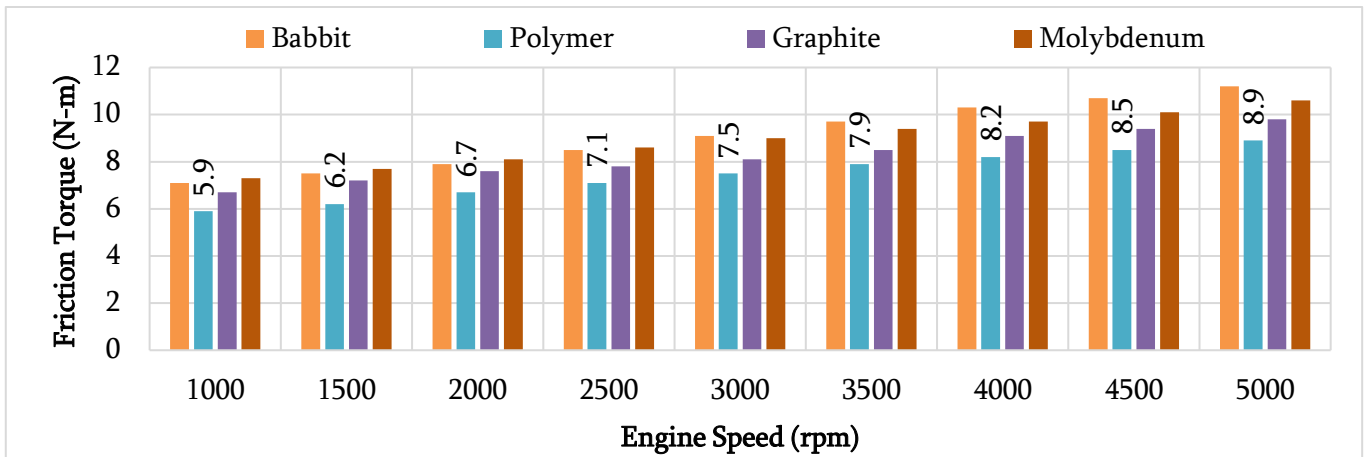


Fig 5: Friction torque from the engine using different AFC coatings

To evaluate the friction from engine due to change in bearing overlay material, full engine is reduced to the base-engine configuration by deactivating all engine auxiliary devices. This enables to full focus on the base engine friction losses during the friction loss investigations. The first measurements are then carried out on the base engine to obtain the engine friction torque over the entire load and speed range of interest. The engine friction torque is measured at constant engine media supply temperatures to analyze the influence of different AFC coatings on the friction losses of the engine due to bearings. Plot shown above depicts the different frictional torque with respect to overlay layer of anti-friction layers.

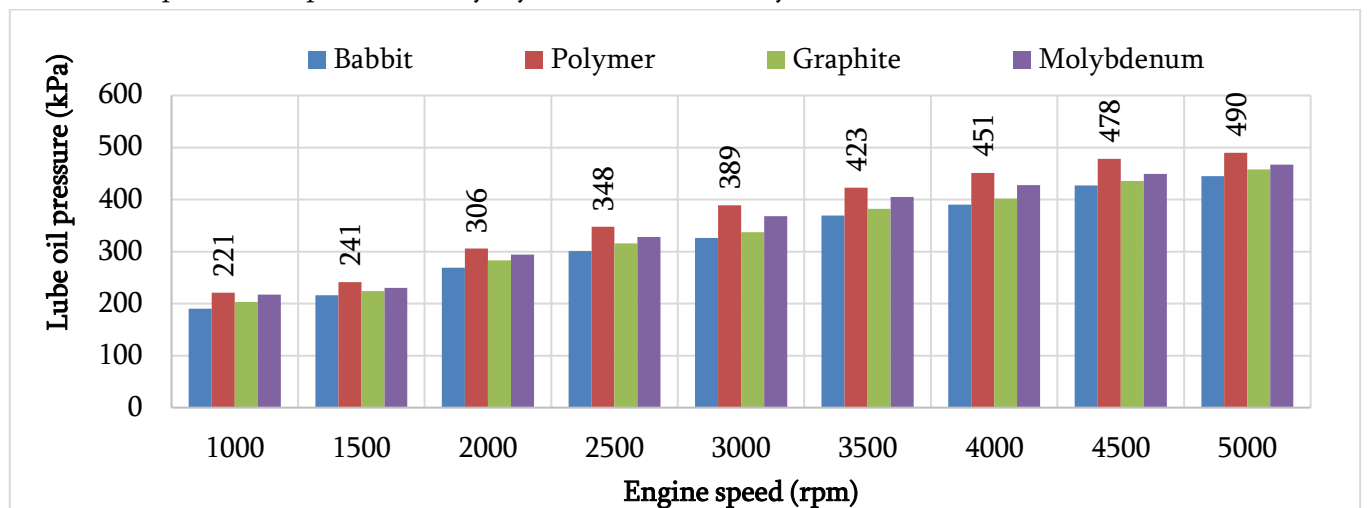


Fig 6: Lube oil pressure with different AFC coatings

The above bar chart is plotted with lube oil pressure data conducted in trial engine with different coatings on the main and journal bearings as well as camshaft bearings. The data shows the oil pressure is higher side with polymer coated overlay bearing. To keep this oil cushion working well, we need a very accurate gap between the bearing shell and the crankshaft journal. It's a very small gap in the order of hundredths of a millimeter. The polymer coating being less hard compared to other coatings the gap between the bearings and crankshaft (Minimum oil film thickness) maintained as required in most of the engine speed conditions

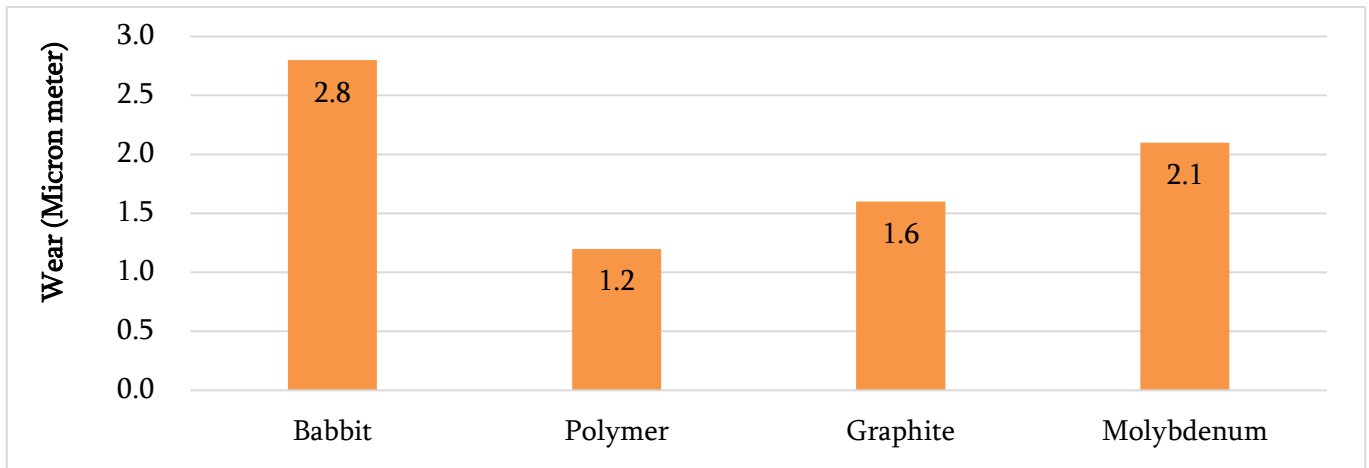


Fig 7: Wear rate with different AFC coatings

Above plot indicates the wear of coating layer after testing an engine for 200 hours on test bench. Different coatings worn out with different pattern and overall dimension is measured to assess the wear rate in micron meters. The lowest wear notices with polymer coated bearings. The coating applied is said to be 'solid lubricant' or 'dry lubricant' films, and it basically polymer coatings with a low coefficient of friction. Incorporation of solid lubricant particles into a metallic coating improves its anti-friction properties decreases the coefficient of friction and increases Seizure resistance (compatibility) and wear resistance. The most popular composite anti-friction coatings are nickel based with co-deposited PTFE. Copper-graphite and cobalt-BN are other examples of depositions with incorporated particles of solid lubricants.

V. CONCLUSION

This work investigated the frictional behavior of different overlay coated bearings and subsequently assessed whether the performance of coatings with respect to hardness, wear rate, frictional power and lube oil pressure sustenance. Based on the test results following conclusions are derived

1. The important part is the oil pressure inside the engine: this is piped to the crankshaft bearings, and it's this pressure that makes the plain bearings work. Based on the experimental results it is recommended to use polymer coated (AFC) bearings for this engine to achieve the best lube oil pressure in all rpms, to nullify the starting torque and reducing friction over engine operation.
2. The crank spins on a cushion of high-pressure oil, so the bearings should never really wear in normal use – there's a little bit of contact when the engine starts, but this will quickly stop once the oil pump starts working. If the oil pressure drops, then the bearings start to touch the crank journal surface, and the bearing shell quickly wears away. Based on the experimental results it is observed that polymer coated bearings wear rate is very less compared to other coatings, so we can conclude that based on the tested materials polymer coated overlay is good for the engine which is under trials.
3. Engine friction represents a non-negligible part of engine power loss, which determines engine efficiency. By optimizing bearings and their environment, which means the lubricant circuit and structural components like the camshaft, crankshaft, conrod, it seems possible to reach 25% bearing friction

- reduction. Without a large improvement of technology in component friction, this target will remain unreachable. Looking at the experimental results polymer coated bearings created less friction in engine in comparison to other materials. So, it can be concluded as the polymer coatings are good for this engine.
4. After various engine design background, low friction bearing design has to go hand in hand with improvements in reliability. The new trends in development try to define properties in more mechanical and quantified terms like hardness, yield strength, ductility and fatigue resistance. Based on the hardness results the polymer coatings have lowest hardness in comparison to other materials under trials. Polymer coatings requires addition particles to increase the hardness as well as fatigue strength. With polymer coatings, the main worry is binding quality as polymer material has quite a different thermal expansion to the metallic substrate.
 5. Polymer coated engine bearings offer the end user superior protection and performance in extreme scenarios, extend engine life, and provide vastly improved lubricity over non-coated bearings.

VI. FUTURE SCOPE

With improved hardness, fatigue strength of the bearings we can achieve better reliability of engine bearings. There is a need of improvement in base material and the most common solutions are MoS_x or DLC coatings. However, new coatings, composite coatings or deposits with WC/Co, TiN, TiC, TiB₂, WS₂, nanostructured coatings are also under investigation. Bearing manufacturers are in an intervention to solve this potential delamination problem by adopting a specific surface preparation and to add adhesion promoters to the polymer.

VII. REFERENCES

- [1]. N. Marina, D. Marin, Analysis of the properties of anti-friction materials of sliding bearings of diesel vehicles, Samara – Orenburg, 2013.
- [2]. S. Kosarev, N. Marina, I. Kardashev, Dynamic loading of high-performance diesel engine connecting rod bearing in the conditions of use of surfactants, Heavy Machinery. 10 (2012) 26-29
- [3]. K. Mutyala, H. Singh, R. Evans, and G. Doll, “Deposition, characterization, and performance of tribological coatings on spherical rolling elements,” Surface and Coatings Technology, vol. 284, pp. 302–309, 2015.
- [4]. K. Bobzin and T. Brögelmann, “Minimizing frictional losses in crankshaft bearings of automobile powertrain by diamond-like carbon coatings under elastohydrodynamic lubrication,” Surface and Coatings Technology, vol. 290, pp. 100–109, 2016
- [5]. Holmberg, K.; Andersson, P.; Erdemir, A. Global energy consumption due to friction in passenger cars. Tribol. Int. 2012, 47, 221–234.
- [6]. Praca, M.; Uehara, S.; Ferreira, M.; Mian, O. New polymeric coating on sputtered bearings for heavy duty diesel engines. SAE Int. J. Engines 2013, 6, 623–628, doi:10.4271/2013-01-1724.

- [7]. Nyberg, H.; Sundberg, J.; Sarhammar, E.; Gustavsson, F.; Kubart, T.; Nyberg, T.; Jansson, U.; Jacobson, S. Extreme friction reductions during initial running-in of W-S-C-Ti low friction coatings. *Wear* 2013, 302, 987–997.
- [8]. Beaurepaire, O.; Uehara, S.; George, J. Engine Bearings with a Durable Polymer Coating for Hybrids and Start-stop Applications; Articles techniques R-011608010; SIA: Versailles, France, 2011.
- [9]. Wang, G.; Nie, X.; Tjong, J. Surface Effect of a PEO Coating on Friction at Different Sliding Velocities; SAE Paper 2015-01-06897; SAE International: Warrendale, PA, USA, 2015.
- [10]. Braun, D.; Greiner, C.; Schneider, J.; Gumbsch, P. Efficiency of laser surface texturing in the reduction of friction under mixed lubrication. *Tribol. Int.* 2014, 77, 142–147.
- [11]. Nannan X and Wencheng T 2015 Modeling analysis and experimental study for the friction of a ball screw *Mech. and Mach. Theory* 87 pp 57-69
- [12]. Yuchao W, Fuyan L, Huazhuang J and Wenming Y 2015 Investigation on frictional characteristic of deep-groove ball bearings subjected to radial loads *Advances in Mechanical Engineering* 7 pp1-12



Profile Generation of a Subsonic Aircraft Wing with NACA 64-215 at the Root and NACA 64-210 at the Tip

Nataraj Kuntoji¹, Vinay V Kuppast^{2*}

¹Research Scholar, Department of Mechanical Engineering, Basaveshwar Engineering College, (Affl. to Visvesvaraya Technological University, Belgaum) Bagalkot, Karnataka, India

^{2*}Professor, Department of Mechanical Engineering, Basaveshwar Engineering College, (Affl. to Visvesvaraya Technological University, Belgaum) Bagalkot, Karnataka, India

ABSTRACT

Design of an aircraft is a multidisciplinary and a complex process that includes a broad range of disciplines and proficiency in aerodynamics, propulsion, structures, and flight control systems. Most important step in the any aircraft design process is its conceptual design phase. The primary design of any aircraft emphasizes on the balance the four aerodynamic forces namely weight, lift, thrust and drag. The most of the lift is generated by the wing. In the present work the design of the subsonic wing is considered based on these aerodynamic forces. The aircraft wing is modelled in the CATIA V5 considering NACA aerofoil standards, NACA 64-215 and NACA 64-210, which are used at the wing root and tip respectively. Stations and ordinates given in percent of airfoil chord for particular NACA profile are used in the modeling of wing profile. "GSD_PointSplineLoftFromExcel" in-built excel file in the CATIA V5 software is used to generate the points in the construction of airfoil profile at the root and tip. The smooth surface, generated by joining the airfoil profiles at the root and at the tip, is considered as the 'Numerical Master Geometry' in the construction of structural elements of the wing viz., spars, ribs and stringers. This model is further used for aero dynamic analysis.

Keywords: Aircraft Wing Structure, NACA, Wing Profile, CATIA V5

I. INTRODUCTION

During the conceptual design phase of an aircraft design process flight dynamics plays vital role [1, 2], wide variety of aircraft configurations are comprehensively studied and analyzed. Viability studies for different or non identical concepts and designs are carried out and the aim is to come up with the best concept design that is able to achieve the defined design objectives. One of the extremely important studies in any design process of aircraft is the conceptual design study of an aircraft wing.

The conceptual design phase of an aircraft design process flight dynamics plays vital role [1, 2], wide variety of aircraft configurations are comprehensively studied and analyzed. Viability studies for different or non identical concepts and designs are carried out and the aim is to come up with the best concept design that is able to achieve the defined design objectives. One of the extremely important studies in any design process of aircraft is the conceptual design study of an aircraft wing.

The prime function of any wing is to produce sufficient lift (L), Drag (D) and nose-down pitching moments (M) are the two components of the wing. The main aim of the aircraft wing design is to maximize the lift and minimize the drag and nose-down pitching moment. Wing is considered as lifting surface, based on Boundary Layer Principle, lower and upper surface of the wing profile produces the lift.

The wing design of the aircraft depends on many parameters like geometrical dimension, weight, uses of aircraft, required speed of takeoff and landing, required climb rate etc. sometimes space left unused in the wing may be used as storage tank for fuel and also for storage tank of other oils used for any other purpose in the aircraft. Left wing and right wing are decided based on the pilot seating arrangement. Pilot left side is called left wing and right side is called right wing.

Designs of an aircraft in CAD tool three reference planes are required. These reference planes in aircraft terminology termed as stations. Fuselage stations (FS) are used along the length of the aircraft in this case fuselage station zero is considered at the nose of the aircraft. Negative stations will not be considered in the fuselage stations. Reference planes along the height of the aircraft are termed as Water Lines (WL). Reference planes along the span of the wing are termed as Butt Lines (BL). In this research washout is considered along the wing to take care of stalling.

Usually in the case of subsonic aircraft wing two primary spars are constructed along the wing span [3]. Ribs are placed perpendicular to the spars to give aerodynamic shape to the wing. Since it is a subsonic aircraft two spar constructed wing is considered in the modeling. Spars are directly attached to the fuselage so they are considered as main structural member of the aircraft wing. Spars take high bending strength. The transfer of air load in the case of wing takes place from skin to ribs and from ribs to spars. Based on the location of the ribs they are termed as nose ribs, mid ribs and tail ribs. Since wing analysis is tedious and time consuming process and can be made easy by using numerical methods like Finite Element Method (FEM) and Computational Fluid Dynamics (CFD).

A. AIRFOIL:

An airfoil is the shape of a wing or blade as seen in cross-section and is shown in the Figure 1.

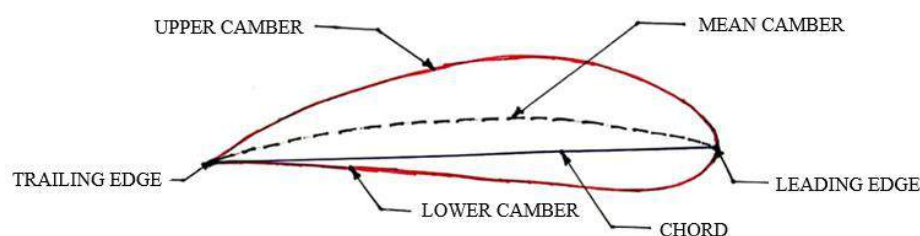


Figure 1. Cross section of an airfoil

It is passed through a fluid in order to provide either lift or down force, depending on its application. Subsonic-flight airfoils have a characteristic shape with a rounded leading edge, followed by a sharp trailing edge, and often with camber (Figure 2).

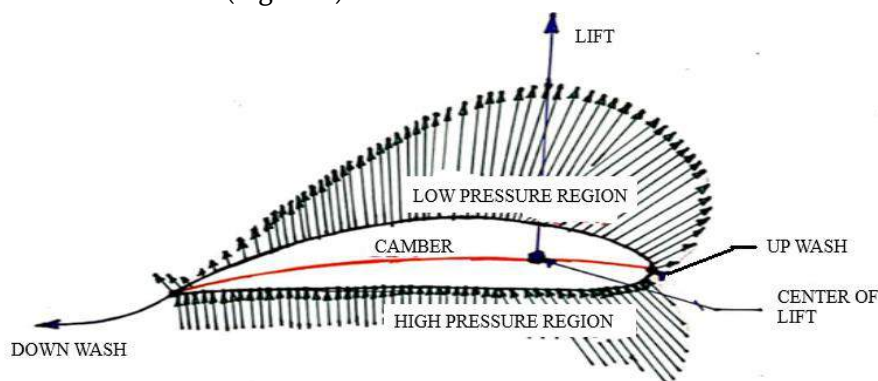


Figure 2. Pressure vector flow over an airfoil

Leading edge: The Wing front edge

Trailing edge: The Wing back edge

Span: Distance measured from wing tip to wing tip

Chord : Distance between wing front edges to wing back edge, usually measured parallel to the long axis of the fuselage

Aspect ratio: Ratio of span to standard mean chord

Twist: Gradual change of the airfoil (aerodynamic twist) and/or angle of incidence of the wing cross-sections (geometrical twist) and/or angle of incidence of the wing cross-sections.

B. AIRFOIL GEOMETRY

Many times we will see airfoils described as NACA XXXX or NACA XXXXX or NACA XXY-XXX series [4]. The following definitions are given to this nomenclature.

The NACA 4-digit airfoil- 4412 has a maximum camber of 4% of chord located at 40% chord back from the leading edge and is 12% thick, while 0006 is a symmetrical section of 6% thickness. The NACA 5 digit series airfoil - 23012 has a maximum camber of about 2% of the chord located at 15% of the chord from the leading edge (3 tenths divided by 2) and is 12% thick. The NACA six, seven and even eight series were designed to highlight some aerodynamic characteristic. For example, NACA 65₃-421 is a 6-series airfoil for which the minimum pressure's position in tenths chord is indicated by the second digit (here, at the 50% chord location), the subscript 3 means that the drag coefficient is near its minimum value over a range of lift coefficients of 0.3 above and below the design lift coefficient, the next digit indicates the lift coefficient in tenths (here, 0.4) and the last two digits give the maximum thickness in percent chord (here, 21% of chord)[3]. Non symmetrical (cambered) airfoils may have a wide variety of upper and lower surface designs. The advantages of the non symmetrical airfoil are increased lift-drag ratios and more desirable stall characteristics.

Here, in this work, *NACA 64-215* is used for the root end and *NACA 64-210* for the tip end of wing. This belongs to NACA six series airfoil and is non symmetrical airfoil.

II. GENERATION OF WING PROFILE

In the present scenario there are many Computer Aided Design (CAD) tools available for preliminary aircraft design. Preliminary Aircraft Design and Optimization (PrADO) is a comprehensive library of about 500 FORTRAN programs initiated in the early '90s at TU Braunschweig [5,6,7]. It is used in the modeling of different airplane configurations, which are further used in the preliminary design analysis. The airfoil generated without struts, ribs and stringers using PrADO and is not CAD-based. Multidisciplinary Interactive Design and Analysis System (MIDAS), based on graphical CAE tools structural analysis is combined with aerodynamics [8, 9]. Framework for Interdisciplinary

Design Optimization (FIDO), in the late 90's NASA Langley Research Center has developed this tool and used in the creation of airfoil geometry, with set of points, creation of airfoil geometry was improved with the use of Non-Uniform Rational B-Splines (NURBS)[10]. In 2002, a new and promising approach was presented by TU Munich [11] using CATIA V5 as a framework. Two concepts like K-operator and D-operator were used to create the aircraft structure using CAD software CATIA V5, which could be used for repetitive aircraft structure generation. [12]. The airfoil was modeled in CATIA V5 considering NACA 4412 coordinates later modeled the wing of the aircraft [13]. S. Senthilkumar et al in their paper considered NACA 65-210 airfoil coordinates in the taper wing CATIA V5 model [14]. Guguloth Kavya and B.C Raghukumar Reddy in their research paper they modeled aircraft wing in ProE with spars and ribs [15]. Ghassan M. et al constructed the wing model using ProE CAD software and later imported to COSMOL analysis software [16]. Kakumani Sureka and R Satya Meher in their research they modeled aircraft wing in CATIA V5 R20 CAD software considering the NACA 64-215 airfoil coordinates [17]. Continuation of previous research we found the research gap that no researcher has explained how to generate the aircraft wing by considering NACA standards in CAD software's which is the basic necessary requirement to carry out the further analysis of the wing. In this paper we focused on the generation of wing profile comprehensively step by step in CAD software CATIA V5. In continuation of previous research the research gap is identified that how to generate the aircraft wing by considering NACA standards in CAD tool to carry out the further analysis of the wing. In this paper the generation of wing profile is focused comprehensively using CATIA V5. The dimensions required for the generation of wing profile have been adopted from the previous design outcomes of various aircraft models. The design details are given in the TABLE 1 and few more considerations in the present research are given in TABLE 2

TABLE 1. Dimensions for modelling wing profile[18]

Parameters	Values
Root chord	2400 mm
Tip chord	700 mm
Semi Span length	5500 mm
Exposed Span	4750 mm
Airfoil (root)	NACA 64-215
Airfoil (Tip)	NACA 64-210
Aircraft weight	1400 kg
Lift Load	6g

FOS	1.5
-----	-----

TABLE 2. Considerations in this Research Work

Sweep at $\frac{1}{4}$ Chord	0°
Angle of Attack at root	0°
Angle of Attack at $\frac{1}{4}$ Span	0.6°
Angle of Attack at Midspan	1°
Angle of Attack at $\frac{3}{4}$ Span	1.6°
Angle of Attack at Tip	2°

It is apparent that all the subsonic aircrafts are relatively having similar values of capacity, length, wing span, height, wing area, empty weight, gross weight, power plant, maximum speed, cruising speed, stall speed, range, and rate of climb and 'g' limit. Hence, for the present study the dimensions required for the generation of wing profile are based on the design details given in the Table 1.

Table 3 gives the coordinates for NACA 64-215 airfoil section [19] and Table 4 gives the coordinates for NACA 64-210 airfoil section [19]

TABLE 3. Co ordinates for NACA 64-215 airfoil

Upper Surface		Lower Surface	
Station	Ordinate	Station	Ordinate
0	0	0	0
0.5	1.3414	0.5	-0.9871
0.75	1.5937	0.75	-1.2205
1.25	2.0067	1.25	-1.5737
2.5	2.7796	2.5	-2.2002
5	3.887	5	-3.0428
7.5	4.7301	7.5	-3.6551
10	5.4313	10	-4.1526
15	6.5361	15	-4.9143
20	7.3702	20	-5.4689
25	7.988	25	-5.8598
30	8.4231	30	-6.1125
35	8.6864	35	-6.2341
40	8.7634	40	-6.2077
45	8.6223	45	-5.9979
50	8.3055	50	-5.6467
55	7.8435	55	-5.1874
60	7.2614	60	-4.6481
65	6.5726	65	-4.0462

70	5.793	70	-3.4045
75	4.9429	75	-2.7543
80	4.0361	80	-2.1328
85	3.0595	85	-1.5834
90	2.057	90	-1.0531
95	1.0473	95	-0.5449
100	0	100	0
L.E. radius = 1.481 percent c			
slope of mean line at LE = 0.0951			

TABLE 4. Calculated Coordinates for chord length 2400mm

Upper Surface		Lower Surface	
Station	Ordinate	Station	Ordinate
0	0	0	0
12	32.1936	12	-23.6904
18	38.2488	18	-29.292
30	48.1608	30	-37.7688
60	66.7104	60	-52.8048
120	93.288	120	-73.0272
180	113.5224	180	-87.7224
240	130.3512	240	-99.6624
360	156.8664	360	-117.9432
480	176.8848	480	-131.2536
600	191.712	600	-140.6352
720	202.1544	720	-146.7
840	208.4736	840	-149.6184
960	210.3216	960	-148.9848
1080	206.9352	1080	-143.9496
1200	199.332	1200	-135.5208
1320	188.244	1320	-124.4976
1440	174.2736	1440	-111.5544
1560	157.7424	1560	-97.1088
1680	139.032	1680	-81.708
1800	118.6296	1800	-66.1032
1920	96.8664	1920	-51.1872
2040	73.428	2040	-38.0016
2160	49.368	2160	-25.2744

2280	25.1352	2280	-13.0776
2400	0	2400	0
L.E. radius = 1.481 percent c			
slope of mean line at LE = 0.0951			

Similarly stations and ordinates are calculated for NACA 64-210 standard given in the TABLE 5 considering the chord length as 700 mm at the tip for both upper and lower surfaces and the calculated values are given in the TABLE 6.

TABLE 5. Co ordinates for NACA 64-210 airfoil section

Upper Surface		Lower Surface	
Station	Ordinate	Station	Ordinate
0	0	0	0
0.5	0.9339	0.5	-0.7026
0.75	1.1132	0.75	-0.8544
1.25	1.4035	1.25	-1.0743
2.5	1.9434	2.5	-1.4517
5	2.7218	5	-1.9464
7.5	3.3193	7.5	-2.3017
10	3.8186	10	-2.5886
15	4.6112	15	-3.0233
20	5.2138	20	-3.3355
25	5.6653	25	-3.5513
30	5.9884	30	-3.6853
35	6.1926	35	-3.7426
40	6.2733	40	-3.7162
45	6.2054	45	-3.5787
50	6.0119	50	-3.3524
55	5.7125	55	-3.0585
60	5.3237	60	-2.716
65	4.8542	65	-2.3372
70	4.3111	70	-1.9353
75	3.7066	75	-1.5333
80	3.0449	80	-1.1598
85	2.3124	85	-0.8543
90	1.559	90	-0.5674
95	0.788	95	-0.292
100	0	100	0

L.E. radius = 0.735 percent c
slope of mean line at LE = 0.0951

TABLE 6. Calculated coordinates for chord length 700mm

Upper Surface		Lower Surface	
Station	Ordinate	Station	Ordinate
0	0	0	0
3.5	6.5373	3.5	-4.9182
5.25	7.7924	5.25	-5.9808
8.75	9.8245	8.75	-7.5201
17.5	13.6038	17.5	-10.1619
35	19.0526	35	-13.6248
52.5	23.2351	52.5	-16.1119
70	26.7302	70	-18.1202
105	32.2784	105	-21.1631
140	36.4966	140	-23.3485
175	39.6571	175	-24.8591
210	41.9188	210	-25.7971
245	43.3482	245	-26.1982
280	43.9131	280	-26.0134
315	43.4378	315	-25.0509
350	42.0833	350	-23.4668
385	39.9875	385	-21.4095
420	37.2659	420	-19.012
455	33.9794	455	-16.3604
490	30.1777	490	-13.5471
525	25.9462	525	-10.7331
560	21.3143	560	-8.1186
595	16.1868	595	-5.9801
630	10.913	630	-3.9718
665	5.516	665	-2.044
700	0	700	0
L.E. radius = 0.735 percent c			
slope of mean line at LE = 0.0951			

The points calculated in the Table 4 and Table 6 as per NACA profile standards are used to generate the airfoil profile. The profiles used are NACA 64- 215 at the root and NACA 64-210 at the tip. The splines are drawn

starting from the trailing edge to the leading edge except the leading edge point. Thus creating the top and bottom splines of the wing. This is done on both root and the tip

A. Creating the primary wing surface using CATIA V5:

- Plotting the NACA profile points.
- Plot the points using the option: "GSD_PointSplineLoftFromExcel"

FIGURE 3. shows the co-ordinates generation at root and tip as per NACA standards in CATIA V5 platform.

1. Create the splines making the top and bottom part of the aerofoil. Leave the leading edge point to give the leading edge radius as per NACA standard. FIGURE 4. shows the creation of spline except leading edge radius.

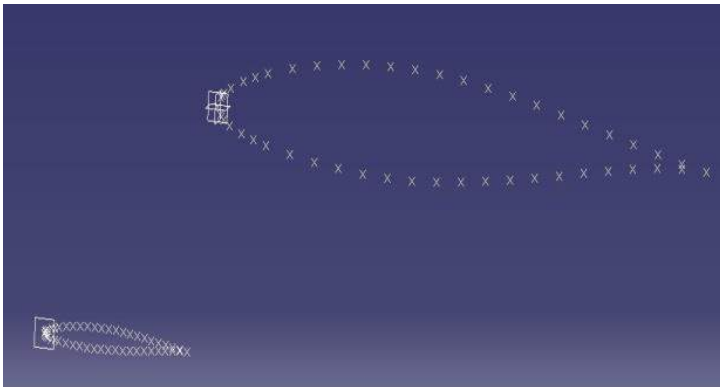


FIGURE 3. Coordinates generation at root and tip as per NACA standards

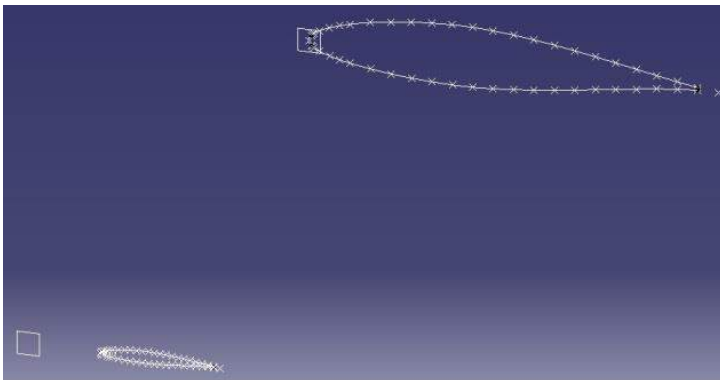


FIGURE 4. Creation of spline except leading edge radius

B. Incorporating the leading edge radius

1. Using the NACA standards for leading edge;

At Root

Slope= 0.0842, Radius= 1.556% of the chord length

At Tip

Slope= 0.0842, Radius= 0.701% of the chord length.

The following calculations are made using empirical relations for the creation of leading edge radius and slope.

At Root (NACA 64-215)

Leading edge radius – 1.556% chord length

$$= \frac{1.556}{100} \times 2400 = 37.344 \text{ mm}$$

Slope of mean line at leading edge = 0.0842

$$\tan \theta = 0.0842$$

$$\theta = \tan^{-1}(0.0842)$$

$$\theta = 4.8129^\circ$$

At Tip (NACA 64-210)

Leading edge radius – 0.701% chord length

$$= \frac{0.701}{100} \times 700 = 4.907 \text{ mm}$$

Slope of mean line at leading edge = 0.0842

$$\tan \theta = 0.0842$$

$$\theta = \tan^{-1}(0.0842)$$

$$\theta = 4.8129^\circ$$

2. Creating a point in the sketcher mode as per the given standards for both root and tip airfoil profiles and it is shown in the FIGURE 5.

3. Exit the sketcher and draw the arcs of radius as per the standards for the profiles. FIGURE 6 shows the drawing procedure of the arc at the root and tip of the wing.

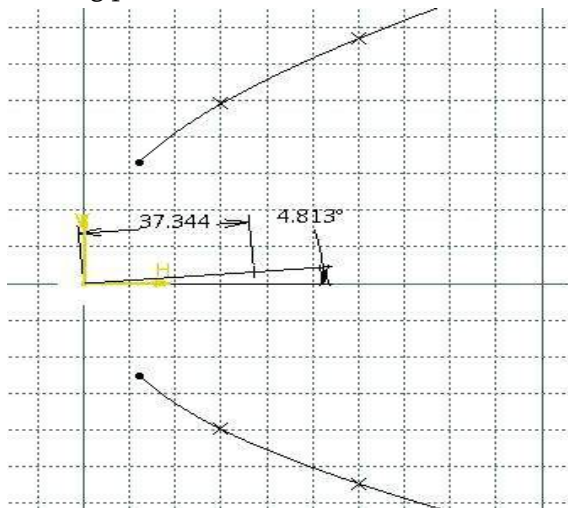


FIGURE 5. Leading edge radius centre point

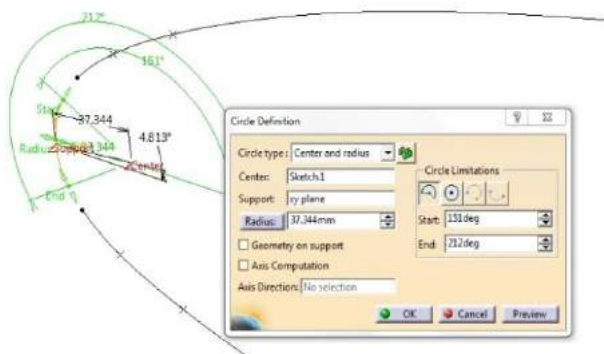


FIGURE 6. Creation of arc for leading edge

5. Using the connect curve option join the arc and the splines choosing curvature continuity for both the ends and it is shown in FIGURE 7.

6. Generation of wing surface using the aerofoil profiles at the root and the tip. Creation of wing surface is shown in FIGURE 8.

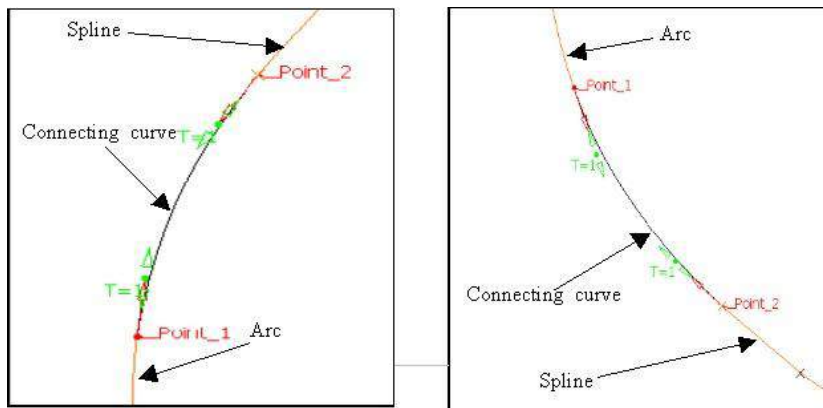


FIGURE 7. curve connecting arc and spline

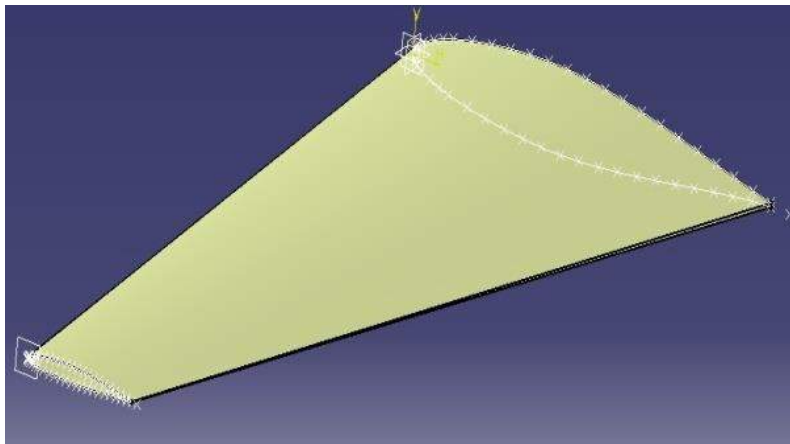


FIGURE 8. Wing surface connecting root and tip sections

III. WING SURFACE WITH WASHOUT

A. Creating profiles at sections

1. Construct the planes at $1/4^{\text{th}}$, $1/2$ and $3/4^{\text{th}}$ of the spans of the wing.
2. Intersect the wing surface at the constructed planes to get the aerofoil sections at each of them and it is shown in the FIGURE 9.
3. Create a line along a point at quarter chord distance.
4. Rotate the profiles keeping the line as a reference.
5. The rotation angles are 0° at the root of the wing, 0.6° at $1/4^{\text{th}}$ span of the wing, 1° at the mid span, 1.6° at $3/4^{\text{th}}$ of the span and 2° at the tip of the wing. Introducing the angle of attack into the CATIA model is shown in the FIGURE 10.
6. Create the surface using multi sections surface option

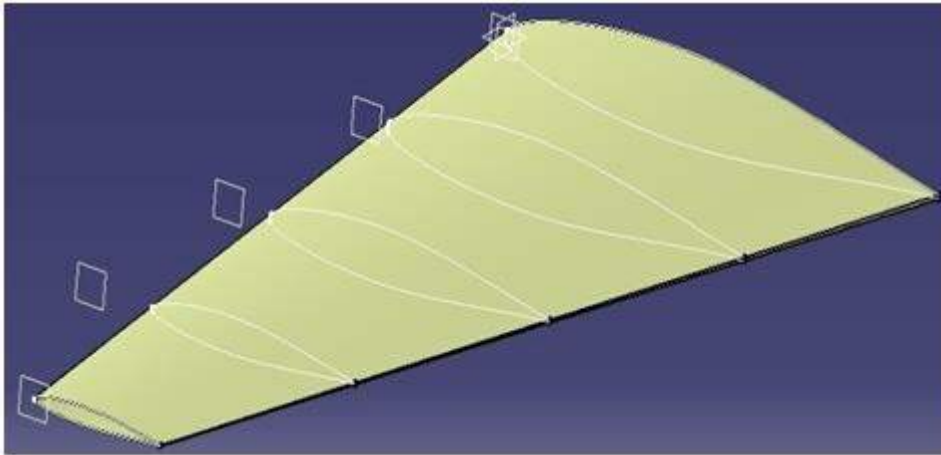


FIGURE 9. Intersection of the wing surface at 3 different planes

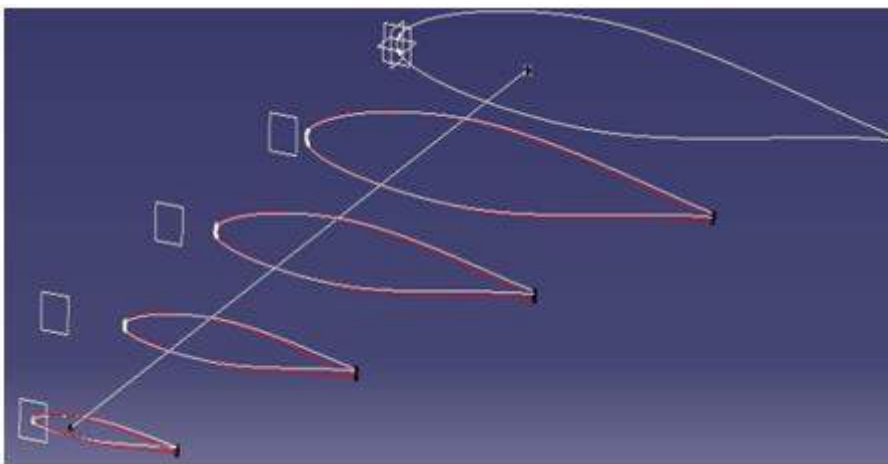


FIGURE 10. Introducing angle of attack

By considering the profiles generated with angle of attack at different sections, the wing surface is created using multi-section surface option. Wing surface with washout is shown in FIGURE 11.

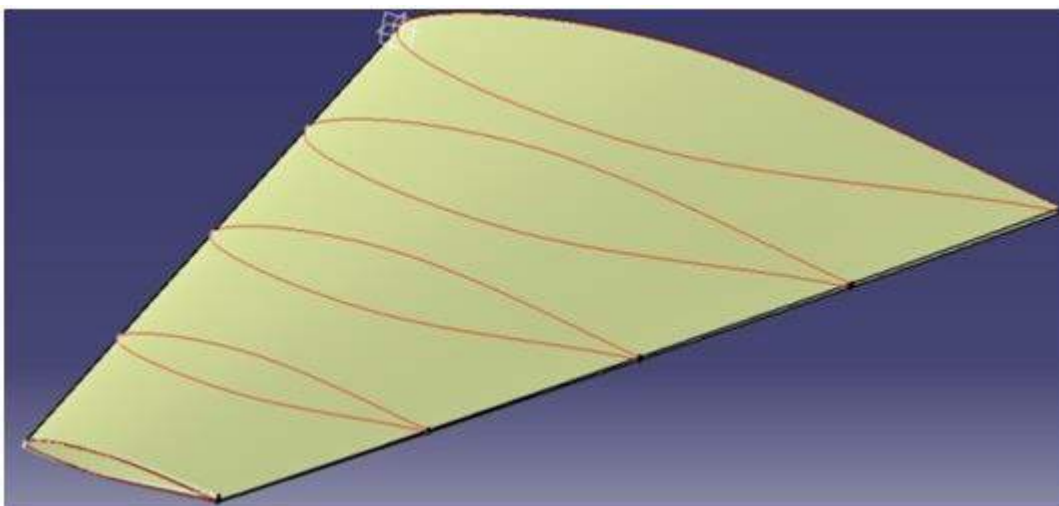


FIGURE 11. Wing surface with washout

Thus the wing surface is constructed as per the NACA standards incorporating all the requirements considered in this research work.

IV. CONCLUSION

Wing profile generation is the prime requirement of a researcher to carry out any kind of design and analysis on aircraft wing model. Existing Literature would not give clear idea in the generation of subsonic aircraft wing profile. 2 to 14 seater aircrafts are subsonic in nature. NACA standards are used in most of the aircrafts to build the wing profile. In this research NACA 64-215 at the root and NACA 64-210 at the tip are considered for building the wing profile. Washout is also considered along the length of the wing at the root, 1/4th, 1/2, 3/4th and at the tip of the wing as 0°, 0.6°, 1°, 1.5° and 2° respectively for reducing the lift distribution across the wing span of the aircraft to provide the continued aileron control during stalling of the aircraft. CATIA CAD tool is used in the generation of wing profile.

V. REFERENCES

- [1]. Warren, F.P. Mechanics of Flight; Wiley: Hoboken, NJ, USA, 2009.
- [2]. Kermode, A.C. Mechanics of Flight; Longman Pub Group: London, UK, 1996.
- [3]. ATSB Transport Safety Report Occurrence Investigation, AO-2013-226, Final -21 January 2016, Australian Transport Safety Bureau.
- [4]. Airplane Aerodynamics, by Dommasch, Sherby and Connally, Pitman Press, 1967
- [5]. W. Heinze, C.M. Österheld, P. Horst, Multidisziplinäres Flugzeugentwurfsverfahren PrADO-Programmwurf und Anwendung im Rahmen von Flugzeug-Konzeptstudien, Technical Report, Institut für Flugzeugbau und Leichtbau (IFL), Technische Universität Braunschweig, 2002.
- [6]. A. Lubis, H. Kossira, W. Heinze, PrADO-Pa: Ein parallelisiertes Programmsystem für den Entwurf von Verkehrsflugzeugen, in: DGLR Jahrestagung 1992, Bremen, DGLR-Jahrbuch 1992 III, Bonn, 1992
- [7]. C.M. Österheld, W. Heinze, P. Horst, Preliminary design of a blended wing body configuration using the design tool PrADO, in: Proceedings of the CEAS Conference on Multidisciplinary Aircraft Design and Optimisation, Köln, Juni 25–26, 2001.
- [8]. X. Luo, H. Rajagopalan, R. Grandhi, MIDAS: Multidisciplinary Interactive Design and Analysis System – integration of ASTROS and I-DEAS, in: 37th AIAA/ASME/ASCE/AHS/ASC Structures, Structural Dynamics, and Materials Conference and Exhibit, Salt Lake City, UT, 1996
- [9]. H. Sobieczky, R. Seebass, J. Mertens, G. Dulikravich, A. Van der Velden, New Design Concepts for High Speed Air Transport, CISM Courses and Lectures, vol. 366, International Center for Mechanical Sciences, Springer-Verlag, 1997.
- [10]. J.C. Townsend, J.A. Samaresh, R.P. Weston, W.E. Zorumski, Integration of a CAD system into an MDO framework, Technical Report NASA/TM1998-207672, NASA – Langley Research Center, Hampton, VA, 1998.

- [11]. T. Richter, M. Mechler, D. Schmitt, Integrated parametric aircraft design, Technical Report, Institute of Aeronautical Engineering, Technical University Munich, 85747 Garching, 2002.
- [12]. Christof Ledermann, Paolo Ermanni, and Roland Kelm, "Dynamic CAD objects for structural optimization in preliminary aircraft design" *Aerospace Science and Technology* 10 (2006) 601–610.
- [13]. Sudhir Reddy Konayapalli and Y Sujatha "Design and Analysis of Aircraft Wing" *International Journal and Magazine of Engineering, Technology, Management and Research*. Volume No: 2 (2015), Issue No: 9 (September).
- [14]. S. Senthilkumar, A. Velayudham, and P. Maniarasan "Dynamic Structural Response Of An Aircraft Wing Using Ansys" *International Journal of Engineering Research & Technology (IJERT)*, Vol. 2 Issue 6, June – 2013.
- [15]. Guguloth Kavya and B.C Raghukumar Reddy "Design and Finite Element Analysis of Aircraft Wing using Ribs and Spars" *International Journal and Magazine of Engineering, Technology, Management and Research*. Volume No: 2 (2015), Issue No: 11 (November).
- [16]. Ghassan M. Atmeh, Zeaid Hasan and Feras Darwish "Design and Stress Analysis of a General Aviation Aircraft Wing" Excerpt from the Proceedings of the COMSOL Conference 2010 Boston.
- [17]. Kakumani Sureka and R Satya Meher "Modeling and Structural Analysis on A300 Flight Wing by using ANSYS" *International Journal of Mechanical Engineering and Robotics Research* Vol. 4, No. 2, April 2015.
- [18]. T.S.Vinoth Kumar, A.Waseem Basha, M.Pavithra, V.Srilekha "Static and Dynamic Analysis of a Typical Aircraft Wing Structure using MSC Nastran" *International Journal of Research in Aeronautical and Mechanical Engineering*, Volume: 3 Issue 8, August 2015.
- [19]. <http://www.pdas.com/sections6a.htm>



Mechanical Characterization of Micro B₄C Particles Reinforced Al6061 Alloy Metal Composites

Murali Mohan R¹, Madeva Nagaral²

¹Assistant Professor, Department of Mechanical Engineering, Government Engineering College, Hasan, Karnataka, India

²Deputy Manager, Aircraft Research & Design Centre, HAL, Bangalore-560037, Karnataka, India

ABSTRACT

The current work intended to synthesize Al6061 alloy with 5 wt. % of micro B₄C particulate metal matrix composites using liquid metallurgy technique. Scanning electron microscopic images of the synthesized composites were obtained to demonstrate the uniform dispersion of the reinforced micro B₄C particles in the matrix. EDS spectrums confirmed the various elements present in the Al6061-B₄C composites, XRD patterns reveal the Al and B₄C phases in the composites. Hardness, tensile and impact tests were carried out to find out the impact of micro B₄C on the various mechanical properties of the composites. Synthesized composites hardness, tensile and impact strength were found to be more with the incorporation of B₄C particles.

Key words: Al6061 Alloy, B₄C Particles, Microstructure, Mechanical Properties, Fractography

I. INTRODUCTION

Composites are materials made up of a continuous constituent stage assembled network that holds and supports more grounded, stronger support constituents, resulting in a material with an optimal blend of main qualities that is clearly superior to its constituent parts alone. Design flexibility, high specific strength, high specific modulus, high fatigue endurance limit, corrosion, and wear resistance, thermal cycling tolerance, tolerable coefficient of thermal expansion, and other features make composites superior to normal primary materials [1, 2]. The relative number and attributes of constituent stages, as well as the geometry of the distributed stage, which includes molecule size, shape, and orientation in grid coordinates, are all properties of composites [3]. High stiffness, a high strength-to-weight ratio, and good wear resistance are only a few of the qualities [4]. For light weight structural applications and electronic enclosures, metal matrix composites (MMCs) using aluminium (Al) as the matrix are used. In contrast to the same monolithic materials, MMCs were increased as a critical material class for simple structural, wear, and electrical applications principally because they were able to show greater efficiency than weight-strength to cost ratios [5, 6]. Aluminum metal matrix composites (AMMCs) are regarded as a new class of propellants in MMCs because of their light weight, high resistivity, high modulus, low CTE (Coefficient of Thermal Expansion), and increased wear resistance.

Ashwath and team [7] explain the importance of aluminium metal matrix composites and their importance in high strength application in line with fatigue strength. This study tells us advantages and disadvantages in employing aluminium alloy metal matrix composites (AAMMC) for superior strength applications. They claimed that AAMMC fabricated by advanced manufacturing methods have certain degree of impact in the evaluation of replacement of high strength materials.

Jayashree and team [8] did this study to address the role of SiC addition in aluminium metal matrix composites on the welded microstructure and to relate the microstructural changes to the observed mechanical behaviour of the welded joints. Their study reveals that strength depends not only on average value of misorientation but also on the distribution of misorientation in the microstructure. It briefs us some important observations on the strength and behaviour of the welds of aluminium MMCs prepared through the TIG technique with different composition of SiC subjected to age hardening and relating the noticed characteristics of the welds to its microstructure in terms of distribution of grain size, grain boundary nature, misorientation and stored energy.

Harish Munnur [9] and others tried to summarize the effects of reinforcements such as SiC and CNT in the aluminium matrix by various fabrication Techniques. They discussed about mechanical properties like hardness, tensile strength and compressive strength improvement related with percentage of reinforcement, fabrication and processing of the MMCs. They also briefed about methodology for mixing condition and behaviour of Aluminium metal matrix composites which gives information about processing conditions.

In the present study, alumina particles with 90 micron size were incorporated into the Al6061 alloy to fabricate Al6061 – 5 wt. % of B₄C composites. The composites were developed using stir cast method. Thus developed composites were tested for microstructural and mechanical characterization as per ASTM testing standards.

II. EXPERIMENTAL DETAILS

Materials Used

The stir method of casting was used to create metal composites containing 5% B₄C particles with a size of 90 microns. Due to its greater casting properties, strength, formability, heat treatment nature, good corrosion resistance, machinability, and wide applications in several sectors, aluminium 6061 alloy (Fenfee Metallurgical Pvt. Ltd., Bangalore) was chosen as the matrix, while B₄C particles with a size of 90 m were used as reinforcements (Fig.1). The chemical arrangement of the Al6061 alloy used in the current experiments is shown in Table 1.

Table 1 Chemical configuration of Al6061 alloy

Elements (wt. %)	Al6061 (actual)
Mg	0.91
Si	0.67
Fe	0.21
Cu	0.23
Ti	0.07
Cr	0.02
Zn	0.03

Mn	0.06
Al	Balance

B₄C particles of 90 μm (Supplied by Speedfam Ltd, Chennai, Karnataka, India) are used in the present study. The SEM and EDS analysis of B₄C particulates are carried by using SEM as in Fig. 1 (a-b).

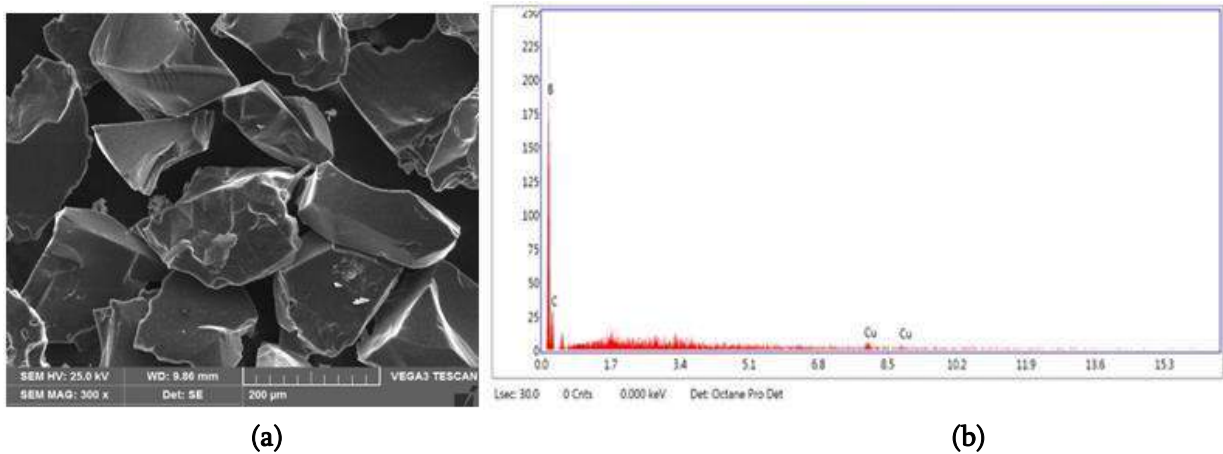


Fig. 1 (a) SEM micrograph of B₄C particles (b) EDS spectrum of B₄C particles

Preparation of Composites

The stir casting approach is used to create Al6061-B₄C metal composites. A weighing kit is used to weigh a known amount of Al6061. The graphite-based crucibles are used to hold the Al6061 ingots. Inside the electro-mechanical stir cast machine is a crucible containing Al6061 alloy. The Al6061 ingot is heated to 750°C till it becomes liquid metal. Simultaneously, known amounts of B₄C particles are warmed in the preheater at a temperature of 500 degrees Celsius. This aids in the removal of humidity and increases the wettability of the particles. Degassing specialist hexochlorthene is introduced to the liquid metal to remove unwanted gases caught inside. After that, 5 wt. percent B₄C particles are added into the produced vortex of the melt in two phases rather than one at a time, and the melt is further stirred for 10 minutes with a zirconia coated steel impeller. The molten slurry is then poured into a cast iron mould and allowed to solidify completely. After complete solidification, the hybrid composite is drawn from the mould and subjected to SEM, hardness, tensile test, and impact test, all in accordance with their specifications. In the tensile and impact failure investigation, SEM microphotographs were employed to examine the various fracture modes.

SEM is used to examine the size, shape, and circulation of B₄C and B₄C found in Al6061 composites (TESCAN VEGA, Czech Republic). For EDX study, the apparatus is connected to the JED 2300 examination software application. Specimens for SEM are cut to a diameter of 15 mm and a height of 5 mm. The sliced samples are flattened with a belt grinder. The samples are then polished with silicon carbide emery sheets with grit sizes ranging from 300 to 1000. Fine cerium oxide is used to finish the piece by hand on a micro cloth. Keller's reagent is used to etch the samples to disclose the right granular structure. 95 mL H₂O, roughly 2.5 mL HNO₃, 1.5 mL HCl, and 1 mL HF make up the etching solution. The samples are rinsed and completely dried after etching.

To determine the degree of difficulty The Vickers hardness tester is employed, with a load range of 25 to 1000 g. For testing, the ASTM E384 [10] standard is utilised. Dead weight is used to apply loads. A precision diamond indenter is utilised on the material, and a load of 100 g is applied for 30 seconds across a specimen with a diameter of 15 mm and a length of 10 mm. The indentation is then microscopically measured, and the applied load is utilised to calculate the Vickers hardness number (VHN). On each sample, three readings were taken at different points and the mean value was calculated.

Tensile tests are performed using an Instron computerised universal testing machine (UTM) with a 60 kN capacity and a minimum count of 4 N. Figure 2 shows a tensile specimen with a 45 mm gauge length that meets the ASTM E8 [11] standard. Following the test, the fracture surfaces are provided for microstructural analyses with a scanning electron microscope (SEM) to better understand the fracture mechanism.



Fig. 2 Tensile test specimen

Impact strength of the Al6061 alloy and Al6061 with 5 weight percentages of B₄C particles reinforced composites are evaluated as per ASTM E23 standard [12]. The standard size of the Charpy impact test sample is shown in the Fig. 3.

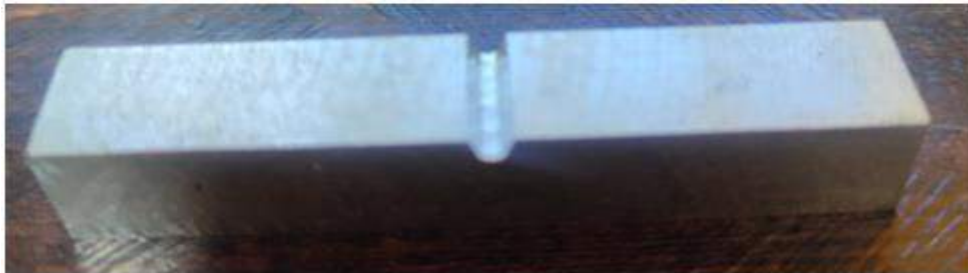
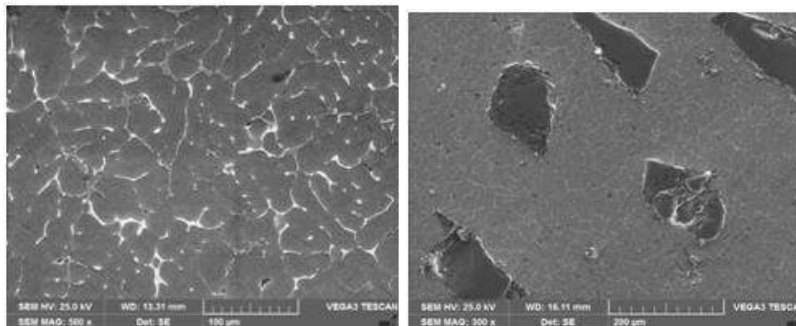


Fig. 3 sample of Charpy impact test specimen

III. RESULTS AND DISCUSSION

Microstructural Studies

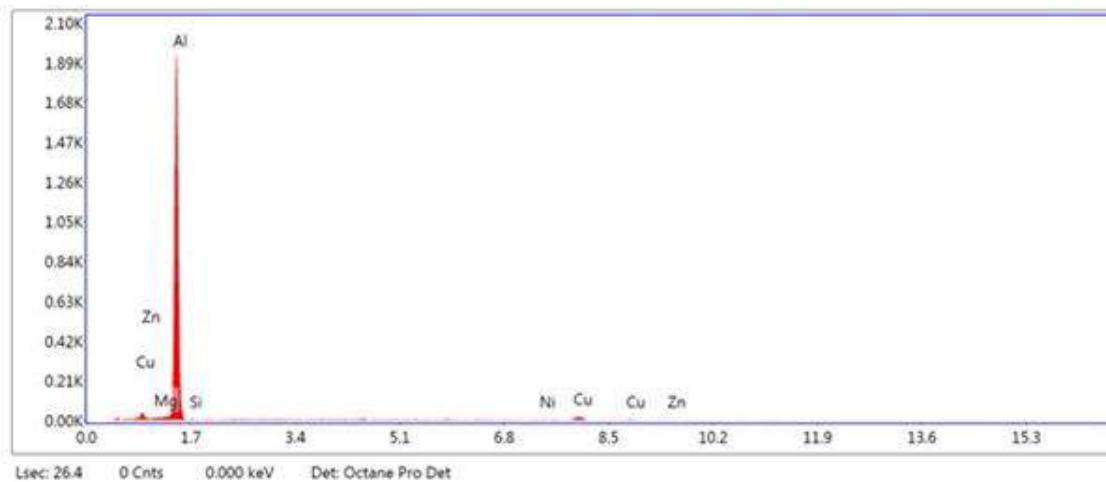


(a)

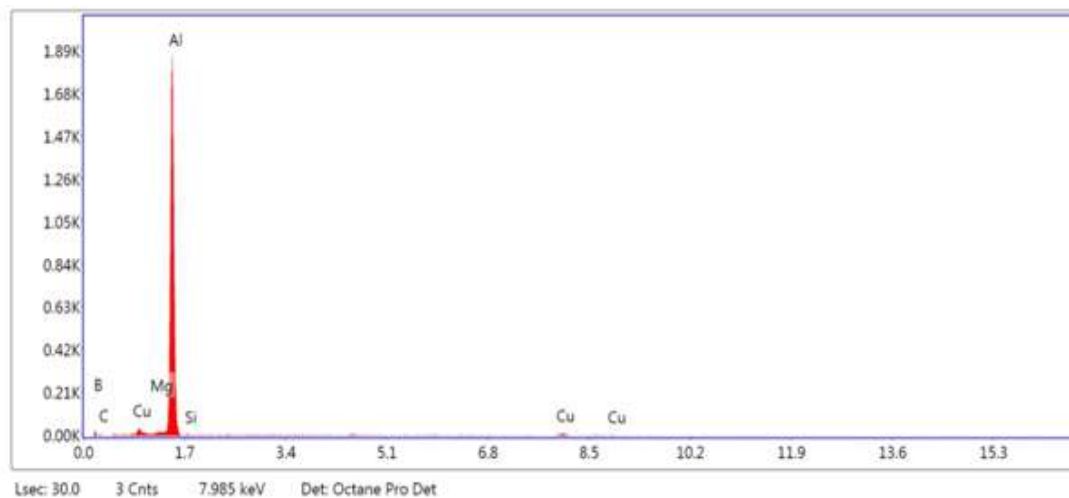
(b)

Fig. 4 Scanning electron microphotographs of (a) Al6061 alloy (b) Al6061-5 wt. % of B₄C composites

Scanning electron microphotographs of Al6061 alloy as cast and Al6061 with 5% B₄C composites are shown in Figure 4 (a-b). SEM microstructures of Al6061 compound and Al6061 amalgam with 5 weight rates of micro B₄C supported composites are shown separately in Figs. 4 (a) and 4 (b). The micrograph of Al6061 alloy with fine grains and no pores is shown in Figure 4 (a). Furthermore, as shown in Fig. 4 (b), B₄C is present in the Al6061 alloy, and there is a strong link between the Al6061 matrix and B₄C particles. The Al6061 alloy's particle distribution was enhanced using a two-stage reinforcement addition process. As a result, dispersed particles aid in the improvement of composite qualities.



(a)



(b)

Fig. 5 EDS spectrums of (a) Al6061 alloy (b) Al6061-5 wt. % of B₄C composites

The EDS spectrums of Al6061 alloy and 5 wt. percent B₄C particles supported composites are shown in Fig. 5(a-b). The alloying components included in Al6061 compound are shown in Fig. 5 (a), with Mg and Si being the most important alloying components, along with Cu, Mg, Zn, and Si. The EDS analysis of Al6061-5 wt. percent of B₄C composites is shown in Fig. 5 (b); the spectrum verifies the presence of B₄C particles in the generated composites in the form of Al and B elements.

To examine the presence of Al and B₄C particulates in the Al6061-B₄C metal composites, the XRD investigation is made. Fig. 6 is the XRD pattern of 5 wt. % of B₄C particles reinforced composites, which contains B₄C phases at 38°, 42°, 69° and 74°.

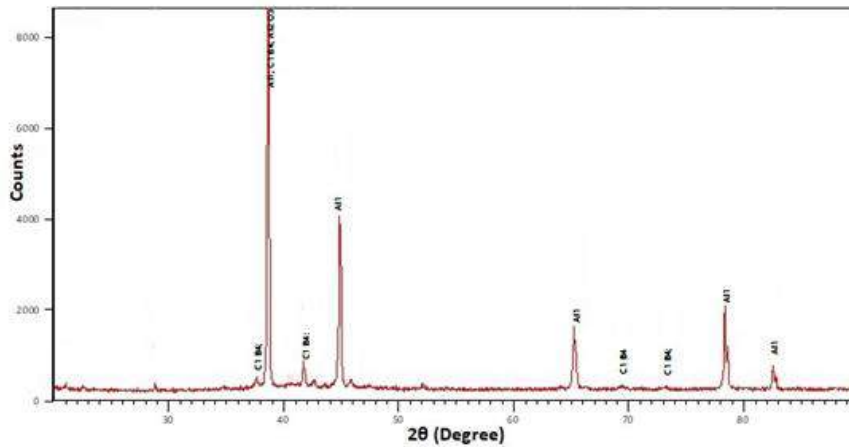


Fig. 6 XRD patterns of Al6061-5 wt. % of B₄C composites

Hardness Measurements

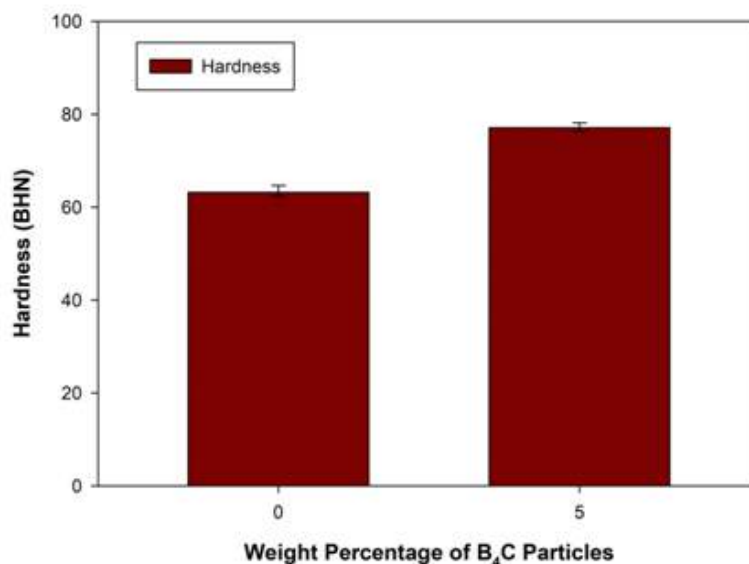


Fig. 7 Hardness of Al6061 alloy and B₄C composites

Hardness of Al6061 compound and Al6061 with 5 weight level of B₄C supported metal grid composites are addressed in Fig. 7. The hardness of the Al6061 compound expands with the addition of support B₄C particles, as seen in Fig. 7 plots. The hardness of the base material cast Al6061 combination is estimated to be 63.5 BHN, however after the expansion of B₄C particles using a two-way unique technique, the hardness increases to 76.3 BHN. The hardness of Al6061-5 wt. percent of B₄C composites has improved by 20.15 percent. The inclusion of hard particles B₄C in the delicate pliable lattice contributes to Al6061's increased hardness. The delicate framework's hardness increased because the hardness of B₄C particles is 2875 BHN, which increases the hardness of the Al6061-B₄C grid.

Ultimate Tensile and Yield Strength

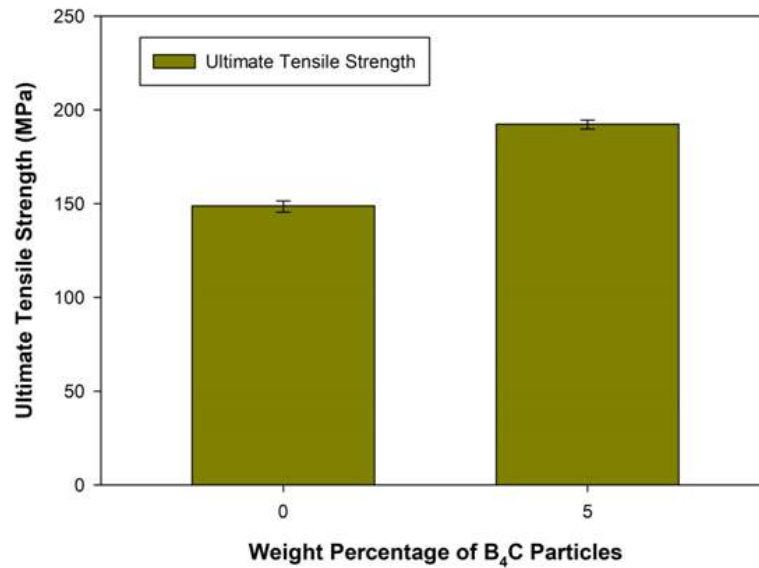


Fig. 8 Ultimate tensile strength of Al6061 alloy and B₄C composites

The ultimate strength of supported B₄C particles on Al6061 amalgam is shown in Fig.8. The basic material cast Al6061 combination has a UTS of 146.8 MPa; however, after expanding B₄C particles in two ways using a unique technique, the UTS increases from 146.8 MPa to 192.3 MPa. The strength of Al6061-5 wt. percent of B₄C composites has improved by 30.9 percent. The strong interfacial connection of Al6061 matrix and B₄C particles was clearly seen in SEM micrographs; this bonding aids in the transfer of axial tensile load from matrix to B₄C particles [13]. This hard particle prevents Al matrix plastic flow, increasing the load carrying capability of Al6061 alloy. The two-step technique also contributed to the Al6061 alloy having a strong bond and homogeneous particles.

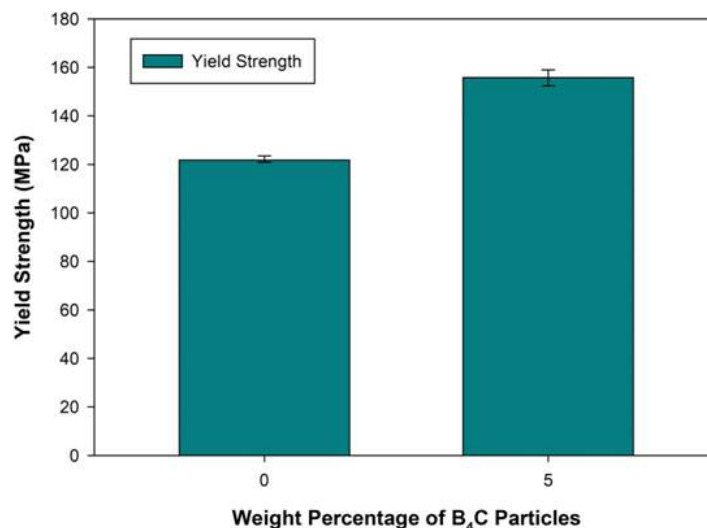


Fig. 9 Yield strength of Al6061 alloy and B₄C composites

The yield strength of Al6061 alloy and Al6061 alloy with 5% B₄C composites is plotted in Fig. 9. The yield strength of Al6061 alloy is 121.6 MPa, with a slight increase following the addition of 5% micro B₄C to the Al matrix. The strength of Al6061 composites containing 5% B₄C is 154.3 MPa. These hard oxide particles are responsible for a 26.9% increase in yield strength. The strong interfacial connection of Al6061 matrix and B₄C particles was clearly seen in SEM micrographs; this bonding aids in the transfer of axial tensile load from matrix to B₄C particles. This hard particle prevents Al matrix plastic flow, increasing the load carrying capability of Al6061 alloy.

Percentage Elongation

When compared to the cast Al6061 matrix alloy, Fig. 10 shows the decrease in percentage elongation of the resulting composite after adding 5 wt. percent B₄C. The decrease in ductility is due to the following factors: i) void nucleation caused by raising the reinforcing level. The specific explanation for this difference could be that the B₄C particle works like a stress concentrator, and that ii) the solid interfacial strength with the reinforcement and matrix is extremely high, resulting in increased reinforcement load and breaking at lower stresses [14].

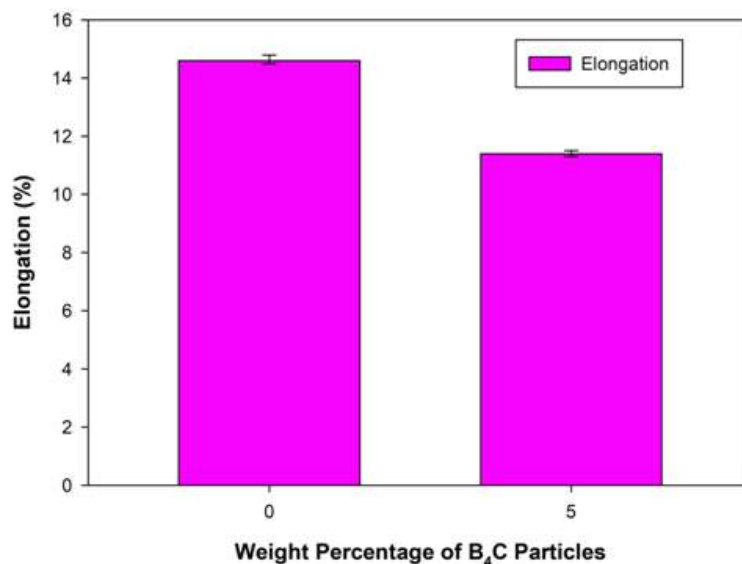


Fig. 10 Ductility of Al6061 alloy and B₄C composites

Impact Strength

The impact strength of Al6061 alloy reinforced metal composites with 5% B₄C particles is shown in Fig. 11. The impact strength of as-cast Al6061 alloy is 1.6 J, however with the inclusion of oxide particles, the impact strength of Al6061-5 wt. percent B₄C composites increased to 1.95 J. When compared to the as-cast Al matrix, composites absorb more energy due to the strong connection between the particle and matrix interface. The development of a clean interface between the matrix and reinforcement is dependent on load transfer, hence it is important for boosting composite strength. When strong ceramic particles are present, a dislocation shortage occurs, causing dislocations to pile up, resulting in increased impact strength.

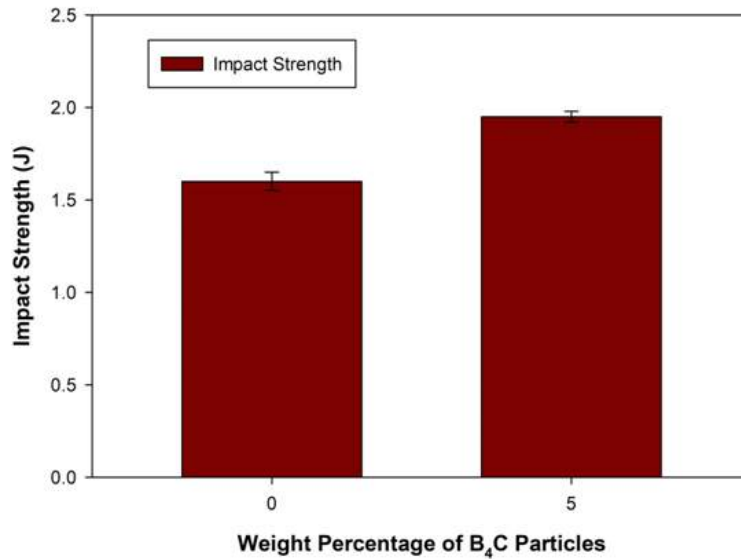


Fig. 11 Impact strength of Al6061 alloy and B₄C composites

IV. CONCLUSIONS

By using stir casting technology, Al6061-B₄C composites with 5% micro B₄C and an average particle size of 90 microns were successfully manufactured in the current study. Microstructural analysis and major mechanical performance, such as hardness, UTS and YS, % elongation, and impact strength, are all ASTM requirements. The matrix is virtually pore-free as a cast-alloy and evenly distributed micro B₄C composite, as shown in SEM micrographs. The Al6061 alloy matrix contains B₄C particles, according to EDS and XRD measurements. When compared to unreinforced Al6061 as-cast alloy, the characteristics of Al6061 and 5 wt. percent B₄C composites are superior.

V. REFERENCES

- [1]. Pankaj R jadhav, B R Sridhar, Madeva Nagaral and Jayasheel I Harti, "Mechanical behavior and fractography of graphite and boron carbide particulates reinforced A356 alloy hybrid metal matrix composites", *Advanced Composites and Hybrid Materials*, 3, 2020, pp. 114-119.
- [2]. Madeva Nagaral, V. Auradi, S. A. Kori, "Microstructure and Mechanical Properties of Al6061-graphite Composites Fabricated by Stir-Casting Process", *Applied Mechanics and Materials*, 766-767, 2015, pp. 308-314.
- [3]. Madeva Nagaral, V Auradi, S A Kori, VeenaShivaprasad, "Mechanical characterization and wear behavior of nano TiO₂ particulates reinforced Al7075 alloy composites", *Mechanics of Advanced Composite Structures*, 7 (1), 2020, pp. 71-78.

- [4]. H.R. Ezatpour, S.A. Sajjadi, M.H. Sabzevar, Y.Z. Huang, "An investigation of the tensile and compressive properties of Al6061 and its nano composites in as-cast state and in extruded condition", *Materials Science and Engineering A*, Volume 607, Issue 23, 2014, pp. 589-595.
- [5]. Fazil N, V Venkataramana, Madeva NagaraI, V Auradi, "Synthesis and mechanical characterization of micro B4C particulates reinforced AA2124 alloy composites", *International Journal of Engineering and Technology UAE*, 7 (2.23), 2018, pp. 225-229.
- [6]. N. G. Siddesh Kumar, G. S. Shivashankar, S. Basavarajappa, R. Suresh, Some studies on mechanical and machining characteristics of Al2219/n-B4C/MoS2nano hybrid metal matrix composites, *Measurement*, 107, 2017, pp. 1-11.
- [7]. P. Ashwath, "Surface modification on aluminium metal matrix composite for high strength application-Current state of art", *Materials today: Proceedings*,46,17, 2021, 2130-7134.
- [8]. Jayashree P.K, "The effect of SiC content in aluminium based metal matrix composites on the microstructure and mechanical properties of welded joints ", *Journal of Materials Research and Technology*, 12, 2021, 2325-2339.
- [9]. Harish Munnur, "Characterization & tribological behaviour of aluminium metal matrix composites-A review", *Materials today: Proceedings*, 47, 10, 2021, 2570-2574.
- [10]. G Pathalinga Prasad, H C Chittappa, Madeva NagaraI, V Auradi, 'Effect of the reinforcement particle size on the compressive strength and impact toughness of LM29 alloy-B4C composites', *Structural Integrity and Life*, 19, br. 3, 2019, pp. 231-236.
- [11]. HS Vasanth Kumar, UN Kempaiah, Madeva NagaraI, K Revanna, "Investigations on mechanical behaviour of micro B4C particles reinforced Al6061 alloy metal composites", *Indian Journal of Science and Technology*, 14, 22, 2021, pp. 1855-1863.
- [12]. V AAnjanBabu, R Saravanan, M Raviprakash, M NagaraI, "Microstructure, Tensile and Flexural Strength of Boron Carbide Particles Reinforced Al2030 Alloy Composites", *Indian Journal of Science and Technology*, 14, 28, 2021, pp. 2342-2350.
- [13]. Madeva NagaraI, V Auradi, V Bharath, ShanawazPatil, Mahantesh S Tattimani, "Effect of micro graphite particles on the microstructure and mechanical behavior of aluminium 6061 (Al-Mg-Si) alloy composites developed by novel two step casting technique", *Journal of Metals, Materials and Minerals*, 31, 2, 2021, pp. 38-45.
- [14]. H S Kumar, U N Kempaiah, Madeva NagaraI, V Auradi, "Impact, Tensile and Fatigue Failure Analysis of Boron Carbide Particles Reinforced Al-Mg-Si (Al6061) Alloy Composites", *Journal of Failure Analysis and Prevention*, 21, 6, 2021, pp. 2177-2189.



Study on Effect of Process Parameters on Kerf Width using Wire Electrical Discharge Machining of Cu-Al-Mn Shape Memory Alloys

N Praveen^{*1}, U S Mallik², A. G. Shivasiddaramaiah³

^{*1}Research Scholar, Department of Mechanical Engineering, Siddaganga Institute of Technology (Affiliated to VTU), Tumkur-572103, Karnataka, India

²Professor, Department of Mechanical Engineering, Siddaganga Institute of Technology, Tumkur-572103, Karnataka, India

³Assistant professor, Department of Mechanical Engineering, Siddaganga Institute of Technology, Tumkur-572103, Karnataka, India

ABSTRACT

Wire cut EDM machining is a popular specialised thermal machining technique for conductive materials. During the process, molybdenum wire with a diameter of 0.18 mm acts as an electrode. The present study aims to identify the process parameters affecting the kerf width (Kw) of the Cu-Al-Mn shape memory alloy (SMA), which was machined using wire-cut EDM. For the conduction of experiments, Taguchi's L9 orthogonal array was chosen based on the design of experiments (DOE). The kerf width is used to classify the accuracy. From ANOVA, the main parameter which is responsible for affecting the Kw was identified and percentage contribution to obtain the accuracy. The lowest kerf can be achieved keeping the both pulse on time and peak current at low. From SEM Analysis, the kerf width profile obtained after the machining process were examined.

Keywords: Cu-Al-Mn SMAs, Wire cut EDM, Kerf width, Taguchi method, ANOVA.

I. INTRODUCTION

Wire electric discharge machining (WEDM) is a non-conventional type of Electro Discharge Machining (EDM). [1]. This machining method can precisely machine a complex and irregular shape of an electrically conductive component that is difficult to machine. To achieve the optimal three-dimensional shape and accuracy of the work material, the wire movement is numerically controlled [2]. The machining principle is based on a series of discontinuous discharges between the electrode (wire) and the work-piece eroding the work-piece material [3]. The commonly used Wire cut EDM wires are from brass, copper, tungsten or molybdenum, zinc or brass coated. However recently multi coated wires are also have been used Wire cut EDM is appropriate for stamping dies,

extrusion dies, and prototype parts manufacturing applications. the conventional machining process took long hours for fabrication of precision work piece because of manual grinding and polishing [4][5][6].

The main challenge with EDM is surface integrity difficulties such as kerf width and heat impacted zone. As a result, choosing the right cutting parameters is critical for mitigating this issue. Kerf width, also known as working gap, is a term used to describe the width of a kerf. The working gap is the result of an erosion pulse discharge between the workpiece and the electrode wire. The breadth of this working gap varies according to the cutting parameter, dielectric fluid, and material to be cut. It was noted that peak current has a big impact on the WEDM micro milling process. Working gap is also linked to excessive thermal stress that exceeds the material's ultimate tensile strength and pulse energy fluctuations that cause the Kerf width to increase. The Kerf width decreases as the pulse on time, pulse off time, spark gap voltage, peak current, and wire tension rise [7].

Ashish goyal et al. have investigated the surface roughness and the kerf width of shape memory alloy using wire EDM. They have revealed that the most important factor affecting was pulse on time. Both Ra and kerf width of the alloy. The increased thickness of the recast layer is due to the greater discharge energy value [8]. Vinayak N. Kulkarni et al, have reported the machinability analysis of Nitinol shape memory alloy and its optimization using wire EDM. The Servo voltage (SV) was found to be the most important factor in achieving improved surface quality, followed by Ton and Toff. The higher the SV, the better the surface quality. High MRR can be obtained at lower SV by increasing the Ton and Toff. Wire feed (WF) was found to be unimportant when it comes to maximizing MRR. When machining medical grade NiTiNOL SMA, the electrode material made of zinc- coated brass wire provides better machining results when compared with the uncoated brass wire electrode in terms of lower SR, TWR, and greater MRR [9].

Abhinaba Roy et.al.,have reported the machining accuracy of TiNiCu SMA using wire EDM. As per ANOVA results, servo voltage (SV) followed by pulse on time (Ton) are proved to be most influential parameters when kerf width is concerned. When compared to Ti40Ni50Cu10, Ti50Ni40Cu10 had a better propensity for broader kerf formation and a larger material removal rate under equivalent machining conditions, which can be attributed to Ti50Ni40Cu10's lower thermal conductivity value. For a medium to average VMRR, testing runs 7 and 11 produce satisfactory kerf width accuracy and are adequate for machining with average accuracy for the specified alloys [10]. Vinayak N Kulkarni et.al.,reported the Wire EDM process characteristics of medical grade Ni-Ti SMAs. The main factor pulse on time affects the output responses such as MRR and Ra, followed by wire feed rate, according to ANOVA. However, Toff is the least significant parameter and has no effect on the output responses. WEDM process parameter optimization for NiTi SMA shows the best results obtained with the parameters Ton =115 μ s, Toff =25 μ s, and WF =4 m/min [11]. Shivangi Paliwal et.al., have evaluated machining of SMAs using non- conventional machining process. investigated the impact of various critical parameters such as voltage, pulse off time, pulse on time, current, and electrode wear rate on material removal rate, electrode wear rate, and surface roughness. The material removal rate of NiTi shape memory alloys is highly influenced by pulse current and pulse on time [12].

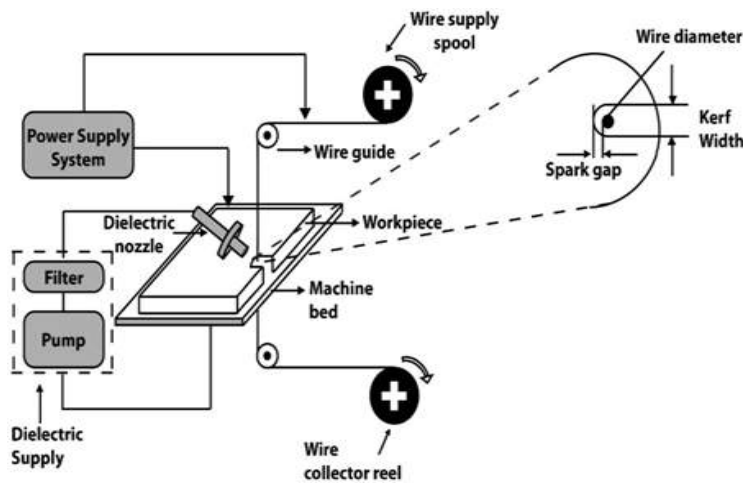


Fig.1: Mechanism of wire cut EDM of Kerf width [13]

The effect of machining factors on MRR, surface roughness, cutting speed, wire rupture, and wire craters has been studied in the literature for Nitinol shape memory alloy. However, to the best of the authors' knowledge, there is no published work on examining the effect of machining parameters and their level of relevance exclusively on kerf width by using Taguchi Method has not been carried out for copper based SMAs (i.e., Cu-Al-Mn SMA).

II. METHODOLOGY

The Cu-Al-Mn SMAs was the sample used in this investigation. The flat specimen measured 100X50X3mm in dimensions (LxWxT). Cu-89wt.%, Al-10.5wt.%, and Mn-0.5wt.% are the chemical compositions of the chosen alloy. Concord DK7720 wire cut EDM was used for the test. Because of its inexpensive cost and ability to be reused as many times as feasible during the machining, molybdenum wire with a diameter of 0.18 mm is used as a cutting tool in wire cut EDM machining. Distilled water, which works as a dielectric medium, was employed as a lubricant during the cutting operation.

The Kw was measured using SEM after the machining process. The kerf width of Cu-Al-Mn SMAs was determined by measuring Kw in three different locations and taking the average of those measurements. The machined Kw, which changes with machining parameters, has a considerable influence on machining precision. The width of the kerf determines a machined part's dimensional precision. The Kw is affected by the diameter of the gap wire, the spark gap, debris in the gap, and wire vibration. The present work was carried out using wire cut EDM shown in fig.2 and fig.3 indicates the flat Cu-Al-Mn SMA specimen setup image in wire EDM equipment. Table.1 shows the parameters and their ranges of wire cut EDM considered for the present investigation.

Table.1: Input factors and their ranges

Parameters	Level-1	Level-2	Level-3
Pulse on time (μ s)	90	95	100
Pulse off time (μ s)	5	10	15
Peak current (A)	2	3	4



Fig.2: Wire cut EDM



Fig.3: Setup image of SMA

III. RESULTS AND DISCUSSION

Fig.4 shows the main effect plot for kerf width. From Table.1, It was found that pulse on time obtained rank-1 position, peak current as rank-2 position followed by pulse off time as rank-3. Table.2 shows the kerf width results throughout 9 test runs. At the first glance, there was not a lot of variation observed that the result ranging from 223 to 325 μm . Further investigation by statistical analysis, the main factor that affected kerf width was discovered using ANOVA. From fig.4 it was found that as the T_{on} and I_p increases, the kerf width increases but when increase in T_{off} tends to decrease in width of kerf. Table 3 shows ANOVA, T_{on} and I_p were found significant since P-Values were less than 0.05. Based on the P-value the ranks for the individual parameter were obtained from the analysis. The contribution is more for pulse on time (45.26%), Peak current

(38.75%) and for pulse off time (0.30%). Since the pulse off time was found least significant parameter affecting the Kw.



Fig.4: Main effect plot for kerf width

Table.1 Shows the data for main effect plot

Levels	Pulse on time	Pulse off time	Peak current
1	253.3	282.7	26
2	290.7	280.7	280.7
3	298.3	279	301.7
Delta	45	3.7	41.7
Rank	1	3	2

Table.2: Machined data of kerf width (Kw)

Sl. No	Pulse on time (µs)	Pulse off time (µs)	Peak current (A)	Kerf width (µm)
1	90	5	2	223
2	90	10	3	257
3	90	15	4	280
4	95	5	3	300
5	95	10	4	298
6	95	15	2	272
7	100	5	4	325
8	100	10	2	284
9	100	15	3	287

Table.3 ANOVA for Kerf width (Kw)

Source	DF	Seq SS	Adj SS	Adj MS	F-value	P-value	Contribution
Pulse on time	1	3082.67	3082.67	3082.67	15.52	0.011	46.34%
Pulse off time	1	13.5	13.5	13.5	0.07	0.805	0.20%
Peak current	1	2562.67	2562.67	2562.67	12.9	0.016	38.52%
Error	5	993.17	993.17	198.63			14.93%
Total	8	6652					100%

IV. EFFECT OF PROCESS PARAMETERS ON KERF WIDTH (KW)

The kerf width, which is the gap left by the wire electrode after passing through a certain point, can be used to determine the precision of a Wire cut EDM-machined component. The wire diameter and spark gap on both sides of the wire determine the kerf width. The input factors of the Wire cut EDM process define the spark gap, which changes based on the parameter values. Fig.4 indicates the SEM image of the kerf width of Cu-Al-Mn SMAs. The influence of Ton, Toff, and Ip on Kw was investigated. For the selected alloys, Kw increases as the pulse duration (Ton) increases, which may be explained by the fact that as the discharge duration increases, more material is melted, resulting in a larger kerf and thus reduced accuracy. The influence of increasing pulse duration on kerf width is clearly shown in Fig. 7, as more re-solidified molten debris is present at the kerf boundary due to the increasing explosive nature of the molten material. Because of the uniform distribution of the spark, resulting in the generation of more heat and, as a result, an increase in the width of the kerf. This causes a dimensional variation in the profile. Dimensional accuracy can be achieved at lower Ton and Ip values.

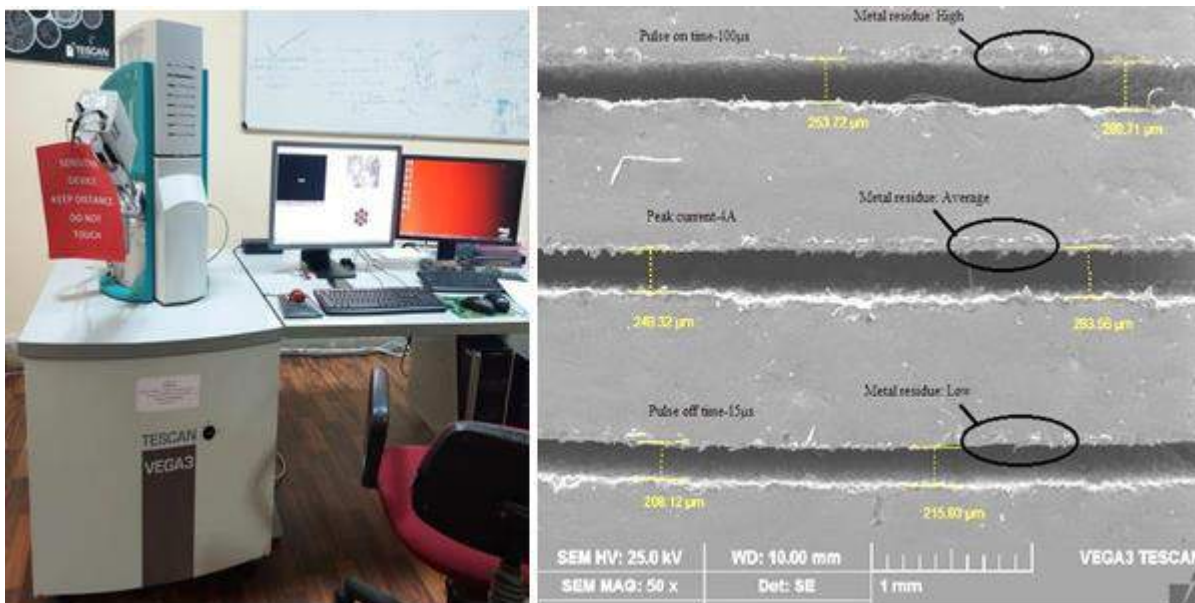


Fig.6 SEM equipment Fig.7: SEM image of kerf width of Cu-Al-Mn SMA

As the Toff increases, the kerf width tends to decrease because the higher the value of Toff, the more debris is flushed away from the machining zone, improving dimensional accuracy [8][14]. A.Ikram et al. found that the overall influence of pulse off time on kerf width is minimal when compared to other parameters since the net change in pulse off time from starting to final value is not significant [3].

Fig. 6 shows the SEM equipment and fig.7 indicates profile of kerf width observed from SEM. When pulse on time is set to 100 μ s, more metal residues were observed along the boundary of the machined zone. Similarly, when the peak current was increased to 4A, the average amount of metal residue that was formed along the machined area increased, resulting in an increase in kerf width. Similarly, a small width of kerf can be observed when the Ton is set to 15 μ s and found very less metal residue along the boundary of the kerf width.

V. CONCLUSIONS

The following are the conclusions obtained from the experimental results,

- The Taguchi method was used to evaluate the impact of cutting parameter on Kw.
- From ANOVA, it was noticed that pulse on time is the most significant factor affecting kerf width followed by peak current and pulse off time. As the pulse off time increases, the kerf width tends to decrease.
- From the SEM image, the width of the kerf was identified and observed a recast layer formation along the around the kerf boundary of the alloy for all three parameters. Maximum pulse on time and peak current values resulted in the increase of recast layer. The obtained recast layer is free from crack formation and results in good accuracy of the kerf width of the alloy.
- A thorough experimental examination is also necessary to assess the machinability of Cu-Al-Mn SMA in Wire cut EDM using various multi optimization techniques.

ACKNOWLEDGEMENT:

The authors would like to thank Siddaganga Institute of Technology for providing research assistantship support to carry out the research work.

VI. REFERENCES

- [1]. N. Praveen, U. S. Mallik, L. Shivaramu, A. G. Shivasiddaramaiah, R. Suresh, and S. Prashantha, "Synthesis and evaluation of machining characteristics of Cu-Al-Mn ternary shape memory alloys using CNC wire electric discharge machining," AIP Conf. Proc., vol. 2247, 2020.
- [2]. M. Divya, N. Sateesh, B. C. Nookaraju, A. A. Lakshmi, and S. Ram, "Multi performance optimisation of wire-cut EDM process parameters of Incoloy 800 alloy using grey relational analysis," Mater. Today Proc., vol. 44, pp. 2416–2420, 2021.
- [3]. A. Ikram, N. A. Mufti, M. Q. Saleem, and A. R. Khan, "Parametric optimization for surface roughness, kerf and MRR in wire electrical discharge machining (WEDM) using Taguchi design of experiment," J. Mech. Sci. Technol., vol. 27, no. 7, pp. 2133–2141, 2013.

- [4]. T. Method, R. Ramli, R. Ahmad, and J. A. Ghani, "Kerf Width Optimization in Wire-Cut Electrical Discharge Machine by using Jurnal Teknologi Full paper Kerf Width Optimization in Wire-Cut Electrical Discharge Machine by using Taguchi Method," no. October, pp. 3–8, 2012.
- [5]. N. Tosun, C. ÇOĞUN, and G. Tosun, "A study on kerf and material removal rate in wire electrical discharge machining based on Taguchi method," *J. Mater. Process. Technol.*, vol. 152, pp. 316–322, 2004.
- [6]. N. Praveen, U. S. Mallik, A. G. Shivasiddaramaiah, and G. N. N. Reddy, "Materials Today : Proceedings A study on material removal rate of Cu-Al-Mn shape memory alloys in WEDM," *Mater. Today Proc.*, no. xxxx, pp. 2–6, 2021.
- [7]. P. Gupta, R. Khanna, R. D. Gupta, and N. Sharma, "Effect of Process Parameters on Kerf Width in WEDM for HSLA Using Response Surface Methodology," vol. 2, no. 1, pp. 1–6, 2012.
- [8]. A. Goyal and H. Ur Rahman, "Experimental studies on Wire EDM for surface roughness and kerf width for shape memory alloy," *Sadhana - Acad. Proc. Eng. Sci.*, vol. 46, no. 3, 2021.
- [9]. V. N. Kulkarni, V. N. Gaitonde, S. R. Karnik, M. Manjaiah, and J. Paulo Davim, "Machinability analysis and optimization in wire EDM of medical grade NiTiNOL memory alloy," *Materials (Basel)*, vol. 13, no. 9, pp. 1–17, 2020.
- [10]. A. Khan, K. Academy, W. Jappes, K. Academy, S. R. Kumar, and J. Mashinini, "Machinability Of Shape Memory Alloy Using Electro Spark Erosion Process," pp. 1–13, 2021.
- [11]. V. N. Gaitonde and K. S. Nalavade, "OPTIMIZATION OF WIRE EDM PROCESS PARAMETERS FOR MEDICAL GRADE NICKEL TITANIUM SHAPE MEMORY ALLOY," vol. 70, no. 1, pp. 69– 80, 2020.
- [12]. S. Paliwal and P. S. Rao, "Machining of f Shape Memory Alloys through Different Non Conventional Machining Process," no. March 2020, 2019.
- [13]. V. Lalwani, P. Sharma, and C. I. Pruncu, "Response Surface Methodology and Artificial Neural Network-Based Models for Predicting Performance of Wire Electrical Discharge Machining of Inconel 718 Alloy."
- [14]. A. Roy and S. Narendranath, "Study of Wire Electro Discharge Machining Accuracy of TiNiCu Shape Memory Alloys through Kerf Analysis," pp. 929–932.



Dielectric Properties of Lanthanum Doped Nano Copper Ferrite

Chikkappa Udagani

Department of Physics, University College of Science, Tumkur University, Tumkur-572103, Karnataka, India

ABSTRACT

Nano magnetic ferrites are one of the important classes in the family of nanomaterials. In the recent days the Nano magnetic ferrites draw greater attention of the researchers all over the world due to their significant applications in the field of electronics, gas sensing, catalysis, magnetic drug delivery and magnetic resonance tomography. In the present work copper ferrite (CuFe_2O_4) and lanthanum doped CuFe_2O_4 were synthesized by using nitrates as source materials and citric acid as fuel via self-combustion reaction. The synthesized CuFe_2O_4 and lanthanum doped CuFe_2O_4 were characterized using XRD, FTIR and SEM-EDAX. The XRD reveals the high crystallinity of the synthesized nano ferrites. The effective synthesis of the nano ferrite samples were further confirmed by FTIR and SEM-EDAX. The dielectric study plays an important role in understanding the electric nature of the materials. The dielectric and ac conductivity studies on the CuFe_2O_4 and lanthanum doped CuFe_2O_4 have been carried out using AAI LCR meter over the frequency range 100Hz-100 kHz. The frequency dependence of ac conductivity, dielectric constant and dielectric loss factor of the synthesized CuFe_2O_4 and lanthanum doped CuFe_2O_4 were investigated and reported in this paper.

Keywords: ac conductivity, copper ferrite, dielectric constant, dielectric loss, self-combustion

I. INTRODUCTION

The nano magnetic ferrites are attracting the researchers and scientists due to their variety of applications. The ferrites are represented by general formula MFe_2O_4 ($\text{M} = \text{Zn, Mn, Cu, Mg, Ni, Co}$ etc). The ferrites have wider applications in high-density storage media, ferromagnetic fluids, catalysts, magnetic separation, magnetic resonance tomography, gas sensors and other applications [1]. Copper ferrite belongs to the class of inverse spinel structure [2]. The spinel structure of the copper ferrite has 8 Cu^{2+} ions in octahedral B-site while among 16 Fe^{3+} ions, 8 Fe^{3+} ions occupy the tetrahedral (A-sites) and 8 Fe^{3+} ions occupy octahedral (B-sites) site of the unit cell. CuFe_2O_4 shows thermal stability, high resistance to corrosion, excellent catalytic properties, photocatalyst and ferrimagnetism [3-6]. The Copper ferrite is commonly used in cell labeling, gas sensing and electrochemistry [7-9]. Lanthanum is rare earth element and shows strong photo-luminescence and magnetic moment. It was reported in the literature that the substitution of the minute amount of rare earth ions in ferrites causes a notable change in electrical and magnetic properties [10, 11].

II. EXPERIMENTAL WORK

For synthesis of CuFe_2O_4 and lanthanum doped CuFe_2O_4 , the Copper nitrate [$\text{Cu}(\text{NO}_3)_2 \cdot 3\text{H}_2\text{O}$ (MW 241.6 g/mol)], Ferric nitrate [$\text{Fe}(\text{NO}_3)_3 \cdot 9\text{H}_2\text{O}$ (MW 404 g/mol)], Citric acid [$\text{C}_6\text{H}_8\text{O}_7$ (MW 192.12 g/mol)], Lanthanum nitrate [$\text{La}(\text{NO}_3)_3 \cdot 6\text{H}_2\text{O}$ (MW 324.92 g/mol)] and Ammonia solution [NH_3OH (17.037 g/mol)] of high purity have been used. The 0.02M of ferric nitrate solution is prepared by dissolving 1.01 gm of $\text{Fe}(\text{NO}_3)_3 \cdot 9\text{H}_2\text{O}$ in 50 ml of DI water. The 0.02M ferric nitrate solution is added to 50ml of 0.05M citric acid solution. The solution of ferric nitrate and citric acid solution is stirred for 10 minutes. This solution is labelled as solution A. 0.02M copper nitrate solution is prepared by dissolving 0.604 gm of $\text{Cu}(\text{NO}_3)_2 \cdot 3\text{H}_2\text{O}$ in 50ml of DI water. The 0.02M of copper nitrate solution is added to 50ml of 0.05M citric acid solution. The solution of copper nitrate and citric acid solution is stirred for 10 minutes. This solution is labelled as solution B. Mix the solutions A and B in the Molar Ratio 2:1 and stir the mixture using magnetic stirrer for 25 min to get homogeneous reaction mixture. After complete dissolution, Ammonia was added drop wise into the solution to adjust the PH -7 to 8 and the stirring is continued at 90 until the concentrated gel of CuFe_2O_4 is formed. The gel is then taken in a glass petry dish and heated at 200 to allow self-combustion reaction to take place. After the self-combustion reaction, powder of CuFe_2O_4 is collected in the petry dish. The powder of CuFe_2O_4 is then calcinated at 400 for 4 hours in the vacuum furnace to exhaust any moisture content in the sample. To prepare lanthanum doped CuFe_2O_4 , the same procedure is used. Here 5wt% of lanthanum nitrate relative to ferric nitrate is mixed with 0.05M citric acid and $\text{Fe}(\text{NO}_3)_3 \cdot 9\text{H}_2\text{O}$ solution to get solution A.

III. RESULTS AND DISCUSSION

The phase purity, surface morphology and composition of the synthesized nanoferrite samples were characterized by XRD, FTIR and FESEM-EDAX.

A. XRD:

The XRD patterns of the samples were recorded using the Bruker 8 advance in the range of 0-100 . The XRD pattern of CuFe_2O_4 is depicted in the Figure (1). At 2theta angles of 18.33 , 29.88 , 30.59 , 34.75 , 35.90 , 37.13 , 41.86 , 43.80 , 46.87 , 52.73 , 53.88 , 55.34 , 57.07 , 57.89 , 62.13 , 63.68 , 66.23 , 69.07 , 71.91 , 73.19 , 74.63 , 76.16 and 79.15 sharp XRD peaks are observed.

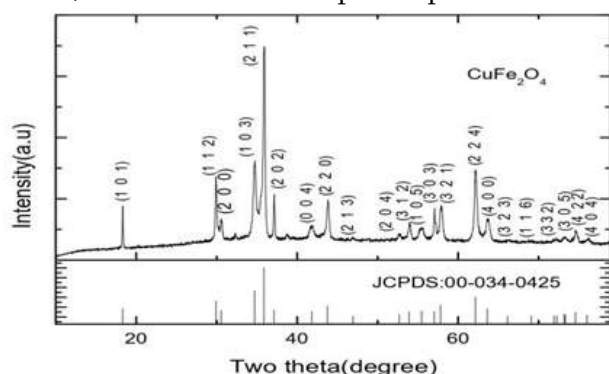


Figure (1): XRD of CuFe_2O_4

The absence of impurity peaks in the xrd pattern shows the high purity of CuFe₂O₄ and the sharp XRD peaks confirm the high crystallinity of the synthesized CuFe₂O₄. The peaks are indexed for reflecting planes; (1 0 1), (1 1 2), (2 0 0), (1 0 3), (2 1 1), (2 0 2), (0 0 4), (2 2 0), (2 1 3), (2 0 4), (3 1 2), (1 0 5), (3 0 3), (3 2 1), (2 2 4), (4 0 0), (3 2 3), (1 1 6), (3 3 2), (3 0 5), (4 2 2) and (4 0 4) of tetragonal CuFe₂O₄ with a =5.8444 and c = 8.6304 and the results obtained were in close agreement with the JCPDS Card No.034-0425. The Figure (2) shows the XRD pattern of lanthanum doped CuFe₂O₄. By observing the XRD pattern of lanthanum doped CuFe₂O₄, it is seen that all the major CuFe₂O₄ peaks of CuFe₂O₄ reappear in the case of lanthanum doped CuFe₂O₄. The XRD peaks of lanthanum doped CuFe₂O₄ are sharper due to higher crystallinity compare to pure CuFe₂O₄.

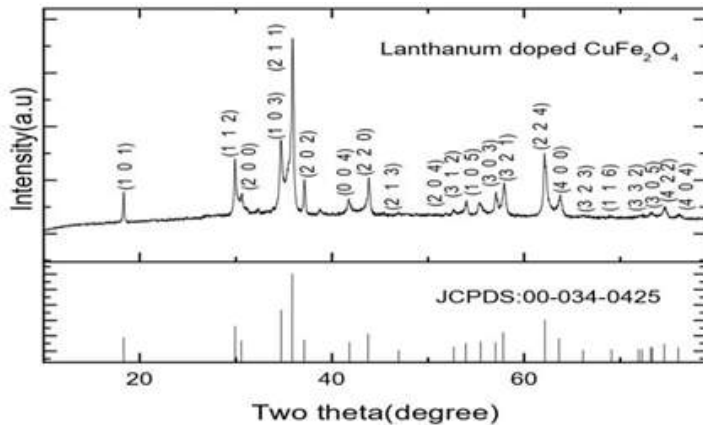


Figure (2): XRD of lanthanum doped CuFe₂O₄

The crystallite size of the nanoferrites was estimated using the FityK software [12]. Figure (3) shows the Gaussian fit to the major peak of CuFe₂O₄ corresponding to reflection (2 1 1) using FityK and Figure (4) shows the Gaussian fit to the major peak of lanthanum doped CuFe₂O₄ corresponding to reflection (2 1 1) using FityK. The crystallite size (D) was estimated using the following Equation:

$$D = K\lambda / \beta \cos \theta$$

Where K is shape factor and its typical value is 0.94 for spherical crystallites with cubic symmetry, λ the X-ray wavelength (Cu), β the FWHM (Full Width Half Maximum) of XRD peak in radians and θ the Bragg's angle. The β is found to be 0.276 and crystallite size is estimated to be 31.61nm for pure CuFe₂O₄. For lanthanum doped CuFe₂O₄, the β is found to be 0.314 and crystallite size is turned out to be 27.79nm. Decrease in crystalline size of the lanthanum doped copper ferrite is attributed to the inclusion of lanthanum ions in the lattice of copper ferrite.

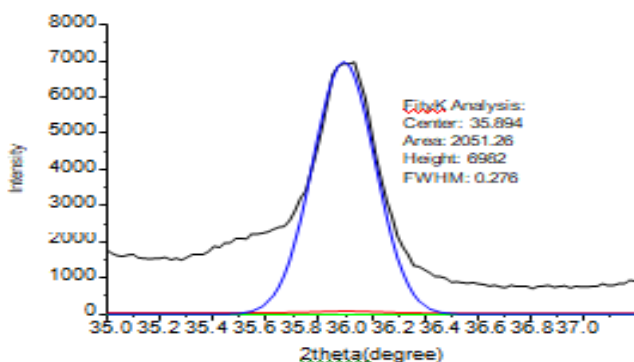


Figure (3): Gaussian fit for CuFe₂O₄

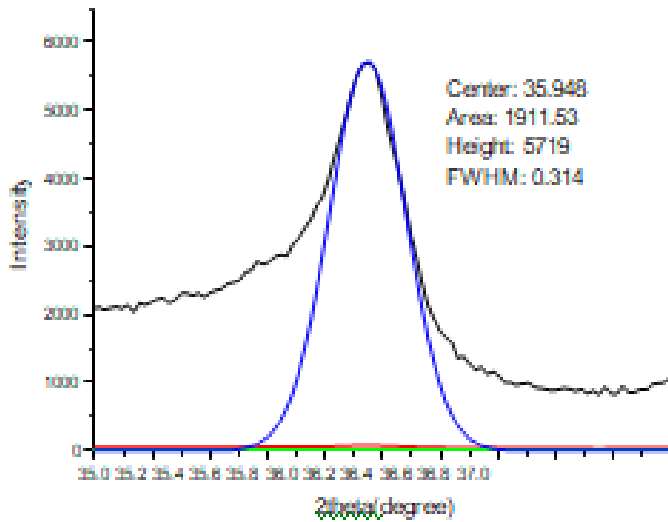


Figure (4): Gaussian fit for lanthanum doped CuFe_2O_4

B. FTIR

The FTIR technique is useful for identification of functional groups present in the sample. The FTIR spectra for the CuFe_2O_4 samples have been carried out using Bruker spectrometer in the wave number range 400 to 4500 cm^{-1} . The FTIR spectrum of CuFe_2O_4 is shown in the Figure (5). The spectrum shows two characteristic absorption peaks at 575.61 cm^{-1} and 399.18 cm^{-1} which corresponds to the octahedral and tetrahedral sites of +ve ions of CuFe_2O_4 respectively [13]. The FTIR spectrum of lanthanum doped copper ferrite is depicted in the Figure (6). In the case of lanthanum doped CuFe_2O_4 the characteristic absorption observed at 590.53 cm^{-1} and 407.08 cm^{-1} . It is observed that the characteristic absorption peaks are shifted to longer wavenumber side in the case of lanthanum doped CuFe_2O_4 . The presence of lanthanum ions in the lattice of CuFe_2O_4 is the reason for the shift in wavenumber of the characteristic absorption peaks.

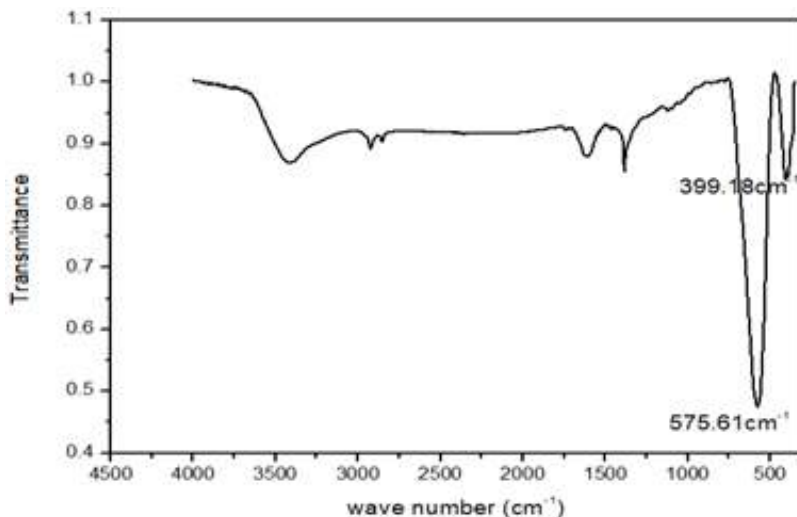


Figure (5): FTIR of CuFe_2O_4

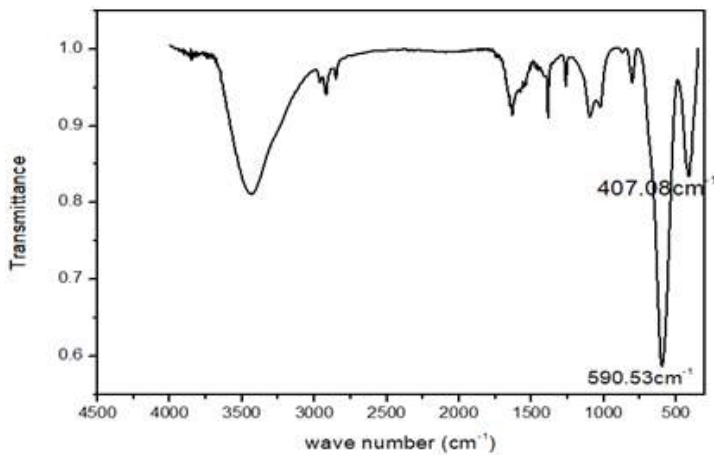


Figure (6): FTIR of lanthanum doped CuFe_2O_4

C. FESEM –EDAX

The FESEM–EDAX of the nanoferrite samples were recorded using ZEISS with the accelerating voltage 5.0kV and higher magnification of the order of 50.00- 100.00kX. The surface morphology and shape of the nanoferrite samples were analysed through FESEM. The Figure (7) is the FESEM micrograph of CuFe_2O_4 . The FESEM micrograph visualizes the polyhedron shape of the copper ferrite. There is uniform distribution of grains in the space with no porosity.

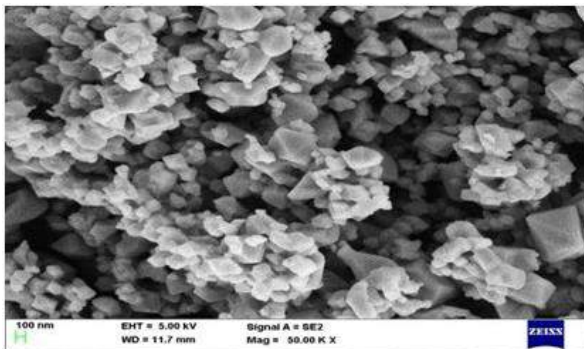


Figure (7): SEM image of CuFe_2O_4 The Figure (8) is the FESEM micrograph of lanthanum doped CuFe_2O_4 is shown in the Figure (8). The micrograph clearly reflects the accumulation of lanthanum on the polyhedron CuFe_2O_4 .

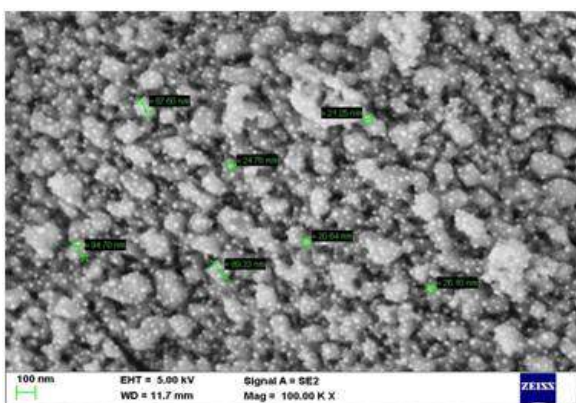


Figure (8): SEM image of lanthanum doped CuFe_2O_4

The chemical content of the nanoferrite samples were analysed by EDAX. The Figure (9) is EDAX of pure copper ferrite. The peaks observed at 0.930keV and 8.040keV correspond to Cu, the peaks observed at 0.705keV and 6.403keV correspond to Fe and peak observed at 0.532 keV corresponds to O. presence of sharp peaks of Cu, Fe and O is the clear indication of formation of copper ferrite.

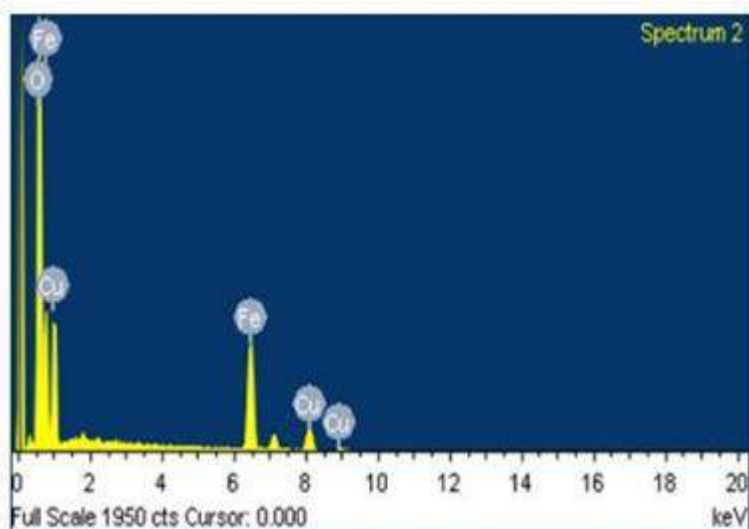


Figure (9): EDAX of CuFe_2O_4 .

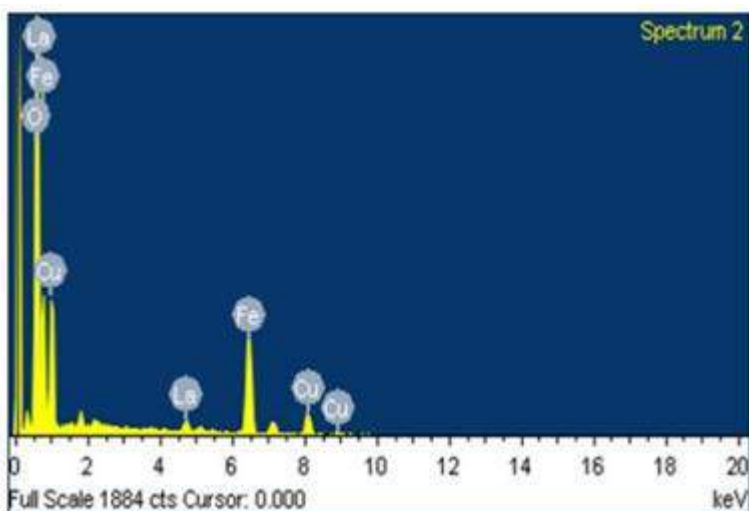


Figure (10): EDAX of lanthanum doped CuFe_2O_4

The EDAX of lanthanum doped copper ferrite is depicted in the Figure (10). In the EDAX of lanthanum doped CuFe_2O_4 ; there are sharp peaks of lanthanum at 0.833keV, 4.650 keV and 5.888 keV in addition to Cu, Fe and O peaks. FESEM –EDAX analysis supports the inclusion of lanthanum ions in the lattice of copper ferrite and the results obtained from the XRD and FTIR confirm this.

D. Dielectric measurement

The fine powder of nanoferrite was pelletized using hydraulic press at a pressure around 2tons. The pellet was polished carefully to get smooth surface. The silver paste was coated on either faces of the pellet. Utmost care

was taken to ensure no electric connection between two faces of the pellet while coating the silver paste. The pellets were allowed to dry for twenty days to completely evaporate moisture. The dielectric measurement was carried out using LCR meter AAI. AAI can measure the dielectric parameters up to frequency 100 kHz. The Figures (11a) and (11b) depict the variation of dielectric constant of CuFe₂O₄ and lanthanum doped CuFe₂O₄ with applied frequency.

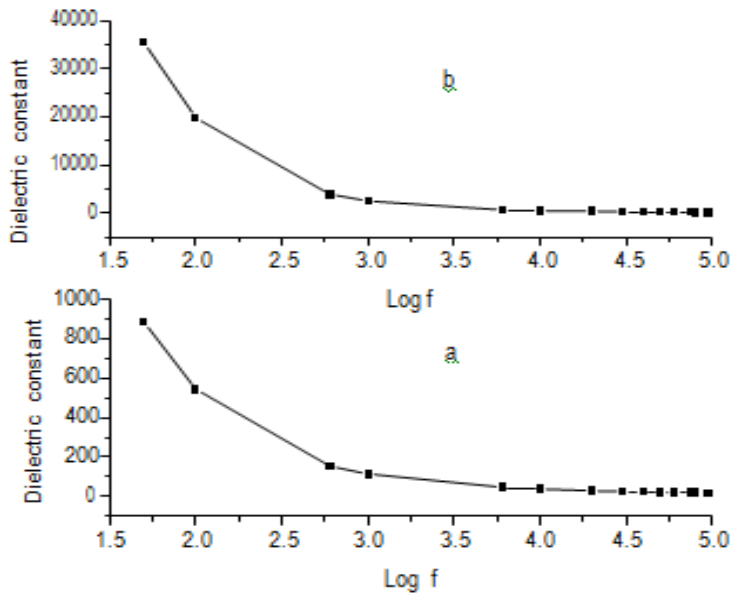


Figure (11): Frequency dependence of dielectric constant of (a) CuFe₂O₄ and (b) lanthanum doped CuFe₂O₄. The dielectric constant, decreases with increasing frequency. The dielectric constant of lanthanum doped CuFe₂O₄ is higher than that of the CuFe₂O₄ which means that the lanthanum doped CuFe₂O₄ seems to be more capable of storing electric energy than the CuFe₂O₄.

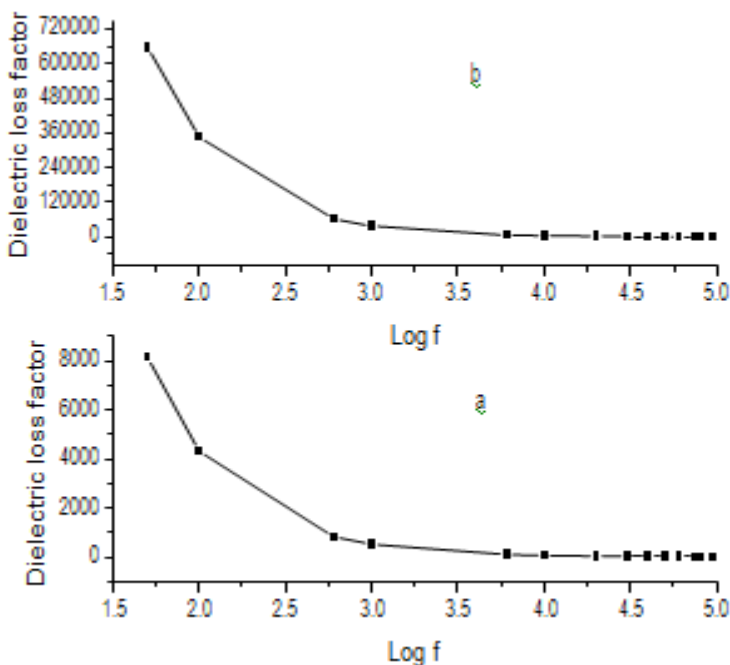
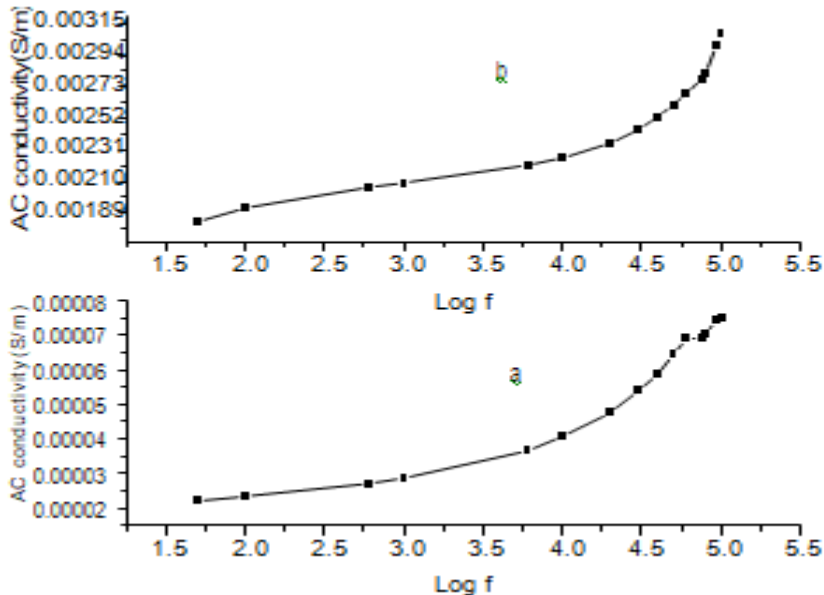


Figure (12): Frequency dependence of dielectric loss of (a) CuFe₂O₄ and (b) lanthanum doped CuFe₂O₄

The Figures (12a) and (12b) show the frequency dependence of dielectric loss factor, of the CuFe_2O_4 and lanthanum doped CuFe_2O_4 . The dielectric loss factor gives information about the energy dissipation in dielectric material when the material of interest is subjected to an external ac signal. The dielectric loss factor of the nano ferrites varies inversely with applied frequency. The lanthanum doped CuFe_2O_4 shows greater dielectric loss than the CuFe_2O_4 .



The Figures (13a) and (13b) show the frequency dependence of ac conductivity of the CuFe_2O_4 and lanthanum doped CuFe_2O_4 . It is found that the ac conductivity of CuFe_2O_4 increases with increasing frequency of the applied voltage. This increase in ac conductivity with frequency may result due to increase in charge carriers hopping in the ferrite with frequency. The ac conductivity of lanthanum doped CuFe_2O_4 is higher compared to CuFe_2O_4 .

IV. CONCLUSION

Copper ferrite (CuFe_2O_4) and lanthanum doped CuFe_2O_4 were synthesized effectively using citric acid as fuel via self-combustion reaction. The synthesized samples have been characterized using XRD, FTIR and FESEM-EDAX. The dielectric study shows decreasing trend of both the dielectric constant and dielectric loss with frequency. In the lower frequency range there may be faster response of dipoles to the frequency of the applied field and dipole polarization has maximum value. At higher frequencies dipole polarizability will reach minimum value due to slow response of dipoles to the frequency of the applied field. Therefore, dielectric values; dielectric constant and dielectric loss saturate at minimum value at higher frequency range. The ac conductivity increases with increasing frequency due to the hopping of charge carriers. The ac conductivity of lanthanum doped CuFe_2O_4 is more than that of the CuFe_2O_4 . In the octahedral site, lanthanum ions replace Cu^{2+} ions. Some of the Fe^{3+} ions in the tetrahedral site will diffuse to octahedral site. This will increase the ac conductivity of lanthanum doped CuFe_2O_4 .

V. REFERENCES

- [1]. Kuznetsov, M., Morozov, Y., & Belousova, O. (2013). Synthesis of copper ferrite nanoparticles. *Inorganic Materials*, 49(6), 606-615. doi: 10.1134/s0020168513050063.
- [2]. Mounkachi, O., Hamedoun, M., Belaiche, M., Benyoussef, A., Masrour, R., El Moussaoui, H., & Sajieddine, M. (2012). Synthesis and magnetic properties of ferrites spinels $Mg_xCu_{1-x}Fe_2O_4$. *Physica B: Condensed Matter*, 407(1), 27-32. doi: 10.1016/j.physb.2011.09.023
- [3]. Iqbal, M., Yaqub, N., Sepiol, B., & Ismail, B. (2011). A study of the influence of crystallite size on the electrical and magnetic properties of $CuFe_2O_4$. *Materials Research Bulletin*, 46(11), 1837- 1842. doi: 10.1016/j.materresbull.2011.07.036
- [4]. Dar, M., & Varshney, D. (2017). Effect of d -block element Co spinel copper ferrites. *Journal of Magnetism and Magnetic Materials*, 436, 101-112. doi: 10.1016/j.jmmm.2017.04.046
- [5]. Mohanty, D., Mallick, P., Biswal, S., Behera, B., Mohapatra, R., Behera, A., & Satpathy, S. (2020). Investigation of structural, dielectric and electrical properties of $ZnFe_2O_4$ composite. *Materials Today: Proceedings*, 33, 4971-4975. doi: 10.1016/j.matpr.2020.02.827
- [6]. Mohanty, D., Satpathy, S., Behera, B., & Mohapatra, R. (2020). Dielectric and frequency dependent transport properties in magnesium doped $CuFe_2O_4$ composite. *Materials Today: Proceedings*, 33, 5226-5231. doi: 10.1016/j.matpr.2020.02.944
- [7]. Ahmad, J., Alhadlaq, H., Alshamsan, A., Siddiqui, M., Saquib, Q., & Khan, S. et al. (2016). Differential cytotoxicity of copper ferrite nanoparticles in different human cells. *Journal of Applied Toxicology*, 36(10), 1284-1293. doi: 10.1002/jat.3299
- [8]. Singh, S., Yadav, B., Prakash, R., Bajaj, B., & lee, J. (2011). Synthesis of nanorods and mixed shaped copper ferrite and their applications as liquefied petroleum gas sensor. *Applied Surface Science*, 257(24), 10763-10770. doi: 10.1016/j.apsusc.2011.07.094
- [9]. Lavela, P., Tirado, J., Womes, M., & Jumas, J. (2009). ^{57}Fe Mössbauer Spectroscopy Study of the Electrochemical Reaction with Lithium of MFe_2O_4 ($M = Co$ and Cu) Electrodes. *The Journal of Physical Chemistry C*, 113(46), 20081-20087. doi: 10.1021/jp9056362
- [10]. Rezlescu N, Rezlescu E, Pasnicu C, Craus M (1994). Effects of the rare-earth ions on some properties of a nickel-zinc ferrite. *Journal of Physics: Condensed Matter* 6:5707-5716. doi: 10.1088/0953- 8984/6/29/013
- [11]. Satpute S, Wadgane S, Desai K, Mane D, Kadam R (2020) Substitution effect of Y^{3+} ions on the structural, magnetic and electrical properties of cobalt ferrite nanoparticles. *Cerâmica* 66:43- 49. doi: 10.1590/0366-69132020663772734.
- [12]. Marcin Wojdyr. (2010) Fityk: a general-purpose peak fitting program. *J. Appl. Cryst.* 43, 1126–1128.
- [13]. Kanagaraj, M., Sathishkumar, P., Kalai Selvan, G., Phebe Kokila, I., Armugam, S. (2014). Structural and magnetic properties of $CuFe_2O_4$ as-prepared and thermally treated spinel nanoferrites. *Indian Journal of Pure & Applied Physics*, 52, 124-130.



Spatial Variation and Fluoride Contamination of Drinking Water using GIS in the Bagepallitaluk of Chikkaballapura District, Karnataka, India

Sridhara M K¹, Sadashivaiah C², Kiran D A^{3*}

¹Department of Civil Engineering, Government Engineering College, Chamarajanagara, Karnataka, India

²Department of Civil Engineering, Dr. Sri Sri Shivakumara Mahaswamy College of Engineering, Byranayakanahalli, Bangalore Rural District, Karnataka, India

^{3*}Department of Civil Engineering, Dayananda Sagar College of Engineering, Bengaluru, Karnataka, India

ABSTRACT

A high concentration of fluoride in ground water beyond the permissible limit of 1.5 mg/L is a major health problem in India. The goal of this work is to use Geographic Information System (GIS) techniques to understand the fluoride concentration in the drinking water of Bagepalli Taluk (BPT). For the present study, 184 and 23 samples were collected from the rural and urban areas of BPT. This study reveals that, fluoride content in rural areas of BPT varied from 0.1 to 1.74 mg/l with an average of 0.946 mg/l. Also, out of 24 Grama Panchayaths (GPs), 16 GPs were contaminated with high fluoride content. A very high concentration of 1.74 mg/l and 1.71 mg/l were recorded from Thollapalli and Pathapalya GPs. In urban areas, fluoride concentrations varied from 0.47 to 1.39 mg/l with an average of 0.96 mg/l. The majority of the samples exceeded the standard limit of 1 mg/l given by BIS 10500:2012, so drinking fluoride contaminated water causes major health problems in the areas of BPT. The present study is helpful in proper planning and management of available water resources for drinking purposes.

Keywords: Fluoride, GIS, Bagepalli, Chikkaballapura, Drinking water, Groundwater

I. INTRODUCTION

According to WHO 1984, due to the poor quality of drinking water, the world is affected with 80% of diseases [1]. Fluoride (F) is one of the prominent elements found in ground water. When consumed in moderation, fluoride in drinking water has some health benefits, such as reducing dental cavities. However, an excessive presence of this anion in the drinking water (> 1.5 mg/L) can lead to health problems such as dental and skeletal fluorosis [2, 3]. Generally, a limited concentration of fluoride is present in groundwater and soil. However, certain anthropogenic activities, such as the application of fertilisers in agricultural activities and the untreated discharge of industrial waste, aggravate the fluoride concentration and become the cause of ground and surface water contamination [4]. India is one of the most affected countries by fluoride contamination in groundwater.

According to [5], approximately 12 million tonnes of fluoride deposits are present in the earth's crust of Indian topography, and both geogenic and anthropogenic activities have a role in aggravating this presence.

The impact of geogenic activities and climatic conditions on the fluoride level in ground water Yadav et al. [5] was one of the focal points of the researchers. Suthar et al. [6], who conducted a study on the villages in northern Rajasthan, which is a part of the peninsular plateau, indicated the association of geogenic sources with the presence of fluoride in the ground water. The study demonstrated higher levels of fluorides in the ground water and vaguely hinted at the role of semi-arid conditions and the rocky geography, with the presence of bedrock of gneisses and schists, in the increased concentration of fluorides. Reddy et al. [7] indicated that the ground water originated from fractured hard rock terrain could be the reason for the higher fluoride presence in the ground water in those areas. The relationship between fluoride presence and geogenic sources as well as climatic conditions was further highlighted by Mishra et al. [8]. Naaz[9] also pointed out the geogenic sources like granite and gneissic rocks as the reason for the exceedingly high presence of fluorides in the drinking water. Several studies have highlighted the role of geogenic sources in the increased presence of fluorides in ground water. The study by Singaraja [10] hinted at the role of climatic conditions. The author demonstrated the higher concentration of fluoride in the pre-monsoon season in comparison with the post monsoon season, indicating the dilution effect. This was further supported by Batabyal and Gupta [11], who also highlighted the effect of natural and climatic activities on the presence of fluorides in groundwater. Anthropogenic activities can also be the source of fluoride pollution. Ravindra and Garg[12] provided an indication of the role of anthropological activities, such as agricultural activities and improper water treatment, in determining fluoride levels.

Fluoride contamination of groundwater has irreversible consequences for plants and human health. In humans, high fluoride intake causes physiological problems, skeletal and dental fluorosis, thyroxin changes, and kidney damage. Fluoride levels above a certain level hinder germination, create ultrastructural deformities, lower photosynthetic capabilities, alter membrane permeability, reduce productivity and biomass, and cause various physiological and biochemical problems in plants. The uncontrolled exploitation of groundwater has resulted in elevated fluoride levels in the water. People's health has been affected as a result of their consumption of this water [13].

TABLE I HARMFUL EFFECTS OF DIFFERENT LEVELS OF FLUORIDE IN DRINKING WATER [13]

Fluoride Level (mg/l)	Harmful Effects
Less than 1	No dental caries
1.00 – 1.50	Acceptable
1.50 – 3.00	Mottling and pitting of teeth
3.00 – 6.00	Skeletal Fluorosis
More than 10.00	Crippling Fluorosis (Skeleton)

Chikkaballapura is a district in the state of Karnataka, just north of the capital Bengaluru. Groundwater plays an important role in the economy of the farmers of the Chikkaballapura district of Karnataka. Agriculture was mainly dependent on irrigation facility by numerable widely distributed tanks during earlier days. Due to drought situations farmers are now mainly depending upon borewells for their agriculture needs. As per

Central Ground Water Board (CGWB) report, there is no scope for further ground water development. All the taluks are over exploited especially Bagepalli. Fluoride concentration of more than 1.5 mg/l is reported from many parts in Bagepalli. However, some of the exploratory bore wells also have recorded fluoride concentration of 2mg/l and above [13]. The main objective of the present study is to assess the fluoride concentration in drinking water in the Bagepallitaluk of Chikkaballapura district using GIS.

The quality of groundwater has particularly received immense attention since water of high quality is required. Until recently, groundwater assessment has been based on laboratory investigation, but the advent of satellite technology and GIS has made it very easy to integrate various databases. GIS can be a powerful tool for developing solutions for water resources problems, assessing water quality, preventing flooding, determining water availability, understanding the natural environment and for managing water resources on a local or regional scale [14].

II. MATERIALS AND METHODS

Bagepallitaluk is in the Chikkaballapura district of Karnataka. The district has no perennial water sources for both agriculture and drinking water purposes and its only source of water is ground water. According to Chikkaballapura district at a glance report 2019, the BPT consists of 25 GPs and has the total area of 929 sq. km with a total population of 1,83,498. Normal rainfall in BPT was 667mm. The topography of the district is undulating to plain, the types of soils distributed range from red loamy soil to red sandy soil and lateritic soil. Drinking water sampling was carried out in November to December 2020 in urban and rural areas of the BPT taluk. 184 and 23 samples were collected from the rural and urban areas of BPT, respectively. In the rural areas of BPT, the samples were collected from 24 GPs. The geographical location of each sample was determined with the help of GPS. Samples were collected in pre-cleaned polypropylene bottles as per the standard procedures. On the same day, after collecting water samples, they were stored in the laboratory at a 4 °C temperature level and analysed for fluoride content to check their suitability for drinking as per BIS 10500:2012. Figure 1 and figure 2 shows the location map of Bagepallitaluk of Chikkaballapura district and sampling locations in the study area, respectively.

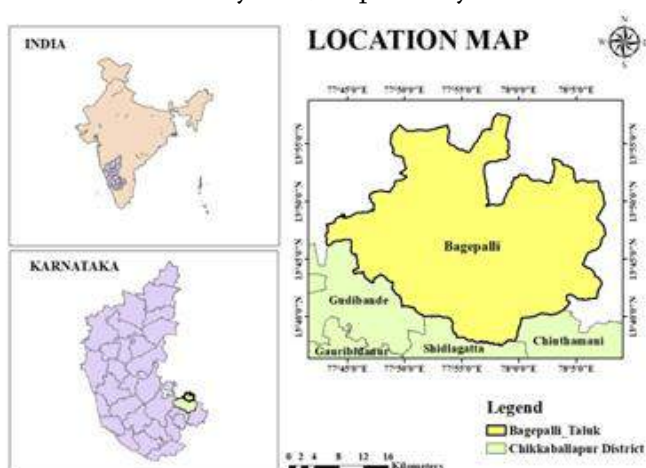


Figure 1: Location map of Bagepallitaluk of Chikkaballapura district, Karnataka

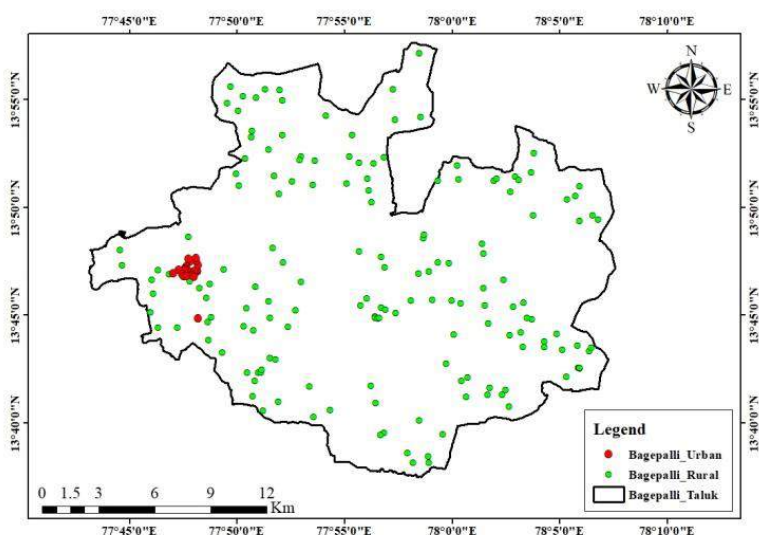


Figure 2: Sampling locations in the study area

III. RESULTS AND DISCUSSIONS

The table 2 shows the fluoride content in BPT. Fluoride content in rural areas of BPT was varied from 0.1 to 1.74 with an average of 0.946 mg/l. In the case of MittemariGP, high fluoride (1.48 mg/l) was recorded at Chinnampalli village. Likewise, InKanagamakalapalli, Yellampalli, Gulur, Nallapareddypalli, Chakavelu, Rascheruvu, Somanathapura, Palyakere, Naremaddepalli, Pathapalya, Thollapalli, Thimmampalli, Devaragudipalli, Gantavaripalli, Paragodu, Marganakunte, Kothakota, Billur, Gorthapalli, Chelur, Nallaguttapalli, Polanayakanahalli, and JulapalyaGPs, high concentrations of fluoride were recorded at the village Pillagutta (1.52 mg/l), Patravarapalli (1.67 mg/l), Chinnakayalapalli (1.72 mg/l), M Cherlopalli (1.7 mg/l), Maddireddipalya (1.34 mg/l), Aragevarigutta (1.46 mg/l), Mangalamaduguvarapalli (1.37 mg/l), Gollapalli (1.50 mg/l), Kamatampalli (1.46 mg/l), Gondipalli (1.71 mg/l), Nallacheruvunagarlu (1.74 mg/l), Gujjavandlapalli (1.61 mg/l), Peddathunkepalli (0.4 mg/l), Puttaparthi (0.39 mg/l), Srinivasapura (0.46 mg/l), Nanjireddipalli(0.37 mg/l), Krishnapura (0.34 mg/l), Kottur (0.33 mg/l), Kothur (0.37 mg/l), Byrappanapalli (0.97 mg/l), Kottakotavandlapalli (1.18 mg/l), Dugginayakanahalli(1.23 mg/l) and Vadigere (1.22 mg/l) respectively. Out of 24 GPs, 16 GPs were contaminated with high fluoride content.

In urban areas, fluoride concentrations varied from 0.47 to 1.39 mg/l with an average of 0.96 mg/l. In Table 3, ward numbers indicate that drinking water from various points was supplied to those particular wards. High fluoride content was noticed in the water supplied to wards 2, 3, and 6. From the results, it was observed that high fluoride concentrations were recorded in many parts of the taluk and most of sample were exceeds the acceptance limit of 1 mg/l as per BIS 10500:2012. Hence, they were not fit for drinking purposes. The cause of this contamination is linked to decreased rainfall, which has resulted in longer periods of drought in the area, forcing residents to dig deeper and deeper in search of water, resulting in a decrease in groundwater level. Figure 3 shows the spatial variation map of fluoride in the rural areas of Bagepalli.

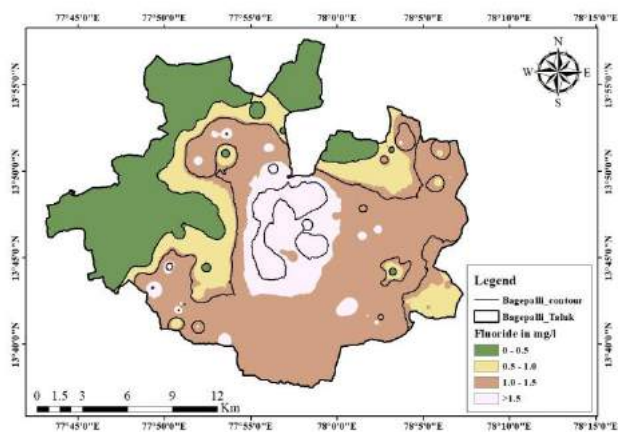


Figure 3: Spatial variation map of fluoride in the rural areas of Bagepalli

TABLE II FLUORIDE CONCENTRATIONS IN BAGEPALLI TALUK (RURAL)

GramaPanchayaths	No. of samples	F, mg/l		
		Min.	Max.	Mean
Mittermari	5	0.91	1.48	1.14
Kanagamakalapalli	11	0.66	1.52	1.19
Yellampalli	7	0.36	1.67	0.96
Gulur	4	0.56	1.72	1.15
Nallapareddypalli	7	1	1.7	1.33
Chakavelu	9	0.83	1.34	1.09
Rascheruvu	9	0.84	1.46	1.15
Somanathapura	7	1.15	1.37	1.24
Palyakere	9	0.88	1.50	1.24
Naremaddepalli	5	0.92	1.46	1.24
Pathapalya	9	1.12	1.71	1.47
Thollapalli	8	1.45	1.74	1.61
Thimmampalli	14	1.06	1.61	1.33
Devaragudipalli	9	0.11	0.4	0.25
Gantavaripalli	5	0.12	0.39	0.26
Paragodu	8	0.1	0.46	0.25
Marganakunte	9	0.19	0.37	0.30
Kothakota	7	0.26	0.34	0.3
Billur	6	0.21	0.33	0.26
Gorthapalli	6	0.17	0.37	0.26
Chelur	9	0.46	0.97	0.79
Nallaguttapalli	11	0.17	1.18	1.01
Polanayakanahalli	6	1.11	1.23	1.18
Julapalya	4	1.02	1.22	1.10

TABLE III FLUORIDE CONCENTRATION IN BAGEPALLI TALUK (URBAN)

Town	Ward No. (Drinking water supplied to)	F, mg/l	Min.	Max.	Mean
Bagepalli Town	1	0.55	0.47	1.39	0.96
	2, 3	0.89			
	2, 3, 6	1.39			
	3	1.28			
	2, 3	0.92			
	4	0.53			
	2, 3, 4	1.22			
	10, 11, 12	0.57			
	18	1.13			
	10	1.06			
	14	1.2			
	15, 17	0.8			
	19	1.23			
	10, 12, 13	0.88			
	20	1.2			
	21	0.99			
	23, 22	1.28			
	16	0.95			
	Chithravathi Filter Water	0.47			
	9	0.59			
7, 5	0.89				
5	1.08				
5	1.1				

IV. CONCLUSIONS

The results indicate that most of the samples from urban and rural areas were beyond the acceptable limits as per BIS. The fluoride content in rural areas of BPT varied from 0.1 to 1.74 mg/l with an average of 0.946 mg/l. A very high concentration of 1.74 mg/l and 1.71 mg/l were recorded from Thollapalli and Pathapalya GPs. In urban areas, fluoride concentrations varied from 0.47 to 1.39 mg/l with an average of 0.96 mg/l. As a result, there is an urgent need to reduce fluoride contamination in Bagepallitaluk. Consumption of high concentrations of fluoride can lead to serious health issues. The long exposure and use of groundwater that has high fluoride results in fluorosis. The present study is helpful in proper planning and management of available water resources for drinking purposes.

V. REFERENCES

- [1]. Manivannan R, Chidambaram S, Anandhan P, Karmegam U, Sinagaraja C, Johnsonbabu G, Prasanna MV (2011) Study on the significance of temporal ion chemistry in groundwater of Dindigul District, Tamilnadu, India. *J Chem* 8(2):938–944
- [2]. Raj, D., &Shaji, E. (2017). Fluoride contamination in groundwater resources of Alleppey, southern India. *Geoscience Frontiers*, 8(1), 117-124.
- [3]. Yadav, K. K., Gupta, N., Kumar, V., Sharma, S., &Arya, S. (2015). Water quality assessment of Pahuj River using water quality index at UnnaoBalaji, MP, India. *Int J Sci Basic Appl Res*, 19(1), 241-250.
- [4]. Gupta, N., Yadav, K. K., Kumar, V., Kumar, S., Chadd, R. P., & Kumar, A. (2019). Trace elements in soil-vegetables interface: translocation, bioaccumulation, toxicity and amelioration-a review. *Science of the Total Environment*, 651, 2927-2942.
- [5]. Yadav, K. K., Kumar, S., Pham, Q. B., Gupta, N., Rezanian, S., Kamyab, H., ...& Cho, J. (2019). Fluoride contamination, health problems and remediation methods in Asian groundwater: A comprehensive review. *Ecotoxicology and environmental safety*, 182, 109362.
- [6]. Suthar, S., Garg, V. K., Jangir, S., Kaur, S., Goswami, N., & Singh, S. (2008). Fluoride contamination in drinking water in rural habitations of Northern Rajasthan, India. *Environmental Monitoring and Assessment*, 145(1), 1-6.
- [7]. Reddy, D. V., Nagabhushanam, P., Sukhija, B. S., Reddy, A. G. S., &Smedley, P. L. (2010). Fluoride dynamics in the granitic aquifer of the Wailapally watershed, Nalgonda District, India. *Chemical Geology*, 269(3-4), 278-289.
- [8]. Misra, A. K. (2013). Influence of stone quarries on groundwater quality and health in FatehpurSikri, India. *International Journal of Sustainable Built Environment*, 2(1), 73-88.
- [9]. Naaz, A. (2015). Hydrogeochemistry of fluoride-rich groundwaters in semiarid region of Central India. *Arabian Journal of Geosciences*, 8(12), 10585-10596.
- [10]. Singaraja, C., Chidambaram, S., Anandhan, P. et al. (2014). Geochemical evaluation of fluoride contamination of groundwater in the Thoothukudi District of Tamilnadu, India. *Appl Water Sci* 4, 241–250.
- [11]. Batabyal, A. K., & Gupta, S. (2017). Fluoride-contaminated groundwater of Birbhum district, West Bengal, India: interpretation of drinking and irrigation suitability and major geochemical processes using principal component analysis. *Environmental monitoring and assessment*, 189(8), 1-24.
- [12]. Ravindra, K., &Garg, V. K. (2006). Distribution of fluoride in groundwater and its suitability assessment for drinking purpose. *International Journal of Environmental Health Research*, 16(2), 163-166.
- [13]. DDMA- District Disaster Management Authority, Chikkaballapur District Disaster Management Plan, 2019.
- [14]. Ketata-Rokbani M, Gueddari M, Bouhlila R (2011) Use of geographical information system and Water Quality Index to assess groundwater quality in El Khairat Deep Aquifer (Enfidha, Tunisian Sahel). *Iran J Energy Environ* 2(2):133–144



WSN Framework for Rose Greenhouse Monitoring

Devika¹

¹*Department of Computer Science & Engineering, Government Engineering College, K R Pet -571426,
Karnataka, India

ABSTRACT

Current world is rapidly forward towards smart systems to incarnate easy and versatile in all actions of development using Wireless sensor network (WSN) technologies. WSN is applied in smart farming to assist in monitoring and controlling as advances in technology. The applications based on WSN are similar to those components used in industries, control applications, automation and security systems. WSN can be designed and implemented for commercial crop rose in a greenhouse to provide best growing conditions. In this paper a new device namely Smart panel, a system helps person with inferior knowledge of technology to understand and maintain rose green house will be considered. The system allows agricultural environment data collection from each sensor such as temperature, humidity, and light in rose greenhouse a smart panel will be designed. The data mining techniques will be used to identify behavioral patterns according to environmental conditions captured by sensor network. The monitoring includes functions like crops management, harvesting, water supply control, animal control, pesticide distribution, humidity and temperature. The actuators to automate farming and provide precision farming experience. The smart panel assists in e-governance by setting simple data exchange between farmers and government. Farmers will be benefitted by system as to keep them up to date agricultural related announcements.

Keywords: WSN, data mining, smart agriculture, precision farming, smart panel, e governance, Crop yield, pest control, green house

I. INTRODUCTION

The collection of large set of mobile or static sensor nodes featured with self-organization and self-location assisted single or multi-hop network is known as Wireless Sensor Network (WSN). The sensors will be embedded with capability to interact with each other in network environment be processing information and communication to each other wirelessly. Mainly WSN is deployed with purpose to detect, process and to communicate sensed information in remote areas. Hence it has greater impacts in seismic, low sampling magnetic, thermal, visual, infrared, acoustic and radar real time applications (1). The typical WSN network is shown in figure 1.

The WSN has been employed in precision agriculture with an aim to prevent to manage routine to a crop regardless of site circumstances to improve in several circumstances such as minimize the water requirement,

wastage of pesticides, control pests and diseases, supply of required nutrients to soil and others(2). The tradition farming varies from PA sense that this process accurately identifies variations and relates the spatial data to management activities. PA involves five stages, namely, (i) data collection, (ii) diagnosis, (iii) data analysis, (iv) precision field operation, and (v) evaluation [4].

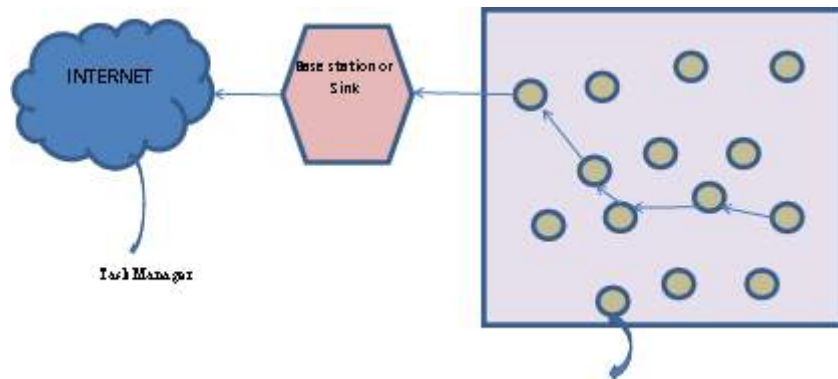


Figure 1: Typical WSN architecture

A. Motivation

One of the primary basic needs of human beings is food due to increase in population throughout world is facing shortage of food. Though according to world statistics India being in 27th position in production of food face problem to feed everyone in the country. The changes in climate and scarcity of water alarm adaptation of new improvement methods (Mueller et al., 2012). So, agricultural sector must increase yield by adopting modern technologies in order to meet gap ((Chen et al., 2015);). the most favorable facilities for Agriculture can be considered as one of WSNs to improve food crop yields and minimize the burden of farmers[3]. Hence, out main objective of proposed work is to assist a farmer with very less or absolute technical knowledge by introducing smart panel concept.

The main contributions of this paper are summarized as follows:

- Automatic watering and pesticide supply system for rose greenhouse
- The identification of smart sensor potentials in terms of best power consumption and communication distance for PA application.
- The taxonomy of energy-efficient and energy harvesting techniques to resolve problems of communication
- To develop an environmental conditions identification system to high precision agriculture within controlled environment by applying to rose green house
- The smart panel will be provided interface to sensor and actuators
- The existing solutions, applicability, and limitations of applying WSNs in agriculture will be reviewed and compared
- The applicability of data mining techniques to obtain prediction model will be dealt.

II. RELATED WORK

This section briefs some compiled works which aligns with proposed by highlighting key focus and progress. Since from time of PA adaptation around 1994 have gone through various modifications with the advancement in technologies. Few researchers have also incorporated IOT and cloud computing to assist in PA functionalities [4]. For processing and to get accurate results at faster rate machine learning techniques are being introduced [5]. The key concern of PA is smart irrigation system. The automatic watering system based on Arduino UNO design in [8] detecting level of moisture in the soil using soil moisture sensors. A similar project developed in [9] by applying increased technology ATmega32 microcontroller, where an automatic watering of plants from tank is developed. IOT based automated irrigation system was developed in (10). Decision support system based on PH levels for watering of plants adopted in (11). The Raspberry Pi, humidity and temperature sensors based automatic system irrigation system developed to increase crop production [2]. Wi-Fi enabled play house implemented in [3], low power Bluetooth and Low Power Wide Area Networks (LPWAN) communication modules and MQ Telemetry Transport (MQTT) communication method is used in monitoring and control systems of PA in [4]

The crop estimation has been another major research concern in PA, the image based crop estimation was implemented in [12], satellite image based prediction adopted in [13], machine learning model based prediction in [5], prediction based on data mining knowing soil quality designed in [6]

In [1] an IoT based monitoring and controlling system designed using moisture sensors. For pest control initially manual techniques were applied by trapping those in pheromone trap [6] later moved on to image based pest fine grained optimization [7].the crop suggestion system based on soil fertility was developed in [7].

A zigbee based WSN drip watering system designed measuring soil moisture, temperature, light intensity and electric conductivity for making decisions in (Xinjian Xiang14). A monitoring system to monitor agricultural environment using System on Chip to reduce cost and physical size was constructed in (Jzau-Sheng Lin et al.15). A decision system for producer using WSN is implemented in (Zhao Liang et al). the knowledge base and diffuse inference rules providing intelligent watering mechanisms implemented in this system.

Initially smart board concept was adopted for teaching purpose [14], and mainly to teach math [15], later similar concept was adopted in (16) identifying benefits of smart board.

The prediction system for apple plagues constructed based on WSN in (Bharava, 13). The system is used to identify temperature and foliar humidity measurements. The watering for cherry plant by detecting specific area and implementing drip watering system with Bluetooth build in (Dursen and Ozden16). An automated agriculture system to monitor and control the growth process of melon in green house was implemented in (Yoo S. et al.17). Most of the works presented systems are only proposals, few works are implemented and very few works are specific to applications. So, forward trending actions are required for better productivity.

TABLE 1 SUMMARY OF RELATED WORK

Author	Title	Year	Domain	Application of interest
Jonathan Jao, Bo Sun Kui Wu	A Prototype wireless Sensor Network for Precision Agriculture	2013	WSN in agriculture	Utilizes solar panels and rechargeable battery to address the problem of limited battery supply
Ravi Kishore Kodali, Nisheeth Rawat, Lakshmi Boppana	WSN Sensors for Precision Agriculture	2015	WSN In Precision Agriculture	Different Sensors used in Agriculture and mathematics behind them
Santoshkumar, Udaykumar R.Y	Development of WSN system for precision agriculture	2015	Precision Agriculture	Smart low cost WSN is used for monitoring and control in Precision Agriculture
G.Sahitya,Dr.N.Balaji,Dr. C.D Naidu	Wireless Sensor Network for Smart Agriculture	2016	Agriculture	To give real input according to the environment, Sensor network designing and transferring sensed values to zigbee

III. PROPOSED WSN SYSTEM CONSTRUCTION

Agriculture includes growing, maintaining and yielding of crops. Our aim is to construct smart panel to assist in monitoring all such actions remotely in a green house. Also, this paper tries to reduce problems of farmer. The modules included to assist are, automated calculation of crop yield, automatic watering of field, timely reporting of disorder and automatic pesticide application.

The prediction of crop yield requires temperature, humidity, moisture and nutrient sensors. The counter sensors will be installed to figure out ripe crops with in green house area. The sensors will be communicating one to another to get live details regarding temperature or moisture detector will collect information within detection range(13). PH, temperature and moisture sensors will be installed in fields to function in automatic watering. PH level i.e nutrient index from PH sensors, dielectric constant index of the soil from moisture sensor and temperature of field from temperature sensors will be collected to make decision on movement of motor and amount of watering to rose plant. The water supply will be automatically made to start when sensors data shows information more than 800ohm, 700ohm and 7 for temperature, moisture and PH respectively which is considered as non-ideal situation for rose plant (11). -Suitable mechanism will be installed such as ultrasonic pest detector with range between 20-50 kHz band and transducers to recognize pest through sound. The scale

from 1-5 will be designed to identify level of disorder based on portion area being infected. Through the information collected farmer will be able to supply suitable amount of pesticide via pump. Pesticide can be automatically supplied using motor as in water distribution or supplied manually. To establish communication between sensors wireless sensor network will be construct assisted with 802.15.4 technical standard and Zigbee Full Function Device to transmit data and GSM remote network distribution for storage and processing of information or federator-network technology like WLAN and WWAN can also be equipped or if all functions are to be carried in a system without Internet connection then WiMAX technology setup will be done (19,20). The data storage and result analysis can be suitably made to compute in smart panel so that smart panel will be able to communicate back to required sensor through commands. The proposed smart panel architecture to equip fro rose greenhouse is shown in figure 3 to assist in remote greenhouse monitoring.

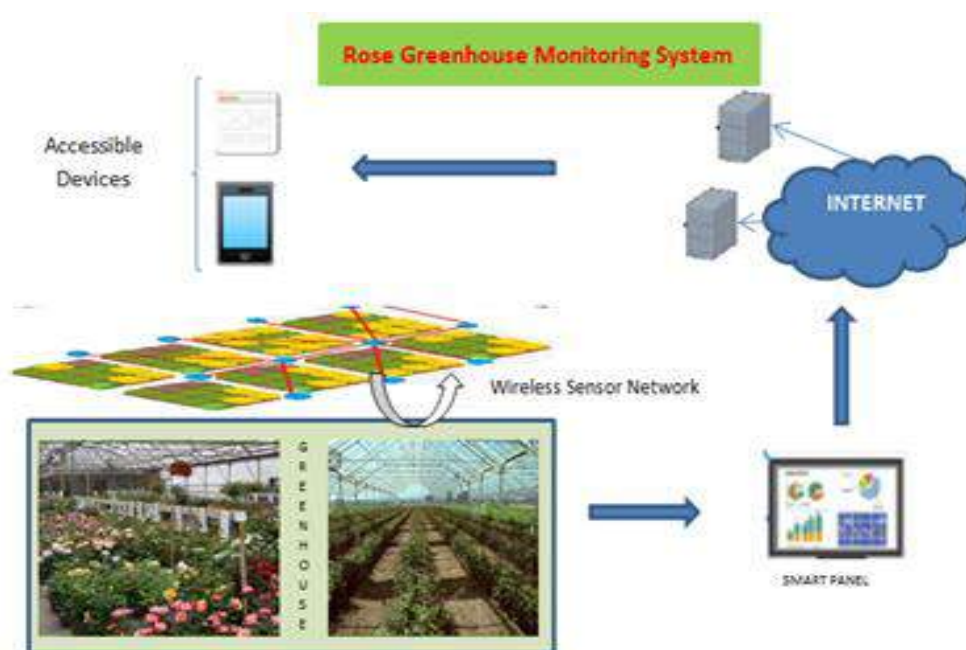


Figure 3: The Architecture of Rose Greenhouse Monitoring System

The major advantage of introduction of smart panel will be to help farmer with very less technical knowledge. It is observed from many precision farming systems that embedding and collaborating functionalities between modules to make it operative will be an issue. In such cases smart panel concept will be useful where it can be handled with minimum knowledge as person need not to interact directly with sensors or actuators. Further, the green house will be divided into small areas. It avoids overuse of water or pesticides by supplying only to required areas in correct proportions. If portion on is not having ideal values only sensors in that location will be active and rest portions sensors and actuators will be in sleep.

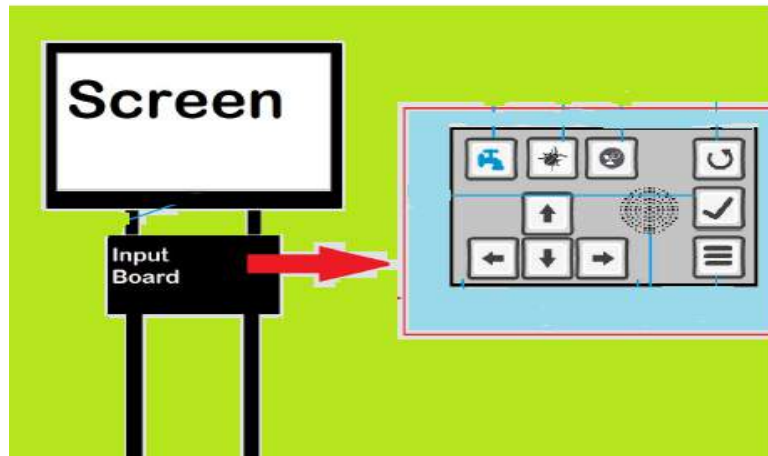


Figure 4: Smart panel

An interactive smart panel will be designed as in figure 4. It will consist of buttons to accept commands or made to accept input and output voice messages. Further the operating system with simple functions required to support interface in smart panel. The interactive dash board and farmers assistant tool box to alert regarding information of any warnings for farmers, any news alert for any coming cyclone of flood will be designed. The flow of operations in the proposed model is described in figure 5. Governmental services notifications or suggestions regarding current crop yield information are accessible via smart panel.

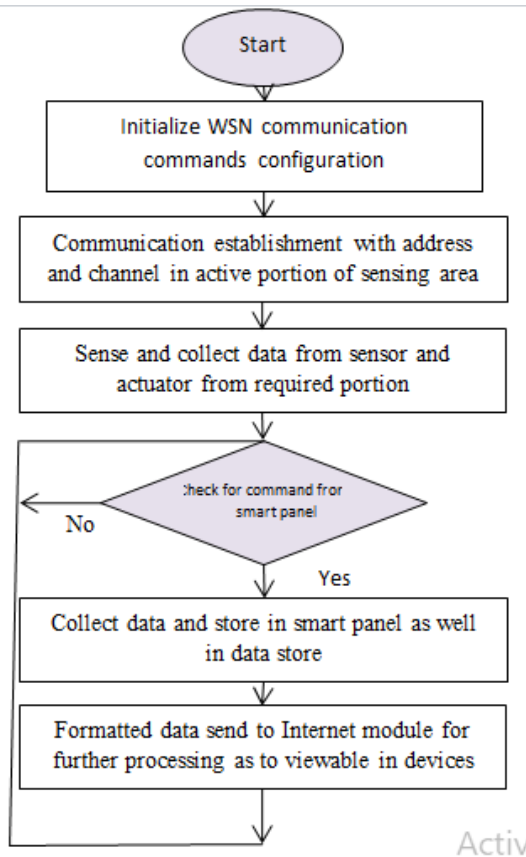


Figure 5 : Flow diagram of Rose Greenhouse Monitoring

IV. PREDICTIVE MODEL

The proposed rose greenhouse monitoring system model is a completely implementation model but still not yet instrumented practically. The rate of success of proposed model is estimated collecting economic data of components as in table 2(22,21). The price list of sensors and smart panel are estimated based on current market information.

TABLE 2: ESTIMATED COST OF ROSE GREENHOUSE MONITORING SYSTEM

Name of the Component	Required Number of Units	Cost
Temperature sensor	4	2000
Moisture sensor	10	5000
PH sensor	2	12000
UV sensor	2	1000
Servo motor	8	5000
Smart panel components	1	10000
Total cost		35000

A. Application Feature:

The smart panel will be interactive for farmer to know about field information and to operate remotely. The data will be stored for further decisions making or for instant data fetching in web interactive pages or in mobiles. The information is provided to only authenticate persons through a Log-invalidating via a confirmation email. The data collected will be scripted with suitable parameters for further mining and subsequently to generate prediction model through learning tool. The temporal and numerical data will adjust itself to the algorithm which gives the best results and can show a prediction with the least amount of deviation to the parameters that were taken for the study probably. The dataset will be designed to include both raw; data collected from sensors and normalized data between zero and on. The three predictive models will be used to perform test linear regression, neural networks and support vector machines.

V. CONCLUSION

Thus, smart farming helps farmers to make sure to earn more money thereby improving economy of our county considering in large scale. Technology applied in proposed model is fundamentally a support, monitor and management tool for agricultural domain which can be extended to other domain also. Generally monitoring and predictive system being developed influences much on decision making on parameters temperature, humidity, moisture, luminosity and others. Normally, the goal of recording such value is to characterize crop by size, duration, sanitary status and others which assist farmers to take earlier actions. The learning algorithms tuned up in order to enhance greenhouse environmental conditions forecasting and a comparison with other

techniques will be put into effect. In the future, a complete solution using different hardware and software components designed during proposed work will be put in place. Further improvement for proposed work can be focused with automatic control of data regarding phenological status with introduction of cameras applying image processing concepts. Similarly nodes can be made to operate on solar energy minimizing energy requirement.

VI. REFERENCES

- [1]. Díaz, S.E.; Pérez, J.C.; Mateos, A.C.; Marinescu, M.-C.; Guerra, B.B. A novel methodology for the monitoring of the agricultural production process based on wireless sensor networks. *Comput. Electron. Agric.* 2011, 76, 252–265.
- [2]. Jawhar, I.; Mohamed, N.; Al-Jaroodi, J.; Zhang, S. A framework for using unmanned aerial vehicles for data collection in linear wireless sensor networks. *J. Intell. Robot.Syst.* 2014, 74, 437–453.
- [3]. Kim, Y.-D.; Yang, Y.-M.; Kang, W.-S.; Kim, D.-K. On the design of beacon based wireless sensor network for agricultural emergency monitoring systems. *Comput. Stand. Interfaces* 2014, 36, 288–299.
- [4]. Valente, J.; Sanz, D.; Barrientos, A.; Cerro, J.D.; Ribeiro, Á.; Rossi, C. An air-ground wireless sensor network for crop monitoring. *Sensors* 2011, 11, 6088–6108.
- [5]. Ojha, T.; Misra, S.; Raghuvanshi, N.S. Wireless sensor networks for agriculture: The state-of-the-art in practice and future challenges. *Comput. Electron. Agric.* 2015, 118, 66–84.
- [6]. Tuna, G.; Gungor, V.C. Energy harvesting and battery technologies for powering wireless sensor networks. In *Industrial Wireless Sensor Networks*; Kolavennu, S., Ed.; Woodhead Publishing: Sawston, UK, 2016; pp. 25–38.
- [7]. Tan, Y.K.; Panda, S.K. Review of energy harvesting technologies for sustainable wireless sensor network. In *Sustainable Wireless Sensor Networks*; Seah, W., Ed.; InTech: Rijeka, Croatia, 2010; pp. 15–43.
- [8]. Ilie-Ablachim, D.; Patru, G.C.; Florea, I.-M.; Rosner, D. Monitoring Device for Culture Substrate Growth Parameters for Precision Agriculture: Acronym: Monisen. In *Proceedings of the 15th RoEduNet Conference: Networking in Education and Research, Bucharest, Romania, 7–9 September 2016*; pp. 1–7.
- [9]. Andreev, S.; Galinina, O.; Pyattaev, A.; Gerasimenko, M.; Tirronen, T.; Torsner, J.; Sachs, J.; Dohler, M.; Koucheryavy, Y. Understanding the IoT connectivity landscape: A contemporary M2M radio technology roadmap. *IEEE Commun. Mag.* 2015, 53, 32–40.
- [10]. Ratasuk, R.; Vejlgard, B.; Mangalvedhe, N.; Ghosh, A. Nb-IoT system for M2M communication. In *Proceedings of the IEEE Wireless Communications and Networking Conference, Doha, Qatar, 3–6 April 2016*; pp. 1–5.
- [11]. Lin, X.; Adhikary, A.; Wang, Y.-P.E. Random access preamble design and detection for 3GPP narrowband IoT systems. *IEEE Wirel. Commun. Lett.* 2016, 5, 640–643.
- [12]. Cancela, J.; Fandiño, M.; Rey, B.; Martínez, E. Automatic irrigation system based on dual crop coefficient, soil and plant water status for *Vitis vinifera* (cv Godello and cv Mencía). *Agric. Water Manag.* 2015, 151, 52–63.

- [13]. Rani, M.U.; Kamalesh, S. Energy efficient fault tolerant topology scheme for precision agriculture using wireless sensor network. In Proceedings of the International Conference on Advanced Communication Control and Computing Technologies (ICACCCT), Ramanathapuram, India, 8–10 May 2014; pp. 1208–1211.
- [14]. Rao, Y.; Jiang, Z.-H.; Lazarovitch, N. Investigating signal propagation and strength distribution characteristics of wireless sensor networks in date palm orchards. *Comput. Electron. Agric.* 2016, 124, 107–120.
- [15]. Raheemah, A.; Sabri, N.; Salim, M.; Ehkan, P.; Ahmad, R.B. New empirical path loss model for wireless sensor networks in mango greenhouses. *Comput. Electron. Agric.* 2016, 127, 553–560.
- [16]. Huircán, J.I.; Muñoz, C.; Young, H.; Von Dossow, L.; Bustos, J.; Vivallo, G.; Toneatti, M. Zigbee-based wireless sensor network localization for cattle monitoring in grazing fields. *Comput. Electron. Agric.* 2010, 74, 258–264.
- [17]. Azaza, M.; Tanougast, C.; Fabrizio, E.; Mami, A. Smart greenhouse fuzzy logic based control system enhanced with wireless data monitoring. *ISA Trans.* 2016, 61, 297–307.
- [18]. Nadimi, E.S.; Jørgensen, R.N.; Blanes-Vidal, V.; Christensen, S. Monitoring and classifying animal behavior using zigbee-based mobile ad hoc wireless sensor networks and artificial neural networks. *Comput. Electron. Agric.* 2012, 82, 44–54.
- [19]. Sabri, N.; Aljunid, S.A.; Ahmad, R.; Malek, M.; Yahya, A.; Kamaruddin, R.; Salim, M. Smart prolong fuzzy wireless sensor-actor network for agricultural application. *J. Inf. Sci. Eng.* 2012, 28, 295–316.
- [20]. Edwards-Murphy, F.; Magno, M.; Whelan, P.M.; O'Halloran, J.; Popovici, E.M. b+ WSN: Smart beehive with preliminary decision tree analysis for agriculture and honey bee health monitoring. *Comput. Electron. Agric.* 2016, 124, 211–219.



A survey on Performance Analysis and Comparison among Different Task Scheduling Algorithms in Cloud Computing

Sakshi T¹, Rachana S B¹, Prof. Annaiah H²

¹Student, Department of CSE, GEC, Hassan, Karnataka, India

²Department of CSE, Government Engineering College, Hassan, Karnataka, India

ABSTRACT

The enhanced form of client-server, cluster and grid computing is termed as Cloud Computing. The cloud users can virtually access the resources over the internet. Task submitted by cloud users are responsible for efficiency and performance of cloud computing services. The number of tasks in the cloud is huge and the system is dealing with massive tasks all the time, so it is difficult to handle and manage. Scheduling means the order in which the set of tasks to be executed.

Cloud computing provides various scheduling algorithms considering various parameters that can increase the performance of the system. Task scheduling is an essential downside within the cloud computing that has to be optimized by combining different parameter. Here the comparison of several job scheduling techniques with respect to several parameters, like response time, load balance, execution time and makespan of job to find the best and efficient task scheduling algorithm under these parameters.

Already a lot of scheduling algorithm exists targeting to various goals like reducing execution time, cost, makespan and increase resource utilization, load balancing, etc. In this work, we have mainly carried out the performance analysis and comparison among various well-known task scheduling algorithms.

I. INTRODUCTION

Cloud computing is a new technology derived from grid computing and distributed computing and refers to using computing resources (hardware, software, and platforms) as a service and provided to beneficiaries on demand through the Internet. It is the first technology that uses the concept of commercial implementation of computer science with public users. It relies on sharing resources among users through the use of the virtualization technique.

High performance can be provided by a cloud computing, based on distributing workloads across all resources fairly and effectively to get less waiting time, execution time, maximum throughput, and exploitation of resources effectively. Still, there are many challenges prevalent in cloud computing, Task scheduling and load balance are the biggest yet because it is considered the main factors that control other performance criteria such as availability, scalability, and power consumption.

II. TASKS SCHEDULING ALGORITHMS OVERVIEW

Tasks scheduling algorithms are defined as the mechanism used to select the resources to execute tasks to get less waiting and execution time or They can be defined as a set of rules and policies used to assign tasks to the suitable resources (CPU, memory, and bandwidth) to get the highest level possible of performance and resources utilization.

Scheduling levels

In the cloud computing environment there are two levels of scheduling algorithms:

First level: in host level where a set of policies to distribute VMs in host.

Second level: in VM level where a set of policies to distribute tasks to VM.

III. TASK SCHEDULING ALGORITHMS ADVANTAGES

1. Manage cloud computing performance and QoS.
2. Manage the memory and CPU.
3. The good scheduling algorithms maximizing resources utilization while minimizing the total task execution time.
4. Improving fairness for all tasks.
5. Increasing the number of successfully completed tasks.
6. Scheduling tasks on a real-time system.
7. Achieving a high system throughput.
8. Improving load balance.

IV. TASK SCHEDULING SYSTEM IN CLOUD COMPUTING

The task scheduling system in cloud computing passes through three levels. The first task level: is a set of tasks (Cloudlets) that is sent by cloud users, which are required for execution. The second scheduling level: is responsible for mapping tasks to suitable resources to get highest resource utilization with minimum makespan. The makespan is the overall completion time for all tasks from the beginning to the end. The third VMs level: is a set of (VMs) which are used to execute the tasks as in Figure.

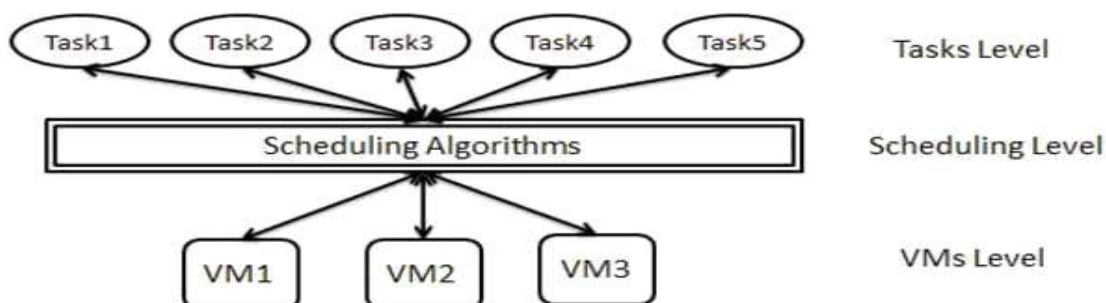


Fig 1: Task scheduling system

V. TASK SCHEDULING ALGORITHMS IN CLOUD COMPUTING

1.1 FCFS

FCFS: the order of tasks in task list is based on their arriving time then assigned to VMs. FCFS is a most popular and simplest scheduling algorithm. It is fairer than other simple scheduling algorithms and it depends on FIFO rule in scheduling task. It has less complexity when compared to other scheduling algorithms. But it also has few demerits such as tasks have high waiting time and it won't give any priority to tasks. That means when we have large tasks in the begin tasks list, all tasks must wait a long time until the large tasks to finish.

The resources are not consumed in an optimal manner. And In order to measure the performance achieved by this method, we will be testing them and then measuring its impact on (fairness, ET, TWT, and TFT).

1.2 Shortest Job First (SJF)

Tasks are sorted based on their priority. Priority is given to tasks based on tasks lengths and begins from (smallest task \equiv highest priority). Some of the advantages of SJF are the wait time is lower than FCFS and SJF has minimum average waiting time among all tasks scheduling algorithms. And it has disadvantages such as it shows unfairness to some tasks when tasks are assigned to VM, due to the long tasks tending to be left waiting in the task list while small tasks are assigned to VM. And it takes long execution time and TFT.

1.3 MAX-MIN Scheduling Algorithm

In MAX-MIN tasks are sorted based on the completion time of tasks; long tasks that take more completion time have the highest priority. Then assigned to the VM with minimum overall execution time in VMs list. This algorithm is working to exploit the available resources in an efficient manner. And it has better performance than the FCFS, SJF, and MIN-MIN algorithm. But It increases waiting time to small and medium tasks; if we have six long tasks, in MAX-MIN scheduling algorithm they will take priority in six VMs in VM list, and short tasks must be waiting until the large tasks finish. And it shows unfairness to some or most small and medium tasks when tasks are assigned to VM.

1.4 Min-Min scheduling Algorithm

This algorithm is split into 2 stages. The estimated completion time of each assignment in a Meta task is determined for each resource in the first stage. In the second stage, the task is chosen and assigned to the corresponding element by shortest estimated completion time. Then the chosen task is erased from the meta-list. This process is repeated before you map all the tasks in the Meta task. This raises the cumulative completion time of all the tasks and thereby raises the makespan. To finish their operation, the long tasks have to pause for smaller tasks.

It causes for unbalancing load in Min-Min. The min-min method is easy, but at the time of the number of tasks in the Meta task is small relative to large tasks, it gives instant results. On the other hand, if the number of smaller tasks is overlaid by large-size, it offers bad utilization of resources and bot good makespan since large tasks have to pause until all low size tasks to be done.

1.5 Particle Swarm Optimization (PSO)

This is meta-heuristic population-based algorithm exhilarated by social manners of fish schooling and bird flocking. The algorithm contains set of particles, and each particle depicts a solution for the problem in given search space which is then used to approach convenient solutions . This algorithm is initialized by a set of random particles and then finding a best solution in problem space. In PSO we use iteration to find out each particles position which is referred as Personal best P_b achieved by particle I and global best P_g . Position found by neighbour particle.

VI. COMPARASION PARAMETERS

Scheduling of the jobs/tasks, consider certain parameters through which the performance of the system can be improved by improving those parameters. Various parameters used to compare various scheduling algorithms are discussed in this section:

- **Makespan:** It is defined as the total completion time of all the tasks in a job queue. The makespan should be reduced to increase the performance of particular algorithm.
- **Resource utilization:** Resource utilization is the use of the resource in such a way that increases the throughput of the system.
- **Deadline:** It is the period of time from submitting a task to the time by which it must be completed.
- **Execution time:** The exact time taken to execute the given task is known as execution time. The ultimate goal of any scheduling algorithm is minimizing the execution time.
- **Completion time:** The time taken to complete the whole execution of a job. It also includes the execution time and the delay caused by the cloud system.
- **Load balancing:** It is the method of distributing the entire load in a cloud network across different nodes so that at a time no nodes remain under loaded. The load should be balanced to increase the efficiency of the system.
- **Energy consumption:** Many different scheduling algorithms has designed to reduce the power consumption and improving the performance.
- **Performance:** Performance indicates the overall efficiency given by the scheduling algorithm in order to provide good services to the user as per their requirements.
- **Quality of service:** This includes various user input constraints like meeting execution, performance, deadline, cost, makespan, etc.
- **Response time:** The elapsed time between the end of an inquiry or demand on a computer system and the beginning of a response.
- **Scalability:** It is the ability of the system to function well when it is changed in size to satisfy the user need.

VII. COMPARISON OF VARIOUS TASK SCHEDULING ALGORITHMS

Algorithms	Methodology	Parameters	Merits	Demerits
Particle Swarm Optimization	The algorithms use population to find the optimal minimum values that help in creating a correct order of tasks and schedule task to a suitable resource	1. Inertia, 2. C1, C2 constants	1. high utilization of resources, finding the optimal solution, minimizing processing time	1. Slow convergence speed if search space is large
Min-Min Algorithm	This algorithm works on strategy in which task having minimum execution time is selected for all task	1. Makespan	1. Better makespan	1. load imbalance 2. poor QoS
First Come First Serve	This algorithm manages the task scheduling with FIFO queue. Task which comes first will be executed first on VM	1. Arrival time	1. Simple and fast execution	1. Task scheduling is based on arrival time, doesn't consider any other criteria Less utilization of VM

VIII. CONCLUSION

This paper introduces the meaning of the different tasks scheduling algorithms and also a comparative study between the static task scheduling algorithms in a cloud computing environment such as FCFS, SJF, and MAX-MIN, MIN-MIN, PSO in terms of average waiting time, turnaround time, makespan, load balancing, and throughput, fairness between tasks, and when becoming suitable to use.

IX. REFERENCES

- [1]. Peter Mell and Tim Grance, "The nist definition of cloud computing", 2011.
- [2]. A. Gupta, H. S. Bhaduria, A. Singh and J. C. Patni, "A theoretical comparison of job scheduling algorithms in cloud computing environment", 2015 1st International Conference on Next Generation Computing Technologies (NGCT), Dehradun, 2015, pp. 16-20, doi: 10.1109/NGCT.2015.7375074.

- [3]. Malhotra, Agarwal, and Jaiswal, "Virtualization in cloud computing", *Journal of Information Technology Software Engineering*, doi:10.4172/2165-7866.1000136, vol. 04, 2014.
- [4]. Neha Sharma and D. Sanjay Tyagi, "A comparative analysis of min-min and max-min algorithms based on the makespan parameter", *International Journal of Advanced Research in Computer Science*, vol. 8, no. 03, April 2017.
- [5]. Sanjay Kumar and Atul Mishra, "Application of min-min and maxmin algorithm for task scheduling in cloud environment under time shared and space shared vm models", *International Journal of Computing Academic Research (IJCAR)*, vol. 04, no. 06, pp. 182–190, December 2015.
- [6]. R. JeminaPriyadarsini and L. Arockiam, "Performance evaluation of min-min and max-min algorithms for job scheduling in federated cloud", *International Journal of Computer Applications (0975 a 8887)*, vol. 99, ^ no. 18, August 2014.
- [7]. M. Joundy, S. Sarhan, and S. Elmougy, "Task scheduling algorithms in cloud computing: A comparative study", *International Journal of Intelligent Computing And Information Science*.
- [8]. EssaiesMeriam and Nabil Tabbane, "A survey on cloud computing scheduling algorithms", 2016 Global Summit on Computer Information Technology, DOI: 10.1109/GSCIT.2016.6, 2017.



Locomotive Aid for Paralysed People

Leelavathi V V

Department of Electronics and Communication Engineering, Government Engineering College,
Chamarajanagar-571313, Karnataka, India

ABSTRACT

This project discusses about a brain-controlled wheel chair based on Brain-computer interfaces (BCI). BCI's are systems that can bypass conventional channels of communication (i.e., muscles and thoughts) to provide direct communication and control between the human brain and physical devices by translating different patterns of brain activity into commands in real time. The intention of the project work is to develop a robot that can assist the disabled people in their daily life to do some work independent of others. Here, we analyse the brain wave signals. Human brain consists of millions of interconnected neurons, the pattern of interaction between these neurons are represented as thoughts and emotional states. According to the human thoughts, this pattern will be changing which in turn produce different electrical waves. A muscle contraction will also be generating a unique electrical signal. All these electrical waves will be sensed by the brain wave sensor and the different pattern is used for controlling a wheel chair.

Keywords: brain-computer interface, wheel-chair, eeg sensor

I. INTRODUCTION

Paralysis is the inability whether temporary or permanent to move a part of the body. In almost all cases, paralysis is due to nerve damage, and it is not because of injury to the affected region. For instance, an injury in the middle or lower regions of the spinal cord is likely to disrupt function below the injury, including the ability to move the feet or feel sensations, even though the actual structures are as healthy as ever. Because of this in patients at least one of the following symptoms results. The brain is unable to relay a signal to an area of the body due to injuries to the brain. Brain- Computer Interface (BCI) also known as "direct neural interface" can provide a direct communication and interaction channel between the user's brain and the computer. BCI helped to direct in assisting, augmenting, or repairing human cognitive or even sensory-motor functions. BCI provides a new direction to construct an interactive system which can translate human Channel based on brain waves and muscles to allow users to communicate without movement with the external world. A BCI system is just to translate EEG signals from a reflection of brain activity into user action through system's hardware and software. [1].

II. OVERVIEW

- 2.1. PROBLEM STATEMENT DISABLED PERSON HAS TROUBLE MOVING FROM ONE PLACE TO OTHER WITHOUT THE HELP OF OTHERS. THE PRESENT SYSTEM DOESN'T PROVIDE MUCH HELP SINCE THEY ARE MANUALLY OPERATED WHEEL CHAIR. HENCE THERE IS NEED FOR AUTONOMOUS SYSTEM WHICH AID DISABLED PERSON TO MOVE ON THEIR OWN.
- 2.2. EXISTING SYSTEM EXISTING SYSTEM CONSIST OF MANUALLY OPERATED WHEEL CHAIR WHICH CONSISTS OF WHEEL PULLY WHICH SHOULD BE ROTATED BY HAND TO MOVE THE WHEEL CHAIR .THE OTHER VERSION CONSISTS OF MOTORIZED WHEEL CHAIR WHICH IS ALSO OPERATED BY A REMOTE ON THE WHEEL CHAIR. THESE SYSTEMS ARE INEFFICIENT WHEN THE PERSON USING IT IS PHYSICALLY CHALLENGED OR DISABLED DUE TO OLD AGE / PARALYSIS.
- 2.3. PROPOSED SYSTEM OUR PROPOSED IDEA CONSISTS OF A MOTORIZED WHEEL CHAIR, WHICH IS CONTROLLED USING BRAIN SIGNALS. THIS SYSTEM DOESN'T DEPEND ON OPERATING SWITCHES MANUALLY OR ROTATING A PULLY.SINCE THE CONTROL MECHANISM WORKS BY INTERCEPTING BRAIN SIGNAL, IT OVERCOMES THE MAIN LIMITATION OF EXISTING SYSTEM. THUS, ALLOWING PHYSICALLY CHALLENGED AND DISABLED PERSON TO USE WITHOUT EFFORT.
- 2.4. MOTIVATION BEHIND PROPOSED WORK THE MOTIVATION OF THE EEG-CONTROLLED WHEELCHAIRS IS TO FACILITATE ASSISTANCE IN MOBILITY IN ORDER TO ACCOMPLISH COMPLEX NAVIGATIONAL TASKS IN REALISTIC ENVIRONMENTS FOR THE PARALYZED PATIENTS. IT INCLUDES THE DEVELOPMENT OF AUTOMATIC NAVIGATION STRATEGIES AND PERSONALIZED INTERACTIVE ASSISTANCE TO ENABLE THE PATIENTS TO MOVE EFFECTIVELY AND EASILY. ONE ATTEMPT ATTRACTING CONSIDERABLE ATTENTION IN THOSE FIELDS INVOLVES THE UTILIZATION OF BIO- SIGNALS SUCH AS AN ELECTROENCEPHALOGRAM (EEG) OR ELECTROMYOGRAM (EMG); OBTAINABLE FROM THE HUMAN BODY AS A MEANS FOR INTERACTION WITH THE SURROUNDING WORLD. IN THE FIELD OF BRAIN- COMPUTER INTERFACE (BCI), MEANINGFUL INFORMATION DERIVED DIRECTLY FROM A USER'S BRAIN ACTIVITY HAS BEEN USED TO MANIPULATE SYSTEMS. HOWEVER, DESPITE THE DEFINITE ADVANTAGE UNIQUE TO EEG SIGNALS THAT ALLOWS A SYSTEM TO BE CONTROLLED ONLY BY ONE'S THOUGHTS, THE POOR SIGNAL-TO-NOISE RATIOS IN THE SPONTANEOUS EEG SIGNALS AND THE LACK OF CONSISTENCY IN THE SIGNAL ` PATTERNS STILL MAKE THEIR APPLICATION IMPRACTICAL.
- 2.5. **Scope of the proposed project**
 - Advancements in robotics, sensor technology and artificial intelligence promises enormous scope for developing an advanced wheelchair.
 - The proposed work deals with engineering an interface between the human brain and an electric wheelchair using a portable EEG brainwave headset and firmware signal processing and filtering.

- The project eliminates the drawbacks of conventional EEG by using a dry sensor technology to pick up EEG signals instead of using a conductive gel and reducing the time it takes to setup.
- This project aims at creating a cost-efficient solution, later intended to be distributed as an add-on conversion unit for a normal wheelchair. Doing so would be of noble and of importance to “brain-active-body-paralyzed patients providing them the independence of mobility.
- The main purpose of this project is to design a wheelchair for severely disabled person move them voluntarily. Their movement of wheelchair can be controlled with their own mind waves.

2.6. Objectives

Independent mobility is a necessity to live everyday life for human beings. A person with physical challenges has restricted mobility. For these people, Brain Computer Interface (BCI) provides a promising solution. The major design objectives of this project are given below.

- To reduce user effort in controlling the wheelchair.
- To ensure the safety during movement.
- A smart wheelchair using inexpensive hardware and open-source software.
- To monitor the activity of the person in real time using sensors
- The designed system should be portable for the user.

III. LITERATURE SURVEY

Cecilia L. Maeder; Claudia Sannelli; Stefan Haufe; Benjamin Blankertz: PreStimulus “Sensorimotor Rhythms Influence Brain-Computer Interface Classification Performance”: The influence of pre-stimulus ongoing brain activity on post-stimulus task performance has recently been analysed in several studies. While pre-stimulus activity in the parieto-occipital area has been exhaustively investigated with congruent results, less is known about the sensorimotor areas, for which studies reported inconsistent findings. In this work, the topic is addressed in a brain-computer interface (BCI) setting based on modulations of sensorimotor rhythms (SMR). The goal is to assess whether and how peristimulus SMR activity influences the successive task execution quality and consequently the classification performance. Grand average data of 23 participants performing right and Lefthand motor imagery were analysed. Trials were separated into two groups depending on the SMR amplitude in the 1000ms interval preceding the cue, and classification by common spatial patterns (CSPs) pre-processing and linear discriminant analysis (LDA) was carried out in the post-stimulus time interval, i.e., during the task execution. The correlation between trial group and classification performance was assessed by an analysis of variance. As a result of this analysis, trials with higher SMR amplitude in the 1000 ms interval preceding the cue yielded significantly better classification performance than trials with lower amplitude. A further investigation of brain activity patterns revealed that this increase in accuracy is mainly due to the persistence of a higher SMR amplitude over the ipsilateral hemisphere. Our findings support the idea that exploiting information about the ongoing SMR might be the key to boosting performance in future SMR-BCI experiments and motor related tasks in general.

Murat Akcakaya; Betts Peters; Mohammad Moghadamfalahi; Aimee R Mooney; Umut Orhan; Barry Oken; Deniz Erdogmus: "Noninvasive Brain- Computer interfaces for Augmentative and Alternative Communication": Brain-computer interfaces (BCIs) promise to provide a novel access channel for assistive technologies, including augmentative and alternative communication (AAC) systems, to people with severe speech and physical impairments (SSPI). Research on the subject has been accelerating significantly in the last decade and the research community took great strides toward making BCI-AAC a practical reality to individuals with SSPI. Nevertheless, the end goal has still not been reached and there is much work to be done to produce real-world worthy systems that can be comfortably, conveniently, and reliably used by individuals with SSPI with help from their families and care givers who will need to maintain, setup, and debug the systems at home. This paper reviews reports in the BCI field that aim at AAC as the application domain with a consideration on both technical and clinical aspects.

C Guger, H Ramoser, G Pfurtscheller: "Real time EEG analysis with subjectspecific spatial patterns for a brain-computer interface (BCI)": Electroencephalogram (EEG) recordings during right and left motor imagery allow one to establish a new communication channel for e.g., patients with amyotrophic lateral sclerosis. Such an EEG-based brain-computer interface (BCI) can be used to develop a simple binary response for the control of a device. Three subjects participated in a series of on-line sessions to test if it is possible to use common spatial patterns to analyses EEG in real time in order to give feedback to the subjects. Furthermore, the classification accuracy that can be achieved after only three days of training was investigated. The patterns are estimated from a set of multichannel EEG data by the method of common spatial patterns and reflect the specific activation of cortical areas. By construction, common spatial patterns weight each electrode according to its importance to the discrimination task and suppress noise in individual channels by using correlations between neighbouring electrodes. Experiments with three subjects resulted in an error rate of 2,6 and 14days of training and make common spatial patterns a promising method for an EEG -based brain -computer interface.

Md. Arif Abdulla Samy; Md. Mirazur Rahman; Tafsir Ahmed Khan: "Extracting and discriminating selective brain signals in non-invasive manner and using them for controlling a device": A cost-efficient approach to brain computer interface (BCI):Publisher: IEEE: The interface through which a human brain establishes links with external devices is generally called Brain Computer Interface. Although there are some significant amounts of ongoing researches on how an overall efficient BCI can be developed are going on, making a cost-efficient approach while dealing with limitless brain patterns is found to be more challenging. In this work, feasibility of a cheaper but appropriate way of extracting and discriminating of several non-invasive. EEG signals and using those for controlling devices such as a wheel chair has been proved. To assist the argument of this project, numerous experimental data has been processed to produce several signals, such as, right turn, moving forward, stop etc. for the wheel chair. In the experiment the above mentioned three signals were well distinguished from each other. A microcontroller has been used for processing the signals collected from the brain and hence sending to the wheel chair controlling motors. Despite the challenges of dealing with very low but noise sensitive brain signals, their limitless patterns, and limited scope of necessary circuitries, this work has opened up the scope of feasibility of BCI technology in practical life with a simpler and easier approach.

R. S. Naveen; Anitha Julian: "Brain computing interface for wheel chair control:Publisher: IEEE:" Brain-computer interfaces (BCIs) or mind machine interface (MMI) is the direct communication path between brain

and external devices. Currently it is difficult for the persons suffering from strokes, amyotrophic lateral sclerosis (ALS) can lead to complete paralysis. Therefore, the BCI system may be used to improve the quality of life of such patients. In this paper we overcome this challenge by introducing a BCI system which helps the patient to navigate the wheelchair from one place to another based-on motor imagery model to control a brain actuated wheelchair. This allows the user to control the direction for four movements left turn, right turn, forward and backward movement, of the simulation or real wheelchair. Experimental trials are to be conducted to assess the BCI control; both a simulated wheelchair in a virtual environment and a real wheelchair were tested. The system will be realized as a standalone hardware unit and will be tested in the field.

Nafiul Hasan; Md. Mahmudul Hasan; Md. Akramul Alim: "Design of EEG Based Wheel Chair by Using Color Stimuli and Rhythm Analysis Publisher": IEEE: A novel methodology of brain controlled intelligent wheelchair by using color stimuli is proposed here. A general methodology is applied to find out most effective rhythm for color classification. Primary colors RGB and secondary color yellow were chosen for left, right, forward and stop command. Alpha, Beta, Theta, Delta rhythms were analysed for three different subjects. Using dissimilar features of time and frequency domain twelve artificial neural network were built to decide the best rhythm. Principal component analysis was made for each EEG signal to remove the background effect of color stimuli. Comparing the findings, it is visualized that beta rhythm is the most efficient rhythm with minimum mean square error of 4.845×10^{-9} among all designed ANN for color classification.

Danny Wee-Kiat Ng; Ying-Wei Soh; Sing-Yau Goh: "Development of an Autonomous BCI Wheelchair Publisher: IEEE:" In the society, most of the disabled people especially completely movement impaired ones live like burdens and suffer from severe depression as they have to depend on others for day-to-day activities and cannot contribute to the community. These people may not be able to move their arms or legs but they can certainly think. If their ability to think and make decisions can be utilized in decision making situations and also if they can further be included in industrial automation structure, they will no longer be burden rather they will become man-power to the society. One of the major challenges of involving these people in such processes is making a low-cost device that is affordable by the mass, made with locally available components and also interprets the person's choice accurately. As these people are physically disable, comprehending their electroencephalogram (EEG) signal for blink detection can be an effective solution for translating their choices. EEG-based controlling devices are mobile and can serve as powerful aids for severely disabled people in their daily life. In this work, a low-cost EEG sensor is made with readily available components and a framework is developed to detect voluntary eye blinks. A graphical user interface (GUI) is also developed which is suitable for the impaired person. The eye blinks of the person act as bridge between a set of choices pointed in the GUI and his/her selection interest and thus help the person control home appliances, wheel chair and even computer without depending on others.

Soumya Sen Gupta; Sumit Soman; P. Govind Raj; Rishi Prakash: "Detecting eye movements in EEG for controlling devices. Publisher: IEEE:" Eye blinks and lateral eye movements are prominent in EEG signals which are obtained by placing electrodes in the frontal region of the brain. This paper presents a machine learning approach to detect eye movements and blinks from EEG data and map them as intents to control external devices like a computer desktop or a wheel chair.

C. S. Ashwin; K. R. Rangarajan; S. Ramachandran: "Disance (enhance the disabled) brain mapped mobility for physically challenged. Publisher: IEEE." This paper proposes an intelligent robotic wheelchair with user-friendly human computer interface (HCI) based on EEG signal, face directional gesture, and voice. Electroencephalography (EEG) is the recording of electrical activity along the scalp produced by the firing of neurons within the brain. The user has to just think the direction in which the wheel chair has to move. Additionally, at unavoidable circumstances he can use voice or other gestures to signal the movement. The user's intention is transferred to the wheelchair via the HCI, and then the wheelchair is controlled to the intended direction. Additionally, the wheelchair can detect and avoid obstacles autonomously using sonar sensors. By combining HCI into the autonomous functions, it performs safe and reliable motions while considering the user's intention. The proposed robotic Wheelchair is feasible for the disabled and the elderly with severe motor disabilities. This concept gives the user the flexibility to use the device in unknown and evolving scenarios.

Lamiya Rahman; Jannatul Adan; Quazi Mutasim Billah; Md Kamrul Islam; A.H.M Mostafa Kamal; Sazzad Hossain: "A low-cost Human Computer Interface for Disabled People based on Eye Blink detection using Brain Signal :Publisher: IEEE." In the society, most of the disabled people especially completely movement impaired ones live like burdens and suffer from severe depression as they have to depend on others for day-to-day activities and cannot contribute to the community.

These people may not be able to move their arms or legs but they can certainly think. If their ability to think and make decisions can be utilized in decision making situations and also if they can further be included in industrial automation structure, they will no longer be burden rather they will — 25 become man-power to the society. One of the major challenges of involving these people in such processes is making a low-cost device that is affordable by the mass, made with locally available components and also interprets the person's choice accurately. As these people are physically disable, comprehending their electroencephalogram (EEG) signal for blink detection can be an effective solution for translating their choices. EEG-based controlling devices are mobile and can serve as powerful aids for severely disabled people in their daily life. In this work, a low-cost EEG sensor is made with readily available components and a framework is developed to detect voluntary eye blinks. A graphical user interface (GUI) is also developed which is suitable for the impaired person. The eye blinks of the person act as bridge between a set of choices pointed in the GUI and his/her selection interest and thus help the person control home appliances, wheel chair and even computer without depending on others.

IV. COMPONENTS USED IN THE SYSTEM

4.1. Software Requirement:

1. Arduino IDE

4.2. Hardware Requirement:

1. Arduino Uno
2. Heart beat sensor
3. Blood oxygen sensor (spO₂)(MAX30100)

4. Temperature sensor(LM35)
5. Motor Driver(LM239D)
6. DC motor
7. Battery(12V)
8. EEG sensor
9. LCD Display

4.3. Hardware Description

1. ARDUINO UNO

The Arduino Uno is an open- source microcontroller board based on the Microchip ATmega328P microcontroller and developed by Arduino.cc. The board is equipped with sets of digital and analog input/output (I/O) pins that may be interfaced to various expansion boards (shields) and other circuits. The board has 14 digital I/O pins (six capable of PWM output), 6 analog I/O pins, and is programmable with the Arduino IDE (Integrated Development Environment), via a type B USB cable. It can be powered by the USB cable or by an external 9-volt battery, though it accepts voltages between 7 and 20 volts. It is similar to the Arduino Nano and Leonardo. While the Uno communicates using the original STK500 protocol, it differs from all preceding boards in that it does not use the FTDI USB-to-serial driver chip. Instead, it uses the ATmega16U2 (ATmega8U2 up to version R2) programmed as a USB-to-serial converter.

Features of Arduino

The key features of Arduino have been discussed below as follows:

- Arduino boards are able to read analog or digital input signals from different sensors and turn it into an output such as activating a motor, turning LED on/off, connect to the cloud and many other actions.



Figure 4-1 ARDUINO UNO

- You can control your board functions by sending a set of instructions to the microcontroller on the board via Arduino IDE (referred to as uploading software).
- Unlike most previous programmable circuit boards, Arduino does not need an extra piece of hardware (called a programmer) in order to load a new code onto the board. You can simply use a USB cable.
- Additionally, the Arduino IDE uses a simplified version of C++, making it easier to learn to program.

Finally, Arduino provides a standard form factor that breaks the functions of the microcontroller into a more accessible package. Arduino UNO board description We chose the Arduino UNO board because it is the most popular board in the Arduino board family. In addition, it is the best board to get started with electronics and coding. Some boards look a bit different from the one given below, but most Arduino have majority of these

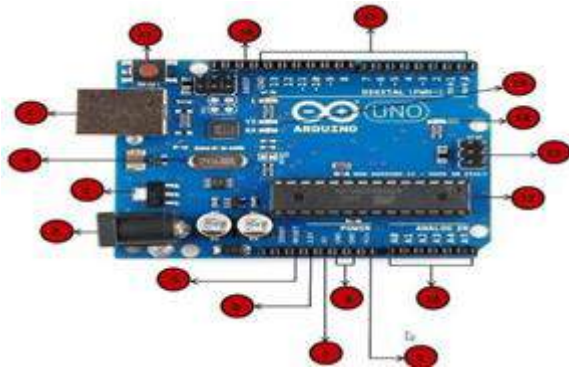


Figure 4 - 2 Arduino UNO Board components in common. The pin configuration of the Arduino UNO Board is discussed in the below Table 4-1:

Pin No.	Description
1	Power USB: Arduino board can be powered by using the USB cable from your computer. All you need to do is connect the USB cable to the USB connection (1).
2	Power (Barrel Jack): Arduino boards can be powered directly from the AC mains power supply by connecting it to the Barrel Jack (2).
3	Voltage Regulator: The function of the voltage regulator is to control the voltage given to the Arduino board and stabilize the DC voltages used by the processor and other elements.
4	Crystal Oscillator: The crystal oscillator helps Arduino in dealing with time issues. How does Arduino calculate time? The answer is, by using the crystal oscillator. The number printed on top of the Arduino crystal is 16.000H9H. It tells us that the frequency is 16,000,000 Hertz or 16 MHz
5, 17	Arduino Reset: You can reset your Arduino board, i.e., start your program from the beginning. You can reset the UNO board in two ways. First, by using the reset button (17) on the board. Second, you can connect an external reset button to the Arduino pin labelled RESET (5).
	Pins (3.3, 5, GND, Vin) 3.3V (6) : Supply 3.3 output volt

2. DC MOTOR




- A DC motor converts DC electrical energy into mechanical energy.
- Basic principle: When a current-carrying conductor is placed in a magnetic field, it experiences a torque and has a tendency to move.
- DC Motor – 100RPM – 12Volts geared motors are generally a simple DC motor with a gearbox attached to it.
- These motors have a 3 mm threaded drill hole in the middle of the shaft thus making it simple to connect it to the wheels or any other mechanical assembly.
- They are very easy to use and available in standard.

<p>6,7 8,9</p>	<p>5V (7) : Supply 5 output volt (Most of the components used with Arduino board works fine with 3.3 volt and 5 volts.) GND (8- Ground): There are several GND pins on the Arduino, any of which can be used to ground your circuit. Vin (9) : Even this pin can be used to power the Arduino UNO board from an external power source, like AC mains power supply.</p>
<p>10</p>	<p>Analog pins: This board has six analog input pins A0 to A5. These pins can read the signal from an analog sensor like the humidity sensor or temperature sensor and convert it into a digital value that can be read by the microprocessor.</p>
<p>11</p>	<p>Main microcontroller: Each Arduino board has its own microcontroller (11). You can assume it as the brain of your board. The main IC (integrated circuit) on the Arduino is slightly different from board to board. The microcontrollers are usually of the ATMEL Company. You must know what IC your board has before loading up a new program from the Arduino IDE. This information is available on the top of the IC. For more details about the IC construction and functions, you can refer to the data sheet.</p>
<p>12</p>	<p>ICSP pin: Mostly, ICSP (12) is an AVR, a tiny programming header for the Arduino consisting of MOSI, MISO, SCK, RESET, VCC, and GND. It is often referred to as an SPI (Serial Peripheral Interface), which could be considered as an "expansion" of the output. Actually, you are slaving the output device to the master of the SPI bus.</p>



Figure 4 - 3 DC motor

<p>13</p>	<p>Power LED indicator: This LED should light up when you plug your Arduino into a power source to indicate that your board is powered up correctly. If this light does not turn on, then there is something wrong with the connection.</p>
-----------	--

	<p>TX and RX LEDs: On your board, you will find two labels: TX (transmit) and RX (receive). They appear in two places on the Arduino UNO board. First, at the digital pins 0 and 1, to indicate the pins responsible for serial communication. Second, the TX and RX led (13). The TX led flashes with different speed while sending the serial data. The speed of flashing depends on the baud rate used by the board. RX flashes during the receiving process.</p>
	<p>Digital I/O: The Arduino UNO board has 14 digital I/O pins (15) (of which 6 provide PWM (Pulse Width Modulation) output. These pins can be configured to work as input digital pins to read logic values (0 or 1) or as digital output pins to drive different modules like LEDs, relays, etc. The pins labelled “~” can be used to generate PWM.</p>
	<p>AREF: AREF stands for Analog Reference. It is sometimes, used to set an external reference voltage (between 0 and 5 Volts) as the upper limit for the Analog input pins.</p>

3. MOTOR DRIVER (L298N)

Motor driver is a small Current Amplifier whose function is to take a low- current control signal and then turn it into a higher- current signal that can drive a motor. The most popular L298N H-bridge module with onboard voltage regulator motor driver can be used with this motor that has a voltage of between 5 and 35V DC. Nuts and threads on the shaft to easily connect and internally threaded shaft for easily connecting it to the wheel.

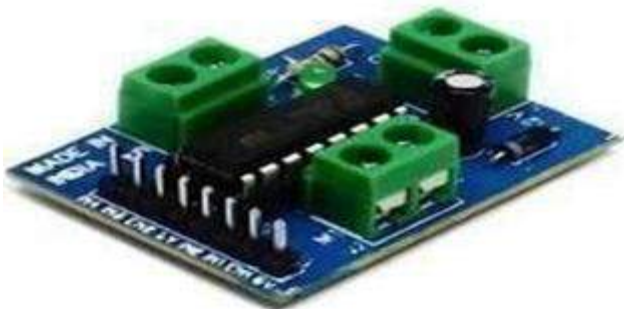


Figure 4 - 4 Motor driver

4. EEG SENSOR

- The Electroencephalography (EEG) sensor is a non- invasive sensor.
- It has a bipolar configuration with two measurement electrodes which detects the electrical potentials in the specific scalp region and is used in combination with a reference electrode, placed at a region of low muscular activity. The resulting signal is the amplified difference between these two signals and the result of the brain's electrical activity in the monitored scalp region.
- EEG Muscle Sensor Module V3.0 with Cable and electrodes will measure the filtered and rectified electrical activity of a muscle and gives the output 0-Vs Volts depending on the amount of activity in the selected muscle, where Vs signifies the voltage of the power source.

- This Muscle Sensor V3 measures, filters, rectifies and amplifies the electrical activity of a muscle and produces an analog output signal that can easily be read by Arduino microcontroller. Important Features:
- Improved adjustable gain (more rugged).
- Onboard port for new cables .
- Connects to the board straight out of the box.
- Power Supply: Normally $\pm 9V$ dual power supply, minimum voltage is $\pm 3.5V$.
- The body temperature of the patient is measured using this sensor.
- Any abnormality in body temperature will be alerted.
- LM35 is a precision Integrated circuit Temperature sensor, whose output voltage varies based on the temperature around it.
- It is a small and cheap IC which can be used to measure temperature anywhere between $-55^{\circ}C$ to $150^{\circ}C$.
- It can easily be interfaced with Arduino.
- The body temperature of the patient is measured using this sensor.



Figure 4 - 5 Electroencephalography (EEG) sensor

- Power the IC by applying a regulated voltage like +5V (VS) to the input pin and connected the ground pin to the ground of the circuit. Now, you can measure the temperature in form of voltage as shown below:

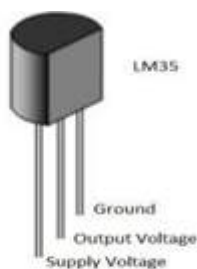


Figure 4 - 6 Temperature sensor: (LM35)

First, we must have an Arduino board and a USB cable. In case we use Arduino UNO, Arduino Duemilanove, Nano, Arduino Mega 2560, or Diecimila, we will need a standard USB cable (A plug to B plug), the kind we would connect to a USB printer .In case we use Arduino Nano, we will need an A to Mini-B cable instead as shown in Fig.4.8



Figure 4-8 A to Mini-B Cable

Step 2 - Download Arduino IDE Software:

One can get different versions of Arduino IDE from the Download Page on the Arduino Official website. We must select our software, which is compatible with our operating system (Windows, IOS, or Linux). Unzip the file, after downloading it completely.

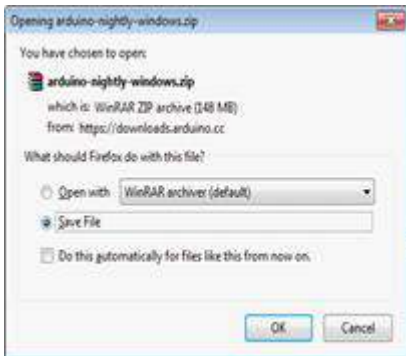


Figure 4 -9 Downloading Arduino IDE

Step 3 - Power up your board:

The Arduino Uno, Mega, Duemilanove and Arduino Nano automatically draw power from either, the USB connection to the computer or an external power supply. If you are using an Arduino Diecimila, you have to make sure that the board is configured to draw power from the USB connection. The power source is selected with a jumper, a small piece of plastic that fits onto two of the three pins between the USB and power jacks. Check that it is on the two pins closest to the USB port. Connect the Arduino board to computer using the USB cable. The green power LED (labelled PWR) should glow.

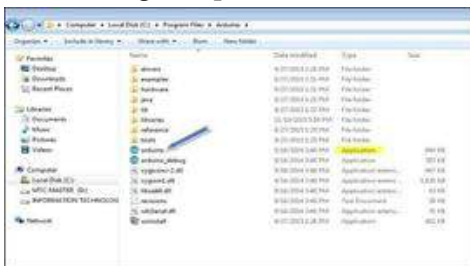


Figure 4 - 10 Launch Arduino IDE

Step 4 -Launch Arduino IDE :

After your Arduino IDE software is downloaded, you need to unzip the folder. Inside the folder, you can find the application icon with an infinity label (application.exe). DoubleClick the icon to start the IDE.

Step 5 - Open your first project:

Once the software starts, we have two options:

Create a new project. To create a new project, select File →New, as shown in Fig 4-11.

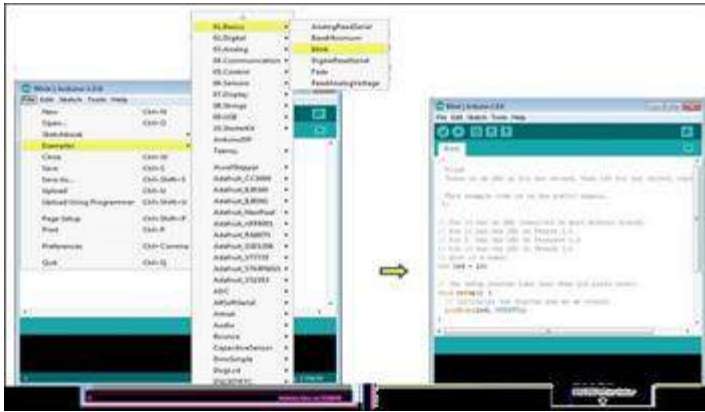


Figure 4 - 11 Creating a New Project

Open an existing project example. To open an existing project example, select File → Example → Basics → Blink, as shown in Fig. 4.-12. Here, we are selecting just one of the examples with the name Blink. It turns the LED on and off with some time delay. We can select any example from the list.

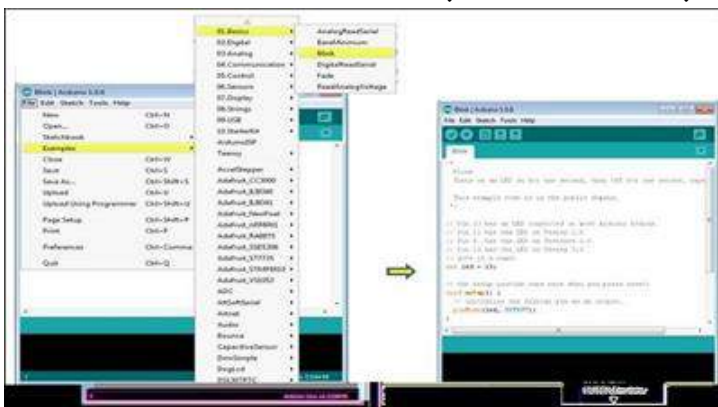


Figure 4 - 12 Opening an Existing Project

Step 6 -Select the respective Arduino board:

To avoid any error while uploading our program to the board, we must select the correct Arduino board name, which matches with the board connected to our computer. Go to Tools → Board and select the board.

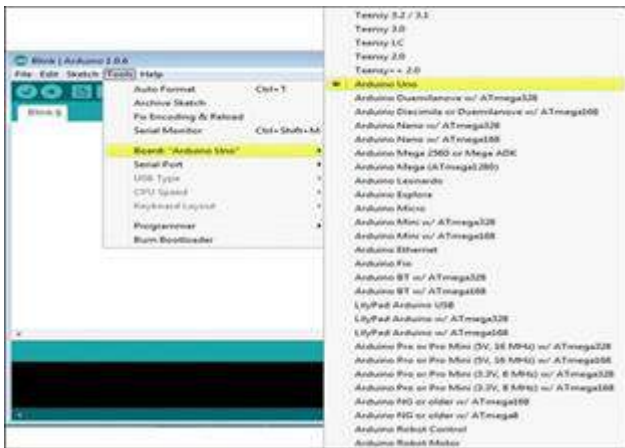


Figure 4 - 13 Selecting the Arduino Board

Step 7 - Select the serial port:

Select the serial device of the Arduino board. Go to Tools → Serial Port menu.

This is likely to be COM3 or higher (COM1 and COM2 are usually reserved for hardware serial ports).

To find out, you can disconnect your Arduino board and re-open the menu, the entry that disappears should be of the Arduino board. Reconnect the board and select that serial port.

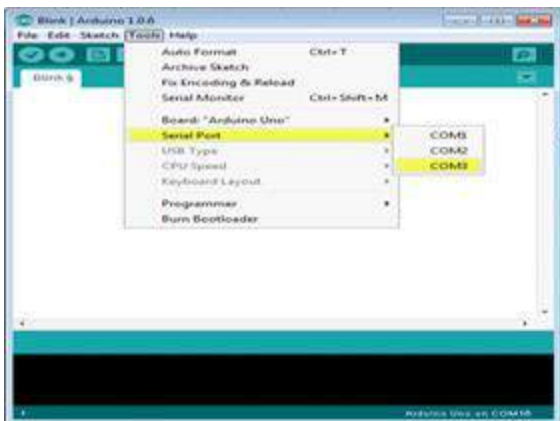


Figure 4 - 14 Selecting the Serial Port

Step 8 -Upload the program to the board:



Figure 4 - 15 Arduino IDE Toolbar

Before explaining how to upload our program to the board, we should know the function of each symbol appearing in the Arduino IDE toolbar.

- A. Used to check if there is any compilation error.
- B. Used to upload a program to the Arduino board.

- C. Shortcut used to create a new sketch.
- D. Used to directly open one of the example sketches.
- E. Used to save your sketch.
- F. Serial monitor used to send and receive the serial data from the board.

Now, simply click the "Upload" button in the environment. Wait few seconds; we will see the RX and TX LEDs on the board, flashing. If the upload is successful, the message " Done uploading" will appear in the status bar.

Program Structure

In this section, we will study in depth, the Arduino program structure and we will learn more new terminologies used in the Arduino world. The Arduino software is open-source. The source code for the Java environment is released under the GPL and the C/C++ microcontroller libraries are under the LGPL. Arduino programs are called "sketch".

Arduino programs can be divided in three main parts: Structure, Values (variables and constants), and Functions. Let us learn about the Arduino software program, step by step, and how to write the program without any syntax or compilation error. Let us start with the Structure. Software structure consist of two main functions:

Setup() function

Loop() function

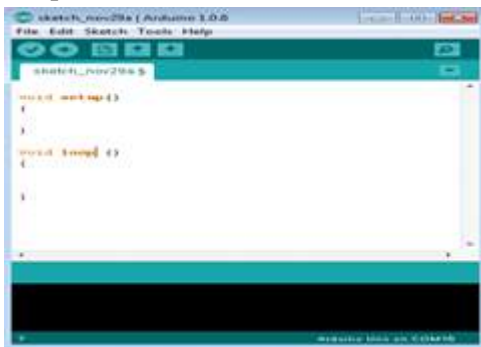


Figure 4 - 16 Structure of a Sketch

The setup () function is called when a sketch starts. It is used to initialize the variables, pinmodes, start using libraries, etc. The setup function will only run once, after each power up or reset of the Arduino board.

After creating a setup () function, which initializes and sets the initial values, the loop() function does precisely what its name suggests, and loops consecutively, allowing our program to change and respond. It actively controls the Arduino board.

Programming using Embedded C

C is a high-level programming language intended for system programming. Embedded C is an extension that provides support for developing efficient programs for embedded devices. Yet, it is not a part of the C language. In our internship program, we employed Embedded C programs to write sketches to be dumped on Arduino Uno.

Introduction to Embedded C

Embedded C programming language is an extension to the traditional C programming language that is used in embedded systems.

The only extension in the Embedded C language from normal C Programming Language is the I/O Hardware Addressing, fixed-point arithmetic operations, accessing address spaces, etc.

Basic Structure of Embedded C Program: The embedded C program has a structure similar to C programming. The five layers of Embedded C programming structure are:

- Comments
- Pre-processor directives
- Global declaration
- Local declaration
- Main function()

The whole code follows the below outline. This is the basic structure of the embedded c program. Each code has a similar outline. Now let us learn about each of this layer in detail.

Outline of an Embedded C code is as shown below:

1. Multiline Comments Denoted using `/*.....*/`
2. Single Line Comments. Denoted using `//`
3. Pre-processor Directives `#include` or `#define`
4. Global Variables Accessible anywhere in the program
5. Function Declarations. Declaring Function
6. Main Function. Main Function, execution begins here
7. {
8. Local Variables. Variables confined to main
9. function.
10. Function Calls. Calling Other Functions
11. Infinite Loop Like while (1) or for (;;) Statements
12.
13.
14. }
15. Function Definitions Defining the Functions
16. {
17. Local Variables. Local Variables confined to
18. this Function Statements
19.
20.
21. }

Comment Section: Comments are simple readable text, written in code to make it more understandable to the reader. Usually comments are written in `//` or `/* */`. Example: `//Test program`

Global Declaration Section: The global variables and the user-defined functions are declared in this part of the code. They can be accessed from anywhere.

void delay (int);

Local Declaration Section: These variables are declared in the respective functions and cannot be used outside the main function.

Main Function Section: All C programs need to have the main function. So does an embedded C program. Each main function contains 2 parts. A declaration part and an Execution part. The declaration part is the part where all the variables are declared. The execution part begins with the curly brackets and ends with the curly close bracket. Both the declaration and execution part are inside the curly braces.

Example:

```

1. void main(void) // Main Function
2. {
3. P1 = 0x00;
4. while(1)
5. {
6. P1 = 0xFF;
7. delay(1000);
8. P1 = 0x00;
9. delay(1000);
10. }
11. }

```

Function Definition Section: The function is defined in this section.

Arduino Code libraries – Library Structure

A library is a folder comprised with C++ (.cpp) code files and C++ (.h) header files.

The .h file describes the structure of the library and declares all its variables and functions.

The .cpp file holds the function implementation. –

Importing Libraries

The first thing to do is to find the library we want to use out of the many libraries available online. After downloading it to our computer, we just need to open Arduino IDE and click on Sketch Include Library Manage Libraries. We can then select the library we want to import. Once the process is complete the library will be available in the sketch menu.

Arduino Code Explanation Arduino code is written in C++ with an addition of special methods and functions. C++ is a human-readable programming language. When we create a ‘sketch’ (the name given to Arduino code files), it is processed and compiled to machine language.

Code Structure

The basic concepts which one should know to write a program on Arduino IDE are discussed below:

– Libraries

In Arduino, much like other leading programming platforms, there are built-in libraries that provide basic functionality. In addition, it’s possible to import other

libraries and expand the Arduino board capabilities and features. These libraries are roughly divided into libraries that interact with a specific component or those that implement new functions. To import a new library, we need to go to Sketch > Import Library.

In addition, at the top of our file, we have to use 'include' to include external libraries. We can also create custom libraries to use in isolated sketches.

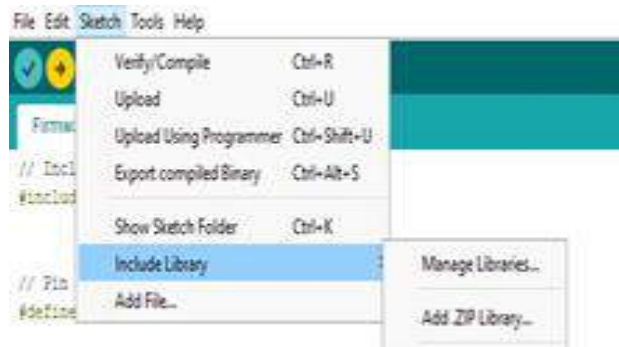


Figure 4 - 17 Include library

Pin Definitions

To use the Arduino pins, we need to define which pin is being used and its functionality. A convenient way to define the used pins is by using: 'define pinName pinNumber'. The functionality is either input or output and is defined using the pinMode () method in the setup section.

Declarations

Variables Whenever we're using Arduino, we need to declare global variables and instances to be used later on. In a nutshell, a variable allows us to name and store a value to be used in the future. For example, we would store data acquired from a sensor in order to use it later. To declare a variable, we simply define its type, name and initial value. It's worth mentioning that declaring global variables isn't an absolute necessity. However, it's advisable to declare variables to make it easy to utilize our values further down the line.

Instances

In software programming, a class is a collection of functions and variables that are kept together in one place. Each class has a special function known as a constructor, which is used to create an instance of the class. In order to use the functions of the class, we need to declare an instance for it.

Setup()

Every Arduino sketch must have a setup function. This function defines the initial state of the Arduino upon boot and runs only once. Here we'll define the following:

- * Pin functionality using the pinMode function
- * Initial state of pins
- * Initialize classes
- * Initialize variables
- * Code logic

Loop()

The loop function is also a must for every Arduino sketch and executes once setup () is complete. It is the main function and as its name hints, it runs in a loop over and over again. The loop describes the main logic of our circuit.

Code Logic

The basic Arduino code logic is an “if-then” structure and can be divided into 4 blocks:

Setup

It will usually be written in the setup section of the Arduino code, and performs things that need to be done only once, such as sensor calibration.

Input

At the beginning of the loop, read the inputs. These values will be used as conditions (“if”) such as the ambient light reading from an LDR using analogRead ().

Manipulate Data

This section is used to transform the data into a more convenient form or perform calculations. For instance, the AnalogRead () gives a reading of 0-1023 which can be mapped to a range of 0- 255 to be used for PWM. (See analogWrite ()).

Output

This section defines the final outcome of the logic (“then”) according to the data calculated in the previous step. Looking at an example of the LDR and PWM, turns on an LED only when the ambient light level goes below a certain threshold.

From Software to Hardware

There is a lot to be said of Arduino’s software capabilities, but it’s important to remember that the platform is comprised of both software and hardware. The two works in tandem to run a complex operating system. Code → Compile → Upload → Run At the core of Arduino, is the ability to compile and run the code.

After writing the code in the IDE we need to upload it to the Arduino. Clicking the Upload button (the rightfacing arrow icon), will compile the code and upload it if it passed compilation. Once the upload is complete, the program will start running automatically.

V. PROPOSED SYSTEM DESIGN (HARDWARE)

5.1. Detailed block diagram

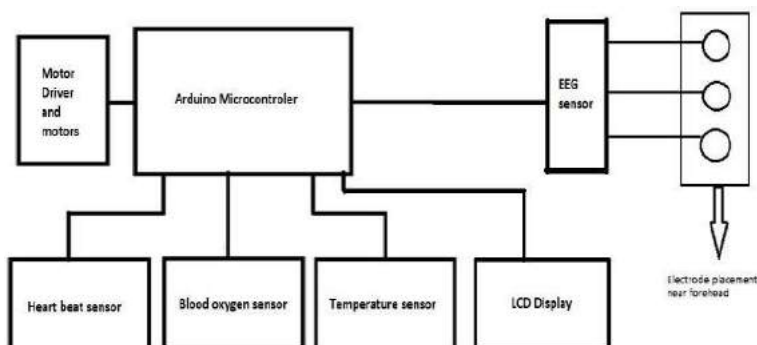


Figure 5 - 1 Block Diagram

5.2. Detailed design

The brain of the system is Arduino microcontroller. The system is designed to control the movement of wheel chair using EEG sensor. EEG sensor intercepts and measures the electrical signal sent by brain to control muscle movement. The electrodes from EEG sensors are attached near forehead when person tries to move eyes, The signal is intercepted. The system is de-signed to recognize different pattern of eye movement, like blinking, blinking fast, hard blink and these patterns are used to control the direction of wheel chair.

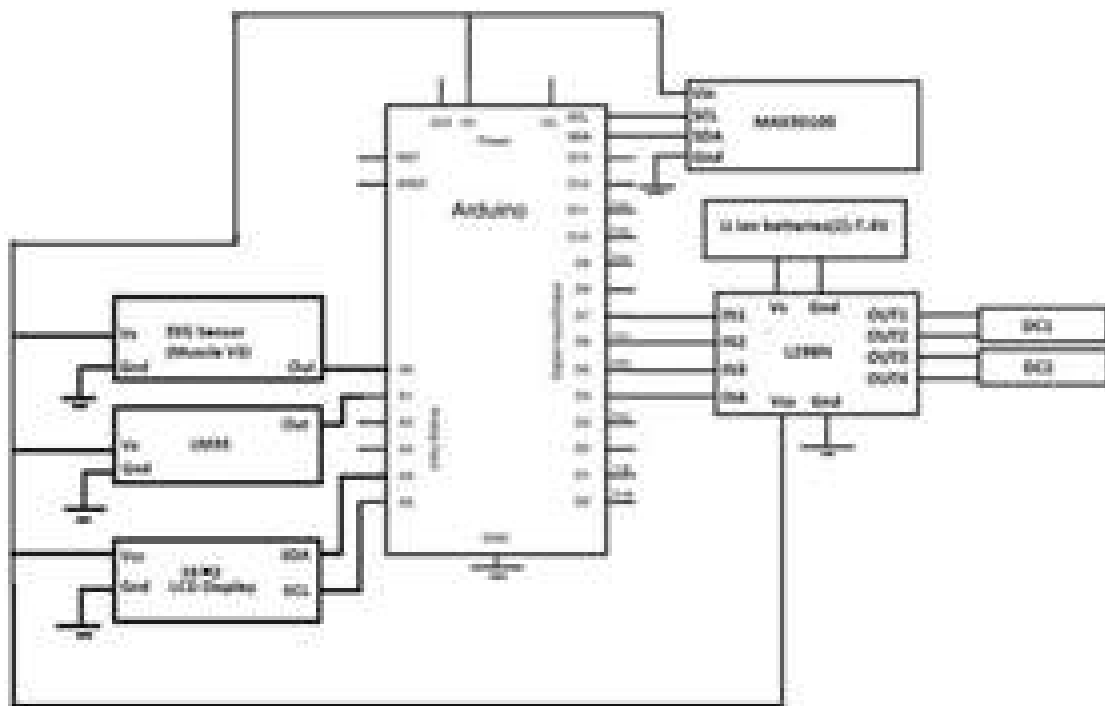
Various other sensors are used to monitor the health of the patient.

1. Heart beat sensor: The heart beat sensor is attached to micro controller, it measures the heart rate of patient, and if the heart rate is too low or high than the threshold value, micro controller gives alert sound.

2. Blood Oxygen Sensor: This sensor measures the oxygen concentration level in blood of patient. This is very important parameter to be checked because paralyzed patients don't have control on their lungs and other diseases like asthma may worsen the effect. If the measured value is less than threshold value an alert will be given by the system.

3. Temperature sensor: The body temperature of the patient is measured using this sensor, any abnormality in body temperature will be alerted.

5.3. Designed circuit



VI. PROPOSED SYSTEM DESIGN (SOFTWARE)

6.1. Flowchart

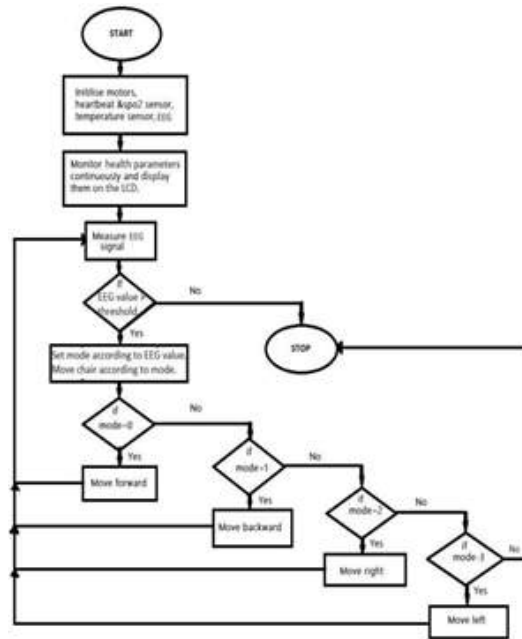


Figure 6-1 Flow chart

VII. RESULTS AND DISCUSSION

Project model result. CASE 1: Temperature and Heartbeat is measured continuously and displayed on LCD screen.

In this case, Temperature sensor reading showing 85 degrees Celsius.



Figure 7 - 1 Temperature sensor reading

In this case, MAX30100 sensor readings showing pulse rate as 102 bpm and oxygen concentration as 95%.



Figure 7 - 2 MAX30100 sensor readings

CASE 2: Direct modes can be changed by concentrating greater than 1 second and less than 2 seconds. The modes are FORWARD, BACKWARD, RIGHT and LEFT. • In this case, Display showing wheelchair moving in FORWARD direction



Figure 7 - 3 Display showing FORWARD movement

In this case, Display showing wheelchair moving in BACKWARD direction.



Figure 7-4 Display showing BACKWARD movement

In this case, Display showing wheelchair moving in LEFT direction.



Figure 7-5 Display showing LEFT direction

In this case, Display showing wheelchair moving in RIGHT direction.



Figure 7-6 Display showing RIGHT direction

CASE 3: The wheelchair can be moved in set direction mode by concentrating for more than 2 seconds.

Final Result Image

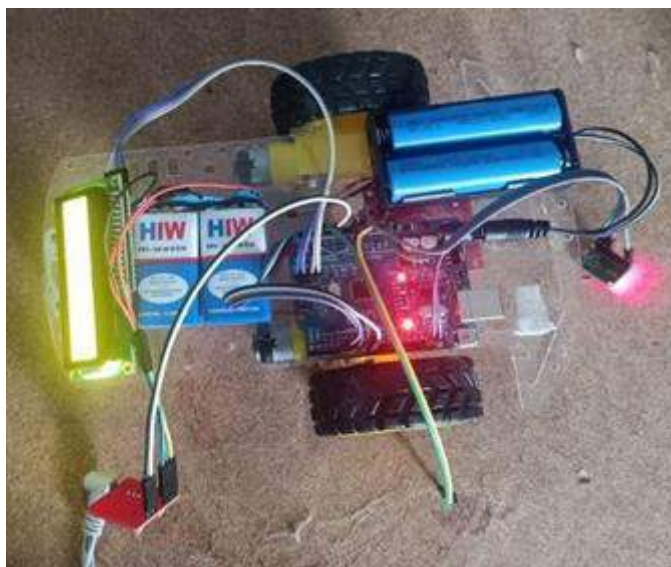


Figure 7-7 Working model of wheelchair controlled using brain as bio-sensor

Advantages

The wheel chair without the tiresome turning of the wheels is a simple step ahead of the electrical wheelchairs. It may prove beneficial for every individual for locomotion purposes without the need of manual labour. The simultaneous EEG acquisition may detect any substantial improvement in the condition of the body.

Disadvantages

The fixing of the electrodes must be done before any further course.
The mental state must be stable at all times.
Some training is must before it is fully efficient and used for practical purposes.

Applications

The developments in the field of brain computer interface are a juvenile step towards the improvement of the wheel chair.
The wheel chair controls only two wheels whereas the same condition may be used to drive a car with four wheels.
The functionality of the brain can be used to trounce many other manual works at industries as well as household levels.
The day today gadgets may be evolved to work using mind waves.

VIII. CONCLUSION

Appropriate assistive technology often helps people with disabilities compensate, at least in part, for a limitation. This specialized technology promotes independence and decreases the need for other support.

IX. REFERENCES

- [1]. Cecilia L. Maeder; Claudia Sannelli; Stefan Haufe; Benjamin Blankertz: PreStimulus Sensorimotor Rhythms Influence Brain- Computer Interface Classification Performance.
- [2]. Murat Akcakaya; Betts Peters; Mohammad Moghadamfalahi; Aimee R Mooney; Umut Orhan; Barry Oken; Deniz Erdogmus: Noninvasive Brain-Computer interfaces for Augmentative and Alternative Communication.
- [3]. C Guger, H Ramoser, G Pfurtscheller: Real time EEG analysis with subject-specific spatial patterns for a brain- computer interface (BCI).
- [4]. Md. Arif Abdulla Samy; Md. Mirazur Rahman; Tafsir Ahmed Khan:Extracting and discriminating selective brain signals in non-invasive manner and using them for controlling a device: A cost-efficient approach to brain computer interface (BCI):Publisher: IEEE.
- [5]. R. S. Naveen; Anitha Julian:Brain computing interface for wheel chair control:Publisher: IEEE.
- [6]. Nafiul Hasan; Md. Mahmudul Hasan; Md. Akramul Alim:Design of EEG Based Wheel Chair by Using Color Stimuli and Rhythm Analysis Publisher: IEEE.
- [7]. Danny Wee-Kiat Ng; Ying-Wei Soh; Sing-Yau Goh:Development of an Autonomous BCI Wheelchair Publisher: IEEE.
- [8]. C. S. Ashwin; K. R. Rangarajan; S. Ramachandran:Disance (enhance the disabled) brain mapped mobility for physically challenged Publisher: IEEE.
- [9]. Lamiya Rahman; Jannatul Adan; Quazi Mutasim Billah; Md Kamrul Islam; A.H.M Mostafa Kamal; Sazzad Hossain:A low- cost Human Computer Interface for Disabled People based on Eye Blink detection using Brain Signal :Publisher: IEEE.
- [10].Soumya Sen Gupta; Sumit Soman; P. Govind Raj; Rishi Prakash: Detecting eye movements in EEG for controlling devices Publisher: IEEE.



Development of a 2D-DWT based Image Compression and Decompression Algorithm

Nandeesh R¹, Shanmugam M¹

¹Assistant Professor, Department of ECE, Government Engineering College, Krishnarajapete-571426, Mandya, Karnataka, India

ABSTRACT

The rapid growth of digital imaging, especially in the fields of hospital, education, and e-commerce, has made data maintenance and transmission over networks a difficult task. So, the development and use of image compression techniques have become essential for overcoming the problems of storage and transmission of digital image data. In this paper, an efficient discrete wavelet transform (DWT) architecture for image compression is presented. The proposed scheme of DWT with capacity of compressing and reconstructing image data without data loss. Using DWT which has better reconstruction quality and also better compression. The difficulties posed by transfer of large file sizes in image processing will be reduced and method gives better accuracy in compression and reconstruction. The simulation is done in MATLAB, applied method to various popular images and obtained promising PSNR, CR, and SSIM that highlight the advantages of our approach and the efficiency of our algorithms.

Keywords— DWT, MATLAB, 2D-DWT, Huffmancoding, scalarquantization, Image compression, Image Decompression.

I. INTRODUCTION

For image compression, transform-based compression demonstrates greater robustness than spatial domain-based compression. Image compression is data compression method applied to digital images, in order to reduce the cost for storage or transmission. The aim is to reduce the number of bits required to represent an image by removing the spatial and spectral components to lowest possible level. During image compression the redundancy and irrelevancy in the image will be reduced. It aims in reducing the size of multispectral image using image compression techniques. The objective is to reduce the transmission and storage requirements of image data.

The two types of compression which describes image compression are:

Lossless compression: In this compression type it reduces the image size by changing the way in which the data is stored. Therefore this type of compression will make no changes in your image. The noise will not be added to the image.

Lossy compression: In this Compression type, the size of the image will be reduced by removing some data from it which in turn reduces the quality of the image but will not affect the quality of that image [5]. The compression ratio of data loss, however, is very high, but it suffers from lossy compression. Yet this is a high compression ratio, really. In the lossless compression method, the decompressed image is identical to the original one, but with the compression ratio [2]. Discrete cosine transform (DCT) is one of the most popular transforms in image processing. It is widely used for image compression because of its high energy packing capabilities. The spatial domain image is converted into frequency domain image using DCT. Image is represented as a sum of sinusoidal of varying magnitudes and frequencies. At high data compression ratio, DCT is capable of achieving higher quality. This property is termed as energy compaction. Lossy image compression uses discrete cosine transform for image compression. [5] Lossless compression techniques, on the other hand, conserve all the information of the original image even after compression. Fractal algorithm is an example of Lossy Compression. Discrete Wavelet Transform (DWT) and Huffman Coding are Lossless Image Compression techniques. Discrete wavelet converts the image into four separate frequency bands called LL, LH, HL, and HH, where image characteristics are reflected by LL sub-bands and signal noise is shown by HH sub-bands [2]. DWT is used to separate the image into a pixel. DWT is used in signal and image processing especially for lossless image compression. DWT is also used for Lossy compression. The Lossless image compression is mostly used in DWT Lossless image compression give the good quality of the image and also the compression ratio of the image also good. The PSNR ratio of the image is also good in the Lossless compression. In this technique lossless gives the best compression result. The PSNR value of Lossless Image is good quality. The lossless image compression ratio was good, and also the quality of the lossless image compression also good. The aim of this study is to propose a technique based on Discrete Wavelet Transforms and Scalar Quantization to compress grayscale images in an efficient manner to achieve high compression ratios and high quality.

II. RELATED WORK

S. Nosratian, M. Moradkhani and M. B. Tavakoli have proposed an approach that provides security and compression for data and emphasizes the use of the fuzzy Huffman coding algorithm for compression and the use of fuzzy logic encryption for data security.[1] Their proposed method uses a fuzzy logic mechanism based on the frequency of the symbols to determine Huffman compression weights. These symbols are derived from the classification of information codes that are moved by fuzzy logic for data security under a dedicated key. Their proposed method uses symmetric key encryption. In fact, it uses a public key for encryption that based on the data structure, the number of symbols and this public key, a proprietary key that varies for each data set is achieved and security encryption and decryption is done based on this key. Their proposed method has been tested under matlab2017b software for image and text information data and shows that it has been successful in data compression and security [1].

Rajiv Ranjan in “Canonical Huffman Coding Based Image Compression using Wavelet” [4] have combined DWT with Canonical Huffman Coding to get a highly compressed reconstructed image and compared the results and parameters with other Huffman Coding method. To do so, it has tested many well-known images cited in relevant literature at slice resolutions of 256×256 , considering it to be the minimum industrial

standard size. It has been matched that computing time and codebook size with Huffman coding to establish the superiority of Canonical Huffman coding. [4]

III. METHODOLOGY

Proposed DWT architecture is designed by choosing 3 levels of discrete wavelet decomposition. Image is taken through 3 levels of discrete wavelet decomposition. The compressed image is reduced in bit size using the Huffman coding system. Huffman coding is based on the frequency of occurrence of a data item (pixel in images). The principle is to use a lower number of bits to encode the data that occurs more frequently. Codes are stored in a Code Book which may be constructed for each image or a set of images. To ensure accurate decoding, the encoded sequence along with their code is used by the decoder to successfully recover the original data. To restore the image, the compressed image goes through a reverse of the compression process. The Huffman encoded data is first decoded to recover the indexes. Inverse discrete wavelet transform (IDWT) is applied to get back the original image.

A. Proposed Block Diagram.

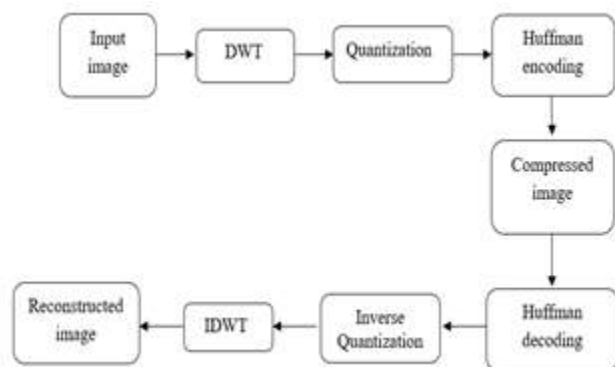


Fig 1. Block diagram of proposed system.

Image is taken through 3 levels of discrete wavelet decomposition, three level decomposition of image, the approximation and detail coefficients are obtained. These coefficients are quantized after that the quantized coefficients are coded in a bit stream using Huffman coding and compressed data is obtained.

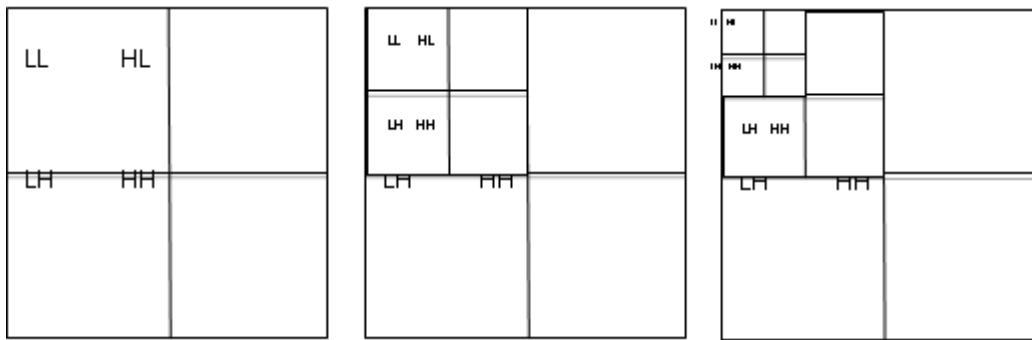
To decompress images, compressed data is decoded and then Inverse quantized. In this step wavelet coefficient are obtained. Using inverse discrete wavelet transform original image is reconstructed.

B. Discrete Wavelet Transform

The Discrete Wavelet transform (DWT) can decompose images into various multi-resolution sub bands [4]. Basically, the low frequency coefficients contain the most energy of the image, while the high frequency coefficients reflect the significant visual information.

The vital key role of the decomposition procedure is separating the low frequency coefficients from the high frequency to a small number of coefficients. Meanwhile, the remaining coefficients have been quantized

indecently or minimized to zero with insignificant image distortion. Sub bands for 3-levels Haar filter as a basic function of the wavelet decomposition [4]. The figure 2 shows the decomposition of image.



a) Single level decomposition b) Two level Decomposition c) Three level Decomposition

Figure 2. Decomposition of image in 3 levels

Three Level Decomposition of Image.

- Apply the DWT transformation on the input image to get four sub-bands; LL, LH, HL, and HH. The approximation sub-band is the LL sub-band.
- Transforming LL sub-band again to gain a new set of sub-bands and that LL sub-band is also transformed. This ensures that the input grayscale image goes through three levels of decomposition. At last LL band obtained at level three decomposition is used for further process.

C. Quantization

Quantization, involved in image processing, is a lossy compression technique achieved by compressing a range of values to a single quantum value.

Quantization step is applied at the cost of image quality to the sub-band coefficients produced by the DWT to reduce the number of bits needed to represent them. The output is a sequence of integer numbers which must be encoded bit-by-bit. The quantization steps according to different bands are tuning to control the quality of reconstructed image. For the high compression ratio, the large quantization step is required but this lead to degrade the image quality and the technique will be lossy. With no quantization step the compression is lossless. To maintain the image quality, the approximation coefficients (LL) need the smaller step of quantization.

Quantization is the process of reducing the number of bits needed to store an integer value by reducing the precision of the integer.

Quantization is of two types:

- Scalar quantization
- Vector quantization

As we compare to Vector Quantization Scalar quantization has less complexity, therefore we have used scalar Quantization for quantizing the Image.

Scalar quantization is a phenomenon on which, each pixel is quantized either by reducing the number of gray levels or by reducing the resolution.

Gray level is defined as

$$L = 2^K$$

Gray level = number of bits per pixel (BPP). (K in the equation)

D. Huffman coding

Huffman coding is an entropy encoding algorithm used for lossless image compression. Huffman coding is efficient technique for image compression to some extent [11]. The Huffman encoding starts with calculating the probability of each symbol in the image. The symbols probabilities are arranged in descending order [11]. Huffman coding is one of the basic compression method that have proven useful in image and video compression standards. When applying Huffman encoding technique on an image, the source symbols can be either pixel intensities of the image or the output of an intensity mapping function. Huffman coding is a lossless data compression algorithm where each character in the data is assigned a variable length prefix code. This can be applied for different values whereas the run length only works for the data that have repeated values. This coding could compress the data significantly if certain symbols occur more frequently than others, whereas LZW is not going to be able to compress the data very well. After Huffman encoding, we get encoded data and dictionary that will be used in reconstruction process.

E. Proposed Algorithm

Compression Process

1. Read the input grayscale image.
2. Apply 2-DWT on image for decomposing into four Sub-bands (LL, LH, HL, and HH).
3. Consider LL sub-band (Approximation coefficients), Apply 2-DWT for another two levels and get the resultant image LL3
4. Apply Scalar Quantization on LL3
5. Apply Huffman encoding on Quantized Image to get Encoded Data and calculate encoded length

Decompression Process

6. Encoded data is decoded using Huffman Decoding process and Image is obtained after reshaping Decoded Data.
7. Inverse Quantization is applied on Decoded Image.
8. IDWT is used for reconstruction by using Inverse Quantized image and other Zero filled Sub-bands, IDWT is applied for 3 times .
9. Calculate SSIM, PSNR, Original image length, Encoded Length and Compression Ratio for the input and Reconstructed Image.

IV. PERFORMANCE EVALUATION

The performance of compression methods can be estimated with the help of certain indicators mentioned below.

Peak-Signal-to-noise-ratio (PSNR):

PSNR is a standard measure for computing the quality of the compressed image.

For the general case of 8-bits images, the PSNR [4] is expressed as

$$psnr(dB) = 10 \log_{10} \left(\frac{255^2}{mse} \right) \text{ ----- (1)}$$

Where worth 255 is the maximum possible value that can be attained by the image signal.

MSE in Eq. (2) [4] denotes the mean squared error of the image expressed as

$$mse = \frac{1}{n} \sum_i \sum_j (X(i,j) - Y(i,j))^2 \text{ ----- (2)}$$

MSE = 1/n, Here n is the total number of pixels, Y (i, j) indicates the pixel value in the compressed image and X (i, j) expresses a pixel value in the original image.

Compression Competence

Compression ratio (C.R) [4] is a scale for measuring compression competence, which is defined.

Mathematically as follows:

$$C.R = \frac{Y_{compressed}}{X_{original}} \text{ ----- (3)}$$

Where $Y_{compressed}$ is the dimension of the compressed image data and $X_{original}$ is the dimension (numeral of bits) of the original image data.

V. RESULTS AND COMPARISION

A. Lena image

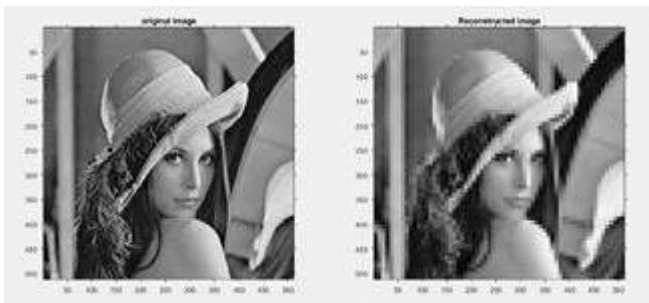


Image	SSIM	PSNR	Compressed length	Compression Ratio
Lena	0.6318	23.664	30083	98.4375

B. Results

We have considered various images for the experimentation and obtained the result as shown in Table I and Table II.

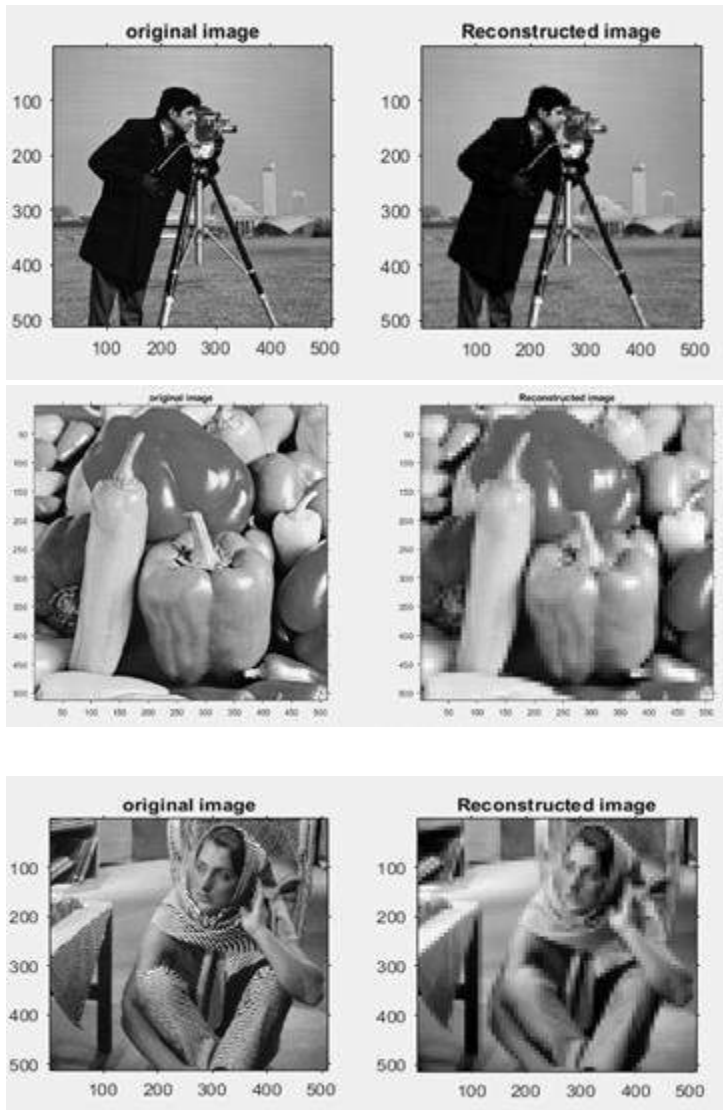
C. Result table

Image (512X512)	SSIM	PSNR	Compressed length	Compression Ratio
Lena	0.632	23.66	30083	98.4375
Cameraman	0.705	22.21	28678	98.4375
Barb	0.499	21.81	30009	98.4375
Peppers	0.606	22.85	30860	98.4375

Fishing-boat	0.499	22.04	28867	98.4375
--------------	-------	-------	-------	---------

TABLE I. RESULT OBTAINED FOR DIFFERENT IMAGES

D. Images



VI. CONCLUSION

The proposed scheme uses DWT based-compression technique to compress and decompress image for reduced transmission times with superior data compressibility. DWT is used for decompose the image and the wavelet coefficients are then encoded with use of Huffman encoding after the quantization. The usage of wavelet and Huffman encoding ensure the compression performance. Our proposed method provides 98% compression ratio and high SSIM. Scalar quantization helps to reduce the number of bits required to represent the image pixel value. Further Huffman coding reduces the bits required to represent an image and Inverse is applied to get the reconstructed image which has high similarity index. The values of PSNR and CR received through our

algorithm and their comparison with such values produced by competing methods justify our expectations. We can therefore conclude that our method can prove to be extremely beneficial for the storage and transmission of image data over digital networks.

VII. REFERENCES

- [1]. S. Nosratian, M. Moradkhani and M. B. Tavakoli "Hybrid data compression using fuzzy logic and Huffman coding in secure IOT",2021.
- [2]. Nancy Awadallah Awad and AmenaMahmoud "Improving Reconstructed Image Quality via Hybrid Compression Techniques",2021.
- [3]. Rajaa Khalaf Gaber, Ahmed Abdulqader Hussein, Manal Kadhim Oudah and Ahmed Hameed Reja "Image Compression Using High Level Wavelet Transformer with Non Uniform Quantizer and Different Levels Human Codes",2020.
- [4]. Rajiv Ranjan "Canonical Huffman Coding Based Image Compression using Wavelet" in 2020.
- [5]. Prasantha H S and Likitha C Raju "An Approach For Multispectral Image Compression" in 2020.
- [6]. Ankur Gupta , Muskan Garg , Apurv Verma, Dushyant Kaushik "Implementing lossless compression during image processing by integrated approach" in 2020.
- [7]. Sukhendu Janaa, Soumaya Mandalb " Dwt Based Image Compression Using Quadtree Decomposition And Huffman Encoding" in 2020.
- [8]. Jan Carlo T. Arroyo¹, Charisse P. Barbosa, Meljohn V. Aborde, Fe B. Yara⁴, Allemar Jhone P. Delima "An Improved Image Steganography through Least Significant Bit Embedding Technique with Data Encryption and Compression Using Polybius Cipher and Huffman Coding Algorithm" in 2020.
- [9]. Anu Sri¹, Sitanshu Sekhar Sahu " Improved fractal-SPIHT hybrid image compression algorithm", 10th ICCNT 2019.
- [10]. Mohammed Babatunde Ibrahiim, Kazeem Allagbe Gbollagade "Performance Enhancement of Huffman coding Image Compression with Chinese Remainder Theorem", Anale. Seria Informatică. Vol. XVII fasc. 2 – 2019.
- [11]. Md. Atiqur Rahman & Mohamed Hamada,"A semi-lossless image compression procedure using a lossless mode of JPEG", 2019 IEEE.
- [12]. Shree Ram Khaitu¹, Sanjeeb Prasad Panday "Fractal Image Compression Using Canonical Huffman Coding" Journal of the Institute of Engineering January 2019.
- [13]. Rana Krisnanda, Irma Safitri, Achmad Rizal "Huffman Coding Medical Image Watermarking with Compressive Sensing L1 Norm". 2018 ICITISEE
- [14]. Arka Provo Mukhopadhyay, Saurav Mohapatra, Budhaditya Bhattacharya,"ROI based Medical Image Compression using DWT and SPIHT Algorithm" 2019 ViTECoN.
- [15]. Tresor Oteko Lisungu, Mbuyu Sumbwanyambe "Image Compression-Encryption Scheme Based on 2D DWT, SPIHT and Qi Hyper-chaos" 2019 SAUPEC/RobMech/PRASA Conference
- [16]. Abhilasha Sharma, Sarita S. Bhadauria, Rekha Gupta "Image Compression and Sparsity Measurement by using Multilevel and Different Wavelet Functions", I-SMAC 2019

- [17]. Tewelde Tekeste, Pallavi Gupta “Selection of Lifting Scheme based Wavelet Filters for Image Compression in Resource Constrained Wireless Multimedia Sensor Networks”, 2019 ICCIS.
- [18]. Fauhan Handay Pugar and Aniati Mumi Arymurthy “Blind Color Image Watermarking Based on 2-level Discrete Wavelet Transform, M-ary Modulation, and Logistic Map” 2019 ICTS.
- [19]. Chuxi Yang , Yan Zhao, (Member, Ieee), And Shigang Wang “Deep Image Compression in the Wavelet Transform Domain Based on High Frequency Sub-Band Prediction” 2019.
- [20]. Taranath N L, C.K.Subbaraya, Darshan L M, Gopalakrishna C, Sourabh Saklecha, Varun A S, Sandesh S “Image Compression and Decompression using Fence Decimation” 2019
- [21]. Yusra Salih ,Loay E. George, “Improved Image Compression Scheme Using Hybrid Encoding Algorithm” in 2019.
- [22]. P .Sreenivasulu Dr S.Varadharajan “Medical Image Compression Using DCT based MRG Algorithm”, ICSSIT 2019.
- [23]. N. Varuna Shree T. N. R. Kumar “Identification and classification of brain tumor MRI images with feature extraction using DWT and probabilistic neural network”, Brain Informatics 2018.
- [24]. S. Boopathiraja1, P. Kalavathi “A Near Lossless Multispectral Image Compression using 3D-DWT with application to LANDSAT Images”, Vol-6, Special Issue-4, May 2018 E-ISSN: 2347-2693.
- [25]. Sandhya Kadam and Vijay Rathod “Medical and Color Image Compression with Fractal Quadtree with Huffman Coding for Different Threshold Values”, Springer Nature Singapore Pte Ltd. 2019.
- [26]. Irma Safitri Ratri Dwi Atmaja Azharudin Hidayat “Wavelet Huffman Coding Image Watermarking in the Presence of Compressive Sensing”, 2018 3rd International Conference on Information Technology, Information Systems and Electrical Engineering (ICITISEE), Yogyakarta, Indonesia.
- [27]. Paul Nii Tackie Ammah, Ebenezer Owusu “Robust medical image compression based on wavelet transform and vector Quantization”, Informatics in Medicine Unlocked 15- 2019.
- [28]. Jones T, Townsend DW. History and future technical innovation in positron emission tomography. J Med Imaging 2017;4:011013.
- [29]. Reinhard E, Heidrich W, Debevec P, Pattanaik S, Ward G, Myszkowski K. High dynamic range imaging: acquisition, display, and image-based lighting. Morgan Kaufmann; 2010.
- [30]. Al-Qershi OM, Khoo BE. High capacity data hiding schemes for medical images based on difference expansion. J Syst Softw 2011;84:105–12.
- [31]. Hashem IAT, Yaqoob I, Anuar NB, Mokhtar S, Gani A, Khan SU. The rise of “big data” on cloud computing: review and open research issues. Inf Syst 2015;47:98–115.
- [32]. House MJ, Bangma SJ, Thomas M, Gan EK, Ayonrinde OT, Adams LA, Olynyk JK, St Pierre TG. Texture-based classification of liver fibrosis using MRI. J Magn Reson Imaging 2015;41:32



Statistical Assessment of Water Quality Parameters for Bellandur Lake Water, Bangalore Urban Area

Ramesh. N

Department of Civil Engineering, Government Engineering College, K R Pet -571426, Karnataka, India

ABSTRACT

Statistical techniques such as Karl Pearson's coefficient of correlation and Principal Component Analysis (PCA) were used to analyze the data. Fifteen variables for twelve sampling locations used to evaluate the status of the water quality. The correlation co-efficient of pH, calcium, magnesium, alkalinity, sulphate, DO, BOD and COD were significantly correlated with a large set of variables and the BOD and COD are significantly negative correlation with other physico-chemical parameters. There is a high positive correlation of 0.99 between BOD and COD. The Principal Component Analysis (PCA) showed that the eigenvalues of the first 2 components accounts for 55% in the total variance whereas first four components accounted for almost 79% of the total variations. The PCA biplot axis 1 and 2 together 96.81% of variation in the physico - chemical parameters of the 12 sampling sites are consistently different in their characteristics.

Keywords: Water quality, Correlation, Principal Component, Biplot, Lake Water

I. INTRODUCTION

Statistical techniques such as Karl Pearson's coefficient of correlation and Principal Component Analysis (PCA) interpret the data. They help to better understand the behaviour of the water body [1]. Karl Pearson's correlation analysis will indicates the relationship between various physico-chemical parameters. The correlation coefficient indicates positive and negative correlation with each other. Positive correlation mean, one parameter increase with increase in other parameters and negative correlation mean one parameter increase with other parameters decrease [2]. The PCA was developed to summarize and it reduces a multidimensional complex data set into two or three dimensions by computing principal component. In study PCA was used to produce an ordination of independent descriptors based on water quality parameters [3]. The Bellandur lake water is an important source for the activities of drinking, fishing, recreation, cultural etc., in Bangalore urban area. There are different factors including sewage and industrial wastes which are posing threat on water quality of the lake water. The purpose of this study to assess the relationship between the various analyzed physico-chemical parameters applies statistical techniques such as pearson's correlation coefficient and PCA.

II. MATERIALS, METHODS AND DATA ANALYSIS

Investigations involving a large number of observed variables can often be simplified by considering a smaller number of linear combinations of the original values, with a Standardized Linear Combination (SLC), it is possible to make meaningful comparisons between various choices of linear combinations. PCA finds a set of SLC called the Principal Components (PCs), which taken together can explain all the variables obtained by multiplying the original correlated variables with a list of coefficients (loadings or weightings). There are generally as many PCs as variables. However, because of the way they are calculated, it is usually possible to consider only a few of them which together explain most of the original variation. PCA therefore imparts information on the most important parameters, explaining the whole data set while permitting data reduction with the least amount of loss of original information it is a potent method for pattern detection that attempts to explain the variance of a huge set of inter-correlated variables and convert them into a smaller set of independent (uncorrelated) variables (PCs). The correlation coefficient matrix determines how well the variance of each element can be explained by each relationship with each of the others (4). A rotation of principal components can achieve a simpler and more meaningful representation of the underlying factors by decreasing the contribution to PCs of variables with minor significance and increasing the more significant ones (5).

PCA is one of the best statistical techniques for extracting the linear relationships between sets of variables. PCA are linear combinations of original variables and are the eigen vectors (6). The analysis was applied to assess the significance of parameters that explain the patterns of the monitoring stations on the basis of water quality parameters. The correlation matrix consists of 15 water quality parameters.

Data Analysis

A statistical technique such as Pearson's correlation and PCA were used to evaluate the water quality of Bellandur lake. SAS 9.3 software was used to carry out the analysis. Proc princomp and proc prinqual procedure are used to get correlation matrix, eigenvalues, scree plot and biplot.

III. RESULTS AND DISCUSSION

In this study, statistical methods including correlation matrix (Pearson's correlation) and principal component analysis were applied to a data set obtained from the analytical data.

Correlation matrix

The spatial correlation matrix of the water quality parameters obtained using the Spearman coefficient is shown in table No.1. There exists good and strong correlation between the parameters if r more or equal to The 15 variables generated 121 correlation coefficients when analyzed in pairs and 31 were statistically significant [9]. According to table-1, all the variables are correlated with each other. The variables that showed only one significant correlation were EC with calcium (0.43). Some variables had a moderate number of significant correlations. Turbidity is positive correlation with alkalinity. The TDS showed significant positive correlation

with pH (0.51), total hardness (0.97) and magnesium (0.77). The pH showed significant positive correlation with TDS (0.51), total hardness (0.48), magnesium (0.57), alkalinity (0.41), DO (0.43) and negative correlation with BOD (-0.42) and COD (-0.40). The total hardness showed significant positive correlation with TDS (0.97), pH (0.48) and magnesium (0.67). The calcium showed significant positive correlation with EC (0.43), BOD (0.41), COD (0.42) and negative correlation with sulphate (-0.46). The magnesium showed significant positive correlation with TDS (0.77), pH (0.57), TH (0.67), alkalinity (0.46), DO (0.61) and negative correlation with BOD (-0.56) and COD (-0.56). The alkalinity showed significant positive correlation with turbidity (0.48), pH (0.41), magnesium (0.46), chloride (0.59), phosphate (0.54) and negative correlation with nitrate (-0.43). The sulphate is positive correlation with DO (0.47) and significant negative correlation with calcium (-0.46), BOD (-0.42) and COD (-0.45). The nitrate is significant negative correlation with alkalinity (-0.43), chloride (-0.60) and phosphate (-0.62). The chloride is significant positive correlation with alkalinity (0.59) and DO (0.42) and negative correlation with nitrate (-0.60). The phosphate is positive correlation with alkalinity (0.54) and negative correlation with nitrate (-0.62). The DO is significant positive correlation with pH (0.43), magnesium (0.61), sulphate (0.47), chloride (0.42) and negative correlation with BOD (-0.92) and COD (-0.94). The BOD is positive correlation with calcium (0.41) and COD (0.99) and significant negative correlation with pH (-0.42), magnesium (-0.56), sulphate (-0.42) and DO (-0.92). The COD is positive correlation with calcium (0.42) and BOD (0.99) and significant negative correlation with pH (-0.40), magnesium (-0.56), sulphate (-0.45) and DO (-0.94). Examples of the above mentioned pattern were compared with the pH, calcium, magnesium, alkalinity, sulphate, DO, BOD and COD were significantly correlated with a large set of variables.

The correlation co-efficient that of BOD and COD are negative correlation with other water quality (physico-chemical) parameters namely turbidity, total dissolved solids, pH, total hardness, magnesium, sulphate, nitrate, chloride and dissolved oxygen might be due to different pollution loads from different origin.

The physico-chemical properties showed significant correlations except few with the sulphate, nitrate, BOD and COD. There is a high positive correlation of 0.99 between BOD and COD. This implies that BOD is derived from COD.

Principal Component Analysis

The principal component analysis biplot graph executed on 15 variables for 12 sampling locations in order to identify quality of lake water were performed measured on physico-chemical parameters of Bellandur lake. Each observed variable contributes one unit of variable to the total variance in the data set. Any component that displays an eigenvalue greater than 1.0 is accounting for a greater amount of variance and is retained; the remaining factors have eigenvalues of less than unity [8]. Eigenvalues greater than one was taken as criterion for extraction of the principal components required to explain the variance in the data. The obtained factor loading values and variance calculated by the PCA are tabulated in table 2 and the figure 1 shows the scree plot of the eigenvalues of principal component. The first component accounted for one third of all the variance in the data (32%). Second component accounted for one fourth of all the variance in the data (23%). First two components (with eigenvalues of 4.86 and 3.39) accounted for 55% in the total variance where as first four components accounted for almost 79% and rest of the components accounted for 21%. The scree plot is a graph

of eigenvalues in decreasing order. The y-axis has shows the eigenvalue and the x- axis show their principal component in order is as shown in figure 1.

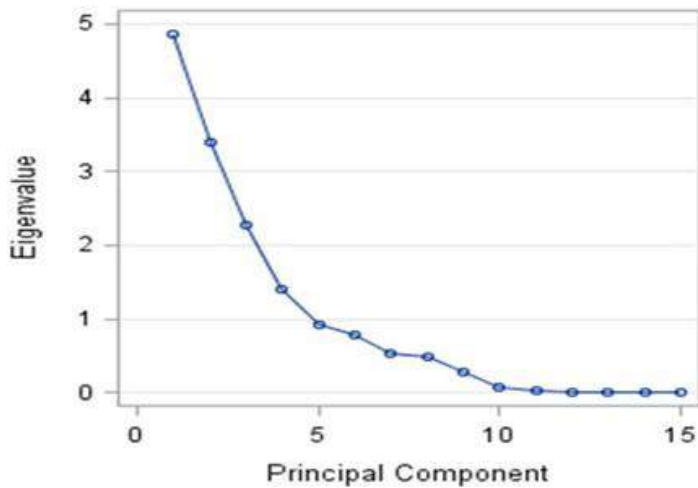
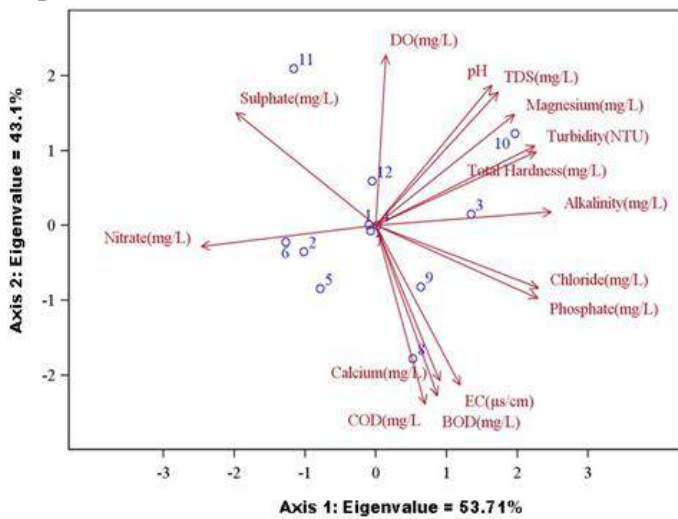


Figure 1. Scree-plot for the principal component analysis

The PCA biplot analysis performed on the entire set of measured physico- chemical parameters [3,7] of Bellandur lake showed in figure 2. Biplot showed a projection of the initial variables in the factor space. Variables on right side showed positive correlation among themselves but negative correlation with the factors on left side [1]. The PCA axis 1 and 2 together 96.81% of variation in the physico- chemical parameters of the 12 sampling sites are consistently different in their characteristics. The parameters DO, pH, TDS, magnesium, turbidity, total hardness, alkalinity, chloride, phosphate, electrical conductivity, BOD, COD and calcium which is positively associated with physico- chemical parameters. The gradient was negatively associated with sulphate and nitrate.



Arrows represent variables

◦ Symbols represent sampling sites

Figure 2. Biplot of standardized PCA-analysis performed on entire set of physico- chemical parameters of Bellandur lake

TABLE 1. CORRELATION MATRIX OF THE 15 PHYSICO- CHEMICAL PARAMETERS OF BELLANDUR LAKE.

	TU	EC	TDS	pH	TH	Ca	Mg	ALK	SO ₄	NO ₃	Cl	PO ₄	DO	BOD	CO D
TU	1														
EC	0.27	1.00													
TDS	0.24	0.31	1.00												
pH	0.32	0.31	0.51	1.00											
TH	0.15	0.29	0.97	0.48	1.00										
Ca	0.30	0.43	0.13	-0.14	-	1.00									
Mg	0.27	-	0.77	0.57	0.67	-0.08	1.00								
ALK	0.48	0.16	0.37	0.41	0.28	0.16	0.46	1.00							
SO ₄	-0.33	-	-	-0.07	-	-0.46	-0.07	-0.18	1.00						
NO ₃	0.33	0.17	0.05	-0.27	0.02	0.27	-0.08	-0.43	-0.08	1.00					
Cl	0.32	0.17	0.30	0.33	0.27	0.05	0.30	0.59	-0.05	-0.60	1.00				
PO ₄	-0.26	-	0.29	-0.04	0.20	0.27	0.32	0.54	-0.27	-0.62	0.35	1.00			
DO	0.16	-	0.38	0.43	0.37	-0.36	0.61	0.02	0.47	-0.06	0.42	-	1.00		
BOD	-0.24	0.02	-	-0.42	-	0.41	-0.56	0.06	-0.42	-0.04	-0.27	0.33	-	1.00	
COD	-0.14	-	-	-0.40	-	0.42	-0.56	0.12	-0.45	-0.05	-0.23	0.32	-	0.99	1.00
		0.02	0.29		0.29								0.94		

TU = Turbidity; EC = Electrical Conductivity; TDS = Total Dissolved Solids; TH= Total Hardness; Ca = Calcium; Mg = Magnesium; ALK = Alkalinity; SO₄ = Sulphate; NO₃ = Nitrate; Cl = Chloride; PO₄ = Phosphate; DO = Dissolved Oxygen; BOD = Biological Oxygen Demand; COD = Chemical Oxygen Demand

TABLE 2. FACTOR LOADING VALUES AND VARIANCE.

Parameter	PC1	PC2	PC3	PC4
Turbidity	0.166	0.144	0.352	0.485
EC	0.083	0.200	0.340	0.158
TDS	0.334	0.229	0.140	-0.382
pH	0.326	0.083	0.027	0.093
Total Hardness	0.317	0.178	0.114	-0.428
Calcium	-0.096	0.333	0.277	0.122
Magnesium	0.387	0.088	-0.015	-0.231
Alkalinity	0.191	0.355	-0.179	0.291
Sulphate	0.048	-0.389	-0.219	0.060
Nitrate	-0.077	-0.132	0.588	-0.139
Chloride	0.251	0.181	-0.246	0.407
Phosphate	0.030	0.362	-0.399	-0.202
DO	0.375	-0.262	-0.029	0.059
BOD	-0.345	0.314	-0.043	-0.123
COD	-0.346	0.322	-0.042	-0.031
Eigenvalues	4.86	3.39	2.27	1.40
Total Variance (%)	32	23	15	9
Cumulative Variance (%)	32	55	70	79

IV. CONCLUSION

In this study correlation matrix and principal component analysis were applied to analytical water quality data of physico-chemical parameters of Bellandur lake. The correlation coefficient indicates positive and negative correlation of physico-chemical parameters with each other.

The correlation co-efficient of pH, calcium, magnesium, alkalinity, sulphate, DO, BOD and COD were significantly correlated with a large set of variables. The BOD and COD are significantly negative correlation with other physico-chemical parameters might be due to different pollution loads from different origin. There is a high positive correlation of 0.99 between BOD and COD. This implies that BOD is derived from COD.

The PCA explains the variances of a large dataset on inter-correlated variables with a smaller set of independent variables. Biplot circle is useful in interpreting the meaning of the axis. The main object of the PCA to determine the hidden factors responsible for the data structure when whole set of data set was considered. The PCA biplot axis 1 and 2 together 96.81% of variation in the physico - chemical parameters of the 12 sampling sites are consistently different in their characteristics. The parameters DO, pH, TDS, magnesium, turbidity, total hardness, alkalinity, chloride, phosphate, electrical conductivity, BOD, COD and calcium which is positively associated with physico- chemical parameters. The gradient was negatively

associated with sulphate and nitrate. The study indicated that the lake polluted which poses a great danger to aquatic life, people using it for domestic purposes and other activities. This might be due to improper disposal of sewage, surface runoff and wastewater from different activities. The water is thus not suitable for human activity without physico-chemical treatment. Hence, there is a urgent need for public awareness on the state of lake water and proper treatment is required before discharge of sewage and effluent into the Bellandur lake and its catchment area.

V. REFERENCES

- [1]. Altaf Hussain, Abdul Qayyum Khan Sulehria, Muhammad Ejaz and Asma Maqbool; Assessment of water quality of a flood plain reservoir for the development of aquaculture in Pakistan; *Biologia(Pakistan)*, 2014, 1-9.
- [2]. Gayathri. S, Latha. N. and Ramachandra Moha. M ; Impact of climate change on water quality of Shoolkere Lake, Bangalore; *JAIR*; Volume 2, Issue 6, November 2013, pp-362-368.
- [3]. Jacinto Elias Sedeno-Diaz and Eugenia Lopez-Lopez; *Water Quality in the Lerma, Mexico*; Springer; 2007, pp-1797-1812.
- [4]. Ibrahim Mohamed. Faridah Othman, Adriana I. N. Ibrahim. M.E. Alaa-Eldin and Rossita M. Yunus; Assessment of water quality parameters for Klang River basin, Malaysia; Springer; 2015, 4182, pp-1-12.
- [5]. Yared Kassahun Kebede and Tesfu Kebedee ; Application of principal component analysis in surface water quality monitoring, Ethiopia; 2012, pp-83-100. www.intechopen.com
- [6]. Nirmal Kumar Jangala Isaiah, Basil George, Rita Nirmal Kumar, Sajish Poliyaparambil Ravi and Shailendra Viyol ; An assessment of physico-chemical characteristics of Narmada Estuary, Gujarat; *Ekologia*; Volume 31, 2012, pp-65-74
- [7]. Ftsun Gebreyohannes, Abraha Gebrekidan, Amanual Hadera and Samuael Estifanos; Investigations of Physico-Chemical Parameters and its pollution implications of Elala River, Ethiopia; *MEJS*, V7(2) , 2015, pp-240-257
- [8]. Salim Aijaz Bhat, Gowhar Meraj, Sayar Yaseen and Ashok K. Pandit ; Statistical assessment of water quality parameters for pollution source identification in sukhnag stream, Kashmir, Himalaya; *Journal of Ecosystems*, 2014, pp-1-18
- [9]. Rodrigues-Filho, Gatti-Junior, Medeiros, Degani, Blanco, Faria, Campanelli, Soares, Sidagis-Galli, Teixeira-Silva, Tundisi, , Matsmura-Tundisi, and Tundisi ; Spatial patterns of water quality in Xingu River Basin, Amazonia; *Braz. J. Biol*, Volume 75, 2015, pp-34-46



P₃O₄ Contents Present in The Soil, After Spraying the Distillery Spent Wash Obtained from Optimized Bio Methanation Process

Lalitha D¹, Ramesh N², Sathish Ns², Manju B³

¹*Department of Chemistry, Government Engineering College, KRPet-571426, Karnataka, India

²Department of Civil Engineering, Government Engineering College, KRPet-571426, Karnataka, India

³Department of Chemistry, Maharaja Institute of Technology, Mysore, Mandya Dist., Karnataka, India

ABSTRACT

Waste water obtained from the industries generally known as Spent wash it contains lots of organic beneficial contents varied with its range values but without treatment if we discard the same contents to outer environment leads to many environmental defects may arise among that neighbouring lands defects and fresh water resources defects, but stimulated substantial changes in waste water treatment to achieve the objectives were based primarily on aesthetic and environmental concerns. The P₃O₄ contents present in the spent wash will also leads hazardous affects, after treatment the same spent wash will act as a benefited resource as “PHOSPHOROUS(III)TETRAXIDE” for soil to enhance germination and soil fertility.

Index Terms— ETHONAL, Molasses, Spent wash, Anaerobic, Bio-methanation, Phosporous(3) tetraxide.

I. INTRODUCTION

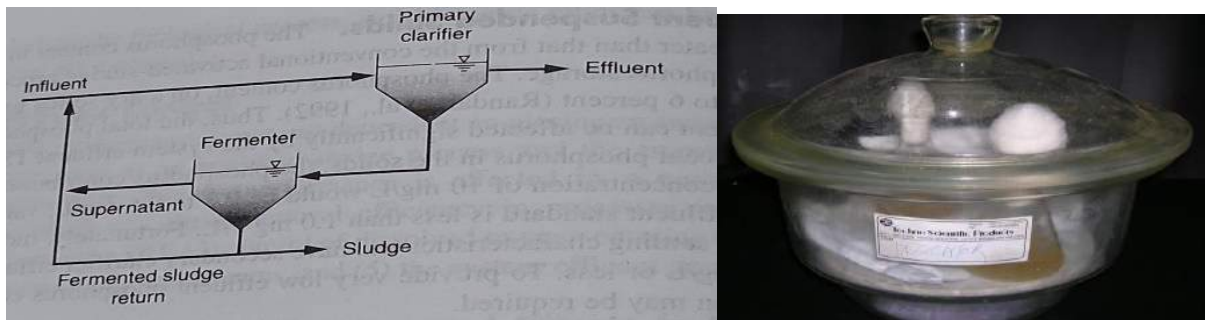
Spent wash is a rich source of organic contents and nutrients like nitrogen, sulphur, phosphorous, potassium and calcium, Industrial waste water even contains sufficient micronutrients like manganese, iron, zinc, copper, boron and molybdenum etc. in spent wash nutrients are highly rich and its acidity or alkalinity may also affect very largely so it may directly affects on the pH values as well as phosphorous contents present in the spent wash. Waste water obtained from the industries generally known as Spent wash it contains lots of organic beneficial contents varied with its range values but without treatment if we discard the same contents to outer environment leads to many environmental defects may arise among that neighbouring lands defects and fresh water resources defects, but stimulated substantial changes in waste water treatment to achieve the objectives were based primarily on aesthetic and environmental concerns. The P₃O₄ contents present in the spent wash will also leads hazardous affects, after treatment the same spent wash will act as a benefited resource as “PHOSPHOROUS(III)TETRAXIDE” for soil to enhance germination and soil fertility.

It is used for Bio-Gas generation (biomethanation), the techniques now used by distilleries for the treatment of distillery waste are biomethanation followed by 2 types (stage) biological treatment and discharge in fresh water

outlets with neutralization and also reduction or optimization of Phosphorous values and for use on land for irrigation purposes or for compositing with or without concentration,biomethanation and incineration. Certain drawbacks are also there in this method. Much energy in the form of methane gas will also be looses by this Process. This is also of national Importance. This type of work is an initiation to neutralize the waste water followed by pH study of the gained products through continues process and for Biomethanation for high TDS spent wash.

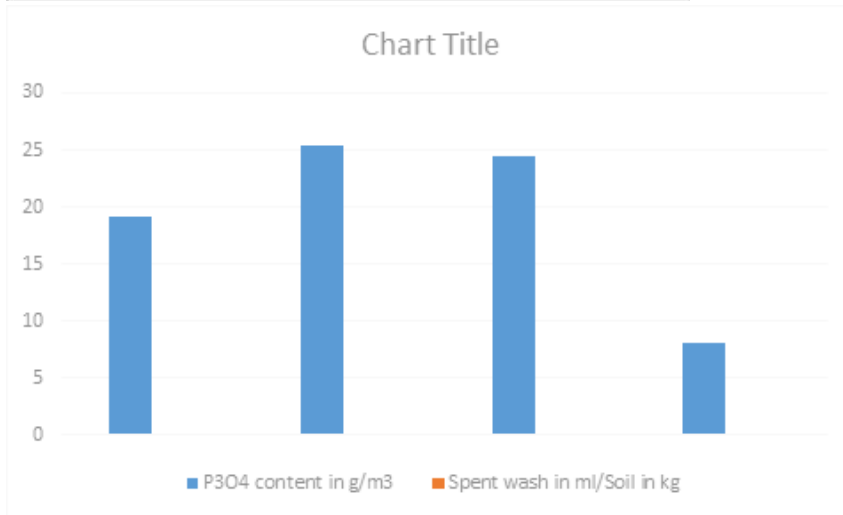
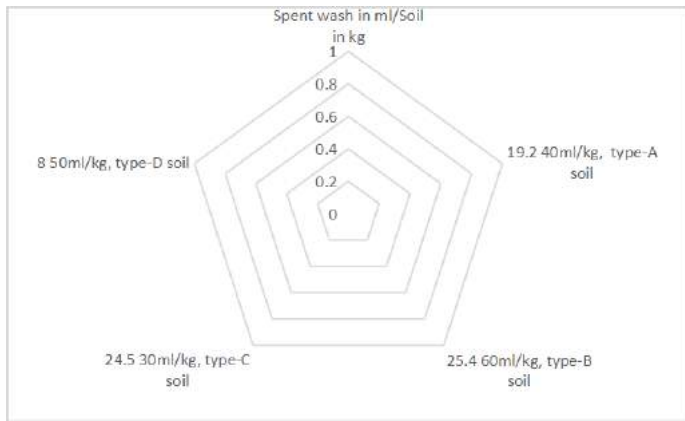
II. METHODOLOGY

BPR System is very specific and -site and also depends on the waste water characteristics and the plant process design and working, effluent phosphorous concentrations may exceed 1.0 to 2.0 mg per liter, but effluent concentrations below 0.5 / 1.0 mg per liter have been shown for high TDS spent wash, Depending upon the availability “ fermentation reactors for producing volatile fatty acids (VFAs) used for phosphorous removal” .Biological Phosphorous -Removal process are some what complex with many dependent interactions and comprehensive simulation methods(models) are very useful for evaluating biological Phosphorous and analysis.



Table

S.N	P ₃ O ₄ content in g/m ³	Spent wash in ml/Soil in kg	Result
1	19.2	40ml/kg, type-A soil	It is observed that depending upon the soil type P ₃ O ₄ is moderately available in all type.
2	25.4	60ml/kg, type-B soil	
3.	24.5	30ml/kg, type-C soil	
4.	8.0	50ml/kg, type-D soil	



III. RESULTS AND DISCUSSION

Based upon the obtained data result is interpreted as,

It is observed that depending upon the soil type, P_2O_4 is moderately available in all soil type. So after proper treatment spent wash is not much toxic to soil based on the above mentioned data and spent wash added in milliliter to soil type in kilogram. So fertility does not effecting much as the spent wash sprinkled on soil outlets in the type of press mud.

IV. CONCLUSION

Waste water obtained from sugar industries as spent wash can be used in dual beneficial mode as a biogas generator and also as fertilizer to sprinkle upon the mud especially for irrigation purposes so that enriches fertility and yield rate too.

V. REFERENCES

- [1]. © July 2021 | IJIRT | Volume 8 Issue 2 | ISSN: 2349-6002 IJIRT 152268 INTERNATIONAL JOURNAL OF INNOVATIVE RESEARCH IN TECHNOLOGY 926 ph Study in Optimization of Bio-Methanation Process of High TDS Spent Wash Obtained from Distillery LALITHA D1 , DR. N S SATHISHA2 , DR B MANJU2 , DR. B M KIRAN3
- [2]. ISSN: 2454-132X Impact Factor: 6.078 (Volume 7, Issue 4 - V7I4-1261) Available online at: <https://www.ijariit.com> Characteristic study in optimization of Biomethanation process for high TDS spent wash from Distilleries Lalitha Devaraju lalithadevaraju@yahoo.co.in Government Engineering College, K. R. Pete, Krishnarajpete, Karnataka Dr. Manju B. hodchemistry@mitmysore.in Maharaja Institute of Technology, Mysore, Karnataka Dr. Sathisha N. S. sathish.env@gmail.com Government Engineering College, K. R. Pete, Krishnarajpete, Karnataka Dr. Kiran B. M. kirangowda.82@gmail.com Adichunchanagiri Institute of Technology, Chikmagalur, Karnataka
- [3]. Smt.Lalitha D, Dr.N S Sathisha,Dr B Manju, Dr. B M Kiran. Optimization of biomethanation process for high TDS spent wash from distilleries IJSRR Volume 10 (2018).
- [4]. DISTILLERY WASTE WATER TREATMENT AND DISPOSALBY Lt Col Mantha Nagaraj*,Dr Arvind Kumar
- [5]. MethanEmissionbyGutSymbiontsofTe1mites1V.Gomathi,1K.Ramasamy,M .R.V.P.Red dy,1A.Ramalakshmiand1A.Ramanathan
- [6]. online resources.



K₂O Contents Present in The Soil, After Spraying the Distillery Spent Wash Obtained from Optimized Biomethanation Process

Lalitha D¹, Manju B², Ramesh N³, Sathish Ns³

¹*Department of Chemistry, Government Engineering College, KRPet-571426, Karnataka, India

²Department of Chemistry, Maharaja Institute of Technology, Mysore, Mandya Dist., Karnataka, India

³Department of Civil Engineering, Government Engineering College, KRPet-571426, Karnataka, India

ABSTRACT

Distillery Waste water obtained from the industries commonly named as Spent leese or Spent wash it contains lots of organic constituents but they varied with range of values but without treatment if we dispose the same constituents to outer space increases many environmental causes, it may lead to that agricultural lands toxifies and water resources also affects, but substantial stimulated changes in Spent wash treatment to effectively achieve the objectives which based on environmental concerns primarily on aesthetic. The K₂O contents present in the distillery spent wash will also leads toxic effects, after treatment the same waste water will act as a beneficiary resource as “ POTASSIUM OXIDE” for soil to enrich its germination capacity and also increases in soil fertility.

Index Terms— Alcohol, Molasses, Spentwash, Anaerobic, Biomethanation, Potassium oxide.

I. INTRODUCTION

Distillery waste is a enrich source of Nutrients and organic biodegradable contents like N₂,K,S,P,Ca etc.,Spent wash even contains much micro nutrients like Zn, Mn, B,Cu, Mb,Fe etc in this waste more than sufficient nutrients are available and its acidic or basic nature may also effect highly, so it may directly effects on the pH values as well as Potassium contents present in the industrial waste. Spent wash obtained from the distillery generally known as Distillery waste water and it contains heavy organic matters vary with its high range values, before treatment if it discarded to the surrounding environment creates many environmental problems among the neighbouring lands and outer water sources, but substantial stimulated changes in distillery spent wash treatment need to achieve the objectives, which were based upon first aesthetic and environmental pollutants concerns.The K₂O contents present in the distillery waste will also creates toxic affects, so after treatment the same waste water will act as a benefited resource as “ POTASH or Potassium oxide” for soil fertility.

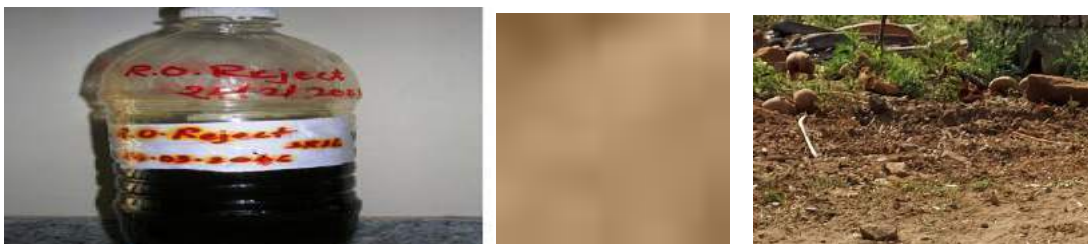
Distillery Waste water obtained from the industries commonly named as Spent leese or Spent wash it contains lots of organic constituents but they varied with range of values but without treatment if we dispose the same constituents to outer space increases many environmental causes, it may lead to that agricultural lands toxifies and water resources also affects, but substantial stimulated changes in Spent wash treatment to effectively achieve the objectives which based on environmental concerns primarily on aesthetic. The K_2O contents present in the distillery spent wash will also leads toxic effects, after treatment the same waste water will act as a beneficiary resource as "POTASSIUM OXIDE" for soil to enrich its germination capacity and also increases in soil fertility.

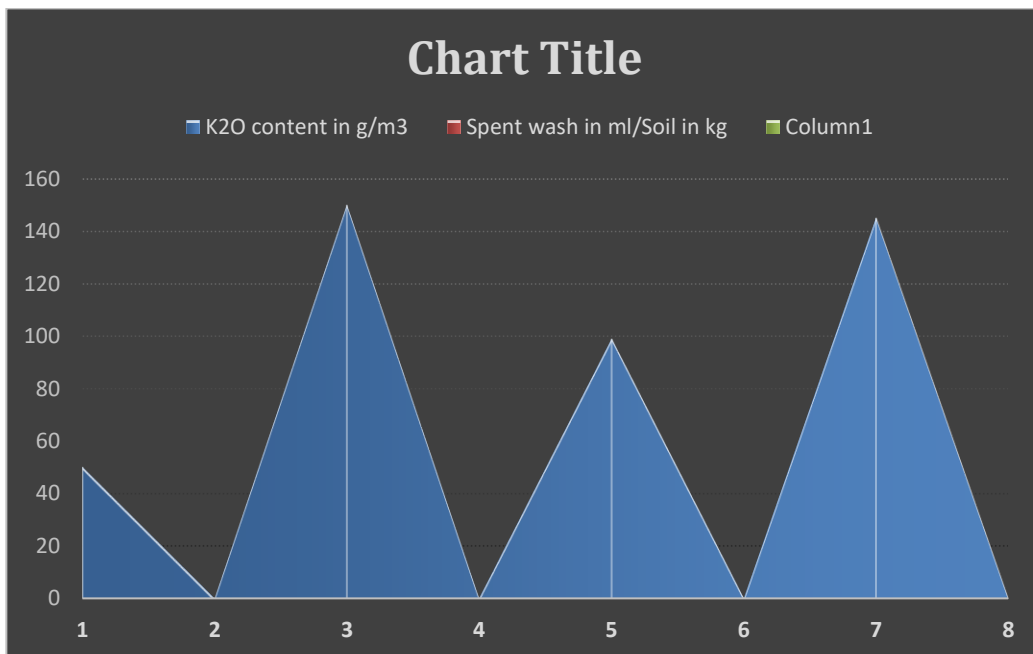
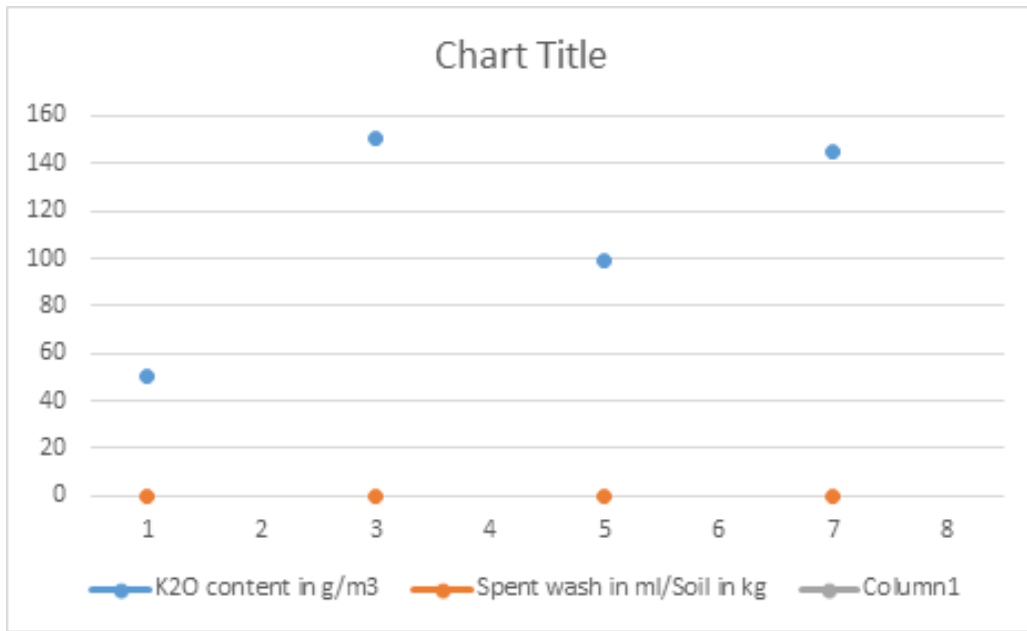
It is used for Biogas generation(Methanogenesis), and the method now used by industries for the treatment of Spent wash are Methanogenesis or biomethanation followed by 2 stage biological treatment and discharge in water resource outlets by neutralization and also suppression or optimization of Potassium values and use on irrigation land for Agricultural purposes and also for compositing without or with concentration, Methanogenic and incineration. Certain setbacks are also there in this method. Vast energy in the form of CH_4 gas will also be loses by this Method. This is also of national Prioritize task. So our work is an attempt and initiation to neutralize the SPent wash followed by pH study of the highly concentrated products through continues process and for Biomethanation for high TDS waste water.

II. METHODOLOGY

The Spent wash sample is collected from the Samson Distillery, Duggavathi, Davangere, Karnataka. In poly-carbonyl container the spent wash is collected and it is sealed thoroughly stored in $2-4^{\circ}C$ for further Analysis, And with Stander ed methods the chemical-physical parameters were identified. To check the soil quality soil sample was collected near the site at around 20-25 cm depth, air dried powdered, added spent wash in 30, 40, 50, 60 ml / kg depending upon the site sample and finally analyse d the K_2O present in that, the following results were obtained and tabulated and graphical representation also noted.

Spent wash before treatment Soil dried after addition of optimized bio methanated spent wash





Table

S.N	K ₂ O content in g/m ³	Spent wash in ml/Soil in kg	Result
1	50.26	40ml/kg, type-a soil	It is observed that depending upon the soil type K₂O content is moderately available in all type soil.
2	150.19	60ml/kg, type-b soil	
3.	99.1	30ml/kg, type-c soil	
4.	145.2	50ml/kg, type-d soil	

III. RESULTS AND DISCUSSION

Based upon the obtained data result is interpreted as,

It is observed that depending upon the soil type, K₂O is moderately available in all soil types. So after proper treatment Distillery spent wash is not much toxic to soil, instead it is a beneficial product like fertilizer, based on the above tabulated data and waste water added in 'ml' to soil type in 'kg'. The soil fertility rate is increasing as the spent wash sprinkled on soil outlets as in the type of press mud.

IV. CONCLUSION

Spent wash or Waste water obtained from distillery industries can be used as a beneficiary products like biogas production, steam utilization in boilers and also as fertilizer to sprinkle upon the soil especially for irrigation/agricultural purposes so that it enriches the fertility nature of soil and crops yield will also enhances.

V. REFERENCES

- [1]. © July 2021 | IJIRT | Volume 8 Issue 2 | ISSN: 2349-6002 IJIRT 152268 INTERNATIONAL JOURNAL OF INNOVATIVE RESEARCH IN TECHNOLOGY 926 ph Study in Optimization of Bio-Methanation Process of High TDS Spent Wash Obtained from Distillery LALITHA D1 , DR. N S SATHISHA2 , DR B MANJU2 , DR. B M KIRAN3
- [2]. ISSN: 2454-132X Impact Factor: 6.078 (Volume 7, Issue 4 - V7I4-1261) Available online at: <https://www.ijariit.com> Characteristic study in optimization of Biomethanation process for high TDS spent wash from Distilleries Lalitha Devaraju lalithadevaraju@yahoo.co.in Government Engineering College, K. R. Pete, Krishnarajpete, Karnataka Dr. Manju B. hodchemistry@mitmysore.in Maharaja Institute of Technology, Mysore, Karnataka Dr. Sathisha N. S. sathish.env@gmail.com Government Engineering College, K. R. Pete, Krishnarajpete, Karnataka Dr. Kiran B. M. kirangowda.82@gmail.com Adichunchanagiri Institute of Technology, Chikmagalur, Karnataka
- [3]. Smt.Lalitha D, Dr.N S Sathisha,Dr B Manju, Dr. B M Kiran. Optimization of biomethanation process for high TDS spent wash from distilleries IJSRR Volume 10 (2018).
- [4]. DISTILLERY WASTE WATER TREATMENT AND DISPOSALBY Lt Col Mantha Nagaraj*,Dr Arvind Kumar
- [5]. MethanEmissionbyGutSymbiontsofTe1mites1 V.Gomathi, 1K.Ramasamy, M R.V.P.Red dy,1A.Ramalakshmiand1A.Ramanathan



Fabrication and Characterization of Hybrid Fibers Thermoplastic Blend Composites

Lingesh B V^{1*}, B M Rudresh²

¹Department of Mechanical Engineering, Bangalore Institute of Technology, Bangalore -560004, Karnataka, India

^{2*}Department of Mechanical Engineering, Government Engineering College, K R Pet -571426, Karnataka, India

ABSTRACT

Polymer matrix composites (PMCs) can be found in almost every aspect of modern life, from consumer electronics to a wide variety of automotive accessories. Polymer matrix composites are materials made up of fibres that are embedded in an organic polymer matrix. These fibers are introduced to enhance selected properties of the polymer matrix composites. In the present investigation the composites were prepared by using basalt and glass fibers as reinforcements. The composite materials are thermoplastic blend of Polyamide 66 and polypropylene (Blend), glass fiber reinforced thermoplastic blend (Blend/SGF), basalt fiber reinforced thermoplastic blend (Blend/SBF) and hybrid fibers reinforced thermoplastic blend composites (BG hybrid). The composites and specimens were prepared by twin screw extrusion and injection molding technique.

The mechanical properties of hybrid composites such as tensile, flexure and impact strength were investigated using ASTM standards. The findings of the experiments demonstrated that hybrid fibers significantly improved the mechanical behavior of thermoplastic (PA66/PP) blend.

The BG hybrid composites exhibited 77.22 % increase in tensile strength, 109 % increase in flexural strength and 15.92 % reduction in elongation respectively. The hybrid fibers effect resulted in a significant increase in composite strength. The fibers and matrix synergistic effect contributed in improving mechanical behavior. Due to the brittle nature of the fibers, the impact strength of composites was lowered. Scanning electron microscopy (SEM) photos reveal the failure of composites due to fiber fracture, fiber pull out and fiber misalignment.

Keywords: Hybrid, Blend, SGF, SBF, SEM

I. INTRODUCTION

Many of our modern technologies necessitate materials with peculiar qualities that traditional metal alloys, ceramics, and polymeric materials cannot provide. This is especially true for materials that are needed for aerospace, underwater and transportation applications. For example, aviation engineers are increasingly looking for low-density structural materials that are robust, stiff, abrasion and impact resistant, and corrosion resistant.

This is a powerful combo of qualities. Strong materials are mostly thick; also, increasing strength or stiffness usually leads in a reduction in impact strength [1-4]

The development of composite materials has expanded material property combinations and ranges, and it continues to do so. In general, any multiphase material that exhibits a considerable fraction of the properties of both component phases, resulting in a better combination of properties, is deemed a composite. Better property combinations are fashioned by the appropriate combining of two or more separate elements, according to this principle of combined action. Many composites have property trade-offs as well.

In designing composite materials, scientists and engineers have ingeniously combined various metals, ceramics and polymers to produce a new generation of extraordinary materials. The majority of composites were developed to improve a combination of mechanical properties like stiffness, toughness and ambient and high-temperature strength.

The most important composites in terms of technology are those in which the dispersed phase is in the shape of a fibre. High strength and/or stiffness on a weight basis are frequently design goals for fiber-reinforced composites [5-7]. Specific strength and specific modulus parameters are used to express these properties, which correspond to the ratios of tensile strength to specific gravity and modulus of elasticity to specific gravity respectively. Low-density fibre and matrix materials have been used to create fiber-reinforced composites with extremely high specific strengths and moduli. [8]. Composite material performance and properties depend on the properties of individual components, mixture proportions and their inter-facial compatibility. The composite materials primarily consist of two constituents, one of which is the reinforcement material that could be treated with chemicals for surface modification [9] in order to improve binding and handling properties. The second component is the matrix which serves to protect the reinforcement material from environmental and external damage by transfer of the load [10]. Dan-mallam et al studied mechanical properties of hybrid fibers (kenaf/polyethylene terephthalate) reinforced polyoxymethylene hybrid composite. The hybrid composite samples showed increases in the modulus and strength [11].

II. MATERIALS, COMPOSITION, PROCESSING AND TESTING OF COMPOSITES

The materials used for the fabrication and development of composites are shown in the table 1. The compositions for the preparation of composites are selected as per the data shown in the table 2.

TABLE I MATERIALS USED IN THE FABRICATION PROCESS

Material	Designation	Size (μm)	Density (g/cc)
Polyamide 66	PA66	----	1.14
Polypropylene	PP	----	0.9
Short glass fibers	SGF	10-20	2.54
Short basalt fibers	SBF	10-20	2.65

TABLE II FORMULATIONS OF COMPOSITES

Composition	Mt. ID	Wt.%			
		PA66	PP	SGF	SBF

Blend (PA66/PP)	Blend	80	20	--	--
Blend/glass fibers	Blend/ SGF	80	20	10	--
Blend/basalt fibers	Blend/SBF	80	20	--	10
Blend/glass/basalt fibers	BG Hybrid	80	20	10	10

A. Processing of fiber reinforced composites

The processing and fabrication of composite is carried out through melt mix method using twin screw extrusion equipment. The injection molding process is used to prepare the specimens as per ASTM standards. The following diagram explains the details of production process of composites [12].

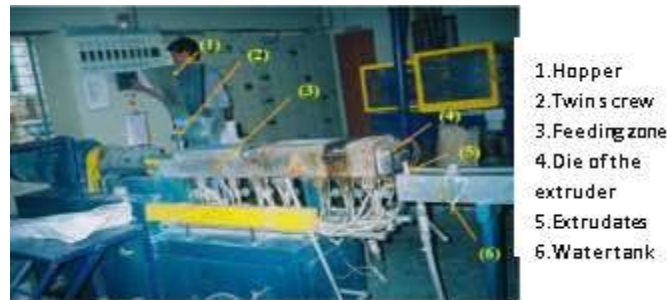


Fig. 1. Processing of composites

B. Testing of fiber reinforced composites

The mechanical properties such as tensile, flexural and impact test of fiber reinforced composites have been tested using universal testing machine (JJ Loyd) as per ASTM D638, D790 and D256 respectively [13].

III. RESULTS AND DISCUSSION

A. Tensile behavior of fiber reinforced composites

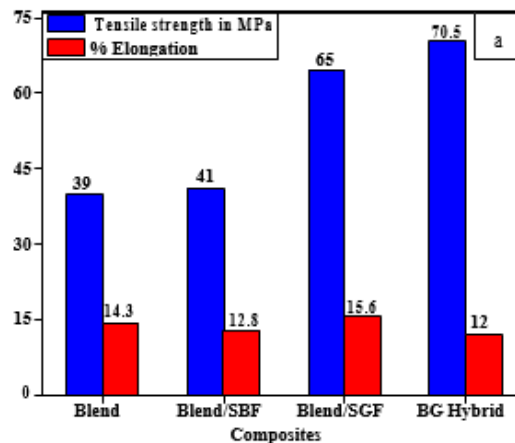


Fig. 2. Tensile behaviour of composites

The effect of fiber loading on tensile behaviour of thermoplastic blend based hybrid composites is shown in the figure 2. The tensile test of composites was carried out at room temperature as per ASTM D638 with a strain rate of 5 mm/min.

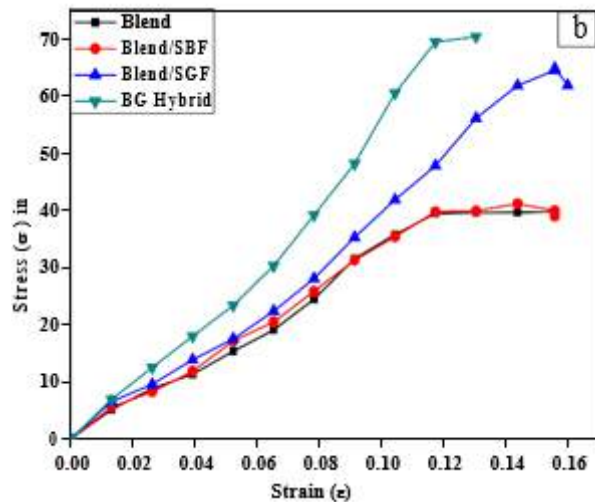


Fig. 3. Stress – Strain curve of composites

It is observed from the figure 2, that the tensile behavior of BG hybrid composites is a function of hybridization effect of fibers. The tensile strength of 39 MPa has been exhibited by the blend PA66/PP. The reinforcement of 10 wt. % SGF into the blend improved the tensile strength of Blend/SGF composites to 65 MPa which is observed that the effect of high modulus and good strength SGF improved the strength of BG hybrid composites. Further, the strength improvement is one of the contributions by the silane coupling agent which intensifies the bonding between the fibers and matrix. This behavior matches with the results of others work [16].

The effective mean length of fibers decreases during hybridization of fibers. The maximum interfacial shear strength is exhibited at fiber ends. The magnitude of shear stress has been found to be maximum at short basalt fiber ends because of high stiffness and good aspect ratio than short glass fibers. Therefore, as per stress transfer theory, the short basalt fiber ends exhibit the maximum shear stress. Hence, debonding starts at SBF ends which may be the initiation for development of cracks in composites. The strong network between SBF and SGF has been created and short glass fibers as an effect of hybridization, they act as crack arresters. This improves the strength of composites. Further, the 66.67% increase. This is due to the effect of high modulus SGF addition into the blend. The SGF has been coated with coupling agent silane which establishes the bond between the matrix and the surface of fibers. The geometry of fibers such as slenderness ratio, length, surface area and also the volume of fibers establishes the good compatibility between the thermoplastic matrix. The good stiffness and high specific strength of SGF, when reinforced into blend PA66/PP, the tensile strength of short glass fiber reinforced composites shoots to a very high level [14-15].

The slight increase in tensile strength over the blend has been observed by reinforcing 10 wt. % SBF into the blend. Blend/SBF composites exhibited the tensile strength of 41 MPa which is 5% increase over the blend. Basalt fiber is a low load carrying member but it can retain its strength at very high temperature. The basalt fibers are rich in potential fillers such as SiO₂, Alumina, and Fe₂O₃. These fillers have improved the brittle nature of Blend/SBF composites and deteriorated the matrix – fiber interface bonding. This is the main reason, why there is no substantial increase in the strength of Blend/SBF filled composites.

The hybridization effect of SGF and SBF significantly improved the tensile strength of BG hybrid composites. The BG hybrid composites exhibited the tensile strength of 70.5 MPa which is 81%, 72 % and 8 % increase over tensile strength of blend, basalt fiber filled and glass fiber filled composites. It has been silane compounds established the network for improving the strength of BG hybrid composites. The profile of silane molecule is: $R-(CH_2)_n-SiX_3$. This molecule creates bonding with fiber at one end while the other end establishes the bond with the matrix. Trihydroxysilane has been produced during the process of hydrolysis of silane compounds. Trihydroxysilane develops the covalent or hydrogen bond with hydroxyl groups on the surface of basalt fibers and glass fibers [17]. Hence, the hybridization effect of glass and basalt fibers improved the tensile strength of BG hybrid composites. The obtained results match with the work of researchers [15, 16].

The effect of fibers on percentage elongation of PA66/PP composites is depicted in figure 3. It is observed from the figure that the percentage elongation is a function of fiber reinforcement. Hybridization of fibers impaired the percentage elongation of hybrid composites. The blend PA66/PP had the least stress but highest strain. This is due to the ductile nature of PA66/PP blend. The ductile nature of blend improved the extension capacity of composites with less load carrying capacity. Similarly, the load bearing capacity of Blend/SGF composites is high due to strong and ductile nature of SGF fibers. But the load bearing capacity of SBF filled composites is slightly lesser and their elongation is also small when compared to Blend/SGF composites. But the hybridization effect of fibers decreased the elongation of composites by increasing the load bearing capacity. The BG hybrid composites exhibited the strain range from 0.01 to 0.015. The slight improvement in strain rate of BG composites is due to the presence of SGF in the BG hybrid composites. The effect of hybrid fibers improved the brittleness of composites and slight improvement in elongation has been exhibited by BG hybrid composites [14,15].

B. Flexural behavior of fiber reinforced composites

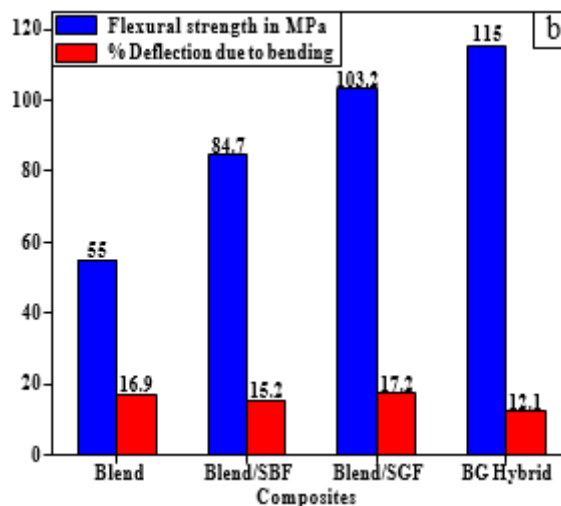


Fig. 4. Flexural behavior of composites

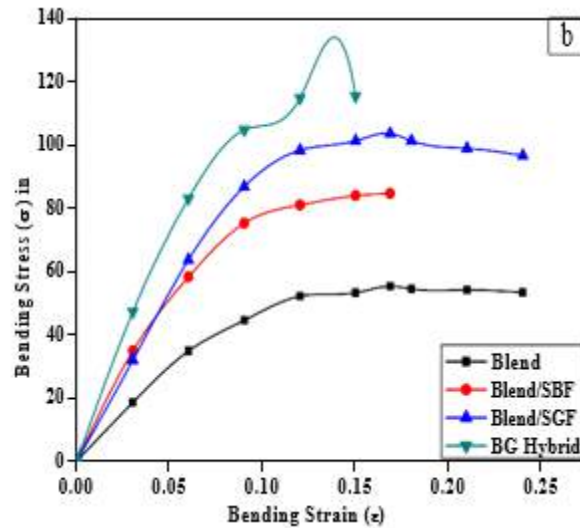


Fig. 5. Stress – Strain curve of composites

The flexural strength of the neat blend PA66/PP is 55 MPa. The reinforcement effect of 10 wt. % Blend/SBF composites exhibited the flexural strength of 84.7 MPa which is 54% increase over blend PA66/PP. This is the least value among the flexural strength of fiber filled composites. The degree of compatibility of SBFs with the matrix seemed to be poor. The filled compounds such as SiO₂, Alumina and Fe₂O₃ are rich in basalt fibers. The hard nature of these filled compounds deteriorates the flexural strength of Blend/SBF composites. The hard nature of these compounds results in the loss of ductility of composites. This made the composites to receive less bending load during performance of composites. The brittle nature of SBF, made the composite material to become brittle and hence there is no much increase in flexural strength. SBF has been recommended as a fiber for composites because of their retention strength at very high temperatures. Hence, they are potential supporters for thermal applications.

The addition of 10 wt. % SGF improved the flexural strength of Blend/SGF composites to 103.2 MPa which is 87.6% increase over blend. This is purely attributed to the silane coupling agent which establishes the good bonding between the matrix and fibers. The high modulus, high stiffness and good specific strength of SGF enabled the Blend/SGF composites to resist the load during bending. During bending, outer fibers are in tension and inner fibers were in compression. The intensity of shear strength of SGF has been decided by the amount coupling agent sized on the surface of glass fibers. Further, the ductile nature of Blend/SGF composites found to exhibit the good ductility and deflection of these composites further increases to receive more load [14].

It is found from the figure that the flexural The individual fibers and their hybridization effect on flexural properties of PA66/PP blend based hybrid composites are shown in figure 4. It is found from the figure that the hybridization of fibers has greatly developed the flexural behavior of composites. The hybridization effect of fibers is quite greater than effect of individual fibers on flexural behavior of hybrid composites. strength of BG hybrid composites has been improved due to the effect of hybridization of fibers. The flexural strength of BG hybrid composites is 115 MPa which is 109% increase blend. Further, the load bearing capacity of composites has been improved due to high modulus and good strength glass fibers [14]. The stiffness and aspect ratio of SBF is more than SGF. Therefore, shear stress is maximum at SBF ends according to stress transfer theory [18]. The

ends of SBF are therefore subjected to debonding first. The micro cracks as a result of debonding starts as a source of defects. The hybrid effect of both SGF and SBF arrested the cracks development due to hybridization effect. Therefore, the hybridization effect improved the flexural strength of BG hybrid composites. The decrease in length of short fibers to a very low value is due to shearing stresses which developed during polymer processing. The improved interfacial adhesion is due to the compensation of critical length of fibers. Therefore, the hybridization effect has improved the flexural strength of hybrid fibers filled composites.

It has been observed that the effect of fiber reinforcement decreased the percentage elongation due to deflection. The percentage deflection of blend PA66/PP exhibited the highest value due to absence of fibers. The blend exhibited the highest percentage deflection of 16.86. But the percentage of deflection due to bending of Blend/SGF composites was superior due to their higher modulus. But the effect of hybridization has reduced the percentage deflection.

The S – S behavior of fiber filled and BG hybrid composites is shown in the figure 5. The load bearing capacity of BG hybrid composites have been improved due to hybridization of fibers. But the strain of corresponding composites has been slightly decreased because of their brittle nature. The Blend/SGF composites exhibited the better strain rate due to ductile nature of composites. The load bearing capacity of blend PA66/PP is low when compared to fiber reinforced composites experiencing highest strain. But the BG hybrid composites had the better strain rate and also strength due to high strength and high modulus glass fibers.

C. Impact Behavior of fiber reinforced Composites

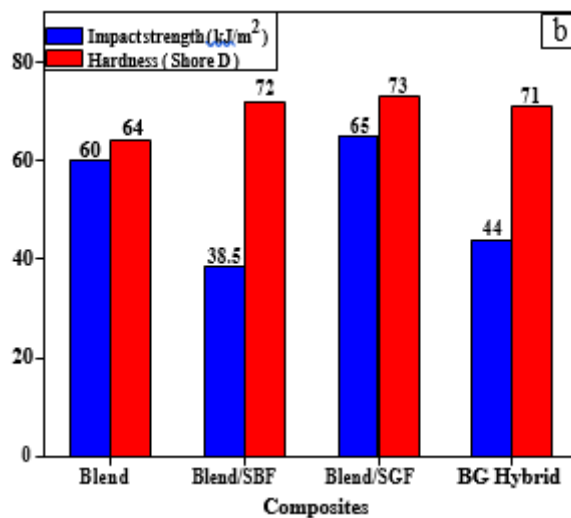


Fig. 6. Impact strength & Hardness of composites

The individual and hybrid fibers effect on hardness and impact strength of composites is shown in figure 6. It is found from the figure that the impact strength and hardness of hybrid composites is purely a function of composites composition.

The blend exhibited the impact strength of 60 kJ/m². The Blend/SGF composites exhibits the impact strength of 65 kJ/m², which is 8% more. Blend/SBF composites exhibited the impact strength of 38.5 kJ/m² against the blend which is 35.8% decrease. The impact strength of 44 kJ/m² has been exhibited by BG hybrid composites. But the effect of short glass fiber reinforcement influenced the impact strength of glass fiber reinforced

composites significantly. Among the composites studied, short glass fiber reinforced composites exhibited the highest impact strength. Basalt fibers effect improved the brittle nature of Blend/SBF composites. Inclusion of SBF leads to the creation of voids by introducing cracks. Hence, the impact strength reduces.

Unique observation has been noticed as result of reinforcement of fibers on the hardness (shore D) of composites. The increase in hardness of SBF and SGF reinforced composites has been observed due to the addition of fibers. But hybridization effect of fibers has been found to decrease the hardness slightly below the value of Blend/SGF composites. This is due to the fact that the hybridization of fibers results in overlapping of fibers, creation of voids, debonding of fibers and poor interfacial bond strength. This may reduce the hardness of polymer composites.

D. Fractography analysis of composites

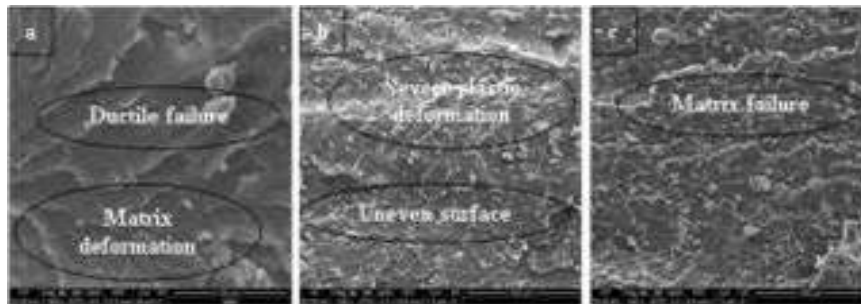


Fig. 7. SEM photographs of fractured surfaces of Blend Tensile (a) Flexure and (c) Impact test

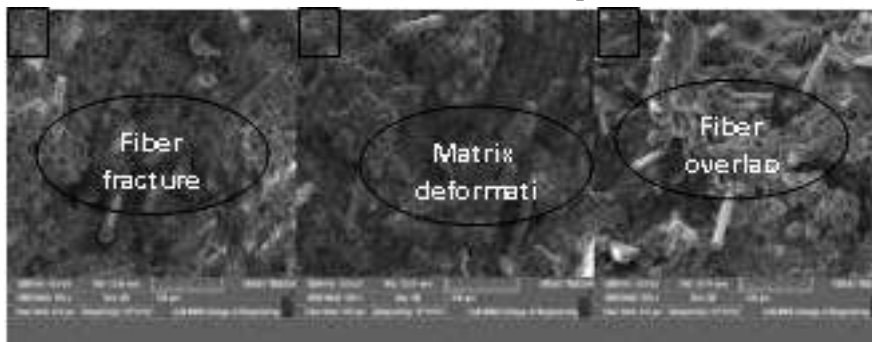


Fig. 8. SEM photographs of fractured surfaces of BG Hybrid Composites (a) Tensile (b) Flexure and (c) Impact test

The SEM image of fractured surface of tensile behavior of BG hybrid composites is depicted in the figure 8 (a). It has been revealed from the figure that the fiber pull out impressions are more along with the matrix deformation. The overlapping of fibers has been exhibited in the figure. The uneven surface is exhibited by the composites. The SEM image of flexural behavior of BG hybrid composites is shown in the figure 8 (b). It is observed from the figure that the fiber fracture is more common with matrix deformation. Fiber aggregates are collected at the surface which is clearly seen in the picture. The fiber pulled out impressions is clearly shown in the figure. The SEM image of impact fracture of BG hybrid composites is depicted in the figure 8 (c). It is exhibited by the figure that the fiber overlap and fiber pulled out mechanisms are common. The aggregates of

broken fibers are also seen in the figure. Further, the rough and brittle nature of composites has been witnessed by the SEM picture of BG hybrid composites.

IV. CONCLUSION

Following are the important facts drawn from the study.

- The tensile and flexural characteristics of fiber reinforced composites have been significantly improved by the addition of individual fibers of SGF and SBF. But the impact behavior of composites is slightly impaired.
- The effect of hybridization of fibers (Basalt and Glass) is very much effective in improving the tensile and flexural behavior of BG hybrid composites. But it has been found that the impact strength of hybrid composites found to be impaired due to the effect of hybrid fibers

V. REFERENCES

- [1]. Pickering KL, Efendy MGA, Le TM. A review of recent developments in natural fibre composites and their mechanical performance. *Compos A Appl Sci Manuf*. 2016;83:98–112.
- [2]. Budhe S, de Barros S, Banea M. Theoretical assessment of the elastic modulus of natural fiber-based intralaminar hybrid composites. *J Braz Soc Mech Sci Eng*. 2019;41(6):263.
- [3]. Rohit K, Dixit S. A review-future aspect of natural fiber reinforced composite. *Polym Renew Res*. 2016;7(2):43– 59.
- [4]. Pereira AL, Banea MD, Pereira AB. Effect of intralaminar hybridization on mode I fracture toughness of natural fiber-reinforced composites. *J Braz Soc Mech Sci Eng*. 2020. <https://doi.org/10.1007/s40430-020-02525-w>.
- [5]. De Araujo Alves Lima R, Kawasaki Cavalcanti D, de Souza e Silva Neto J, da Meneses Costa H, Banea MD. Effect of surface treatments on interfacial properties of natural intralaminar hybrid composites. *Polym Compos*. 2020;41(1):314–25.
- [6]. Pereira AL, Banea MD, Neto JS, Cavalcanti DK. Mechanical and thermal characterization of natural intralaminar hybrid composites based on sisal. *Polymers*. 2020;12(4):866.
- [7]. Cavalcanti D, Banea M, Neto J, Lima R, da Silva L, Carbas R. Mechanical characterization of intralaminar natural fibre-reinforced hybrid composites. *Compos B Eng*. 2019;175:107149.
- [8]. Andrews R and Weisenberger M C 2004 Carbon nanotube polymer composites. *Current Opinion Solid State and Materials Science* 8(1): 31–37
- [9]. Belgacem, M.N.; Gandini, A. The surface modification of cellulose fibres for use as reinforcing elements in composite materials. *Compos. Interfaces* 2005, 12, 41– 75. [CrossRef]
- [10]. Masuelli, M. *Fiber Reinforced Polymers: The Technology Applied for Concrete Repair*; Intech Open Limited: London, UK, 2013

- [11].Dan-mallam, Y.; Abdullah, M.Z.; Yusoff, P. Mechanical properties of recycled kenaf/polyethylene terephthalate (PET) fiber reinforced polyoxymethylene (POM) hybrid composite. *J. Appl. Polym. Sci.* 2014, 131.
- [12].B M Rudresh, ; B N Ravikumar.; Lingesh B V, Hybridization Effect on the Mechanical Behavior of Monophase Reinforced PA66/Teflon Blend Based Hybrid Thermoplastic Composites. *Transactions of the Indian Institute of Metals.* 2017,
- [13].BV Lingesh, BN Ravi Kumar, BM Rudresh, HN Reddappa, Hybridization effect of fibers on mechanical properties of PA66/PP blend-based thermoplastic composites, *Advanced Composites and Hybrid Materials*, 2018
- [14].B V Lingesh, B N Ravikumar, B M Rudresh, Mechanical Characterization of Hybrid Thermoplastic Composites of Short Carbon Fibers and PA66/PP, *Indian J. Adv. Chem. Sci*, 2016.
- [15].B M Rudresh, B N Ravi Kumar, B V Lingesh, Hybridization Effect on the Mechanical Behavior of Monophase Reinforced PA66/Teflon Blend Based Hybrid Thermoplastic Composites, 2017
- [16].B M Rudresh, B N Ravi Kumar, B V Lingesh, Fibrization effect on the mechanical behavior of PA66/PTFE blend based fibrous composites, 2017
- [17].Y. A. Ei-Shekeil, S. M. Sapuan, K. Abdan and E. S. Zainudin, Influence of fiber content on the mechanical and thermal properties of kenaf fiber reinforced thermoplastic polyurethane composites, *Materials and design.* 40, (2012), 299-303
- [18].Sultan Ozturk, The effect of fiber content on the mechanical properties of hemp and basalt fiber reinforced phenol formaldehyde composites, *J. Mater. Sci.*, 40(17), (2005), 4585-4592



Effect of Aerobic Exercises on Selected Motor Fitness Variables Among School Level Soccer Players

Dr. Kanthraj S

Physical Education Director, CBR National College of Law, Shivamogga, Karnataka, India

ABSTRACT

The purpose of the study was to investigate the effect of aerobic exercises on selected motor fitness variables among school level soccer . To achieve the purpose of this study, thirty college level football players were randomly selected as a subjects from shivamogga, Karnataka. boys age between 15 and 17 years. True randomized experimental group design has been employed with two groups, namely aerobic exercises group and control group with 15 subjects each. Group I participated the training for a period of six weeks and no training were given to the control group. Speed was measured by 40 yard dash, agility was measured by “T” agility run test and explosive strength was measured by standing broad jump. The two groups were statistically analyzed by using analysis of covariance (ANCOVA). The result of the study reveals that there was a significant improvement in the experimental groups on selected variables when compared to the control group after the completion of six weeks of aerobic exercises program.

Keywords: Aerobic Training, School Boys, Motor fitness, Soccer.

I. INTRODUCTION

The word Aerobic literally means “with oxygen or in the presence of oxygen”. Aerobic exercises are any activity that uses large muscle groups can be maintained continuously for long period of time and is rhythmic in nature. Aerobic activity trains the heart, lungs and cardiovascular system to process and deliver oxygen more quickly and efficiently to every part of the body. As the heart muscle becomes stronger and more efficient (Wolach and Harold, 2000). Aerobic exercise is a moderate intensity workout that extends over a certain period of time and uses oxygen in this process. Well, in the present times, carrying out aerobics has become the most happening workout trend among the youth. Not only is performing aerobic exercise interesting, but also is very beneficial for health. There are various types of aerobic exercise. In general, aerobic exercise is one performed at a low to moderate level of intensity over a long period of time (Gillette and Elseman, 1987). Basic motor abilities and skills are of crucial importance in the early phases of the motor learning process (Ackerman, 1998). The basis of motor learning is a specific motor program, which is created by the motor cortex based on external and internal information. Fundamental movement skills are common

motor activities with specific observable patterns. Most skills used in sports and movement activities are their advanced versions. From a phylogenetic point of view, fundamental movement skills represent a cultural heritage enabling a purposeful and effective evaluation of human abilities and skills. The expansion of specialized motor skills is popular today, especially when it comes to sport-specific motor skills. Therefore, kinesiological scientific investigations are aimed at defining the quality and quantity of any knowledge on the performance level, primarily in the case of children and the young, while focusing primarily on the relationship between the process of motor learning and a learner's age (Carroll and Bandura, 1987).

Performing aerobics helps in maintaining all round fitness and also turns out to be a delightful experience while playing soccer. In this modern era soccer is played worldwide with entertainment. Nowadays school girls are participating in sports and games not only for the sake of fitness but also for exposure. Aerobics is a activity which can be performed with interest. To find out whether the aerobic exercises training has a positive outcome on selected motor fitness variables the investigator formulated the study to find the solution.

II. METHODOLOGY

The purpose of the study was to investigate the effect of aerobic exercises on selected motor fitness variables among college soccer girls. To achieve the purpose of this study, thirty college level football players were randomly selected as a subjects from Shivamogga, boys age between 15 and 17 years. The investigator selected the following variables for the present investigation.

TABLE - I

S.NO.	VARIABLES	TEST ITEMS	UNITS
1	Speed	40 Yard Dash	In Seconds
2	Agility	"T" Agility Run	In Seconds
3	Explosive Strength	Standing Broad Jump	In Metres

True randomized experimental group design has been employed with two groups, namely aerobic exercises group and control group with 15 subjects each. Group I participated the training for a period of six weeks and no training were given to the control group. The two groups were statistically analyzed by using analysis of covariance (ANCOVA). (Rothstein,1985).

III. RESULTS AND DISCUSSION

The detailed procedure of analysis of data and interpretation were given below,

Table-II Summary of Descriptive Statistics on Selected Motor Fitness Variables among School Level Soccer Players (Boys)

Sl.No	Variables	AEG					CG				
		Pre	SD (\pm)	Post	SD (\pm)	Adjusted Mean	Pre	SD (\pm)	Post	SD (\pm)	Adjusted Mean

1	Speed	6.54	0.39	5.94	0.31	5.94	6.54	0.24	6.53	0.22	6.53
2	Agility	11.26	0.20	10.35	0.40	10.35	11.19	0.54	11.15	0.58	11.16
3	Explosive Strength	1.67	0.11	1.77	0.04	1.76	1.64	0.10	1.65	0.09	1.65

AEG – Aerobic Exercise Group

CG - Control Group

The table II shows that the pre and post test means and standard deviation of two groups on selected motor fitness variables among school level soccer players (Boys)

Table – III Analysis of Variance of Pre Test Scores on Selected Motor Fitness Variables among School Level Soccer Players (Boys)

Sl. No	Variables	Source of Variance	Sum of Squares	Df	Mean Squares	F- Value
1	Speed	BG	0.000	1	0.000	0.003
		WG	3.03	28	0.10	
2	Agility	BG	0.03	1	0.03	0.22
		WG	4.74	28	0.16	
3	Explosive Strength	BG	0.006	1	0.006	0.51
		WG	0.32	28	0.01	

* P < 0.05 Table F, df (1,28) (0.05) = 4.19

In table III, the results of analysis of variance of pre test scores on speed (0.003), agility (0.22) and explosive power (0.51) were lesser than the table value of 4.19 indicating that it was not significant for the degrees of freedom (1,28) at 0.05 level of confidence indicating that the random sampling was successful.

Table-IV Analysis of Variance of Post Test Scores on School Level Soccer Players (Boys) Selected Motor Fitness Variables among

Sl. No	Variables	Source of Variance	Sum of Squares	Df	Mean Squares	F-Value
1	Speed	BG	2.58	1	2.58	34.24*
		WG	2.11	28	0.07	
2	Agility	BG	4.79	1	4.79	18.72*
		WG	7.16	28	0.25	
3	Explosive Strength	BG	0.11	1	0.11	19.02*
		WG	0.16	28	0.006	

* P < 0.05 Table F, df (1,28) (0.05) = 4.19

In table IV, the results of analysis of variance of post test scores on speed (34.24), agility (18.72) and explosive power (19.02) were greater than the table value of 4.19 indicating that it was not significant for the degrees of freedom (1,28) at 0.05 level of confidence.

Table-V Analysis of Covariance of Adjusted post test scores on Selected Motor Fitness Variables among School Level Soccer Players (Boys)

Sl. No	Variables	Source of Variance	Sum of Squares	df	Mean Squares	F-Value
1	Speed	BG	2.59	1	2.59	35.12*
		WG	1.99	27	0.07	
2	Agility	BG	4.83	1	4.83	18.32*
		WG	7.12	27	0.26	
3	Explosive Strength	BG	0.09	1	0.09	22.39*
		WG	0.10	27	0.004	

* $P < 0.05$ Table F, $df(1,27)$ (0.05) = 4.21

In table V, the results of analysis of covariance of adjusted post test scores on speed (35.12), agility (18.32) and explosive power (22.39) were greater than the table value of 4.21 indicating that it was not significant for the degrees of freedom (1,27) at 0.05 level of confidence.

Figure-I Shows the Mean Values of Control Group on Selected Motor Fitness Variables among College Soccer Girls

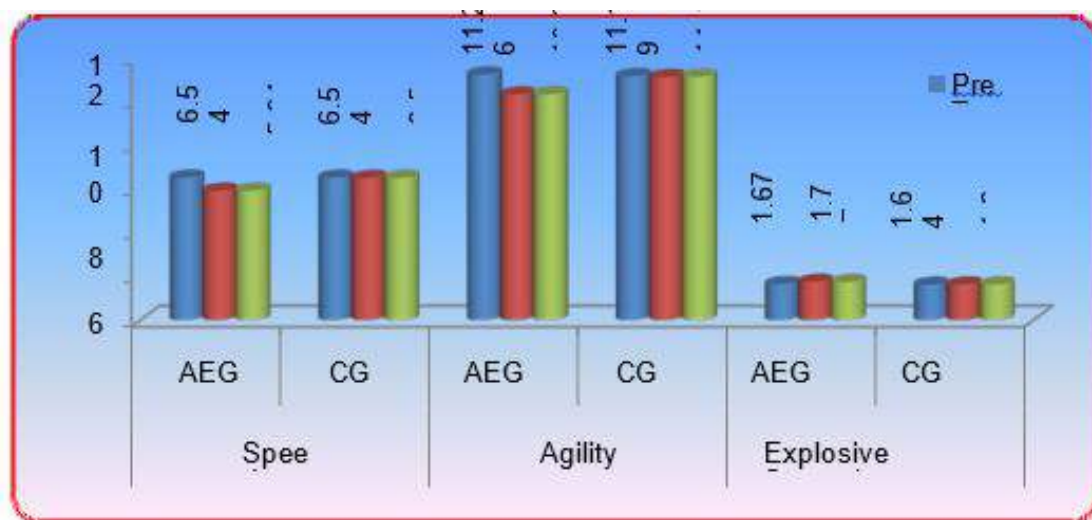


Figure-I Shows the Mean Values of Control Group on Selected Motor Fitness Variables among College Soccer Girls

IV. CONCLUSIONS

In the light of the study undertaken with certain limitations imposed by the experimental conditions, the following conclusions were drawn. The result of the study reveals that there was a significant improvement in the experimental groups on selected variables when compared to the control group after the completion of six weeks of aerobic exercises programme. This type of aerobic exercises can be incorporated in the training programme for college soccer girls.

V. REFERENCES

- [1]. Ackerman, L., Tzetzis, G., Mantis. (1998). Determinants of individual differences during skill acquisition: cognitive abilities and information processing. *Journal of Experimental Psychology*, 117, 288-318.
- [2]. Barrow, H.M., Mc. Gee. M. and Kathleen A. Tritschler (1989). *Practical measurements in Physical Education and Sports*, Philadelphia: lea Fibiger.
- [3]. Barry, L. Johnson, L. Barry and Jack K. Nelson, (1982). *Practical Measurement for Evaluation in Physical Education*, New Jersey; Englewood Cliffs Prentice Hall, Inc.
- [4]. Carroll, W. R., & Bandura, A. (1987). Translating condition into action: The role of visual guidance in observational learning. *Journal of Motor Behavior*, 19,385-398.
- [5]. Gillette ,P,A., and Elseman,P,A.(1987). The effect of intensity controlled aerobic dance exercise aerobic on capacity of middle aged, over weightwomen. *Res NursHealth.*;10(6):383-90.
- [6]. Wolach,M,B., and Harold M,M.(2000) Effect of aerobic and anaerobic exercise on the phagocytic in old trained female. *Journal of women and health*, Vol.50(77):639-51.
- [7]. Anne, L. Rothstein. (1985). *Research Design and Statistics for Physical Education*: Englewood Cliffs, N.J: Prentice Hall, Inc.



Effect of Muscle Relaxation Training on Competitive Anxiety of School Level Boys Foot Ball Players

Srinivasa Murthy

Assistant Director, Physical Education and Sports, Government Engineering College Krishnarajapete, Mandya, Karnataka, India

ABSTRACT

The present study investigated the effect of psychological skill training techniques such as progressive muscle relaxation on competitive anxiety. The three sub-scales of competitive anxiety were also examined; cognitive anxiety, somatic anxiety, and state self-confidence. The study consisted of 24 School level Foot Ball players from Mandya District Karnataka, their age ranged from 14 to 16 years. The competitive state anxiety inventory-2 (CSAI-2) also developed by martens, vealey, and Burton (1990) were used. Subjects were randomly assigned to either a relaxation training experimental group, or a no relaxation training control group. Both the experimental groups were given training for 3 days a week and for 6 weeks in total. Paired t-test was used to test the effect of treatment groups individually between pre and post-test of all the groups on variables used in the present study. The result of the study reveals that there was significant difference in 0.05 levels of competitive anxiety among the School level Foot Ball players Foot Ballplayers.

Keywords: Relaxation Training, Competitive Anxiety.

I. INTRODUCTION

The present study is mainly concerned with foot ball players who participated in the high level competitions. Now days, the game foot ball is becoming a professional sport rather than the competitive sport. So the competitiveness among the foot ball players is growing up day by day with different color. Reason for such competitiveness is arise naturally among the players, because of pressures such as equal competition, concern about fulfilling the expectation of their teachers, coaches, parents and peer group and personal needs. It leads to mental and physical stress. In high level stress, the player's are unable to show their real effort in matches though they are having the needed physical and mental resources. Hence the physical education teachers and coaches are in need to study the means and methods needed to face such competitive pressures whereby they can equip their players to perform well. As far as means and methods for high performance in sports are concerned, they are varied with the nature and type of competition such as low level competition and high level competition. In high level competition, sport is demanding high level mental toughness. Mental toughness of player can be strengthened only through the implication of internal and external pressures

whereby they can easily face the competition pressures and to show their talents in time. Having this thirst, the investigator has impelled to study.

II. PARTICIPANTS

The purpose of the study was to find out the effect of progressive muscle relaxation training on competitive anxiety of male Inter-collegiate foot ball players. To achieve the purpose of the study twenty-four boys football players were selected from State level tournaments. Their age was ranged from 14 to 16 years. The purpose of the present study was explained to them clearly where by their consent to serve as samples were obtained. The present study is an experimental one and to test the effects of varied forms of intervening strategies, the care was taken in distributing the samples to each experimental group. For this, the selected samples (N=24) were divided into two equal groups. Group I was considered as progressive relaxation training group (PRTG) in which they underwent progressive muscle relaxation practices. Group II was considered as control group and they did not undergo any practices. Both the experimental groups were given training for 3 days a week and for 6 weeks in total.

Selection of variables Anxiety Related

- Cognitive anxiety.
- Somatic anxiety.
- Self-confidence.

Tools Used in the Study Competitive Sport Anxiety

Competitive state anxiety was assessed by using the competitive state anxiety inventory-2 (CSAI-2, Martens et al. 1990) which is a self-report, psychometric state anxiety inventory. Consisting of 27 items. The CSAI-2 normally takes less than five minutes to complete and was administered ten minutes before competition and practice session. Before allowing subjects to begin complete the CSAI-2, instruction was explained, and researchers ensured that all instruction was completely understood. State anxiety was measured by the competition state anxiety inventory-2. (CSAI-2) Martens et al 1990). The CSAI-2 assesses two components of state anxiety, cognitive worry and somatic anxiety and related constructs self-confidence. The CSAI-2 contains 9 items that reference each sub-scale. Thus, each sub-scale has range from 9 to 36. Higher scores on cognitive and somatic anxiety indicate higher level of anxiety whereas higher scores on self-confidence sub-scale correspond to higher level self-confidence (Martens et al 1990 and McKay et al. 1997)

Tester Competency and Reliability of Tests

To ensure that the investigator was well versed with the techniques of conducting the tests, the investigator had a number of practice sessions in testing procedure, the reliability of the data was established through test and retest method. Tester reliability was established by t-test process whereby consistencies of results were obtained by product moment correlation. The data collected from a randomly selected sample of ten subjects in test was correlated with the data taken by the expert and coefficient of correlation thus obtained is presented in Table I. Since very high correlations from .806 to .897 were obtained for the variables, the

competency of the tester to administer the test was accepted. The interclass correlation coefficient obtained from selected criterion variables were presented in Table.1

Table I Intra-class correlation co-efficient values on selected criterion variables

Sl. No	CRITERION VARIABLES	COEFFICIENT OF CORRELATIONS
1	Cognitive anxiety	.897
2	Somatic anxiety	.860
3	Self confidence	.806

III. TRAINING PROGRAMME

Psychological Skills Training Provided to the Foot Ball Players

Psychological skill training involved meeting with the football team to provide the psychological skills training. The psychological skill training sessions were conducted once a week. The sessions lasted between 30 and 60 minutes and they were audio taped for foot ballplayers who were unable to attend. At the conclusion of a session, the foot ball players received a handout de- scribing the activities completed during that session. Additional copies of the handouts were available to foot ball players who were unable to attend. The meetings were not requiring. Rather, the foot ball players were free to choose whether or not to participate in the psychological skill training program.

Progressive Relaxation Training

The football players were comfortable with the breathing technique. This activity involved a programmatic relaxation technique called developed by Jacobson (1926, 1976). Jacobson's technique, called progressive relaxation, involves the systematic tension and relaxation of muscle groups. A football player is asked to inhale and tense a specific muscle group for approximately five seconds. The foot ball player then exhales and releases the tension from the specified muscle group, concentrating on the feelings of relaxation, this procedure is repeated for a number of muscle groups with each group begin tensed and relaxed three times. The muscles groups used with the foot ball team are listed.

The Muscle Groups Used In the Progressive Relaxation Exercise

- Muscle Group1:** right hand and fingers (make a fist)
- Muscle Group2:** right forearm
- Muscle Group3:** right upper arm
- Muscle Group4:** left hand and fingers (make a fist)
- Muscle Group5:** left forearm
- Muscle Group6:** left upper arm
- Muscle Group7:** head and face
- Muscle Group8:** shoulders
- Muscle Group9:** chest

- Muscle Group10:** stomach and abdomen
MuscleGroup11: right upper leg
Muscle Group12: right lower leg
Muscle Group13: right foot and toes
Muscle Group14 :left upper leg
Muscle Group15:left lower leg
Muscle Group16 :left foot and toes.

IV. STATISTICAL TECHNIQUES

The following statistical techniques were used to find out the effect of progressive relaxation training on competitive anxiety of school level foot ball players. Paired t-test was used to test the effect of treatment groups individually between pre and post tests of all the groups on variables used on the present study. As one of the objectives of present study was to test the effects of progressive muscle relaxation training on competitive anxiety, the initial test means and final test means were tested treatment wise by using the paired sample t-test. The obtained 't' ratio's of progressive relaxation training were postulated in the following **table II**.

Table II. Significance of mean gains/losses between pre and post test of progressive relaxation training (PRTG) on competitive anxiety of foot ballplayers

Variables	Pre-test mean	Post-test mean	Mean diff.	Standard error mean	't'-ratio
Cognitive anxiety	21.50	20.08	1.42	.148	9.53*
Somatic anxiety	22.08	20.50	1.58	.148	10.60*
Self confidence	21.25	22.75	-1.50	.151	9.95*

*significance at 0.05 level

Table II indicates that the obtained' ratios were 9.53 for cognitive anxiety, 10.65 for somatic anxiety, 9.95 for self-confidence. The obtained' ratios on competitive anxiety. When compared with the critical value of 2.201 for degrees of freedom of 1,112 it was found that the mean gains and mean losses statistically significant. Resulting of these confirm that six-week practice of progressive relaxation training produced a significant improvement in cognitive anxiety (1.42; $p < 0.05$), somatic anxiety (1.58; $p < 0.05$), self-confidence (-1.50; $p < 0.05$), statistically significant and explained its effect positively.

V. CONCLUSIONS

1. The purpose of the present study was to examine if progressive muscle relaxation decreased competitive anxiety, and if so, which of the three sub-scales: cognitive anxiety, somatic anxiety, and self-confidence were most affected by the training. The only statistically significant effects found between the

- experimental group and the control group occurred on the cognitive anxiety, somatic anxiety and self-confidence sub-scale of competitive anxiety.
2. The competitive anxiety of the subjects was tested first producing no statistically significant effects between the experimental and control group. Although, previous research suggests that various relaxation training techniques, including progressive muscle relaxation, decrease full-scale competitive a-state anxiety (Bethany and Forrest, 1998), the results of the present study did not confirm these observations.
 3. The competitive state anxiety inventory (CSAI-2) (Martens, Veale, and Burton, 1990) produced no statistical significance for the overall a-state anxiety levels between the relaxation training experimental group (group 1) and the no training control group (group 2). However, the mean scores of trait and state for group I exhibited a greater decrease from competitive anxiety.
 4. The competitive state anxiety inventory (CSAI-2) (Martens, Vealey, and Burton, 1990) produced no statistical significance for the overall a-state anxiety levels between the relaxation training experimental group (group 1) and the no training control group (group 2). However, the mean scores of trait and state for group I exhibited a greater decrease from competitive anxiety

VI. REFERENCES

- [1]. Anshel, m., & porter, A. (1996). Self-regulatory characteristics of competitive swimmers as a function of skill level and gender. *Journal of sport behavior*, 1 2), 91.
- [2]. Bethany, L., & Forrest, S. (1998). Effect of self- administered visual-motor behavioral rehearsal on sport performance of collegiate athletes. *Journal of sport behavior*, 21(2),206.
- [3]. Broucek, M., & Bartholomew, J. (1993). The effects of relaxation with a warning cue on pain and tolerance.-*journal of sport behavior*, 16(4), 239.
- [4]. Fisher, C., & Zwart, E. (1982). Psychological analysis of athletes' anxiety responses. *Journal of sport psychology*, 4.139-158.
- [5]. Jacobson, E., (1938). *Progressive relaxation*. Chicago, IL: University of Chicago.



Publisher

Technoscience Academy

Website : www.technoscienceacademy.com

Email: info@technoscienceacademy.com

**International Conference on
Recent Trends In Mechanical
Engineering
(ICRTIME-2022)**

Organized By

Department of Mechanical Engineering,
Government Engineering College, K R Pet – 571426,
Mandya District, Karnataka, India

Email: editor@ijsrset.com Website : <http://ijsrset.com>